Advances in Intelligent Systems and Computing 215

Fuchun Sun
Dewen Hu
Huaping Liu *Editors*

Foundations and Practical Applications of Cognitive Systems and Information Processing

Proceedings of the First International Conference on Cognitive Systems and Information Processing, Beijing, China, Dec 2012 (CSIP2012)

Springer

Advances in Intelligent Systems and Computing

Volume 215

Series Editor

J. Kacprzyk, Warsaw, Poland

For further volumes:
http://www.springer.com/series/11156

Fuchun Sun · Dewen Hu · Huaping Liu
Editors

Foundations and Practical Applications of Cognitive Systems and Information Processing

Proceedings of the First International Conference on Cognitive Systems and Information Processing, Beijing, China, Dec 2012 (CSIP2012)

Springer

Editors
Fuchun Sun
Huaping Liu
Department of Computer Science and Technology
Tsinghua University
Beijing
People's Republic of China

Dewen Hu
College of Mechatronics and Automation
National University of Defense Technology
Changsha
People's Republic of China

ISSN 2194-5357 ISSN 2194-5365 (electronic)
ISBN 978-3-642-37834-8 ISBN 978-3-642-37835-5 (eBook)
DOI 10.1007/978-3-642-37835-5
Springer Heidelberg New York Dordrecht London

Library of Congress Control Number: 2013947347

Printed on acid-free paper

Springer is part of Springer Science+Business Media (www.springer.com)

Preface

This book is part of the Proceedings of the Seventh International Conference on Intelligent Systems and Knowledge Engineering (ISKE2012) and the First International Conference on Cognitive Systems and Information Processing (CSIP2012) held in Beijing, China, during December 15–17, 2012. ISKE is a prestigious annual conference on Intelligent Systems and Knowledge Engineering with the past events held in Shanghai (2006, 2011), Chengdu (2007), Xiamen (2008), Hasselt, Belgium (2009), and Hangzhou (2010). Over the past few years, ISKE has matured into a well-established series of International Conferences on Intelligent Systems and Knowledge Engineering and related fields over the world. CSIP2012 is the first conference sponsored by Tsinghua University and Science China Press, and technically sponsored by IEEE Computational Intelligence Society, Chinese Association for Artificial Intelligence. The aim of this conference is to bring together experts from different expertise areas to discuss the state-of-the-art in cognitive systems and advanced information processing, and to present new research results and perspectives on future development. Both ISKE2012 and CSIP2012 provide academic forums for the participants to disseminate their new research findings and discuss emerging areas of research. It also creates a stimulating environment for the participants to interact and exchange information on future challenges and opportunities of intelligent and cognitive science research and applications.

ISKE2012 and CSIP2012 received 406 submissions in total from about 20 countries (United States of America, Singapore, Russian Federation, Saudi Arabia, Spain, Sudan, Sweden, Tunisia, United Kingdom, Portugal, Norway, Korea, Japan, Germany, Finland, France, China, Argentina, Australia, and Belgium). Based on rigorous reviews by the Program Committee members and reviewers, among 186 papers contributed to CSIP2012, high-quality papers were selected for publication in the proceedings with the acceptance rate of 40.9 %. The papers were organized in 25 cohesive sections covering all major topics of intelligent and cognitive science and applications. In addition to the contributed papers, the technical program includes four plenary speeches by Jennie Si (Arizona State University, USA), Wei Li (California State University, USA), Chin-Teng Lin (National Chiao Tung University, Taiwan, China), and Guoqing Chen (Tsinghua University, China).

As organizers of both conferences, we are grateful to Tsinghua University, Science in China Press, Chinese Academy of Sciences for their sponsorship, grateful to IEEE Computational Intelligence Society, Chinese Association for Artificial Intelligence, State Key Laboratory on Complex Electronic System Simulation, Science and Technology on Integrated Information System Laboratory, Southwest Jiaotong University, University of Technology, Sydney, for their technical co-sponsorship.

We would also like to thank the members of the Advisory Committee for their guidance, the members of the International Program Committee and additional reviewers for reviewing the papers, and members of the Publications Committee for checking the accepted papers in a short period of time. Particularly, we are grateful to thank the publisher, Springer, for publishing the proceedings in the prestigious series of Advances in Intelligent Systems and Computing. Meanwhile, we wish to express our heartfelt appreciation to the plenary speakers, special session organizers, session chairs, and student volunteers. In addition, there are still many colleagues, associates, and friends who helped us in immeasurable ways. We are also grateful to them all. Last but not the least, we are thankful to all authors and participants for their great contributions that made ISKE2012 and CSIP2012 successful.

December 2012

Fuchun Sun
Dewen Hu
Huaping Liu

Organizing Committee

General Chairs:	Bo Zhang, Tsinghua University, China Yen Gray, Oklahoma State University, USA
Honorary Chairs:	Jiaguang Sun, China Deyi Li, China
Advisory Committee Chairs:	Nanning Zheng, China Wei Li, China Sam Shuzhi Ge, National University of Singapore
Steering Committee Chairs:	Chin-Teng Lin, Taiwan, China Zongben Xu, China
Organizing Committee Chairs:	Zengguang Hou, China Xiaorong Gao, China Huaping Liu, China
Program Chairs:	Fuchun Sun, China Jenni Si, USA Dewen Hu, China
Plenary Sessions Chair:	Derong Liu, Chicago, USA
Sessions Chairs:	Haibo He, USA Fei Song, China
Publications Chairs:	Dianhui Wang, Australia Guangbin Huang, Singapore
Publicity Chair:	Jun Zhu, China
Finance Chair:	Hongbo Li, China
Registration Chairs:	Jianmin Li, China Caixia Chen, China
Local Arrangements Chairs:	Huaping Liu, China Linmi Tao, China
Electronic Review Chair:	Xiaolin Hu, China

Advisory Committee

Advisory Committee Chairs

Nanning Zheng	President of Xi'an Jiaotong University, Member of Chinese Academy of Engineering, China
Wei Li	Previous president of Beijing University of Aeronautics and Astronautics, Member of Chinese Academy of Sciences, China
Sam Shuzhi Ge	Vice President of IEEE Control System Society, National University of Singapore, IEEE Fellow

Members

Tianyou Chai	Member of the Chinese Academy of Engineering, Northeastern University, China
Aike Guo	Member of the Chinese Academy of Science, Chinese Academy of Sciences,China
Okyay Kaynak	Bogazici University, Turkey
Yanda Li	Member of Chinese Academy of Science, Tsinghua University, China
Shoujue Wang	Member of Chinese Academy of Sciences, Chinese Academy of Sciences, China
Donald Wunsch II	Missouri University of Science and Technology, USA
Xin Yao	IEEE Fellow, University of Birmingham, UK
Lei Xu	The Chinese University of Hong Kong, Hong Kong
Jacek M. Zurada	IEEE Fellow, University of Louisville, USA
Shangkai Gao	IEEE Fellow, Tsinghua University, China
Lin Chen	Member of Chinese Academy of Engineering, Chinese Academy of Science, China

Steering Committee

Steering Committee Chairs

Chin-Teng Lin	Deputy President of National Chiao Tung University, Taiwan, China
Zongben Xu	Vice President of Xi'an Jiaotong University, Member of Chinese Academy of Science, China

Members

Guangren Duan	Harbin Institute of Technology, China
Jinde Cao	Southeast University, China
Wen Yu	National Polytechnic Institute, Mexico
Aiguo Song	Southeast University, China
Cong Wang	South China University of Technology, China
Jianwei Zhang	Hamburg University, Germany
Zhigang Zeng	Huazhong University of Science and Technology, China

Sponsors

Tsinghua University

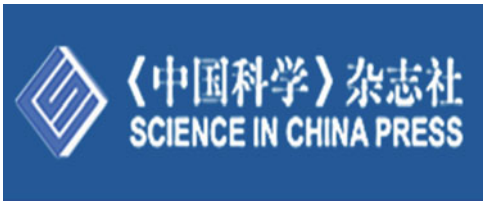

Science in China Press

Chinese Academy of Sciences

Institute of Electrical and Electronics Engineers

Contents

Effects of Stimulus Views on Mental Rotation of Hands: An Event-Related Potential Study

Xiaogang Chen, Guangyu Bin and Xiaorong Gao

Abstract Mental rotation of hands, which is subject to biomechanical constrains, involves participants engaging in motor imagery processing. To contribute to a better understanding of the process of hand mental rotation, reaction times and event-related potential were measured while participants were performing a left–right hand recognition task. Participants apparently solved the task by imagining their own hands rotating to the orientation of the stimulus for comparison. In line with previous studies, the behavioral results showed that slower reaction times were found for the hand views that could not be easily reached with real movement. More importantly, the event-related potential results revealed that the amplitude of rotation-related negativity (RRN) decreased with the difficulty of the hand views increasing. The previous results are complemented by this study; it is stimulus views that modulate reaction times and the amplitude of RRN during mental rotation task of hands.

Keywords Biomechanical constrain · Mental rotation · Motor imagery · Event-related potential

1 Introduction

Mental rotation is a well-known paradigm used to study the cognitive process of mentally rotating objects. It was first observed by Shepard and Metzler in 1971 when participants were shown pairs of three-dimensional block drawings at

X. Chen · G. Bin · X. Gao (✉)
Department of Biomedical Engineering, School of Medicine, Tsinghua University, Beijing 100084, China
e-mail: gxr-dea@tsinghua.edu.cn

G. Bin
The College of Life Science and Bio-Engineering, Beijing University of Technology, Beijing 100124, China

F. Sun et al. (eds.), *Foundations and Practical Applications of Cognitive Systems and Information Processing*, Advances in Intelligent Systems and Computing 215,
DOI: 10.1007/978-3-642-37835-5_1,

different orientations and required to distinguish whether both drawings were presented as the same or the mirrored image version [1]. Results showed that the reaction times (RTs) increased with increasing angles of rotation. At the psychological level, this effect saliently explained that the image is mentally rotated to align it with its upright position. Since their discovery, mental rotation has been widely investigated [2–6]. The mental rotation paradigm has been extensively applied not only for rotation of 3-D cubes but also for letters, numbers, hands, and feet pictures [7, 8].

The investigation of hand mental rotation is classically performed by judgment of hand laterality. In such mental rotation tasks, participants tend to use a set of mental transformations of their own hands in order to closely match the stimulus. The reaction times for judging hand laterality also increased with increasing angle of rotated stimulus from its vertical position. Furthermore, hand mental rotation is sensitive to proprioceptive constraints, leading to longer reaction times for stimulus depicting anatomically difficult postures. These reaction times profiles were interpreted as evidence of kinesthetic limitations on movement imposed by the biomechanical constrains of the muscles and joints [9]. These constrains led to the postulation that participants utilized an embodied cognitive processing, which was classically referred to as motor imagery.

With the development of functional brain imaging methods such as positron emission tomography (PET) and functional magnetic resonance imaging (fMRI), a number of neuroimaging studies have been conducted to illustrate brain regions involved in mental rotation tasks [10–12]. Kosslyn et al. measured the regional cerebral blood flow (rCBF) while participants were performing mental rotation of Shepard–Metzler's drawings and hands. For the Shepard–Metzler type of stimuli, increased rCBF was observed in the parietal lobe and Area 19. In contrast, for mental rotation task of hands, there was significantly greater rCBF in the precentral gyrus, superior and inferior parietal lobes, primary visual cortex, insula, and frontal Areas 6 and 9. The authors claimed that at least two different mechanisms were involved in mental rotation, one for objects like hands related to motor preparation processes and another for objects like Shepard–Metzler's drawings that did not [13]. A recent fMRI study compared activation regions while participants performed mental rotation task of hands and tools. In addition to replicating classic activation regions in mental rotation of hands and tools (bilateral superior parietal lobes and visual extrastriate cortex), there was an important difference in premotor area activation. Pairs of hands engendered bilateral premotor activation while tools only activated the left premotor cortex. The authors concluded that participants might simulate moving objects with their hands [14]. Results of PET and fMRI indicated that mental rotation was correlated with activity in parietal, occipital, frontal regions, as well as primary motor cortex, and the supplementary motor region of the precentral sulcus [15–17]. The involvement of the motor cortex in mental rotation task of hands is also supported by evidence from transcranial magnetic stimulation (TMS) studies. Pelgrims et al. found Brodmann area 4 (BA4) virtual lesions selectively increased reaction times in the left–right hand recognition task while leaving the mental rotation task of letters

unaffected. The authors suggested that BA4 contribution to mental rotation task of hands [18]. Activation in motor-related cortical areas implied that motor imagery was being applied during hand mental rotation task, indicating that motor structures might play an important role in supporting the mental rotation task of hands.

In contrast to neuroimaging techniques such as PET and fMRI, electroencephalography (EEG) has exquisite temporal resolution that make it possible to measure the timing and order of activity of brain regions during the unfolding of mental rotation task. Electrophysiological studies by event-related potential (ERP) showed that the mental rotation tasks elicited a modulated positive component approximately between 300 and 700 ms after stimulus presentation located at parietal region. This component was known as rotation-related negativity. The amplitude of this component was inversely related to the rotation angle and becomes more negative with increasing angles of rotation [19, 20]. Wijers et al. suggested that the gradual decrease of the positivity was caused by a modulation of a slow negativity that would be understood as a direct electrophysiological correlate of the mental rotation process [21]. This notion was extensively validated in various studies, suggesting that the ERP effect observed during mental rotation was highly specific to the process of mental rotation itself.

In this study we employed a hand mental rotation task similar to that used in the upper limb amputees' study by Nico et al. on the basis that there was a close similarity in brain activity between mental rotation of a movement and its real counterpart. Participants were presented with left–right hands at four different views and were asked to perform left–right hand recognition task. Previous studies have focused on the effect of rotational angle in general. To our knowledge, this is the first study investigating view effect on mental rotation of hands. If the mental rotation of hands relied on a first person perspective, we expect that it will be also more sensitive to the stimulus view. Accordingly, for more awkward stimulus view, we expect longer reaction times and more negative ERP component in the mental rotation task of hands.

2 Materials and Methods

2.1 Participants and Stimuli

Fourteen healthy participants (seven males) aged between 19 and 26 years [mean ± standard deviation (SD): 24.3 ± 1.93 years] took part in this experiment. All participants were right-handed, had normal or corrected to normal vision and had no history of psychiatric or neurological disorders. All participants signed an informed consent prior to the experiment and were paid for their participation.

Participants sat approximately 60 cm away from a 19-inch CRT monitor. Stimuli were black and white line drawings of both left and right hands presented from different views (thumb, back, palm, and pinkie side). Each of the eight hands

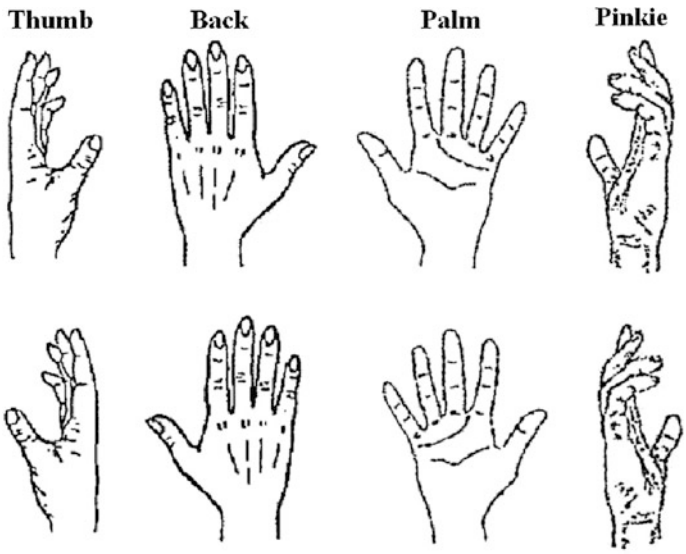

Fig. 1 The stimuli used in the hand rotation task

was rotated clockwise in a step of 30° (12 rotations), which produced a total of 96 pictures (Fig. 1). The pictures were displayed randomly at the center of the screen on a background, which created an approximate 8° viewing angle. The stimulus presentation was managed by a computer program (VC++) written by the authors.

2.2 Procedure

Participants sat comfortably in a sound attenuated and electrically shielded EEG room. They were instructed to rest their right index and ring fingers on the left and right arrow of the keyboard, representing the left and right hand, respectively. Participants were asked to respond as quickly and accurately as possible, with a motor imagery strategy on how to solve the task, and not to be too cautious in their response. The experiment began with a practice phase to familiarize participants with the procedure. When the accuracy rate reached 75 %, the practice phase was ended. During the formal test phase, participants were instructed to respond by the fingers alone, without any hand, arm, or wrist movement. Furthermore, they were told to keep their eyes fixated on the central area of the screen while keeping their hands on their laps and out of sight, avoiding eye blinking and any sort of movement. After finishing one block, each participant was asked whether the motor imagery strategy was used or not.

The experiment was separated into three blocks of 96 trials. Each trial began with a green fixation cross lasting for 1,500 ms at the central area of the screen.

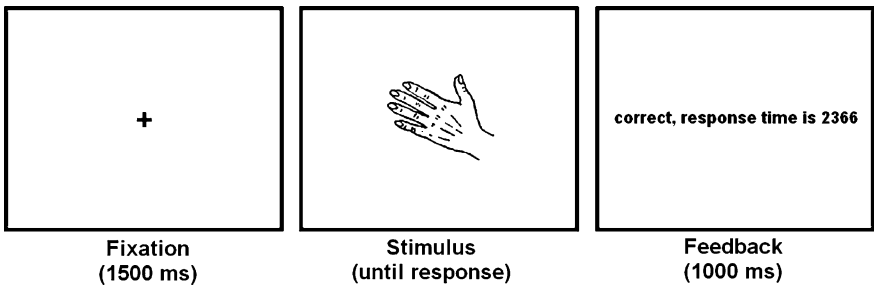

Fig. 2 Sequence of events within one trial in the mental rotation paradigm

Subsequently, the stimulus was displayed and did not disappear until the participant made a response. Then feedback on their performance of the participants were shown and lasted for 1,000 ms in the center of the screen, including the reaction time and whether the stimulus was correctly sorted (Fig. 2). At the end of each block, the accuracy rate and reaction time were presented to give participants insight into their progress.

2.3 Data Acquisition

For behavioral data acquisition, reaction times were defined as the period during which the stimulus appeared on the screen and the onset of the participant's response. Corresponding information regarding the participant's response was automatically recorded by appropriate software.

EEG data were recorded continuously using SynAmps2 amplifiers and Scan 4.3 software (Compumedics Neuroscan, EI Paso, TX, USA) with a 64-channel ElectroCap according to the international 10–20 system. EEG data were referenced online to a point midway between Cz and CPz and grounded midway between Fz and FPz. Electrode impedances were kept below 10 kohm. The horizontal electrooculogram (EOG) was recorded from electrodes placed next to the outer canthi of each eye. For the vertical EOG, electrodes were placed at the supraorbital and infraorbital regions of the left eye. Data were digitally amplified and collected at a sampling rate of 1,000 Hz.

2.4 Data Analysis

Reaction times and accuracy rates were analyzed to ensure that the participants used the motor imagery strategy in the procedure of the task. If they did, it would be expected that more time was taken for difficult hand views [22]. Reaction times and accuracy rates were calculated in separate analyses of variance (ANOVA)

with factor view (thumb, back, palm, and pinkie side). Errors and trials with RTs shorter than 200 ms or longer than 3 standard deviations from the mean were removed before analysis of reaction times and left out from the EEG analyses; 7.9 % data were eliminated for all participants in this task. The Greenhouse–Geisser correction was applied if the data did not conform to the sphericity assumption by Mauchly's Test of Sphericity. Whenever a main effect reached significance, pairwise comparisons were conducted by using Bonferroni adjustments for multiple comparisons. The alpha level was set at 0.05.

Raw EEG data were bandpass filtered between the frequency ranges from 0.5 to 40 Hz (24 dB/octave) and digitally re-referenced to the average of the left and right mastoids. Ocular artifacts were corrected using a linear regression procedure [23]. The continuous EEG was segmented subsequently into epochs of −200 to +1000 ms relative to the stimulus onset. Then, the prestimulus baseline of 200 ms was performed for baseline correction. Epochs with amplitude above ±100 μV were rejected (0.9 % of the whole trials). Then epochs were averaged separately for each of the four conditions.

In the present study, there was no statistically significant difference between left- and right-hand stimuli, thus these data were pooled for further study. The view effect was studied by analyzing mean amplitude measures in the 400–550 ms time window, spanning the RRN component, selected according to visual inspection of grand average ERP waveforms. A 4 × 6 × 3 repeated-measures ANOVA was performed on the mean amplitudes at 18 electrodes (F3, Fz, F4, FC3, FCz, FC4, C3, Cz, C4, CP3, CPz, CP4, P3, Pz, P4, PO3, POz, and PO4), tasking as factors view (thumb, back, palm, and pinkie), region (frontal, fronto-central, central, central-parietal, parietal, and occipito-parietal), and laterality (left, middle, and right). Statistical analyses were carried out by the same way described for behavioral data.

To investigate the relationship between reaction times and RRN amplitudes, we conducted a linear regression analysis. Two-tailed Pearson correlation was implemented to compare the resulting regression slope coefficients across participants.

3 Results

3.1 Behavioral Data

All participants engaged in the mental rotation task of hands, with a mean accuracy of 94.37 %. A one-way ANOVA on accuracy was conducted and a marginal main effect of view was observed [mean ± standard error of the mean (SEM); $F(3,39) = 3.23$, $P = 0.07$]. Pairwise comparisons revealed significant mean differences between the palm and pinkie condition ($P < 0.01$). In contrast to accuracy, reaction times revealed a significant effect of view [mean ± SEM; $F(3,39) = 14.27$, $P < 0.01$; thumb, 1462 ± 134 ms; back, 1508 ± 126 ms; palm,

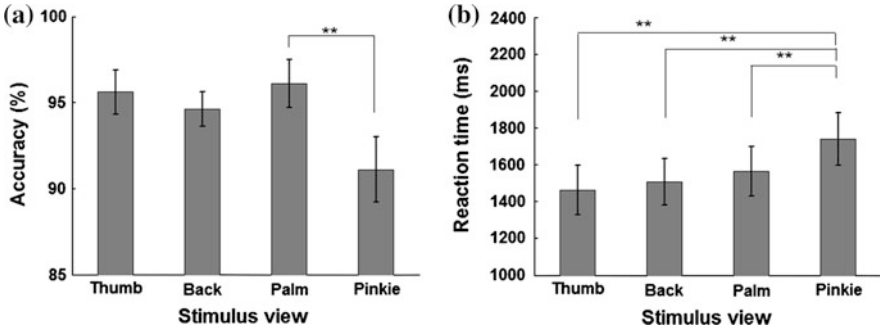

Fig. 3 **a** Accuracy and **b** reaction times as a function of stimulus viewpoint. The sign "**" indicates significance $P < 0.01$. Error bars represent standard error of the mean

1563 ± 135 ms; pinkie, 1740 ± 143 ms]. Pairwise planned comparisons confirmed that hands presented in pinkie-side views took significantly longer RTs than those presented in more usual perspectives, such as thumb, back, or palm views (all $P < 0.01$), but there were no differences among thumb, back, and palm views, as shown in Fig. 3.

3.2 ERP Data

Figure 4 shows the grand average ERP for each view at Fz, FCz, Cz, CPz, and Pz sites. As can be seen in Fig. 4, the rotation-related negativity component becomes more negative for stimuli depicting hands in unnatural views. That is, views difficult to reach with a real movement. Figure 5 shows the mean amplitude in the 400–550 ms time window as a function of stimulus view at Fz, FCz, Cz, CPz, Pz, and POz sites. The plots show again that response to pinkie-side views are more negative than the others views. Voltage maps in Fig. 6 show the spatial distribution of the view effect over all electrodes at the scalp surface in the 400–550 ms time window. These topographic maps show that the greatest mean amplitude was found at the CPz site.

The statistical analysis performed on the average ERP amplitude from 400 to 550 ms supports these observations. Three-way repeated-measures ANOVA showed that a significant main effect of view [mean ± SEM; $F(3,39) = 8.79$, $P < 0.01$; thumb, 1.01 ± 0.17 μV; back, 1.10 ± 0.13 μV; palm, 1.10 ± 0.14 μV; pinkie, 0.83 ± 0.15 μV]. Pairwise planned comparisons revealed that pinkie-side views were distinctly different from back and palm views (all $P < 0.01$) and marginally different between pinkie-side views and thumb views ($P = 0.09$). Specially, the amplitude decreased with increasingly awkward/uncomfortable views. There were also significant effects of region [mean ± SEM; $F(5,65) = 5.24$, $P < 0.05$], laterality [mean ± SEM; $F(2,26) = 4.53$, $P < 0.05$], and region × laterality [mean ± SEM; $F(10,130) = 3.55$, $P < 0.01$], indicating

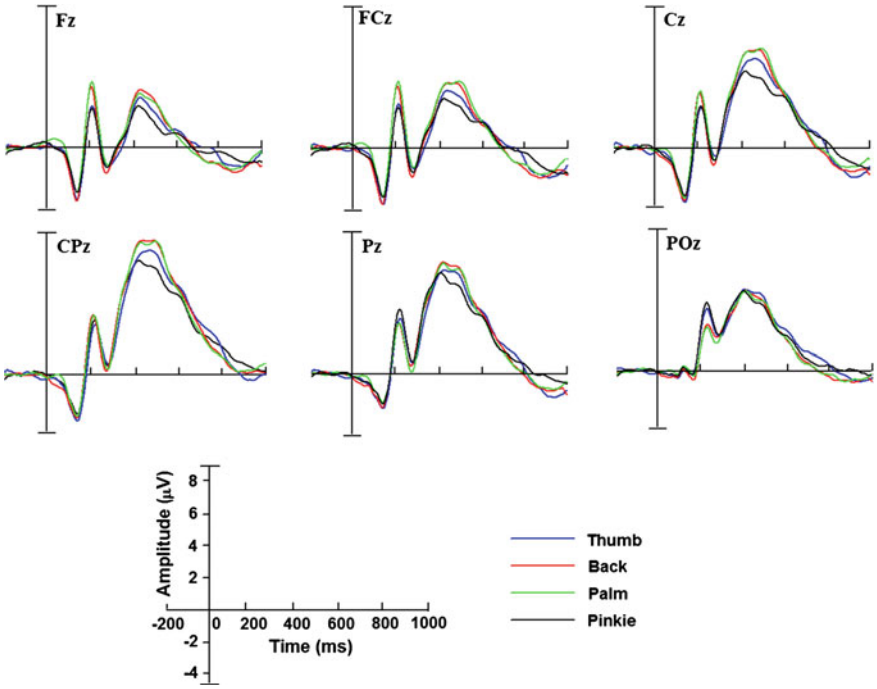

Fig. 4 Grand average ERP ($n = 14$) in each view at the Fz, FCz, Cz, CPz, Pz, and POz electrodes

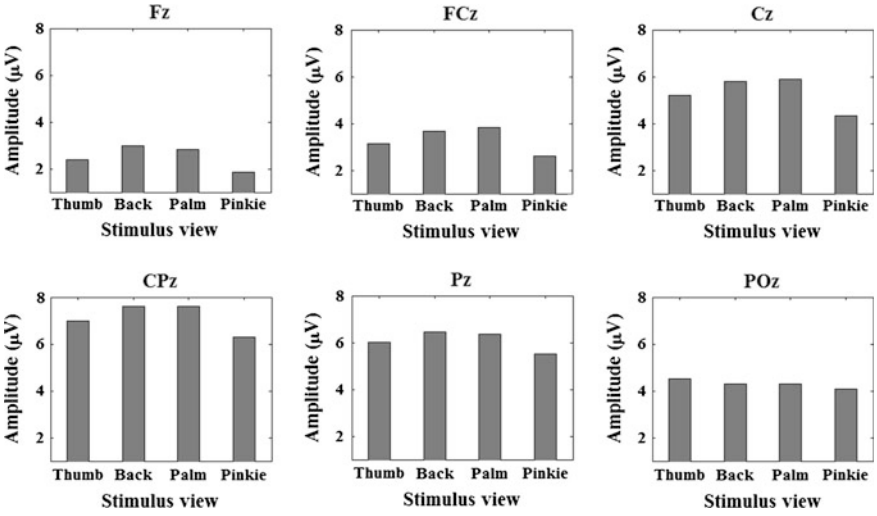

Fig. 5 Mean amplitude in the 400–550 ms time window as a function of stimulus view at the Fz, FCz, Cz, CPz, Pz, and POz sites

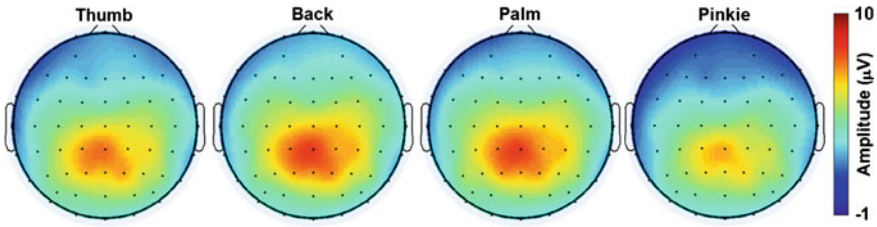

Fig. 6 Topographical maps of the view effect based on the average ERP amplitude from 400 to 550 ms

Table 1 The view effects reflected by the mean amplitudes of RRN in each of the six regions

Region	RRN	
	F	*P*
Frontal	9.72	0.002
Frontal-central	13.02	0.001
Central	23.06	<0.001
Central-parietal	13.16	0.001
Parietal	3.12	0.070
Occipito-parietal	1.19	0.358

the topographic specificity of the RRN component. The interaction of region × view [mean ± SEM; $F(15,195) = 3.51$, $P < 0.05$] was also significant. Pairwise planned comparisons showed that the largest effect size was in the central region, suggesting the most significant view effect in this region (Table 1). However, no other significant interactions were obtained.

The three-way repeated-measures ANOVA was performed for these analyses. The significant level was set at $P < 0.05$.

Since pairwise planned comparisons revealed no significant difference between the mean amplitude with the thumb, back, and palm views. These results were pooled (Poolviews) for comparison with pinkie views. A significant reduction in mean amplitude was observed in the pinkie views (Fig. 7a) and topographic maps of difference wave Poolviews versus pinkie (Fig. 7b) showed the following spatio-temporal distribution for the ERP data. The amplitude was more negative in pinkie than in Poolviews in the 400–550 ms time window over the central region.

The mean values of strongest correlations between RRN amplitudes and reaction times for each electrode are depicted in Fig. 8a. The strongest and statistically significant correlations were obtained only for POz site. In Fig. 8b, a scatter plot illustrating the relationship between RRN amplitudes change and reaction times for participants during hand mental rotation task. Change in RRN amplitudes showed a significant negative correlation with reaction times [Pearson correlation coefficient $(r) = -0.49$; $P < 0.01$], which indicated that more negative RRN amplitude was associated with slower responses to hand stimuli.

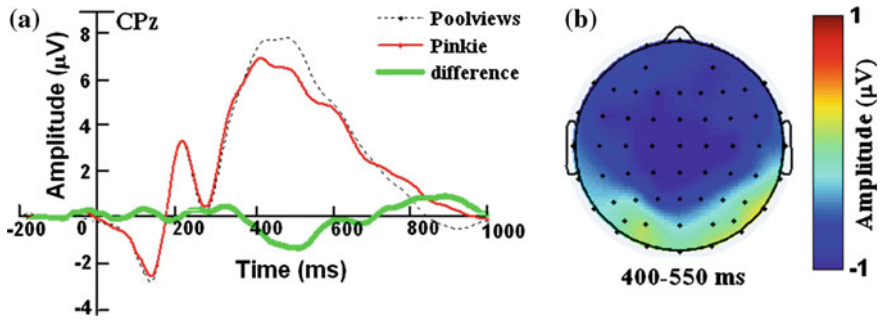

Fig. 7 **a** Grand average ERP to Poolviews (average of thumb, back, and palm) and pinkie conditions and the difference wave (pinkie-Poolviews) at Cz site. **b** Topographical maps of the voltage amplitudes for the Poolviews versus pinkie condition difference wave in the 400–550 ms time window

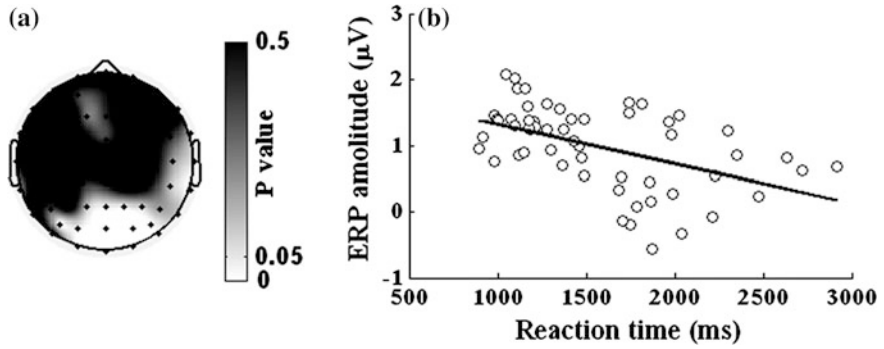

Fig. 8 **a** The *P* value at each electrode, as assessed the statistical significance by a linear regression analysis between reaction times and ERP amplitudes from 400 to 550 ms. **b** Association of individual mean ERP amplitudes from 400 to 550 ms and reaction times for stimulus view (thumb, back, palm, and pinkie) at the POz site

4 Discussion

The primary purpose of the present study was to further understand the process of hand mental rotation task. We investigated reaction times and event-related potential for the neural dynamics of mental hand rotation task by using EEG.

4.1 Behavioral Response

For all participants with low error rates, it was found that significantly longer reaction times were taken for pinkie-side views compared to the other three

conditions, which was in line with previous studies [22] (see Fig. 1). It can be concluded that the pinkie-side views were the most biomechanically difficult mental spatial transformations. This modulation of reaction times has been linked to the increase of biomechanical constraints when imaging the hand rotation to match the difficult stimulus view. Therefore, the biomechanical constraints might be primarily responsible for the greater mental simulation times and play an important role in stimuli-related cognitive processing. In addition, it has been reported that this cognitive processing can be affected by both current and desired states [24]. In a hand mental rotation task, the desired state is the presented stimulus view. Because motor imagery is subject to biomechanical constraints, reaction times are increased to judge the stimuli oriented in anatomically difficult positions if participant uses the motor imagery strategy to solve this task. In an informal debriefing following the experimental session, all participants reported to have solved the task by using a set of mental transformations of their own hands in order to closely match the view presented in the line drawing (motor imagery strategy). These behavioral results and participants' debriefings indicated the engagement in motor imagery.

4.2 ERP Amplitude Modulation Association with Mental Rotation

Our ERP data showed that this mental rotation task had its main impact on neural activity during the RRN segment. In contrast to natural views such as thumb, back, and palm, the pinkie views elicited more negative component. This slow ERP component was functionally related to the P3b component of the P300 complex, which was generally interpreted as reflecting quality of information processing and the amount of effort allocated to a task. Therefore, we conclude that it takes more effort for the mental rotation in a difficult view than that in an easier one.

The RRN showed a maximal correlation with reaction times at parieto-occipital sites. Increased reaction time was associated with reduced ERP amplitude over parieto-occipital regions. Therefore, we can conclude that this effect may be an index of the increase in posterior parietal/occipital cortex activity. This notion is in accord with numerous previous studies that have reported that a large region of activation centered in the intraparietal sulcus and extending into the transverse occipital sulcus during mental rotation task [13, 25, 26]. Participants were slower and less accurate when making a 'same' judgment for a difficult view in comparison to an easy one. Therefore, the tendency of RRN amplitude in the partieto-occipital region to be negatively correlated with the reaction time might also indicate that attention to the mental rotation task is more demanding in a difficult view than in an easy one.

4.3 Role of Central Motor Regions in Mental Rotation

There is growing evidence that the parietal lobe play an important role in mental rotation. A variety of studies using PET, fMRI, and EEG have shown parietal lobe activation during mental rotation [13, 14, 19]. Furthermore, as task demands are increased, parietal lobe activation increases. In addition to activating the parietal lobe, there is also considerable evidence reporting activity in the precentral sulcus during mental rotation tasks [18].

In the current study we observed view-sensitive amplitude modulations and the most significant view effect in the central region. Thus, we conclude that mental rotation of hands is based on biomechanical constraints related to motor simulation and the central region is indeed involved in mental rotation of hands. Regions in the central cortex are associated with motor planning and motor execution. Motor imagery shares many cognitive aspects of movement with actual motor execution. These results suggest that the central lobes activity may reflect the use of action simulation to solve this task. In other words, participants use a set of mental transformations of their own hands in order to closely match the view presented in the line drawing. Evidence from PET and fMRI has provided support for the notion that when participants use the motor imagery strategy to solve the mental rotation tasks, medial/superior motor regions are activated [13, 14].

5 Conclusion

We employed a mental rotation task of hands which is similar to that previously adopted to involve in motor imagery [22]. The behavioral data showed that reaction times were subject to biomechanical constraints because longer reaction times were found for those views when hands are not able to reach easily with real movement. ERP results showed that the RRN amplitude was more negative for difficult to maintain or unfamiliar views with the most significant view effect in the central region. Behavior was closely linked with the slope of the parieto-occipital ERP amplitude modulation. These results suggest that the neural activity underlying mental rotation of hands are primarily conducted in parietal, occipital, and central lobes.

Acknowledgments This work is supported by National Basic Research Program (973) of China (No. 2011CB933204), National Natural Science Foundation of China under Grant 90820304, 91120007, 61105123, Chinese 863 Project: 2012AA011601.

References

1. Shepard RN, Metzler J (1971) Mental rotation of three-dimensional objects. Science 171:701–703
2. Prime DJ, Jolicoeur P (2010) Mental rotation requires visual short-term memory: evidence from human electric cortical activity. J Cogn Neurosci 22:2437–2446
3. Milivojevic B, Hamm JP, Corballis MC (2009) Functional neuroanatomy of mental rotation. J Cogn Neurosci 21:945–959
4. Quinn PC, Liben LS (2008) A sex difference in mental rotation in young infants. Psychol Sci 19:1067–1070
5. Peters M, Battista C (2008) Application of mental rotation figures of the Shepard and Metzler type and description of a mental rotation stimulus library. Brain Cogn 66:260–264
6. Chu M, Kita S (2008) Spontaneous gestures during mental rotation tasks: insights into the microdevelopment of the motor strategy. J Exp Psychol Gen 137:706–723
7. Parsons LM (1987) Imagined spatial transformations of one's hands and feet. Cognitive Psychol 19:178–241
8. Ionta S, Blanke O (2009) Differential influence of hands posture on mental rotation of hands and feet in left and right handers. Exp Brain Res 195:207–217
9. Petit LS, Harris IM (2005) Anatomical limitations in mental transformations of body parts. Vis Cogn 12:737–758
10. Mourao-Miranda J, Ecker C, Sato JR, Brammer M (2009) Dynamic changes in the mental rotation network revealed by pattern recognition analysis of fMRI data. J Cognitive Neurosci 21:890–904
11. Vingerhoets G, Santens P, Laere KV, Lahorte P, Dierckx RA, Reuck JD (2001) Regional brain activity during different paradigms of mental rotation in healthy volunteers: a positron emission tomography study. Neuroimage 13:383–391
12. Shimoda N, Takeda K, Imai I, Kaneko J, Kato H (2008) Cerebral laterality differences in handedness: a mental rotation study with NIRS. Neurosci Lett 430:43–47
13. Kosslyn SM, Digirolamo GJ, Alpert NM, Thompson WL (1998) Mental rotation of objects versus hands: neural mechanisms revealed by positron emission topography. Psychophysiology 35:151–161
14. Vingerhoets G, de Lange FP, Vandemaele P, Deblaere K, Achten E (2002) Motor imagery in mental rotation: an fMRI study. Neuroimage 17:1623–1633
15. de Lange FP, Helmich RC, Toni I (2006) Posture influences motor imagery: an fMRI study. Neuroimage 33:609–617
16. Zacks JM (2008) Neuroimaging studies of mental rotation: a meta-analysis and review. J Cognitive Neurosci 20:1–19
17. Beste C, Heil M, Konrad C (2010) Individual differences in ERPs during mental rotation of characters: lateralization, and performance level. Brain Cogn 72:238–243
18. Pelgrims B, Michaux N, Olivier E, Andres M (2011) Contribution of the primary motor cortex to motor imagery: a subthreshold TMS study. Hum Brain Mapp 32:1471–1482
19. Núñez-Peña MI, Aznar-Casanova JA (2009) Mental rotation of mirrored letters: evidence from event-related brain potentials. Brain Cogn 69:180–187
20. Makeig S, Delorme A, Westerfield M, Jung TP, Townsend J, Courchesne E, Sejnowski TJ (2004) Electroencephalographic brain dynamics following manually responded visual targets. PLoS Biol 2:e176
21. Wijers AA, Otten LJ, Feenstra S, Mulder G, Mulder LJM (1989) Brain potentials during selective attention, Memory search, and mental rotation. Psychophysiology 26:452–467
22. Nico D, Daprati E, Rigal F, Parsons L, Sirigu A (2004) Left and right recognition in upper limb amputees. Brain 127:120–132
23. Semlitsch HV, Anderer P, Schuster P, Presslich O (1986) A solution for reliable and valid reduction of ocular artifacts, Applied to the P300 ERP. Psychophysiology 23:695–703

24. de Lange FP, Roelofs K, Toni I (2008) Motor imagery: a window into the mechanisms and alterations of the motor system. Cortex 44:494–506
25. Gogos A, Gavrilescu M, Davison S, Searle K, Adams J, Rossell SL, Bell R, Davis SR, Egan GF (2010) Greater superior than inferior parietal lobe activation with increasing rotation angle during mental rotation: an fMRI study. Neuropsychologia 48:529–535
26. Koscik T, Leary DO, Moser DJ, Andreasen NC, Nopoulos P (2009) Sex differences in parietal lobe morphology: relationship to mental rotation performance. Brain Cogn 69:451–459

Predictive Coding with Context as a Model of Image Saliency Map

Duzhen Zhang and Chuancai Liu

Abstract Predictive coding/biased competition (PC/BC) is a computational model of primary visual cortex (V1). Recent literature demonstrates that PC/BC model provides an implementation of the V1 bottom-up saliency map hypothesis. In this paper, we propose a novel approach toward natural color images saliency detection via the PC/BC model with top-down cortical feedback as context. We compare our method with the five state-of-the-art models of saliency detectors. Experimental results show that our method performs competitively for visual saliency detection task.

Keywords Saliency map · PC/BC model · Primary visual cortex (V1) · Top-down · Bottom-up · Context

1 Introduction

The visual system pays attention to the salient object. A number of psychophysical experiments suggest that primary visual cortex (V1) may be involved in the computation of visual salience. Spratling introduced the nonlinear predictive coding/biased competition (PC/BC) model [1], a reformulation of predictive

D. Zhang (✉) · C. Liu
School of Computer Science and Engineering, Nanjing University of Science and Technology, NJUST, Nanjing, China
e-mail: zhduzhen@yahoo.cn

C. Liu
e-mail: liu.ccnj@yahoo.com.cn

D. Zhang
School of Computer Science and Technology, Jiangsu Normal University, JSNU, Xuzhou, China

F. Sun et al. (eds.), *Foundations and Practical Applications of Cognitive Systems and Information Processing*, Advances in Intelligent Systems and Computing 215,
DOI: 10.1007/978-3-642-37835-5_2,

coding consistent with the biased competition theory of attention, that can simulate a very wide range of V1 response properties including tuning and suppression [2, 3]. The paper [4] extends his previous work by showing that the PC/BC model of V1 can also simulate a wide range of psychophysical experiments on visual salience, and demonstrates that PC/BC provides a possible implementation of the V1 bottom-up saliency map hypothesis. It proposes that the perceptual saliency of the image is consistent with the relative strength of the prediction error calculated by PC/BC. Saliency can therefore be interpreted as a mechanism by which prediction errors attract attention in an attempt to improve the accuracy of the brain's internal representation of the world [4].

Visual saliency plays important roles in natural vision in that saliency can direct eye movements, deploy attention, and facilitate tasks like object detection and scene understanding. Many models have been built to compute saliency map. There are two major categories of factors that drive attention: bottom-up factors and top-down factors [5]. Bottom-up factors are derived solely from the visual scene. Regions of interest that attract our attention are in a bottom-up way and the responsible feature for this reaction must be sufficiently discriminative with respect to surrounding features. Most computational models focused on bottom-up attention, where the subjects are free-viewing a scene and salient objects attract attention. Inspired by the feature-integration theory [6], Itti et al. [7] proposed one of the earliest bottom-up selective attention models by utilizing color, intensity, and orientation of images. Bruce et al. [8] introduced an idea of using Shannon's self-information to measure the perceptual saliency. Saliency using natural image statistics (SUN) is a bottom-up bayesian framework [9]. Recently, Hou et al. [10] proposed a dynamic visual attention approach to calculate the saliency map based on Incremental Coding Length (ICL). Bottom-up attention can be biased toward targets of interest by top-down cues such as object features, scene context and task-demands. Bottom-up and top-down factors should be combined to direct attentional behavior. A recent review of attention models from computational perspective can be found in [11].

Reference [4] uses synthetic stimuli to test the saliency of the PC/BC model. In this paper, inspired by the work of Spratling, we propose an approach toward natural color images saliency detection via the PC/BC model with top-down cortical feedback as context. We compare our method with the five state-of-the-art models of saliency detectors. Experimental results show that our method performs competitively for visual saliency detection task. The rest of this paper is organized as follows. Section 2 introduces and analyzes Spratling's PC/BC model, and based on his work, a novel method combining top-down cortical feedback for measuring image saliency is proposed. Experimental results and comparisons with state-of-the-art models are presented in Sect. 3, and discussions are given in Sect. 4.

2 The Model Description

Figure 1 illustrates the retina/LGN model and the PC/BC model of V1, from left to right, capital characters I, X, E, Y, and A represent input image, image preprocessing stage by the retina/LGN, the error-detecting neurons, the prediction neurons, feedback from higher cortical regions, respectively.

2.1 The Retina/LGN Model

To simulate the effects of circular-symmetric center-surround receptive fields (RFs) in lateral geniculate nucleus (LGN) and retina, input image (I) preprocessed by convolution with a Laplacian-of-Gaussian (LoG) filter (l) and a saturating nonlinearity:

$$X = \tanh\{2\pi(I * l)\}. \tag{1}$$

The positive and rectified negative responses were separated into two images X_{ON} and X_{OFF} simulating the outputs of cells in retina and LGN with on-center/off-surround and off-center/on-surround RFs, respectively. These ON- and OFF-channels provided the input to the PC/BC model of V1.

2.2 The V1 Model

The PC/BC model of V1 is described by the following equations:

$$E_O = X_O \oslash \left(\varepsilon_2 + \sum_{k=1}^{p} (\hat{\omega}_{ok} * Y_k)\right). \tag{2}$$

$$Y_k \leftarrow (\varepsilon_1 + Y_k) \otimes \sum_{o} (\omega_{ok} \circ E_O). \tag{3}$$

$$Y_k \leftarrow Y_k \otimes (1 + \eta A_k). \tag{4}$$

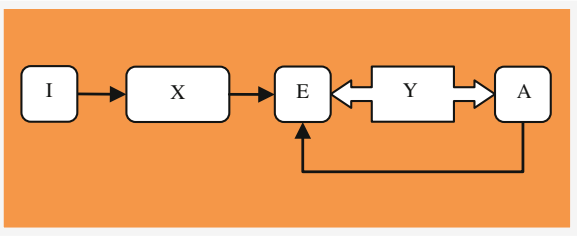

Fig. 1 The retina/LGN model and the PC/BC model of V1

where $o \in$ [ON, OFF]; X_o represents the input to the model of V1, E_o represents the error-detecting neuron responses, Y_k represents the prediction neuron responses, A_k represents the weighted sum of top-down predictions, all of them are two-dimensional array, equal in size to the input image; ω_{ok} is a two-dimensional kernel representing the synaptic weights for a particular class (k) of neuron normalized so that the sum of all the weights is equal to ψ, $\hat{\omega}_{ok}$ is a two-dimensional kernel representing the same synaptic weights as ω_{ok} but normalized so that the maximum value is equal to ψ, the Gabor function is used to define the weights of each kernel ω_{ok} and $\hat{\omega}_{ok}$ (a family of 32 Gabor functions with eight orientation (0°–157.5° in steps of 22.5°) and four phases (0°, 90°, 180°, and 270°) were used); p is the total number of kernels; $\varepsilon_1, \varepsilon_2, \eta$ and ψ are parameters; $\varnothing$ and $\otimes$ indicate element-wise division and multiplication, respectively; o represents cross-correlation (which is equivalent to convolution without the kernel being rotated 180°); and * represents convolution (which is equivalent to cross-correlation with a kernel rotated 180°). Parameter values $\psi = 5000, \varepsilon_1 = 0.0001, \varepsilon_2 = 250$, and $\eta = 1$ were used in the experiments.

Equation (2) describes the calculation of the neural activity for each population of error-detecting neurons. The activation of the error-detecting neurons can be interpreted as representing the residual error between the input and the reconstruction of the input generated by the prediction neurons. The values of E are related to the image saliency, with high error values corresponding to high saliency.

Equation (3) describes the updating of the prediction neuron activations. The values of Y_k represent predictions of the causes underlying the inputs to the model of V1. If the input remains constant, the values of Y_k will converge to steady-state values that reconstruct the input with minimum error.

2.3 Modeling the Top-Down Effects

Equation (4) describes the effects on the V1 prediction neuron activations of top-down inputs from prediction neurons at later processing stages (i.e., in extra-striate cortical regions). In Eq. (4), the effects of cortical feedback are modeled by using an array of inputs (A) to the V1 model which represents the weighted sum of top-down predictions. In the simulations of Ref. [4], feedback was either simple orientation preferences, the elements of A were set to values of 0.25 and zero, or assumed to be negligible, the elements of A were given a value of zero, in which cases Eq. (4) had no effect. We add the following equation between Eq. (3) and Eq. (4) to model the top-down effects:

$$A_k \leftarrow \sum_{k=1}^{p} (\hat{\omega}_{ok} * Y_k). \tag{5}$$

This top-down feedback will have two effects on the PC/BC model of V1. (1) Increasing the response of the prediction neurons that represent information consistent with the top-down expectation [see Eq. (4)]. This will result in these prediction neurons sending stronger feed-forward activation, and hence, make this information more conspicuous for cortical regions at subsequent stages along the processing hierarchy. (2) The enhanced activity in the prediction neurons consistent with top-down expectations will in turn decrease the response of the error-detecting neurons from which these prediction neurons receive their input [see Eq. (2)] [4]. Since the strength of the responses of the error-detecting neurons is assumed to be related to saliency, in this way, top-down feedback modulates bottom-up saliency.

3 Experimental Comparisons

3.1 Saliency Results Comparison

We evaluated our method on human visual fixation data from natural images. The dataset we used was collected by Bruce and Tsotsos [8] as the benchmark dataset for comparing human eye predictions between methods. The dataset contains eye fixation data from 20 subjects for a total of 120 natural images.

Figure 2 affords a qualitative comparison of the output of the proposed models (without/with context) for a variety of images. Visually, top-down effects increase the performance of salient object detection, i.e., top-down signals modulate bottom-up saliency. This is in line with preceding analysis. Figure 2d is fixation density map based on experimental human eye tracking data as the "ground truth" saliency map of each image.

3.2 Comparing Our Saliency Results with Other Methods

We compare our saliency method with context against other five state-of-the-art methods using the database from the publicly available database used by Achanta et al. [12]. Each of the 1,000 images in the database contains a salient object or a distinctive foreground object, so we can compare the performance of different algorithms.

The five saliency detectors are Itti et al. [7], Harel et al. [13], Hou and Zhang [14], Achanta [12], and Goferman et al. [15], hereby referred to as IT, GB, SR, IG, and CA. We refer to our proposed method as PC. The choice of these algorithms is motivated by the following reasons: citation in literature (the classic approach of IT is widely cited), recency (IG, and CA are recent), and variety (IT is biologically

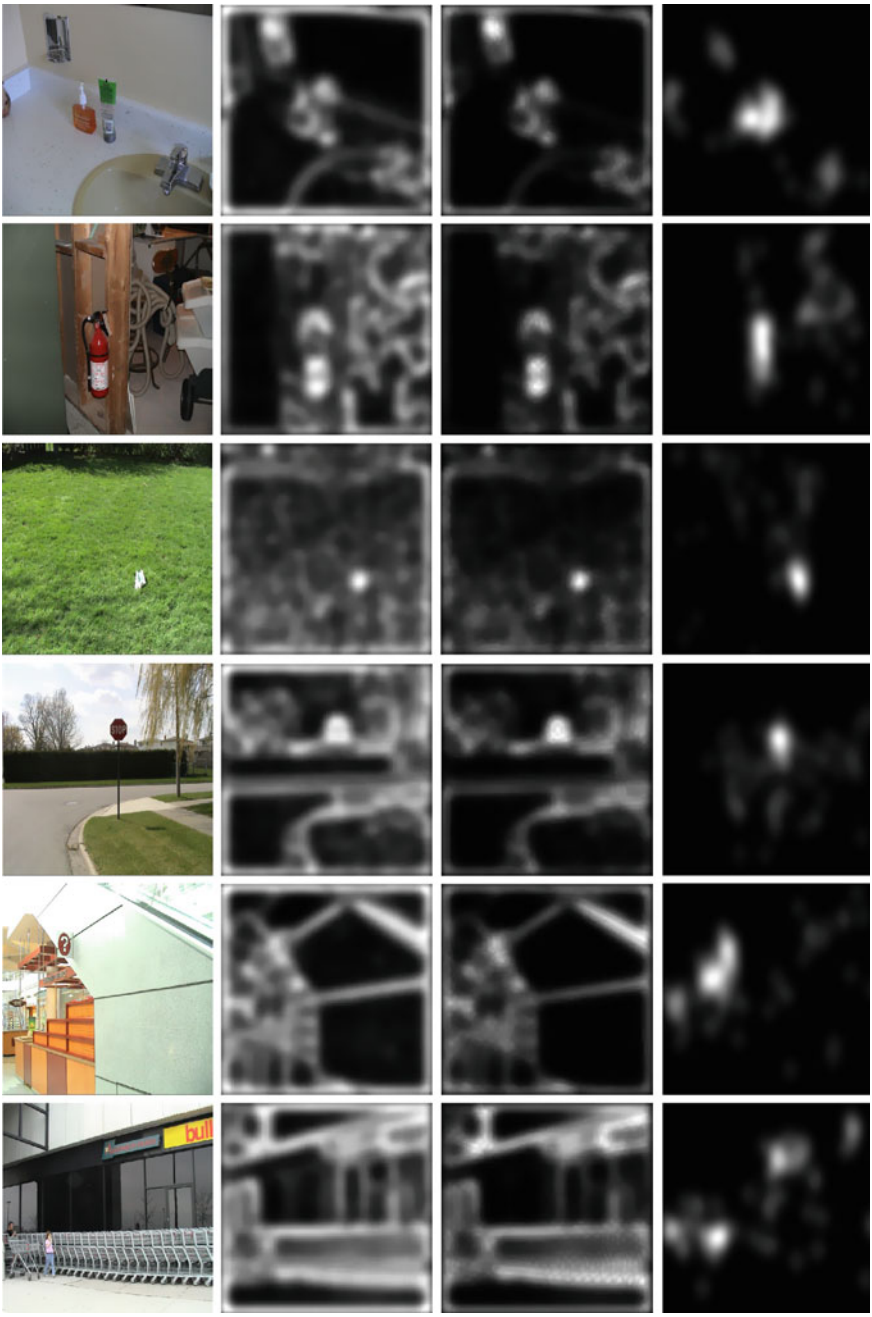

Fig. 2 Results for qualitative comparison: **a** Original image; **b** Saliency map without context; **c** Saliency map with context; **d** Fixation density map based on experimental human eye tracking data

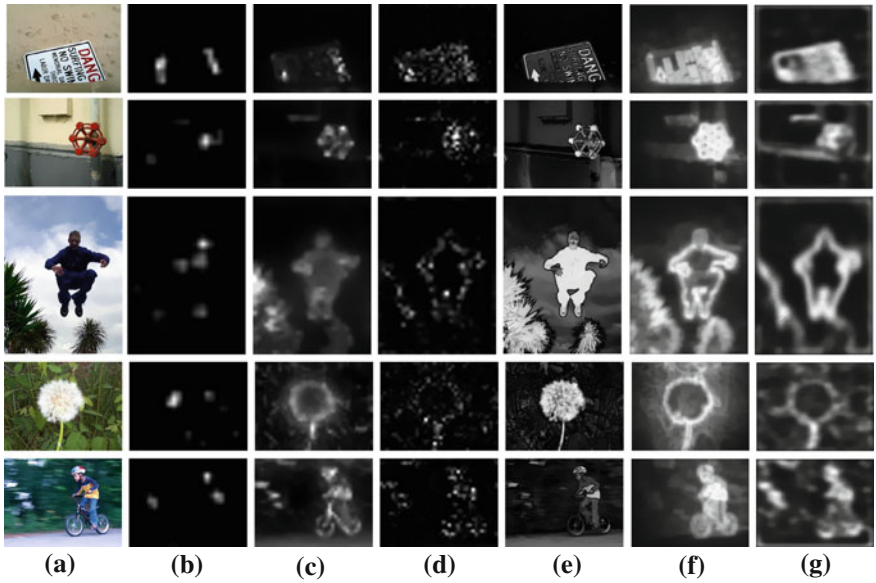

Fig. 3 Visual comparison of saliency map. **a** Original, **b** IT [7], **c** GB [13], **d** SR [14], **e** IG[12], **f** CA [15], **g** PC

motivated, CA is purely computational, GB is a hybrid approach, SR and IG estimates saliency in the frequency domain).

We randomly choose some images from the database. Figure 3 is the output of the five state-of-the-art methods and our method for comparison. Our method is a competitive, promising algorithm.

3.3 Quantitative Evaluation

To obtain a quantitative evaluation we compare ROC curves and Area Under Curve (AUC) on the database presented in [8]. Figure 4 is the result of our method and other three methods.

4 Discussions

PC/BC is a computational model of primary visual cortex (V1) which provides an implementation of the V1 bottom-up saliency map. In this paper, we propose a novel approach to natural color image saliency detection method with top-down cortical feedback as context. Our experimental result is consistent with recent literature conclusion: top-down signals modulate (override) bottom-up saliency (in

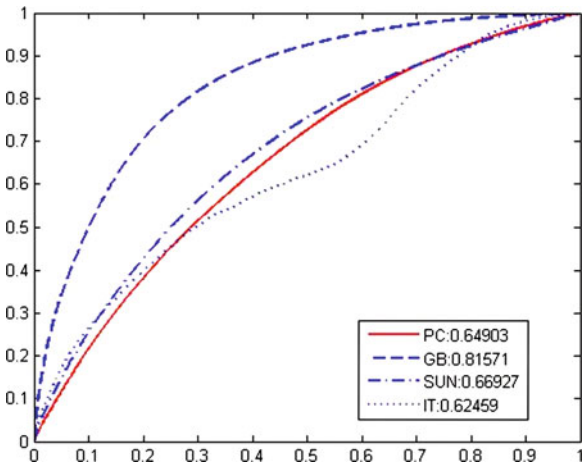

Fig. 4 ROC curves for the database of [8]

a feature-specific way) [16]. We compare our method with the five state-of-the-art models of saliency detectors. Experimental results show that our method performs competitively for visual saliency detection task.

When the organism is not actively searching for a particular target (the free-viewing condition), the organism's attention should be directed to the most salient points which potential targets in the visual field. Bottom-up attention mechanisms have been more thoroughly investigated than top-down mechanisms. One reason is that data-driven stimuli are easier to control than cognitive factors such as task-demands, knowledge, and expectations. Even less is known on the interaction between the two processes [17].

In future work, we will incorporate color feature and other task-demands features as context to detect saliency, "Combining such features-specific top-down signals with (learnt) contextual priors on target location therefore may provide a promising approach to searching for real-world objects in their natural context [16]", and develop applications of our model.

Acknowledgments This work is supported by the National Natural Science Fund of China (Grant Nos. 60632050, 9082004) and by the basic key technology project of Ministry of Industry and Information Technology of China (Grant No. E0310/1112/JC01).

References

1. Spratling MW (2008) Predictive coding as a model of biased competition in visual attention. Vis Res 48:1391–1408
2. Spratling MW (2010) Predictive coding as a model of response properties in cortical area V1. J Neurosci 30:3531–3543
3. Spratling MW (2011) A single functional model accounts for the distinct properties of suppression in cortical area V1. Vis Res 51:563–576

4. Spratling MW (2011) Predictive coding as a model of the V1 saliency map hypothesis. Neural Networks 20:1–22
5. Desimone R, Duncan J (1995) Neural mechanisms of selective visual attention. Ann Rev Neurosci 18:193–222
6. Treisman A, Gelade G (1980) A feature-integration theory of attention. Cogn Psychol 12:97–136
7. Itti L, Koch C, Niebur E (1998) A model of saliency-based visual attention for rapid scene analysis. IEEE Trans Pattern Anal Mach Intell 20:1254–1259
8. Bruce N, Tsotsos J (2005) Saliency based on information maximization. In: Proceedings in advances in neural information processing systems, vol 18, pp 155–162
9. Zhang L, Tong MH, Marks TK, Shan H, Cottrell GW (2008) SUN: a Bayesian framework for saliency using natural statistics. J Vis 8:1–20
10. Hou X, Zhang L (2008) Dynamic visual attention: searching for coding length increments. In: Proceedings of advances in neural information processing systems, pp 681–688
11. Borji A, Itti L (2012) State-of-the-art in visual attention modeling. http://doi.ieeecomputersociety.org/10.1109/TPAMI.2012.89
12. Achanta R, Hemami S, Estrada F, Süsstrunk S (2009) Frequency-tuned salient region detection. In: Proceedings of IEEE international conference on computer vision and pattern recognition, pp 1597–1604
13. Harel J, Koch C, Perona P (2007) Graph-based visual saliency. Adv Neural Inf Proc Syst 19:545–552
14. Hou X, Zhang L (2007) Saliency detection: a spectral residual approach. In: Proceedings of IEEE conference on computer vision and pattern recognition, pp 18–23
15. Goferman S, Zelnik-Manor L, Tal A (2010) Context-aware saliency detection. In: Proceedings of IEEE international conference on computer vision and pattern recognition, pp 2376–2383
16. Einhäuser W, Rutishauser U, Koch C (2008) Task-demands can immediately reverse the effects of sensory-driven saliency in complex visual stimuli. J Vis 8:1–19
17. Frintrop S, Rome E, Christensen HI (2010) Computational visual attention systems and their cognitive foundations: a survey. ACM Trans Appl Percept 7:1–46

Multiclass Pattern Analysis of Whole-Brain Functional Connectivity of Schizophrenia and Their Healthy Siblings

Yang Yu, Hui Shen, Ling-Li Zeng and Dewen Hu

Abstract Recently, a growing number of neuroimaging studies have begun to pay attention to exploring the brains of schizophrenic patients to identify heritable biomarkers for this disorder involving their healthy siblings. Based on whole-brain resting-state functional connectivity of schizophrenic patients, their healthy siblings and healthy controls, the objective of the present study aimed to use multiclass pattern analysis to reveal three types of neural signature: (i) state connectivity patterns, reflecting the state of having schizophrenia; (ii) trait connectivity patterns, reflecting the genetic vulnerability to develop schizophrenia; and (iii) compensatory connectivity patterns, underlying special brain connections by which healthy siblings compensate for an increased genetic risk for developing schizophrenia. The current study may provide additional insights into the pathophysiological mechanisms underlying schizophrenia and be helpful in further highlighting genetic contribution to the etiology of schizophrenia.

Keywords Schizophrenia · Healthy siblings · Functional magnetic resonance imaging · Resting-state · Functional connectivity · Multiclass pattern analysis

Y. Yu · H. Shen · L.-L. Zeng · D. Hu (✉)
College of Mechatronics and Automation, National University of Defense Technology, Changsha 410073 Hunan, China
e-mail: dwhu@nudt.edu.cn

Y. Yu
e-mail: yy87724@sina.com

H. Shen
e-mail: shenhui_nudt@126.com

L.-L. Zeng
e-mail: losernudt@163.com

F. Sun et al. (eds.), *Foundations and Practical Applications of Cognitive Systems and Information Processing*, Advances in Intelligent Systems and Computing 215,
DOI: 10.1007/978-3-642-37835-5_3,

1 Introduction

Schizophrenia is a highly heritable psychiatric disorder, and evidence from family and twin studies demonstrated that heritable factors play an important role in the pathogenesis of schizophrenia [1–4]. It was suggested that the similar genetic backgrounds between schizophrenic patients and their healthy siblings contribute to approximately ninefold higher risk for siblings to develop schizophrenia than the general population [5, 6], whereas the healthy siblings of schizophrenic patients behave normally in their daily lives and do not actually meet the diagnostic criteria for schizophrenic disorder. Thus, comparison among schizophrenic patients, healthy siblings of schizophrenic patients, and healthy controls likely provides additional insights into the pathophysiological mechanisms underlying this disorder and may be helpful in further highlighting genetic contribution to the etiology of schizophrenia.

In recent years, a growing number of neuroimaging studies have begun to pay attention to exploring the brains of schizophrenic patients to identify heritable biomarkers for this disorder involving their healthy siblings [7–10]. Increasing rs-fcMRI studies have demonstrated altered functional connectivity in the brain of schizophrenic patients and their healthy siblings [11–15]. However, most of these previous studies focused mainly on the functional connectivities associated with one or a few preselected seed regions of interest (ROIs), ignoring other potentially informative connectivity patterns. Or they focused on group-level statistical methods which are less helpful to clinical diagnosis on individual-level. In this study, we investigated the whole-brain functional connectivity patterns of schizophrenic patients, healthy siblings, and healthy controls, which could make full use of information contained in the neuroimaging data.

Recent years, multivariate pattern analyses based on machining learning have aroused great interest for its capacity of extracting functional patterns from neuroimaging data and its potential capability of finding valuable neuroimaging-based biomarkers [16]. Our recent study [17] based on multivariate pattern analysis has applied nonlinear support vector machine (SVM) to whole-brain rs-fMRI data to train a one-against-one classifier between schizophrenic patients and their healthy siblings, resulting in significant separation. However, one limitation of this work is that reconstruction is unavailable for the use of nonlinear SVM classifiers, so that it is difficult to discover informative functional connectivity patterns revealing the pathophysiological mechanisms of schizophrenia.

In the present study, we used a multiclass pattern classifier to explore the whole-brain resting-state functional connectivity patterns of schizophrenic patients, healthy siblings and healthy controls based on rs-fMRI. Instead of using a one-against-one classifier, we established our one-against-rest classifier for addressing this multiclass pattern classification issue. There were three procedures involved in this study: (i) dimensional reduction of the original feature space using principal component analysis (PCA), (ii) one-against-rest classification based on

linear SVM was trained to solve the multiclassification problems, and (iii) reconstruction to identify features with high discriminative power.

2 Materials and Methods

2.1 Participants

Subjects consisted of 24 schizophrenic patients, 25 healthy siblings, and 22 healthy controls. Schizophrenic patients were recruited from outpatient departments and inpatient units at the Department of Psychiatry, Second Xiangya Hospital of Central South University, and all the patients were evaluated by the Structured Clinical Interview for DSM-IV, and fulfilled the criteria for schizophrenia according to DSM-IV. Symptom severity for patients was assessed using the positive and negative syndrome scale [18]. No patients had a history of neurological disorders, severe medical disorder, substance abuse, or electroconvulsive therapy. Six of the schizophrenic patients were medication-free, while the others accepted atypical psychotropic drugs during time of scanning (risperidone [$n = 10$, 2–6 mg/day], clozapine [$n = 4$, 200–350 mg/day], quetiapine [$n = 4$, 400–600 mg/day], and sulpiride [$n = 1$, 200 mg/day]). Twenty-five healthy siblings of schizoprenia were recruited so that each schizophrenic patient had a corresponding sibling, and they do not fulfill the DSM-IV criteria for any Axis-I psychiatric disorders. Twenty-five healthy controls who had no first-degree relatives with a history of psychiatric disorders were recruited from Changsha City, China. The schizophrenic patients, healthy siblings, and the healthy controls were well demographically similar on age, gender, and education levels.

All participants gave their written informed consents to participate in the study and they were studied under protocols approved by the Second Xiangya Hospital of Central South University.

2.2 Resting Experiment and Data Acquisition

MRI scans were performed with a 1.5 T GE Signa System (GE Signa, Milwaukee, Wisconsin, USA) via using a gradient-echo EPI sequence. The imaging parameters are as follows: TR = 2000 ms, TE = 40 ms, FOV = 24 cm, FA = 90°, matrix = 64 × 64, slice thickness = 5 mm, gap = 1 mm, slices = 20. In the experiment, subjects were instructed simply to keep their eyes closed, to relax, remain awake, and perform no specific cognitive exercise. Foam pads and earplugs were used to minimize head motion and scanner noise, respectively. Each functional resting-state session lasted 6 min, resulting in 180 volumes.

2.3 Data Preprocessing

Image preprocessing is performed for all rs-fMRI images using the statistical parametric mapping software package (SPM8, Welcome Department of Cognitive Neurology, Institute of Neurology, London, UK, http://www.fil.ion.ucl.ac.uk/spm). For each subject, the first 5 volumes of the scanned data were discarded for magnetic saturation effects. The remaining volumes were corrected by registering and reslicing for head movement. All subjects in this study had less than 1.5 mm translation and/or 2° of rotation in each axis. After the head motion effect was removed, the volumes were normalized to the standard EPI template in the Montreal Neurological Institute (MNI) space. The resulting images were then spatially smoothed with a Gaussian filter of 8 mm full-width half-maximum kernel to increase signal-to-noise ratio and temporally filtered with a Chebyshev band-pass filter (0.01–0.08 Hz). All the registered fMRI volumes with the MNI template were further divided into 116 regions according to the anatomically labeled template previously validated and reported by Tzourio-Mazoyer et al. [19].

Regional mean time series were acquired for each individual by averaging the fMRI time series over all voxels in each of the 116 regions. For each regional mean time series, we further regressed out the global mean signals and the effects of translations and rotations of the head estimated in the course of initial movement correction by image realignment. The residuals of the above regressions constituted the set of regional mean time series used for functional connectivity analysis [20]. We then calculated the Pearson's correlation coefficients between the time series of all ROIs, resulting in a 6,670 dimensional feature vector.

2.4 Multiclass Pattern Analysis

Before training the multiclass classifier, PCA was applied to reduce the dimensionality of original feature space [21]. We used one-against-rest strategy in designing our classifiers. A leave-one-out cross-validation (Loocv) strategy was used to estimate the generalization ability of our classifier [13]. Statistical significance of the classification accuracy was determined by permutation test [22], involving repeating the classification procedure 1,000 times with a different random permutation of the classification labels of the training data.

2.5 Identification of Features with High Discriminative Power

In this study, we determined the functional connectivity features with the highest discriminative power by reconstruction based on the performance of each one-

against-rest classifiers. Because each feature influenced the classification via its weight, the larger the absolute magnitude of a feature's weight is, the stronglier it affected the classification result. For every one-to-rest classifier, we obtained a weight vector in each Loocv experiment. The weight vector for the one-against-rest classifier was finally acquired by averaging these above weight vectors. We therefore obtained three weight vectors respectively representing the features' discriminative power for each one-against-rest classifiers. Because we performed the classification in the dimension-reduced subspace, in order to determine the original functional connectivities which have significantly contribution to the classification, we used the method detailed in previous study [23] to map back each weight vector to the original high-dimensional space. Thus, for all the 6,670 resting-state functional connectivities, we obtained the order of their contribution to the classification for each one-against-rest classifier.

Similar to the definition in the previous study [24], we defined three types of neural signature patterns: (i) state connectivity pattern, functional connectivity patterns responding to the state of having schizophrenia which potentially underlying the nature of abnormal in brain network of schizophrenic patient; (ii) trait connectivity pattern, functional connectivity patterns of dysfunction shared by schizophrenic patients and their healthy siblings, providing a possible neuroendophenotype to help to bridge genomic complexity and disorder heterogeneity and thereby accelerate the investigate of pathophysiological mechanism; and (iii) compensatory connectivity pattern, unique to healthy siblings, underlying special brain connectivities by which healthy siblings might compensate for an increased genetic risk for developing schizophrenia.

3 Results

3.1 Classification Results

The classification results indicated that the correct classifications of schizophrenic patients, healthy siblings, and healthy controls were respectively 62.5, 48.0, and 63.64 % (details were shown in Table 1) and the generalization rate (GR) achieved an accuracy of 57.75 %. Permutation test results ($p < 0.001$) indicated that the overall classification accuracy was statistically significance. The permutation distribution of the estimate is shown in Fig. 1.

Table 1 Confusion matrix for results in leave-one-out cross-validation

Classes	Schizophrenia (%)	Healthy siblings (%)	Healthy controls (%)
Schizophrenia	62.5	12.5	25.0
Healthy siblings	16.0	48.0	36.0
Healthy controls	13.7	22.7	63.6

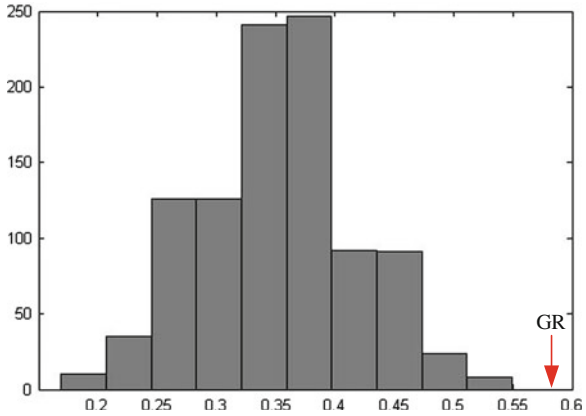

Fig. 1 Histogram of the permutation distribution of the estimate (repetition times: 1,000). x-label and y-label represent the generalization rate and occurrence number, respectively. GR is the generation rate obtained by the classifier trained on the real class labels. With the generalization rate as the statistic, this figure reveals that the classifier learned the relationship between the data and the labels with a probability of being wrong of <0.001

3.2 Functional Connectivity with High Discriminative Power

To identifying the three kinds of brain neural signature patterns: state, trait, compensatory, we selected 5 % (330) of the total functional connectivities with the highest discriminative power for each classifier. The regions related to the three types of connectivity patterns were widely distributed throughout the entire brain rather than restricted to a few specific brain regions (See Fig. 2 for details).

4 Discussion

To the best of our knowledge, this was the first study that used a multiclass pattern analysis method based on resting-state functional magnetic resonance imaging to investigate the difference of whole-brain functional connectivity among schizophrenic patients, healthy siblings, and healthy controls. PCA was employed to reduce the dimensionality of the original feature space for its ability to perform a direct connectivity mapping of the whole brain within a reasonable time frame. And the use of PCA leads to a minimum loss of information, which did not affect the functional connectivity analysis [25]. We chose the generalization rate as the statistic to estimate the statistical significance of the classification accuracy by permutation test. The results demonstrate that the multiclass classifier learned the relationship between the data and the labels with a probability of being wrong of <0.001.

Our classification accuracies for these three groups were respectively 62.5, 48.0, and 63.64 %, resulting in a total accuracy of 57.75 %, which is significantly above

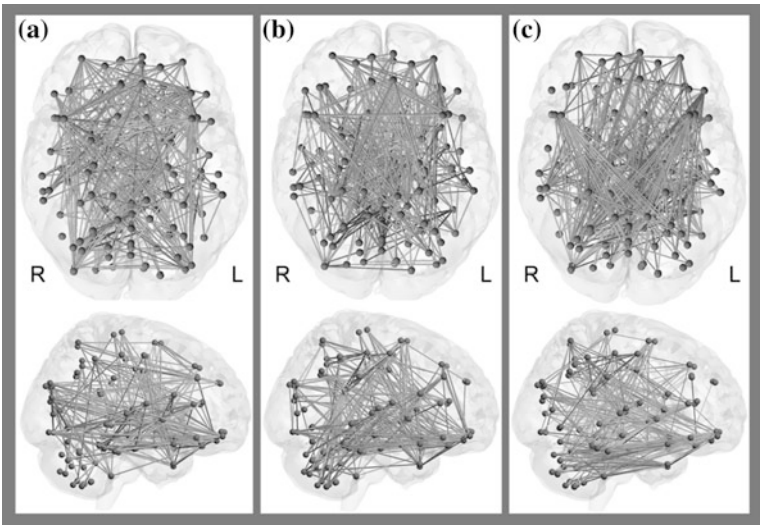

Fig. 2 Region weights and the distribution of the 330 discriminative functional connectivities responding to the state patterns **a** trait pattern **b** and compensatory pattern **c** in bottom and right view, respectively. Regions are color-coded by category. The line colors represent the discriminative power of the connectivities

the chance level of 1/3. These results suggested our methods reliably captured discriminative resting-state functional connectivity patterns among schizophrenic patients, their healthy siblings, and healthy controls at the individual subject level with a high degree of accuracy. From the confusion matrix for classification results, we found that the classification accuracy of the healthy siblings was comparatively lower, and the healthy siblings were easier to be misclassified as schizophrenic patients than healthy controls. In addition, the healthy siblings were much easier to be misclassified as the healthy controls than as the schizophrenic patients. There results might help to explain the normal daily behaviors exhibition of the healthy siblings and demonstrated that healthy siblings of schizophrenic patients have an potential higher risk for developing schizophrenia compared with the general population, which was consistent with previous finds [17].

The identified state connectivity patterns represented the brain functional connectivities which are observably different in schizophrenic patients and non-psychotic individuals (including healthy siblings and healthy controls), and they might reveal the nature of abnormality in brain connectivity pattern of schizophrenic patients. The trait patterns, obtained from the healthy controls against rests (including schizophrenia patients and their healthy siblings) classifier, likely reflect the genetic vulnerability to develop schizophrenia. The compensatory connectivity patterns, composed of connectivities which contributed most in separating the healthy siblings from schizophrenia patients and healthy controls, potentially reveal unique brain functional connectivity pattern owned by the healthy siblings. Interestingly, we found few shared connectivities among these

three types of connectivity patterns, this raises the question that whether the functional connectivity patterns of the brains of schizophrenia patients, their healthy siblings, and healthy controls are different in a whole-brain level rather than restricted to a few specific brain regions This is an interesting finding need to be considered with caution and confirmed by further investigations.

5 Limitations

There are two possible limitations in the current study that should be considered. First, due to the limited size of samples and various noises resulting from acquisition hardware, our findings needed to be confirmed with a larger sample size in the future. Second, we focused on the whole-brain functional connectivity pattern, and identified the discriminative connectivities using multiclass pattern analysis, while how do these connectivities interact remained to be further investigated, i.e., whether these connectivities were decrease or increase what might reflect the dysfunctional mechanism in the pathophysiology of schizophrenia was ignored in this study. Finally, some of the schizophrenic patients in this study were medicated. Previous studies suggest antipsychotic treatments that tend to change aberrant connectivity [26]. We are yet unable to exclude the possibility effects of antipsychotic treatment.

6 Conclusion

We used multiclass pattern analysis to investigate the functional connectivities throughout the entire brain in the schizophrenia patients and their healthy siblings with resting-state fMRI. We identified brain connectivity pattern related to the state of having schizophrenia, provided a possible neuroendophenotype reflecting the genetic vulnerability to develop schizophrenia, and revealed unique brain functional connectivity pattern owned by the healthy siblings. Our investigation suggested that the schizophrenia patients, their healthy siblings, and healthy controls might have different brain connection patterns, which needs to be considered with caution and confirmed by further investigations.

References

1. Laursen TM, Labouriau R, Licht RW, Bertelsen A, Munk-Olsen T, Mortensen PB (2005) Family history of psychiatric illness as a risk factor for schizoaffective disorder: a Danish register-based cohort study. Arch Gen Psychiatry 62:841–848

2. Cardno A, Marshall E, Coid B, Gottesmann I, Farmer A, McGuffin P (1999) Heritability estimates for psychotic disorders. Arch Gen Psychiatry 56:162–168
3. Tuulio-Henriksson A, Arajarvi R, Partonen T, Haukka J, Varilo T, Schreck M, Cannon T, Lonnqvist J (2003) Familial loading associates with impairment in visual span among healthy siblings of schizophrenia patients. Soc Biol Psychiatry 54:623–628
4. Li X, Sundquist J, Hemminki K, Sundquist K (2009) Familial risks of psychotic disorders and schizophrenia among siblings based on hospitalizations in Sweden. Psychiatry Res 166:1–6
5. Gottesman II, Shield J (1973) Genetic theorizing and schizophrenia. Br J Psychiatry 122:15–30
6. Sadock B (2007) Kaplan and Sadock's synopsis of psychiatry: behavioral sciences/clinical psychiatry (10th ed). Indian J Psychiatry 51:331
7. Brahmbhatt SB, Haut K, Csernansky JG, Barch DM (2006) Neural correlates of verbal and nonverbal working memory deficits in individuals with schizophrenia and their high-risk siblings. Schizophr Res 87:191–204
8. Calabrese DR, Wang L, Harms MP, Ratnanather JT, Barch DM, Cloninger CR, Thompson PA, Miller MI, Csernansky JG (2008) Cingulate gyrus neuroanatomy in schizophrenia subjects and their non-psychotic siblings. Schizophr Res 104:61–67
9. Fan Y, Gur RE, Gur RC, Wu X, Shen D, Calkins ME, Davatzikos C (2008) Unaffected family members and schizophrenia patients share brain structure patterns: a high-dimensional pattern classification study. Biol Psychiatry 63:118–124
10. Li X, Branch CA, Nierenberg J, DeLisi LE (2010) Disturbed functional connectivity of cortical activation during semantic discrimination in patients with schizophrenia and subjects at genetic high-risk. Brain Imag and Behav 4:109–120
11. Huang XQ et al (2010) Localization of cerebral functional deficits in treatment-naive, first-episode schizophrenia using resting-state fMRI. NeuroImage 49:2901–2906
12. Liang M, Zhou Y, Jiang TZ, Liu ZN, Tian LX, Liu HH, Hao YH (2006) Widespread functional disconnectivity in schizophrenia with resting-state functional magnetic resonance imaging. Neuroreport 17(2):209–213
13. Shen H, Wang L, Liu Y, Hu D (2010) Discriminative analysis of resting-state functional connectivity patterns of schizophrenia using low dimensional embedding of fMRI. NeuroImage 49:3110–3121
14. Zhou Y, Shu N, Liu Y, Song M, Hao YH, Liu HH, Yu CS, Liu ZN, Jiang TZ (2008) Altered resting-state functional connectivity and anatomical connectivity of hippocampus in schizophrenia. Schizophr Res 100:120–132
15. Repovs G, Csernansky JG, Barch DM (2011) Brain network connectivity in individuals with schizophrenia and their siblings. Biol Psychiatry 69:967–973
16. Pereira F, Mitchell T, Botvinick M (2009) Machine learning classifiers and fMRI: a tutorial overview. NeuroImage 45:S199–S209
17. Liu M, Zeng L-L, Shen H, Liu Z, Hu D (2012) Potential risk for healthy siblings to develop schizophrenia: evidence from pattern classification with whole-brain connectivity. Neuroreport 23:265–268
18. Kay SR, Fiszbein A, Opler LA (1987) The positive and negative syndrome scale (PANSS) for schizophrenia. Schizophr Bull 13:261–276
19. Tzourio-Mazoyer N, Landeau B, Papathanassiou D, Crivello F, Etard O, Delcroix N, Mazoyer B, Joliot M (2002) Automated anatomical labeling of activations in SPM using a macroscopic anatomical parcellation of the MNI MRI single-subject brain. NeuroImage 15:273–289
20. Achard S, Salvador R, Whitcher B, Suckling J, Bullmore E (2006) A resilient, low-frequency, small-world human brain functional network with highly connected association cortical hubs. J Neurosci 26:63–72
21. Maćkiewicz A, Ratajczak W (1993) Principal components analysis. Comput Geosci 19(3):303–342
22. Golland P, Fischl B (2003) Permutation tests for classification: towards statistical significance in image-based studies. Inf Process Med Imaging 2732:330–341

23. Wang L, Shen H, Tang F, Zang Y, Hu D (2012) Combined structural and resting-state functional MRI analysis of sexual dimorphism in the young adult human brain: an MVPA approach. NeuroImage 61:931–940
24. Kaiser MD et al (2010) Neural signatures of autism. Proc Natl Acad Sci USA 107:21223–21228
25. Zhou Z, Chen Y, Ding M, Wright P, Lu Z, Liu Y (2009) Analyzing brain networks with PCA and conditional Granger causality. Hum Brain Mapp 30:2197–2206
26. Schlosser R, Gesierich T, Kaufmann B, Vucurevic G, Hunsche S, Gawehn J, Stoeter AP (2003) Altered effective connectivity during working memory performance in schizophrenia: a study with fMRI and structural equation modeling. NeuroImage 19:751–763

Network Organization of Information Process in Young Adults' Brain

Shao-Wei Xue, Yi-Yuan Tang and Lan-Hua Zhang

Abstract In order to characterize non-random organization patterns of information process in the brain, we combine complex network analysis and resting-state functional magnetic resonance imaging to investigate brain activity derived from young adults, and then extract the tree layout and module structure of whole-brain network. These network organizations may be associated with the emergence of complex dynamics that supports the brain's moment-to-moment responses to the external world and widen understanding potentially biological mechanisms of brain function.

Keywords Brain networks · Maximum spanning tree · Modularity · Hubs

1 Introduction

Complex networks have attracted great attention as a compelling framework with which complex systems are being studied in many fields, such as computer science, physics, social sciences, and neuroscience [1]. Under this framework, many natural and man-made networks generated from different datasets have been exhibited common principles that govern network behavior and can be quantitatively characterized by the same parameters [2].

In neuroscience, studies on relationship between brain and neural networks have deep historical roots. However, the application of complex networks theory to the brain is under development during recent years. Newly developed recording

S.-W. Xue · L.-H. Zhang
Institute of Neuroinformatics, Dalian University of Technology, Dalian 116024, China

Y.-Y. Tang (✉)
Department of Psychology, Texas Tech University, TX 79409, USA
e-mail: yy2100@126.com

F. Sun et al. (eds.), *Foundations and Practical Applications of Cognitive Systems and Information Processing*, Advances in Intelligent Systems and Computing 215,
DOI: 10.1007/978-3-642-37835-5_4,

and imaging techniques help us to acquire large brain activity-based datasets dynamically and noninvasively. Especially, resting-state functional magnetic resonance imaging offers a novel approach to assess the spontaneous brain activity as low-frequency (usually <0.1 Hz) fluctuations in blood oxygen level-dependent signals. These low-frequency fluctuations potentially provide insight into the brain's functional organization because their extremely disproportionate allocation of energy resources is devoted to functionally significant intrinsic activity. Moreover, such fluctuations are not random noise, but demonstrate temporal synchrony within widely distributed brain regions. Communication between neurons and neuronal ensembles is probably established to a large extent through the synchronization of their activity [3]. Network analysis of these datasets is helpful for uncovering the organizational principles that underlies information process in the brain.

However, what can we extract about non-random organization patterns of information process in the brain? Graph theory-based network analysis techniques are employed to characterize brain activity data derived from young adults. Functional brain networks are regarded as graph representations of brain activity, where the nodes represent anatomically defined regions and the edges describe their functional connectivity between each pair.

2 Datasets and Network Construction

The experimental data for network construction were acquired from 33 healthy volunteers (17 males, mean age: 21.6 ± 2.23 (SD), right-handed) on a 3.0 Tesla Philips Achieva MR imaging system. Images of the whole brain using an echo-planar imaging (EPI) sequence were collected in 36 slices (TR = 2000 ms, TE = 30 ms, flip angle = 80°, FOV = 23 cm, matrix = 64 × 64, 4 mm thickness and 0 mm gap). Images preprocessing and further analysis are performed including slice timing, head motion correction, spatial normalization and smoothing with an 8 mm Gaussian kernel, full width at half maximum. Finally, temporal band-pass filtering (between 0.01 and 0.08 Hz) is performed in order to reduce the effects of low-frequency drift and high-frequency noise. Thus, the dataset available for network analysis comprise thirty-three multivariate time series.

In this paper, we investigate the topological characters of brain networks derived from resting-state functional magnetic resonance imaging. Detailed steps include: (1) using a used anatomical automatic labeling atlas [4, 5] to parcellate the whole brain into 90 cortical and sub-cortical regions as network nodes, (2) estimating functional relationship between network nodes by partial correlation analysis of 90 regional time series, (3) generating a correlation matrix (90 × 90) by compiling all coefficients between nodes and applying a network density threshold to each element to produce a binary adjacency matrix or undirected graph, (4) calculating the network parameters of interest in this graphical model of a brain network.

3 Experimental Results

Figure 1 shows a maximum spanning tree derived from the mean matrix across 33 participants using Kruskal's algorithm [6], which connects all nodes ($N = 90$) such that the sum of their 89 connectivity coefficients is maximal. Each vertex is first regarded as a separate tree, and then extra edges are added in order of the decreasing correlation coefficients if those edges connect two different trees, until all nodes form a maximum spanning tree. The resulting connectivity skeleton is represented using a procedure known as the Kamada-Kawai algorithm [7] implemented in Network Workbench Tool (http://nwb.slis.indiana.edu). The algorithm generates the layout in an esthetically pleasing way, and positions the network nodes in two dimensional spaces so that all the edges are of more or less equal length and there are as few crossing edges as possible. As shown in Fig. 1, most pairs of inter-hemispheric homogenous regions are tightly coupled, and two major sub-networks with intrinsic functional activity (the default brain activity and attention-related regions) seem to be at the center of the network layout, whose nodes are highlighted in black.

A maximum spanning tree can be used as a sparse representation of whole-brain networks. However, tree is by definition acyclic and its edges do not form clusters. Accordingly, we grow the tree by adding extra edges in order of the decreasing coefficients. The corresponding binary adjacency matrices are obtained for further mesoscale analysis. The brain network comprising about 200 edges or 5 % of the possible $N(N-1)/2$ edges (4005) is selected for modularity analysis by Newman's spectral optimization algorithm [8]. Modularity is used to evaluate the goodness of a partition of a graph in terms of a modularity matrix and its eigenvector associated with the largest positive eigenvalue. Thus, the module identification problem becomes a modularity optimization problem. The brain network is supposed to consist of n nodes connected by m edges. The index vector s represents any partition in two groups, whose component s_i is +1 if vertex i is in one group and -1 if it is in the other group. Modularity function is expressed as follows:

$$Q = \frac{1}{4m} s^T B s. \tag{1}$$

The modularity can be optimized using the eigenvalues and eigenvectors of a special matrix, the modularity matrix, whose elements are

$$B_{ij} = A_{ij} - \frac{k_i k_j}{2m}, \tag{2}$$

where k_i and k_j are the degrees of the nodes. Like a Laplacian matrix, B has always an eigenvector (1, 1, 1 …) with eigenvalue 0, because the elements of each of its rows and columns sum to zero. The algorithm generates a modularity matrix with an associated modularity score. The modularity score ($Q = 0.52$) of the brain network is significantly higher ($P < 0.05$) than the mean value of the equivalent

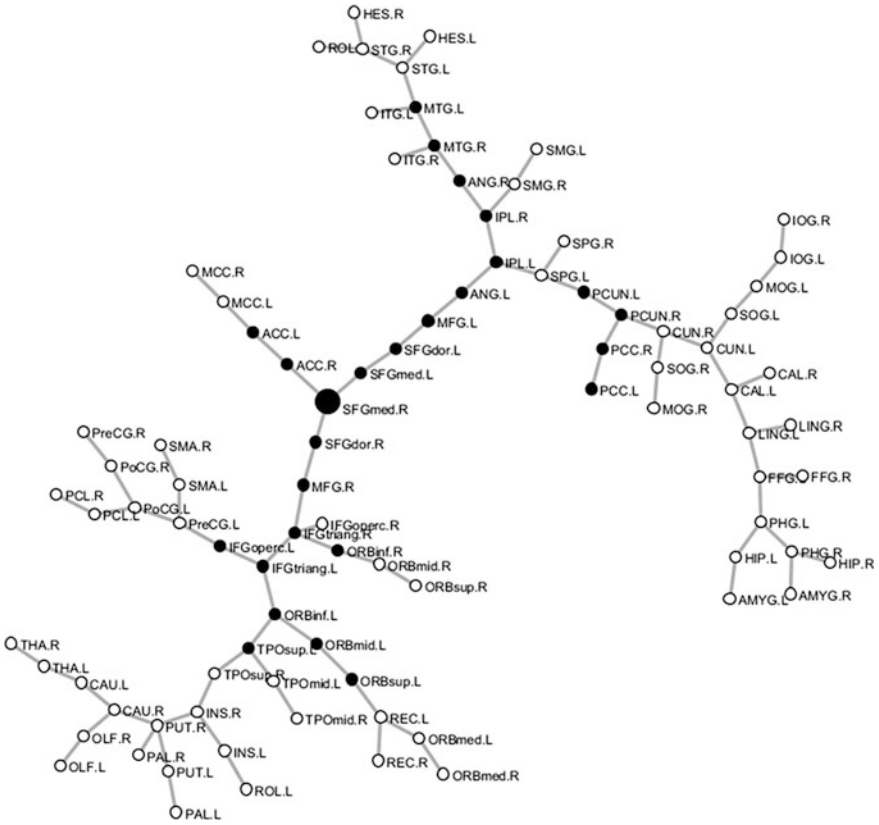

Fig. 1 The whole-brain network layout illustrated by a maximum spanning tree. Ninety regional nodes defined by automated anatomical labeling template can be seen in the Ref. [4]

random networks ($Q_{\text{rand}} = 0.39$). Figure 2 shows six connected modules in the brain network, whose spatial distribution of these identified modules is closely associated with some biologically meaningful functional systems of the brain including attention control in prefrontal areas, visual processing module, temporo-insular zones, limbic/paralimbic and subcortical systems, temporal gyrus, and default system in fronto-cingulo-parietal. Notably, the modular detection algorithm does not take into account prior knowledge of the anatomical locations and functions of brain regions.

To further characterize how each module is organized, we determine the roles of network nodes and edges by their connectivity patterns. We first distinguish nodes that play the role of hubs in their own modules from those that are non-hubs by the intra-modular degree z-score. The z-score of a node is defined as

$$z_i = \frac{k_i(m_i) - \overline{k}(m_i)}{\sigma_{k(m_i)}}, \tag{3}$$

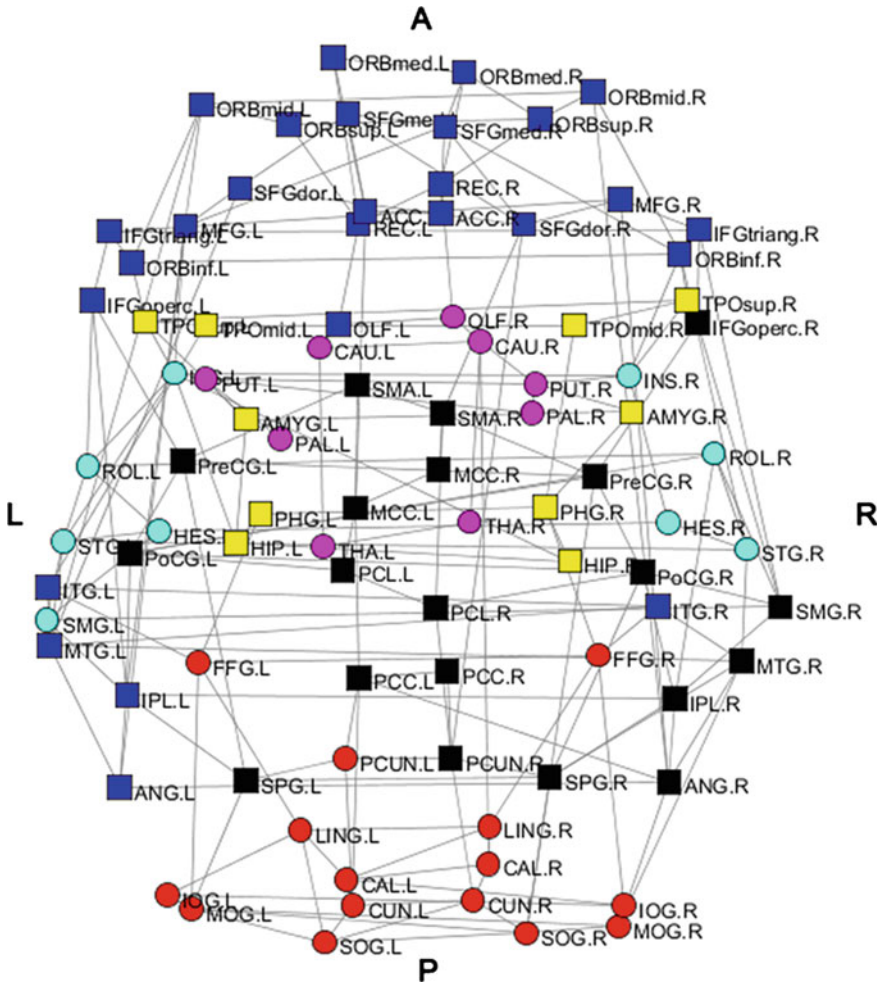

Fig. 2 Module structure of brain networks. *P* posterior, *L* left, *R* right

where m_i is the module containing node i, $k_i(m_i)$ is the number of links of node i to other nodes in its module m_i, and $\overline{k}(m_i)$ and $\sigma_{k(m_i)}$ are the respective mean and standard deviation of the within-module m_i degree distribution. Two nodes with the same z-score play different roles if one is connected to several nodes in other modules and another is not.

We then classify nodes based on their connections to nodes in other modules than their own. The participation coefficient P_i of node i is computed as

$$P_i = 1 - \sum_{m \in M} \frac{k_i(m_i)^2}{k_i}, \tag{4}$$

where M is the set of modules, and $k_i(m_i)$ is the number of links between i and all nodes in module m_i, and k_i is the total degree of node i. Thus the participation coefficient of a node tends to one if its links are uniformly distributed among all the modules and zero if all links are within its own module.

We assign four roles to the nodes of the brain network. We first classify nodes with $z \geq 1$ as module hubs and nodes $z < 1$ as non-hubs. Both hub and non-hub nodes are then more finely characterized by using the values of P_i, and the hub nodes are further subdivided into R1 connector hubs ($P_i > 0.3$) and R2 provincial hubs ($P_i < 0.3$), and non-hub nodes are divided into R3 connector non-hubs ($P_i > 0.3$) and R4 peripheral non-hubs ($P_i < 0.3$).

Figure 3 shows the distribution of the roles obtained from the brain network over the z–P parameter space. Most of the nodes (76/90; 84 %) can be assigned as non-hubs. The anatomical distribution of the node roles is depicted in Fig. 4. Interestingly, these parameter distributions could help us to characterize the complex statistical properties and heterogeneity of edges and nodes.

We further characterize global roles of an individual node or edge in the brain network by calculating betweenness centrality [9]. The betweenness centrality of a node can be defined as follows:

$$N_i = \sum_{s \neq t, s \neq i, t \neq i} \frac{g_{st}(i)}{g_{st}}, \tag{5}$$

where g_{st} is the total number of all shortest paths from node s to node t, and g_{st}(i) is the number of shortest paths from node s to node t that pass through the node i. Betweenness measures the ability of a node over information flow between other

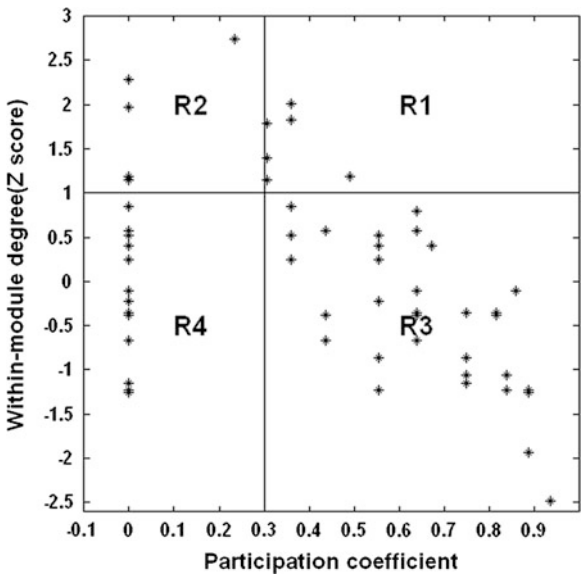

Fig. 3 Regional node roles

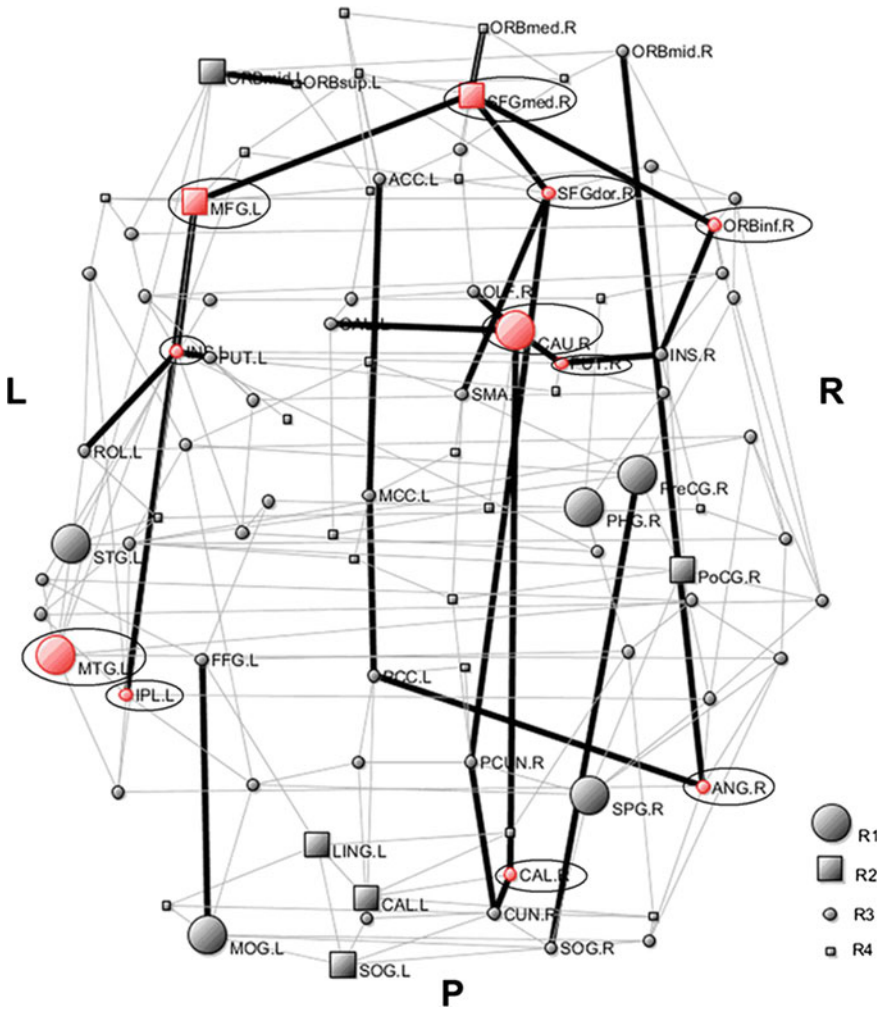

Fig. 4 The spatial distribution of hubs and bridges in the brain network

nodes in the whole-brain network. The brain regions with high betweenness ($N_i >$ mean + SD) are considered global hubs in the brain network. The identified hub regions include 6 association cortex regions, 2 limbic/paralimbic cortex regions, 1 primary motor cortex region and 2 subcortical regions. Red nodes in Fig. 4 are used to represent the global hubs. The roles of these global hub regions in multiple highly integrated functional systems have been previously reported [10]. Similarly, edges are identified as the bridges in the brain network, if their edge betweenness [9] values are at least one standard deviation (SD) greater than the average edge betweenness of the network. Thick lines in Fig. 4 show the bridge connections between the two brain regions. It should be noted that most of

the hub nodes (10 of 11) are linked with the identified bridge edges, suggesting there is a tendency for these hub nodes and bridge edges to converge on functionally integrated core system.

4 Discussion

In this paper, we measure brain activity and employ network analysis approach based on graph theory to reveal functional organization in young adults' brain. This approach, unlike previous conventional functional imaging studies, quantitatively assesses functionally integrated core at various levels. At a global level of tree analysis, most brain areas of the default and attention-related network activity are distributed at the center of the network layout and form important functional hubs of information processing at rest to support the brain's moment-to-moment responses to the external world [11].

At a mesoscale level of modularity analysis, our identified module structure of brain networks is closely associated with some biologically meaningful functional systems of the brain, and the non-random structure with a balanced interplay between local segregation and global integration of distant anatomofunctional brain regions can contribute to efficiency of parallel information transfer at low physical connection cost [12]. Moreover, modularity has the advantage of allowing evolutionary adaptation of one functional subsystem, without risking loss of function in others [13].

At individual node or edge level, we found hub nodes and bridge edges of brain networks had a tendency to converge on functionally integrated core system or rich-club organization [14], indicating playing key roles in integration of information process in the brain [15].

5 Conclusion

In summary, we have applied graph theory-based network analysis techniques to study the organization of intrinsic spontaneous information process in the young adults' brain at rest. Several specific non-random network organization patterns including whole network layout and modular structure have been found. This non-randomness may be associated with the brain's moment-to-moment responses to the external world. Many applications of this work to brain dysfunction will be performed in our future work.

Acknowledgments The authors thank the Institute of Neuroinformatics staffs for assistance with data collection. This work was supported by National Natural Science Foundation of China 60971096, 2012CB518200.

References

1. Seung HS (2011) Neuroscience: towards functional connectomics. Nature 471:170–172
2. Costa LdF, Oliveira ON, Travieso G, Rodrigues FA, Villas Boas PR, Antiqueira L, Viana MP, Correa Rocha LE (2011) Analyzing and modeling real-world phenomena with complex networks: a survey of applications. Adv Phys 60:329–412
3. Zhou C, Zemanová L, Zamora-Lopez G, Hilgetag CC, Kurths J (2007) Structure–function relationship in complex brain networks expressed by hierarchical synchronization. New J Phys 9:178
4. Liu Y, Liang M, Zhou Y, He Y, Hao Y, Song M, Yu C, Liu H, Liu Z, Jiang T (2008) Disrupted small-world networks in schizophrenia. Brain 131:945–961
5. Tzourio-Mazoyer N, Landeau B, Papathanassiou D, Crivello F, Etard O, Delcroix N, Mazoyer B, Joliot M (2002) Automated anatomical labeling of activations in SPM using a macroscopic anatomical parcellation of the MNI MRI single-subject brain. Neuroimage 15:273–289
6. Kruskal JB (1956) On the shortest spanning subtree of a graph and the traveling salesman problem. Proc Am Math Soc 7:48–50
7. Kamada T, Kawai S (1989) An algorithm for drawing general undirected graphs. Inf Process Lett 31:7–15
8. Newman MEJ (2006) Modularity and community structure in networks. Proc Natl Acad Sci U S A 103:8577–8582
9. Freeman L (1977) A set of measures of centrality based on betweenness. Sociometry 40:35–41
10. Tomasi D, Volkow ND (2010) Functional connectivity density mapping. Proc Natl Acad Sci U S A 107:9885–9890
11. Fox MD, Corbetta M, Snyder AZ, Vincent JL, Raichle ME (2006) Spontaneous neuronal activity distinguishes human dorsal and ventral attention systems. Proc Natl Acad Sci U S A 103:10046–10051
12. Bullmore E, Sporns O (2009) Complex brain networks: graph theoretical analysis of structural and functional systems. Nat Rev Neurosci 10:186–198
13. Kashtan N, Alon U (2005) Spontaneous evolution of modularity and network motifs. Proc Natl Acad Sci U S A 102:13773–13778
14. Zhou S, Mondragón RJ (2004) The rich-club phenomenon in the internet topology. IEEE Commun Lett 8:180–182
15. Bullmore E, Sporns O (2012) The economy of brain network organization. Nat Rev Neurosci 13:336–349

Reconfigurable Control Allocation of Multi-Surfaces Aircraft Based on Improved Fixed Point Iteration

Kejun Bi, Weiguo Zhang, Chengzhi Chi and Jingkai Zhang

Abstract For the real-time requirement of reconfigurable control allocation problem in the field of multi-surfaces aircraft, the control allocation scheme based on max direction derivative increment (MDDI) fixed point (FXP) iteration is proposed. The increment update for current iteration along the MDD and the design steps are given. Moreover, the convergence of the improved method is also proved. Comparisons of different methods are simulated in multi-surfaces aircraft model. The simulation results show the rapidity of MDDIFXP method compared with the original one and the effectiveness of the method in solving reconfigurable control allocation problem of multi-surfaces aircraft.

Keywords Multi-surfaces aircraft · Control allocation · Fixed point arithmetic · Pseudo-inverse method · Reconfiguration · Improvement

1 Introduction

Due to the increasing requirements on the reliability, maneuverability, and survivability of modern aircraft, control surfaces are no longer limited to three conventional ones: aileron, elevator, and rudder, and many more control surfaces have been introduced. With these redundant control surfaces, the problem of allocating these controls to achieve the desired moments becomes non-unique and far more complex [1]. So effective control allocation schemes has been studied following the work of Durham [2] to distribute the required control moments over the control surfaces [3]. In particular, in the case of control surface failures or damages [4], an effective and rapid reallocation of the control surface deflections

K. Bi (✉) · W. Zhang · C. Chi · J. Zhang
School of Automation, Northwestern Polytechnical University, Xian 710072, China
e-mail: chengzhi.chi@gmail.com

F. Sun et al. (eds.), *Foundations and Practical Applications of Cognitive Systems and Information Processing*, Advances in Intelligent Systems and Computing 215,
DOI: 10.1007/978-3-642-37835-5_5,

with the remaining healthy control surfaces is needed in order to maintain acceptable performance, and this requirement asks for the so-called reconfigurable control allocation or control reallocation technique, which is a necessary part of the reconfigurable (or fault tolerant) flight control systems, and that is important for continuing flight mission or safe landing.

Control allocation is the problem of distributing the control requirements among redundant control surfaces for satisfying the optimized objectives within their range of position and rate limits [5–7]. A comparison of different control allocation methods are documented in [8]. However, the fault-tolerant control reallocation problem has not been well investigated except a few notable works presented in [1, 9–11].

In this paper, we propose control allocation scheme based on an improved fixed point (FXP) algorithm, which is evaluated in ADMIRE aircraft model. The paper is organized as follows: The improved FXP algorithm max direction derivative increment fixed point (MDDIFXP) is presented in Sect. 2. MDD can be achieved by computing the derivative along all directions of current iteration, and the increments of the former and current iteration are taken as the update for current iteration along the MDD, also, the convergence of the method is proved. Simulations of the control allocation scheme compared to different methods in the normal situation and fault-tolerant reconfiguration in the presence of different partial control surface faults are presented in Sect. 3. Finally, conclusions and future work are described in Sect. 4.

2 MDDIFXP Based Quadratic Programming

The control allocation problem studied in the paper is achieved by solving a quadratic programming (QP) problem which involves the minimization of a quadratic cost function subject to both equality and inequality constraints. In this section, we will first discuss the establishment of FXP and MDDIFXP method for QP problem. We then prove the convergence of MDDIFXP method.

2.1 FXP Method

The optimal control input is given by the solution to a weighted optimization problem [8]:

$$\min_{u} \quad J = \|W_u(u - u_d)\|_2^2 + \gamma \|W_v(Gu - v)\|_2^2 \tag{1a}$$

$$\text{Subject to } \underline{u} \le u \le \bar{u} \tag{1b}$$

Here u_d is the desired control input and v is virtual control input, W_u and W_v are weighting matrices. G is control effectiveness matrix, $\gamma > 0$ is the weighting factor. Equation (1a) can be rewritten by:

$$\begin{aligned} J =& (u-u_d)^T W_u (u-u_d) + \gamma (Gu-v)^T W_v (Gu-v) \\ =& u^T W_u u - u^T W_u u_d - u_d^T W_u u + u_d^T W_u u_d + \gamma \big(u^T G^T W_v G u \\ & - u^T G^T W_v v - v^T W_v G u + v^T W_v v \big) \\ =& u^T \big(W_u + \gamma G^T W_v G \big) u + u^T \big(-2 W_u u_d - 2\gamma G^T W_v v \big) \\ & + u_d^T W_u u_d + \gamma v^T W_v v \\ =& \frac{1}{2} u^T T u + u^T d + r \end{aligned}$$

Here $T = 2W_u + 2\gamma G^T W_v G, \quad d = -2W_u u_d - 2\gamma G^T W_v v, \quad r = u_d^T W_u u_d + \gamma v^T W_v v$.

Because r is a constant value in a sampled cycle, so the solution will be the same if we remove r from the cost function. Then, the control allocation problem based on QP can be reduced to

$$\min_u \quad J = \tfrac{1}{2} u^T T u + u^T d \tag{2a}$$

$$\text{Subject to } \underline{u} \le u \le \bar{u} \tag{2b}$$

When $u_d = 0$, Eq. (1) can be rewritten by [8, 9]:

$$J = \frac{1}{2} \left[(1-\varepsilon)(Gu-v)^T Q_1 (Gu-v) + \varepsilon u^T Q_2 u \right] \tag{3a}$$

$$\text{Subject to} \quad \underline{u} \le u \le \bar{u} \tag{3b}$$

Here $Q_1 = W_v^T W_v > 0, \quad Q_2 = W_u^T W_u > 0, \quad \varepsilon = (1+\gamma)^{-1}$.

Suppose $u = (u_1, \ldots, u_m)^T \in R^m$, which satisfies

$$s_i(u) = \begin{cases} \underline{u}, & u_i \le \underline{u} \\ u_i, & \underline{u} < u_i < \bar{u}, \\ \bar{u}, & u_i \ge \bar{u} \end{cases} \quad i = 1, 2, \ldots, m \tag{4}$$

$s(\cdot)$ is the vector saturator, then the algorithm becomes

$$u = s\left[(1-\varepsilon)\omega G^T Q_1 v - (\omega T - I) u \right] \triangleq f(u) \tag{5}$$

Here $\omega = \|T\|_F^{-1} = (tr(T^T T))^{-\frac{1}{2}}$, which decides the step length. $T = (1-\varepsilon) G^T Q_1 G + \varepsilon Q_2, \varepsilon \in (0, 1)$.

So the iterative formula of FXP method is listed as follows:

$$u^{k+1} = f\left(u^k\right) (k = 0, 1, \ldots, N) \tag{6}$$

2.2 MDDIFXP Method

The principle of MDDIFXP is improvement of increment update for current iteration along the MDD, in order to fasten the process of iteration.

Definition 1 Suppose that $f : R^n \to R^n$ is a continuous function, and for the unit vector $e_i = \left(\delta_1^i, \ldots, \delta_n^i\right)^T$, $\delta_i^i = 1$, $\delta_j^i = 0 \quad (j \neq i, i = 1, 2, \ldots, n)$, the derivative of function $f(u0 + te_i)$ at point $t = 0$ (if it exists) is named as the first partial derivative of $f$at point $u0$ with respect to u_i $(i = 1, 2, \ldots, n)$. For $\forall i = 1, 2, \ldots, n$, if the first partial derivative of f at point u with respect to u_i exists, then the gradient of $f(u)$ at point u is defined as follows:

$$\nabla f(u) = \left(\frac{\partial f(u)}{\partial u_1}, \frac{\partial f(u)}{\partial u_2}, \ldots, \frac{\partial f(u)}{\partial u_n}\right)^T \tag{7}$$

Definition 2 For $u0 \in R^n$, $d \in R^n$, the directional derivative of f at point $u0$ with respect to direction d is defined as follows:

$$\frac{\partial f(u0)}{\partial d} = \lim_{t \to 0^+} \frac{f(u0 + td) - f(u0)}{t} \tag{8}$$

Suppose $Df(u0; d)$ is the directional derivative of f at point $u0$ with respect to direction d. When the first partial derivative of f is continuously differentiable, the directional derivative can be computed by:

$$Df(u0; d) = \nabla f(u0)^T d. \tag{9}$$

Then, the gradient of FXP function $f(u)$ at point u is defined as:

$$\overset{f}{\nabla} f(u) = \left(\frac{f(u + \Delta t e_1) - f(u)}{\Delta t}, \ldots, \frac{f(u + \Delta t e_n) - f(u)}{\Delta t}\right)^T. \tag{10}$$

Here, the f at the top left corner of the left side of the equation means FXP. Δt is the iteration interval, and which is set to 1 normally. So the directional derivative of f at point $u0$ with respect to direction d can be computed by:

$$Df(u0; d) = \overset{f}{\nabla} f(u0)^T d \tag{11}$$

Then, MDD is the unit vector e_i satisfies

$$\text{Max}\left[\frac{f(u0 + \Delta te) - f(u0)}{\Delta t}\right] \quad (i = 1, 2, \ldots, n) \tag{12}$$

Definition 3 For $u^k, u^{k+1} \in R^n$ and unit vector e_i, the increment of f at point u^{k+1} with respect to direction e_i is defined as:

$$\Delta f\left(u^{k+1};\, e_i\right) = \frac{f\left(u^{k+1} + \Delta t e_i\right) - f\left(u^{k+1}\right)}{\Delta t} - \frac{f\left(u^{k} + \Delta t e_i\right) - f\left(u^{k}\right)}{\Delta t} \tag{13}$$

MDDIFXP method takes the increments of the former and current iteration as the update of current iteration along the MDD, and the design steps are:

1. Compute $f\left(u^k\right)$, $f\left(u^{k+1}\right)$;
2. Compute $\overset{f}{\nabla} f\left(u^{k+1}\right)^T e_i (i = 1, 2, \ldots, n)$, take the unit vector e_i as the MDD vector e_M, which satisfies Max $\left[\frac{f\left(u^{k+1}+\Delta t e_i\right)-f\left(u^{k+1}\right)}{\Delta t}\right]$;
3. Compute $\Delta f\left(u^{k+1};\, e_M\right)$ and update $f\left(u^{k+1}\right) = f\left(u^{k+1}\right) + \Delta f\left(u^{k+1};\, e_M\right) e_M$;
4. Take $u^{k+2} = f\left(u^{k+1}\right)$ as the new iteration point, and compute $f\left(u^{k+2}\right), f\left(u^{k+3}\right)$;
5. If $k < K (K \in N)$ and $\left\| \overset{f}{\nabla} f\left(u^{k+1}\right) \right\| > \xi (\xi > 0)$, repeat step 1–4, or turn to basic FXP algorithm.

Note that the updated $f\left(u^{k+1}\right)$ should also satisfies constraint condition.

2.3 The Convergence of MDDIFXP Method

Before discussing the convergence of MDDIFXP algorithm, we introduce the convergence of basic FXP algorithm.

When the cost function is convex, every optimization algorithm should meet Kuhn-Tucker condition [12]. For convex programming, Kuhn-Tucker condition is the necessary and sufficient condition. And the necessary and sufficient condition of u^* is the solution to problem of positive definite quadratic programming is that u^* is the Kuhn-Tucker point [12]. From [13], we can see the solution to Eq. (5) is also the solution to Eq. (2), so FXP algorithm can solve the QP problem accurately [14]. Then, the convergence of basic FXP algorithm is proved.

Hence, u^* is the globally optimal solution to the control allocation QP problem. Suppose $\{u^n\}$ is the sequence of iterations for basic FXP algorithm, then the sequence should converge to u^*. According to the design steps of MDDIFXP algorithm, the improved algorithm changes only finite term of the sequence $\{u^n\}$; therefore, the convergence of the sequence is not changed. Further, due to the limit of sequence is unique, the iteration sequence of MDDIFXP converge to u^*.

3 Simulation and Performance Evaluation

3.1 MDDIFXP in Normal Control Allocation

ADMIRE aircraft model is used in the simulation, and the main data of simulation are listed as follow:

$$G = \begin{bmatrix} 0.7984 & -0.7984 & -4.5787 & -3.9413 & 3.9413 & 4.5787 & 2.6919 \\ 1.3841 & 1.3841 & -1.0906 & -1.7433 & -1.7433 & -1.0906 & 0.0046 \\ -0.3970 & 0.3970 & -0.2014 & -0.4256 & 0.4256 & 0.2014 & -1.6265 \end{bmatrix}$$

$$Wv = \begin{bmatrix} 1 & 0 & 0 \\ 0 & 10 & 0 \\ 0 & 0 & 12 \end{bmatrix}, \quad Wu = \mathrm{I}_7,\ \varepsilon = 1\mathrm{e}-3,\ K = 3,\ \xi = 1\mathrm{e}-3$$

The control surfaces are

$$u = [\,\delta_{c_l} \quad \delta_{c_r} \quad \delta_{\mathrm{roe}} \quad \delta_{\mathrm{rie}} \quad \delta_{\mathrm{lie}} \quad \delta_{\mathrm{loe}} \quad \delta_r\,]^T$$

And the ranges of limits are listed in Table 1.

Two series of virtual inputs are generated in the simulation, as showed in black line in Figs. 1 and 2. The algorithms such as Pseudo-inverse (PINV), Linear Programming (LP), Interior point (IP), FXP, and MDDIFXP are compared. All algorithms are simulated 100 times, and the average computation time is listed in Table 2.

According to Table 2, we can see that among all the methods, MDDIFXP has a minimum computation time for two series of virtual inputs except PINV. Moreover, for two series of virtual inputs, MDDIFXP saves 2.12 and 2.21 % of the computation time, respectively. Figures 1 and 2 show that the outputs can track the corresponding virtual inputs with MDDIFXP, and from Fig. 1, we can see the outputs cannot track the corresponding virtual inputs well with PINV. According to the above analyzing, rapidity of the MDDIFXP method compared with the original FXP is demonstrated.

3.2 MDDIFXP in Fault Reallocation

In the above section, we have verified the rapidity and effectiveness of MDDIFXP in normal control allocation. Then, we apply MDDIFXP method to the reconfigurable control allocation of multi-surfaces aircraft. In the following, two scenarios are simulated: (1) a floating fault to be occurred at 2.3 s in right inner elevon; (2) a 50 % of loss of control effectiveness to be occurred at 2 s in right outer elevon. It is assumed that the FDD information is available for control re-allocation, but with

Table 1 Ranges of limits of control surfaces

Control surface	Control variable	Minimum deflection (°)	Maximum deflection (°)	Maximum rate (°/s)
Canards	δ_{c_l}, δ_{c_r}	−55	25	50
Elevons	δ_{lie}, δ_{rie} δ_{roe}, δ_{loe}	−30	30	150
Rudder	δ_r	−25	25	100

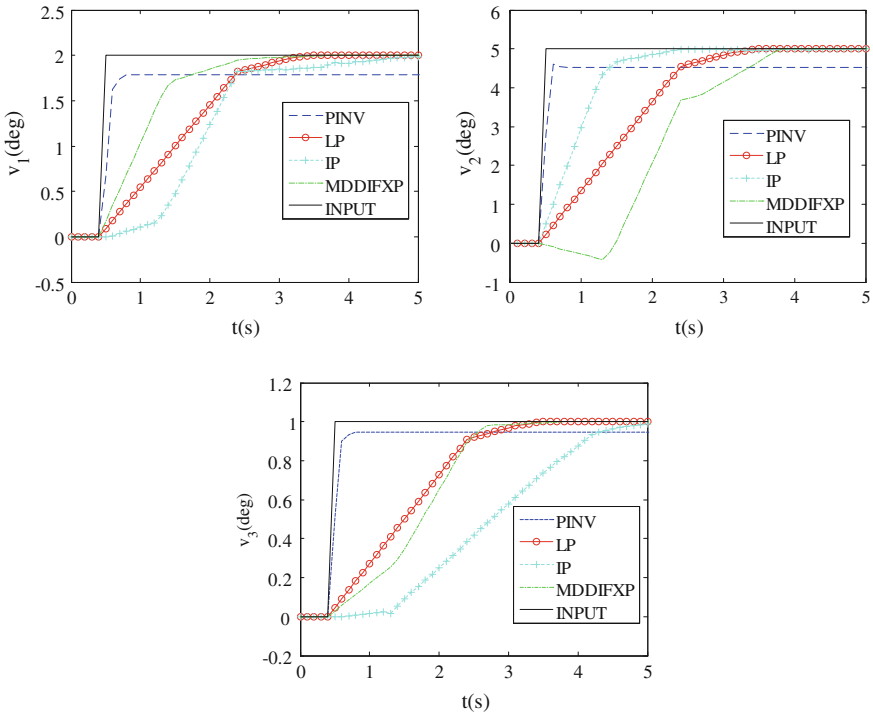

Fig. 1 Comparison of different methods on virtual input V_1

0.3 and 0.5 s FDD time delay simulated for floating fault and loss of control effectiveness fault control reconfiguration, respectively.

As shown in Figs. 3 and 4, without reconfiguration, the outputs cannot track the inputs. With reconfiguration, the reconfigured outputs track the inputs with zero steady-state error. Meanwhile, the effectiveness of the MDDIFXP method in the reconfiguration control allocation problem is indicated.

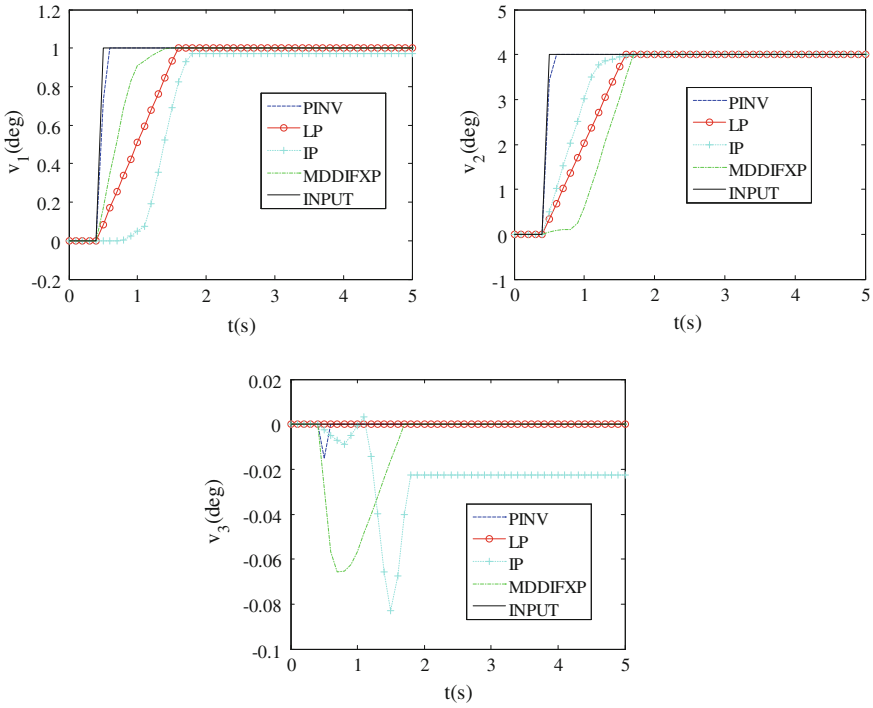

Fig. 2 Comparison of different methods on virtual input V_2

Table 2 Comparison of different algorithms

No	CPU computation time (s)				
	PINV	IP	LP	FXP	MDDFXP
1	0.0280	0.0522	0.4517	0.0519	0.0508
2	0.0295	0.0472	0.4506	0.0452	0.0442

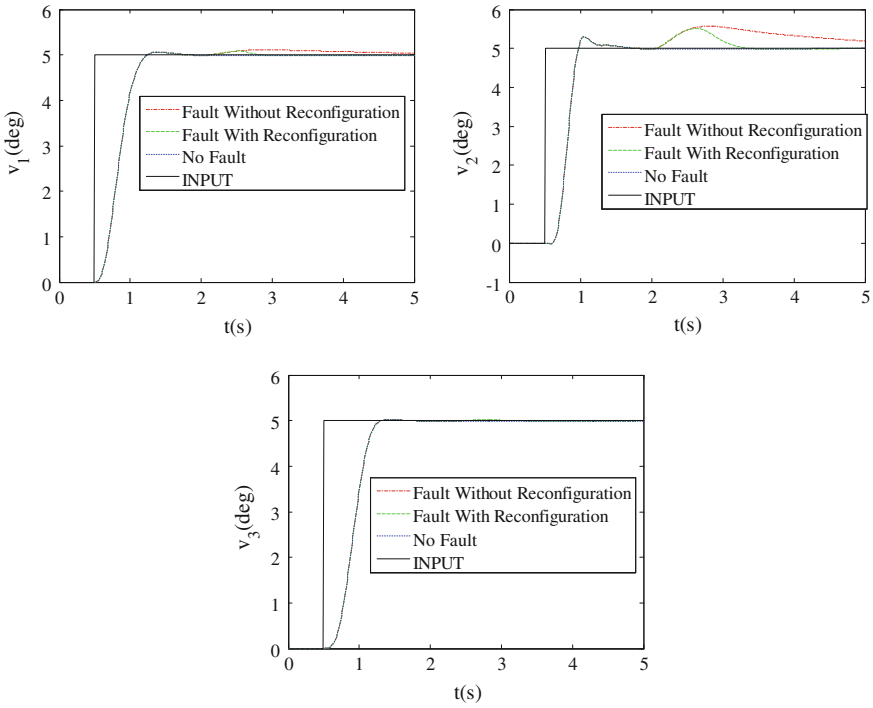

Fig. 3 Responses of virtual inputs with floating fault

4 Conclusion and Future Work

In this paper, an improved FXP method MDDIFXP is applied to control allocation and fault reallocation in ADMIRE model. The design steps of MDDIFXP are given, among which, the increment update for current iteration along the MDD is discussed in detail. Moreover, the convergence of the method is also proved. The comparisons of different methods applied to ADMIRE model show the rapidity of the MDDIFXP method, and the effectiveness of MDDIFXP method in the reconfiguration control allocation problem is also verified. Future work includes incorporation of FDD schemes in the ADMIRE model and further investigation on the conditions of step 5 in order to improve the performance of MDDIFXP method.

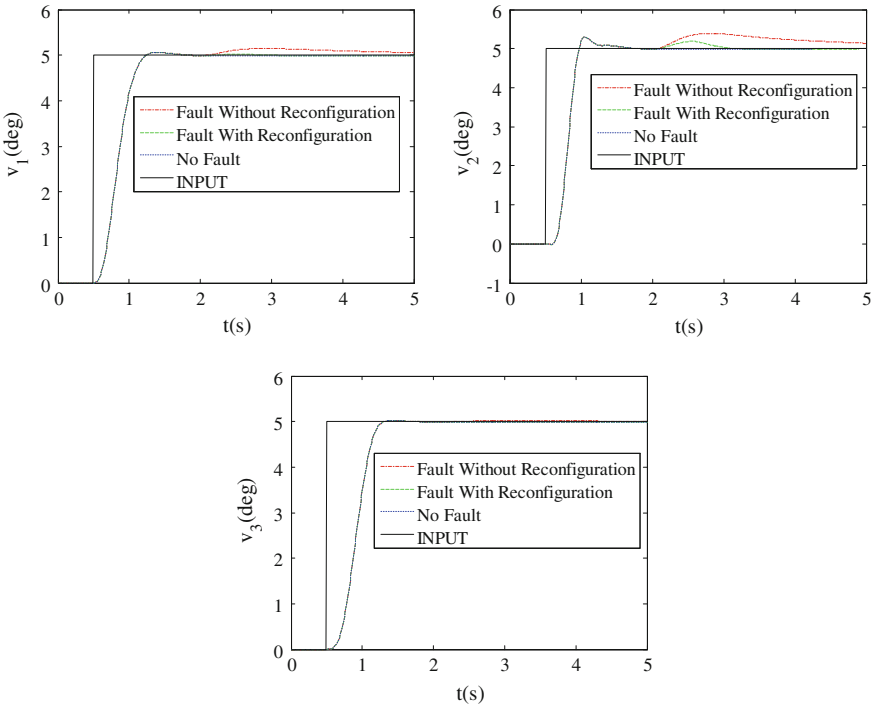

Fig. 4 Responses of virtual inputs with loss of control effectiveness

References

1. Zhang YM, Suresh VS, Jiang B, Theilliol D (2007) Reconfigurable control allocation against aircraft control effector failures. In: IEEE international conference on control applications. IEEE Press, New York, pp 1197–1202
2. Durham WC (1993) Constrained control allocation. J Guidance Control Dyn 16:717–725
3. Shi JP, Zhang WG, Li GW, Liu XX (2010) Research on the allocation efficiency of redistributed pseudo-inverse algorithm. Scientia Sinica (Informationis) 40:519–525
4. Lombaerts T, Schravendijk MV, Chu P, Mulder JA (2011) Adaptive nonlinear flight control and control allocation for failure resilience. Adv Aerosp Guidance, Navig Control I:41–53
5. Schofield B, Hägglund T (2008) Optimal control allocation in vehicle dynamics control for rollover mitigation. In: American control conference. IEEE Press, New York, pp 3231–3236
6. Johansen TA, Fuglseth TP, Tøndel P, Fossen TI (2008) Optimal constrained control allocation in marine surface vessels with rudders. Control Eng Pract 16:457–464
7. Ahmadia J, Khaki-Sedighb A, Ohadia A (2012) Robustification of input redundant feedback systems using robust actuator weighting in the control allocation problem. Int J Control 85:1380–1400
8. Härkegård O (2003) Backstepping and control allocation with applications to flight control. Linköping University, Linköping
9. Burken JJ, Lu P, Wu ZL, Bahm C (2001) Two reconfigurable flight-control design methods: robust servomechanism and control allocation. J Guidance Control Dyn 24:482–493

10. Davidson JB, Lallman FJ, Bundick WT (2001) Integrated reconfigurable control allocation. In: AIAA guidance, navigation and control conference, American Institute of Aeronautics and Astronautics, Alexander, pp 1–11
11. Omerdic E, Roberts G (2004) Thruster fault diagnosis and accommodation for open-frame underwater. Control Eng Pract 12:1575–1598
12. Huang HX, Han JY (2006) Mathematical programming. Tsinghua University Press, Beijing
13. Wang J, Longoria RG (2009) Coordinated and reconfigurable vehicle dynamics control. IEEE Trans Control Syst Technol 17:723–732
14. Lu P (1996) Constrained tracking control of nonlinear systems. Syst Control Lett 27:305–314

Particle Filter-Based Object Tracking and Handover in Disjoint View Multi-Cameras

Xiaoyan Sun, Faliang Chang and Wenhui Dong

Abstract In intelligent video surveillance, multiple cameras, even a distributed network of video sensors, have to be employed to monitor activities over a complex area nowadays. Hence, the continuous object tracking across multiple cameras and object handover between adjacent cameras is urgently needed, in which many appearance cues and spatial–temporal information can be employed. This paper fuses the spatial–temporal cues with appearance cues into a particle filter to handle the camera handover with multiple cameras having non-overlapping view. The spatial–temporal cues, including source and sink regions, their transition probabilities, and transition time among adjacent regions, are learned offline. Then a spatial–temporal progressive matching scheme using particle filter is proposed to deal with camera handover among adjacent cameras. In particle filter matching course, the commonly used appearance cue, i.e. the histogram in HSV color space is used. Once an object enters into sink region, we first continuously scatter particles in source regions related to this sink region according spatial–temporal information until the object emergence detected, and secondly, based on the particle weights of every source region, adjust their particle numbers till the camera handover is successfully completed. Encouraging experiment results show the efficiency of this scheme.

Keywords Multi-camera surveillance · Camera handover · Particle filter · Spatial–temporal information

X. Sun · F. Chang (✉) · W. Dong
School of Control Science and Engineering, Shandong University, Shandong, China
e-mail: flchang@sdu.edu.cn

X. Sun
e-mail: sxy@sdjzu.edu.cn

X. Sun
School of Computer Science and Technology, Shandong Jianzhu University, Jinan, China

F. Sun et al. (eds.), *Foundations and Practical Applications of Cognitive Systems and Information Processing*, Advances in Intelligent Systems and Computing 215,
DOI: 10.1007/978-3-642-37835-5_6, © Springer-Verlag Berlin Heidelberg 2014

1 Introduction

Intelligent video surveillance has been one of the most active research areas in computer vision, with a wide variety of applications both in public and private environments, such as homeland security, crime prevention, traffic control, accident prediction and detection, and monitoring patients, elderly and children at home. These applications require monitoring indoor and outdoor scenes of airports, train stations, highways, parking lots, stores, shopping malls, and offices [1, 2]. Since a single camera has a limited field of view, multiple cameras, even a distributed network of video sensors, have to be employed to monitor activities over a complex area nowadays. Hence the continuous object tracking across multiple cameras and consistent labeling of objects between adjacent cameras is urgently needed. Continuously tracking objects across cameras and consistent labeling of objects between adjacent cameras is usually termed as "object handover." The objective of object handover is to maintain the identity of moving objects when they are traveling from one camera to another. More specifically, when an object appears in one camera, we need to determine whether it has previously appeared before in other cameras or is a new object [3]. Moreover, it is usually not feasible to completely cover large areas with cameras having overlapping views due to economic and/or computational reasons. Thus, in realistic scenarios, the system should be able to handle multiple cameras with non-overlapping fields of view. In this paper, we use particle filter to solve object handover with multiple cameras having non-overlapping fields of view.

Possible cues for tracking across cameras include appearance information and spatial–temporal information. Thus, existing algorithms of camera handoff can be classified as: (1) Camera handover based on environment information, such as dealing with the handoff problem based on 3D environment model and calibrated cameras [4], tracking objects on a single global ground plane [5], or based on the homography between camera views [6], the limits of fields of view to establish correspondence between objects in multiple cameras [7]. All these handoff methods need either the common fields of view or camera calibration, which restricts their applications. (2) Camera handoff based on object model. Appearance is the inherent feature of object, so using one cue or multiple cues of object to construct the object model is a more popular method of camera handoff, especially in cases where spatial–temporal reasoning is not feasible or accurate [8]. The most widely used cues are spatial position, shape, color, intensity and motion. A lot of research work has been done on this field only using visual information of appearance to associate objects, which can be named as object re-identification [9, 10]. However, the appearance cues are easily fouled by many factors, such as illumination, view angles, object deformation, etc. (3) Hybrid methods. Combining appearance information with spatial–temporal information into Bayesian theory or other fusion methods is more common since these two cues have their own defects and merits. [11] integrates spatial position, shape, and color information to track object blobs in single camera tracking, calibrates two fixed cameras using five

coplanar control points, then tracks objects across them using Extended Kalman Filter (EKF) to handle occlusion. [12, 13] learn the spatial–temporal relationship of non-overlapping cameras and the appearance relationship of objects, then track them, while the computation speed is slow for learning [14] using a map of the surveillance area, which provides information about possible path trajectories across the non-overlapping region in particle filter to help track prediction when the subject leaves the field of view of a camera and enters another camera.

In order to solve the camera handoff of multiple cameras with disjoint view, a camera handoff method using particle filter is proposed in this paper. We integrated appearance information with spatial–temporal information to label consistent objects in multiple cameras. The spatial–temporal information includes the source, sink regions among cameras, their transition probabilities, and transition time. In this paper, these spatial–temporal cues are learned offline. Based on these spatial–temporal cues particles are sampled and adapted till the correct camera handover is found. Histogram in HSV color space is used to compute the fitness of particle. This algorithm is called particle filter handover. The work most similar with ours is [14], who also use particle filter to resolve the problem of within field of view visual tracking and track prediction when targets leave the field of view of any camera; however, they do not involve the spatial–temporal cues, and their applied environment is restricted in in-house scene.

The remainder of the paper is organized as follows: Section 2 introduces our tracking initialization and intra-camera object detection and tracking, Sect. 3 discusses the camera handover scheme based on particle filter, experiments results are given in Sects. 4, 5 conclude the paper.

2 Intra-camera Object Detection and Tracking

Tracking objects continually across cameras involves mainly two parts: Intra-camera object tracking and inter-camera tracking. The first, tracking objects within a camera view is the basic following process, so we discuss our tracking initialization and intra-camera object detection and tracking scheme in this section.

2.1 Tracking Initialization

Tracking initialization has been little investigated although it is very important. Most works set the initial target by drawing a rectangle to enclose the object in the first frame. Our initialization can realize an automatic target setting, in which one can directly input the description of target, for example, “a person dressed in red shirt and black pants,” or else one can set the target by friendly man–machine interface, only using drawing or filling. The reason we do this is because we first detect a moving foreground, and then find the assigned object in all moving blocks

using color matching. When comparing the color of moving objects with that of assigned target, we quantified the HSV color space into 53 pieces based on fussy logic [15] and named them like Joost [16]. Hue slice is quantified into 12 pieces defined as: red, orange, yellow, green and yellow, green, blue, cyan, blue, purple, magenta, pink, and red. Saturation S is divided into three parts, taking green for example, the three parts are: white, light green, and green. Value V is divided into three parts, also taking green for example, the three parts are: black, dark green, green. If saturation S is less than the threshold range of 0.16, all the colors are degenerated to grayscale, so this region is quantified alone to five parts: black, dark gray, gray, light gray, and white. Thus the HSV color space is quantified as 12 * 2 * 2 + 5 = 53 sub-regions. Considering the vagueness of color border, we use Trapezium membership function in fuzzy quantification.

2.2 Particle Filter-Based Intra-camera Object Tracking

Once the original target is determined, particle filter is used to track the object in single camera. The principle of particle filter is derived from the sequential Monte Carlo method [17] that recursively generates random measurements to approximate the distribution of unknown variables. Particle filter technique has proved to be robust and is widely used in many applications, especially object tracking [1, 18]. The principle of particle filter-based tracker is maintaining a probability distribution over the state (location, scale, etc.) of the object being tracked [18]. Particle filters represent this distribution as a set of weighted particles. In general, tracking using cameras is a nonlinear problem, thus the dynamic model is expressed as (1)

$$\begin{aligned} x_k &= f_k(x_{k-1}, u_k) \\ z_k &= h_k(x_k, v_k). \end{aligned} \tag{1}$$

In (1), k is time stamp, x_k is the state sequences, and z_k represents the observation measurement. The notation u_k and v_k are noise matrices. The first equation is the function that predicts the current state given the previous state and a noise vector. The second equation defines a measurement model, i.e., it determines how well the prediction of current state based on current observation. Hence particles can be denoted by $\left\{x_{1:k}^{(i)}, w_k^{(i)}\right\}_{i=1}^{N}$, where i is the particle index, N is the total number of particles, $x_{1:k}^{(i)}$, and $w_k^{(i)}$ represent the predicted state and weight of particle i. Each particle is a guess representing one possible location of the object being tracked. The set of particles contains more weight at locations where the object being tracked is more likely to be. This weighted distribution is propagated through time using a set of equations known as Bayesian filtering equations, and the trajectory of the tracked object can be drawn from the density $p(x_{0:k}|z_{1:k})$, which is expressed in (2)

$$p(x_{0:k}|z_{1:k}) \approx \sum_{i=1}^{N} w_k^{(i)} \delta\left(x_{0:k} - x_{0:k}^{(i)}\right). \tag{2}$$

Then the estimation of the state observation can be determined by taking the weighted mean of the particle set at each time step, denoted by (3), where $h(\cdot)$ is the observation of statement.

$$E(h(x_{1:k})) = \sum_{i=1}^{N} w_k^{(i)} h\left(x_{1:k}^{(i)}\right). \tag{3}$$

A general framework of particle filter algorithm can be described as:

1. Initialize: a particle set of N particles.
2. Prediction: for each particle using second order auto regressive dynamics in (4), where $\omega_{k-1}^{(i)}$ is the noise and $\omega_{k-1}^{(i)} \sim N(0, \sigma^2)$.

$$x_k^{(i)} - x_{k-1}^{(i)} = x_{k-1}^{(i)} - x_{k-2}^{(i)} + \omega_{k-1}^{(i)}. \tag{4}$$

3. Importance: weighting each particle based on current observation by histogram distance.
4. Resample: a process to maintain the diversity of all particles according to their re-normalized weights.

3 Camera Handover Based on Particle Filter

The objective of camera handover is to maintain the identity of moving objects when they are traveling from one camera to another, it is parallel with maintaining the identity of moving objects when they are traveling from one frame to another in certain extent, so we consider using particle filter in camera handover as in inter-frame tracking. When the object is traveling from one camera to another, although the sights and illuminations of cameras are quite different, the appearance of object remains consistent. For example, the color and texture of object considered as not changing excludes the impact of light, the velocity of subject remains constant in two adjacent cameras if the angle change of two cameras is small. Thus we employ a spatial–temporal progressive matching scheme in particle filter among adjacent cameras, which extracts the template and velocity of target in prior camera and fuses them into matching the next camera. First we learn the spatial–temporal relationship of camera network in Sects. 3.1, and 3.2 describes the algorithm of camera handover using particle filter.

3.1 Spatial–Temporal Information of Inter-camera

We learn the spatial–temporal relationship among adjacent cameras from video sequences of a long time. We group locations where objects appear (source region) and disappear (sink region) by k-means clustering, and the sources and sinks are represented by two-element Gauss distribution. The spatial transition probability and transition time of each pair of source and sink can be calculated by statistics. The spatial transition probability is defined as $P(S_k^i S_l^j)$, where S_k^i is the kth source region of camera i and S_l^j is the lth sink region (or exit zone) of camera j, which can be represented by a digraph in Fig. 1. Figure 1a shows the original sources and sinks, dark and bright ellipses represent source and sink, respectively, in one way. Figure 1b is the digraph, and Fig. 1c is the topology of cameras. In Fig. 1b, vertexes represent source and sink regions, verges represent the transition of source and sink, and the weight of verge is the transition probability of each pair of source and sink. The Transition time is represented by $P_{S_k^i S_l^j}(t)$. Each $P(t)$ is modeled as a mixture of Gaussian distribution. In this paper, we choose K as 3, three Gaussian distributions correspond to people walking slowly, at normal speed, and walking quickly. The probability of transition time t is as follows

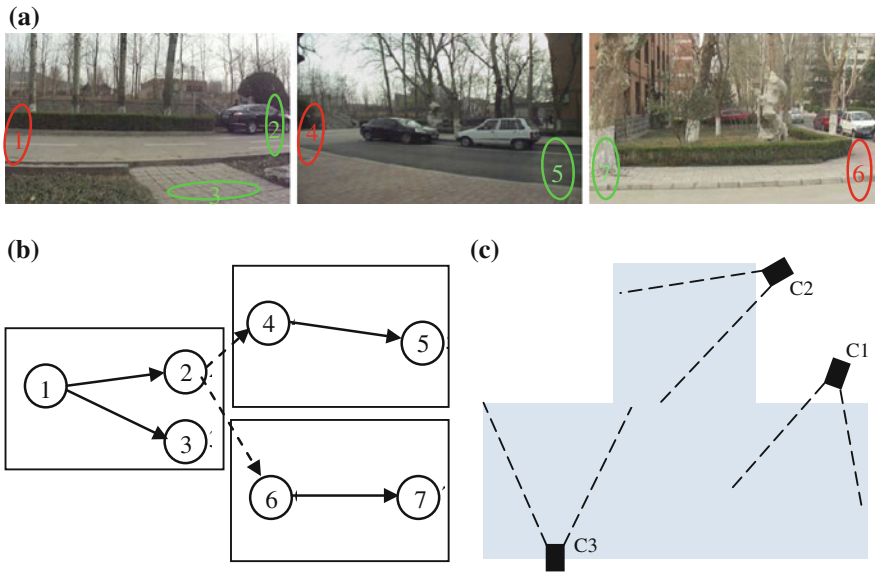

Fig. 1 Spatial–temporal constraint of inter-camera. **a** Original source and sinks of three cameras C1, C2 and C3. **b** Digraph representation. **c** Topology of C1, C2 and C3

$$P(t) = \sum_{j=1}^{3} \omega_j * n_j(t, \mu_j, \sigma_j)$$
$$n_j(t, \mu_j, \sigma_j) = \frac{1}{\sqrt{2\pi} \cdot \sigma_j} e^{-\frac{(t-\mu_j)^2}{2\sigma_j^2}} \tag{5}$$

where ω_j is the weight of the jth Gaussian in the mixture, which can be interpreted as a prior probability of the random variable generated by the jth Gaussian distribution, μ_j and σ_j are the mean value and standard deviation of the jth Gaussian, n_j is the Gauss probability density function.

3.2 Description of Camera Handoff Based on Particle Filter

In order to get effective camera handover, we employ a spatial–temporal progressive matching scheme in particle filter among adjacent cameras. Taking camera handover in Fig. 1 as example, the steps of camera handover are described below in detail.

- S1. When the target goes into the sink region of C1, extract the object model H and speed V_h, push the object model H into targetlist, start the handover judgment. For maximize repression the influence of illumination changes, histogram in HSV space is used in the object model.
  - S1.1 according to the probability of transition time $P_{S_k^i S_l^j}(t)$ and spatial transition probability $P(S_k^i S_l^j)$, scatter particles in source regions of other cameras corresponding to the sink region of C1 (that is, region 4 in C2 and 6 in C3).
  - S1.2 calculates the similarity of all particles with the object model H according to histogram Intersection in (6).

$$w_k^{(i)} = d\left[h_k^{(i)}, H_k\right] = \sum_{j=1}^{m} \min\left(h_{kj}^{(i)}, H_{kj}\right) \tag{6}$$

    where $h_k^{(i)}$ is the histogram of ith particle in HSV color space of t time, h_k is the object template of k moment.
  - S1.3 If all similarities are less than a certain threshold T_S, judge the target that does not emerge in other cameras, in the next time step go S1.1 continue scatter particles based on the spatial–temporal probability. Once the similarity of some particle appears larger than threshold T_S, which means target appears, go S2 particle filter handover.
- S2 Particle filter handover.
  - S2.1 motion predictions for all particles in regions 4 and 6 separately at the same time. Motion model is shown in (7) and (8).

$$v_k = \alpha \cdot V_h + (1 - \alpha) \cdot v_{k-1} + G_{k-1} \tag{7}$$

$$x_k = x_{k-1} + v_k \tag{8}$$

where V_k is the speed of k time step, V_h is the object speed in prior camera, G_{k-1} is two-element Gauss random noise, and α is fusion coefficient.

– S2.2 computer the weights $w_k^{(i)}$ of all particles according to histogram Intersection coefficient in (6) and normalized according to (9).

$$w_k^{(i)} = \frac{1}{\sum_i^N w_k^{(i)}} \tag{9}$$

In order to improve the accuracy, we use (10) to renew the template H_t when computing the weights.

$$H_k = \beta \cdot H + (1 - \beta) \cdot H_{k-1} \tag{10}$$

where H is the object model of the prior camera, H_k is the template of k moment, and β is fusion coefficient.

– S2.3 calculate the weight sums of each source, if the sum of some source is larger than others, increase the particle number of this source and decrease particle number of other sources correlated with the sink. Taking Fig. 1 for example, if the weight sum of source region 4 in C2 is larger than that of region 6 in C3, increase particle number of region 4, decrease number of region 6 at the same time, so that the total particle number is constant.
– S2.4 resample particles according the weights and numbers of each sources.
– S2.5 go to S2.1 recursive motion prediction and increase/decrease the particles. If the number of some source decreases to less than 5 % of the total number, set it to 0. If the particle number of some source is more than 95 % of the total number, or particle numbers of all the other sources are 0, the object in current source is judged as the correct handover, and camera handover is completed.
– S2.6 After particle filter handover is started for a long time T, there is no particle's similarity larger than threshold T_S or the case that one particle's similarity larger than T_S remains short time, we judged the camera handover as failed. Object detection in subsequent cameras is restarted. If some object is detected, compare it with targetlist, judge it as new subject if its model is not similar to any target in targetlist, and then add it to targetlist.

• S3 In the next process, object tracking in single camera view keep going on.

In the above steps, fusion coefficients α and β are two important parameters, which determine to what extent is the template consistent with prior camera and how fast it adapts to the current scene. The impact of prior template is slowly

reduced with time, so we name this scheme as spatial–temporal progressive matching.

3.3 Mathematical Description of Particle Filter Handover

In (2), the trajectory of the tracked object can be drawn from the density $p(x_{0:k}|z_{1:k})$. In fact, the density in multiple cameras can be expressed by

$$p(x_{0:k}|z_{1:k}) \approx \sum_{j=1}^{C} \sum_{i=1}^{N_j} w_k^{(ji)} \delta(x_{0:k} - x_{0:k}^{(ji)}) \tag{11}$$

in which, C is the number of source regions related to the sink region. If we denote density of each source region as $p_j(x_{0:k}|z_{1:k})$, S2.3 in Sect. 3.2 increases the particle number of region with $\max(p_j(x_{0:k}|z_{1:k})$, that is, increases the density of maximal likelihood; decreases that of other source regions, until it finds the correct handover.

4 Experiments

In this part, the particle filter handover scheme above is tested by an outdoor scenario taken by us. The experimental environment is: CPU, Intel Pentium 2.93G Hz, and memory, 3.25 GB, developing tools are Visual Studio 2008 and OpenCV 2.3.

In our outdoor scenario, the topology of cameras is shown in Fig. 1, in which the three cameras have no or little overlap view, so the homography-based or limits of fields of view-based methods cannot be used. Some frames of C1, C2, and C3 are shown in Fig. 2, from which one can see that the illuminations of three cameras are quite different for different camera types and views of angles. So the appearance-based method is not reliable. The only effective way is combining appearance information with spatial–temporal information.

The space–time information of three cameras is first learned using a 2 h dataset. In our test scenario, a person passes through C1, then exits from C1 and enters into C2 after 266 frames, not C3. The types of these three cameras are different, and the

Fig. 2 Some frames of three cameras

Fig. 3 Particle distribution in frames target first emerged

resolutions are also different: Resolutions of C1 and C2 are 320*240, and that of C3 is 640*480, so normalization should be done first.

When the target enters into sink region 2 in C1, the camera handover judgment is started, and particles are sampled according to the spatial–temporal constraints. In the first few frames of C2 and C3 into which target did not enter, the camera handover is not started as the similarities of particles with object model H in prior camera are small. Continue scatter particles in next frame. Once the similarity of some particle appears larger than threshold, it means the target goes in (in this experiment, first similarity larger emerges in frame 266 of C2), does not scatter

Fig. 4 Camera handover successfully completed in frame 271 of C2

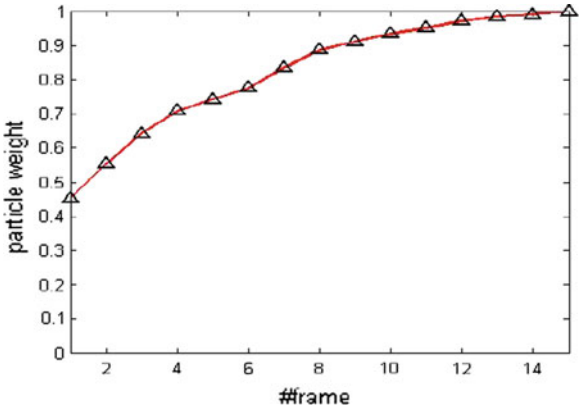

Fig. 5 Weight change of particles in C2

particles in the next frame, and switches to the particle filter camera handover. The particle state of frame where target first emerged in source regions 4 and 6 is shown in Fig. 3 where the dots represent a particle. The motion prediction, resample based on weights and number adjustment of particles are carried out with the time. Another parameter setting is: $T_S = 16$, $\alpha = 0.9$, $\beta = 0.95$. Experiment results show that in 15 frames after the target first emerged, all particles are transferred into C2 and focus on the target, which indicates the handover is successfully completed. Figure 4 is the handover ending in frame 271 of C2, in which the pixels are particle positions and the rectangle is the estimation of object location. The weight sum change of particles in 15 frames of C2 is given in Fig. 5.

5 Conclusion

In multiple camera intelligent surveillance, continuously object tracking across cameras, i.e., object handover is an unresolved problem and has attracted many research works in recent years. This paper proposed a particle filter camera tracking and handover method to solve the continuous tracking across multiple cameras with non-overlapping fields of view. The spatial–temporal constraints, including source and sink regions, transition probabilities, and transition time of each pair of source and sink are learned offline. Then a spatial–temporal progressive matching scheme is used to scatter particles and renew the number of particles in source regions according to the spatial–temporal information among adjacent cameras. Experiment shows that this particle filter camera handover scheme is effective. Further and deeper employment should be done to extend this scheme to camera handover and camera management in more complicate camera networks.

Acknowledgments We would like to acknowledge the support from China Natural Science Foundation Committee (No. 60975025, No. 61273277), the Scientific Research Foundation for the Returned Overseas Chinese Scholars, State Education Ministry (20101174), Shandong province Natural Science Foundation Committee (No. ZR2011FM032), and the University Innovation Program from Jinan Science and Technology Bureau (No. 201004002).

References

1. Yilmaz A, Javed O, Shah M (2006) Object tracking: a survey. ACM Compu Surv 38(4):45
2. Wang X (2012) Intelligent multi-camera video surveillance: a review. Pattern Recogn Lett pp 1–25
3. Cai Y, Chen W, Huang K, Tan T (2007) Continuously tracking objects across multiple widely separated cameras ACCV. LNCS 4843:843–852
4. Focken D, Stiefelhagen R (2002) towards vision-based 3d people tracking in a smart room. In: Proceddings of IEEE international conference multimodal interfaces

5. Chang T-H, Gong S (2001) Tracking multiple people with a multi-camera system. In: Proceedings of IEEE workshop on multi-object tracking
6. Khan SM, Shah M (2006) A multiview approach to tracking people in crowded scenes using a planar homography constraint. ECCV 2006
7. Omar J, Sohaib K, Zeeshan R, Mubarak S (2000) Camera handoff: tracking in multiple uncalibrated stationary cameras. In: Proceedings workshop on human motion 2000
8. Nicholas J, Redding J, Fabian O, Judd K, Tristrom C (2008) Cross-matching via feature matching for camera handover with non-overlapping fields of view. In: Proceedings of digital image computing: techniques and applications
9. Omar J, Khurram S, Mubarak S (2005) Appearance modeling for tracking in multiple non-overlapping cameras. In: Proceddings of IEEE international conference computer vision and pattern recognition (CVPR)
10. Doretto G, Thomas S, Peter T, Jens R (2011) Appearance-based person reidentification in camera networks: problem overview and current approaches. J Ambient Intell Humaniz Comput 2:127–151
11. Zhou Q, Aggarwal JK (2006) Object tracking in an outdoor environment using fusion of features and cameras. Image Vis Comput 4(11):1244–1255
12. Kuo C-H, Huang C, Nevatia R (2010) Inter-camera association of multi-target tracks by on-line learned appearance affinity models. ECCV 2010 Part I, LNCS 6311
13. Chen K-W, Lai C-C, Lee P-J, Chen C-S, Hung Y-P (2011) Adaptive learning for target tracking and true linking discovering across multiple non-overlapping cameras. IEEE Trans Multimed 13(4):625–638
14. Lim FL, Leoputra W, Tan T (2007) Non-overlapping distributed tracking system utilizing particle filter. J VLSI Sig Proc 49:343–362
15. Cheng M-Y, Wang C-K (2007) Dynamic visual tracking based on multi-cue matching. In: Proceedings of international conference on mechatronics
16. Weijer Jvd, Schmid C, Verbeek J (2007) Learning color names from real-world images. In: Proceddings of IEEE international conference computer vision and pattern recognition (CVPR)
17. Bolic M (2004) Architectures for efficient implementation of particle filters. Ph.D. thesis, electrical engineering, Stony Brook University, August 2004. http://www-sigproc.eng.cam.ac.uk/smc/smcpapers.html
18. Isard M, Blake A (1998) Condensation-conditional density propagation for visual tracking. Int J Comput Vision 29(1):5–28

Analyzing Effects of Pressing Radio Button on Driver's Visual Cognition

Huacai Xian, Lisheng Jin, Haijing Hou, Qingning Niu and Huanhuan Lv

Abstract An approach is presented based on driver simulator and SmarteyeII eye tracking system to examine the effects of pressing in-vehicle radio button on driver's visual cognition. Parameters of glance frequency, glance duration, eye movement speed, and visual line moving in different regions of interest (ROIs) in task of pressing the radio button, closely related with driver's visual cognition, were collected and analyzed. Based on the experimental data, driver's visualization model with secondary tasks was built by CogTool. Driver's vision, eye movement, cognition, and hand motion were tracked and recorded by the model. Results of experiment and running model show that pressing the in-vehicle radio button while driving has adverse influence on driver's visual cognition and occupies a lot of the driver's visual resources.

Keywords In-vehicle radio · Secondary task · Visual cognition · Visualization model · CogTool

1 Introduction

Amelia Stenson reports that 90 % of causes of traffic accidents are related to driver's factor [1]. Some researchers consider that 80 % of the driver's perception of information origins from vision. Thus, it is put in a significant place while driving and accident controlling [2, 3]. Thus, it is of remarkable significance to study the driver's visual cognition with the secondary task which is an important factor for driver distraction. Secondary tasks are tasks that the driver voluntarily or involuntarily engages in which do not directly pertain to the primary task of safe vehicle operation [4], such as taking a look at the navigation system, listening to

H. Xian (✉) · L. Jin · H. Hou · Q. Niu · H. Lv
Transportation and Traffic College, Jilin University, ChangChun 130024, China
e-mail: xianhuacai1983@163.com

F. Sun et al. (eds.), *Foundations and Practical Applications of Cognitive Systems and Information Processing*, Advances in Intelligent Systems and Computing 215,
DOI: 10.1007/978-3-642-37835-5_7,

music or radio, talking on the phone, etc. These tasks occupy driver's visual resource, cognitive resource, and motion resource in different degrees and distract the driver's attention simultaneously as well. As the most important factor for safe driving, the driver's visual cognition remains largely unexplored, which is the focus of this study.

Most previous studies paid close attention to eye movements and driving performance while using cell phone [5–7], music and music tempo [8–10], text messaging, and device position while driving [11, 12]. However, few have made detailed and thorough analysis on driver's visual cognition in secondary tasks while driving. Therefore, it is of important significance to study the driver's visual cognition in secondary task.

With this motivation in mind, the overall goal of this paper is to develop a method of examining the effects of pressing radio button on driving performance. In particular, it has the following purposes:

(1) Collect parameters of drivers' visual cognition behavior, taking an in-vehicle radio as the secondary task while driving and coordinating Driving Simulator with SmarteyeII system, which is separated from driver's head and thus relieves discomfort.
(2) Use SPSS and Matlab for analyzing parameters of driver's glance frequency, glance duration, eye movement speed, and visual line moving.
(3) Build driver's visualization model in task and achieve prediction of driver's vision, eye movement, cognition, and hands motion using CogTool.

2 Description of Experiment

2.1 Experiment Equipments

The experiment equipment mainly includes the SmarteyeII system, an in-vehicle radio, and a platform composed of a BESTURN B50 car and a Driving Simulator.

(1) Secondary task

The secondary task was performed on the in-vehicle radio button. The center of radio-button coordinate was (29, −23, −13.5) and 23° away from the steering wheel center (see Fig. 1).

(2) Eyes tracking system

Eyes tracking system of the Smarteye was mainly responsible for capturing driver's eye movement during the whole driving procedure. The Smarteye used four cameras (shown in Fig. 1) mounted in front of the windscreen towards driver's face to capture driver's eye movement. Besides, to pick driving environment out of the vehicle, three panoramic cameras were also mounted between two back seats.

Fig. 1 In-vehicle radio and SmarteyeII

(3) Driving simulator

Driving simulator is composed of a BESTURN B50 car, modules of dynamics simulation, image simulation, and monitor simulation (see Fig. 2).

2.2 Participants

Eight participants (six male and two female) between the ages of 20 and 23 (mean = 21.5, SD = 1.18) were recruited from the University of Jilin. All participants were required to hold a valid class C driver's license for more than 2 years and drive a minimum of 5,000 km per year. Divers were also required to be in good health.

2.3 Experimental Design

The performing course was divided into 13 steps. A four-lane divided highway with an 80–120 km/h velocity limit was chosen. Each lane of the highway was 3.75 m wide and the middle belt was 3 m wide. The experiment was performed in multi-vehicles and non-vehicle environment, respectively, in the following steps:

Fig. 2 Driving environment

(1) Participants were taught to operate the radio and then practice performing the task and driving the simulator under multi-vehicles and non-vehicle road conditions repeatedly, first separately and then together.
(2) Lead driver to complete secondary tasks at any time they feel safe while driving. Each driver completed a drive without performing the in-vehicle radio task and a drive with in-vehicle radio task under different highway road conditions, after which parameters of driver's eye behavior were recorded.
(3) Driver's visual data was collected while driving and then analyzed.

3 Analysis of Drivers' Visual Cognition Behavior

Eye movement was collected by SmarteyeII Recorder. A glance is defined as consecutive focuses on an area of interest, not including saccade transition and blinking behavior. As four regions of interest (ROI), the road, in-vehicle radio, and two rearview mirrors were extracted in the experiment for further research.

Figure 3 shows the tracking of eye movement. From Fig. 4, four ROIs are divided by rectangles of different colors. ROI-0 (blue area) and ROI-3 (green area) are areas of on-road and in-vehicle radio conditions. ROI-1 (red area) and ROI-2 (light yellow area) stand for the right and left rear mirrors respectively.

3.1 Mean Glance Frequency

Glance frequency is defined as the number of glances at a target during the task where each glance is separated by at least one glance to a different target [13]. Apart from glances at the lane, the more intensive the driver's gaze points is, the more visual resources the area occupies, resulting in driver's visual distraction.

The glance frequency distribution without and with secondary tasks on multi-vehicles road is shown in Figs. 5 and 6 respectively. Comparing the ROI0 and ROI1, it can be perceived that the number of glances on rearview mirrors with radio task is

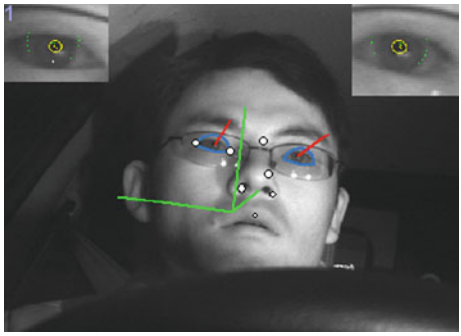

Fig. 3 Eye movement tracking

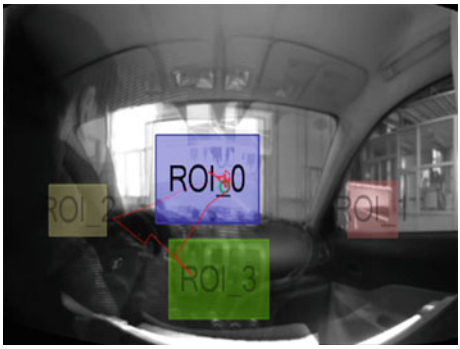

Fig. 4 Eye interested regions

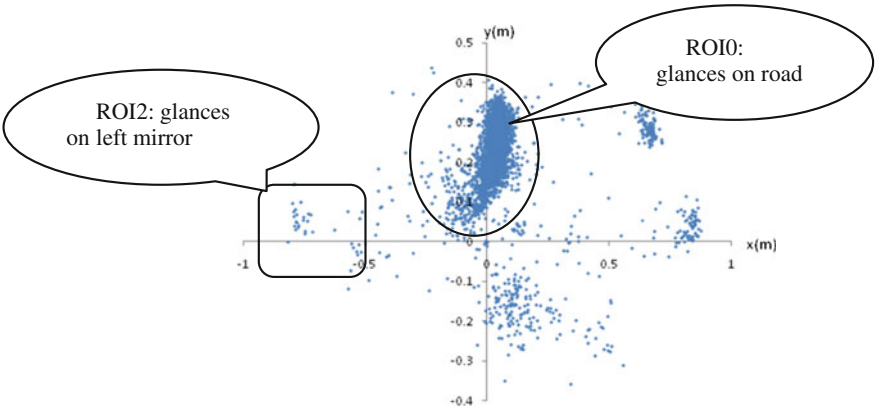

Fig. 5 Distribution of glance frequency on multi-vehicles road without in-vehicle radio task

more than that without secondary task. From ROI3, it can be seen that the glances significantly increase and gaze points become intensive while with the task.

In addition, it is obvious that driver's visual location on road is mainly concentrated within the range of 0.4 m without secondary task, while under the secondary-task condition, driver's visual location on road is partly more than 0.4 m and the distribution of gaze points is more dispersed. According to the statistics data, the number of glances for completing pressing radio button on non-vehicle road is 28, and 89 on multi-vehicles road.

3.2 Mean Glance Duration

Glance duration was calculated along the time (in seconds) from first looking at an ROI until gaze was moved off that area. The mean duration of each glance in seconds was extracted and categorized into various ROIs for secondary task [14].

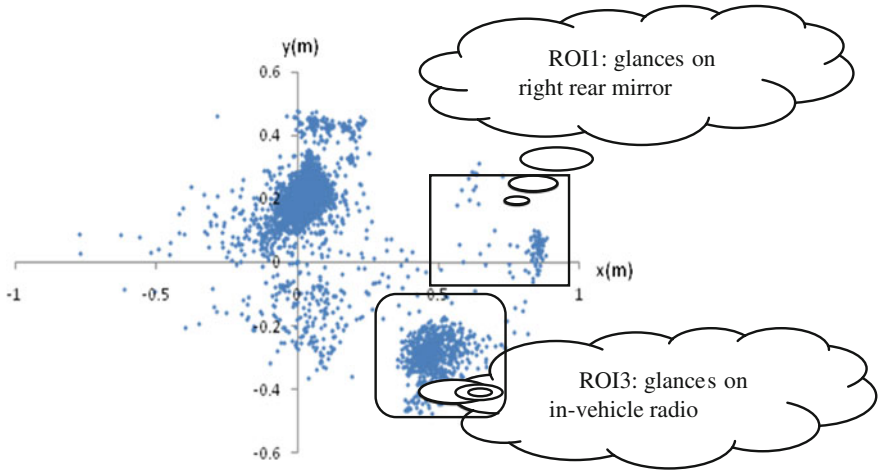

Fig. 6 Distribution of glance frequency on multi-vehicles road with secondary task

The duration of glances significantly differed depending on the ROIs, see Fig. 7. Figure 8 shows the maximum glance duration in different ROIs. Driver's single maximum glance duration on non-vehicle road without secondary task is 2.33 s from the bar chart. Statistics indicate that under that condition and excepting the long gaze on the road, each driver has an average of three times of a single glance, of which the duration exceeds 1.6 s, largely threatening the driving safety. Furthermore, almost all of the dangers occurred under the condition of operating the in-vehicle radio task.

A conclusion can be obtained that the glance duration on ROIs with secondary task is longer than that without task on the corresponding ROI under any road condition. Further, except for gazes on road, some driver's single glances exceed 1.6 s with secondary task, which is an important factor to cause traffic accidents. In addition, long glances are concentrated on areas where the radio button is seated on any road condition.

3.3 Eye Movement Speed

Eye movement speed stands for the transfer angle of driver's gaze point from one position to another. If the speed of eye movement is faster, the glance duration on a fixed area is shorter, driver's distraction is smaller, and the driving safety is higher. Figure 9 shows the curves of driver's eye movement speed including left eye, right eye, and resultant angular rate on non-vehicle road without secondary task using Matlab. LGAZE velocity and RGAZE velocity stand for the left and right eyes movement speeds respectively. CGAZE velocity is the average of left and right eye speeds. The blue, green, and red lines stand for driver's eye yaw angular, pitch

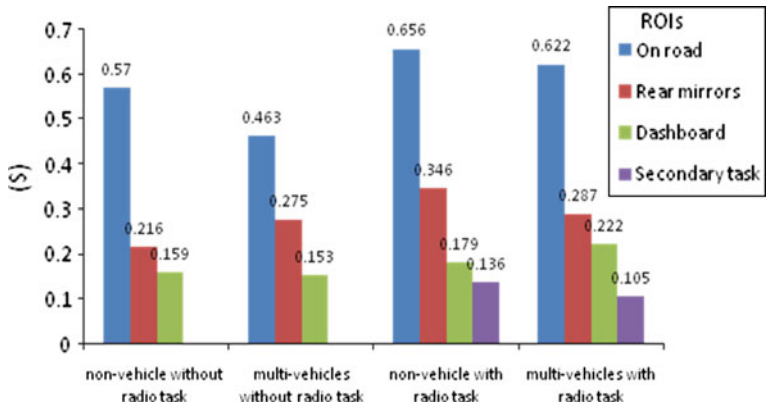

Fig. 7 Glance duration on different ROIs

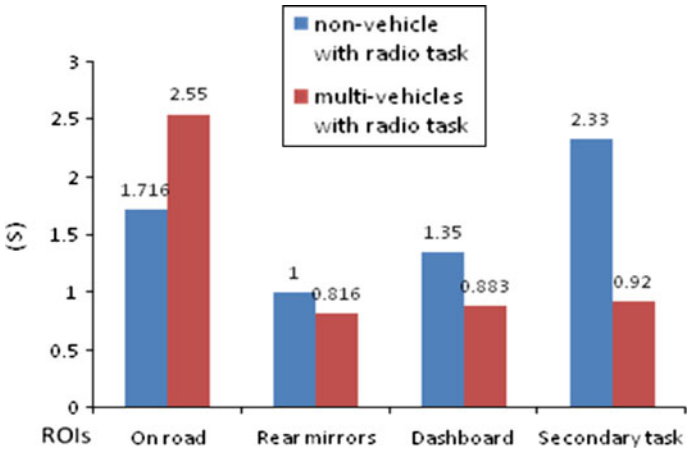

Fig. 8 Maximum of glance duration

angular rate, and resultant angular rate respectively. The similar curves can be obtained on multi-vehicles road with or without task.

According to the statistics, the eye yaw angular rates without secondary task on non-vehicle (21.85 °/s) and multi-vehicles road (28.22 °/s) are less than that with secondary task (non-vehicle: 30.88 and multi-vehicles: 31.30). The same trend is found in pitch angular rate. On non-vehicle road, the resultant angular rate is 32.82 °/s without secondary task and 42.08 °/s with secondary task, while on multi-vehicles road it is 38.44 and 45.54 °/s respectively. Except that, the angular rate on multi-vehicles road is higher than that on non-vehicle road at any task condition. This is because on multi-vehicles road, driver's visual load increases.

From the analysis above we can infer that, in order to ensure safe driving, drivers had to increase glance frequencies and shorten the gaze time on a certain

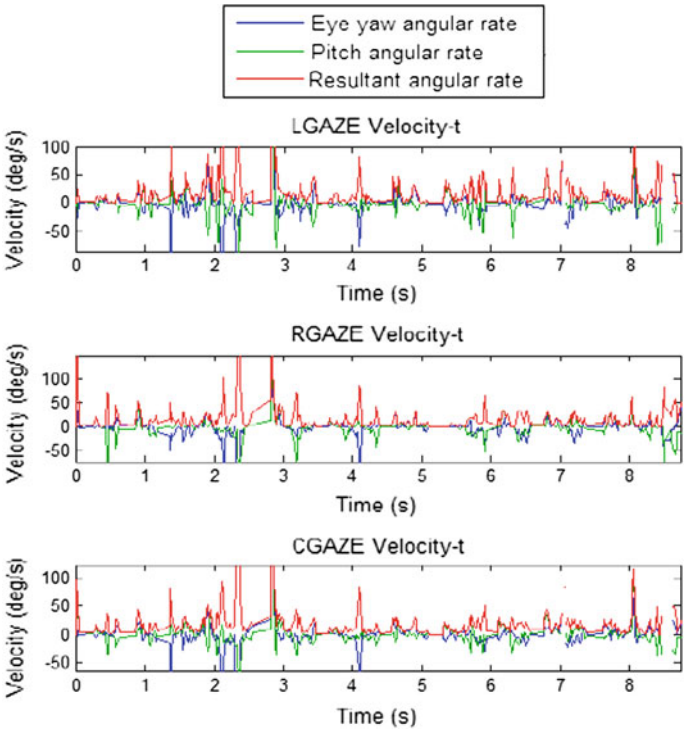

Fig. 9 Driver's eye movement speed

area. So the driver's eye yaw angular, pitch angular rate, and resultant angular rate with secondary task are greater than that without secondary task on any road condition.

4 Study on Driver's Visualization Model Using Cogtool

CogTool is a cognitive modeling tool to demonstrate focuses on HCI task, which itself is an integration of several tools: Dreamweaver^{TM}, Behavior Recorder, ACT-Simple, and ACT-R environment [15, 16]. Based on the experiment results and CogTool [17], driver's visualization model with in-vehicle radio secondary task was built in the study. All operation interfaces of in-vehicle radio were combined by transition function. Results of model trace and visualization are shown in Fig. 10.

The trace window shows the time each action needs in detail. In the left pane, time runs from left to right and the widths of the boxes are proportional to the time it takes to execute. An export command then creates a KLM of in-vehicle radio

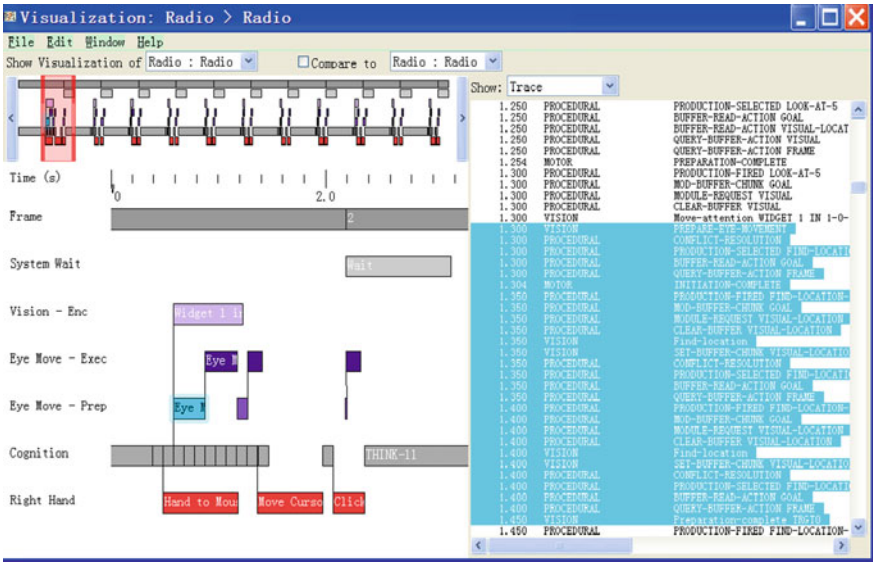

Fig. 10 Results of model trace and visualization

task expressed in ACT-Simple, a simplified language that is compiled into ACT-R productions.

From the model running results, 20.159 s is needed to finish the in-vehicle radio operation. The in-vehicle radio task occupied driver's visual resource, cognitive resource and motion resource in different degrees, which competes with driver's major task and gives rise to the possibility of traffic accidents.

Frame (darker gray): represents the Frame that is visible on the screen. System Wait (lighter gray): represents the system response time. Vision-Enc (light purple): represents the eye's encoding objects on the Frame. Eye Move-Exec (darkest purple): represents the eyes moving to objects on the screen. Eye Move-Prep (mid purple): represents the eyes preparing to move to objects on the screen. Cognition-center row (gray): represents the thoughts the model has when performing the Task.

5 Conclusions

This study examined the effects of in-vehicle radio task on driver's visual cognition. A number of parameters were collected and then analyzed. Based on results of the experiment and the Cogtool software, a driver's visualization model with in-vehicle radio secondary tasks was built. Furthermore, driver's visualization and action when pressing the radio button were also obtained, thus to predict driver's visual cognition successfully.

The presented study is concentrated on effects of pressing the button at a fixed location. Interaction with other devices such as GPS, in-vehicle computer, and television still remains to be analyzed deeply. Apart from that, the study only selected eight young drivers to participate in the experiment. Therefore, further studies are required to be continued on different age ranges and on more drivers.

Acknowledgments This research was supported partly by the Doctoral Study Special Research Foundation of Higher Education (20110061110036), Major Projects of Jilin Science and Technology Department (20116017), New Century Excellent Talent Foundation Program under Grant (NCET-10-0435) and National Nature Science Foundation of China (No. 50908098).

References

1. Amelia Stenson, The most common causes of car accidents. http://www.Articlesbase.com
2. China highway, http://www.chinahighway.com
3. Lappe M, Grigo A, Bremmer F, Frenz H (2000) Perception of heading and driving distance from optic flow. In: Proceedings of the driving simulation conference DSC 2000, Paris, France, pp 25–31
4. Kenneth MB et al (2008) You can touch, but you can't look: interacting with in-vehicle systems. In: Proceedings tangibles: input & output, pp 1139–1148
5. Brookhuis KA, de Vries G, de Waard D (1991) The effects of mobile telephoning on driving performance. Accid Anal Prev 23:309–316
6. Jan EBT, Anne KB (2005) Mobile phone use-effects of handheld and hands free phones on driving performance. Accid Anal Prev 37:902–909
7. Tova R (2006) Driving performance while using cell phones: an observational study. J Saf Res 37l:207–212
8. Daniel TB, Costas IK, Noel PK (2009) Effects of musically-induced emotions on choice reaction time performance. Sport Psychol 23:1–19
9. Warren B (2002) The effects of music tempo on simulated driving performance and vehicular control. Trans Res 4:219–241
10. Brian HD, David GB (2007) Effects of noise and music on human and task performance: a system review. Occup Ergonomics 7:143–152
11. Hosking SG, Young KL, Regan MA (2005) The effects of text messaging on young novice driver performance. The National Roads and Motorists' Association Motoring Services, Melbourne
12. Helen J, Fuller A (2010) The virtual driver: integrating physical and cognitive human models to simulate driving with a secondary in-vehicle task. The University of Michigan, Ann Arbor pp 25–92
13. Salmon PM, Lenné MG et al (2011) The effects of motion on in-vehicle touch screen system operation: A battle management system case study. Transp Res Part F 14:494–503
14. Chisholm SL, Caird JK, Lockhart J (2008) The effects of practice with MP3 players on driving performance. Accid Anal Prev 40:704–713
15. Salvucci DD, Lee FJ (2003) Simple cognitive modeling in a complex cognitive architecture. In: Human factors in computing systems: CHI 2003 conference proceedings. ACM Press, New York pp 265–272
16. Bothell D, ACT-R environment manual. http://act-r.psy.cmu.edu/software
17. Bonnie EJ, CogTool user guide. http://cogtool.org

MAC Protocol Used Progressive Reservation Mechanism in Ad hoc Networks

Hai-dong Yang, Bo Jing, Jian-hai Li and Xin Xiang

Abstract Guarantee to QoS for real-time traffic is the bottleneck to Ad hoc Networks' development. In the distributed network, packet contention is so high that nodes always fail to access channels in limited time. Although there are many protocols, for example FPRP, which could eliminate collision remarkably, they usually need a large quantity of control packets, which lead to high access delay. By studying dynamical slot-distribution MAC protocol, a protocol using progressive reservation mechanism for Ad hoc Networks was laid out, named PR-MAC. In the new protocol, nodes access channel by gradation, coordinated competition, and also the idle data slot is reconstructed to resolve the confliction. Therefore, PR-MAC possesses the merit of high utilization of resources, few data-packets collision, and low access delay; in addition, it can also support data traffic fine.

Keywords Ad hoc networks · MAC · Slot-reconstruction · Progressive reservation

1 Introduction

Providing effective delay guarantee for real-time traffic, such as voice and video, is always a technical difficulty for MAC protocol designing in Ad hoc networks. Because for voice and video, packet access delay required usually is less than milliseconds. While for Ad hoc network with dynamic topology and distributed operating mechanism, problems that lack center of scheduling and management node, also special hidden terminals, exposure terminals, and invasion of terminal

H. Yang (✉) · B. Jing · J. Li · X. Xiang
Aviation and Aerospace Engineering Institute, Air Force Engineering University, Xi'an, China
e-mail: yanghd2008@163.com

F. Sun et al. (eds.), *Foundations and Practical Applications of Cognitive Systems and Information Processing*, Advances in Intelligent Systems and Computing 215,
DOI: 10.1007/978-3-642-37835-5_8,

problem make the packet conflict frequently; node is difficult to access channels successfully in a limited amount of time.

In order to support real-time traffic, the existing MAC protocol prefers to use distinguished mechanism (such as IEEE802.11 DCF [1, 2]), wireless token ring technology (such as WTRP [3]), and dynamic channel allocation techniques (including TDMA, CDMA, FDMA, etc.).

Among them, due to the use of random competition to access the channel, MAC protocol using a distinguished mechanism, such as IEEE802.11 DCF, inevitably causes conflict between control packet and data packet, which lead to great instability in access performance when load changes, and does not provide a fine delay guarantee.

Wireless token ring technology can avoid packet conflict effectively, and has good fairness, but token ring structure is subjected to token-losing and multi-token problem in large-scale networks. Where nodes cannot reach each other, there is subnet dividing problem and synchronization problem within multi-token, and these problems have not been solved so far. Second, in denser network, this kind of method will make token ring and the polling cycle too long, even if many nodes in the network do not send information; it will also waste a lot of polling circle leading to high access delay.

Dynamic channel allocation mechanism is also called dynamic resource reserve mechanism, that is, through time and frequency or code division, the data channel shared is divided into several independent sub-channels. Each sub-channel is allocated to one or more users, and is adjusted dynamically according to the network state, which makes different nodes not to interfere with each other in communication. Among them, the frequency division multiple access, or code division multiple access, is not suitable for Ad hoc network, because it is difficult to realize strict time synchronization and power control between the nodes in Ad hoc networks. Hence, for CDMA, the near–far effect caused by multi-address interference is serious [4]. For frequency division multiple access protocol, the hardware realization is complicated, and compatibility is poor, so it is difficult to apply widespread. Some simplified frequency division multiple access protocols, such as FAMAC [5], DCA-PC [6], employ frequency hopping method to reduce the complexity of hardware, but it will result in "node exclusive" [6, 8]; Thus it tends to be more of concern to employ TDMA MAC protocol for QoS guarantee in Ad hoc network, That is, dynamic slot allocation protocol.

The dynamic slot allocation protocol combines the advantages of reservation and competition. It not only has a "conflict-free" characteristic for fixed allocation, which makes packet congestion, delay, and bandwidth allocation controllable, but also adapts to the dynamics slot adjustment caused by changed network topology. Moreover, it is of better reliability, flexibility, fairness and can provide QoS guarantee for delay-sensitive traffic. Therefore, the dynamic slot allocation protocol is a suitable access mechanism for real-time traffic transmission.

However, the dynamic allocation protocol currently does not have good delay performance, faces the problem of poor ability to eliminate conflict, load flexibility and higher complication. For example, once the protocol with embedded signaling,

such as CATA [7], HRMA [8], and SRMA/PA [9], suffer conflict, it is difficult to determine the time when the node can access, and at the same time the corresponding data-slot time will be wasted. As for FPRP [10], RBRP [11] agreement as a representative of independent signaling structure, although they are able to eliminate conflicts better, they need a lot of signaling slot (FPRP need $5 \times M \times N$ control slot, RBRP need $M \times (m + 2) + 6N$ control slot), which also can cause high access delay. Another protocol with complex signaling structure such as MAC-RSV [12], although using less number of signaling slots, easily suffers detective interrupt and delay jitter problem [13], causing uncertainty of access delay. Therefore, the key problems for slot allocation protocols are how to effectively reduce the number of control slots, fully resolve packet conflict in short time, and shorten the access delay, all of which help to improve the QoS performance.

2 The Progressive Reserved Channel Access Control Protocol

After intensive research on the slot distribution MAC protocol, this paper introduces a MAC protocol for Ad hoc network using gradual reserve mechanism, called progressive reserved channel access control protocol (PR-MAC), i.e., Progressive Reservation.

2.1 The Idea of Design

In order to reduce access delay and increase the utilization rate of the channel, the new protocol adopted the following design thought:

(i) Make full use of free data slot. Data slot will be converted to control channel when at leisure, which can increase the eliminate ability for packet conflict, and promote channel utilization ratio and space reuse.

(ii) Hierarchical reservation. Different reservation level is set up between reserved nodes and prepared-reservation nodes. The access order in sequence is reserved nodes, prepared-reservation nodes, real-time traffic competition node (divided into single competition node and multiple competition node), and data traffic node, that is, the new protocol uses a hierarchical channel access method. The above node types described in Sect. 2.2 below.

(iii) The nearest principle is employed in data access process. Prepared-reservation nodes in the access data channel use the first free data slot it listened, and single competition node in successful competition after shaking hands can directly use the rest of the data slot, so as to provide as small access delay for real-time traffic packet as possible.

(iv) In each free data slot, the successful number of nodes in the competition is not more than one, that is, only one prepared-reservation nodes is generated in unit time, so the conflict between nodes can be cut down remarkably in channel access process.

2.2 Protocol Description

The slot structure of PR-MAC is shown in Fig. 1.

PR-MAC protocol is made up of frame units, each frame consists of N slots, each slot is composed of two parts: flag domains T_{RC} for reservation and data-sending domain T_{DSC1}, of which the T_{RC} domain includes reserve cycle RB and Prepared reserve cycle RES, its structure remains the same for all nodes, while in T_{DSC1} domain, the structure is different for different types of nodes.

Definition: Reservation node is one that has successfully sent real-time traffic packet formerly. The **c**orresponding slot will still send the data in current slot; Prepared-reservation node refers to the nodes that successfully get the right to use the channel in the past through the slot competition, but has not sent real-time traffic yet.

In the protocol, reservation node has the highest priority in channel access process, followed by Prepared-reservation node, and then the real-time traffic competition node, and finally datagram traffic node. Reserved node prevents other nodes from sending data by sending RB packet, and Prepared-reservation node can reserve the slot by sending RES packet when RB circle is free, meanwhile, send real-time traffic in T_{DSC1} in the format of DATA/ACK.

For real-time traffic competition node, T_{DSC1} domain converts into T_{SCC} and T_{DSC2} when T_{RC} domain is free, of which, T_{SCC} used for channel competition, if a reservation is successful, then nodes immediately send DATA through T_{DSC2} in the form of DATA/ACK, otherwise they continue to compete in the domain T_{MCC}. Because only single real-time traffic node can compete successfully in T_{SCC}, therefore, it is also called the single-node competition domain, and T_{MCC} is called the corresponding multi-node competition domain. The following is the detailed process of channel competition of real-time traffic competition node;

(1) Before nodes access the channel they monitor RB and RES cycle; if RB and RES are idle, real-time traffic transceiver node shake hands through RTS/CTS

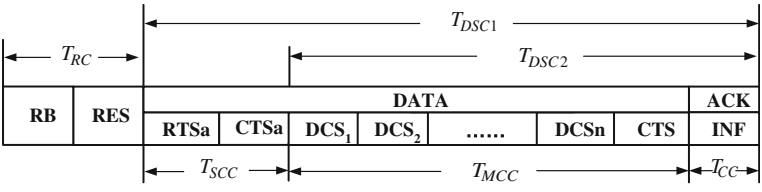

Fig. 1 The slot structure of PR-MAC protocol

in domain T_{SCC}, then go to step (2), otherwise, the nodes give up competition in current slot and go into the next slot;

(2) If handshake succeeds, transceiver nodes will send real-time traffic data directly in the subsequent T_{DSC2} domain, and at the same time become the reserved node. Otherwise, enter step (3);

(3) The sending node randomly selects a DCS cycle to send RTS packet in T_{MCC} domain, while receiving node send CTS packet based on the following rules: the receiving node j maintains a listening state in the whole DCS domain (DCS1–DCSn), and marks all the DCS packets sent by adjacent emission node k, denoted by the Number (k), the Number (k) = 1, 2,…, M. If i is the sending node of j corresponding, and to meet Number (i) > Number (k), where k is any adjacent emission node of j, the receiving node j sends CTS packet to reply, and go to step (4); otherwise, if there is a node r, meet Number (i) < Number (r), the receiving node give up sending CTS packet, and quit the competition on the current slot. The above mechanism determines that the receiving node whose serial number is biggest can send a CTS packet. Therefore, the successful node in competitive process in domain T_{MCC} will not exceed one.

(4) After receiving the corresponding CTS packet, emission node i becomes Prepared-reservation node.

One can see, in T_{SCC}, the single-node competition domain, if there is only one real-time traffic competition node, it can immediately access the channel to send data, and at the same time become the reservation node; when there are several competitive nodes they will fail to compete in T_{SCC}, while through slot expanding in T_{MCC} and CTS packet collaborative-sending mechanism, it can still make a couple of competition nodes successful in nodes competition, which then becomes the Prepared-reservation node.

Datagram node is allowed to access channel only when T_{RC} and T_{SCC} is idle, it is certain that real-time service node will not access now. Specifically, the emission node can send only when RB, RES CTSa is idle, the receiving node can answer only when RTSa cycle is idle. When permitted to access, the datagram nodes send data in domain T_{DSC2} using the basic access mode (Data/ACK) of IEEE802.11DCF.

That shows that PR-MAC protocol adopted a new hierarchical channel access method, on the basis of full use of free data slot. The packet conflict between real-time traffic nodes can be reduced in the process of reservation. In addition, only sending node was provided with competition slot in domain T_{MCC}, which can further reduce the occupation of the control slot. Furthermore, there are not more than one Prepared-reservation node produced per data slots, so in PR-MAC protocol, Prepared-reservation node can use the first free data slot without conflicts, which helps to provide lower packet access delay.

2.3 Collaborative Competition Mechanism of Multi-Node

Now, cooperative competition mechanism for real-time traffic node will be described below based on Sect. 2.2.

To provide the support capacity that each free data slot accesses a node, in different connected domain conditions, node competition process of PR-MAC protocol is as follows:

(1) Fully connected domain: all transmitting and receiving nodes are in the same emission coverage area, as shown in Fig. 2 (in Figure "① ②" behalf the priorities in the domain to select the DCS cycle). In accordance with the competition rules of the multi-node of the PR-MAC protocol, node B will not send the CTS packet, thus nodes C, D, are able to compete successfully.

(2) Strongly connected domains: that is, only one node is within the coverage area each other between two pairs of transmitting and receiving nodes. Three cases, respectively, as shown in Fig. 3a and c below.
In Fig. 3a, node B will not send CTS packet, while nodes C, D compete successfully. If exchanging the sending order of DCS packet, the nodes B and D will send CTS packet all, so nodes A and B compete successfully, and the node C compete failed due to receiving conflicted CTS. In Fig. 3b, node b will not send CTS packet, node C, D compete successfully. In Fig. 3c, node A will not send CTS packet, nodes C, D compete successful.

(3) Weakly connected domains: there is only one link between two pairs of sending and receiving nodes. The three cases are shown in Fig. 4.
In Fig. 4a, node B will not send CTS packet, nodes C, D, compete successfully. If the order they were sent is interchangeable, then nodes B and D will send CTS packet to all, node C will compete failure due to receiving conflicted CTS packet, and nodes A, B, compete successfully. In Fig. 4b, nodes B, C, will only receive the DCS packet from corresponding transmitting node, and successfully return the CTS packet. Nodes A, B and C, D, compete successfully. In Fig. 4c, nodes A, D, are to send to the CTS packet, two pairs of nodes A, B, and C, D are able to compete successfully each.

It can be seen, when DCS cycle packet does not conflict in signaling competition between the two pairs of nodes, it can be ensured that at least one pair of nodes will compete each slot successfully. In fact, once conflicts take place in T_{SCC}, the

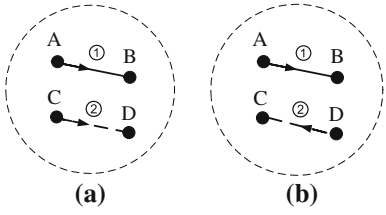

Fig. 2 Competition between the nodes in fully connected domain

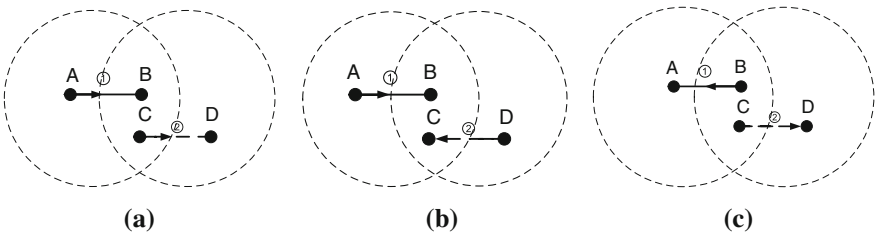

Fig. 3 Competition between the nodes in strongly connected domain

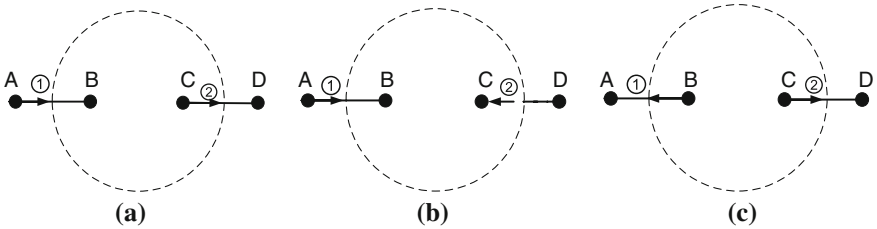

Fig. 4 Competition between the nodes in weakly connected domain

domain T_{MCC} will immediately differentiate n DCS cycle for competitive, in unit slot, real-time traffic competition nodes are usually far less than n, therefore, not all DCS packets in T_{MCC} may completely conflict. So, the max Number (k) that nodes listened is always in existence, so there is always node to receive the corresponding DCS packet at the domain and successfully send CTS packet.

3 Performance Analysis

3.1 System Model and Assumption

Thinking channel is the ideal error-free symmetric channel; node can distinguish between channel free, collisions, and received correctly in several circumstances. Each node is in the receiving state when there are no data to send. Each node sends one packet at most every slot and each packet takes up one data slot. Because the mobile node impacts little on channel access [14], therefore, it does not take account of the mobile terminal and node invasion influence in the following analysis.

Suppose there are N total slots every frame, adjacent nodes for M, the network state for k, k is the number of both the reserved node with the prepared-reserved node in a frame, $0 \leq k \leq N$. Because of the randomness and independence of each node's traffic, the arrival rate of the new real-time traffic packet obeys Poisson process with parameter λ, that is: $\boldsymbol{P}_{\xi}(\lambda \boldsymbol{t}) = \frac{(\lambda \boldsymbol{t})^{\xi}}{\xi!}\boldsymbol{e}^{-\lambda \boldsymbol{t}}$, the total arrival rate:

$\lambda_a = \sum_{i=1}^{M} \lambda_i, i = 1, 2, 3\ldots$, suppose $\lambda_1 = \lambda_2 = \lambda_3 = \ldots = \lambda_M$, therefore $\lambda_a = M\lambda_i$.

3.2 Success Rate of Channel Reservation

The distribution probability of new arrival packet number of real-time traffic in unit slot is given in Sect. 3.1.

Assumptions are as follows: $P_{\xi}(\lambda_a T_S) = \frac{(\lambda_a T_S)}{\xi!} e^{-\lambda_a T_S}$, where T_S is the length of a slot. Therefore, probabilities of no new packet to send, one packet to send, and i'th new packet to send in unit slot are:

$$\begin{cases} P_{\xi=0}(\lambda_a T_S) = e^{-\lambda_a T_S} \\ P_{\xi=1}(\lambda_a T_S) = \lambda_a T_S e^{-\lambda_a} T_S \\ P_{\xi=i, i>1}(\lambda_a T_S) = \dfrac{(\lambda_a T_S)^i}{i!} e^{-\lambda_a T_S} \end{cases} \tag{1}$$

So, the probability of successful competition of real-time traffic nodes in T_{SCC} cycle and T_{MCC} cycle in a data slot is:

$$\begin{cases} \Phi_{\mathrm{SCC}} = \dfrac{N-k}{N} \cdot P_{\xi=1}(\lambda_a T_S), \\ \Phi_{\mathrm{MCC}} = \dfrac{N-k}{N} \cdot \sum\limits_i P_{\xi=i, i>1}(\lambda_a T_S)/i \end{cases} \tag{2}$$

Therefore, the probability of real-time service nodes to compete successfully in every data slot is

$$\begin{aligned} \Phi_S =& \Phi_{\mathrm{SCC}} + (1 - \Phi_{\mathrm{SCC}})\Phi_{\mathrm{MCC}} \\ =& \frac{N-k}{N} \cdot \left[\lambda_a T_S e^{-\lambda_a T_S} + \left(1 - \frac{N-k}{N} \lambda_a T_S e^{-\lambda_a T_S}\right) \sum_i \frac{(\lambda_a T_S)^i}{i \cdot i!} e^{-\lambda_a T_S} \right] \end{aligned} \tag{3}$$

The probability of t $(t < N)$ real-time nodes to compete successfully in a frame is

$$\Phi_F(t) = C_{N-K}^t (\Phi_S)^t (1 - \Phi_S)^{N-K-t} \tag{4}$$

3.3 The System Throughput

The throughput S defined as the data packet number sent in a slot or the ratio of payload slot to total slot in a frame. Suppose the probability of released slot by reserved node is as follows:

$q = 1 - e^{-\lambda' T_f}$, Assume that the system state is k, then after a frame the probability of r slot released is:

$$\boldsymbol{F}_{\boldsymbol{k}}^{\boldsymbol{r}}(\boldsymbol{q}) = \boldsymbol{C}_{\boldsymbol{k}}^{\boldsymbol{r}}\boldsymbol{q}^{\boldsymbol{r}}(1-\boldsymbol{q})^{\boldsymbol{k}-\boldsymbol{r}}, 0 \le \boldsymbol{r} \le \boldsymbol{k} \tag{5}$$

So the transition probability is as follows:

$$\boldsymbol{P}_{\boldsymbol{kh}} = \begin{cases} \sum_{r=0}^{k} \boldsymbol{F}_{\boldsymbol{k}}^{\boldsymbol{r}}(\boldsymbol{q})\Phi_F(\boldsymbol{h}-\boldsymbol{k}+\boldsymbol{r}), & \mathrm{k} < \mathrm{h} \\ \sum_{r=k-h}^{k} \boldsymbol{F}_{\boldsymbol{k}}^{\boldsymbol{r}}(\boldsymbol{q})\Phi_F(\boldsymbol{h}-\boldsymbol{k}+\boldsymbol{r}), & \mathrm{k} > \mathrm{h} \end{cases} \tag{6}$$

where, $\boldsymbol{P}_{\boldsymbol{kh}}$ is the probability of system from state k into state h. Assumption $\boldsymbol{P}_{\boldsymbol{k}}$ is the probability system is in state k, then there are:

$$\sum_{\boldsymbol{k}=0}^{N} \boldsymbol{P}_{\boldsymbol{k}} = 1, \quad \boldsymbol{P}_{\boldsymbol{k}} = \sum_{\boldsymbol{h}=0}^{N} \boldsymbol{P}_{\boldsymbol{h}}\boldsymbol{P}_{\boldsymbol{hk}} \tag{7}$$

So:

$$\boldsymbol{S} = \frac{1}{\boldsymbol{N}}\sum_{k=0}^{N} \boldsymbol{P}_k \left[\begin{array}{l} \sum_{r=0}^{k}\sum_{t=0}^{N-k} (\boldsymbol{k}+\boldsymbol{t}-\boldsymbol{r})\boldsymbol{F}_{\boldsymbol{k}}^{\boldsymbol{r}}(\boldsymbol{q})\Phi_F(\boldsymbol{t}) \\ + \sum_{r=0}^{k}\sum_{t=N-k}^{N-k+r} (\boldsymbol{k}+\boldsymbol{t}-\boldsymbol{r})\boldsymbol{F}_{\boldsymbol{k}}^{\boldsymbol{r}}(\boldsymbol{q})\Phi_F(\boldsymbol{t}+\boldsymbol{r}) \end{array} \right] \tag{8}$$

where t and r are the slot number successful reserved and released in the current frame.

3.3.1 Access Delay

Suppose the node did not compete successfully until slot w from the data was generated, then under the conditions that the channel is not saturated, there is.

$$\begin{aligned} \tau &= \sum_{w=1}^{N} [(w-1)\cdot T_S + (T_{\mathrm{RC}} + T_{\mathrm{SCC}})] \cdot P_{\mathrm{fail}}(w-1) P_{\mathrm{succ\_SCC}}(w) \\ &\quad + \sum_{w=1}^{N} [(w-1)\cdot T_S + T_{\mathrm{RC}}] \cdot P_{\mathrm{fail}}(w-1) \cdot P_{\mathrm{succ\_MCC}}(w) \cdot P_{\mathrm{fail}}(w+V) \\ &= \sum_{w=1}^{N} [(w-1)\cdot T_S + (T_{\mathrm{RC}} + T_{\mathrm{SCC}})] \cdot \sum_{d=1}^{w-1} P_i^d (1-\Phi_{\mathrm{MCC}})^{(w-1-d)} \cdot \Phi_{\mathrm{SCC}} \\ &\quad + \sum_{w=1}^{N} [(w-1)\cdot T_S + T_{\mathrm{RC}}] \cdot \sum_{d=1}^{w-1} P_i^d (1-\Phi_{\mathrm{MCC}})^{(w-1-d)} \cdot \Phi_{\mathrm{MCC}} \cdot P_i^{v-1}(1-P_i) \end{aligned} \tag{9}$$

where the first means the statistical average of access delay for successful node in the single-node competition period and the second means value for the delay statistics in the multi-nod competition period. $P_{\text{fail}}(w-1)$ is the probability of continuous w-1 slot channel is occupied or unsuccessful, $P_{\text{succ\_SCC}}(w)$ is the probability node successfully access in single-node competitive domain in w slots, $P_{\text{succ\_MCC}}(w)$ for the probability of successful access in multi-node competitive domain, $\boldsymbol{P}_i$ is the occupancy rate of slot, that $\boldsymbol{P}_i = \sum_{k=0}^{N} \frac{k}{N} \boldsymbol{P}_k$.

4 Simulation

Performance simulation was carried out for PR-MAC protocol in OPNET platform. The simulation parameters set is as shown in Table 1, the maximum communication distance of node is 25 km.

Assume the number of data packets PL (Packet Length) that each message contains obeys the truncated geometric distribution, the maximum PL is 1000 and the new packet reached the proportion of 1/10 of all. That is, $\lambda_0 = \lambda/10$. Figure 5 shows the simulation results of packet reservation success rate in a frame under different arrival rate, the references are FPRP and CATA (the main parameters of PR-MAC are same, in FPRP, $M = N = 10$). The figure shows that FPRP protocol has the highest successful access rate in same load, while the PR-MAC protocol followed, but is much larger than CATA. The success rate of packet reservation in PR-MAC protocol every frame is generally greater than 80 % under $\lambda \leq 0.5$, while CATA reaches the performance under $\lambda \leq 0.1$. Even in $\lambda = 0.8$, success rate of PR-MAC can still reach 50 %, it can be seen, that PR-MAC protocol showed fine collision resolution and channel access capability under high overload. Although collision resolution capability of PR-MAC protocol still lags far behind the FPRP protocol, this does not explain that FPRP protocol is better than PR-MAC. From the point of protocol structure, the PR-MAC is more streamlined in control slot than the FPRP protocol, and thus it may get smaller access delay.

Figure 6 shows the simulation results of system throughput under different packet arrival rate λ. It shows that the normalized channel utilization and system throughput here which is in agreement with Sect. 3.3. As seen, the throughput of the three kinds of protocols show a similar increasing trend in the low load conditions, and as the load increased, the throughput of CATA rapidly declines when $\lambda > 0.6$, which is attributed to CATA's collision resolution mechanism. It is

Table 1 Simulation parameters setting

Parameters	Simulation data	Parameters	Simulation data
Channel rate	10 Mbit/s	RB, RES, ACK	12.8 us
Neighbor node (M)	20	RTSa, CTSa, DCS, CTS	25.6 us
Total channel (N)	20	Slot safeguard (GP)	100 us
Number of DCS (n)	20	Length of T_S	3.2272 ms

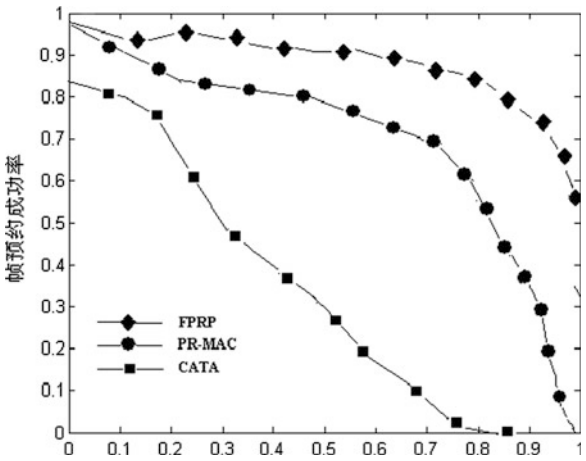

Fig. 5 Packet reservation success rate under arrival rate λ

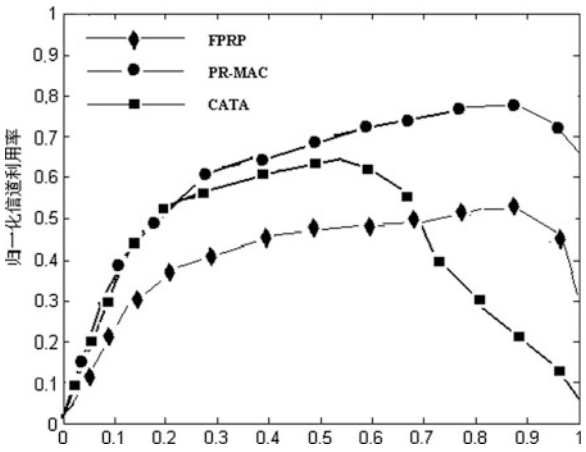

Fig. 6 Channel utilization under arrival rate λ

still relatively simple and difficult to respond to more packet collision. In contrast, FPRP still maintained a high throughput by virtue of the conflict decomposition under high load, but the maximum channel utilization of FPRP is generally lower than CATA and PR-MAC protocol, which is mainly due to that FPRP protocol using too much control slot, resulting in substantial loss of channel resources. In the figure, the channel utilization of PR-MAC protocol achieves a higher level in the entire load range, which is due to the PR-MAC protocol which is a relatively simple slot structure, taking full advantage of the idle data slot.

Figure 7 shows the simulation results of average packet access delay under arrival rate λ. The figure shows, under the conditions of $\lambda \leq 0.8$, the average packet access delay of PR-MAC protocol is below 60 ms, then with increasing of λ, the value of delay also increases, but is still far less than CATA. In other words, the packet access delay of PR-MAC protocol can remain at a lower level in a wide

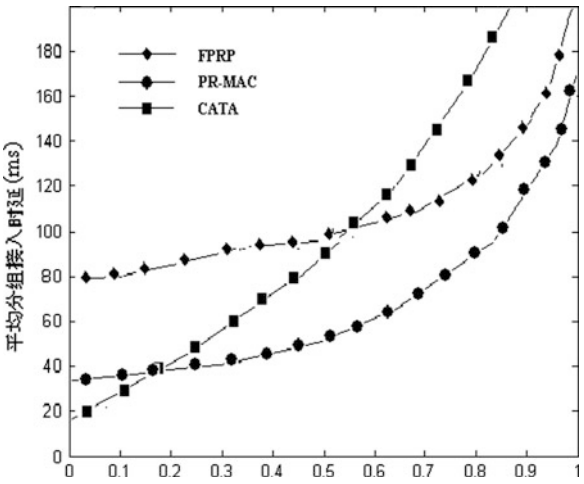

Fig. 7 Average packet access delays under arrival rate λ

load range, $0 \leq \lambda \leq 0.8$, which will undoubtedly provide better transmission support for real-time traffic. In contrast, delay performance of CATA under high load deteriorated sharply, in order to provide the access delay supporting video transmission, that is, 50 ms below the load λ is not greater than 0.3. While regardless of the load being high or low, FPRP contains more than 80 ms of fixed delay, which is mainly caused by its complex control slot. Packet access delay is at least $5 \times M \times N \times 100\,\text{us} = 50\,\text{ms}$ only considering the propagation delay in control slot. Thus, relative to the other two protocols, PR-MAC protocol has a better adaptability of the load and delay access performance.

5 Conclusion

The particularity of Ad hoc networks makes them much more complex than other networks in the use of channel resources. How to use less channel resources to eliminate much of packet conflicts, and success access channel in a limited time, are the goals that Ad hoc network MAC algorithms strive for, that is, the fairness of the MAC protocol, efficiency, and effectiveness. By full integration of the channel characteristics of distributed network and the needs of delay-sensitive traffic, the Progressive Reservation Protocol, relative to other slot allocation access protocols, present with the following characteristics:

(1) uses two reservation mechanisms, that is, reservation mechanisms and potential reservation mechanism;
(2) has the capacity of efficient use of idle data slot;
(3) progressive access, accumulated less conflict;
(4) supports both real-time traffic and datagram traffic, whose datagram packet access grade is less than the real-time traffic packet; and

(5) time slot structure is relatively simple with less consumption of resources.

Exactly speaking, PR-MAC protocol is an embedded signaling MAC protocol in structure, but through the hierarchical, progressive access, as well as the reconstruction of idle data slot, it attained the advantages of high channel utilization and less conflict like stand-alone signaling MAC protocol. PR-MAC protocol not only has excellent characteristics of small packet access delay under low load, but can also maintain good delay performance under heavy load. These features make the PR-MAC protocol have better adaptability for different network environments and different types of traffic.

References

1. Aad I, Castelluccia C Differentiation mechanisms for IEEE 802.11 (2001). In: Proceedings of the twentieth annual joint conference of the IEEE Computer and Communications Societies, Anchorage, Alaska, pp 209–218
2. Banchs A, Perez X (2002) Distributed weighted fair queuing in 802.11 wireless LAN. In: Proceedings of the .IEEE ICC, New York
3. Lee D et al (2001) A wireless token ring protocol for intelligent transportation systems. In: Proceedings of the 4th international IEEE conference on intelligent net transportation system
4. Li X-Q, Quan Q-Y, Hu J-D (1999) A novel interference canceled scheme combined with adaptive antenna in CDMA system. In: APCC/OECC'99, pp 739–742
5. Zhao Z-F et al (2001) MAC protocol for Ad hoc networks based multi-channel: FAMAC. Technological report of Communication Engineering College Interchanging Technology and ATM Research Centre
6. Wu SL, Tseng YC, Lin CY, Sheu JP (2002) A multi-channel MAC protocol with power control for multi-hop mobile Ad hoc networks. Computer (SCI) 45(1):101–110
7. Tang Z, Garcia-Luna-Aceves JJ (1999) A protocol for topology-dependent transmission scheduling in wireless networks. In: Proceedings of the IEEE wireless communications and networking conference, WCNC
8. Tang Z, Garcia-Luna-Aceves JJ (1999) Hop-reservation multiple access (HRMA) for Ad-hoc networks. In: Proceedings of the IEEE INFOCOM, pp 231–236
9. Chang Wook AHN et al (2003) Soft reservation multiple access with priority assignment (SRMA/PA): a distributed MAC protocol for QoS-guaranteed integrated services in mobile ad-hoc networks. In: Proceedings of the IEEE transactions on communication, vol E86-B, No 1
10. Zhu C, Corson MS (1998) A five phase reservation protocol (FPRP) for mobile Ad hoc networks. In: Proceedings of the IEEE INFOCOM
11. Marina MK et al (2001) RBRP: a robust broadcast reservation protocol for mobile Ad hoc networks. In: Proceedings of the IEEE INFOCOM
12. Jennifer CF and George DK (2003) A synchronous, reservation based medium access control protocol for multihop wireless networks. Wireless Communications and Networking. WCNC 4(1):994–998
13. Yang H-D et al (2009) Monitor broken problem and solving scheme of MAC-RSV protocol. J Chin Comput Syst 30(10):2096–2099
14. Haas ZJ et al (2002) Dual busy tone multiple access (DBTMA)—a multiple access control scheme for Ad hoc networks. IEEE Trans Commun 50(6):975–985

An Automatic SSVEP Component Selection Measure for High-Performance Brain-Computer Interface

Zimu Zhang and Zhidong Deng

Abstract This paper proposed an automatic steady-state visual evoked potential (SSVEP) component selection (SCS) measure for a high-performance SSVEP-based brain-computer interface (SBCI) system. First, multi-electrode raw electroencephalogram signals are spatially pre-processed using a blind source separation technique resulting in multi-source components. The SCS measure of each component is then calculated by continuous wavelet transform (CWT), and the ensemble features that contain the weighted CWT energy of individual SSVEP harmonic are extracted. Second, the SSVEP component with maximal SCS measure is considered to have the highest signal-to-noise ratio. In our SBCI system, six stimulus frequencies served as the input patterns. Offline analyses were performed, through which the common electrode locations, the time window size, and the number of harmonics were defined. Thereafter the results of our method were compared with those of others. We next carried out an online test of the SBCI for 11 subjects using eight common electrode locations, a 1.5-s time window, and the first and second harmonics. The test results showed that our method achieved an average accuracy of 95.2 % and a practical bit rate of 68.2 bits/min.

Keywords Brain-computer interface (BCI) · Electroencephalogram (EEG) · Steady-state visual evoked potential (SSVEP) · Automatic SSVEP component selection measure

Z. Zhang (✉) · Z. Deng
State Key Laboratory of Intelligent Technology and Systems, Tsinghua National Laboratory for Information Science and Technology, Department of Computer Science and Technology, Tsinghua University, Beijing 100084, China
e-mail: zzm09@mails.tsinghua.edu.cn

Z. Deng
e-mail: michael@tsinghua.edu.cn

F. Sun et al. (eds.), *Foundations and Practical Applications of Cognitive Systems and Information Processing*, Advances in Intelligent Systems and Computing 215,
DOI: 10.1007/978-3-642-37835-5_9,

1 Introduction

Brain-computer interface (BCI) transforms neural activations to control commands, building a direct connectivity between human and external devices [1]. It is believed that disabled people with severe neurological dysfunction could significantly benefit from emerging interdisciplinary technology involving neural science, signal processing, machine learning, and pattern recognition. As a classical BCI paradigm, the steady-state visual evoked potential (SSVEP) signal that is generated by gazing at a frequency-encoded visual stimulus can be detected over the occipital sites, which is sensitive to rhythmic noise [2]. The analyses of such weak signal indicate that the response contains the fundamental (first) and higher harmonic components of the target stimulus frequency [3]. In recent decades, the use of SSVEP in BCI systems has attracted increasing research interest due to its superiority over other BCI systems with regard to a higher information transfer rate (ITR) and fewer training requirements [2–18].

In most publications on SSVEP-based BCI, the electroencephalogram (EEG) signals were derived from sparse electrodes, mostly O1, O2, or Oz (international 10/20 system) [2–11]. However, in this case, considerable inter-user variation in performance might occur [12]. To effectively manage inter-user variability, a variety of manual selection methods for individual optimal single- or dual-electrode locations have been widely investigated [12–14]. For example, Wang et al. used an independent component analysis (ICA) technique to select two optimal leads [13], and Wu et al. presented a stability coefficient method to select an optimal single-electrode location [14]. In addition, discrete Fourier transformation (DFT)-based power spectral density analysis (PSDA) is often used to extract these features.

Although these methods work well in BCI systems, they have some drawbacks. First, as signals from only one or double electrodes are used, these methods might not provide sufficient detection information or be sensitive to noise. Second, these optimal electrodes selection methods require time-consuming manual offline analyses that are specific for each subject, hence reducing the ease-of-use of BCI applications.

However, information fusion methods with multiple electrode locations may overcome these shortcomings and significantly improve system performance. To date, several such multi-electrode EEG-based methods have been reported [15–19]. For instance, Friman et al. proposed a minimum energy combination method, which was greatly superior because no calibration data were required and its recognition accuracy was high [15]. Bin et al. proposed a canonical correlation analysis (CCA)-based method, which gave a better performance than others [16]. In this method, the Fourier series of the first harmonic at each of the stimulus frequencies and multi-electrode electroencephalogram (EEG) signals are used to obtain the CCA coefficients, the largest of which serves as the frequency feature. The target frequency is then defined as the stimulus frequency with maximal feature value. However, there may exist a frequency interference problem for this CCA-based method when the stimulus frequencies are in the range of rhythmic

noise. In our study, we incorporated the first and higher harmonics. Since frequency interferences like occipital alpha wave do not contain higher harmonics, thus in the case of rhythmic noise, using the multi-harmonic features of SSVEP may be potential to reduce the interferences deteriorating the system performance.

The objective of this study is to explore possible ways to address the above challenging issues. First, we kept SSVEP and interference signals apart using a blind source separation (BSS) technique for multi-electrode raw EEG signals, resulting in multi-source components. Second, we proposed a new automatic SSVEP component selection (SCS) measure that combines features of individual harmonics, which can automatically identify the SSVEP component from the multiple components, in order to discriminate input patterns accurately. Based on the proposed method, an SSVEP-based BCI (SBCI) system with six stimulus frequencies was developed. In an offline analyses phase, we investigated a scope of key parameters and compared the performance of our method with that of the CCA of Bin et al. and the DFT-based PSDA as well. Our analyses illustrated that the proposed method gave better performance and reduced frequency interference. In an online test phase, the experimental results showed that the proposed method attained an average accuracy of 95.2 % and a practical bit rate (PBR) of 68.2 $\pm$ 15.9 bits min. The proposed method provides a promising solution to improve the ease-of-use and performance of SBCI. It could also be applied to the development of self-paced or hybrid BCI.

2 Methods

As shown in Fig. 1, the proposed SCS method mainly includes: (1) the BSS for the multi-electrode EEG raw signals, which produces multi-dimension source components; (2) multiple SCS measures for the components, of which the one with maximal value is defined as the SSVEP component; and (3) target recognition for the chosen component. In this way, the control intention of users can be decoded into a sequence of executable commands. The detailed procedure is described below.

2.1 Design of Stimuli Layout and EEG Records

In our SBCI system, a liquid crystal display (60 Hz refresh rate, 1024 $\times$ 768 screen resolution) was employed to generate stimuli, which was similar to that used by Bin et al. [16]. Six squares served as stimulus sources, flickering at six frequencies, i.e., 15, 12, 10, 8.6, 6.7, and 5.5 Hz, corresponding to six characters. Figure 2 shows the layout of the stimuli. EEG raw signals were measured from 32 scalp electrodes mounted in an elastic cap using a BioSemi ActiveTwo device (band pass, 3–45 Hz; sampled at 256 Hz). Electrodes were placed at 10–20 sites and the impedance was kept below 5 kΩ.

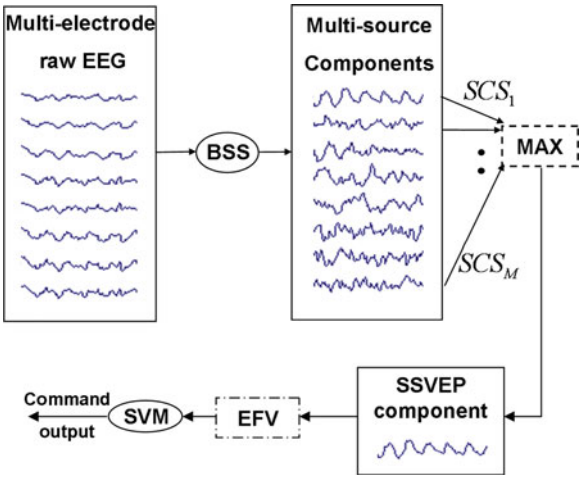

Fig. 1 Block diagram of the proposed method

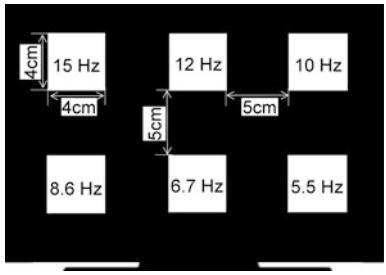

Fig. 2 Spatial configuration of the six stimuli on the screen

2.2 Subjects and Experimental Settings

Eleven healthy right-handed adults (5 women and 6 men; age range of 20–30 years old) with normal or corrected-to-normal vision served as paid volunteers after giving their informed consent. They were seated in a comfortable chair in a shielded recording chamber. Subjects 1 and 2 had taken part in SBCI tests before but the remaining was uninitiated in BCI use. During data acquisition, participants were asked to relax but remain attentive and avoid unnecessary movement. Our experiments consisted of offline analyses and online test phases. For the offline analyses, each subject performed six runs, each comprising 60 trials. Each trial started with the appearance of an arrow (1 s) in central vision, indicating subjects' attention to one stimulus. Then a black background was shown followed 1.5 s later by stimuli presentation (2 s). Each of the 6 stimuli was randomly indicated 10 times in one run, leading to 60 trials for each stimulus. Subjects were allowed to rest between runs to eliminate visual fatigue. For the online test, each stimulus represented one character, and the 15 Hz one served as a backspace option to correct errors. Each trial began with a cue presentation (0.3 s) of the next

character. Subjects were asked to input 30 predefined characters and received feedback at the top of the display at the end of each trial.

2.3 Multi-Electrode SSVEP Enhancement Based on BSS

In the presence of strong rhythmic noise, the SSVEP signal is too weak to extract effectively, and enhancement of the response is a challenging task for any SBCI. Our method uses robust BSS technology to address this problem. The assumption model on which our method is based is given below.

Assume that signals $X(t) \in R^{M\times 1}$ (t = T,…, NT) from M electrodes within an NT-s time window are recorded for each trial, where N is the number of sampling points and T the sampling period. The multi-electrode signals $X(t)$ are then expressed as

$$X(t) = A\sum_{i=1}^{N_h}(\sin(2\pi ift) + \cos(2\pi ift)) + BE(t), \tag{1}$$

where N_h denotes the number of harmonics and f the individual stimulus frequency. It indicates that (1) can be decomposed into two parts: the first part is the SSVEP signal that contains $\sin(2\pi ift)$ and $\cos(2\pi ift)$ pairs; the second, i.e., $E(t)$, is task-independent noise such as baseline drift, spontaneous EEG, specifically occipital alpha wave interference, and measurement error. The SSVEP signal and noise are added to each electrode signal, scaled with the weights vector $A \in R^{M\times 1}$ and matrix B, respectively. Assume the time window to be short enough for the SSVEP signal and noise to be stationary within this window, so the weights are time-invariant.

Since the SSVEP signal is an exogenous response [20], it is reasonable to suppose that there is statistical correlation among SSVEP harmonics, whereas the SSVEP signal is uncorrelated with strong noise including endogenous components and artifacts. Hence, enhancement of the SSVEP can be considered as a decorrelation problem, which is suitably addressed by BSS. Since BSS relies on the assumption that the source signals do not correlate with each other, it separates multi-dimension mixed signals into multi-source components so that the statistical correlation among the resulting components is minimized [21]. Hence, using proper BSS technology, the buried weak SSVEP response, including higher harmonics, could be extracted and enhanced as one source component of the highest signal-to-noise ratio (SNR). Inspired by the second-order blind identification technique [22], the robust decorrelation procedure in our method is detailed as follows:

Step 1: This is the so-called sphering process. First, the common average Ref. [19] for $X(t)$ is performed to correct the baseline. Subsequently, the one-step covariance matrix is used to reduce the interference of white noise. It can be transformed by singular value decomposition as

$$E\left[X(t)X(t-T)^T\right] = U\Sigma V^T. \tag{2}$$

We then have

$$Z(t) = SX(t) = \sqrt{\Sigma^{-1}}U^T X(t), \tag{3}$$

where $S = \sqrt{\Sigma^{-1}}U^T$ is a sphering matrix and $Z(t) \in R^{M\times 1}$ pre-sphered data.

Step 2: The covariance matrix of $Z(t)$ is given by

$$R_Z(k) = E\left[Z(t)Z(t-kT)^T\right], \tag{4}$$

where the time delay $k = 1,\ldots, d$. In this study, we set $d = \min(100, N/3)$ based on [21]. The decorrelation matrix $H \in R^{M\times M}$ is computed by

$$H = Q^T S, \tag{5}$$

where the orthogonal matrix $Q \in R^{M\times M}$ is obtained as a joint diagonalizer of the set $\{R_z(k)|k = 1,\ldots, d\}$. Belouchrani et al. [22] detailed the proof of the essential uniqueness of the joint diagonalizer and the approximate joint diagonalization algorithm. This approach is intended to reduce the probability that an unfortunate choice of time delay k results in a failure of decorrelation of Q from $R_z(k)$. Importantly, this approach generally increases the statistical efficiency of the procedure by using a larger set of statistics. Hence, robustness is significantly increased at little additional cost by processing a matrix set rather than a single covariance matrix, which enables reliable extraction of the SSVEP-only component. Moreover, unlike widely employed BSS procedures like ICA using higher order statistics, the BSS one only relies on second-order statistics, which enables fast calculation for online BCI.

Subsequently, the multi-source components $Y \in R^{M\times 1}$ can be extracted as

$$Y = HX, \tag{6}$$

where H^{-1} indicates a mixing matrix.

2.4 SSVEP Component Selection Based on the SCS Measure

However, it is unknown to us which of the multi-source components are the SSVEP one, due to inter-user variation and the intrinsic permutation uncertainty of BSS. Thus, it is difficult to define the SSVEP component automatically. To address this challenge, inspired by the physiological mechanism of SSVEP, we designed an automatic SCS measure based on CWT. In a previous study, we exploited CWT for one-electrode SSVEP detection [9] and indicated the superiority of complex Morlet CWT over FFT-based methods. In this paper, we attempt to extend the CWT-based method for multi-electrode SSVEP detection.

CWT is a well-established approach for time–frequency analysis [23]. Unlike short-time Fourier transform (STFT), the time–frequency kernel of CWT can efficiently utilize the correlation between time and frequency spaces. For a specific application, a properly chosen wavelet can provide optimal resolution and closely match the temporal properties. In our study, complex Morlet wavelet [23] is chosen as the mother wavelet due to the advantage of nonstationarity analysis for EEG signals.

Let us consider the single channel data $y(t)$ from any component of Y. The wavelet coefficient $W(a,b)$ can be obtained by CWT for $y(t)$, where $a > 0$ is the scale factor, which is inversely proportional to frequency f and b the position factor. According to the correlation between a and f [24], we have

$$W(f,b) = W(a,b)|_{a=f_s f_c/f,\ b\in[1,\ N]} \tag{7}$$

where f_s denotes the sampling frequency and f_c the complex Morlet wavelet center frequency. Then we define

$$\rho(f) = \frac{1}{N}\sum_{b=1}^{N} |W(f,b)|^2. \tag{8}$$

Over the whole time-domain, $\rho(f)$ represents the average energy of the component at f for $y(t)$. We then give the definition of CWT-based SNR (CSNR) as

$$\mathrm{CSNR}(f) = \frac{\rho(f)}{\frac{1}{q}\sum_{m=1}^{q/2}\left(\rho(f - mf_{\mathrm{res}}) + \rho(f + mf_{\mathrm{res}})\right)}, \tag{9}$$

where f_{res} is the frequency resolution, m the frequency step and q the step size. In practice, we empirically set 1 Hz as the band of adjacent frequencies ($f_{\mathrm{res}} = 0.25$ and $q = 4$).

In our study, we noted that for most users, higher SSVEP harmonics are very likely to have lower CWT energy but background noise is weak. Thus, higher harmonics generally have a higher CSNR. We also noted that the relative significance of different harmonics is user-specific. Hence, it is more reasonable to weight $\rho(f)$ at individual harmonic based on the significance of the corresponding CSNR. Then the frequency feature is as follows:

$$V_f = \sum_{i=1}^{N_h} w_i \rho(if), \tag{10}$$

subject to the constraint $\sum_{i=1}^{N_h} w_i = 1$. In our analyses, weight w_i is computed using offline data. After summing the CSNR at individual harmonic averaged over all stimulus frequencies, the proportion of each component to the sum is designated as the weight of the corresponding harmonic, resulting in N_h weights. This weighting strategy can flexibly decrease the relative significance of the harmonics with a low CSNR and increase that of harmonics with a high CSNR, thus improving the classification performance of the ensemble CWT energy feature. Further, using the ensemble feature can lower inter-user variation.

Subsequently, given the stimulus frequencies f_1, f_2,..., and f_r, we present an automatic SCS measure,

$$\mathrm{SCS} = \frac{\sum_{j=1}^{r} \left(V_{f_j} - \overline{V_f}\right)^2}{\sum_{j=1}^{r} \left(-\frac{V_{f_j}}{\sum_{j=1}^{r} V_{f_j}} \cdot \ln\left(\frac{V_{f_j}}{\sum_{j=1}^{r} V_{f_j}}\right)\right)}, \tag{11}$$

which is actually the ratio of the ensemble CWT energy variance to entropy and

$$\overline{V_f} = \frac{1}{r}\sum_{j=1}^{r} V_{f_j}. \tag{12}$$

The SCS is a contrast measure. For the SSVEP component, compared with other stimulus frequencies, V_f tends to have an almost distinct peak at the target frequency, leading to a high SCS measure value, and vice versa for the other components. We compute the SCS measure values separately for each of the source components Y, resulting in M measure values. Then the SSVEP component is automatically recognized by

$$c = \underset{l}{\mathrm{argmax}}(\mathrm{SCS}_l),\ l \in [1, M], \tag{13}$$

where SCS_l is the SCS value of the lth component in Y.

For the chosen SSVEP component, define the ensemble feature vector (EFV) using the previously obtained $V_{f_1}, \ldots, V_{f_r}$

$$\mathrm{EFV} = [V_{f_1}, V_{f_2}, \ldots, V_{f_r}]^T, \tag{14}$$

Then taking EFV as input feature vector, the support vector machine (SVM) [25] is used to perform online decoding of users' control intention. As a supervised learning method, SVM can obtain marked generalization performance based on statistical learning theory [26].

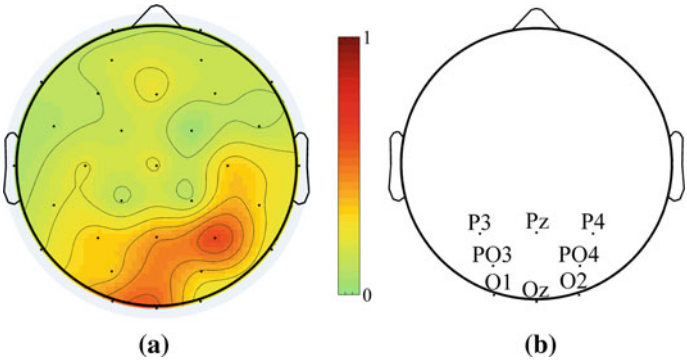

Fig. 3 **a** Scalp topography of grouped average absolute weights. **b** Common electrode locations for all subjects in our SBCI system. The *dots* denote the electrode locations on the scalp

2.5 Common Electrodes Selection

SSVEP is a localized potential [20]. Due to the introduction of less relevant EEG features, the use of considerable broad area for analyses may be not proper for the detection of features from multi-electrode signals. Therefore, it is preferable to perform the analyses on a scalp patch. To improve the universality and the ease-of-use of the SBCI, we located common electrodes for all subjects using the offline data with a 2-s time window.

For the chosen SSVEP component, the corresponding column in the mixing matrix H^{-1} can be normalized and adopted as a weight vector to obtain approximate SSVEP source distribution over the scalp [27], which can be helpful to determine electrode locations for the SBCI. The weights with relatively large absolute values indicate the relevance of the SSVEP component to corresponding locations. Figure 3a shows the scalp topography of the grouped average absolute weights for all subjects determined by EEGLAB [28]. Consistently with the fact that SSVEP is generated in this region [20], strong activities with large weights occurred in the occipital region, based on which, Fig. 3b gives the eight fixed common occipital electrode locations, which were used in the following offline analyses and online test phases unless otherwise specified.

2.6 Comparison Methods

For comparison, we performed the PSDA and the CCA of Bin et al. and contrasted the results with those of our approach. The electrodes for PSDA were selected from a set of 32 EEG sites according to [13], which manually chose two optimal leads with a highly normalized amplitude spectrum of SSVEP. The power

spectrum is then estimated using the differential signal of these leads. The target frequency defined for the PSDA is one that has maximal normalized amplitude. In the CCA, the fixed eight-electrode data were used to calculate the CCA coefficients with a Fourier series that consists of N_h harmonics for each of the stimulus frequencies. The target frequency is the one with the largest coefficient.

2.7 Evaluations

For offline analyses, a 10-fold cross-validation procedure was used to avoid overfitting [12], during which 90 % of the offline trials randomly selected were used to calculate the weights (w_i) and train the SVM model. The average of the cross-validated classification accuracy was used to evaluate the performance of the above three methods. The size of the time window (NT), and the number of harmonics (N_h) are critical for system performance. To explore proper parameters, the accuracy was computed for different NT (1.5, 2 s) and N_h (1, 2, 3). In all following analyses of variance (ANOVA) for statistical evaluation, p values were adjusted for sphericity violations using the Huynh–Feldt approach. If suitable, significant main and interaction effects were followed by post hoc tests including subsidiary ANOVAs or paired t tests with Bonferroni correction. All reported p values were significant with respect to adjusted α levels ($\alpha = 0.05$).

The alpha wave of most people ranges from 8 to 12 Hz [29]. In our study, the stimulus frequencies coincided with the alpha band, and thus the interference from alpha activity occurred in the SBCI [2]. As for this case, we performed an alpha band analysis detailed below to evaluate the sensitivity of the three methods to rhythmic noise.

Classification accuracy and traditional ITR separately are not sufficient to evaluate the effectiveness of an online BCI system [30]. For the online test, the PBR presented by Townsend et al. [30] was used to estimate the actual online performance of our system in this study, because it considers that every error results in a penalty of two additional selections. The PBR is calculated by (ITR $\times$ (1 – 2 $\times$ ER)), where ITR is measured in bits/min and ER the online error rate of the BCI system. In this way, a high bit rate cannot be achieved if performance accuracy is poor as PBR is used to assess the online speed.

3 Experimental Results

3.1 Offline Analyses

Figure 4 shows the overall comparisons among SCS and the other two methods applied to all subjects when different NT and N_h were selected. As for each subject,

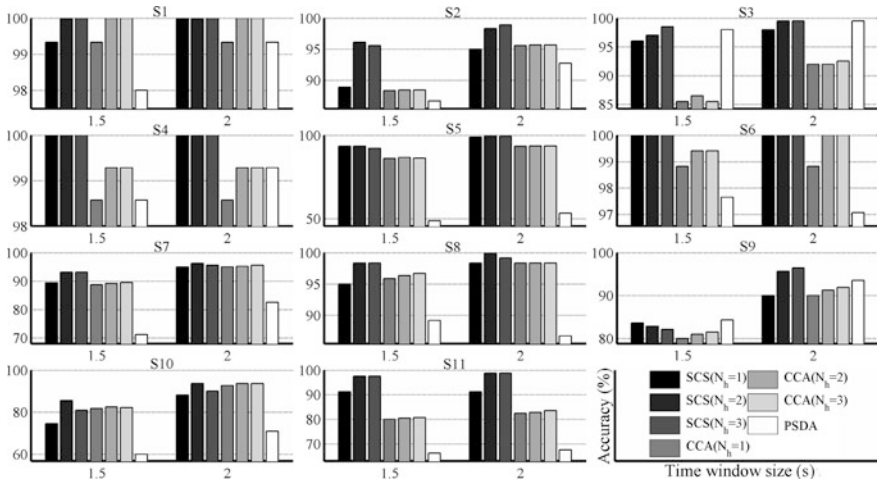

Fig. 4 Accuracy with respect to the time window size and number of harmonics for each subject using the three methods

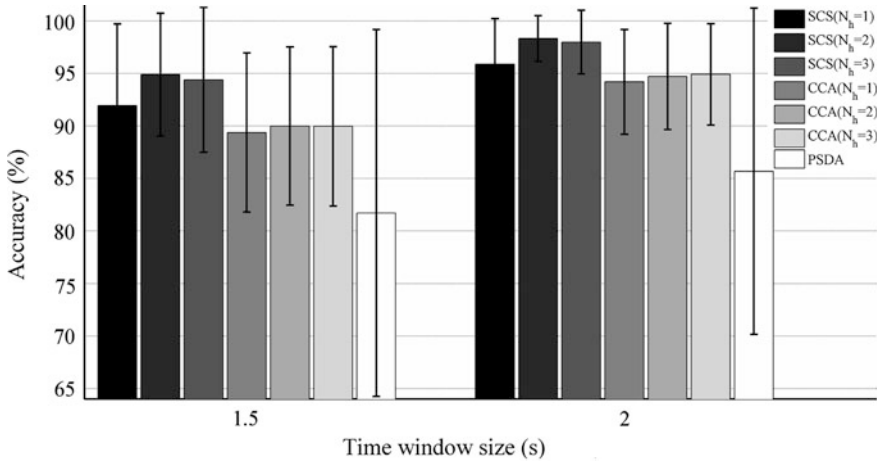

Fig. 5 Group average accuracy with different time window sizes and numbers of harmonics. The error bars denote standard deviations

the first three and the following three (from the 4 to 6th) bars of each time window size represent the performance of the SCS and CCA methods, respectively, with different N_h, and the last bar gives the accuracy of PSDA. It indicates that our method obtained higher recognition accuracy than the other two at various time window sizes for most of subjects, especially in the case of using higher harmonics ($N_h = 2, 3$).

As shown in Fig. 5, both the group average accuracy and the standard deviations were obtained using the three methods. The relatively smaller standard

deviations of our approach indicate less inter-user variation. Further, a repeated-measures ANOVA was performed with *NT* (1.5/2 s) and method of specific parameter (SCS($N_h = 1$)/SCS($N_h = 2$)/SCS($N_h = 3$)/CCA($N_h = 1$)/CCA($N_h = 2$)/CCA($N_h = 3$)/PSDA) as factors. Analyses showed that the 2-s time window yielded greater accuracy than the 1.5-s one ($F(1,10) = 12.5$, $p < 0.006$). Also, a main effect of method was found ($F(1.6,16) = 5.9$, $p < 0.02$). Post hoc tests revealed that in our method, using the first harmonic showed lower accuracy than two ($F(1,10) = 9.7$, $p < 0.02$) or three ($F(1,10) = 10.5$, $p < 0.01$) harmonics, but there was no significant difference ($F(1,10) = 1.2$, $p > 0.29$) between higher harmonics ($N_h = 2, 3$). Thus the first and second harmonics of SSVEP contain enough effective discrimination information. Besides, with N_h of being equal to 2, our method outperformed the CCA ($N_h = 1$) ($F(1,10) = 11.1$, $p < 0.009$), ($N_h = 2$) ($F(1,10) = 8.3$, $p < 0.02$), and ($N_h = 3$) ($F(1,10) = 8.1$, $p < 0.02$), as well as the PSDA ($F(1,10) = 8$, $p < 0.02$). To obtain acceptable performance and a higher PBR in the following alpha band analysis and online test, we thus set N_h to 2 and used a 1.5-s rather than a 2-s time window.

3.2 Alpha Band Analysis

Using CWT, the average value of $\rho(f)$ within 8–12 Hz was calculated as an index to evaluate the alpha activity of each subject in his or her idle state. A high index value denotes strong alpha activity and vice versa. Using the group average alpha activity as a threshold, the subjects were divided into two groups: group A, five subjects (S1, S3, S7, S10, and S11) with the index values greater than the threshold; group B, the remaining six with the index values equaling to or less than the threshold. To compare group A with B, we analyzed the 8.57, 10 and 12 Hz offline data in the alpha band using the above three methods, respectively. Table 1 lists the average results of both groups. The analyses were performed by a mixed-measures ANOVA, with group as between factor and method as within factor. Significant main effect of method was found ($F(1.5,13.1) = 6.2$, $p < 0.02$). Post hoc tests showed that in both groups, our method yielded higher accuracy than the PSDA ($F(1,10) = 9.4$, $p < 0.02$). In group A with strong alpha activity, the SCS approach attained greater performance than the CCA ($F(1,9) = 6.4$, $p < 0.04$). The above evidence verifies the robustness of our method to interference.

Table 1 Overview of average results for different methods among two groups

Group	Method		
	SCS (%)	CCA (%)	PSDA (%)
A	95.4 ± 6.1	89.3 ± 8.2	83.2 ± 19.1
B	95.3 ± 7.9	94.6 ± 6.5	82.3 ± 15.3

Table 2 Results of the online test

Subject	Accuracy (%)	PBR (bits/min)
S1	100	86
S2	96.7	72
S3	96.7	72
S4	100	86
S5	93.3	60
S6	100	86
S7	93.3	60
S8	96.7	72
S9	86.7	42
S10	86.7	42
S11	96.7	72
Average ± standard deviation	95.2 ± 4.8	68.2 ± 15.9

3.3 Online Test

The online test for the SBCI was carried out on 11 subjects. We used the parameters below: the eight electrode locations shown in Fig. 3b, the 1.5-s time window, and the two harmonics ($N_h = 2$). A character was produced every 1.8 s. From Table 2, it can be observed that the average accuracy of 30 commands reached 95.2 ± 4.8 %. The proposed method achieved an average PBR of 68.2 ± 15.9 bits/min.

4 Discussion

We proposed an SCS method for high-performance multi-electrode SBCIs. The advantages of our method are summarized as follows.

First, during our study, we observed that SSVEP-dominated component existed for each subject, due to the efficient separation between the SSVEP and the background noise via the BSS procedure. Thus, the proposed method is robust to noise interference, including the disturbance of non-target stimulus frequencies, spontaneous oscillation, and artifacts with similar frequencies to the stimulus responses, specifically the occipital alpha wave, as shown in Table 1.

Second, our method used higher SSVEP harmonics to further effectively improve the robustness to frequency interference and lower inter-user variation. Generally, SSVEP might have a user-specific distribution for different harmonics of the target frequency. Incorporating higher harmonics can provide sufficient descriptors of SSVEP. Several previous reports have shown that the adoption of higher harmonics could achieve better performance in SBCI than using only the first harmonic [3, 11, 12]. However, in the study by Lalor et al. adding the second harmonic reduced recognition accuracy [2]. These conflicting results led us to

hypothesize that traditional simple incorporation methods might not be appropriate for all users and that the use of higher harmonics was not effective enough. The proposed method thus used the ensemble CWT energy with weighted multi-harmonic according to the specific distribution of each user, which could further reduce frequency interference and improve group performance. Moreover, Fig. 5 shows that the use of the first two harmonics may be adequate to achieve high performance.

Third, satisfactory performance can be achieved fusing a few localized common electrode locations. The unsatisfactory results obtained with PSDA, as shown in Fig. 5, illustrate that dual electrodes provide insufficient detection information and are sensitive to noise. Although specific optimization for each user would certainly improve the performance of SBCI, common electrode locations can improve the ease-of-use of the SBCI application because the same electrode cap can be used for all users. The use of signals from multiple occipital channels may have contributed to the greatly improved results of the SCS and CCA methods. In addition, employing multi-electrode creates greater robustness against noise, whereas the use of signals within a broader area may bring greater noise interference and negatively affect performance. In our method, the eight occipital common electrode locations are capable of providing sufficient information to detect the SSVEP component automatically. In the meantime, key parameters such as the time window size and the number of harmonics were fixed, which further enhanced the convenience of the application. No complicated pre-processing is required other than having the steps to calculate harmonic weights and train the SVM model. These advantages make our method more practical for use in the real world. The online test results showed that we could achieve high performance and low inter-user variation with an average PBR of 68.2 $\pm$ 15.9 bits/min. Thus, based on our method, the SBCI can work well for any user after minimal training.

In addition, our method still has room for further improvement. The linearity of the human visual pathway is the underlying hypothesis of this study. However, there was sufficient evidence that the human visual pathway involves multiple neural mechanisms, each of which is preferentially sensitive to one abstract feature of the visual input through nonlinear processing [20]. Therefore, we are working on enhancing the proposed method to take this nonlinear dynamics into account.

5 Conclusion

This paper proposed the BSS and the SCS measure for SSVEP enhancement and extraction in high-performance SSVEP-BCI systems. In our system, eight common occipital electrode locations were defined for both offline analyses and online test. The offline results illustrated that our method achieved better performance than the widely used PSDA and CCA ones. Subsequently, we conducted an online test of the SBCI with a 1.5-s time window and two harmonics. The experimental results showed that the proposed method obtained an average accuracy of 95.2 % and a

PBR of 68.2 bits/min. In addition, the analyses also confirmed the robustness of our method with respect to frequency interference. Overall, the new method is believed to be applicable to the development of self-paced or hybrid BCI due to the ease-of-use and simplicity to comprehend.

Acknowledgments This work was supported in part by the National Science Foundation of China (NSFC) under Grant Nos. 90820305 and 60775040. The authors would like to thank all subjects for their participation.

References

1. Wolpaw JR, Birbaumer N, McFarland DJ, Pfurtscheller G, Vaughan TM (2002) Brain-computer interfaces for communication and control. Clin Neurophysiol 113:767–791
2. Lalor EC, Kelly SP, Finucane C, Burke R, Smith R, Reilly RB, McDarby G (2005) Steady-state VEP-based brain-computer interface control in an immersive 3D gaming environment. EURASIP J Adv Signal Process 2005(19):3156–3164
3. Müller-Putz GR, Scherer R, Brauneis C, Pfurtscheller G (2005) Steady-state visual evoked potential (SSVEP)-based communication: impact of harmonic frequency components. J Neural Eng 2:123–130
4. Shyu KK, Lee PL, Liu YJ, Sie JJ (2010) Dual-frequency steady-state visual evoked potential for brain computer interface. Neurosci Lett 483(1):28–31
5. Shyu KK, Lee PL, Lee MH, Lin MH, Lai RJ, Chiu YJ (2010) Development of a low-cost FPGA-based SSVEP BCI multimedia control system. IEEE Trans Biomed Circuits Syst 4(2):125–132
6. Lopez-Gordo MA, Prieto A, Pelayo F, Morillas C (2010) Use of phase in brain-computer interfaces based on steady-state visual evoked potentials. Neural Process Lett 32(1):1–9
7. Luo A, Sullivan TJ (2010) A user-friendly SSVEP-based brain-computer interface using a time-domain classifier. J Neural Eng 7(2)
8. Cheng M, Gao X, Gao S (2002) Design and implementation of a brain–computer interface with high transfer rates. IEEE Trans Biomed Eng 49(10):1181–1186
9. Zhang ZM, Li XQ, Deng ZD (2010) A CWT-based SSVEP classification method for brain-computer interface system. In: Proceedings of the IEEE international conference on intelligent control and information processing. Dalian, pp 43–48
10. Jia C, Gao X, Hong B, Gao S (2011) Frequency and phase mixed coding in SSVEP-based brain—computer interface. IEEE Trans Biomed Eng 58(1):200–206
11. Brunner C, Allison BZ, Krusienski DJ, Kaiser V, Müller-Putz GR, Pfurtscheller G, Neuper C (2010) Improved signal processing approaches in an offline simulation of a hybrid brain-computer interface. J Neurosci Meth 188(1):165–173
12. Müller-Putz GR, Eder E, Wriessnegger SC, Pfurtscheller G (2008) Comparison of DFT and lock-in amplifier features and search for optimal electrode positions in SSVEP-based BCI. J Neurosci Meth 168(1):174–181
13. Wang YJ, Wang RP, Gao XR, Hong B, Gao SK (2006) A practical VEP-based brain-computer interface. IEEE Trans Neural Syst Rehabil Eng 14(2):234–239
14. Wu ZH, Yao DH (2008) Frequency detection with stability coefficient for steady-state visual evoked potential (SSVEP)-based BCIs. J Neural Eng 5(1):36–43
15. Friman O, Volosyak I, Graser A (2007) Multiple channel detection of steady-state visual evoked potentials for brain–computer interfaces. IEEE Trans Biomed Eng 54(4):742–750
16. Bin G, Gao X, Yan Z, Hong B, Gao S (2009) An online multi-channel SSVEP-based brain-computer interface using a canonical correlation analysis method. J Neural Eng 6(4):046002

17. Pan J, Gao X, Duan F, Yan Z, Gao S (2011) Enhancing the classification accuracy of steady-state visual evoked potential-based brain—computer interfaces using phase. J Neural Eng 8(3):036027. doi:10.1088/1741-2560/8/3/036027
18. Yan Z, Gao X, Bin G, Hong B, Gao S (2009) A half-field stimulation pattern for SSVEP-based brain-computer interface. Proc IEEE Eng Med Biol Soc 2009(2006):6461–6464
19. Peters BO, Pfurtscheller G, Flyvbjerg H (2001) Automatic differentiation of multichannel EEG signals. IEEE Trans Biomed Eng 48(1):111–116
20. Regan D (1989) Human brain electrophysiology: evoked potentials and evoked magnetic fields in science and medicine. Elsevier, New York
21. Cichocki A, Amari S (2002) Adaptive blind signal and image processing: learning algorithms and applications (ch. 4). Wiley, Chichester
22. Belouchrani A, Abed-Meraim K, Cardoso J-F, Moulines E (1997) A blind source separation technique using second-order statistics. IEEE Trans Signal Process 45(2):434–444
23. Goupillaud P, Grossman A, Morlet J (1984) Cycle-octave and related transforms in seismic signal analysis. Geoexploration 23(1):85–102
24. Wang SY, Aziza TZ, Steina JF, Liu X (2005) Time–frequency analysis of transient neuromuscular events: dynamic changes in activity of the subthalamic nucleus and forearm muscles related to the intermittent resting tremor. J Neurosci Meth 145(1–2):151–158
25. Cortes C, Vapnik V (1995) Support-vector network. Mach Learn 20:273–297
26. Vapnik VN (1995) The nature of statistical learning theory. Springer-Verlag, New York
27. Sanei S, Chambers JA (2007) EEG signal processing (ch. 2). Wiley, Chichester
28. Delorme A, Makeig S (2004) EEGLAB: an open source toolbox for analysis of single trial eeg dynamics. J Neurosci Meth 134:9–21
29. Chatrian GE, Bergamini L, Dondey M, Klass DW, Lennox-Buchthal M, Petersén I (1974) A glossary of terms most commonly used by clinical electroencephalographers. Electroenceph Clin Neurophysiol 37:538–548
30. Townsend G, Lapallo BK, Boulay CB, Krusienski DJ, Frye GE, Hauser CK, Schwartz NE, Vaughan TM, Wolpaw JR, Sellers EW (2010) A novel P300-based brain-computer interface stimulus presentation paradigm: moving beyond rows and columns. Clin Neurophysiol 121(7):1109–1120

Human Gender Differences in Cognitive Preferences Toward Attractive Faces in a Visual Oddball Paradigm: An ERP Study

Zimu Zhang and Zhidong Deng

Abstract In this study, employing event-related potential (ERP) in response to faces and object stimuli, we explored the temporal course of cognitive biases and sex differences for facial attractiveness during a visual oddball paradigm. 10 women and 10 men were confronted with this task, within which they were asked to point out, as fast as possible, rare attractive or unattractive faces of neutral expression among a series of frequent stimuli (neutral objects). Behavioral analyses showed that men yielded longer reaction times than women, and deviant attractive faces were detected more slowly compared with deviant unattractive ones only for men. In accordance with the behavioral results, the ERP results showed that with respect to women, the N2b peak latencies were prolonged for both attractive and unattractive faces in men, perhaps reflecting early implicit attention to distinctive faces. Thereafter, for both sexes, deviant attractive faces evoked greater P3b amplitudes in comparison to deviant unattractive faces, revealing the cognitive biases toward facial beauty. Importantly, only in men, the P3b peak latencies were longer for attractive faces as opposed to their unattractive counterparts. Thus, it is likely that sex differences found in the detection of facial attractiveness could begin quite early in the information processing mechanism. Moreover, from an evolutionary view, the ERP and behavioral evidence together confirmed a reasonable supposition that although both men and women showed processing preferences for attractive faces, compared with women, men might attribute more value to distinctive evolution-related cues, especially to attractive information.

Keywords Facial attractiveness · Cognitive preferences · Gender differences · Event-related potential (ERP) · Oddball paradigm

Z. Zhang (✉) · Z. Deng
State Key Laboratory of Intelligent Technology and Systems, Tsinghua National Laboratory for Information Science and Technology, Department of Computer Science and Technology, Tsinghua University, Beijing 100084, China
e-mail: zzm09@mails.tsinghua.edu.cn

Z. Deng
e-mail: michael@tsinghua.edu.cn

F. Sun et al. (eds.), *Foundations and Practical Applications of Cognitive Systems and Information Processing*, Advances in Intelligent Systems and Computing 215,
DOI: 10.1007/978-3-642-37835-5_10,

1 Introduction

Cognitive preferences in visual processing have been explored mainly in the condition of emotional stimuli. For instance, cognitive psychologists have suggested that threatening or unpleasant images, like angry faces or snakes, capture our attention more quickly [1] and sustain it for a long period [2]. Likewise, functional magnetic resonance imaging (FMRI) and positron emission tomography (PET) researches have revealed that such images yielded greater neural activations with respect to neutral ones [3]. The vast majority of these findings have been elucidated from an evolutionary view, suggesting that it is adaptive to pay quick and persistent attention to items threatening to survival [1]. Since faces convey not only configural information but also great nonverbal aspects associated, inspired by the above findings, similar cognitive biases might likewise occur for attractive faces as evolution-relevant stimuli.

As previous evidence for this idea, so far, numerous recent brain imaging researches have suggested that some brain regions are distinguishingly sensitive to attractive with respect to unattractive faces [4–6]. For instance, O'Doherty et al. observed that medial prefrontal areas, as well as the medial orbitofrontal cortex and lateral areas, were more sensitive to attractive compared with unattractive faces [5]. However, what cannot be inferred from these findings is the timing of this attractiveness effect. The time course of neural responses can be explored using scalp-measured event-related potential (ERP) with its great high time resolution. This leads us to the first purpose of this study: to explore the temporal dynamics of likely cognitive preferences toward attractive faces during a variant of visual oddball paradigm by ERP technology.

Several ERP researches have employed a classical visual "oddball" task, in which subjects have to point out, among a train of frequent stimuli, a rare one. In this paper, we designed a variant of the oddball task, during which participants were confronted with a frequent stimulus (a neutral object) and two rare ones (an attractive and an unattractive face) that they are instructed to point out as fast as possible. The detecting of stimulus switch may be involved in orienting attention to biologically significant items [7]. This is marked by two representative ERP components. First, when participants are positioned in attention phase, rare stimulus elicits a N2b component, reaching a minimum on occipital sites at about 250 ms, which implies a change of attention to items of biological importance so as to facilitate subsequent processing [7, 8]. Next, a P3b component is yielded peaking mainly over parietal leads at about 400 ms, which is associated with later conscious, decisional, and premotor reaction-related phases [8]. Thus, in this attractiveness detection paradigm, employing ERP will enable us to explore the neural mechanisms of different processing phases.

Until now, several researchers have used ERP to explore the temporal course of neural activations in response to facial attractiveness. Images of attractive face may belong to the class of pleasant items. In accordance with this respect, during a latency range from 400 to 600 ms since stimulation onset, an enhanced centro-parietal positivity of the late positive component (LPC) was evoked by attractive faces with respect to unattractive ones [9–12], as well as by faces of beloved ones

compared with those of friends [13]. Using mixed-sex subjects, Werheid et al. showed that a more marked early posterior negativity (EPN); (230–280 ms) was evoked by attractive faces with respect to unattractive ones through an attractiveness categorization experiment [14]. This ERP influence has been considered to index significant emotion, allocating attentional resources to the processing of high-priority items [15]. Several lines of evidence revealed that attractive stimuli also yielded a greater occipitotemporal negativity at around 300 ms [11, 14]. Beside the above results, other studies have reported that a larger P2 was elicited by pleasant and unpleasant pictures [16], as well as attractive and unattractive faces [17]. Together, the above findings indicate that the encoding of facial attractiveness and emotion perhaps interact during not only one information processing phase, thus showing the significance of exploring the time dynamics of cognitive preference effects. In this study, we thereby explored ERP evidence for distinguishing processing resources allocation as a function of attractiveness degree within both typical N2b and P3b temporal periods in our oddball paradigm.

The second purpose of this study is: to confirm the supposition that men would yield a greater cognitive preference for the detection of attractive faces than women during the oddball task. More explicitly, from the evolutionary view, it is worth building if there are function-related sex differences in line with the distinguishing aspects that adapted men and women value, respectively, in their social behaviors. Using an emotional oddball paradigm, Campanella et al. found a prolonged N2b component, functionally linked to an attentional directing mechanism, in men for happy stimuli with respect to fearful ones [18]. Given the relationship between emotion and facial attractiveness (detailed above), it is likely that if humans are actually biased to focus on attractive faces, this should be more remarkable in men compared with women. As earlier findings for this idea, van Hooff et al. have reported an enhanced late slow wave only in men for attractive opposite-sex faces, marking promoted attention processing [17]. Based on previous results, in this study, we thus anticipated pronounced oddball-specific components modulations for attractive faces in men subjects.

In sum, in this study, we designed a visual oddball task in men and women as confronted with rare attractive or unattractive faces, independently of emotional expressions. Through the ERP technology, the principal objects were to investigate the time course of cognitive biases for attractive faces and to confirm the neural mechanisms of the evolution-related sex differences.

2 Methods

2.1 Participants

As paid volunteers, 10 men (mean age: 22.4) and 10 women (mean age: 21.9), participated in this experiment. All were right-handed, heterosexual, had normal or corrected to normal vision, and no psychiatric or neurological history. The study

was designed according to tenets of the Declaration of Helsinki. All subjects gave informed signed consent, and the study was approved by the departmental ethics committee.

2.2 Stimulus Materials

Before performing the experiment, each subject selected four neutral objects and eight faces (4 females) with the most attraction and non-attraction in one's view within an set of images, which included 328 unfamiliar young Chinese faces (164 females) from the oriental face database collected under the research of the Artificial Intelligence and Robotics (AI&R) [19] and 33 objects collected from different public-accessed websites. Using Adobe Photoshop, the faces were digitally edited to remove ears and hair, leaving merely a facial mask and all images converted to a unitary format (15 by 15 cm) in gray with a black background. These pictures were collected based on a prior behavioral study, in which a three-step rating on emotional expression (1: positive; 2: neutral; 3: negative) was performed as well as five-step rankings on factors of attractiveness, happiness, and arousal by 30 Chinese University students (15 men and 15 women; mean age: 21.5). Finally, 164 attractive face images, 164 unattractive faces, and 33 neutral objects were used as the choosing collection in the ERP experiment. T tests were conducted for the faces on the above factors, as listed in Table 1. Besides, faces were collected based on the following features: neutral expression, head position forward, forward eye-gaze, and with no aversive or odd characteristics.

2.3 Procedure

The testing procedure consisted of 8 blocks (4 blocks each repeated twice) of 100 stimuli (76 frequent stimuli: for example, object A neutral; 12 deviant face A attractive; 12 deviant face A unattractive). The order of the eight blocks varied across subjects. Each trial began with the presentation of a fixation cross (300 ms) followed by a random (range 1000–1300 ms) interstimulus interval. Then, a stimulus was presented (800 ms duration). Since the end of stimulation presentation, subjects had 1000 ms to detect each deviant face as ''attractive'' or

Table 1 Mean rankings of the choosing collection in the ERP experiment

Ranking factor	Non-attraction	Attraction	*P*	Objects
Emotional expression	2	2	>0.05	–
Attractiveness	2.09	4.10	<0.001	–
Happiness	2.12	3.84	<0.001	2.81
Arousal	3.32	3.35	>0.05	1.48

''unattractive'' as quickly and accurately as possible by pressing one of two horizontally arranged keys. The response to hand assignment was balanced across subjects. The order of stimuli was determined randomly. During the ERPs recording, subjects were seated in front of a computer screen on a chair in a soundproof, electrically shielded, dark room. All stimuli were presented in central vision. The duration of the experiment was about 45 min. Prior to the experiment, subjects were acquainted with the task in a training session.

2.4 ERP Recording and Data Processing

The electroencephalogram (EEG) was recorded (Neuroscan) from 64 electrodes mounted on an elastic cap according to the standard 10–20 system. The left mastoid served as reference. ERP waveforms were re-referenced to left and right mastoid off-line [20]. The ground electrode was on the medial frontal aspect. The vertical electrooculogram (EOG) was recorded by two electrodes positioned below and above the left eye. The horizontal EOG was detected from the external canthus of both eyes. The EEG and EOG were amplified, filtered (0.01–100 Hz), and digitized at 1000 Hz. The impedance of all electrodes was kept below 5 kΩ. Epochs beginning 200 ms prior to stimulation onset and continuing for 800 ms were made. ERPs were aligned to a 200-ms baseline. Trials contaminated with eye movements, blinks, EEG drifts, A/D saturation muscular and other artifacts (mean voltage exceeding ±80 μV) were excluded. Incorrect behavioral responses had to be rejected from further data processing. The EEG was averaged separately for all stimulus types [deviant attractive, deviant unattractive, and standard (where merely the standard stimuli prior to the rare ones were calculated to obtain the same number of averaged standard stimuli)]. The average waveforms were low-pass filtered at 30 Hz.

2.5 Data Analysis

(1) *Behavior*. As mean performance was correct at 98.72 %, only correct reaction times (RTs) were analyzed by mixed-measures ANOVA with sex (men, women) as between factor and attractiveness (attractive, unattractive) as within factor. Here and in all following ANOVAs, *P* values were corrected for deviation from sphericity according to the Huynh–Feldt method. If suitable, significant main and interaction effects were followed by post hoc tests including subsidiary ANOVAs with Bonferroni correction. All reported *P* values were significant with respect to adjusted α levels ($\alpha = 0.05$).
(2) *ERP*. For the difference-waveforms computed as we subtract the ERPs elicited by standard stimuli from those by the deviants, individual peak amplitude and

latency were analyzed for particular sets of sites in selected time windows: 200–300 and 350–550 ms, corresponding to the N2b and P3b components, respectively. These temporal periods were defined according to visual inspection of grand average waveforms and to prior studies of ERP about oddball designs. The sites included in the analyses were: FP1, FPz, FP2, F3, Fz, F4, FC3, FCz, FC4, C3, Cz, C4, CP3, CPz, CP4, P3, Pz, P4, O1, Oz, and O2. For exploring the modulations on the N2b that are considered to be evoked over the occipital area, a mixed-measures ANOVA was performed factoring sex (men, women), attractiveness (attractive, unattractive), and occipital lead (O1, Oz and O2). The effects of attractiveness on the P3b were analyzed via another mixed-measures ANOVA with sex (men, women) as between factor and attractiveness (attractive, unattractive), location (fronto-polar, frontal, fronto-central, central, centroparietal and parietal), and side (left, middle and right) as within factors.

3 Results

3.1 Behavioral Reactions

In women, the mean RT was 286.8 ms for attractive and 288.9 ms for unattractive faces. These values in men were 441.1 ms for rare attractive and 417 ms for unattractive faces. ANOVA revealed that there were significant main effects for sex ($F(1,18) = 7.8$; $P < 0.02$) and attractiveness ($F(1,18) = 4.7$; $P < 0.05$) as well as a significant interaction between sex and attractiveness ($F(1,18) = 6.7$; $P < 0.02$). Post hoc tests showed that independently of attractiveness levels, men reacted slower in comparison to women, but only for men, longer RTs were observed in response to rare faces detected as attractive than to those detected as unattractive ($F(1,18) = 11.3$; $P < 0.01$).

3.2 ERP Results

Grand average ERPs at representative midline sites are presented by Fig. 1 that shows, for women and men, respectively, the difference-waveforms obtained by the subtraction of ERPs in response to frequent stimuli and to rare ones. Visual inspection revealed that independently from whether rare faces were attractive or unattractive, two primary components, well known in visual oddball paradigms, were pronouncedly evoked: (1) the N2b component, mostly recorded over occipital location at about 250 ms; and (2) the P3b one, measured from parietal to frontal leads at approximately 400 ms [8].

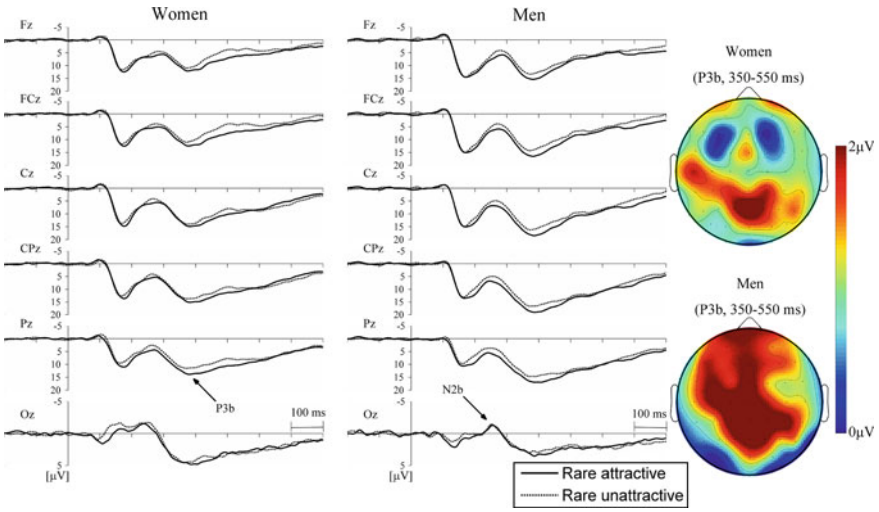

Fig. 1 Grand average ERP waveforms at representative midline sites for *women* and *men*, respectively, in response to the detection of *rare attractive* and *unattractive faces*. In the time period of 200–300 ms, a significant N2b component was found in the occipital leads. Also, a significant P3b effect was found in the temporal range of 350–550 ms from parietal to frontal locations. Differential scalp topographic maps for the P3b modulation are depicted in the *right part* of the figure in *women* and *men*, respectively (deviant attractive minus unattractive faces)

(1) *N2b* (200–300 ms). For peak amplitudes, the sex × attractiveness × lead ANOVA showed only a main effect of lead ($F(2,36) = 8.9$; $P < 0.001$) on the N2b component. No other comparisons were significant. However, for peak latencies, there were main effects for sex ($F(1,18) = 4.5$; $P < 0.05$) and lead ($F(2,36) = 4.4$; $P < 0.02$). Since neither main effect for attractiveness nor interaction (attractiveness × sex) was found, this means that men yielded longer N2b latencies with respect to women, regardless of attractiveness degrees and leads.

(2) *P3b* (350–550 ms). For peak amplitudes, the sex × attractiveness × location × side ANOVA showed main effects for attractiveness ($F(1,18) = 9.8$; $P < 0.01$), location ($F(2.1,37.8) = 15.5$; $P < 0.001$), side ($F(2,36) = 16.6$; $P < 0.001$), and a significant location × side interaction ($F(6,107) = 11.3$; $P < 0.001$) on the P3b, which suggests, for both sexes, an enhanced amplitude in response to deviant attractive faces than to deviant unattractive ones, as shown in Fig. 1 that gives the differential topographies of the P3b peak amplitudes (rare attractive faces minus their unattractive counterparts). For peak latency values, the statistical analyses revealed main effects for attractiveness ($F(1,18) = 4.5$; $P < 0.05$), location ($F(1.7,31.3) = 5.8$; $P < 0.01$), and a significant attractiveness × sex interaction ($F(1,18) = 10.8$; $P < 0.01$). Post hoc tests showed that the P3b peak amplitudes had at a later latency for deviant attractive faces in comparison to deviant unattractive ones, but only for men ($F(1,18) = 14.6$; $P < 0.01$).

3.3 Summary of the Results

Overall, the behavioral results were in agreement with the observed ERP patterns. Longer RTs were found for men than women, whereas men yielded slower RTs for rare attractive faces with respect to rare unattractive ones. In the mean time, longer peak latencies were observed for men as opposed to women on the N2b component. Subsequently it was revealed that merely for men, the P3b peak latencies were longer for rare attractive stimuli than their counterparts. Besides, it is worth noting that attractive faces evoked greater ERP amplitudes compared with unattractive ones on the P3b over anterior sites, independently of the subjects' sexes. In summary, the findings revealed marked sex differences and positive effects of rare attractive faces.

4 Discussions

4.1 Effects of Facial Attractiveness on Behavioral Reactions

The first important finding of this study is that men showed slower reactions to attractive faces than to unattractive ones. More time taken in detecting attractive faces might have revealed more attention directed to processing beautiful facial features. Corroborating evidence in this respect has been provided by Aharon et al. who suggested that more effort was exerted by the key press procedure in rating beautiful females as attractive with respect to attractive males [4]. Correspondingly, significantly slower RTs for attractive faces might have reflected that attractive faces made relatively deeper impressions on men, and men were more deliberate in detecting these than unattractive ones. These results are somewhat in accordance with those of Zhang et al. who found that subjects were significantly slower in recognizing attractive stimuli [12]. Marzi and Viggiano also reported enhanced accuracy in retrieving highly attractive faces compared with medium, low attractiveness, or unattractive ones [11]. Further, RTs in detecting attractive faces may be prolonged because attractive features more closely match men's cultural bias toward facial beauty. This explanation is consistent with the finding showing that attractive female faces led men to discount higher future rewards rather than smaller immediate ones [21].

4.2 Effects of Facial Attractiveness on ERP Components

In both men and women, N2b peak amplitudes and latencies yielded no difference between attractive and unattractive faces. In processing faces, early ERP effects reveal the detection of facial configurations or perceptual features that are related

to stimulus-driven attention mechanisms [22]. Thus, a likely explanation is that the N2b component found here may reflect an automatic triggering of attention and reveal pre-categorical low-level face features perceptual processing in face-specific ventral visual regions that produce structural representations used in subsequent stages of facial attractiveness detection [23]. Since in our task, with respect to neutral standard stimuli, the rare attractive and unattractive faces selected by the subjects were both distinctive, like the EPN that has been found on temporooccipital leads when watching emotional images [24], or for threatening in comparison to neutral faces [25], the N2b amplitudes have more been related to early stimulus-driven attention to distinct stimuli in general. This result is somewhat comparable to van Hooff et al.'s finding that no P2 amplitudes difference has been found between attractive and unattractive faces [17].

Moreover, for both sex, attractive faces yielded an enhanced anterior P3b component that was associated with several psychological functions including decision making, premotor response preparation, and context updating [18]. An ERP correlate of evaluation biases toward facial attractiveness is reflected by the augmented P3b component revealing the response-related phase. The previous results of Johnston and Oliver-Rodriguez indicated that an enhanced (LPC, 350–550 ms) was elicited by attractive faces [9], which is analogous to the P3b effect in our findings.

On the whole, the N2b and P3b components in our task could reveal different cognitive functions, covering perceptual attention, stimulus judgment, and decision making [18]. It is worth noting that the P3b modulation reflected cognitive biases toward detecting attractive faces. The result was consistent with the evolutionary theory, which suggests that attractive faces can influence reproductive success and mate choice [26]. Thus, such preferences found in our finding may be the adaptations of selecting good mates.

4.3 Effects of Facial Attractiveness on Reward and Emotional Processing

Several recent brain imaging researches have suggested that unpleasant and pleasant visual stimuli activate different neuronal regions [27, 28]. Thus, according to the prior behavioral evaluation for the face stimuli on dimensions of happiness and arousal, a reasonable hypothesis of our ERP patterns is that attractive faces are more emotionally rewarding to process and activate areas associated with emotion arousal. Previous results have shown more activation in the amygdala as viewing attractive than unattractive faces [4, 5]. Further, it is suggested that the amygdala could play some role in tuning the visual system to become more sensitive to vital cues by means of efferent projections to primary sensory areas [29]. Thus, the greater processing resources devoted to attractive faces can be considered as adaptive. Our studies are also in accordance with those of Aharon et al. who

suggested that variable reward value was yielded by attractive faces in both fMRI and behavioral experiments [4]. Besides, Senior reported that people focus predominantly on beautiful faces, possibly due to the higher intrinsic reward value that produced by them [6]. It is also assumed that the high reward value of attractive faces elicited enhanced ERP activity [10]. Under these suppositions, attractive faces promote synchronous activation of reward and emotional processing. Subsequently, these systems could enhance perceptual processing. Heightened P3b amplitudes in detecting attractive faces than unattractive ones support this respect.

4.4 Sex Differences During the Oddball Task

In accordance with behavioral results, we observed the important sex differences during the temporal course of oddball task. On the one hand, men yielded longer posterior N2b peak latencies than women, regardless of attractiveness levels, presumably revealing that during the early attentional phase in our target detection task, men recruited more processing resources to distinctive faces than women. On the other hand, as detailed above, the P3b component reflects a response-related phase of the information processing system that can be featured by its peak latencies [18]. Significantly, we found that although women and men did not differ in the peak latencies of the P3b for any attractiveness level, there was a significant attractiveness difference in the delay only for men. Specifically, at the response-related phase, women reacted almost simultaneously to attractive and unattractive faces, whereas men yielded later P3b peak latencies for attractive faces with respect to its counterparts, showing a complete accordance between neurophysiological and behavioral data. Actually, a behavioral delay was computed for RTs, indicating that attractive faces were detected by men more slowly than unattractive ones. An ERP correlate of men's behavioral delay was reflected by the corresponding prolonged P3b component. However, for both sexes, rare attractive faces all evoked greater P3b peak amplitudes than rare unattractive ones. This suggests that during the response-related phase, both men and women showed processing preferences for facial beauty. More importantly, men allocated more cognitive resources to attractive facial information than women.

These sex differences could be somewhat helpful for us to comprehend sexual strategy theory, which suggests that attractiveness is a more salient feature of potential mating for men with respect to women [30]. Our results were also analogous to the findings of van Hooff et al. who revealed that only men subjects yielded an augmented late slow wave for attractive opposite-sex faces, marking enhanced processing associated with promoted attention [17]. However, unlike them, in this study, men and women viewed faces of both sexes. This design enabled us to explore the hypothesis that with respect to women, men focus more on attractive faces in general, yet likewise there are some inferential limitations in our study. For instance, the supposition that men just pay more attention to

opposite-sex beauty than women during our oddball paradigm needs further exploration. Overall, the sex differences found within different processing phases indexed by the N2b and P3b confirm that in comparison to women, men value distinctive looks more, especially beautiful faces.

5 Conclusion

In summary, through the ERP technology, our findings indicated possible processing biases toward the detection of attractive faces in the visual oddball task. A temporal and functional association with these preferences was shown by observing the P3b effects in the information processing system. Plausible explanations for these results include higher intrinsic reward value and more positive emotional activation aroused by attractive faces compared with unattractive ones. Base on the evolutionary theory, attractive faces also denote mating value and reproductive fitness. More important, the neural differences due to sex were verified by revealing modulations of the N2b and P3b components, which indicated men's more cognitive preference toward distinctive faces especially facial beauty. This may be of significance to understand adapted men's mind in response to evolution-relevant information with respect to women. Further researches are needed to explore this issue.

Acknowledgments This work was supported by the National Science Foundation of China (NSFC) under grants No. 90820305 and No. 60775040. The authors are grateful to all subjects for their interest and participation as well as the Laboratory of Neural Engineering of Tsinghua University for offering the Neuroscan Synamps recording equipment.

References

1. Ohman A, Flykt A, Esteves F (2001) Emotion drives attention: detecting the snake in the grass. J Exp Psychol Gen 130(3):466–478
2. Fox E, Russo R, Bowles R, Dutton K (2007) Do threatening stimuli draw or hold visual attention in subclinical anxiety? J Exp Psychol Gen 130(4):681–700
3. Vuilleumier P (2005) How brains beware: neural mechanisms of emotional attention. Trends Cognitive Sci 9(12):585–594
4. Aharon I, Etcoff N, Ariely D, Chabris CF, O'Connor E, Breiter HC (2001) Beautiful faces have variable reward value: fMRI and behavioral evidence. Neuron 32(3):537–551
5. O'Doherty J, Winston J, Critchley H, Perrett D, Burt DM, Dolan RJ (2003) Beauty in a smile: the role of medial orbitofrontal cortex in facial attractiveness. Neuropsychologia 41(2):147–155
6. Senior C (2003) Beauty in the brain of the beholder. Neuron 38(4):525–528
7. Halgren E et al (1994) Spatio-temporal stages in face and word processing. 2. Depth-recorded potentials in the human frontal and rolandic cortices. J Physiol Paris 88(1):51–80

8. Campanella S, Gaspard C, Debatisse D, Bruyer R, Crommelinck M, Guerit J-M (2002) Discrimination of emotional facial expressions in a visual oddball task: an ERP study. Biol Psychol 59(3):171–186
9. Johnston VS, Oliver-Rodriguez JC (1997) Facial beauty and the late positive component of event-related potentials. J Sex Res 34(2):188–198
10. Oliver-rodríguez JC, Guan Z, Johnston VS (1999) Gender differences in late positive components evoked by human faces. Psychophysiology 36(2):176–185
11. Marzi T, Viggiano MP (2010) When memory meets beauty: insights from event-related potentials. Biol Psychol 84(2):192–205
12. Zhang Y et al (2011) Identifying cognitive preferences for attractive female faces: an event-related potential experiment using a study-test paradigm. J Neurosci Res 89(11):1887–1893
13. Langeslag SJ, Jansma BM, Franken IH, Van Strien JW (2007) Event-related potential responses to love-related facial stimuli. Biol Psychol 90(3):211–217
14. Werheid K, Schacht A, Sommer W (2007) Facial attractiveness modulates early and late event-related brain potentials. Biol Psychol 76(1–2):100–108
15. Schupp HT, Stockburger J, Bublatzky F, Junghöfer M, Weike AI, Hamm AO (2007) Explicit attention interferes with selective emotion processing in human extrastriate cortex. BMC Neurosci 8(1):16
16. Carretié L, Hinojosa JA, Martín-Loeches M, Mercado F, Tapia M (2004) Automatic attention to emotional stimuli: neural correlates. Hum Brain Mapp 22(4):290–299
17. van Hooff JC, Crawford H, van Vugt M (2011) The wandering mind of men: erp evidence for gender differences in attention bias towards attractive opposite sex faces. Soc Cognitive Affect Neurosci 6(4):477–485
18. Campanella S et al (2004) Human gender differences in an emotional visual oddball task: an event-related potentials study. Neurosci Lett 367:14–18
19. Oriental Face Database (OFD). http://www.aiar.xjtu.edu.cn/groups/face/Chinese/Homepage.htm
20. Luck SJ (2005) Basic principles of ERP recording, in an introduction to the event-related potential technique. MIT Press, Cambridge, p 107
21. Wilson M, Daly M (2004) Do pretty women inspire men to discount the future? Proc Roy Soc B Biol Sci 271(4):S177–S179
22. Chen A, Luo Y, Wang Q, Yuan J, Yao D, Li H (2007) Electrophysiological correlates of category induction: PSW amplitude as an index of identifying shared attributes. Biol Psychol 76(3):230–238
23. Eimer M (2000) The face-specific N170 component reflects late stages in the structural encoding of faces. NeuroReport 11(10):2319–2324
24. Foti D, Hajcak G, Dien J (2009) Differentiating neural responses to emotional pictures: evidence from temporal-spatial PCA. Psychophysiology 46(3):521–530
25. Schupp HT, Ohman A, Junghöfer M, Weike AI, Stockburger J, Hamm AO (2004) The facilitated processing of threatening faces: an ERP analysis. Emotion 4(2):189–200
26. Rhodes G (2006) The evolutionary psychology of facial beauty. Annu Rev Psychol 57(1):199–226
27. Gur RC, Gunning-Dixon F, Bilker WB, Gur RE (2002) Sex differences in temporo-limbic and frontal brain volumes of healthy adults. Cereb Cortex 12(9):998–1003
28. Wrase J (2003) Gender differences in the processing of standardized emotional visual stimuli in humans: a functional magnetic resonance imaging study. Neurosci Lett 348(1):41–45
29. Davidson RJ, Irwin W (1999) The functional neuroanatomy of emotion and affective style. Trends Cognitive Sci 3(1):11–21
30. Buss DM, Schmitt DP (1993) Sexual strategies theory: an evolutionary perspective on human mating. Psychol Rev 100(2):204–232

An Optimized Particle Filter Based on Improved MCMC Sampling Method

Aili Sang and Zhiquan Feng

Abstract Particle filter (PF) is used in the three-dimensional (3D) free hand tracking system, which is nonlinear and non-Gaussian. Markov chain Monte Carlo (MCMC) plays a positive role in Bayesian statistical calculation and the maximum likelihood estimation. This paper focuses on using of MCMC algorithm in the PF sampling to reduce the time cost. The 3D free hand tracking system is real-time by using the improved PF algorithm. First, do experiments in the virtual platform with data gloves and establish constraints of 3D free hand. Second, we analyze the obtained data to get the sampling model, which is applied into the PF algorithm. Finally, use VC++ to code the algorithm in 3D gesture tracking system, and then compare with correlation algorithms. The results show that the cost of time is reduced by more than 15 % than the human gesture part recognition sample method (HGPRS) with the high tracking accuracy.

Keywords Human–computer interaction · Particle filter (PF) · MCMC · Metropolis-Hasting sampling method · 3D free hand tracking system

1 Introduction

Human–computer interaction (HCI) [1] is the study of interaction techniques between the human and computers. That is the knowledge of the interaction connecting system with user and it connects the computer with people. The trend

A. Sang · Z. Feng (✉)
School of Information Science and Engineering, Shandong Provincial Key Laboratory of Network Based Intelligent Computing, University of Jinan, Jinan, China
e-mail: fzqwww@263.net

A. Sang
e-mail: specialshang@gmail.com

F. Sun et al. (eds.), *Foundations and Practical Applications of Cognitive Systems and Information Processing*, Advances in Intelligent Systems and Computing 215,
DOI: 10.1007/978-3-642-37835-5_11,

of HCI development is to be more natural, more harmonious, more intelligent, anytime, anywhere, and everywhere. Hands, face, and limbs as the most important organs of human play important roles and occupy irreplaceable positions not only in interpersonal interaction of social activities but also in the HCI. In recent years, interaction interface of free hand is a hot research topic in the field of HCI, and the tracking of the 3D free hand motion is one of the crucial and basic problems [2]. The paper [3] refers to the root, fingertips, and other key features of real-time video image and the process divided into two stages: coarse positioning and fine positioning. Complete the 2D hand recognition and the 3D hand tracking. Finally, complete the interactive tasks on real-time and precisely.

The main feature of the PF is its strong robustness against illumination, complex background, and self-occlusion. But the PF method requires a large number of samples to represent the posterior distribution [4]. For high-dimensional articulated object, assuming state X is a ten-dimensional variable, if consider each state takes 20 discrete values, and assume the general case $H = 5$, then the minimum required number of samples is 320,000,000, which is not acceptable [5]. Because hand is a typical high-dimensional articulated object and it is at least 26 degrees of freedom (DOF), achieve real-time tracking with great difficulty.

In 3D tracking, Paper [6] uses MCMC and PF to track multiple interacting targets. Paper [7] proposed a combination of the motion trajectory and the dynamic model to structure the sampling model, then use MCMC to estimate each basic piece of graph state independently, and use the consistency rule of motion region to choose the effective feature of target, occlusion state is defined as the disappearance of the corresponding part of picture, determined the foreseeable probability of the target by the combination of effective piece pictures. In machine learning and pattern recognition, combine with the PF to positioning robots [8]. In the finance file, study on China's futures market liquidity combined with MCMC [9].

There are articles of the simulation combined with the MCMC-PF algorithm [10]. In order to solve the problem of the loss of particle diversity after the resampling in PF algorithm, adding a MCMC moving step to increase the diversity of particles in the resampling step of PF, results simulating the target tracking show that the MCMC-PF algorithm outperforms the PF algorithm. Tao [11] proposed the improved tracking method, that is the PFMC based on MCMC which outperforms the PF algorithm from the tracking results. From the computational analysis, carrying out MCMC combining with the Metropolis-Hasting (MH) algorithm which is the improved method PFMC based on MCMC is heave computing, so the real-time is the inadequacies of the algorithm. The introduction of MCMC being part in the PF algorithm [10–13] is all aimed at the depletion of particles, particle degradation, increased particle's diversity, and effectiveness in the PF resampling step, while it also resulted that time consumption is relatively large.

From a fresh perspective, this article is not just in order to enhance the particle diversity but also to reduce time cost combined the MCMC with PF method. The improved PF combined with the MCMC sampling algorithm in 3D hand tracking is to get better sampling particles, prediction accuracy, tracking accuracy, and reduce the time cost. The main idea of this algorithm: One hand is to reduce the

sampling DOF, the other hand focus on using the MCMC algorithm to construct the PF sampling algorithm with high precision.

2 An Optimized PF Based on Improved MCMC Sampling

2.1 MCMC, the Metropolis-Hasting Sampling Method

MCMC algorithm, the idea is: get samples ($\boldsymbol{x}$) through the establishment of the stationary distribution of Markov chain $\prod(\boldsymbol{x})$.

The MCMC [14] is shortly represented as the following three steps:

(1) Select the corresponding stationary distribution of Markov chains of ($\boldsymbol{x}$), whose transfer nuclear is $\boldsymbol{p(X, X')}$;
(2) Starting from a point $\boldsymbol{X(0)}$ in the X, the Markov chain which is mentioned in step (1) to generate point sequence $\boldsymbol{X1}$,...,$\boldsymbol{Xn}$;
(3) A $\boldsymbol{m}$ and a $\boldsymbol{n}$, $\boldsymbol{n} \gg \boldsymbol{m}$, the expectations of any function $\boldsymbol{f(x)}$ is estimated as follows:

$$\hat{E}_x f = \frac{1}{n-m} \sum_{t=m+1}^{n} f(X^{(t)}) \tag{1}$$

Among them, the $\{X(t)\}\ t \geq 0$ is the Markov chain of X, the one step transition probability function is:

$$p(x \to B) = \int_B p(x, x')\mathrm{d}x' \tag{2}$$

The proposed algorithm uses the MH sampling method to construct MCMC methods. Steps are as follows [14, 15]:

1. Select an initial state of the Markov chain randomly, $\boldsymbol{X0 = x0}$.
2. By the transfer function $\boldsymbol{p(x, x')}$ to produce a try of movement $\boldsymbol{x'}$.
3. Generate random number $\boldsymbol{u(0, 1)}$, if $\boldsymbol{u < a(x, x')}$, then make $\boldsymbol{X1 = x'}$, otherwise to maintain the current status, that is $\boldsymbol{X1 = X0 = x0}$.
4. Repeat the above steps to generate $\boldsymbol{X1}$,…, $\boldsymbol{Xn}$.

2.2 The Kinematical Constraints

Three-dimensional skeleton model of the free hand in this article uses 1* 33 dimensional vector that is an array ***X[33]*** to represent the DOF, ***X[0]–X[33]*** parameters are as [16].

The range of joint angles and the constraint relations of joint angle are discussed in the literature [17, 18]. That refers the flexion/extension angle and the range of exhibition/adduction angle. Another constraint relation between the joint angles is the constraint of the natural posture. According to the study of statistical data, the angles of hand knuckles under a natural posture have strong linear constraints [18]:

$$\theta_{DIP}^{f/e} = \frac{2}{3}\theta_{PIP}^{f/e} \tag{3}$$

$$\theta_{PIP}^{f/e} = 2\theta_{MCP}^{f/e} \tag{4}$$

DIP is short for distal interphalangeal joint. The PIP is short for proximal interphalangeal joint. The MCP is metacarpophalangeal joint [18].

Data got through multiple data glove experiments is shown in Fig. 1, the results roughly fit with the conclusion of Cui Jinshi's [18] research, but the data got from data glove experimental platform are greatly different according to the different experimenters' habit, based on this, this paper through the 3D virtual platform gets the hands relationship, which is discrete, linear, simple, and more accord with the relationship of the changing angles in 3D virtual system.

Through the adjustment, the angle relationship of the index finger, middle finger and ring finger meet the following general relations:

$$\theta_{PIP}^{f/e} = \frac{2.99}{5}\theta_{MCP}^{f/e} \tag{5}$$

$$\theta_{DIP}^{f/e} = \frac{1.66}{5}\theta_{MCP}^{f/e} \tag{6}$$

And get each Angle range of index finger, middle finger and ring finger:

$$0 \leq \theta_{MCP}^{f/e} \leq 85 \tag{7}$$

$$0 \leq \theta_{PIP}^{f/e} \leq 50 \tag{8}$$

$$0 \leq \theta_{DIP}^{f/e} \leq 20 \tag{9}$$

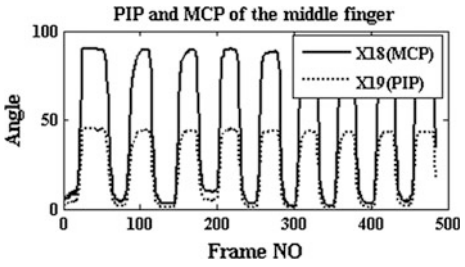

Fig. 1 Middle finger bended many times, the MCP and PIP relationship

This article reduces the parameter dimensions through the mutual relationship constraints.

2.3 Improved Particle Filter Algorithm with MCMC Sampling

Particle filter algorithm based on MCMC has been applied in vehicles tracking; the literature [19] put forward a real-time vehicles tracking and classification system using the MCMC-PF algorithm based on the kinematics model of vehicles; the number of sampling particles is 200, the algorithm is able to track and classify ten cars. However, method in the literature [19] is used in tracking high-dimensional joint object, 200 particles, and 26 DOF; this will not be real-time for the tracking. The literature [10–13, 20] focus on using MCMC to solve degradation and exhaustion of particles and then put forward the MCMC-PF algorithm to enhance robustness.

In conclusion, general MCMC-PF algorithm mainly uses MCMC algorithm to increase particle diversity, prevents particles exhaustion phenomenon, and can get very good enhancement robust algorithm but it cannot realize real-time effectively. According to this problem, this paper puts forward the improved PF algorithm based on the MCMC sampling algorithm to reduce time costs, enhance the real-time, and ensure the basis of high precision in 3D hand interactive platform.

In this paper, improved MH sampling method is used in the PF algorithm. Delete the PF resampling process to reduce time spending with ensuring a high quality conditions, then apply the algorithm in the 3D hand tracking interactive platform.

The specific procedures are as follows:

Vector parameter is $\boldsymbol{x_i}$.

Step 1: set state B as the current state, initialization:

$$x(0) = B \tag{10}$$

Step 2: get particle $\boldsymbol{x_i}$ +1 namely y by $\boldsymbol{x_i}$, structure the transfer nuclear equation as follows:

When $\boldsymbol{x_i = x(0)}$;

$$p(x_i, y) = (f(A, B) + x_i) + \text{Random}(0, 0.5) \tag{11}$$

When $\boldsymbol{x_i \neq x(0)}$;

$$p(x_i, y) = r^{-1} * \begin{bmatrix} f(x_{i-1}, x_i) * r_1 + f(A, B) * r_2 \\ + \text{Random}(0, f(A, B)) * r_1 + h(x_i) * r_2 \end{bmatrix} \tag{12}$$

$0 < \boldsymbol{r_1} < 1$, $0 < \boldsymbol{r_2} < 1$, which is experience value, and $\boldsymbol{r_1} + \boldsymbol{r_2} = \boldsymbol{1}$; $\boldsymbol{f(x, y)}$ is state transfer vector for the state transition $\boldsymbol{x \rightarrow y}$, including size and direction,

$\boldsymbol{f(A, B)}$ as experience value is used to adjust the size and direction of sampling particles; $\boldsymbol{h(x_i)}$ is linear interpolation function decided by state transfer $A \rightarrow B$. The bigger mold of $\boldsymbol{f(A, B)}$, the greater speed the $\boldsymbol{h(x_i)}$, $\boldsymbol{h(x_i)}$ and $\boldsymbol{f(A, B)}$ are with the same direction.

Step 3: get judgment toward particles, divided into two steps as the following:

(a) Adjust particle $\boldsymbol{x_i + 1}$ with constraints, for example, when the angle of middle finger MCP is greater than 85°, according to $0 \leq \boldsymbol{\theta}_{MCP}^{f/e} \leq 85$, it is to be 85°.
(b) After the adjustment, get the Hausdorff distance between particles and observations, when the Hausdorff distance is greater than the threshold value which set in the initialization, it should be abandoned, returned to the second step, and regain the particles.

Repeat the second and the third step, get $\boldsymbol{n + 1}$ sampling particles including $\boldsymbol{x(0)}$.

Step 4: get predicted state C:

$$C = \mathrm{E}(x) \tag{13}$$

State C is for sampling particle expectations, and:

$$\mathrm{E}(x) = \sum_{i=1}^{n} (x_i * \overline{\mathrm{Weight}_i}) \tag{14}$$

$$\overline{\mathrm{Weight}_i} = \mathrm{Weight}_i \Big/ \sum_{k=1}^{n} \mathrm{Weight}_k \tag{15}$$

$$\mathrm{Weight}_i = \exp(-\lambda * D_{\mathrm{hausdorff}}(x_i, g_i))^{\frac{b}{a}} \tag{16}$$

3 The Experimental Results

The experiment uses 3D skeleton model of hands in the literature [17]. The paper [17] expounds each of the DOF of 3D skeleton model. It states the joint of the kinematics constraint, angle changes in between -3^{o} and 90^{o}, the planes' angle of adjacent fingers excepted the thumb range from -20^{o} to $+20^{o}$, Angle range between thumb and the index finger is 0^{o} to $+90^{o}$, in addition, fingers are not overlap [17]. The experiment uses the constraints in Sect. 2.

The similarity function is the similar level between 3D information which is estimated from tracking method and 2D image features got after hand extraction from video. Particles' selection, precision of tracking system are closely related to the similarity function; so an effective similarity function can perform better in the PF algorithm, get high precision, and better evaluation of the final prediction. In this article, the Hausdorff distance is as the similarity function.

For two point set A and B the Hausdorff distance [21] of them is defined as follows:

$$D_{\text{hausdorff}}(A, B) = \text{Max}\left(\max_{a_i \in A}\min_{b_j \in B}\left\|a_i - b_j\right\|, \max_{b_j \in B}\min_{a_i \in A}\left\|b_j - a_i\right\|\right) \tag{17}$$

The equipment: A CCD camera of ZhongTeAnDing Technology Co. Ltd. The DH-CG410 image acquisition card produced Beijing China DaHeng (group) Co. Ltd. The PC with Intel (R) Core (TM) 2, 2.66 GHz CPU, and 4 GB memory. Programming environment is VC6.0. The Opengl technique builds virtual reality scenes. Platform uses parts of Opencv interface to process image.

(1) Track hand motion only and need not to complete interactive tasks. The experiment process is shown in Fig. 2. Figure 2a initialization success and starting tracking. Figure 2b except the thumb, other four fingers stop bending, that is their angle must stop changing, the virtual hand of 3D scene also stops. Figure 2c hands bending certain angles (hand does not completely hold) move in the 3D space, this time the finger bending angles is unchanged. Figure 2d hand is in the process of moving in with fingers bending.
(2) Apply the algorithm into the virtual reality platform with the assembly task, realize human–machine interaction. And complete contrast experiments using the assembly platform, verify the effectiveness of our proposed algorithm. The experiment process is shown as Fig. 2e. Establish assembly task scene. Assembly task process is: Move the screw and the nut from the original destination to the target destination. Assemble the crew and the nut in the target destination, complete assembly task. As shown in Fig. 2e, hand clutching screw moves to the target destination, then place screws on the target destination (table).

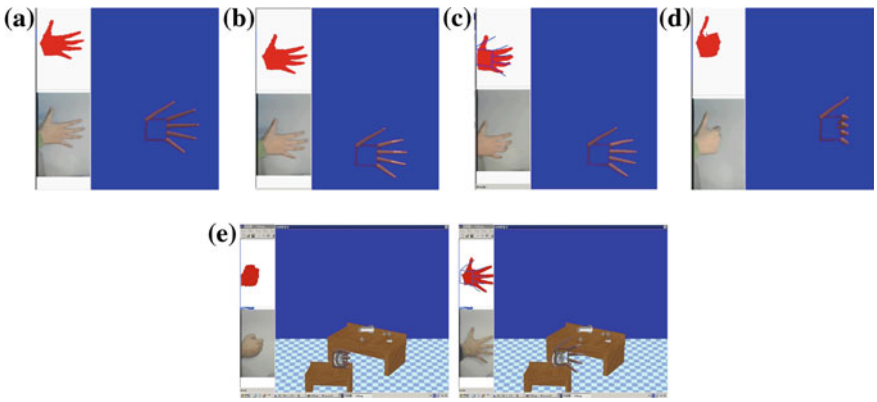

Fig. 2 **a** initialization, **b** fingers stop bending, **c** hand moves, **d** hand moves and fingers bend, **e** assembly platform of the screw and the nut

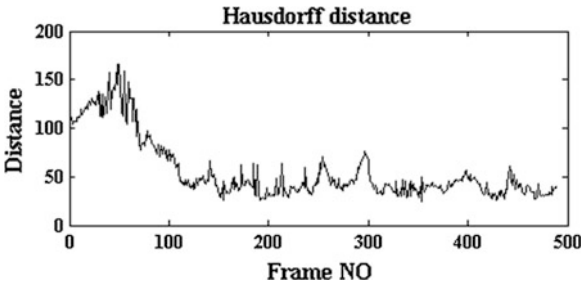

Fig. 3 The Hausdorff distance trend with the corresponding frame number

Data analysis results are as follows: Fig. 3, for an experiment the relationship between Hausdorff distance and frame number, the figure shows that data shock highly before the 100th frame. After the 100th frame, stabilize, so in this article accuracy obtained when frame state calculation stable from the 100th frame.

Precision [16] definition formula is as follows:

$$p_n = 2.5 * ((1/\sqrt{d_n - hd}) - 0.2) \tag{18}$$

$\boldsymbol{P_n}$ stands the precision, n is the number of particles, $\boldsymbol{hd}$ is for a experience value, which is 20 and $\boldsymbol{d_n}$ is the Hausdorff distance between the 2D projection of tracking result and the actual image observation information, the greater the $\boldsymbol{d_n}$, the lower the accuracy, the less the $\boldsymbol{d_n}$, the higher the accuracy [16], and $\boldsymbol{P_n}$ is the normalized result.

"S-M-H" is short for the improved MCMC sampling algorithms in this paper. The experiments take four different algorithms as comparative experiments, S-M-H stands for this paper's algorithm, Gauss is short for the PF algorithm based on gauss sampling, algorithm based on variable long markov chain is marked as VLMM, SMD stands method of [22] tracking algorithm, HGPRS marks human gesture part recognition sample [23]. Complete 20 interactive experiments with all algorithms, respectively, the method is different, the environment, the number of particles, the test machine, virtual scene, and other conditions are under the same condition. Results build experimental precision figure, is shown in Fig. 4, the precision of the improved method adopted in this paper is similar with HGPRS [16, 23] and higher than other sampling methods.

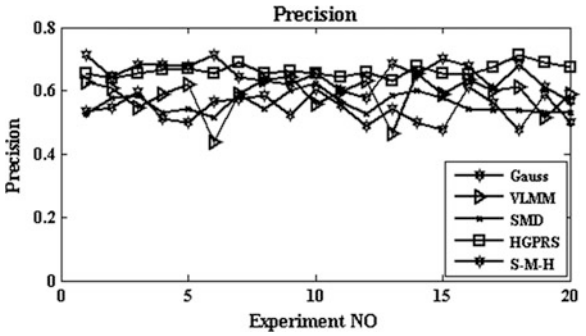

Fig. 4 Precisions of different tracking algorithms

Table 1 Average accuracy of 20 experiments of different algorithms

Algorithm	Gauss	VLMM	SMD	HGPRS	S-M-H
Precision	0.54	0.58	0.55	0.66	0.65

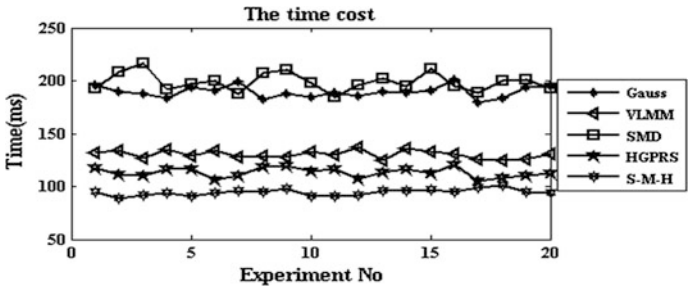

Fig. 5 Time cost of different tracking algorithms

Table 2 Average time of 20 experiments of different algorithms

Algorithm	Gauss	VLMM	SMD	HGPRS	S-M-H
Time (ms)	189.65	130.45	198.8	113.05	94.55

The average accuracy of different algorithms' 20 experiments is shown in Table 1, it can be seen that S-M-H algorithm and the HGPRS tracking precision are above 60 % higher than the other algorithms.

The experiments consume different time with the different number of particles, different experimental environment, and other factors such as the machine configuration changes. So ensure that the experimental results comparable, experiments are in the same experiment environment, the same particle number, the same PC, and the same virtual scene, do 20 times with each algorithm. Get the results is shown in Fig. 5, Time cost of S-M-H sample tracking algorithm is less than HGPRS and VLMM, far less than SMD and Gauss.

Average time of the different algorithms' 20 experiments, which is shown in Table 2, it can be seen that S-M-H algorithm is less than 100 ms (ms), and the others in time are larger than 100 ms, even more than 180 ms. Altogether, it is known that our algorithm has a distinct advantage in time.

4 Conclusion

The real-time and accuracy are taken into account in the PF process, we proposed S-M-H sampling algorithm to construct an optimized PF which is based on improved MCMC and combined with kinematical constraints, finally applied it in 3D hand tracking experiments. Compared to the HGPRS [16, 23], our algorithm

reduced by 16.3644 % in time cost in the condition of the similar accuracy and reduce by more than 50 % compared to other algorithms including VLMM, SMD, Gauss, the results verifies the effectiveness and the superiority of our algorithm.

References

1. http://en.wikipedia.org/wiki/Human%E2%80%93computer_interaction
2. Zhu D (2011) Research on 3D hand tracking based on interactive analysis. University of Jinan, Jinan
3. Feng Z, Yang B, Chen Y, Zheng Y, Xu T, Li Y, Xu T, Zhu D (2011) Features extraction from hand images based on new detection operators. Pattern Recogn 44:1089–1105
4. Feng Z, Yang B, Li Y, Zheng Y, Zhang S (2009) Research on hand gestures tracking based on particle filtering aiming at optimizing time cost. Acta Electronica Sin 37:1989–1995
5. Chen R, Liu G, Zhao G, Zhang J, Li H (2005) 3D human motion tracking based on sequential Monte Carlo method. J Comput Aided Des Comput Graph 17:85–92
6. Khan Z, Balch T, Dellaert F (2004) An MCMC-based particle filter for tracking multiple interacting targets. Computer Vision-ECCV 17:85–92
7. Lu J, Cai A, Li L (2011) Moving object tracking based on part template matching. J Optoelectron Laser 22:297–301
8. Xu S, Xie L, Liu J (2007) Robot localization based on MCMC particle filter. J Zhejiang Univ (Eng Sci) 41:1083–1087
9. Lu B, Hua R (2010) Research on liquidity of Chinese futures markets via MCMC method. J Manage Sci China 13:98–106
10. Gao J, Li S, Shao K (2009) Application and research of MCMC particle filter algorithm. Electron Test 12:19–22
11. Tao W, Wang L, Lin X (2007) The improved particle filter algorithm based on MCMC methods. J Hangzhou Dianzi Univ 27:52–55
12. Zhang M, Liu X (2009) Target tracking algorithm based on MCMC unscented particle filter. Syst Eng Electron 31:1810–1813
13. Feng C, Zhao N (2009) Research on MCMC particle filter algorithm based on effective particles. Appl Sci Technol 36:19–22
14. Cao C (2007) The parameter estimation of the statistics models based on the MCMC method. Nanjing University of Aeronautics and Astronautics, Nanjing
15. Tian F (2007) Markov chain Monte Carlo algorithm. Hubei University, Hubing
16. Xu T (2011) Research on moving hand tracking based on behavior analysis. University of Jinan, Jinan
17. Feng Z, Meng X, Lin Y (2006) Research on moving human-hand tracking based on dynamic visual fingers. J Syst Simul 18:2351–2354
18. Cui J (2004) Studies on three-dimensional model based posture estimation and tracking on articulated objects. Tsinghua University, Beijing
19. Bardet F, Chateau T (2008) MCMC particle filter for real-time visual tracking of vehicles. In: Proceedings of 11th international IEEE conference on intelligent transportation systems, ITSC 2008, pp 539–544
20. Jing L, Vadakkepat P (2010) Interacting MCMC particle filter for tracking maneuvering target. Digit Signal Process 20:561–574
21. Song X (2010) Research on 3D hand tracking based on cognitive model. University of Jinan, Jinan
22. Bray M, Koller-Meier E, Van Gool L (2007) Smart particle filter for high-dimensional tracking. Comput Vis Image Underst 106:116–129
23. Feng Z, Yang B, Li Y, Xu T, Shang A, Liu C, Jiang Y (2012) Hand tracking method based on interactive behavioral analysis. Comput Integr Manuf Syst 18:31–39

A Novel Spectrum Sensing Algorithm in Cognitive Radio System Based on OFDM

Liu Yun, Qicong Peng, Fuchun Sun, Huaizong Shao, Xingfeng Chen and Ling Wang

Abstract In cognitive radio (CR) networks, spectrum sensing which attracts a lot of interest is a significant task. Aiming at the problem that conventional spectrum sensing technique is usually focused on signal band. This paper introduces a multi-band joint spectrum detection based on multiple signal classification (MUSIC) algorithm for orthogonal frequency division multiplexing (OFDM) cognitive ratio system. The proposed eigenvalue-construct method only uses signal autocorrelation of OFDM symbols and simple sorting to achieve the spectrum detection. The computer simulations show that the proposed approach has a good performance compared with the conventional energy sensing method which uses the same threshold over multiple frequency bands.

Keywords Cognitive radio · Multiple signal classification · Orthogonal frequency division multiplexing · Spectrum sensing

1 Introduction

The cognitive radio (CR), as a revolutionary technology of the spectrum sharing, is considered as the best schedule of resolving the spectrum "scarcity" and improving the spectrum utilization [1–4]. Spectrum sensing is a key task in a CR.

L. Yun (✉) · Q. Peng · H. Shao · L. Wang
School of Communication and Technology Engineering, University of Electronic Science and Technology of China, Chengdu 610054, China
e-mail: liuyun001@uestc.edu

F. Sun
State Key Lab of Intelligent Technology and Systems, Department of Computer Science and Technology, Tsinghua University, Beijing 100084, China

X. Chen
State Key Laboratory of Remote Sensing Science, Institute of Remote Sensing Applications, CAS, Beijing 100101, China

F. Sun et al. (eds.), *Foundations and Practical Applications of Cognitive Systems and Information Processing*, Advances in Intelligent Systems and Computing 215,
DOI: 10.1007/978-3-642-37835-5_12,

It allows identification of spectral holes and helps in exploiting them efficiently. Moreover, it helps in controlling the level of interference caused to primary users (PUs) of the spectrum. Sensing provides awareness of the radio operating environment. A CR may then adapt its parameters such as carrier frequency, power, and waveforms dynamically in order to provide the best available connection and to meet the user's needs within the constraints on interference.

Orthogonal frequency division multiplexing (OFDM) will be a key technology in broadband wireless communication systems. Among OFDM systems are: IEEE 802.11a/gWireless LANs, IEEE 802.16 or WiMAX Wireless LANs, IEEE 802.20 or mobile broadband wireless access (MBWA) systems, long-term evolution (LTE), for example. Therefore, it is reasonable to assume that the PUs will often use OFDM transmission. Hence, the problem of detecting OFDM signals is very relevant.

Several spectrum sensing methods have existed in the literatures. Energy detection has been considered in [5–7], matched filter detection in [5] and [8], cyclostationary feature detection in [9] and recently emerged eigenvalue-based detection in [10–12]. Each of these techniques has its strengths and weaknesses. For example, matched filter detection and cyclostationary feature detection require knowledge on the wave form of the primary user, which is impractical for certain applications. Energy detection and eigenvalue-based detection belong to the so-called blind detection methods which do not need any a priori information of the signal. However, energy detection suffers from the noise-uncertainty problem [6], in which inaccurate estimation of noise power will lead to the SNR wall [13]. The newly proposed eigenvalue-based detection algorithms circumvent the need of knowledge about noise power. Therefore, they outperform energy detection in the case of noise uncertainty [10]. The eigenvalue-based detection schemes proposed so far are based on asymptotical analysis. Specifically, these schemes rely on the distribution of the ratio between the largest and smallest eigenvalues of the received covariance matrix. This distribution has only been derived for the case when the number of received samples tends to infinity [12]. An exact analysis of eigenvalue-based detection, however, requires the knowledge of the ratio distribution of finite dimensional covariance matrices, which is generically mathematically intractable. In this paper, we propose a new detection scheme based on the eigenvalue of autocorrelation matrix in frequency domain to estimate the number of subcarriers occupied by the PUs and to detect free subcarrier frequency bands by simple energy sorting for OFDM cognitive ratio system.

The rest of this paper is organized as follows. In Sect. 2, we introduce the signal model of the OFDM cognitive ratio system. In Sect. 3, the proposed statistical blind estimation algorithm is derived. Computer simulation results are given in Sect. 4, and conclusions are drawn in Sect. 5.

2 The Signal Model of the Cognitive Radio System Based on OFDM

We consider a CR system based on OFDM with N subcarriers signaling through the additive white Gaussian noise (AWGN) channel. At the transmitter end, N complex data symbols are modulated onto the N sub-carriers by using IFFT. The last NCP samples of the IFFT outputs are then copied and added to form cyclic prefix (CP) at the beginning of each OFDM symbol. So the time-domain transmitted signal can be expressed as:

$$r(t) = \sum_{l=-\infty}^{\infty} \left[\sum_{k=-K}^{K} X_{l,k} e^{i2\pi(f_{c,j}+k\Delta f)(t-T_{CP}-lT)} \right] U_T(t - lT) + u(t) \tag{1}$$

where $T = T_{\text{FFT}} + T_{\text{CP}}$ is OFDM symbol interval, T_{FFT} and T_{CP} denote the FFT/IFFT period and CP $X_{l,k}$ is data of the kth subcarrier during the lth OFDM symbol duration. It may be safely approximated as zero-mean random variables with the correlation $E\left\{X_{l,k}X^*_{l',k'}\right\} = \sigma_s \delta(k-k')\delta(l-l')^*$ denotes conjugate operator. Δf is the subcarrier frequency spacing and $f_{c,j}$ is carrier frequency of the jth sub-band. $U_T(.)$ is a rectangular function.

The baseband-modulated digital signal $r(n)$ is available after sampling and parallel to serial conversion. Thus, $r(n)$ can be expressed as:

$$r(n) = \sum_{l=-\infty}^{+\infty} \sum_{k=0}^{N} \frac{X_{l,k}}{N} e^{j\frac{2\pi k(n-N_{CP}-lM)}{N}} \text{rect}(n - lM) + u(n) = s(n) + u(n) \tag{2}$$

where $u(n)$ is a white complex Gaussian noise with variance σ_u^2, and independent of the signal $s(n)$. If we only consider one OFDM symbol, the received signal with the normalized carrier frequency offset (CFO) ε can be written as follows:

$$x(n) = \frac{1}{N} \sum_{k=0}^{N} X_{0,k} e^{j\frac{2\pi kn}{N}} e^{j\frac{2\pi \varepsilon n}{N}} + u(n) = \sum_{k=0}^{N} A_k e^{j\omega_i n} + u(n) \tag{3}$$

where $A_k = X_{0,k}/N$, $\omega_k = 2\pi(k+\varepsilon)/N$.

3 Multi-Band Joint Spectrum Detection Algorithm

In this section, we proposed a new scheme to realize spectrum sensing. The method which is not the conventional spectrum sensing technique usually focusing on signal band uses all subcarrier dates to detect the spectrum holes.

First, the method estimates the number of subcarriers occupied by PUs (PUs) based on MUSIC method. The proposed algorithm is a blind approach which is spatial spectrum estimation method using eigenvalue-construct method to estimate

the number of subcarriers occupied by the PUs. The algorithm uses the orthogonality between signal subspace and noise subspace, which is easily satisfied for OFDM system, to estimate subcarrier number by searching the maxima of the pseudo spatial spectrum.

The baseband-modulated signal can be seen as stationary stochastic process. We arrange the received signals into the following observation vector:

$$X(n) = \begin{pmatrix} x(n) \\ x(n-1) \\ \vdots \\ x(n-P+1) \end{pmatrix} = \begin{pmatrix} 1 & 1 & \cdots & 1 \\ e^{-j\omega_1} & e^{-j\omega_2} & & e^{-j\omega_N} \\ \vdots & \vdots & & \vdots \\ e^{-j(P-1)\omega_1} & e^{-j(P-1)\omega_2} & \cdots & e^{-j(P-1)\omega_N} \end{pmatrix} \cdot \begin{pmatrix} A_1 e^{-j\omega_1 n} \\ A_2 e^{-j\omega_2 n} \\ \vdots \\ A_N e^{-j\omega_N n} \end{pmatrix} + \begin{pmatrix} u(n) \\ u(n-1) \\ \vdots \\ u(n-P+1) \end{pmatrix} = A(w)S(n) + U(n) \tag{4}$$

Where *U(n)* is the noise vector, *S(n)* is the signal vector, and $A(w) = [a(\omega_1), a(\omega_2), \ldots, a(\omega_N)]$ is the steering matrix, $a(w_i) = [1, e^{-jw_i}, \ldots\ldots, e^{-j(P-1)w_i}]^T$ is the steering vector, where the superscript T denotes the transposition operation.

From the above analysis and the characteristics of OFDM symbols in CR systems, we can see that $a(\omega_i)$ is linear independent for different ω_i and the signal and the noise are not related. We define the correlation matrix by the expectation of the outer product of the observation vector *X(n)* with itself. Let *Rxx* denotes the $P \times P$ autocorrelation matrix defined in this way. We thus write

$$\begin{aligned} Rxx =& E\{X(n)X^H(n)\} = A(w)E\{S(n)S^H(n)\}A^H(w) + E\{U(n)U^H(n)\} \\ =& AS_PA^H + \sigma_u^2 I \end{aligned} \tag{5}$$

For a stationary discrete time stochastic process, the*Rxx* can be expressed as:

$$Rxx = \lim_{N_s=\infty} \frac{1}{N_s} \sum_{n=1}^{N_s} X(n)X^H(n)N_s \tag{6}$$

where the superscript H denotes Hermitian transpose operation, $\sigma_u^2 I \in C^{P\times P}$ is the noise covariance matrix, and $S_P = E\{S(n)S^H(n)\} = \text{diag}\left\{|A_1|^2, |A_2|^2, \ldots, |A_N|^2\right\}$ is the signal covariance matrix. When $P \geq N, \text{RANK}(A) = N$ A is column full rank, thus $\text{RANK}(AS_PA^H) = N$.

Take eigen decomposition to AS_PA^H as follows:

$$AS_PA^H = \sum_{i=1}^{P} \lambda_i' u_i u_i^H = S\Lambda S^H \tag{7}$$

where $S = [u_1, u_2, \cdots, u_N]$, $\Lambda = \mathrm{diag}\{\lambda'_1, \lambda'_2, \cdots, \lambda'_N\}$, and $\lambda'_1 \geq \lambda'_2 \geq \cdots \geq \lambda'_N > 0$, $\lambda'_{N+1} = \lambda'_{N+2} = \cdots = \lambda'_P = 0\,\lambda'_i$ and u_i denote eigenvalue and normalized eigenvector of matrix AS_PA^H, respectively. The matrix Rxx is hermit matrix, thus the eigen decomposition of Rxx can be expressed as:

$$Rxx = \sum_{i=1}^{N} (\lambda'_i + \sigma_u^2) u_i u_i^H + \sigma_u^2 \sum_{i=N+1}^{P} u_i u_i^H = \sum_{i=1}^{P} \lambda_i u_i u_i^H \tag{8}$$

The eigenvalue of Rxx can be written as follows:

$$\lambda_i = \begin{cases} \lambda'_i + \sigma_u^2, i = 1 \ldots N \\ \sigma_u^2, i = N+1 \ldots P \end{cases} \tag{9}$$

From Eq. (9), the eigenvalue of Rxx includes two parts: the first N eigenvalues is the sum of λ' and variance of noiseσ_u^2; the other $P - N$ eigenvalues only include variance of noise σ_u^2.λ' is significantly larger than the σ_u^2 when the signal-to-noise-power-ratio (SNR) is high enough. So we can easily find the number of larger eigenvalues N from all values. In the CR system based on OFDM, N is the number of subcarriers occupied by the PUs.

Since we have estimated the number of subcarriers occupied by the PUs, so just sorting the data in all subcarrier channels according to the energy in frequency domain, the N subcarrier channels which have larger energy are occupied by the PUs and the others are free subcarrier frequency bands which can be used by secondary users (SUs).

The eigen decomposition of autocorrelation matrix Rxx is the key technology for the proposed scheme from the above description and analysis. The CFO has no influence for the estimation of subcarrier number in the algorithm from Eq. (3). The number of symbols used for the calculation of correlation matrix Rxx should be large enough from Eq. (6). Whereas the complexity will augments with the increasing of Ns. Thus, the correct choice of Ns is very important in the approach. The decision threshold is also not necessary in this scheme from the above description.

4 Simulation Results and Comparisons

Numerical results are presented to demonstrate the performance of the proposed spectrum sensing in CR system based on OFDM. Throughout the simulations, the OFDM model selected from IEEE802.15.3a for simulation in this paper consists of 128-point FFT, a guard interval of 32 samples, i.e., 1/4 of the useful data interval, and QPSK modulation mapping scheme. Our simulation is carried out in AWGN and SUI-2 channel with uniform power delay profiles [14], respectively. The input signal vector $X(n)$ in Eq. (4) includes 256 samples, that is to say $P = 256$. The

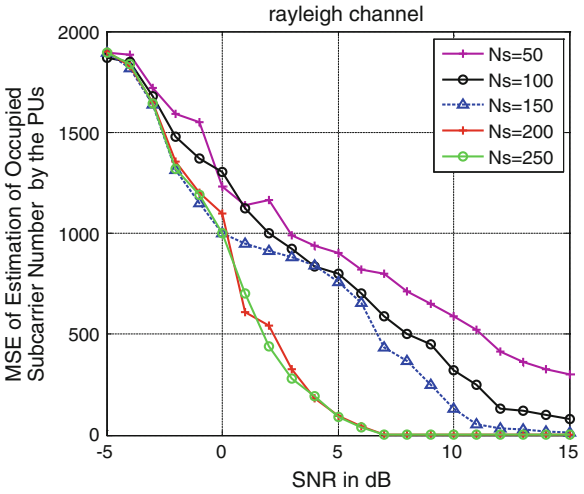

Fig. 1 Performance comparison of the estimation of occupied subcarrier number by the PUs for different Ns in rayleigh channel

SNR is defined as $SNR = 10\lg \sigma_s^2/\sigma_u^2$. All results were obtained by averaging over 1,000 independent Monte Carlo trials.

Figure 1 shows the performance of the estimation of occupied subcarrier number by the PUs rayleigh channel, respectively. From Fig. 1, we observe that the algorithm's performance is improved a lot with increasing the detection symbol numbers and SNR, while the estimation performance has almost no change when Ns $>$ 200. Thus, Ns $=$ 200 is the optimal value.

Figures 2 and 3 show the performance of the proposed MUSIC-ES method for the fixed Ns(Ns $=$ 200) in AWGN and rayleigh channel, respectively. From Fig. 2, we can see that the probability detection curves almost overlap when SNR $>$ 2 dB in AWGN channel, that is to say the two methods have the same

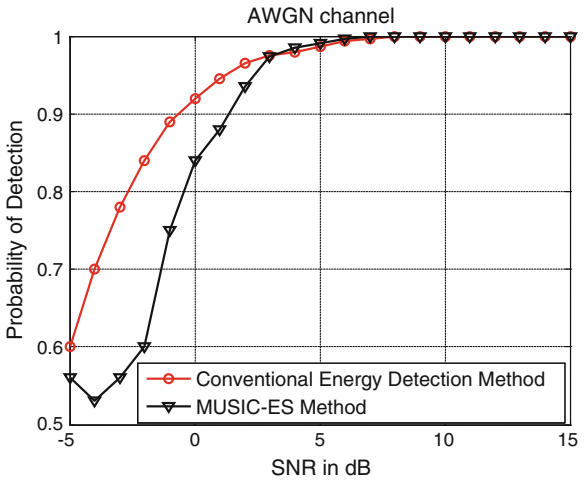

Fig. 2 Performance comparison of the two method for the fixed Ns(Ns $=$ 200) in AWGN channel

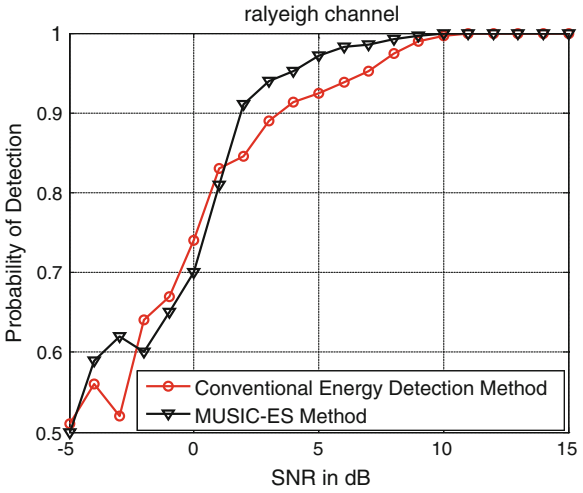

Fig. 3 Performance comparison of the two method for the fixed Ns(Ns = 200) in rayleigh channel

performance. We can easily observe that the MUSIC-ES method has a better features compared with conventional energy detection method when SNR > 3 dB from Fig. 3. Further, by comparing Fig. 2 with Fig. 3, we can realize that the algorithm's performance descends largely in rayleigh channel and the MUSIC-ES method has a higher detection probability when SNR > 7 dB.

5 Conclusions

In this paper, we have provided a new spectrum sensing scheme based on eigenvalue-construct of the received autocorrelation signal matrix in CR system. The approach based on MUSIC algorithm only uses the orthogonality between signal subspace and noise subspace to realize the spectrum detection. Thus, channel information is not indispensable for the proposed algorithm and the CFO has no influence for the algorithm's detection performance. And the decision threshold is also not necessary in this scheme. While the optimal value of Ns should be designated for realization of the algorithm in this paper. Simulations show that the approach suits the CR system based on OFDM with higher SNR.

References

1. Prasad RV, Pawelczak P, Hoffmeyer JA, Steven Berger H (2008) Cognitive functionality in next generation wireless networks: standardization efforts. IEEE Commun Mag 46(4):72–78
2. Kim S, Lee J, Wang H, Hong D (2009) Sensing performance of energy detector with correlated multiple antennas. IEEE Signal Process Lett 16:671–674

3. Shen J, Liu S, Zeng L, Xie G, Gao J, Liu Y (2009) Optimization of cooperative spectrum sensing in cognitive radio network. IET Commun 3:1170–1178
4. Wang Y, Feng C, Zeng Z, Guo C (2009) A robust and energy efficient cooperative spectrum sensing scheme in cognitive radio networks, Institute of Electrical and Electronics Engineers Inc., Phoenix Park, Korea, pp 640–645
5. Sahai A, Cabric D (2005) Spectrum sensing: fundamental limits and practical challenges. In: Proceedings of IEEE international symposium on new frontiers in dynamic spectrum access network, November 2005, pp 546–551
6. Tandra R, Sahai A (2005) Fundamental limits on detection in low SNR under noise uncertainty. Wirel Commun 1:464–469
7. Ruttik K, Koufos K, Jantti R (2009) Spectrum sensing with multiple antennas. In: Proceedings of 2009 IEEE international conference on systems, man, and cybernetics, October 2009, pp 2281–2286
8. Kay SM (1993) Fundamentals of statistical signal processing: estimation theory. Prentice-Hall, Englewood Cliffs
9. Gardner WA (1991) Exploitation of spectral redundancy in cyclostationary signals. IEEE Signal Process Mag 8(2):14–36
10. Zeng Y, Liang YC (2008) Eigenvalue based spectrum sensing algorithms for cognitive radio. http://arxiv.org/PS_cache/arxiv/pdf/0804/0804.2960v1.pdf. Accessed Apr 2008
11. Cardoso LS, Debbah M, Bianchi P, Najim J (2008) Cooperative spectrum sensing using random matrix theory. In: 3rd international symposium on wireless pervasive computing, May 2008, pp 334–338
12. Penna F, Garello R, Spirito MA (2008) Cooperative spectrum sensing based on the limiting eigenvalue ratio distribution in Wishart matrices. http://arxiv.org/PS_cache/arxiv/pdf/0902/0902.1947v1.pd. Accessed Feb 2008
13. Tandra R, Sahai A (2008) SNR walls for signal detection. IEEE J Sel Top Sign Proces 2(1):4–17
14. Batra A, Balakrishnan J, Dabak A et al (2004) Multi-band OFDM physical layer proposal for IEEE 802.15 task group 3a. IEEE P802.15-04/0493r1, September 2004

Target Tracking Algorithm Based on Multi-Subblock Feature Matching

Faliang Chang, Wenhui Dong and Li Ma

Abstract Real-time target tracking is an important subject in modern intelligent surveillance and security defense systems. However, due to the natural scene's complexity and variability, the tracking becomes complex and difficult especially when the target is occluded in complex background. This paper proposes a tracking algorithm of moving target based on adaptive blocking and feature correlation matching. We compute target's grayscale first, and judge the target's grayscale attribute. Then according to it, we choose a more suitable algorithm to track moving target from edge correlation matching algorithm and grayscale correlation matching algorithm based on multi-subblock. To edge matching algorithm, target's displacement in two successive frames is determined by optimal matching of current unoccluded edge with real-time updated target template. For grayscale correlation matching based on multi-subblocks, the algorithm first estimates occluded region accurately by subblocks with distinct feature, and then tracks the target by residual unoccluded subblocks to participate in grayscale correlation matching. The experimental results of our tracking system show that the algorithm is effective for tracking moving targets.

Keywords Target tracking · Computer vision · Pattern recognition · Image blocking · Feature matching

1 Introduction

Moving target tracking is an important research subject in computer vision and has great practical value in robot visual navigation, medical diagnosis, traffic surveillance, etc. But due to the scene's complexity and variability, the tracking

F. Chang (✉) · W. Dong · L. Ma
School of Control Science and Engineering, Shandong University, Jinan, China
e-mail: flchang@sdu.edu.cn

F. Sun et al. (eds.), *Foundations and Practical Applications of Cognitive Systems and Information Processing*, Advances in Intelligent Systems and Computing 215,
DOI: 10.1007/978-3-642-37835-5_13,

becomes complex and difficult especially when the target is occluded. To solve the occlusion problem during target tracking, researchers have done a lot of studies and put forward many effective methods as follows: (1) Algorithm based on target feature matching [1–5], where features might be target's gray image, edge points (corner points). For example, generalized Hough transform solves occlusion problems by selecting corner points as the feature points, and using residual feature points to locate the target [6]. (2) Multi-subblock template matching method. In [7], matching error is employed to judge whether the subblocks are occluded, then by grayscale correlation matching the target is tracked continuously. In [8], based on maximum posteriori probability criterion, the multi-target mutual occlusion problem is solved by distributing sub-template to correct target according to correlation matching results. (3) Modeling the occlusion process by using dynamic Bayesian network [9, 10]. (4) Particle filter based on color histogram may solve target's partial occlusion [11]. (5) The model based on grid may also solve occlusion problems [12, 13].

Additionally, many researchers also pay close attention to the optimal methods based on statistic model which look for the optimal matching of the target, such as Mean-Shift algorithm, which is a real-time tracking algorithm, but can converge to local maximum and has poor performance under occlusion. Stochastic tracking algorithms mainly evaluate the states of the targets, such as particle filter [11, 14, 15], which is successfully used in tracking algorithms for maintaining multiple hypotheses with many particles and can efficiently describe randomicity of the tracking process. Although particle filter can provide robustness, it is usually computationally intense and not so real-time.

Mean-Shift and particle filter were combined efficiently in the literature [16–18]. Every particle was moved to a nearby local maximum by Mean-Shift iterations in the literature [17, 18], which solved the degeneracy problem and reduced the computational cost preferably, but could not maintain the diversity of the particles, especially when there was little information about the target and severe disturbance, under which case, most particles converged to disturbance and were difficult to recover when occlusion disappeared. In [18], Mean-Shift and particle filter were performed simultaneously and the tracking result whose matching value was larger were used as the real result. However, under severe occlusion, the largest matching value may not correspond to the real result, so the tracking does not always recover after occlusion. Moreover, under normal conditions, it is not necessary to use so many particles for Mean-Shift tracking, which will have good performance in this case.

The rest of this paper is organized as follows. In Sect. 2, how to judge target's gray attribute and how to select right matching algorithm are introduced. Section 3 describes Kalman prediction method based on current statistical model. In Sect. 4, we give the edge matching algorithm. Section 5 deals with the grayscale matching algorithm based on multi-subblock when the target is occluded. Finally, experimental results and analysis are given in Sect. 6, and in Sect. 7, we conclude with some remarks.

2 Target Attribute Judging and Matching Algorithm Selecting

To guarantee reliable feature matching and reliable tracking, we selected correctly target's features according to the difference in target's attributes. The method to judge target's gray attribute is based on the following steps.

Step 1: We divide the rectangle containing target into subblocks of size 8×8 pixels, and then eliminate the subblocks lying in the boundary of the rectangle because the subblocks usually contain background rather than target.

Step 2: Calculate the histogram of each subblock i ($i = 1 \sim$ n) and smooth it.

Step 3: Find the maximum and minimum of the gray in each subblock. If the difference between the two gray values is larger than 50, this subblock will be marked as a subblock with rich grayscale. Otherwise, it will be marked as a uniform grayscale subblock.

Step 4: When the number of subblocks with rich grayscale is larger than $n/4$, the target will be considered to have rich grayscale and the grayscale matching method will be chosen. Otherwise edge matching method will be selected.

3 Kalman Prediction Based on Current Statistical Model

Target moving information (position, velocity, and acceleration) can be predicted accurately through Kalman filter. Neighborhood centered in prediction position may be used as searching window to match target in two successive frames. In most cases, this searching method is efficient and can reduce computational cost. Thus, when the target is tracked under complete occlusion, we choose the position predicted by Kalman filter as the target's real position.

The basic idea of the current statistical model is as follows: If the target is maneuvering with certain acceleration, the acceleration in the next time is limited in the neighborhood of current acceleration [19].

The state equation and observation equation of the system are expressed as (1) and (2). We can get optimal one-step prediction $\hat{X}_{k,k-1}$ through Kalman filter.

$$X_k = \Phi_{k,k-1} X_{k-1} + U_{k,k-1}\overline{a} + \Gamma_{k,k-1} W_{k-1} \tag{1}$$

$$Z_k = H_k X_k + V_k \tag{2}$$

where k is the time index; X_k and X_{k-1} are state variables in time k and $k-1$ respectively; Z_k is the observed variable in time k; $\overline{a}$ is the current acceleration(i.e. the acceleration corresponding to one-step prediction state variable $X_{k,\ k-1}$); $U_{k,}$

$_{k-1}$ is the coefficient matrix corresponding to $\overline{a}$; W and V are process noise matrix and measurement noise matrix respectively; $\Phi_{k,\ k-1}$ is state displacement matrix; H_k is observation matrix and $\Gamma_{k,\ k-1}$ is noise matrix.

In our target tracking system, system state variable is defined as $X_k = [s_x, s_y, v_x, v_y, a_x, a_y]$, where (s_x, s_y) is target's position, v_x and v_y are target's velocity, a_x and a_y are target's acceleration in x and y directions respectively. The observed variable is target's position $Z_k = [s_x, s_y]^T$.

4 Edge Matching Algorithm

As mentioned above, if target's grayscale is uniform, edge matching algorithm will be chosen to solve the occlusion problem. Granted the target position in previous frame is $k-1$, the key to track the target in the current frame k is to calculate the displacement $(\Delta x, \Delta y)$.

4.1 Edge Detection

First, we detect the moving target by background subtraction. To adapt to the illumination change [1], the background will be updated real-time as (3).

$$B_{k+1}(x,y) = \begin{cases} I_k(x,y) + \alpha[B_k(x,y) - I_k(x,y)], \alpha \approx 1 \\ \text{if } I_k(x,y) \in O_j, j = 1,\ldots,N \\ I_k(x,y) + \beta[B_k(x,y) - I_k(x,y)], \beta \ll 1 \\ \text{if } I_k \notin O_j, j = 1,\ldots,N \end{cases} \tag{3}$$

where O_j is the jth moving target, N is the total number of moving targets in the kth frame, I_k is the current image, B_k is the current background, B_{k+1} is the background in next frame. The values of α and β are limited in the interval [0, 1]. If the current pixel belongs to a moving target, the background is not updated, so we let coefficient α be near 1, and then $B_{k+1}(x, y) \approx B_k(x, y)$. On the contrary, if the current pixel does not belong to moving target, we let coefficient β be near 0, and then $B_{k+1}(x, y) \approx I_k(x, y)$, i.e., the pixel value in background is updated using the value of the current pixel.

If the real-time updated background is subtracted by current image, the moving target will be detected more exactly. Then with Canny edge detector, edge features are extracted from difference images.

4.2 Edge Matching Algorithm

The essential idea of edge matching algorithm is performing the correlation matching between target's edge module and unoccluded edges in current frame. The calculating formula is defined as (4).

$$\begin{aligned} C_t(\Delta x, \Delta y) &= \sum_{k=1}^{N} \sum_{l=1}^{M} \mathrm{AND}[M_t(k,l), I_t(k+\Delta x, l+\Delta y)] \\ (\Delta x*, \Delta y*) &= \arg \max_{(\Delta x, \Delta y)} C(\Delta x, \Delta y) \\ \Delta x_0 - w/2 \le \Delta x \le \Delta x_0 + w/2, &\ \Delta y_0 - w/2 \le \Delta y \le \Delta y_0 + w/2 \end{aligned} \tag{4}$$

where $C_t(\Delta x, \Delta y)$ is matching degree between template M_t in the tth frame and I_t $(k + \Delta x, l + \Delta y)$ which is the target's region in current frame corresponding to displacement vector $(\Delta x, \Delta y)$. Larger $C_t(\Delta x, \Delta y)$ indicates higher similarity. When $C_t(\Delta x, \Delta y)$ is maximum, we get the optimal displacement vector $(\Delta x^*, \Delta y^*)$. Δx_0 and Δy_0 are displacement vectors predicted by Kalman filter. $w \times w$ is the size of tracking window centered in predicted position, $N \times M$ is the size of searched area.

4.3 Affine Transformation

The target may be deformed during movement. We solve this problem through affine transformation. Since occlusion is usually short time, and the target cannot change abruptly, the affine transformation is calculated every 10 frames, which will adapt to the changes efficiently. After displacement, scaling, and rotation, coordinate point (x, y) is denoted as (x', y'), which is expressed with affine transformation (5).

$$\begin{bmatrix} x' \\ y' \end{bmatrix} = k \begin{bmatrix} \cos\theta & \sin\theta \\ -\sin\theta & \cos\theta \end{bmatrix} \begin{bmatrix} x \\ y \end{bmatrix} + \begin{bmatrix} \Delta x \\ \Delta y \end{bmatrix} \tag{5}$$

where k is the scaling factor; θ is the rotation factor; and Δx, Δy are the displacement vectors in x and y directions respectively.

The number of target edge points will become fewer during occlusion. To guarantee the effectivity of affine transformation, affine transformation is performed only when the number of detected edge points is larger than half of edge points before occlusion.

4.4 Template Update

Template update is the key in edge matching algorithm, and the template should reflect target's current state in time.

For the case that the moving target is occluded by stationary object, we first preserve the target edges in the frame before occlusion, and denote the number of whole edge points as A_0. During occlusion, A_0 will be adjusted every 10 frames by affine transformation to adapt to target's current state. By combining A_0 with the detected edges at time $t - 1$ as the common template at time t, the algorithm not only preserves the whole edge of the target but also absorbs current edge information. Furthermore, it can cope with the problem caused by abrupt change of edges at time $t - 1$. If there are only few edges detected in current frame, it indicates almost complete occlusion, and the prediction position of Kalman filter will be used as the target position.

For the case that the moving target is occluded by other moving target (suppose only two objects A and B for simplification), the detected edges in current frame are the sum of the edges of the two targets. We cannot distinguish exactly which edges belong to target A and which belong to target B. In such case, we select edges A_0 and B_0 under unocclusion as target template A and B, where A_0 and B_0 need to be adjusted by affine transformation every 10 frames. When the matching edge points between the template and current occluded target are few, the target is considered to be completely occluded. Then the prediction position through Kalman filter is used as the target position.

5 Gray Matching Based on Multi-subblock under Occlusion

When moving target has rich grayscale, the grayscale matching algorithm based on multi-subblock is adopted to solve occlusion problem. According to the subblock with distinct features, we can judge if the target is occluded. The occluded subblocks will not be considered in correlation matching calculation, only the unoccluded subblocks are used in tracking the target.

5.1 Target Adaptive Dividing

Target adaptive dividing is intended to provide distinct features for each subblock, and to improve the confidence level in subblock matching. It is the key step to determine whether the subblocks are occluded. If the subblocks do not have obvious features and have similar gray level with occluding obstacles, occlusion may fail to be detected. However, when subblocks with distinct features are

occluded, the confidence level will be greatly improved. The main process of adaptive dividing is: Divide target's rectangular area into n subblocks with 8×8 pixels; then merge and divide the subblocks according to their features. Variance can reflect the distinction of grayscale and the number of edges inside subblocks, so it is a proper measurement to divide or merge subblocks.

Block target as the following steps:

(1) Calculate the variance for every subblock; if the variance of any subblock is less than a predetermined threshold, this subblock will merge into subblock with the largest variance in neighborhood. The threshold should not be too large; otherwise this will produce too big subblocks and cause inaccurate matching. Only when subblocks are sufficient enough, the target position can be determined accurately by residual subblocks even partial occlusion.
The threshold selection method is as follows: After dividing target into subblocks with 8×8 pixels, calculating variances of subblocks within tracking window (exclude the surrounding subblocks in surrounding), sort the variances and choose the median as the threshold of adaptive division. Then we can get sufficient subblocks with distinct features.
(2) Divide the subblock with large variance into two small ones satisfying the condition in step (1).
(3) Make sure the size of the merged and divided subblock is not less than 8×8.
(4) The surrounding subblocks in tracking window contain background pixels which will change with time and cannot express target's feature, so we should diminish these subblocks' influence. They are not of much importance in matching calculation.

To adapt to target's small changes under occlusion, we detect the subblocks every 10 frames according to the above criterions. To improve the robustness, ensure the real-time performance, and reduce computation cost, the subblocks that do not satisfy above criteria will be adjusted. Figure 1a, b shows the results of adaptive division of a deforming target during occlusion. From the figure, we can

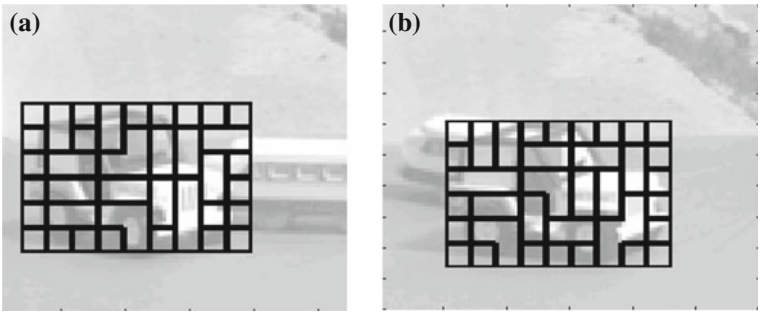

Fig. 1 Adaptive division of moving vehicle. **a** Division in frame 120. **b** Division in frame 150

know that the surrounding subblocks in tracking window changed slightly because most of them described the background. However, the subblocks within the target have distinct features.

5.2 Gray Correlation Matching Based on Multi-subblock Under Occlusion

The Determination of Occluded Subblocks. After adaptive dividing of the moving target, grayscale correlation matching algorithm of the target will be performed in successive frames. The matching region is centered in (Δx_0, Δy_0) which is obtained through Kalman filter, with size $w \times w$. Every point within this region is corresponding to a possible displacement of the target, which is denoted as (Δx, Δy), where $\Delta x_0 - w/2 \leq \Delta\ x \leq \Delta x_0 + w/2$ and $\Delta y_0 - w/2 \leq \Delta y \leq \Delta y_0 + w/2$. The matching error of each subblock is calculated as (6).

$$S_p(\Delta x, \Delta y) = \sum_{i=1}^{m} \sum_{j=1}^{n} \left| M_p(i,j) - I_p(i + \Delta x, j + \Delta y) \right|^2 \tag{6}$$

$$p = 1, \ldots, N$$

where M_p is the pth subblock in the previous frame, I_p is the pth subblock corresponding to displacement of (Δx, Δy) in the current frame, m and n are the height and width of the pth subblock, respectively, and N is the number of subblocks. From above equation, each subblock will obtain an optimal displacement (Δx^*_p, Δy^*_p) corresponding to the minimum of $S_p(\Delta x, \Delta y)$.

The matching error of the whole target is computed as (7).

$$\text{sum}(\Delta x, \Delta y) = \sum_{p=1}^{N} S_p(\Delta x, \Delta y) \tag{7}$$

The target's optimal displacement is corresponding to the minimum of sum (Δx, Δy), which is denoted as (Δx^*, Δy^*). If the optimal displacement of the subblocks are not coincident with that of the target (i.e. difference in x or y direction is larger than two pixels), then the subblocks will be considered to be occluded.

Tracking in Occlusion Process. The matching algorithm during occlusion is as follows:

Calculate the matching error $S_p(\Delta x, \Delta y)$ for each subblock according to (6), then gain the optimal displacement of each subblock (Δx^*_p, Δy^*_p). The occluded subblocks will not be used as matching calculation. The matching error of the target during occlusion is expressed as (8).

$$\text{sum}(\Delta x, \Delta y) = \sum_{p=1.p\neq q_i}^{N} S_p(\Delta x, \Delta y) \tag{8}$$

where p is the index of the unoccluded subblock and $q_i (i = 1,\ldots, l)$ is occluded subblock. We choose the minimum of sum(Δx, Δy) as the optimal displacement still, which is represented by (Δx^*, Δy^*).

Updating Occluded Region. During occlusion, the occluded subblocks will change real-time. Thus, the occluded region should be updated real-time to achieve accurate tracking. The occluded region is updated as follows:

(1) For occluded subblock $q_i (i = 1,\ldots, l)$, if its optimal displacement (Δx^*_{qi}, Δy^*_{qi}) is not coincident with (Δx^*, Δy^*), it is considered still in occlusion, otherwise, it is considered out of occlusion.
(2) For unoccluded subblock p, when its optimal displacement (Δx^*_p, Δy^*_p) becomes not coincident with (Δx^*, Δy^*), it will be considered occluded at this frame, otherwise, it is considered not yet occluded.

6 Experimental Results and Analysis

6.1 Experiment 1

As shown in Fig. 2, a moving car is occluded by a stationary car in the natural background outside our laboratory. The target (the moving car) possesses rich grayscale through calculation, so grayscale matching algorithm based on multi-subblock is chosen to track the vehicle. In the tracking process, the vehicle is divided into 39 subblocks. But the subblocks lying in the boundary of rectangle usually contain the background rather than the vehicle, thereby the subblocks will be regarded as occlusion and will not participate in matching operation. With the vehicle occluded gradually, the subblocks marked as "occlusion" will increase. The frame where the target is occluded most severely is shown in Fig. 2c, only 8 subblocks are effective (i.e. not occluded), but the target still can be tracked accurately. When the target moves away from occlusion, the effective subblocks increase and the tracking becomes more reliable. Figure 2a shows the tracking rectangle before occlusion, Fig. 2b is the case of occlusion beginning, Fig. 2c illustrates the tracking result under severe occlusion, and Fig. 2d presents the tracking when the car is moving away from the occlusion. The experiment results show that the grayscale matching algorithm based on multi-subblock can track the vehicle accurately during the whole course. Furthermore, the stage of occlusion can be determined according to the change of numbers of the occluded subblocks.

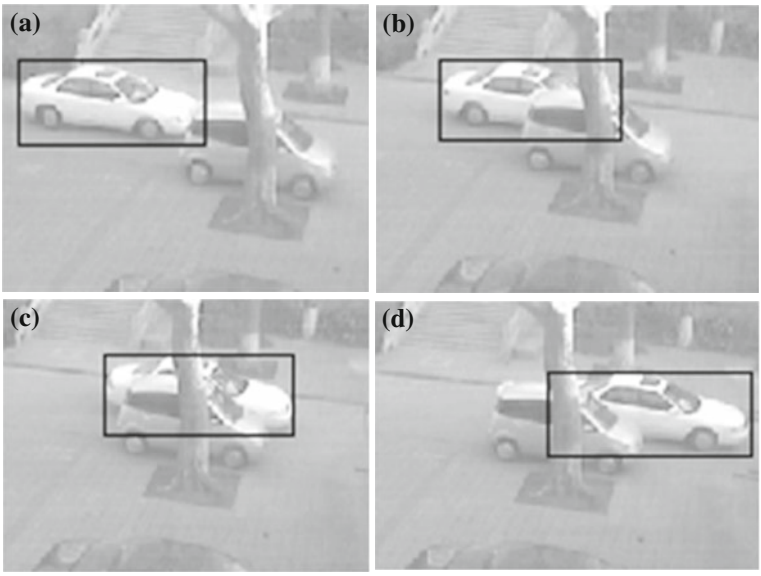

Fig. 2 A car with rich *grayscale* is occluded by another stationary car. **a** Tracking before occlusion. **b** Tracking under occlusion. **c** Tracking under severe occlusion. **d** Tracking the car away from occlusion

6.2 Experiment 2

In this experiment, the target movement and the background are more complicated than the above two experiments. Figure 3 shows the tracking results of a car running along different trajectories in the natural complex scene in which there are many other cars looking similar to the tracking target. The car travels first at high speed, then slows down, turns back, turns a corner, finally speeds up to leave. In this complex process, the target has the cases as rotation, scale changes, maneuvering, speed changes, and so on. Figure 3a–c give some tacking frames of the video sequence in which the rectangles illustrate the tracking results in the tracking process.

In Fig. 3d, the curve is the moving trajectory of the target's centroid, and the small rectangles look like dots. Results show that the tracking algorithm has good adaptability to rotation, deformation, maneuvering, etc.

6.3 Experiment 3

Differing from the above experiments which use a video sequence, this experiment use an experimental system developed by us which adopts a PTZ camera to track vehicles actively outside our laboratory in a complex natural scene. That is, by

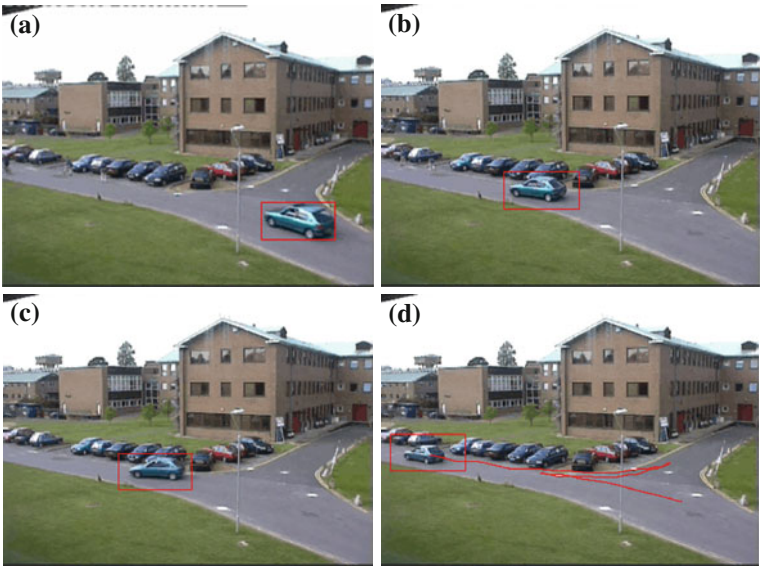

Fig. 3 The tracking results to vehicle with multi-trajectory. **a** Frame 163. **b** Frame 190. **c** Frame 230. **d** Moving trajectory

controlling PTZ camera's movement, we make the vehicle always lie in the vicinity of monitor's center when the vehicle is moving. So our main task is controlling the PTZ camera's movement according to the tracking algorithm mentioned in this paper.

Controlling Strategies of the PTZ Camera. In our experimental tracking system, we employ Fuzzy controlling idea to control the PTZ camera movement. The control idea is as follows:

(1) Compute the distance vector between image center position and target center-of-gravity position given by the tracking algorithm.
(2) Put the distance vector as the Fuzzy vector of the Fuzzy controller, and compute direction and position control value for camera movement according to relationship of the Fuzzy vector and Fuzzy control rules.
(3) Transform the Fuzzy control output to the electric control signal to control the camera.

Figure 4 shows the image plane coordinate system in which the rectangle region illustrates the range of image. (x_c, y_c) denote the coordinate of the central point C, and (x_i, y_i) is the coordinate of the tracking target in current frame. Hence the tracking position vector $\vec{r}$ is expressed as (9)

$$\vec{r} = (x_i - x_c)\hat{i} + (y_i - y_c)\hat{j} \tag{9}$$

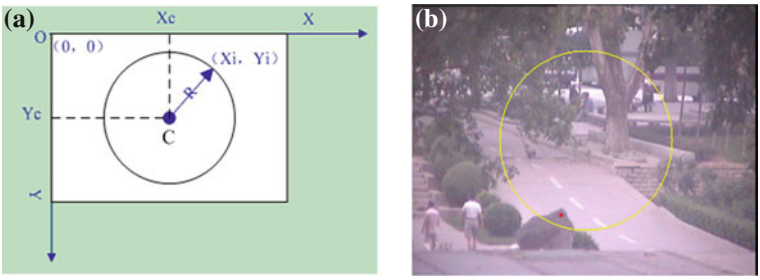

Fig. 4 Image coordinates. **a** Coordinate diagram. **b** Real scene

When $|r| < R$, we can continue to track the moving target in the range of vision-field of the camera without camera's movement; when $|\bar{r}| \geq R$, which indicates the tracking target will move away from the central region of camera's vision-field, we control the camera's movement to keep the target image in vicinity of monitor's center where the threshold value R, which indicates the range of the central region of the camera's vision-field, can be adjusted according to the practical situation.

We divide the turning direction of the camera into eight cases according to the relationship between tracking target center and the center of camera's vision-field: right, left, up, down, right-up, right-down, left-up and left-down. The turning control algorithm is as follows:

If $x_i - x_c > L \wedge |y_i - y_c| \leq L$, turns to right;
if $x_i - x_c > L \wedge y_i - y_c < -L$, turns to right-up;
if $|x_i - x_c| \leq L \wedge y_i - y_c < -L$, turns to up;
if $x_i - x_c < -L \wedge y_i - y_c < -L$, turns to left-up;
if $x_i - x_c < -L \wedge |y_i - y_c| \leq L$, turns to left;
if $x_i - x_c < -L \wedge y_i - y_c > L$, turns to left-down;
if $|x_i - x_c| \leq L \wedge y_i - y_c > L$, turns to down;
if $x_i - x_c > L \wedge y_i - y_c > L$, turns to right-down;

where L is a threshold value which determine the direction of the camera, its value can be defined as (10).

$$L = R \times \sin(\pi/4) \tag{10}$$

The Tracking Experiment Results. Figure 5 shows the results of tracking vehicles outside our laboratory using an experimental system developed by us. The system adopts PTZ camera to track a car actively. That is, by controlling PTZ camera's movement, vehicles can always lie in the vicinity of the monitor's center. The experimental results show that the PTZ camera tracking system can achieve continuous tracking to vehicle very well in a complex and wide natural scene. Figure 5a–d gives some tacking frames of the video sequence in which the rectangle illustrates the tracking results.

Fig. 5 An example of tracking a vehicle using a PTZ camera. **a** Frame 7. **b** Frame 129. **c** Frame 459. **d** Frame 507

7 Conclusion

This paper studies vehicle tracking algorithm based on multi-subblock correlation matching in a complex and large scene. The algorithm presented by this paper solves effectively the occlusion problem of running vehicle. The contributions of this algorithm are summarized as follows: (1) According to target's different attribute, the algorithm may choose edge matching method or grayscale correlation matching method based on multi-subblock. Through choosing more suitable matching method, the algorithm can solve occlusion problem more effectively and track more reliably. (2) Only logical "AND" operation is calculated in edge matching, which can satisfy the real-time request. Moreover, affine transformation can update matching template and make the tracking more accurate. (3) Compared with fixed division, adaptive division is more efficient to deal with occlusion question when target has similar grayscale with the occluding obstacles. Furthermore, the stage of occlusion can be evaluated according to the occluded subblocks, and thus improve the tracking accuracy.

The algorithm studied in this paper still has some questions that need to be advanced. For example, we adopt target's grayscale and mean gray information when dividing subblocks adaptively. If color and its distribution information are adopted, the tracking will be more reliable, but will need more calculation cost. This is our next work.

Acknowledgments We would like to acknowledge the support from China Natural Science Foundation Committee (No. 60975025, No. 61273277), Shandong province Natural Science Foundation (No. ZR2011FM032) and the Scientific Research Foundation for the Returned Overseas Chinese Scholars, State Education Ministry (the contract number is No. 20101174).

References

1. Marecenaro L, Ferrari M, Marchesottl L (2002) Multiple object tracking under heavy occlusions by using Kalman filter based on shape matching. In: IEEE international conference on image processing, Rochester, pp 341–344
2. Pterfreund N (1999) Robust tracking of position and velocity with Kalman snakes. IEEE Trans Pattern Anal Mach Intell 22:564–569
3. Galvin B, McCane B, Novins K (1999) Visual snakes for occlusion analysis. In: IEEE computer society conference on computer vision and pattern recognition, pp 294–299
4. Loutast E, Diamantarast K, Pitast I (2001) Occlusion resistant object tracking. IEEE international conference on image processing, pp 65–68
5. Nguyen HT, Worring M, van den Boomgaard R (2001) Occlusion robust adaptive template tracking. In: Proceedings. Eighth IEEE international conference on computer vision, pp 678–683
6. Oberti F, Calcagno S, Zara M, Regazzoni CS (2002) Robust tracking of humans and vehicles in cluttered scenes with occlusions. In: IEEE international conference on image processing, pp 629–632
7. Ito K, Sakane S (2001) Robust view-based visual tracking with detection of occlusions. In: IEEE international conference on robotics and automation, pp 1207–1213
8. Kamijo S, Matsushita Y, Ikeuchi K, Sakauchi M (2000) Occlusion robust tracking utilizing spatio-temporal Markov random field model. In: Proceedings. 15th International conference on pattern recognition, pp 140–144
9. Wu Y, Yu T, Hua G (2003) Tracking appearances with occlusions. In: IEEE computer society conference on computer vision and pattern recognition, pp 789–795
10. Hu M, Hu W, Tan T, Tracking people through occlusion. In: 17th international conference on pattern recognition, pp 724–727
11. Nummiaro K, Koller-Meier E, Van Gool L (2003) An adaptive color-based particle filter. Image Vis Comput 21:99–110
12. Altunbasak Y, Murat Tekalp A (1997) Occlusion-adaptive, content-based mesh design and forward tracking. IEEE Trans Image Process 6:1270–1280
13. Zhao J-W, Wang P, Liu C-Q (2002) An object tracking algorithm based on occlusion mesh model. In: International conference on machine learning and cybernetics, pp 288–292
14. Stern H, Efros B (2005) Adaptive color space switching for tracking under varying illumination. Image Vis Comput 23:353–364
15. Isard M, Blake A (1998) Condensation-conditional density propagation for visual tracking. Int J Comput Vision 29:5–28
16. Shan CF, Wei YC, Tan TN, Ojardias F (2004) Real time hand tracking by combining particle filtering and mean shift. In: Sixth IEEE international conference on automatic face and gesture recognition, pp 669–674
17. Chang C, Ansari R (2005) Kernel particle filter for visual tracking. IEEE Signal Process Lett 12:242–245
18. Deguchi K, Kawanaka O, Okatani T (2004) Object tracking by the mean-shift of regional color distribution combined with the particle-filter algorithm. In: International conference on pattern recognition. Cambridge, pp 506–509
19. Hongren Z, Kumar KSP (1984) A current statistical model and adaptive algorithm for estimation maneuvering targets. AIAA J Guidance Control Dyn 7:596–602

Intuitive Systemic Models and Intrinsic Features for Radar-Specific Emitter Identification

Tao Han and Yiyu Zhou

Abstract An intuitive systemic model based on the systemic Yoyos and stochastic differential geometry is provided for finding a meaningful geometric description of radar-specific emitter identification (SEI) problems in this paper. According to this model, we show that intrinsic parameters of signals can be used to explain and find the effective fingerprints feature of specific emitters. Experiments on actual intercepted radar signals with the same type verify the correctness and validity of the proposed model.

Keywords Radar · Specific emitter identification · Systemic Yoyos · Differential geometry

1 Introduction

Specific emitter identification (SEI) is a high priority task in modern electronic intelligence (ELINT) and electronic support measurement (ESM) systems [1, 2]. The aim of the SEI algorithm is the identification a specific radar emitter or the other wireless radio of interest within a single class of emitters. It is also used in various applications such as cognitive radio and network security [3, 4].

An effective implementation of SEI depends on appropriate definitions and strict measurements of features, which represent those intrinsic and distinctive characteristics of a specific emitter. There has been a certain amount of research on achieving features. Conventional approaches, which perform SEI by clustering decisions made by estimating the pulse descriptor word characteristics [5], include radio frequency (RF), pulse width (PW), direction-of-arrival (DOA), time-of-arrival (TOA), and pulse repetition interval (PRI) [6]. Other than the above

T. Han (✉) · Y. Zhou
School of Electronic Science and Technology, National University of Defense Technology, Changsha, China
e-mail: dr.hannibal.h@gmail.com

F. Sun et al. (eds.), *Foundations and Practical Applications of Cognitive Systems and Information Processing*, Advances in Intelligent Systems and Computing 215,
DOI: 10.1007/978-3-642-37835-5_14,

features, the unintentional modulation on pulse (UMOP) features are used to demonstrate SEI technology in [7, 8], which consist of the spurious output, the pulse shape, and phase noise [9]. Different kinds of spurious outputs can be caused by the crosstalk and leakage of the frequency source and the power ripple and vibration in an individual emitter [10]. The distribution capacitance, lead inductance, and continual varying of voltage and current arouse distortions of the pulse shape [11]. In [12] is present the complicated structure in each pulse caused by both UMOP and intentional modulations on pulse (IMOP), which can be used for SEI.

Although a great deal of features and their combinations are presented for performing SEI in prior open research, the mechanism and framework for finding meaningful intrinsic description of features are hardly ever studied. Radar systems usually consist of many nonlinear devices, e.g., power amplifiers and frequency multipliers. All the nonlinearities of the whole radar are the source of features for SEI. Besides, they will become the obstruction on the further evolution of SEI if they are not properly understood.

Systemic Yoyos was officially proposed in 2008 [13], which provides a tool of theoretical analysis for studying nonlinear structures and organizations from diverse areas [14]. According to the theory, in terms of physical objectivity, mutual reactions of a specific radar's nonlinear devices generate signals with intrinsic signature information. The information obtained from real-time surveillance by EINT systems enables threat avoidance, countermeasures analysis, and the situational awareness. In this paper, we propose an intuitive systemic evolution model based on Systemic Yoyos to study the nonlinear mechanism of features. A framework is also given to find a meaningful geometric description of intercepted signals, by using the knowledge of stochastic differential geometry (SDG). With the model, we investigate the intrinsic forms of signals for finding the effective features and their combinations, and then define some new features based upon diffusion processes for achieving better classification performances.

The paper is organized as follows. Section 2 presents the intuitive systemic models and its mathematical descriptions. The derivation and analysis of intrinsic forms of signals are also presented in this section. Section 3 introduces the approximate intrinsic location parameter, and deals with the intrinsic features. The results of experiments are presented in Sect. 4. Finally, the conclusions are drawn in Sect. 5.

2 Intuitive Model for SEI

The vectors attributed to the intrinsic signatures, which can be measured and associated with the relevant specific radar emitter, are referred to as features. Determining and extracting the intrinsic features from the intercepted radar pulses and finding the optimum set of them are the two most difficult problems of SEI. In this section, we analyze these two problems by using Systemic Yoyos and SDG.

Systemic Yoyos suggest an evolutionary model to describe the relationship between nonlinearities of the specific radar and its intrinsic signatures, which also provides intuitive understanding of SEI, and SDG works as a powerful mathematical tool.

2.1 Intuitive Models Based on Systemic Yoyos

A modern radar system is highly complex and nonlinear. When a specific radar works, it should be treated as a higher order nonlinear evolution system. The nonlinearity of the working radar is the source of intrinsic features, which represents eddy motions [13]. Based on the aforementioned observations, the intuitive model of a specific radar can be proposed as follows (Fig. 1).

Because nonlinear structures of the radar system and EINT are eddy sources, leading to eddies instead of waves (see Fig. 2) these intuitive models provide tools of theoretical analysis for studying the intrinsic features for SEI.

2.2 Mathematical Models

A radar pulse signal s_t can be totally described by three instantaneous parameters, which are the instantaneous amplitude A_t, the instantaneous frequency f_t and the instantaneous phase ϕ_t. Consider reaction mechanisms of a specific radar as a Markov process $\{\boldsymbol{X}_t | \boldsymbol{X}_t = (A_t, f_t, \phi_t), t \geq 0\}$ with values in the connected manifold S of dimension 3 determined by the radar system, represented by

$$\mathrm{d}\boldsymbol{X}_t^{(i)} = \alpha^{(i)}(\boldsymbol{X}_t)\mathrm{d}t + \sum_{j=1}^{3} \sigma^{(i,j)}(\boldsymbol{X}_t)\mathrm{d}\boldsymbol{W}_t^{(j)}, \tag{1}$$

where $i, j = 1, 2, 3$, the $\sum \alpha^{(i)}\left(\partial / \partial x^{(i)}\right)$ is a vector field on S, $\sigma(x) \stackrel{\wedge}{=} (\sigma^{(i,j)}(x)) \in L(\mathbb{R}^3, T_x S)$, $T_x S$ is the tangent space at point $x \in S$, and $\boldsymbol{W}$ is a Winner process in S.

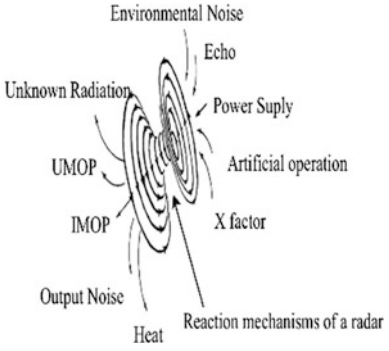

Fig. 1 The intuitive model of a radar system

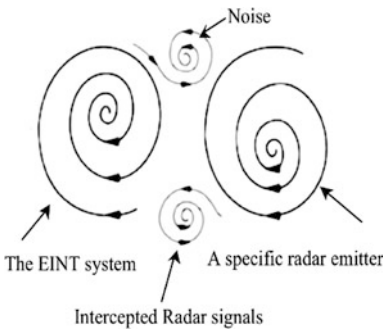

Fig. 2 The intuitive model of SEI

In this paper, we assume that the coefficients $\alpha^{(i)}$ and $\sigma^{(i,j)}$ are $\mathbb{C}^2$-continuous with the first bounded without loss of generality.

Based on the well-known SDG knowledge and the given Eq. (1), one can define a $\mathbb{C}^2$ semi-definite metric on the cotangent bundle of the manifold S.

$$\left\langle \mathrm{d}x^i \mid \mathrm{d}x^j \right\rangle = (\sigma \cdot \sigma)^{(i,j)} = \sum_{k=1}^{3} \sigma^{(j.k)} \sigma^{(j.k)}. \tag{2}$$

This semi-definite metric is intrinsic, which means, it remains the same while the matrix is changed by different coordinates for the state process of the radar. In the physical point of view, the intrinsic metric describes varying patterns of the instantaneous parameters. These patterns represent mutual reaction mechanisms of nonlinear structures of a specific radar. Consequently, we postulate that the intrinsic semi-definite metric is the appropriate metric for studying the SEI problem. From the above, the effectiveness criterion of features for SEI is given as follows.

Proposition A *If a set of features consist of feature vectors which represent the varying patterns of instantaneous parameters of a specific radar, then the set should be reliable and effective.*

3 Intrinsic Features for SEI

For normal radars, we assume for simplicity that the state variable only consists of the instantaneous frequency and phase in pulse. The Markov diffusion process $\boldsymbol{S_t} = (\boldsymbol{X}_t, \dot{\boldsymbol{X}}_t, \ddot{\boldsymbol{X}}_t)$ is defined as

$$\begin{bmatrix} \mathrm{d}\boldsymbol{X}_t \\ \mathrm{d}\dot{\boldsymbol{X}}_t \\ \mathrm{d}\ddot{\boldsymbol{X}}_t \end{bmatrix} = \begin{bmatrix} \mathbf{0} & \boldsymbol{I} & \mathbf{0} \\ \mathbf{0} & \mathbf{0} & \boldsymbol{I} \\ \mathbf{0} & -P(\boldsymbol{S_t})\boldsymbol{I} & -\lambda Q(\dot{\boldsymbol{X}}_t) \end{bmatrix} \begin{bmatrix} \boldsymbol{X}_t \\ \dot{\boldsymbol{X}}_t \\ \ddot{\boldsymbol{X}}_t \end{bmatrix} + \begin{bmatrix} 0 \\ 0 \\ \gamma Q(\dot{\boldsymbol{X}}_t)\mathrm{d}\boldsymbol{W}_t \end{bmatrix}, \tag{3}$$

where λ, γ are proposed constants, $\boldsymbol{W}$ is a Winner process in $\mathbb{R}^2$, and $\boldsymbol{s}^T = (x^T, \dot{x}^T, \ddot{x}^T)$, so we have

$$P(\boldsymbol{s}) = \|\ddot{\boldsymbol{x}}\|^2 \Big/ \|\dot{\boldsymbol{x}}\|^2, \tag{4}$$

$$Q(\dot{\boldsymbol{x}}) = (\boldsymbol{I} - \dot{\boldsymbol{x}}\dot{x}^T) \big/ \|\dot{\boldsymbol{x}}\|^2. \tag{5}$$

The intrinsic semi-definite metric is

$$(\sigma \cdot \sigma)^{(i,j)} = \begin{bmatrix} 0 & 0 & 0 \\ 0 & 0 & 0 \\ 0 & 0 & \gamma^2 Q(\dot{\boldsymbol{x}}) \end{bmatrix}. \tag{6}$$

Based on (1), (2), and (6), the intrinsic vector field on the manifold is

$$\xi(\boldsymbol{s}) = \begin{bmatrix} \dot{\boldsymbol{x}} \\ \ddot{\boldsymbol{x}} \\ -P(\boldsymbol{s})\dot{\boldsymbol{x}} - \lambda Q(\dot{\boldsymbol{x}})\ddot{\boldsymbol{x}} \end{bmatrix}. \tag{7}$$

According to references [15], we define the approximate intrinsic location parameter (AILP) $\{m_i, i = 1, 2, 3, \ldots, N_p\}$ to be the original feature set, where N_p is the number of samples in a radar pulse. This feature set is reliable and effective based on proposition A. Assuming the sampling frequency is f_s, intrinsic features can be calculated by the following formulas:

$$AILP_i = \tau(AILP_{i-1} + H_{i-1} f_s/2) + H_i f_s/2. \tag{8}$$

$$\tau = \exp\{[D\xi(\boldsymbol{s}_i) + D\xi(\boldsymbol{s}_{i-1})] f_s/2\}. \tag{9}$$

$$H_i = \frac{1}{2}(D^2 \xi(\boldsymbol{s}_i)). \tag{10}$$

where D is the Euclidean differential operator. In the next section, experiments on actual intercepted radar signals of the same type verify the correctness and validity of the aforementioned models and features.

4 Experiments and Results

In this section, we discuss the performance of the proposed models and features. The actual pulses are intercepted by the same one ELINT receiver. As shown in Fig. 3a, b, the pulses are actual intercepted signals of Identification Friend of Foe (IFF). The sampling frequency is 250 MHz. There are four radars with the same type. Each of them has collected 500 pulses at one time.

Figure 4 shows the nice separabilities of the proposed intrinsic features, which are calculated from two different specific emitters' instantaneous parameters.

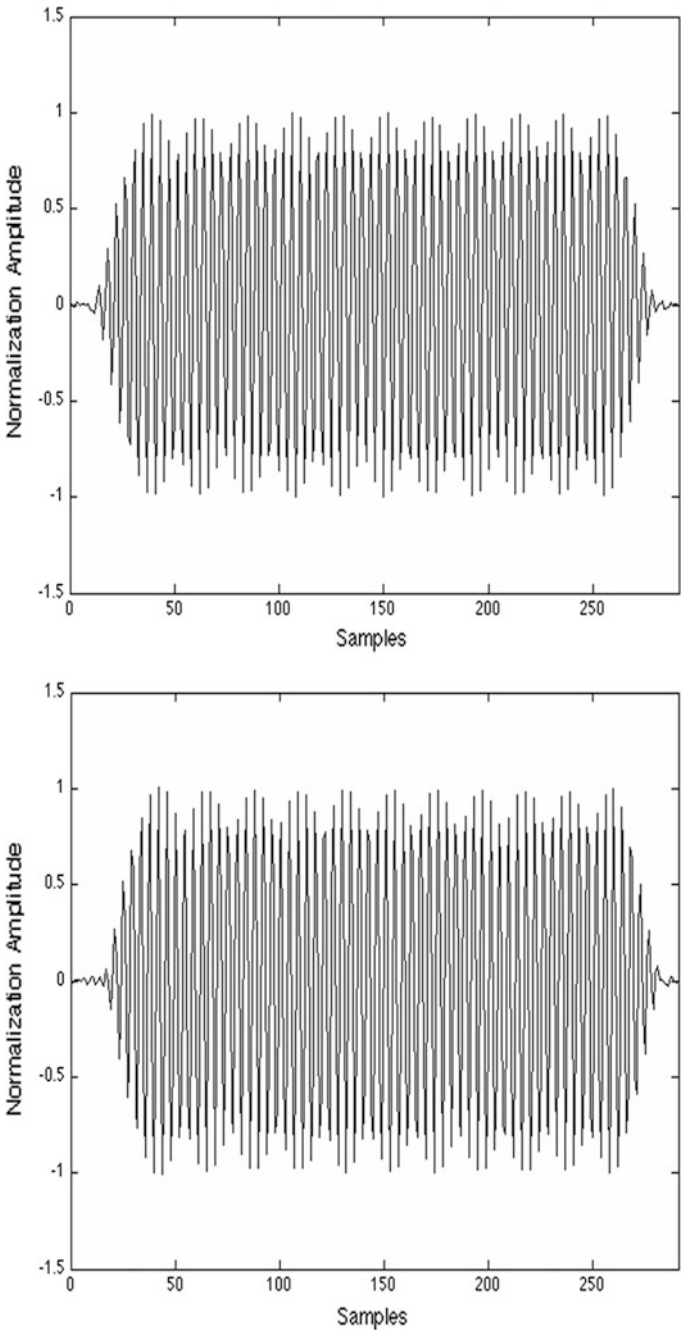

Fig. 3 Samples of two specific emitters: **a** emitter 1, **b** emitter 2

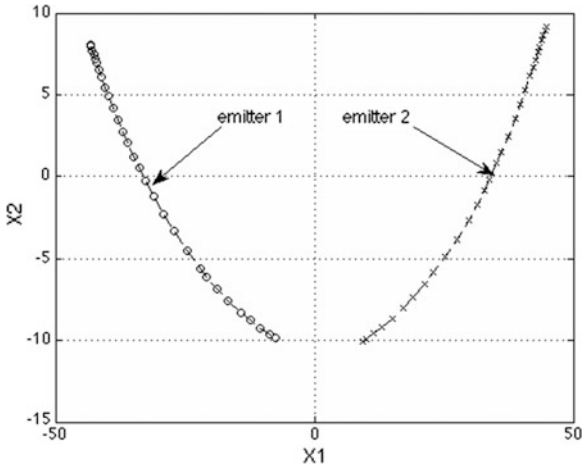

Fig. 4 Intrinsic features in two dimensions

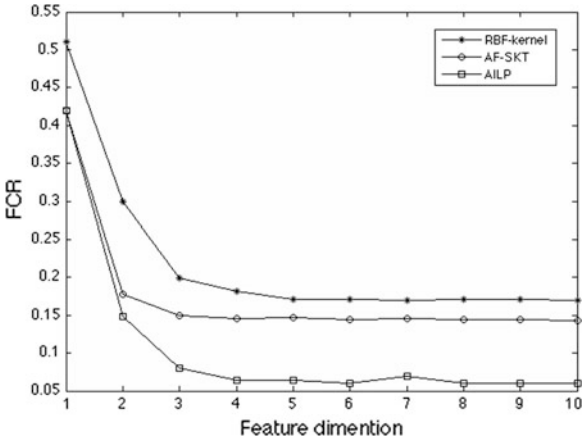

Fig. 5 Performance comparisons

This result testifies the correctness of the intuitive models and the Preposition A aforementioned.

We use two different kernel principal component analysis (KCPA) methods, RBF kernel and Asymmetric Frobenius Subspace Kernel Function (AF-SKF), to extract features form the instantaneous parameters and compare identification performances with the proposed intrinsic features. By using the same K-means classifier to identify the four radar emitters, we show the false classification rate (FCR) in Fig. 5.

From Fig. 5, we find that with increasing of the dimension of the features, all the FCR decreases, and the FCR of proposed features is the smallest, which means that the intrinsic features are better than the others. The performance of SEI is increased by nearly 15 % when the dimension of features is big enough.

5 Conclusions

The intuitive model and SDG can exact the extremely good feature sets of individual radar. These intrinsic features have the ability of rejection of the nonlinear interference and noise signals. Experiments on actual intercepted radar signals with the same type verify the correctness and validity of the proposed model.

Acknowledgments We thank professor Wenli Jiang, Xiang Wang and Peng Yang for useful discussions regarding this work. We also thank professor Yi Lin for his thesis, and Yifei Li for her comments. We are grateful to the reviewers for their helpful suggestions.

References

1. Wiley RG (2002) ELINT: the interception and analysis of radar signals. Artech House Inc, Norwood
2. Spezio AE (2002) Electronic warfare systems. IEEE Trans Microw Theory Tech 50(3):633–644
3. Goodman G (2009) New horizons for shipboard EW. JED 32(1):25–32
4. Jackson EA (2006) Detecting intrusions at layer one: device fingerprinting for network access authorization. Ph.D. dissertation, Iowa State University, Ames, Iowa
5. Shieh CS, Lin CT (2002) A vector neural network for emitter identification. IEEE Trans Antenn Propag 50(8):1120–1127
6. Langley LE (1993) Specific emitter identification (SEI) and classical parameter fusion technology. In: Proceedings of IEEE Western electronic show conference, San Francisco, CA, pp 377–381
7. Dagostino S, Foglia G, Pistoia D (2009) Specific emitter identification: Analysis on real radar signal data. In: Proceedings of the 6th European conference on radar, Rome, Italy, pp 242–245
8. Kawalec A, Owczarek R (2004) Specific emitter identification using intrapulse data. In: Proceedings of the European radar conference, Amsterdam, The Netherlands, pp 249–252
9. Lin Y (2008) Systemic Yoyos: some impacts of the second dimension. Taylor and Francis, London
10. Diego R (2010) Systemic Yoyos: some impacts of the second dimension, Kybernetes. Int J Syst Cybern Manag Sci 39(6):1075–1078
11. Xu D (2008) Research on the mechanism an method on the specific emitter identification. National University of Defense Technology, Changsha, Hunan (in Chinese)
12. Lin Y, OuYang S (2010) Irregularities and prediction of major disasters. CRC Press, Boca Raton
13. Song Chunyun S, Zhan Y, Guo L (2010) Specific emitter identification based on intrinsic time-scale decomposition. In: Proceedings of the IEEE wireless communications networking and mobile computing (WiCOM) conference, Chengdu, pp 1–4
14. Lunden J, Koivunen V (2007) Scaled conjugate gradient method for RADAR pulse modulation estimation. In: Proceedings of the IEEE ICASSP
15. Darling RWR, Intrinsic location parameter of a diffusion process. http://www.stat.berkeley.edu/tech-reports/

RGBD SLAM for Indoor Environment

Rongyi Lin, Yangzhu Wang and Songpu Yang

Abstract This paper presents an implementation of indoor Simultaneous Localization and Mapping (SLAM) using RGBD images. Such system can be used in applications such as indoor robot navigation and environment perception. We perform coarse frame alignments using visual features. The coarse alignment results are then refined by applying Iterative Closest Point (ICP) algorithm to the point clouds. We create a pose graph which consists of keyframes which will be optimized if a new loop is detected. The performances of coarse alignment are tested using four methods—KLT tracker, SIFT, SURF and ORB. The experiment results show that ORB is a good trade-off between accuracy and efficiency. The performances and limitations of ICP are also explored. The results indicate that ICP is very sensitive to the initial value and the size of the point clouds. We also find that the loop closing largely reduces the alignment error. The maps of our laboratory are created using both the 3D point clouds and octomap.

1 Introduction

GPSs and IMUs are typically used to determine the positions and orientations of a robot, respectively. However, in many occasions like indoors or urban environment, GPSs are denied and IMUs suffer from quick drift. In some applications, we also need a representation of the environment where a robot is working.The past decade has seen extensive research in Simultaneous Localization and Mapping (SLAM). SLAM endows the robots with the ability to build map online and simultaneously utilize the built map to determine their own poses and correct

R. Lin (✉) · Y. Wang · S. Yang
School of Automation Science and Electrical Engineering, Beihang University, Beijing, China
e-mail: rongyilin87@gmail.com

F. Sun et al. (eds.), *Foundations and Practical Applications of Cognitive Systems and Information Processing*, Advances in Intelligent Systems and Computing 215,
DOI: 10.1007/978-3-642-37835-5_15,

errors of previous estimations. SLAM is considered as the Holy Grail in the robotics society which makes a robot truly autonomous, since SLAM does not need any prior information of the environment.

The SLAM problems are traditionally solved using filtering techniques such as Extended Kalman Filter (EKF), Rao-Blackwellized Particle Filter (RBPF) [1] and Unscented Kalman Filter (UKF) in which key points locations and robot poses (or trajectories) are simultaneously estimated. The graph-based SLAM [2], especially the implementation using pose graph [3], have gained popularity in recent years. The graph-based SLAM typically consists of two parts: the *front-end* and the *back-end*. The front-end interprets sensor data, finds the constraints among frames and constructs the graph. The back-end adjusts the nodes in the graph using non-linear optimization techniques to obtain the best consistency with the spatial constraints encoded in the edges.

The SLAM system also concerns two other problems: *data association* and *loop closing*. Data association aims to find the which landmarks (or so-called feature points in visual SLAM) in a new observation best match with those in the current map (or in old observations). The job of loop closing is to associate the current observations with the previously mapped region. This process will largely reduce the pose and mapping errors accumulated along the trajectory.

Visual-based SLAM is a hot topic in recent years, which is closely related to computer vision problems such as Structure from Motion (SFM), Bundle Adjustment (BA) and Visual Odometry (VO). The mono-vision systems [4] have the problem with the unknown image scale factor and the additional techniques should be applied to initialize features. The maps generated from visual-based SLAM systems typically consist of sparse feature points which are not good representations of the complex 3D world. However, visual-based SLAM has the advantage in data association by using informative visual features compared to laser-based solutions. One of the major difficulties of visual-based SLAM is that it is non-trivial to obtain the dense depth information.

The advent of Kinect sensor has aroused intensive interests in the field of robotics and computer vision. Kinect is a cheap sensor but it can output both RGB images and depth images at full rate [5]. In this paper, we build a SLAM system using Kinect sensor as the front-end and pose graph as the back-end. Figure 1 shows the architecture which will be explained in detail in the following sections. In general, we use features detected from two intensity images to estimate the sensor motion (or relative sensor pose). The point clouds generated from two depth images are then utilized to refined the relative sensor pose and create the dense 3D structures of the environment. The motion sensing is done on frame-by-frame basis, but only keyframes are added to the pose graph and optimized.

Unfortunately, Kinect sensors have some shortcomings including the limited depth range ($<$5 m), narrow field of view ($\approx 60^\circ$), shadow effects (due to the obstacles), sensitivity to the sunlight and increased errors or failures introduced by reflective, refractive surfaces or IR absorbing materials [6].

This paper is organized as follows: Section 2 discusses Kinect sensor model. Section 3 presents the implementation of the front-end which consists of coarse

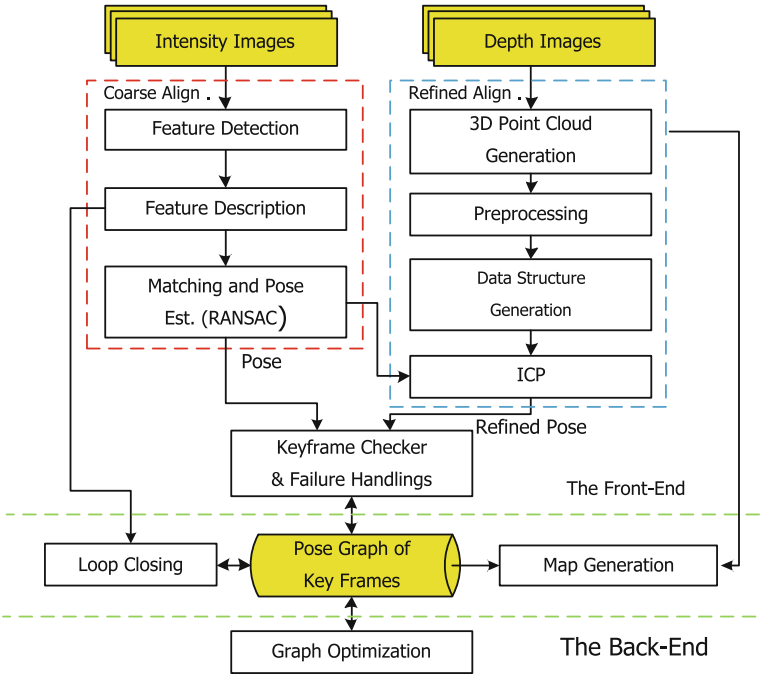

Fig. 1 The RGBD SLAM framework

alignment and refined alignment. Section4 covers SLAM based on the pose graph including problem formulation and loop closing. Section 5 presents the results of our experiments.

2 The Kinect Sensor

The Kinect sensor outputs both RGB intensity image $\mathcal{I}_{rgb}(u, v)$ and depth image $\mathcal{I}_d(u, v)$, both with the resolution 680×480 at 30 Hz. The depth image has the precision up to 11 bits, whereas the valid range is from 500 to 1000. The mapping from a depth image pixel value d in bits to the actual distance x in meters is nonlinear and can be modeled as

$$x = \frac{1}{-k_1 d + k_2}$$

with the coefficients $k_1 \approx -0.00307$ and $k_2 \approx 3.33$. The Kinect sensor can be parametrized as a tuple:

$$(c_u^d, c_v^d, f_u^d, f_v^d; c_u^I, c_v^I, f_u^I, f_v^I; T_c^d; k_1, k_2)$$

where $c_.$'s denote the optical centers (in pixels), $f_.$'s denote focal lengths (in pixels) and $T_c^d \in \mathbb{SE}(3)$ is 6D relative pose from depth camera to intensity camera. For simplicity, we ignored the distortion coefficients in both cameras.

$\mathcal{I}_{rgb}$ and $\mathcal{I}_d$ are first aligned using sensor parameters. For a pixel (u, v) in the image, the corresponding 3D coordinate (x, y, z) w.r.t. the sensor coordinate system can be obtained using the following procedures:

$$x = \frac{1}{-k_1 \mathcal{I}_d(u, v) + k_2}, \; y = \frac{-x}{f_u} u + \frac{c_u}{f_u}, \; z = \frac{-x}{f_v} v + \frac{c_v}{f_v} \tag{1}$$

We refer the readers to [7] and [6] for detailed modeling and calibration of Kinect sensors.

3 The Front-End

The front-end of our system can be seen as a Visual Odometry (VO) with depth information, which calculates the sensor motion $\delta\mathbf{x}$ with two consecutive frame of Kinect data. The Kinect data input are processed on a *coarse-to-fine* basis.

3.1 Feature Detection and Description Algorithms

Finding features in an image includes two steps: first, identify the 2D coordinate of a feature in an image; second, summarize the information of the feature (using the information of neighborhood) as a feature descriptor (typically in the form of a vector). An ideal image feature shall be discriminative, fast to extract, and immune to the changes of viewpoint, lighting and scale.

Corner features such as Harris or more recent FAST features are typically used as feature detectors which are fast to compute. But FAST and Harris are sensitive to scale and rotation. The problem with scale can be handled using scale space. SIFT [8] and SURF [9] features are scale and viewpoint invariant but computationally demanding. SURF is faster than SIFT but suffers from a slight discount in accuracy. SIFTGPU [10] is a paralleled version of SIFT and largely enhances the efficiency (reportedly about 3.5 times as fast as non-parallel SURF).

SIFT and SURF have both detector and descriptor which can operate separately. Generally, we can use different combinations of detector and descriptor. But detector and descriptor must be designed to work well with each other [11].

BRIEF [12] is a new feature descriptor which is very fast both to generate and to match. BRIEF is formulated as a 256-bit binary sequence. Every bit in the sequence represents the result of a binary intensity test (of a pair of points within the patches around the candidate feature). *Hamming distance* which is defined as number different bits in two binary sequence is used to calculate the distance of two descriptors. Hamming distance can be computed fast on CPUs which typically

provide instructions to perform XOR and bit count. BRIEF is easy to use in that only two parameters are needed to produce a BRIEF descriptor: (1) the kernel and size; (2) the spatial distributions of the pairs for binary tests.

One major disadvantage of BRIEF is that it is not designed for viewpoint change (only tolerates small rotation $<15°$). [13] proposed the enhanced version of BRIEF - Orientation Resistant BRIEF (ORB). ORB uses multi-scale FAST detector and then filtered by Harris. ORB determines the orientation of a feature point by evaluating the direction of the vector from the feature point to the centroid of the patch surrounding the feature point. ORB is reportedly faster than GPUSIFT by one order of magnitude [5], and has the potential for further improvement since it is yet fully optimized using GPU/SSE.

3.2 Visual Features Matching and Coarse Alignment

Let $\mathcal{F} = \{\mathbf{f}_i\}$ be a set of sparse visual features in an image. Every feature $\mathbf{f}_i$ can be represented as a concatenated vector that consists of its information, e.g.,

$$\mathbf{f}_i = [\mathbf{p}_i, \mathbf{d}_i, \mathbf{c}_i, \cdots]$$

where $\mathbf{p}_i$ is the 3D coordinate, $\mathbf{d}_i$ is the feature descriptor, and $\mathbf{c}_i$ is the RGB color. We use (1) to retrieve 3D coordinate $\mathbf{p}_i$ of a feature. Note that the depth information for some feature points may be invalid, hence they must be removed from the feature set.

Given two sets of features $\mathcal{F}^1 = \{\mathbf{f}_i^1\}$ and $\mathcal{F}^2 = \{\mathbf{f}_j^2\}$, the objective of feature matching problem is to find a set of pairs $\mathcal{C} = \{(\mathbf{f}_{i_k}^1, \mathbf{f}_{j_k}^2)\}_k$ such that

$$\mathbf{f}_{j_k}^{t_2} = \arg\min_{\mathbf{f}\in\mathcal{F}^2} \|\mathbf{f} - \mathbf{f}_{i_k}^1\|^2, \quad \mathbf{f}_{i_k}^{t_1} = \arg\min_{\mathbf{f}\in\mathcal{F}^1} \|\mathbf{f} - \mathbf{f}_{j_k}^2\|^2 \tag{2}$$

Equations in (2) are solved using Nearest Neighbor Search (NNS). Note that here we perform bi-directional NNS to avoid ambiguous matches. The nearest neighbors can be determined using brute force search, k-D tree or k-means-based search. These techniques have been implemented in FLANN library. [14] shown that a GPU-based brute-force search outperforms a CPU-based kd-trees.

In NNS, we can define different distances between two features. Here we simply define $\|\mathbf{f}_i - \mathbf{f}_j\|^2 = \|\mathbf{d}_i - \mathbf{d}_j\|^2$ where only feature descriptors are concerned.

Except from direct feature descriptor matching, we also test data association using tracking algorithms. We use KLT (Kanade-Lucas-Tomasi) [15] algorithm to track features in a sequence of images. The main idea of KLT tracker is to calculate the motion of images. The motion of image can be estimated by solving the minimization problem:

$$(A, d) = \arg\min_{A,d} \sum_{w\in\mathcal{W}} \sum_{x\in w} \|\mathcal{I}_2(x + d) - \mathcal{I}_1(x)\|^2$$

where $\mathcal{I}_1$ and $\mathcal{I}_2$ are two intensity images, x denote a image point, A and d are parameters of affine motion model and $\mathcal{W}$ is a set of image patches in the reference image $\mathcal{I}_1$. KLT tracker does not guarantee the corresponding points in the next frame is a feature points, since it only applies the KLT criterion (other criteria such as Harris and are allowed) in the first frame but not for other frames. But we can re-check the tracked features to ensure that they are 'good'. Since some previous features will be lost in the new frame, new features will be detected and added to the list of features. KLT tracker is fast and can track features in a new image within several tens of milliseconds. But KLT tracker is not robust against changes in scale and viewpoint and only accurate for short sequences.

With matched feature correspondences $\mathcal{C}$, we can estimate the relative sensor pose between frame 1 and frame 2 by solving the problem

$$\delta\mathbf{x} := \arg\min_{\delta\mathbf{p}\in\mathcal{C}'} \sum_k \|\mathbf{p}^1_{i_k} - \delta\mathbf{x} \oplus \mathbf{p}^2_{j_k}\|^2$$

where $\mathcal{C}'$ is a subset of $\mathcal{C}$. Our implementation uses Random Sample Consensus (RANSAC). For simplicity, we use $\oplus$ and $\ominus$ operation to express the *composition* and *inverse composition* of 6D poses $\in \mathbb{SE}(3)$ or 3D points $\in \mathbb{R}^3$, as was in MRPT [16].

3.3 Refined Alignment using ICP

We have a coarse guess of inter-frame transformation using visual-based approaches discussed in Sect. 3.2. The next step is to refined this transformation using Iterative Closest Point (ICP).

Let $\mathcal{P}^1 = \{\mathbf{p}^1_i\}$ and $\mathcal{P}^2 = \{\mathbf{p}^2_j\}$ be two point clouds. The objective is to estimate the relative pose $\delta\mathbf{x}$ between two $\mathcal{P}^1$ and $\mathcal{P}^2$. The ICP generally consists of two steps [17]:

(1) Find correspondences $\mathcal{S} = \{(\mathbf{p}^1_{i_k}, \mathbf{p}^2_{j_k})\}_k$ such that $\mathbf{p}^2_{j_k}$ is the nearest neighbor of $\mathbf{p}^1_{i_k}$ and the reprojected Euclidean distance $\|\mathbf{p}^1_{i_k} - \delta\mathbf{x} \oplus \mathbf{p}^2_{j_k}\|_2 < d_{max}$. Here, d_{max} is chosen to limit search region and reduce mismatches.
(2) Estimate the relative pose $\delta\mathbf{x}$ by solving the following optimization problem:

$$\delta\mathbf{x} := \arg\min_{\delta\mathbf{x}} \sum_k w_k \cdot \text{dist}(\mathbf{p}^1_{i_k}, \delta\mathbf{x} \oplus \mathbf{p}^2_{j_k}) \tag{3}$$

where the $\text{dist}(\cdot,\cdot)$ is user-defined error metric and w_k's are the weights.

The solution of ICP with dense point clouds has high probability to been trapped in local minima. Conversely, ICP using sparse point clouds will cause large alignment error. Therefore, it is important to seek a proper cloud size. We down-sample the point clouds using voxelization. We test the ICP performances by setting the leaf size (the size of voxel) from 0.01m to 0.5m. In addition, the invalid points and distant points (>5 m) are removed.

As descriptors matching in Sect. 3.2, a distance metric should be specified. The simplest one is *point-to-point* metric, i.e.,

$$\text{dist}(\mathbf{p}_i^1, \mathbf{p}_j^2) \triangleq \|\mathbf{p}_i^1 - \delta\mathbf{x} \oplus \mathbf{p}_j^2\|_2^2$$

Some metrics exploit the surface information. For example, *point-to-plane* metric measures the distance from a point to tangent plane of the other point. Here,

$$\text{dist}(\mathbf{p}_i^1, \mathbf{p}_j^2) \triangleq \|\mathbf{n}_i^{1T}(\mathbf{p}_i^1 - \delta\mathbf{x} \oplus \mathbf{p}_j^2)\|_2^2$$

where $\mathbf{n}_i^1$ is the surface normal at the point $\mathbf{p}_i^1$. One of the drawbacks of the plane-to-point metric is that the error along the directions orthogonal to the surface normals is not controlled. The *plane-to-plane* metric [17] takes the surface information in both scans into account, which needs additional computation to calculate surface normals.

In some schemes like [14], colors are incorporated to compensate the regions without salient geometric structure. As intensity images, we can extract (geometric) features from point clouds and generate the descriptor for each feature. These features can be used if we fail to calculate the transformation using visual features.

It has been shown that ICP is less robust than the technique using visual features. If the transformation calculated by ICP is largely inconsistent with the initial value, we simply discard the ICP result. Another feasible approach is to take the visual features into account throughout the whole optimization process. In this case, the optimization problem becomes

$$\delta\mathbf{p} := \arg\min_{\delta\mathbf{p}}(1-\alpha)\cdot\text{error}(\mathcal{C}) + \alpha\cdot\text{error}(\mathcal{S}) \tag{4}$$

where $\mathcal{C}$ is the set of correspondences of visual features, $\mathcal{S}$ is the set of inter point cloud correspondences, error$(\cdot)$ is the sum of re-projection errors, and α is the weight. Although it is advantageous to use (4), it is not trivial to determine α.

There are some termination criteria for ICP: (1) the max number of iteration reached, (2) the difference of successive transformation estimation is lower than a threshold, and (3) the sum of re-projection error is smaller than a threshold. The ICP stops if any the above criteria is satisfied.

In our implementation, we use the Point Cloud Library (PCL) [18] for point cloud operations and ICP.

4 The Back End

4.1 Problem Formulation for Pose Graph SLAM

The task of SLAM back-end is to seek for a configuration of nodes that maximizes the likelihood of measurements encoded in the constraints.

A pose graph can be represented as a direct graph $\mathcal{G} = (\mathcal{V}, \mathcal{E})$, where $\mathcal{V} = \{\mathbf{x}_n\}$ is a set of keyframes and $\mathcal{E} = \{(i_k, j_k, \delta\mathbf{x}_k)\}_k$ is a set of edges where the relative poses $\delta\mathbf{x}_k = \mathbf{x}_{i_k} \ominus \mathbf{x}_{j_k}$ are encoded. The loop closing procedure add edges between non-consecutive frames. The objective of pose graph optimization is to obtain $\mathcal{V}^*$ such that

$$\mathcal{V}^* = \arg\min_{\mathcal{V}} \sum_k \|\mathbf{p}_{i_k} \ominus (\mathbf{p}_{j_k} \oplus \delta\mathbf{x}_k)\|^2$$

which is in fact a Nonlinear Least Squared (NLS) problem. Because of the sparse nature of pose graph, this problem is cheap to compute. However, if excessive revisits occur, many node in the graph may become redundant. [19] and [20] presented approaches to reduce the graph complexity. Graph optimization is performed each time a loop closing is detected.

Let $\delta\mathbf{x}^\dagger = (x^\dagger, y^\dagger, z^\dagger, \text{yaw}^\dagger, \text{pitch}^\dagger, \text{roll}^\dagger)$ be the relative pose of current frame w.r.t. the previous *keyframe*. In our implementation, the current frame is considered as a *keyframe* if $\sqrt{(x^\dagger)^2 + (y^\dagger)^2 + (z^\dagger)^2} > 0.2\text{m}$, or $\text{yaw}^\dagger > 6°$, or $\text{pitch}^\dagger > 3°$, or $\text{roll}^\dagger > 3°$.

4.2 Loop Closing

Loop closing generally covers two steps: *loop detection* and *loop correction*. Loop detection recognizes that the camera has returned to the previously visited location. Loop correction merges duplicated regions in the map. For visual-based SLAM, loop detection is also known as Place Recognition (PR). In our implementation, loop correction is done by optimizing pose graph.

Visual place recognition can be considered an image classification problem in which new views are classified against a set of previously seen views. [21] proposed a technique based on Bag-of-Words (BoW). An image can be treated as a document described using words from a vocabulary. A vocabulary is built by clustering features extracted from a large dataset. A word is defined as the center of a learned cluster. The number of the clusters equals to vocabulary size. The vocabulary tree can be used to hierarchically tag an image to a certain topic.

For visual-based SLAM, the classifier must support efficient online learning of new reference image. FAB-MAP [22] is a notable framework which learns a probabilistic model of scene appearance online using a generative model of visual word observations and a sensor model which explains missed observations of visual words.

5 Experiments

This section presents some of our experiment results although we have not completely fulfilled the proposed scheme. We run the tests on an work station with Intel Xeon E5504 CPU and 4GB RAM.

We use a 165-frame dataset acquired by a hand-holding Kinect sensor which consists of one loop. This dataset is a 360° scan of our laboratory in which the frame 20−80 consist of mainly far objects. We sub-sample the full-rate Kinect data stream by 4.

5.1 Coarse Alignment

We test the performances of coarse alignment using SIFT/SIFT, SURF/SURF, ORB/ORB and KLT tracker. SIFT, SURF and ORB are configured by default in OpenCV. KLT tracker is provided by MRPT. We have not currently tested the GPU-based algorithms. To reduce the computation, we detect at most 500 'good' key points w.r.t. their KLT responses for each frame. Since we do not have the ground truth of inter-frame transformations, we use the following *alignment score* to evaluate the accuracy,

$$\text{score} = \frac{1}{|\text{inliers}|} \sum_{(\mathbf{p}^1, \mathbf{p}^2) \in \text{inliers}} \|\mathbf{p}^1 - \delta\mathbf{x} \oplus \mathbf{p}^2\|_2$$

where $\mathbf{p}^{\cdot}$ is the coordinate of a feature (w.r.t. the sensor coordinate system) and $\delta\mathbf{x}$ is the relative pose.

Figure 2 shows the alignment score each frame. We can find in Fig. 2 that SURF has generally lowest alignment errors whereas SIFT is no better than SURF although it is most computationally demanding. Since ORB and tracking approaches have fewer features (correspondences), thus more vulnerable to large errors or even failures. The accuracy of ORB and KLT is comparable to that of SIFT/SURF in most cases.

We also investigate the ratio η of inliers which pass RANSAC to all candidate matching pairs found by NNS. This indicates the susceptibility to mismatching and the uniqueness of features. Figure 3, shows that SURF and KLT (except the cases of where the alignment fails) have highest inlier ratios. This is expected for KLT tracker since the image motions are taken into account and features have higher probability to be tracked. The η of SIFT is smaller than that of SURF by approximately 10 % whereas ORB is comparable to SIFT with more downward peaks. For SIFT and SURF, we use both L_1 and L_2 norm for feature descriptor matching. We find that L_1 and L_2 norm have similar accuracies. Hence, we ignore the curves

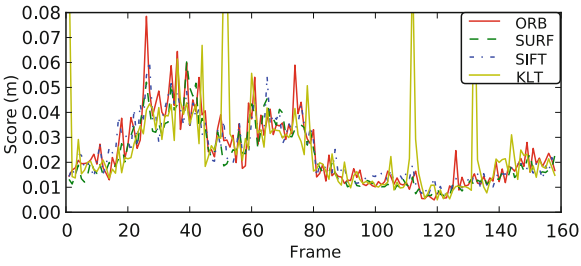

Fig. 2 Alignment scores of coarse alignment process for each frame in the 165-frame dataset

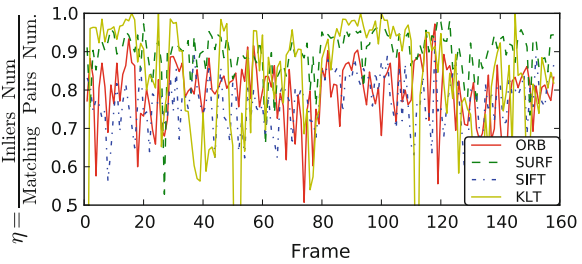

Fig. 3 Correspondence inliers ratios of coarse alignment process for each frame in the 165-frame dataset

related to L_1 norm to keep the plots succinct. According to Figs. 2 and 3, there is an inverse relationship between the alignment score and inlier ratios.

We also test the execution time for each approach. We divide the execution time into for categories: feature detection, descriptor calculation, descriptor matching, and pose estimation. For KLT tracker, we only record the overall tracking time per frame. We found that the time for feature matching using BruteForce-L_1 and BruteForce-L_2 is nearly the same. But the calculation of L_1 norms can be optimized using SSE instructions which is out of the scope of this papers. From Table 1, we can see that matching using FLANN is much faster than BruteForce approach. SIFT is most time consuming because it requires more time to detect, describe and match SIFT features. SIFT and SUFT are hard to satisfy the requirement real-time application. The ORB is faster than SURF by a scale of magnitude and KLT is fastest among our four approaches. Note that the RANSAC take a large percentage of execution time which should be further optimized in the future work.

To sum up, we prefer ORB and Tracking approaches, since their accuracy comparable to that of SIFT and SURF but are much faster. But KLT is not suitable when the frame rate is slow, and a feature has higher likelihood to be lost in the next frame. SURF can serve as a backup if ORB or KLT fails.

5.2 ICP

Since we do not have ground truth dataset, we test the ICP performances according to following steps: (1) Select a point cloud to be tested and voxelize this point

Table 1 Execution time for coarse alignment

	Detection (ms)	Description (ms)	Matching (ms)	RANSAC (ms)
ORB	18.5	14.9	7.5	89.4
SURF-L_1	239.7	105.9	84.4	213.2
SURF-L_2	241.3	106.2	84.4	213.5
SURF-FLANN	105.6	105.6	31.8	214.1
SIFT-L_2	388.4	390.2	218.7	178.3
SIFT-L_1	368.3	377.3	217.7	173.7
SIFT-FLANN	364.7	370.0	57.1	177.2
KLT	11.2 (Tracking)			65.2

cloud with user-defined leaf size. Denote $\mathcal{A}$ the voxelized point cloud. Make a copy of $\mathcal{A}$ which is taken as $\mathcal{B}$. (2) To make two cloud not fully overlap, we remove points in $\mathcal{B}$ whose $y-$coordinate (lateral) are out of the a user-defined range $[y_1, y_2]$. (3) Add Gaussian noise to $\mathcal{A}$ and $\mathcal{B}$. In our test we set $\sigma_x = 3$ cm (depth), $\sigma_y = 1$ cm (lateral), $\sigma_z = 1$ cm (vertical). (4) We run ICP with an initial guess and the resulting transformation, which is expected converge to identity, indicates the alignment error in the real scenario.

We select a point cloud from our dataset which consists of both near and far points, and apply the procedures presented above. In our application, the primary rotation motions are in the channel of yaw. Hence, we fix the initial roll and pitch to 1°. In all ICP experiments, we set max iteration number to 50. For simplicity, the x, y and z of initial translation are set with the same t_{init}.

We have investigated how d_{max} affects ICP performances. Our results show that a carefully selected d_{max} does not do better than $d_{max} = \infty$. Hence, we do not restrict the value of d_{max}.

We investigate how leaf size will affect the ICP alignment result. Generally speaking, the selection of leaf size is a trade-off between convergence rate to accuracy: ICP with a large leaf size converges fast but it is more likely that the solution is pulled to a wrong value. On the other hand, small leaf size may results in local minima. We set the $t_{init} = 5$ cm, yaw $= 5°$, pitch $= 1°$, roll $= 1°$. The leaf size ranges from 0.01 to 0.5. We can see from Fig. 4a that in this test, ICP enlarges the translation error to around 15 cm for leaf size in the range $[0.01, 0.2]$. In contrast, ICP generally reduces the rotation errors into an acceptable ranges. Surprisingly, when leaf size > 0.3 (the corresponding size of point cloud is less than 150), both angular and translation errors decrease drastically. This may be explained by the fact that we use a pair of artificial point clouds and ICP will easily converge to the true value with sparse points. However, in real scenarios, it is not feasible to use point cloud which is too sparse since we have obtained a rather

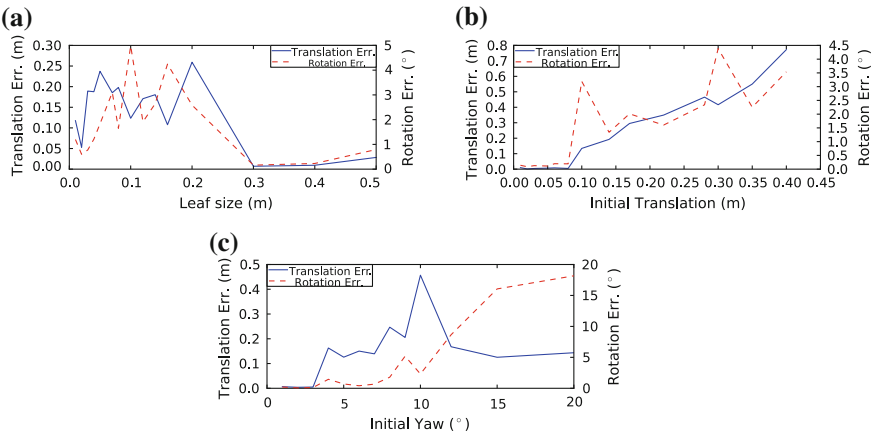

Fig. 4 ICP performance as **a** the leaf size, **b** the initial translation, and **c** the initial yaw

accurate initial guess and we need ICP to refine the relative pose. We think point clouds with sizes around 5000 is a good choice for ICP.

We also investigate how large the deviation of the initial guess will affect the final alignment result. We consider the initial translation and rotation (yaw) separately. Intuitively, larger deviation will cause worse result. But we are interested to find a safe range.

We consider the how initial translation will influence the final transformation. We set leaf size $= 0.04$, yaw $= 1^\circ$, pitch $= 1^\circ$ and roll $= 1^\circ$. The initial translation t_{init} are chosen from 0.01 m to 0.40 m. Figure 4b shows the final rotation errors and rotation error as the function of t_{init}. It shows that on the premise that the initial rotation is small $(<1^\circ)$, the resulted translation errors tend to converge below 1 cm if initial translation is less than 10 cm. If the initial translation reaches to 10 cm, the resulted translation error will jump to more than 10 cm and continue to increase as initial translation. The tendency of rotation error is similar to that of translation error.

We investigate the extent to which the initial deviation of yaw influences the final alignment result. We set the leaf size $= 0.04$, $t_{init} = 1$ cm, pitch = 1°, roll = 1°. We choose initial yaw from 1° to 20°. Figure 4c shows that the translation error decreases to near-zero value if initial yaw is less than 3°, followed by a drastic jump. Figure 4c shows that angular error is more robust to initial yaw with the critical point at 8°.

To summarize, ICP is less stable than the frame alignment using visual features. The parameters are difficult to be tuned. Although we have not seen a persuasive reason to use ICP to refined frame alignment, our mapping using the 165-frame dataset shows that visual + ICP combination do better than solution without ICP [cf. Fig. 5a and b]. We think that if there are sufficient inliers of visual features correspondences between consecutive frames, ICP can be ignored.

5.3 Pose Graph Optimization and Loop Closing

Since we have not implemented the place recognition, we close the loop manually. We set the covariance matrix of each edge uniformly to

$$\Sigma \approx [\text{diag}(0.1\text{m}\,(x), 0.1\text{m}\,(y), 0.1\text{m}\,(z), \\ 0.1^\circ\,(\text{yaw}), 0.1^\circ\,(\text{pitch}), 0.1^\circ\,(\text{ roll}))]^2$$

This is obviously not a good assumption since the alignment error might vary frame by frame. Hence we suggest that a more accurate edge covariance be derived to avoid large adjustment between accurately aligned frames.

Figure 5b shows the map of our lab using point clouds of keyframes where the global pose of the point clouds is obtained using SURF and refined by ICP. We can find a large inconsistency near the middle of the left edge in Fig. 5b between 'head' frame and 'tail' frame. Then we close the loop by re-computing the relative

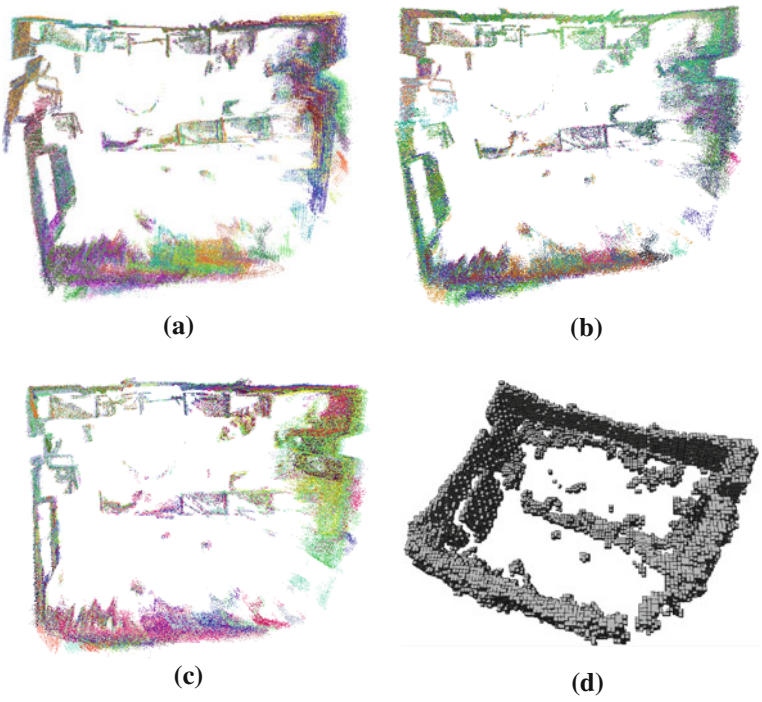

Fig. 5 **a** Point cloud map using SURF without ICP. **b** Point cloud map using SURF and ICP before loop closed. **c** Point cloud map using SURF and ICP with loop closed. **d** Visualization using Octomap

transformation between 'head' frame and 'tail' frame and add it as a new edge in the pose graph. We can see in Fig. 5c that the 'tail' frame and the 'head' frame have been perfectly aligned and the poses of remaining frames are adjusted slightly. The occupancy grid map in Fig. 5d is the Octomap [23] version of Fig. 5c.

6 Conclusion and Future Work

In this paper we present a pose-graph-based SLAM using RGBD images. We perform coarse frame alignment using visual features. Then, we refine the alignment using ICP. We construct a pose graph with keyframes and perform graph optimization if a new loop is detected. We create the maps of our laboratory using both the 3D both point clouds and octomap.

We currently focus on off-line processing and the code is not fully optimized. Techniques using parallel computing and GPU will be implemented. In next step, we will incorporate the IMU to our system. The IMU data can be fused with the visual odometry to generate more precise estimation of robot motion. On the other

hand, pose increments calculated from the IMU can serve as the initial guess for other processes which may reduce convergence time. The IMU is also a backup when the front-end fails.

References

1. Montemerlo M, Thrun S, Koller D, Wegbreit B (2003) Fastslam 2.0: an improved particle filtering algorithm for simultaneous localization and mapping that provably converges. In: International joint conference on artificial intelligence, vol 18. Citeseer, pp 1151–1156
2. Thrun S, Montemerlo M (2006) The graph slam algorithm with applications to large-scale mapping of urban structures. Int J Robot Res 25(5–6):403–429
3. Konolige K, Grisetti G, Kummerle R, Burgard W, Limketkai B, Vincent, R (2010) Efficient sparse pose adjustment for 2d mapping. In: Intelligent robots and systems (IROS), (2010) IEEE/RSJ international conference on, IEEE, pp 22–29
4. Klein G, Murray D (2007) Parallel tracking and mapping for small ar workspaces. In: Proceedings of the (2007) 6th IEEE and ACM international symposium on mixed and augmented reality. IEEE Computer Society, pp 1–10
5. Endres F, Hess J, Engelhard N, Sturm J, Cremers D, Burgard W (2012) An evaluation of the rgb-d slam system
6. des Bouvrie B (2011) Improving rgbd indoor mapping with imu data
7. Herrera CD, Kannala J, Heikkilä J (2011) Accurate and practical calibration of a depth and color camera pair. In: Computer analysis of images and patterns, Springer, pp 437–445
8. Lowe D (2004) Distinctive image features from scale-invariant keypoints. Int J Comput Vision 60(2):91–110
9. Bay H, Tuytelaars T, Van Gool L (2006) Surf: Speeded up robust features. Comput Vis ECCV 2006 1:404–417
10. Wu C (2007) SiftGPU: A GPU implementation of scale invariant feature transform (SIFT). http://cs.unc.edu/ ccwu/siftgpu
11. Hertzberg C, Wagner R, Birbach O, Hammer T, Frese, U.: Experiences in building a visual slam system from open source components. In: Robotics and automation (ICRA), (2011) IEEE international conference on, IEEE, pp 2644–2651
12. Calonder M, Lepetit V, Strecha C, Fua P (2010) Brief: Binary robust independent elementary features. Comput Vis ECCV 2010 6314:778–792
13. Rublee E, Rabaud V, Konolige K, Bradski G (2011) Orb: an efficient alternative to sift or surf. In: International conference on computer vision, Barcelona, 2011
14. Neumann D, Lugauer F, Bauer S, Wasza J, Hornegger, J.: Real-time rgb-d mapping and 3-d modeling on the gpu using the random ball cover data structure. In: Computer vision workshops (ICCV Workshops), (2011) IEEE international conference on, IEEE, pp 1161–1167
15. Tomasi C, Shi J (1994) Good features to track. CVPR94, pp 593–600
16. Blanco JL (2010) A tutorial on se(3) transformation parameterizations and on-manifold optimization. Technical report, University of Malaga
17. Segal A, Haehnel D, Thrun S (2009) Generalized-icp. In: Proceedings of robotics: science and systems (RSS)
18. Rusu RB, Cousins S (2011) 3D is here: point cloud library (PCL). In: IEEE international conference on robotics and automation (ICRA), Shanghai, China, 9–13 May 2011
19. Stachniss C, Kretzschmar H (2011) Pose graph compression for laser-based slam
20. Konolige K, Agrawal M (2008) Frameslam: from bundle adjustment to real-time visual mapping. IEEE Trans Rob 24(5):1066–1077

21. Sivic J, Zisserman A (2003) Video google: a text retrieval approach to object matching in videos. In: Computer Vision, Proceedings. Ninth IEEE International Conference on, IEEE, pp 1470–1477
22. Cummins M, Newman P (2008) Fab-map: probabilistic localization and mapping in the space of appearance. Int J Robot Res 27(6):647–665
23. Wurm KM, Hornung A, Bennewitz M, Stachniss C, Burgard W (2010) OctoMap: a probabilistic, flexible, and compact 3D map representation for robotic systems. In: Proceedings of the ICRA 2010 workshop on best practice in 3D perception and modeling for mobile manipulation, Anchorage, AK, USA, May 2010. http://octomap.sf.net/

Neighborhood-Based Variable-Scale Model in Mobile Maps

Chaode Yan, Wang Guo, Jianjun Bai and Tian He

Abstract Mobile maps, which integrates mobile positioning, mobile computing, and mobile communication technologies, differ from desktop and Web maps. Due to their small sizes, maintaining good legibility in mobile maps is very challenging. The variable-scale map model can be used in mobile maps to improve their legibility. Current variable-scale models often require human expertise to select appropriate parameters or models for generating variable-scale maps. However, these models ignore the effect of uneven distribution of spatial objects in map views. In this paper, a variable-scale model based on neighborhood is proposed, which selects the user's focus region based on the neighborhood, identifies the focus region shape and automatically selects the variable-scale range and model. The principle and algorithm are introduced and described. Finally, the proposed model is evaluated. Results of the experiment show that the new model is feasible and valid to overcome the problem mentioned above.

Keywords Mobile map · Variable-scale · Neighborhood

C. Yan (✉) · W. Guo · T. He
Water Conservancy and Environment College, Zhengzhou University, Zhengzhou, China
e-mail: nettalk@sina.com

C. Yan
Research Group Cartography, Institute for Geoinformation and Cartography, Vienna University of Technology, Vienna, Austria

J. Bai
School of Tourism and Environment, Shanxi Normal University, Xi'an, China
e-mail: jianjunb@sina.com

F. Sun et al. (eds.), *Foundations and Practical Applications of Cognitive Systems and Information Processing*, Advances in Intelligent Systems and Computing 215,
DOI: 10.1007/978-3-642-37835-5_16,

1 Introduction

With the development of computer hardware and wireless networks, mobile smart devices, e.g., smart phone, tablet PC, have been widely used. Mobile map, as a kind of general application mode of mobile application, has highly dynamic, interactivity. But the mobile device's display is smaller compared to desktop computer's screen, and it is inconvenient in operation, especially in move environment. These disadvantages limit the use and development of the mobile map. Is there an approach to be able to give detail as well as overviews in mobile map? The answer is "Yes". The variable-scale model is helpful to realize it.

Variable-scale maps abandon the uniform scale in a map. The scales change according to the importance of map area. Variable-scale maps can fully use the map space and the load of map information also the map function are improved observably [1, 2]. This paper proposes a variable-scale model based on neighborhood trying to improve the legibility of mobile map. The paper is organized as follows. Section 2 introduces previous studies of variable-scale maps. Section 3 studies the method of calculating focus area with neighborhood. Section 4 describes the variable-scale mobile map model based on neighbor region. Conclusion is presented in Sect. 5.

2 Previous Studies of Variable-Scale Maps

There are two main categories of variable-scale mobile map. The one abandons uniform scale, changes scale along with importance of region. Different scales are used in different parts in the map. Another category changes the scale based on user's location. This kind of map takes a uniform scale in a single map sheet, but the scale will be changed according to the positions while user is moving.

Much research has been devoted to developing variable-scale mobile map that have as better the results as possible. Harrie divided map of small screen into three regions, and changed the scales of regions with the circle or rectangle variable-scale coordinate conversion formula [3, 4]. This method's computing is simple, distortion is little, and display is more appropriate than traditional mobile map. Li proposed variable-scale maps model according to region of interesting (ROI) [5]. This method divides mobile map into several ROIs, and has a very good expression for relative uniform road net.

There was a common problem in these models. The size, shape, and scale of the focus region had to be predesigned or fixed by user. It cannot be automatically adjusted variable-scale range according to the spatial distribution around user's points of interest (POI), whether Harrie's model based on measurement or Li's based on the region of interest. The display effect depends on experience of user or designer. Both methods hardly make the key geographic information completely and prominently displayed in the focus area.

Yan et al. proposed an adaptive map expression method based on the real-time neighbor relationship of mobile user [6–8]. The uneven distribution of spatial objects and POIs and the cognitive demands of the small display mobile map are considered. In this method, a map has a suitable uniform scale based on dynamic calculation of user's neighbor relationship. An adaptive model was proposed, which applied a suitable map view and reduced user's operation.

3 The Calculation and Measurement of Focus Area

3.1 Neighbor POIs and Neighbor Region

Generally, a variable-scale mobile map is divided into focus area and outlying area. The focus area is the concern area around the user, usually use larger scale. And the outlying area is lower attention area, use smaller scale. The information in user's ROI can be displayed as clear as possible and the information in outlying region can also be displayed as more as possible, by this magnifying-glass effect, like Fig. 1.

Figure 1a is ordinary mobile map and Fig. 1b is variable-scale mobile map. We can see the details of the map center in Fig. 1b as well as Fig. 1a, and the overview is better than Fig. 1a. Shapes of features in Fig. 1b are deformed by variable-scale.

Through the study of human way-finding process, Golledge believe that the human awareness of the space environment has continued to spread through the neighbor regions outside the spillover effects, and the environment or elements in the neighbor regions are most likely to first perception and cognition by mobile

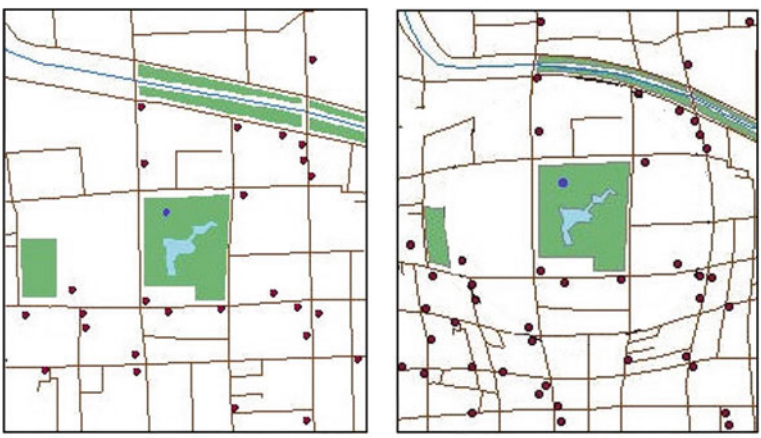

Fig. 1 Difference between ordinary mobile map (**a**) and variable-scale mobile map (**b**)

users [9]. Therefore, a spatial area can be determined by the user and the closest POI, according to the neighbor relationship of users and the surrounding POI.

The geometry neighbor relationship applies to the situation which is relatively a uniform distribution of POI. But in reality, spatial distribution of geometry features is uncertain and imbalance. It is prone to appear much POI in a small area, or little POI in a large area. By traditional variable-scale model with uniform range parameters, mobile map is difficult to be observed with too much POI or nothing to observe with too little POI. The uneven distribution of POI easily leads to imbalances information and reducing legibility. These problems can be effectively reduced by neighbor relationship based on the topology. Take neighbor relationship of POI based on Delaunay triangulation for example. Delaunay triangulation is a connected graph, and each edge of the Delaunay triangle implies the neighbor relationship between the two points. Selected POI based on the Delaunay triangulation, the number is relatively stable. The information of mobile map is not prone to the imbalance.

Define the user's neighbor regions as an Area by first-order neighbor POI of user location. The neighbor region is composed by triangles of the most neighbor POI. To a certain extent, the range of user current attention and high concern can be reflected by neighbor region. The setting parameter of range could be replaced, based on human experience in the past. The neighbor region could guarantee the number of POI in center scope and is relatively stable. In neighbor region, hardly occurred situation which the POIs were too much or too little. In addition, the balance map load was effectively ensured.

3.2 Focus Region Calculation Based on Neighbor Region

Topology neighbor POI and topology neighbor region can be used to determine user's focus range. The focus range balance map display, adjust map information load, and improve map legibility.

The triangle in the Delaunay triangulation is suitable for expressing the neighbor relationship of the spatial point set. It is also able to reflect the geometrical relationship. There are four characteristics of Delaunay triangulation as follows:

(1) Empty the circumcircle: In Delaunay triangulation of the point set V, each circumcircle of triangle does not contain in any other point in the point set V.
(2) Maximizes the minimum angle: Compared to any other triangulation of the points, the smallest angle in the Delaunay triangulation is at least as large as the smallest angle in any other.
(3) Uniqueness: No matter where to start networking, the same Delaunay triangulation will be obtained.
(4) Minimum Edge length: Total edge length of triangle in the Delaunay triangulation is the minimum.

In summary, shape of triangle in the Delaunay triangulation is relatively stable. The design of the calculation method based on the neighbor adaptive focus area is discussed in this section. The calculation method applies to the topology relationship by Delaunay triangulation instead of the traditional geometry relationship. In order to conveniently conclude and calculate, neighbor region were divided into two types of rectangular and circular by the approximate shape of neighbor region. When the shape of neighbor region is approximate circle, the Algorithm of focus region is described as follows:

Step 1: Establishing Delaunay triangulation by the user's POI.
Step 2: Getting the user's location (O). Judging O within the triangle circumcircle or not. If O is within, the vertexes of the triangle are included in set S of the neighbor POI.
Step 3: Calculating the distance of point O to P_i (point P_i belongs to the set S) and getting the maximum as D in Eq. (1)

$$D = \max\{D_{OP_i}\}, \quad P_i \in S \tag{1}$$

Step 4: Getting the focus region which is a circle. O is the center and D is the radius.

When approximate rectangle, the Algorithm is described as follows:

Step 1: Like circle Steps 1, 2.
Step 2: Calculating the horizontal and vertical distance of point O to P_i (point P_i belongs to the set S) and getting the horizontal maximum as X and vertical maximum as Y in Eq. (2)

$$X = \max\{X_{OP_i}\}, \quad Y = \max\{Y_{OP_i}\}, \qquad P_i \in S \tag{2}$$

Step 3: Getting the focus region which is a rectangle. O is the center, X is the half of long side, and Y is the half of short side.

Calculation of variable-scale map is simplified by regular shape of the focus region instead of original irregular shape of the neighbor region. The integrity of geometry features in neighbor region is ensured. Regular shape is easier to predict and control the deformation of geometry features in the process of variable-scale. Furthermore, the shape distortion of geometry features is avoided in variable-scale map.

3.3 Shape Measurement of Neighbor Region

In this section, the method to calculate the neighbor region is discussed, which based on topology neighborhood. In this section, a model is derived that divided the approximate neighbor region into a circular or rectangular.

3.3.1 Characteristic of Neighbor Region

(1) POIs in neighbor region always distribute around the user, which is very close to human's observation by eyes.
(2) POI number is relatively stable. The average number of neighbor POI is about 5, so that the number of neighbor POI is hardly too much or too little.
(3) Although the neighbor region is dynamically calculated, it is relatively fixed when user only move within a certain range.

The appropriate variable-scale model is selected according to the shape of the neighbor region, thus the shape of feature is without distortion. As the user's location changes, the shape of the neighbor region will be changed. In addition, model also should be automatically switched in different variables-scale models.

3.3.2 Shape Measurement

Haggett et al. [10] introduced a circular rate measure model to describe the closeness of the city and circle [10]. Corrected the model, and neighbor region circular rate is defined as (3):

$$C_r = \frac{4\pi A}{P^2} \tag{3}$$

where A is neighbor region area, P is neighbor region perimeter, and C_r is neighbor region circular rate. When C_r equals 1, the neighbor region is circular. And while the neighbor region is a square, C_r is approximately 0.7854. If C_r value approaches 1, the shape of neighbor region will approach a circle. Since the appropriate variable-scale model is selected, the deformation of geometry features is effectively reduced. A circular variable-scale model is appropriate to the circular and radial distribution of geometry features. Rectangular geometry features distribution is not distorted in the rectangle variable-scale model. Depending on the value of the C_r, a circular or rectangular variable-scale model is chosen for the suitable mobile map.

4 Variable-Scale Mobile Map Model Based on Neighbor Region

This paper proposes an adaptive variable-scale mobile map model. In mobile environment, the model can automatically select the variable-scale model and transform the map based on topological relationship between user and POI.

4.1 Principle of Model

Through the thorough analysis above, the key to solve these problems is that user neighbor regions are measured with topological relationship instead of geometry relationship. Topological relationship between the user and POI determine the user's focus region, moreover, focus region change map by variable-scale model. As a result, center of mobile map display is more clearly and surrounding area shows a more range.

The mobile map display area is small and operation is inconvenient. The variable-scale mobile map allows the user not only to more clearly view the region of interest (with large scale), but also to see a more extensive area without interest (with small scale). In the mobile map, neighbor relations not only reflect the topology relationship of the map features, but also reflect the distribution density of the map features. In this way, information distribution of mobile map is balanced, and the readability of the map is improved. In addition, the number of user's actions is reduced by this adaptive variable-scale way of mobile map.

Considering the limited computing power of mobile devices, the geometry features of interest are set to POI in advanced by user. Then, POIs were integrated into a layer or data sets. Delaunay triangulation was established, as well as the topological relations between POIs were obtained. In the mobile environment, the user's current location is acquired. Then, neighbor POIs and neighbor region are dynamic calculated according to topological relationship between users and POIs. Furthermore, measurement value of neighbor region shape is calculated by shape measurement model. Little deformation variable-scale model is selected according to the shape measurement value of the neighbor region. Finally, an appropriate variable-scale model is automatically selected and switched. Harrie's circular and rectangular model is used to change the map display as variable-scale models in test. In the circular model, map can be constructed by a radial displacement function where r_{new} (the new radial distance) is a function of r (the original radial distance) [3]:

$$\begin{cases} r_{\text{new}}(r) = r, & r < r_0 \\ r_{\text{new}}(r) = r + \frac{(r-r_0)^2 \cdot (s_s - s_1)}{2 \cdot s_1 \cdot (r_1 - r_0)}, & r_0 < r \le r_1 \\ r_{\text{new}}(r) = r_1 + \frac{(r_1 - r_0) \cdot (s_s - s_1)}{2 \cdot s_1} + (r - r_1) \cdot \frac{s_s}{s_1}, & r > r_1 \end{cases} \tag{4}$$

The radial direction in rectangular case is dependent on the angle φ:

$$\begin{cases} r_0(d_0, \varphi) = \frac{d_0}{\cos(\varphi)}, & |\varphi| \le \frac{\pi}{4} \\ r_0(d_0, \varphi) = \frac{d_0}{\cos(|\varphi| - \pi/2)}, & \frac{\pi}{4} < |\varphi| \le \frac{3\pi}{4} \\ r_0(d_0, \varphi) = \frac{d_0}{\cos(|\varphi| - \pi)}, & \frac{3\pi}{4} < |\varphi| \le \pi \end{cases} \tag{5}$$

There is a problem, when user around the complex shape geometry features or the distribution of features extreme irregular, shape distortion is hardly avoided.

4.2 Algorithm and Experiment

4.2.1 Algorithm

Neighborhood-based variable-scale mobile map is complicated mechanism, which includes computation of neighbor relation, selection of the neighbor regions, calculation of the measurement of neighbor region shape and visualization of variable-scale map. The algorithm (Fig. 2) is described as follows:

Step 1: Establishing the topological relationships of user-selected POI based on Delaunay triangulation.
Step 2: Inputting the user's location.
Step 3: Computing the user neighbor triangle and combining triangles into a neighbor region.
Step 4: Calculating the value of neighbor region shape measure.
Step 5: Computing the user's focus region based on value of shape measure.
Step 6: Selecting the appropriate variable-scale model, according to shape measurement value.
Step 7: Visualizing the mobile map with variable-scale model.

4.2.2 Experiment

In order to verify the feasibility and validity of our model, we adopted Visual Studio 2005 C#, ArcGIS Server Mobile SDK and Windows Mobile SDK 6.0 as tools under Windows OS. A simulated mobile experimental system was developed. In the system, the geo-data from an east part of Zhengzhou city were used. The important building was set POI-layer. Figure 3 is the panel of experiment system.

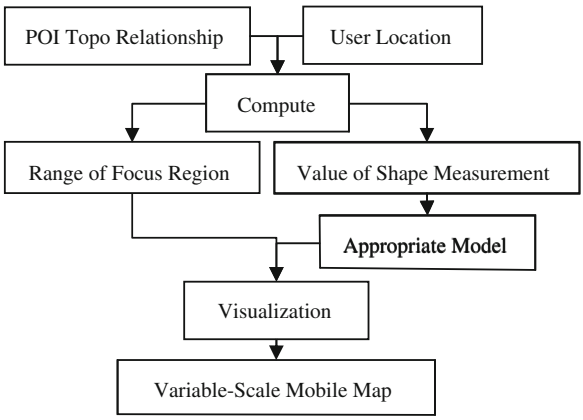

Fig. 2 Algorithm of neighborhood-based variable-scale model

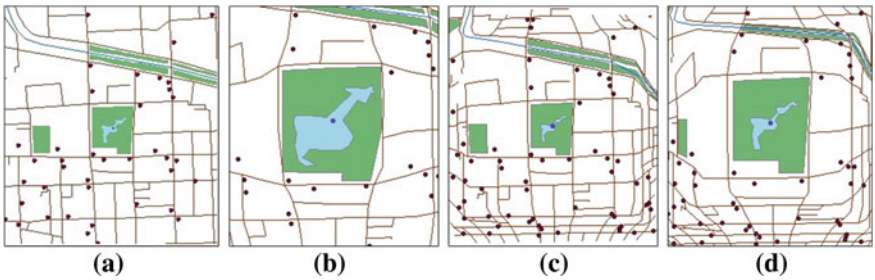

Fig. 3 Experiment system of variable-scale model. **a** Display of normal map, **b** display of traditional variable-scale map (radius 100 m), **c** display of traditional variable-scale map (radius 1000 m), and **d** display of neighbor variable-scale map

Figure 3a is the normal map display. The geometry features distribution of this part approach to circular. Figure 3b is traditional variable-scale map display and radius of focus area is 100 m, but Fig. 3c's focus area radius is 1000 m. Figure 3d is the neighbor variable-scale map display. Not only the center part is more amplified, but also the surrounding part has more geometry features than Fig. 3a–c. In this area, the shape of geometry feature has changed, but is less distortion.

5 Conclusion

This paper proposes a variable-scale mobile map model based on neighborhood, which takes topological relation instead of geometry relation to generate and present mobile map in moving environment. The adaptive variable-scale range is accessed according to neighbor relation. Two variable-scale models, circle and rectangle, are automatically switched based on the shape measurement of neighbor region. An experiment has been done and shows that not only center part is clearly detailed, but also overview information of other part was well displayed. As a result, the display area of mobile is effectively utilized, and the operation number is markedly reduced.

Acknowledgments This work described in this paper was supported under the grant numbers 40971238 and 40971213 from the Natural Science Foundation of China (NSFC).

References

1. Wang Q, Hu Y (1993) A kind of adjustable map projection with magnifying glass effect. Acta Geod Cartograph Sin 22(4):270–278
2. Zipf A, Richter KF (2002) Using focus maps to ease map reading. Kunstliche Intelligenz 4:35–37

3. Harrie L, Sarjakoski LT, Lehto L (2002) A mapping function for variable-scale maps in small-display cartography. J Geospatial Eng 4(2):111–123
4. Harrie L, Sarjakoski LT, Lehto L (2002) A variable-scale map for small-display cartography. Int Arch Photogram Rem Sens Spatial Inform Sci 34(4):237–242
5. Li Q (2009) Variable-scale representation of road network on small mobile devices. Comput Geosci 35:2185–2190
6. Yan C, Zhao R, Chen J, Zhao X (2006) Neighborhood-based adaptive geovisualization on mobile map. J Wuhan Univ (information edition) 31(12):1112–1115
7. Yan C, Zhao R, Chen J (2006) Adaptive model of mobile map. Geogr Geo-Inform Sci 22(2):42–45
8. Chen J, Yan C, Zhao R, Zhao S (2009) Voronoi neighbor-based self-adaptive clipping model for mobile maps. Acta Geod Cartograph Sin 38(2):153–155
9. Golledge G (1978) Learning about urban environment. Timing space and spacing time. Edward Arnold, London, pp 76–98
10. Haggett P, Cliff AD, Frey A (1977) Locational analysis in human geography. Edward Arnold, London, 309 pp

ODE-LM: A Hybrid Training Algorithm for Feedforward Neural Networks

Li Zhang, Hong Li and Dazheng Feng

Abstract A hybrid training algorithm named ODE-LM, in which the orthogonal differential evolution (ODE) algorithm is combined with the Levenberg-Marquardt (LM) method, is proposed to optimize feedforward neural network weights and biases. The ODE is first applied to globally optimize the network weights in a large space to some extent (the ODE will stop after a certain generation), and then LM is used to further learn until the maximum number of iterations is reached. The performance of ODE-LM has been evaluated on several benchmarks. The results demonstrate that ODE-LM is capable to overcome the slow training of traditional evolutionary neural network with lower learning error.

Keywords Feedforward neural network · Differential evolution · Orthogonal crossover · Levenberg-Marquardt method

1 Introduction

Feedforward neural networks (FNNs) have been extensively applied to various areas, such as function approximation, pattern classification, system identification, and signal processing, etc. [1–6]. Since the development of the back-propagation (BP) method, many modified and new algorithms have been proposed for training FNNs. Although BP is now a commonly used algorithm, it has some drawbacks [2, 6–10]. For example, BP converges to a local minimum of the error function,

L. Zhang (✉) · H. Li
Department of Mathematics, Xidian University, Xi'an 710071, China
e-mail: lzhang@xidian.edu.cn

H. Li
e-mail: lihong@mail.xidian.edu.cn

D. Feng
National Lab of Radar Signal Processing, Xidian University, Xi'an 710071, China

F. Sun et al. (eds.), *Foundations and Practical Applications of Cognitive Systems and Information Processing*, Advances in Intelligent Systems and Computing 215,
DOI: 10.1007/978-3-642-37835-5_17,

especially for nonlinearly separable problems [10]. Additionally, its convergence speed is too slow even though the learning can be achieved. The main reason for the slow convergence rate is due to the derivative of the activation function that may cause premature saturation, often referred as a 'flat spot' [10]. The convergence of BP algorithm is highly dependent on the initial values of weights, biases, and its parameters such as learning rate and momentum [9].

Using evolutionary algorithms or other heuristic methods is a popular tool to enhance the BP-based learning algorithms [9]. These commonly used heuristic algorithms include Differential Evolution (DE) [1], Genetic Algorithm (GA) [3, 4], Evolutionary Programming (EP) [12], Particle Swarm Optimization (PSO) [2, 9, 13], Memetic algorithms [11], etc. They are regarded as global optimization algorithms and could reduce the probability of trapping in local minima, but they still suffer from slow convergence rates and time-consuming course.

This paper presents a hybrid training algorithm synthesizing orthogonal differential evolution algorithm and Levenberg-Marquardt method for the optimization of FNNs, and is thus named ODE-LM. In order to evaluate the performance of ODE-LM, it has been tested on some function approximation and benchmark classification problems.

The rest of this paper is organized as follows: Three-layer FNN is simply described in Sects. 2 and 3 develops a hybrid training algorithm to optimize FNNs. The experimental results and some discussions are presented in Sect. 4. Finally, Sect. 5 draws the conclusion.

2 Three-Layer FNN

A typical FNN topology that takes the form of three-layer perceptron is considered. The network consists of I input nodes, J hidden nodes, and K output nodes. Assume w_{ij} is the network weight between input node i and hidden node j, and w_{jk} is the network weight between hidden node j and output node k. b_j and b_k denote the biases of the hidden node and the output node, respectively. Let h_{pj} and o_{pk} be the outputs of hidden node j and output node k, respectively, which are produced from input pattern p. The number of training patterns is P. Also, let x_{pi} be the input value in input node i for input pattern p, and let y_{pk} be the desired or target output value in output node k for input pattern p.

Input a pattern $X_p = [x_{p1}, x_{p2}, \ldots, x_{pI}]^\top$ from the training set, and compute $H_p = [h_{p1}, h_{p2}, \ldots, h_{pJ}]^\top$, $O_p = [o_{p1}, o_{p2}, \ldots, o_{pK}]^\top$ by using the following equations:

$$h_{pj} = f_1\left(\sum_{i=1}^{I} w_{ij} x_{pi} + b_j\right) \tag{1}$$

$$o_{pk} = f_2\left(\sum_{j=1}^{J} w_{jk} h_{pj} + b_k\right) \tag{2}$$

where the sigmoid function $f_1(x) = 1/(1+\exp(-x))$ and the pure line function $f_2(x) = x$ are used as the activation functions for the hidden layer and the output layer, respectively.

Use the desired target $Y_p = [y_{p1}, y_{p2}, \ldots, y_{pK}]^\top$ associated with X_p to compute the normalized mean squared error E for all input patterns. Then the error function of the network is provided as follows:

$$E = \frac{1}{PK}\sum_{p=1}^{P}\sum_{k=1}^{K}(y_{pk} - o_{pk})^2 \tag{3}$$

3 ODE-LM Training Algorithm

DE, first introduced in [14], can be classified as a floating-point encoded evolutionary algorithm for global optimization over continuous spaces. In this study, we first develop an orthogonal DE (ODE) to globally search the weights and biases of a three-layer FNN, and then refine the obtained network weights and biases via LM method.

3.1 The ODE Algorithm

3.1.1 Coding scheme

Considering three-layer FNN as an example, all the connection weights and biases are expressed as different row vectors, and then these row vectors are connected to form a big row vector, simply called network weights vector, i.e., $W = (w_1, w_2, \ldots, w_D)$, where $D = (I+1)\cdot J + (J+1)\cdot K$.

DE operates on a population of candidate solutions, which are the individuals of the population. DE maintains a population of constant size that consists of NP, real-value vectors, W_t^G, where t is the index of the population and G is the generation to which the population belongs. Thus each population contains NP network individuals, and each network individual is a D-dimensional weights vector: $W_t^G = (w_{t,1}^G, w_{t,2}^G, \ldots, w_{t,D}^G)$, $t = 1, 2, \ldots, NP$, $G = 0, 1, 2, \ldots$.

3.1.2 Fitness value

The fitness function, which measures the performance of network individual, is defined as the normalized mean squared error (MSE) of the network individual on the training set. For example, the fitness value of the network individual W_t^G $(t = 1, 2, \ldots, NP)$ is computed as follows.

$$\text{fitness}\ (W_t^G) = \frac{1}{PK}\sum_{p=1}^{P}\sum_{k=1}^{K}(y_{pk} - o_{pk})^2 \tag{4}$$

where y_{pk} is the expected output of input pattern p, and o_{pk} is the calculated network output of input pattern p related to network individual W_t^G. P is the number of training set examples, and K is the number of output nodes.

3.1.3 Initialization of population

At the initial generation $G = 0$, randomly generate NP initial network individuals $W_1^G, W_2^G, \ldots, W_{NP}^G$, where $W_t^G = (w_{t,1}^G, w_{t,2}^G, \ldots, w_{t,D}^G)$, $w_{t,i}^G \in [-1, 1]$, $t = 1, 2, \ldots, NP$, $i = 1, 2, \ldots, D$.

3.1.4 Mutation

For each parent vector W_t^G, $t = 1, 2, \ldots, NP$, a mutant vector V_t^G is generated using DE/best/1 bin:

$$V_t^G = W_{\text{best}}^G + F \cdot (W_{r_1}^G - W_{r_2}^G) \tag{5}$$

where random indexes $r_1, r_2 \in \{1, 2, \ldots, NP\}$, $r_1 \neq r_2$, and they are different from the running index t. W_{best}^G denotes the best network individual in the Gth generation. Scaling factor $F \in (0, 1)$ is a real-value control parameter.

3.1.5 Crossover

In classic DE algorithm, the crossover offspring is generated by randomly selecting the components of parent individual W_t^G or mutation individual V_t^G. The crossover operator in DE algorithm, called DE crossover is described as follows.

The crossover offspring $U_t^G = (u_{t,1}^G, u_{t,2}^G, \ldots, u_{t,D}^G)$ is generated by randomly mixing the parent vector $W_t^G = (w_{t,1}^G, w_{t,2}^G, \ldots, w_{t,D}^G)$ and mutated vector $V_t^G = (v_{t,1}^G, v_{t,2}^G, \ldots, v_{t,D}^G)$:

$$u_{t,i}^{G} = \begin{cases} v_{t,i}^{G}, & \text{if } R_i \leq CR \text{ or } i = rn(t) \\ w_{t,i}^{G}, & \text{otherwise} \end{cases} \tag{6}$$

where $i = 1, 2, \ldots, D$, $R_i \in (0, 1)$ is a random number, $rn(t) \in \{1, 2, \ldots, D\}$ is the randomly selected index chosen once for each t, and CR is a real-valued crossover rate constant in the range $(0, 1)$.

In order to improve the effect of DE crossover, the orthogonal crossover based on orthogonal experimental design is combined with the DE crossover. The orthogonal crossover is considered as a determinate combination method because the offspring generated by the orthogonal crossover is not worse than its parent and mutant individuals.

The used orthogonal crossover is provided as follows.

First, a suitable orthogonal array corresponding to dimension of individual needs to be selected. A two-level orthogonal array similar to one in [15] is used in this paper. A two-level standard orthogonal array for $N - 1$ factors with 2 levels and N combinations is often denoted by $L_N(2^{N-1})$, which is an $N \times (N - 1)$ matrix or array. According to the individual dimension D, a suitable two-level orthogonal array $L_N(2^{N-1})$ is selected to execute the matrix experiments. If $D = N - 1$, the standard orthogonal array $L_N(2^{N-1})$ is directly adopted. If $D < N - 1$, the first D columns of the standard orthogonal array $L_N(2^{N-1})$ or the available orthogonal array $L_N(2^D)$ from source is only adopted. Several orthogonal arrays are available from http://www2.research.att.com/~njas/oadir/.

Secondly, N combinations taken as trial individuals are generated by executing the matrix experiments according to the selected two-level orthogonal array $L_N(2^D)$. The D components of the parent individual W_I^G and mutation individual V_I^G are considered as D factors, where the index $I \in [1, NP]$ is randomly selected integer. For $j = 1, 2, \ldots, D$, the jth component of W_I^G is regarded as level 1 of the jth factor, and the jth component of V_I^G is regarded as level 2 of the jth factor. Levels 1 and 2 of the jth factor in orthogonal array $L_N(2^D)$ are replaced with the jth components of W_I^G and V_I^G, respectively. A new $N \times D$ matrix is then obtained, in which every row is a combination of factor level representing a trial individual. Thus N trial individuals are generated.

Finally, the summarized data is analyzed using the factor analysis after evaluation of each individual in the N combinations. Factor analysis can evaluate the effects of individual factors on the fitness value, rank the most effective factors, and determine the better level for each factor. In this paper, the factor analysis in [16] is adopted in this algorithm. Let $fitness_i$ denote a fitness value of the combination corresponding to the experiment i, $i = 1, 2, \ldots, N$, where N is the total number of experiments. Define the main effect of factor j with level l as E_{jl} where $j = 1, 2, \ldots, D$ and $l = 1, 2$:

$$E_{jl} = \sum_{i=1}^{N} \text{fitness}_i \cdot \chi_i \tag{7}$$

where $\chi_i = 1$ if the level of factor j of experiment i is l; otherwise, $\chi_i = 0$. Considering the case that the problem is to be minimized (smaller-the-better), the level 1 of factor j makes a better contribution to the fitness value than level 2 of factor j does when $E_{j1} < E_{j2}$, so the better level is level 1 for factor j. If $E_{j1} > E_{j2}$, level 2 is the better one. If $E_{j1} = E_{j2}$, levels 1 and 2 have the same contribution. After the better level for each factor is selected, a potentially best individual can also be obtained. This best individual has the lowest fitness value among those of parents and N combinations of factor levels, where N is the total number of experiments. The purpose for the use of the orthogonal crossover is to produce a potentially best individual from randomly selected parent and mutant individuals.

The proposed hybrid crossover scheme formed by DE crossover and the orthogonal crossover is provided in detail as follows: `Algorithm 1`:

Step 1. Randomly choose an integer I in the range $[1, NP]$.

Step 2. For $t = 1, 2, \ldots, NP$, if $t = I$, the parent individual W_I^G and mutant individual V_I^G are selected to execute the orthogonal crossover. A potentially best combination U_I^G with the better factor level is finally obtained.

Step 3. For the other indices $t \neq I$, execute DE crossover for the other parent individuals W_t^G and mutant individuals V_t^G by using Eq. (6), and generate $(NP - 1)$ individuals U_t^G.

Step 4. A total of NP individuals U_t^G are obtained by combining orthogonal crossover with DE crossover.

3.1.6 Selection

To decide the next generation, the crossover vector U_t^G and the parent vector W_t^G are compared. The individual of the next generation W_t^{G+1} is decided according to the following rule for the minimization:

$$W_t^{G+1} = \begin{cases} U_t^G, & \text{fitness}(U_t^G) < \text{fitness}(W_t^G) \\ W_t^G, & \text{otherwise} \end{cases} \tag{8}$$

The above-mentioned operators compose a modified DE algorithm, called the ODE. When the generation G achieves a given constant, ODE stops and output the best individual as network weights vector. In this paper, the given constant in the stopping condition is equal to half of the maximum number of iterations $G_{\max}$ of ODE-LM algorithm.

3.2 LM Optimization Method

In order to improve the network efficiency and reduce the network error, we resort to Levenberg-Marquadt (LM) optimization method for local search.

When the generation G achieves a given constant $G_{\max}/2$, ODE stops, and start to call LM method from MATLAB Toolbox of Neural Networks with the best weights vector outputted by ODE as the initial weights vector. By using LM method, repeatedly optimize and refine network weights until the maximum number of iterations $G_{\max}$ arrives.

3.3 Steps of ODE-LM Training Algorithm

`Algorithm 2`:

Step 0. Parameter setup: population size NP; standard two-level orthogonal array used in the orthogonal crossover $L_N(2^{N-1})$; scaling factor F; crossover rate CR; maximum number of iterations $G_{\max}$.

Step 1. Set $G = 0$. Randomly generate NP initial network individuals $W_1^G, W_2^G, \ldots, W_{NP}^G$, where $W_t^G = (w_{t,1}^G, w_{t,2}^G, \ldots, w_{t,D}^G)$, $w_{t,i}^G \in [-1, 1]$, $t = 1, 2, \ldots, NP$, $i = 1, 2, \ldots, D$. Calculate their fitness values, and determine the best individual.

Step 2. Generate NP mutant individuals V_1^G, V_2^G, ..., V_{NP}^G by using DE mutation operator.

Step 3. Generate NP crossover individuals U_1^G, U_2^G, ..., U_{NP}^G by `Algorithm 1`, and calculate their fitness values.

Step 4. Decide NP new individuals W_1^{G+1}, W_2^{G+1}, ..., W_{NP}^{G+1} for the next generation by using DE selection operator.

Step 5. When $G < G_{\max}/2$, let $G = G + 1$, and return to step 2; Otherwise, output the best weights vector.

Step 6. Set some parameters related to LM training algorithm, and start to perform LM training algorithm with the best weights vector outputted by Step 5 as the initial weights vector.

Step 7. By using LM training algorithm, repeatedly optimize and refine network weights until the maximum number of iteration $G_{\max}$ arrives. Finally output the results.

4 The Experimental Results and Discussions

To evaluate the performance of the proposed ODE-LM training algorithm, several experiments were conducted on the training problems from two commonly used problem domains.

- function approximation

  (1) $y = f_1(x) = \frac{\sin(3x)}{3x}$, $x \in [0.1, 9.9]$;
  (2) $y = f_2(x) = [1 - 5\cos(6x)^2]\exp(-\frac{x^2}{2})$, $x \in [-3, 3]$;
  (3) $y = f_3(x) = \sin(5x) + \cos(3x)$, $x \in [-2\pi, 2\pi]$;

- data classification

All data sets come from the UCI machine learning benchmark repository [17].

(1) The breast cancer data set is a two-class problem with nine features. The total number of examples is 699. The first 349 examples were used for the training set, and the last 175 examples for the testing set.
(2) The diabetes data set is a two-class problem with eight features. The total number of examples is 768. The first 384 examples were used for the training set, and the last 192 examples for the testing set.
(3) The heart data set is a two-class problem with 13 features. The total number of examples is 270. The first 134 examples were used for the training set, and the last 68 examples for the testing set.

The training set is used to train the *NP* network individuals, and then select the best one (with the lowest MSE) from them, while the testing set is used to test the generalization performance of the best network.

4.1 Experimental Setup

There are some parameters in ODE-LM which need to be specified by the user. These parameters were set to the same for all these problems: population size $NP = 50$; scaling factor F and crossover rate CR are random parameters, i.e., $F = 0.5 + \alpha \cdot 0.1$, $CR = 0.4 + \beta \cdot 0.2$, where α and β are random numbers in the range (0,1) related to the generation. In the training, three-layer FNNs are adopted with a sigmoid transfer function between the input nodes and hidden nodes and a pure linear transfer function between the hidden nodes and output nodes. Network structure, vector dimension D, orthogonal array $L_N(2^{N-1})$, and maximum number of iterations $G_{\max}$ for all problems are provided in Table 1.

In the experiments, 50, 30, 60 points are sampled in the given intervals for the functions $f_1(x)$, $f_2(x)$ and $f_3(x)$, respectively; the input attributes of all the data sets are rescaled between -1.0 and 1.0 by a linear function. The outputs are encoded

Table 1 Network structure and other parameters used in the experiments

Problem	Network structure	D	$L_N(2^{N-1})$	$G_{\max}$
$f_1(x)$	1-8-1	25	$L_{32}(2^{31})$	1500
$f_2(x)$	1-16-1	49	$L_{64}(2^{63})$	2000
$f_3(x)$	1-18-1	55	$L_{64}(2^{63})$	3000
Breast cancer	9-3-2	38	$L_{64}(2^{63})$	400
Diabetes	8-3-2	35	$L_{64}(2^{63})$	400
Heart	13-3-2	50	$L_{64}(2^{63})$	400

by the $1-of-c$ representation for c classes. The winner-takes-all method is used in the proposed approach, i.e., the output with the highest activation designates the class.

4.2 Experimental Results and Comparison

ODE-LM is compared with DE and ODE to illustrate the performance of ODE-LM. ODE-LM is a two-stage algorithm, and ODE is the proposed DE algorithm, in which the orthogonal crossover is combined with DE crossover. These algorithms utilize the same parameters and computational cost. ODE-LM, ODE, and DE are performed for all problems over 30 independent runs, and the training results are provided in Table 2, including the mean MSE, standard deviation (SD) of MSE, minimum (Min) MSE, maximum (Max) MSE on the training examples. MSE is the normalized mean squared error.

From Table 2, it can be seen that ODE-LM has the smallest MSE for all problems among three algorithms, next comes ODE, and the third rank is DE.

Figure 1 shows the curves of the original sample points and the best network output (with minimum MSE) after training with ODE-LM algorithm for three functions. It is found that the best network output with ODE-LM training algorithm are the same as the original sample points.

Table 3 presents the error rate results of ODE-LM, ODE, and DE for training and testing sets over 30 independent runs on 3 data sets, respectively (the Mean, SD, Max, and Min indicate the mean error rate, standard deviation, maximum error rate, and minimum error rate, respectively). The error rate in the table refers to the percentage of wrong classification produced by the trained FNNs on the training or testing set. Table 3 compares the training and testing results of ODE-LM with those of DE and ODE for the three data sets, respectively (with same computational cost). From Table 3, we can find that the training error rates of ODE-LM are lower than those of DE and ODE for three training data sets. But it is noted that the generalization performance of ODE-LM is not better than ODE, because the mean testing error rates of ODE-LM are larger than those of ODE for three testing data sets.

Table 4 compares the mean testing results of ODE-LM, ODE, and DE with those of IPSONet [2] and EPNet [12] for the three data sets. ODE-LM, ODE, DE,

Table 2 The training MSE are provided by DE, ODE, ODE-LM for all the problems over 30 independent runs

Problem	Method	Mean MSE	SD	Min MSE	Max MSE
	DE	4.32e−3	6.13e−4	3.34e−3	5.66e−3
$f_1(x)$	ODE	2.56e−3	5.41e−4	1.52e−3	3.79e−3
	ODE-LM	1.59e−4	1.63e−4	1.68e−7	5.63e−4
	DE	9.00e−1	3.97e−3	8.84e−1	9.08e−1
$f_2(x)$	ODE	7.93e−1	1.13e−1	5.74e−1	9.13e−1
	ODE-LM	7.54e−2	1.53e−1	1.57e−23	5.02e−1
	DE	9.71e−1	2.82e−2	8.62e−1	9.87e−1
$f_3(x)$	ODE	8.24e−1	7.75e−2	6.62e−1	9.82e−1
	ODE-LM	1.56e−1	1.45e−1	9.66e−7	7.20e−1
	DE	2.78e−2	3.68e−3	2.07e−2	3.31e−2
Breast cancer	ODE	2.72e−2	2.35e−3	1.95e−2	3.17e−2
	ODE-LM	1.91e−2	4.60e−3	5.60e−3	2.51e−2
	DE	1.50e−1	4.43e−3	1.46e−1	1.62e−1
Diabetes	ODE	1.57e−1	3.62e−3	1.51e−1	1.64e−1
	ODE-LM	1.45e−1	7.90e−3	1.25e−1	1.57e−1
	DE	6.44e−2	8.30e−3	4.46e−2	8.23e−2
Heart	ODE	7.29e−2	7.54e−3	5.00e−2	8.61e−2
	ODE-LM	5.28e−2	1.16e−2	2.93e−2	8.01e−2

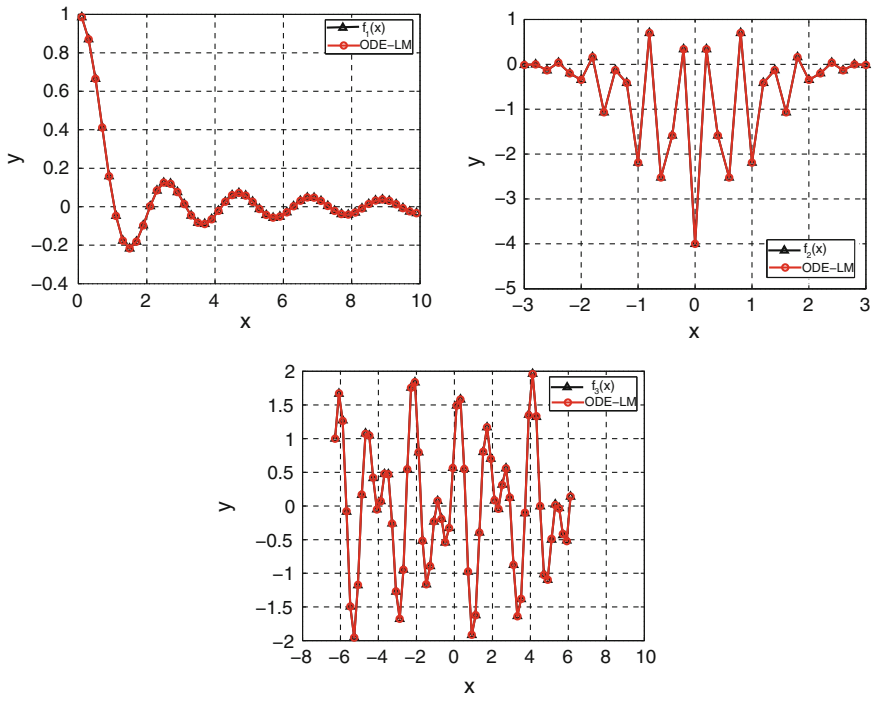

Fig. 1 Results of training experiments for three functions

Table 3 The training and testing error rates are provided by DE, ODE, and ODE-LM for three data sets over 30 independent runs

Data set	Error rate	Training set			Testing set		
		DE	ODE	ODE-LM	DE	ODE	ODE-LM
Breast cancer	Mean	0.0324	0.0311	0.0258	0.0118	0.0112	0.0162
	SD	0.0054	0.0030	0.0069	0.0091	0.0057	0.0089
	Min	0.0201	0.0201	0.0057	0	0.0057	0.0057
	Max	0.0430	0.0344	0.0315	0.0400	0.0286	0.0457
Diabetes	Mean	0.2132	0.2216	0.2065	0.2260	0.2128	0.2219
	SD	0.0107	0.0080	0.0126	0.0116	0.0135	0.0225
	Min	0.1953	0.2083	0.1745	0.1875	0.1823	0.1719
	Max	0.2500	0.2396	0.2292	0.2448	0.2344	0.2760
Heart	Mean	0.0689	0.0853	0.0634	0.1765	0.1623	0.1716
	SD	0.0190	0.0173	0.0164	0.0370	0.0290	0.0245
	Min	0.0448	0.0522	0.0299	0.1176	0.1176	0.1324
	Max	0.1119	0.1418	0.0970	0.2500	0.2353	0.2206

Table 4 Comparison of ODE-LM, ODE, DE, IPSONet, and EPNet in terms of the average testing error rate for three data sets

Data set	ODE-LM	ODE	DE	IPSONet	EPNet
Breast cancer	0.0162	0.0112	0.0118	0.0127	0.0137
Diabetes	0.2219	0.2128	0.2260	0.2102	0.2238
Heart	0.1716	0.1623	0.1765	0.1814	0.1677

IPSONet, and EPNet used the same training set, and testing set for the three problems. The results of ODE-LM, ODE, DE, IPSONet, and EPNet are the average testing error rates over 30 independent runs on the three data sets. It should be noted that IPSONet and EPNet spends much additional computation cost to evolve FNNs than ODE-LM, ODE, and DE. Moreover, the number of hidden nodes of IPSONet is larger than those of ODE-LM, ODE, and DE. In comparison with IPSONet and EPNet, ODE has a better generalization performance, while ODE-LM has a slightly poorer generalization performance, but spends less computation cost.

5 Conclusion

In this paper, the ODE is developed, in which the orthogonal crossover is employed to improve the original DE, then a new hybrid training algorithm, named ODE-LM, is proposed for optimizing FNNs. In the proposed training algorithm, first ODE can globally search some weight vectors in the large space to a certain extent, and obtain a best weight vector. Then LM algorithm further explores the accurate weight vector with the best weight vector obtained by ODE

as its initial network weight vector. This will improve the convergence rate and reduce the training error. The performance of ODE-LM has been evaluated on some benchmark problems. The results are produced by ODE-LM in comparison with other algorithms. The experimental results indicate that ODE-LM performs well in function approximate, while it has a general performance in data classification.

Acknowledgments This work was supported by the Fundamental Research Funds for the Central Universities (K50511700004).

References

1. Ilonen J, Kamarainen JK, Lampinen J (2003) Differential evolution training algorithm for feed-forward neural networks. Neural Process Lett 17:93–105
2. Yu J, Xi L, Wang S (2007) An improved particle swarm optimization for evolving feedforward artificial neural networks. Neural Process Lett 26:217–231
3. Su CL, Yang SM, Huang WL (2011) A two-stage algorithm integrating genetic algorithm and modified newton method for neural network training in engineering systems. Expert Syst Appl 38:12189–12194
4. Ding S, Su C, Yu J (2011) An optimizing BP neural network algorithm based on genetic algorithm. Artif Intell Rev 36:153–162
5. Jing X (2012) Robust adaptive learning of feedforward neural networks via LMI optimizations. Neural Netw 31:33–45
6. Szczuka M, Slezak D (2011) Feedforward neural networks for compound signals. Theoret Comput Sci 412:5960–5973
7. Nasr MB, Chtourou M (2006) A hybrid training algorithm for feedforward neural networks. Neural Process Lett 24:107–117
8. Ahmed SU, Shahjahan M, Murase K (2011) Injecting chaos in feedforward neural networks. Neural Process Lett 34:87–100
9. Mirjalili S, Mohd Hashim SZ, Moradian Sardroudi H (2012) Training feedforword neural networks using hybrid particle swarm optimization and gravitational search algorithm. Appl Math Comput 218:11125–11137
10. Ng SC, Cheung CC, Leung SH (2004) Magnified gradient function with deterministic weight modification in adaptive learning. IEEE Trans Neural Netw 15:1411–1423
11. Chandra R, Frean M, Zhang M (2012) Crossover-based local search in cooperative co-evolutionary feedforward neural networks. Appl Soft Comput 12:2924–2932
12. Yao X, Liu Y (1997) A new evolutionary system for evolving artificial neural networks. IEEE Trans Neural Netw 8:694–713
13. Yu J, Wang S, Xi L (2008) Evolving artificial neural networks using an improved PSO and DPSO. Neurocomputing 71:1054–1060
14. Storn R, Price K (1997) Differential evolution-a simple and efficient heuristic for global optimization over continuous spaces. J Global Optimiz 11:341–359
15. Tsai JT, Liu TK, Chou JH (2004) Hybrid Taguchi-genetic algorithm for global numerical optimization. IEEE Trans Evol Comput 8:365–377
16. Ho SY, Shu LS, Chen JH (2004) Intelligent evolutionary algorithms for large parameter optimization problems. IEEE Trans Evol Comput 8:522–540
17. Asuncion A, Newman DJ (2007) UCI machine learning repository. School of information and Computer Science, University of California, Irvine. http://www.ics.uci.edu/

Weather Condition Recognition Based on Feature Extraction and K-NN

Hongjun Song, Yangzhou Chen and Yuanyuan Gao

Abstract Most of vision based transport parameter detection algorithms are designed to be executed in good-natured weather conditions. However, limited visibility in rain or fog strongly influences detection results. To improve machine vision in adverse weather situations, a reliable weather conditions detection system is necessary as a ground base. In this article, a novel algorithm for weather condition automatic recognition is presented. This proposed system is able to distinguish between multiple weather situations based on the classification of single monocular color images without any additional assumptions or prior knowledge. Homogenous area is extracted form top to bottom in scene image. Inflection point information which implies visibility distance will be taken as a character feature for current weather recognition. Another four features: power spectral slope, edge gradient energy, contrast, saturation, and image noisy which descript image definition are extracted also. Our proposed image descriptor clearly outperforms existing descriptors for the task. Experimental results on real traffic images are characterized by high accuracy, efficiency, and versatility with respect to driver assistance systems.

Keywords Weather condition recognition · Image inflection point · Power spectral slope · Edge gradient energy · Noise estimation

H. Song · Y. Chen
Institute of Autonomous Technology and Intelligent Control, Beijing University of Technology, Beijing 100124, China
e-mail: songhongjun2001@yahoo.cn

Y. Chen
e-mail: yzchen@bjut.edu.cn

Y. Gao (✉)
College of Information and Engineering, Zhejiang A&F University, Hangzhou 311300, China
e-mail: gyyshj@yahoo.cn

F. Sun et al. (eds.), *Foundations and Practical Applications of Cognitive Systems and Information Processing*, Advances in Intelligent Systems and Computing 215,
DOI: 10.1007/978-3-642-37835-5_18,

1 Introduction

Driver assistance systems based on vision (DASV) are currently designed to perform under good-natured weather conditions. However, limited visibility which strongly affects the accuracy or even the general function of vision systems often occurs in daily life [1] (e.g., heavy rain or fog). Actual weather condition is valuable information for assistance systems because specialized approaches for each class can be invoked to improve cognition based on the results of weather classification. This will form a key factor to expand the application of DASV from special environmental conditions to an overall approach. Little work has been done on weather related issues for in-vehicle camera systems so far. Nayar [2] studied visual effects of rain and discussed a photometric rain drop model that describes refraction and reflection of light by rain drop. Additionally, they determined the effect of camera parameters on image disturbance and developed an approach of detecting and removing rain from videos. Narasimhan [3] analyzed images taken under poor static weather conditions and used the Koschmieder model to estimate scattering coefficients of the atmosphere, and then restore the contrast of weather degraded images. Kurihata [4] used a machine learning approach with raindrop templates called eigendrops to detect rain drops on windshields. However, this method lacks a holistic approach to deal with all kinds of adverse weather conditions.

Whereas little work has been done on DASV for bad weather situations, scientific research in image classification or categorization is very broad. Generally, the goal is to decide whether an image belongs to a certain category or not. Depending on the application, categories can include various natural scenes [5], but often images are tested for the presence of a certain object category [6]. All modern approaches are based on the extraction of local image features, as global features turned out to be not robust enough to deal with variations in view, lighting, and occlusion and object variations. Different kinds of local features have been proposed with histogram-based features like SIFT [7], HOG [8], and shape context [9] being among the most discriminator. However, these features perform weakly for the intended task. In this article, a novel algorithm for automatic weather condition recognition in traffic scene is presented. This proposed system is able to distinguish between multiple weather situations based on the classification of single monocular color images without any additional assumptions or prior knowledge. Homogenous area is extracted form top to bottom in traffic image. The inflection point information will be taken as a character for current weather recognition. Another four features: spectral slope, edge gradient energy, contrast, saturation, and image noisy, respectively, which descript image clarity are extracted also. This proposed image descriptor clearly outperforms existing descriptors for the task. Figure 1 shows this proposed algorithm flow.

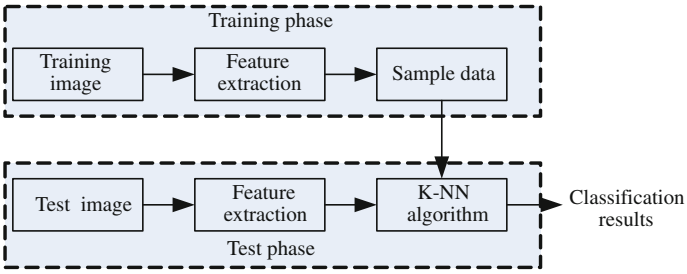

Fig. 1 Algorithm flowchart

2 Image Inflection Character Based on Homogenous Area Searching

Based on light transmission theory in suspended particulate weather conditions (fog, haze, cloudy), pixels from the top to the bottom of traffic scene will change in the form of hyperbola and the inflection point indicates visibility distance, while sunny and snowy weather do not conform this law. In this section, we will extract inflection point's longitudinal coordinate as feature for weather recognition.

Light traveling through a scattering medium is attenuated along its original course and is distributed to other directions. This process is commonly modeled mathematically by assuming that along short distances there is a linear relation between the fractions of light deflected and the distance traveled.

Koschmieder proposed the light transmission law in particulate weather conditions in 1924. Koschmieder presents a simple relationship between the distance d of an object with intrinsic luminance J_x and its apparent luminance $I_{(x)}$ as follows:

$$I(x) = t(x)J(x) + (1 - t(x))A \tag{1}$$

where A denotes the luminance of the sky and k is the extinction coefficient of the atmosphere, $t(x)$ describes the scene transmission. Direct attenuation describes the scene radiance and its decay in the medium, while air-light results from previously scattered light and leads to the shift of the scene color.

Scene transmission and scene distance have the following relationship:

$$t(x) = e^{-kd(x)} \tag{2}$$

From the top to the bottom (as the scene distance increase), image intensity will change in the form of hyperbola if sky included, because intensity of road and sky is union (Formula 2).

2.1 Characters for Recognition

In order to search homogenous area five major characters calculated based on GLCM are taken. These five major characters are Angular Second Moment (ASM), Entropy (ENT), Contrast (CON), Variance (VAR), and Inverse Difference Moment (IDM). Detail calculation formulas are as following:

$$\mathrm{ASM} = \sum_{i=0}^{L-1} \sum_{j=0}^{L-1} P^2(i,\ j) \tag{3}$$

$$\mathrm{CON} = \sum_{n=0}^{L-1} n^2 \sum_{i=0}^{L-1} \sum_{j=0}^{L-1} P(i,\ j) \tag{4}$$

where $|i - j| = n$

$$\mathrm{ENT} = \sum_{i=0}^{L-1} \sum_{j=0}^{L-1} p(i,j) \lg\ p(i,\ j) \tag{5}$$

$$\mathrm{VAR} = \sum_{i=0}^{L-1} i \sum_{j=0}^{L-1} (i - m)^2 P(i,\ j) \tag{6}$$

where m stand for mean value of GLCM

$$\mathrm{IDM} = \sum_{i=0}^{L-1} \sum_{j=0}^{L-1} \frac{P(i,\ j)}{1 + (i - j)^2} \tag{7}$$

where $p(i,j)$ stands for pixel value in GLCM of difference image, parameters W and H stand for the width and height of difference image.

2.2 Area for Judging Searching Method Based on Texture Characters

In this section, we will discuss how to extract the identifying area in current traffic frame. Although sky and road's color are different, texture characters are similar between them. So we could use road model to replace sky model. Road surface, sky, and the rest of the traffic scene have difference texture structure. Main steps of searching method are listed as followings:

(1) *Start algorithm from first line of background image*: Initial the searching rectangle window $T_{1,\,1}$ by 8×6, calculate texture value in $T_{1,\,1}$ and save it. Slide this rectangle from left to the right in traffic background image. Every time we only move one pixel. The rectangular regions obtained are defined as

$T_{1,i}$. All the texture value of these rectangles is calculated and saved. Corresponding to each rectangle, these texture values compose character vector sequences $C_{1,i} = (\mathrm{ASM}_i, \mathrm{CON}_i, \mathrm{ENT}_i, \mathrm{VAR}_i, \mathrm{IDM}_i) \quad i = 1, 2, \ldots, 320$. The character vector for prepared model in Fig. 4 is assumed as C_0. Before comparison, a constancy threshold T is set. The area with minimal value is selected as candidate region:

$$\varepsilon_{1,i} = |C_{1,i} - C_0| \quad i = 1, 2, \ldots 320 \tag{8}$$

where $|C_{1,i} - C_0|$ stand for sum of the absolute value of corresponding elements of two vectors $C_{1,i}$ and C_0. Then the smallest (we may assume it is $\varepsilon_{1,j}$) will be compared with T (threshold). The rectangle $T_{1,j}$ will be selected into our searching sequence only if $\varepsilon_{1,j} < T$, and then the algorithm turns to step (2). Otherwise it will go to step (3).

(2) *Move window along the longitudinal axis of the image from the top to the bottom*: Like step (1), we may assume the current line is m, the area we got will be marked as $T_{m,j}$. The search window will move down from the current line until all the pixels from the top to the bottom of scene are finished.
(3) *Reduce the height of searching window*: The height of searching window will be cut to be half if $\varepsilon_{i,j} < T$. Then turn to step (2).

The average value for each line from top to bottom will be calculated after the target area is selected. For each line:

$$P_i^A = \frac{\sum_{k=1}^{8} P_{i,k}}{8} \quad i = 1, 2, \ldots, 240 \tag{9}$$

For each background image, a sequence will be got: $\left(P_1^A, P_2^A, \ldots, P_n^A\right)$.

2.3 Extracted and Curve Fitting Results

This area searching algorithm has been tested on three classic weather conditions for two different traffic scenes that are captured in Beijing highway. One scene includes three different weather conditions (Scene I). Experiment shows that changing mode in fog and rain is appropriate hyperbola, while in sunny and snowy, it does not obey this rule.

Figure 2 shows the traffic scene images and their corresponding area extraction results. It is clear that in fog weather condition, pixel value from the top to the bottom change as the form of hyperbola (Fig. 3). Other weather conditions are not in line with this fact.

In fact, most homogenous weather conditions (cloudy, rainy, fog, haze), the area extraction and curve fitting results will be in line with hyperbola. However,

Fig. 2 Traffic scene and the corresponding extracted area which are enlarged. **a** original image and extraction result for sunny in scene I, **b** original image and extraction result for snowy in scene I, **c** original image and extraction result for fog in scene I

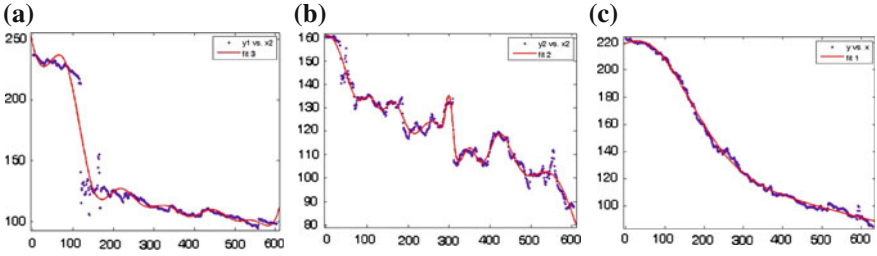

Fig. 3 Function fitting results corresponding to Fig. 2. **a** sunny, **b** snowy, **c** fog

visibility distance in these weather conditions is different. Inflection of hyperbola curve indicates visibility distance, the calculation formal is flowing. We could use the infection extraction results as feather to distinguish current weather condition. While in sunny and snowy, because there is no inflection point, this feather will be set to be zero.

$$\mathrm{VIS} = \frac{3\lambda}{2(v_i - v_h)} \tag{10}$$

where VIS stands for traffic meteorological visibility distance, λ stand for camera parameter, v_i stand for image inflection point, and v_h stand for horizon line.

3 Other Characters for Weather Condition Recognition

3.1 Blur Feature Based on Power Spectrum Slope

Some high frequency components of a blurred region are lost though low-pass filtering. So the amplitude spectrum slope of a blurred region tends to be steeper than that of an unblurred region.

The power spectrum [10] of an image I with size $N \times N$ is calculated by taking the squared magnitude after Discrete Fourier Transform (DFT)

$$S(u, v) = \frac{1}{N^2} |I(u,\ v)|^2 \tag{11}$$

where $I(u,\ v)$ denotes the Fourier transformed image. We represent the two dimensional frequency in polar coordinates, set $u = f \cos\theta,\ v = f \sin\theta$ and construct $S(f,\ \theta)$. By summing the power spectra Sover all directions $\theta,\ S(f)$, using polar coordinates, can be approximated by

$$S(f) = \sum_{\theta} S(f,\ \theta) \approx {}^{A}/_{f^{-\alpha}} \tag{12}$$

where A is an amplitude scaling factor for each orientation and α is the frequency exponent, called slope of power spectrum. Field [11] demonstrated that using image wise computation, the power spectra of most natural images make $\alpha \approx 2$. A blurred image usually has a large value, while an unblurred image corresponds to a small α. However, a natural image may contain objects with different boundary sharpness. A simple threshold will be set by the value of α for blur estimation. Applying formula (12), we could get [12]

$$\alpha = \ln\ A - \frac{\ln(S(f))}{\ln(f)} \tag{13}$$

3.2 Noise Feature

Noise can be estimated within an image (intra-image estimation) or between two or more successive images (inter-image estimation). Inter-image estimation requires

more memory and is, in general, more computationally demanding. Intra-image noise estimation methods can be classified as smoothing based or block based. In smoothing-based methods, the image is first smoothed, for example, using an averaging filter, and then the difference between the noisy and enhanced image is assumed to be the noise; noise is then estimated at each pixel where the gradient is smaller than a given threshold. In block-based methods, the variance over a set of blocks of the image is calculated and the average of the smallest variances is taken as an estimate. In rain and snow and other dynamic weather conditions, point noise and motion noise could be generated because of attenuation caused by all sorts of atmospheric particles. Noise character standing for different particles could be extracted by noise estimation. In this paper, we use fast noise estimation method [12]. Laplasse template N is defined first to detect noise in image.

$$N = \begin{bmatrix} 1 & -2 & 1 \\ -2 & 4 & -2 \\ 1 & -2 & 1 \end{bmatrix} \tag{14}$$

Image is proposed by the use of template N, standard deviation for each point in the image is calculated, then, mean variance for whole image will be obtained:

$$\delta = \frac{1}{6(W-2) \times (H-2)} \sum_{\text{image } I} |I(x, y) * N| \tag{15}$$

where W stands for image width, H stands for image height, $I(x, y)$ stands for intensity at the point of (x, y).

3.3 Edge Energy Evaluation Operator for Image Definition

In edge detection, sobel operator commonly used as a template, there are two sobel operators: one is horizontal operator S_{hor} and the other is vertical operator S_{ver}.

$$S_{\text{hor}} = \begin{bmatrix} -1 & 0 & 1 \\ -2 & 0 & 2 \\ -1 & 0 & 1 \end{bmatrix}, \quad S_{\text{ver}} = \begin{bmatrix} -1 & -2 & -1 \\ 0 & 0 & 0 \\ 1 & 2 & 1 \end{bmatrix} \tag{16}$$

Progressing different images with different definition, we could get different images with different edge energy. Figure 4 compares different edge detection results for sunny and fog, respectively.

Sobel operator maintains simple and fast processing speed. Edge detected by sobel operator is smooth, continuous. Its disadvantage is coarse. Edge energy evaluation function can detect edge energy value and it does not require strict edge result. In our algorithm, edge threshold of starting position of image will be first estimated and this threshold value will be used to detect the other image sequences. Based on sobel edge detection principle, edge energy evaluation function could be defined as:

(a) **(b)** **(c)** **(d)**

Fig. 4 Sobel operator detection results. **a** sunny, **b** fog, **c** sobel result for sunny, **d** sobel result for fog

(1) Filter image by operators S_{hor} and S_{ver}.

$$H = G(m,\ n) * S_{\text{hor}}, \quad V = G(m,\ n) * S_{\text{ver}} \tag{17}$$

where $G(m,\ n)$ stand for the image detected and $*$ stand for convolution operation.

(2) Set $|I(i,\ j)| = \sqrt{H^2(i,\ j) + V^2(i,\ j)}$, edge detection threshold parameter $T = 2\delta(I)$, where $\delta(I)$ is the standard deviation of matrix I.
(3) In the position $(i,\ j)$, select the larger one between $H(i,\ j)$ and $V(i,\ j)$, if there is a local maximum in the direction and the matrix element $I(i,\ j) > T$, then this edge information will be restored, otherwise $I(i,\ j) = 0$.
(4) Evaluation function is set to be $E_{\text{edge}} = \sum_{i=1}^{m}\sum_{j=1}^{n} |I(i,\ j)|^2$, namely the edge energy is taken as definition evaluation function.

3.4 Image Contrast

Traveling light in atmosphere of various media is affected by attenuation and refraction effect. Contrast will be different even if images are captured in the same scene behind different weather conditions. Through the contrast features, we could classify current weather. EliPeli [13] propose a definition of local band-limited contrast in images that assigns a contrast value to every point in the image as a function of the spatial frequency band. For each frequency band, the contrast is defined as the ratio of the band pass-filtered image at that frequency to the low pass image filtered to an octave below the same frequency (local luminance mean). In this paper, we use Root Mean Square to calculate contrast:

$$C = \left[\frac{\sum I^2(x,\ y) - \frac{\left(\sum I(x,\ y)\right)^2}{N}}{N}\right]^{\frac{1}{2}} \tag{18}$$

where $I(x,\ y)$ stand for the intensity of point $(x,\ y)$ and N stand for total pixel number.

3.5 Maximum Saturation

Color in formation is also considered as blur feature. It is observed that in blurred traffic images, pixels tend to have less vivid colors than in unblurred images because of the smoothing effect of the blurring process. So saturation degree descript blurs is computed as

$$S_P = 1 - \frac{3[\min(R, G, B)]}{(R + G + B)} \tag{19}$$

4 Results and Analysis

In order to verify our algorithm, two image sequences for different weather conditions are captured from scene I. Both of these two sequences contain 3000 frames, the total is 6000 frames. The classification algorithm here we use is Nearest Neighbor Classification algorithm. 2000 frames (each weather condition contains about 250 frames) for each scene are used to extract samples to train and the other 1000 frames are used to test the effect of these six feathers. Figure 5 shows four different image samples for each scene. Table 1 shows the corresponding character extraction results.

In our recognition stage, each frame is calculated and feathers are extracted. Then distance between this pattern vector and the samples are calculated. Weather condition for this test image will be classified to the category that has the nearest vector distance. Figure 6 shows the final recognition results. From the result we could find that the recognition right ratio surpasses 90 %. All of the algorithms are run on a PC with a 2.0 GHz Intel Pentium 4 processor. All traffic video sequences are sized by 320 × 240. The average running time for these four main stages (image inflection point finding, power spectrum slope, and other characters calculation, category judging) take about 20, 30, and 10 ms, respectively, to process an image. The total time consumed is 40 ms. This running time could maintain real-time detection. Experiment results verify the effective of this proposed algorithm.

Fig. 5 Sample images in scene I **a** sunny, **b** snowy, **c** fog, **d** rain

Table 1 Sample feature calculation results corresponding to Fig. 5

Feature value	Inflection point	Spectrum slope	Edge energy	Saturation	Contrast	Noise estimation δ
Sunny I	0	−2.6	328	0.72	0.83	2.19
Fog I	200	−2.4	269	0.62	0.58	2.51
Snowy I	0	−2.0	280	0.43	0.66	2.69
Rain I	182	−1.9	240	0.36	0.53	2.31

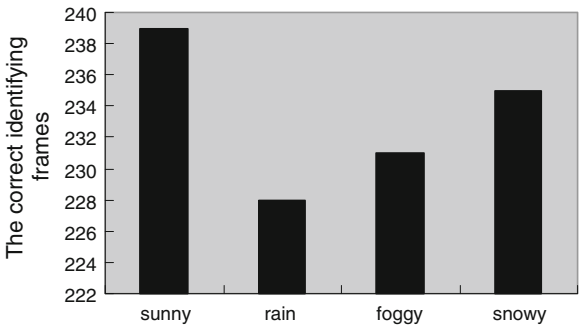

Fig. 6 Recognition precision

5 Conclusion

In this article, a novel algorithm for automatic weather condition recognition in traffic scene is presented. This proposed system is able to distinguish between multiple weather situations based on the classification of single monocular color images without any additional assumptions or prior knowledge. Homogenous area is extracted form top to bottom in traffic image. The inflection point information will be taken as a character for current weather recognition. Another four features: spectral slope, edge gradient energy, contrast, saturation, and image noisy, respectively, which descript image clarity are extracted also. Our proposed image descriptor clearly outperforms existing descriptors for the task. The average running time for these four main stages (image inflection point finding, power spectrum slope and other characters calculation, category judging) take about 20, 30, and 10 ms, respectively, to process an image. The total time consumed is 40 ms. This running time could maintain real time detection. Experiment results verify the effective of this proposed algorithm.

Acknowledgments This work is supported by the National Natural Science Foundation of China (No. 61079001), China's 863 Program (No. 2011AA110301), and China's PH.D Program Foundation (No. 20111103110017).

References

1. Roser M, Moosmann F (2008) Classification of weather situations on single color images. In: 2008 IEEE intelligent vehicles symposium, IEEE Press, pp 798–803
2. Garg K, Nayar SK (2007) Vision and rain. Int J Comput Vis 75(1):3–27
3. Narasimhan SG, Nayar SK (2000) Chromatic framework for vision in bad weather. In: IEEE conference on computer vision and pattern recognition, vol 1, pp 598–605
4. Kurihata H, Takahashi T, Ide I et al (2005) Rainy weather recognition from in-vehicle camera images for driver assistance. In: Proceedings of the IEEE intelligent vehicles symposium, IEEE Press, pp 205–210
5. Lazebnik S, Schmid C, Ponce J (2006) Beyond bags of features: spatial pyramid matching for recognizing natural scene categories, computer vision and pattern recognition. In: 2006 IEEE computer society conference on computer vision and pattern recognition, IEEE Press, vol 2, pp 2169–2178
6. Fergus R, Fei–Fei L, Perona P, Zisserman A (2005) Learning object categories from google's image search. In: Proceedings of the tenth IEEE international conference on computer vision, IEEE Computer Society, pp 1816–1823
7. Lowe DG (1999) Object recognition from local scale-invariant features. Proceedings of the international conference on computer vision, Corfu, pp 1150–1157
8. Dalal N, Triggs B (2005) Histograms of oriented gradients for human detection. In: International conference on computer vision and pattern recognition, IEEE Computer Society Press, vol 2, pp 886–893
9. Belongie S, Malik J, Puzicha J (2000) Shape context: a new descriptor for shape matching and object recognition. Adv Neural Inf Process Syst 831–837
10. Liu R, Li Z, Jia J (2008) Image partial blur detection and classification. In: IEEE conference on computer vision and pattern recognition, IEEE Press, p 8
11. Field D (1987) Relations between the statistics of natural images and the response properties of cortical cells. J Opt Soc Am A 4(12):2379–2394
12. Li Q, Fam Y, Zhang J, Li BQ (2011) Method of weather recognition based on decision-tree-based SVM. J Comput Appl 31(6):1624–1627
13. Eli P (1990) Contrast in complex images. J Opt Soc Am 7(10):2032–2040

Improvements of UMHexagonS Algorithm for Fast Motion Estimation in H.264

Hong-jian Cao and Gang Song

Abstract Motion estimation is the most time consuming part in H.264. UMHexagonS algorithm was accepted as the fast motion search algorithm in H.264 reference software JM because of its short motion estimation time (MET) and good rate-distortion performance. In this paper, an improved algorithm based on UMHexagonS is proposed. Improved initial search point prediction, improved premature termination rule, octagon-diamond pattern, and new uneven multi-hexagon-grid search pattern are adopted. Experiment results showed that, it can reduce MET by at least 27.46 % compared with that of UMHexagonS without degrading video quality significantly.

Keywords UMHexagonS · Fast motion estimation · H.264 · Video coding

1 Introduction

H.264 [1] is a video coding standard proposed by ITU-T's Video Coding Experts Group and ISO/IEC's Moving Pictures Experts Group in 2003. Although its coding rate could be improved by 50 % [2] than previous standard such as MPEG-4 and H.263, the significant improvement is at the cost of higher algorithm complexity, which restricts the coding efficiency of H.264. MET takes about 80–90 % of encoding time of H.264. The key to improve coding efficiency of H.264 is decreasing MET. Full search (FS) [3] algorithm is the most accurate search algorithm. Using FS, we can find the best matching point. However, the computation and MET are very large because we should search every point in

H. Cao (✉) · G. Song
School of Information Science and Engineering, Shandong University, Jinan, China
e-mail: generalchj@yahoo.com.cn

G. Song
e-mail: sddxsg@163.com

F. Sun et al. (eds.), *Foundations and Practical Applications of Cognitive Systems and Information Processing*, Advances in Intelligent Systems and Computing 215,
DOI: 10.1007/978-3-642-37835-5_19,

search range. Recently, many fast block motion search algorithms such as three-step search (TSS) [4], new three-step search (NTSS) [5], four-step search (4SS) [6], diamond search (DS) [7], hexagon-based search (HEX) [8] were proposed. H.264 accepted a hybrid search algorithm named UMHexagonS [9]. Compared with FS algorithm, UMHexagonS could decrease the computation by 90 % with good rate-distortion performance [2]. Compared with the other fast search algorithm, the computation improvement is also significant, local optimum problem can also be avoided. But UMHexagonS algorithm does not perform well in real-time coding, because the MET is not short enough.

The rest of this paper is organized as follows: At first we introduced UMHexagonS algorithm. Then based on UMHexagonS algorithm, we proposed an improved algorithm. Experiment results showed that the algorithm could reduce the MET without degrading video quality significantly followed by conclusion.

2 UMHexagonS Algorithm

UMHexagonS algorithm consists of four steps, step 2, 3, 4 are shown in Fig. 1.

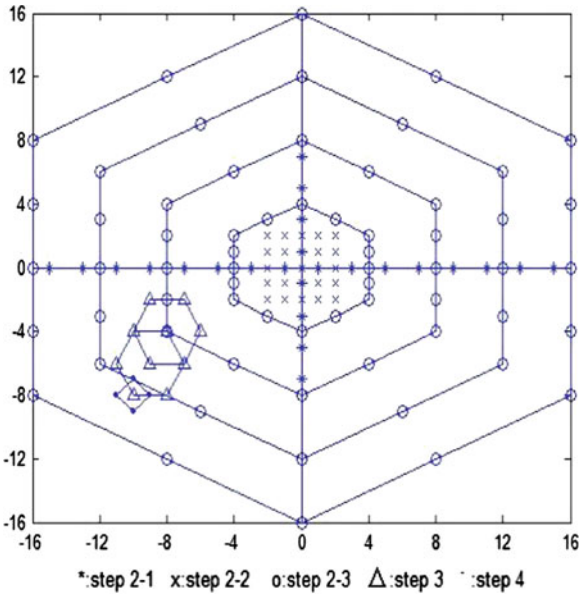

Fig. 1 Steps of UMHexagonS algorithm

2.1 Initial Search Point Prediction (Step 1)

There are four prediction modes to estimate the initial search point. They are median prediction, up layer prediction, corresponding block prediction, and neighboring reference frame prediction. The sum of absolute differences (SAD) of each mode was calculated and the minimum SAD, as in (1), was chosen. The point with minimum SAD is named Minimum block distortion (MBD) point. If the SAD is larger than threshold1 (Th1), go to step 2-1; if it is between Th1 and threshold2 (Th2), go to step 3; if it is less than Th2, go to step 4.

$$\mathrm{SAD}(i,j) = \sum_{m-1}^{M}\sum_{n-1}^{N} \mathrm{f_c}(m,n) - \mathrm{f_R}(m+i, n+j). \tag{1}$$

Here the block size is $M \times N$, $\mathrm{f_c}(m,n)$ is the pixel grey value in current block, $\mathrm{f_R}(m+i, n+j)$ is the pixel grey value in reference block.

Median prediction: As shown in Fig. 2, the motion vector of current block (D) is predicted by the motion vector of the adjacent left block (A), top-left or top-right block (B), top block (C) of the current block. As in (2), the mean of the four motion vectors is the predicted value of the motion vector of current block, where MVA, MVB, MVC are the motion vector of block A, B, C

$$\mathrm{MV_{MP}}=(\mathrm{MV_A} + \mathrm{MV_B} + \mathrm{MV_C})/4 \tag{2}$$

$$\mathrm{MV_{UP}} = \mathrm{MV_{up\,layer}}. \tag{3}$$

.

Up layer prediction: Considering the block size, H.264 defines seven inter-frame prediction modes. They are 16 × 16 mode (mode 1), 8 × 16 mode (mode 2), 16 × 8 mode (mode 3), 8 × 8 mode (mode 4), 4 × 8 mode (mode 5), 8 × 4 mode (mode 6), 4 × 4 mode (mode 7). As in (3), the motion vector of up layer (for example, mode 1 is the up layer of mode 2 and 3) is prediction of the lower layer.

Corresponding block prediction: There is close correlation between neighboring frames. Usually the project in current block can be found in neighboring frames. As Fig. 3 shows, the motion vector of the last frame's corresponding block can be used as a prediction. The equation is as followed, where MVCB is the motion vector of corresponding block.

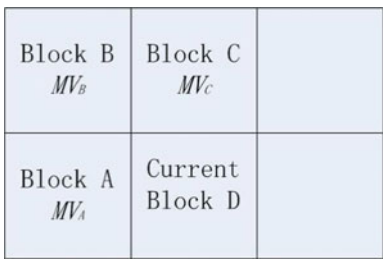

Fig. 2 Median prediction

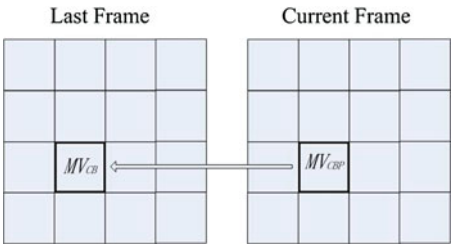

Fig. 3 Corresponding block prediction

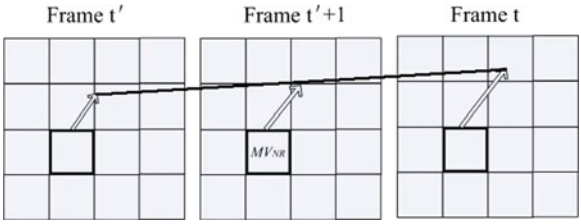

Fig. 4 Neighboring reference frame prediction

$$\mathrm{MV_{CBP}} = \mathrm{MV_{CB}} \tag{4}$$

Neighboring reference frame prediction: As Fig. 4 shows, the motion vector of the reference frame can be predicted by the motion vector of neighboring reference frame by scaling the motion vector by time. Because there is close correlation between them. The equation is as followed, where MVNRFP is the motion vector prediction in frame t', MVNR is the motion vector in frame $t' + 1$.

$$\mathrm{MV_{NRFP}} = \mathrm{MV_{NR}} \times \frac{t - t^{'}}{t - t^{'} - 1} \tag{5}$$

2.2 Unsymmetrical Multi-Resolution Hexagon Search (Step 2)

Step 2-1: Run an unsymmetrical-cross search to get the new MBD point. The point with the minimum SAD was chosen to be the new MBD point. If the SAD is larger than Th1, go to step 2-2; if it is between Th1 and Th2, go to step 3; if it is less than Th2, go to step 4.

Step 2-2: Run a 5 × 5 full search to get the new MBD point. The 5 × 5 area around the MBD point is chosen. The point with the minimum SAD was chosen to be the new MBD point. If the SAD is larger than Th1, go to step 2–3; if it is between Th1 and Th2, go to step 3; if it is less than Th2, go to step 4.

Step 2-3: Run an uneven multi-hexagon-grid search (UMHS) with a 33 long and wide search window to get the new MBD point. This step is run from middle to the edge. The point with the minimum SAD was chosen to be the new MBD point. If the SAD is less than Th2, go to step 4; otherwise go to step 3.

2.3 Iterative Hexagon Search (Step 3)

Run an iterative hexagon search get the new MBD point. Set the MBD point as the center of the hexagon pattern. Calculate the SAD of six search points of the hexagon pattern. Run the iterative hexagon search until the new MBD point is the center point of the hexagon pattern. Go to step 4.

2.4 Iterative Diamond Search (Step 4)

Run an iterative diamond search get the new MBD point. Set the MBD point as the center of the diamond pattern. Calculate the SAD of four search points of the diamond pattern. Run the iterative hexagon search until the new MBD point is the center point of the diamond pattern, it is the ultimate MBD point, the search is terminated.

3 Improved Algorithm

The procedure of the proposed algorithm is shown in Fig. 5. There are four improvements.

3.1 Improved Initial Search Point Prediction

UMHexagonS algorithm adopts four modes to estimate the initial search point. The best initial search point can be found accurately by making full use of the motion vector correlation of inner-frame, inter-frame macro blocks with different sizes. However, if they are all checked, it will take a long time and large space to do the computation. It is not practical to adopt all of the four modes in real-time application. Sometimes some modes can not be used. For example, up-layer prediction is not available for 16 × 16 block. Neighboring reference frame prediction is not available for the nearest reference frame. Besides, there are many static blocks in video sequences. For example, in video conference and news video the background is almost static all the time. The probability of (0,0) being the motion vector prediction is 45.49 % [10]. So (0,0) is set as the initial motion vector. If the SAD is small enough, go to step 4 to run the iterative diamond search. Otherwise, goto median prediction. The point with smaller SAD is set as the initial search point.

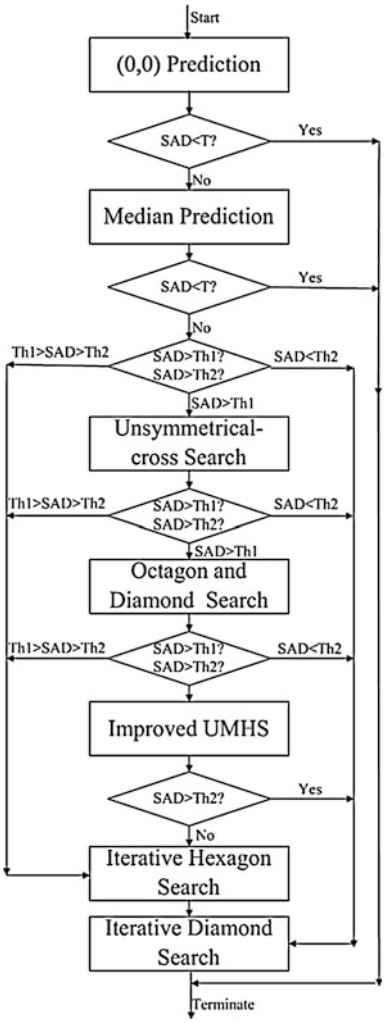

Fig. 5 Procedure of the proposed algorithm

3.2 Improved Premature Termination Rule

In UMHexagonS algorithm even if the best MBD point is got, the search still goes on until the best MBD point is in the center of the hexagon or diamond pattern. It is a waste of time. In natural video sequences, many blocks are static or have corresponding block in neighbor frame which is the same as the block. When the block is static, the SAD is less than 512. And 512 is set as a threshold (T). Generally, if the SAD is less than T after (0,0) prediction, median prediction, or during diamond search, the point is the ultimate MBD point. The SAD during

other search patterns is not checked like this because other search patterns are for motive blocks, it is not likely to find static blocks, comparing the SAD frequently is a waste of time. The termination rule can be described as followed: if the SAD is less than 512 after (0,0) prediction, median prediction, or during diamond search, the point is set as the ultimate MBD point. The search is terminated.

3.3 Improved Full Search Pattern

In UMHexagonS algorithm, if the SAD of the MBD point is larger than Th1 after unsymmetrical-cross search, 5 × 5 full search is run. There is close correlation between neighboring search points, it is unnecessary to search all points. Considering the spatial correlation, we propose an octagon-diamond pattern which is as shown in Fig. 6 to displace the 5 × 5 full search pattern. Twelve points form five diamonds. Compared with 5 × 5 full search, the MBD point can be easily found with 50 % search points reduction.

3.4 Improved Uneven Multi-Hexagon-Grid Search

In UMHexagonS algorithm adopts uneven multi-hexagon-grid search pattern because there are more horizontal movements than vertical movements. However, in mode 2 and mode 5, the movement is more likely vertical. A new uneven multi-hexagon-grid search is proposed to increase vertical search points for mode 2 and 5, which is as shown in Fig. 7.

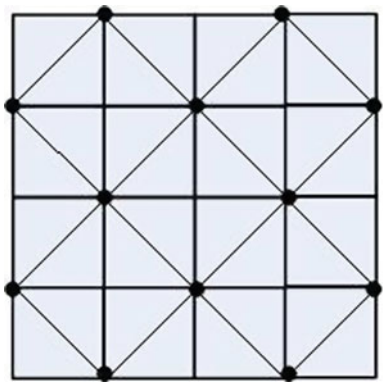

Fig. 6 Octagon-diamond pattern

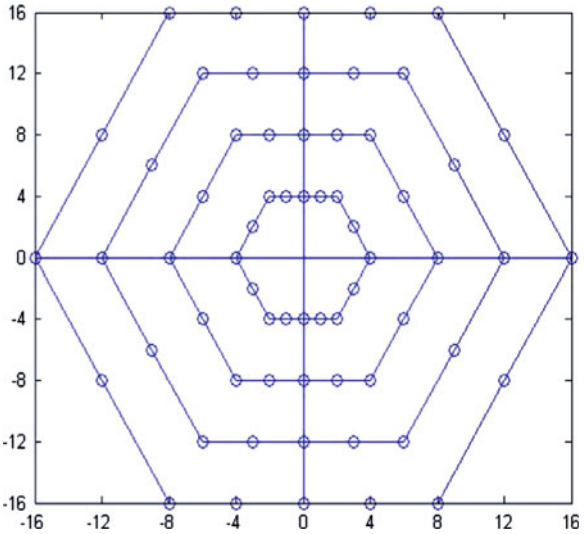

Fig. 7 New uneven multi-hexagon-grid search pattern

4 Experiment Results and Analysis

To evaluate our algorithm, H.264 reference software JM 11.0 [11] is used. Original UMHexagonS algorithm and proposed algorithm were set as the search algorithm. Five test video sequences in QCIF (176 × 144) are chosen including less motive sequences and motive sequences. They are 'akiyo,' 'foreman,' 'carphone,' 'coastguard,' and 'mobile' sequence. The computer parameters were Intel Pentium D processor 1.6G Hz, 1 GB RAM. The main software parameters are listed in Table 1. The motion estimation time (MET), peak signal to noise ratio (PSNR), and bitrate of the two search algorithms were calculated and compared. The difference and improvement rate is defined in (6) and (7).The unit of MET, PSNR, and bitrate are *s, dB,* and *kb/s.*

$$\text{Difference} = \text{Pro} - \text{Ori} \tag{6}$$

Table 1 Main software parameters

Parameter	Value
YUV type	4:2:0
Sequence type	IPPP
Entropy coding method	CAVLC
Frames to be encoded	100
Number reference frames	5
Search range	16
Frame rate	30
UseHadamard	Used

Table 2 Experiment results

	Original			Proposed		
	MET	PSNR	Bitrate	MET	PSNR	Bitrate
Akiyo	38.65	39.30	29.12	21.32	39.28	29.61
Foreman	59.69	37.99	131.91	43.30	37.96	136.24
Carphone	50.77	38.45	94.10	35.28	38.42	96.00
Coastguard	75.84	37.23	245.20	49.88	37.19	248.81
Mobile	72.74	33.92	422.95	47.21	33.89	433.82

Table 3 Differences and improvement rates

	Difference			Improvement rate (%)		
	MET	PSNR	Bitrate	MET	PSNR	Bitrate
Akiyo	−17.33	−0.02	+0.49	−44.83	−0.05	+1.68
Foreman	−16.39	−0.03	+4.33	−27.46	−0.08	+3.28
Carphone	−15.49	−0.03	+1.90	−30.51	−0.08	+2.02
Coastguard	−25.96	−0.04	+3.61	−34.23	−0.11	+1.47
Mobile	−25.53	−0.03	+10.87	−35.10	−0.09	+2.57

$$\text{Improvement Rate} = \frac{\text{Difference}}{\text{Ori}} \times 100\,\% \tag{7}$$

Here Pro is proposed algorithm result, Ori is original algorithm result.

As shown in Tables 2 and 3, compared with original UMHexagonS algorithm, the MET of proposed algorithm can be reduced by 27.46–44.83 %. The reduction is particularly significant when encoding less motive sequences such as 'akiyo' sequence. Because in 'akiyo', the background is almost static. Although the degradation of PSNR and increase of bitrate are little, we should do more research to make them less while achieve more MET reduction.

5 Conclusion

Based on UMHexagonS algorithm, an improved algorithm is proposed, in which improved initial search point prediction, improved premature termination rule, octagon-diamond pattern, and new uneven multi-hexagon-grid search pattern are adopted. Experiment results showed that MET was reduced a lot without degrading video quality significantly. This proposed algorithm is a very efficient algorithm for video coding. To reduce more MET with less video quality degradation, further research is necessary.

References

1. Wiegand T, Sullivan GJ (2003) Senior member: overview of the H.264/AVC video coding standard. IEEE Trans CSVT 13(7):560–576
2. Yang YH, Xu X, Ji XY (2006) An improvement on the motion estimation algorithm UMHexagonS. Comput Eng Appl 42(11):31–50
3. Dufaux F, Moscheni F (1995) Motion estimation techniques for digitalTV: a review and a new contribution. In: Proceedings of the IEEE, pp 858–876
4. Koga T, Linuma K, Hirano A, Ishi-guro T (1981) Motion-compensated interframe coding for video conferencing. In: Proceedings of national telecommunication conference, New Orleans, USA, pp C9.6.1–C9.6.5
5. Li R, Zeng B, Liou ML (1994) A new three-step search algorithm for block motion estimation. IEEE Trans CSVT 4(4):438–442
6. Po L-M, Ma W-C (1996) A novel four- step search algorithm for fast block motion estimation. IEEE Trans CSVT 6(3):313–317
7. Zhu S, Ma K-K (1997) A new diamond search algorithm for fast block matching motion estimation. In: Proceedings of the international conference on information communication on signal processing, pp 292–296
8. Zhu C, Lin X, Chau L (2002) Hexagon-based search patten for fast block motion estimation. IEEE Trans CSVT 12:349–355
9. Chen Z, He Y, Xu J (2003) Hybrid unsymmetrical cross multi-hexagon-grid search strategy for integer pel motion estimation in H.264. In: Proceedings of PCS, pp 17–22
10. Lam CH, Po LM, Cheung CH (2004) A novel kitecross-diamond search algorithm for fast block motion estimation. In: Proceedings of 2004 IEEE international symposium on circuits and systems, Canada, pp 729–732
11. JM Reference software. http://bs.hii.de/suehring/tml/download

Research on Middle-Semantic Manifold Object Annotation

Wengang Feng and Shaozhong Wu

Abstract A novel bionic, middle-semantic object annotation framework is presented in this paper. Moreover, we build the model based on the perception as defined by the human visual system. At first, the super-pixel is used to represent the images, and conditional random field could label each of the super-pixels, which means annotating the different classes of objects. In next step, on the basis of the previous result, image pyramid is used to represent the image, and get the sub-region of some objects of the same class. After extracting descriptor to represent the patches, all the patches are projected to a manifold, which could annotate the different views of objects from the same class. Experiments show that the bionic, middle-semantic object annotation framework could obtain superior results with respect to accuracy, and it could verify the correctness of WordNet indirectly.

Keywords Semantic manifold · Object annotation · Conditional random field · Pyramid presentation

W. Feng (✉) · S. Wu
Department of Policing Intelligence, Chinese People's Public Security University, Beijing 100038, China
e-mail: wengang.feng@gmail.com

S. Wu
e-mail: weshaoz@sina.com

W. Feng
Public Security Intelligence Research Center, Chinese People's Public Security University, Beijing 100038, China

F. Sun et al. (eds.), *Foundations and Practical Applications of Cognitive Systems and Information Processing*, Advances in Intelligent Systems and Computing 215,
DOI: 10.1007/978-3-642-37835-5_20,

1 Introduction

A person can recognize visually more than 10,000 categories of objects [1]. For humans, visual recognition is fast, effortless, and robust with respect to viewpoint, lighting conditions, occlusion, and clutter [2]. Moreover, learning new categories requires minimal supervision and a handful of exemplars. A challenging problem, resulted from the creation of huge image databases, is the effective search, navigation, and management of large image archives.

Human beings utilize the eyes, ears, nose, tongue, and body to obtain the information and perceive the world, but about 75 % information is acquired through the visual system, therefore, the vision is the most advanced perception of human being [3]. The aim of computer vision system is to build the model of real world, and those representations are used to interact with real world. Due to these reasons, there has been a surge of interest in image auto-annotation and object recognition in recent years. Researchers have tried to define ways to automatically assign keywords onto images or image regions and proposed many learning models [4]. Generally, if we want computer to "see" the world, the same as biological visual system, the key is that the framework should be bionic.

Object annotation could be treated as the high-level task of image understanding, because it usually has to use the information from last two steps. There are roughly two major techniques for image annotation: text-based and content-based. Text-based approaches utilize textual keywords or descriptions generated by human annotators. Given the rapid growth in the number of digital images, manual image annotation is time-consuming and annotator dependent. Content-based image annotation was developed to address some of the shortcomings of the manual annotation. It is based on the idea of annotating images using information automatically extracted from pixels.

1.1 Related Work

The main challenge in content-based image retrieval is to bridge the semantic gap between low-level features and conceptual contents. The problem of automatic image annotation is closely related to that of content-based image retrieval. As for automatic image annotation, most of the researchers worked in two directions: using discriminative or generative method.

In the former one, Pan et al. [5] leveraged a graph structure. They constructed a two-layer graph whose nodes are images and their associated captions and proposed a random-walk-with-restart algorithm to estimate the correlations between new images and the existing captions. Then, in another work [6], they extended the model to a three-layer graph with image regions added. In contrast, a few researchers have proposed discriminative models. Li et al. [7] proposed a Confidence-based Dynamic Ensemble model, which is a two-stage classifier. Carneiro and Vasconcelos [8] attempted to establish a one-to-one mapping between

semantic classes and sets of images with the criterion to minimize the error rate. All of the works mentioned above require a supervised learning stage. Hence, the generalization capability is a crucial assessment to their effectiveness.

As a different kind of approach, generative models were proposed. For example, Duygulu et al. [9] represented images in blobs and then adopted a statistical machine translation model to translate the blobs into a set of keywords. Blei and Jordan proposed a Corr-LDA model [10]. It assumes that there is a hidden layer of topics, which is a set of latent factors, such that words and image regions are independently generated by the topics. It used 7,000 Corel photos and a vocabulary of 168 words for evaluation. Li and Wang [11] proposed a 2D multi-resolution hidden Markov model to couple images and concepts. They used 60,000 Corel photos with 600 concepts. In one of their recent works, they improved this model and built an interesting real-time annotation system named Alipr, which attracted a great deal of attention from both academic and industry.

1.2 Novelty of our Approach

Instead of low-level method mentioned before, our method will use the middle-semantic information, by extracting a representative set of features from the interrelated patches and identifying an appropriate measure of similarity in the high-dimensional feature space.

In detail, our framework has two steps. First is image segmentation, which annotates different types of object. Here we use super-pixel representation and conditional random field to segment, which is coarse annotation. Second is precise annotation, which is the key point of the paper. Here uses an image pyramid to obtain every patch which has part of object, then extract the descriptor of the patches, finally project on the manifold.

The contributions of the bionic, middle-level semantic framework are: (1) the bionic, in order to simulate the human visual system, especially the prominence of behavioral bias in eye guidance, we use image pyramid to express one image, which includes the global and local manners, and use manifold to get the distribution of object patches, which makes the decision like human beings. (2) the middle-level semantic, one image is divided into several layers (the depth depends on the image resolution and object area), whose feature extraction and model training are independent. (3) the visual words, we combine the SIFT descriptor with color feature.

The rest of this paper is organized as follows. Section 2 outlines the proposed framework with various components such as super-pixel, conditional random field, image pyramid, feature extraction, and manifold learning described in various subsections. Experimental results are presented in Sect. 3 followed by the conclusions in Sect. 4.

2 Model Description

In visual cognition experiment, researchers found that alternative levels of selection for eye guidance are very important. A new cognition research is that there are two qualitatively different modes of viewing during scene inspection: An ambient mode for discerning overall spatial layout and a focal mode for more detailed, local processing [7]. Velichkovsky and colleagues argue that these two modes are separable on the basis of eye movements: Ambient processing is characterized by short duration fixations associated with large amplitude saccades; focal processing is characterized by long duration fixations associated with small amplitude saccades. Basis on this result, we want to extend object annotation into two parts.

First, we use the super-pixel to represent the images, and we will use the conditional random field to label each of the super-pixels, which means annotate the different classes of objects, which means analysis of the inter-class variation. In next step, on the basis of the previous result, we want to analyze the intra-class variation. We will use pyramid to represent the image, and to get the subregion of some objects of the same class, and then use different histogram to annotate them. The low-level factors are totally inadequate descriptors of where people fixate. Furthermore, even motion cues cannot explain fixation placement. They find that looking at the center of the screen has some predictive power, but that the single best explanation of fixation placement is a world-centered bias to look slightly below the horizon (which of course changes position considerably throughout the video clips). That's the evidence that supports pyramid representation is a good way to express the images. The flowchart of the algorithm is shown in Fig. 1.

2.1 Inter-Class Annotation

Super-Pixel Representation
Model is built based on a higher level image representation than the pixel image, in which a small patch of similar pixels are grouped together to form a larger unit, a super-pixel. Segmentation methods based on the bottom-up image cues can be utilized to generate such an image representation by over-segmenting the image into small but coherent regions. When the regions are small enough, their boundaries are usually consistent with the boundaries between object categories, and the potential error induced by such decomposition will be relatively small.

Conditional Random Field
The probabilistic model assigns labels to the super-pixels for a given input image by combining top-down category-based information with image cues. Let $X = \{x_i\}_{i \in S}$ be the input image, where S is a set of sites associated with the super-pixels and x_i is the image descriptor from the ith super-pixel. Each super-pixel x_i will be

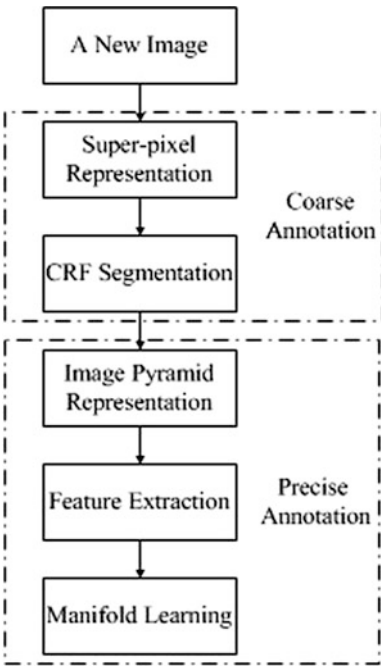

Fig. 1 Flowchart of the algorithm

assigned a label l_i from a finite label set L. The set of label variables $\{l_i\}_{i \in S}$ for image X forms a structural output L. So we define a conditional distribution over the output L given input X:

$$P(L|X) = \sum P_M(L|X, c)P_G(c|X) \tag{1}$$

where $P_M(L|X, c)$ is a conditional random field for the context c, and $P_G(c|X)$ is a gating function which yields the probability distribution of context given the information from image X. The inter-class annotation result is shown in Fig. 2.

2.2 Intra-Class Annotation

After we get the previous result, we will focus on the intra-class variation. Although we have annotated different kind of objects in the scene, there could be some parts of the image annotated/segmented as the same label, which means they are in the same class. How to treat such regions to get more detail of intra-class? Deeper annotation!

Spatial pyramid, which is by partitioning the image into increasingly fine sub-regions and computing histograms of local features found inside each sub-region, could be used only to represent the regions which obtain the same labeling object.

Fig. 2 **a** Original image, **b** Super-pixel representation, **c** Segmentation result

Image Scale Space

The human's observation of the scene and object is a hierarchical model moving from global to local. According to the pyramid data structure [1, 11], the image could be defined as a sequence $D = \{D_k\}_{k=1}^{K}$, and "K" is the depth which is the key point observed by a human. On the basis, the image is further divided into a planar sequence, $D_k = \{D_i^k\}_{i=1}^{4^{k+1}}$, where D_i^k is the image content of the subscript area R_i^k in the image D.

$$D_i^k = \left\{D_{x,y}, (x,y) \in R_i^k\right\}_{i=1}^{4^{k+1}} \tag{2}$$

where R is the subscript matrix of the image D, and R_i^k is the subscript set of the ith patch of the kth layer in the pyramid.

$$R = \left\{R_i^k\right\}_{i=1}^{4^{k+1}}, R = \{(x,y)|x = 1,\ldots,X, y = 1,\ldots,Y\} \tag{3}$$

where (X, Y) is the pixel resolution of image D.

The image scale space maintains the entropy structure of the image. This is because there is no filter processing on the original image and every layer of an image region description is coherent with the constraint of scale consistency. The image pyramid is constructed by placing a sequence of increasingly detailer grids over the image space.

2.2.1 Feature Extraction

Since we use little sub-regions to represent the regions, now we will extract descriptors to represent the patches in the manifold.

First, we use "weak features," which are oriented edge points, i.e., points whose gradient magnitude in a given direction exceeds a minimum threshold.

For better discriminative power, we also utilize higher dimensional "strong features," which are SIFT descriptors of 16 × 16 pixel patches computed over a grid with spacing of 8 pixels.

Color provides more discriminatory information than simple intensities particularly in case of the image. Although RGB (Red, Green, and Blue) color space is simple and very common, HSI (Hue, Saturation, and Intensity) features have been shown to have the best discriminatory potential among several perceptually relevant color spaces. Hence, we compute in this work SIFT descriptors over all three channels of the HSV color model. Thus, there will be a threefold increase in the dimensionality of the SIFT feature vector, and hence the key-point descriptors in color space would be having 3 × 128 (= 384) components.

Since annotation performance could also depend not only on the color space used but also the way color features are extracted, we did not outright reject the RGB color space. We conducted our experiments also with the 384 component feature vectors obtained by a concatenation of the SIFT descriptors computed over the three channels of the RGB color model.

The H color model is scale-invariant and shift-invariant with respect to light intensity. We also compute SIFT descriptors for every RGB channel independently. Because the SIFT descriptor operates on derivatives only, the subtraction of the means in the transformed color model is redundant, as this offset is already canceled out by taking derivatives. Similarly, the division by the standard deviation is already implicitly performed by the normalization of the vector length of SIFT descriptors.

Manifold Learning

Isomap aims to extract a low-dimensional data representation that best preserves all pair wise distances between input points, as measured by their geodesic distances along the manifold. It approximates the geodesic distance as a series of hops between neighboring points. This approximation becomes exact in the limit of infinite data. Isomap can be viewed as an adaptation of Classical Multidimensional Scaling [4], in which geodesic distances replace Euclidean distances.

Computationally, Isomap requires three steps: (1) Find t nearest neighbors for each point in input space and construct an undirected neighborhood graph, G, with points as nodes and links between neighbors as edges. This requires $O(n^2)$ time. (2) Compute approximate geodesic distances, Δ_{ij}, between all pairs of nodes (i,j) by finding shortest paths in G using Dijkstra's algorithm at each node. Construct a dense, $n \times n$ similarity matrix, G, by centering Δ_{ij}^2, where centering converts distances into similarities. This step takes $O(n^2 \log n)$ time, dominated by calculation of geodesic distances. (3) Find the optimal k dimensional representation, $Y = \{y_i\}_{i=1}^n$, such that $Y = \arg\min \sum_{ij} \left(\left\| y_i' - y_j' \right\|_2^2 - \Delta_{ij}^2 \right)$. The solution is given by, $Y = \left(\Sigma^k\right)^{1/2} \left(U^k\right)^T$ (1) where Σ^k is the diagonal $k \times k$ matrix storing the top k eigen-values of G, and U^k are the associated eigenvectors. This step requires $O(n^2)$

space for storing G, and $O(n^3)$ time for its eigen-decomposition. The time and space complexities for all three steps are intractable for $n = 18M$.

3 Experiment

The implementation details and experimental results of proposed algorithm are described in this section. We will analysis three aspects of the performances of the model. At first, we test the ability of the model to annotate the objects which have the same semantic and the different vision feature. Second, the rightness of WordNet will be tested by the proposed model indirectly. Finally, the influence of model parameters will be discussed. The baseline methods here are Mixed Media Graph (MMG) [12] and Latent Dirichlet Allocation (LDA) [13].

3.1 Experiment 1

The first experiment wants to test performance of the model. The evaluation is performed on the data set by us, because there is no data set which has several types of object having the same semantic and the different vision features. We use four different look chairs, and take the pictures in different viewpoints and angels. The data set has 200 pictures (all the resolution of the images in the experiment are 480×720), and each chair has the same number of pictures. We used 50 % of the randomly sampled pictures for model training, and used the remaining 50 % for testing.

Shown in Fig. 3, we could see that the proposed method could recognize about the objects which have the same semantic and about 30 % vision difference. But for both of the baseline methods, they did not work on such situation.

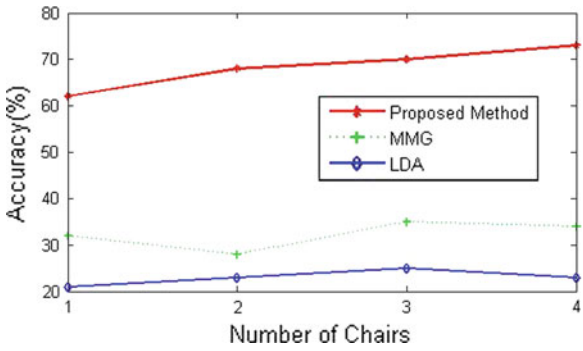

Fig. 3 The comparison of proposed method and baseline methods

3.2 Experiment 2

In this part, we want to check the performance influenced by the number of visual words. Since the performance of the model could depend upon the size of the codebook (vocabulary), we wanted to study the size of our codebook (equivalently, the number of clusters formed in our k-means approach to vector quantization) on the accuracy of object annotation. In this experiment, the size of codebook varied from 100 to 400 in intervals of 100. From these results, we can observe that the highest annotation accuracy is when the codebook sizes are 200, 300, and 400, respectively, and the result is shown in Fig. 4.

3.3 Experiment 3

This part of experiment analyzes the performance of the proposed model by the depth of image pyramid. The cause novelty of proposed method is to use middle semantic, which obtain the descriptors from the patches having parts of the object. So how to decide the depth of image pyramid is a key point.

Shown in Fig. 5, the depth of image pyramid has a great influence on the performance of the proposed model. If the depth is 1 or 2, which means the patches are just like original image, and the accuracy is very low. If the depth is 6 or 7, which means the patches are too small, and all the descriptors are just the same as low-level features. Due to the resolution being 480×720, the best depth is 5. But that is not fixed, because it 'is due to the image resolution and the area of the object in the image.

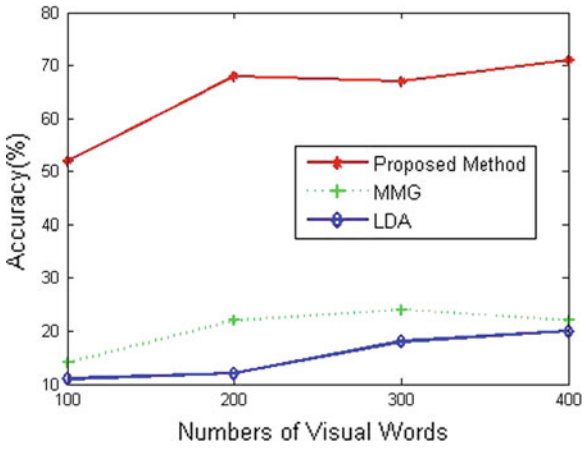

Fig. 4 The comparison of proposed method and baseline methods

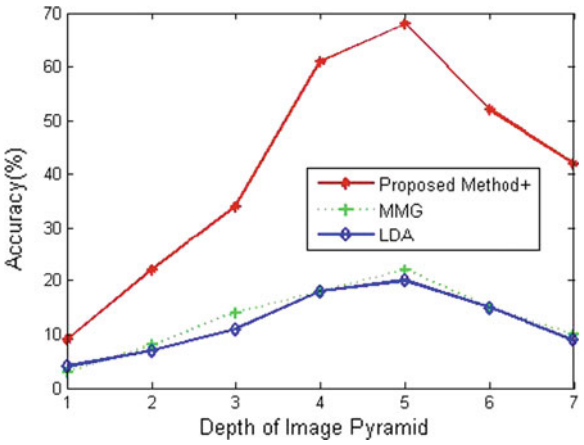

Fig. 5 The comparison of proposed method and baseline methods

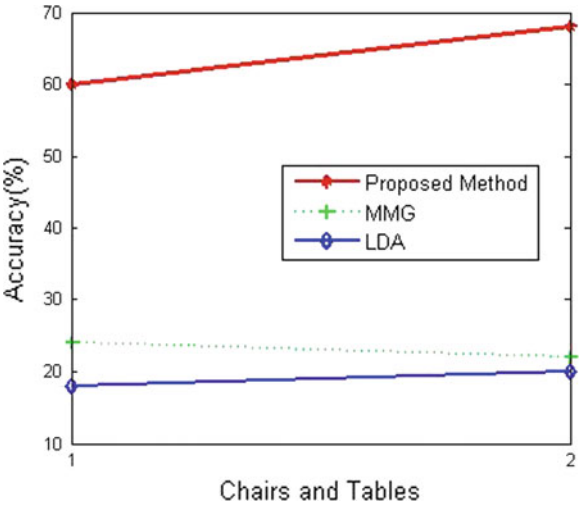

Fig. 6 The comparison of proposed method and baseline methods

3.4 Experiment 4

WordNet is an on-line lexical reference system whose design is inspired by current psycholinguistic theories of human lexical memory. English nouns, verbs, and adjectives are organized into synonym sets, each representing one underlying lexical concept.

WordNet is designed by people, which means it belongs to Cognitive science. The proposed model could verify the rightness of WordNet indirectly. Here, the training dataset is the indoor pictures, which have the desks and chairs (The most part of pictures should be occupied by the desk and chair). And the testing dataset has the pictures which just have chair or desk in them.

From Fig. 6, the chairs or tables could be found in the indoor pictures, which mean they have the same manifold. So from such aspect, the table and chair belong to indoor set is meaningful.

4 Conclusion

Why does the proposed framework obtain the more accurate results? As opposed contrast to generative or discriminative models, the proposed framework uses the image pyramid to obtain the patches, and project the patches into manifold, which have middle-level semantic. Besides such advantages, combining SIFT with color feature upgrades the performance of the proposed framework.

This paper investigates the bionic, middle-semantic object annotation framework, which could apply on both common scene datasets and other particular datasets. We use the image pyramid to acquire the information at scales to emulate human perception. We build new codebook to simulate long stare and short saccade to imitate human vision. One improvement was shown in descriptor combinations in the multi-feature space contrary to using only individual descriptors. The other improvement is combining image pyramid and manifold. This leads to improved performance and reduction of background noise in object-based image retrieval.

Acknowledgments This work was financially supported by the Chinese People's Public Security University Natural Science Foundation (2011LG08).

References

1. Smith TF, Waterman MS (1981) Identification of common molecular subsequences. J Mol Biol 147:195–197
2. Foster I, Kesselman C (1999) The grid: blueprint for a new computing infrastructure. Morgan Kaufmann, San Francisco
3. Czajkowski K, Fitzgerald S, Foster I, Kesselman C (2001) Grid information services for distributed resource sharing. In: 10th IEEE international symposium on high performance distributed computing. IEEE Press, New York, pp 181–184
4. Foster I, Kesselman C, Nick J, Tuecke S (2002) The physiology of the grid: an open grid services architecture for distributed systems integration. Technical report, Global Grid Forum
5. Pan J-Y et al (2004) GCap: Graph-based automatic image captioning. In: Proceedings of the conference on computer vision and pattern recognition workshop, 9:146–154
6. Felzenszwalb P, Huttenlocher D (2006) Pictorial structures for object recognition. In: Proceedings of the IEEE conference on computer vision and pattern recognition, pp 2066–2073
7. Li BT, Goh K, Chang E (2003) Confidence-based dynamic ensemble for image annotation and semantics discovery. In: Proceedings of ACM international conference on multimedia, pp 195–206

8. Carneiro G, Vasconcelos N (2005) A database centric view of semantic image annotation and retrieval. In: Proceedings of the 28th annual international ACM SIGIR conference on research and development in information retrieval, pp 559–566
9. Duygulu P et al (2002) Object recognition as machine translation: learning a lexicon for a fixed image vocabulary. In: Proceedings of the European conference on computer vision, pp 97–112
10. Pan JY, Yang HJ (2004) Automatic multimedia cross-modal correlation discovery. In: KDD'04, pp 322–330
11. Li J, Wang JZ (2006) Real-time computerized annotation of pictures. In: Proceedings of the ACM international conference on multimedia, pp 911–920
12. Barnard K (2003) Matching Words and Pictures. J Mach Learn Res 3:1107–1135
13. Vailaya A, Figueiredo A, Jain A, Zhang H (2001) Image classification for content-based indexing. IEEE Trans Image Process 10:117–129

Research on HVS-Inspired, Parallel, and Hierarchical Scene Classification Framework

Wengang Feng and Xiping Zhou

Abstract A novel bionic, parallel, and hierarchical scene classification framework is presented in this paper. Moreover, we build the model based on the perception as defined by the human visual system. At first, we use an image pyramid to present both the global scene and local patches containing specific objects. Second, we build our own codebooks, which satisfy both long stare and short saccade similar to humans. Next, we train the visual words by generative and discriminative methods, respectively, which could obtain the initial scene categories based on the potential semantics using the bag-of-words model. Then, we use a neural network to simulate a human decision process. This leads to the final scene category. Experiments show that the parallel, hierarchical image representation, and classification model obtain superior results with respect to accuracy.

Keywords Image pyramid · Visual codebook · Generative method · Discriminative method · Neural network

1 Introduction

Nowadays, as it becomes increasingly viable to capture, store, and share large amounts of image and video data, automatic image analysis is crucial to managing visual information. The amounts of the image data and the number of the users

W. Feng (✉) · X. Zhou
Department of Policing Intelligence, Chinese People's Public Security University, Beijing 100038, China
e-mail: Wengang.feng@gmail.com

X. Zhou
e-mail: pxz95010672@sina.com

W. Feng
Public Security Intelligence Research Center, Chinese People's Public Security University, Beijing 100038, China

F. Sun et al. (eds.), *Foundations and Practical Applications of Cognitive Systems and Information Processing*, Advances in Intelligent Systems and Computing 215,
DOI: 10.1007/978-3-642-37835-5_21,

have an exponential increase. Image scene classification, which can be used for indexing, searching, filtering, and mining large amounts of image data, becomes increasingly important for users.

Scene classification [1–3] plays an important role in efficient image resource management and automatic image classification and is very important in computer vision and pattern recognition domain as well as content-based retrieval. The goal of a computer vision system is to build a model of the real world that allows a user to interact with it. The ultimate goal is to allow a computer to "see" the world in a manner similar to the biological visual system. First it must build the framework then realize cognition and inference. The goal of this research is to allow images to be quickly, accurately, and efficiently classified based on the image semantics and relevance. This work also can be used in domains such as image retrieval, video surveillance, and navigation.

In cognitive theory [4–6], the majority of research on scene classification has focused on the roles of either low-level visual feature cues or high-level factors such as object-, semantic-level cues, or behavioral task demands. However, latest research in cognitive neuroscience finds evidence of the importance of periods of localized scanning separated by "global" relocations to new regions of the scene, as well as evidence to support the existence of small amplitude "corrective" saccades in natural image viewing. So both global features and local features are good visual feature candidates for targets on which the eyes fixate. They should be used together for scene modeling, in a parallel fashion.

The perception in the human visual system follows a hierarchical model in which the information of scale space is not changed by altering the scale [7]. Humans can recognize one scene in a very short time because they have a large and complex scene dataset in the brain. The model needed to classify a scene has been trained sufficiently to fit most situations. Based on cognitive neuroscience, we propose a novel parallel, hierarchical scene classification framework that has superior results for scene recognition.

This paper is organized as follows: In the next section, we describe the related work in traffic scene classification and the unique features of our approach. Following that, we discuss the proposed traffic scene classification framework and then describe the experimental results. Finally we draw a few conclusions.

2 Proposed Scene Classification Framework

2.1 Scene Classification Framework

In the training step, there are five stages: First, each one image will be presented as 21 images (patches) in three layers using an image pyramid. Second, we will build codebooks, which have a clustering part (scale-invariant feature transformer [1]) and non-clustering part (color, texture, gist, and fractal features) for each patch.

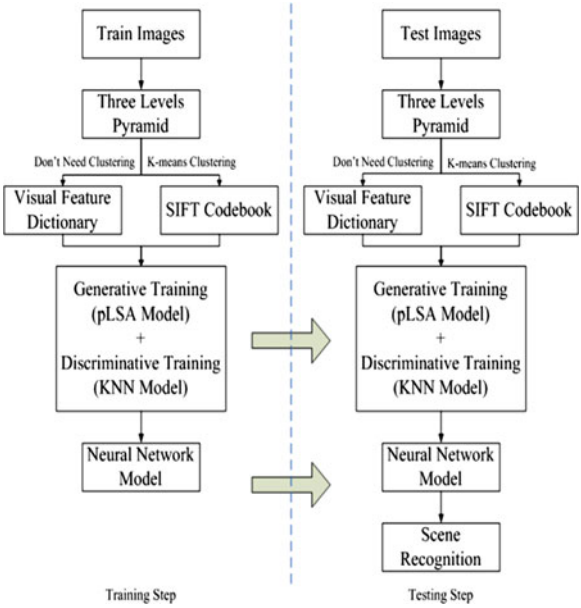

Fig. 1 Flowchart of the algorithm

Third, each visual word extracted from one image patch is trained in a generative way using pLSA model. Each training patch is then represented by z-vectors ($p(z|d)$) where z is a topic and d is a document (image). The cardinality of the $z$vector is the number of the topics. Fourth, the z-vectors obtained from last step are subjected to discriminative training (KNN model). Finally, we use a neural network to get the final one classification category based on the 21 patches scene categories. This approach simulates human's decision process based on local and global visual perception.

The test step also proceeds in five stages. The difference is that the test image is projected onto the simplex spanned by the vector learned during training. This is achieved by running Expectation Maximization (EM) in a similar manner to that used in learning, but now, only the z-vectors are updated in each M-step with the other learned vectors ($p(w|z)$) fixed. The result is that the test image is represented by a z-vector. The test image is then classified by the multiclass discriminative classifier. Figure 1 shows graphically the parallel, hierarchical framework for both the training and testing steps.

2.2 Image Pyramid

The human's observation of the scene and object is a hierarchical model moving from global to local. According to the pyramid data structure [1, 7], the image could be defined as a sequence $I = \{I_k\}_{k=1}^{K}$, and "K" is the depth which is the key

point observed by a human. On the basis, the image is further divided into a planar sequence, $I_k = \{I_i^k\}_{i=1}^{4^{k+1}}$, where I_i^k is the image content of the subscript area R_i^k in the image I.

$$I_i^k = \left\{I_{x,y}, (x,y) \in R_i^k\right\}_{i=1}^{4^{k+1}} \tag{1}$$

where R is the subscript matrix of the image I, and R_i^k is the subscript set of the ith patch of the kth layer in the pyramid. Here we use three layers:

$$R = \left\{R_i^k\right\}_{i=1}^{4^{k+1}}, R = \{(x,y)|x = 1,\ldots,X, y = 1,\ldots,Y\} \tag{2}$$

where (X, Y) is the pixel resolution of image I.

The image scale space maintains the entropy structure of the image. This is because there is no filter processing on the original image and every layer of an image region description is coherent with the constraint of scale consistency.

2.3 Feature Extraction

In the framework, first an input image is separated into three layers and 21 patches by an image pyramid. We treat each patch from the original image as one independent image. That means that the scene dataset will have 21 subsets. This is the parallel property shown in Fig. 2.

For each patch we extract two types of features to build codebooks used in the experiments of Sect. 3. First, we have the so-called "clustering codebook," which

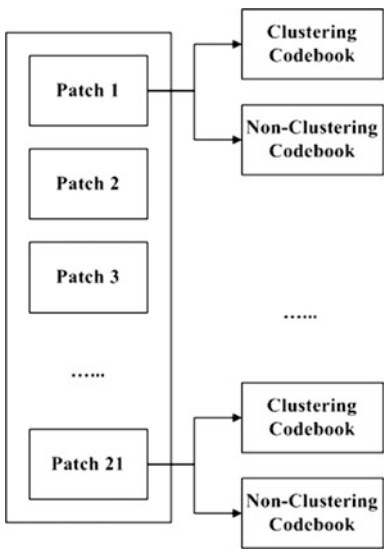

Fig. 2 Codebook structure

are SIFT [1] (scale-invariant feature transformer) features. The SIFT feature is highly distinctive, shown to provide robust property of affine distortion, image scale and rotation, change in 3D viewpoint, addition of noise, and change in illumination.

In detail, we have four steps to get SIFT features [8]: (1) Scale-space extreme detection: The first stage of computation searches over all scales and image locations. It is implemented efficiently by using a difference-of-Gaussian function to identify potential interest points that are invariant to scale and orientation. (2) Keypoint localization: At each candidate location, a detailed model is fit to determine location and scale. Keypoints are selected based on measures of their stability. (3) Orientation assignment: One or more orientations are assigned to each keypoint location based on local image gradient directions. All future operations are performed on image data that has been transformed relative to the assigned orientation, scale, and location for each feature, thereby providing invariance to these transformations. (4) Keypoint descriptor: The local image gradients are measured at the selected scale in the region around each keypoint. These are transformed into a representation that allows for significant levels of local shape distortion and change in illumination. After we get the SIFT features, we perform k-means clustering to form a visual codebook.

We also utilize a "non-clustering codebook," which combines color, texture, gist, and fractal feature. All color descriptors can be extracted from an image or an image region. Color structure is a histogram of color distribution and spatial color structure. Texture descriptors can be extracted from an image or an image region. There are five common texture descriptors: right boundary texture-histogram, left boundary texture-histogram, top boundary texture-histogram, bottom boundary texture-histogram, and interior texture-histogram, which describe the local spatial distribution of image structure. Fractal dimension could represent the complexity and irregularity of the image, and we could use the global and local fractal dimension as a histogram. The gist feature [7] is extracted from one whole image, which includes all levels of processing, from low-level features (e.g., spatial frequencies) to intermediate image properties (e.g., surface, volume) and high-level information (e.g., objects, activation of semantic knowledge). Therefore, gist can be studied at both perceptual and conceptual levels.

2.4 Generative Model Training

Probabilistic Latent Semantic Analysis (pLSA) is a generative model from statistical text literature [9]. In text analysis, this is used to discover topics in a document using the bag of words document representation. Here, we treat images as documents, and object categories as topics (for example, mountain and street), so that an image containing instances of several objects is modeled as a mixture of topics. The model is applied to images by using a visual analog of words, formed by clustering and non-clustering codebooks. pLSA is appropriate here because it

provides a correct statistical model for clustering in the case of multiple object categories per image.

In detail, each image is modeled as a mixture of Z topics, and each topic is a distribution over the vocabulary of words. More formally, we have a set of images $D = d_1, \ldots, d_N$, each modeled as a histogram of word counts over a vocabulary of $W = w_1, \ldots, w_V$. The corpus of images is represented by a co-occurrence matrix of size $V \times N$, with entry $n(w, d)$ listing the number of times the words w occurred in an image d. Image d has N_d words in total.

The key values used or obtained from training via pLSA are probabilities. $p(d_j)$ denotes the probability of observing a particular image d_j. $p(w_i|z_k)$ signifies the probability of a specific word conditioned on the unobserved topic variable z_k. Finally, $p(z_k|d_j)$ expresses an image-specific probability distribution over the latent variable space. Based on these, we can express the specific pLSA model for the problem. First, an image d_j is selected with the probability $p(d_j)$; second, a latent topic z_k is picked with the probability $p(z_k|d_j)$; finally, a word w_i is generated with the probability $p(w_i|z_k)$. It is the probability of the latent variable, $p(w_i|z_k)$, for which we must solve.

It shows indirectly the marginal decomposition of the joint probability $p(w, d, z)$. More explicitly:

$$p(w, d) = \sum_{z=1}^{Z} p(w, d, z) = \sum_{z=1}^{Z} p(d)p(w|z)p(z|d) \tag{3}$$

$p(w, d)$, we obtain by examining the image/document directly. From the chain rule, we obtain $p(w, d) = p(d)p(w|d)$. Summing across all values for the latent variable, we obtain the expression for $p(w|d)$:

$$p(w|d) = \sum_{z=1}^{Z} p(w|z)p(z|d) \tag{4}$$

We see that a $W \times D$ matrix is decomposed into a $W \times Z$ matrix and a $Z \times D$ matrix. $p(w|z)$ captures the co-occurrence of words within a topic while $p(z|d)$ gives the weighting of each topic within a image. For every image, the marginal distribution $p(z|d)$ is convex.

We use maximum likelihood for parameter iteration, the likelihood is,

$$L = \log P(D, W) = \prod_{i=1}^{M} \prod_{j=1}^{N} n(w, d) \log P(w, d) \tag{5}$$

This is equivalent to minimizing the Kullback–Leibler divergence between the measured empirical distribution and the fitted model. The standard procedure for maximum likelihood estimation in latent variable models is the Expectation Maximization (EM) algorithm [8]. EM alternates two steps: (i) an expectation (E) step where posterior probabilities are computed for the latent variables, based on the current estimates of the parameters, (ii) a maximization (M) step, where parameters

are updated based on the so-called expected complete data log–likelihood which depends on the posterior probabilities computed in the E-step. Here, the densities of the model, $p(w|z)$ and $p(z|d)$, are learnt using EM, in the E-step computes the posterior over the topic, $p(z|w,d)$ and then the M-step updates the densities.

2.5 Discriminative Model Training

For a discriminative model, one needs only the conditional probabilities of the target labels, $p(z|d)$. For each patch, we now have a vector for each image whose cardinality equals the number of the topics, $\langle p(z_1|d), p(z_2|d), \ldots, p(z_n|d)\rangle$. Two discriminative models are used, one to obtain the best estimate of the label (and its probability) for each patch and one to obtain the best label for the overall scene.

To obtain the single-estimate probability and label for one patch we use KNN over an R^2-space, in which the training set is embedded, KNN where $k = 7$ is used to select the best label. The probability is estimated as the average probability over neighbors having similar labels. The probability is used in the next discriminative step.

2.6 Neural Network Model Training

Radial basis function (RBF) networks [10] typically have three layers: an input layer, a hidden layer, and a linear output layer. The hidden layer consists embeds of an RBF (Gaussian) activation function, each having stronger responses when the N inputs are nearer the mean. The output, y, of the network is a weighted sum of the responses of the hidden neurons,

$$y = \sum_{i=1}^{S} \alpha_i \rho(\|x - c_i\|) \tag{6}$$

where S is the number of neurons in the hidden layer, c_i is the center vector of neuron i, α_i are the weights of the neuron, and $\rho(.)$ is the response of hidden neuron:

$$\rho(\|x - c_i\|) = \exp\left[-\beta_i \|x - c_i\|^2\right] \tag{7}$$

Here, we set the initial value of weights, $\beta_{i,}$ but in the training, all weights are changed to optimum values. The norm is taken to be the Euclidean distance.

The number of inputs, N, is 21—one for each patch. The value of the input is the value $p(z|w,\ d)$ instantiated by the KNN step described earlier. There is one output, y, from which a Z-way decision is extracted by Z–1 thresholds.

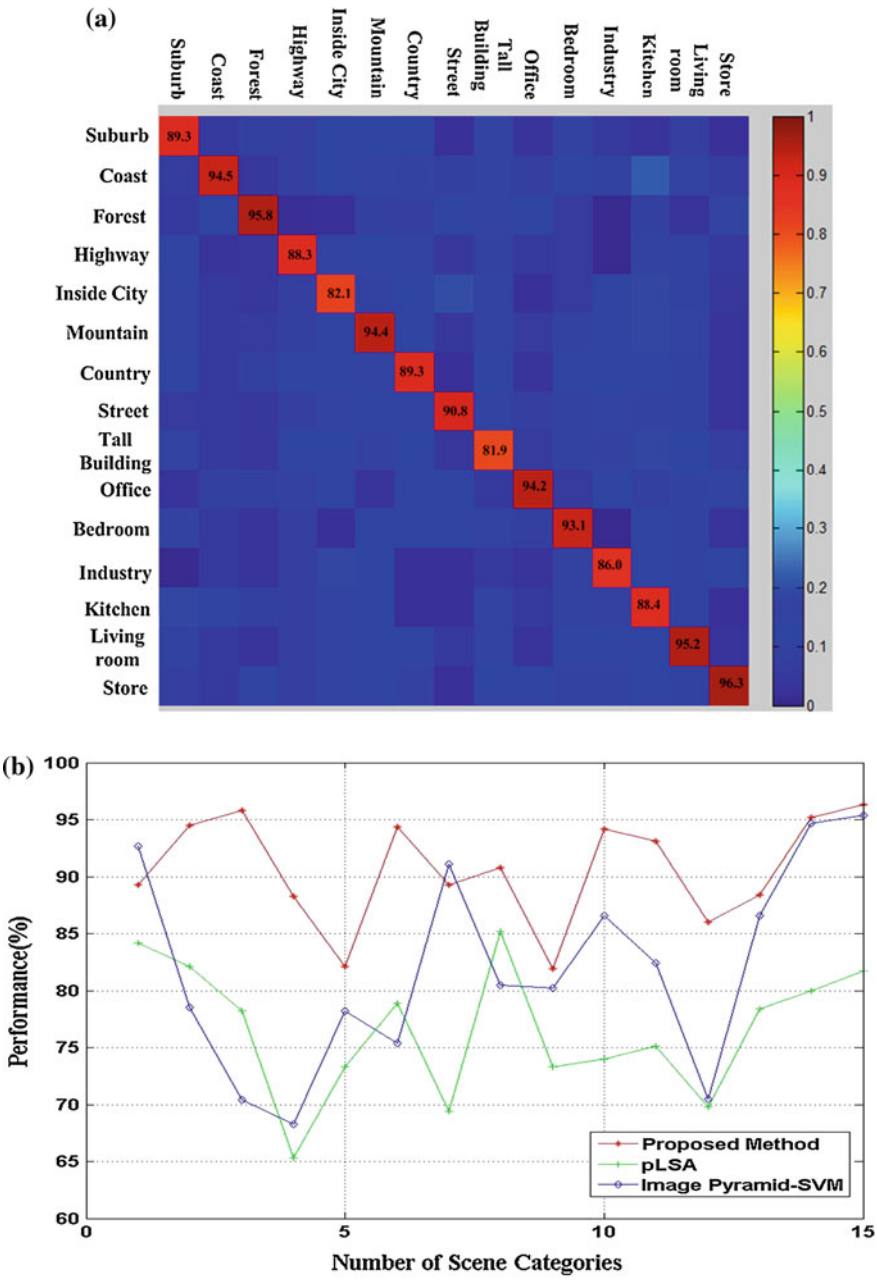

Fig. 3 **a** Confusion matrix for fifteen scene categories. The result of our method, **b** The result of the baseline pLSA method

3 Experiment

The implementation details and experimental results of our proposed algorithm are described in this section. At first, we describe the three image database used to evaluate our framework and our testing methodology. Then we analyze the results and compare the results with the baseline method (pLSA model [9] and image pyramid-SVM [1]).

Since the accurateness of the classification result is the key point for the scene classification framework, our first experimentation is on identification of the best classifier for the common dataset. We use UIUC 15 scene categories dataset as the common dataset, which are bedroom, suburb, industry, kitchen, living room, coast, tree, highway, inside city, mountain, country, street, tall building, office, and store. The dataset contains 200 images per category, respectively. The images are medium resolution, i.e., about 500 × 330 pixels. Namely, most images feature relatively little clutter, and the objects are centered and occupy most of the image. In addition, a number of categories, such as chimney, are affected by "corner" artifacts resulting from artificial image rotation. Though these artifacts are semantically irrelevant, they can provide stable cues resulting in misleadingly high recognition rates.

In Fig. 3, we could see the result of our classification framework and the comparison of our method and baseline methods. In Fig. 3a, the confusion matrix shows that the accurateness of our classification framework is around 90 %, which is better than all the state-of-art method. Especially for the coast, forest, mountain, living room, and store, the accurateness of such classes is near 100 %, because in such scene images, all the nature scene characteristics are unique, and it could be distinguished in very high precise result. In Fig. 3b, it is easy to discover that the result of the proposed framework is much better than the baseline methods.

4 Conclusion

Why does the proposed framework obtain more accurate results? In contrast to the pLSA-only model, the proposed framework uses the image pyramid to connect the global and local semantic information, thus make better choices. Besides this advantage, choosing the different visual words and using a neural network upgrade the performance.

We have proposed a scene classification framework, which can recognize the traffic scene category enabling automatic selection of the most efficous vehicle tracking and traffic surveillance algorithms for the conditions. The model is able to obtain semantic information from global and local manners despite using coarse features. We use the image pyramid to acquire the information at scales to emulate human perception. We build different codebooks to simulate long stare and short saccade to imitate human vision. We use generative method, discriminative

method, and neural network to train the visual words to get the semantic information from images to simulate human beings visual system. Finally we could get a traffic scene classification result depending on our generic framework.

Acknowledgments This work was financially supported by the Chinese People's Public Security University Natural Science Foundation (2011LG08).

References

1. Lazebnik S, Schmid C, Ponce J (2006) Beyond bags of features: spatial pyramid matching for recognizing natural scene categories. In: IEEE conference on computer vision and pattern recognition, pp 1–8
2. Malisiewicz T, Efros AA (2008) Recognition by association via learning per-exemplar distances. In: Proceedings of the IEEE conference on computer vision and pattern recognition, pp 1–8
3. Fei–Fei L, Perona P (2005) A Bayesian hierarchical model for learning natural scene categories, In: IEEE conference on computer vision and pattern recognition, pp 524–531
4. Talter BW (2009) Current understanding of eye guidance. Vis Cognition 17:777–789
5. Talter BW, Vincent BT (2008) Systematic tendencies in scene viewing. J Eye Mov Res 2:1–18
6. Talter BW, Vincent BT (2009) The prominence of behavioural biases in eye guidance. Vis Cognition 17:1029–1054
7. Grauman K, Darrell T (2005) Pyramid match kernels: discriminative classification with sets of image features. In: Proceedings of the international conference on computer vision, pp 1–8
8. Lowe DG (1999) Object recognition from local scale-invariant features. In: International conference on computer vision, Corfu, Greece, pp 1150–1157
9. Hofmann T (1998) Probabilistic latent semantic indexing. In: Proceedings of the SIGIR conference research and development in information retrieval, pp 1–13
10. Torralba A (2003) Contextual priming for object detection. Int J Comput Vision 53(2):169–191

Adaptive Sub-Channel Allocation Based on Hopfield Neural Network for Multiuser OFDM

Sufang Li, Mingyan Jiang, Anming Dong and Dongfeng Yuan

Abstract A kind of adaptive sub-channel allocation method utilizing Hopfield neural network (HNN) is studied in this paper. In order to find the power optimal sub-channel allocation under the constraints that only one sub-channel can be allocated to one user and all users are allocated the same number of sub-channels, a kind of new energy constrained function is constructed for the HNN. It is shown through numerical simulation that the proposed method can find the optimal allocation with less complexity compared with the exhaustive method.

Keywords Sub-channel allocation · Multiuser OFDM · HNN · Optimization algorithm

1 Introduction

As a kind of promising technology that can meet the demand of next generation wireless communication systems, Orthogonal Frequency Division Multiplexing (OFDM) technology based on the concept of multi-carrier transmission has been proposed for many years. The idea is to divide a broadband channel into multiple narrowband parallel sub-channels. In multiuser OFDM systems, a centralized base

S. Li · M. Jiang (✉) · A. Dong · D. Yuan
School of Information Science and Engineering, Shandong University, Jinan 250100, China
e-mail: jiangmingyan@sdu.edu.cn

S. Li
e-mail: sufangli@mail.sdu.edu.cn

A. Dong
e-mail: anmingdong@mail.sdu.edu.cn

D. Yuan
e-mail: dfyuan@sdu.edu.cn

F. Sun et al. (eds.), *Foundations and Practical Applications of Cognitive Systems and Information Processing*, Advances in Intelligent Systems and Computing 215,
DOI: 10.1007/978-3-642-37835-5_22,

station is needed to communicate with multiple users and there should be a multiple access scheme to allocate the limited number of sub-channels to the users. Because the adaptive modulation can greatly enhance the system efficiency by changing its modulation constellation and transmit power according to the instantaneous Channel State Information (CSI), how the resources are allocated among the users in an OFDM system is a key problem.

The problem above can be formulated as an optimization problem. Two major classes of adaptive resource allocation methods have been reported in the literature: (1) Margin Adaptive (MA) and (2) Rate adaptive (RA). The MA resource allocation method refers to minimizing the total transmit power while providing each user with its required quality of service in terms of data rate and bit error rate (BER) [1]. The aim of RA resource allocation method is to maximize the total throughput of the system with the constraint on the transmit power [2]. The MA method is used in this paper, which is to minimize the total transmit power while satisfying the rate requirement and bit error rate (BER) constraints of each user. A kind of genetic algorithm has been proposed [1] to solve this problem by adding some individuals with 'good' genes to the initial population. However, the converging speed is slow and the transmission characteristic deteriorates when the number of users and sub-channels increases. An iterative water-filling algorithm has been declared [3] with near-optimal solution, but the complicated computation makes it impractical. With the advantage of parallel processing, the HNN has the potential to search the optimal solutions with a relative fast convergence speed. It is especially powerful in solving combinatorial optimization problems. For the reason that the sub-channel allocation for multiuser OFDM can be mapped into such combinatorial optimization problem, which can be seen in Section III. B of the following context, a new MA sub-channel allocation method based on HNN is proposed in this paper.

The main contributions of our work include the formulation of sub-channel allocation with the objective to minimize transmit power and the mapping of this formulation into the energy function of the HNN. Numerical simulations are taken to verify the proposed algorithm and the results show that the adaptive sub-channel allocation method by HNN can achieve minimum transmit power with a faster convergence speed and lower computational complexity.

2 Multiuser OFDM and the Sub-channel Allocation

In order to achieve adaptive resource allocation for a multiuser OFDM system, multiple users should be scheduled to transmit on different sub-channels within one OFDM symbol. The resources for the downlink of OFDM systems include the total transmit power and the bandwidth, i.e., sub-channels. Because different users have different locations and independent fading characteristics, the sub-channels can be allocated to the users according to their channel conditions [4]. The data bits are then modulated to the sub-channels that have been assigned to each user under the constraints of power [5].

The problem of sub-channel allocation in a multiuser OFDM system with N sub-channels and K users is basically to determine the matrix $C = [c_{k,n}]_{K\times N}$ which sub-channels should be assigned to each user, where $c_{k,n}$ indicates whether sub-channel n is used by user k or not, and it can only be either 1 or 0. When the sub-channel is occupied, the value of $c_{k,n}$ is 1, otherwise it is 0. A sub-channel can only be allocated to one user, and it is forbidden for multiple users to share one sub-channel, i.e., each column of C can only have one 1. The matrix C is known as allocation matrix. Throughout this paper, we assume that $N/K = M$ is an integer and the number of sub-channels allocated to every user is M. To determine the elements of C, the problem is formulated in the form of an optimization problem with one or more constraints according to the objective of the system. The optimization problem that allocates sub-channels to different users according to channel conditions of these users under the equal resource constraint to minimize the total transmit power can be formulated as follows:

$$\begin{aligned} \text{minimize} \quad & P_T = \sum_{k=1}^{K}\sum_{n=1}^{N} P_{k,n}c_{k,n} = \sum_{k=1}^{K}\sum_{n=1}^{N} \frac{f_k(c_{k,n})}{h_{k,n}^2} c_{k,n}, \\ \text{subject to} \quad & \sum_{k=1}^{K} c_{k,n} = 1, \quad n \in \{1,2,\cdots,N\}, \\ & \sum_{n=1}^{N} c_{k,n} = M, \quad k \in \{1,2,\cdots,K\}, \\ & \sum_{n=1}^{N}\sum_{k=1}^{K} c_{k,n} \end{aligned} \tag{1}$$

where $P_{k,n}$ is the power allocated to user k on the sub-channel n. P_T is the total power of an OFDM symbol. The parameter $h_{k,n}$ is the channel gain for user k on sub-channel n. Under the constraint of equal number of sub-channel allocation for every user, the sum of every row of allocation matrix is M, while the sum of every column is 1. The parameter $f_k(c_{k,n})$ is the minimum signal power that can be demodulated correctly by receivers. For different modulation patterns, the power needed to transmit OFDM bits data are different. The most common modulation method used in OFDM is the M-QAM. Given the BER p_e, it is known that the power needed for c bits data for M-QAM modulation is given as

$$f(c) = N_0\left[Q^{-1}\left(\frac{p_e}{4}\right)\right]^2(2^c - 1), \tag{2}$$

where N_0 is the unilateral frequency spectral density of white Gaussian noise. The Q function is defined as

$$Q(x) = \frac{1}{2\pi}\int_x^{\infty} e^{-t^2/2}dt. \tag{3}$$

The function $Q^{-1}(x)$ denotes the inverse function of the Q function. Note that in this paper the power function is normalized to 1 for the reason that it is not correlated with the MA optimization algorithm presented in the paper. Nevertheless, the power function is indeed important for the related future work, and it should be used in other RA optimization problems.

The objective is to determine the adaptive sub-channel allocation scheme based on HNN which can search the optimal sub-channel allocation matrix adaptively according to the CSI of users to minimize the global transmit power.

3 Adaptive Sub-channel Allocation Algorithm Based on HNN

3.1 Optimization Using HNN

Hopfield and Tank initiated the use of HNN to solve optimization problem in [6]. Since then the HNN model was used in many fields to deal with optimization problems, including the adaptive subcarrier allocation [7]. The HNN is a kind of fully connected recurrent network. Hopfield and Tank introduced the idea of energy function, which was helpful to understand the computation performed by HNN and showed that the combinatorial optimization problem could be solved by the neural networks.

As for the MA allocation problem, each element of the allocation matrix C is mapped into a neuron in the HNN, and the outputs of neurons are the final allocation matrix results if the iteration of the HNN converges. A total of $K \times N = N_0$ neurons are needed to construct the HNN for the MA optimization. The output of the neuron is defined as

$$v_i = g(u_i) = g\left(\sum_{j=1, i\neq j} w_{ij} v_j + b_i\right), \quad v_i \in R^r, \tag{4}$$

where w_{ij} is the connection of the *jth* neuron to the *ith* neuron, u_i and v_i is the input and output of the *ith* neuron respectively, b_i is the threshold value, $g(.)$ is the activation function of neurons, which is often a kind of sigmoid function.

An energy function E is indispensable for the HNN to evolve into its stable states. The energy function is in fact a Lyapunov function. The network performs gradient descent on the Lyapunov function, and the neurons develop into their stable states finally. In general, the problem of minimizing or maximizing the energy function is always converted into the problem of finding the derivative condition of the output state of the neurons. Then the dynamic functions of HNN can be written as [8].

$$\frac{\partial E(u_i, v_i)}{\partial u_i} = -\frac{du_i}{dt}. \tag{5}$$

From the Eq. (5) we can obtain the state function of the HNN for specific applications.

3.2 Algorithm of HNN Based on Sub-channel Allocation

3.2.1 Design of Energy Function

Assume the objective function is $g(u)$, where $u \in R^r$ and it is the state of the Artificial Neural Network (ANN) or the variable of the objective function. The optimization problem can be transformed into the problem of minimizing the objective function with some constraint conditions. Hence the corresponding energy function E is given by

$$E = g(u) + \sum_{i=1}^{N_0} |g_i(u)|, \tag{6}$$

where $|g_i(u)|$ is a kind of constraint function or penalty function. It has been shown that if the activation function is bounded, continuously differentiable and monotonically increasing, eventually the network could converge to a stable point, which is the minimum point of the energy function.

3.2.2 HNN Formulation

After the model mapping, an energy function and its state function of the HNN are constructed. The energy function consists of two parts, which are objective function and constraint function based on the mapped matrix and the constraints. A kind of energy function and dynamic equation have been proposed in [9] by Liu and Jiang. They constructed the energy function only including the column constraints and the row constraints of the mapping matrix were unconsidered and the convergence property could not be guaranteed. Because the row constraints play very important roles on the convergence characteristic of the HNN, the new energy function and dynamic equation which include the row constraints are constructed in this paper. The new energy function is given by

$$\begin{aligned} E = {} & A \sum_{n=1}^{N} \sum_{k=1}^{K} \frac{P}{h_{k,n}^2} c_{k,n} + \frac{B}{2} \sum_{n=1}^{N} \left(\sum_{k=1}^{K} c_{k,n} - 1 \right)^2 \\ & + \frac{C}{2} \sum_{k=1}^{K} \left(\sum_{n=1}^{N} c_{k,n} - M \right)^2 + \frac{D}{2} \left(\sum_{n=1}^{N} \sum_{k=1}^{K} c_{k,n} - N \right)^2. \end{aligned} \tag{7}$$

The first part of Eq. (7) is the objective function, the middle two are the constraint functions, which are column and row constraints, respectively, the last part is the total sub-channel number constraints.

From the equation above, we can derive the dynamic state equation as

$$\frac{dU_{k,n}}{dt} = -A\frac{P}{h_{k,n}^2} - B\left(\sum_{k=1}^{K} c_{k,n} - 1\right) - C\left(\sum_{n=1}^{N} c_{k,n} - M\right) - D\left(\sum_{n=1}^{N}\sum_{k=1}^{K} c_{k,n} - N\right), \tag{8}$$

where the constants A, B, C and D are all positive, and they can be determined through experiments.

Thirdly, the initialization of HNN occurs. The initial output of every neuron can be set as arbitrary little values

$$U_{k,n} = U_0(rand(K, N)), \tag{9}$$

where U_0 is the scaling factor of the activation function of HNN, and rand (K, N) denotes a random $K \times N$ matrix.

Finally, when the above work has been done, the iterative progress for the optimization is much easier. Algorithm 1 shows the detailed steps of the HNN optimization algorithm. The iteration terminates when the algorithm has converged with the difference between the current energy and the previous energy less than a tolerance, or the iteration number is greater than a constant number.

Algorithm 1 Detailed steps of the HNN optimization algorithm.

1: Initialization of the HNN;
2: Calculate the dynamic function, preparing for the iterative optimization based on (8). Utilizing the steepest descend method

$$U(t+1) = U(t) + \mu\Delta U, \tag{10}$$

where μ is the simulation step;
3: Calculate the output of the network, which can be acquired from the follow equation

$$V_{k,n} = g(U_{k,n}) = \frac{1}{2}(1 + tansig(U_{k,n}/U_o)), \tag{11}$$

where $tansig(n) = 2/(1 + exp(-2 * n)) - 1$, which is a neural transfer function;
4: Calculate the energy function (7);
5: Check if the sum of each column is 1. If the sum of each column is 1 then continue, otherwise go to step 2;
6: Check if the sum of each row is M. If the sum of each column is not M, go to step 2, otherwise stop.

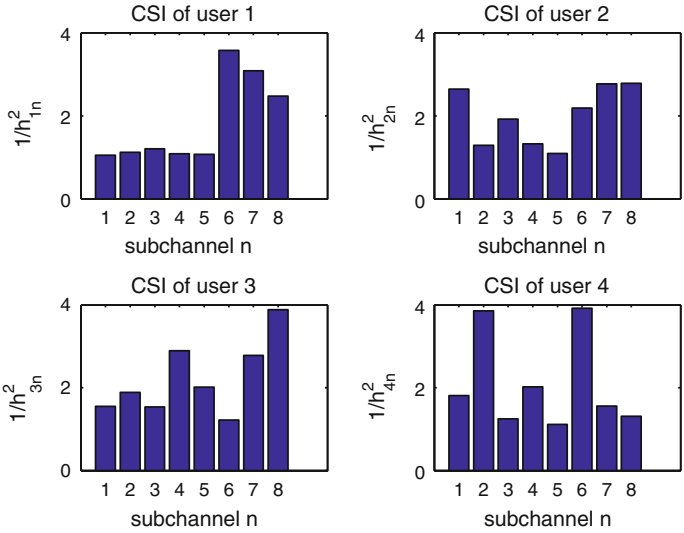

Fig. 1 Snapshot of the channels, $K = 4, N = 8$

4 Numerical Results

Numerical simulations are performed to validate the proposed algorithm. The channel parameters are generated randomly between 0 and 1 with a mean 0.5. There are $K = 4$ users and the sub-channel number N is chosen as 8 and 16 respectively. It can be seen that the channel is frequency selected because of the random nature of the channel factors. The parameters A, B, C, and D are chosen empirically in the simulation. The proposed algorithm can converge almost surely.

A snapshot picture of channel parameters for $K = 4, N = 8$ is illustrated in Fig. 1. The algorithm can converge within less than 100 iterations as shown in Fig. 2 and the state of the network evolves into a stable state quickly. The sub-channel allocation matrix calculated through the HNN algorithm is given in Table 1. In the sub-channel allocation matrix, there are two 1 in each row and only one 1 in each column, which are consistent with the constraints. To validate if the HNN algorithm can find the optimal sub-channel allocation with the minimum sum power, a comparison of the HNN method and the exhaustive method is illustrated in Fig. 3, from which we can see that the minimum total transmit power is found using the proposed HNN method.

As a comparison, the number of calculations using exhaustive method can be formulated as follows:

$$N_{times} = \prod_{i=0}^{K-1} \binom{M}{N - Mi}, \quad M = \frac{N}{K}. \tag{12}$$

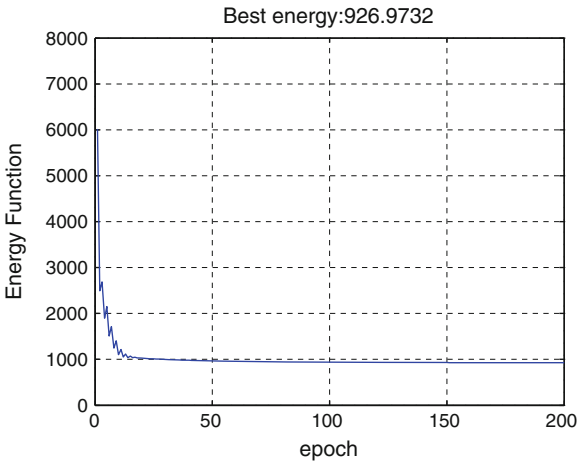

Fig. 2 Convergence curve of energy function, $K = 4,\ N = 8$

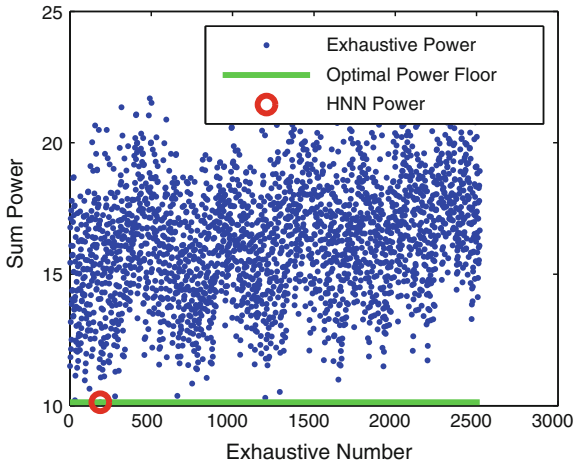

Fig. 3 Comparison of transmit power between the HNN method and the exhaustive method

The number of calculations is much more complicated than the HNN algorithm which can converge within hundreds of steps of iteration. When $K = 4, N = 8$, the number of calculations needed for the exhaustive algorithm is 2,520. When the number of sub-channels or users increases, there will be a great increase in the computational complexity of the algorithm. For example, if $K = 4, N = 16$, the number of calculations needed for the exhaustive algorithm is 8.1730×10^{10}. For $K = 4, N = 16$, the HNN method can still converge within 100 steps iteration as in Fig. 4. The sub-channel allocation matrix for $K = 4, N = 16$ calculated through the HNN algorithm is given in Table 2. Comparing with the results of the two methods above, we can draw a conclusion that the HNN MA method can find the optimal sub-channel allocation with lower computational complexity than the exhaustive method.

Table 1 Results of sub-channel allocation for $K = 4, N = 8$

	N1	N2	N3	N4	N5	N6	N7	N8
User1	1	0	0	1	0	0	0	0
User2	0	1	0	0	1	0	0	0
User3	0	0	1	0	0	1	0	0
User4	0	0	0	0	0	0	1	1

Table 2 Results of sub-channel allocation for $K = 4, N = 16$

	N1	N2	N3	N4	N5	N6	N7	N8	N9	N10	N11	N12	N13	N14	N15	N16
User1	0	0	1	0	1	0	0	1	1	0	0	0	0	0	0	0
User2	0	0	0	0	0	1	0	0	0	0	0	0	0	1	1	1
User3	1	1	0	0	0	0	0	0	0	0	1	1	0	0	0	0
User4	0	0	0	1	0	0	1	0	0	1	0	0	1	0	0	0

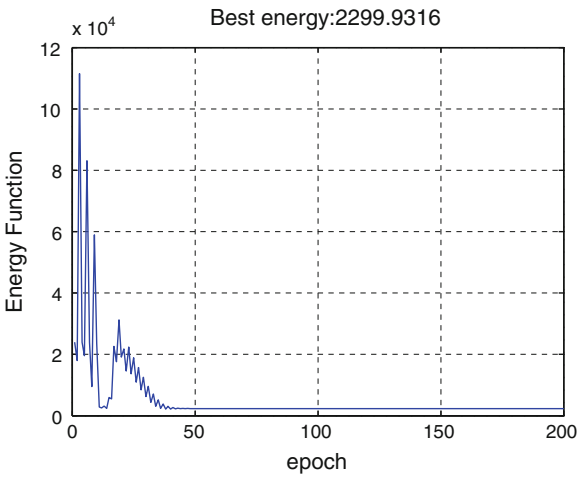

Fig. 4 Convergence curve of energy function, $K = 4, N = 16$

5 Conclusion

A novel minimum transmit power sub-channel allocation algorithm based on HNN is presented in the paper. The MA resource allocation problem for sub-channels of OFDM can be mapped into a kind of combinatorial optimization problem which can be resolved efficiently using HNN. Through this mapping, the energy function for the HNN is constructed. Simulation results show that the proposed algorithm can find the optimal channel allocation with the minimum transmit power almost surely and with lower computational complexity than the exhaustive method. It is believed that the energy function constructing method proposed in this paper could be further used to solve a lot of similar problems related to the resource allocation in wireless communications.

Acknowledgments This work is supported in part by the Natural Science Foundation of Shandong Province (No. ZR2010FM040), and the Graduate Independent Innovation Foundation of Shandong University (GIIFSDU) (No. yzc12071).

References

1. Wang Y, Chen F, Wei G (2005) Adaptive subcarrier and bit allocation for multiuser ofdm system based on genetic algorithm. In: Proceedings of the international communications, circuits and systems conference, vol 1, pp 242–246
2. Jang J, Lee KB (2003) Transmit power adaptation for multiuser ofdm systems. IEEE J Sel Areas Commun 21(2):171–178
3. Wang D, Li Z, Wang X (2012) Joint optimal subcarrier and power allocation for wireless cooperative networks over ofdm fading channels. IEEE Trans Veh Technol 61(1):249–257
4. Sadr S, Anpalagan A, Raahemifar K (2009) Radio resource allocation algorithms for the downlink of multiuser ofdm communication systems. IEEE Commun Surv Tutor 11(3):92–106
5. Shen Z, Andrews JG, Evans BL (2005) Adaptive resource allocation in multiuser ofdm systems with proportional rate constraints. IEEE Trans Wirel Commun 4(6):2726–2737
6. Hopfield J, Tank D (1985) Neural computation of decisions in optimization problems. Bioll Cybern 52(3):141–152
7. Lazaro O, Girma D (2000) A hopfield neural-network-based dynamic channel allocation with handoff channel reservation control. IEEE Trans Veh Technol 49(5):1578–1587
8. Gomez-Barquero D, Calabuig D, Monserrat J, Garcia N, Perez-Romero J (2006) Hopfield neural network—based approach for joint dynamic resource allocation in heterogeneous wireless networks. In: Proceedings of the IEEE 64th vehicular technology Conference, VTC-2006 Fall 2006, pp 1–5
9. Jiang M, Liu Y (2010) Adaptive resource allocation in multiuser ofdm system based on hopfield neural network. J Circuits Syst 15:47–51

CUDA on Hadoop: A Mixed Computing Framework for Massive Data Processing

Zhanghu Wang, Pin Lv and Changwen Zheng

Abstract Data processing can achieve desirable efficiency on a Graphics Process Unit cluster in the Compute Unified Device Architecture (CUDU) environment. However, the storage power and computing power of CUDA in the single-node environment has become the bottleneck of massive data processing. In order to process massive data efficiently in the CUDA environment, a computing framework for massive data processing is provided: CUDA on Hadoop. It combines CUDA and Hadoop that enhances the data throughput of CUDA applications by utilizing the distributed computing technology of Hadoop through a general interface for CUDA applications. In this paper, the details of the design and implementation of CUDA on Hadoop are illustrated as well.

Keywords CUDA · GPU · Hadoop · Massive data · Distributed computing

1 Preliminaries

1.1 Hadoop

Hadoop is an open source distributed computing framework which is organized by Apache Software Foundation. It provides reliable and scalable massive data

Z. Wang (✉) · P. Lv · C. Zheng
Science and Technology on Integrated Information System Laboratory, Institute of Software, Chinese Academy of Sciences, Beijing, China
e-mail: wangzhanghu@gmail.com

P. Lv
e-mail: lvpin@iscas.ac.cn

C. Zheng
e-mail: zhengchangwen@iscas.ac.cn

F. Sun et al. (eds.), *Foundations and Practical Applications of Cognitive Systems and Information Processing*, Advances in Intelligent Systems and Computing 215,
DOI: 10.1007/978-3-642-37835-5_23,

processing. Hadoop consists of two key parts: Hadoop Distributed File System (HDFS) and MapReduce [1].

As the storage of Hadoop, HDFS is characterized by fault-tolerance, massive data capability, and highly access performance [2]. MapReduce is a programming model. The most important concept of MapReduce is dividing the data set into many data splits and processing each data split in a different Map task. All the Map tasks execute parallelly on a large cluster of commodity machines. Then the Reduce tasks merge the outputs of Map tasks and return the final results.

1.2 GPU and CUDA

Compute Unified Device Architecture (CUDA) is a programming environment based on the Graphics Process Unit (GPU) general computing which is proposed by NVIDIA corporation. The GPU cluster makes big progress on efficiency of data processing by parallel computing. In the CUDA environment CPU is the host and GPU is the coprocessor. Both of them work together. CPU is responsible for serial computing tasks which have strong logic and GPU does some parallel computing tasks.

1.3 CUDA on Hadoop

Data processing can achieve desirable efficiency on a GPU cluster in the CUDA environment. However, the storage power and computing power of CUDA in the single-node environment have become the bottleneck of massive data processing. Therefore, CUDA is just used for compute-intensive data processing rather than data-intensive processing.

Hadoop is a distributed computing framework which has massive data storage power and computing power. In order to enhance the data throughput of CUDA applications, we propose a mix computing framework for massive data processing: CUDA on Hadoop. It transplants CUDA to Hadoop and has the massive data processing power for CUDA applications. We also design and implement the general interface for CUDA applications. Therefore, the users can use the framework conveniently.

The organization of the paper is as follows. Section 2 gives an overview of the related work on the combination of distributed computing and the GPU multi-core computing. Section 3 presents the design of the framework in detail. Section 4 explains the implementation of CUDA on Hadoop. The conclusion and the future work are explained in Sect. 5.

2 Related Work

There are mainly two ways to combine the distributed computing and the GPU multi-core computing according to the different implementations and different goals.

2.1 The Combination of MapReduce and CUDA

Hadoop is one kind of open source implementation of MapReduce paradigm and there are different ways to implement MapReduce paradigm. In Ref. [3], a special MapReduce framework named Mars is proposed and implemented. Mars improves the efficiency of data processing obviously by the computing power of MapReduce and it also provides a simple interface which hides the complexity of the programming in the GPU environment.

Phoenix is a distributed framework which is proposed in [4]. It combines MapReduce and the multi-core computing. In Phoenix, every node in the cluster has the multi-core environment instead of the single-core environment. The goal of Phoenix is to process massive data more efficiently. Phoenix has the same interface as Hadoop does.

2.2 The Combination of Hadoop and CUDA

In Ref. [5], the authors propose a method to combine CUDA and Hadoop. They implement the RSA algorithm which can be running parallelly in two levels: thread level and computer level. In the thread level, the parallel RSA algorithm is realized with CUDA and in the computer level the parallel RSA algorithm is running on Hadoop. However, this method is only for RSA algorithm and it is not suitable for other applications. In this paper, our CUDA on Hadoop is different: This framework is not for only one algorithm or one application. It applies for all the CUDA applications (or exactly a class of CUDA applications), and provides a general interface for CUDA programmers. The goal of CUDA on Hadoop is to enhance the data throughput of CUDA applications.

3 The Design of CUDA on Hadoop

3.1 The Comparison of CUDA and Hadoop

Hadoop is a distributed computing framework while CUDA is a parallel computing platform based on GPU. Both of them have many differences. For example,

the data type, the application scenarios, the goals, and so on. Otherwise they have a common character: splitting the data and processing it parallelly. Table1 illustrates the comparison of characters between Hadoop and CUDA.

As we can see in Table1, Hadoop is mainly used for massive data processing in the Internet in which the data exists in the form of text that is unstructured or semi-structured [6]. The data association is weak and each data split can be processed in an independent node in the cluster.

CUDA is mainly used for image processing, graphics rendering, matrix calculation, and so on. The data in these applications is always structured. The data association varies according to different application scenarios. The data which has no association can be processed in different threads within one block while the data which has strong association can synchronize through the shared memory.

The big difference of Hadoop and CUDA is the data throughput. Hadoop gets large data throughput while CUDA gets small one. CUDA on Hadoop is to improve the data throughput of CUDA applications.

The common point of CUDA and Hadoop is splitting the data and processing it parallelly.

3.2 The Principle of CUDA and Hadoop

CUDA on Hadoop deploys the CUDA platform to each node in the Hadoop cluster. Therefore, the Map tasks can run in the CUDA environment instead of the original CPU environment. Because of the supporting of Hadoop, the data throughput of CUDA applications is improved obviously. Figure 1 shows the principle of CUDA on Hadoop. As we can see in Fig.1, HDFS is the storage in the distributed environment. The data is split into many data splits. Each of them is formatted to some records formed as <key, value>. Then the records are processed in the Map task. Each Map task is running in the GPU multi-core environment after the combination of CUDA and Hadoop. So the GPU multi-core environment is embedded in the distributed environment and the data throughput of CUDA applications gets a big improvement.

The common point of Hadoop and CUDA is splitting the data and processing it parallelly. Hadoop splits the input data into equal parts by default. Each data split is 60 MB (the user can change it). Every data split is processed in a Map task.

Table 1 The comparison of Hadoop and CUDA

	Differences			Similarities
	Data type	Data association	Data throughput	
Hadoop	Unstructured or semi-structured	Weak	Large	Splitting the data and processing it parallelly
CUDA	Structured	Strong	Small	

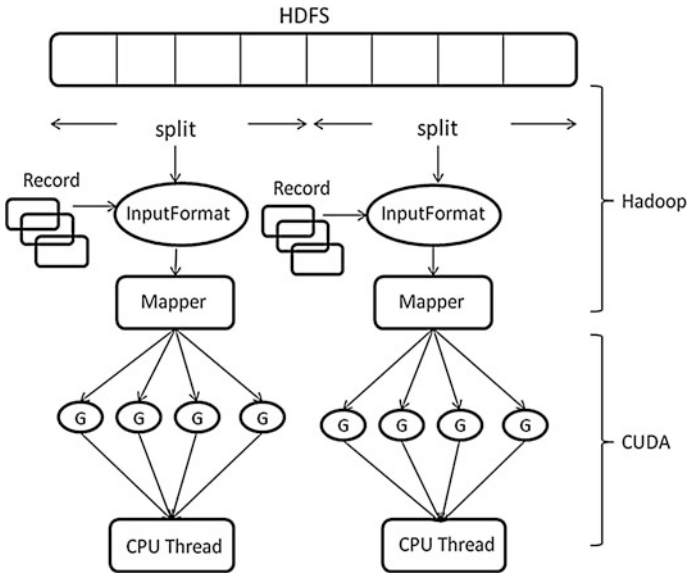

Fig. 1 The principle of CUDA on Hadoop

Then the Reduce tasks collect the outputs of Map tasks and output the final result. In the CUDA environment the data structure and the data splitting are decided by the programmer. Therefore, the data structure and data splitting method differs according to the different applications. In this paper, the framework CUDA on Hadoop takes the CUDA application as a Map task in Hadoop and every Map task executes the same CUDA application.

The goal of CUDA on Hadoop is to provide a general CUDA application interface and improve the data throughput of CUDA applications.

The key problem of achieving the goal is how to input and split the data of CUDA applications. The CUDA application is just a Map task in Hadoop and the input data is a data split which comes from the job of Hadoop in which the data split is 60 MB by default. Because the data in Hadoop is always unstructured and the data association is weak, each data split can be processed in a dependent node in the cluster. However, it is not a right way for CUDA applications because the data in CUDA applications is always structured. Therefore, we must change the default data input and data splitting method in Hadoop.

CUDA on Hadoop is used for the CUDA application. So the data input and data splitting method should be the same as the CUDA application and it is necessary to change the data input and data split method in Hadoop.

In order to provide a general CUDA application interface, CUDA on Hadoop needs to recognize the data splitting method of the CUDA application and then splits the data in the same way as in Hadoop.

In order to solve this problem, we analyze a large number of CUDA applications and sum up the input data model. Then, the input data can be classified in the following three aspects:

Dimension. The frequently used data are one-dimension data and two-dimension data. For example, linear list is one-dimension data and matrix is two-dimension data.

The number of the operand. The common data processing has one or two operands. Especially for two-operand data processing, we need to split both of the operands and make a cartesian product of the data splits of the two operands. Then we get all the pairs of the data splits. At last, we delete the useless pairs by a filtration.

Splitting method. There are lots of splitting methods. For example, equal-part splitting, fixed-size splitting, and so on. Hadoop splits the data in HDFS dynamically according to the data splitting method in CUDA.

CUDA on Hadoop analyze the data format and splitting method from the above classification and split the input data dynamically. It provides a general interface for CUDA applications.

4 The Implementation of CUDA on Hadoop

CUDA on Hadoop gives a general interface toward CUDA programmers. As we can see in Fig.2, the client submits the CUDA program and the input data to CUDA on Hadoop. The CUDA program is running as a Map task and the input data is put into HDFS. CUDA on Hadoop recognizes the data splitting method of the CUDA application and then changes the default data input format of Hadoop to be the same as in CUDA. After that, CUDA on Hadoop distributes the data splits to the Map tasks, which are CUDA applications. CUDA applications are running in the GPU multi-core environment as Map tasks. After all the Map tasks are finished, Reduce tasks collect the outputs and then give the final result to the client.

The implementation of CUDA on Hadoop includes the following three aspects:

The integration of CUDA and Hadoop. Because CUDA on Hadoop need the GPU multi-core environment, each node in Hadoop cluster (except the control node Jobtracker) deploys the CUDA platform. CUDA programs execute as Map tasks in the cluster.

Besides, we need to embed the CUDA program to MapReduce framework by a tool named Hadoop Streaming [7]. Hadoop Streaming can help the user to create and run a special class of Map/Reduce tasks. These Map/Reduce tasks can be executable files or script files. They read the data from the standard input and output the result to the standard output. The executable CUDA program can be a Map task running in Hadoop.

Recognize the data splitting method by the configuration file. In order to split the data of the CUDA program in Hadoop, we need to know the data splitting method in the CUDA environment. To solve this problem, a configuration file written by the CUDA programmer can help. The configuration file presents the data splitting

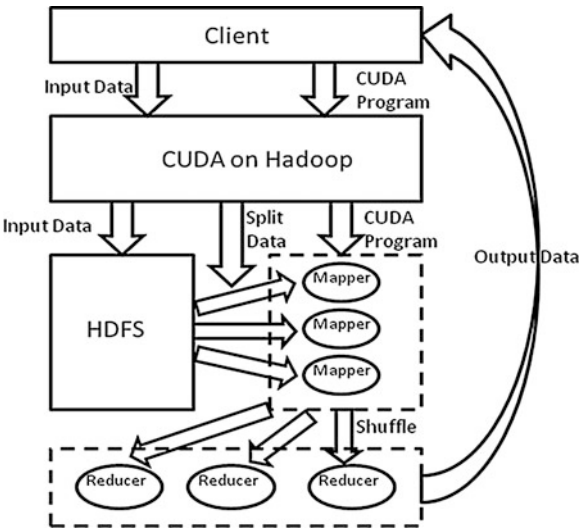

Fig. 2 The data flow of CUDA on Hadoop

method in the CUDA environment. The parameters are just as mentioned in Sect. 3. The CUDA programmer inputs the data dimension, the number of operands and so on. CUDA on Hadoop recognizes the data splitting method through the configuration file and splits the input data in HDFS dynamically.

Change the default input data splitting method by overloading the class InputFormat in Hadoop. Hadoop splits the input data into equal parts by default. Now we need to overload a class in Hadoop named InputFormat, so that we can change the default data splitting method.

InputFormat is responsible for creating the input data splits and dividing them into records. One input data split is processed in one Map task. Each split is divided into some records form as <key, value> and Map tasks process them one by one. The InputFormat interface is as follows [7]:

```
public interface InputFormat<K ,V>{
          InputSplit[]  getSplits  (JobConf  job,  int
numSplits) throws IOException;
          RecordReader<K,       V>       getRecordReader
(InputSplit split, JobConf job, Reporter reporter)

     throws IOException;

}
```

The class InputSplit represents the data split. The function getSplits splits the data. Class RecordReader represents the records (<key, value>) which are separated from the data split. The function getRecordReader implements how to get the records from the data split [7].

The framework CUDA on Hadoop implements the interface again. It gets the data splitting method from the configuration file written by the CUDA programmer

and splits the input data in HDFS dynamically, then gets the data splits and the records. CUDA on Hadoop distributes the executable CUDA program to each node in Hadoop cluster. The CUDA programs process the data splits as Map tasks. After all the Map tasks are finished, Reduce tasks collect the outputs and return the final result to the client. So the CUDA application can run in Hadoop cluster, which makes the data throughput improved obviously.

5 Conclusion and Future Work

CUDA on Hadoop is a mixed computing framework for massive data processing. It provides a general interface toward CUDA applications and achieves the goal of improving the data throughput of CUDA applications. CUDA programmers can expand the data volume conveniently without the MapReduce programming knowledge.

CUDA on Hadoop also have some limitations. Because CUDA applications have a wide range and the data splitting method varies according to different scenarios, the data format summed up in Sect. 3 is not suitable for all the CUDA applications. CUDA on Hadoop is often used for the CUDA application which has explicit data format and data splitting method which can be presented in a configuration file.

The future work is mainly as the following two aspects: First, analyze more CUDA application scenarios and try to find some regular pattern. Then we can detail the data format and the data splitting method information and make the framework that could support more CUDA applications. Second, we will try to get the data information from the CUDA source codes, so that the CUDA programmers do not need to write the configuration file.

References

1. Apache Hadoop, http://hadoop.apache.org/
2. HDFS, http://hadoop.apache.org/hdfs/
3. He B, Fang W, Govindaraju NK, Luo Q, Wang T (2008) Mars: a MapReduce framework on graphics processors. In: Proceedings of the 17th international conference on parallel architectures and compilation techniques, pp 260–269
4. Ranger C, Raghuraman R, Penmetsa A, Bardski G, Kozyrakis C (2007) Evaluating MapReduce for multi-core and multiprocessor systems. In: HPCA'07 Proceedings of the 2007 IEEE 13th international symposium on high performance computer architecture, Washington, DC, USA. IEEE Computer Society, pp 13–24
5. Fan W, Chen X, Li X (2010) Parallelization of RSA algorithm based on compute unified device architecture. In: Proceedings of the 9th international conference on grid and cooperative computing (GCC)
6. Dean J, Ghemawat S (2008) MapReduce: simplified data processing on large clusters. Commun ACM 51(1):107–113
7. White T (2009) Hadoop: the definitive guide, 1st edn. O'Reilly Media, Inc, Sebastopol

Human Appearance Matching Based on Major Color and Spatio-Texture Features Across Disjoint Camera Views

Biao Yang and Guoyu Lin

Abstract Human tracking across disjoint camera views has obtained extensive concern with the increasing use of multi-camera surveillance with non-overlapping camera views. Human appearance matching is the key to continuous human tracking. Accurate human appearance matching among disjoint camera views is difficult due to various factors such as different view angles and illumination change. In this paper a method incorporating major color and spatio-texture features is proposed. Both features used are robust to illumination change. Major color describing global information is robust to the changes in view angles. A subtractive clustering method is used to extract major color representations from each object and then a formulation based on the normalized RGB color distance is proposed to weight the similarity among different major colors. The major color matching is calculated in an anniversary way. For objects owning similar color information, a spatio-texture feature concerning detailed information is exploited for further matching. In this paper, canny operators extracted from selected area are used as textural information. We test our approach indoor, and the results show that this method has successfully achieved a high matching accuracy in spite of general illumination change.

Keywords Human appearance matching · Non-overlapping FOVs · Major color representations · Illumination change

B. Yang (✉) · G. Lin
School of Instrument Science and Engineering, Southeast University, Nanjing, China
e-mail: yb6864171@126.com

F. Sun et al. (eds.), *Foundations and Practical Applications of Cognitive Systems and Information Processing*, Advances in Intelligent Systems and Computing 215,
DOI: 10.1007/978-3-642-37835-5_24,

1 Introduction

Human tracking across non-overlapping field of views (FOVs) is one of the most demanded tasks in computer vision for wide area video surveillance and traffic monitoring because in most cases, it is impossible for a single camera to cover the entire region of interest. Exact human appearance matching is one of the key problems for human tracking across non-overlapping FOVs, which requires accurate feature matching between detected observation which just appears in one camera's FOV and past observations stored in the history database. A history database exists in the camera network to store observations with identity confirmed. Color and texture features are commonly used for matching non-rigid objects. Meanwhile they are robust to different camera view angles and object sizes.

However, the sensitivity of these features to illumination change should be considered, and the complexity of the algorithm taken into account for real-time performance.

A lot of work has been done on features used for matching, but not all of them can be used across disjoint camera views due to illumination change and different camera view angles. Huang and Russell use RGB color histogram with time information for vehicle matching in the highway as in [1]. Color histogram is one of the most popular color features used in object matching; it describes color information of the entire image. However, it is a kind of global feature which ignores geometric characteristics and spatial locations which are important for object recognition. Some methods are based on color histograms like color coherence vector (CCV) proposed by Pass in [2] and Color correlograms proposed by Ojala in [3]. The former extends the color histogram by considering color spatial distributions and the latter depicts the proportions and spatial correlation between different colors. Massimo Piccardi proposes a method of incremental major color spectrum histogram representation (IMCSHR) for object matching across disjoint camera scenes in [4]. Each object is modeled by its major color and then an advanced histogram comparing approach is used to calculate the similarity of different observations. The model built by major color is more accurate than general RGB histograms, however, illumination change existed in disjoint camera views influences the accuracy of appearance matching.

In this paper we propose a method incorporating major color and spatio-texture features together to associate the observations under different camera scenes which share no common area. Supposing A and B are two observations. The overview of our method would be introduced in Sect. 2. For major color feature which is used as a principle cue, the normalized RGB values which are robust to illumination change are adopted for similarity calculating of different major colors. Algorithm of major color matching is raised in Sect. 3. Major color matching rate $M(AB)$ can be calculated if A and B are considered as matched using color information. Meanwhile, for the suspected matching such as different objects owning similar color appearances, the spatio-texture feature based on canny operators is adopted as an assistant. Algorithm of the spatio-texture matching method is introduced in

detail in Sect. 4. Spatio-texture matching rate $S(AB)$ can also be calculated. The final matching rate using our method is $P_{\text{final}}(AB)$ which can be calculated as follows. The weight α is always larger than 0.7 which indicates that the major color cue plays a dominant role in matching. $P_{\text{final}}(AB)$ equals 0 if the suspected matching is denied by spatio-texture matching. Experimental results and conclusions are given in Sects. 5 and 6 respectively.

$$\mathrm{P}_{\text{final}}(AB) = \begin{cases} \alpha * M(AB) + (1-\alpha) * S(AB) & \text{If } S(AB) > T \\ 0 & \text{Else} \end{cases} \tag{1}$$

2 Overview of the Algorithm

Figure 1 shows all the processes of proposed algorithm for human matching across disjoint camera views. Major color and spatio-texture features adopted in this paper are both illumination-tolerant. People to be matched walk indoor arbitrarily under different illuminations and foreground extraction is done using background subtraction method. After the object is extracted well from test videos with little noise and distortion, the major color feature is extracted from this detected object initially. The body of detected human is divided into two parts according to known anatomical proportions, one is clothes part and the other is pants part. Unlike one's head, color information in these two parts is discriminative. Then, a subtractive clustering method based on RGB color space is proposed to obtain major colors of each part. A normalized RGB color distance which is robust to illumination change is adopted to calculate the similarity of different major colors. An advanced color histogram matching method is used to calculate the major color matching rates of two parts. Two thresholds, $\sigma 1$ and $\sigma 2$, are needed for human appearance matching. Suppose r_{MC} is the matching rate acquired by the major color method. If r_{MC} of any part is smaller than the threshold $\sigma 2$ then we could say these two observations are not corresponding. If r_{MC} of both parts are larger than the threshold $\sigma 1$, it is considered that two observations are corresponding. And if r_{MC} of any or both parts are larger than the threshold $\sigma 2$ and less than the threshold $\sigma 1$, it means that the major color information is not enough for accurate human matching, and spatio-texture feature is needed for further matching. The spatio-texture feature is extracted from the selected area which contains abundant textural information. This area is subdivided into nine uniform parts to encode spatial locations. In this paper canny operators are used for textural feature extraction. If the textural matching rate of suspected matched case is larger than a given threshold T, then the suspected matched case is a real matched case.

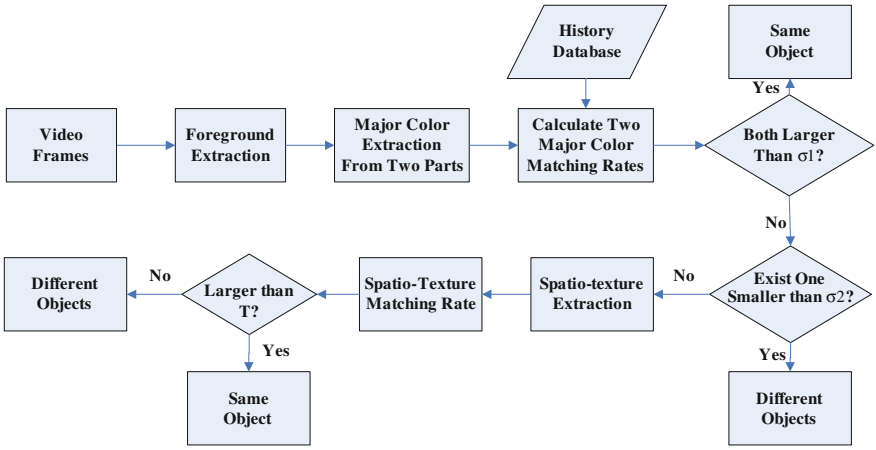

Fig. 1 Flowchart of the proposed algorithm

3 Major Color Matching

Traditional RGB color histograms describe the global feature and thus ignore geometric characteristics and spatial locations which are important for object recognition. HSV in [5] or LUV in [6] are more robust to illumination change than RGB, but the conversion from RGB to HSV or LUV is time wasting and both methods are not discriminative due to low saturation and low value of indoor environment.

This paper proposes a new color feature based on major color. Pixels with similar *R*, *G*, *B* values are merged into clusters and a subtractive clustering method proposed in [7] that pays no attention to initial centers and cluster numbers is adopted to extract several final major colors without losing much accuracy in representing and comparing. Unlike most clustering methods like K-Harmonic clustering method in [8], Fuzzy C-Means clustering method in [9] and Nearest Neighbor clustering method in [10], the subtractive clustering method pays no attention to cluster number and initial centers. Finally, these major colors are represented by histograms whose bins are all of a same and predetermined size, bin colors are determined by *R*, *G*, *B* values of relevant major colors, while bin heights indicate the pixel numbers of major colors. As shown in Fig. 2, major color representations are extracted from the detected person in the red bounding rectangles.

An advanced color histogram matching method is used in this paper for major color matching. It is different from the traditional one like the Bhattacharyya distance method because color number is unknown beforehand. A normalized RGB color distance which is robust to illumination change is proposed to calculate the distances of different major colors.

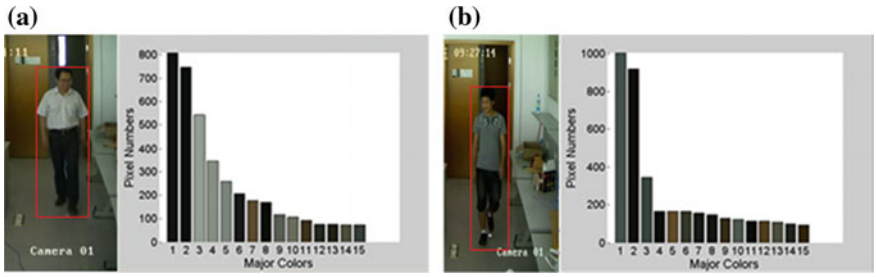

Fig. 2 (**a**) Major color representation of a man with white shirt and black trousers. (**b**) Major color representation of a man with gray T-shirt and gray jeans

We assume that M and N major colors are extracted from objects A and B separately. Major colors in object A can be expressed as $H(A) = \{H(A_1),\ldots,H(A_i),\ldots,H(A_M)\}$, while $H(A_i)$ $(i = 1,2,\ldots,M)$ is one of the major colors in observation A. Each major color of A has a frequency $p(Ai)$, then the frequencies of A can be expressed as $p(A) = \{p(A_1),\ldots,p(A_i),\ldots,p(A_M)\}$.

Similarly, for object B, there are $H(B)$ and $p(B)$ which can be expressed as $H(B) = \{H(B_1),\ldots,H(B_j\},\ldots,H(B_N)\}$ and $p(B) = \{p(B_1),\ldots,p(B_j),\ldots,p(B_N)\}$.

In order to weight the similarity of major colors extracted from different observations, a normalized RGB color distance of major colors H_i and H_j is computed as Eq. 2.

$$d(H_i, H_j) = \Delta r_{ij} * \Delta R_{ij}^2 + \Delta b_{ij} * \Delta B_{ij}^2 + \Delta g_{ij} * \Delta G_{ij}^2 \tag{2}$$

In the above equation Δr_{ij}, Δb_{ij} and Δg_{ij} are differences in the normalized RGB values. They are robust to illumination change because RGB values vary almost conformably under illumination change. ΔR_{ij}, ΔB_{ij} and ΔG_{ij} are differences in RGB values. They are essential in the equation because sometimes different colors own similar normalized RGB values.

Similarity between major color $H(A_i)$ and $H(B)$ can be calculated using color distances of different major colors. Distance of $H(A_i)$ and $H(B_j)$ is calculated using the equation given above and then is compared with a given threshold σ. If the distance is smaller than σ, then we can say $H(B_j)$ is similar to $H(A_i)$. For each major color $H(A_i)$ in observation $H(A)$, a probability $p(A_i|B)$ is calculated based on $H(A_i)$ itself and those major colors which are similar to $H(A_i)$ in $H(B)$. $p(A_i|B)$ is computed as

$$p(A_i\,|B) = \min\left\{ p(A_i), \sum_{d(H_{Ai},H_{Bj})<\sigma} p(B_j) \right\} \tag{3}$$

We can obtain $p(B_j|A)$ can be obtained in the same way as $p(A_i|B)$

$$p(B_j|A) = \min\left\{ p(B_j), \sum_{d(H_{Ai},H_{Bj})<\sigma} p(A_i) \right\} \tag{4}$$

Then major color similarity of $H(A)$ and $H(B)$ in the direction from A to B is given as Sim(A,B)

$$Sim(A,B) = \frac{\sum_{i=1,2,\ldots,M} p(A_i|B)}{\sum_{i=1,2,\ldots,M} p(A_i)} \tag{5}$$

Correspondingly, major color similarity of $H(A)$ and $H(B)$ in the direction from B to A is given as Sim(B,A) which can be calculated in the same way.

Finally, similarity of major color M(A,B) between A and B is determined by the smaller one of Sim(A,B) and Sim(B,A) as follows:

$$M(A,B) = \min\{Sim(A,B), Sim(B,A)\} \tag{6}$$

Humans to be matched in this paper are divided into two parts initially, including clothes part and pants part. Thus, two major color matching rates M_{up} and M_{low} are calculated, respectively, using the above traversal major color matching method. Two thresholds are used for initial matching, including a large one $\sigma 1$ and a small one $\sigma 2$. If two major color matching rates are both larger than $\sigma 1$, then the two objects are matched, and if any one of the two rates is smaller than $\sigma 2$, then the two objects are unmatched. The matching that does not belong to the above two conditions are considered as suspected matched, which need further matching using textural feature.

The major color matching rates of A and B can be represented as $M(AB)$.

$$M(AB) = \begin{cases} \frac{1}{2} * (M_{\text{up}}(A,B) + M_{\text{low}}(A,B)) & \text{If } M_{\text{up}}(A,B) > \sigma 2 \text{ and } M_{\text{low}}(A,B) > \sigma 2 \\ 0 & \text{Else} \end{cases} \tag{7}$$

4 Spatio-texture Feature for Further Matching

For the purpose of further matching, the spatio-texture feature including textural intensity and textural distribution are extracted from the selected area. The selected area is defined as the torso part of people except two arms, because motion artifacts which decrease the accuracy of matching exist in the arms. Assuming bounding rectangle of detected human is H in height and W in width, then according to the average anatomical proportions, the height of selected area is about $0.6H$ to $0.8H$ and width is about $0.2W$ to $0.8W$.

After the selected area is ascertained, canny operation is calculated in selected area. Foreground mask is eroded two times and then make "AND" operation with

canny image to eliminate the influence of outer contours of people. The selected area is divided into nine uniform rectangles to encode spatial information. Nonzero pixels of each uniform rectangle are counted and the textural distribution is represented by a structural histogram with nine bins while each bin indicates nonzero pixel number of one rectangle. Figure 3 shows the results of processed canny images and relevant structural histograms.

The textural intensity is represented by the average number of nonzero pixels in nine uniform rectangles. In Fig. 3a, b, textural intensities are 25.11 and 29.67 respectively.

In this paper, spatio-texture matching rate is calculated based on textural intensity and textural distribution using a weighted method. In order to calculate similarity of textural intensity, distance of two structural histograms is needed. Distance of two structural histograms is calculated using method of Bhattacharya distance represented as Ss(AB).

Similarity of textural intensity is calculated based on the difference of two objects in textural intensity. An approximate range [min, max] of difference in textural intensity is obtained empirically. Supposing the difference of textural intensity of two objects A and B is $d_i(AB)$ which is rescaled to [min, max] initially as follows:

$$d_{\mathrm{i}}(AB) = \begin{cases} \min & d_i(AB) < \min \\ d_i(AB) & \min \le d_i(AB) \le \max \\ \max & d_i(AB) > \max \end{cases} \tag{8}$$

Then the similarity of textural intensity can be calculated as

$$S_i\ (AB) = 1 - \frac{\mathrm{d_i(AB)} - \min}{\max - \min} \tag{9}$$

Spatio-texture matching rate $S(AB)$ can be calculated based on $S_s(AB)$ and $S_i(AB)$ with weight β. β adjusted according to the view angles. A large view angle indicates a small β.

$$S(AB) = \beta * S_{\mathrm{s}}(AB) + (1-\beta) * S_{\mathrm{i}}(AB) \tag{10}$$

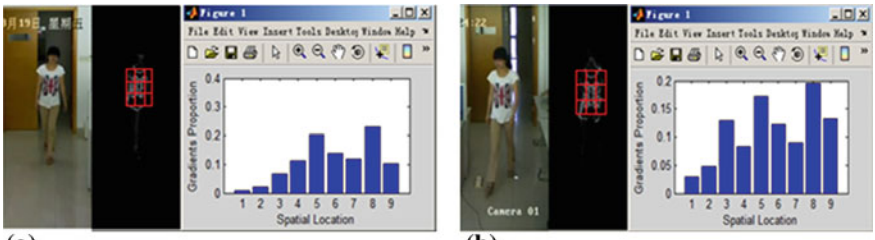

Fig. 3 Gradient image and structural histogram of a girl (**a**) in front door and (**b**) in back door

5 Experiments and Results Analysis

Different experiments were carried out to test the proposed matching algorithm across disjoint camera views. Experiments were done under four different scenes with each scene locating a color camera. The proposed matching algorithm was run in VC++ 6.0 with a P4 2.8 GHz, with the help of OPENCV library.

Humans to be matched are divided into two parts in the proposed algorithm, including clothes part and pants part to encode approximate position information. Figure 4 shows the whole processes of major color matching.

In major color matching experiments, several pairs of objects were used for major color matching. These pairs of objects include the matched and unmatched conditions. They are captured across disjoint camera views, under different illuminations. Thus, general color features are not suitable for appearance matching in such conditions. In our experiments, red rectangle represents the major color matching rate of pants part while the blue circle represents the major color matching rate of clothes. As shown in Fig. 5, the major color matching rates are almost larger than 0.8. For major color matching of unmatched pairs in Fig. 6, one or two low rates, which are always smaller than 0.25, exist. The superiority of our partitioned method over whole-body method is indicated in the ninth pair in Fig. 6; for this pair of observations, major color matching rate of whole-body can achieve 0.892 while matching rates of partitioned method are both smaller than 0.35. The results in both figures indicate the matching ability of proposed major color matching algorithm.

Similar to major color matching experiments, a spatio-texture matching experiment was carried out for further matching of those suspected matched pairs. Figure 7 shows the result of spatio-texture matching experiments. People to be matched own similar color information of clothes (only color information of clothes is considered in experiments) thus it is difficult to distinguish just using the major color information, but the spatio-texture matching rates of these pairs are all smaller than a small value, such as 0.3.

To test the appearance matching ability of proposed algorithm across disjoint camera views, several people walked in the cameras network under different illuminations. The camera network which shares no common area is shown in

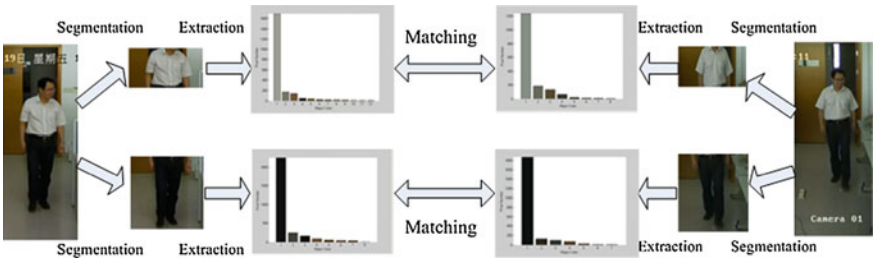

Fig. 4 Major color matching process

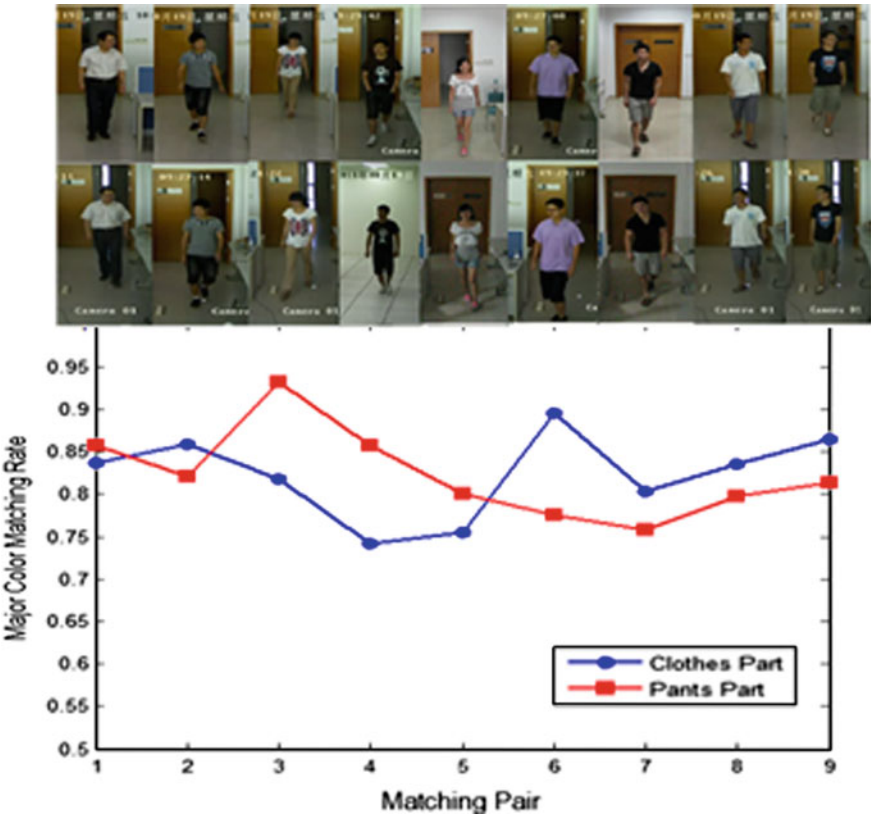

Fig. 5 Major color matching rates of same people

Fig. 8. We give several groups of matching results in Fig. 9. The results indicate that the proposed algorithm can achieve a high appearance matching accuracy. The tracking method used in this paper is the traditional Mean-Shift tracking algorithm as proposed in [11].

The robustness of the proposed algorithm to illumination change was also tested. Twenty observations of people as shown in Fig. 4 are obtained across disjoint camera views and under different illumination conditions like natural light or incandescent lights. We compared our method with other matching methods such as general RGB histograms in [12] and HSV method in [13]. Figure 10 indicates that our method plays well under different illuminations, all matching rates are almost about 0.8–0.9 while matching rates of the other two methods lie approximately between 0.5 and 0.8. HSV plays better than RGB histograms in most cases except in cases of low saturation and low value.

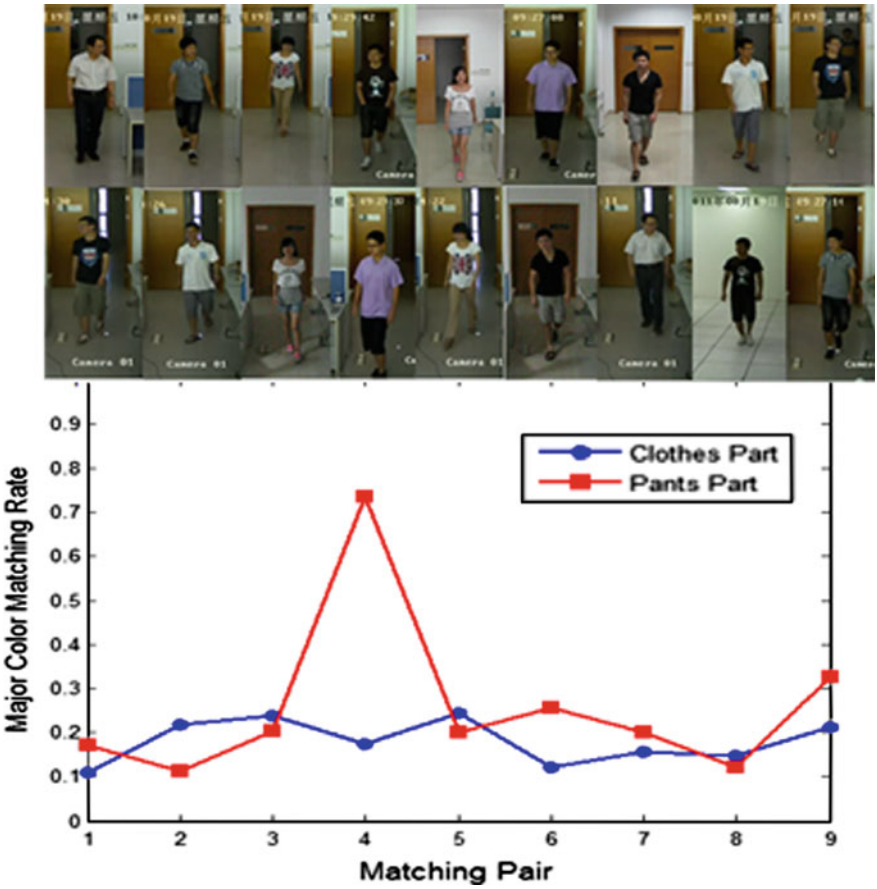

Fig. 6 Major color matching rates of different people

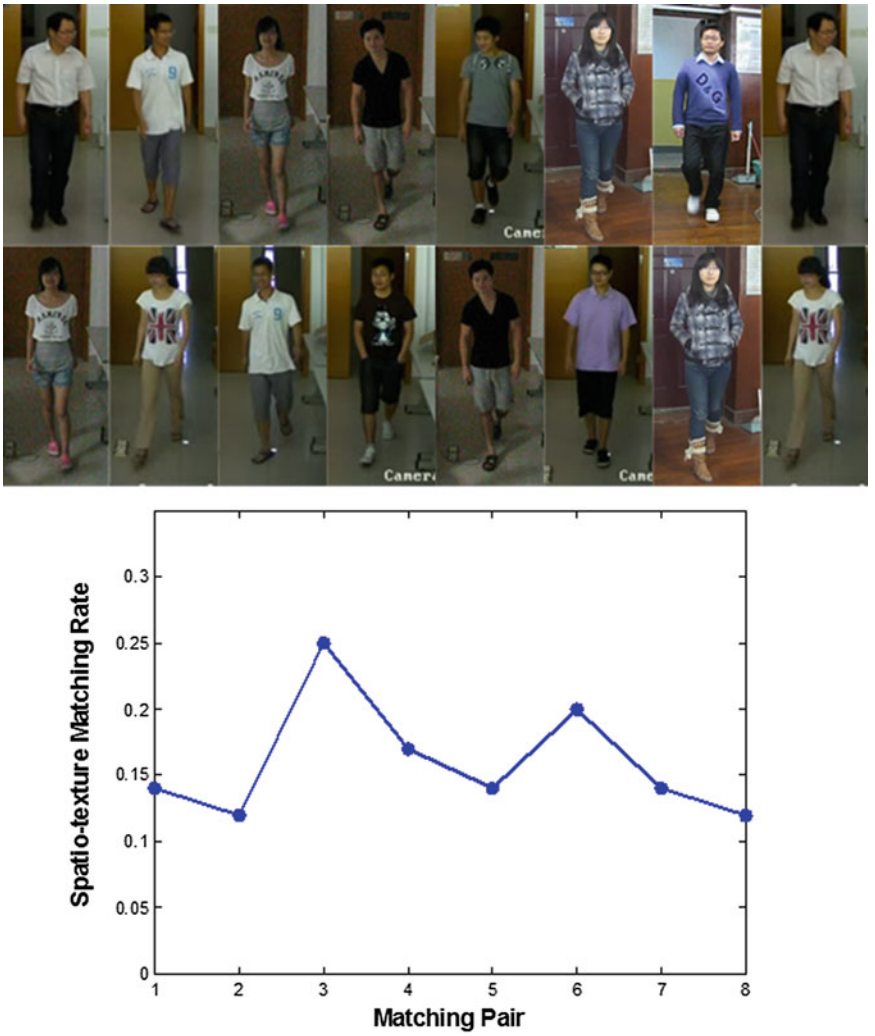

Fig. 7 Spatio-texture matching rates of different people owning similar color information of clothes

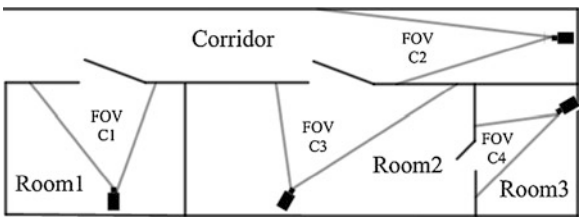

Fig. 8 Cameras network topology in our experiments

Fig. 9 Tracking results of same people from C1–C4

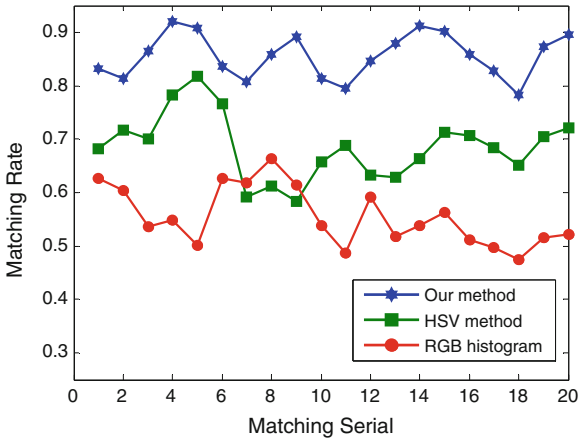

Fig. 10 Robustness to illumination change

6 Conclusions

A new method for human appearance matching across disjoint camera views is proposed in this paper. The contribution of our work focuses on incorporating major color and spatio-texture features together for accurate human appearance matching. The major color matching based on normalized RGB values is used as a

main cue for human appearance matching, while the spatio-texture matching is used as an assistant for the cases of different people owning similar color information. Finally, experimental results show that our method is illumination-tolerant and can achieve a high matching accuracy. Our future work focuses on improving the clustering process and texture features used.

References

1. Huang T, Russell S (1997) Object identification in a Bayesian context. In: International joint conferences on artificial intelligence, Morgan Kaufmann, San Francisco, pp 1276–1682
2. Pass G, Zabih R (1997) Comparing images using color coherence vectors. In: ACM international conference on multimedia. ACM, New York, pp 65–73
3. Ojala T, Rautiainen M (2001) Semantic image retrieval with HSV correlograms. In: 12th Scandinavian conference on image analysin. IEEE Press, New York, pp 621–627
4. Piccardi M, Cheng ED (2005) Track matching over disjoint camera views based on an incremental major color spectrum histogram. In: IEEE conference on advanced video and signal based surveillance, London, pp 147–152
5. Lu YZ, Gao WD, Liu JH (2010) Color matching for colored fiber blends based on the fuzzy c-mean cluster in HSV color space. J Fuzzy Syst Knowl Discov 11:452–455
6. Monari E, Maeker J (2009) A robust and efficient approach for human tracking in multi-camera systems. In: Sixth IEEE international conference on advanced video and signal based surveillance. IEEE Press, Washington, pp 134–149
7. Pan TH, Xue ZK, Li SY (2009) An online multi-model identification algorithm based on subtractive clustering. J Acat Autom Sinica 35:220–224
8. Frackiewicz M, Palus H (2008) Clustering with K-harmonic means applied to color image quantization. In: IEEE international symposium on signal processing and information techonology. IEEE Press, Sarajevo, pp 52–57
9. Zhu YX, Wang YH, Liang HB (2010) A fuzzy C-means clustering based on hybrid color space. In: 2010 International conference on electrical and control engineering. IEEE Press, Wuhan, pp 4605–4607
10. Molina I, Roa LJ, Arrebola F (2000) Hierarchical image segmentation based on nearest neighbour region chains. J Electron Lett 36:1111–1113
11. Li ZY, Liu H, Xu C (2011) Real-time human tracking based on switching linear dynamic system combined with adaptive Meanshift tracker. In: 2011 18th IEEE international conference on image processing. IEEE Press, Brussels, pp 2329–2332
12. Lu YH, Hu J, Huang DC (2006) Study on a image matching algorithm based on sphere similarity of color histogram intersection. J Intell Control Autom 2:9945–9948
13. Huang JG, Kong B (2007) A new method of unstructured road detection based on hsv color space and road features. In: 2007 International conference on information acquisition. IEEE Press, Seogwipo-si, pp 596–606

Fast Image Dehazing Using Fuzzy System and Hybrid Evolutionary Algorithm

Hongjun Song, Yuanyuan Gao and Yangzhou Chen

Abstract A fast approach is proposed for image dehazing using fuzzy system and hybrid evolutionary algorithm through fuzzy contrast enhancement. First, the RGB color space is converted into HSV color space and Gaussian membership function (MF) is used for the fuzzification. Then a parametric sigmoid function is used for the haze image contrast enhancement. Finally, an objective function combining with the entropy and the visual factors is optimal using a hybrid evolutionary algorithm (HEA). HEA is presented based on Partial Swarm Optimization (PSO) algorithm and Genetic algorithm (GA). On comparison, this approach is found applicable for image dehazing and better than the artificial ant colony system (AACS)-based method [1].

Keywords Image dehazing · Fuzzy system · Hybrid evolutionary algorithm · Partial swarm optimization · Genetic algorithm

1 Introduction

Images of outdoor scenes are usually degraded by the turbid medium (e.g., particles, water droplets) in the atmosphere. Haze, fog, and smoke are such phenomena due to atmospheric absorption and scattering. The irradiance received by

H. Song · Y. Chen
Institute of Autonomous Technology and Intelligent Control, Beijing University of Technoloty, Beijing 100124, China
e-mail: songhongjun2001@yahoo.cn

Y. Chen
e-mail: yzchen@bjut.edu.cn

Y. Gao (✉)
College of Information and Engineering, Zhejiang A&F University, Hangzhou, 311300, China
e-mail: gyyshj@yahoo.cn

F. Sun et al. (eds.), *Foundations and Practical Applications of Cognitive Systems and Information Processing*, Advances in Intelligent Systems and Computing 215,
DOI: 10.1007/978-3-642-37835-5_25,

the camera from the scene point is attenuated along the line of sight. Furthermore, the incoming light is blended with the air light [2]. Image dehazing is highly desired in both consumer photography and computer vision applications. First, removing fog can significantly increase the visibility of the scene and correct the color shift caused by the air light. In general, the fog-free image is more visually pleasuring. Second, most computer vision algorithms, from low-level image analysis to high-level object detection, usually assume that the input image (after radiometric calibration) is the scene radiance. The performance of vision algorithms (for instance, feature detection, filtering, and photometric analysis) will inevitably suffer from the biased, low contrast scene radiance.

However, image dehazing is a challenging problem because fog is dependent on the unknown depth information. There are two categories for fog removal, the physical model-based approach, and the approach based on image enhancement method. The success of physical model-based approaches lies in using stronger priors or assumptions. This method is targeted to get the fog effect nature; generally, there will be no loss of information, the key point of the processing is parameters estimated in the model. Tan [3] observes that the fog-free image must have higher contrast compared with the input haze image and he removes the haze by maximizing the local contrast of the restored image. The results are visually compelling but may not be physically valid. Fattal [4] estimates the albedo of the scene and then infers the medium transmission, under the assumption that the transmission and surface shading are locally uncorrelated. However, this approach cannot well handle heavy haze images and may fail in cases that the assumption is broken. He [2] proposes a method for estimating the transmission using dark channel prior in homogeneous fog weather condition. Tare [5] presents a fast fog removal method based on a median filtering approach which is much faster compared to [2, 3, 4]. However, median filtering is not a good edge-preserving filter and inappropriate parameter settings will easily get into the Halo Effect.

Fog image enhancement method does not consider the image degradation reason and has a wide range. It can effectively improve the fog image contrast, to highlight the details of the image, to improve the image of the visual effects, but the prominent part of the information may cause some loss. Fuzzy contrast enhancement is a type of image enhancement method. Kam et al. [6] propose a fuzzy contrast enhancement and parameters are enhanced by trial and error. However, it is likely to cause the enhancement degree differently and over-enhancement in local region. According to the image histogram information and the local neighborhood grayscale information, Cheng et al. [7] present an efficient contrast enhancement algorithm based on fuzzy logic to improve the fog image contrast and suppress the enhance phenomenon. Dhanwan gives the definition of local contrast based on the relative brightness of the image pixel and its neighboring pixels. However, the method may lose detailed information in the large neighborhood. Hanmandlu et al. [8] proposed a fuzzy system for color image enhancement using bacterial foraging (BF). On comparison, this approach is found to be better than the genetic algorithm (GA)-based and entropy-based approaches.

They propose another algorithm using artificial ant colony (AACS) system for optimizing parameters [1].

Partial Swarm Optimization (PSO) algorithm is a type of evolutionary algorithm proposed in 1995 by Kennedy and Eberhart [9, 10]. Many scholars take PSO applied in image enhancement and propose the hybrid PSO model. Angeline [11] introduces selection operator of evolutionary computing in the PSO; Lovbjerg et al. [12] put PSO and GA through fusion, and introduce concepts of breed and population on into the PSO so as to set up two hybrid PSO optimizers and get faster convergence speed.

In this paper we propose a fast approach for image dehazing using fuzzy system and hybrid evolutionary algorithm (HEA) through fuzzy contrast enhancement. HEA is combined with Partial Swarm Optimization (PSO) algorithm and Genetic algorithm (GA). First, the RGB color space is converted into HSV color space and Gaussian membership function (MF) is used for fuzzification. Then a parametric sigmoid function is used for the haze image contrast enhancement. Finally, an objective function combing with the entropy and visual factors is optimal using HEA. On comparison, this approach is found applicable for image dehazing and better than the artificial ant colony system (AACS)-based method [1].

The organization of the paper is as follows. Section 2 describes fuzzification, intensification, and enhancement. Section 3 introduces fuzzy measures and objection optimization with HEA. Results and analysis is discussed in Sect. 4 and conclusions are drawn in Sect. 5.

2 Fuzzification, Intensification, and Enhancement

Fuzzy set theory-based approach is a useful tool to deal with the issue of uncertainty mapping by three-dimensional space to the 2D plane to essentially determine the image memory for the solution of practical problems. Therefore, in recent years more and more domestic and foreign researchers of fuzzy theory are applied to the field of image processing, and achieved satisfactory results. In this paper we propose a fast approach for image dehazing using fuzzy system and hybrid evolutionary algorithm (HEA) through fuzzy contrast enhancement.

In different fog conditions, the degree of image degradation is different; the distribution of gray levels is different which are mostly set to the middle and bright parts and less in the dark part pixel. When the fog condition is more serious, the image degradation is more severe and the gray histogram distribution range is narrower. In order to reduce the impact on the histogram distribution range by different fog conditions, the grayscale range of the input image standardization is necessary. Using Formula (1) standardizing brightness to [0255].

$$v_{mn} = 255 \times (v_{0mn} - v_{0\min})/(v_{0\max} - v_{0\min}) \tag{1}$$

where v_{0mn} is the gray value of input image at point (m, n), $v_{0\max}, v_{0\min}$ are the biggest and smallest gray values of input image.

An image of size $M \times N$ in RGB converted into HSV having intensity levels v_{mn} in the range [0, $L-1$], can be considered as a collection of fuzzy singletons in the fuzzy domain. Accordingly, the fuzzy representation of an image is

$$\begin{aligned} I &= \cup\{\mu(v_{mn})\} = \{\mu_{mn}/v_{mn}\} \\ m &= 1, 2, 3 \ldots M; \quad n = 1, 2, 3 \ldots N \end{aligned} \tag{2}$$

where M and N are the number of rows and columns, respectively, of an image matrix, $\mu(v_{mn})$ or μ_{mn}/v_{mn} denotes the membership function (MF) μ_{mn} of some property. v_{mn} denotes the color intensity at the (m, n)th pixel. To increase the speed of computation, the histogram of V is considered for fuzzification instead of taking the intensity level [8].

Next, use 'S' type membership function for standardization in [0,1]. The function is as follows:

$$\mu(v_{mn}) = \begin{cases} 0, & 1 \le v_{mn} \le a \\ \dfrac{(v_{mn} - a)^2}{(b-a)\cdot(c-a)}, & a < v_{mn} \le b \\ 1 - \dfrac{(v_{mn} - c)}{(c-b)\cdot(c-a)}, & b < v_{mn} \le c \\ 1, & v_{mn} > c \end{cases} \tag{3}$$

where a, b, and c decide the function shape, v_{mn}, $\mu(v_{mn})$ are the values before and after the fuzzification respectively. Parameters a and c are confirmed by the two endpoint values of the statistic histogram of the image after standardization. Parameter b is confirmed through computing the biggest fuzzy entropy to obtain the optimal value. Formula (3) is described as follows:

$$b = \arg\max\{En(v_{mn}; a, b, c) \,|0 \le a < b \le 255\}. \tag{4}$$

We use sigmoid function to transform membership so as to enhance image fuzzy contrast. The formula is as follows:

$$\mu'(v) = \left\{ \frac{1}{1 + e^{-t(\mu(v) - \mu_c)}} \right\} \tag{5}$$

where t is the intensification parameter and μ_c is the crossover point of the foggy image. In the next section we will describe the objection function and indicate how to decision and optimal parameters such as t, μ_c and b.

3 Fuzzy Contrast Measure

We use concepts of fuzzy contrast, average fuzzy contrast, and visual factor proposed by Hanmandlu [1]. Definitions of the quality factor and visual factor are described in detail in [1].

The fuzzy contrast for the image is given by

$$C_f = \frac{1}{L} \cdot \sum_{v=0}^{L-1} (\mu'(v) - \mu_c)^2. \tag{6}$$

The average fuzzy contrast for the image is as follows:

$$\bar{C}_f = \frac{1}{L} \cdot \sum_{v=0}^{L-1} (\mu'(v) - \mu_c) \tag{7}$$

The initial fuzzy contrast and average fuzzy contrast before conversation are shown:

$$C_{af} = \frac{1}{L} \cdot \sum_{v=0}^{L-1} (\mu(v) - \mu_c)^2 \tag{8}$$

$$\bar{C}_{af} = \frac{1}{L} \cdot \sum_{v=0}^{L-1} (\mu(v) - \mu_c) \tag{9}$$

The quality factor Q_f and the initial quality factor Q_{af} are defined as

$$Q_f = \left| \frac{\bar{C}_f}{C_f} \right| \tag{10}$$

$$Q_{af} = \left| \frac{\bar{C}_{af}}{C_{af}} \right| \tag{11}$$

Then the visual factor is given by:

$$V_f = \frac{Q_{af}}{Q_f} \tag{12}$$

Entropy that makes use of Shannon's function is regarded as a measure of quality of information in an image in the fuzzy domain [8]. It gives the value of indefiniteness of an image defined as

$$E = \left(-\frac{1}{L \ln 2} \right) \left(\sum_{v=0}^{L-1} \mu'(v) \ln(\mu'(v)) + (1 - \mu'(v)) \ln(1 - \mu'(v)) \right) \tag{13}$$

The objective function is as follows:

$$J = E + \lambda \left| V_f - V_{sf} \right| \tag{14}$$

V_{sf} is the desired visual factor.

4 Objection Optimization based on HEA

The basic idea is: initialization parameters, all parameters to form a chromosome, initial population to real coding, and each individual evaluation in accordance with the predetermined objective function, to give a fitness value, and sort in accordance with the fitness value. Then abandon particles of the low-value adapt degree according to the abandon probability and give the retained particles particle swarm algorithm operation. Select a certain number of individuals from the current retained individuals with a selection strategy, and give them a cross and mutation operation, respectively, resulting in crossover and mutation offspring. Then the offspring replaces the parent to form a group to form the next generation of groups. Repeat finally to get a good individual. Denote p as the abandon probability and *popsize* as the size of population. The algorithm flowchart of HEA is as follows:

Step 1 Initial particle swarm;
Step 2 Calculate the fitness value of each particle;
Step 3 Sort each particle according to the fitness value and discard the particles with smaller fitness value $popsize * p$;
Step 4 Give the PSO operator to the retained particles $popsize * (1 - p)$;
Step 5 Select $popsize * p$ to give the crossover and mutation operators from $popsize * (1 - p)$ particles;
Step 6 Combine with particle swarm re-experienced the operators of the two algorithms for a particle swarm whose size is *popsize*;
Step 7 If not reach the end conditions, go to step 2; otherwise output the current global particle position as the optimal solution (Fig. 1).

5 Experimental Results

We use our approach for image dehazing using fuzzy system and hybrid evolutionary algorithm (HEA) through fuzzy contrast enhancement. Figures 2, 3, and 4 show our image dehazing results.

In Figs. 2–4 we compare our approach with He's work and the AACS-based method. The colors of He's results recover the structures without sacrificing the fidelity of the colors and the halo artifacts are also significantly small in his results. It may not work for some particular images. When the scene objects are inherently similar to the atmospheric light and no shadow is cast on them, the dark channel prior is invalid [2]. See Figs. 5.

Fig. 1 Algorithm flowchart

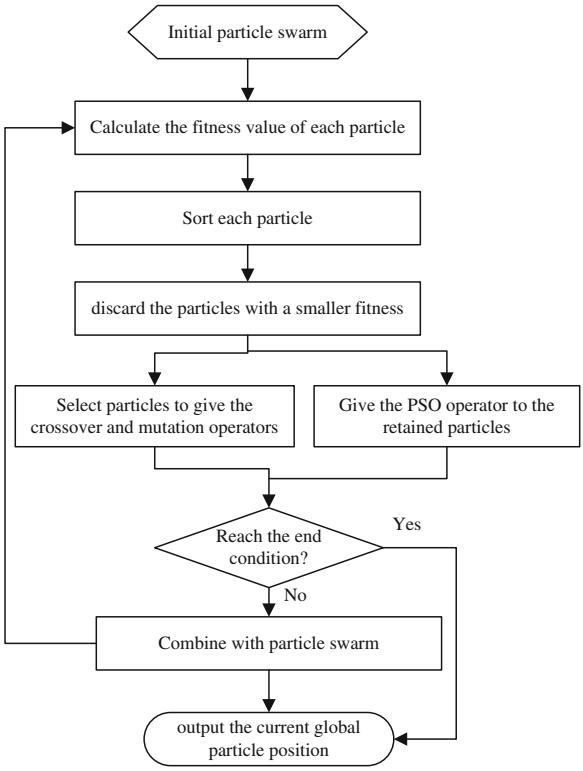

Next, we compare our approach with AACS-based method. For the results of AACS-based method see Fig. 2c–4c. By contrast, we can see that our approach works better than that method.

6 Conclusions

In this paper we propose a fast approach for image dehazing using fuzzy system and hybrid evolutionary algorithm (HEA) through fuzzy contrast enhancement. The concept of dynamic abandoned factor in the HEA is introduced to solve random problems, the convergence speed, and save resources. It improves the search capability and stability, and obtains the optimal or approximate optimal solution, avoids the time cost, and the non-intelligent human intervention. On comparison, this approach is found applicable for image dehazing and better than the artificial ant colony system (AACS)-based method.

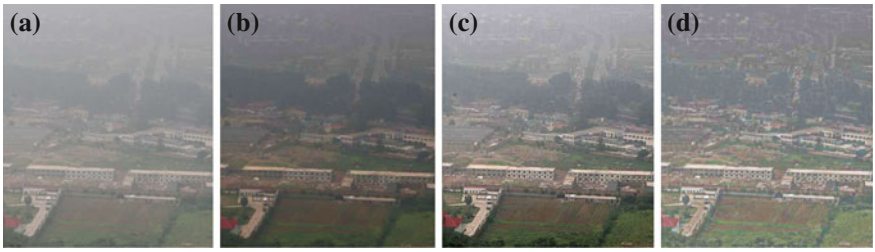

Fig. 2 Example 1 (**a**) Original images (**b**) He's method (**c**) AACS-based method (**d**) Our method

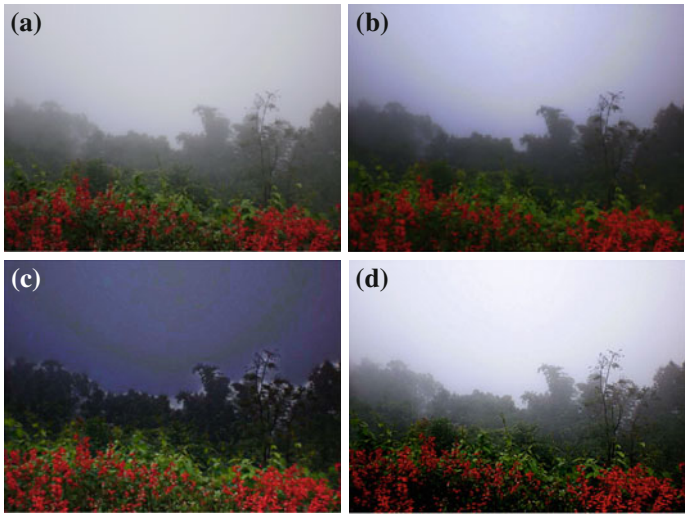

Fig. 3 Example 2 (**a**) Original images (**b**) He's method (**c**) AACS-based method (**d**) Our method

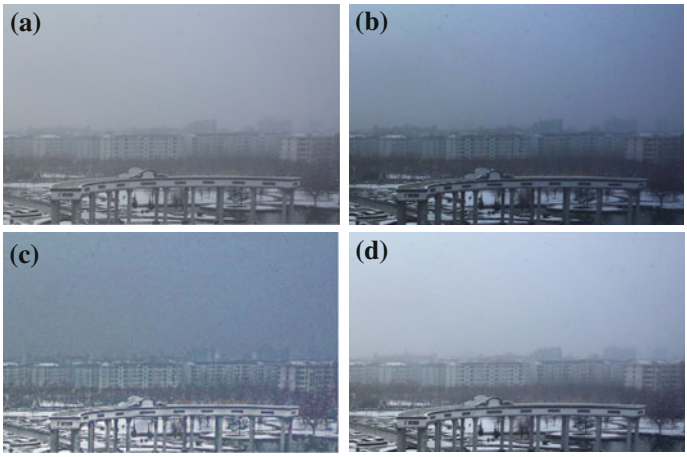

Fig. 4 Example 3 (**a**) Original images (**b**) He's method (**c**) AACS-based method (**d**) Our method

Fig. 5 Example 4 (**a**) Original image (**b**) He's method (**c**) Our method

Acknowledgments This work is supported by the National Natural Science Foundation of China (No. 61079001), China's 863 Program (No. 2011AA110301), China's PH.D. Program Foundation (No. 20111103110017).

References

1. Verma OP, Kumar P, Hanmandlu M et al (2012) High dynamic range optimal fuzzy color image enhancement using artificial ant colony system. Appl Soft Comput 12(1):394–404
2. He K, Sun J, and Tang X (2009) single image haze removal using dark channel prior. In: Proceedings on 2009 IEEE computer society conference on computer vision and pattern recognition (CVPR), pp 1956–1963
3. Tan R (2008) Visibility in bad weather from a single image, CVPR
4. Fattal R (2008) Single image dehazing. In: SIGGRAPH, pp 1–9
5. Kam Y, Hanmandlu M (2003) An improved fuzzy image enhancement by adaptive parameter selection [J]. In: IEEE International conference on systems, man and Cybemetics, 2(5–8):pp 2001–2006
6. Cheng H, Xu H (2000) A novel fuzzy logic approach to contrast enhancement [J]. Pattern Recogn 33(5):809–819
7. Dhnawan AP, Buelloni G, Gordon R (1986) Enhancement of mammographic features by optimal adaptive neigh borhood image processing [J]. IEEE Transaction on Medica Imaging 5(1):8–15
8. Hanmandlu M, Verma OP, Kumar NK, Kulkarni M (2009) Anovel optimal fuzzy system for color image enhancement using bacterial foraging[J]. IEEE Trans Instrum Meas 58(8):2867–2879
9. Kennedy J, Eberhart R (1995) Particle swarm optimization. In: Proceedings of IEEE international conference on neural networks, pp 1942–1948
10. Eberhart R, Kennedy J (1995) A new optimizer using particle swarm theory. In: Proceeding of the 6th international symposium on micro-machine and human science, pp 39–43
11. Angeline P. Using selection to improve particle swarm optimization. Proceedings of IEEE International Conference on Evolutionary Computation, 84-89 (1998)
12. Lovbjerg M, Rasmussen T, Krink T (2001) Hybrid particle swarm optimizer with breeding and subpopulations. In: Proceedings of genetic and evolutionary computation conference, 2001,pp 469–476

Anti-Interference Performance Improvement Using Probability Control in Cognitive CDMA Communication System

Sheng Hong, Bo Zhang and Hongqi Yang

Abstract Cognitive code division multiple access (CCDMA) systems commonly use power control to reduce the interference between the users. But the power control is not always optimal. Probability control is a recently introduced method that allows better mitigation of multiple access interference in CCDMA networks. In this paper, we apply the probability control to CCDMA system. It was found that the performance reflected by the signal to noise plus interference ratio (SINR) resulting from probability control is better than the one resulting from power control by some simulation results.

Keywords Probability control · CCDMA · Communication system · SINR

1 Introduction

Direct sequence code division multiple access (DS-CDMA) systems that use non-continuous transmission were considered throughout the history of CDMA systems. References present the existing research focuses on probability control [1–4]. Itsik Bergel [2] has demonstrated a CDMA system which has an optimal probability control over an AWGN channel is probability controlled optimal, and they draw a conclusion that any CDMA system design must consider the

S. Hong (✉) · H. Yang
School of Reliability and System Engineering, Beihang University, Beijing, China
e-mail: fengqiao1981@gmail.com

H. Yang
e-mail: yang13161322@sina.com

B. Zhang
School of Electronics and Information Engineering, Beihang University, Beijing, China
e-mail: bozhang@buaa.edu.cn

F. Sun et al. (eds.), *Foundations and Practical Applications of Cognitive Systems and Information Processing*, Advances in Intelligent Systems and Computing 215,
DOI: 10.1007/978-3-642-37835-5_26,

implementation of a probability control mechanism. The analysis showed that the presented probability controlled system can operate in severe near far scenarios, in which power controlled systems are completely jammed.

The high anti-interference requirements on downlink throughput in CDMA systems, especially in Wideband CDMA had motivated many works [5]. With the rapid proliferation of a variety of consumer oriented wireless devices, demand for access to radio spectrum has been growing dramatically, but much of the pre-licensed radio spectrum experiences low utilization. Cognitive radio (CR) is an emerging technology aiming at improving spectrum utilization efficiency by allowing secondary users/networks to opportunistically share radio spectrum originally licensed by primary users/networks without causing harmful interference to them [6, 7]. The user cooperation concept used in CR system had been studied in CDMA communication system [8, 9]. The existing works mainly concentrate on power control in CCDMA [10–15]. Farrokh Rashid-Farrokhi proposed joint power allocation and user-to-base assignment, which generally termed as multiple base power control in [10]. In [11], the author proposed a distributed resource allocation (DRA) algorithm that considers the subchannel and power allocation comprehensibly. Although the power control has obtained some achievements, it is not always optimal, and typically systems performance is limited by the MAI [15].

It is difficult to adjust the transmit power according to the change of channel condition in fast fading channel or when the users are in a fast moving state, and even when the interference is small, we usually use large transmit power to suppress the interference, which results in the waste of energy. Replacing the power control with the control of the pulse strength (another form of transmission probability) can suppress the interference more effective [16–18], and most cognitive users are power-constrained. So we study on the application of the probability control in CCDMA. In the CCDMA communication system, there are two kinds of users: the licensed user and the cognitive user. The communication scenario we studied is presented in Fig. 1. Both of the cognitive user and licensed user can receive the interest signal and interference signal from the base station and the other users, and we analysis the performance of CCDMA communication system through numerical simulation results under the probability control.

2 System Model of Probability Control

In this paper, the CDMA communication system which implements non-continuous transmission via including the zero in the spreading sequences is used. In this way, the system model is presented in Fig. 2. So the spreading sequence $c_{k,d,v}$ may contain zero and non-zero elements.

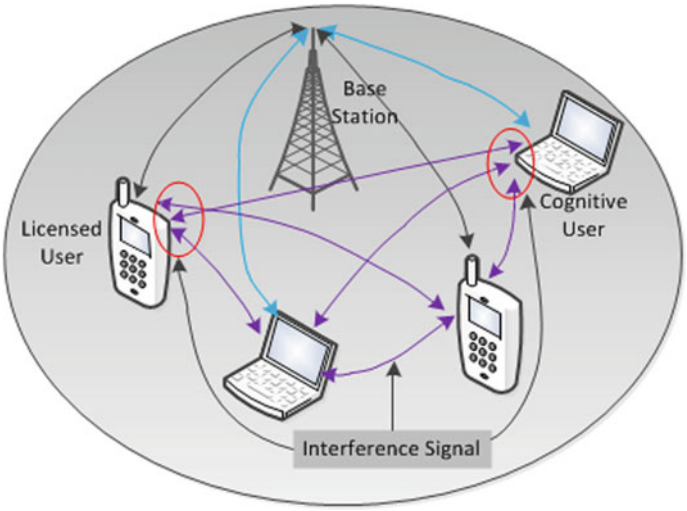

Fig. 1 The communication scenario of CCDMA

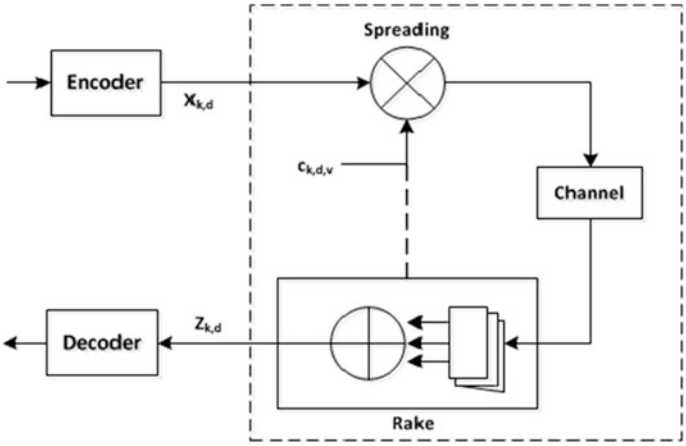

Fig. 2 The system model of code division multiple access system

We assume that the spreading sequence of licensed user is binary sequence. The spreading sequence of cognitive user is ternary sequence. The transmitted signal of the *k*th cognitive user is defined as follows,

$$s_k(t) = \sqrt{E_{k,d}} \sum_{d} x_{k,d} \sum_{m=0}^{N_1-1} c_{k,d,m}\, p(t - (d N_1 + v)\, T_c) \tag{1}$$

where $p(\ t)$ is the transmitted pulse shape, $E_{k,d}$ is the dth data symbol of kth cognitive user's chip energy, Tc is the chip time, N1 is the spreading factor, $x_{k,d}$ is

the dth data symbol of kth cognitive user, $c_{k,d,m}$ is the spreading sequence of kth cognitive user, $c_{k,d,m} \in \{+1, 0, -1\}$.

We assume there is a frequency-selective slow-fading channel model. The interest signal received by the kth receiver is as follows,

$$r_k(t) = \sum_{i=1}^{K} \int_{-\infty}^{\infty} h_{k,j}(\tau)\, s_j(t-\tau)\mathrm{d}\tau + n_k(t) \tag{2}$$

where $h_{k,j}(\tau)$ is the impulse response of the channel from the jth transmitter to the kth receiver, K is the number of the cognitive users, and $n_k(t)$ is the noise measured by the receiver, modeled as white Gaussian noise with spectral density $N_0/2$.

The kth user employs a RAKE receiver with L_k fingers. Each finger uses a spreading waveform correlator to dispread the signal for each symbol. Because of the unideal correlation properties of the spreading sequence of the licensed user and cognitive user, the received signal of cognitive user will contain the interference term. We can write the vector of RAKE finger output of cognitive user as follows,

$$y_{k,d} = \mu_{k,d}\, x_{k,d} + M_{k,d} \tag{3}$$

where $\mu_{k,d} = \sqrt{E_{k,d}}\ r_{k,k,d,d}$ is a vector of gains corresponding to the symbol of interest. $r_{k,k,d,d}$ is the interest signal received by the kth receiver, and $r_{k,j,a,d}$ is the interference received by the kth cognitive user when it receives the ath data symbol caused by the dth data symbol of jth cognitive user. It can be expressed,

$$r_{k,j,a,d} = \sum_{q=0}^{N_j-1} \sum_{i=0}^{N_k-1} c_{j,a,q}\, c_{k,d,i} f_{q,i} \tag{4}$$

where,

$$f_{q,i} = \int_{-\infty}^{\infty} h_{k,j}(\zeta)\, R_p\big(\tau_{kl} - \zeta + \big(d\,N_k + i - a\,N_j - q\big)\, T_c\big)\mathrm{d}\zeta \tag{5}$$

$c_{j,a,q}$ and $c_{k,d,i}$ are the spreading sequences of the cognitive user on the transmitting terminal and receiving terminal respectively, $R_p(t)$ is the autocorrelation function of $p(t)$, $\mathrm{Pr}_{k,j,a,d}$ is the interference received by the kth cognitive user when it receives the ath data symbol caused by the dth data symbol of jth licensed user.

So the noise plus interference part can be expressed as,

$$\begin{aligned} M_{k,d} = &\sum_{j\neq k} \sum_{a} \sqrt{E_{j,a}}\, x_{j,a}\, r_{k,j,a,d} + \sum_{a\neq d} \sqrt{E_{k,a}}\, x_{k,a}\, k, k, a, d \\ &+\ n_{k,d} + \sum_{j} \sum_{a} \sqrt{Q_{j,a}}\, x_{j,a}\, \mathrm{Pr}_{k,j,a,d} \end{aligned} \tag{6}$$

$Q_{j,a}$ is the chip energy of licensed user. We can get that the noise plus interference term is a random vector with zero mean and the covariance matrix is,

$$\sigma_{k,d} = \sum_{j \neq k} \sum_{a} E_{j,a}\, r_{k,j,a,d}\, r_{k,j,a,d}^{T} + \sum_{a \neq d} E_{k,d}\, r_{k,k,a,d}\, r_{k,k,a,d}^{T} + \sum_{j} \sum_{a} Q_{j,a}\, \mathrm{Pr}_{k,j,a,d}\, \mathrm{Pr}_{k,j,a,d}^{T} \tag{7}$$

Denoting the weight vector by $w_{k,d}$, the decision variable is described,

$$e_{k,d} = w_{k,d}^{T}\, y_{k,d} \tag{8}$$

so the SINR achieved for the reception of the dth symbol by the kth user can be derived as follows,

$$\mathrm{SINR}_{k,d} = \frac{E\left[e_{k,d}\right]^{2}}{VAR\left[e_{k,d}\right]} = \frac{w_{k,d}^{T}\, \mu_{k,d}\, \mu_{k,d}^{T}\, w_{k,d}}{w_{k,d}^{T}\, \sigma_{k,d}\, w_{k,d}} \tag{9}$$

The type of receiver we used is minimal mean square error (MMSE) RAKE receiver. The optimal weight vector is given by [19],

$$w_{k,d} = \sigma_{k,d}^{-1}\, \mu_{k,d} \tag{10}$$

substituting the weight vector (9), back in the expression for the SINR (8), we can get,

$$\mathrm{SINR}_{k,d} = \frac{\left(\sigma_{k,d}^{-1}\, \mu_{k,d}\right)^{T}\, \mu_{k,d}\, \mu_{k,d}^{T}\, \sigma_{k,d}^{-1}\, \mu_{k,d}}{\left(\sigma_{k,d}^{-1}\, \mu_{k,d}\right)^{T}\, \sigma_{k,d}\, \sigma_{k,d}^{-1}\, \mu_{k,d}} = \mu_{k,d}^{T}\, \sigma_{k,d}^{-1}\, \mu_{k,d} \tag{11}$$

In this paper, the optimization object is the SINR of each cognitive user. According to the condition of coexistence and the constraints of the spreading sequence, we can conclude the optimization problem as follows,

$$\begin{array}{lll} \max\limits_{i} & \mathrm{SINR}_{i}, & i = 1, \ldots, K \\ s.t. & I_{j} < \gamma_{j}, & j = 1, \ldots, J \\ & & \mathrm{SINR}_{i} > \rho_{i} \\ & & 1 > p_{i} > 0 \end{array} \tag{12}$$

where,

$$I_{j,a} = w_{j,a}^{T}\, P\sigma_{j,a}\, w_{j,a} \tag{13}$$

$$P\sigma_{j,a} = \sum_{k} \sum_{d} E_{j,a}\, \mathrm{Pr}_{k,j,a,d}\, \mathrm{Pr}_{k,j,a,d}^{T} \tag{14}$$

I_j is the interference caused by cognitive users to jth licensed user, γ_i is the threshold value for the interference not to affect the licensed user, ρ_i is the minimum value for the cognitive user to satisfy the quality of service, p_i is the transmission probability of the ith cognitive user, which is related to the spreading sequence (namely $c_{k,d}$, $c_{j,a}$) it uses. We can obtain the optimal solution by calculating the correct transmission probability and finding the corresponding spreading sequence.

Assuming each transmitter only transmits one symbol each time, which contains N1 chips. Then the transmission probability of the transmitter is equal to the transmission probability of the spreading sequence. We can optimize the SINR of each cognitive user using probability control mechanism to optimize the spreading sequence.

When $K > 2$, it is a multi-objective optimization problem. So we can use the Pareto optimization criterion to solve the problem according to the existing research [2, 20–22]. We can obtain the weak Pareto solutions under the probability control mechanism. The proposed algorithm can be described as follows.

Step 1. Initialization. **G** is solution space, including the whole possible solution $\mathbf{g_i} = (\mathbf{g_{i1}},\mathbf{g_{i2}})$. **S** is Pareto optimal solution set. $\mathbf{s_j} = (\mathbf{s_{j1}},\mathbf{s_{j2}})$ is the element of the set S, and it is initialized to be empty.

Step 2. Judgment 1. If the set of G is empty, jump to Step 6.

Step 3. Search. Taking out a possible solution $\mathbf{g_i}$ from **G** and compare it with all the Pareto solutions $\mathbf{s_j}$ in **S**.

Step 4. Judgment 2. If $\mathbf{s_{j1} < g_{i1}}$ and $\mathbf{s_{j2} < g_{i2}}$, then $\mathbf{s_j}$ is worse than $\mathbf{g_i}$, we remove $\mathbf{s_j}$ from **S**. For all the solutions $\mathbf{s_k}$ in S, If $\mathbf{g_{i1} > s_{k1}}$ or $\mathbf{g_{i2} > s_{k2}}$ (cannot be true at the same time), then $\mathbf{g_i}$ is noninferior solution, we put $\mathbf{g_i}$ into **S**.

Step 5. Update solution set. Removing $\mathbf{g_i}$ from **G**. Jump to Step 2.

Step 6. End.

3 Simulation Results and Discussion

In order to analyze the performance of CCDMA communication system under the probability control, we performed several simulations, and the channel model used is the one adopted by the IEEE-802.15.3a standard committee for the line-of-sight case at ranges of 0–4 m. This model, which is based on the well-know Saleh-Valenzuela model, has many multipath components which are grouped in clusters. The average chip energy $\left(E_k^{av}\right)$ of cognitive user is 2, and the peak chip energy $\left(Q_k^{pk}\right)$ of licensed user is 20. The spectral density of white Gaussian noise is 1(namely N0 = 2). The time of chip (Tc) is 1/1.3. The ratio of Tc to sampling time (Ts) is 30. The number of the RAKE receiver's finger is 6.

When p2 is fixed the variation of SINR1 about p1 is presented in Fig. 3. We can conclude from the figure: (1) When the value of p1 is fixed, SINR1 decreases with the increase of p2. (2) When p2 is fixed, the larger the value of p1, the larger

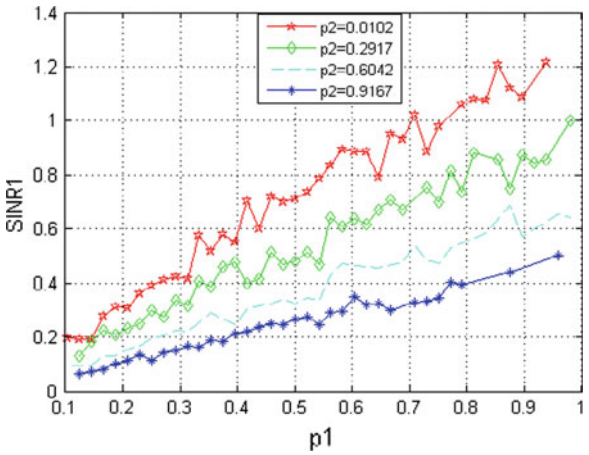

Fig. 3 SINR1 versus p1 with different p2 in channel 1

SINR1 is. It is easy to explain. When the chip energy of the cognitive user and licensed user are given, if p1 is fixed, then the energy of the interest signal is constant, so the interference term will be larger with the increase of p2, which will cause the decrease of the SINR1.

In order to be more intuitive to see the relationship of SINR and the transmission probability, we present the three-dimensional graphics of SINR1 and SINR2 vary with p1 and p2 in Fig. 4.

We can easily find the variation of SINR1 and SINR2 with the change of p1 and p2. For the 1st cognitive user, the smaller the value of p2, the less its interference term caused by the 2nd cognitive user is. For any point (p1, p2), either the value of

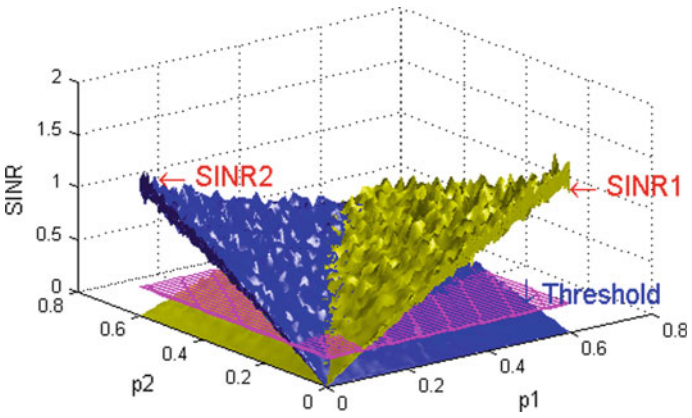

Fig. 4 Three-dimensional graphics of SINR1 and SINR2 vary with p1 and p2 under the condition of CCDMA in channel 1

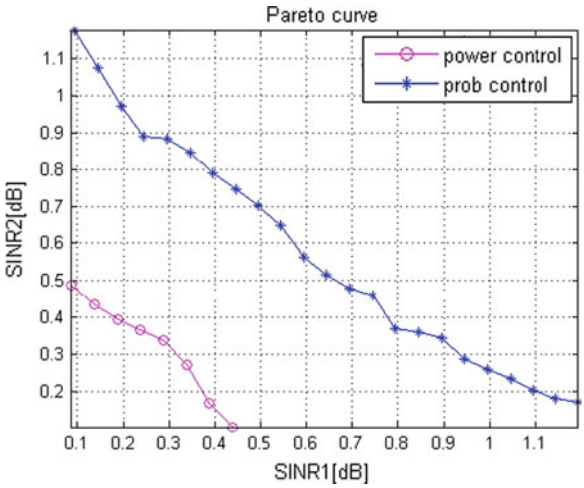

Fig. 5 Pareto curve of probability control and power control in channel 1

SINR1 or the value of SINR2 is less than Threshold, it cannot be used in the scenario.

In order to get the general performance, we obtain the Pareto optimal solutions according to the algorithm above. They are presented in Fig. 5. It can be found the value range of SINR1 and SINR2 are greater under the probability control than power control in Fig. 5.

For example, the maximum of SINR2 is 0.5 dB with the power control mechanism, while the maximum of SINR2 can be about 1.2 dB with the probability control mechanism under the same conditions. Moreover, the curve obtained by probability control mechanism is above the curve obtained by power control mechanism within the entire range. If we use *D*-value it represents the difference of two data, then the minimum *D*-value of SINR2 under probability control and power control when the value of SINR1 is equal to about 0.53 dB according to the figure. So we can conclude that the probability control is better than power control in the scenarios according to the simulation results.

It is found that the interference ratio has an effect on the performance, and the result is presented in Fig. 6.

From Fig. 6, we can see that the smaller the interference ratio is, the better the Pareto boundary curve is, and the *D*-value of results obtained with probability control and the one obtained with power control increases when the value of interference ratio becomes large. For example, when SINR1 is 0.39 dB, the *D*-value obtained with ratio equals to 16 is about 0.71 dB, while the one obtained with ratio equals to 4 is about 0.41 dB. Because interference ratio reflects the channel gain between interference signal and interest signal. The larger the ratio is, the more severe the interference to the system performance. The minimum *D*-value of SINR2 under probability control and power control when the value of SINR1 is equal to about 0.33 dB with the value of ratio 4, and it is about 0.63 dB when ratio is 16.

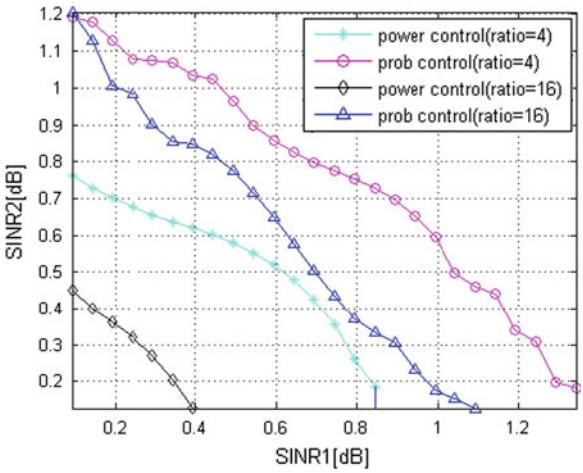

Fig. 6 Comparison of probability control and power control when interference ratio is 4 and 16 in channel 1

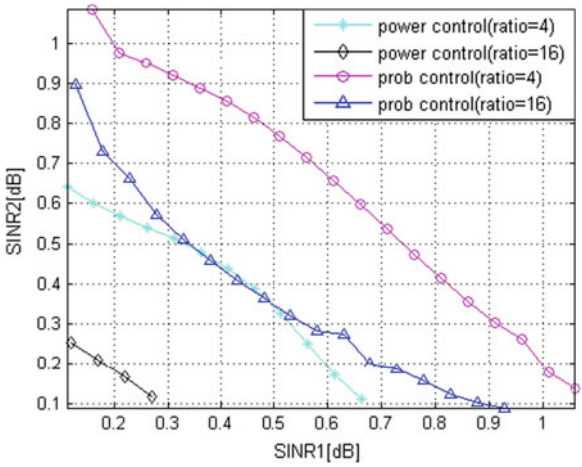

Fig. 7 Comparison of probability control and power control when interference ratio is 4 and 16 in channel 2

Further, the results obtained in different channels are given in Fig. 7 to illustrate the universality of the study. The average additional delay and the multipath components within 10 dB are 5 ns, 12.5 respectively in channel 1. While the corresponding parameters in channel 2 are 9.9 ns and 15.3.

The whole tendency reflected in Fig. 7 is the same as it in Fig. 6. Because of the increase of multipath components, the channel environment of channel 2 is worse than channel 1, so the performance of it becomes worse. The value ranges of SINR1 and SINR2 in channel 2 is smaller than that in channel 1. For example, the maximum value of SINR1 is about 0.93 dB when interference ratio is 16 under probability control, which is smaller than it obtained in channel 1 (1.1 dB). It can be found that the Pareto curve obtained by probability control when interference ratio is 16 (marked by triangle) can be equal to it obtained by power control when

interference ratio is 4 (marked by asterisk) in the worst period (the value of SINR1 varies from 0.3 to 0.5 dB). The conclusions can be arrived that the performance reflected by SINR under probability control is better than that under power control, the performance will be worse when the interference ratio increases and the superiority of probability control will be prominent with the increase of interference ratio according to the analysis above.

4 Conclusion

In this paper, we challenge the traditional practice to use power control to optimize the CCDMA communication by applying the probability control mechanism to cognitive radio system. We present the detailed theoretical analysis through the construction of system model and formulas' derivation. Basing on the theoretical analysis, some simulation results and the analysis about these results are given, it can be concluded that the probability control can be a substitution or at least an addition to power control and its performance is better than power control in the scenarios we assumed in this paper.

In addition, the comparisons of the performance when the interference ratio and channel type are different are presented. The conclusion can be arrived that the superiority of probability control to power control in CCDMA communication system will becomes more obvious with the increase of the ratio and it is valid in different channels.

Acknowledgments This project is financially supported by the National Natural Science Foundation of China (NSFC 61171070) and Fundamental Research Funds for the Central Universities of china (YWF-11-03-Q-063).

References

1. Bergel I, Messer H, Messer M (2008) Optimization of CDMA systems with respect to transmission probability, part I: mutual information rate optimization. IEEE Trans Wirel Commun 7(6):2075–2083
2. Bergel I, Messer H (2008) Optimization of CDMA systems with respect to transmission probability, part II: signal to noise plus interference ratio optimization. IEEE Trans Wirel Commun 7(6):2084–2093
3. Babaei A, Jabbari B (2010) Transmission probability control game for coexisting random aloha wireless networks in unlicensed bands. In: The 71st IEEE vehicular technology conference, pp 1–5
4. Bergel I, Dorfand Y, Shtessman E (2008) Implementation of probability control over convolutional codes. In: Proceedings of IEEE 19th international symposium on indoor and mobile radio communications, pp 1–5
5. Smolyar L, Bergel I, Messer H (2007) Joint downlink power allocation, beamforming weights and base assignment. In: IEEE 8th workshop on signal processing advances in wireless communications, pp 1–5

6. Mitola J III, Maguire, GQ Jr (1999) Conitive radio: making software radios more personal. Pers Commun IEEE 6(4):13–18
7. Haykin S (2005) Cognitive radio: Brain-empowered wireless communications. IEEE J Sel Areas Commun 23(2):201–220
8. Sendonaris A, Erkip E, Aazhang B (2003) User cooperation diversity. Part II. implementation aspects and performance analysis. IEEE Trans Commun 51(11):1939–1948
9. Ganesan G, Li Y (2007) Cooperative spectrum sensing in cognitive radio, part I: two user networks. IEEE Trans Wireless Commun 6(6):2204–2213
10. Farrokh R-F, Ray Liu KJ, Tassiulas L (1997) Downlink power control and base station assignment. IEEE Commun Lett 1(4):102–104
11. Liu S, Chang Y, Wang G, Yang D (2012) Distributed resource allocation in two-hierarchy networks. ETRI J 34(2):159–167
12. Buzzi S, Saturnino D (2011) A game-theoretic approach to energy-efficient power control and receiver design in cognitive CDMA wireless networks. IEEE J Sel Top Signal Process 5(1):137–150
13. Mahyari MM, Shikh-Bahaei MR (2012) Joint optimization of rate and outer loop power control for CDMA-based cognitive radio networks. In: International conference on computing, networking and communications, pp 392–396
14. Choi K, Kim S (2003) Optimum uplink power/rate control for minimum delay in CDMA networks. ETRI J 25(6):437–444
15. Kim N-M, Kim M-R, Kim E-J, Shin S-J, Yu H-I, Yun S-B (2008) Robust cognitive-radio-based OFDM architecture with adaptive traffic allocation in time and frequency. ETRI J 30(1):21–32
16. Gariby M, Gariby T, Zamir R 92008) Managing the degree of impulsiveness of other cell interference. In: IEEE international conference on communications, pp 1398–1403
17. Gariby M, Gariby T, Zamir R (2006) The most favorable impulsive interference for ternary CDMA. In: IEEE international symposium on information theory, pp 942–946
18. Gariby M, Gariby T, Zamir R (2008) Capacity of impulsive modulation over multipath interference channels. In: 4th IEEE international conference on circuits and systems for communications, pp 191–195
19. Verdu S (1998) Multiuser dection. Cambridge University Press, New York
20. Mueller-Gritschneder D, Graeb H, Schlichtmann U (2009) A successive approach to compute the bounded Pareto front of practical multiobjective optimization problems. SIAM J Optim 20:915–934
21. Petko JS, Werner DH (2011) Pareto optimization of thinned planar arrays with elliptical mainbeams and low sidelobe levels. IEEE Trans Antennas Propag 99:1748–1751
22. Boche H, Naik S, Schubert M (2011) Pareto boundary of utility sets for multiuser wireless systems. IEEE/ACM Trans Netw (TON) 19(2):589–601

A Stereo Matching Algorithm Based on Outline-Assisted Dynamic Programming

Pei Wang, Chen Chen and FangFang Wei

Abstract In the stereo vision researches, global matching algorithms are widely used in the preference of high matching accuracy. This paper presents a new stereo matching algorithm based on global matching philosophy. The proposed method, which is called 3D dynamic programming-oriented matching method with filter-box acceleration, utilizes the edge information obtained by wavelet transform from the stereo images got from Middlebury University. We then compared the computational cost and matching accuracy among by the new method and other conventional stereo matching algorithms. We show that it gets advantages beyond those results. Finally, we make a conclusion about current works and look forward to feature jobs.

Keywords Stereo matching · Wavelet transform · 3D dynamic programming · Filter-box acceleration

1 Introduction

Stereo vision is the basic and important branch in machine learning. It is mainly to obtain 3D information from the 2D information carrier, images, for example. While stereo matching is the key point in the field of stereo vision, the basic principle is to determine the pixels of the same object point between left and right images. Coordinate difference between the corresponding pixels of the object in stereo image is called disparity. Stereo matching is to obtain a 2D disparity map by finding all correspondences of entire pixels in the images [1]. Binocular stereo

P. Wang (✉) · C. Chen · F. Wei
Information and Electrical Mechanism Engineering College, Shanghai Normal University, Shanghai 200000, China
e-mail: peiwang@shnu.edu.cn

F. Sun et al. (eds.), *Foundations and Practical Applications of Cognitive Systems and Information Processing*, Advances in Intelligent Systems and Computing 215,
DOI: 10.1007/978-3-642-37835-5_27,

matching is the most popular research direction in this field because it is bionic to get the depth information just like the eye system of mankind does.

Stereo matching algorithm can be commonly divided into two categories: area based and feature based [1]. Feature-based algorithm utilizes the features of image such as corner or edge and obtains a sparse disparity map with low computational cost and high matching accuracy. The area-based algorithms calculate the correlations of pixels in a matching window among stereo images. The correlations could be Sum Absolute Difference (SAD), Sum Squared Difference (SSD), and Normalized Cross Correlation (NCC) to determine disparities of entire image pixels which will create a dense disparity map from stereo images. The area-based matching algorithm falls into two types: local and global optimization. Local optimization is calculating the correlations of pixels using the method mentioned above and finding a best and optimized disparity with some restraints and hypotheses such as polar constraint, disparity continuity constraint, etc. Global optimized algorithm is to minimize a global cost function such as energy function for a pixel to get the certain disparities. These kinds of algorithms can provide accurate disparity maps, however, their computational cost is usually higher than other algorithms mentioned above if no optimization is applied. Examples are Belief Propagation (BP) [2], Graph Cuts (GC) [3, 4], Dynamic Programming (DP) [5–7], etc. In this paper, we present an improved algorithm using DP first mentioned by Sun [5]. We use wavelet transform [8] to get the edge information and preprocessing to restrict the DP processing. The results show that it will not only enhance the accuracy but also improve the computational cost.

2 The Proposed Matching Algorithm

In this section, we describe a stereo matching algorithm based on efficient 3D dynamic programming. The key idea behind dynamic programming is quite simple. In general, to solve a given problem, we need to solve different parts of the problem (sub-problems), then, combine the solutions of the sub-problems to reach an overall solution. Among stereo image matching researchers, Dynamic Programming is usually defined as a global energy limited function. We need to define the regulations which are usually called cost functions between every two sub-problems to minimize the whole energy sum perfectly. We define the NCC as the cost function, and present an edge information-based restrict to not only accelerate the process, but also improve the accuracy of dynamic programming. In this paper, we used and improved a special dynamic programming called Two-Step Dynamic Programming (TSDP) which was first mentioned by SUN [5] by involving the edge information-based restrict.

We utilize the wavelet transform and advanced preprocessing to get the image outline information and box-filter is implemented to sharply decrease the process time in calculating the NCC value between each pix-pair of stereo images. Finally, a dense disparity is obtained with low computational cost and high accuracy.

2.1 Edge Information Obtaining

In this section, we propose a method to obtain the edge information which will be used in the 3D dynamic programming to improve the cost efficiency and matching accuracy. Edge has two conceptions; one is the outline of the object and another is the high frequency noises. Getting the outline of objects is the main purpose of obtaining edge-information. Unfortunately, we do not have a common method to perfectly differentiate the two kinds of edge. In order to get the outline of the image, we designed two-step processing; step one is to use the wavelet transform to obtain the whole edge information and step two is casting out the high frequency noise part.

2.1.1 Wavelet Transform-Based Edge Detection

We used a new method of wavelet transform-based edge detection presented by Tao Yang, Guoxia Sun, and Xiuman Duan [8]. Its main philosophy is to multiply the Digital Wavelet Transform (DWT) coefficients in the adjacent scale, then calculate the proper threshold to separate the coefficients that come from wavelet transform so that edge information can be determined. As a result of this edge processing, a two-value image is gained in which 1 stands for pixels in the edge area and 0 presents the pixels in continuous area.

2.1.2 Casting Out the High Frequency Noise Information

Let $\varphi(i,j)$ as the edge image obtained using wavelet transform. We are about to fill the threshold image $\varphi'(i,j)$ by utilizing the following expressions:

$$\varphi'(i,j) = \begin{cases} \arg\limits_{n \in \text{Range}} \begin{cases} \varphi(i+0,j) \neq 0 \\ \varphi(i+1,j) \neq 0 \\ \cdots \\ \varphi(i+n,j) \neq 0 \end{cases} & , \varphi(i,j) \neq 0 \\ 0 & , \varphi(i,j) = 0 \end{cases} \tag{1}$$

The range in Eq. (1) stands for the search range for image filling. Now we define the $\varphi''(i,j)$ as the filling image.

$$\begin{cases} \varphi''(i,j) = \varphi''(i+1,j) = \cdots = \varphi''(i+\varphi'(i,j),j) = \varphi'(i,j), 0 < \varphi'(i,j) < th1 \\ \varphi''(i,j) = 0 \qquad\qquad , \text{else} \end{cases} \tag{2}$$

The threshold th1 in Eq. (2) determines how many continuous zero-value pixels show up at the right position of a nonzero-value pixel will be filled with the same value as the nonzero-value pixel in order to eliminate the high frequency noise.

Finally, the outline image is defined as:

$$\varphi'''(i,j) = |\varphi''(i,j) - \varphi''(i+1,j)| + |\varphi''(i,j+1) - \varphi''(i+1,j)| \tag{3}$$

Two constants (th1 and range) should be determined by the experiments according to different image size and quality.

2.2 Matching Algorithm

In this section, we describe the global matching algorithm based on a 3D dynamic programming.

Matching cost function is defined to calculate the similarity degree between the pixels of the image pair. So far, SSD, SAD and NCC are the three main common matching cost functions in matching researches. In this paper, we choose NCC to be the matching cost function in consideration of its robustness of alteration of light intensity. NCC is defined as the following formula:

$$NCC(p1,p2,d) = \left| \frac{\sum_{m=-k}^{k}\sum_{n=-l}^{l}\left[I_1(i+m,n+j) - \overline{I_1(i,j)}\right] \times \left[I_2(i+m+d,n+j) - \overline{I_2(i+d,j)}\right]}{\sqrt{\left\{\sum_{m=-k}^{k}\sum_{n=-l}^{l}\left[I_1(m+i,n+j) - \overline{I_1(i,j)}\right]^2\right\} \times \left\{\sum_{m=-k}^{k}\sum_{n=-l}^{l}\left[I_2(m+i+d,n+j) - \overline{I_2(i+d,j)}\right]^2\right\}}} \right| \tag{4}$$

Match window is a 2 l × 2 k square, is the average value of the pixels in the window . p1 and p2 are the pair points between the different stereo images with the specific disparity d. It will be a huge computation cost if we just follow formula (5) to take the whole pixels matching process. To accelerate the NCC calculating, the filter-box mentioned in [9] was chosen for use.

The main philosophy of the box-filter could be summarized as the following formulas:

$$NCC(p1,p2,d) = \frac{\mathrm{cov}(i,j,d)}{\sqrt{\mathrm{var}(i,j,I_1)\mathrm{var}(i+d,j,I_2)}} \tag{5}$$

$$\mathrm{cov}(i,j,d) = \sum_{m=-k}^{k}\sum_{n=-l}^{l} I_1(m+i,n+j)I_2(m+i+d,n+j) - (2k+1)(2l+1)\overline{I_1(i,j)I_2(i+d,j)} \tag{6}$$

$$\mathrm{var}(i,j,I_1) = \sum_{m=-k}^{k}\sum_{n=-l}^{l} I_1^2(m+i,n+j) - (2k+1)(2l+1)\overline{I_1(i,j)}^2 \tag{7}$$

$$\mathrm{var}(i+d,j,I_2) = \sum_{m=-k}^{k}\sum_{n=-l}^{l} I_2^2(m+i+d,n+j) - (2k+1)(2l+1)\overline{I_2(i+d,j)}^2 \tag{8}$$

Let,

$$\begin{cases} I_{1C}(x,y) = \sum\limits_{n=-l}^{l} I_1(x,n+y) \\ I_{2C}(x,y) = \sum\limits_{n=-l}^{l} I_2(x,n+y) \\ I_{1s}(x,y) = \sum\limits_{n=-l}^{l} I_1^2(x,n+y) \\ I_{1s}(x,y) = \sum\limits_{n=-l}^{l} I_2^2(x,n+y) \end{cases} \tag{9}$$

Then, calculate the window-based average value and sigma value by the recursion programming shown as the formula below:

$$\begin{cases} \overline{I_1(i+1,j)} = \overline{I_1(i,j)} + \dfrac{1}{S}[I_{1C}(i+k+1,j) - I_{1C}(i-k,j)] \\ \overline{I_2(i+1,j)} = \overline{I_2(i,j)} + \dfrac{1}{S}[I_{2C}(i+k+1,j) - I_{2C}(i-k,j)] \\ \sum\limits_{m=-k}^{k}\sum\limits_{n=-l}^{l} I_1^2(i+1,j) = \sum\limits_{m=-k}^{k}\sum\limits_{n=-l}^{l} I_1^2(i,j) + I_{1S}(i+k+1,j) - I_{1S}(i-k,j) \\ \sum\limits_{m=-k}^{k}\sum\limits_{n=-l}^{l} I_2^2(i+1,j) = \sum\limits_{m=-k}^{k}\sum\limits_{n=-l}^{l} I_2^2(i,j) + I_{2S}(i+k+1,j) - I_{2S}(i-k,j) \end{cases} \tag{10}$$

Experiment results show that the filter-box involved programming can sharply accelerate the NCC calculating process. It takes 15.46 s to take the process of NCC calculating without filter-box, while 2.31 s with filter-box between the 512 × 512 stereo images pair under the 9 × 9 match window.

After defining the matching cost function, we specify the matching strategy to obtain the disparity. Inspired by the TSDP mentioned by Sun [5], we proposed an improved TSDP strategy with the restrictions of edge information obtained in Sect. 2. It not only improves the matching accuracy but also reduces the calculating time.

First, calculate the 3D NCC cube of the image pair. Assume the right hand image as the conference image, calculate the NCC value for each disparity d in the d-searching range [0, *dmax*], after pixel NCC and disparity *d* traversal in conference image, we can get the 3D NCC cube *C* which is illustrated as Fig. 1.

Second, we obtain an accumulated NCC 3D cube *Y*. On each vertical plane of the 3D NCC cube, calculate the accumulated NCC value using dynamic programming as defined as the following equation and illustrated in Fig. 2.

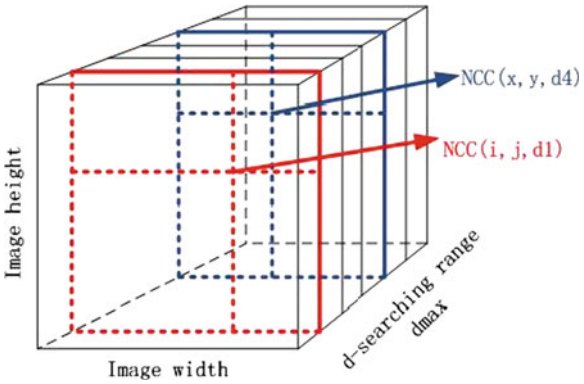

Fig. 1 3D NCC Cube C

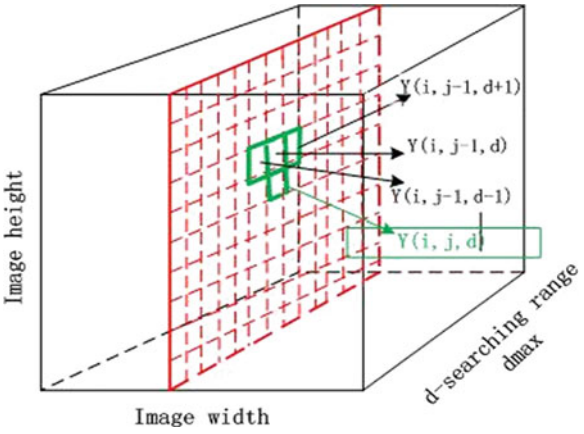

Fig. 2 3D accumulated NCC Cube Y

$$\begin{cases} Y(i,j,d) = C(i,j,d) + \underset{-p \le t \le p}{MAX}[Y(i,j-1,\, d+t)] \\ Y(0,j,d) = C(0,j,d) \end{cases} \tag{11}$$

The constant p in Eq. (11) is the accumulate compare range in the specific vertical plane. It is fluctuant along with the image size. For 512 × 512 image, we let $p = 1$. For each horizon plane in accumulated cube Y, we regard the d information of highest value as the disparity Fig. 3.

To get all the disparities of all the pixels in the reference image, we still use the dynamic programming philosophy, On each horizon plane of accumulated 3D NCC cube, the cost is defined as simply as accumulating the biggest value, and restricts are proposed as using the edge information as illustrated in Fig. 4.

We suppose that in the texture continuous area, the disparity is also continuous or changed very smoothly. Conversely, where texture jumped sharply, where there exists a high possibility the disparity also jumped rapidly. With that philosophy, we designed an edge-information-aided disparity search algorithm to not only

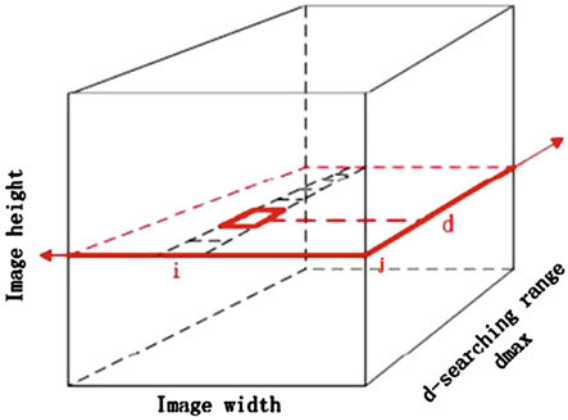

Fig. 3 For special position (i, j), find the highest value of $Y(i, j,d)$, regard this d, as the disparity of the pixel $I(i, j)$

reduce the computational cost in searching the disparity but also enhance its accuracy.

The last optimal path is used as the reference path and an initial search range is given to search the disparity in the current layer. On the one hand, the initial search range is a constant which is smaller than the searching d-max so that it can save the total searching account. On the other hand, we assume texture continuous area has continuous disparities.

The restriction of finding disparity near the former layer if the pixel is not at the edge of object will enhance the accuracy of finding disparities. If the pixel is on the edge of an object, then, the disparity searching range should be enlarged, even search through the whole disparity. Experiments show that the improvement on time saving is significant and so is matching accuracy.

3 Experiment Result

We use the standard stereo image pairs provided by Middlebury University. The proposed algorithm assumes that the geometric distortion and light distortion have been rectified and the polar line is the horizon scan line of the image.

We used the local matching algorithm with NCC directly as cost function and with different window size and disparity searching range. The window size is smoothly increased from 5×5 to 11×11 with stepping 1, while the matching accuracy increases too. The maximum disparity in 3D NCC cube is set as 30 pixels in consideration of the total image size (434×383). It should be adjusted manually when the image size is changed. In Fig. 5, the proposed algorithm is utilized with the same parameters used to create the results in Fig. 6. It is obvious that the proposed method gets better results. The disparity is much more continuous than that got by the NCC direct matching method. The disparity is much more continuous than that got by the NCC direct matching method (Fig. 7).

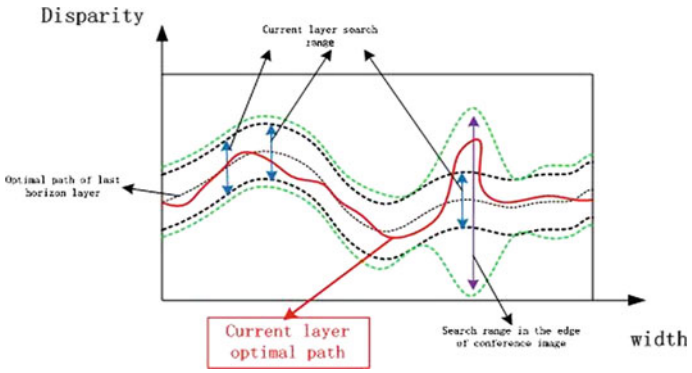

Fig. 4 Edge-information-aided disparity search algorithm

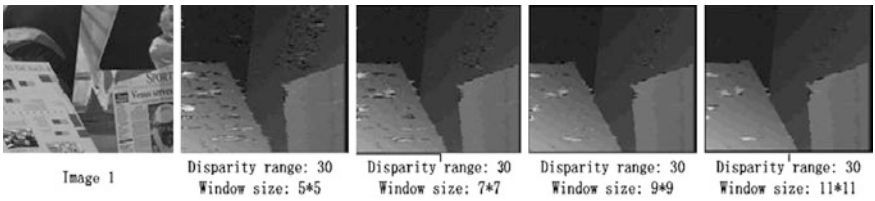

Fig. 5 Experiment result of image 1 with the proposed algorithm

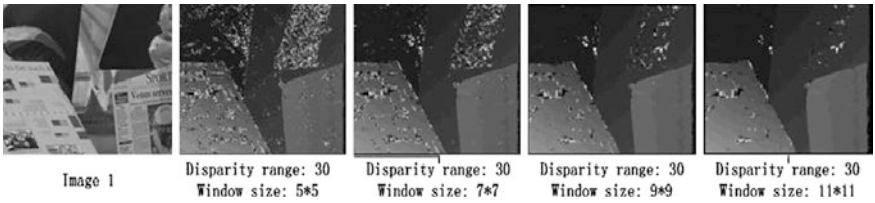

Fig. 6 Experiment result of image 1 with direct NCC algorithm

With the utilization of box-filter, the time consumption of proposed algorithm is contracted into 2 s with the disparity searching range 30.

It is very important to determine the maximum disparity searching range. If the DSR is much higher than the true value, it will not only add the additional computational cost but also reduce the matching accuracy. If the DSR is much lower than the true value on the contrary situation, it will shorten the process time, but mismatching may not be acceptable. We estimated the searching range to 30 pixels and tried the 20 pixels too, according to the image size, 434 $\times$ 383. It is one of our feature works to automatically determine the max searching disparity range.

As shown in Table 1, the proposed algorithm has the advantages in time cost compared with the other two algorithms. The runtime environment is as follows:

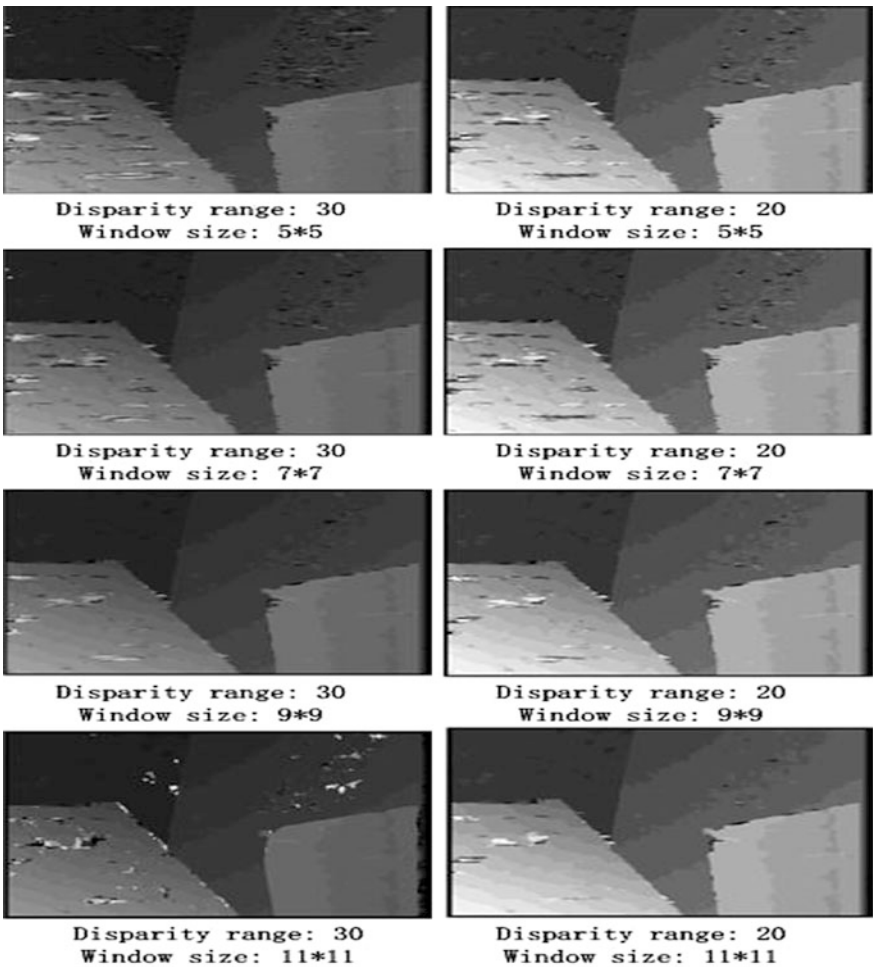

Fig. 7 Experiment results with the proposed algorithm and different disparity searching range

Table 1 Time cost compare

Window/max-d	NCC (s)	Fast NCC (s)	Proposed method (s)
5 × 5/30	11.34	1.43	1.40
7 × 7/30	14.11	1.98	1.87
9 × 9/30	17.23	2.32	2.21
11 × 11/30	23.34	3.42	3.41
5 × 5/20	9.31	1.41	1.32

CPU: Intel core i5
RAM: 4.00 GB

OS: 64-bit windows 7
Software: Visual Studio 6.0 SP6.

Though the time is contracted into approximately 2 s with the disparity range 30, it still does not match the demand in real-time system. This should be one of our future tasks.

4 Conclusion

We proposed an improved algorithm using edge information to guide the process of 3D dynamic programming matching. Dynamic programming is a widely used algorithm for accurate disparity map. But usually it costs more computational resources than other local matching algorithms. We used two main methods to accelerate the process. First, the box-filter technique was utilized to reduce the time calculating the NCC valve. Second, we used the edge information to cut the range of disparity searching width. The edge information also enhanced the accuracy of disparity finding. Reasonable results are obtained. Meanwhile, some future works are required, such as automatically determining the max searching disparity range of different image pairs and improvement of computational cost to match the requirement of real-time applications and etc.

Acknowledgments This work is supported by the project of Shanghai Normal University (No.3434532), the Program of Shanghai Normal University (DZLA-7001-12-002006), and Shanghai Normal University (SK201127)

References

1. Kim C-I, Park S-Y (2011) Fast Stereo Matching of Feature Links. In: 2011 international conference on 3D imaging, modeling, processing, visualization and transmission
2. Boykov Y, Veksler O (2001) Fast approximate energy minimization via graph cuts. Trans Pattern Anal Mach Intell 23:1222–1239
3. Sun J, Li Y, Kang SB, Shum H–Y (2005) Symmetric strereo matching for occlusion handling. Comput Vision Pattern Recognit (CVPR) 2:399–406
4. Yang Q, Wang L, Yang R, Stewenius H, Nister D (2009) Stereo matching with color-weighted correlation, hierachical belief propagation, and occlusion handling. Trans Pattern Anal Mach Intell 31(3):492–504
5. Sun C (2001) Rectangular subregioning and 3-D maximum-surface techniques for fast stereo matching. In: Proceedings of the IEEE workshop on stereo and multi-baseline vision, pp 44–53
6. Donate A, Liu X, Jr Gollins EG (2011) Efficient path-based stereo matching with subpixel accuracy. IEEE Trans Syst Man Cybern-PartB: Cybern 41(1):183–195
7. Chen C, Pei W, FangFang W (2011) Efficient multichannel and edge information based on stereo matching algorithm. Digital Video 35:17–21
8. Tao Yang G, Sun C, Duan X (2011) A new method of wavelet transform-based edge detection. In: 2011 IEEE 13th international conference on communication technology pp 789–792
9. Sun C (1998) Muli-resolution rectangular subregioning stereo matching using fast correlation and dynamic programming techniques CMIS Report No. 98/246

Dynamic Visual Time Context Descriptors for Automatic Human Expression Classification

Yi Ji, Shengrong Gong and Chunping Liu

Abstract In this paper, we propose two fast dynamic descriptors Vertical-Time-Backward (VTB) and Vertical-Time-Forward (VTF) on spatial–temporal domain to catch the cues of essential facial movements. These dynamic descriptors are used in a two-step system to recognize human facial expression within image sequences. In the first step, the system classifies static images and then it identifies the whole sequence. After combining the visual-time context features with popular LBP, the system can efficiently recognize the expression in a single image, and is especially helpful in highly ambiguous ones. In the second step, we use the evaluation method through the weighted probabilities of all frames to predict the class of the whole sequence. The experiments were performed on 348 sequences from 95 subjects in Cohn–Kanade database and obtained good results as high as 97.6 % in seven-class recognition for frames and 95.7 % in six class for sequences.

Keywords Facial expression classification · LBP · Spatial–temporal descriptor

1 Introduction

Automatic facial expression recognition (FER) is one of the most active fields in computer vision and has attracted many proposals over the past several decades. On a human face, the expressions come from the movements of facial muscles and

Y. Ji (✉) · S. Gong · C. Liu
School of Computer Science and Technology, Soochow University,
No.1 Shizi Street, Suzhou, China
e-mail: jiyi@suda.edu.cn

S. Gong
e-mail: shrgong@suda.edu.cn

C. Liu
e-mail: cpliu@suda.edu.cn
URL: http://www.suda.edu.cn

F. Sun et al. (eds.), *Foundations and Practical Applications of Cognitive Systems and Information Processing*, Advances in Intelligent Systems and Computing 215,
DOI: 10.1007/978-3-642-37835-5_28,

are influenced by internal emotion states. In everyday life, the interpretation of facial expressions occupies an important role in interpersonal and nonverbal communication. Ekman and Friesen [1] proposed to use Facial Action Code System (FACS) as the standard to systematically categorize the facial expression of emotions. They also defined six basic emotions: Anger, Disgust, Fear, Happiness, Sadness, and Surprise. The task to interpret these universal expressions, by applying recognition algorithm or, even manually, by human beings, is difficult because of individual differences and culture background, regardless of complexion, gesture or facial hair. In this work, we propose to exploit the appearance based and dynamic visual-time information to classify not only the image frames but also the sequences.

From the early survey of Pantic and Rothkrantz [2] in 2000 to Huang's review of facial image analysis [3] in 2011, many related works are summarized and compared. Their survey concluded that the ideal system for facial expression analysis includes three important stages: the detection of faces, the representation of faces, and the classification of the representations.

After face detection, the next step is to extract discriminative information to represent the face regions. In one category of approaches [2, 4], which are based on geometric features, models are established by a set of important points on the face or face contour deformation. Recently, surface descriptor under 3D model became more and more popular [3]. In another category of methods, face is represented by appearance-based features. Some handled the image wise problem [5–7] and identified six basic classes plus the neutral class to label images. As these static approaches cannot capture the movements of essential facial parts, some new approaches recently focused on taking into account dynamic information so as to handle the sequence wise problem. Six-class classification for the sequences was processed for the six basic expressions. Yeasin et al. [8] used K-NN to classify the optical flow information which is neither invariant to illumination change nor considering the texture of appearance on static faces. Xiang et al. [9] analyzed a fixed size sequences with 11 frames using fuzzy C means computation to general the expression model. Their method is inflexible for sequence with variable sizes. Zhao and Pietikäinen [10] divided the whole sequences to subvolumes and connected the features on three orthogonal planes to represent the video, but their motion treatment is just the same as the treatment of appearance regardless of their different texture pattern. Yang et al. [11] built dynamic Harr-like codebook in the same position along the temporal window. Their coded features are fixed size on time span. The speed to which different expressions are changing cannot be handled and influences their recognition results. Buenaposada et al. [12] introduced a probabilistic procedure to combine the information from input image sequence to compute the posterior probability. Their system is robust to realistic environment but only obtained around 80 % recognition rates in expressions as fear, sadness, and angry. Roduvic et al. [13] noticed the temporal evolution and intensity estimation during the observation. Their manifold learning method obtained modest rates from 71 to 96 % for different emotion catagories. Here, we introduce two new descriptors to help our automatic system for the

challenge. The system separated the feature extraction for static images and dynamic information estimation. The proposed system can also evaluate the intensity of expressions and handle the temporal information for image sequences.

2 Image Representation by Non-Dynamic and Dynamic Features

Most of researches in this area are either image based [2, 6] or sequence based [10, 11]. We are inspired by their progress and try to improve their approaches by combining the method for static images and the method to integrate the dynamic information.

The first part uses the face detection algorithm proposed by Kienzle et al. [14], and enhanced by facial parts location [15]. All faces were detected and automatically scaled to 64×64 pixels. The cropped region is processed through histogram equalization and pixel normalization in the same way as in CSU Face Identification Evaluation System [16] to remove the illumination changes.

2.1 Local Binary Pattern for Non-Dynamic Feature

The representation of a non-dynamic feature on a static image is based on appearance descriptors, extracted from the face images obtained in previous section. To select proper descriptors, we consider the computation efficiency and discriminative ability of LBP operator [7, 17]. The original LBP operator labels the pixels of an image by thresholding the 3×3 neighborhood of each pixel with the value of the central pixel and by considering the results as a binary number. In our approach, as the facial organs have been detected as in Sect. 2.1 we propose to use a designed mask of 10 blocks as in Fig. 3 for division. Our method is derived from facial parts detection, and considers the natural distribution of facial organs. The size of the final vector is 2,560 components. It is a concatenation of the histograms related to the 10 blocks in Fig. 3, and its dimension is much smaller than the one of the vectors used by Shan [6] or Zhao and Pietikäinen [10].

2.2 Visual-Time Context Descriptor for Dynamic Feature

In 1979, Bassili et al. [18] suggested that motion in a face would allow expressions to be identified even with minimal information about the spatial arrangement of features. His pioneer work reported that facial expressions were more accurately recognized from dynamic images than from a single static image. Figure 1

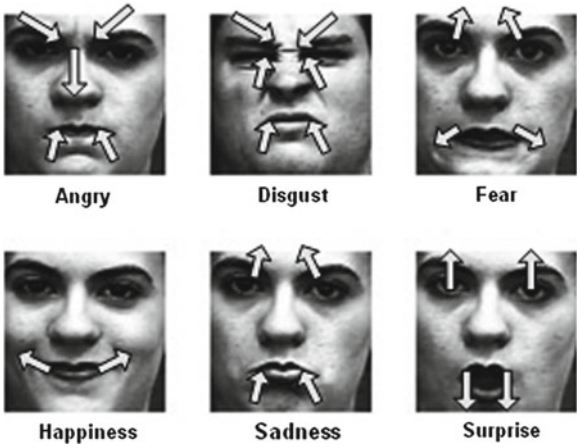

Fig. 1 The cues of facial movements [18]

summarizes Bassili's observation on the motion-based cues for facial expressions. Since then, various attempts are applied to catch the temporal information from neutral face to the expressive one. Zhao and Pietikäinen [10] extracted the traditional LBP features on the three orthogonal planes: XY, XT, and YT as Volume-LBP and LBP-TOP. The treatment is just different in the number of neighboring points for different planes. Considering that the two spatio–temporal planes: VT(YT) as vertical time and HT (XT) as horizontal time, unlike the XY plane as static images, have their own special texture, we propose to apply new LBP-like descriptor VTB and VTF to make the most of the important temporal information.

The VTB and VTF descriptors are also gray-level invariant texture primitive statistic, but designed to be used on spatio–temporal planes. The operator is related to a sequence of three continuous images. In the third image, each pixel is used to threshold its two backward (or forward)neighboring pixels with the same coordinate. Similar to the original LBP operator, we build the descriptor on 3×3 neighborhood as in Fig. 2. The binary result is calculated to label the middle-right pixel ('6' in Fig. 2).

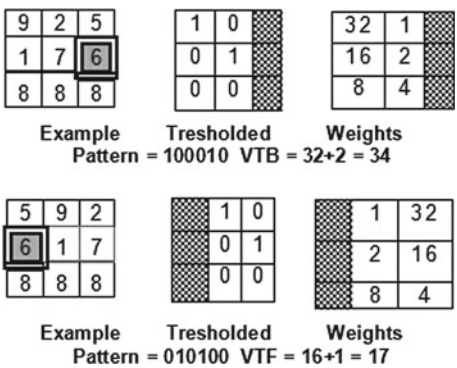

Fig. 2 VTB and VTF computing

For each pixel P with coordinate (x, y) and gray value $g_{x,y}$ in an image of time t, the binary code is produced as Eqs. 1 and 2.

$$\begin{aligned} VTB \quad = \; & s(g_{x,y-1,t-2} - g_{x,y-1,t})2^5 \\ & + s(g_{x,y,t-2} - g_{x,y,t})2^4 \\ & + s(g_{x,y+1,t-2} - g_{x,y+1,t})2^3 \\ & + s(g_{x,y+1,t-1} - g_{x,y+1,t})2^2 \\ & + s(g_{x,y,t-1} - g_{x,y,t})2^1 \\ & + s(g_{x,y-1,t-1} - g_{x,y-1,t})2^0. \end{aligned} \tag{1}$$

$$\begin{aligned} VTF \quad = \; & s(g_{x,y-1,t+2} - g_{x,y-1,t})2^5 \\ & + s(g_{x,y,t+2} - g_{x,y,t})2^4 \\ & + s(g_{x,y+1,t+2} - g_{x,y+1,t})2^3 \\ & + s(g_{x,y+1,t+1} - g_{x,y+1,t})2^2 \\ & + s(g_{x,y,t+1} - g_{x,y,t})2^1 \\ & + s(g_{x,y-1,t+1} - g_{x,y-1,t})2^0. \end{aligned} \tag{2}$$

where,

$$s(x) = \begin{cases} 1, \text{if} \;\; x > 0 \\ 0, \text{if} \;\; x \leq 0 \end{cases} \tag{3}$$

In facial expression, most facial part movements are vertically oriented and the main directions can be up or down for different organs. For example, an expression of surprise is related to eyes moving up and mouth moving down. Therefore, we divide the VT plane into three blocks: eye, nose, and mouth regions as in Fig. 3. Finally, a total vector of $2^6 \times 3 = 192$ bins is used to represent the movements. Now we have 10 blocks from appearance and three blocks from motion. These histograms are concatenated into a single one. Such a representation of an image is obtained from the image itself plus two previous reference images. This extraction can be done per image in the sequence, except for the first two images. The vectors obtained from LBP + VTB + VTF will be used to identify sequences.

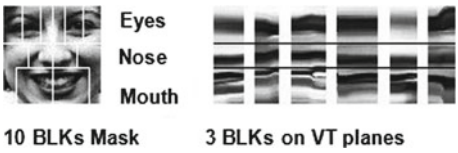

Fig. 3 10 blocks on front faces and three blocks on VT plane

3 Facial Expression Recognition Experiments

In this section, we use the Cohn–Kanade AU-Coded Facial Expression Database [19] as the test bed, which is one of the most used database in current facial image analysis community. It includes 486 sequences from 97 students. Subjects range in age from 18 to 30 years inclusive. 65 % were female; 15 % were African–American, and 3 % Asian or Latino. They were asked to perform different expressions using a camera directly in front of one subject. Each sequence runs from a face in neutral state to a target expression in peak state. A comprehensive comparison is difficult because even though most of the proposed systems worked on this database, they did not use the same selection of sequence sets and their own labelings of expressions. Our choice of sequences and their labels are based on the 333 sequences used by Buenaposada et al. [12]. In our experiments, we added more image sequences and changed several false labels to fix the total number to 348 (40 Anger, 41 Disgust, 45 Fear, 97 Happiness, 48 Sadness, and 77 Surprise). For our study, we also manually labeled the starting frame of expression in every sequence.

As all images from this database show faces with frontal view or nearing frontal view, and as the positions of the head are rather stable, we applied the face detection on the first frame using flib [14] and improved by [15]. The cropped and normalized 64×64 face images are divided into 10 regions shown in Fig. 3. For every image, the motion information, which is relative to its previous or following two images in sequence, is obtained from three blocks on VT plane using VTB or VTF 3. The total histogram length is $256 \times 10 + 64 \times 3 = 2752$ for using of LBP + VTB or LBP + VTF and $256 \times 10 + 64 \times 3 \times 2 = 2944$ for LBP + VTB + VTF. Because of its powerful discriminative ability, the SVM with polynomial kernel is used. The 10-fold validations are applied in all experiments. Our results are compared to other image-based methods and video-based (sequence-based) methods in Table 1, where SN stands for the number of subjects, SqN stands for the number of sequences and LOSO stands for Leave-One-Subject-Out.

3.1 Classification for Neutral and Peak Images

For the previous image-based approaches on Cohn–Kanade database, Bartlett et al. [5] selected the first and last frame as training images and for testing. Shan et al. [6] used the neutral faces and three peak frames for prototypic expression recognition. We did a similar selection to build static image sets. For each sequence, the first two images are not used as there is no VTB descriptor available and the last is leaving out as there is no VTF descriptor. The neutral images and four peak images per sequence are used as training and testing images, thus resulting in 2,124 images (158 Anger, 164 Disgust, 180 Fear, 388 Happiness, 191 Sadness, 305 Surprise, and 738 neutral). Later, the trained classifiers were applied to all 5,670 images (529 Anger, 387 Disgust, 542 Fear, 1,382 Happiness, 547 Sadness, 909 Surprise, and

Table 1 Recognition performances comparisons (%)

	Representation	SN	SqN	Classes	Dynamic	Automatic	Measure	Accuracy (%)
(a) *Image-based methods*								
Bartlett et al.(2005) [5]	Gabor	90	313	7	N	Y	10-Fold	93
Shan et al.(2008) [6]	LBP	96	320	7	N	N	10-Fold	95.1
Ji and Idrissi(2010) [15]	LBP	95	348	7	Y	Y	10-Fold	91.9
Ji and Idrissi(2012) [15]	LBP + VTB	95	348	7	Y	Y	10-Fold	97.2
Ours: Neutral + Peak	LBP + VTF	95	348	7	Y	Y	10-Fold	96.3
Ours: Neutral + Peak	LBP + VTB + VTF	95	348	7	Y	Y	10-Fold	97.6
Ours: ALL	LBP	95	348	7	Y	Y	10-Fold	83.8
Ours: ALL	LBP + VTB	95	348	7	Y	Y	10-Fold	84.1
Ours: ALL	LBP + VTF	95	348	7	Y	Y	10-Fold	85.5
Ours: ALL	LBP + VTB + VTF	95	348	7	Y	Y	10-Fold	91.3
(b) *Sequences-based methods*								
Yeasin et al.(2004) [8]		-	-	6	Y	Y	5-Fold	90.9
Xiang et al. (2007) [9]		95	365	6	Y	Y	10-Fold	88.8
Buenaposada et al.(2008) [12]		94	333	6	N	Y	LOSO	89.13
Zhao and Pietikäinen(2007) [10]		97	374	6	Y	N	10-Fold	95.1
Zhao and Pietikäinen(2009) [10]		97	374	6	Y	Y	2-Fold	93.85
Chang et al.(2009) [4]		-	392	6	Y	N	5-Fold	92.86
Ji and Idrissi(2010) [15]		95	348	6	Y	Y	10-Fold	93.68
Ours:$\mathcal{N}(\mu, \sigma_1^2)$		95	348	6	Y	Y	10-Fold	95.1
Ours:$\mathcal{N}(\mu, \sigma_2^2)$		95	348	6	Y	Y	10-Fold	95.7

1,344 neutral) in the sequences. By comparing the results in Table 1a, we can fairly say that our proposed method is superior to the other ones in classifying the static images. The new descriptor VTB and VTF not only improved the classification of neutral + peak images, but can also provide better performance in the classification of expressive faces in variant degrees between neutral frames and peak frames. Especially, the combination of LBP + VTF + VTB can only slightly improve the performance of neutral + peak images, though for ambiguous ones, this improvement is more evident. The reason may lie in that in ambiguous frames, movement texture provides more context cues than static or peak images. Indeed, among the flows of realistic facial expressions, a typical long video is composed of several neutral frames, a few peak frames, and many ambiguous or less intense frames between neutral and ones.

We suppose a temporal ordered image sequence $S = \{I_1, I_2, \ldots, I_T\}$, where T is the number of frames in one sequence. After classifying all the frames except the first two ones, an image I_i, with $3 \leq i \leq T$, is associated with a vector combined by label and probabilities: $\{G_i, p_{i,c_0}, p_{i,c_1}, \ldots, p_{i,c_6}\}$, where G_i is one of the seven class labels, and $p_{i,c_j}, (0 \leq j \leq 6)$ is the probability for the seven classes including p_{i,c_0} for neutral expression. For example, the prediction result for one image related to 'Surprise' can be $\{'Surprise', 0.0, 0.143, 0.095, 0.238, 0.048, 0.286 \text{ and } 0.19\}$, which shows that the image is labeled as 'Surprise' according to the highest probability.

3.2 Classification for Sequences

Recently, more and more researches moved from static-based methods to dynamic analysis of video sequences exploration. Similar to Bartlette et al. [5], Chang et al. [4], and Buenaposada et al. [12], we use the classification results from each frame to select the final label for the sequences. The detailed algorithm is presented in Algorithm1.

Algorithm 1 sequence level classification using weighted sum

1. Initiate a vector $P_S = \{P_1, P_2, \ldots, P_6\}$ as $P_k = 0$, where $1 \leq k \leq 6$
2. For $(i = 3 \quad to \quad T)$:
   (a) If $G_i =' Neutral'$, ignore the frame and go to next iteration;
   (b) If $G_i \neq' Neutral'$, $P_k = P_k + w_i * p_{i,c_k}$, where $1 \leq k \leq 6$
3. The final label for sequence

$$G = argmax_k \{P_k\}, \tag{3}$$

where $1 \leq k \leq 6$.

Table 2 Confusion matrix of Ours: $\mathcal{N}(\mu, \sigma_2^2)$ (%)

	An	Di	Fe	Ha	Sa	Su
An	97.5	2.43	0	0	0	0
Di	2.5	92.7	0	0	0	0
Fe	0	0	90.91	2.01	2.08	0
Ha	0	2.43	0	96.91	0	0
Sa	0	0	0	0	97.92	0
Su	0	2.43	9.09	1.06	0	100

In experiments, we built a set of weights $W = \{w_3, w_4, \ldots, w_T\}$, and we associate one weight to one image. Three sets of weights W are tested. In the first set, we consider the same weights $w_i = 1$ for all the images $3 \leq i \leq T$. For the second and third set, the weights will have higher values for the last few frames in sequences as they provide more valuable information. As we can observe [4, 12], face changes are not linear and, for different expressions, the movement patterns are also variant. As the real pattern is unknown, we assume that the relation between distance to peak frame and similarity follows normal distribution $\mathcal{N}(\mu, \sigma^2)$. The maximum is reached for the peak frame, corresponding to the last frame ($\mu = T$). In the second and third sets, σ_1^2 and σ_2^2 are respectively T and $\frac{1}{2}T$. A comparison between our proposed approach and other methods is given in Table 1b. As we can see, better performances are obtained with the three sets of W. The confusion matrix is showed in Table 2, where An stands for Angry, Di for Disgust, Fe for Fear, Ha for Happiness, Sa for Sadness, Su for Surprise, and Av for Average. Here for dynamic recognition of emotions, the results are also better than Rudovic et al. [13] in all six expressions on CK dataset. In the future use of the complete sequences as neutral-expressive-neutral, this setting can be easily extended from applying left bell to full bell. The use of normal distribution is only a rough estimation to approximate the movement patterns of expressions. Future tuning and special pattern build can be achieved.

4 Conclusions

In this work, two fast dynamic descriptors for FER system are proposed to recognize the human facial expressions in image sequences. The system analyzed a single image with static information from appearance-based descriptors and dynamic visual-time context information provided by spatio–temporal plane. Here, the dynamic information is derived from vertical-time plane and specially used to model the evolution of facial parts from neutral state to expressional state. The system further used the predicted probabilities from a single image to classify the whole sequence. After training and testing it on the popular Cohn–Kanade database, the proposed approach yielded better results than other manual or automatic methods. In our future work, we plan to use these descriptors to detect the real

rhythm of human expressions and identify the facial expressions from a video camera under variant environments.

Acknowledgments This work was supported by National Natural Science Foundation of China (61170124& 61272258), Jiangsu Province Natural Science Foundation (BK2009116) and Basic and Applied Research Program of Suzhou City (SYG201116).

References

1. Ekman P, Friesen W (1978) Facial action coding system: a technique for the measurement of facial movement. Consulting Psychologists Press, Palo Alto
2. Pantic M, Rothkrantz L (2000) Automatic analysis of facial expressions: the state of the art. IEEE Trans Pattern Anal Mach Intell 22:1424–1445
3. Huang D, Shan C, Ardabilian M, Wang Y, Chen L (2011) Local binary patterns and its application to facial image analysis: a survey. IEEE Trans Syst Man Cybern Part C: Appl Rev 41(4):1–17
4. Chang K, Liu T, Lai S (2009) Learning partially-observed hidden conditional random fields for facial expression recognition. In: CVPR, Miami, pp 533–540
5. Bartlett M, Littlewort G, Lainscsek C, Fasel I, Frank M, Movellan J (2005) Fully automatic facial action recognition in spontaneous behavior. In: Automatic Face and Gesture Recognition, pp 223–228
6. Shan C, Gong S, McOwan P (May 2009) Facial expression recognition based on local binary patterns: a comprehensive study. Image Vis Comput 27(6):803–816
7. Zhao G, Ahonen T, Matas J, Pietikainen M (2012) Rotation-invariant image and video description with local binary pattern features. Image Process, IEEE Trans 21(4):1465–1477
8. Yeasin M, Bullot B, Sharma R (2004) From facial expression to level of interest: a spatio-temporal approach. CVPR 2:922–927
9. Xiang T, Leung M, Cho S (2008) Expression recognition using fuzzy spatio-temporal modeling. Pattern Recognit 41(1):204–216
10. Zhao G, Pietikäinen M (2009) Boosted multi-resolution spatiotemporal descriptors for facial expression recognition. Pattern Recogn Lett 30(12):1117–1127
11. Yang P, Liu Q, Metaxas DN (2009) Boosting encoded dynamic features for facial expression recognition. Pattern Recogn Lett 30(2):132–139
12. Buenaposada J, Munoz E, Baumela L (January 2008) Recognising facial expressions in video sequences. Pattern Anal Appl 1(2):101–116
13. Rudovic O, Pavlovic V, Pantic M (2012) Multi-output laplacian dynamic ordinal regression for facial expression recognition and intensity estimation. CVPR '12 Proceedings of the 2012 IEEE Conference on Computer Vision and Pattern Recognition (CVPR) pp 2634–2641
14. Kienzle W, Bakir G, Franz M, Schölkopf B (2004) Face detection—efficient and rank deficient. NIPS 17(2005):673–680
15. Ji Y, Idrissi K (Jul. 2012) Automatic facial expression recognition based on spatiotemporal descriptors. Pattern Recognit Lett 33(10):1373–1380
16. Beveridge J, Bolme D, Draper B, Teixeira M (February 2005) The csu face identification evaluation system: its purpose, features, and structure. Mach Vis Appl 16(2):128–138
17. Ojala T, Pietikäinen M, Harwood D (January 1996) A comparative study of texture measures with classification based on feature distributions. Pattern Recognit 29(1):51–59
18. Bassili JN (1979) Emotion recognition: the role of facial movement and the relative importance of upper and lower areas of the face. J Pers Soc Psychol 37(11):2049–2058
19. Kanade T, Cohn J, Tian Y-L (2000) Comprehensive database for facial expression analysis. In Proceedings of the 4th IEEE international conference on automatic face and gesture recognition (FG'00), Grenoble, pp 46–53

Moving Objects Detecting and Tracking for Unmanned Aerial Vehicle

Binpin Su, Honglun Wang, Xiao Liang and Hongxia Ji

Abstract Moving objects detecting and tracking is important for future Unmanned Aerial Vehicles (UAVs). We propose a new approach to detect and track moving objects from the flying UAV. First, estimate the global-motion of the background by tracking features selected by KLT algorithm from frame to frame. In order to avoid features located on the foreground objects participating in motion estimation, feature effectiveness evaluation is employed. Then compensate the background with the transform model computed by RANSAC. Define the undefined area before applying frame difference method to the compensated frame and the current frame. Then initialize the tracking module with information obtained from the detecting module, which overcomes shortcomings of artificial orientation of traditional tracking algorithms. For tracking fast and robustly from UAVs, we design a new tracking algorithm by fusing Kalman prediction and Mean Shift Search together. The experimental results presented effectiveness of the whole detecting and tracking approach.

Keywords Object detecting · Object tracking · Global-motion estimation · Mean Shift · Kalman prediction

1 Introduction

Recently, UAVs have been used more and more widely for news gathering, search, and rescue both in military and civil areas, especially in a reconnaissance and strike integrated system by aerial surveillance. Aerial surveillance is performed primarily using video cameras these days. Exploitation of UAV video data is increasingly

B. Su (✉) · H. Wang · X. Liang · H. Ji
Science and Technology on Aircraft Control Laboratory, Beijing University of Aeronautics and Astronautics, Beijing 100191, China
e-mail: binpin.su@gmail.com

F. Sun et al. (eds.), *Foundations and Practical Applications of Cognitive Systems and Information Processing*, Advances in Intelligent Systems and Computing 215,
DOI: 10.1007/978-3-642-37835-5_29,

critical for surveillance systems. Large numbers of videos from UAVs will overwhelm human operators for visually inspecting the data, so automatic video analysis and processing is essential, which will not only reduce the workload for humans but will also improve the fully-automatic surveillance ability for future UAVs.

Moving objects detecting and tracking for UAVs is a subject of active research. The detection of an interesting moving object is based on the motion information such as optical flow or background subtraction. Tracking is to maintain a consistent identity on the object based on the appearance, shape, or kinematic information over the frames. A large amount of research on moving-object detecting and tracking in a video has been performed in the past years, and a variety of methods have been developed, which include region-based [1–3], feature-based [4–6], and contour-based [7, 8] methods. Although many methods have been proposed, most can only be used for specific applications with reliable assumptions, such as a stationary application in a constrained and uncluttered environment. For UAV videos captured by a fast-moving camera, moving objects detecting and tracking has the following key challenges.

The camera is mounted on the moving UAV, so there are two independent motions involved: the motion of moving objects and the motion of camera. Unfortunately, those two motions are blended together. In order to detect moving objects robustly from the moving background, it should be able to decompose these two independent motions from sensor readings.

A UAV may move very fast, and an object may also move fast. UAV video objects tend to have low resolution and the background is usually cluttered. There are various types of noise added at various stages, including changing lighting conditions, changing appearance, rotations, and scales of objects. Furthermore, UAV objects may be so small that they are similar to noise, and may suffer partial or total occlusions.

UAV video analysis requires fast tracking of moving objects. Hence a compromise typically exists between the achieving of real-time tracking performance and the constructing of a robust tracking algorithm.

Frame difference, which compares two consecutive image frames and finds moving objects based on the difference, is perhaps the most intuitive and fastest algorithm for moving object detection, especially when the viewing camera is static. However, for UAV videos, straightforward differencing is not applicable because a large difference is generated by simply moving the camera even if nothing moves in the environment. The global-motion of the background should be eliminated so that the remaining motions, which are due to moving objects, can be detected.

To overcome the first problem mentioned above, various methods have been proposed to stabilize camera motions by tracking features [9] and computing optical flow [10]. These approaches focus on estimating the transformations between two image coordinate systems. The features associated with the foreground objects should be eliminated since they will lead to wrong estimation of the global-motion of the background.

Once moving objects has been identified, they need to be tracked. Two major components can be distinguished in a typical visual tracker [11]. Target Representation and Localization is mostly a bottom-up process which copes with the changes in the appearance of the target. Filtering and Data Association is mostly a top-down process dealing with the dynamics of the tracked object, learning of scene priors and evaluation of different hypotheses by using a Bayesian filter. The way the two components are combined and weighted is application dependent. They play a decisive role in the robustness and efficiency of the tracker.

In this paper we propose an approach to detect and track moving objects for UAV. The block diagram of the proposed approach is depicted in Fig. 1. It includes three steps: compensation of the image flow induced by a moving camera, detection of moving regions in each frame, and tracking of moving objects in time.

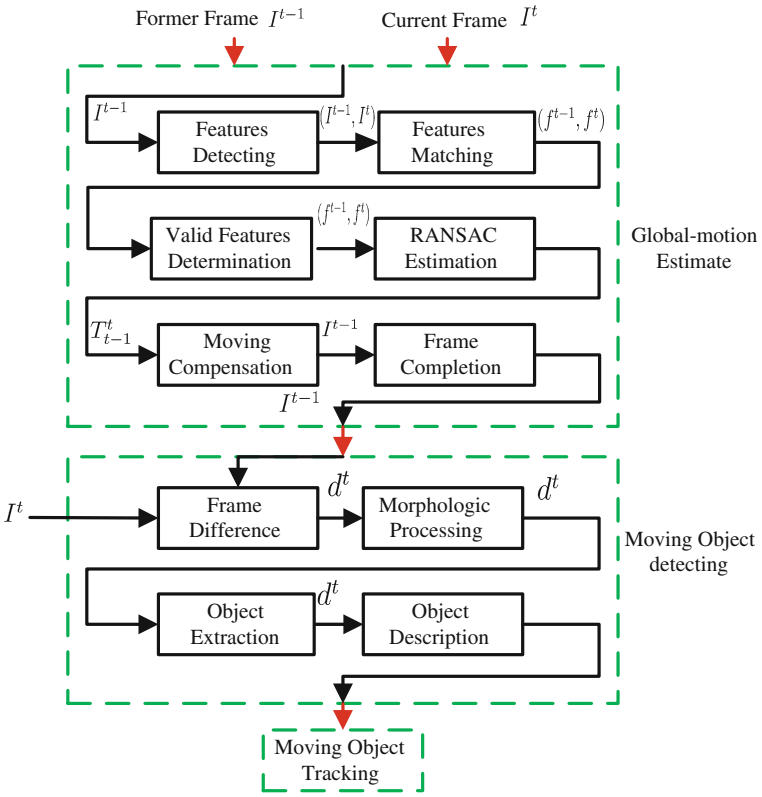

Fig. 1 The proposed detecting and tracking approach

2 Global-Motion Estimation

The motion induced by a moving camera must be canceled before motion detection. The global-motion estimation can be estimated by tracking features between images. When the camera moves, two consecutive images, I^t (the image at time t) and I^{t-1} (the image at time $t-1$), are in different coordinate systems. Global-motion estimation is a transformation from the image coordinates of I^{t-1} to that of I^t so that the two images can be compared directly. The transformation can be estimated using two corresponding feature sets: a set of features f^{t-1} in I^{t-1} and a set of corresponding features f^t in I^t.

2.1 Feature Detecting and Matching

In general, two basic questions must be answered: how to select features and how to track them from frame to frame. Two most successful visual features are corner [12] and SIFT (Scale Invariant Scale Transform) [13] features. A corner feature is characterized by the high intensity changes in both horizontal and vertical directions. SIFT feature is a more advanced visual feature, which is known to be relatively invariant to image translation, scaling, and rotation and partially invariant to changes in illumination and local image deformations. Considering the computational intensive, it is not suitable for real-time applications, unless the algorithm is implemented in hardware. We adopt the KLT [4] feature (a famous corner feature) selection algorithm for corresponding feature set selection due to its computation efficiency. The feature selection algorithm runs on image I^{t-1}, and generates features f^{t-1}. A corresponding feature set f^t is constructed by tracking the same features on the image I^t. Figure 2a shows the outdoor environment. Figure 2b shows the feature selected from the image I^t, and Fig. 2c shows the same features tracked over 5 frames on the image I^{t+5}, while Fig. 2d implies the optical flow between the two frames.

2.2 Valid Feature Determination

Once the correspondence $f = \{f^{t-1}, f^t\}$ is known, the geometric transform to align $I^{t-1}$and I^t can be estimated using a transformation model. However, as mentioned before, some of the features associated with the foreground moving objects may be included, which will lead to an inaccurate estimation of the global-motion of background. Thus, those features should be eliminated from the feature set before the transform is computed. We name features belonging to background as valid features (or insiders) while foreground features are invalid features (or outliers).

Fig. 2 **a** out door environment **b** features detected on image It **c** features detected on image It+5 **d** optical flows between the two images

Since features belonging to the background move in a uniform way, assume that the distribution of the optical flow vectors follows Gaussian distribution. The probability out of the range of $[\mu - 3\sigma, \mu + 3\sigma]$ is very small according to the Gaussian theory, where μ, σ denote the expected value and variance respectively. When the vector of two corresponding features is out of the range, the features are probably belonging to foreground objects. Let V_i represent the optical flow vector of a selected feature between two consequent frames. $\|V_i\|$, $Ang(V_i)$ denotes its vector norm and vector direction, respectively, while $\left(\mu_{\|\cdot\|}, \sigma_{\|\cdot\|}\right)$ and $\left(\mu_{Ang}, \sigma_{Ang}\right)$ represent the expected value, variance of the norm, and direction angle of all selected features respectively. The determinant condition (outlier algorithm) can be defined as follows:

$$\begin{cases} f_i \in F_{\text{in}} & \text{if } \left|\|V_i\| - \mu_{\|\cdot\|}\right| < 3 \cdot \sigma_{\|\cdot\|} \text{ and } \left|Ang(V_i) - \mu_{Ang}\right| < 3 \cdot \sigma_{Ang} \\ f_i \in F_{\text{out}} & \text{otherwise} \end{cases} \tag{1}$$

where F_{in} and F_{out} denote valid and invalid features respectively. Figure 3 shows the result of the valid feature determination algorithm. F_{in} is marked with red circles and F_{out} is marked with green circles. In the frame, the aircraft is moving while the buildings and trees are static. All the features associated with the aircraft are detected and eliminated. Note that the valid feature determination will be violated when moving objects are very close to the camera since they will occupy most of the areas of an image and the features optical flow will not conform to Gaussian distribution.

Fig. 3 Inliers (*red circle*) and outliers (*green circles*)

2.3 Transform Model

Using the remaining insiders (valid features set), we can compute the relatively accurate transformation model. The most-used models include affine model, bilinear model, and pseudo-perspective model. When the interval between consecutive images is very small, most global-motion can be estimated using an affine model, which can cover translation, rotation, shearing, and scaling motions. Hence, we use an affine model here:

$$\begin{bmatrix} f_x^t \\ f_y^t \end{bmatrix} = \begin{bmatrix} af_x^{t-1} + bf_y^{t-1} + t_1 \\ cf_x^{t-1} + df_y^{t-1} + t_2 \end{bmatrix} \tag{2}$$

We compute the transformation model T_{t-1}^t by using RANSAC (RANdom SAmple Consensus) algorithm [14], an iterative method, to estimate the parameters of the affine model due to its ability for robust estimation.

2.4 Moving Compensation

For frame differencing, image I^{t-1} is converted using the transformation model before being compared to the image I^t in order to eliminate the effect of global-motion. For each pixel (x, y)

$$I_{\text{comp}}^{t-1}(x, y) = I^{t-1}\left(\left(T_{t-1}^t\right)^{-1}(x, y)\right) \tag{3}$$

where I_{comp}^{t-1} represents the compensation of global-motion of image I^{t-1}.

3 Moving Object Detecting

The difference image between two consecutive images is computed using the compensated image:

$$I_{\text{diff}}(x,y) = \left| I^{t-1}_{\text{comp}}(x,y) - I^{t}(x,y) \right| \tag{4}$$

Note that some pixels around the border moved out of the frame after compensation, causing undefined area in the compensation frame. To obtain a complete frame, we redefine the difference frame as follows:

$$I_{\text{diff}}(x,y) = \begin{cases} \left| I^{t-1}_{\text{comp}}(x,y) - I^{t}(x,y) \right| & \text{if}(x,y) \in \text{definedarea} \\ 0 & \text{if}(x,y) \in \text{undefinedarea} \end{cases} \tag{5}$$

Figure 4 compares the result of two cases: frame difference without global-motion compensation (Fig. 4a) and with global-motion compensation (Fig. 4b).

With the image processes introduced above, we can detect the moving object in theory, but in fact due to illumination and background variance, there are noises in the frame. Hence, we continue to perform a morphologic closing operation on the result to remove camera noise and to connect object pixels into regions. The morphologic process include erosion and dilation algorithm, which define as follows:

$$A \odot B = \left\{ x \middle| (B)_x \subseteq A \right\} \tag{6}$$

$$A \oplus B = \left\{ x \middle| \left(\hat{B}\right)_x \cap A \neq \varnothing \right\} \tag{7}$$

where A is the image to be processed and B is the erosion matrix of 20×20 pixels. The resultant image is then size-filtered. Only connected regions of size bigger than a threshold are kept. Figure 5 shows the difference of the difference image with noise and with morphologic process. We can extract the detecting moving object clearly after morphologic.

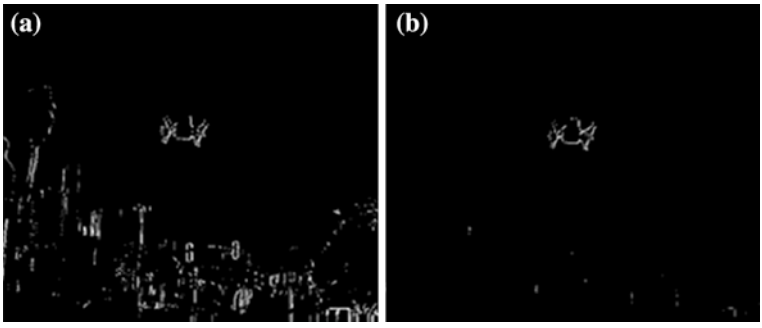

Fig. 4 **a** frame difference without global-motion compensation **b** frame difference with global-motion compensation

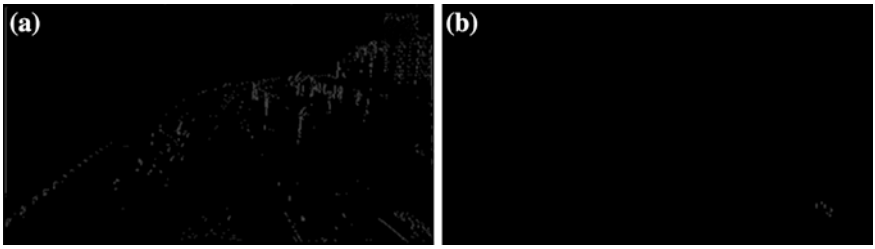

Fig. 5 **a** frame difference without morphologic process **b** frame difference with morphologic process

4 Object Tracking

In the previous work, tracking object was always initialized with a hand-drawn region. As in the surveillance of the aerial video, it is difficult to point the exact interesting region due to the fast video speed, and the region including noise and unrelated information will lead to wrong track. In this paper we propose an approach to initialize the region by the information about the moving object obtained from the object detecting module, which overcomes shortcoming of artificial orientation.

Although KLT algorithm can track feature points, it cannot identify which feature point belongs to the target we want to track. Hence, we choose other feature space. Mean Shift, which is based on the motion of "kernel", is an efficient technique that can automatically sort out local model within a set of data. Here, we employ the Mean Shift algorithm which chooses color information as the object feature.

4.1 Object Tracking Using Mean Shift Algorithm

The Mean Shift tracking algorithm is divided into three parts: target representation, similarity function measure, and target location computation [15]. First, the reference target model is represented by its probability density function (pdf) $\hat{q} = \{\hat{q}_u\}_{u=1\ldots m}$, $\sum_{u=1}^{m} \hat{q}_u = 1$. A target candidate which is defined at location y is characterized by the pdf $\hat{p}(y) = \{\hat{p}_u(y)\}_{u=1\ldots m}$, $\sum_{u=1}^{m} \hat{p}_u = 1$. m represents m-bin histograms. Second, the similarity between the target model and the target candidates in the next frame is measured using the metric derived from the Bhattacharyya coefficient $\hat{\rho}(y) \equiv \rho[\hat{p}(y), \hat{q}] = \sum_{u=1}^{m} \sqrt{\hat{p}_u(y)\hat{q}_u}$. The coefficient determines whether it is the most similar result to a given model, if not then search around. The bigger the value, the more similar the model is to the target. The search procedure uses gradient information which is provided by the Mean Shift vector. Mean Shift was originally presented in 1975 by Fukunaga and Hostetler

[16]. We use Mean Shift iterations to search for the maxima density function of the coefficient, then we can obtain the most reliable candidate. The Mean Shift algorithm calculates local optimal result fast and effectively which is superior to blindness search. Besides color feature using for tracking is simple and effective in most situations.

However, the Mean Shift tracking algorithm has some shortcomings. It cannot be applied to track fast-moving objects. Because the most reliable location y was obtained after some manipulations using Taylor expansion around the probability location $\hat{y}_0$ on $\hat{\rho}(y)$:

$$\rho[\hat{p}(y), \hat{q}] \approx \frac{1}{2}\sum_{u=1}^{m}\sqrt{\hat{p}_u(\hat{y}_0), \hat{q}_u} + \frac{1}{2}\sum_{u=1}^{m}\hat{p}_u(\hat{y})\sqrt{\frac{\hat{q}_u}{\hat{p}_u(\hat{y}_0)}} \tag{8}$$

When the target moves fast, the new location is far from the old one which is not fit for neighborhood expansion analysis.

Besides, the feature color, being described as the target and candidates in Mean Shift tracking algorithm, is a relative weak feature. When some noises which are similar to the target appear in the background, it will cause wrong tracking.

4.2 Kalman Prediction

Mean Shift tracking algorithm is a bottom-up appearance-based tracking method, while Kalman is totally a top-down process. Kalman is an optimal recursive data processing algorithm, which consists of two steps: prediction and correction. In the former step, the state is predicted with the dynamic model, while in the latter step, it is corrected with the observation model. Since the error covariance of the estimator is minimized, it can be regarded as an optimal estimator.

As for tracking, the information characterizing the target is defined by the state sequence $\{X_k\}_{k=0,1,\ldots} = \{x_k, y_k, v_{xk}, v_{yk}\}$, representing the target's location and its velocity, whose evolution in time is specified by the dynamic equation $X_k = FX_{k-1} + w_k$. The available measurements $\{Z_k\}_{k=1,\ldots} = \{x_k, y_k\}$ are related to the corresponding states through the measurement equation $Z_k = HX_k + v_k$. The matrix F is called the system matrix and H is the measurement matrix. The noise sequence w_k and v_k are Gaussian, $w_k \sim N\left(0, \sigma_{\mathrm{w}}^2\right)$, $v_k \sim N\left(0, \sigma_{\mathrm{v}}^2\right)$.

Considering a target may not always runs with uniform velocity, it moves fast and sometimes slowly, turns around quickly, or brakes suddenly. We suppose that it moves in a linear motion with random acceleration noise. We design the state sequence updates in the following way:

$$x_k = x_{k-1} + \upsilon_{x_{k-1}} t + \frac{1}{2} w_k t^2 \tag{9}$$

$$y_k = y_{k-1} + v_{y_{k-1}} t + \frac{1}{2} w_k t^2 \tag{10}$$

$$v_{x_k} = v_{x_{k-1}} + w_k t \tag{11}$$

$$v_{y_k} = v_{y_{k-1}} + w_k t \tag{12}$$

where t denotes the interval frames. Hence, we design the dynamic equation and the measurement equation as follows:

$$\begin{pmatrix} x_k \\ y_k \\ v_{x_k} \\ v_{y_k} \end{pmatrix} = \begin{pmatrix} 1 & 0 & t & 0 \\ 0 & 1 & 0 & t \\ 0 & 0 & 1 & 0 \\ 0 & 0 & 0 & 1 \end{pmatrix} \begin{pmatrix} x_{k-1} \\ y_{k-1} \\ v_{x_{k-1}} \\ v_{y_{k-1}} \end{pmatrix} + \begin{pmatrix} \frac{t^2}{2} \\ \frac{t^2}{2} \\ t \\ t \end{pmatrix} w_k \tag{13}$$

$$\begin{pmatrix} x_k \\ y_k \end{pmatrix} = \begin{pmatrix} 1 & 0 & 0 & 0 \\ 0 & 1 & 0 & 0 \end{pmatrix} \begin{pmatrix} x_{k-1} \\ y_{k-1} \\ v_{x_{k-1}} \\ v_{y_{k-1}} \end{pmatrix} + \begin{pmatrix} 1 \\ 1 \end{pmatrix} v_k \tag{14}$$

where $\sigma_w = \sigma_v = 5$. The object of using Kalman prediction is to estimate the state X_k given all the measurement $Z_{1:k}$ up to that moment, or equivalently to construct the probability density function $p(x_k|Z_{1:k})$.

4.3 Fusing Kalman Prediction and Mean Shift Search

Considering the advantages and disadvantages of the Mean Shift and Kalman, we combine Mean Shift search and Kalman prediction together to track fast and robustly. The framework is shown in Fig. 6. Kalman predicts position of the target first, and Mean Shift searches in the confidence region estimated by Kalman which largely improves the search efficiency since it reduces the search area. The search result of Mean Shift is used in turn as the measurement value of Kalman to predict the position of the target in the next frame. As the search result of Mean Shift may not be accurate which will lead to unreliable prediction computed by Kalman, we add a determination. $(\hat{x}_k, \hat{y}_k)$ which represents predicted value of Kalman, while (x_k, y_k) denotes the search value of Mean Shift. The two values are highly similar in general and $e(k) = \sqrt{(x_k - \hat{x}_k)^2 + (y_k - \hat{y}_k)^2}$ are small. When the difference is large, we can infer that Mean Shift result is invalid so it cannot be used as the measure value of Kalman.

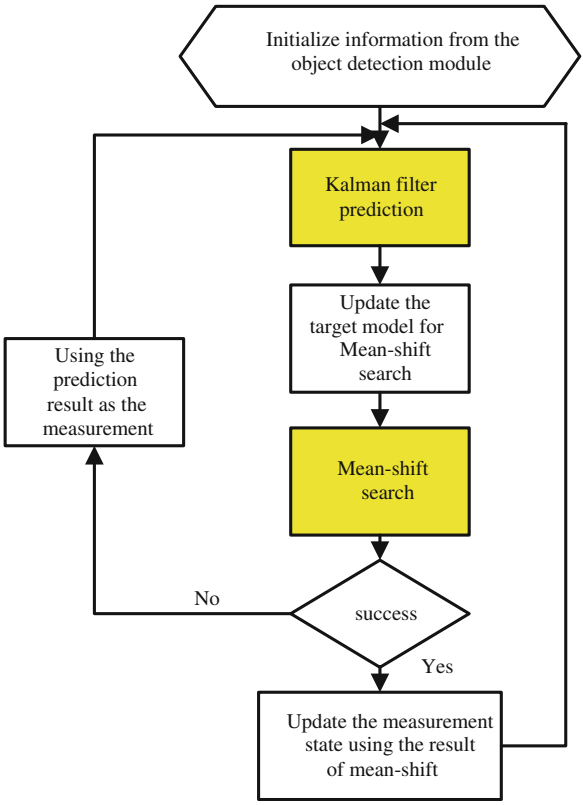

Fig. 6 New tracking algorithm of fusing Mean Shift search and Kalman prediction

5 Experiments

We have developed a system implementation for testing the detecting and tracking method, using visual C++ 2010 platform and OpenCV library. The computer processor is Intel Xeon @2.80 GHz.

5.1 Moving Object Detecting Result

The city video was taken from an airplane. The three rows shown in Fig. 7 represent detection results of frames 37, 41, and 44, respectively, which aims at detecting a moving car along the road. The first column shows the frame difference without global-motion compensation while the second column shows the frame difference with compensation. In the third column, we mark out the detected moving region with red rectangle. There is only one moving car in the scene. We compute the location and velocity of the moving region to prepare for the tracking module. The total process time is 215 ms.

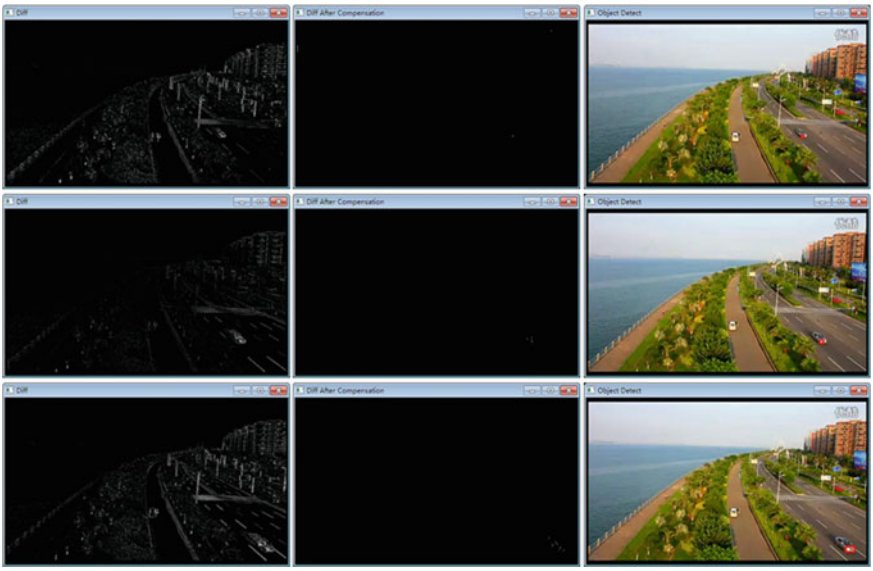

Fig. 7 Moving object detection from a moving camera. The frames 37, 41, and 44 are shown

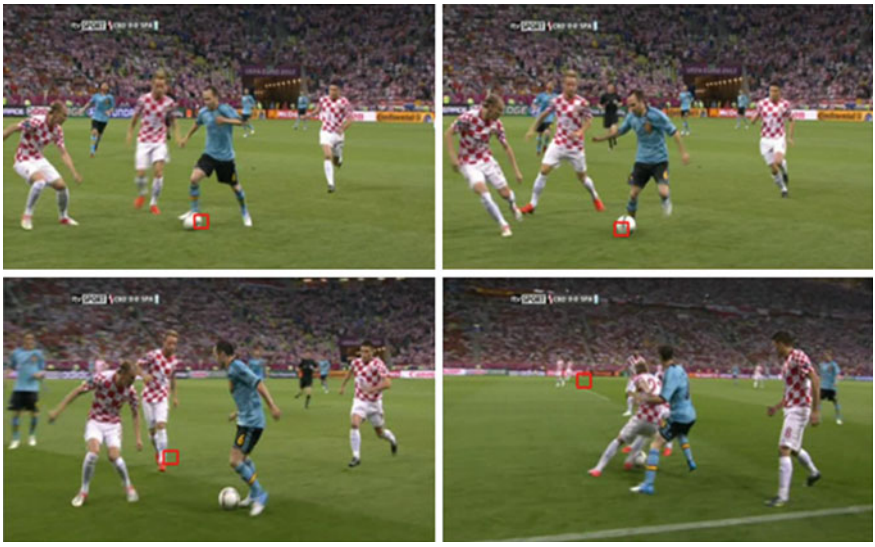

Fig. 8 Results of football tracking with Mean Shift

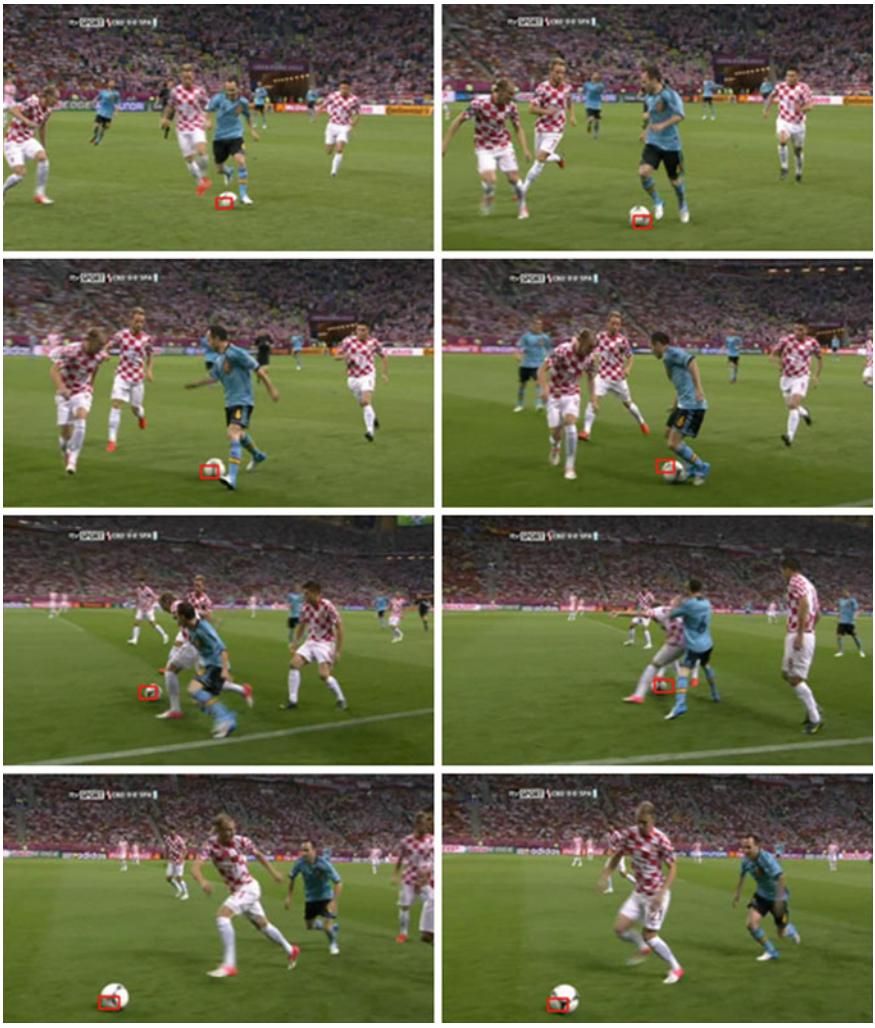

Fig. 9 Results of football tracking by fusing Mean Shift and Kalman. Frames 1, 28, 32, 45, 56, 69, 80, 88 (*left* to *right*, *up* to *down*) are shown

5.2 Moving Object Tracking Results

In a sequence of the game of football, the ball runs fast and moves in a random way. Note that the motion characters of the tracked targets from UAVs are similar to football, so we use the football sequence to test the performance of the tracking algorithms. When tracking the football using Mean Shift only (Fig. 8), it shows

Fig. 10 Results of car tracking with Mean Shift

Fig. 11 Results of tracking by fusing Mean shift and Kalman. Frame1, 110, 171 (*left to right*) are shown

that the ball can be tracked well in the first few frames, but fails later due to its fast movement, just as the theory analyzed in the fourth part.

Figure 9 shows the tracking result of the running football in the same football sequence using the method of fusing Mean Shift search and Kalman prediction together. Whether the football runs relatively slowly which was brought along by the player (frame 1, 28, 32, 45), runs very fast because of being shoot (frame 80, 88), or partially occlusion (frame 69) by the dual meet players, it can all be tracked robustly.

In a car sequence (Fig. 10), which has 200 frames of 512*288 pixels, we intend to track the black car. Since the histogram of the shade is similar to the car itself, Mean Shift tracking converges to the shade.

Figure 11 shows the result of tracking the black car using the fusing method proposed in this paper. Observe that the overall algorithm is able to track the car in the presence of similar objects (car shadow in frame 110) and partially occlusion by the obstacle on the road (frame 171).

In a more concrete analysis of the car sequence, similar objects in the neighborhood and occlusion increase the measurement uncertainty. In Fig. 12, we present the measurements (dotted line) obtained by Mean Shift and the estimated locations of the object computed by Kalman (solid line) in the direction of X and Y

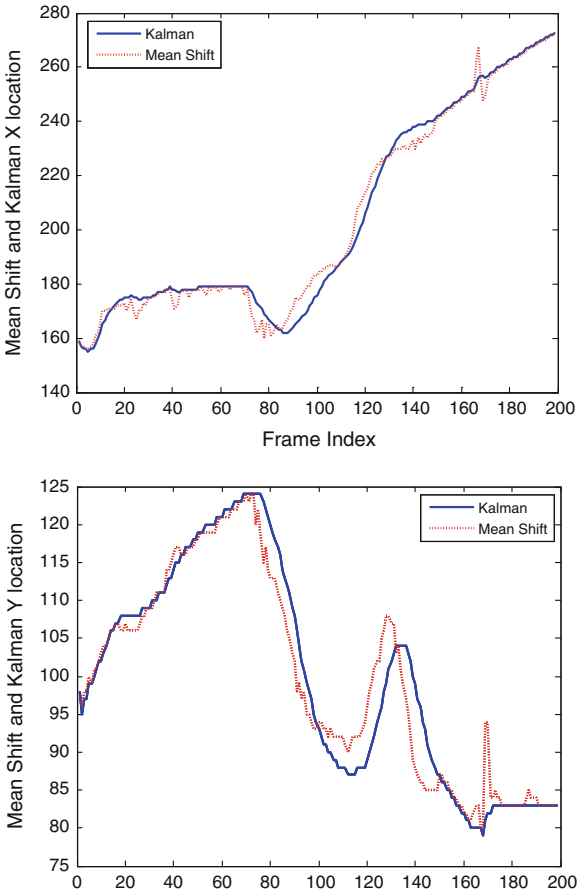

Fig. 12 Measurement and estimated state of car sequence

respectively. In most of the frames, two values are very close to each other. But the presence of car shadow from frame 72 to 149, which determines an increase in state uncertainty, give two values which vary. The sharp curve from frame 169 to 175 in the dotted line represents invalid search by Mean Shift caused by feature occlusion (see Fig. 11). By fusing Mean Shift search and Kalman prediction together, we can conduct a robust track.

Besides achieving a robust detecting and tracking method, we also care much about its real-time performance. When searching the target in one frame of 512*288 pixels, the average cost time using Mean Shift is 31 ms, while the time cost by fusing Mean Shift and Kalman is 26 ms. By fusing Mean Shift search and Kalman prediction together, we can also conduct a faster track. Thus the fusing track algorithm is fit for our aerial video tracking.

6 Conclusion and Future Work

A real-time method for moving object detecting and tracking on an unmanned aerial vehicle was introduced. The global-motion of the background was estimated using corresponding valid feature sets first. Then detect the moving object after compensating the consecutive frames. Use the location and velocity information of the moving object obtained from the object detecting module for object tracking module initialization. Finally we integrated the Mean Shift algorithm and the Kalman prediction to track objects fast and robustly. The results show that the method is general and computationally inexpensive which is fit for aerial video surveillance.

Additional research work is needed to improve the performance of the method, such as optimizing the object detection algorithm to minimize the computation cost. On the other hand, the current system can only estimate the location, direction and speed of the moving objects. Since a single camera has limit on retrieving depth information, the information from a camera alone is not rich enough to construct full 3-dimensional models of moving objects. We can use a laser rangefinder, which provides the depth information of a single plane.

Acknowledgments We appreciate the contributions made by the open source communities to the humanity. We especially thank the developers and sponsors of OpenCV libraries for their valuable work.

References

1. Wang D (1998) Unsupervised video segmentation based on watersheds and temporal tracking. Circuits Syst Video Technol IEEE Trans 8(5):539–546
2. Wong K, Spetsakis M (2002) Motion segmentation and tracking. In: International conference on vision interface, Citeseer, pp 80–87
3. Cavallaro A, Ebrahimi T (2000) Video object extraction based on adaptive background and statistical change detection. Proc of SPIE 4310:465
4. Shi J, Tomasi C (1994) Good features to track. In: Proceedings of the CVPR'94. IEEE computer society conference on computer vision and pattern recognition, pp 593–600
5. Tomasi C, Kanade T (1991) Detection and tracking of point features. Carnegie Mellon Univ, School of Computer Science
6. Trucco E, Petillot Y, Ruiz I, Plakas K, Lane D (2000) Feature tracking in video and sonar subsea sequences with applications. Comput Vis Image Underst 79:92–122
7. Jurie F (1998) Tracking objects with a recognition algorithm. Pattern Recogn Lett 19(3):331–340
8. Drummond T, Cipolla R (2002) Real-time visual tracking of complex structures. Pattern Anal Mach Intell IEEE Trans 24(7):932–946
9. Jung B, Sukhatme G (2004) Detecting moving objects using a single camera on a mobile robot in an outdoor environment. In: International conference on intelligent autonomous systems, Citeseer, pp 980–987

10. Srinivasan S, Chellappa R (1997) Image stabilization and mosaicking using the overlapped basis optical flow field. In: The proceedings of the IEEE international conference on image processing, vol 3, pp 356–359
11. Comaniciu D, Ramesh V, Meer P (2003) Kernel-based object tracking. Pattern Anal Mach Intell IEEE Trans 25(5):564–577
12. Harris C, Stephens M (1988) A combined corner and edge detector. In: Alvey vision conference
13. Lowe D (2004) Distinctive image features from scale-invariant keypoints. Int J Comput Vision 60(2):91–110
14. Xin S (2006) The matching method based on ransac algorithm for estimation of the fundamental matrix. J Shanghai Dianji Univ 9(004):66–69
15. Comaniciu D, Meer P (1999) Mean shift analysis and applications. In: The proceedings of the seventh IEEE international conference on computer vision, vol 2, pp 1197–1203
16. Fukunaga K, Hostetler L (1975) The estimation of the gradient of a density function, with applications in pattern recognition. Inf Theory IEEE Trans 21(1):32–40

Object Recognition and Pose Estimation Based on Principle of Homology-Continuity

Zhonghua Hao and Shiwei Ma

Abstract Based on manifold ways of perception, this paper describes a novel method of object recognition and pose estimation within one integrated work. This method was inspired by bionic pattern recognition and manifold learning. Based on the principle of homology-continuity, we establish shortest neighborhood graph (SNG) for each class and regard it as a covering and triangulation for the hypersurface that the training data distributed on. For object recognition task, we propose a simple but effective classification method, named SNG-KNN. For pose estimation, local linear approximation method is adopted to build a local map between high-dimensional image space and low-dimensional manifold. The projective coordinates on manifold can depict the pose of object. Experiment results suggest that the recognition performance of our approach was similar and sometimes better compared to the SVM method; moreover, the pose of object can be estimated.

Keywords Object recognition · Pose estimation · Shortest neighborhood graph · Local linear estimation · Simplex

1 Introduction

Object recognition and pose estimation are two important goals for an intelligent vision system. Object recognition is the problem of finding a given object in an image or video sequence, and pose estimation is the problem of determining the transformation of an object in a 2D image which gives the 3D object.

Z. Hao (✉) · S. Ma
School of Mechatronic Engineering and Automation, Shanghai Key Laboratory of Power Station Automation Technology, Shanghai University, Shanghai 200072, China
e-mail: hzhaly1102@yahoo.com.cn

S. Ma
e-mail: masw@shu.edu.cn

F. Sun et al. (eds.), *Foundations and Practical Applications of Cognitive Systems and Information Processing*, Advances in Intelligent Systems and Computing 215,
DOI: 10.1007/978-3-642-37835-5_30,

In recent years, statistical learning methods are the primary approach to solve these two problems, such as LDA, SVM, and ADABOOST [1]. The basic thought of these methods is: First, find out the features that have big inter-class difference and little inner-class difference. Then, adopt various algorithms to find out the optimalizing hyperplane for classification to separate two or more classes. However, there are two critical drawbacks of these methods. (1) The recognition result is not satisfactory since the invariance features are hard to extract when the pose, illumination, and other factors vary from scene to scene. (2) Negative samples are needed during the study process. The selection of negative sample data determines the generalization of the classifier. Moreover, how to choose negative samples to obtain the most optimal separating hyperplane is a complicated question. Another critical problem coupled with negative sample is that the classifier model must be trained renewably if adding new kinds of objects to recognition in training data. During increase in the number of categories, the learning process becomes more and more complicated.

2 Motivation and Basic Ideas

To deal with the drawbacks mentioned above, in 2002, Wang Shoujue [2] proposed a new model of pattern recognition called Bionic Pattern Recognition (BPR), which is based on 'matter cognition' instead of 'matter classification'. This method gives us a hopeful way to overcome the drawback mentioned above. However, in BPR method, the topological character of training samples must be analyzed by humans before using artificial neural networks to cover the training image sets.

On the other hand, in 2000, H. Sebastian Seung and Daniel D. Lee proposed the manifold ways of perception [3]. It pointed out that the image of object changes in pose, scale, illumination, and other sources of continuous variability would lie on low-dimensional manifolds embedded in high-image space. Coupled with this theory, many manifold learning algorithms (MLA) are proposed; Isomap [4], LLE [5], and LTSA. Many researches [6, 7] have applied these methods to solve the recognition problem. Unfortunately, these method just take manifold learning algorithm as a preprocess step before classification. They still have the drawback 2.

It is worth to noting that the mathematic foundation of BPR and MLA is Principle of Homology-Continuity (PHC). This principle depicts continuity among samples of the same class, i.e., if two samples are in the same class, the difference between them must be gradually changed.

According to PHC, for the same object, gradual change processes exist between two different pose of the same object. Therefore, if the sampling density is high enough, the dataset with pose change distributes on a hypersurface in high-image space. Moreover, because the process of pose variation has some kind of regularity, e.g., object rotation, human walking, there should be a meaningful low-dimensional manifold hidden in high-dimensional image space.

Based on this assumption, the object recognition task is converted to determine on which hypersurface in high-dimensional image space the test image lies, and pose estimation is to find out the location of the test image on the low-dimensional manifold which reflects pose variation.

In this paper, we simulate the way of human perception, propose an integrated framework that addresses the object recognition and pose estimation problem. As a first step, we establish a Shortest Neighborhood Graph (SNG) for each train image set and regard SNG as a covering and triangulation of the hypersurface that train image distributed. Second, apply KNN algorithm to SNG for classification. The simplex characters divided by SNG are used to determine the parametric '*k*' in KNN and calculate the residual error of linear representation by neighborhood images. This step could point out if the test image belongs to neither class that has been trained and the represented weight could also be determined. The pose estimate process is to use local linear approximation method to build a local map between high-image space and low-dimensional manifold. The projective coordinates on manifold can depict the pose of object in tested image.

There are three main contributions to our framework. The first contribution of this paper is adopting the thought of bionic pattern recognition, regarding SNG as a cover and triangulation of the hypersurface that the training data distributes on. Hence the recognition task is converted into finding on which SNG the test image lies, and is contained in which simplex, more precisely. It makes the algorithm to not need negative samples and establish an SNG if adding new object to recognition. The second contribution of this paper is the SNG-KNN method. This method could adjust parameter '*k*' that determines the research area in KNN algorithm adaptively and judges whether the test image lies on one of the SNGs by analyzing the characteristics of simplex. The third contribution of this paper is adopting local linear approximation method to establish a map between high-image space and low manifold. Hence the pose of test image could be estimated.

The rest of this paper is organized as follows. We briefly summarize the most relevant work and introduce our motivation in Sects.1 and 2. In Sect.3, we present an introduction to SNG-KNN algorithm. In Sect.4, we describe our algorithm for classification and pose estimation. The experiments are present in Sect.5.

3 SNG-KNN Algorithm

3.1 Shortest Neighborhood Graph and Simplex

In the real world, the distribution of data sets is always nonlinear. The Euclidean distance cannot depict the intrinsic geometric distribution of the data sets. The purpose of Shortest Neighborhood Graph (SNG) is to solve this problem. The key point is estimating the geodesic distance between faraway points, given only input-space distances. For neighboring points, input-space distance (Euclidean distance) provides a good approximation to geodesic distance. For faraway points, geodesic

distance can be approximated by adding up a sequence of Euclidean distance between neighboring points. Because all pose transformation of one object is connected in SNG, so if a test image belongs to one class, it must lie on the corresponding SNG. Therefore, the SNG could be regarded as a covering of this class.

In mathematics, triangulation is a method that divides hypersurface into connected simplexes that are used to analyze the hypersurface properties. The simplex is an n-dimensional geometric solid like a triangle. It has $n + 1$ vertexes connected to every pair and linear independent. Regard images as points in high-image space. In SNG, each point connects nearby points with edges. Hence, SNG can be seen as a triangulation for the hypersurface that the training data is distributed on.

For recognition task, we need to determine on the SNG that test image lies on. The KNN algorithm is adopted in this paper. Regard test image as a point in high-image space. Parameter '*k*' which determines research area plays a critical role for effection of the classification result. How to select '*k*' properly remains a challenging question. It can be seen in Fig. 1 that as parameter '*k*' increased from *k1* to *k3* the predict result is vastly different.

3.2 Simplex Analysis

In mathematics, a manifold of dimension *n* is a topological space such that each point has a neighborhood which is homeomorphic to an open set of the Euclidean space of dimension *n*. In our work, the hypersurface is one kind of manifold and simplex is a local area of manifold, so we could analyze the simplex in Euclidean space.

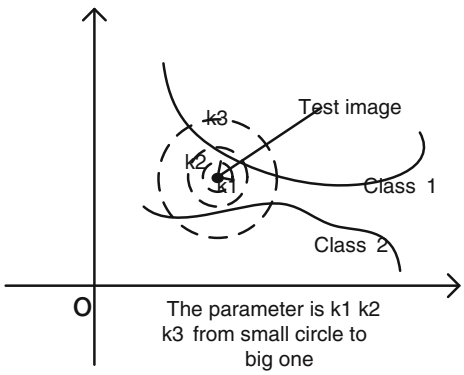

Fig. 1 Two *curves Class 1* and *Class 2* stand for the hypersurfaces of two class data distributed. *k1*, *k2*, and *k3* are the different values of parameter '*k*'. If $k = k1$, test image belongs to neither Class 1 nor Class 2. If $k = k2$, test image belongs to Class 1 with much probability. If $k = k3$, the test image belongs to Classes 1 and 2 with the same probability. It can be seen that '*k*' is a critical parameter to predict result

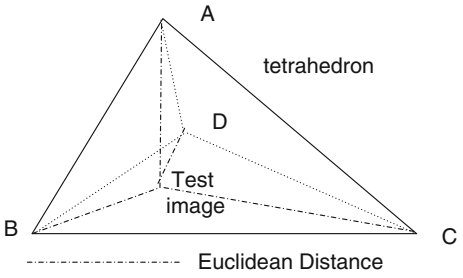

Fig. 2 A tetrahedron that stands for n-dimensional simplex. The distance from an inner point to arbitrary vertex is smaller than the longest edge of the simplex. The inner point can be linear represented by vertexes

It is obvious that if a test image lies on one SNG, it should be an inner point of one certain simplex. Thus the recognition task is converted to find out a simplex that contains test image. It can be seen from Fig. 2 that the distance from test image to arbitrary vertex is smaller than the longest edge of simplex. This conclusion is not proved here. In this paper, we select parameter 'k' equal to the longest edge of simplex that has been calculated in SNG. Therefore, if the test image is an inner point, the research area in KNN must cover the simplex.

However, the research area containing the vertexes of a certain simplex could not guarantee the test image as an inner point of this simplex. The test image may be near the simplex but not in it. Figure 3 shows this case.

On the basis of simplex definition, the vertexes are linear independent. Therefore, if the test image is an inner point of simplex, it can be represented by a linear combination of vertexes. If the test image is outside the simplex, the optimum linear representation is the projection vector of test image. The closer the test image is to simplex, the less difference there is between the length of test image vector and the length of its projection vector. In Fig.4 is defined test image vector as $\vec{T}$, and vertex vectors as $\vec{v}_1, \vec{v}_2 \ldots \vec{v}_N$. The linear combination that minimizes $\varepsilon(W)$ is the projection of test image vector; e is a linear combination error which reflects how close the test image is to simplex. In our experiment, we consider the test image as an inner point of simplex if $e < 0.05$.

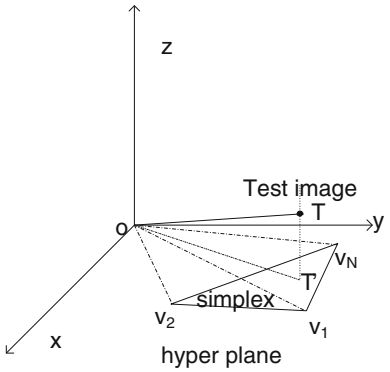

Fig. 3 T is test image near the simplex, v_1, $v_{2,\ldots,}v_N$ are the vertexes. T' is the projection of P

$$\varepsilon(W) = \min\left|\overrightarrow{T} - \sum W_n \vec{v}_n\right|^2; \quad n = 1...N. \tag{1}$$

$$e = \frac{|\vec{T}|^2 - |\sum W_n \vec{v}_n|^2}{|\vec{T}|^2}; \quad n = 1...N. \tag{2}$$

4 Method Description

The procedure of our method is shown in Fig. 4. We use shortest neighborhood graph to cover the training images in the same class. Determine parameter '*k*' by analyzing simplexes, then adopt KNN algorithm to classify roughly. The *K* nearest points could also be determined at this step. Use the linear combination of these points to represent the test image and analyze the error to classify precisely. Finally, adopt local linear approximation method to construct a local map between high-dimensional image space and low-dimensional manifold. The projective coordinates on manifold can depict the pose of object in test image.

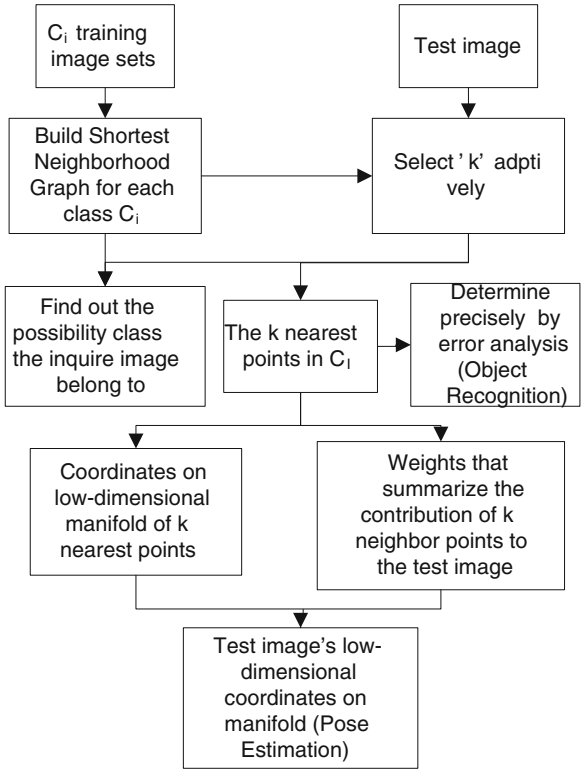

Fig. 4 Flowchart of our new model

In high-dimensional image space, a test image corresponds to a point. Defining that T is A test image; C_n is the data set of Class N; p_{n-i} is the ith data point in Class N; r is the radius of a hyperball; and $d(i, j)$ is Euclid distance between point i and point j.

4.1 Object Recognition

There are three steps to object recognition:

(1) Build shortest neighborhood graph G_n for Class C_n. Select the maximum distance of neighbor points on G_n as parameter 'k', where p_{n-i} and p_{n-j} are shortest neighbors in G_n.

$$k = \max\left\{d\left(p_{n-i}, p_{n-j}\right)\right\}; \quad n = 1 \cdots N. \tag{3}$$

(2) Take the test point T as the center of a hyperball and the value of 'k' as the diameter. The inner points set covered by the hyperball is:

$$B(T, r) = \{x \in C_n | d(x, T) \leq r\}; \; r = k/2; \quad n = 1 \ldots N. \tag{4}$$

If there is no point covered by the hyperball, the test image does not belong to any of the classes that have been trained. If B(T, r) is not an empty set, suppose the points in it come from M different classes.

$$T \notin C_n, IF : \{B(T, r) = \phi\}; \quad n = 1 \ldots N. \tag{5}$$

(3) Reduce the radius of hyperball. For each class, the radio of the hyperball is selected as:

$$r_m = \max\left\{d\left(p_{m-i}, p_{m-j}\right)\right\}, \quad m = 1 \ldots M. \tag{6}$$

Find out the points in the hyperball of each class, where k_m is the number of points of Class M.

$$\left\{p_m^{k_m}\right\} = \{B(T, r) \cap C_m\}; \quad m = 1 \ldots M. \tag{7}$$

Using the points of each class in hyperball to linear represent the test image

$$\varepsilon_m(W_m) = \min\left|\vec{T} - \sum W_{k_m} \vec{p}_m^{k_m}\right|^2; \quad \sum W_m = 1; \quad m = 1 \ldots M. \tag{8}$$

$$e_m = \frac{|\vec{T}|^2 - |\sum W_{k_m} \vec{p}_m^{k_m}|^2}{|\vec{T}|^2}; \quad m = 1 \ldots N. \tag{9}$$

The test image belongs to Class R that has the minimum e and e much less than 0.05.

$$T \in C_R, \{e_R = \min\{e_m\}; \quad m = 1 \cdots M. \tag{10}$$

In object recognition process, the k nearest points of the test image is k_R and the weights W_R that summarize the linear contribution error are also determined.

4.2 Pose Estimation

For pose estimation, we project training image on low-dimensional manifold and find the rule of correspondence between pose and coordinate of an object at first step. Then we use local linear approximation to determine the coordinate of the test image on manifold. The process is as follows:

(1) Adopt MDS algorithm to project G_R on low-dimensional manifold and get the coordinates of p_L.
(2) Project the test point to a low manifold. This is done by choosing the low-dimensional coordinates of the test point T_L to minimize the embedding cost function.

$$\phi(T_L) = \sum \left| \vec{T}_L - \sum W_R \vec{p}_L \right|^2. \tag{11}$$

where T_L is T's coordinate in low-dimensional manifold space and the pose of the object in test image can be determined by T_L.

5 Experiments and Results

In the experiments, we select FacePix database supposed by Arizona State University. It contains 30 face images of persons under pose and illumination variation. For pose variation images, it samples at every 1° while rotating the face from 0 to 180°. In our experiment, we select 5 face images at intervals of every 3°. Thus, there are 60 images for each person. In Fig. 5 we list three of them.

The main steps and results of the experiments are as follows:

(1) Construct shortest neighborhood graph for each class. By calculating, $k = 19.28$ select four untrained images Test 1, Test 2, Test 3, and Test 4 from the database as test samples as shown in Fig. 6. The first two test images are from Class 1 at 58° and −11° respectively. T3 is from Class 2 at 14° and T4 is from an untrained class. Take test images as centers of two hyperballs and select $k/2$ as radius. Therefore, Test 4 does not belong to any of the classes that have been trained.

Fig. 5 The data select from training image. Each row contains one person's face image and the column reflects pose change of the head. From *left* to *right* column is 90, 60, 30, 0, −30, −60, −90°

Fig. 6 Test images. T1, T2, T3, T4 from *left* to *right*

$$\begin{aligned} B(T1,r) &= \{p_{1-50}, p_{1-51}, p_{1-52}\}; B(T2,r) = \{p_{1-27}, p_{1-28}\} \\ B(T3,r) &= \{p_{2-35}, p_{2-36}\}; B(T4,r) = \{\phi\} \end{aligned} \tag{12}$$

(2) Reduce the radius of the hyperball. $r1 = 17.35$ and $r2 = 18.43$. The points near each test image can be found.

$$\begin{aligned} &B(T1,r_1) = \{p_{1-50}, p_{1-51}\}; \\ &B(T2,r_1) = \{p_{1-27}, p_{1-28}\}; B(T3,r_2) = \{p_{2-35}, p_{2-36}\}. \end{aligned} \tag{13}$$

(3) Using these points to linear represent test image. By calculation, the weights are (0.734, 0.266), (0.703, 0.297), (0.236, 0.764) for three test images and the error is: 0.027, 0.042, and 0.048 respectively. Therefore, Tests 1 and 2 belong to Class 1 and Test 3 is a part of Class 2.

(4) Project training image into low-dimensional manifold. Figure 7 shows the result of dimension reduction of Class 1.
The low-dimensional manifold is a curve, because the motion of head rotation has just one degree of freedom. Therefore, the pose of head can be depicted by one-dimensional coordinate. Table 1 lists the corresponding relationship of Class 1. It is worth to notice that the coordinates are relative in low-dimensional space.

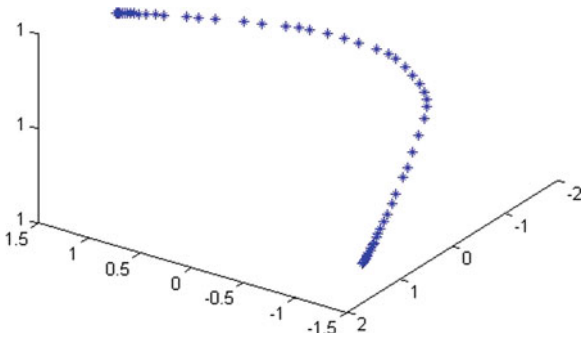

Fig. 7 Dimension reduction result of Class 1

Table 1 Corresponding relationship between coordinates on low manifold and pose parameter

Point	$p_{1\text{-}1}$	$p_{1\text{-}2}$	…	$p_{1\text{-}26}$	$p_{1\text{-}27}$	$p_{1\text{-}28}$	…	$p_{1\text{-}50}$	$p_{1\text{-}51}$	…
Coordinate	0	3.218	…	828	886.7	970.7	…	5999	7385	…
Degree	−90	−87	…	−15	−12	−9	…	57	60	…

(5) The low-dimensional coordinate of test image can be obtained by using local linear approximate method. The pose of Test 3 can be calculated in the same way. Obviously pose estimation is correct and precise.

$$\begin{aligned} \text{angle}_{\text{Test1}} &= \sum W_{\text{Test1}} \cdot \text{Degree} = (-12 \times 0.734) + (-9 \times 0.266) = -11.202 \\ \text{angle}_{\text{Test2}} &= \sum W_{\text{Test2}} \cdot \text{Degree} = (57 \times 0.703) + (60 \times 0.297) = 57.891 \end{aligned} \tag{14}$$

Because of high-density sample of training data, the recognition accuracy is high by SVM which acts as a contrast experiment. However, Test 3 could not be refused when taking the first two persons as training data. Moreover, the pose estimation of the test images cannot be estimated.

6 Conclusion

The proposed method deals with object recognition and poses estimation problem. Based on PHC, we adopt SNG to cover and triangulate the hypersurface of the training image distributed in high-image space. Therefore, the recognition task becomes to find the SNG that the test image lies on. The object in an image can be correctly recognized when its pose is changed largely. Compared with the statistic classification algorithm, this method does not need negative samples and could increase new classes arbitrarily. Different from conventional manifold learning algorithms such as Isomap and LLE, this method employs local linear

approximation algorithm to build a map locally which could project test image on a manifold.

The experiment results on FacePix database show that this new model is effective under condition that the object's appearance varies with rotation and any untrained object cannot be recognized incorrectly. However, it is worth to notice that the pose of object varies in just one DOF in database. The method will be verified experimentally on other more complex databases in further studies.

References

1. Viola P, Jones MJ (2004) Robust real-time face detection. Comput Vis 57(2):137–154
2. Wang S, Chen X (2003) Biomimetic (Topological) pattern recognition- a new model of pattern recognition theory and its application. Neural Netw 3:2258–2262
3. Sebastian Seung H, Lee DD (2000) The manifold ways of perception. Science 290:2268–2269
4. Tenenbaum JB, de Silva V, Langford JC (2000) A global geometric framework for nonlinear dimensionality reduction. Science 290:2268–2323
5. Roweis LS (2000) Nonlinear dimensionality reduction by locally linear embedding. Science 290:2323–2326
6. Vlachos M, Domeniconi C, Gunopulos D, Kollios G, Koudas N (2002) Non-linear dimensionality reduction techniques for classification and visualization. In: Proceedings of the. 8th ACM SIGKDD International Conference on Knowledge discovery and data mining, pp 645–651
7. Kadoury S, Levine MD (2006) Finding faces in gray scale images using locally linear embeddings. In: 5th international conference on image and video retrieval, CIVR, pp 221–230

Vision-Based Traffic Sign Recognition System for Intelligent Vehicles

Jing Yang, Bin Kong and Bin Wang

Abstract The recognition of traffic signs in natural environment is a challenging task in computer vision because of the influence of weather conditions, illuminations, locations, vandalism, and other factors. In this paper, we propose a vision-based traffic sign recognition system for the real utilization of intelligent vehicles. The proposed system consists of two phases: detection and recognition. In detection phase, we employ simple vector filter for chromatic/achromatic discrimination and color segmentation followed by shape analysis to roughly divide traffic signs into seven categories according to the color and shape properties. The Pseudo-Zernike moments features of the extracted candidate traffic sign regions are selected for recognition by random forests which combines bootstrap aggregating (bagging) algorithm and random feature selection to construct collections of decision trees and possesses excellent classification ability. The rationality and effectiveness of the proposed system is validated on our intelligent vehicle—Intelligent Pioneer from a great number of experiments.

Keywords Traffic sign recognition · Simple vector filter · Pseudo-Zernike moments · Random forests

J. Yang (✉) · B. Kong · B. Wang
Institute of Intelligent Machines, Chinese Academy of Sciences, Hefei 230031, China
e-mail: jyang@iim.ac.cn

B. Kong
e-mail: bkong@iim.ac.cn

B. Wang
e-mail: alec.w.ustc@gmail.com

B. Wang
University of Science and Technology of China, Hefei 230027, China

F. Sun et al. (eds.), *Foundations and Practical Applications of Cognitive Systems and Information Processing*, Advances in Intelligent Systems and Computing 215,
DOI: 10.1007/978-3-642-37835-5_31,

1 Introduction

With the rapid urbanization and the increasing number of car ownership, Traffic Safety is becoming increasingly prominent and drawing great attention from the society. As a transport language, traffic sign can be interpreted by drivers with its shape, color, pattern, and text. Traffic signs are very important and they represent the current traffic situation, show danger, and give warnings to drivers. Because of weather conditions, illuminations, locations, vandalism and other factors, vision-based Traffic Sign Recognition (TSR) system has been a challenge task for many years as a component of the Advanced Driver Assistance System (ADAS) of intelligent vehicles.

Traffic sign detection and recognition algorithms have drawn considerable research attentions in recent years. As in the detection phase, color segmentation which is carried out by setting thresholds for some color space to extract the candidate sign regions from the scene is the most common method. For this purpose, many researches employed several kinds of color spaces, such as RGB [1], HSV/HIS [2, 3], CIElab [4] and YCbCr [5], etc. to weaken the influence of the light intensity. Shape-based approaches are also developed for traffic sign detection. Fast Fourier Transform (FFT) was employed to retrieve shape signatures [6]. G. Loy developed a fast shape-based method for road sign detection [7]. For the recognition stage, there are series of approaches which includes Neural Networks [8], Template Matching [9], and Support Vector Machines (SVM) [10]. Reference [11] developed a traffic sign recognition system using Scale Invariant Feature Transform (SIFT) and color classification. A class-specific discriminative features and color distance transform-based nearest neighbor classifier is proposed in [12] for recognition. Other methods such as Fuzzy Shape recognizer [13] and SimBoost [14] have also been used.

In this paper, we aimed at developing a traffic sign recognition system for the real utilization of intelligent vehicles. The proposed system is divided into two phases. In detection phase, we employ simple vector filter (SVF) for chromatic/achromatic discrimination and color segmentation followed by shape analysis to divide traffic signs into seven categories according to their color and shape properties. Candidate traffic sign regions are then normalized into a specified size and image database are built for training. In recognition phase, Pseudo-Zernike moments are selected to represent features of the extracted candidate regions for subsequent classification. Due to the excellent performance of the Ensemble Learning, random forests are used as an ensemble classifier for traffic signs recognition. It combines bootstrap aggregating (bagging) algorithm and the random feature selection to construct a collection of decision trees and outputs the class by a majority vote of individual trees. The system proposed in this paper is out of the ordinary for it not only realizes an entire system for traffic sign detection and recognition, but also covers a wide majority of national Chinese traffic signs rather than being restricted to a certain type of signs.

The remainder of this paper is organized as follows. Brief introduction of national Chinese traffic signs are given in Sect. 2. Section 3 presents an overview over the system including color segmentation, shape analysis, feature extraction, and random forests-based classification. The experiment results are demonstrated in Sect. 4, followed by conclusions in Sect. 5.

2 National Standard Chinese Traffic Signs

The Chinese national standard traffic signs can be divided into four categories according to different applications:

- *Prohibitory signs.* They are used to prohibit or appropriately restrict the vehicle according to the situation of streets and traffic. Normally, they are designed in a circular shape with thick red rim, white background, and black arrow indication.
- *Indicatory signs.* They control the actions of drivers and pedestrians, normally shaped with complete blue circle or rectangle and white arrow or other pictogram.
- *Warning signs.* They indicate a hazard ahead on the road or remind drivers to take measures to deal with in front of traffic information. Usually, they are equilateral triangles with a black symbol and a yellow background rimmed a black border.
- *Supplementary signs.* These types of signs are used to assist with indicating supplementary information such as: road construction, emergency belt, etc.

Figure 1 listed 27 species of Chinese national standard traffic signs which requested by the recognition performance evaluation of "Chinese Future Challenge of Intelligent Vehicle."

Fig. 1 27 species of Chinese national standard traffic signs

3 Vision-Based Traffic Sign Recognition System

As shown in Fig. 2, the proposed vision-based traffic sign recognition system consists of several modules which cooperate to complete the detection and recognition task. These modules are briefly presented in Fig. 2.

3.1 Color Segmentation

As pointed out in the introduction, different color spaces have been used to segment traffic signs in outdoor images. The tough challenge that we encounter when using these color space-based segmentation algorithms is related to illumination changes owing to different weather conditions and possible deterioration of the signs. Thus, there are some works where thresholding is not applied directly using a specific color space. Thresholding by looking for chromatic and achromatic colors is applied in [15] by a simple vector filter which has characteristics that it can extract the specific color at high speed and eliminate all the outlines at the same time, as shown in Fig. 3. The algorithm of SVF is considered through the HIS table color. When the vector direction is the same, the corresponding color element is the same and then achromatic color is expressed by the same direction of vector. Accordingly, the SVF represents the direction of the vector and a corresponding color territory simply. The achromatic color is the center of gravity direction in the triangle as shown in Fig. 3. The vector calculation of achromatic color is given by:

$$F(R,G,B) = \frac{(|R-G| + |G-B| + |B-R|)}{3D} \tag{1}$$

where R, G, B represent the brightness of the respective color, and D is the degree of extraction of an achromatic color. In our case, we get the best segmentation results by setting D to 20. An $F(R, G, B)$ less than 1 represents achromatic colors, and an $F(R, G, B)$ greater than 1 represents chromatic colors.

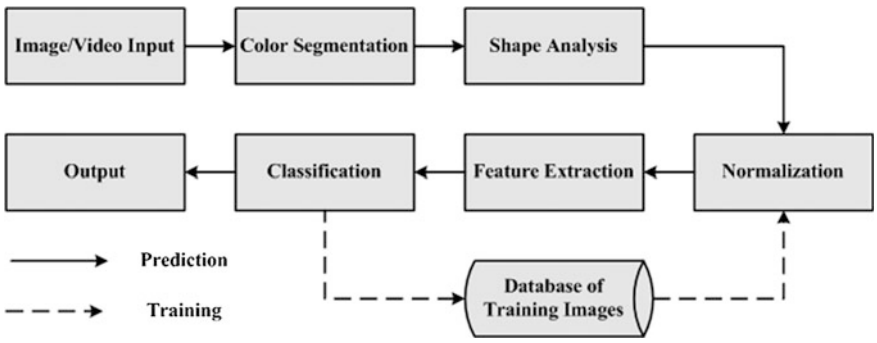

Fig. 2 Flow chart of the proposed system

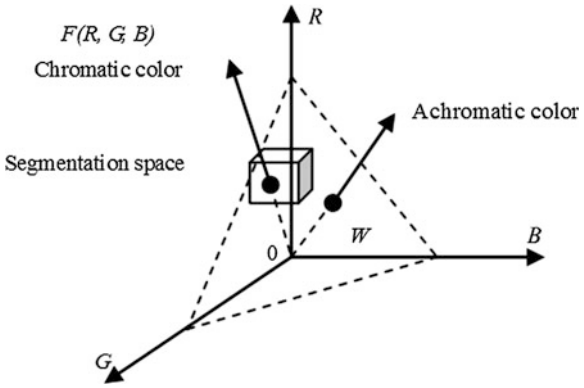

Fig. 3 Concept of simple vector filter

Reference [15] removed the outline of the sign and the shadow of the background by using this algorithm. In our experiments, we found that this algorithm can do well in separating the color element of red, green, blue, and yellow, and it can achieve better color segment performance than other traditional used color spaces, such as RGB, HSV, HIS, etc., in various illumination conditions, like sunny and cloudy days. Meanwhile, because of the low computational complexity, the SVF color segment method is more suitable for real-time application. According to Fig. 3, this four colors could be set to extreme as (255, 0, 0), (0, 255, 0), (0, 0, 255), (255, 255, 0) in the ideal condition, and the pixel element of the color distributes around the corresponding extreme value. Under the limited region, shown as in (1), the pixel element of the color will be preserved if the direction of the vector shows significant differences. Meanwhile, from statistical results, for each RGB pixel $x = [x_R, x_G, x_B]$, a simple SVF color segmentation algorithm is then provided by the following equations:

$$\begin{aligned} \text{Red}: &\quad x_R - x_G > 75 \quad \text{and} \quad x_R - x_B > 30. \\ \text{Green}: &\quad x_G - x_R \geq x_R, x_G \geq x_B \quad \text{and} \quad x_G - x_B < 40. \\ \text{Yellow}: &\quad x_R - x_B > 70 \quad \text{and} \quad x_G > 50. \\ \text{Blue}: &\quad x_B - x_R > 65 \quad \text{and} \quad x_B > 45. \end{aligned} \tag{2}$$

As a result, the algorithm of SVF is appropriate for solving the problem of color segmentation of traffic signs and several single color channel images (e.g., red channel image, green channel image, yellow channel image, and blue channel image) can be obtained, see Fig. 4 for simple illustration.

3.2 Shape Analysis and Normalization

As shown in Fig. 5, according to the different color and shape characteristics of 27 species of traffic signs illustrated in Sect. 2, we can classify these signs roughly

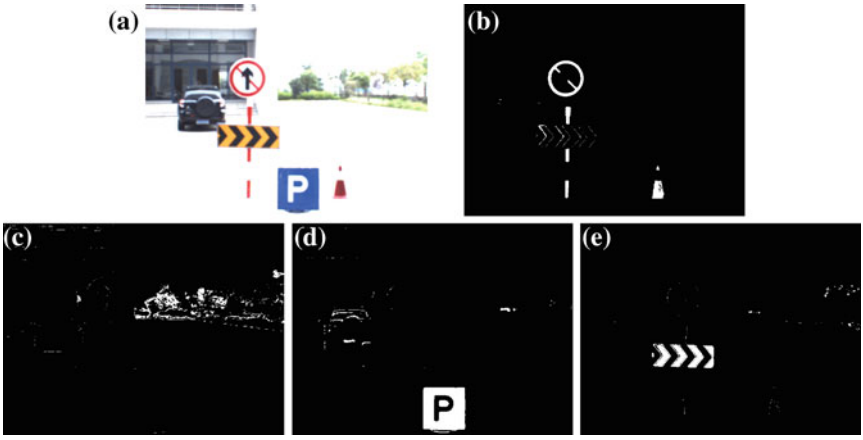

Fig. 4 SVF color segmentation. **a** Original image; **b** Red channel image; **c** Green channel image; **d** Blue channel image; **e** Yellow channel image

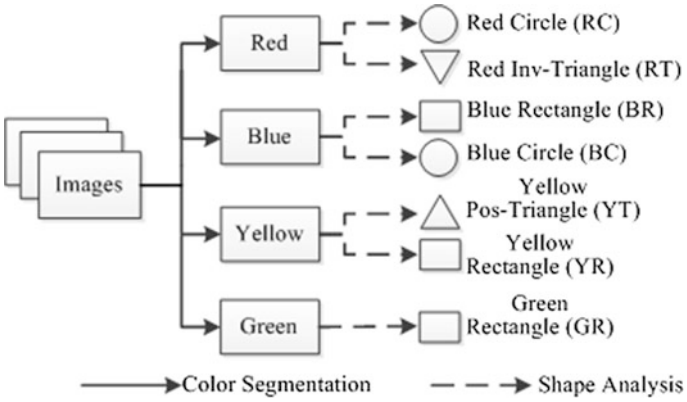

Fig. 5 Roughly classification according to color and shape characteristics

into seven classes, i.e., "RC" class, "RT" class, "BR" class, "BC" class, "YT" class, "YR" class, and "GR" class. Once the single color channel images have been derived from the above SVF color segmentation, we proceed to use hough transform and curve fitting approaches to extract candidate traffic sign regions by having ellipse and triangle detections in red channel image, rectangle and ellipse detections in blue channel image, triangle and rectangle detections in yellow channel image, and rectangle detections in green channel image. Meanwhile, priori knowledge of some constraints is imposed during respective shape detections, such as region size, aspect ratio of the enclosing rectangles, orientation limitation, etc.

Once the shape analyses have been done, candidate traffic sign regions of interests (ROIs) can be obtained. Owing to the different size, these ROIs in binary channel images need to be normalized before calculating the Pseudo-Zernike

moments features which demonstrated to possess translation, scale, and rotation invariance. In order to normalize the candidate regions of traffic sign into uniform size, the bicubic interpolation algorithm is employed in this paper to standardize the dimension of ROIs irrespective of their true scale in original image. Figure 6 depicts results indicating shape analysis, ROIs extraction, ROIs normalization (with 51×51 resolutions) and binarization.

3.3 Feature Extraction

With excellent properties for invariances of translation, rotation, and scale, moments which first introduced by Hu [16], have been widely used in computer vision applications such as image analysis, patter recognition, and image reconstruction. Zernike Moments [17] and Pseudo-Zernike Moments (PZM [18]), consist of a set of complex polynomials that form a complete orthogonal set over the unit disk in polar coordinate space. With the orthogonal property, Zernike Moments and Pseudo-Zernike Moments have the minimum amount of information redundancy and robustness to noise. In this paper, we employ Pseudo-Zernike Moments for ROIs feature representation.

Mathematically, the two-dimensional Zernike moments of order p with repetition q over $D = \{(p,q)|0 \le p \le \infty, |q|, \le p, |p-q| = \text{even}\}$ are defined as:

$$Z_{pq} = \frac{p+1}{\pi} \iint\limits_{x^2+y^2 \le 1} f(x,y)\, V_{pq}^{*}(x,y)\, dxdy \tag{3}$$

where $f(x,y)$ is a discrete image intensity function and $V_{pq}(x,y)$ is defined as follows:

$$V_{pq}(x,y) = R_{pq}(r_{xy}) \exp(-jq\theta_{xy}) \tag{4}$$

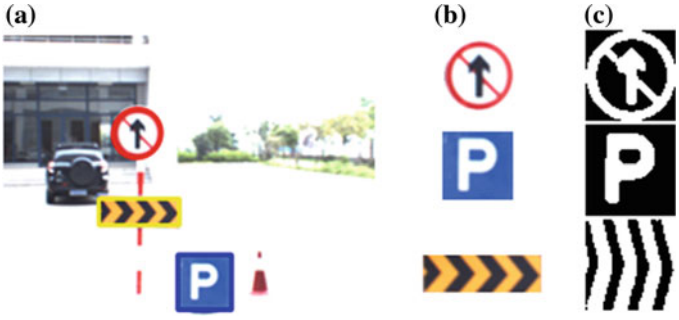

Fig. 6 Shape analysis and normalization. **a** Results of shape analysis and traffic signs labeling; **b** Extracted ROIs images; **c** ROIs normalization and binarization (51 × 51 resolutions)

where $r_{xy} = \sqrt{x^2 + y^2}$, $\theta_{xy} = arc\tan(y/x)$, and the real-valued radial polynomial $R_{pq}(r)$ is given by:

$$R_{pq}(r) = \sum_{k=0}^{\left(\frac{p-|q|}{2}\right)} (-1)^k \frac{(p-k)!}{k!\left(\frac{p+|q|}{2}-k\right)!\left(\frac{p-|q|}{2}-k\right)!} r^{p-2k} \tag{5}$$

The Pseudo-Zernike moments of order p with repetition q differ from Zernike moments in the real-valued radial polynomial, then (5) is replaced by:

$$R_{pq}(r) = \sum_{k=0}^{(p-|q|)} (-1)^k \frac{(2p+1-k)!}{k!(p+|q|+1-k)!(p-|q|-k)!} r^{p-k} \tag{6}$$

Because of the removal of the limitation ($p - |q|$ is even), Pseudo-Zernike moments offer more vectors than Zernike moments when using the same order. Consequently, an efficient algorithm for fast computation of Pseudo-Zernike moments [19] is given as follows:

$$R_{pq}(r) = \sum_{s=q}^{p} D_{pqs} r^s \tag{7}$$

where $s = p - k$ and $D_{pqs} = \frac{(-1)^{p-s}(p+s+1)!}{(p-s)!(s+q+1)!(s-q)!}$.

The recurrence relations as follows can be used for efficient computation of D_{pqs}:

$$\begin{aligned} D_{pqp} &= 1; \quad D_{p(q-1)s} = D_{pqs} \frac{s+q+1}{s-q+1}; \\ D_{pq(s-1)} &= -D_{pqs} \frac{(s+q+1)(s-q)}{(p+s+1)(p-s+1)}. \end{aligned} \tag{8}$$

Algorithm 1 is used to illustrate the extraction of Pseudo-Zernike moments-based feature representation.

Algorithm 1 *PZM_Feature Extraction* (*ROIs*, *Order*)

Require: *ROIs* {the cropped ROIs image} and *Order {*sets of different order combinations}
Ensure: *Feature* {the feature vectors of ROIs image}
1: Map the *ROIs* into the unit disk in polar coordinate space, and take the center as origin;
2: Initialize *PZM_Feature* = [ ];
3: **for** (*p*,*q*) in Order do
4: Calculate R_{pq} using Eqs. (7) and (8);
5: Calculate V_{pq} using Eq. (4);
6: Calculate Z_{pq} using Eq. (3);
7: *PZM_Feature* = [*PZM_Feature* Z_{pq}];
8: **end for**
9: **return** *PZM_Feature.*

Due to the rotation invariance of *PZM_Feature*, it is difficult to distinguish "straight only," "keep left," and "keep right" of blue circle signs. So a second judgment is used for them by a simple template matching algorithm.

3.4 Random Forests-Based Classification

In this section, we employ random forests classifier for traffic sign recognition and *PZM_Feature* evaluation.

Random forests [20] is a kind of ensemble learning which consists of unpruned decision trees and outputs the class by a majority vote of individual trees. It combines bootstrap aggregating (bagging) algorithm and the random feature selection to construct a collection of decision trees with controlled variation. The advantage of random forests, as has been noted by previous authors, is that they are much faster in training, testing and perform very well compared to many other classifiers (such as Support vector machines, Boosting, Discriminant Analysis). They also enable different cues to be "effortlessly combined" [21].

(1) *Growing Trees*
The trees here are binary and are constructed in a top-down manner. The binary test at each node can be chosen in one of two ways: randomly, i.e. data independent or by a greedy algorithm which picks the test that best separates the given training samples. "Best" is measured by the information gain

$$\Delta E = -\sum_i \frac{|Q_i|}{|Q|} E(Q_i) \tag{9}$$

caused by partitioning the set Q of samples into two subsets Q_i according the given test. Here $E(q)$ is the entropy $-\sum_{j=1}^{N} p_i \log_2(p_i)$ with p_i the proportion of samples in q belonging to class j, and $|\bullet|$ is the size of the set. The process of selecting a test is repeated for each nonterminal node, using only the training samples falling in that node. The recursion is stopped when the node receives few samples, or when it reaches a given depth.

(2) *Random forests classification*
The random forests for classification are described as follows in algorithm 2.

Algorithm 2 *Random Forests for Classification*

1: **for** tree numbers $k = 1$ to K do
2: Draw a bootstrap sample of size N from the training data;
3: Grow a random forest tree T_k to the bootstrapped data, by recursively repeating the following steps for each terminal node of the tree, until the minimum node size n_{min} is reached.
a) Select m variables at random from the p variables;
b) Pick the best variable/split-point among the m;
c) Split the node into two daughter nodes;
4: **end for**
5: **Output** the ensemble of trees $\{T_k\}_1^K$;
6: **Classification** of a new point x: Let $C_k(x)$ be the class prediction of the kth random forest tree. Then $C_{rf}^K(x) = majority\, vote\{C_k(x)\}_1^K$

(3) *Out-of-bag samples and error*
In random forests, there is no need for cross-validation or a separate test set to get an unbiased estimation. It is estimated internally, during the run, as follows:

(a) At each bootstrap iteration, predict the data not in the bootstrap sample called "out-of-bag (OOB)" samples using the tree grown with the bootstrap sample.
(b) Aggregate the OOB predictions. (On the average, each data point would be out-of-bag around 36 % of the times, so aggregate these predictions.) Calculate the error rate, and call it the OOB error.

(4) *Variable importance* and *PZM_Feature* evaluation
Random forests also use the OOB samples to construct a different variable importance measure, apparently to measure the prediction strength of each variable (feature). The algorithm estimates the importance of a variable by looking at how much prediction error increases when OOB data for that variable is permuted while all others are left unchanged. Thus, the variable importance of random forests reflects the contribution of each *PZM_Feature* extracted above for classification, and can be used as feature evaluation method.

4 Experiments and Discussions

In order to evaluate the performance of the proposed system, a database of 2643 raw images of traffic signs are used for testing. These pictures were captured under various weather conditions, at different times and locations. CCD video camera mounted on top of the vehicle was used for this task, as shown in Fig. 7. All of them are RGB images with 640 × 480 resolutions. The training database consisting of 744 binary images of 51×51 pixels are used for training of the random forests classifier after calculating 16 dimensional *PZM_Feature*s. The traffic sign

Fig. 7 Intelligent pioneer with cameras mounted on *top* of the vehicle

recognition system has been developed based on visual C++ and Intel® Open Source Computer Vision Library (OpenCV) [22].

4.1 Detection Results

Figure 8 depicts the experimental results for traffic sign detection under various weather conditions. The candidate regions are labeled by corresponding color and shape markers. As we can see that, the proposed method executes effectively under different illumination environments and is robust to rotation and scale variations. The detailed experimental results are summarized in Table 1. The testing images are roughly divided into two types, i.e., "Sunny," "Cloudy" according to different illuminations. Total Images (TI) means the total number of images. Total Signs (TS) means the total number of signs in total images. Correct Detection (CD) is the number of traffic signs correctly detected. Miss Detection (MD) is the number of signs failed to be located. False Detection (FD) indicates the number of non-signs wrongly regarded as signs candidates, and most of them can be excluded in the following recognition phase. Hit Rate (HR) equals CD divided by TS. Experiments results clearly show that, the proposed method is effective and efficient for traffic signs detection.

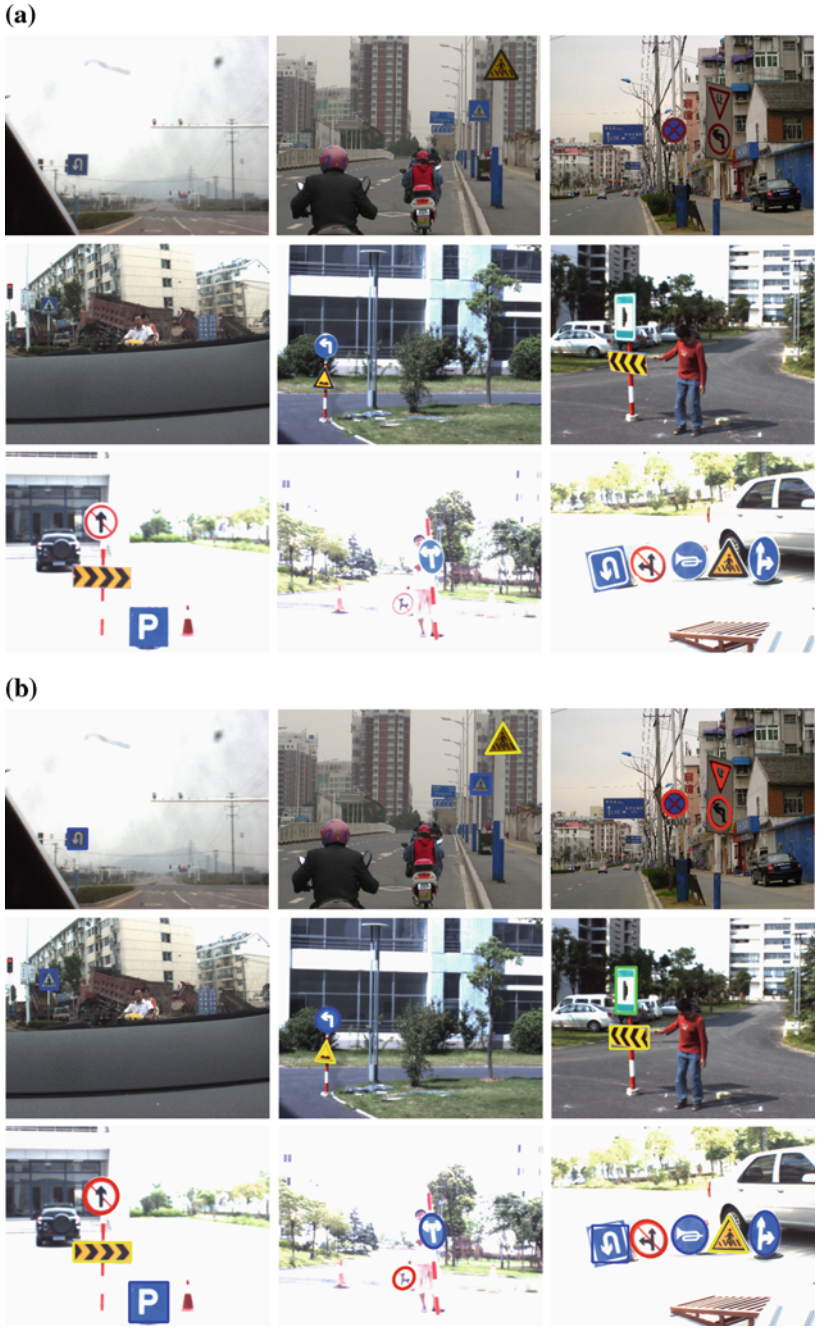

Fig. 8 Traffic signs detections. **a** Original images; **b** Detection results labeled with corresponding color and shape markers

Table 1 Traffic sign detection results

Weather condition	TI	TS	CD	MD	FD	HR (%)
Sunny	976	2173	2113	60	269	97.2
Cloudy	1667	2614	2562	52	299	98.0

4.2 Recognition Results

Due to space limitations here, we only present the recognition results for the red circle traffic signs in the training database (284 binary images of red circle signs) with respect to the parameters of random forests classifier in Figs. 9 and 10. From Fig. 9, we can see a global tendency of the recognition rate to rise for an increasing number of trees. It appears that this increasement is not linear but logarithmic. One can conclude that with respect to an increasing number of trees, the random forests accuracy converges. We also have noticed that the rise of the recognition rate begins to considerably slow down from about 50 trees in the forest which indicating the forest achieved sufficient training. Meanwhile, for a fixed number of trees, for instance $K = 40$, we can see that, the performance of the system becomes to improve from $m = 1$ to $m = 8$, and begins to decrease if m goes on to rise as $m = 12$ and $m = 16$. The reason for this phenomenon can be concluded that a too much important portion of features preselected, makes the diversity decrease between trees in the forests. Indeed the more features are randomly preselected, the more the splits will be identical from one tree to another, since they are then selected according to the splitting criterion. Figure. 10 depicts synthetic 3D representation of the above results. Figure 11 presents the 16 dimensional *PZM_Features* evaluation through variable importance measure. It is helpful to find out the most important features for classification, especially in the field of high dimensional pattern recognition for model complexity reduction.

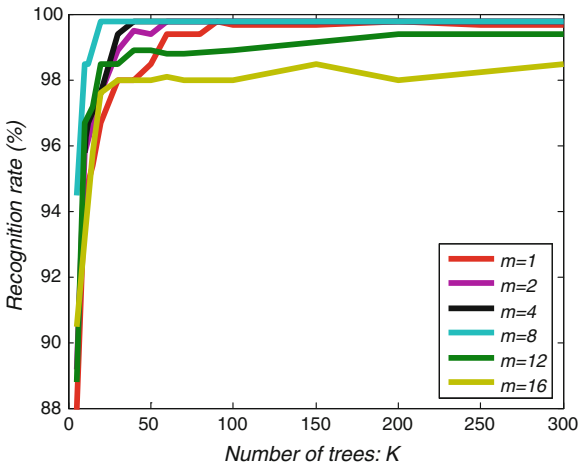

Fig. 9 Recognition rate for *red circle* signs in training database

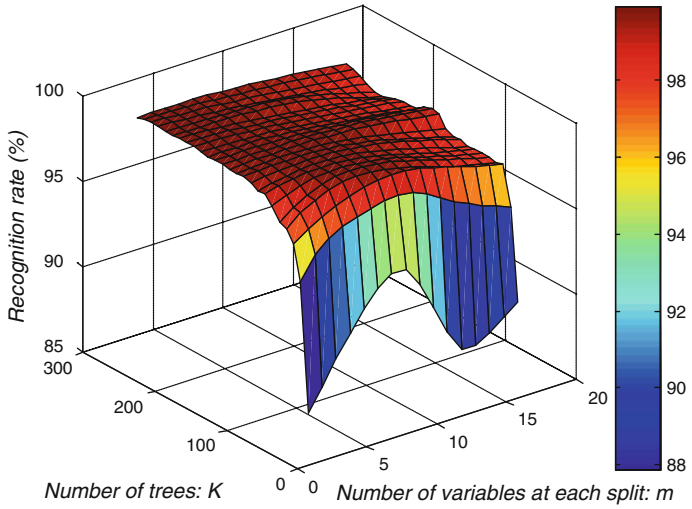

Fig. 10 Synthetic 3D representation of recognition rate for *red circle* signs in training database

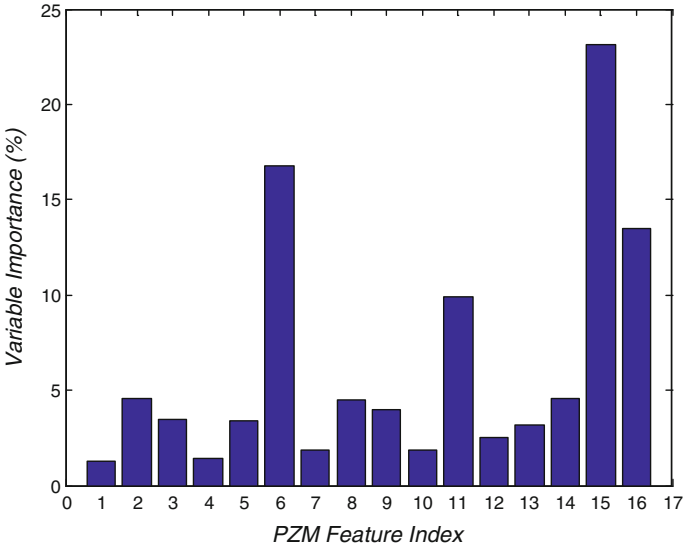

Fig. 11 PZM_Feature evaluation through variable importance measure

The overall system performance results for different type of signs are listed in Table 2. Here we use $K = 200$ and $m = 8$ for designing the random forests classifier. True Positive (TP) denotes the number of traffic signs correctly classified

Table 2 Traffic sign recognition results

Traffic signs	TS	TP	FN	FP	AR (%)
Red Circle	1412	1334	78	56	94.5
Red Inv-Triangle	305	296	9	17	97.0
Blue Rectangle	781	737	44	45	94.4
Blue Circle	1618	1519	99	73	93.9
Yellow Pos-Triangle	358	343	15	24	95.8
Yellow Rectangle	313	287	26	16	91.7

to the corresponding category. Accordingly, False Negative (FN) indicates the number of signs wrongly classified. False Positive (FP) is the number of disturbing noise objects wrongly classified as traffic signs. Accuracy Rate (AR) equals TP divided by TS. From Table 2, it is necessary to point out that the accuracy rates for traffic signs recognition are all over 90 % which indicating the effectiveness and robustness of the proposed system. Red Inv-Triangle signs even achieve 97 % owing to the distinctiveness and uniqueness. Meanwhile, the proposed system takes 170 ms on average to fulfill the whole detection and recognition task. In addition, we analyzed a small amount of images with the trouble in detection and recognition. The reasons in missed, false detection, and wrong classification are as follows: severely faded traffic signs, highlights, occlusion, and the influence of other advertising signs.

5 Conclusion

In this paper, we propose a robust vision-based traffic sign recognition system for intelligent vehicles. Simple vector filter color segmentation algorithm and shape analysis are first employed to quickly establish candidate regions of interests, and roughly divide the traffic signs into seven categories. Pseudo-Zernike moments features of the extracted candidate regions are selected for classification by random forests in recognition phase. Besides, due to the moments' rotation invariance, a simple template matching algorithm is used to make a second judgment for some kinds of signs. Experiment results show that the proposed system can rapidly and accurately recognize traffic signs in a natural environment, and it covers a wide majority of Chinese traffic signs rather than being restricted to a certain type of signs. Future work will include systematic research on more abominable illuminations and other species of traffic signs.

Acknowledgments This work was supported by National Natural Science Foundation of China under grant No. 91120307 and 60875076.

References

1. Soetedjo A, Yamada K (2005) Fast and robust traffic sign detection. In: IEEE international conference on systems, man and cybernetics. IEEE Press, Hawaii, pp 1341–1346
2. Medici P, Caraffi C, Cardarelli E, Porta PP, Ghisio G (2008) Real time road signs classification. In: IEEE international conference on vehicular electronics and safety. IEEE Press, pp 253–258
3. Wu WY, Hsieh TC, Lai CS (2007) Extracting road signs using the color information. World Acad Sci Eng Technol 8:282–286
4. Lopez LD, Fuentes O (2007) Color-based road sign detection and tracking. Image Anal Recogn Lect Notes Comput Sci 4633:1138–1147
5. Eichner ML, Breckon TP (2008) Integrated speed limit detection and recognition from real-time video. In: IEEE intelligent vehicles symposium. IEEE Press, pp 626–631
6. Gil-Jimenez P, Lafuente-Arroyo S, Gomez-Moreno H, Lopez-Ferreras F, Maldonado-Bascon S (2005) Traffic sign shape classification evaluation II: FFT applied to the signature of Blobs. In: Proceedings of the IEEE intelligent vehicles symposium. IEEE Press, Las Vegas, pp 607–612
7. Loy G, Barnes N (2004) Fast shape-based road sign detection for a driver assistance system. In: Proceedings of the IEEE/RSJ international conference on intelligent robots and systems. IEEE Press, Sendai, pp 70–75
8. Hossain MS, Hasan MM, Ali MA, Kabir MH, Ali ABMS (2010) Automatic detection and recognition of traffic signs. In: IEEE conference on robotics automation and mechatronics. IEEE Press, Singapore, pp 286–291
9. Wang YP, Shi MP, Wu T (2009) A method of fast and robust for traffic sign recognition. In: Proceedings of the fifth international conference on image and graphics, IEEE Press, Xi'an, pp 891–895
10. Bascon SM, Rodriguez JA, Arroyo SL, Caballero AF, Lopez-Ferreras F (2010) An optimization on pictogram identification for the road-sign recognition task using SVMs. Comput Vis Image Underst 114:373–383
11. Kus, MC, Gokmen M, Etaner-Uyar S (2008) Traffic sign recognition using scale invariant feature transform and color classification. In: 23rd international symposium on computer and information sciences, pp 1–6
12. Ruta A, Li YM, Liu XH (2010) Real-time traffic sign recognition from video by class-specific discriminative features. Pattern Recogn 43(1):416–430
13. Fleyeh H (2008) Traffic sign recognition by fuzzy sets. In: IEEE intelligent vehicles symposium. IEEE Press, Eindhoven, pp 422–427
14. Ruta A, Li YM, Liu XH (2010) Robust class similarity measure for traffic sign recognition. In: IEEE transactions on intelligent transportation systems, IEEE Press, Piscataway, pp 846–855
15. Asakura T, Aoyagi Y, Hirose OK (2000) Real-time recognition of road traffic sign in moving scene image using new image filter. In: Proceedings of the 39th SICE annual conference, international session papers, pp 13–18
16. Ming-Kuei H (1962) Visual pattern recognition by moment invariants. IRE Trans Inform Theory 8(2):179–187
17. Teague MR (1980) Image analysis via the general theory of moments. J Opt Soc Am 70(8):920–930
18. The CH, Chin RT (1988) On image analysis by the methods of moments. IEEE Trans Pattern Anal Mach Intell 10(4):496–513
19. Chong CW, Raveendran P, Mukundan R (2003) An efficient algorithm for fast computation of Pseudo-Zernike moments. Int J Pattern Recognit Artif Intell 17(6):1011–1023
20. Breiman L (2001) Random forests. Mach Learn 45:5–32
21. Winn J, Criminisi A (2006) Object class recognition at a glance. In: IEEE conference on computer vision and pattern recognition, IEEE Press
22. Intel Corporation: Open Source Computer Vision Library. Reference Manual, Copyright © 1999–2001. http://www.developer.intel.com

An Iterative Method for Classifying Stroke Subjects' Motor Imagery EEG Data in the BCI-FES Rehabilitation Training System

Hao Zhang, Jianyi Liang, Ye Liu, Hang Wang and Liqing Zhang

Abstract Motor imagery-based BCI-FES rehabilitation system has been proved to be effective in the treatment of movement function recovery. Common Spatial Pattern (CSP) and Support Vector Machine (SVM) are commonly used in the feature extraction and classification of Two-classes motor imagery. However, motor imagery signals of stroke patients are irregular due to the damage of the specified brain area. Traditional CSP is not able to detect the optimal projection direction on such EEG data recorded from stroke patients under the interference of irregular patterns. In this paper, an adaptive CSP method is proposed to deal with these unknown irregular patterns. In the method, two models are trained and updated by using different subsets of the original data in every iteration procedure. The method is applied on the EEG datasets of several stroke subjects comparing with traditional CSP-SVM. The results also provide an evidence of the feasibility of our BCI-FES rehabilitation system.

Keywords EEG · Stroke · BCI-FES rehabilitation system · Iteration · Classification · CSP · SVM

1 Introduction

Stroke is the rapid loss of brain function due to disturbance in the blood supply to the brain. The affected areas of stroke sufferers' brain cannot function, leading to an inability to move one or more limbs on one side of the body as well as finish completed left–right motor imagery [1]. Functional Electrical Stimulation (FES)

H. Zhang (✉) · J. Liang · Y. Liu · H. Wang · L. Zhang
MOE-Microsoft Key Laboratory for Intelligent Computing and Intelligent Systems, Department of Computer Science and Engineering, Shanghai Jiao Tong University, Shanghai 200240, China
e-mail: zh_chaos@sjtu.edu.cn

F. Sun et al. (eds.), *Foundations and Practical Applications of Cognitive Systems and Information Processing*, Advances in Intelligent Systems and Computing 215,
DOI: 10.1007/978-3-642-37835-5_32,

has been widely used in clinical rehabilitation for strokes. However, the key problem of the general therapy is that the unidirectional stimulation cannot attract subjects' attention enough, which results in a passive stimulation process with poor rehabilitation performance [2]. While, the motor imagery-based BCI system provides a platform for stroke subjects to follow appointed imagery procedures, such as controlling a wheelchair or finishing BCI game tasks [3], during which we can exploit electrical stimulations to help them conduct imagery tasks appropriately. Our system combines brain activities induced by Central Nervous System (CNS) with FES stimulations on corresponding muscles. Prior and post training have been done before and after the process, respectively [4]. The results, evaluated as feedbacks of the whole process, prove that it is indeed a promising approach for improving the performance of traditional FES therapy.

CSP is commonly applied for calculating an optimal direction which maximizes the differentiation of two kinds of mental states in EEG [5]. Features are extracted by projecting original EEG data onto the hyperspace and then arranged for training an SVM classifier [6, 7]. However, compared with normal subjects, the data of stroke patients mix regular motor imagery signals with unexpected noise such as failed, missed, or mistaken imagery caused by injuries on corresponding brain areas and mental maladjustments. These kinds of noise share common characteristics which are similar to Gaussian and cannot be filtered by general-purpose EEG signal processing methods because they locate at the same frequency band with normal motor imagery signals [8]. Therefore, general CSP may detect a wrong orientation when applied directly on such kinds of datasets. In this paper, we propose an iterative method for filtering the described type of EEG data and apply it in our BCI-FES rehabilitation system.

This paper is organized as follows: Sect. 2 introduces the data acquisitions and experiment design. Section 3 describes the iterative training and classification algorithms in detail. Section 4 gives comparative results when applying the method and traditional CSP-SVM on the datasets of stroke subjects simultaneously, and at the same time provides evidence of the feasibility of our BCI-FES rehabilitation system.

2 Data Acquisition and Experiment Setup

2.1 Introduction to SJTU-BCMI BCI-FES Rehabilitation Training System

Figure 1 provides a brief illustration of our BCI-FES system. Five components, consisting of data acquisition module, offline modeling module, online classification module, data visualization and cognition feedback module, and FES feedback module corporate in the system.

The 19-channel g.USBamp amplifier is adopted in the current research. Raw data are recorded by 19 electrodes with sampling rate 256 Hz, among which the

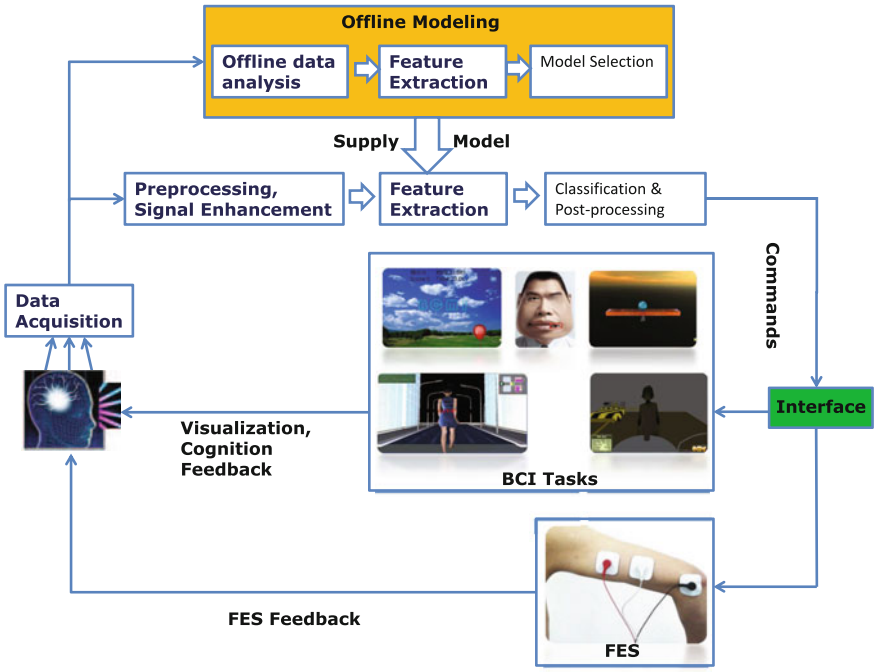

Fig. 1 A general view of our BCI-FES rehabilitation system

forehead and post-ear ones are selected as reference and ground, respectively, as shown in Fig. 2. EEG signals after removed artifacts are then filtered within the band 8–30 Hz, detrended piecewise and converted into the format *time*channel*window*. CSP is utilized in the following step to calculate the optimal projection direction.

Signals with largest eigenvalues maximize the difference of variance of left versus right motor imagery EEG. These signals are the m first and last rows of Z. Normalization is done by using the following equation [5, 9]:

$$f_p = \log\left(\frac{var(Z_p)}{\sum_{i=1}^{2m} var(Z_i)}\right) \tag{1}$$

2.2 Experiment Setup

In general, our experiment consists of three aspects: prior-training for model preparations, FES stimulation for rehabilitation, and post-training for assessments. The fundamental parameters of our system are listed in Table 1. In the first step, subjects are required to take part in different numbers of sessions ranging from 5 to 8 per day and 3 days per week. During each session, subjects sit still on a

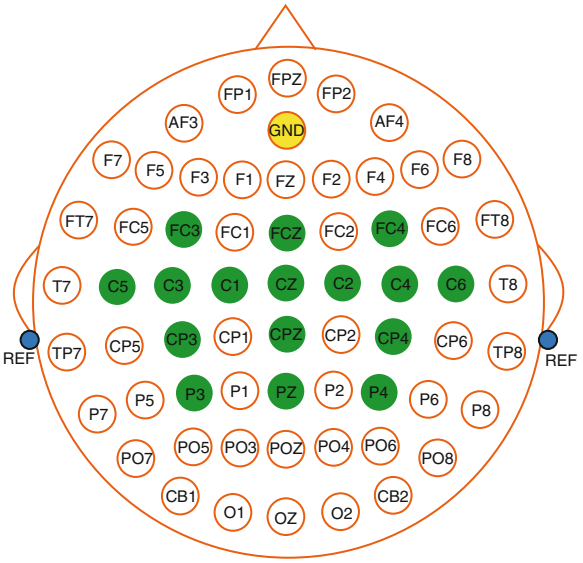

Fig. 2 Positions of the 19 selected channels. The two post-ear ones (marked *blue* in the figure) are averaged as the reference lead

Table 1 Fundamental parameters of our BCI-FES system

Parameter	Value
Number of channels	19 (3 for reference and ground)
Sampling rate	256 Hz
Frequency band	8–30 Hz
Number of trials per session	15–16
Time per trial	4 s
Sliding window size	1 s
Sliding window step length	0.125 s
Dimensions of feature	4

comfortable chair facing a wide-screen monitor. There are 5 min for subjects to relax their minds between sessions. Each session contains 15–16 numbers of 4 s trials including close number of left and right motor imagery tasks. At the beginning of each trial, a bold arrow with randomly left or right direction is shown on the screen, guiding subjects to concentrate imagining movements of their corresponding part of arms. Time sequences of each trial are cut into 25 sliding windows with size 1 s and step length 0.125 s as shown in Fig. 3. After pre-processing and feature extraction, the sliding windows are put into an online classifier. Two scroll bars increase according to the classification results as time goes on. For example, if the classification result (left or right) is the same as what the bold arrow directs, the corresponding scroll bar will increase. Voting strategy is employed to determine the class label of the whole trial. If the voting result matches the direction of the instruction arrow, the system will return a success signal on the screen, indicating the end of this trial. A 2 s interval is given between

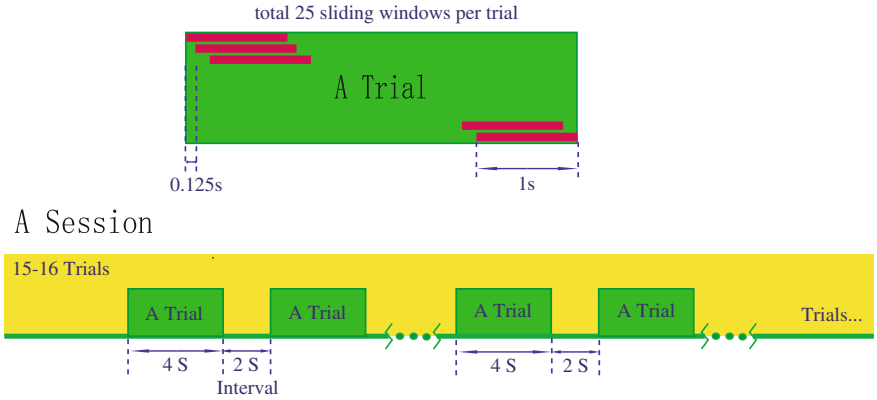

Fig. 3 The time arrangement of each session and each trial

trials while the subjects can adjust their mental state to prevent fatigues and prepare for following trials. The data of the first session are used to train a priori model offline for the following online classifications [10].

After the prior-training procedure, subjects are asked to finish some motor imagery-based games like balancing a beam or lifting balloons appeared randomly in the left or right part of the screen [11, 12]. FES is triggered and stimulates subjects' muscles under an appreciate current when they get stuck, which causes real movement of their hands or arms. The imagination-stimulation process reconstructs the neuroncircuit between paralysis limbs and corresponding pathological brain area of the subject and takes effect in the rehabilitation treatment [13]. Finally, a post-training session with 16 trials is finished for rehabilitation efficacy assessment.

3 An Itearative Method Based on Bilateral Models

Since stroke patients' data are a blend of motor imagery and irregular imagination contents, which are difficult to be filtered by general methods, the iterative method based on bilateral models is put forward for data pre-processing and noise elimination.

This algorithm is based on an assumption that the data of stroke patients are not as pure as that of normal persons. They mix natural motor imagery data with irregular patterns. Here, irregular patterns include failed or mistaken motor imagery caused by impaired brain regions. In the algorithm, *leftmodel* and *rightmodel* are trained for classifying data as left or nonleft and right or nonright, respectively, instead of left or right. Consider the following situation: an EEG segment labeled right is put into *leftmodel* and classified as left, then we are convinced that this segment has a large probability that it actually does not source

from a natural right motor imagery because *leftmodel* is trained by relatively pure left motor imagery data and mixed right ones, so that CSP tends to choose a projection direction that maximizes the difference between pure left and mixed right data. In a similar way, we conclude the corresponding relationships as shown in Table 2. Every time in the iteration, the ability of *leftmodel* for classifying left and nonleft is enhanced because the left labeled data become less noisy. So is the *rightmodel*. The iteration terminates when the number of rejected data is less than a given threshold. Algorithm 1 describes the method in detail and Fig. 4 gives a schematic diagram of how L in the algorithm changes and how a new *leftmodel* is trained in one round of iteration.

Algorithm 1 Iteration training process of *leftmodel* and *rightmodel*.

use the data of the first session to train an initial common model C;
set *leftmodel* = *rightmodel* = C;
set *elimination data number* = infinite large;
set *leftspatialfilter* = *rightspatialfilter* = the projection matrix calculated by CSP on the data of the first session;
while *elimination data number* < *threshold1* **do**
  choose a new session S from the training dataset;
  set $L_1 = L_2 = \{x | x \in S$ and x is labeled left$\}$;
  set $R_1 = R_2 = \{x | x \in S$ and x is labeled right$\}$;
  use *leftspatialfilter* to extract features from R_2;
  put features of R_2 into *leftmodel* for classification;
  use *rightspatialfilter* to extract features from L_2;
  put features of L_2 into *rightmodel* for classification;
  set *count* = 0;
  for each segment $x \in L_2$ **do**
    if the classification result by *rightmodel* = right and $random(0, 1) >$ *threshold2* **then**
      $L_2 = L_2 - \{x\}$;
      count = *count* + 1;
    end if
  end for
  for each segment $x \in R_2$ **do**
    if the classification result by *leftmodel* = left and $random(0, 1) >$ *threshold2* **then**
      $L_1 = L_1 - \{x\}$;
      count = *count* + 1;
    end if
  end for
  combine L_2 and R_1, calculate the new *leftspatialfilter* and use them to train a new *leftmodel*;
  combine R_2 and L_1, calculate the new *rightspatialfilter* and use them to train a new *rightmodel*;
  set *elimination data number* = *count*;
end while

Table 2 Relationships between models and classification results

Original label	Classification model	Result	Processing method
left	*rightmodel*	right	reject
left	*rightmodel*	nonright	accept
right	*leftmodel*	left	reject
right	*leftmodel*	nonleft	accept

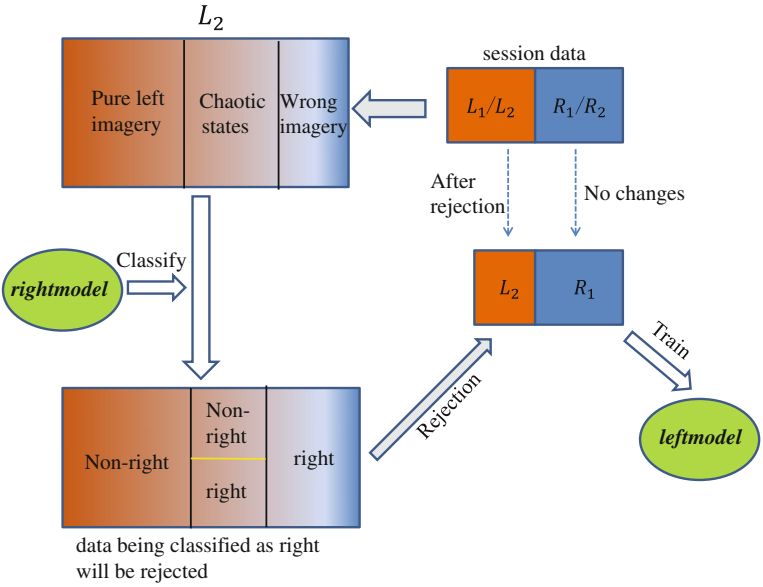

Fig. 4 The change of L in a round of iteration. Initially L is full of noise. After filtered by *rightmodel*, noise reduces and the new L is combined with the original R for training a new *leftmodel*

There is another issue needed to be highlighted that this algorithm is quite sensitive to the model initialization. If the signal-to-noise ratio of the first session data is quite low, the initial left and right models will be trained with poor classification ability, which may lead to a few improper rejections on the following datasets. To avoid this situation, we implement another threshold to reject data with a certain probability so that negative impact of model initialization on rejections is alleviated.

Algorithm 2 instructs the algorithm for testing. Note that segments with classification result "null" do not participate in the voting of its belonging trial.

Algorithm 2 Testing method by using bilateral models

```
for each window segment x in the test dataset do
    use leftspatialfilter to extract features from x;
    put the features into leftmodel and get the classfication result as y1;
    use rightspatialfilter to extract features from x;
    put the features into rightmodel and get the classfication result as y2;
    if y1 = y2 then
        return y1;
    else
        return null;
    end if
end for
```

4 Results

Eight stroke patients from Zhejiang Taizhou Hospital participate in our study. Five of them remain well after 2 months' training while no significant recovery appearances are discovered on the other three patients. We surmise that these three subjects may have missed the best rehabilitation period because all of them have suffered stroke for no less than 8 months [14].

We apply the iterative method on the EEG datasets of three patients (out of the five patients that remain well) for evaluations. We split the original data into two parts: the last session each day for testing and all of remaining sessions for iteration training. The elimination number threshold and rejection threshold are determined by leave-one-out cross validation [15]. The essential information and sliding window classification accuracies of three subjects are demonstrated in Table 3. We choose 6 weeks out of 2 months (3 weeks per month) and represent the mean accuracy of every week on the test dataset.

We also implement the traditional CSP-SVM method on the dataset for comparison. Considering that the number of sliding windows of the whole training set may be too large for general CSP-SVM, to avoid over-fitting, we choose parts of them to train a general CSP-SVM model with best performance and then compare it with our method. Figure 5 shows the graph of accuracies along with time by applying our method and traditional CSP-SVM on the test dataset. It is obvious that our method outperforms the traditional CSP-SVM.

Table 3 Essential information and sliding window accuracies of the three sampled subjects

Subject	Age	Sex	Pathogenesis	1st week (%)	2nd week (%)	3rd week (%)	4th week (%)	5th week (%)	6th week (%)
1	65	Female	Cortex injury	54	59	67	62	68	72
2	71	Male	Basal ganglia injury	47	61	58	68	71	79
3	62	Female	Basal ganglia injury	52	63	55	62	59	66

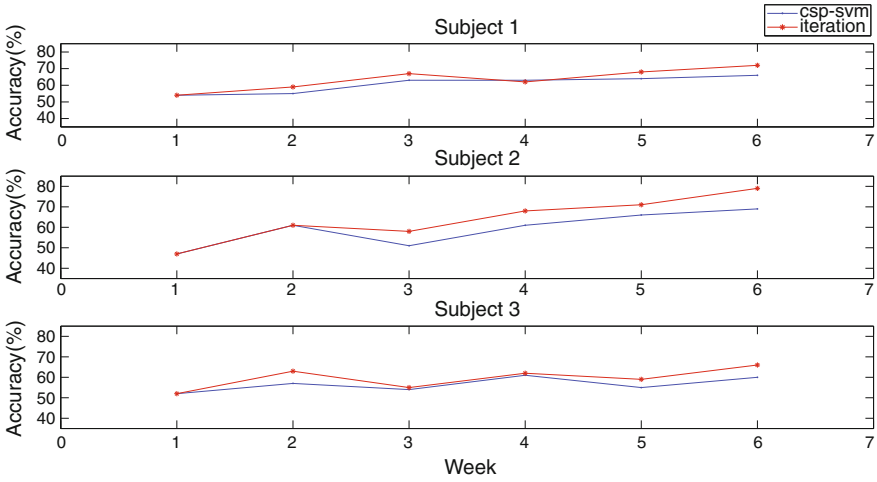

Fig. 5 Comparisons between the iteration method and traditional CSP-SVM on the test datasets of three subjects. *Red lines* represent our method and the *blue* ones represent CSP-SVM. An increasing trend can be observed evidently

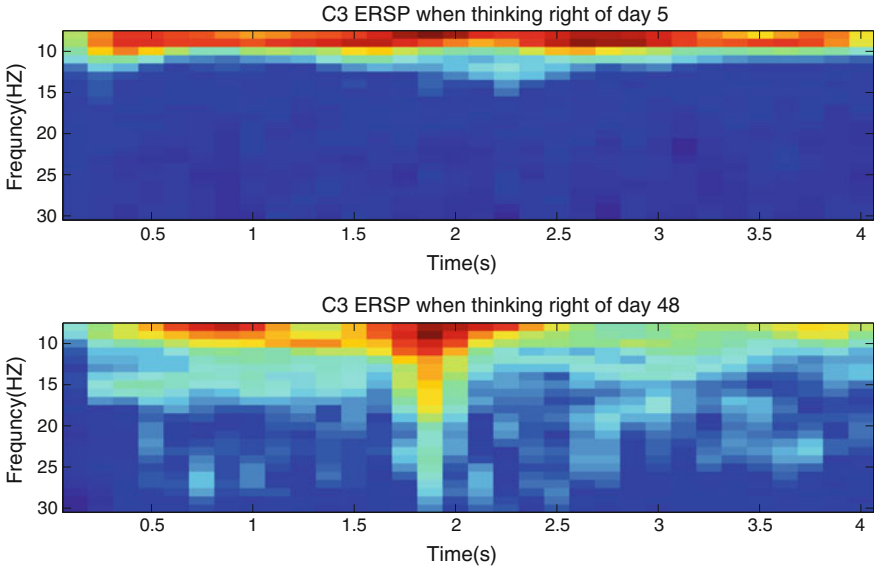

Fig. 6 ERD phenomenon of subject 2 before and after the training process. *Red* represents high power and *blue* represents low power. The duration of ERD becomes longer and the desynchronization appears more obviously, which indicate that the training and rehabilitation process take effects

It is worth mentioning that the whole experiment also provides a powerful evidence of the feasibility of our motor imagery-based BCI-FES rehabilitation system. Three patients reach the accuracy 66 % after 2 months' training and one of them reaches 79 %. The Event Related Desynchronization (ERD) time-frequency graphs of subject 2 in the 5th and 48th day are shown in Fig. 6. It is easy to find that the ERD phenomenon appears longer and more obviously after training [16]. A control group with another three stroke patients is observed and recorded during the experiment. The group is trained with ordinary medical treatments for 2 months. Compared with the experiment group, the clinical rehabilitation parameters of the control group is much lower after post-assessment, which indicates that our system promotes the rehabilitation of impaired cerebric areas and accelerates the reconstructing of the neuroncircuit of stroke patients.

5 Conclusion

In this paper, We propose an adaptive CSP method for classifying two-classes motor imagery EEG of stroke patients. This method builds two models for different classification tasks and trains them by iteration. By selecting appropriate threshold parameters, the iteration will converge and return a robust model in most cases; We apply both the proposed method and the traditional CSP-SVM on the datasets of stroke subjects and compare their classification accuracies. The results have proved that the method outperforms the general CSP-SVM approach. By evaluating the improvement of motor imagery accuracy, observing the changes of ERD phenomenon, and comparing with the control group, we also provide evidence for the feasibility of our BCI-FES rehabilitation system.

A shortcoming of this method is that the performance of two models is very sensitive to the initialization. For future work, besides implementing a rejection threshold, we can also take advantage of the distribution features of EEG recorded from stroke patients for further alleviating the negative impacts of initialization. And the test algorithm needs to be improved such as combining outputs of two models with different weights instead of obtaining the classification result by simple comparisons. Moreover, we plan to apply our BCI-FES system in more post-stroke cases and acquire new EEG data of stroke patients to provide more evidences for our method and further improvements.

Acknowledgments The work was supported by the National Natural Science Foundation of China (Grant No. 90920014 and 91120305) and the NSFC-JSPS International Cooperation Program (Grant No. 61111140019).

References

1. Sims N, Muyderman H (2010) Mitochondria, oxidative metabolism and cell death in stroke. Biochimica et Biophysica Acta (BBA)-Mol Basis Dis 1802(1):80–91
2. Cozean C, Pease W, Hubbell S (1988) Biofeedback and functional electric stimulation in stroke rehabilitation. Arch Phys Med Rehabil 69(6):401
3. Daly J, Wolpaw J (2008) Brain-computer interfaces in neurological rehabilitation. Lancet Neurol 7(11):1032–1043
4. Li J, Zhang L, Tao D, Sun H, Zhao Q (2009) A prior neurophysiologic knowledge free tensor-based scheme for single trial EEG classification. IEEE Trans Neural Syst Rehabil Eng 17(2):107–115
5. Ramoser H, Muller-Gerking J, Pfurtscheller G (2000) Optimal spatial filtering of single trial eeg during imagined hand movement. IEEE Trans Rehabil Eng 8(4):441–446
6. Bishop C, En Ligne SS (2006) Pattern recognition and machine learning, Vol 4. Springer, New York
7. Chang C, Lin C (2011) Libsvm: a library for support vector machines. ACM Transon Intell Syst Technol 2(3):27
8. Neuper C, Müller G, Kübler A, Birbaumer N, Pfurtscheller G (2003) Clinical application of an eeg-based brain-computer interface: a case study in a patient with severe motor impairment. Clin Neurophysiol 114(3):399–409
9. Li J, Zhang L (2012) Active training paradigm for motor imagery BCI. Exp Brain Res 219(2):245–254, Springer
10. Li J, Zhang L (2010) Bilateral adaptation and neurofeedback for brain computer interface system. J Neurosci Methods 193(2):373–379
11. Heidi S (2004) Motor rehabilitation using virtual reality. J Neuro Eng Rehabil 1:10. doi: 10.1186/1743-0003-1-10. http://www.jneuroengrehab.com/content/1/1/10
12. Zhao Q, Zhang L, Cichocki A (2009) Eeg-based asynchronous bci control of a car in 3d virtual reality environments. Chin Sci Bull 54(1):78–87
13. Meng F, Tong K, Chan S, Wong W, Lui K, Tang K, Gao X, Gao S (2008) BCI-FES training system design and implementation for rehabilitation of stroke patients. In: IEEE international joint conference on neural networks IJCNN 2008 (IEEE world congress on computational intelligence), IEEE, pp 4103–4106
14. Wolf S, Winstein C, Miller J, Taub E, Uswatte G, Morris D, Giuliani C, Light K, Nichols-Larsen D et al (2006) Effect of constraint-induced movement therapy on upper extremity function 3–9 months after stroke. JAMA: J Am Med Assoc 296(17):2095–2104
15. Friedman J, Hastie T, Tibshirani R (2001) The elements of statistical learning, Vol 1. Springer Series in Statistics
16. Pfurtscheller G, Lopes da Silva F (1999) Event-related EEG/MEG synchronization and desynchronization: basic principles. Clin Neurophysiol 110(11):1842–1857

The Research and Application of Multi-Resource Heterogeneous Data Fusion on Dynamic Traffic Routing System

Youli Ren, Depin Peng, Jianping Wu and Yuan Zhou

Abstract Traffic data is the basis of Intelligent Transportation Systems (ITS). It is the key problem that how to fuse and share multi-resource heterogeneous data to provide comprehensive traffic information for ITS. This paper takes the Dynamic Traffic Routing System of Nanning City of China as example, multi-resource heterogeneous data fusion model is proposed, multi-resource heterogeneous database is generated, and then the GPS, Loop, and Video data are fused. The fusion results provide comprehensive traffic information for Dynamic Traffic Routing System and Traveler. Finally, the effectiveness of the proposed model was validated by the Dynamic Traffic Routing System of Nanning.

Keywords Intelligent transportation systems · Dynamic traffic routing system · Multi-resource heterogeneous data fusion

1 Introduction

Intelligent Transportation Systems (ITS) is the system of using informationization and intelligentization technology to solve road traffic congestion, improve the environment, reduce traffic accidents, improve road utilization, and transport quality. Informationization and intelligentization technology is the development trend of transportation of the twenty-first century [1, 2]. And the research in this area is close to maturity, achieved very good results in practical applications in

Y. Ren · D. Peng (✉) · Y. Zhou
Department of Information Engineering, Yunnan Land and Resources Vocational College, Kunming, China
e-mail: depinpeng@gmail.com

J. Wu
School of Civil Engineering, Tsinghua University, Beijing, China

F. Sun et al. (eds.), *Foundations and Practical Applications of Cognitive Systems and Information Processing*, Advances in Intelligent Systems and Computing 215,
DOI: 10.1007/978-3-642-37835-5_33,

Japan, Europe, and the United States, while in China, there is a great gap with the developed countries, because the traffic informationization technology started relatively late, and the degree of informationization technology is still relatively low [3]. While, in our country, traffic informationization had a greater degree of development through decades of construction. But in the process of traffic informationization, each department had established a number of application systems according to their needs, and heterogeneity of the database platform used in various application systems make the problem of isolated islands of information more and more obvious and serious, make the traffic data collected cannot achieve the interconnection and sharing [4]. Therefore, the research and realization of multi-source traffic information fusion is one of the key issues for dynamic route guidance under heterogeneous database environment. This paper takes the construction of the subsystems of traffic information fusion and processing for Traffic Guidance System of Nanning as example, study the feasibility and effectiveness of multi-source traffic information fusion from the aspects of traffic flow data preprocessing, GPS location information matching, traffic flow information fusion, and traffic information sharing under heterogeneous database environment, and verify the efficiency of data queuing model based on high speed cache.

The structure of the paper is organized as follows: Collected traffic data was preprocessed to improve the reliability and accuracy in Sect. 1; GPS location information matching was studied in Sect. 2; Sect. 3 researched the multi-source heterogeneous data fusion, and the data queuing model was proposed based on high speed cache to achieve the fusion of traffic flow data collected by loop, video, and GPS, and then the data accuracy is calibrated; The effective conclusions was given in Sect. 6.

2 Traffic Flow Data Preprocessing

Preprocessing the collected traffic data is one of the key to ensure data reliability and accuracy. Therefore, the GPS data, loop data, and video data were preprocessed as follows.

2.1 GPS Data Preprocessing

The key algorithms of GPS data preprocessing combining with GPS historical data are:

- GPS traffic flow data denoising: remove the useless data generated when GPS in the parking, slow, bridge, buildings, and other factors caused data deviate.
- The GPS traffic flow fusion algorithm: GPS location point data are quickly and accurately matched to the corresponding road, generated real-time road running state-velocity data.

- Through the small sample of GPS supplementary algorithm, data supplement is achieved when the GPS sample on the road causing data missing.

2.2 Loop Detector Data Preprocessing

The key preprocessing of loop data are:

- Conversion processing from the traffic data collected by loop for road section to the average speed of the road: real-time traffic flow data collected by loop buried under road section during some time interval, which cannot be complete representation the average speed of the whole road, which need to convert the data from section to road. According to the traditional speed switching model from point to line and combined with the actual road and traffic characteristics, the parameters were amended to ensure data correct [5].
- Loop data denoising: Loop data still has data anomalies which maybe caused by loop damage, equipment precision, environmental catastrophe, etc. These abnormal data will bring a great deal of influence to fusion accuracy of system data. Therefore, it is necessary for data denoising processing prior to fusion. The model used in this paper have calibrated by field data, which can automatically find abnormal data, remove, and repair data.

2.3 Video Data Preprocessing

The video data is identical with loop data preprocessing, the key processing are:

- Convert travel time data collected by video detector to average speed of the road: Video equipments were installed on the bayonet of the rapid ring road in this paper. The detection principle of travel time is based on license plate recognition and the executed time during space distance between the dual video. Because video travel time may contain multiple sections, when fusing video travel time and if only contains a single section, it can be used as the basis of average speed of road section. If video travel time contains multiple sections, it can be used to calibrate the results accuracy of GPS and loop data to improve the accuracy of system data.
- Video traffic flow data denoising: The video detection data sources also have data anomalies, because the detection of travel time depends on the video accuracy for license plate recognition. While the processing technology of license plate recognition was impacted by climate (such as fog, rain, snow, wind, dust, etc.), recognition success rate will often fluctuate including noise data.

3 GPS Location Information Matching

GPS location points were real-time matched to the right road section, which provide a basis for the traffic flow data fusion by confirming its direction, speed, etc. Several important considerations of matching process include: data filtering and denoising, data curve smoothing (points complement of location data), and road section traffic flow speed fusion. And the GPS receive data stream format per vehicle, generate flat data table; data grid division was projected based on road network (small sections grid); GPS data matching with small sections in the grid to complete the data network cell allocation. The matching principle and algorithm are shown in Figs. 1, 2, 3, and 4.

4 Multi-source Heterogeneous Information Fusion

Multi-source traffic flow information fusion was achieved through a series of data fusion model and algorithm which calibrated and validated by a large number of actual data. Multiple traffic flow data fusion model and algorithm are shown in Fig. 5.

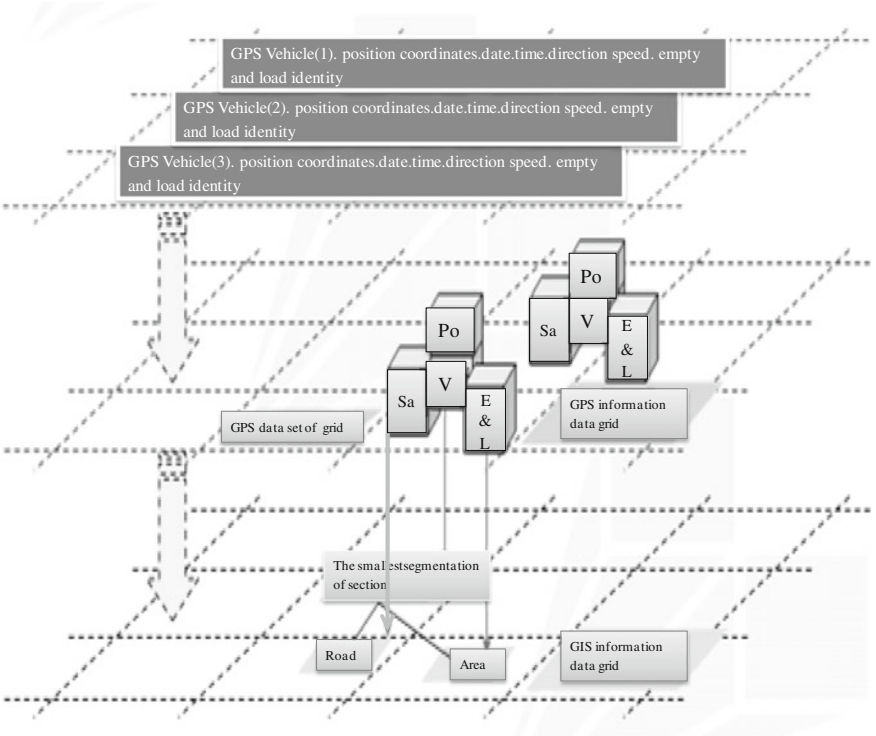

Fig. 1 The principle of GPS location matching model

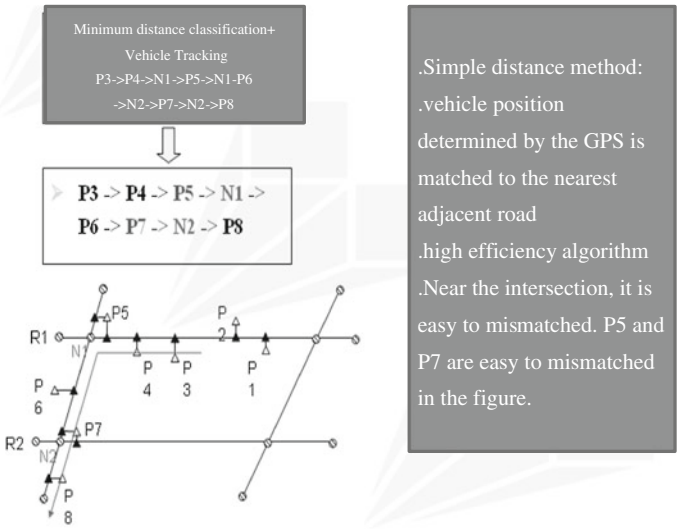

Fig. 2 Long-distance dispersed position complementation point algorithm

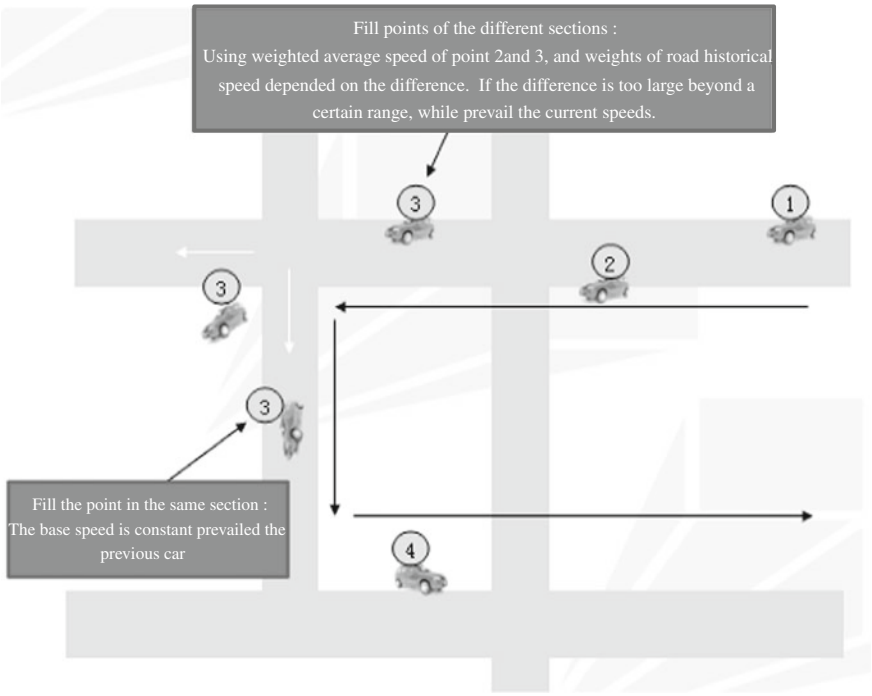

Fig. 3 The principle of GPS complementation point

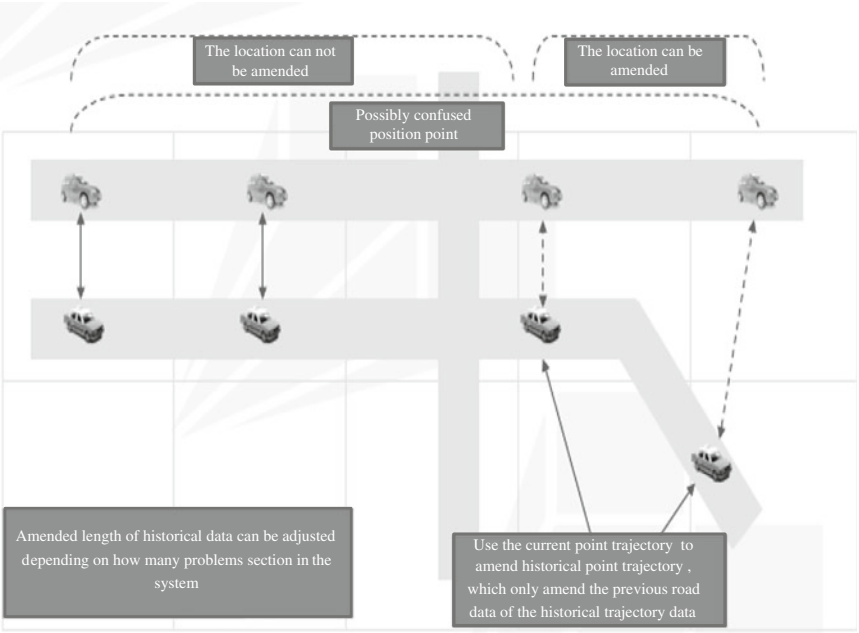

Fig. 4 Parallel, same direction, and close section matching and the principle of historical trajectory amendment

4.1 Multi-source Heterogeneous Traffic Flow Database Structure

The multiple heterogeneous traffic flow database structure using three-dimensional structure grid-based of traffic data is shown in Fig. 6.

This paper generates data set on the same target containing a variety of properties for complex multi-source heterogeneous traffic dynamic data analysis and processing combined with the traffic geographic information system, information processing technology in data grid, it is the traffic dynamic information three-dimensional database. The relationship of the three-dimensional data structure of traffic data was shown in Fig. 7.

Generating the three-dimensional traffic data database structure, the key is to establish a complex relationship between the various data. This study will build Nanning road network dynamic traffic data database. The data for constructing the database include: (1) GIS information; (2) GPS traffic flow, loop traffic flow fusion data; (3) traffic management infrastructure data (restricted access, control information); (4) dynamic traffic information, comprehensive traffic flow data.

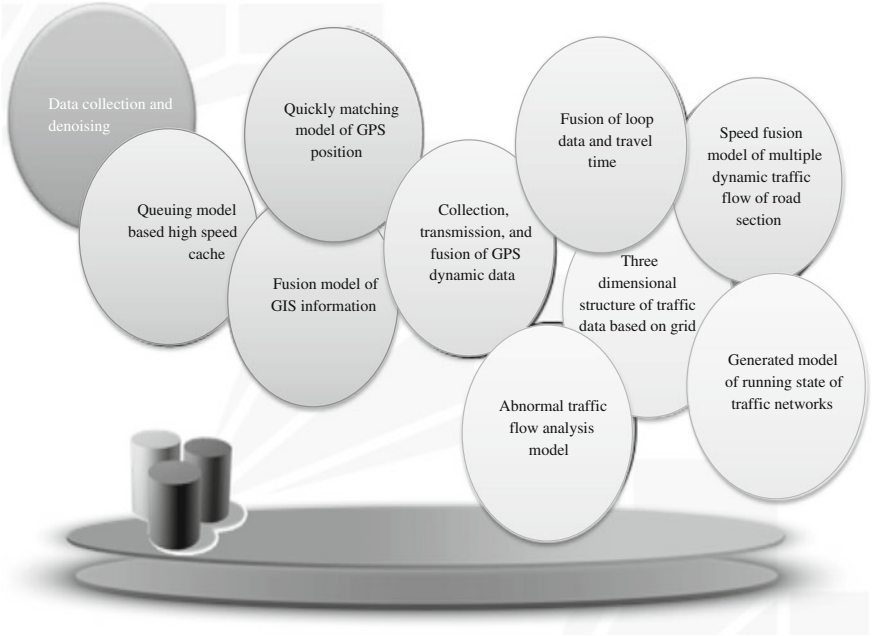

Fig. 5 Data fusion model and algorithm set

4.2 GPS, Loop, and Video Data Fusion

Multiple dynamic traffic data fusion was achieved by fusion model proposed in this paper for different dynamic traffic data collected on the same sections through the dual-grid algorithm (data + map), and the speed and flow information collected by different ways were fused and matched to electronic maps to obtain accurate traffic flow data in the various sections.

Under the condition that of the GPS data accurate, the data fusion accuracy depends on the collection frequency and sample size of the GPS. In this paper, GPS collection frequency must be less than 30 s and sent real time. The main traffic models of the GPS data fusion technology are: GPS Dynamic Traffic Data matching to GIS, GPS traffic flow data fusion model. The multi-source dynamic traffic speed fusion model is shown in Fig. 8.

The procedure of fusion is:

- Remove data noise for different types of data according to different rules, such as smoothing processing of the data curve (supplementary point processing).
- Format the GPS traffic flow data, loop traffic data, and video traffic data get from GPS match model.
- Based on the classification collection of data, aggregate data and generate classified data set, it is that the loop, video, and GPS data classified load; based

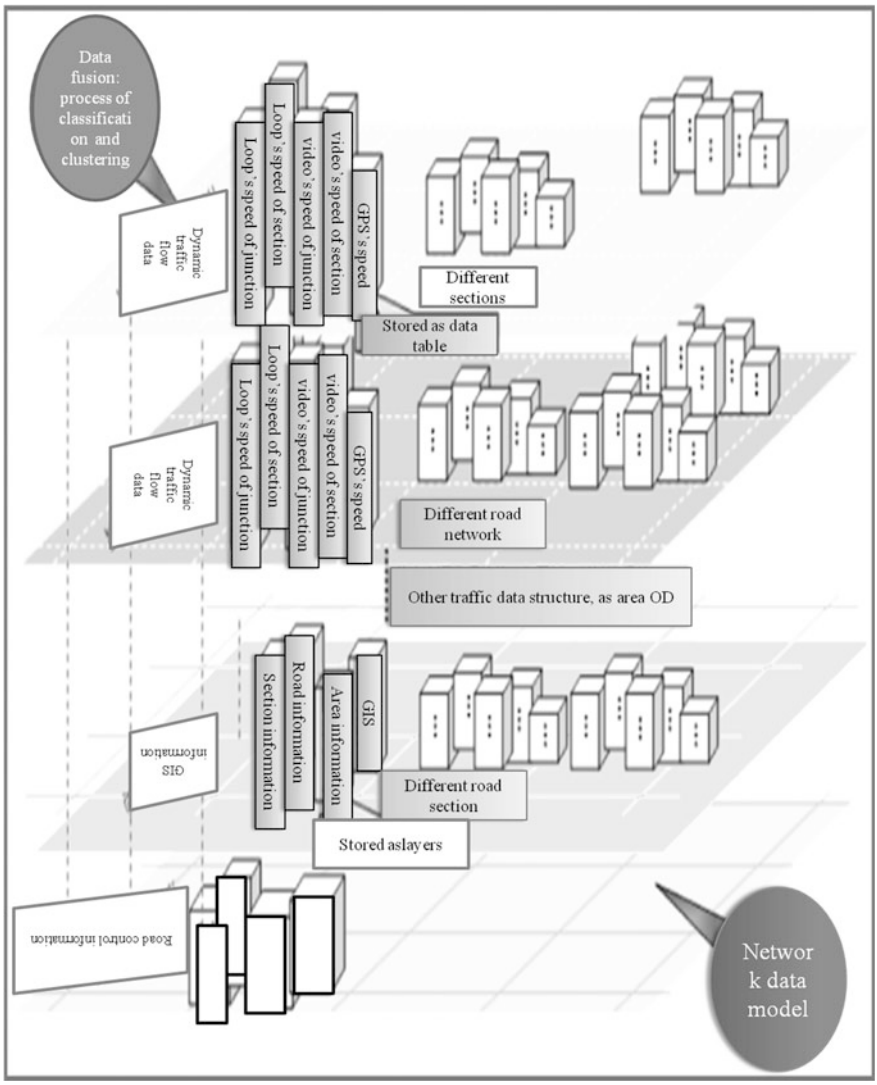

Fig. 6 Three-dimensional structure of traffic flow data-based grid

on the properties of the data, do data clustering, that is, the same attributes data such as speed is fused.

- Data fusion model is the core algorithm used to analyze data from different sources, and distribute the weights for different characteristics. Finally, a single data is formed by multi-source data fusion algorithm. The fused data were again matched to the section.

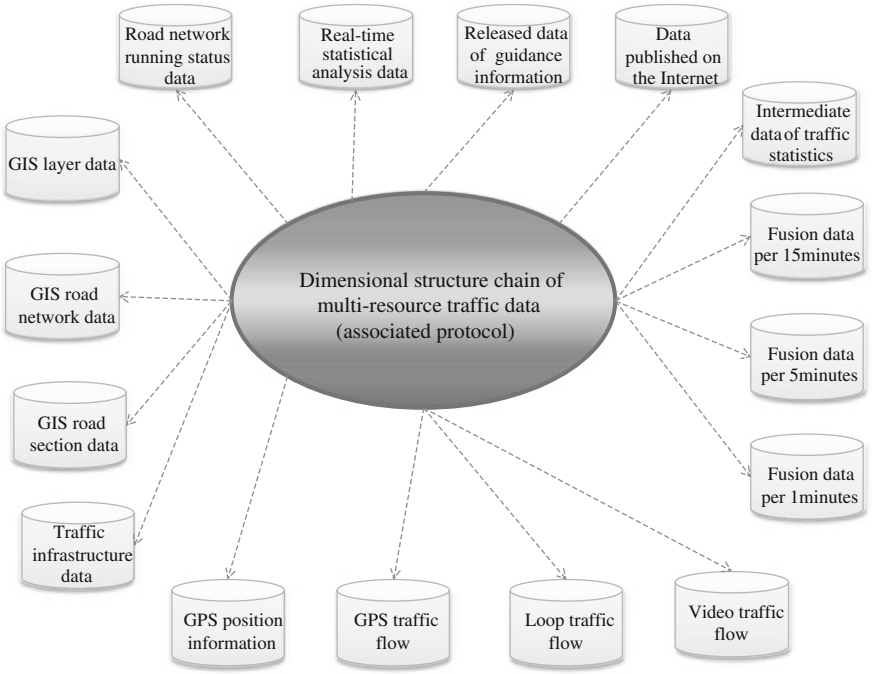

Fig. 7 The diagram of traffic three-dimensional data structure

4.3 Fusion Accuracy Calibration

The purpose of the data accuracy calibration:

To ensure the traffic data obtained after the data fusion with sufficient accuracy, and the traffic state assessment and prediction results in line with the actual situation, must make necessary calibration of data accuracy. The purpose of data calibration is to calibrate and validate accuracy of the system data which analyzed and processed by system software, through actual sampling information of real sections.

In order to ensure data validation, need the following preparations:

- First, need to collect related information of actual sections. In the data collection process, use traffic data collection techniques to ensure the accuracy of data.
- Second, according to the relevant features of software to determine the data calibrated contents, after processed and analyzed the manual data, compared with the system data, analyzed the accuracy of system data, and then obtained the calibrated results.

Contents of data accuracy calibration:

Calibration point selection principle: data calibration should focus on the overall road network in Nanning, but in the actual calibration process, only select

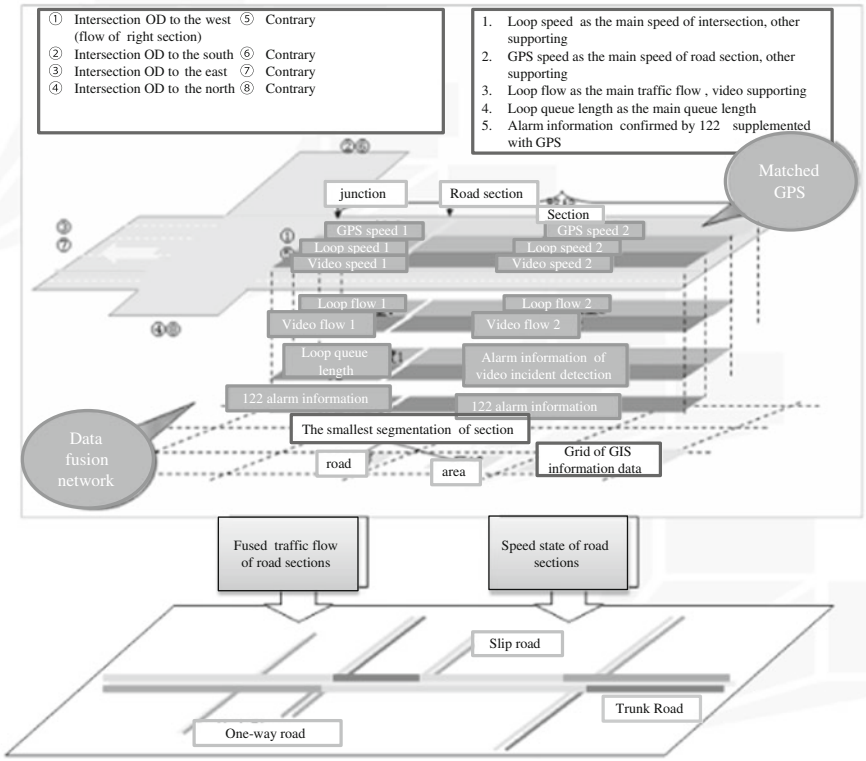

Fig. 8 The sections speed fusion model of multi-source dynamic traffic flow

representative roads to calibrate in the road network. According to Nanning city road network structure, specific calibration object within the scope of the paper are the typical fast road, trunk road, sub-distributors, service road, and a one-way street.

- Independent basic data: collection source is independent for the sections, such as data detection based on loop, or only GPS-based data detection.
- Conveniently collection and analysis: it is conducive to manual data collection.
- Selected calibration parameters: travel time of sections (or average speed).

Data accuracy calibration method.

Data calibration method is main comparing system data with manual data for sampling road in different periods, analyzing law of data error, making system results close to the actual situation by adjusting the parameters of system traffic model to ensure the results accuracy of system data to practical extent.

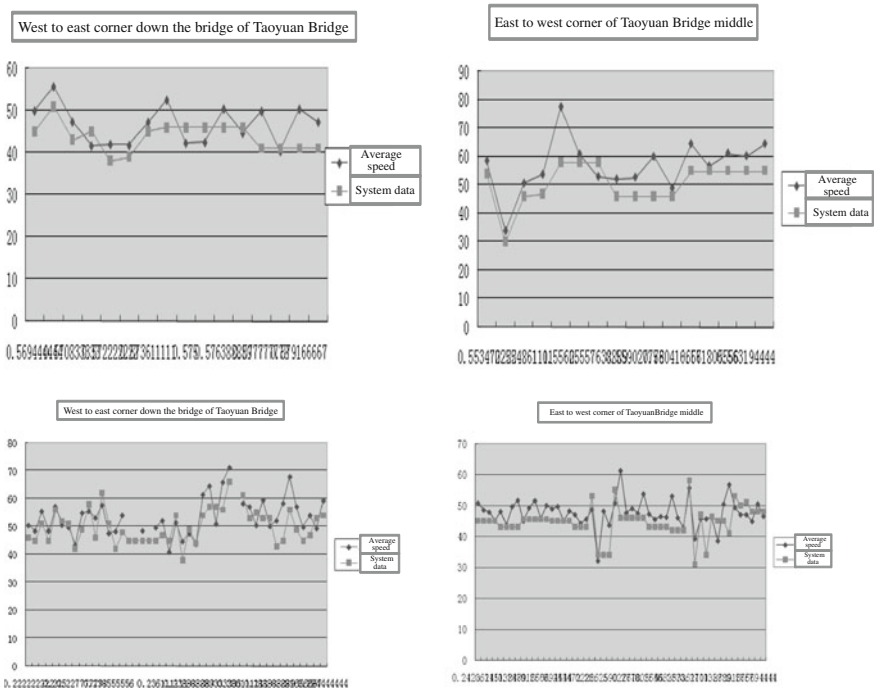

Fig. 9 The comparison of the actual data and system fusion data for Taoyuan bridge

5 Real Traffic Data Testing and Analysis

This paper, selected the Nanning actual traffic data to validate and calibrate fusion model, selected Taoyuan Bridge and Baisha Bridge of Nanning as study fields; the comparison results between real data and system fusion data are shown in Figs. 9 and 10. That average error for Taoyuan Bridge is less than 10 % and that of Baisha Bridge is 11 % by statistical calculations. Since the actual data collection method is by riding a motor vehicle in the National Road more than 20 times in different time periods (morning peak, flat peak, evening peak), and use the stopwatch to record the time of enter and exit of the various sections to calculate the travel time and speed of the various sections in the different time period (the length of each section is known). The inherent errors of the human factors and equipment factors have an impact on the accuracy of the data, through repeated collection and statistical analysis, the data error is reduced to the lowest. Overall, the fusion accuracy basically meets dynamic traffic guidance system data requirements.

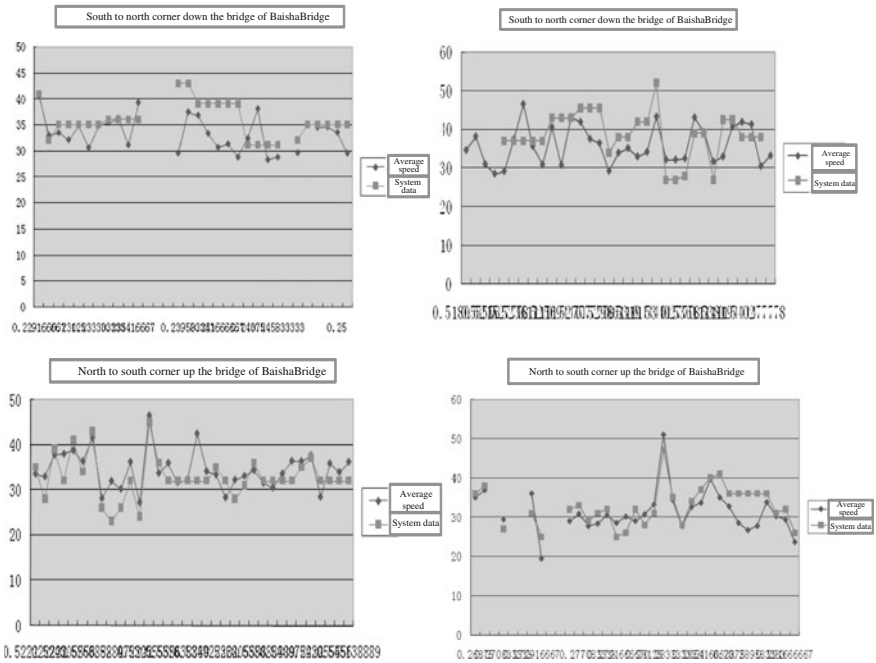

Fig. 10 The comparison of the actual data and system fusion data for Baisha bridge

6 Conclusions

Traffic informationization construction is a complex systems engineering, this paper studies multi-source heterogeneous traffic information fusion model of the dynamic traffic guidance system. Take Nanning as an example, collect traffic data, preprocess traffic data, construct database, fuse multi-source heterogeneous information, and generate multi-source heterogeneous traffic data database. Traffic information data fusion results were stored in database center, and then, the traffic information was released and shared. Finally, the practicality and effectiveness of fusion model proposed in this paper were verified through the construction, implementation, and calibration of Nanning traffic guidance system.

References

1. Xu J-M, Hu Y-C, Zhong H-L (2002) The research of ITS common information platform system framework and operational mechanism. J South China Univ Technol 30(11):55–60 (Natural Science Edition)
2. Guan J-Z (2002) System framework and integration of ITS common information platforms. J Transp Syst Eng Inf Technol 2(4):11–16

3. Li F (1999) The development trend of intelligent transportation systems in foreign countries. Foreign Highway 19(1):1–5
4. Li H, Li M, Luo X et al (2006) Research on traffic information sharing technology in multiple heterogeneous database environment. J Highway Transp Res Develop 23(6):140–144
5. Jiang Z-F, Tan G-L (1996) The development of vehicle detectors. J Highway Transp Res Develop 13(1):62–65

Data Fusion for the Diagnostics, Prognostics, and Health Management of Aircraft Systems

Zheng Liu and Nezih Mrad

Abstract In the diagnostics, prognostics, and health management (DPHM) program for aircraft, enormous data, information, and knowledge relevant to the health states of aircraft are collected from various sources. The proper interpretation and using of these data and information constitute the basis for a sound decision making of maintenance activities. The raw data is pre-processed, extracted, combined, and integrated into reference information for decision making. Data fusion becomes a key technology at varied levels in this process This paper identifies and describes the role of data fusion in the context of modern DPHM program.

Keywords Diagnostics, prognostics and health management · Condition monitoring · Data fusion · Computational intelligence

1 Introduction

The philosophy for aircraft maintenance evolves with modern technology from run-to-failure maintenance, time-based preventive maintenance, to a more cost-effective condition-based maintenance (CBM) so that the major expense on maintenance can be saved [1]. The maintenance is only conducted on the evidence

Z. Liu (✉)
Intelligent Information Processing Laboratory, Toyota Technological Institute, Nagoya 468-8511, Japan
e-mail: zheng.liu@ieee.org

N. Mrad
Department of National Defence, Operational Analysis and Systems Integration Support Defence R&D Canada Atlantic, National Defence Headquarters, Ottawa, ON K1A 0R6, Canada
e-mail: Nezih.Mrad@drdc-rddc.gc.ca

F. Sun et al. (eds.), *Foundations and Practical Applications of Cognitive Systems and Information Processing*, Advances in Intelligent Systems and Computing 215,
DOI: 10.1007/978-3-642-37835-5_34,

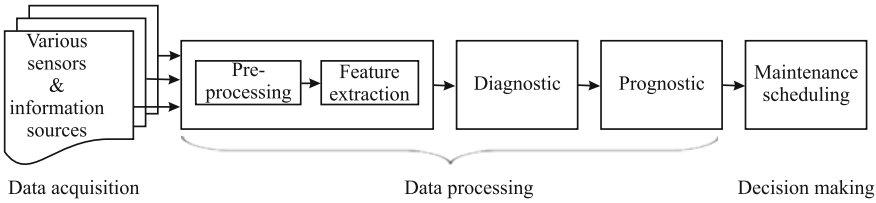

Fig. 1 DPHM for condition-based maintenance of aircraft

of need, which comes from the information collected through health condition monitoring. Thus, the diagnostics, prognostics, and health management (DPHM) program comes into operation. As illustrated in Fig. 1, DPHM is implemented in the condition-based maintenance of aircraft systems. The whole process includes three major steps: data acquisition, data processing, and decision making [2].

For complex systems like aircraft structures, condition monitoring is a key step to implement CBM. Health refers to the ability of a system to continue to preform its intended function in light of the inevitable aging and damage accumulation resulting from the operational environments. Condition monitoring is referred as a process of implementing a damage identification strategy [3]. Advanced sensor technologies are employed to collect information and the acquired signals and data from these sensors are manipulated to get a better awareness of the health states of the aircraft. Sensor-level or signal-level fusion can be applied in this scenario to generate a fused signal of the same type as the original but with greater quality. The computational process has been recognized as one of the statistical pattern recognition problem. According to the description in [3, 4], the condition monitoring process involves the observation of a structure or mechanical system over time with periodical measurements, the extraction of damage-sensitive features from these measurements, and the statistical analysis of these features to determine the current state of system health.

Diagnostics is most commonly performed as classification using feature-based techniques [5]. Those features used for classification are extracted from measurement data. Diagnostics maps the information obtained in the measurement space and/or feature space to the faults in the fault space [2]. Fault diagnosis is to detect, isolate, and identify an impending or incipient failure condition—the affected component (subsystem, system) is still operational even though at a degraded model while failure diagnosis looks at the component that has eased to operate [6]. The diagnostic functionalities include:

- Detection: detecting and reporting the abnormal operating condition.
- Isolation: determining which component (system, subsystem) is failing or has failed.
- Identification: estimating the nature and extent of the fault (failure).

Sensory data are processed to extract features correlated to specific failure modes. Data fusion plays an important role in better understanding and interpretation of the collected information. Fused features can be used to establish the healthy state

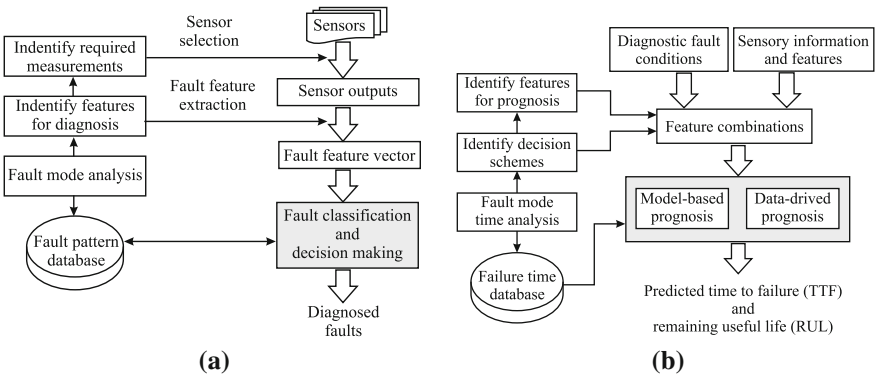

Fig. 2 The diagnostic (**a**) and prognostic processes (**b**)

of the system and can provide a better estimate of the object's performance deviation due to presence of any fault [7]. Figure 2a illustrates the diagnostic process [6, 8]. The whole process starts from fault mode analysis, which determines what to measure (choice of sensors) and the most appropriate features to track fault's status. Fault feature vectors are extracted from sensor outputs and used for fault classification. The information about the diagnosed faults will be used as inputs for the prognosis as illustrated in Fig. 2b.

Prognostics is to project the current health and performance state of a component into the future with the estimates of future usage profiles taken into account [9]. Given the current condition and past operation profile, prognosis will predict the remaining useful life (RUL) and/or the chance of a system that can be operated without a fault or a failure to a future time point [2]. The definition of prognostic by International Organization for Standardization (ISO) is: the estimation of time to failure and risk for one or more existing and future failure modes [10]. As illustrated in Fig. 2b, the prognostic process starts from the fault mode time analysis and subsequently identify the best feature combinations and the best decision schemes to compute these combinations for RUL estimation [6, 8]. The two basic approaches for prognosis are model-based and data-driven approaches. Similarly, data fusion also contributes to the implementation of prognostic process through integrating and incorporating multi-source information and knowledge.

Data fusion combines information from multiple sensors to validate signals and create features at the lowest level. Fusion can also be used to combine features to derive diagnostic information, which achieves an improved level of confidence for the diagnosed results. The diagnostic and prognostic processes can incorporate the experience-based information, such as legacy failure rates and/or physical model predictions with the data fusion technologies for improved accuracy and reliability. To assure the effectiveness of a fusion process, the characteristics of the a priori system information should be fully understood.

This paper surveys the use of data fusion techniques in the context of DPHM of aircraft systems. The role of data fusion in the DPHM system is identified and

described. The detailed implementations for the data fusion algorithms are not the focus of this paper. This paper intends to identify the novel use of these techniques to provide a better solution to the application of aircraft maintenance.

2 Data Fusion for DPHM

A definition of data fusion as recommended by the U.S. Department of Defense Joint Directors of Laboratories Data Fusion Sub-panel is [11]:

> Data fusion is a multilevel, multifaceted process dealing with the automatic detection, association, correlation, estimation, and combination of data and information from multiple sources.

The potential applications of fusion techniques are illustrated in Fig. 3 with numbers one to seven. The sources of information can be roughly categorized into three sections, i.e., from sensor-based approaches, data-driven models, and physics-based models. Thus, the intelligent use of information from these approaches and models may benefit the overall DPHM program.

① Fuse multi-sensor signal/data, feature, and information;
② Fuse multiple physics-based models;
③ Fuse multiple data-driven models;
④ Fuse sensor information with physics-based models;
⑤ Fuse sensor information with data-driven models;
⑥ Fuse physics-based and data-driven models;
⑦ Fuse sensor information with physics-based and data-driven models.

3 The Functionalities of Data Fusion

3.1 Sensor Data Fusion for Condition Monitoring

Sensor-level fusion encompasses the fusion of non-destruction inspection data and the fusion of online sensor measurements [12]. The fusion operation can achieve

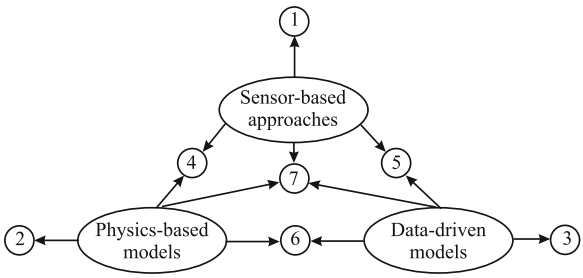

Fig. 3 The potential fusion applications

signal enhancement, denoising, sensor validation, etc. [13]. For example, by fusing the signals from multiple vibration sensors, the effects of random noise are diminished and the subtle signs of a fault can be highlighted [14]. A survey of non-destructive evaluation (NDE) fusion was presented in [15], where most approaches were implemented offline. In [16], multiple piezoelectric transducers (PZT) were used to detect mono- and multi-delamination in carbon fiber-epoxy composite structures. The time-of-flight feature was extracted to characterize such delaminations. Four fusion schemes, i.e., disjunctive, conjunctive, compromise, and hybrid fusion, were proposed to fuse the prior probabilities to derive a posterior consensus. Fusion of conventional and pulsed eddy current with microwave inspection results was carried out to detect the hidden corrosion in aircraft lap joints [17]. An extension of a maximum likelihood approach was used of fuse data obtained from two anomaly detectors, i.e., RX detector and fuzzy logic detector. RX algorithm is an adaptive multi-band constant false alarm rate anomaly detector based upon the generalized maximum-likelihood ratio test [18]. Further investigations on the fusion of ultrasound testing images for lap joint corrosion detection was reported in [19].

As described in [20], sensor data is available in two forms: state awareness and usage. The state awareness sensors provide information about the current state of material health from the initial indications of defect to crack size estimations. The uncertainties from state awareness sensors include false alarms and measurement errors. Usage sensors directly or indirectly measure the external impacts that lead to damage. The data from usage sensor may include information about local stresses and environmental parameters, such as temperature, humidity, and local chemistry. Usage data also has the uncertainty in the form of measurement and mapping errors [20]. Various indicators from multiple sensors can be fused to provide a comprehensive health indicator for a component [21].

Failure models use a variety of parameters, estimates of current state, and anticipates of future usage to project future state as a function of time or usage. The input parameters reflect the material properties. Due to the limited knowledge about the structures and/or the inadequate representation of the physics, the uncertainty of these parameters is characterized statistically. As both models and sensors are imperfect, it is necessary to use the information from models and sensors to dynamically adjust predictions, which is expressed in terms of the health condition at a future point, or a time to reach a specified health condition [20]. The fusion of information from sensors and models is to reduce the uncertainty of the output, which is presented as the probability of failure as a function of time and/or usage. A two-stage process proposed in [20] is illustrated in Fig. 4. In the first stage, sensors are used to detect the presence or absence of a defect. The probability density of the time to form a crack of specific size defines the current state. This assessment is further used to update the input parameters of the failure models through the Bayesian theorem. The second stage combines updated model predictions and its uncertainties with current state estimates to determine the probability of failure as a function of time and/or usage.

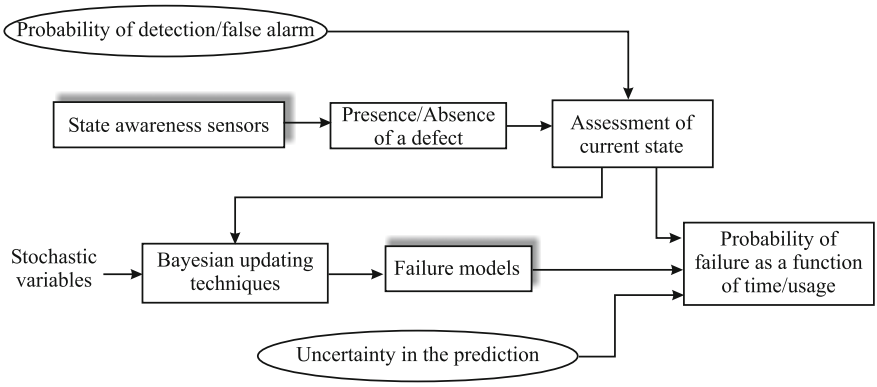

Fig. 4 The process of reasoning and prediction by fusing the information from sensors and models

Another fusion scheme based on Kalman filter was proposed in [22] to fuse imperfect sate information such as environmental measurements with failure models. The fusion enables an adaptive prognosis for structural corrosion damages.

Piezoelectric accelerometers were applied to locate the damages in starboard wing in a Gnat trainer aircraft [23]. Inspection panels were distributed and moved over the wing to simulate the damages. A set of piezoelectric accelerometers were used to detect the damages. The first step is to extract signal features for damage detection and localization. The feature selection process was conducted by inspecting the transmissibility functions [24]. Then, a multi-layer perceptron (MLP) neural network and a Dempster-Shafer neural network were used to classify the damage locations. The results from these two classifiers were fused with Bayesian and Dempster-Shafer methods. An improvement in classification rate was observed [24].

3.2 Data Fusion for Diagnostics

Diagnostics is a higher level understanding of the fault condition and the fuse of sensor information and features extracted from multiple sensors may facilitate the diagnostic process, i.e. detection, isolation, and identification/estimation. Anomaly detection is the first step to extract the underlying structural information from data, define normal status, and identify departures from such normal status [25]. In Ref [25], the anomaly detection was implemented by constructing and fusing an ensemble of diverse detectors for the improved reliability of outputs, where the detectors complement each other.

The fusion of features from multiple sensors can provide a greater diversity of health indicators for detection level reasoning by combing the strengths of the individual features [26]. In Ref [27], fuzzy inference system (FIS) was applied to

fuse various CI values from various sources into one meaningful assessment. The fault detection performance can thus be improved and the severity of the fault can be better characterized [26]. The potentials to fuse measurements for C17-T1 engine diagnostics were investigated and reported in [28, 29]. High-level feature fusion, which transforms multi-source information into a diagnosis knowledge base, was implemented to minimize diagnostic decision errors [29]. A fuzzy belief network was used to assess engine health status in real-time during flight by fusing the input health features from analysis modules.

A health monitoring system was developed in [30] to diagnose the degradation of aircraft hydraulic pumps. The dynamic analysis of high frequency content of pump pressure and case drain signals provided eight reliable diagnostic features. Four each were used for pump pressure and case drain respectively. The performance analysis is based on a physics-based approach, which models the performance characteristics of the pump. Fuzzy logic-based classification was performed for each analysis approach and Bayesian fusion was applied to fuse the classification results.

A dynamic fusion of multiple classifiers for jet engine fault diagnosis is presented in [31]. Three individual classifiers, i.e., neural network, support vector machine, and decision tree, were selected to classify seven classes with 12 parametric inputs [31]. The local performance information of individual classifiers is considered for final classification decision making. A bias adjustment method was implemented to integrate the local performance information into the MEAN rule-based fusion process [31, 32]. The overall performance in terms of overall accuracy, false positive, and negative rates is improved.

In Ref [33], data collected within a flight control system, including pressure, current , and position measurements, were used to extract health features. The health state of actuators was classified with the extracted features. Then, the outputs from the classifiers were fused with the operational mode information to produce a fused health state. A prognostic function based on Kalman filter used such state assessment to predict the RUL. In the in-line health monitoring system for hydraulic pumps and motors, two fuzzy logic classifiers were trained for high-bandwidth and low-bandwidth performance analysis respectively [30, 34]. The classification results, health indicators represented by damage level, were then fused with an adaptive weighting approach [30, 34]. An overall health state was derived from the fusion result. Meanwhile, the diagnostic confidence was updated in a Bayesian framework using historical information and a projected number of operational hours [30, 34].

4 Data Fusion Algorithms

The fusion can be implemented at three levels, i.e., sensor level, feature level, and decision level. At the lowest (sensor) level, the fusion operation combines information from multiple sensors to validate signals and create features. At a higher level, fusion operation will combine derived features to obtain the diagnostic information. At the highest level, fusion will incorporate experience-based

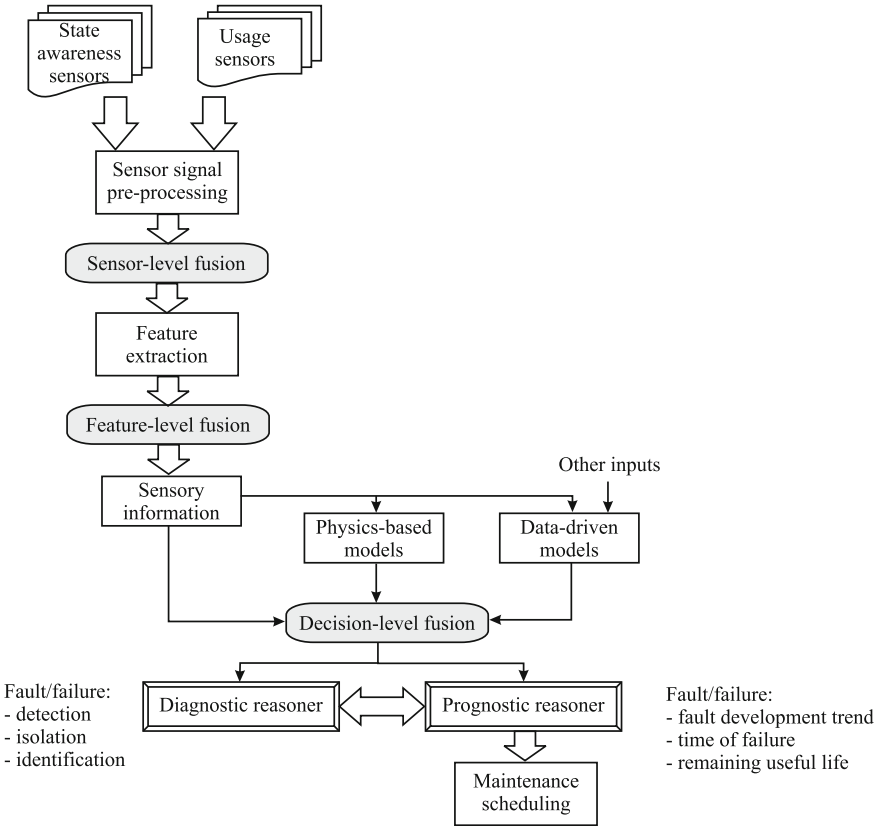

Fig. 5 The three levels of data fusion in DPHM

information or physical model predictions with signal-based information to facilitate the decision making process. This can be illustrated with Fig. 5. The implementations for the fusion at different levels are different.

A multi-sensor fusion tool kit developed by Penn State University provides a standardized visual programming environment for data fusion [35]. This platform can facilitate rapid prototyping and evaluation of data analysis and fusion algorithms for varied applications, such as mechanical power transmission and electrochemical systems [35].

5 Concluding Remarks

This paper presents a survey on the application of data fusion techniques to the DPHM of aircraft systems. The roles of data fusion in the context of condition monitoring, diagnostics, prognostics, and health management are identified and the

potential application areas are highlighted as well. The flow of information from raw sensor data and priori knowledge to the reference for maintenance decision making relies on the operations for information extraction, modeling, and integration, which are facilitated or implemented by the data fusion and mining techniques. The benefits of the data fusion techniques can be understood and evaluated from the performance metrics.

The implementation of data fusion algorithms is a computational issue, which relies on the types of sensors, available data, and application requirements. The TRL (technology readiness level) depends on how the algorithms will be used, e.g., online or offline, on-board or off-board. The technology efficiency also depends on the availability of computational power and resources. The effectiveness or performance of the sensor-level fusion is determined by the choice of the sensors, which can be complementary to each other or totally irrelevant.

The detailed discussions of the implementations and performance of varied fusion algorithms are not available in this paper, instead we first look at the functionality of the data fusion in the context of diagnostics, prognostics, and health management of aircraft systems. How data fusion facilitates the flow of information from raw sensor data to high-level knowledge is described and reviewed. Thus, the benefits of data fusion techniques can be understood from the concrete examples. For future work, we will further look into the existing algorithms and their performance in terms of the requirements of specific applications.

References

1. Mrad N, Lejmi-Mrad R (2011) Advances in health monitoring and management. In: Expert systems for human, materials and automation. InTech, pp 109–136
2. Jardine A, Lin D, Banjevic D (2006) A review on machinery diagnostics and prognostics implementing condition-based maintenance. Mech Syst Signal Process 20:1483–1510
3. Farrar CR, Worden K (2007) An introduction to structural health monitoring. R Soc Lond Trans Ser A 365:303–315
4. Farrar CR, Doebling SW, Nix DA (2001) Vibrationbased structural damage identification. Philos Trans R Soc Lond Ser A Math Phys Eng Sci 359:131–149
5. Byington CS, Garga AK (2001) 23 Data fusion for developing predictive diagnostics for electromechanical systems. In: Handbook of multisensor data fusion. CRC Press, Taylor and Francis Group, New York, pp 1–32
6. Vachtsevanos G, Lewis F, Roemer M, Hess A, Wu B (2006) Intelligent fault diagnosis and prognosis for engineering systems. Wiley, Hoboken
7. Kumar S, Pecht M (2008) Data analysis approach for system reliability, diagnostics and prognostics. In: Pan Pacific microelectronics symposium, Kauai, USA, pp 1–9
8. Lewis FL (2011) Intelligent fault diagnosis and prognosis. Presentation available at http://arri.uta.edu/acs. Accessed Nov 2011
9. Tejedor TA (2007) Towards the future of gas turbine asset and performance management. In: Power industry international, 2007, pp 19–21
10. Dragomier OE, Gouriveau R, Dragomir F (2009) Review of prognostic problem in condition-based maintenance. In: European control conference, Hungary, Budapest, pp 1–6

11. Klein LA (1999) Sensor and data fusion concepts and applications. Society of Photo-Optical Instrumentation Engineers (SPIE), Bellingham
12. Pidaparti RM (2007) Structural corrosion health assessment using computational intelligence methods. Struct Health Monit 6:245–259
13. Roemer M, Orsagh R, Schoeller M, Scheid J, Friend R, Sotomayer W (2002) Upgrading engine test cells for improved troubleshooting and diagnostics. In: IEEE aerospace conference, vol 6, pp 6-3005–6-3013
14. Byington CS, Watson MJ, Lee H, Hollins M (2008) Sensor-level fusion to enhance health and usage monitoring systems. In: AHS 64th annual forum and technology display, Montreal, QC, Canada
15. Liu Z, Forsyth D, Komorowski J, Hanasaki K, Kirubarajan T (2007) Survey: state of the art in nde data fusion techniques. IEEE Trans Instrum Measur 56:2435–2451
16. Su Z, Wang X, Cheng L, Yu L, Chen Z (2009) On selection of data fusion schemes for structural damage evaluation. Struct Health Monit 8:223–241
17. Gupta K, Ghasr M, Kharkovsky S, Zoughi R, Stanley R, Padwal A, OKeefe M, Palmer D, Blackshire J, Steffes G, Wood N (2007) Fusion of microwave and eddy current data for a multi-modal approach in evaluating corrosion under paint and in lap joints. In: Thompson DO, Chimenti DE (eds) Proceedings of the 33th annual review of progress in quantitative nondestructive evaluation, vol 894. AIP, 2007, pp 811–618
18. Thomas A (2008) Extending the rx anomaly detection algorithm to continuous spectral and spatial domains. In: IEEE southeastcon, pp 557–562
19. De S, Gupta K, Stanley R, Steffes G, Palmer D, Zoughi R (2009) A data fusion based approach for evaluation of material loss in corroded aluminum panels. In: IEEE conference on intelligent transportation systems, pp 1–6
20. Papazian JM, Anagnostou EL, Engel SJ, Hoitsma D, Madsen J, Silberstein RP, Welsh G, Whiteside JB (2009) A structural integrity prognosis system. Eng Fract Mech 76:620–632
21. Chin HH Turbine engine hot section prognostics, http://www.appliedconceptresearch.com/Turbine%20Engine%20Hot%20Section%20Prognostics.pdf
22. Kacprzynski GJ, Muench DS (2006) Sensor/model fusion for adaptive prognosis of structural corrosion damage. Technical report, Impact Technologies LLC, Rochester, USA
23. Manson G (2003) Experimental validation of a structural health monitoring methodology: Part III. Damage location on an aircraft wing. J Sound Vibr 259:365–385
24. Worden K, Manson G, Denœux T (2009) An evidence-based approach to damage location on an aircraft structure. Mechl Syst Signal Process 23:1792–1804
25. Bonissone P, Iyer N (2007) Soft computing applications to prognostics and health management (PHM): leveraging field data and domain knowledge. In: Sandoval F, Prieto A, Cabestany J, Graa M (eds) Computational and ambient intelligence. Lecture notes in computer science, vol 4507. Springer, Berlin, pp 928–939
26. Byington C, Watson M, Amin S, Begin M (2008) False alarm mitigation of vibration diagnostic systems. In: IEEE aerospace conference, pp 1–11
27. Schoeller MH, Roemer MJ, Leonard MS, Derriso M (2007) Embedded reasoning supporting aerospace IVHM. Technical report, Impact Technologies LLC, Rochester, USA
28. Volponi A (2005) Data fusion for enhanced aircraft engine prognostics and health management. Technical report, Pratt & Whitney, Connecticut, USA
29. Volponi AJ, Brotherton T, Luppold R (2004) Development of an information fusion system for engine diagnostics and health management. In: 1st intelligent systems technical conference, Chicago, USA
30. Amin S, Byington C, Watson M (2005) Fuzzy inference and fusion for health state diagnosis of hydraulic pumps and motors. In: Proceedings of the annual meeting of the North American fuzzy information processing society, pp 1–6
31. Yan W, Xue F (2008) Jet engine gas path fault diagnosis using dynamic fusion of multiple classifiers. In: IEEE international joint conference on neural networks, IEEE world congress on computational intelligence, China, Hong Kong, pp 1585–1591

32. Bonissone PP, Xue F, Subbu R (2011) Fast meta-models for local fusion of multiple predictive models. Appl Soft Comput 11:1529–1539
33. Byington CS, Watson M, Edwards D (2004) Data-driven neural network methodology to remaining life predictions for aircraft actuator components. In: 2004 IEEE aerospace conference proceedings, IEEE 2004, pp 3581–3589
34. Byington C, Watson M, Edward D, Dunkin B (2003) In-line health monitoring system for hydraulic pumps and motors. In: IEEE aerospace conference, New York, USA
35. Byington CS, Garga AK (2008) Data fusion for developing predictive diagnostics for electromechanical systems. Electrical engineering and applied signal processing series. In: Handbook of multisensor data fusion: theory and practice, 2 edn. CRC Press, Taylor and Francis Group, pp 1–32

Multiscale Image Segmentation via Exact Inference of Hidden Markov Tree

Yinhui Zhang, Zifen He, Jinhui Peng and Yunsheng Zhang

Abstract This paper addresses the problem of exact inference of probabilistic graphical models for multiscale segmentation of objects in the presence of dynamic backgrounds. Previous hidden Markov tree (HMT) based approaches have exploited the Expectation-Maximization (EM) algorithm to compute the optimal estimates of the multiscale parameters that maximize the likelihood function. However, the main problem with the EM algorithm is that it is a "*greedy*" method that converges to a local maxima on the log-likelihood surface. In this paper, we derive the Bethe free energy associated with the HMT which is a lower bound of cumulant energy function so as to recover multiscale posterior likelihoods exactly. This allows both inference and fusion of multiscale classification likelihoods to be computed through bottom-up likelihood estimation and up-bottom posterior inference of HMT. Experimental results on a frame of typical high-speed industrial inspection image demonstrate the correctness and robustness achieved by the proposed method.

1 Introduction

Image segmentation is a fundamental premise of many high-level computer vision applications such as object identification, stereo vision, and content-based image retrieval. However, robust segmentation of objects from dynamic backgrounds poses a challenging task, due to the presence of sensor noise, nonuniform illumination, shading, as well as background occlusions.

Multiscale segmentation provides an alternative perspective to address dynamic conditions across spatial locations, mainly due to the fact that the higher the scale,

Y. Zhang · Z. He (✉) · J. Peng · Y. Zhang
Kunming University of Science and Technology, Yunnan, China
e-mail: zyhhzf1998@163.com

F. Sun et al. (eds.), *Foundations and Practical Applications of Cognitive Systems and Information Processing*, Advances in Intelligent Systems and Computing 215,
DOI: 10.1007/978-3-642-37835-5_35,

the more reliable the feature information is. Crouse et al. [1] first proposed a multiscale modeling method in wavelet domain named hidden Markov tree (HMT) to achieve a concise modeling of the statistical dependencies and non-Gaussian statistics of real-world signals. The key advantage of this approach is that it is capable of performing communication both intra and inter scales; i.e., it allows the fusion of regional and boundary information by using robust higher scale classification likelihoods and accurate fine scale classification likelihoods, respectively.

For this reason, the HMT model has been further extended to aerial photo and document image segmentation by Choi et al. in [2]. Signolle [3] exploited HMT for texture segmentation of very large images. However, the parameters of HMT models in [2, 3] need supervised training by single textures. To overcome the limitations of supervised segmentation, Ye et al. [4] extended HMT to unsupervised segmentation and adjusted to SAR image segmentation.

Although the previous image segmentation approaches based on HMT multiscale fusion are successful to some extent, there are still some open problems. Generally, most of the HMT-based methods have exploited the Expectation-Maximization (EM) algorithm to compute the optimal estimates of the multiscale parameters that maximize the likelihood function. However, the main problem with the EM algorithm is that it is a "*greedy*" method that converges to a local maxima on the log-likelihood surface [5]. While simple each iteration of the EM algorithm is $\mathcal{O}(N)$, it is guaranteed to convergence only to a local maximum of log likelihood.

In addition, previous works for HMT-based segmentation always consist of two stages: raw segmentation by likelihood estimation through expectation maximization (EM) and multiscale fusion by EM [2, 4], Majority vote [3], maximum a posteriori (MAP) [6] to obtain reliable final segmentation. In practice, the convergence of the two-stage EM-based HMT segmentation algorithm can be relatively slow for the reason that there is nothing to limit the number of iterations it takes to converge. To overcome this, Romberg et al. [7] introduced a universal HMT (uHMT) with nine fixed parameters. This model needs not any kind of training. The demerit of uHMT is that the meta-parameters should be fixed with specific, such as photograph-like images.

Several more recent works describe how to fit different classes of HMTs under various conditions [8–10]. For instance, Zhang et al. [11] recast HMT-based image segmentation as a convex optimization problem by defining a multiscale energy function which is convex in terms of marginal distributions and overcome the local minimum associated with multiscale objective.

The main contribution of this work is that we derive the Bethe free energy associated with the HMT which is a lower bound of cumulant energy function so as to recover multiscale posterior likelihoods exactly. This allows both inference and fusion of multiscale classification likelihoods to be computed through bottom-up likelihood estimation and up-bottom posterior inference of HMT.

The paper is organized as follows: Section 2 gives the HMT representation for 2D images; Sect. 3 gives the exact inference strategy of HMT; Experiments and result analysis form Sect. 4; Finally, Sect. 5 concludes the paper.

2 HMT Representation for 2D Images

The statistical image classification frameworks regard the different regions in an image as a random realization from a family of distributions. Since the wavelet transform can represent an image at multiresolutions, thus it provides powerful insight into the spatial and frequency characteristics of the original image. Moreover, each wavelet coefficient can also be regarded as a realization of its class label in wavelet domain. The HMT method proposed in [2] is a well-known wavelets distribution modeling framework. In this framework, the intrascale clustering and interscale persistency properties are modeled by a two-state Gaussian mixture model and a tree-structured probabilistic graph, respectively.

2.1 Discrete Wavelet Transform

Wavelet decomposition provides a sparse and approximately decorrelated representation of images at multiple scales. Using the wavelet transformation scheme, multiple directional and multiscale features can be detected while intra and interscale statistical distributions are naturally established.

Harr wavelet is employed in this paper to perform discrete wavelet transform of the original images. The standard way to obtain 2D wavelet decomposition is to use the tensor product of 1D Haar filters (low-pass: $g = 1/\sqrt{2}[1\ 1]$ and high pass: $h = 1/\sqrt{2}[-1\ 1]$) repeatedly along vertical and horizontal directions of the image F. The outputs are subsampled by a factor of two and consist of three high-pass subbands HL, LH, HH and one low-pass subband LL, corresponding to the four filters $h^T * g$, $g^T * h$, $h^T * h$, $g^T * g$, respectively.

The result of tensor product is represented by the vertical, horizontal, and diagonal wavelet coefficients, respectively. Let $\mathbf{w} = \{w_{h,l}(i)\}$ be the collection of wavelet coefficients at a range of L scales, where $h \in \{HL, LH, HH\}$ is the directional components and $l \in \{1, \ldots, L\}$ denotes the scale.

Most of image energy compacted onto a few wavelet coefficients with large magnitudes, while most of the wavelet coefficients are very small. This compact property allows us to capture the key characteristics of an image from a few large wavelet coefficients. This is very useful in high-level computer vision applications, such as natural image understanding and robot's autonomous navigation. We then employ Gaussian mixture model and hidden Markov tree model to characterize the intrascale clustering and interscale persistence properties of the detail coefficients, respectively.

Figure 1 shows the probabilistic graphical models that are built directly over the original image grid and wavelet domain. In particular, each node of the graphical model over the original grid corresponds to a image pixel, whereas those nodes of the latter models correspond to wavelet coefficients. In addition, note that the original graphical model consists of several circles, while the wavelet domain

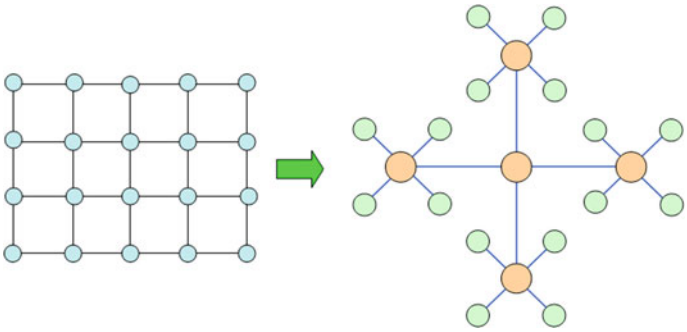

Fig. 1 Probabilistic graphical models that are built directly on the image grid (*left*) and on wavelet coefficients (*right*)

graphical model is tree structured. The key difference between the two graphical models will later lead to an exact inference of the posterior marginal.

2.2 HMT Representation of Wavelet Coefficients

The key idea behind of synchronous inference of HMT is that we view the pixels as the nodes at scale 0 of HMT $\mathcal{T} = (\mathcal{V}, \mathcal{E})$. In this way, the hidden Markov tree $\mathcal{T}$ is an acyclic directed graph and as such it consists of $|\mathcal{V}|$ of nodes and a set of $|\mathcal{E}|$ directed edges, each edge goes from a parent node to a child node. Each node $i \in \mathcal{V}$ takes values from the space of $\mathcal{X}$. Thus, the joint distribution over HMT can be naturally factorized as

$$\begin{aligned} P(\mathcal{T}, \mathcal{X}) = \prod_{i \in \mathcal{V}} p(x_i) \times & \left(\prod_{i \in \mathcal{V}, j \in \mathcal{N}(i)} p(x_i | x_j) \right) \\ & \times \left(\prod_{i \in \mathcal{V}, \text{scale(i)} \in \{1, \ldots, \text{L}\}} p(w_i | x_i) \right) \\ & \times \left(\prod_{i \in \mathcal{V}, \text{scale(i)} = 0} p(f_i | x_i) \right), \end{aligned} \tag{1}$$

where $\text{scale}(i)$ denotes the scale in which node i resides. Note that the Markovian dependencies of hidden states are realized by the following conditions. Given the parent state, the child state is conditionally independent of all other states. Given the hidden state of a node, the corresponding label is conditionally independent of all other variables in the tree. In this sense, the goal of multiscale segmentation is to inference the posterior $p(x_i|O)$ from a joint observation set $O = W \cup F$.

2.3 Modeling of Marginal and Interscale Distribution

Singular marginal distribution To capture intrascale distribution properties, we associate a hidden stochastic state variable x_i to each wavelet coefficient w_i. For single object identification problems, x_i takes two values: either object ($x_i = 1$) or background ($x_i = 0$). Since most of the wavelet coefficients have small values while only a few wavelet coefficients have large values, thus the probability density function (pdf) $p(w_i)$ of each wavelet coefficient is well approximated by a two-density Gaussian mixture model

$$p(w_i) = \sum_{m=0}^{1} p(w_i|x_i = m)p(x_i = m). \tag{2}$$

More specifically, $p(w_i|x_i = m)$ follows zero-mean Gaussian distribution, i.e.,

$$p(w_i|x_i = m) = \frac{1}{\sqrt{2\pi\sigma^2_{i,x_i=m}}} \exp\left(\frac{-w_i^2}{2\sigma^2_{i,x_i=m}}\right) \tag{3}$$

where $\sigma^2_{i,x_i=m}$ is the variance at node i when its state is m, $m \in \{0, 1\}$. This means that, to each coefficient w_i, we associate a hidden state x_i which takes on two values (0 or 1) with probability mass function(pmf) $p(x_i = m)$. Upon the assumption that the wavelet coefficients are mutually independent, the joint probability density function of the wavelet coefficients is given by

$$p(W) = \prod_i p(w_i) \tag{4}$$

where W is a matrix containing the detail coefficients of LH, HL, and HH subband.

Pairwise interscale dependencies Based on the observation that wavelet coefficients tend to retain in the same state across scales, we employ the HMT model for the purpose of capturing interscale persistence properties in wavelet domain. Recall that the HMT we constructed consists of $L + 1$ scales ranging from $j = 0$ to $j = L$. In particular, the nodes in the tree represent wavelet coefficients w_i of each node i for all scale$(i) \in \{1, \ldots, L\}$, whereas the node f_i denotes the observed pixel values at the finest scale, i.e., scale$(i) = 0$. In addition, note that each node at scale l corresponds to four children nodes at scale $l - 1$.

In the HMT model, we use the probability mass function

$$p(x_i = m) = \begin{bmatrix} p(x_i = 0) \\ p(x_i = 1) \end{bmatrix}$$

of node i to denote the distribution of hidden states, where $m \in \{0, 1\}$. The state transition probability $\epsilon_i^{\mathcal{P}(i)}$ is defined to represent the probability for w_i to be small(or large) when its parent $w_{\mathcal{P}(i)}$ is small(or large). Since a wavelet coefficient

has four children, thus $\epsilon_i^{p(i)}$ is a 2×2 probability matrix representing state transition probability from $w_{\mathcal{P}(i)}$ to its four children

$$\epsilon_i^{\mathcal{P}(i)} = \begin{bmatrix} \epsilon(x_i = 0|x_{\mathcal{P}(i)} = 0) & \epsilon(x_i = 0|x_{\mathcal{P}(i)} = 1) \\ \epsilon(x_i = 1|x_{\mathcal{P}(i)} = 0) & \epsilon(x_i = 1|x_{\mathcal{P}(i)} = 1) \end{bmatrix}.$$

For the single object identification problem, the column sums of state transition probability matrix are equal to 1.

With the two models discussed so far, the HMT model is defined by a parameter set

$$\Theta = \left\{ p_l(x_i = m), \epsilon_i^{\mathcal{P}(i)}, \sigma_i^2 | m \in \{0, 1\}, l \in \{0, \ldots, L\} \right\} \tag{5}$$

for each *LH*, *HL* and *HH* subband. Where $p_l(x_i = m)$ denotes the probability mass function $p(x_i = m)$ of node i at the $L + 1$ scales $l \in \{0, \ldots, L\}$.

3 Two-Pass Synchronous Inference of HMT

The inference of HMT uses a two-pass inference modified from the one given in [12]. We have modified the algorithm, so that it retains the prior of unary potentials and allows synchronous fusion of them. The upward sweep for likelihood estimation is first described. Description of the downward sweep for posterior inference then follows.

3.1 Upward Likelihood Estimation

Given the hidden state of node i we can factorize the likelihood of subtree $\mathcal{T}(i)$ by exploiting the structure of HMT as

$$\alpha(\mathbf{o}_i|x_i) = \alpha(o_i|x_i) \prod_{j \in \mathcal{C}(i)} \alpha(\mathbf{o}_j|x_i), \tag{6}$$

where $\mathcal{C}(i)$ denotes the children of node i. By making the assumption of conditional independence that when the hidden state x_j is known, then no knowledge from x_i will alter the probability of $\mathbf{o}_j$, we can decompose the conditional likelihood of $\mathbf{o}_j$ in Eq. (6) into

$$\alpha(\mathbf{o}_j|x_i) = \sum_{x_j} \alpha(\mathbf{o}_j|x_j)\alpha(x_j|x_i). \tag{7}$$

By substituting (7) into (6), we obtain the subtree likelihood expression at higher scale in terms of those at the lower scale. In particular, the likelihood of subtree

$\mathcal{T}(i)$ can be viewed as the unary potential of node i multiplies all incoming subtree likelihoods from its children weighted by their parent–child state transition probabilities. This children-parent likelihood passing process proceeds up the tree, culminating at the root node.

3.2 Downward Posterior Inference

Once the likelihood of HMT has been learned through upward sweep, we can use Bayes' rule to derive posterior inference of HMT through downward sweep. Given the complement of the observation of subtree $\mathcal{T}(i)$, the posterior of node i is given as

$$\beta(x_i|\mathbf{o}_i^c) \propto \beta(\mathbf{o}_i^c|x_i)\beta(x_i). \tag{8}$$

Again, by making the assumption of conditional independence that when the hidden state $x_{\mathcal{P}(i)}$ is known, then no knowledge from x_i will alter the probability of $\mathbf{o}_i^c$, the likelihood term in Eq. (4) can be decomposed as

$$\beta(\mathbf{o}_i^c|x_i) = \sum_{x_{\mathcal{P}(i)}} \beta(\mathbf{o}_i^c|x_{\mathcal{P}(i)})\beta(x_{\mathcal{P}(i)}|x_i). \tag{9}$$

Substituting Eq. (5) into Eq. (8) and again using Bayes' rule

$$\beta(x_i|\mathbf{o}_i^c) \propto \sum_{x_{\mathcal{P}(i)}} \beta(\mathbf{o}_i^c|x_{\mathcal{P}(i)})\beta(x_i|x_{\mathcal{P}(i)})\beta(x_{\mathcal{P}(i)}). \tag{10}$$

Using HMT structure decomposition of $\mathbf{o}_i^c$

$$\begin{aligned}\beta(\mathbf{o}_i^c|x_{\mathcal{P}(i)}) = \beta(o_{\mathcal{P}(i)}|x_{\mathcal{P}(i)})\beta(\mathbf{o}_{\mathcal{P}(i)}^c|x_{\mathcal{P}(i)}) \\ \prod_{j\in\mathcal{B}(i)} \beta(o_j|x_{\mathcal{P}(i)}),\end{aligned} \tag{11}$$

where $\mathcal{B}(i)$ denotes the three brothers of node i, i.e., $\mathcal{B}(i) = \mathcal{C}(\mathcal{P}(i)) \setminus i$. Substituting Eq. (9) into Eq. (8) and using Bayes' rule again,

$$\begin{aligned}\beta(x_i|\mathbf{o}_\mathbf{i}^\mathbf{c}) = \frac{1}{Z}\sum_{x_{\mathcal{P}(i)}}[\beta(o_{\mathcal{P}(i)}|x_{\mathcal{P}(i)})\beta(x_{\mathcal{P}(i)}|\mathbf{o}^\mathbf{c}{}_{\mathcal{P}(i)}) \\ \prod_{j\in\mathcal{B}(i)} \beta(o_j|x_{\mathcal{P}(i)})\beta(x_i|x_{\mathcal{P}(i)})],\end{aligned} \tag{12}$$

where Z is a normalizing constant. In this way, the posterior of node i can be iteratively inference from that of its parent, by multiplying all unary potentials of its three brothers as well as that of its parent weighted by state transition probability. This parent–child likelihood passing process proceeds down the tree, terminating at the leaf nodes of HMT.

The main advantage of the inference algorithm is that it performs synchronous fusion of all scales of HMT model by using only twice the computation of upward and downward pass in the same tree.

3.3 Exact Inference on HMT

Fixed points of the bottom-up and up-bottom inference of HMT correspond to fixed points of the Bethe free energy [13]:

$$\mathcal{F}_{\text{Bethe}}(\beta) = \sum_{i \in \mathcal{V}} H(\beta(x_i)) - \sum_{(i,\mathcal{P}(i)) \in \mathcal{E}} I\big(\beta(x_i|x_{\mathcal{P}(i)})\big), \tag{13}$$

where $H(\beta(x_i))$ denotes the singleton entropy of the marginal distribution of node i and $I(\beta(x_i|x_{\mathcal{P}(i)}))$ denotes the mutual information of the pairwise distributions between a pair of neighboring nodes i and its parent $\mathcal{P}(i)$.

The pseudomarginal probabilities β should satisfy the following three constrains. The unary marginal probabilities should be nonnegative, i.e., $\beta(x_i) \geq 0$. β should satisfy the normalization constraints, $\sum_{x_i} \beta(x_i) = 1$ for all $i \in \mathcal{V}$. For two connected nodes, the single marginal must be consistent with the joint marginal, also known as weak tree consistency constraints, formalized as $\sum_{x_j} \beta(x_i|x_j) = \beta(x_i)$.

One of the most interesting property lies in the fact that the fixed point β^* is guaranteed to be the unique solution of the bottom-up and up-bottom synchronous inference algorithm. In addition, the elements of the fixed points correspond to the exact singleton and pairwise marginal distributions of the hidden Markov tree. In particular, consider a pairwise Markov random field with binary variables, the cumulant function value could be decomposed according to the loop series expansion:

$$\mathcal{F}(\beta) = \mathcal{F}_{\text{Beth}}(\beta) + \log(1 + \Delta), \tag{14}$$

where Δ represents the loop series expansion terms of the graph

$$\Delta = \sum_{\tilde{E} \subseteq E} \gamma_{\tilde{E}} \prod_{i \in \mathcal{V}} \mathbf{E}_{\alpha_i} (x_i - \alpha_i)^{d_i(\tilde{E})} \tag{15}$$

where $\gamma_{\tilde{E}}$ denotes the subgraph weight which is the product of all edge weights in this subgraph $\tilde{E}$. In addition, $d_i(\tilde{E})$ denotes the degree of node i in a generalized loop of the graph. Consequently, for any $\tilde{E} \subseteq \mathcal{T}$ such that $d_i(\tilde{E}) = 1$ for at least one $i \in \mathcal{V}$, then the associated term in the expansion vanishes. We refer the reader to the paper of Sudderth et al. [14] for a thorough treatment. Since our tree-structured graphs do not contain any nontrivial generalized loops, which provide a proof of the exactness of the Bethe approximation for HMT model.

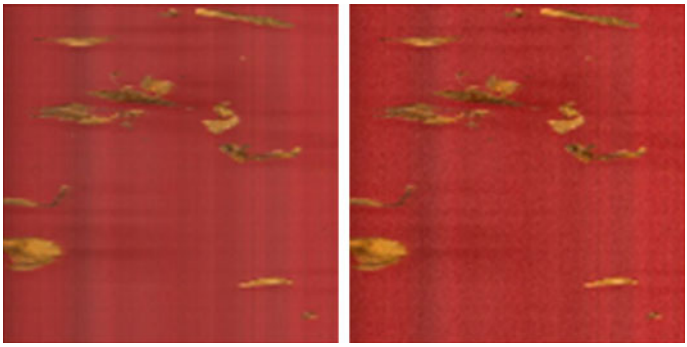

Fig. 2 Original image (*left*) captured by SPYDER 3 CCD imaging sensor and the noisy image (*right*) corrupted by white noise

4 Experiment and Result Analysis

To validate the performance of our method, we choose to use a sequence of industrial inspection images, which are captured by a high-speed line-scan CCD camera equipped on a tobacco packaging machine. The size of each frame is 1024×1024. Due to the computationally intensive nature, we have carried out the evaluation on images that have been down sampled by a factor of 8 from its original size. The input image has a size of 128×128 pixels. One frame of the original images is shown in Fig. 2. We used a personal computer with CPU 2.67 GHz and 3 G memory to perform the testing. The programs are written in Matlab 7.10.

In the following experiments, the model parameter σ_i^2 is initialized by setting $\sigma_i^2 = 3$ for all $i \in \mathcal{T}$ to characterize singular marginal distributions. We assign $p(x_i) = [0.5 \quad 0.5]^T$ to each of the probability mass function of the HMT model, which is an unbiased initialization for total nodes within the hidden Markov tree. In addition, the 2×2 probability matrix that representing state transition probability from $w_{\mathcal{P}(i)}$ to its four children is initialized as

$$\epsilon_i^{\mathcal{P}(i)} = \begin{bmatrix} 0.8 & 0.2 \\ 0.2 & 0.8 \end{bmatrix}.$$

Initializing the state transition matrix in this way, the interscale consistency constraints across the hidden Markov trees are moderately imposed on each of the edges $(i,j) \in \mathcal{E}$.

To evaluate the robustness of the proposed multiscale segmentation method in the presence of dynamic backgrounds, original image corrupted by Gaussian white noise has been considered. An example is provided at the right of Fig. 1, where the noisy image has been obtained by corrupting each RGB channel with Gaussian

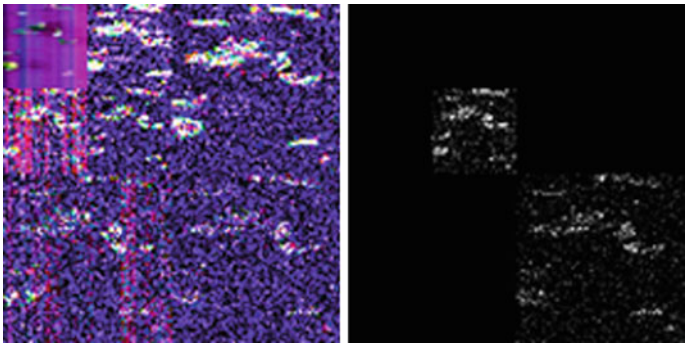

Fig. 3 Wavelet coefficients (*left*) of the noisy image and the features (right) under subband and color independence assumption

noise (standard deviation $\sigma = 0.01$). We use Peak Signal to Noise Ratio (PSNR) as the distortion metric. The PSNR between the original and noisy image is 34.76 dB.

After Haar wavelet decomposition, the noisy image is decomposed into a 2-scale, 3-orientation pyramid representation which is shown at the left of Fig. 2. We observe that the wavelet coefficients have been contaminated by noise, which would make the segmentation less reliable. Under the assumption of subband and color independence, corresponding wavelet coefficients residing at three subbands and three color channels are multiplied by each other and normalized to [0 1].

The multiplication result under subband and color independence assumption is shown at the right of Fig. 2. We find that the multiscale features at scales 1 and 2 are more robust against background noise than the original wavelet coefficients. We assign unary prior potentials of each node at scales 1 and 2 as the normalized magnitude of the wavelet coefficients.

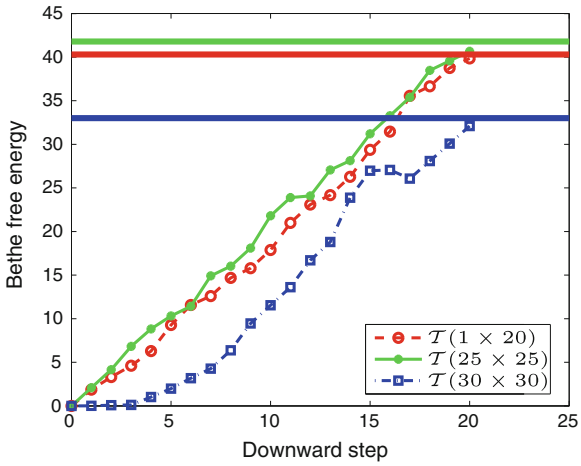

Fig. 4 Bethe free energy versus number of downward steps during posterior inference of HMT

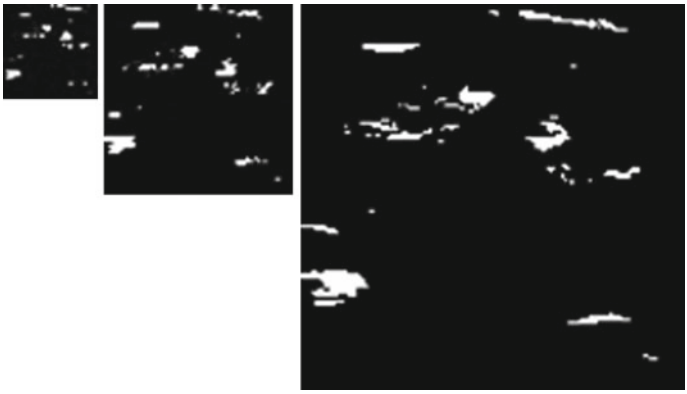

Fig. 5 Segmentation result of the proposed method at scales 2, 1, and 0 (from *left to right*)

At the pixel resolution scale, we compute the mean color vector of foreground and background by K-means algorithm in RGB color space. The cluster centers of foreground and background are, respectively, $[172.74 \quad 106.91 \quad 55.28]^T$ and $[161.68 \quad 55.78 \quad 51.80]^T$. The unary prior potentials at scale 0 are assigned with the Euclidean distance between the color vectors of each pixel to each corresponding cluster centers.

Each node of the HMT at scale 2 corresponds to a subtree $\mathcal{T}(i)$ with 21 nodes and 20 edges. At upward sweep through HMT, the likelihood of the nodes in a subtree is estimated. Then the posterior of each node is calculated by a downward sweep through HMT. Figure 3 shows the Bethe free energy of subtrees $\mathcal{T}(1 \times 20)$, $\mathcal{T}(25 \times 25)$ and $\mathcal{T}(30 \times 30)$ as a function of the number of downward steps during posterior inference. We find the free energy of the three subtrees increase approximately linearly with the number of downward step. Most importantly, the Bethe free energies of the three HMTs finally arrived at the exact boundary value after $|\mathcal{E}| = 20$ iterations of up-bottom posterior inference updates.

After two sweeps through HMT, the segmentation results at three scales are shown in Fig. 4. The performance is over 95 % in terms of segmentation accuracy at the finest scale, whereas the segmentation accuracy by using HMT seg [2] achieves about 91 %. The inference time of each subtree is 0.01 s, since there are 32×32 nodes in scale 2, the total segmentation time is about 10 s (Fig. 5).

5 Conclusion

In this paper, we extend the HMT-based multiscale segmentation algorithm to exact inference and adapted it to the application of industrial image segmentation in the presence of dynamic backgrounds. We derive the Bethe free energy associated with the HMT which is a lower bound of cumulant energy function so as to

recover multiscale posterior likelihoods exactly. This allows both inference and fusion of multiscale classification likelihoods to be computed through bottom-up likelihood estimation and up-bottom posterior inference of HMT. Multiscale segmentation experimental results on a frame of typical high-speed industrial inspection image demonstrate the correctness and robustness achieved by the proposed method to a wide range of scales of the dynamic background image in the presence of stochastic Gaussian white noise. Our future work will focus on improving the speed of the two-pass synchronous inference of HMT.

Acknowledgments This work was supported by the National Science Foundation of China (NSFC) under Grant 60962007 and by the KMUST under Grant 2011-02. In addition, this work was supported by Major Program of National Natural Science Foundation of China (No. 51090385), International S&T Cooperation Program of China (No. 2012DFA70570) as well as Yunnan Provincial International Cooperative Program (No. 2011IA004).

References

1. Crouse MS, Nowak RD, Baraniuk RG (1998) Wavelet-based statistical signal processing using hidden Markov models. IEEE Trans Signal Process 46:886–902
2. Choi H, Baraniuk RG (2001) Multiscale image segmentation using wavelet-domain hidden Markov models. IEEE Trans Image Process 10:1309–1321
3. Signolle N, Revenu M, Plancoulaine B, Herlin P (2010) Wavelet-based multiscale texture segmentation: Application to stromal compartment characterization on virtual slides. Signal Process 90:2412–2422
4. Ye Z, Lu CC (2002) Wavelet-based unsupervised SAR image segmentation using hidden Markov tree models. In: Proceedings of international conference on pattern recognition. IEEE Press, pp 729–732
5. Reddy CK, Chiang HD, Rajaratnam B (2008) TRUST-TECH-based expectation maximization for learning finite mixture models. IEEE Trans Pattern Anal and Mach Intell 30:1146–1157
6. Chang S, Carin L (2006) A modified SPIHT algorithm for image coding with a joint MSE and classification distortion measure. IEEE Trans Image Process 15:713–725
7. Romberg JK, Choi H, Baraniuk RG (2001) Bayesian tree-structured image modeling using wavelet-domain hidden Markov models. IEEE Trans Image Process 10:1056–1068
8. Kivinen J, Sudderth E, Jordan M (2007) Learning multiscale representations of natural scenes using Dirichlet processes. In: Proceedings of international conference on computer vision, pp 1–8
9. Spence C, Parra L, Sajda P (2006) Varying complexity in tree-structured image distribution models. IEEE Trans Image Process 15:319–330
10. Milone D, Persia L, Torres M (2010) Denoising and recotnition using hidden Markov models with observation distributions modeled by hidden Markov trees. Pattern Recogn 43:1577–1589
11. Zhang Y, He Z, Zhang Y, Wu X (2011) Global optimization of wavelet-domain hidden Markov tree for image segmentation. Pattern Recogn 44:2811–2818
12. Wainwright M (2002) Stochastic process on graphs with cycles: geometric and variational approaches. PhD Dissertation, MIT
13. Minka T (2001) The EP energy function and minimization schemes. MIT: Media Lab Technical Report
14. Sudderth EB, Wainwright MJ, Willsky AS (2004) Embedded trees: estimation of Gaussian processes on graphs with cycles. IEEE Trans Signal Process 52:3136–3150

Cognitive Emotion Research of Humanoid Expression Robot

Jizheng Yan, Zhiliang Wang and Siyi Zheng

Abstract Humanoid expression robot is a rising hot spot in the field of Artificial Intelligence (AI), and is very important to the human–computer harmonious interaction. People never stop the humanoid research of robots, which is the trend of the future. This paper wants to discuss three issues. First, can robot have cognitive emotion and show us? Second, how computer or analogous machines simulate complex emotions of human? Can the current emotion theory support and guide the development of cognitive robot? Third, combined with the current techniques and cognitive theory basis, how to design and build humanoid expression robot? Finally, the authors analyze the cognitive basis of emotion theory, and give the robot model and emotion model of cognitive expression.

Keywords Humanoid expression robot · Cognitive emotion · AI

J. Yan (✉)
School of Automation and Electrical Engineering,
University of Science and Technology Beijing, Beijing,
People's Republic of China
e-mail: happynanhu@163.com

Z. Wang
School of Computer and Communication Engineering,
University of Science and Technology Beijing,
Beijing, People's Republic of China
e-mail: wzl@ustb.edu.cn

S. Zheng
Beijing Command College of Chinese People's Armed Police Force, Beijing,
People's Republic of China
e-mail: sisizheng@163.com

F. Sun et al. (eds.), *Foundations and Practical Applications of Cognitive Systems and Information Processing*, Advances in Intelligent Systems and Computing 215,
DOI: 10.1007/978-3-642-37835-5_36,

1 Introduction

With the rapid development of modern science and technology, human civilization gradually enters the stage of knowledge-based economy from physical labor, the robots play an increasingly important role in our life and work, assist and even replace the human work in more and more fields [1]. Traditional robots are mostly concentrated task-specific, and also have achieved great success in the execution of specific tasks, but with the expanding fields of robotic applications, robots need to work in complex unknown and dynamic environment, many shortcomings are also beginning to show, for example, they are task specific, just for the good performance of one task, and cannot develop new capabilities to adapt new environments and even cannot solve the problems, thus we need robots with humanoid intelligence [2]. For humans, robots are not just production tools, no longer dead machines, but friends to assist person's work, study, and life [3, 4].

Many laboratories in the world began to study in this field of humanoid expression robot [5–7], such as Klaus Scherer's emotional research laboratory, which is in the University of Geneva. D. Canamero in Free University of Brussels has his emotional robot research team and A. Sloman in University of Birmingham is a leader of Cognition and Affect Project. In China research in this area began in the 1990, and most of the research work is about the theory and technology of artificial emotion unit, such as multi-functional perceptron, including facial expression recognition, face recognition, face detection and tracking, sign language recognition, face synthesis, lip reading of the robot control architecture based on artificial emotion. Pro. Hegao Cai in Chinese Academy of Engineering developed a humanoid speech robot in 1996, this robot head with eye movement, the mouth speech driven facial muscles function. The humanoid Avatar Robot Research Center of Harbin Institute of Technology for the first time in 2004, successfully develop robot H & F ROBOT-I of eight basic facial expressions (including a natural expression, serious, happy, smiling, sadness, surprise, fear, anger).

2 Robot Cognitive Basis

Cognitive science is a new research category of the world's scientific landmark in the twentieth century, study human perception and thinking process, including from the sensory input to the complex problem solving, the individual human being to the intelligence activities of human society, as well as the nature of human intelligence and machine intelligence, is the result of the interdisciplinary development of modern psychology, information science, neuroscience, mathematics, anthropology, and even natural philosophy, and is an inter-discipline studying the mysteries of human mind.

Environment provides people with a lot of stimulation, some are very important to people, some are not important, some are meaningless. To normal work, study

and life, people must select the important information, and exclude the interferences of irrelevant stimulus. Cognitive science take the human cognitive system as an information processing system, and this system is based on physiological mechanism, guided by the psychological mechanism, coupled with human-specific social attributes, which constitutes the human cognition. As shown in Fig. 1.

The physiological mechanisms of human cognition have three main parts, including neurons, nervous system, and brain. Neurons, also known as nerve tissue, is to constitute the basic unit of structure and function in the nervous system, with long protrusions cells, constituted by the cell body and cell processes. The cell body is located in the brain, spinal cord, and ganglion, cell processes, which is divided into dendrites and axons, can be extended to the body organs and tissues. Each neuron can have one or more dendrites, accept stimulation and send to cell body. Each neuron has only one axon can be excited from the cell body sent to another neuron or other organizations, such as muscles or glands. The nervous system is playing a leading role in the body system,and is divided into two parts of the central nervous system and peripheral nervous system. The structure and function of human body are under the control of the nervous system directly or indirectly, regulate and influence each other, closely coordinate to achieve and maintain normal life activities. Brain embrace the telencephalon and diencephalon, telencephalon comprise the left and right cerebral hemispheres, which is the main part of the higher nervous system of the vertebrate brain, and control movement, sensory and senior nerve center of higher brain function.

The psychological mechanism of human cognition is divided into four main parts, including attention, perception, memory and thinking. Thought attention was the concentration of mental effort on sensory events or psychological event, but believed attention was defined as the currently active node. Cognitive science deems that attention is the starting point of human cognition, and short of attention,there are difficult to achieve the input of information, coding, storage, and extraction. According to the breadth, stability, distribution, and transfer characteristics, attention can be divided into three kinds, selective, distributive, and sustained attention. Selective attention was to choose one in the simultaneous presentation of two or more to stimulate the individual, while ignoring the other's attention. Distributive attention was that at the same time two or more stimulation in the individual, attention will be assigned to different activities, which is an important condition for completion of complex tasks. Sustained attention was that

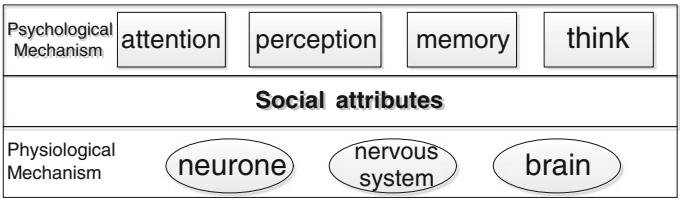

Fig. 1 The basis of human cognition

in a certain period of time to maintain the stability of an understanding of the object or activity, vigilance is a special form of sustained attention.

Compared with other animals, the fundamental difference is that people always live and work in a certain social relationship. Marx said: "the nature of human is not inherent in the single individual abstraction, reality it is the sum of all social relations." People is concrete, living in real life, they inevitably occur in a variety of relationships, such as production relations, sexual relationships, kinship, relationship between colleagues. People living in the real world, must be living in a certain social relations. This complex social relations determine the nature of social property, social attributes is a focus of cognitive science research, also a major difficulty.

Humanoid expression robot is to use artificial methods and techniques to imitate, extend, and expand human emotion, so that robot has the ability to distinguish, understand, and express emotion. It requires the following special ability to have emotional intelligence features, learning knowledge, using knowledge, and computing knowledge. Emotional robot research can be divided into two categories, one is the physical emotional robot, and another is the virtual emotional robot. The direction of the theory and technology of these two studies complement each other, together promote the development of emotional robot.

3 Emotion Theory

3.1 Affective Computing

Numerical methods for signal acquisition, transformation, processing, valuation, and recognition, belong to the areas of logical computing [8]. Typically, we use computers to process digital signal, then have rational thinking, and logical reasoning, just like brain. Emotional information processing is on the basis of the theory of artificial intelligence to mimic human emotions, moods, and feelings; like heart, in order to achieve a harmonious human–computer interaction, the study of emotional information processing is very important.

In the academia, Picard from the MIT Media Lab earlier began to study emotion systematically [9]. In 1997, Picard published "Affective Computing", thought the so-called affective computing was trying to give computer the ability to observe, understand, and generate emotional features like human. Affective computing is an attempt to create a computing system, which can perceive, identify, and understand human emotions, and make intelligent, sensitive, friendly response to human.

3.2 Kasnei Engineer

Japanese researchers have proposed the concept of Kansei Engineering, think person's feelings, and perception have two-sided and double constructive. Heretofore, in pattern recognition, we can resolve feeling, perceive agencies, and make information model, and build the engineering information processing system on the opinion of the "known", but feeling and perception have another important function and features—that is "sensitive", which is from the point of view of the "feeling" to look at the feeling, perception agencies.

Kansei engineering is to combine perceptual and engineering technology, on the basis of inductive science, through the analysis of human sensibility, add person's need to the product design. Kansei engineering can bring people happiness and comfortable, and also known as "happy and comfortable" science, production of goods based on Kansei engineering technology called "emotional goods".

3.3 Artificial Psychology

China's understanding of emotional information processing is also gradually improving and Professor Wang Zhiliang from University of Science and Technology Beijing, in 1999, first proposed the concept of artificial psychology. Artificial Psychology use information science and artificial machine (computer, model algorithms, etc.) to achieve a more comprehensive content of human mental activity (emphasis is human emotion, will, character, create) again, on the basis of artificial intelligence, combined with new theories and methods of psychology, brain science, neuroscience, information science, computer science, automation, and scientific to accomplish a comprehensive manual machine simulation of human mental activity (especially emotion, will, character, and create).

4 Design Humanoid Expression Robot

The most notable feature of Humanoid expression robot is to interact with the human naturally, understand human, and at the same time, be able to face feedback. This anthropomorphic interaction can increase comfort and satisfaction of the users, and further promote the using range of robots. The Hardware of Humanoid expression robot is based on the design of the humanoid head, by studying the anatomy of the human head bone structure, design humanoid head similar to person, and operation require the support of the six areas, such as facial action coding system, robot vision [10] (Fig. 2).

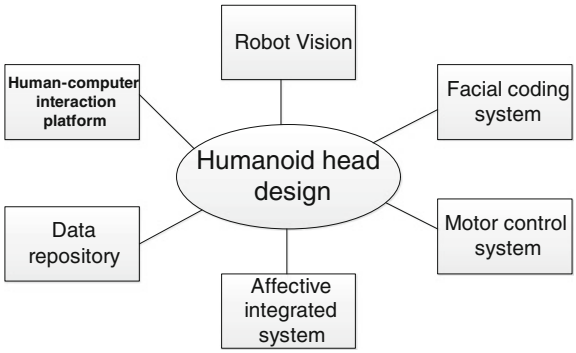

Fig. 2 Design structure of robot

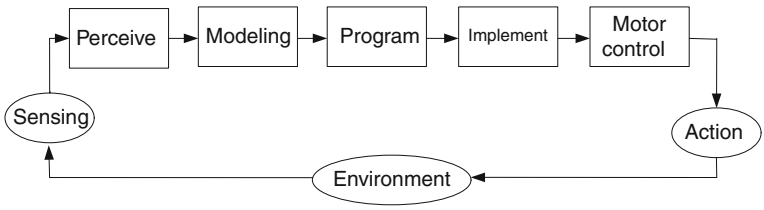

Fig. 3 Information processing of robot

The system of humanoid expression robot is based on affective computing, cognitive theory, multi-channel, and multimode states of human–computer interaction and cooperation, first, sensors and other devices perceive environmental information, perception process information, and extract feature, through modeling emotion, emotional processing system make decision, output corresponding feedback emotional, and plan expression and action, the motor control units execute the command, generate actions response to the environment, and finally it forms a complete feedback chain (Fig. 3).

4.1 Humanoid Head Design

A robot with humanoid expression needs to be able to carry out a series of facial expression and body language, and the shows of facial expression make the human–computer interaction more direct and expeditious, so the head design of humanoid expression robot is a key part [11]. Robots obtain and analyze information, make comprehensive decisions, finally realize their inner emotional states through the head expression, such as showing a smile, upset, happy, or scared expression. As shown in Figs. 4 and 5, though taking advantages of the electronic and mechanical technology more harmony and unity, finally people can make the natural flow of emotional communication with robots.

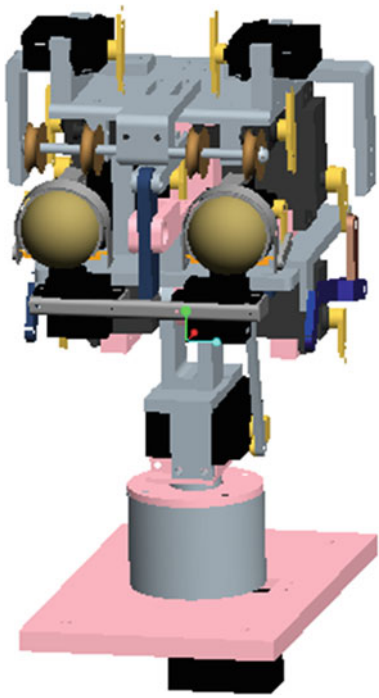

Fig. 4 Three-dimensional structure

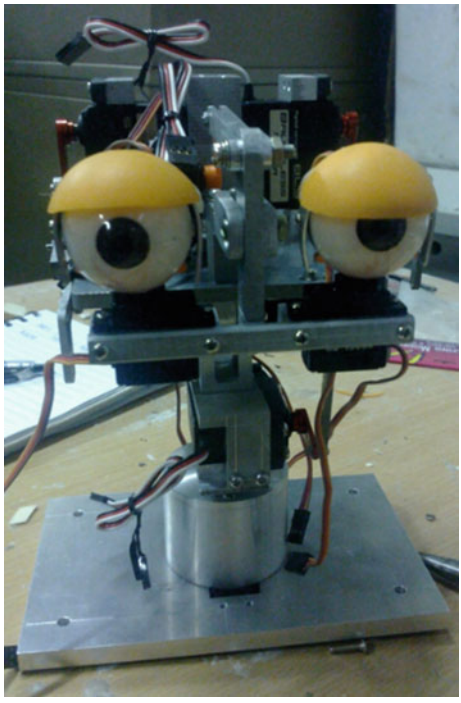

Fig. 5 Mechanical structure

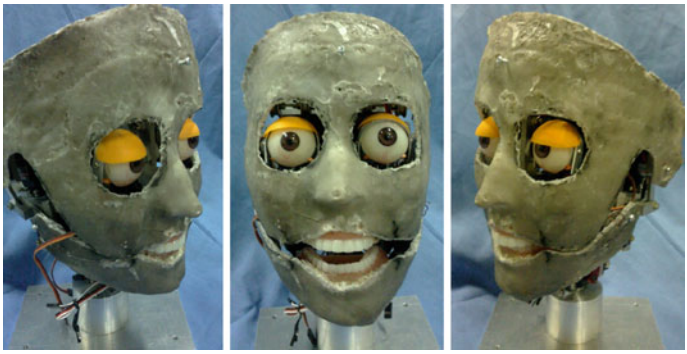

Fig. 6 Shell structure

Fig. 7 Forming structure

4.2 Facial Coding System

When the head expression of the robot was designed, it needs suitable theory to support its expression of what to do under different circumstances. Such as we know a person's face in the normal state, and through each other's facial expressions, we can understand each other just like reading an open book. American psychology Professor Paul Ekman study their movements and gestures in two mutually isolated primitive tribes, and release Facial Action Coding System. He found 43 kinds of action units in the human face, each action unit is constituted by one or several pieces muscles, and units can be freely combined among the various actions, in other words, person's face may have 10,000 kinds of expression, but 3,000 of them maybe have the same emotional significance [12, 13] (Figs. 6 and 7).

The mechanical design of the robot facial expressions is based on FACS, and steering gears drive the emotional robot head, the synthesis of each feature point

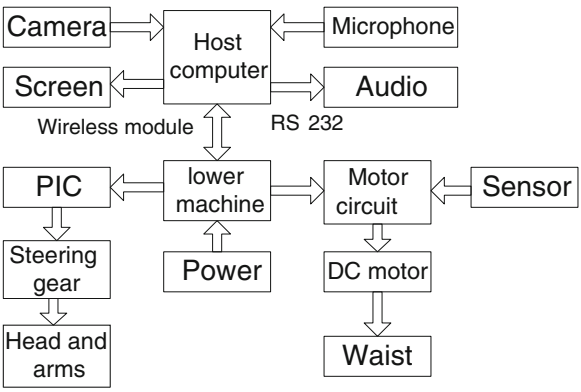

Fig. 8 Robot motor control system

movement form the robot's facial expression. For example, when people expressed surprise, the eyebrows lift and higher bend, eyebrow skin will be stretched. When eyes is wide open, upper eyelid will be pushed up, but when the chin of the face fall, mouth will open. If the head of the emotional robot design is consistent with this, you will get a surprised face.

4.3 Motor Control System

As for the emotional robot, a series of motors control the movements of the head and body, in order to make a variety of facial expressions, so the study of the motor control system is essential. As shown in Fig. 8, emotional robot motors have to meet both the necessary output torque and speed at the same time, and must make the mechanical structure of compact, high transmission accuracy and efficiency, to achieve the requirements of institutional speed and carrying capacity. Therefore, it is important to choose motors, whether motor selection is good or not, even directly related to the success or failure of the emotional robot moves performance.

4.4 Robot Vision

The majority of human information obtained from the external environment comes from eyes, which play an important role in the way to describe and understand people's needs and emotional states, so we must have a visual function of emotional robot to achieve fluent and appropriate communication with human.

Robot vision is to use machines instead of human eyes do the measuring and judgment, through image acquisition devices (CMOS or CCD), convert the intake target to the image signal, send to a dedicated image processing system and is transformed into the digital signal according to the distribution of pixel brightness,

color, and other information. Imaging systems conduct a variety of operations on these signals to extract target features, thus distinguish the results to control the movement of equipment at the scene. In the design of the emotional robot, targets will be detected through the eyes of the robot and converted the image signal, extract target features, and output results according to the default allowed and other conditions, to achieve automatic recognition.

4.5 Human–Computer Interaction Platform

Human–computer interaction (HCI) is not only an interactive computer system about the design, evaluation, and implementation for people, but also is a science to study this main phenomenon. When people interact with the emotional robot, look forward to being harmony and intelligence level, this is necessary to give the emotional robot of the auditory and visual intelligence, so that the computer can recognize the object of the interaction, to understand the form of language expression of the content of speech and the emotions of interacting objects, to do under the requirements of the people, or answer the questions proposed, finally achieve the purpose of interaction (Fig. 9).

4.6 Affective Integrated System

We consider a robot if it wants to show its own feelings in a moment, not only needs to analyze the external environment and its own emotional state, but also analysis signal of human language, body movements, and facial expressions, this requires modeling of the emotional state of the robot [14]. As shown in Fig. 10, at

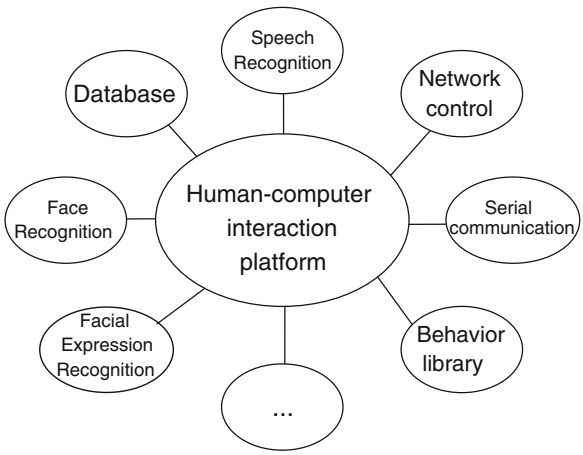

Fig. 9 Interaction platform structure

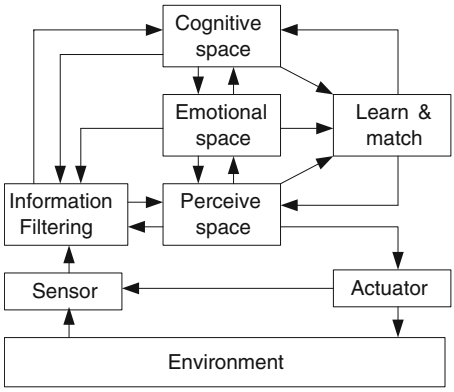

Fig. 10 Humanoid robot control architecture

home and abroad have been many emotional algorithms to model emotion, machine learning algorithms show the advantages in these emotions algorithm, and play the vitally important role in human–computer interaction [15].

4.7 Database

We use database in our lives all the time, for example, books in the library, bus card, case information, which all managed through the database. Brain is the memory or storage of data for human, but in terms of a completely intelligent robot system, database is the part of the stored data, and knowledge in its interior, like the brain of human.

5 Conclusion

By analyzing the structure of humanoid robot, we can build a robot to meet our requirements. In Fig. 11, humanoid robot can make six basic expressions to test and verify our design concept.

Through the above analysis and implementation, robots must have a cognitive emotion. Humanoid expression robot has the characteristic of personalized, user-friendly, and is able to achieve a harmonious human–computer interaction. It can be include more interacting systems, which can distinguish different users and situation. In addition, robot can judge the users emotional state as people, and this function makes a better communication with the owners. Under the guidance of the emotional theories, such as Artificial Emotion, Kansei Engineering and Artificial Psychology, use computer, MEMS and related technologies, people can create a cognitive expression robot, which harmoniously interact with people.

Fig. 11 Humanoid robot emotional expression

But there are some shortcomings in this design, robot has lacked related equipment to collect sufficient data information, which makes the emotional decision-making extremely difficult, sometimes its decision is wrong even is ironic. Existing technology and theory cannot give the robot a lot of support, and robots do not have brain and heart to learn and think like human being, but with technology advancing, these problems will be a good solution.

Acknowledgments This work is supported by the National Natural Science Foundation of China (61170117 and 61105120), thanks for the natural science foundation (NSFC), which provides financial aid for the research.

References

1. Gates B (2007) Robot in every home. Sci Am 296(1):58–65
2. Breazeal C, Scassellati B (1999) How to build robots that make Mends and influence people. In: IROS99, pp 858–863
3. Breazeal CL (2002) Designing sociable robots. The MIT Press, Cambridge
4. Breazeal CL (2003) Emotion and sociable humanoid robots. Int J Hum Comput Stud 59(1–2):119–155
5. Hirai K, Hirose M, Haikawa Y, Takenada T (1998) The development of Honda humanoid robot. In: IEEE international conference on robotics and automation, Leuven, Belgium, pp 1321–1326
6. Ogura Y, Aikawa H, Shimomura K, Morishima A, Lim H-O, Takanishi A (2006) Development of a new humanoid robot WABIAN-2. In: Proceedings of the 2006 IEEE international conference on robotics and automation, Orlando, FL, pp 76–81

7. Hashimoto T, Hitramatsu S, Tsuji T, Kobayashi H (2006) Development of the face robot SAYA for rich facial expressions. In: 2006 SICE-ICASE international joint conference, Busan, South Korea, pp 3558–3563
8. Inokuchi S (1999) Non-verbal interaction for Kansei communication. In: IEEE
9. Picard RW (1997) Affective computing. MIT Press, London
10. Kobayasbi H, Hara E (1996) Real time dynamic control of 6 basic facial expressions on face robot. J Robot Soc Jpn 14:677–685
11. Huang Q, Li K, Wang T (2002) Control and mechanical design of humanoid robot BHR-01. In: Proceedings of the third IARP international workshop on humanoid and human friendly robotics, pp 10–13
12. Ekman P, Friesen WV (1978) Facial action coding system. Consulting Psychologists Press Inc, Palo Alto
13. Ekman P, Friesen W, Hager J (2002) Facial action coding system. A Human Face, Salt Lake
14. Huang Q, Nakamura Y (2005) Sensory reflex control for humanoid walking. IEEE Trans Robot 21(5):977–984
15. Miwa H et al (2003) Introduction of the need model for humanoid robots to generate active behavior. In: Proceedings of the 2003 IEEE/RSJ international conference on intelligent robots and systems, pp 1400–1406

Detecting System of Ink Cells in Gravure Cylinder via Neural Network

Zifen He, Zhaolin Zhan and Yinhui Zhang

Abstract We apply neural network to build up a detecting system of ink cells in gravure cylinder. First, ink cells images are gained in the images capturing device and histogram equalization. The edge of cells is extracted by use of Canny operator. We use different thresholds and experimental sigma values that compare to experimental results. Canny edge extraction operator is best when the value of sigma is 16. According to the image used in this research to determine the standard ink cells carving, the value of gaps d_0 equals 125, the value of dark tone s_0 equals 394, and so its standard value of gaps and dark tone are $d_0 \pm 10$ and $s_0 \pm 10$. The values of gravure outlets gaps and dark tone are measured, while d and s are in the scope of standard range, of which output 1 of the ink cells determined to pass and output 0 deemed to fail. Binarization images are obtained through adaptive threshold segmentation, which regards the value of gaps and dark tone as the characteristic value when they start to detect. Finally, we extract size and surface defects of ink cells for grading. Segmentation pictures are extracted by *K*-means clustering. The areas of ink cells are deemed to size characteristics. Then we classify the ink cells into two classes using neural network. The experimental results consider a neural network model that produces consequences.

Keywords Ink cells in gravure cylinder · Detecting systems · Neural network · Value of gaps and dark tone

Z. He · Y. Zhang (✉)
Faculty of Mechanical and Electrical Engineering, Kunming University of Science and Technology, Kunming 650500, China
e-mail: yinhui_z@yahoo.com.cn

Z. He
e-mail: zyhhzf1998@163.com

Z. Zhan
Faculty of Materials Science and Engineering, Kunming University of Science and Technology, Kunming 650093, China
e-mail: zl_zhan@tom.com

F. Sun et al. (eds.), *Foundations and Practical Applications of Cognitive Systems and Information Processing*, Advances in Intelligent Systems and Computing 215,
DOI: 10.1007/978-3-642-37835-5_37,

1 Introduction

Gravure quality products depend largely on the quality of gravure cylinder. However at present, the vast majority of gravure manufacturing enterprises produced good gravure test sample cells by use of artificial or semi-automatic method [1]. Machine vision inspection system is mainly used in the quality of printed matter rather than printing plates.

Studies on offset and gravure on the automatic detection system by Rafail Bronstein, Omer Karp, and Goldstein have been advanced by the United States Scitex Vision Technology Co. Ltd and proxy, which applied for the patent [2].

Based on machine vision detecting technology it is mainly used in quality inspection of agricultural products [3–8]. Since 2000, the machine vision technology has also been applied in sorting timber, ore, chemicals, and other products classification.

In this paper, we apply neural network to build up a detecting system of ink cells in gravure cylinder. The experimental results consider a neural network model that produce proper sorting and gain true systematization consequences.

The rest of the paper is organized as follows. In Sect. 2, we present the system structure of computer-aided detecting system. Section 3 analyzes the detecting system program. Section 4 gives the pattern recognition results aiming at the model of neural network, and the results show the effectiveness of the proposed method. Finally, a brief summary is discussed in Sect. 5.

2 Computer-Aided Detecting System

A computer-aided ink cells quality assessment and detecting system has two subsystems: a computer vision system and an ink cells handling system [9]. The computer vision system has two modules, namely the image processing module and the pattern recognition module. The computer vision system captures the image of the underlying cell and transmits it to an image processor. The recognizer performs the quality assessments and classifies the underlying cell into prespecified quality classes. Figure 1 show computer-aided sorting system processes.

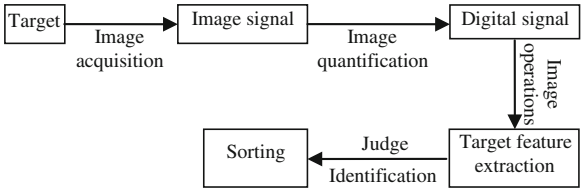

Fig. 1 Computer-aided sorting system

3 Analysis of Detecting System Program

3.1 Gain Images

The gain images system consists of camera, camera lens, light source, and illumination box. The model is shown in Fig. 2. It shows that a camera (the same camera) is installed separately on both sides of the conveyor belt. Cameras are mounted on light boxes, two opposites, the object distance of 200 mm; two light bars were placed on top of both sides of the camera light and angle of the center line of conveyor belt 45°, the belt color is also black.

3.2 The Structure of Ink Cells

In the process of laser engraving of ink cells, each ink cell is formed when the graver has completed a movement rather than time after time engrave. The formation of the ink cells is shown in Fig. 3.

Depth of variable. The ink color reproduction depends on the depth of variable of the ink cells. The image is darker and the ink cell is deeper. The area of ink cell is constant and the thickness of ink cell wall is equal. The formation of the ink cells is shown as in Fig. 4a.

Area of variable. The ink color reproduction depends on the open area of the ink cells. The image is darker and the area of ink cell is bigger. The depth of the ink cell is constant. The formation of the ink cells is as shown in Fig. 4b.

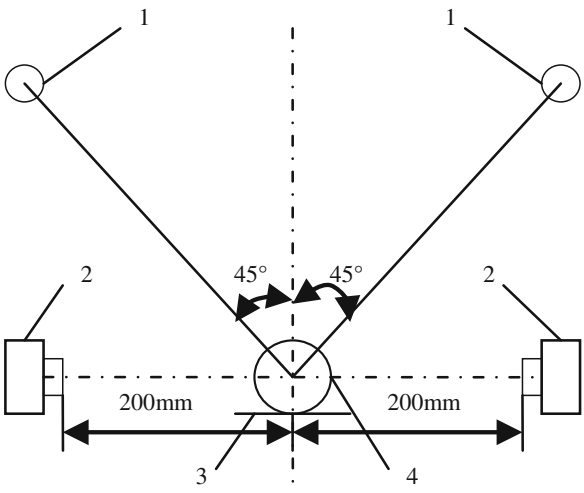

Fig. 2 Gain image device.*1* light source, *2* camera, *3* conveyor, *4* gravure cylinder

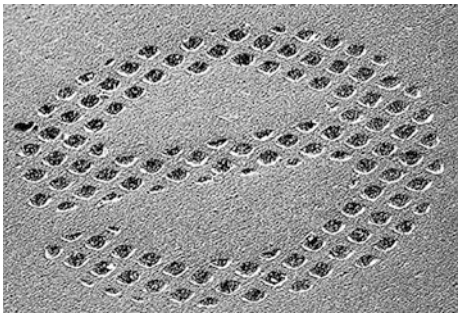

Fig. 3 The ink cells of gravure

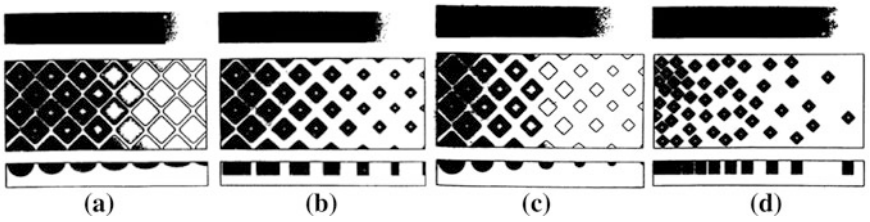

Fig. 4 The structure of ink cells gravure. **a** Depth of variable, **b** Area of variable, **c** Depth and area of variable, **d** FM

Depth and area of variable. The image is darker, the ink cell is deeper, and the area of ink cell is bigger. The thickness of ink cell wall is unequal. The formation of the ink cells is as shown in Fig. 4c.

FM. The open area of ink cell is constant, but the spatial location on the gravure cylinder is changed randomly. Similarly, large area cell wall "zone" does not appear as the image darkened area. The spatial position of the FM ink cell should be subject to reasonable control, it cannot be completely random. The formation of the ink cells is shown as in Fig. 4d.

3.3 Image Processing

The first piece of cell information test image is read and displayed by use of MATLAB image processing software [10, 11]. The information is shown in Fig. 5. When T and sigma are default values, the edge in Fig. 5c is extracted by use of Canny operator [12], Binarization images are obtained through adaptive threshold segmentation. It is obtained by the programming in Matlab [10].

In this paper, we chose the threshold equal to 0.10. The values of gaps and dark tone are the mainly tested objects in the processing of the deformation cells of gravure cylinder. So they are the image feature values. The bright value is 1, the

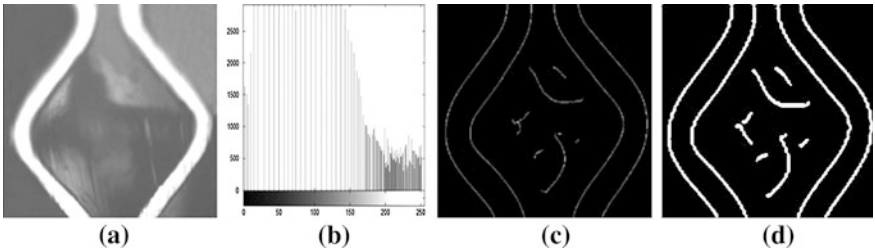

Fig. 5 Read the results of information cell. **a** Original image, **b** the histogram of equalization, **c** Canny operator extraction sigma = 16, **d** Binarization images $t = 0.10$

other part is 0 in the detected edge image. The detected edge image analysis shows that the value of dark tone corresponds to the image matrix of horizontal distance of two points. At first, there are highlights of the location coordinates in the edge image, they are i and j, the jm is the largest horizontal coordinate, and the js is the smallest horizontal coordinate. Hypothesis s is the value of dark tone and s is the difference with the js and jm. In addition to using the progressive test, the calculation of value of the gaps is the same as the dark tone. On the edge of the image all the columns of matrix of the first transverse are scanned so that the results have no bright spots; then the second line is scanned and the values of r and c are obtained.

3.4 The Identification of the Gravure Cells Quality

According to the image used in this research to determine the standard cells carving gaps value of d_0 equal 125, the value of dark tone s_0 equals 394, and so the standard ranges are $d_0 \pm 10$ and $s_0 \pm 10$. The value of gravure outlets gaps and dark tone are measured, while d and s is in the scope of standard range, of which output 1 of the cells determined to pass and output 0 deemed to have failed. The first piece of the original image runs the program; the result of z is 1, therefore it is qualified.

In this article, four experimental original manuscripts run all programs whose results are shown in Table 1. The experimental results of the second, third, and fourth pieces of the original images are shown in Figs. 6, 7, 8.

4 Simulation Pattern Recognition

4.1 Segmentation of Ink Cells

In data mining, k-means clustering is a method of cluster analysis which aims to partition n observations into k clusters in which each observation belongs to the cluster with the nearest mean [13].

Table 1 The test data of four experimental original manuscripts

Name	Original manuscripts			
	1	2	3	4
jm	421	418	429	431
js	19	20	26	27
s	402	398	403	405
r	1, 1, 1, 1	1, 1, 1, 1	1, 1, 1, 1	1, 1, 1, 1
c	143, 189, 235, 280	142, 189, 238, 289	139, 189, 245, 291	138, 190, 246, 290
cm	280	285	291	290
cs	143	142	139	140
d	137	143	152	153
z	1 (Qualified)	0 (Unqualified)	0 (Unqualified)	0 (Unqualified)

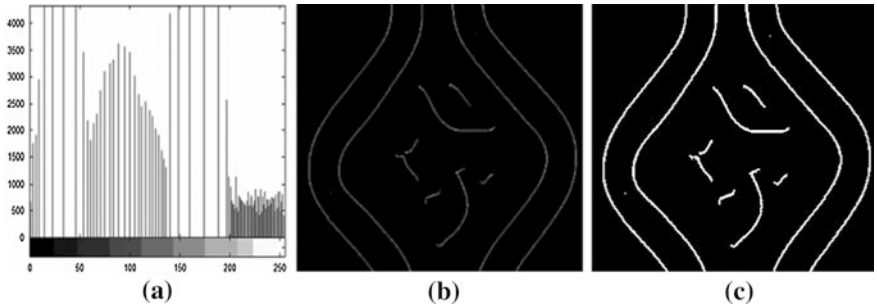

Fig. 6 The results of experiments original manuscript 2. **a** Histogram of equalization, **b** Edge extraction, **c** Einarization images

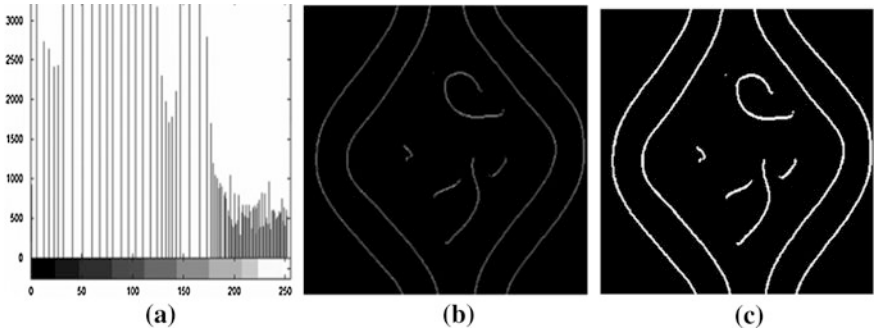

Fig. 7 The results of experiments original manuscript 3. **a** Histogram of equalization **b** Edge extraction **c** Binarization images

Given a set of observations $(x_1, x_2, \ldots, x_n)$, where each observation is a d-dimensional real vector, k-means clustering aims to partition the n observations into k sets $(k \leq n)\, S = \{S_1, S_2, \ldots, S_k\}$ so as to minimize the within-cluster sum

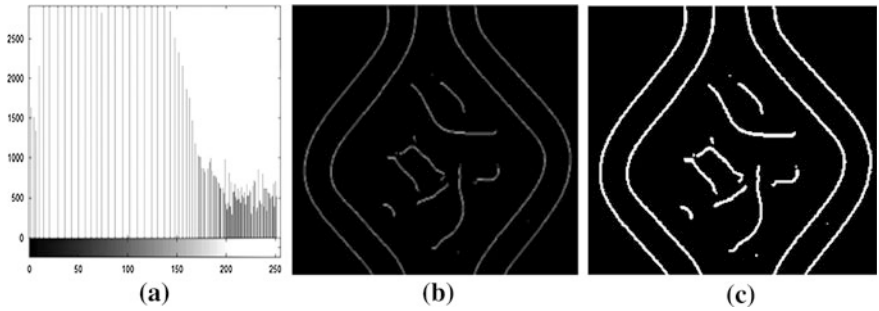

Fig. 8 The results of experiments original manuscript 4. **a** Histogram of equalization, **b** Edge extraction, **c** Binarization images

of squares $\arg\min_{S} \sum_{i=1}^{k} \sum_{x_j \in S_i} \left\| X_j - \mu_i \right\|^2$ where $\boldsymbol{\mu}_i$ is the mean of points in S_i (Fig. 9).

Segmentation pictures are extracted by *K*-means clustering. The areas of ink cells are deemed to size characteristics.

4.2 Neural Network

The American computer scientist F. Rosenblatt proposed the perceptron convergence theorem in 1957 [14], where n_i is the ith weighted neuron total inputs. a_i is the ith neuron output, $i = 1, 2, \ldots, s$.

$$n_i = \sum_{j=1}^{r} w_{ij} p_j. \tag{1}$$

$$a_i = f(n_i + b_i). \tag{2}$$

Fig. 9 The results of Segmentation

The basic function of the perceptron is that the input vector is converted to the output vector which is 0 or 1. According to the test the total weighted output value is located on left and right of the threshold function to classify the input data.

$$a_i = \begin{cases} 1 & n_i + b_i > 0 \\ 0 & n_i + b_i < 0 \end{cases}. \tag{3}$$

This function can be explained by mapping the input vector space. For example, the input vector $r = 2$, for the selected weight w_1, w_2 and b, we regard P_1 and P_2 as horizontal and vertical axes, respectively, which draw the geometric locus of $w * p + b = w_1 * p_1 + w_2 * p_2 + b = 0$ that is a straight line when $w_1 * p_1 + w_2 * p_2 + b > 0$, the values of P_1 and P_2 locate the straight line and above, the output of perception is 1, else 0.

When we apply the perceptron to classification for different input vectors for the desired output 0 or 1, the problem can be transformed into the input vector in the input space formed by different points of location to design perceptron weights w and b. The purpose of perceptron weight parameter is to design a path of $w * p + b = 0$ according to the learning law to achieve the desired division for the input vectors.

We calculated the new weight matrix W and bias B of new algorithms. Changing the amount of weight equals it to the input vector. Assume the input vector to be P, the output vector to be A, and the target vector to be T.

$$\begin{aligned} \Delta w_{ij} &= (t_i - y_i) \times p_j \\ \Delta b_i &= (t_i - y_i) \times 1. \end{aligned} \tag{4}$$

The role of the input vector P, the actual of A is calculated to compare with the corresponding target vector T and check whether A is equal to T, and then to adjust the weights and bias according to the learning rules by use of the error amount. The right to recalculate the value of the network under the new input, the weight adjustment process is repeated when the network output vector A is equal to target output vector T or the number of training to achieve pre-set maximum by the end of training.

In this article, determine the input vector P, the target vector T, and determine the vector dimension and number of neurons: r, s, and q.

First, we classify the cells in gravure cylinder according to the characteristic, namely, given the value of perceptron input vector P and the target output vector T. Figure 10 determines the location of the border.

We use the trained perceptron to classify samples of unknown type. We are trained to detect 14 samples of gravure cells, and use the perceptron test for new samples. The results are shown in Fig. 11.

The simulation results show that gravure cells have been successfully sorted using perceptron neural network. This shows the validity of the proposed method.

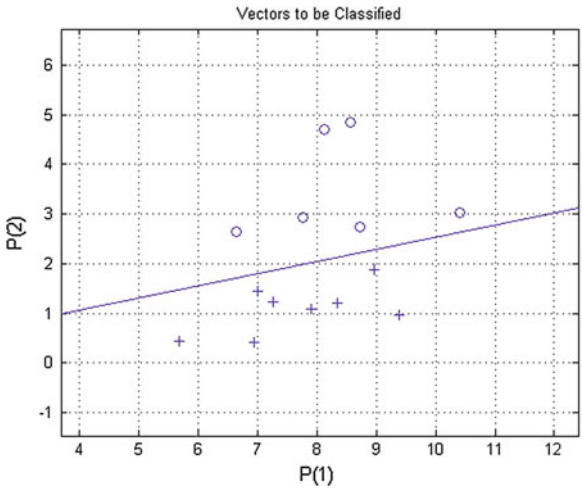

Fig. 10 Perceptron training

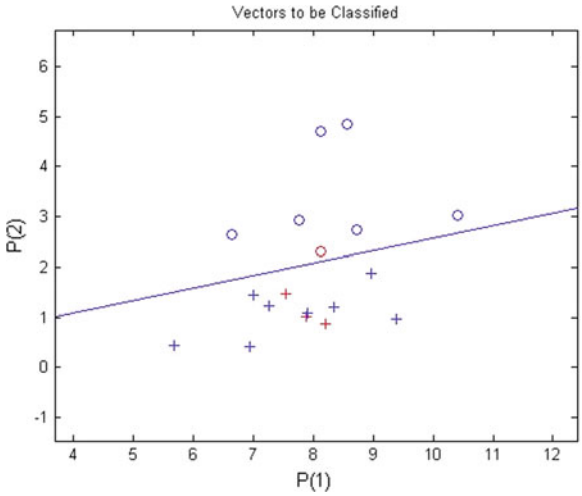

Fig. 11 Application of perceptron

5 Conclusions

In this paper, the main contents of cells in gravure cylinder are extract image feature value and sorting. We regard the machine vision as the theoretical basis for establishing the sorting system of cells in gravure cylinder. First, the cell images are gained in the images capturing device. We have applied the MATLAB to read the experiment images and histogram equalization. The edge of cells is extracted by use of Canny operator. The values of gravure outlets gaps and dark tone are measured and Binarization images are obtained through adaptive threshold segmentation, which regard the values of gaps and dark tone as the characteristic value when they start sorting. Then we apply neural network to classify the cells

into two classes. The experimental results consider a neural network model that produces properly sorting and gain true systematization consequences.

Acknowledgments This work was supported by Project 60962007 of the National Science Foundation of China and Foundation of Kunming University of Science and Technology under Grant 2011-02.

References

1. Deng PJ, Jin Y (2006) Printer dot overlap for gravure cylinder. Packag Eng 27:19–21
2. Bronstein R (2000) The United States. Patent, 6031932[P]
3. Anderson R, Hauaggeb DC, Jacques W, Goldenstein S (2010) Automatic fruit and vegetable classification from images. Comput Electron Agric 70:96–104
4. Riquelme MT, Barreiro P, Ruiz-Altisent M, Valero C (2008) Olive classification according to external damage using image analysis. J Food Eng 87:371–379
5. Blasco J, Aleixos N, Gomeza J, Molto E (2007) Citrus sorting by identification of the most common defects using multispectral computer vision. J Food Eng 83:384–393
6. Xu L, Zhao Y (2010) Automated strawberry grading system based on image processing. Comput Electron Agric 71S:32–39
7. Blasco J, Cubero S, Gómez-Sanchís J, Mira P, Moltó E (2009) Development of a machine for the automatic sorting of pomegranate (*Punica granatum*) arils based on computer vision. J Food Eng 90:27–34
8. Lee D-J, Schoenberger R, Archibald J, McCollum S (2008) Development of a machine vision system for automatic date grading using digital reflective near-infrared imaging. J Food Eng 86:388–398
9. Yousef AO (2011) Computer vision based date fruit grading system: design and implementation. Comput Info Sci 23:29–36
10. Rafael CG, Woods RE (2005) Digital image processing using MATLAB. Publishing House of Electronics Industry, Beijing
11. Shapiro LG (2005) Computer vision. China Machine Press, Beijing
12. Zhu Z, Liu G, Liu Q (2009) Modern Electronics Technique 24:89–90
13. MacQueen JB (1967) Some methods for classification and analysis of multivariate observations, Proceedings of 5-th Berkeley symposium on mathematical statistics and probability, vol 1. University of California Press Berkeley, pp 28–297
14. Hagan MT, Demuth HB, Beale MH (2002) Neural network design. China Machine Press, Beijing

An Underwater Laser Image Segmentation Algorithm Based on Pulse Coupled Neural Network and Morphology

Bo Wang, Lei Wan and Tie-dong Zhang

Abstract Range-gated underwater laser imaging technology, which is very promising in oceanic research, deep sea exploration, and robotic works, is one of the most effective methods to suppress the effect of backward scattering of water medium. However, the special features of underwater laser images, such as speckle noise and nonuniform illumination, bring great difficulty for image segmentation. In this paper, an image segmentation algorithm which combines improved pulse coupled neural network with morphology is proposed. The morphology is applied to eliminate the speckle noise, while the cross-entropy is calculated as an optimization criterion for determination of the optimal segmentation. The experimental results of the proposed algorithm are compared with those of NCut, Mean-shift, Fuzzy C-means, and Watershed methods, and the quantitative evaluation confirms that the proposed algorithm is significantly superior to the other four algorithms in segmentation accuracy and robustness against speckle noise and nonuniform illumination.

Keywords Underwater laser image · Pulse coupled neural network · Morphology · Cross-entropy

B. Wang (✉) · L. Wan · T. Zhang
National Key Laboratory of Science and Technology on Underwater Vehicle, Harbin Engineering University, Harbin 150001, China
e-mail: wb@hrbeu.edu.cn

L. Wan
e-mail: wanlei@hrbeu.edu.cn

T. Zhang
e-mail: zhangtd@hrbeu.edu.cn

F. Sun et al. (eds.), *Foundations and Practical Applications of Cognitive Systems and Information Processing*, Advances in Intelligent Systems and Computing 215,
DOI: 10.1007/978-3-642-37835-5_38,

1 Introduction

There are quite limited means of obtaining images of objects in underwater environment. Acoustic and optical imaging technology are conventional underwater object detecting methods, however, the spatial resolution of acoustic images, as a result of long wavelength, is not so satisfying, and because of the attenuation and scattering effect of water medium the detection range of optical imaging is restrained, especially in deep water where little natural light can reach, artificial light source is often needed to illuminate the target, but a lot of backscattered light degrades the quality of obtained images seriously [1]. One of the most effective solutions to above problems is to apply range-gated underwater laser imaging technology.

Range-gated underwater laser imaging technology, which takes advantage of phenomenon that the attenuation of blue–green light between 470 and 580 nm in spectrum is much less than that of other bands of light in water, adopts blue–green pulsed laser generator as the illuminator, and eliminates most of the backscattering through introducing range-gated controlling technique. Consequently, it has a detection range of 4–6 times that of a conventional underwater camera in intervening water medium, and it is widely preferred not only due to its longer range and higher resolution, but also its robustness in terms of motion insensitivity [2]. However, in the imaging process some backscattering still enters the range-gated CCD (RGCCD) camera, and the noise known as speckle is present in obtained images as a result, and furthermore underwater laser images associated with range-gated underwater laser imaging system are blurred due to absorption and scattering of water medium.

The blurred underwater laser images which are stained by speckle noise bring great difficulty for image segmentation. Therefore, traditional segmentation algorithms, such as statistical methods, energy-based, region-based, and graph-based methods, which often show high sensitivity to speckle noise or consume much computation, always give inaccurate segmentation results when applied on underwater laser images, and other hybrid methods which can give better results suffer from huge computational complexity, and furthermore image preprocessing is usually required to suppress the speckle noise or enhance the images. In order to achieve optimal segmentation results and reduce the computational complexity, an image segmentation algorithm which combines improved pulse coupled neural network (PCNN) with morphology is proposed in this paper. Utilizing the synchronous pulse burst and dynamic threshold of PCNN, a series of image segmentation results can be obtained, and morphological operations are applied to eliminate the effect of speckle noise, while an optimization criterion based on cross-entropy (CE) is used to determine the optimal segmentation result. To evaluate the performance of our proposed algorithm, the segmentation results are compared with those of other four traditional algorithms in terms of image entropy, contour disagreement and area overlap with respect to the ground truth, and conclusion about the segmentation performance of our proposed algorithm is given in the end.

2 Range-Gated Underwater Laser Imaging System

In the trials, LSV-W range-gated underwater laser imaging system (RGULIS) is used to obtain underwater laser images of objects, as is shown in Fig. 1. The LSV-W RGULIS consists of an Nd^{+3}:YAG solid–state pulsed laser generator and a RGCCD camera. The pulse duration of the pulsed laser generator is 10 ns, and the pulse energy output into the water is noy less than 25 mJ at the wavelength 532 nm, which is corresponding to the blue–green light in spectrum. The pulsed laser is utilized to illuminate the underwater object and part of pulse is reflected by the object. When sufficient time has passed for the pulse to propagate from the illuminator to object, and then back to RGCCD camera, the RGCCD camera is activated for a very short-time interval that a laser image including reflection from the object is produced. By sending special instructions to regulate the moment the RGCCD camera is activated and inactivated, the selected layer is determined accordingly. Object in the selected layer is revealed in underwater laser images, while object beyond the selected layer is not.

In the propagation in water medium, the pulsed laser is strongly scattered and absorbed by water molecules and floating particles and the backscattering has great influence over underwater laser images. In order to improve image quality, after that the pulsed laser is emitted from the pulsed laser generator the RGCCD camera retains inactivated. When the pulse reflected from object in the selected layer arrives, the RGCCD camera is activated for a short interval, and then it becomes inactivated again. This regime ensures that most of the backscattering is shielded off in time domain, but still some backscattering enters the RGCCD camera together with reflection from object that obtained underwater laser images are stained by speckle noise as a result (See Fig. 2). Besides, after that the pulse is

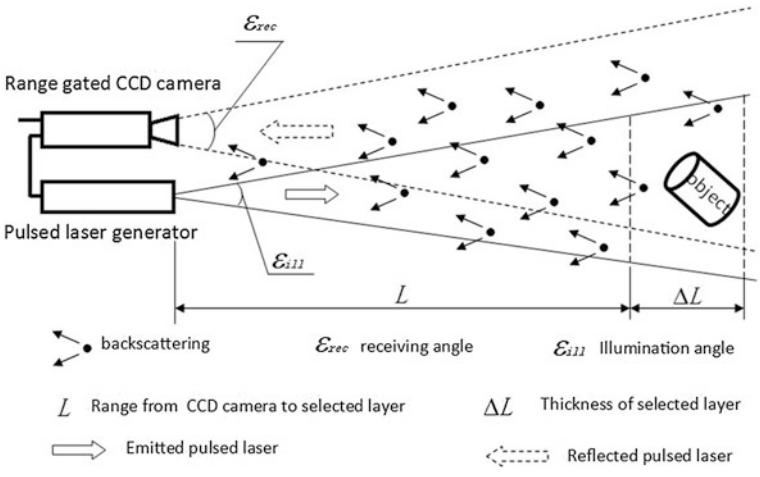

Fig. 1 LSV-W range-gated underwater laser imaging system

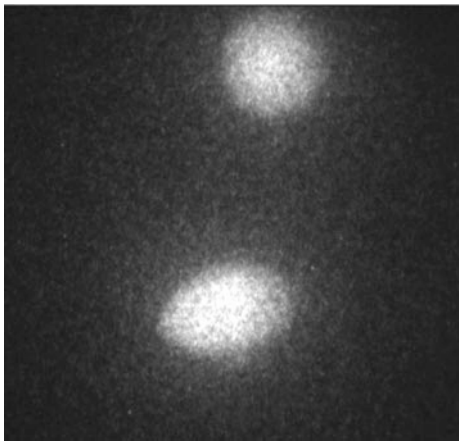

Fig. 2 An typical underwater laser image

reflected from underwater object, the reflection which consists of imaging information of the underwater object is strongly absorbed and scattered by water molecules and floating particles. Thus, the detailed information in the obtained underwater laser images such as edges and points are always blurry, as is shown in Fig. 2. Moreover, because of the laser pulse stretching, the obtained images usually have obvious nonuniformly illuminated character, such as brighter center and darker edge [2]. Consequently, the traditional segmentation algorithms are not suitable for underwater laser images anymore due to these special features, and a novel image segmentation method based on improved PCNN and morphology is proposed.

3 Improved PCNN Model

The PCNN is a biological inspired neural network based on the experimental observations of synchronous pulse bursts in cat and monkey visual cortex [3, 4]. Differing from traditional neural networks, the neurons of PCNN have the same parameter values and PCNN needs not to be trained, furthermore because of its biological foundation, it has original advantage in image processing, especially for image segmentation due to its synchronous pulse burst and dynamic threshold. However, the original PCNN suffers from a large number of feedback iterations, various parameter adjustments, and computational complexity, which are difficult to implement and time consuming [5], thus an improved PCNN model is proposed in this paper. The neuromime of the improved PCNN is shown in Fig. 3.

The neuromime consists of three parts: the receptive field, the modulation product, and the pulse generator [3]. In the receptive field of neuron (i,j) the feeding input F_{ij} only receives external stimulus S_{ij}, and linking input L_{ij} receives output from neighboring neurons with synaptic weight strengths W. The linking

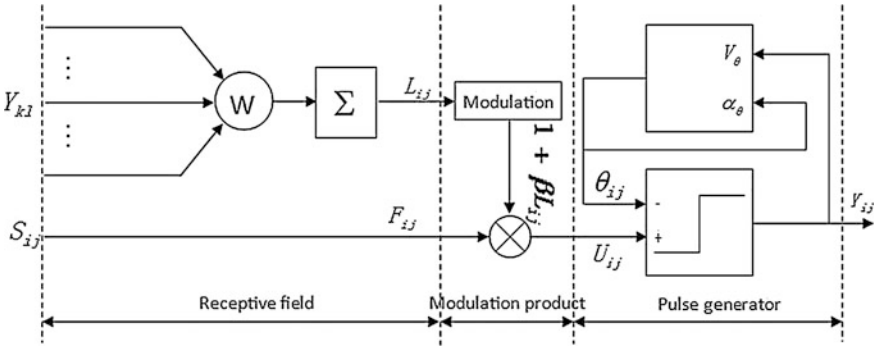

Fig. 3 The neuromime of the improved PCNN

input L_{ij} is modulated through linking strength β and multiplied with feeding input F_{ij} to produce internal activity U_{ij}. The pulse generator compares internal activity U_{ij} with dynamic threshold θ_{ij}, if U_{ij} is larger than θ_{ij}, the neuron (i,j) fires (output $Y_{ij} = 1$), otherwise it does not (output $Y_{ij} = 0$). Y_{kl} is the output of neighboring neuron (k,l) and the parameters V_θ and α_θ denote the amplitude and decay coefficient of dynamic threshold θ_{ij}, respectively.

The discrete mathematical description of its neuron is formulated as follows:

$$F_{ij}[n] = S_{ij} \tag{1}$$

$$L_{ij}[n] = \sum_{k,l} w_{ij,kl} Y_{kl}[n-1] \tag{2}$$

$$U_{ij}[n] = F_{ij}[n](1 + \beta L_{ij}[n]) \tag{3}$$

$$\theta_{ij}[n] = \alpha_\theta \theta_{ij}[n-1] + V_\theta Y_{ij}[n-1] \tag{4}$$

$$Y_{ij}[n] = step(U_{ij}[n] - \theta_{ij}[n]) \tag{5}$$

where n denotes the nth iteration, V_θ denotes the amplitude of dynamic threshold, $step(\bullet)$ is the step function, and $w_{ij,kl}$ refers to the synaptic weight for linking input L_{ij}. Feeding input F_{ij} only receives external stimulus S_{ij} (e.g., intensity of a pixel in the image), and linking input L_{ij} is modulated through linking strength β and multiplied with feeding input F_{ij} to produce internal activity U_{ij} if internal activity U_{ij} is larger than dynamic threshold θ_{ij}, the neuron fires (output $Y_{ij} = 1$) and a pulse is emitted, otherwise it does not fire (output $Y_{ij} = 0$) and dynamic threshold would decay by coefficient α_θ. When a neuron fires, its output is delivered to each interacting neuron that if it has a similar external stimulus, it will fire simultaneously. This phenomenon is called synchronous pulse burst, which present itself theoretical foundation for image segmentation.

4 Underwater Laser Image Segmentation Algorithm

The improved PCNN applied to underwater laser image segmentation is a two-dimensional single layer neural network, the intensity of each pixel is supposed to be the external stimulus of corresponding neuron in PCNN. If the dynamic thresholds of all the neurons begin to decay from the same initial value, which can be accomplished simply by setting $\theta_{ij}[0] = 0$ for all the neurons, the neurons corresponding to pixels of higher intensity will fire first, then the neurons corresponding to pixels of lower intensity will fire at the next iteration. Consequently, in the obtained binary image sequences all the pixels are segmented into different sets according to their intensity, from which the optimal segmentation result is determined by defined optimization criterion. Furthermore, the dynamic thresholds decay in proportion so that obtained binary image at each iteration approximate to optimal segmentation result fast and accurately enough. Moreover, when certain neurons fire, the corresponding pixels probably represent the speckle noise of high intensity that has great influence over the segmentation result. Thus, a morphological opening is applied on the binary image sequences to elimination of the speckle noise.

4.1 Morphological Operations on Binary Images

Based on set theory, morphology obtains description of images' internal structure utilizing defined structuring element (SE) as a 'probe'. Image components that are useful in the representation and description of region shape, such as boundaries, skeletons, and convex hull are extracted through morphological operations, and also morphology can be applied to filtering, thinning, and pruning. There are four basic morphological operations on binary images: erosion, dilation, opening, and closing [6].

Term 1. The erosion of binary image A by SE B, denoted $A \odot B$, is defined as

$$A \odot B = \left\{ z | (B)_z \subseteq A \right\} \tag{6}$$

Term 2. The dilation of binary image A by SE B, denoted $A \oplus B$, is defined as

$$A \oplus B = \left\{ z | (\hat{B})_z \cap A \neq \varnothing \right\} \tag{7}$$

Term 3. The opening of binary image A by SE B, denoted $A \circ B$, is defined as

$$A \circ B = (A \odot B) \oplus B \tag{8}$$

Erosion shrinks or thins objects in binary images, while dilation grows or thickens objects. Thus, they are not usually applied to image processing separately for shifting the boundaries of objects. The opening, which is a combination of erosion with dilation, eliminates all bright regions and dots that are smaller than the SE while distorting the objects as little as possible. In this paper, the opening operation is used to eliminate most of the speckle noise in the image segmentation results.

4.2 Optimization Criterion Based on Cross-Entropy

In the iterative process PCNN outputs a series of matrices called firing arrays, which are considered as binary image sequences, i.e., image segmentation results. For selecting the optimal segmentation result from obtained binary image sequences, an optimization criterion based on CE is applied to measure the discrepancy between the objects and the backgrounds in the segmentation results. Given two probability distributions $P = \{p_1, p_2, \ldots, p_N\}$ and $Q = \{q_1, q_2, \ldots q_N\}$, the CE can be calculated as follows:

$$D(P:Q) = \sum_{i=1}^{N} p_i \ln \frac{p_i}{q_i} + \sum_{i=1}^{N} q_i \ln \frac{q_i}{p_i} \tag{9}$$

According to each image segmentation result underwater laser image is segmented into two parts: the object region and the background region, which are considered as two probability distributions, denoted O and B,, respectively. Consequently, the CE can be formulated as follows [7]:

$$D(O:B) = \sum_{f \in B} fh(f) \ln \frac{f}{\mu_b} + \sum_{f \in O} fh(f) \ln \frac{f}{\mu_o} \tag{10}$$

where f is intensity of underwater laser image and $h(f)$ refers to the probability density function of f. μ_o and μ_b denote the average intensity of object region and background region, respectively, and they are calculated as follows:

$$\mu_o = \frac{\sum_{f \in O} fh(f)}{\sum_{f \in O} h(f)}, \quad \mu_b = \frac{\sum_{f \in B} fh(f)}{\sum_{f \in B} h(f)} \tag{11}$$

The CE is a measure of discrepancy between the object and the background, and the smaller the CE is, the greater discrepancy there is between the object and the background, which means the better segmentation result is obtained. And furthermore, the CE is insensitive to noise, which is quite meaningful for underwater laser image. The CE is calculated for underwater laser images, and the optimal segmentation result corresponds to the minimum CE.

4.3 Algorithm Description

The underwater laser image segmentation algorithm can be described as follows:

Step 1. Read the underwater laser image, initialize the improved PCNN with necessary parameters, and set the initial value of dynamic threshold as $\theta_{ij}[0] = 0$;

Step 2. Calculate the linking input $L_{ij}[n]$ and internal activity $U_{ij}[n]$, output the firing array considered as binary image segmentation result, if iteration counter $n = 0$, jump to step 4;

Step 3. Apply morphological opening on the obtained binary image to eliminate the speckle noise, and calculate the CE of segmented underwater laser image based on current filtered binary image. If minimum CE is achieved, the algorithm ends and output current filtered binary image as the optimal segmentation result.

Step 4. Update the dynamic threshold $\theta_{ij}[n]$ and iteration counter: $n = n + 1$, jump to step 2.

5 Experimental Results and Discussion

In this paper, we demonstrate the superiority of the proposed algorithm by comparing its performance to four popular traditional methods segmenting underwater laser images. Image acquisition was implemented at the depth of 5 m underwater without natural light illumination, and three different objects, which is a sphere, a triangular prism, and an ellipsoid, were placed about 12 m away from the RGU-LIS. Four obtained underwater laser images are shown in Fig. 4. In order to segment the obtained image using the proposed algorithm, we need to initialize PCNN with necessary parameters. The linking strength, the amplitude, and the decay coefficient are set as $\beta = 0.08$, $V_\theta = 200$ and $\alpha_\theta = 0.78$, respectively. And the synaptic weight is defined as the reciprocal of the Euclidean distance between two interacting neurons in linking area that is a region of 7×7 pixels, considering the scattering effect of water medium.

The segmentation process of the proposed algorithm is shown in Fig. 4, as we can see that the optimal segmentation results could be obtained at the fourth iteration of PCNN for current experimental image samples. Actually, the CE function performs as a concave function, which means the CE of segmentation results decreases first, and then it increases in accordance with iterations of PCNN, so that if a local minimum is found, the optimal segmentation result will be determined accordingly. Thus the proposed algorithm quits running as the local minimum of CE is detected in the iterations. Figure 4 also indicates that although underwater laser images are very blurry and there exist speckle noise and non-uniform illumination, which causes the special intensity distributions of the object

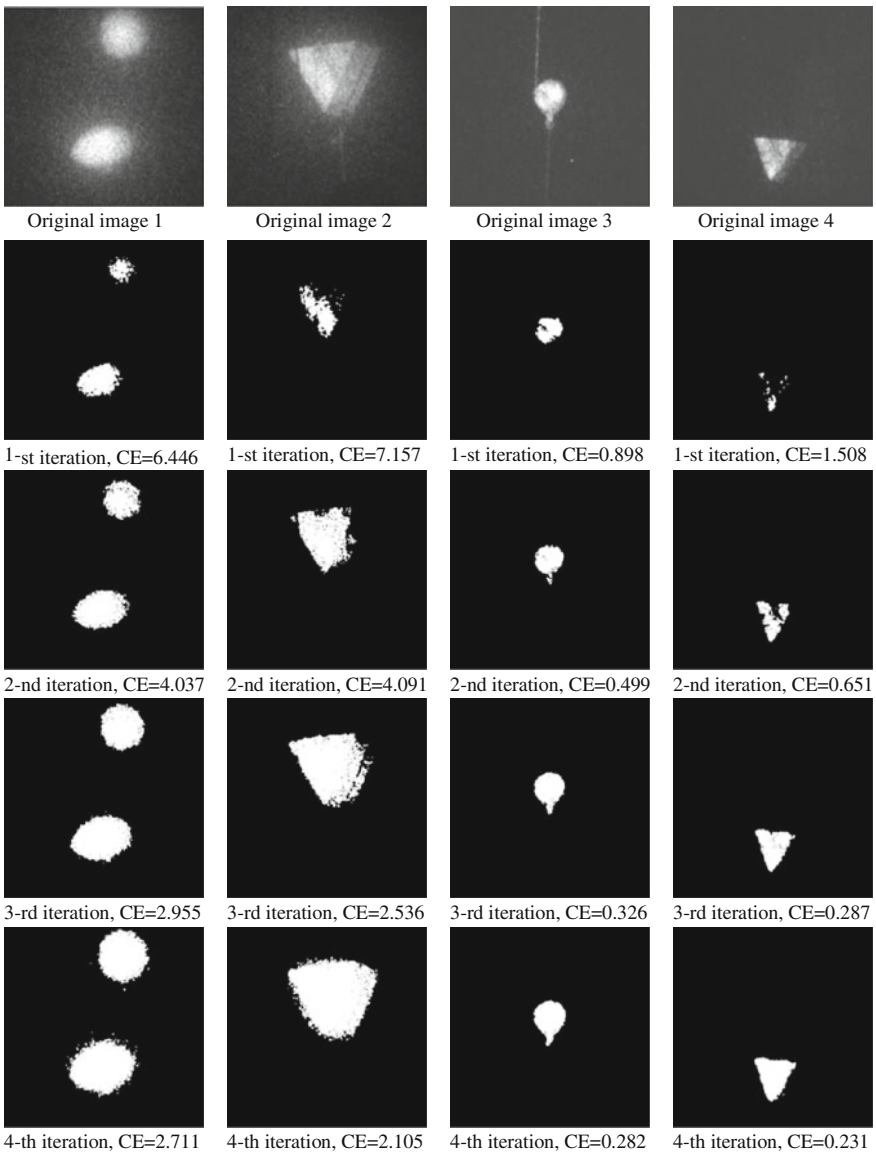

Fig. 4 Examples of image segmentation process using the proposed algorithm, all the optimal segmentation results are obtained at the fourth iteration

regions in the underwater laser images, the proposed algorithm in this paper still can extract all the objects accurately through several iterations.

To evaluate the segmentation performance of our proposed algorithm, we compared its segmentation results with those of other four algorithms, which were Normalized Cut, Mean-shift, Fuzzy C-means, and Watershed methods. The Fuzzy

C-means method and Watershed method are quite sensitive to speckle noise, so they both need the underwater laser images to be filtered before segmentation. The Normalized Cut method is proved to be NP-hard problem, i.e., the computation becomes extremely complex as the pixels of images increases, so the underwater laser images need to be resized to reduce the number of pixels before segmentation, which will result in the loss of contour and region information. The Mean-shift method shows robustness against speckle noise, but its performance is seriously decreased by the nonuniform intensity distribution.

Examples of the segmentation results by the five aforementioned methods are shown in Fig. 5. As we can see, the Normalized Cut method worked unstably and obtained under-segmentation results or over-segmentation results, it is because that the existence of speckle noise and nonuniform distribution in the underwater laser images increases the intergroup similarity in the weighted undirected graph that inaccurate edges are obtained among the nodes. The Fuzzy C-means method, the Mean-shift method, the Watershed method, and the proposed algorithm successfully extracted all the object regions from underwater laser images.

To get a quantitative evaluation, the CE, the area overlap metric (AOM), the Hausdorff distance (HD), and the average minimum Euclidean distance (AMED) have been calculated as evaluation indices with each of the aforementioned methods for the underwater laser images shown in Fig. 5, regarding manually segmented image by experience as the ground truth (GT) [8]. The AOM, which estimates the similarity between the automatically segmented area and the GT, is defined as the ratio of the intersection to the union of them:

$$\mathrm{AOM} = \frac{A_{\mathrm{seg}} \cap A_{\mathrm{gt}}}{A_{\mathrm{seg}} \cup A_{\mathrm{gt}}} \tag{12}$$

where A_{seg} and A_{gt} denote the area of the automatically segmented area and corresponding GT, respectively. Generally, the higher the value of AOM is, the better the segmentation result is considered to be. The HD and AMED are used to quantify the discrepancy between the contours of automatically segmented area and corresponding GT, denoted $A = \{a_1, a_2, \ldots, a_n\}$ and $B = \{b_1, b_2, \ldots, b_m\}$, respectively. The HD and the AMED are calculated as follows:

$$\mathrm{HD} = \max\left\{ \max_{a_i \in A} \min_{b_j \in B} \|a_i - b_j\|, \max_{a_i \in A} \min_{b_j \in B} \|b_i - a_j\| \right\} \tag{13}$$

$$\mathrm{AMED} = \left(\frac{1}{n}\sum_{i=1}^{n} \min_{b_j \in B} \|a_i - b_j\| + \frac{1}{m}\sum_{i=1}^{m} \min_{a_j \in A} \|b_i - a_j\|\right)/2 \tag{14}$$

where $\|\bullet\|$ denotes the Euclidean distance. From the formulas above we can see that the HD measures the worst disagreement between two contours, while AMED estimates the average disagreement between them. Obviously, the smaller the value of HD or AMED is, the better the segmentation result is considered to be.

The evaluation indices for different segmentation algorithms applied to the underwater laser images shown in Fig. 5 are presented in Tables 1, 2, 3, 4. All the

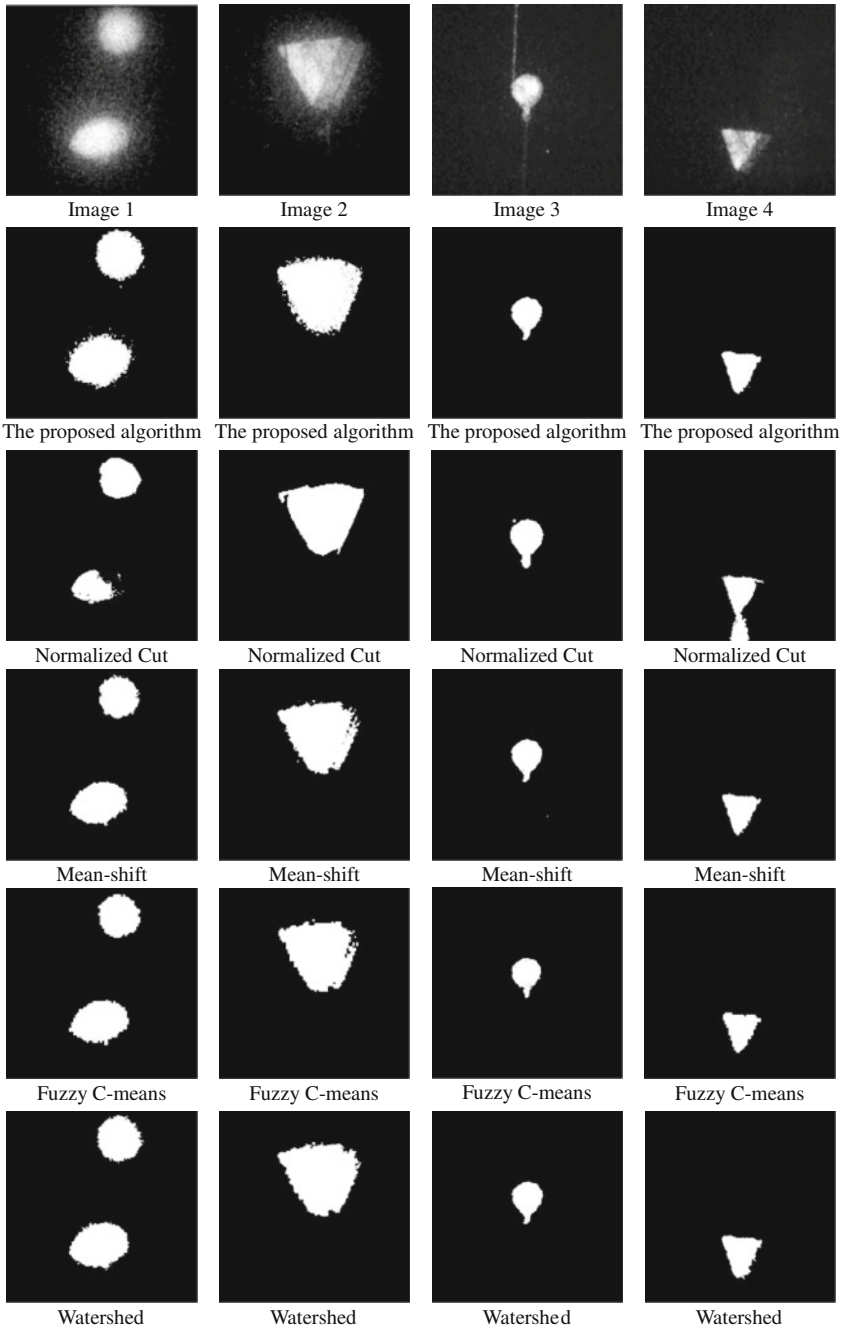

Fig. 5 Examples of segmentation results by the five segmentation methods

Table 1 Evaluation indices of different segmentation methods for Image 1

Segmentation method	CE	AOM	HD	AMED
The proposed method	2.711	0.881	19.217	2.826
Normalized cut	3.134	0.768	45.362	6.875
Mean-shift	2.981	0.879	16.0	3.274
Fuzzy C-means	2.897	0.874	20.157	4.323
Watershed	2.737	0.883	21.180	3.252

Table 2 Evaluation indices of different segmentation methods for Image 2

Segmentation method	CE	AOM	HD	AMED
The proposed method	2.105	0.847	29.65	5.281
Normalized Cut	2.132	0.859	29.860	6.007
Mean-shift	2.162	0.871	31.016	5.989
Fuzzy C-means	2.183	0.795	37.651	8.955
Watershed	2.126	0.832	29.180	12.252

Table 3 Evaluation indices of different segmentation methods for Image 3

Segmentation method	CE	AOM	HD	AMED
The proposed method	0.282	0.880	13.038	2.683
Normalized Cut	0.312	0.779	25.674	4.728
Mean-shift	0.296	0.881	95.525	13.361
Fuzzy C-means	0.308	0.806	21.360	4.833
Watershed	0.293	0.868	13.928	2.498

Table 4 Evaluation indices of different segmentation methods for Image 4

Segmentation method	CE	AOM	HD	AMED
The proposed method	0.231	0.690	26.967	7.759
Normalized cut	0.295	0.613	34.256	9.587
Mean-shift	0.233	0.653	27.295	8.421
Fuzzy C-means	0.238	0.622	35.917	9.668
Watershed	0.234	0.701	26.301	8.285

evaluation indices demonstrate that the segmentation performance of our proposed algorithm is better than that of Normalized Cut, Fuzzy C-means, and Mean-shift methods, while it is similar but slightly superior to that of Watershed method in terms of image entropy, contour disagreement, and area overlap. It is because that in the Mean-shift algorithm when in a wide bandwidth range there are not enough sample points, some small object regions will not be segmented from the original images due to the function convergence, as is seen in Fig. 5. And the performance of Fuzzy C-means method is seriously reduced by speckle noise in spite of applying filter and it is often affected by the initial values, which will result in inaccurate segmentation. The Watershed method can extract the weak blurry edges

well enough, but the nonuniform intensity distribution often results in oversegmentation. Overall our proposed algorithm shows better segmentation accuracy and robustness against noise and nonuniform illumination.

6 Conclusion

Underwater laser imaging technology is a promising advanced technology in underwater imaging field. In this paper, a novel image segmentation algorithm based on improved PCNN and morphology is proposed to segment underwater laser images. The morphological operations are applied to eliminate the effect of speckle noise, while the CE of segmentation results is calculated as an optimization criterion for determination of optimal segmentation result. Experimental results show that our proposed algorithm is able to successfully segment underwater laser images, and the segmentation results are compared with those of Normalized Cut, Mean-shift, Fuzzy C-means, and Watershed methods in terms of image entropy, contour disagreement, and area overlap with respect to the ground truth, all the evaluation indices demonstrate the potential of our proposed algorithm to allow more accurate segmentation and robustness against speckle noise and nonuniform illumination. We will concentrate our future work on studying speckle noise suppression methods and improving segmentation accuracy.

Acknowledgments This work is supported by fundamental research funds for central universities (HEUCF110111), by National Natural Science Foundation of China (51009040\E091002), by National High-tech R&D Program of China (863 Program) (2011AA09A106), and by the China Postdoctoral Science Foundation (Award: 2012M510928).

References

1. Tulldahl HM, Anderson P, Olsson A (2006) Experimental evaluation of underwater range-gated viewing in natural waters. In: Electro-optical and infrared systems. Proceedings of SPIE, vol 6395, p 639506
2. Li H, Wang X, Bai T (2008) Nonuniformly illuminated image enhancement based on range-gated underwater imaging system. In: 2008 International conference on optical instruments and technology. Proceedings of SPIE, vol 7156, pp 71563E
3. Eckhorn R, Reitboeck HJ, Arndt M (1990) Feature linking via synchronization among distributed assemblies: simulation of results from cat cortex. Neural Comput 2(3):293–307
4. Eckhorn R, Frien A, Bauer R (1993) High frequency oscillations in primary visual cortex of awake monkey. NeuroReport 4(3):243–246
5. Wang ZB, Ma YD, Chen FY (2010) Review of pulse-coupled neural networks. Image Vision Comput 28(1):5–13
6. Rafael CG, Richard EW (2010) Digital Image Processing, 3rd edn. Publishing house of electronics industry, Beijing
7. Li CH, Lee CK (1993) Minimum cross entropy thresholding. Pattern Recogn 26(4):617–625
8. Xu SZ, Liu H, Song EM (2011) Marker-controlled watershed for lesion segmentation in mammograms. J Digit Imaging 24:754–763

Locality Preserving Discriminant Projection for Total-Variability-Based Language Recognition

Xianliang Wang, Jinchao Yang, Chunyan Liang, Ruohua Zhou and Yonghong Yan

Abstract In this paper, we introduce a new subspace learning algorithm in language recognition called locality preserving discriminant projection (LPDP). Total variability approach has been the state of art in language recognition, and it preserves most of the discriminant information of languages. Locality preserving projection (LPP) has been proved effective in language recognition, but it can only preserve the local structure of languages. LPDP method used in the total variability subspace can preserve both local structure and global discriminant information about the languages. Experiments are carried out on NIST 2011 Language Recognition Evaluation (LRE) database. The results indicate that LPDP language recognition system performs better than LPP language recognition system and total variability language recognition system in 30 s tasks. In addition, we also give the results of the total variability and LPDP language recognition systems on NIST 2007 LRE 30 s database.

1 Introduction

Language recognition aims to determine the language given a segment of speech. Many language recognition techniques have been developed over the past few decades. Total variability method has been proposed and widely used recently [1, 2]. Total variability uses factor analysis technique to find a low-dimensional subspace called total variability space which contains both the speaker and the channel variability.

Total variability is an effective dimension-reduced method. In total variability, high-dimensional GMM supervector is projected onto a low-dimensional space

X. Wang (✉) · J. Yang · C. Liang · R. Zhou · Y. Yan
Key Laboratory of Speech Acoustics and Content Understanding, Institute of Acoustics, Chinese Academy of Sciences, Beijing, China
e-mail: wangxianliang@hccl.ioa.ac.cn

F. Sun et al. (eds.), *Foundations and Practical Applications of Cognitive Systems and Information Processing*, Advances in Intelligent Systems and Computing 215,
DOI: 10.1007/978-3-642-37835-5_39,

with few discriminative and language-dependent information lost. LDA [3] is also a successfully subspace learning method, and has been one of the most popular techniques for speaker recognition and language recognition. Locality preserving projection (LPP) [4, 5] is a new linear dimensionality reduced algorithm, and it gains an embedding that preserves local and linear information. It is different from LDA which effectively preserves global structure and linear manifold.

Total variability method can be seen as a new feature extractor. New features extracted from it capture most of the discriminative language dependent information in low-dimensional subspace. LDA takes consideration of the label information for recognition which maximizes the between-class scatter matrix while minimizing the within-class scatter matrix in the project subspace. Thus, it has strongly discriminant ability. Results show that dimension-reduced method such as LDA after total variability in language recognition can obtain better performance.

In [6], Jinchao Yang introduced LPP to language recognition. LPP gains an embedding preserving local and linear information by building a graph incorporating neighborhood information of the data set. In Jinchao Yang's work, LPP combining with state-of-the-art systems such as total variability, MMI, and GMM-SVM systems made great improvement in both EER and minDCF.

However, LPP fails to take account of the discriminant information of the languages, which is important for language recognition. A new subspace learning method based on LPP and LDA called locality preserving discriminant projection (LPDP) [7] was successfully used in face recognition, and it contains the global discriminant structure while preserving the local information. LPDP outperforms LPP for which LPDP tries to find the subspace that maximizes the between-class distance while minimizing the within-class distance. We can call both LPP and LPDP laplacian supervector extraction methods.

In this paper, we introduce LPDP to the total variability subspace. The total variability subspace preserves most of the discriminant information about languages because it contains both the speaker and the channel variability. Hence LPDP after total variability analysis can reduce the transformation difference between total variability and LPDP factor, and in the meanwhile make different languages more discriminative.

SVM [1] classifiers are used to model the laplacian supervector and LDA and diagonal covariance Gaussians are used as the backend in Language Score Calibration.

This paper is organized as follows: In Sect. 2, we give an introduction of total variability language recognition system and Support Vector Machines. Section 3 shows the proposed LPDP language recognition system in detail. The experimental results are presented in Sect. 4. Finally, conclusions are given in Sect. 5.

2 Background

2.1 Total Variability Language Recognition System

The total variability approach has become the state of the art in both speaker verification and language recognition. It defines a new low-dimensional space mapping the high-dimensional GMM supervector to a low-dimensional and length-fixed vector.

For a given utterance, the language and variability dependent supervector is denoted as Eq. (1)

$$\mathbf{M} = \mathbf{m} + \mathbf{Tw} \tag{1}$$

where $\mathbf{m}$ is the UBM supervector, $\mathbf{T}$ is language total variability space, and $\mathbf{w}$ is a standard-normally distributed latent variable called language total factor vector. We can assume the language total factor vector model as a new feature extractor that projects an utterance into a low rank space $\mathbf{T}$ to get a language and channel-dependent language total factor vector $\mathbf{w}$.

Total variability method can be used to reduce the dimension of GMM supervector before SVM model. Total variability has been successfully used in language recognition. It preserves most of the language-dependent information in a low-dimensional subspace.

2.2 Support Vector Machines

SVM [8] is a popular technique for discriminative classification. We employed SVM classifiers to model the laplacian supervector. The best separator of an SVM is defined by a kernel function as follows:

$$f(\mathbf{x}) = \sum_{\mathbf{i=1}}^{\mathbf{N}} \alpha_{\mathbf{i}} \mathbf{t_i} \mathbf{K}(\mathbf{x}, \mathbf{x_i}) + \mathbf{b} \tag{2}$$

where N is the number of support vectors, α_i and b are the SVM parameters during the training step, and t_i is the label of the support vectors $\mathbf{x_i}$. The value of the label is either 1 or -1, depending upon whether the corresponding support vector belongs to class 0 or 1.

The kernel function $K(\cdot, \cdot)$ can be expressed as

$$K(\mathbf{x}, \mathbf{x_i}) = \phi(\mathbf{x})' \phi(\mathbf{x_i}) \tag{3}$$

where $\phi(\mathbf{x})$ is a mapping from the input space to a possibly infinite dimensional SVM expansion space.

3 Locality Preserving Discriminant Projection

LPP reserves important aspects of the intrinsic nonlinear manifold structure by preserving local structure. LDA has the advantage that it can maximize the discrimination of different classes while minimizing the intra-class variability. We introduce a new subspace learning algorithm LPDP based on LPP and LDA which preserves both local characteristic and global discriminant structures. The details of LPDP are stated as follows.

3.1 Locality Preserving Projection

Given N samples, $\mathbf{X} = [\mathbf{x_1}, \mathbf{x_2}, \ldots, \mathbf{x_N}]$, LPP aims to find a transformation matrix $\mathbf{A}$ that can map the N samples to a new subspace. LPP is a minimization problem as [5]

$$arg \min_{\mathbf{a}:\mathbf{a}^T\mathbf{X}\mathbf{L}\mathbf{X}^T\mathbf{a}=1} \mathbf{a}^T\mathbf{X}\mathbf{L}\mathbf{X}^T\mathbf{a} \tag{4}$$

The transformation vector $\mathbf{a}$ is given by the minimum eigenvalue solution to the generalized eigenvector problem:

$$\mathbf{X}\mathbf{L}\mathbf{X}^\mathbf{T}\mathbf{a} = \lambda\mathbf{X}\mathbf{D}\mathbf{X}^\mathbf{T}\mathbf{a} \tag{5}$$

where $\mathbf{D}$ is a diagonal matrix and D_{ii} is column sums of $\mathbf{W}$, $D_{ii} = \sum_j W_{ij}$, **L=D-W** is the Laplacian matrix.

We used k-nearest-neighbor graph method. Let G denote a graph with m nodes. We put an edge between nodes i and nodes j if nodes i is among k nearest neighbors of j or nodes j is among k nearest neighbors of i.

The elements of similarity matrix $\mathbf{W}$ is calculated as follows:

$$W_{ij} = e^{-\frac{(w_i - w_j)^2}{t}} \tag{6}$$

The justification for this choice of weights can be traced back to [9].

Let $\alpha_0, \alpha_1, \ldots, \alpha_{l-1}$ be the solution of (5), ordered according to their eigenvalues, $\lambda_0, \lambda_1, \ldots, \lambda_{l-1}$. Thus, the embedding is as follows:

$$\mathbf{x_i} \rightarrow \mathbf{y_i} = \mathbf{A}^\mathbf{T}\mathbf{x_i}, \mathbf{A} = (\alpha_\mathbf{0}, \alpha_\mathbf{1}, \ldots, \alpha_{\mathbf{l-1}}) \tag{7}$$

where $\mathbf{y_i}$ is a l dimension vector, and $\mathbf{A}$ is a transformation matrix.

3.2 Linear Discriminant Analysis

LDA is a well-known method for encoding discriminant information. It encodes discriminant information by maximizing the variance between languages and minimizing the intra-class variance. The LDA subspace is derived from the within-class variance $\mathbf{S_w}$ and the between-class variance $\mathbf{S_b}$. $\mathbf{S_w}$ and $\mathbf{S_b}$ are defined as follows:

$$\begin{aligned}\mathbf{S_w} &= \sum_{i=1}^{c}\sum_{k=1}^{N_i}(\mathbf{X_{ik}} - \mathbf{m_i})(\mathbf{X_{ik}} - \mathbf{m_i})^{\mathbf{T}} \\ \mathbf{S_b} &= \sum_{i=1}^{c} N_i(\mathbf{m_i} - \mathbf{m})(\mathbf{m_i} - \mathbf{m})^{\mathbf{T}}\end{aligned} \tag{8}$$

where c is the total number of language class, N_i is the number of utterances for language i, $\mathbf{m_i}$ is the mean vector of the language i, and $\mathbf{m}$ is the mean of the entire vectors. The columns of the projection matrix $\mathbf{A}$ are obtained by solving the general eigenvalue problem as follows:

$$\mathbf{S_b}\upsilon = \lambda\mathbf{S_w}\upsilon \tag{9}$$

where λ is the diagonal matrix of eigenvalues.

3.3 Locality Preserving Discriminant Projection

The introduced LPDP algorithm combines the advantages of both LPP and LDA. LPP fails to capture the discriminant language-dependent information. We propose LPDP algorithm which adds discriminant information to LPP. It aims to find an optimal subspace for classification which maximizes the following optimized function:

$$J = max\ \mathrm{tr}(\mathbf{a^T}(\mathbf{S_b} - \mathbf{S_w})\mathbf{a}) \tag{10}$$

It maximizes the between-class variance and minimizes the within-class variance. If it combines with the optimized function of LPP, the whole samples will be more discriminant. The LPDP algorithm is the following optimal problem:

$$\begin{aligned}&min\ \mathrm{tr}(\mathbf{a^T}\mathbf{X}\mathbf{L}\mathbf{X^T}\mathbf{a}) \\ &max\ (\mathbf{a^T}(\mathbf{S_b} - \mathbf{S_w})\mathbf{a}) \\ &\mathbf{a^T}\mathbf{X}\mathbf{L}\mathbf{X^T}\mathbf{a} = \mathbf{1}\end{aligned} \tag{11}$$

We get the generalized eigenvector problem using Lagrangian multiplier:

$$(\mathbf{X}\mathbf{L}\mathbf{X^T} - (\mathbf{S_b} - \mathbf{S_w}))\mathbf{a} = \lambda\mathbf{X}\mathbf{D}\mathbf{X^T}\mathbf{a} \tag{12}$$

The vectors $\mathbf{a_i}$ that minimize the objective function are given by minimum eigenvalues solutions to the generalized eigenvalues problem. Let the column vectors $\mathbf{a_0}, \ldots, \mathbf{a_{l-1}}$ be the solutions of Eq. (12), ordered according to their eigenvalues, $\lambda_0 < \lambda_1 < \cdots < \lambda_{l-1}$. The transformation matrix is composed of the vectors $\mathbf{a_i}$.

The embedding was as follows:

$$\mathbf{x} \rightarrow \mathbf{y} = \mathbf{A}_{\mathbf{LPDP}}^{\mathbf{T}}\mathbf{x} \tag{13}$$

where $\mathbf{x}$ is the total variability factor, $\mathbf{y}$ is the low-dimensional vector, and A_{LPDP} is a transformation matrix.

In this way, the total variability is projected to LPDP subspace to reduce transformation difference between total variability and LPDP factor, and in the meanwhile enhance intrinsic difference between the languages.

4 Experiments

Our experiments were carried out on the NIST LRE 2011 and 2007 evaluation database. The training data was primarily from CallFriend corpora, CallHome corpora, Mixer corpora, OHSU corpora, OGI corpora, and data from VOA as supplied by NIST. The 2011 development data consist of LRE03, LRE05, LRE07, LRE09Train. There were 24 target languages in corpora of 2011 evaluation database: Arabic Iraqi, Arabic Levantine, Arabic Maghrebi, Arabic MSA, Bengali, Czech, Dari, English American, English India, Farsi/Persian, Hindi, Lao, Mandarin, Panjabi, Pashto, Polish, Russian, Slovak, Spanish, Tamil, Thai, Turkish, Ukrainian, and Urdu. LRE 2007 evaluation database contained 14 languages: Arabic, Bengali, Chinese (Cantonese, Mandarin, MinNan, and Wu), English (American, Indian), Farsi, German, Hindustani (Hindi, Urdu), Japanese, Korean, Russian, Spanish (Caribbean, Non-caribbean), Thai, Tamil, and Vietnamese. We used equal error rate (EER) and the minimum decision cost value (minDCF) as metrics for evaluation.

4.1 Setup

The feature we used in our system was MSDC feature, which was 7 MFCC coefficients concatenated with SDC 7-1-3-7 feature. Each frame was totally in 56 dimension coefficients. The feature warping and cepstral variance normalization were applied on the previously extracted MSDC feature which results that each feature was normalized to mean 0 and variance 1. Eigenchannel adaptation [10] technique was used to compensate the intersession variability in feature domain.

After MSDC feature was extracted, total variability spaces were estimated as Sect. 2.1. The GMM supervector was projected to total variability spaces. The total variability factor vectors can be seen as new features in a low-dimension space. We then used LPDP technique to the new features. The LPDP transformation matrix A_{LPDP} was learned as Sect. 3.3.

Our experiments were implemented using the SVMTorch [11] with a linear inner-product kernel function, and the laplacian supervector was modeled by SVM. LDA and diagonal covariance Gaussians [12, 13] were used to calculate the log-likelihoods for each target language and achieved improvement in detection performance.

4.2 Results

First, total variability language recognition system followed by LDA is experimented on 2011 NIST LRE database. Then, we export to Laplacian language recognition system (LPP) and LPDP language recognition systems.

In Table 1, we give the performance of the total variability language recognition system, Laplacian language recognition system, Laplacian followed by LDA language recognition system and the proposed Local Preserving Discriminant Projection language recognition system on NIST 2011 Language Recognition Evaluation 30 s corpus. EER and minDCF are observed. From the table, we can see that LPDP performs better than the state-of-the-art total variability method, and LPDP has great advantage over the Laplacian approach. We can also see that LDA after LPP does not receive better result than only LPP or LPDP.

In Table 2, we presented the score fusion results of the total variability and LPP language recognition system, the total variability and LPDP language recognition

Table 1 Results of the total variability, LPP, and LPDP systems on 2011 LRE database

System	EER	MinDCF
Total variability (a)	9.72	10.29
LPP (b)	11.42	11.90
LPP + LDA (c)	11.94	12.29
LPDP (d)	9.14	9.55

Table 2 Score fusion results of total variability and LPP language recognition system, total variability, and LPDP language recognition system on 2011 LRE database

System	EER	MinDCF
a + b	9.57	10.05
a + c	9.71	10.13
a + d	9.02	9.46

Table 3 Results of the total variability and LPDP systems on 2007 LRE database

System	EER	MinDCF
Total variability (a)	3.15	2.61
LPDP (b)	3.15	2.77
a + b	2.92	2.45

system. For simplicity, we added the corresponding scores together simply as the fusion results.

Results show that LPDP is more suitable for language recognition than LPP, and it has improved by 5.97 % on EER and 7.19 % on minDCF compared to the total variability system, and 4.49 % on EER and 4.98 % on minDCF compared to the fusion system of the total variability and LPP. The fusion system of the total variability and LPDP had an improvement of 5.75 % on EER and 5.87 % on minDCF compared to the fusion system of the total variability and LPP. Combining the results of Tables 1 and 2, we realize that LPDP can obtain better performance than state-of-the-art total variability language recognition system, the recently proposed LPP language recognition system, and the fusion system of the total variability and LPP.

By the way, we give the results of the total variability and LPDP language recognition systems on NIST 2007 Language Recognition Evaluation (LRE) database in Table 3.

Results show that on 2007 LRE database, LPDP has almost equivalent performance to the total variability system, but the fusion system of LPDP and the total variability system gains 7.3 % improvement on EER and 11.55 % improvement on minDCF. Results on 2007 LRE database are basically consistent with the results on 2011 LRE database.

All the results presented above indicate that LPDP is an effective method in the total variability subspace for language recognition.

5 Conclusion

In this paper, we propose a new subspace learning algorithm called LPDP based on LPP language recognition system. LPP language recognition system performs better when combining with the state-of-the-art total variability language recognition systems. LPP preserves local structure while suffering from a limitation that it does not encode discriminant information. LPDP language recognition algorithm introduces discriminant information into the objection function of LPP. It not only retains the locality preserving characteristic but also preserves the global discriminant structures. Experiment results show that LPDP is an effective method for language recognition.

Acknowledgments This work is partially supported by the National Natural Science Foundation of China (Nos. 10925419, 90920302, 61072124, 11074275, 11161140319).

References

1. Dehak N, Dehak R, Kenny P, Brummer N, Ouellet P, Dumouchel P (2009) Support vector machines versus fast scoring in the low-dimensional total variability space for speaker verification. In: Tenth Annual conference of the international speech communication association
2. Dehak N, Kenny P, Dehak R, Dumouchel P, Ouellet P (2011) Front-end factor analysis for speaker verification. IEEE Trans Audio Speech Lang Process 19(4):788–798
3. Balakrishnama S, Ganapathiraju A (1998) Linear discriminant analysis-a brief tutorial. In: Institute for signal and information processing
4. Niyogi X (2004) Locality preserving projections. In: Advances in neural information processing systems 16. Proceedings of the 2003 conference, vol 16. The MIT Press, Cambridge, p 153
5. He X, Yan S, Hu Y, Niyogi P, Zhang H (2005) Face recognition using laplacianfaces. IEEE Trans Pattern Anal Mach Intell 3:328–340
6. Yang J (2011) Language recognition with locality preserving projection. In: ICDT 2011 the 6th international conference on digital telecommunications, pp 51–55
7. Gui J, Jia W, Zhu L, Wang S, Huang D (2010) Locality preserving discriminant projections for face and palmprint recognition. Neurocomputing 73(13):2696–2707
8. Hearst M, Dumais S, Osman E, Platt J, Scholkopf B (1998) Support vector machines. IEEE Intell Syst Appl 13(4):18–28
9. Belkin M, Niyogi P (2001) Laplacian eigenmaps and spectral techniques for embedding and clustering. Adv Neural Inf Process Syst 14:585–591
10. Castaldo F, Colibro D, Dalmasso E, Laface P, Vair C (2007) Compensation of nuisance factors for speaker and language recognition. IEEE Trans Audio Speech Lang Process 15(7):1969–1978
11. Collobert R, Bengio S (2001) SVMTorch: support vector machines for large-scale regression problems. J Mach Learn Res 1:143–160
12. Campbell W, Campbell J, Reynolds D, Singer E, Torres-Carrasquillo P (2006) Support vector machines for speaker and language recognition. Comput Speech Lang 20(2):210–229
13. Singer E, Torres-Carrasquillo P, Gleason T, Campbell W, Reynolds D (2003) Acoustic, phonetic, and discriminative approaches to automatic language identification. In: Eighth European conference on speech communication and technology

Adaptive Spectrum Detecting Algorithm in Cognitive Radio

Yun Liu, Qicong Peng, Fuchun Sun, Huaizong Shao, Xingfeng Chen and Ling Wang

Abstract Cognitive radio (CR) network can make an opportunistic access of spectrum licensed to a primary user (PU). The CR must perform spectrum sensing to detect active PU, thereby avoiding interfering with it. This chapter focuses on adaptively spectrum sensing, so that negative impacts to the performance of the CR network are minimized when CR users experience both stochastic data arrival and time-varying channel. Since the frequency of the spectrum sensing has a directly impact on system throughput and the probability of collision between the PU and CR user, the PU activity is modeled based on the characteristic analysis of the PU spectrum utilization. Based on that, an efficient adaptive sensing algorithm that takes into account the system stability, collision, and throughput is proposed. The CR users can make a balance between them by utilizing a "periodic control factor" which controls the adaptive adjustment of the spectrum sensing frequency. The simulation results indicate that the proposed algorithm has excellent performance on collision probability and throughput compared with conventional periodic spectrum sensing scheme. Meanwhile, it is shown that the proposed algorithm has low implementation complexity for practical applications.

Keywords Cognitive radio (CR) · Adaptive spectrum sensing · Random distribution · Spectrum hole · Virtual transmitting slot

Y. Liu · Q. Peng · H. Shao · L. Wang
School of Communication and Technology Engineering, University of Electronic Science and Technology of China, Chengdu 610054, China
e-mail: liuyun001@uestc.edu

F. Sun (✉)
State Key Lab of Intelligent Technology and Systems, Department of Computer Science and Technology, Tsinghua University, Beijing 100084, China
e-mail: fcsun@mail.tsinghua.edu.cn

X. Chen
State Key Laboratory of Remote Sensing Science, Institute of Remote Sensing Applications, CAS, Beijing 100101, China

F. Sun et al. (eds.), *Foundations and Practical Applications of Cognitive Systems and Information Processing*, Advances in Intelligent Systems and Computing 215,
DOI: 10.1007/978-3-642-37835-5_40,

1 Introduction

With the increasing popularity of wireless services, especially the Wi-Fi and 3G wireless technology in the last decade, the application of 4G and the Internet of Things (IOT) [1] in the future will face no spectrum available. In fact, recent measurements by Federal Communications Commission (FCC) [2] have shown that 15–85 % of the allocated spectrum resources in the US are not utilized because of the traditional approach of fixed spectrum allocation to licensed networks [3, 4]. The conflict between the scarcity of unallocated spectrum resources and the low utilization of most allocated spectrum bands motivated the emerging of CR. The CR as a revolutionary technology of the spectrum sharing is considered as the best schedule of resolving the spectrum "scarcity" and improving the spectrum utilization [5–7]. In a CR system, secondary users (SUs) can make opportunistic use of unoccupied spectrum bands as long as it do not cause harmful interference to primary users (PUs). Such opportunistic spectrum sharing technology can improve spectrum efficiency and the system capacity significantly, thereby receiving much attention recently.

How to discover spectrum access opportunities and avoid harmful interference are the key issues to be solved in CR system [8]. We term the functionality of CR as spectrum sensing. A number of detection techniques [9–12] have been investigated for spectrum sensing in the Port Physical Layer (PHY). Since the SU cannot achieve full-band and real-time spectrum detection in the PHY subject to the limitations of the hardware and energy, the implementation of spectrum sensing should be scheduled in the Medium Access Control (MAC) layer. So the spectrum sensing is not just a binary hypothetical test in the PHY layer, but also includes the sensing mechanism design in the MAC layer. We note that most of the existing work on scheduling spectrum sensing in the CR networks adopts a periodic sensing strategy [13–21], e.g., sensing activities are carried out in fixed interval as depicted in Fig. 1. The proposed approaches [19–21] suggest a statistical model of the PU activity based on empirical data and proposed channel-access strategies that maximize the channel utilization while limiting interference to the PU. The authors have proposed the adaptive sensing methods that select the frequency channels based on the historical information about the PU channel usage in [22] and [23]. In general, cognitive devices aimed not to cause interference to PU postpone the entire transmitting on that channel, i.e., quiet sensing periods

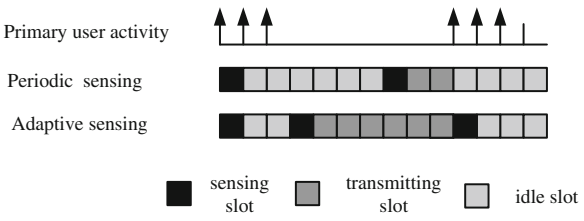

Fig. 1 The adaptive sensing compared with the periodic sensing

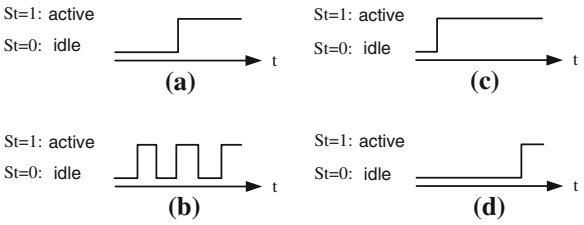

Fig. 2 The "idle/active" characteristics of authorized channel

must be scheduled. Note that scheduling quiet sensing periods results in negative impacts to system throughput. An approach is to improve the spectrum utilization by reducing the sensing time [24, 25], but an impact is imposed on the reliability of spectrum sensing. In the actual network, the characteristics of PU's spectrum utilization will inevitably vary with different operation loads of users in different time periods, as shown in Fig. 2. In this case, the periodic sensing mechanism will be unable to well meet the dynamic time-varying requirement of spectrum utilization characteristics, which will cause performance degradation. In the literature [26, 27], a variable periodic adaptive spectrum sensing and data transmission algorithm was proposed, thus effectively reducing the probability of system conflict and increasing system capacity.

In the existing literatures, CR system achieves adaptive sensing according to the characteristics of PU's spectrum state. In fact, under the fixed spectrum occupancy of PU, behavior frequency is also a major factor to constrain CR system. It can be seen from Fig. 2 that in the same observation time (a) and (b) have the same spectrum occupancy, but in the case of (b), PUs appear more frequently, causing frequent switching of CR users, which may lead to system instability, and even drop-calls. Therefore (a) has a better stability. The existing spectrum sensing algorithms does not make full study on this aspect. Based on the above considerations, this article takes into account the behavior frequency of PU. On the basis of predicting the idle spectrum duration, an adaptive sensing algorithm is proposed, called ASCFSIC algorithm (Adaptive sensing algorithm based on change frequency and state information of channel). Compared with the previous fixed periodic sensing (Fig. 1), this algorithm can adaptively adjust the sensing frequency of CR user based on the behavior change characteristics of PU, so as to effectively improve the utilization of spectrum holes and reduce the probability of system conflict and sensing overhead based on ensuring a certain stability of the system.

The rest of this article is organized as follows: Sect. 2 analyzes the behavior characteristics of PU and CR user, and proposes the principle of optimal sensing algorithm; Sect. 3 describes the adaptive sensing algorithm based on licensed spectrum characteristics and the implementation process; Sect. 4 gives the simulation results and performance analysis; finally, Sect. 5 summarizes the whole article.

2 Algorithm Principle

In CR system, the idle spectrum is constrained by the behaviors of PUs. To protect the primary users from interference, whenever the primary users become active, CR users have to vacate the current channel. Therefore, this type of spectrum is different from fixed-allocation spectrum, characterized by instability, i.e., the uncertainty in idle duration. Based on the characteristic analysis of the PU spectrum utilization, the detection model is established to ensure a certain stability of the system and maximize channel capacity in this article. By adaptively adjusting the detection frequency of CR users, it achieves the balance between channel capacity, conflict probability, and system stability. Therefore, even in a case of the same CR system, when the targets are different, the detection frequency of secondary users may also be different.

2.1 System Description

In CR system, when PU does not occupy the channel, CR user is allowed to access the channel. When PU uses the channel and CR user is still transmitting data, a conflict will be generated. In order to protect PU from interference, conflict probability must be limited within a certain range. Therefore, data transmission of each frame must be assigned with spectrum sensing slot. Moreover, in order to achieve accurate spectrum sensing, CR device must remain silent in spectrum sensing time; otherwise, the interference will be caused between CR users, thereby increasing the probability of false alarm. Silent sensing means that CR system must take centralized control over CR users.

2.2 Problem Description

2.2.1 The PU Behavior

The spectrum used by licensed system (referred to as licensed spectrum) has two states, i.e., “idle” and “active”, as shown in Fig. 2. The variable is defined to indicate the state of licensed spectrum at the time: represents that the licensed spectrum is idle at the time, while represents that the spectrum is occupied by primary user at the time. Thus, the occupancy characteristics of PU over licensed spectrum (can also be referred to as the characteristics of licensed spectrum) can be characterized by two parameters: (1) the spectrum occupancy within the observation time; (2) the refresh times of “idle–active” spectrum within the observation time.

It can be seen from Fig. 2 that in the same observation time (a) and (b) have the same spectrum occupancy, but in the case of (b), PUs appear more frequently, causing frequent switching of CR users. Therefore, (a) has a better stability; (c) and (d) have the same occurrence number of primary users, but (c) has higher spectrum occupancy. Therefore (d) has a better usability. Within the observation time, the occupancy of PU over licensed spectrum characterizes the availability of this spectrum. The higher the occupancy is, the poorer the availability of spectrum will be for CR system. However, the occupation number of PU over this spectrum characterizes the stability of spectrum. The fewer the occurrence number of PU is, the higher the stability of this spectrum will be for CR system. Therefore, in order to fully and accurately describe the characteristics of licensed spectrum, both factors should be jointly considered.

The statistical occupancy of licensed spectrum in the observation time can be expressed as below:

$$\bar{U} = E\left[\sum_{k-1}^{L} Y_k/\Delta t\right] \tag{1}$$

where L is the change times of PU in the observation time Δt, Y_k indicates kth active duration of licensed channel in Δt. Thus, in the next time period, the idle duration of licensed channel, i.e., the available duration for CR user, can be expressed as below:

$$T_{\text{license}} = [1 - \bar{U}] * \Delta t/L \tag{2}$$

The reliability of licensed spectrum can be defined as below:

$$S = T_{\text{license}}/\Delta t = [1 - \bar{U}]/L \tag{3}$$

The value changes in the range [0, 1]. It can be seen from Eq. (3) that in the condition of equal spectrum occupancy, the more frequently the PU changes, i.e., the greater the L is, the smaller the S will be, and the worse the reliability of licensed spectrum will be. In order to ensure the stability of the system, S should be higher than the threshold $S_{\text{thresh}}^{\text{CR}}$ which CR system can tolerate.

In this article, the spectrum occupancy of PU, i.e. R_{PU}, is defined as below:

$$R_{\text{PU}} = T_{\text{occupy}}/T = 1/(1 + T_{\text{vacant}}/T_{\text{occupy}}) \tag{4}$$

where T_{occupy} and T_{vacant} indicate the duration of active channel and idle channel for PU respectively, and T indicates the time interval between the two occurrences of PU. These three are all random variables, of which the probability density function may change with different CR systems. It can be seen from Eq. (4) that R_{PU} represents the occupancy of licensed spectrum. When R_{PU} is greater than the preset threshold, the channel is considered as busy; when R_{PU} is lower than the preset threshold, the channel is considered as idle, and CR users have more opportunities to access this channel at this time. In order to maintain R_{PU} below the threshold, it is required to meet the condition of smaller T_{occupy} or larger T_{vacant}, or

the both. When T_{vacant} larger, CR user can reduce the sensing times and increase the data transmission slot, so as to improve the system capacity.

2.2.2 The CR User Behavior

Spectrum sensing is the first task in CR systems which aim achieving efficient detection of the presence of PU in addition to avoid interfering to the licensed user. Generally, the longer the value of sensing time, the higher reliability of sensing. In order to increasing the system throughput, CR device achieves reliable sensing as quickly as possible under the performance constraint of probability of detection P_{d} and probability of false alarm P_{f}. In [13], the author derived the minimum sensing time of energy detection as follows:

$$T_{\text{s}} = \frac{\tau}{\gamma^2}(Q^{-1}(P_{\text{f}}) - Q^{-1}(P_{\text{d}})\sqrt{2\gamma + 1})^2 \tag{5}$$

where τ is the interval of channel sampling, γ is signal-to-noise-ratio (SNR), and $Q(.)$ is the complementary distribution function of a standard Gaussian variable.

Different from the licensed system with fixed spectrum allocation, the spectrum used in CR system is obtained by sensing. Therefore, in CR system, the data of each frame must contain a sensing slot. In this article, the first slot of each frame is assumed as spectrum sensing slot, while the remaining slots of a frame are data transmission slots. When PU is detected to be existent, data are transmitted in data transmission slot; when PU is detected to be existent, CR user immediately vacates the channel or remains silent, so that the transmission is empty in data transmission slot, called "virtual transmitting slot". Therefore, the frame structure in this article is unified in the form of 1 sensing slot plus n data transmission slots

$$T_{\text{frame}} = T_{\text{s}} + n * T_{\text{t}} \tag{6}$$

where n is dynamically allocated by algorithm in real time rather than by the traditional fixed-allocation mode, T_{frame} indicates the time of a frame, and T_{t} indicates a data transmission slot. From Eq. (6), the benefits of maximizing the proportion of data transmission slot can be clearly seen: (1) when PU vacates the channel, more slots in transmitting data are used to improve the capacity of CR system; (2) when a PU exists, the "virtual transmitting slot" does not consume system power, so that the increase in transmitting slot means reducing the proportion of sensing slot, thus reducing the overhead of system sensing and saving power consumption.

PUs behavior may change at any moment, i.e., change from idle to active, or from active to idle. Therefore, the data transmission slot of a frame cannot be infinitely long. In data transmission, due to random access of PU, the occupancy of licensed spectrum may change to be different from sensing results, which is called a conflict in this article. Obviously, the conflict probability increases with the increase of data transmission time. The conflict probability in the time interval t is defined as $P_{\text{c}}(t)$.

Thus, in order to protect PU's communication from interference, the conflict probability should be less than the threshold $P_{\mathrm{c}}^{\mathrm{PU}}$ which PU can tolerate.

According to the above analysis, the optimal spectrum sensing algorithm should solve the following problems: (1) the channel is allocated to CR user with the maximum transmission rate, when the licensed channel is idle, i.e., when PU vacates the channel; (2) the change frequency statistics of licensed channel is estimated to determine whether data transmission slot is "virtual transmitting slot" or not; (3) the data transmission slot of each frame is dynamically controlled according to the channel occupancy characteristics of PU.

2.2.3 Optimal Sensing Algorithm

Due to different needs, the optimal sensing algorithms of CR system are generally different. The algorithm which meets the need of CR system and maximizes the system capacity is defined as the optimal spectrum sensing algorithm in this article. Assuming that CR users in CR system have the same data transmission rate, and thus the maximization of system capacity is converted into the maximization of data transmission slot. The cost function is defined as Eq. (7):

$$\gamma = R_{\mathrm{PU}}(t), \quad st.P_{\mathrm{c}}(t) \le P_{\mathrm{c}}^{\mathrm{SU}}, \quad S \le S_{\mathrm{thresh}}^{\mathrm{CR}} \tag{7}$$

When the licensed spectrum is "idle", i.e., PU vacates the channel, the optimal algorithm can be expressed as follows:

$$\begin{aligned} \max_{n} \gamma_{\mathrm{vacant}}(n) = & \frac{n * T_{\mathrm{t}}}{T_{\mathrm{s}} + n * T_{\mathrm{t}}} (1 - P_{c0}(n * T_{\mathrm{t}})) \\ & st.P_{c0}(n * T_{\mathrm{t}}) \le P_{c0}^{\mathrm{PU}} \\ & S \ge S_{\mathrm{thresh}}^{\mathrm{CR}} \end{aligned} \tag{8}$$

where $\gamma_{\mathrm{vacant}}(n)$ indicates the time proportion of data transmission of each frame for CR user, $P_{c0}(n * T_{\mathrm{t}})$ indicates the spectrum occupancy probability of PU in the time $n * T_{\mathrm{t}}$, and P_{c0}^{PU} indicates the maximum conflict probability which PU can tolerate.

When the licensed spectrum is "active", i.e., PU occupies the channel, the data frame of CR user is the "virtual transmitting slot", i.e., the data of each frame has only the spectrum sensing slot, and at this time the maximization of data transmission slot represents the minimization of sensing slot. Thus, the optimal criterion can be expressed as follows:

$$\begin{aligned} \min_{n} \gamma_{\mathrm{occupy}}(n) = & \frac{T_{\mathrm{s}}}{T_{\mathrm{s}} + n * T_{\mathrm{t}}} e^{\frac{n * T_{\mathrm{t}}}{\lambda_i}} \\ & st.1 - e^{\frac{n * T_{\mathrm{t}}}{\lambda_1}} \le P_{c1}^{\mathrm{PU}} \\ & S \ge S_{\mathrm{thresh}}^{\mathrm{CR}} \end{aligned} \tag{9}$$

where $\gamma_{\text{occupy}}(n)$ indicates the time proportion of CR user to use the data of each frame for sensing, $P_{c1}(n * T_t)$ indicates the probability of PU vacating spectrum in the time $n * T_t$, and P_{c1}^{PU} indicates the maximum frame wastage rate which CR user can tolerate.

3 Adaptive Sensing Algorithm Based on Change Frequency and State Information of Channel (ASCFSIC)

Taking into account the stability of CR system, conflict probability, and system capacity, ASCFSIC algorithm achieves a balance between the three by setting threshold to, so as to obtain the optimal spectrum sensing algorithm meeting the system requirements. From Eqs. (8) and (9), it can be seen that the nature of the algorithm is the solution of n under optimal criteria. n represents the data transmission slot of each frame for CR user, and controls data transmission and system performance of CR user. Therefore, n is also referred to as the "control factor".

3.1 Algorithm Description

In this article, assuming that the times of PU vacating and occupying channel within a certain time Δt are subject to Poisson distribution, and thus the random variables T_{vacant} and T_{occupy} obey the exponential distribution with the parameters of $1/\lambda_0$ and $1/\lambda_1$ respectively:

$$T_{\text{space}} \sim f(t) = \frac{1}{\lambda_0} \mathrm{e}^{-\frac{t}{\lambda_0}} \tag{10}$$

$$T_{\text{occupy}} \sim f(t) = \frac{1}{\lambda_1} \mathrm{e}^{-\frac{t}{\lambda_1}} \tag{11}$$

where $f(t)$ is the probability density function of random variables, $1/\lambda_0$ and $1/\lambda_1$ are the exponential parameters of T_{vacant} and T_{occupy} respectively, meeting $E\{T_{\text{vacant}}\} = \lambda_0$ and $E\{T_{\text{occupy}}\} = \lambda_1$. Therefore, the above random variables can be used to analyze the occupancy of licensed channel R_{PU}.

In this article, through statistical analysis on historical information of PU activity, the maximum likelihood algorithm is used to estimate the parameters of λ_0 and λ_1. Because the density functions form of the two random variables is the same, so the maximum likelihood estimation function can be adopted in the form of Eq. (12):

$$L(\lambda) = f(t_1, t_2, \ldots, t_n|\lambda) \tag{12}$$

Thus, the parameter estimation can be obtained as shown in Eq. (13):

$$\hat{\lambda} = \frac{1}{N}\sum_{i=1}^{N} t_i \tag{13}$$

where t_i indicates the ith sample value of random variable, and indicates the change times of PU in the time Δt.

Random variables of T_{vacant} and T_{occupy} obey the exponential distribution with the parameters of $1/\lambda_0$ and $1/\lambda_1$ respectively, and thus the probability distribution function can be expressed as below:

$$F(t) = 1 - \mathrm{e}^{-\frac{t}{\lambda}} \tag{14}$$

In the literature [13], it was proposed that under a certain correct sensing probability P_{d}, the probability of conflict occurrence $P_{\text{c}}(t)$ can be obtained $P_{\text{c}}(t) = F(t) * P_d$.

According to Eqs. (8) and (9), when the licensed spectrum is "idle", i.e., PU does not occupy the channel, ASCFSIC algorithm can be expressed as below:

$$\begin{aligned} \max_n \gamma_{\text{vacant}}(n) = & \frac{n * T_{\text{t}}}{T_{\text{s}} + n * T_{\text{t}}} \left(1 - \left(1 - e^{-\frac{n*T_{\text{t}}}{\lambda_0}}\right) * P_{\text{d}}\right) \\ & st. \left(1 - e^{-\frac{n*T_{\text{t}}}{\lambda_0}}\right) * P_{\text{d}} \le P_{c0}^{\text{PU}} \\ & S \ge S_{\text{thresh}}^{\text{CR}} \end{aligned} \tag{15}$$

When the licensed spectrum is "active", i.e., PU occupies the channel, the algorithm is expressed as below:

$$\begin{aligned} \min_n \gamma_{\text{occupy}}(n) = & \frac{T_{\text{s}}}{T_{\text{s}} + n * T_{\text{t}}} \left(1 - \left(1 - e^{-\frac{n*T_{\text{t}}}{\lambda_1}}\right) * P_{\text{d}}\right) \\ & st. \left(1 - e^{-\frac{n*T_{\text{t}}}{\lambda_1}}\right) * P_{\text{d}} \le P_{c1}^{\text{PU}} \\ & S \ge S_{\text{thresh}}^{\text{CR}} \end{aligned} \tag{16}$$

ASCFSIC algorithm obtains the value n meeting the requirements by solving Eqs. (15) and (16), so that the number of data transmission slot for each frame can be allocated dynamically, in order to adaptively adjust the spectrum sensing frequency and data transmission, effectively improve the spectrum utilization and reduce the probability of system conflict and sensing overhead.

3.2 Algorithm Implementation

(1) Initial stage

At this stage, CR user is ready for access to the licensed channel, and n is initialized as the number of data transmission slot for the first frame. The sensing

slot T_s is calculated in accordance with Eq. (5). The counter is set in the local to calculate the frame number m of PU occupying or vacating spectrum. According to the sensing results of the previous frame and conflict information, the time of occupying or vacating spectrum for one behavior of PU, i.e., $m * (T_s + n * T_t)$, can be calculated and stored in the registers.

(2) Adaptive sensing stage

Two buffers were set with the length of N. When PUs behavior changes, the time of PU occupying and vacating channel, i.e., t^i_{occupy} and t^i_{vacant}, are respectively stored in two buffers. The latest N values are only stored in the buffer. The estimated values of parameter λ_1 and λ_0 are obtained by Eq. (13), $\hat{\lambda_1} = \frac{1}{N}\sum_{i=1}^{N} t^i_{\text{occupy}}$, $\hat{\lambda_0} = \frac{1}{N}\sum_{i=1}^{N} t^i_{\text{space}}$.Through Eqs. (1) and (2), the estimated reliability parameter S of licensed spectrum can be obtained, i.e.,

$$\hat{S} = \frac{\sum_{i=1}^{N} t^i_{\text{space}}}{\sum_{i=1}^{N} t^i_{\text{space}} + \sum_{i=1}^{N} t^i_{\text{occupy}}}.$$

$\hat{\lambda}_0$ is substituted into Eq. (15) to solve the optimal equation, so as to obtain n_{vacant} meeting the conditions, n_{vacant} indicates that the licensed spectrum is "idle", i.e., the number of data transmission slot for each frame allocated to CR user when PU vacates the channel. Similarly, $\hat{\lambda}_1$ is substituted into Eq. (16) to obtain n_{occupy}. n_{occupy} Indicates that the licensed spectrum is "active", i.e., the number of data transmission slot for each frame allocated when PU occupies the channel.

According to the calculated n_{vacant} and n_{occupy}, the data transmission slot of each frame is allocated in real time. When PUs behavior changes, we repeat the above steps to obtain the new n.

4 Simulation Results and Analysis

In this section, simulation verification is conducted on the performance of AS-CFSIC algorithm proposed on the basis of channel state and change frequency. A data transmission slot is set as $T_t = 10$ ms, the licensed spectrum contains ten channels with the bandwidth of 1 MHz, SNR of $\delta = -10$ dB and simulation time of $\Delta t = 100 * T$, i.e., the time interval of 100 consecutive changes of licensed spectrum. A total of 500 Monte Carlo simulations are carried out on the algorithm. In order to analyze and compare the performance of ASCFSIC algorithm, the fixed periodic sensing algorithm in the literature [28] and the QCST algorithm based on channel state in the literature [27] are selected for algorithm contrast in this article,

where the parameters are set as $\lambda_0 = 3\,s$ and $\lambda_1 = 1\,s$. It can be known from Eq. (3) that the maximum stability degree can theoretically reach 0.75 in CR system.

Figure 3 shows the relationship between the threshold required by the stability of CR system and the actual stability of the system. It can be seen from the figure that when the requirement of system stability is lower, the stability of CR system in the three algorithms can all achieve the threshold requirement. With the increase of threshold, i.e., the requirement of system stability is increased, QCST algorithm and periodic algorithm cannot meet the system requirements, but the ASCFSIC algorithm proposed in this article can well meet the system requirements, even when the threshold is less than 0.7. However, when the threshold is greater than 0.75, with the increase of threshold, the actual stability of the interval is only maintained around 0.7, which is because the maximum stability degree which can be theoretically reached in CR system is only 0.75. When the requirement of system stability is greater than 0.75, there are no spectrum resources meeting both threshold requirement and bandwidth requirement.

The change curve of system capacity with the requirement of system stability is shown in Fig. 4. It can be seen from the figure that the capacity of CR system in ASCFSIC algorithm is slightly decreased with the increase of threshold, while the system capacities of periodic algorithm and QCST algorithm are almost not influenced by the requirement of system stability. In addition, the system capacity of periodic sensing algorithm is significantly lower than those of ASCFSIC algorithm and QCST algorithm. Comparing Figs. 3 and 4, it can be seen that QCST algorithm sacrifices the stability of the system to achieve the maximum system capacity, so that it cannot well meet the requirement of system stability. However, the ASCFSIC algorithm proposed in this article meets the requirement of system stability by reducing very small system capacity. Obviously, ASCFSIC algorithm has significant advantages for CR system required to satisfy certain stability.

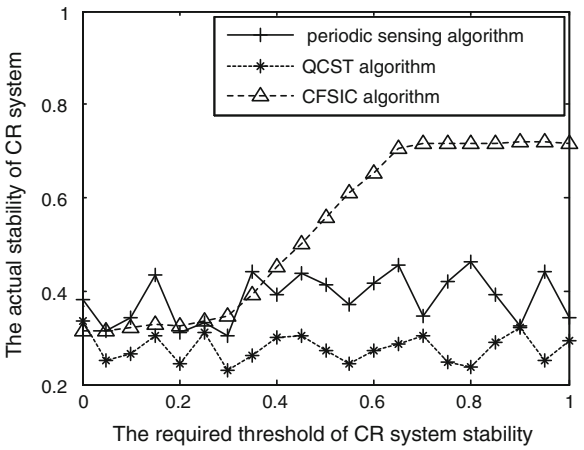

Fig. 3 The actual stability of CR system under different requirements of system stability

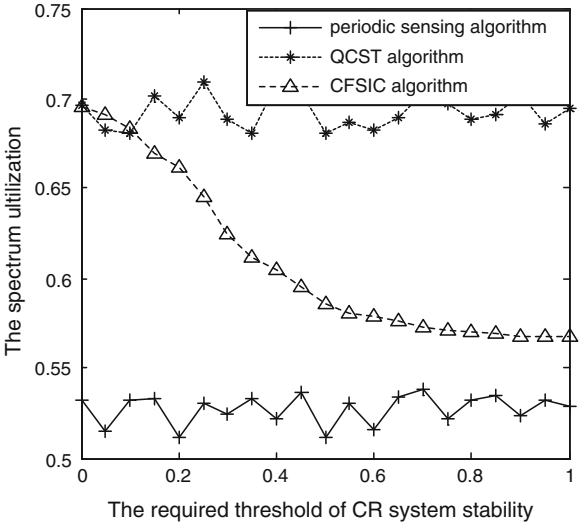

Fig. 4 The system capacity of CR under different requirements of system stability

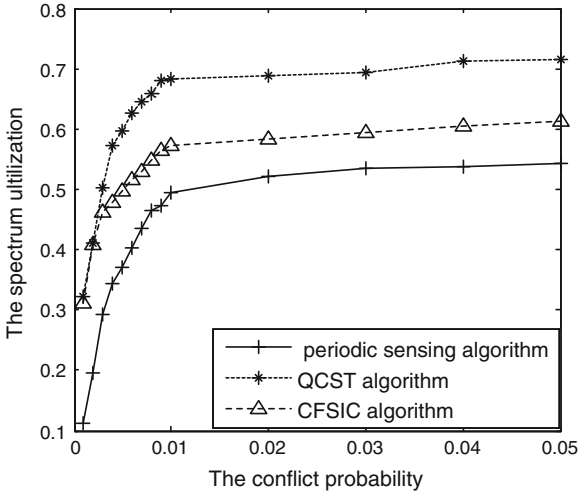

Fig. 5 The spectrum utilization under different conflict probabilities (stability degree of CR system $S > 0.5$)

Figure 5 shows the change curves of spectrum utilizations of three algorithms in different conflict probabilities, when the stability of CR system is greater than 0.5, i.e., It can be seen from the figure that the spectrum utilizations of three algorithms all increase to a certain extent with the increase of conflict probability. When conflict probability is smaller $(P_c \leq 0.01)$, spectral utilization is greatly influenced by conflict probability; when conflict probability reaches a certain level $(P_c \geq 0.015)$, spectrum utilization is almost free from the impact of conflict probability; in the conditions of equal conflict probability, QCST algorithm has the maximum spectrum utilization and ASCFSIC algorithm has slightly poorer

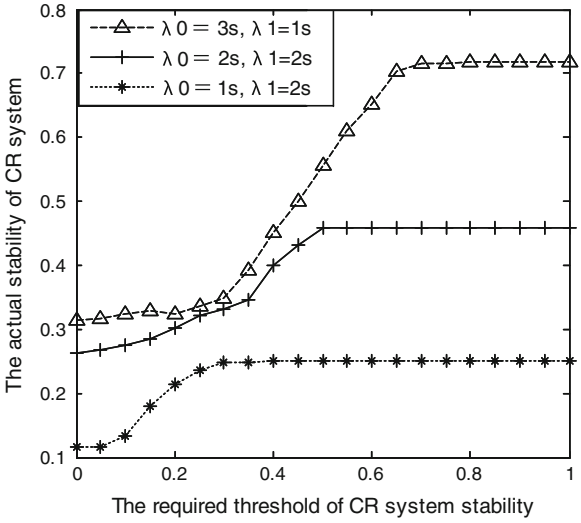

Fig. 6 The actual stability of the system under different parameter values

performance than QCST algorithm due to the constraints of system stability, while the periodic sensing algorithm has the poorest performance.

Figure 6 shows the change curves of the actual stability which CR system using ASCFSIC algorithm can reach according to the threshold of stability requirement, when the parameters λ_0 and λ_1 are different. It can be seen from the figure that the selection of threshold $S_{\text{thresh}}^{\text{CR}}$ needs to consider not only the stability requirement of CR system itself, but also the spectrum occupancy characteristics of PU. For example, when $\lambda_0 = 2\,s$ and $\lambda_1 = 2\,s$, it can be seen from Eq. (3) that the maximum stability degree can theoretically reach 0.5 in CR system. It is obviously impossible to require the stability degree of this system greater than 0.5. Therefore, $S_{\text{thresh}}^{\text{CR}}$ should be less than this theoretical value.

5 Conclusions

In order to reduce the negative impacts from silent spectrum sensing in CR system, based on the characteristic analysis of licensed spectrum, an adaptive sensing algorithm is proposed. This algorithm takes into account the requirements of communication stability and spectrum utilization, and sacrifices very small system capacity for the stability of CR system. CR users change the sensing frequency according to the estimated status and change frequency of licensed spectrum, which meets the requirement of the system stability, effectively improves the system capacity and reduces the conflict probability between PU and CR user. The simulation results show that, this method can effectively improve the system

capacity to achieve the stable communication of CR system under the condition of protecting PU from interference.

References

1. ITU Internet Reports (2005) The internet of things. http://www.itu.int/internetofthings/. Accessed 15 Feb 2010
2. Haykin S (2005) Cognitive radio: brain-empowered wireless communications. IEEE J Sel Areas Commun 23(2):201–220
3. Mchenry M, Spectrum white space measurements. http://www.Newamerica.net/.2007.7
4. Federal Communications Commission: Spectrum policy task force report. http://www.Fcc.gov/sptf/.2007.7
5. Prasad RV, Pawelczak P, Hoffmeyer HA, Berger HS (2008) Cognitive functionality in next generation wireless networks: standardization efforts. IEEE Commun Mag 46(4):72–78
6. Mitola J III, Maguire G Jr (1999) Cognitive radio: making software radio more personal. IEEE Pers Commun 6(4):13–18
7. Akyidiz IF, Lee WY, Vuran MC, Mohanty S (2006) Next generation, dynamic spectrum access/cognitive radio wireless networks:a survey. Comput Network J 50(13):2127–2159
8. Haykin S, Thomson DJ, Reed JH (2009) Spectrum sensing for cognitive radio. Proc IEEE 97:849–877
9. Moghimi F, Nasri A, Schober R (2011) Adaptive Lp–norm spectrum sensing for cognitive radio networks. IEEE Trans Commun 59(7):1934–1945
10. Kim S, Lee J, Wang H, Hong D (2009) Sensing performance of energy detector with correlated multiple antennas. IEEE Signal Process Lett 16:671–674
11. Shen J, Liu S, Zeng L, Xie G, Gao J, Liu Y Optimisation of cooperative spectrum sensing in cognitive radio network. IET Commun 3(7):1170–1178
12. Du K-L, Mow WH (2010) Affordable cyclostationarity-based spectrum sensing for cognitive radio with smart antennas. IEEE Trans Veh Technol 59(4):1877–1886
13. Liang YC, Zeng Y, Peh E, Hoang T (2008) Sensing-throughput tradeoff for cognitive radio networks. IEEE Trans Commun 7(4):1326–1337
14. Lee WY, Akyildiz IF (2008) Optimal spectrum sensing framework for cognitive radio networks. IEEE Trans Wirel Commun 7(10):3845–3857
15. Zhao Q, Chen Y (2007) Decentralized cognitive MAC for opportunistic spectrum access in ad hoc networks: a POMDP framework. IEEE J Sel Areas Commun 25(3):589–600
16. Chen Y, Zhao Q, Swami A (2008) Joint design and separation principle for opportunistic spectrum access in the presence of sensing errors. IEEE Trans Inf Theory 54(5):2053–2071
17. Zhao Q, Krishnamachari B, Liu K (2008) On myopic sensing for multichannel opportunistic access: structure, optimality, and performance. IEEE Trans Wirel Commun 7(12):5431–5440
18. Hoang AT, Liang Y-C, Wong DTC, Zeng Y, Zhang R (2009) Opportunistic spectrum access for energy-constrained cognitive radios. IEEE Trans Wirel Commun 8(3):1206–1211
19. Geirhofer S, Tong L, Sadler BM (2007) Dynamic spectrum access in the time domain: modeling and exploiting white space. IEEE Commun Mag 45(5):66–72
20. Geirhofer S, Tong L, Sadler BM (2008) Cognitive medium access: constraining interference based on experimental models. IEEE J Sel Areas Commun 26(1):95–105
21. Zhao Q, Geirhofer S, Tong L, Sadler BM (2008) Opportunistic spectrum access via periodic channel sensing. IEEE Trans Signal Process 56(2):785–796
22. Wellens M, de Baynast A, Mahonen P (2008) Exploiting historical spectrum occupancy information for adaptive spectrum sensing. In: Proceedings of IEEE WCNC, Las Vegas, pp 717–722

23. Datla D, Rajbanshi R, Wyglinski AM, Minden GJ (2007) Parametric adaptive spectrum sensing framework for dynamic spectrum access network. In: Proceedings of DySPAN, Dublin, Ireland, pp 482–485
24. Han N, Shon SH, Joo JO, Kim JM (2006) Spectral correlation based signal detection method for spectrum sensing in IEEE 802.22 WRAN systems. In: Proceedings of the international conference on advanced communication technology
25. Zeng YH, Liang YC (2009) Eigenvalue based sensing algorithms for cognitive radio. IEEE Trans Commun 57(6):1784–1793
26. Choi KW (2010) Adaptive sensing technique to maximize spectrum utilization in cognitive radio. IEEE Trans Veh Technol 59(2):992–998
27. Hoang AT, Liang Y-C, Zeng Y (2010) Adaptive joint scheduling of spectrum sensing and data transmission in cognitive radio networks. IEEE Trans Commun 58(1):235–246
28. Kim H, Shin KG (2008) Efficient discovery of spectrum opportunities with MAC-layer sensing in cognitive radio networks. IEEE Trans Mob Comput 7(5):533–545

The Autonomous Positioning Method for the Mars Probes Based on Cognizing Optical Information

Yingli Chang, Xiaohua Yuan and Dongmei Huang

Abstract Since Mars probe is very far from the earth during the flight, and the radio delay is up to tens of minutes, it is difficult to provide effective real-time information for the conventional ground-based radio navigation such as DSN of NASA. For probe in communication failure with the earth, it is very important to measure its position and speed based on its surrounding environment information, thus, probe autonomous navigation technology based on the target optical becomes a research focus. This paper first analyzes environment optical information easily perceived by the probe, then designs an autonomous position method based on optical information, at last, conducts a mathematical simulation to the positioning and speed measuring in the assumed Mars exploration Missions 2016. Simulation results show that the accuracy of the proposed method is very close to that of ground radio navigation, and the proposed method is feasible for engineering application.

Keywords Autonomous positioning · Angle between planets · Phase angle · Apparent magnitude formatting

1 Introduction

The distance from Mars Probe to the earth is more than three orders of magnitude of that from Moon Probe to the earth, thus causes a communication delay of tens of minutes. For probe, it is a key issue to obtain its precise position and velocity information, which can support the midcourse correction orbit control tasks and a variety of point control tasks.

Y. Chang (✉) · X. Yuan · D. Huang
Information College, Shanghai Ocean University, Shanghai, China
e-mail: ylchang@shou.edu.cn

Y. Chang
Shanghai Key Lab for Astrophysics, Shanghai, China

F. Sun et al. (eds.), *Foundations and Practical Applications of Cognitive Systems and Information Processing*, Advances in Intelligent Systems and Computing 215,
DOI: 10.1007/978-3-642-37835-5_41,

Currently, probe position and velocity information obtained from ground-based radio measurement networks (such as NASA's DSN network), can satisfy the needs of deep space exploration. But when a transit occurs, the probe antenna direction will be abnormal, which will lead to communication failure between the probe and the earth, the probe can not directly obtain its own location information from ground-based radio measurement networks, and the risk of mission failure will Increase. Therefore, if the flying probe measure its position and speed based on the surrounding environment information, this can not only improve the autonomy of the probe, but also can guarantee the reliability of the probe, thus, autonomous navigation technology based on optical environment information becomes a research focus.

To an assumed Mars exploration mission 2016, in Sect. 1 this paper analyzes environment optical information easily perceived by the probe, in Sect. 2 designs an autonomous optical information-based position method, and in Sect. 3 conduct a mathematical simulation to test the positioning accuracy and the practicality of the proposed method.

2 Information Could be Cognized During Flight

After several centuries of astronomical observations, the ephemeris of giant planets in solar system is very accurate. So usually planet and their satellites are taken as the observation target of autonomous position in deep space exploration. During probe flight to Mars, the optical information in the deep space can be cognized includes planets, moons, or small bodies chord width, land interpersonal dimensions, starlight angular distance, Lu interpersonal angle, angular distance among planets, stellar angular distance. These types of information are shown in Fig. 1.

In theory, the more optical target can be cognized, then the more accurate target ephemeris can be used, and the higher precision of probe positioning can be obtained. But usually, simultaneous observing of more than one planet needs a huge field of view, and there is a big difference between apparent magnitude and phase angle, so it is very difficult to design satisfied navigation sensors. Therefore, during one flight phase, usually only one planetary system is selected as the observed target.

The following analysis is related to angle between planets, phase angle, apparent magnitude, and so on.

2.1 Analysis of the Angle Between Planets

Angle between planets is an important physical quantity to determine the view parameters of navigation sensor field. According to the parameters of the orbit probe transfer from the Earth to the Mars, in following, the angle between planets

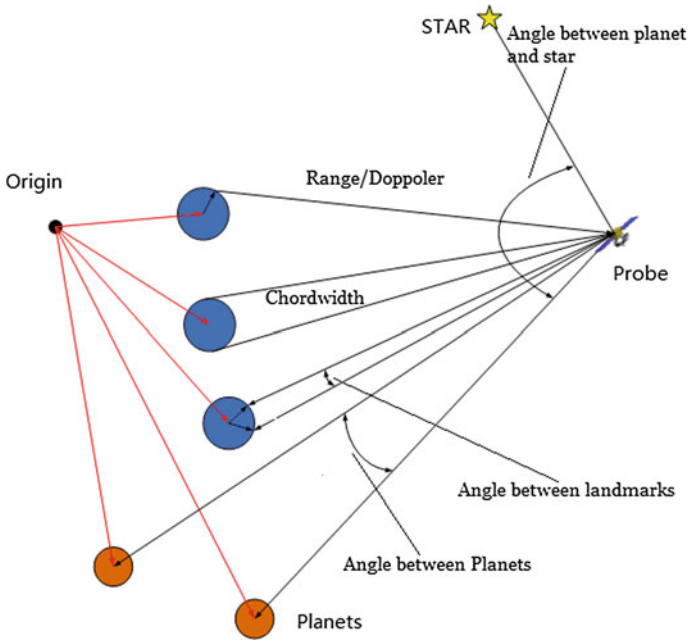

Fig. 1 Information can be cognized in the deep space

after the probe entered in the capture phase has been calculated and analyzed. The change curves of the angle of planets along with the distance between probe and Mars are shown in Fig. 2.

From Fig. 2, we can see if during the preparation for capture multiple planetary systems are needed, on one hand the optical camera must have hundreds of metric-class fields of view, in which it is difficult to obtain higher observation accuracy. And on the other hand, from the following calculation of apparent magnitude and phase angle we can see that besides the target planetary system, it is difficult to find other planetary systems that satisfy the requirements of observation.

2.2 Analysis of Phase Angle

Target phase angle is an important parameter determining the target observability. According to the probe flight orbit, we calculate the angles of each planet during the whole flight of probe. Figure 3 shows the changes of the phase angle of planets along with the distance between probe and Mars.

From Fig. 3, we can see that during probe flight, the phase angle of the Jupiter is the best one for the observability (about more than ten degree), at which nearly the whole of the Jupiter can be observed.

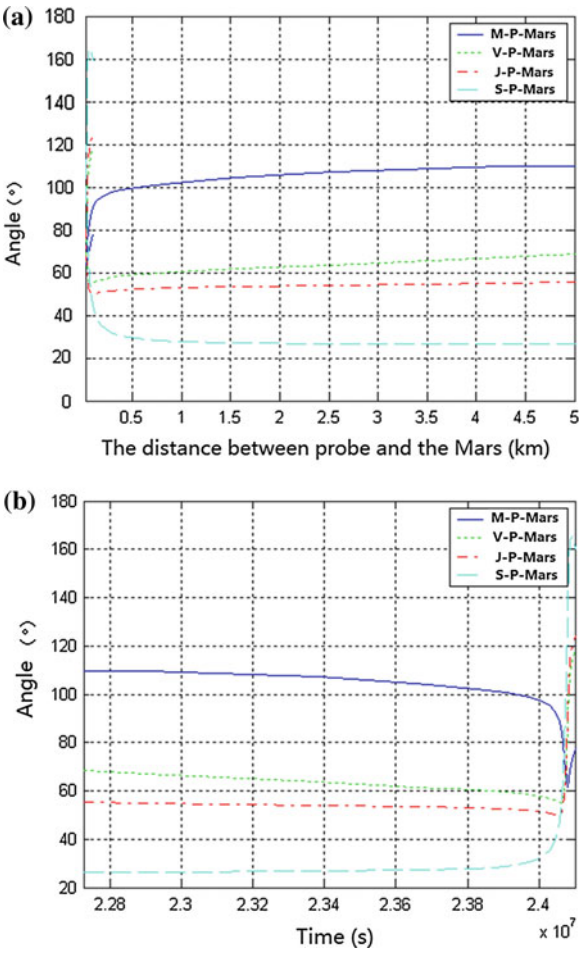

Fig. 2 The changes of the angle of planets along with the distance between probe and mars (**a**) and flying time (**b**)

2.3 Analysis of Target Apparent Magnitude

The apparent magnitude of planet is an important parameter to determine whether the target can be observed.

Similarly according to the parameters of the orbit probe transfer from the Earth to the Mars, in following, the apparent magnitude after the probe entered in the capture phase has been calculated and analyzed. The change curves of the apparent magnitude along with the distance between probe and Mars are shown in Fig. 4.

The results in Fig. 4 show that apparent magnitudes of Jupiter and Saturn are very low (which is about 10), thus the two planets are difficult to be observed. And apparent magnitudes of outer solar planets, such as Mercury, Venus, Earth, and Mars, are higher, thus these planets can be easily observed. Since the apparent

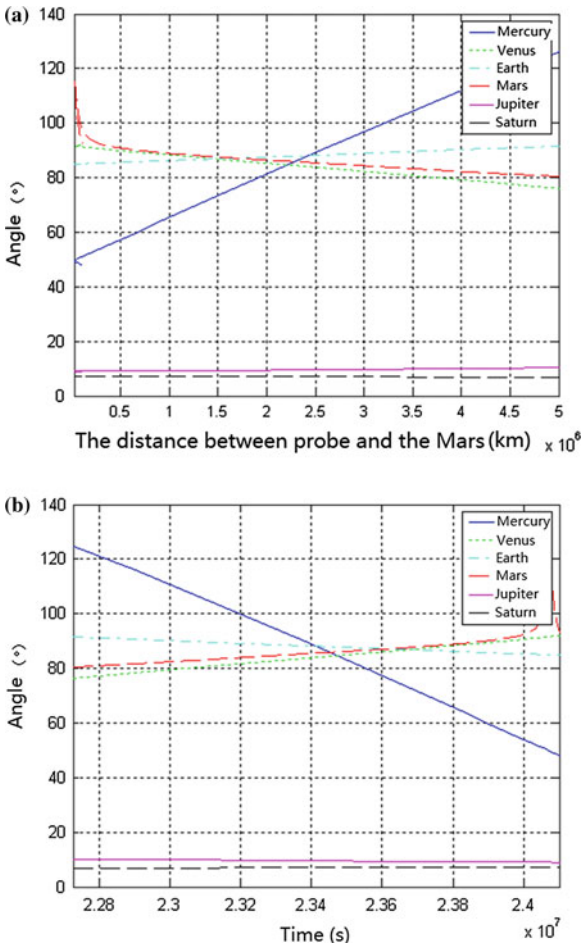

Fig. 3 The changes of the phase angle of planets along with the distance between probe and mars (**a**), and that of flying time (**b**)

magnitude of Mars is the highest one, and it increases with the decrease of distance between probe and Mars, so it can be observed very easily.

2.4 The Choice of Information to be Cognized

Associated with the orbit of probe, the angle of planets, phase angle, apparent magnitude of different object observed, have been calculated and compared. The result shows that the Mars system own good optical condition and is suitable for observing during the flight. The Mars system can be chosen as the target of the optical autonomous navigation system. The Mars chord width and the angle between landmarks on Mars is difficult to be determined precisely, while the

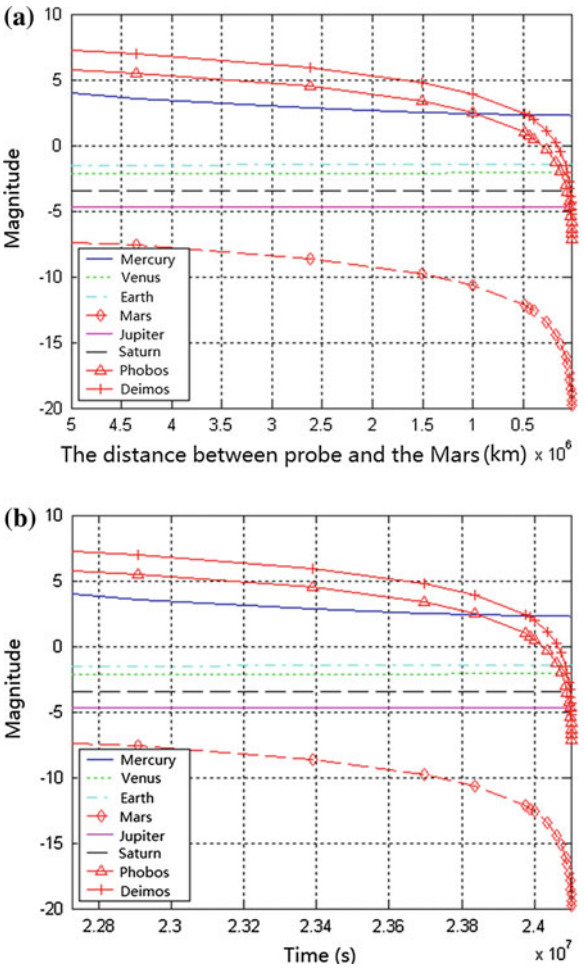

Fig. 4 The change of apparent magnitude of planets along with the distance between probe and mars (**a**), and that of flying time (**b**)

distance between probe and the Mars is far away as hundreds of thousands of kilometers. So, the angle between the Mars vector and stars is the most suitable information which to be cognized for autonomous navigation in the flight.

3 The Autonomous Positioning Method Based on Cognizing Optical Information

3.1 The Theory of Autonomous Positioning

If the value of the probe's velocity refer to the target celestial body is known, the position of probe refer to the celestial body can be determined by cognizing the

aspect of the optical center of the body three times with the camera equipped on the probe. If the aspect of the velocity is also known, the position can be determined by cognizing twice. The observing geometry relations are shown in Fig. 5. In fact, the velocity can be estimated accurately as the magnitude of 1 m/s during the cruise period, therefore it is feasible to navigating autonomously by observing the optical center of the target body. The equation of state is the orbital dynamics equation in mars-center J2000 Inertial coordinate system, and the observation equation is the expression of the line of sight. In order to obtain the more precise estimation, as well as the nonlinear quality of observing the vector of sight and the limited calculating ability of computer equipped on the probe, the Extend Kalman Filter is adopted.

3.2 The Arithmetic of Autonomous Positioning

In the autonomous positioning arithmetic, the equation of state is the orbital dynamics equation in mars-center J2000 Inertial coordinate system. $X = [\vec{r} \quad \vec{v}]^T$ is chosen as the state variable, according to the orbital dynamic model, the equation of state is

$$\dot{X} = \begin{bmatrix} -\frac{\mu}{r^3}x + a_x + a_{1x} \\ -\frac{\mu}{r^3}y + a_y + a_{1y} \\ -\frac{\mu}{r^3}z + a_z + a_{1z} \end{bmatrix} + w \tag{1}$$

In which w is the system modeling error, $a_x\, a_y\, a_z$ is the solar gravity in the mars Inertial coordinate system, $a_{1x}\, a_{1y}\, a_{1z}$ is the mars J2 Perturbation term represented

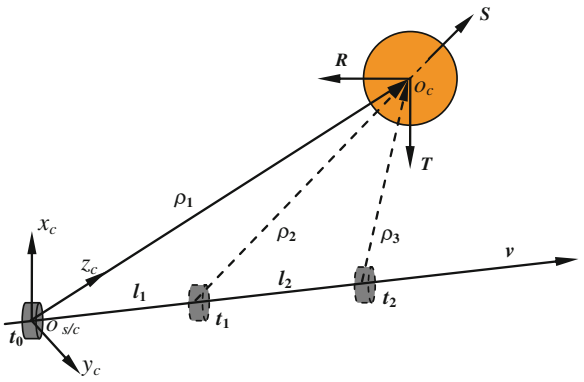

Fig. 5 Schematic diagram of autonomous OpNav

in the mars Inertial coordinate system. So, the equation of state can be determined by Eq. 1 as

$$\dot{X} = f(X) + w \tag{2}$$

The observation equation is the expression of sight. In order to calculating the pixels correspond to the Mars center, the vector of the sigh from the Mars to probe in the mars inertial coordinate system need to be transited to pixel coordinate in the camera. Neglecting the electromagnetic and optical aberration, using the pixel coordinate of the target as observation variable, from simple geometric relationship, we can get

$$\begin{aligned} p &= f\frac{R_{\mathrm{cI}}(1,1)x + R_{\mathrm{cI}}(1,2)y + R_{\mathrm{cI}}(1,3)z}{R_{\mathrm{cI}}(3,1)x + R_{\mathrm{cI}}(3,2)y + R_{\mathrm{cI}}(3,3)z} \\ l &= f\frac{R_{\mathrm{cI}}(2,1)x + R_{\mathrm{cI}}(2,2)y + R_{\mathrm{cI}}(2,3)z}{R_{\mathrm{cI}}(3,1)x + R_{\mathrm{cI}}(3,2)y + R_{\mathrm{cI}}(3,3)z} \end{aligned} \tag{3}$$

In which, p and l is the coordinate of the image of the Mars optical center, R_{cI} is the attitude transiting matrix from the camera coordinate system to inertial coordinate system. Using Eq. 3, the observation equation can be expressed as

$$z = h(X) + v \tag{4}$$

In which, z is observation, v is measurement noise.

In order to estimating the orbit elements more accurately, the choice of filter is very important, which is related with the form of navigation system, the feature of measurement noise, the flight trace, and so on. Taking into account the nonlinear quality of observing the sight vector and the fast calculating requirement in the spacecraft, the navigation arithmetic based on the extend Kalman filter is suitable.

4 Mathematical Simulation

We adopt the autonomous navigation method based on cognizing the optical information of the Mars System mentioned above in an assumed typical Mars exploration mission, and simulate the accuracy of this method mathematically.

Table 1 Mathematical simulation parameters

Parameters	Value
Orbit elements	$a = -4266729.5$ m, $e = 1.854751$, $i = 95°$ Omega = 337.66°, omega = 148.76°, f = −268.26°
Initial position error	[100 km 100 km 100 km]
Initial velocity error	[0.5 m/s 0.5 m/s 0.5 m/s]
The light of sight error	38″

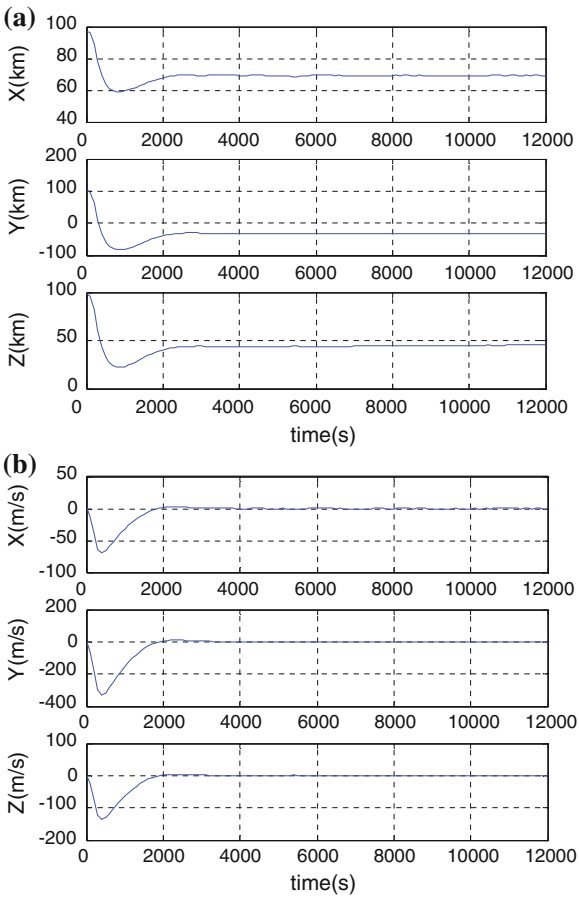

Fig. 6 The error of position and velocity in inertial coordinate system

The value of parameters involved in the mathematical simulation shown in following Table 1.

Using the parameter above, the mathematical simulation platform is constructed. The estimation error of autonomous positioning in inertial coordinate system is shown in Fig. 6, while that in B-plane is shown in Fig. 7.

As Figs. 6 and 7 show the accuracy of autonomous positioning method based on cognizing the optical information of the Mars system is about 90 km, and have slight advantage over ground-base radio navigation whose accuracy is about 100 km.

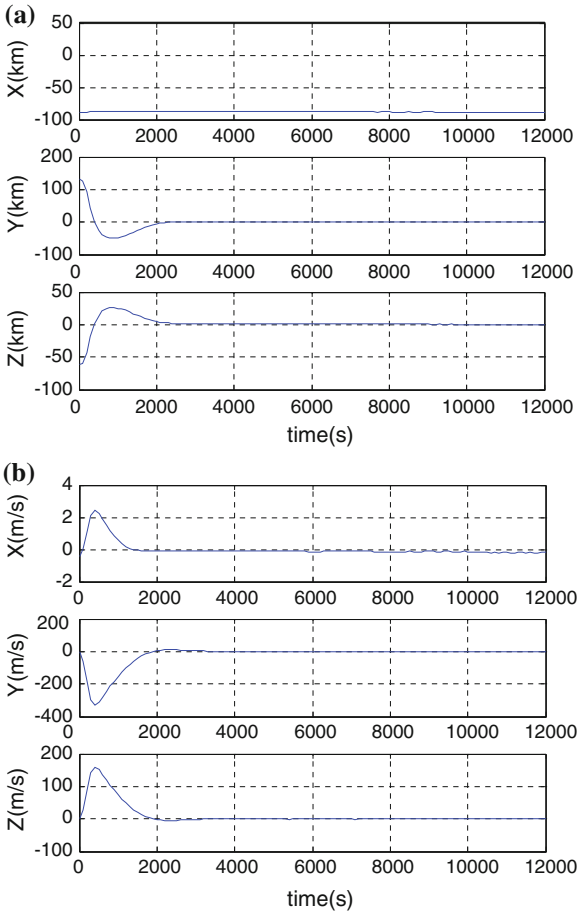

Fig. 7 The error of position and velocity in B-plane

5 Conclusions

To an assumed Mars exploration mission, the optical information cognized possibly has been compared from the angle between planets, observation phase angle, apparent magnitude, and so on. The analysis shows that the angle between the Mars vector and stars is the most suitable information which is to be cognized for autonomous navigation in the flight. The autonomous positioning method is designed based on the information cognized. According to the mathematical simulation, the position accuracy of this method is slightly advantageous over ground-base radio navigation. Mars probe autonomous position in orbit in the case of communication failure with the ground, improve the reliability of the probe, by adopting the method.

Acknowledgments This project is partly supported by the Science and Technology Commission of Shanghai Municipality Program No. 09DZ2274600, the Major State Basic Research Development Program of China (973 Program) under Grant No. 2012CB316200, and the Special Fund Project for Scientific Research of the Marine Public Welfare Industry under Grant No. 20905014.

References

1. Paluszek MA et al (2010) Optical navigation system, AIAA Infotech@Aerospace 2010
2. Riedel JE et al (2010) Optical navigation plan and strategy for the Lunar Lander Altair; OpNav for Lunar and other crewed and robotic exploration applications, AIAA guidance, navigation, and control conference
3. Jun'ichiro Kawaguchi et al (1997) Autonomous optical guidance and navigation, strategy around a small body. J Guidance Control Dyn 20(5):1010–1017

A Cognitive-Heuristic Framework for Optimization of Spaceplane-System Configurations

Ali Sarosh, Yun-Feng Dong and Shi-Ming Chen

Abstract A cognitive-heuristic framework for interconnecting analytical aerothermodynamics and mass-modeling parameters to heuristic optimizer is proposed. It evaluates a complex highly-integrated forebody-inlet configuration and representative hypersonic spaceplane based on minimal input data of flight altitude and Mach number only. SHWAMIDOF-FI design tool is used which incorporates salient features of multi-stage cognitive work approach integrated to heuristic optimization. Results show substantial improvement in geometric, performance, and flow parameters as compared to baseline configuration.

Keywords Cognitive-heuristic framework · Heuristic optimization · Analytical aerothermodynamics · Mass-modeling · Forebody-inlet configuration

1 Introduction

Fully reusable spaceplanes do not exist as yet; therefore, designing spaceplane systems using conventional methods that rely on archival data may not be possible. Cognitive intelligence may therefore offer a framework methodology for evolution of

An erratum to this chapter is available at DOI 10.1007/978-3-642-37835-5_77

A. Sarosh (✉)
Department of Aerospace Engineering, College of Aeronautical Engineering, National University of Sciences and Technology (NUST), PAF Academy Risalpur 24080 KPK, China
e-mail: alisarosh@sa.buaa.edu.cn

Y.-F. Dong · S.-M. Chen
Department of Flight Vehicle Design, School of Astronautics, Beihang University (BUAA), 37 Xueyuan Road, Beijing 100191, China
e-mail: sinosat@buaa.edu.cn

S.-M. Chen
e-mail: csm7531@sa.buaa.edu.cn

F. Sun et al. (eds.), *Foundations and Practical Applications of Cognitive Systems and Information Processing*, Advances in Intelligent Systems and Computing 215,
DOI: 10.1007/978-3-642-37835-5_42,

system/vehicle configurations for future space transportation systems (STS). Design of STS entails a chain of complex, interconnected, and interrelated systems that constitute functionally heterogeneous artifacts. This would mean the evolution of a complex system based on limited information. It implies that collective reasoning must be employed to evolve intelligent information systems for the design process. Barnaby [1] has proposed fast and frugal ways of reasoning by applying *cognitive heuristics*. To form a framework methodology, Gavan [2] and Naikar [3] have described a multi-stage analytical framework of cognitive work analysis (CWA). The framework is based on six stages for analysis of complex information systems. In previous works, Rasmussen [4] and Vicente [5] had identified other multi-stage models depending on different forms of analysis. Since complex systems yield extensive, deeply embedded connection between variables and factors that govern evolutionary design processes, therefore external frameworks may be a viable option. In general, frameworks are used extensively within systems engineering. In the design process, they are used because they aid in assimilating complex concepts, practices, and metrics [2]. Moreover, they also depict interconnections, and interdisciplinary dependencies with a clarity that is difficult to achieve by other strategies.

In the evolution of slender non-trivial configurations for systems of hypersonic spaceplanes that can feature either as lower stage cruise vehicles (CAV) on two-stage-to-orbit (TSTO) spaceplanes or as solitary single stage (SSTO) STS vehicles; high-fidelity configuration solutions based on interdisciplinary methods for highly-integrated surfaces—typically the forebody-inlet system must be employed. In the aerothermodynamic discipline, methods such as stream thrust analysis (STA) [6, 7] or kinetic energy methods (KEM) [6] can help evolve configurations for highly-integrated forebody-inlet systems. In mass-modeling discipline, hypersonic energy partition (HEP) [6, 7] and initial mass ratio comparison [8] can be useful in evolving overall masses for the STS vehicle. However, the real problem lies in evolving information system for interconnection and solution of these disciplines. Intelligent systems such as cognitive frameworks are therefore proposed within the context of cognitive frameworks; this new approach is called as *cognitive-heuristic work analysis* (CHWA) method. In this paper, the CHWA framework uses heuristic algorithms together with a baseline configuration [9] to evolve an optimal aerothermodynamic configuration of hypersonic compression system and respective mass-model for the vehicle. Results show that cognitive framework interconnects the two disciplines with heuristic methods to yield marked improvement in vehicle geometry and performance parameters that satisfy the requirements of both SSTO and TSTO vehicles.

2 CHWA Framework Implementation: SHWAMIDOF-FI Design Tool

SHWAMIDOF-FI design tool [10] is evolved on the basis of cognitive heuristics. It aims to provide simple and efficient set of design methods/rules coupled to evolutionary algorithms for design, optimization, and analysis of a complex

highly-integrated cone-derived waverider forebody attached to planar ramps and supersonic inlet and isolator assembly. In the implementation of CHWA framework, specific features of CWA and cognitive-heuristic methods are integrated into SHWAMIDOF's program. These features include:

(a) Multi-stage models of CWA method.
(b) Framework features of CWA method.
(c) *Take the best heuristic* approach [1] from one-reason decision-making class of cognitive-heuristic.
(d) *Adjustment from an anchor* approach [11] as proposed for decision making under uncertain conditions implemented in cognitive-heuristic method.
(e) *Building-blocks* approach for heuristic decision algorithms.

Minimal input parameters are used; these include Mach number of hypersonic flow and design altitude of CAV stage. A cognitive framework of rules, constraints, and approximations is generated for heuristic optimization and analysis. Optimal solutions for configurations and mass-modeling are obtained. This method can be explained using four key points that include:

(a) Three-step cognitive-heuristic approach.
(b) Integrated cognitive-heuristic framework model: SHWAMIDOF-FI program.
(c) Intelligent heuristic decision method: DF-APSO.
(d) Parallel-mode heuristic optimizers: TIPSO.

In general, the CHWA methodology offers decision solution to a complex problem of highly-integrated configurations, for which minimal input parameters of Mach number and flight attitude are used, a cognitive framework of rules, constraints, and approximations is generated and optimal solution for configurations and mass-modeling is obtained. Some of the vital features of implementation of CHWA in SHWAMIDOF design framework are discussed as follows.

2.1 Three-Step Cognitive-Heuristic Approach

A cognitive framework (as shown in Fig. 1) is used to integrate the approximate analytical aerothermodynamics to mass-modeling approach in a three-step cognitive process.

In the first step, limited parameters are input and the together with framework parameters heuristic models are evolved. Cognitive intelligence is used to select the most suitable model and in step 2, the subject model is heuristically optimized for integrated aerothermodynamic and mass-modeling solution. In step 3, the analytical framework parameters are used to analyze the cognitively evolved-heuristically optimized configuration.

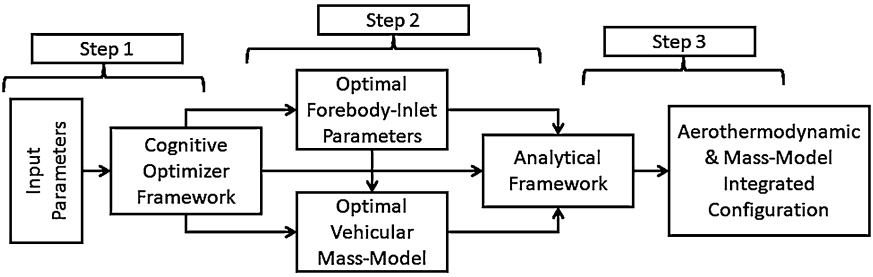

Fig. 1 Schematics of cognitive approach in SHWAMIDOF-FI

2.2 Integrated Framework Model

In SHWAMIDOF-FI, the three-step cognitive approach is represented by a tri-modular framework (refer Fig. 2), one module each, for evolution/selection of baseline surrogate, aerothermodynamic and mass-model integrated optimization of baseline configuration and analysis of the optimal configuration along with generation of data sheets and charts. Typical cognitive system tasks of knowledge, planning, decision making, problem solving, analyzing, assessing etc. are incorporated into the three modules. Sarosh [9] has evolved surrogates of forebody-inlet configurations using baseline module SHWAMIDOF design tool and proposed an intelligent-heuristic method called DF-APSO for selection of suitable baseline surrogate. This baseline surrogate configuration is processed through 17 solvers that simultaneously and heuristically optimize the solution in the optimizer module. The optimal configuration is finally analyzed and its results validated by the third module that produces requisite charts and data sheets.

2.3 Intelligent-Heuristic Decision Method

Surrogate data (i.e., configurations) are generated for spaceplane systems using the baseline module of SHWAMIDOF. A decision method based on difference and fractional parameters of actual, perfect, scaled, and heuristically optimized configurations is utilized for selection of appropriate surrogate as baseline

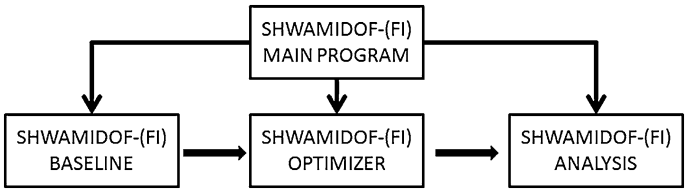

Fig. 2 SHWAMIDOF-FI cognitive heuristic framework model

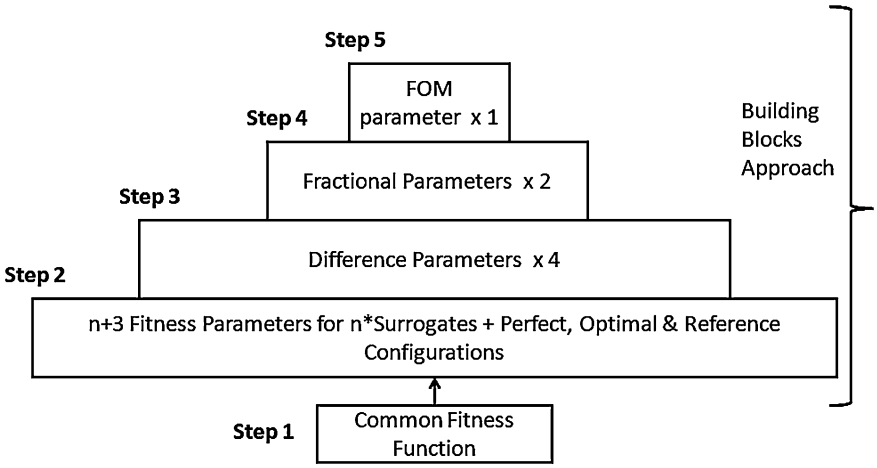

Fig. 3 Schematic of DF-APSO algorithm

configuration. This method is called as DF-APSO algorithm [12]. It uses performance data together with stochastic, probabilistic functions to evolve a cognitive five-step criterion that satisfies *building-block* approach in a *bottom-up* sequence. Figure. 3 describes the building-block layout that DF-APSO algorithm satisfies to evaluate and select the baseline configuration in accordance with the framework explained in Figs. 1 and 2. Each of the blocks corresponds to an equivalent DF-APSO step. All steps form a pyramidal arrangement. Starting from a large fitness parameters' data which gets halved at each subsequent level (block) a final heuristic decision is obtained at the top level. The outcome of this heuristic decision uses the *take the best heuristic* approach to select the baseline configuration with best FOM parameter value.

2.4 Decision Under Uncertainty Conditions

In the mathematical modeling of cognitive heuristics, simple efficient rules laid out on the basis of hard-coded evolutionary processes are modeled for resolution of complex problems with incomplete (i.e., minimal) information. Tversky [11] has described three heuristics that could be employed for decision making under uncertain condition. In the present formulation, we consider the case where no benchmark configurations are available as reference; therefore, the third heuristic, i.e., *adjustment from an anchor* is employed. The anchor in this case is the evolved baseline configuration; the relevant values of adjustment are geometrical, flowfield, and mass-modeling parameters. The anchor or baseline configuration and adjustment parameters are in turn used to evolve an optimal configuration for forebody-inlet system. In this way, an optimal configuration can be obtained for a system for which uncertainty exists due non-availability of benchmarks as reference parameters.

2.5 Parallel-Mode Heuristic Optimizer

The step 2 of cognitive approach (in Fig. 1) is represented by the optimizer module in SHWAMIDOF program (refer Fig. 2). The cognitive framework parameters, which consist of assumptions and nominal values, essential to the optimization of baseline configuration, get generated and are read into the optimizer module. A heuristic algorithm called TIPSO [13] that uses a genetically evolved search space together with decision possibilities for identification of globally optimal result is solved for optimal configuration parameters. A systematic arrangement of aerothermodynamic and mass-modeling solvers (as shown in Fig. 4) is executed by parallel processing labs using multiobjective optimization method to solve objective functions (OFs) which are linked together through a central metric into an aggregate objective function (AOF).

The parallel processing labs play a vital role in evolving cognitive solution because these tend to mimic the behavior of employing different people in an iterative process to evolve an optimal solution. Here each lab produces a unique set of optimal solution that gets refined (improved) over defined number iterations. Since each solution explicitly communicates with the upwind data. Therefore, a solution that employs n number of labs for I number of per-lab iterations, will eventually mimic the behavior of employing $T = m*I$ people to discuss and propose a solution to the problem. The optimized parameters alongwith cognitive framework parameters are finally passed onto the analyzer module for systematic

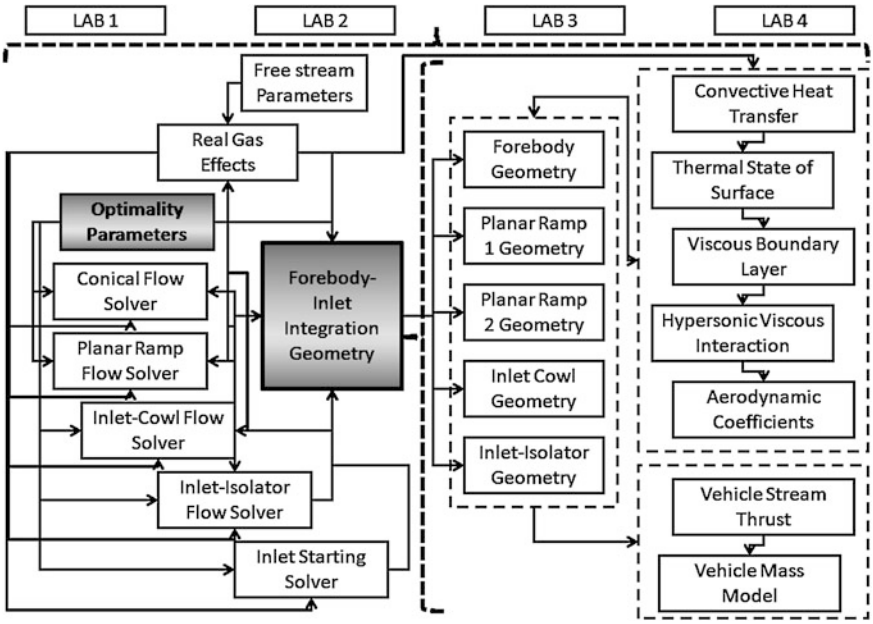

Fig. 4 Schematic of parallel processing of optimization

processing through analytical solvers to generate data sheets and graphical plots of solution as depicted in Fig. 2. The optimization problem, within the cognitive heuristic of forebody-inlet configuration and vehicle's mass-modeling is classified as multi-objective, linearly constrained, static optimization problem of non-separable, nonlinear objective functions with real-valued, stochastic design variables.

3 Mathematical Formulation of Cognitive-Heuristic Problem

In the mathematical modeling of cognitive heuristics, simple efficient rules laid out on the basis of hard-coded evolutionary processes are modeled for resolution of complex problems with incomplete (i.e., minimal) information. Since *adjustment from an anchor* is employed and the anchor is the baseline configuration the relevant values of adjustment are shown in Fig. 6. These parameters define the configuration items of forebody-inlet system which have been identified in Fig. 5. Once the above geometry has been ascertained, the solver progresses toward evaluating the exact performance parameters based on the system geometry and predefined (i.e., framework) parameters of combustor and nozzle efficiencies. The overall performance parameters so determined then provide necessary uplink to correlate HEP-based mass-modeling parameters to the forebody-inlet system configuration. In this way, the optimizer module fulfills the cognitive-heuristic's preconditions of solving complex problems with minimal input parameters in the most fast and frugal way.

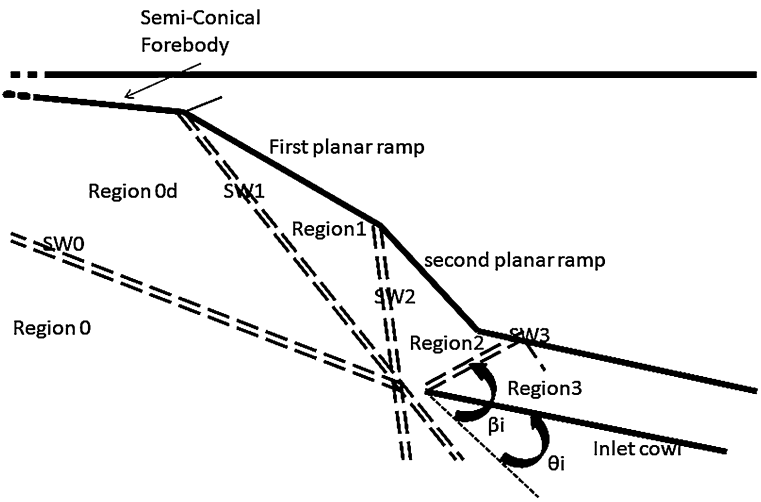

Fig. 5 Geometry and flow parameters for configuration optimization

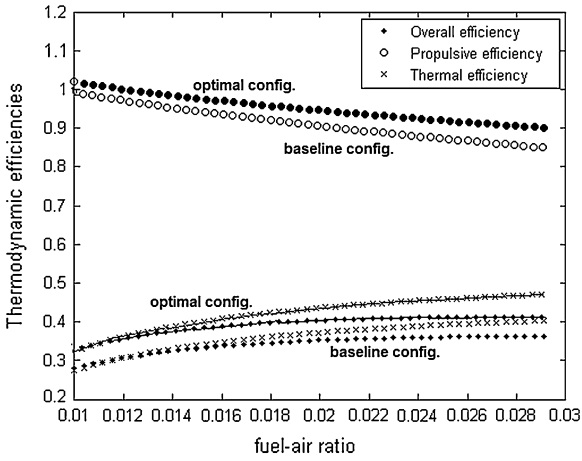

Fig. 6 Aerothermodynamic performance comparison

The design problem is defined by the design vector (**X**) as:

$$\mathbf{X} = [R_{\mathrm{N}},\ R_{\mathrm{L}},\ \varepsilon,\ k_{\mathrm{w}},\ \psi_{\mathrm{LT}},\ \beta_{0\mathrm{d}},\ \beta_{1\mathrm{d}},\ \beta_{2\mathrm{d}},\ \beta_{3\mathrm{d}},\ \mathrm{Re}_{\theta},\ \phi_{23},\ L_{\mathrm{gen}},\ \Pi_{\mathrm{e1}},\ \Pi_{\mathrm{e2}},\ (L/D)_{\mathrm{Stg1}}] \tag{1}$$

The design variables are defined in Table 1 (below). The minimization of multiobjective function $g(\boldsymbol{X})$ is defined as; max $g(\boldsymbol{X}) = \min\{-f(\boldsymbol{X})\}$. These result in the maximization of the actual fitness function $f(\boldsymbol{X})$, that is defined as an aggregate objective function (AOF) which is a function of individual objective functions (OFs) that aim to maximize fitness functions of each of the aerothermodynamic, mass-modeling, and geometric solvers as follows:

$$f(\mathbf{X}) = [f_1(\mathbf{X}),\ f_2(\mathbf{X}),\ \ldots\ldots,\ f_{17}(\mathbf{X})] \tag{2}$$

Subject to inequality constraints, the relevant values of 15 design variables are selected relevant to anchor parameters as shown in Table 1.

The AOF to be maximized is expressed in terms of OFs by Eq. 3 (below):

$$f(\mathbf{X}) = \left[\sum_{i=1}^{17} \omega_i f_i(\mathbf{X})\right] \Big/ \omega_0 \tag{3}$$

where $\omega_1 = \omega_2 = \omega_3 = \omega_6 = \omega_{14} = \omega_{17} = \boldsymbol{O}(1)$; $\omega_4 = \omega_{13} = \boldsymbol{O}(-2)$; $\omega_5 = \omega_{11} = \omega_0 = \boldsymbol{O}(2)$; $\omega_7 = \boldsymbol{O}(14)$; $\omega_8 = \omega_9 = \boldsymbol{O}(-4)$; $\omega_{10} = \boldsymbol{O}(0)$; $\omega_{12} = \boldsymbol{O}(-1)$; $\omega_{15} = \boldsymbol{O}(7)$; $\omega_{16} = \boldsymbol{O}(-3)$.

Using the aforementioned formulation, the design space for static optimization problem of non-separable, nonlinear objective functions with real-valued, stochastic design variables is solved as a real-valued, stochastic programming problem. It is optimized using heuristic swarm algorithms of TIPSO. It uses two-step stochastic process to generate a primed swarm population for TIPSO algorithm. That in turn generates competitive particles for PSO solution.

Table 1 Bounded constraints and anchor data

Parameter	Anchor	Lower bound	Upper bound
Nose radius (m)−(R_N)	0.0025	≥0.001	≤0.0015
Lip radius (m)−(R_L)	0.0025	≥0.003	≤0.0045
Emissivity (ε)	0.90	≥0.90	≤0.97
Wall conductivity (W/m−K)−(K_w)	200	≥100	≤110
Wall temp. ratio turb./lam. (Ψ_{LT})	1.50	≥1.40	≤1.50
Forebody shock angle (o)−(β_{0d})	10	≥9.6	≤11
1st planar ramp shock angle (o)−(β_{1d})	23.11	≥22	≤24
2nd ramp shock angle (o)−(β_{2d})	27.57	≥26	≤28
Inlet cowl shock angle (o)−(β_{3d})	43.29	≥40	≤45
Momentum boundary Re no. (Re_θ)	8000	≥10000	≤15000
Press. ratio across isolator (φ_{23})	1.5	≥1.4	≤1.5
Length of generator cone (m)−(L_{gen})	15	≥10	≤12
Empty mass fraction of stage 1−(Π_{e1})	0.40	≥0.35	≤0.42
Empty mass fraction of stage 2−(Π_{e2})	0.21	≥0.19	≤0.22
Lift-to-drag of 1st stage ($(L/D)_{stg1}$)	4.5	≥4.0	≤5.0

4 Configuration Optimization Results and Analysis

In the evolution of baseline configuration, several configuration items (CI) such as forebody under-belly, planar ramps, inlet cowl lip, sidewalls etc., were identified as primary surfaces for geometrical optimization. Hence, beginning with a baseline configuration of sharp-edged forebody with flat sides, pointed nose profile, and well-defined attachments of aerodynamic surfaces typical of cruise vehicle with low drag profile; the configuration is optimized for aerothermodynamic and mass-modeling parameters to yield an evolved optimal geometry. The new geometry shows, among other features, blunting of nose profile and blending of forebody with sidewalls of ramps and inlet. This indicated that insofar as aerothermodynamics is concerned, the vehicle could now possibly sustain both ascent as well re-entry loads. In Table 2 some of the leading parameters of aerothermodynamic performance, geometry, and mass-modeling are presented as computed using SHWAMIDOF-FI program.

These results show that cognitive-heuristic framework yields an optimized configuration with higher overall efficiency. An increase in cycle temperature and pressure is seen as useful for combustion efficiency and equivalent specific thrust. However, temperature and pressure gains cause increment in entropy and flow momentum losses which are compensated by forebody blending. A comparative plot of aerothermodynamic efficiencies for baseline and optimal configurations is given in Fig. 8. These results are plotted by varying the fuel–air ratio in the burner from an extremely lean mixture up to stoichiometric fuel–air ratio. Results show that in all three cases, the general trend of both configurations is identical; however, the optimized configuration exhibits higher efficiency parameters on all accounts and for all fuel–air ratios. Geometrically, the optimal configuration has a

Table 2 Key parameters of optimal configuration

Parameters	Baseline configuration	Optimal configuration
Compression efficiency (η_c)	0.8932	0.8873
Cycle temperature ratio (Ψ)	4.76	5.56
Cycle pressure ratio (φ)	121.6	172.97
Mass flow specific thrust (F_{sp})	685 m/s	766 m/s
Overall (aeroth.) efficiency (η_o)	0.3634	0.4064
C_{Lmax} (forebody-inlet config.)	0.3296	0.5091
C_{Dmax} (forebody-inlet config.)	0.15562	0.3377
Wall temp. windward ($T_w = T_{ra}$)	1524–1576 K	1459–1571 K
Coefficient of skin friction (C_f)	0.004–0.0025	0.0036–0.0023
Hypersonic energy partition (α)	0.63	0.87
Payload mass (m_{pay})	7000	7000
Empty mass of TSTO (m_e)	48391	22160
Fuel mass TSTO (m_f)	55303	29812
Launch mass TSTO (m_{total})	110695	58972
SSTO versus TSTO (Z/Z_e)	1.15/1.08	0.90/0.80

larger air inlet resulting in weaker sidewall and boundary layer interaction effects and improved starting performance. Aerodynamically, the optimal configuration has higher lift coefficient and reduced drag coefficient. Optimal radiation-adiabatic cooling ensures that wall temperature and coefficient of skin friction are also reduced. Optimized results show (Fig. 7) that energy split parameter (α) shifts in favor of lower stage of TSTO vehicle, an improved TSTO mass configuration is achieved with as much substantial reduction in launch weight. Under improved configuration, both Z and Ze parameters reduce below unity value; hence, the mass ratio of CAV stage holds good for both SST and TSTO configurations.

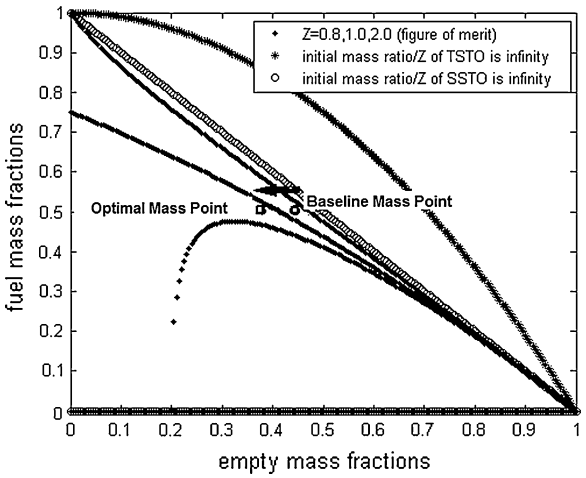

Fig. 7 SSTO versus TSTO mass ratio plot

5 Conclusion

A cognitive-heuristic work analysis (CHWA) framework for integrated aerothermodynamic and mass-modeling solution has been developed. Using SHWAMI-DOF-FI design tool, heuristic solution parameters of highly-integrated hypersonic forebody-inlet configuration are extended to obtain mass-modeling parameter for an equivalent TSTO vehicle. A semi-elliptical waverider forebody is integrated to planar ramps and inlet. Decision heuristic is employed in DF-APSO algorithm for selection of surrogates. Decision possibilities are used in heuristic TIPSO algorithm for global optimization. An improved configuration is successfully evolved and analysis showed considerable improvement in aerothermodynamic performance, thermo-viscous behavior, geometric sizing, and mass-modeling of the vehicle. Vehicle mass ratio showed that the evolved lower stage CAV could be used in both SSTO and TSTO roles.

References

1. Marsh B, Todd PM, Gigerenzer G (2004) Cognitive heuristics: reasoning the fast and frugal way. In: Leighton JP, Sternberg RJ (eds) The nature of reasoning, Cambridge University Press, New York, p 273–287
2. Lintern G (2009) The framework of cognitive work analysis. Found Pragmatics Cogn Work Anal 20–26
3. Naikar N, Sanderson P (2001) Evaluating design proposals for complex systems with work domain analysis. Hum Factors 43(4):529–542
4. Rasmussen J, Pejtersen AM, Goodstein LP (1994) Cognitive systems engineering. Wiley, New York
5. Vicente K (1999) Cognitive work analysis: towards safe, productive, and healthy computer-based work. Lawrence Erlbaum Associates, Mahwah
6. Heiser WH, Pratt DT (1994) Hypersonic airbreathing engine performance analysis. Hypersonic airbreathing propulsion, AIAA education series, American Institute of Aeronautics and Astronautics, Washington, pp 150–193
7. Ortwerth PJ (2000) Scramjet flowpath integration. Scramjet Propulsion, AIAA, Washington, pp 1105–1293
8. Heiser WH (2010) Single-stage-to-orbit versus two-Stage-to-orbit airbreathing systems. J Spacecraft Rockets 47(1):222–223. (doi:10.2514/1.46631)
9. Sarosh A, Feng DY Adnan MA (2011) Configurational aerothermodynamics methodology for derivation of baseline configuration on elliptical cone-wedge integrated waverider. In: 2011 international conference on aerospace engineering and information technology (Aeit 2011), pp 102–107
10. Sarosh A, Yun-Feng D Kamarinchev D (2012) STS forebody material selection method using integrated aerothermodynamic optimization approach. Adv Mater Res J TransTech Publications Inc. (ISSN 1022-6680 doi:10.4028/www.scientific.net/AMR 488-489.1103), 2012, 488–489, 1103–1108
11. Tversky A, Kahneman D (1974) Judgement under uncertainity: heuristics and biases. Science, J Am Assoc Adv Sci 185: 1124–1131

12. Sarosh A, Yun-Feng D, Shi-Ming C (2011) A difference-fractional FOM decision method for down-selection of hypersonic compression system configurations. Aerospace science and technology, Elsevier Inc, USA. doi:http://dx.doi.org/10.1016/j.ast.2012.08.001
13. Hu D, Sarosh A, Dong YF (2011) An improved particle swarm optimizer for parametric optimization of flexible satellite controller. Appl Math Comput 217(21): 8512–8521(ISSN 0096-3003, doi:10.1016/j.amc.2011.03.055)

Artificial Bee Colony Algorithm for Parametric Optimization of Spacecraft Attitude Tracking Controller

Shan Zhong, Yun-Feng Dong and Ali Sarosh

Abstract To satisfy the rapidly and accurately attitude tracking for spacecraft, artificial bee colony (ABC) algorithm is introduced to the controller parametric optimization of spacecraft attitude tracking. The spacecraft attitude tracking dynamics model, kinematics model and a sliding model controller using radial basis function neural network are build up. The concept of ABC algorithm is presented and the steps are also given. For the fitness function of ABC algorithm, the weighted index of error and angular velocity error with the simulation time are used. The optimization result compared between particle swarm optimization (PSO) and ABC algorithm shows the efficient of the ABC algorithm. The simulation result with the optimized controller shows that the controller could guarantee robustness against uncertainties and external disturbances increased.

1 Introduction

Extensive studies on spacecraft attitude tracking problem have been carried out during past few decades [1–7]. The attitude tracking control has important applications ranging. For example, spacecraft applications such as spacecraft formation flying, spacecraft surveillance and communication often have need of highly accurate slewing and/or pointing maneuvers. A series of applications in these need rapidly and accurately tracking.

S. Zhong (✉) · Y.-F. Dong · A. Sarosh
School of Astronautics, Beijing University of Aeronautics and Astronautics, Beijing 100191, People's Republic of China
e-mail: csm7531@sa.buaa.edu.cn

Y.-F. Dong
e-mail: sinosat@buaa.edu.cn

A. Sarosh
e-mail: alisarosh@sa.buaa.edu.cn

F. Sun et al. (eds.), *Foundations and Practical Applications of Cognitive Systems and Information Processing*, Advances in Intelligent Systems and Computing 215,
DOI: 10.1007/978-3-642-37835-5_43,

Sliding mode control has been considered as a useful scheme to deal with uncertainties and disturbances. Jin [2] introduced time-varying sliding mode controller under consideration of control input constraints. Pukdeboon and Zinober [3] designed infinite-time optimal sliding mode control laws. For reducing chattering and providing better accuracy, Pukdeboon [4] proposed higher order sliding-mode control law. Wu [5] also developed robust sliding mode controller with fast stability and convergence in finite time. Chebyshev neural network and radial basis function neural network (RBFNN), were introduced into the sliding mode controller for attitude tracking by Zou [6] and Chen [7], respectively.

However, there are few papers giving guidelines for the selection of the controller gains in these literatures, which plays an important role in tracking rapidly and accurately. Luo [1] analyze the performance of the optimal controller and establish tuning guidelines for the selection of the controller gains. Optimization is another method to selecting the controller gains. Genetic algorithm (GA) was introduced in optimizing the sliding mode controllers parameters by [2]. But it is very difficult for a classic genetic algorithm to effectively explore the solution space [8].

As a swarm intelligence algorithm, artificial bee colony (ABC) algorithm was originally presented by Dervis Karaboga [9] in 2007, under the inspiration of collective behavior on honey bees, and it has been proved to process a better performance in function optimization problem, compared with GA, differential evolution algorithm and particle swarm optimization algorithm [10, 11]. ABC algorithm can be efficiently used for solving multimodal and multidimensional optimization problems [10]. So for this multi-variable and complicated parametric optimization problem for spacecraft attitude tracking controller, ABC will has advantage than GA algorithm.

This paper considers a controller optimization problem by ABC algorithm as an example, which is a complicated RBFNN sliding model controller in [7]. A comparison between ABC and PSO algorithm is also presented, and the result shows the efficient of the ABC algorithm in satellite attitude tracking controller parametric optimization. The rest of the paper is organized as follows. In Sect. 2, the spacecraft attitude tracking problem is proposed. The ABC algorithm is presented in Sect. 3. Section 4 is dedicated to the illustration of the effectiveness of the approach through simulations results. Finally, we draw a conclusion about this work.

2 Spacecraft Attitude Tracking Problem

2.1 Dynamics and Kinematics of Spacecraft

Consider a rigid spacecraft with N reaction wheels, the dynamic equations of the spacecraft can be written as Eq. 1 [7].

$$\mathbf{J}\dot{\boldsymbol{\omega}} = -\boldsymbol{\omega}^{\times}\mathbf{J}\boldsymbol{\omega} - \boldsymbol{\omega}^{\times}\mathbf{A}_s\mathbf{h}_s - \mathbf{A}_s\mathbf{u}_s + \mathbf{T}_d \tag{1}$$

Where $\mathbf{J}$ is the total body inertia matrix minus the radial moments of inertia of wheels, and $\boldsymbol{\omega} = [\omega_1, \omega_2, \omega_3]^T$ is the body rate vector of the spacecraft. The notation $\boldsymbol{\omega}^{\times}, \forall \boldsymbol{\omega} = [\omega_1, \omega_2, \omega_3]^T \in \mathbb{R}^3$ denotes the skew-symmetric matrix. $\mathbf{A}_s = [a_1, a_2, \cdots, a_N]$ is the setup matrix of N wheels. The angular momentum of wheels is and the control torques are $\mathbf{u}_s = [u_{s1}, u_{s2}, \cdots, u_{sN}]^T \in \mathbb{R}^N$.$\mathbf{T}_d = [T_{d1}, T_{d2}, T_{d3}]^T \in \mathbb{R}^3$ is the external torques on the satellite. The details of parameters are defined in [7].

The differential equation that governs the kinematics in terms of the Modified Rodrigues Parameters (MRPs) is given by Eq. 2.

$$\dot{\boldsymbol{\sigma}} = \mathbf{G}(\boldsymbol{\sigma})\boldsymbol{\omega} \tag{2}$$

Where $\boldsymbol{\sigma} = [\sigma_1, \sigma_2, \sigma_3]^T \in \mathbb{R}^3$, and $\mathbf{G}(\boldsymbol{\sigma})$ is $\mathbf{G}(\boldsymbol{\sigma}) = \frac{1}{2}(\frac{1-\boldsymbol{\sigma}^T\boldsymbol{\sigma}}{2}\mathbf{I}_{3\times3} + \boldsymbol{\sigma}^{\times} + \boldsymbol{\sigma}\boldsymbol{\sigma}^T)$ and $\mathbf{I}_{3\times3}$ is the 3×3 identity matrix.

2.2 Tracking Error Equations

Introduce the orbital frame as the reference frame. Assume the $\boldsymbol{\sigma}_d$ denotes the desired attitude with the orbital frame to inertial frame, and define $\boldsymbol{\sigma}_e$ as the attitude error from the body frame to the orbital frame. Then the tracking error dynamics are given by Eqs. 3 and 4, as described in [7].

$$\begin{aligned}\mathbf{J}\dot{\boldsymbol{\omega}}_e = &-(\boldsymbol{\omega}_e + \mathbf{R}(\boldsymbol{\sigma}_e)\boldsymbol{\omega}_d)^{\times}\mathbf{J}(\boldsymbol{\omega}_e + \mathbf{R}(\boldsymbol{\sigma}_e)\boldsymbol{\omega}_d) - \mathbf{A}_s\mathbf{u}_s + \mathbf{T}_d \\ &+\mathbf{J}(\boldsymbol{\omega}_e{}^{\times}\mathbf{R}(\boldsymbol{\sigma}_e)\boldsymbol{\omega}_d - \mathbf{R}(\boldsymbol{\sigma}_e)\dot{\boldsymbol{\omega}}_d) - (\boldsymbol{\omega}_e + \mathbf{R}(\boldsymbol{\sigma}_e)\boldsymbol{\omega}_d)^{\times}\mathbf{A}_s\mathbf{h}_s\end{aligned} \tag{3}$$

$$\dot{\boldsymbol{\sigma}}_e = \mathbf{G}(\boldsymbol{\sigma}_e)\boldsymbol{\omega}_e \tag{4}$$

2.3 Sliding Mode Tracking Controller

In [7], a sliding mode controller using RBF neural network is proposed. The sliding mode controller is described in Eqs. 5 and 6.

$$\begin{aligned}\mathbf{A}_{s0}\mathbf{u}_s = &-(\boldsymbol{\omega}_e + \mathbf{R}(\boldsymbol{\sigma}_e)\boldsymbol{\omega}_d)^{\times}\mathbf{J}_0(\boldsymbol{\omega}_e + \mathbf{R}(\boldsymbol{\sigma}_e)\boldsymbol{\omega}_d) \\ &+\mathbf{J}_0(\boldsymbol{\omega}_e{}^{\times}\mathbf{R}(\boldsymbol{\sigma}_e)\boldsymbol{\omega}_d - \mathbf{R}(\boldsymbol{\sigma}_e)\dot{\boldsymbol{\omega}}_d) \\ &-(\boldsymbol{\omega}_e + \mathbf{R}(\boldsymbol{\sigma}_e)\boldsymbol{\omega}_d)^{\times}\mathbf{A}_{s0}\mathbf{h}_s + \mathbf{J}_0\mathbf{K}\mathbf{G}(\boldsymbol{\sigma}_e)\boldsymbol{\omega}_e - \boldsymbol{\tau}_s + \hat{\mathbf{y}}\end{aligned} \tag{5}$$

$$\mathbf{s} = \boldsymbol{\omega}_e + \mathbf{K}\boldsymbol{\sigma}_e \tag{6}$$

where "0" means the system nominal value, so $\mathbf{A}_{s0} = \mathbf{A}_s - \Delta\mathbf{A}_s$ is the nominal setup matrix of wheels, $\mathbf{J}_0 = \mathbf{J} - \Delta\mathbf{J}$ is the nominal value of $\mathbf{J}$, and "Δ" means the uncertainty value.$\boldsymbol{\tau}_s = [\tau_{s1}, \tau_{s2}, \tau_{s3}]^T$, and $\tau_{si} = -k_{ni}\ \text{sign}\ (s_i) - k_{mi}s_i, i = 1, 2, 3,$

the k_{ni} and k_{mi} are positive. $\hat{\mathbf{y}}$ is the estimate value of uncertainties by radial basis function neural network, as described in Eq. 7.

$$\hat{y}_j = \sum_{i=1}^{m} w_{ij} \exp[-\frac{\|\mathbf{s} - \mathbf{C}_i\|^2}{2{b_i}^2}] \tag{7}$$

Where $\mathbf{C}_i = [c_{1i}, c_{2i}, c_{3i}], i = 1, 2, \cdots, m$, represents the center of the ith Gaussian function, b_i is a measure of its width and w_{ij} represents the output weight from that node to the jth output. m is the number of employed neurons at hidden layer. $\mathbf{K} =$ diag (K_1, K_2, K_3) in Eq. (7) is a diagonal positive matrix. For the derived control law, there are 9 parameters $(K_1, K_2, K_3, k_{n1}, k_{n2}, k_{n3}, k_{m1}, k_{m2}, k_{m3})$ that need to be adjusted, which can be optimized by ABC algorithm.

3 Artificial Bee Colony Algorithm

3.1 Concept of ABC Algorithm

In a natural bee swarm, there are generally three kinds of honey bees that search food [9, 10]. These include the employed bees, the onlookers, and the scouts. Employed bees are responsible for exploiting the nectar sources. They explore the site beforehand and give information to the onlooker bees in the hive about the quality of the food at the source sites which they are exploiting. Onlooker bees wait in the hive and decide on a food source to exploit based on the information shared by the employed bees. Scouts randomly search the environment in order to find a new food source, either depending on an internal motivation or based on possible external clues.

In ABC algorithm, each employed bee uses the currently associated food source to determine a new neighboring source, based on the nectar amount at the new source. Equation 8 shows the method to produce a candidate food position $v_i (i \in 1, 2, \cdots, N_e$, where N_e is the number of employed bees) from each employed bees position x_i. From the candidate position v_i, each employed bees get its nectar amount (fitness value).

$$v_{ij} = x_{ij} + \theta_{ij}(x_{ij} - x_{kj}) \tag{8}$$

where $k \in 1, 2, \cdots, N_f$ is randomly chosen indexes, and $j \in 1, 2, \cdots, D$ is the dimension of employed bees variable. D is the variables dimensions, and N_f is the number of food sources which is equal to the number of employed bees N_e. Although k is determined randomly, it has to be different from i. The θ_{ij} is a randomly produced number between $[-1,1]$.

As can be seen from Eq. 8, if the nectar amount of this new food source is higher than that of the currently associated food source, then this employed bee moves to this new food source, otherwise it continues with the old one.

After all employed bees completing the search process, they share the information about their food sources with onlooker bees. An onlooker bee evaluates the nectar information obtained from all employed bees and chooses a food source using a probability related to its nectar amount. Equation 9 refers to the probability function which is known as roulette wheel selection method. This method provides better candidates to have a greater chance of being selected.

$$p_i = \frac{fit_i}{\sum_{n=1}^{SN} fit_n} \tag{9}$$

where fit_i is the corresponding fitness value, i is proportional to nectar amount of the food source in the position i. The fitness function is defined as Eq. 10.

$$fit_i = \begin{cases} 1/(1+f_i) & f_i \geq 0 \\ 1 + abs(f_i) & f_i < 0 \end{cases} \tag{10}$$

where f_i is the objective function value of solution i.

Once all onlooker bees have selected their food source, each of them determines a new neighboring food source and computes its nectar amount. Provided that its nectar contents are higher than that of previous one, the bee stores the new position and discards the old one. This process is the same as the employed bees, and the new position is produced by Eq. 8.

The food source which has been exhausted by the employed and onlooker bees is assigned as 'abandoned'. It's the employed bee becomes a scout. This implies that, if any position cannot be improved further through a predetermined number of cycles, L_{limit}, called as limit parameter, the food source is assumed to be abandoned and employed bee of that source will become a scout. In that position, a new solution is randomly generated by the scout as given in Eq. 11. It assumes that the abandoned source is x_i and $j \in 1, 2, \cdots, D$, the scout discovers a new food source which will be replaced with x_i.

$$x_i^j = x_{min}^j + rand(0,1)(x_{max}^j - x_{min}^j) \tag{11}$$

where j is determined randomly, it should be noticed that it has to be different from i.

3.2 ABC Algorithm for Parametric Optimization

In ABC algorithm, the position of a food source, x_i, represents a possible solution to the optimization problem and the nectar amount, fit_i, corresponds to the fitness of the solution.

According to the analysis of the problem concerning spacecraft attitude tracking control system, many parameters need to be adjusted. In the general control system design, integrated error, integrated absolute error, integrated square error etc. are used as evaluation functions. The objective function is given by Eq. 12.

$$f = w_1 \int_0^{T_m} \boldsymbol{\sigma}_e^T \boldsymbol{\sigma}_e t dt + w_2 \int_0^{T_m} \boldsymbol{\omega}_e^T \boldsymbol{\omega}_e t dt \tag{12}$$

where f is the objective value. T_m is the total simulation time. t is the control system running time. w_1 and w_2 are weights.

In Eq. 12, the first term is the weighted squared error of attitude error, and the second one is the weighted squared error of angular velocity error. To decrease the effect of initial error, the time t is introduced into Eq. 12, and it can be seen that the less of the last error, the better of the objective value. Setting $w_2 = 0$, the objective value only concerns with the angle error, as shown in [2]. In some mission, the angular velocity also plays an important role, so we set $w_2 > 0$ and $w_1 + w_2 = 1$.

The implementation procedure of ABC algorithm can be described as follows:

- Step 1: Build a simulator for spacecraft attitude tracking system. Initialize the parameters for the simulation, such as spacecraft inertia $\mathbf{J}$ and its uncertainty part $\Delta\mathbf{J}$, the external disturbance $\mathbf{T}_d$, the initial MRPs $\boldsymbol{\sigma}_e$, the initial angular velocity $\boldsymbol{\omega}_e(0)$, the desired angular velocity $\boldsymbol{\omega}_d$, the inertia of each reaction wheels $\mathbf{J}_w$, the nominal reaction wheels' install matrix $\mathbf{A}_{s0}$ and its uncertainty part $\Delta\mathbf{A}_s$, and the initial wheel speed $\Omega(0)$.
- Step 2: Initialize the parameters of ABC optimization algorithm, including the population number N, the number of employed bees N_e , the number of the unemployed bees N_u , the limit parameter of the scout bees L_{limit} , the maximum Iteration I_{max}, the dimensions of the variables D, the lower bounds of the variables **lb**, and the upper bounds **ub**. In general, $N_e = N_u = 0.5 \times N$. Initialize the search time of each bee $i_s = 0$, and $Iteration = 1$. Initialize the employed bee's position randomly. These positions are the controller parameters $(K_1, K_2, K_3, k_{n1}, k_{n2}, k_{n3}, k_{m1}, k_{m2}, k_{m3})$. For each position, simulating the attitude tracking and calculate their fitness value using Eqs. 12 and 10.
- Step 3: For each employed bees, calculate the candidate position by Eq.8 and its fitness by Eqs. 12 and 10. Update their positions if the new fitness is lower than the original one.
- Step 4: According to the fitness of the employed bees, calculate the probabilities of each employed bees by Eq. 9. For each onlooker bees, select a food source by apply roulette wheel selection method, and then calculate the candidate position and its fitness, and update its position which is similar like employed bees in Step 3. If the fitness is better than the original one, the search times i_s will be set as 0, or else, i_s plus one.
- Step 5: If the search times is larger than L_{limit}, the employed bee gives up the solution, and re-search the new food resources, which is realized by re-initializing the parameters and calculating the cost value.
- Step 6: Store the best solution parameters and the best fitness.
- Step 7: If $Iteration < I_{max}$, go to Step 3. Otherwise, output the optimal parameters and optimal fitness.

The procedure can also be shown with Fig. 1.

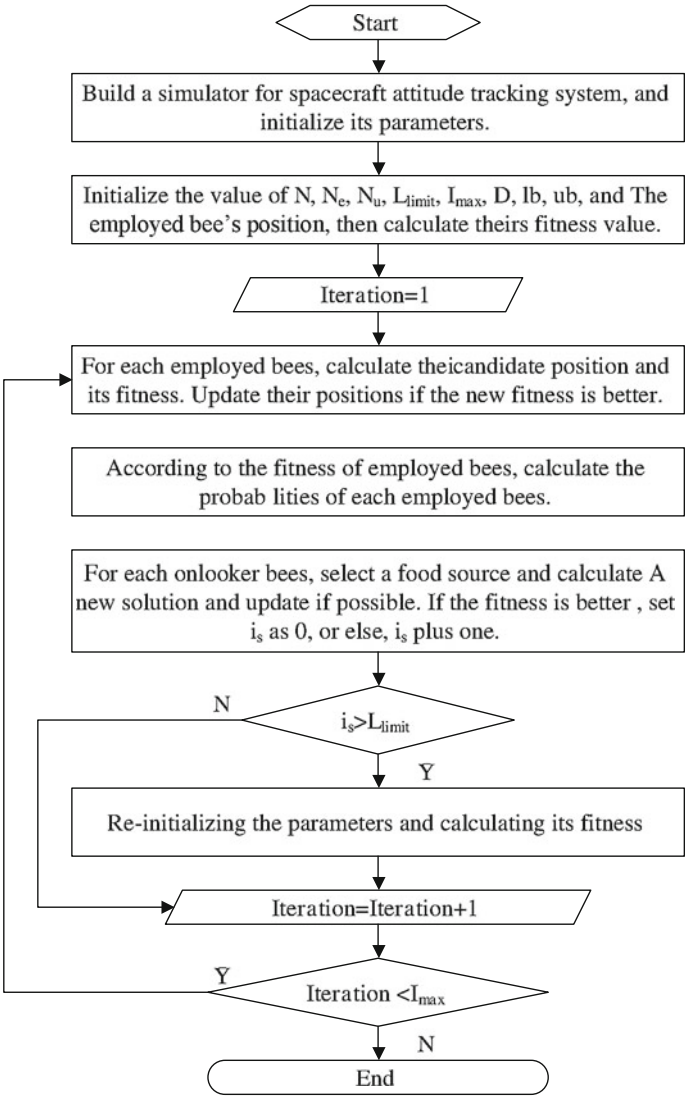

Fig. 1 The procedure of ABC algorithm for spacecraft attitude tracking controller optimization

4 Simulation Results

In order to investigate the feasibility and effectiveness of the ABC algorithm, spacecraft attitude tracking controller parametric optimization experiment is conducted, and further comparative experimental results with the PSO algorithm are also given.

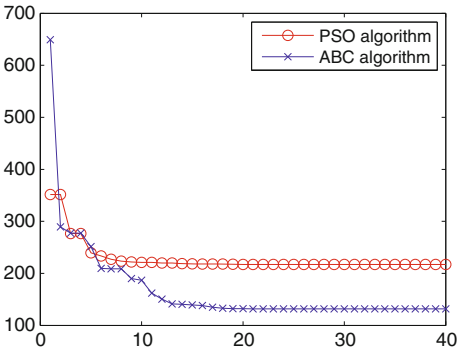

Fig. 2 The evolution curves of ABC and PSO algorithms

Set the initial parameters of ABC algorithm as: $N = 40, N_e = N_u = 20, L_{limit} = 10, I_{max} = 40, D = 9, \mathbf{lb} = [1, 1, 1, 0.05, 0.05, 0.05, 1, 1, 1], \mathbf{ub} = [1000, 1000, 1000, 100, 100, 100, 1000, 1000, 1000]$. The weight $w_1 = 0.9, w_2 = 0.1$, and $T_m = 100$ s.

The initial parameters of PSO algorithm set as the same as ABC algorithm, the population size is 40, the maximum generation is 40, and the parameter dimension is 9. The fitness function defined by Eqs. (14) and (11). Under the advices of [12], learning factor c_1 and c_2 are equal to 2.0. Inertia weight is equal to 0.5.

The spacecraft inertia is $\mathbf{J}_0 = [220, 0, 0; 0, 200, 0; 0, 0, 175]\,\text{kgm}^2$. the uncertainty inertia is $\Delta\mathbf{J} = [-15, 10, -20; 10, 10, 30; -20, 30, -10]\,\text{kgm}^2$. The initial MRPs of the spacecraft is equal to $[0.01, -0.02, 0.04]^T$, and the initial angular velocity is equal to $[-0.005, 0.002, -0.008]^T$ rad/s. The desired angular velocity is $\boldsymbol{\omega}_d = 0.001 \times [\sin(2\pi/600), \sin(2\pi/500), \sin(2\pi/300)]^T$ rad/s .

The external disturbance is $\mathbf{T}_d = [0.001 \times (1 + \sin(2\pi/200)); -0.01 \times (1 + \sin(2\pi/300)); 0.02\times (1 + \sin(2\pi/400))]$ Nm , the inertia of each reaction wheel is taken as 0.4 kgm^2, the nominal reaction wheels' install matrix is $\mathbf{A}_{s0} = [1, 0, 0, -0.5774; 0, 1, 0, -0.5774; 0, 0, 1, -0.5774]$. The uncertainty install matrix of the reaction wheels is $\Delta\mathbf{A}_s = [0.03, 0.03, -0.03, -0.03; -0.03, 0.03, -0.03, 0.03; 0.03, -0.03, 0.03, -0.03]$. The initial wheel speed $\Omega(0) = [3000, 3000, 3000, 3000]^T$ rpm . For the remainder parameters we can refer [7].

The result of the ABC and PSO algorithms is shown in Fig. 2. In Fig. 2, we can see the initial result of PSO algorithm is less than ABC algorithm, but after several iterations, the best fitness value of ABC algorithm is less than PSO algorithm. It turns out that the best fitness value of ABC algorithm is 131.6, while the best fitness value of PSO algorithm is 216.9, apparently showing that ABC algorithm can find the optimal parameters for spacecraft attitude tracking controller more stable than PSO algorithm, and can effectively solve the parametric optimization problem of spacecraft attitude tracking with disturbances and uncertainties.

The simulation result with ABC and PSO algorithms optimization parameters are shown in Fig. 3, which shows the attitude tracking error σ_e in the numeric simulation. Compare to [7], the convergent time of attitude tracking error with

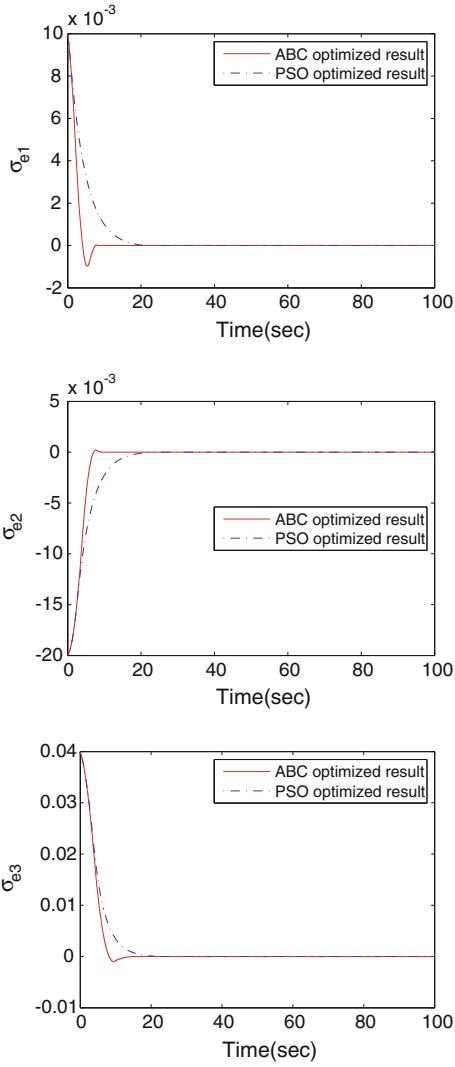

Fig. 3 Time history of the attitude tacking error

PSO and ABC optimized result is decreased from about 200 to 20 s in Fig. 3, and ABC optimized result has better performance than PSO optimized result.

5 Conclusion

An artificial bee colony algorithm is used in spacecraft attitude tracking controller parametric optimization. Define the objective function with the angle error, angular velocity error and the simulation time for the attitude tracking controller

parametric optimization. Compared with PSO algorithm, ABC algorithm has better optimized result. The result shows that the ABC algorithm can be used in the spacecraft attitude tracking controller parametric optimization.

References

1. Luo W, Chu Y, Ling K (2005) H-infinity inverse optimal attitude-tracking control of rigid spacecraft. J Guid Control Dyn 28(3):481–493
2. Jin Y, Liu X, Qiu W et al (2008) Time-varying sliding mode controls in rigid spacecraft attitude tracking. Chin J Aeronaut 21:352–360
3. Pukdeboon C, Zinober ASI (2009) Optimal sliding mode controllers for attitude tracking of spacecraft. In: 18th IEEE international conference on control applications, Saint Petersburg, Russia, pp 1708–1713
4. Pukdeboon C, Zinober ASI, Thein ML (2010) Quasi-continuous higher order sliding-mode controllers for spacecraft-attitude-tracking maneuvers. IEEE Trans Industr Electron 57(4):1436–1444
5. Wu S, Radice G, Gao Y et al (2011) Quaternion-based finite time control for spacecraft attitude tracking. Acta Astronaut 69:48–58
6. Zou A, Kumar KD, Hou Z et al (2011) Finite-time attitude tracking control for spacecraft using terminal sliding mode and chebyshev neural network. IEEE Trans Syst Man Cybern B 41(4):950–963
7. Chen S, Dong Y, Su J (2010) Sliding mode control using RBF neural network for spacecraft attitude tracking. In: IEEE international conference on intelligent computing and intelligent systems (ICIS2010), Xiamen, China, vol 2. pp 211–214
8. Marinakis Y, Marinaki M (2010) A hybrid genetic-particle swarm optimization algorithm for the vehicle routing problem. Expert Syst Appl 37(2):1446–1455
9. Karaboga D, Basturk B (2007) A powerful and efficient algorithm for numerical function optimization: artificial bee colony (ABC) algorithm. J Global Optim 39(3):459–471
10. Karaboga D, Akay B (2009) A comparative study of Artificial Bee Colony algorithm. Appl Math Comput 214(1):108–132
11. Karaboga D, Basturk B (2008) On the performance of artificial bee colony (ABC) algorithm. Appl Soft Comput 8(1):687–697
12. Eberhart RC, Kennedy JA (1995) New optimizer using particle swarm theory. In: Proceedings of the 6th international symposium on micro machine and human science, Nagoya, Japan, pp 39–43

Routing for Predictable LEO/MEO Multi-Layered Satellite Networks

Heyu Liu and Fuchun Sun

Abstract LEO/MEO Multi-Layered Satellite Network (MLSN), consisting of low and medium earth orbit satellites, is capable of providing higher coverage and better service than most Single-Layered Satellite Network. Its performance, however, has been longly encumbered by obsolete routing protocols and algorithms. This paper takes the predictability of satellite movements into consideration, based on which a novel routing protocol—Predictable Satellite Network Routing Protocol (PSNRP), is proposed. In this protocol, all topology changes due to satellite movement are classified into predictable and unpredictable changes. This predictability assists to reduce the protocol overhead. The simulations show that except for obtaining better routing performance, PSNRP also successfully allocates calculation resources evenly among all nodes, separates user data from protocol control data, and achieves stronger robustness on undergoing satellite failures and link congestions.

Keywords MLSN · LEO/MEO · Routing · Predictable · Protocol · Robustness

1 Introduction

Satellite networks are indispensable in modern communication network, especially in the districts where wired accesses are not available. Satellite networks consist of satellites running on earth orbits with Inter-Satellite Links (ISLs) connecting them.

H. Liu (✉) · F. Sun
State Key Laboratory of Intelligence Technology and Systems, Department of Computer Science and Technology, Tsinghua University, Beijing, People's Republic of China
e-mail: liuheyukicker@yahoo.com.cn

F. Sun
e-mail: fcsun@mail.tsinghua.edu.cn

F. Sun et al. (eds.), *Foundations and Practical Applications of Cognitive Systems and Information Processing*, Advances in Intelligent Systems and Computing 215,
DOI: 10.1007/978-3-642-37835-5_44,

In accordance with their altitudes, orbits are classified into Low Earth Orbit (LEO), Medium Earth Orbit (MEO), and Geostationary Earth Orbit (GEO). MLSN, especially LEO/MEO MLSN is becoming a critical issue in the research of satellite network for its lower end-to-end delay and stronger robustness over Single-Layered Satellite Networks. For every communication network, routing scheme is decisive. Different from the fixed topology in conventional ground network, the rapid time-variant topological change and complicated structure in LEO/MEO satellite network make it complicated to design a proper routing protocol.

Three categories of strategy are proposed to deal with topological change: Virtual Topology, Virtual Node, and Strategies dependent on topology [1]. In Virtual Topology, the whole cycle of satellite network T is divided into n timeslots $[t_0 = 0, t_1)$, $[t_1, t_2)$, …, $[t_{n-1}, t_n = T]$, and the topology is deemed as fixed in every timeslot. In another word, topology changes occur only in time nodes $t_1, t_2, \ldots, t_n$. Due to the predictability of satellite movement, all the time nodes and their relevant topologies could be off-line pre-calculated. [2] Virtual Topology strategy was usually adopted in the FSA-based routing [3], the ATM-based routing [4] and snapshot-based routing [5]. The Virtual Node topology attempts to divide the surface of the earth into grids, and every grid is represented by a virtual node whom is described by an invariant logical address. According to the strategy, the satellite covering the grid for the longest time is bounded with this node, and it transfers the relevant information to successive satellite during decoupling. The Virtual Node strategy actually shields satellite relative movement to the ground at the cost of greatly increasing on-board processing data. The IP-based routing [6] and distributed routing [7] belong to this strategy. In recent research, Strategies dependent on topology attract growing attention. Satellites are capable of perceiving the real-time topology and opting different routing strategies. Strategies dependent on topology are, however, designed for some specific topologies [8]. Of these three categories, Virtual Topology is the most widely applied in satellite network routing research for its off-line computation ability and utilization of predictable satellite motion [9].

As for the LEO/MEO MLSN, researchers have designed a number of routing protocols. Predictable Link-State Routing (PLSR) proposed by Fischer successfully takes advantage of satellite movement to simplify protocol. However, it is designed for Single-Layered Satellite Network [10]. Multi-Layer Satellite network Routing algorithm (MLSR) is designed for MLSN [11], but it cannot meet QoS requirements. Chen adopted Virtual Topology Grouping strategy instead of Virtual Topology, and first presented the idea of grouping [12]. But in her SGRP protocol, the whole cycle is divided into too many short time slots that a lot of them are not long enough to deploy subsequent routing protocol and algorithms, resulting in topology jitter. To merge time slots, long proposed NSGRP based on an improved Virtual Topology Grouping strategy [13], but it only applies to GEO/MEO/LEO Triple-Layered Satellite Network.

The above protocols are mainly encumbered by two drawbacks: 1. they do not effectively make use of the predictability of satellite movement. Different from the

mobile ad-hoc network, the movements of satellites are predictable and imply great values. But these protocols only use it to divide time slots; 2. The robustness of satellite network is very weak on facing emergencies. For example, MEO satellites in NSGRP take charge of all the controlling and most of the routing tasks, which often make them hot-spots. Once anomalies occur in these bottlenecks, the whole performance of network degrades. Meanwhile, re-routing strategy is not efficient in handling system anomalies.

In this paper, we improve the idea of treating the topological change as an array of topology snapshot handoffs [5]. Each topology snapshot describes the fixed network linking status in a time slot, and the handoff order reflects the predictable topological change of the network. Based on this topology model, we propose a Predictable Satellite Network Routing Protocol (PSNRP). Simulation results indicate that PSNRP shows a high performance on end-to-end delay and robustness to anomalies.

The constellation model is discussed in Sect. 2 and then topology model in Sect. 3. PSNRP is illustrated in details in Sect. 4. Simulation results and relevant analysis are depicted in Sect. 5. Finally, Sect. 6 is a brief conclusion and future works.

2 Constellation Model

The MLSN in this paper consists of LEO layer and MEO layer, Table 1 shows the parameters of the constellation. The running cycles in the table are calculated using Kepler equation given the orbit height [14].

LEO. The sub-constellation in LEO layer adopts the Walker star constellation model. It is able to provide continuous and complete coverage of the earth surface.

MEO. The sub-constellation in MEO layer adopts Walker-δ constellation model. It also continuously and completely covers both the earth surface and LEO layer.

Ground Station. In our model, there are two kinds of ground stations—GGs (Ground Gateways) and CCs (Control Centers). GGs are used to switch user data with LEO satellites while CCs take charge of switching control data of the routing protocol with MEO satellites.

Four kinds of duplex links connect satellites and ground stations. They are Inter-Satellite Links (ISLs), Inter-Orbital Links (IOLs), User Data Links (UDLs), and User Control Links (UCLs).

Table 1 Parameters of constellation

	Orbit height (km)	Running cycle (hour/h)	Satellite number	Orbit obliquity
LEO	895.5	12/7	6 × 8	90°
MEO	10390	6	2 × 5	45°

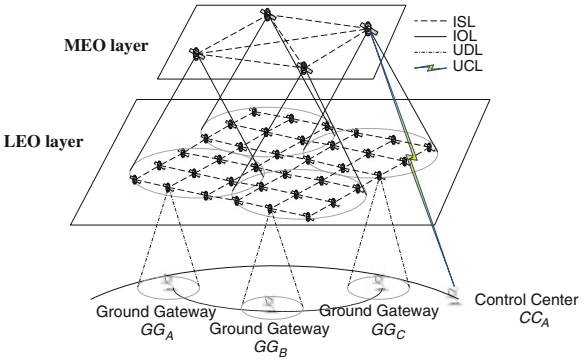

Fig. 1 The structure of a LEO/MEO MLSN

UCLs are first proposed in this paper and they are used to transfer routing protocol control data between CCs and satellites. UCLs are stipulated to exist only between MEO satellites and Control Centers, the reason will be further discussed later.

Figure 1 depicts the LEO/MEO MLSN structure.

3 Topology Model

In this section, a concrete topology model is constructed for LEO/MEO MLSN. The core idea is that the cycle is divided into a number of time slots according to the Virtual Topology Grouping strategy and within a time slot the topology is deemed as fixed. A snapshot is abstracted from a fixed topology to help routing. Given the predictability of network topology, all the snapshots can be calculated previously; therefore, topology change can be deemed as the handoffs of an array of snapshots.

3.1 Snapshots and Division of Time Slot

The definition of topology snapshot was proposed in [5] to describe the mobility for LEO single-layered air-craft network. Now, based on the Virtual Topology Grouping strategy, we formally give the definition of snapshot and division of time slot in LEO/MEO MLSN.

Definition 1 Time slot and time node: a time slot is a short period of time during satellite network running cycle. For t', $t'' \in$ T with $t' < t''$, $[t', t'')$ is used to represent the time slot $\{t \in T | t' \leq t < t''\}$. A time node is a time-point distinguishing two adjacent time slots.

Definition 2 Division of time slot: the moment a LEO satellite leaves a group (see Sect. 4.1 for details of grouping) for another one is defined as a time node, thus a new time slot is generated. In another word, the topology is deemed as fixed if no LEO satellite has changed the group it belongs to. This method for division is proved feasible in [5].

According to this method, the whole running cycle can be divided into n time slots denoted by $[t_0 = 0, t_1)$, $[t_1, t_2)\ldots$ $[t_{n-1}, t_n = T)$. The topology in every time slot is deemed as fixed, it changes only in time nodes $t_1, t_2, \ldots, t_n$. This method of dividing time slot lays the fundamental of the Virtual Topology Grouping strategy [15].

Definition 3 Topology snapshot: the fixed topology in any time slot $[t_i, t_{i+1})$ could be described by a weighted digraph $G_i = (V_i, E_i)$, in which V_i and $E_{i,,}$ respectively, represents the nodes and edges in graph G_i. Two-tuple $S_i =< t_i, G_i >$ is defined as the topology snapshot of time slot $[t_i, t_{i+1})$.

Therefore, all the topology changes in a cycle can be replaced by an array of topology snapshots $<S_0, S_1, S_2, \ldots, S_n>$, of which every S_i can be pre-calculated. In practical operation, the protocol usually sets a mapping function Φ. $S_{i+1} = \Phi(S_i)$ describes the relationship between current snapshot and the next one.

3.2 Predictable Change and Unpredictable Change

In this topology model, predictable changes equal to the handoffs of an array of topology snapshots. The predictability of snapshots makes it possible to cut down OBP overheads. Handling the unpredictable changes caused by anomalies in MLSN is beyond the capability of the topology model itself. Fortunately, PSNRP works on it, which will be further illustrated in Sect. 4.

4 Predictable Satellite Network Routing Protocol

In this section, PSNRP is illustrated in detail.

4.1 Some Definitions

It is necessary to define some concepts first of all.

LEO group and group manager (GM): a LEO group, denoted by $G(M_{i,j})$, refers to a set of LEO satellites all locating in the footprint of the same MEO satellite $M_{i,j}$ and constructing data links with it according to the principle of the

longest covering time. $G(M_{i,j}) = \{L_{i,j,k} | k = 1, 2, \ldots, N_{i,j}\}$, in which $N_{i,j}$ means the number of LEO satellites in group $G(M_{i,j})$. $M_{i,j}$ is the group manager for all LEO satellites in group $G(M_{i,j})$, denoted by $GM(L_{i,j,k}) = M_{i,j}$.

Snapshot Sequence Report (SSR): a snapshot sequence report is a k-number topology snapshot array generated by ground Control Centers. It results from an off-line topology snapshot pre-calculation.

$$SSR(t_k) = < S_{k+1}, S_{k+2}, \ldots, S_{k+n} > , \; n \geq 0; \tag{1}$$

In which S_i refers to a topology snapshot. The equation shows that even before time t_k, S_{k+1} and the successful $n-1$ snapshots have been pre-calculated on the ground.

Snapshot Report (SR): A Snapshot Report is a topology snapshot handoff report. MEO satellite sends it to all its group members in LEO layer.

The report is constituted in the form of the differences between current snapshot and the next one, thus it is a difference report.

Link-state database (LSDB): Compared with conventional link-state protocols, the LSDB in PSNRP does not change a lot. After receiving the SR from group manager, a LEO satellite renews the topology and updates its LSDB with the graph extracted from SR.

Simple Link-State Advertisement (sLSA): When link anomalies are detected, a LEO satellite flood the sLSAs within LEO layer to inform other nodes. To reduce overhead, sLSA retains only four essential parameters: $sLSA(t) = <x, y, t, b>$, $(x, y) \in E_i$, $t_i \leq t \leq t_{i+1}$ $b = \{0, 1\}$; in which x, y are LEO satellites, t is the moment detecting an anomaly, b is a sign bit (0 refers to unplanned shut-down and 1 refers to unplanned turn-on of some link). We will see that due to the potentially unpredictable topology changes, the network may generate a lot of advertisements. In this situation, using sLSA greatly reduces the overhead.

LEO layer routing table: PSNRP provides two kinds of routing service—ordinary routing services and QoS routing services. Ordinary services aim to minimize the end-to-end delay of a call, which could meet the demand of most network traffic today. QoS services are prepared for users with QoS requirements such as delay, bandwidth, jitter, package loss, etc.

To emphasize the protocol itself, we do not consider QoS routing in this section, and leave them for Sect. 5. In PSNRP, generally speaking, all data packets are switched in LEO layer if possible, and MEO layer is just responsible for computing and distributing the control information. So routing tables are completed in LEO satellites, $LT(L_{i,j,k}) = \{<y, \; \text{SPF}(L_{i,j,k}) \rightarrow y> | \; \forall y, \; y \text{ is a LEO satellite}\}$. In which SPF() represents the optimal path to every LEO satellite computed through Dijkstra algorithm.

Anomaly Report (AR): There are two kinds of AR: $\text{AR}_{L \rightarrow M}$ and $\text{AR}_{M \rightarrow G}$. When a LEO satellite detects anomalies, besides flooding sLSAs, it also reports to group manager through $\text{AR}_{L \rightarrow M}$. Once the group manager receives the report, it uses the report to update snapshot S_{i+1} which is to be sent to LEO group members. By this mechanism, underlying sLSA flooding possibility is greatly reduced. If an

anomaly lasts longer than the threshold, after receiving repeated ARs on it, the group manager sends $AR_{M \to G}$ to inform Control Centers of this long-term anomaly. The Control Centers then uses $AR_{M \to G}$ to update the computed snapshots.

Though the improved Virtual Topology Grouping strategy proposed by Long [15] has effectively reduced the total number of timeslots in a cycle, it is still infeasible to store all these snapshots on board.

Algorithm 1 describes steps taken by a LEO satellite node.

Algorithm 1: main loop for a LEO satellite $L_{i,j,k}$

```
1   var sr, x, slsa, ar /*sr is a SR variable; x is an anomaly; slsa is a sLSA variable;
                         ar is an AR variable*/
2   while true do
3       if sr = receive(IOL_{M→L}) then /*receiving SR report from group manager*/
4           update_LSDB(sr);
5       end if
6       if x = detect_change() then /*detecting exception and storing it in x*/
7           update_LSDB(x);
8           slsa = create_sLSA(x); /*generating sLSA report*/
9           send (slsa, neighbor_nodes(L_{i,j,k})); /*flooding sLSA*/
10          ar = creat_AR(x);
11          send(ar, GM(L_{i,j,k})); /*sending AR report to group manager*/
12      end if
13      if slsa = receive(ISL) then /*receiving sLSA*/
14          if is_fresh(slsa) then
15              update_LSDB(slsa);
16              send (slsa, neighbor_nodes(L_{i,j,k}))
17          end if
18      end if
19      update_LT(LSDB); /*updating routing table in LEO layer*/
20  end while
```

Packets are mainly routed in LEO layer. A satellite $L_{i,j,k}$ maintains a LSDB and updates its routing table according to this LSDB. The design for algorithms in LEO is mainly based on how to cope with two kinds of topology changes—predictable changes and unpredictable changes. Lines 3–5 describe the response to predictable changes, which are abstracted into a sequence of snapshots maintained by MEO satellites. When its time to handoff, group managers send new snapshot to all LEO group members through AR reports before the old snapshot expires. After receiving a SR report, a LEO satellite just need to update its LSDB according to the SR report. Lines 6–18 illustrate the mechanism for unpredictable changes. Unpredictable changes are often classified into two categories: the first happens at the initial stage of a new time slot, it is detected when a LEO satellite compares the updated LSDB with the real link-state; the other is that detected after the routing tables have been established. Whatever anomaly is detected, the node updates its LSDB first of all (Line 7) and then generates sLSA and AR (Lines 8–12), which are, respectively, to be sent to neighbor nodes and group managers. Similarly, if the node receives a sLSA, which has not been received yet, the node uses it to

renew LSDB and keeps flooding. Given all the predictable and unpredictable changes, a node always calculates its routing table with the latest LSDB. Reference [16] proved that, for a link-state routing, optimal path re-calculation does not require a complete run of Dijkstra algorithm. Instead, nodes and links affected by SR or sLSA are sufficient. This is particularly beneficial in our model since a topology change usually affects few links or nodes. Our on-board computation ability could totally meet these computational requirements.

Algorithm 2: main loop for a MEO satellite $M_{i,j}$

```
1   var sr, ar /* sr is a SR variable; ar is an AR variable */
2    while true do
3       if timestamp(stack_next) == current_time()/*load back-up sequence*/
4       then stack_now = stack_next;
5            stack_next = 0;
6       end if
7       if timestamp(δ(stack_now)) == current_time()/* handoff time*/
8       then sr = create_SR(δ(stack_now));
9            sr = sr + stack_AR_M ;/*considering anomalies*/
10           send (sr, G(M_i,j ));
11           stack_now = stack_now/δ(stack_now);
12      end if
13      if ssr = receive(UCL_G→M) then/*receiving SSR*/
14         if isfresh(ssr) then
15           stack_next= ssr;
16           send(ssr, neighbor_nodes(M_i,j));    /*flooding*/
17         end if
18      end if
19      if ar = receive(IOL_L→M ) then
20         if isfresh(ar) then
21           update_ stack_AR_M (ar);
22           if isoverthreshold(ar) then /*detecting long-term anomalies*/
23              send(create_AR_M→G(ar), CC);
24           end if
25           send(ar, neighbor_nodes(M_i,j));
26         end if
27      end if
28      if ar = receive(ISL) then /*ordinary anomalies*/
29         if isfresh(ar) then
30           update_ stack_AR_M (ar);
31           send(sr, neighbor_nodes(M_i,j));
32         end if
32      else if ssr = receive(ISL) then /*receiving SSRfrom CCs*/
33            if isfresh(ssr) then
34               stack_next= ssr;
35               send(ssr, neighbor_nodes(M_i,j);
36            end if
37      end if
38    end while
```

Algorithm 2 describes the main loop of algorithm in MEO nodes. MEO layer is the core of the whole PSNRP. Under normal circumstances, this layer does not participate in data routing or forwarding, but it is responsible for controlling all the space-based and ground-based sub-networks. A MEO satellite maintains three databases: stack_now is used to store the sequence whose snapshots are being downloaded to LEO group members one by one; stack_next stores the sequence which has been received from CCs, and the sequence will be sent to stack_now after stack_now being vacuumed up (Lines 3–6); $\text{stack}_{\text{AR\_M}}$ is used to store the anomalies reported by group members. Funtion $\delta()$ returns the first element in an array. When it is time to send a snapshot in stack_now to LEO layer for handoff, a MEO node sends a SR report on the basis of snapshot and latest anomalies in $\text{stack}_{\text{AR\_M}}$ (Line 9). Finally, stack_now eliminates the obsolete snapshot. On receiving a new SSR report from CCs or other nodes, a MEO node extract the sequence and store it in stack_next (Lines 13–18, Lines 32–36). Similarly, the MEO node updates its $\text{stack}_{\text{AR\_M}}$ with arriving AR reports. A very important function is isoverthreshold(), which returns the decision whether an anomaly is long-term or not by a comparison with a threshold. To reduce processing overhead, as illustrated above, long-term anomalies are reported to CCs by $\text{AR}_{\text{M}\rightarrow\text{G}}$ to update SSR report.

PSNRP could effectively handle anomalies by regarding them as unpredictable changes, so it is robust on anomalies.

5 Simulation and Results

In this section, we mainly aim to show the performances of PSNRP, on which runs Dijkstra routing algorithm, by comparing it with SGRP. The simulation is based on the constellation model in Sect. 2, which is the same as that in [12]. Simulation tools are NS2 and OPNET. LEO layer provides accesses to MLSN for the users.

Figure 2 depicts the relationship between average end-to-end delays and their distances in three protocols. The results show that if the distances are short, their performances are similar; but with the increase of the distances PSNRP obviously has a shorter average end-to-end delay than SGRP. The reason is probably that when the distances exceed the radius of the group, most user data are routed through MEO satellites in SGRP—the propagation delays of IOLs are much longer than that of LEO layer ISLs.

We also test protocol's performances under the circumstance of link congestions and satellite failures. PSNRP has a strong robustness on satellite failure and Fig. 3 depicts the result. The simulation studies the relationship between the failing probability of each satellite and the average convergence time. As shown by the figure, PSNRP performs far better than SGRP if the failing probability is not large. It may result from the essential sLSA broadcasting mechanism that makes all LEO nodes be aware of the topology change soon. Instead, in SGRP, after detecting the failure, a LEO node has to report to group manager and wait for the

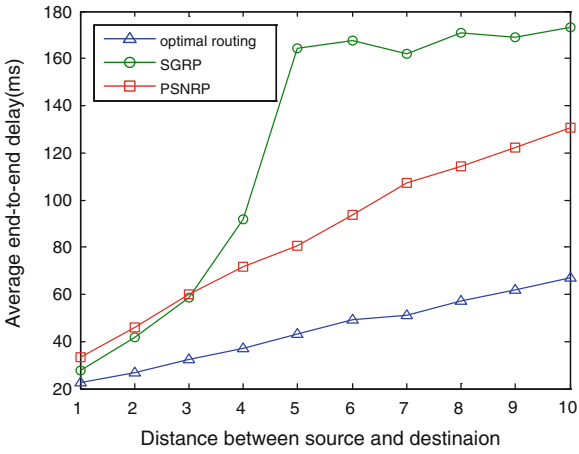

Fig. 2 Average end-to-end delay

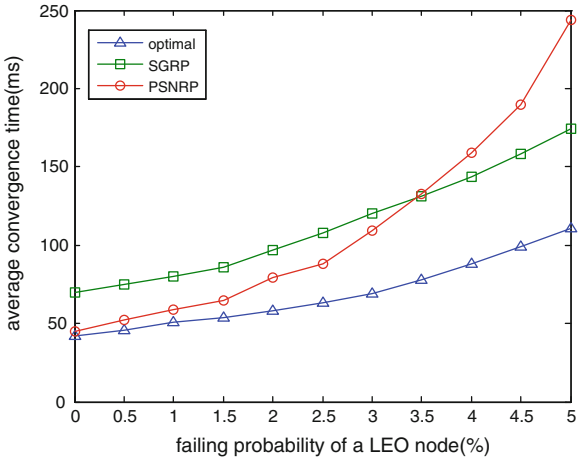

Fig. 3 Robustness on failures

re-calculated routing table. If the number of failed satellites is too large, too many sLSAs are transferred in the network for all the nodes to change LSDB, which causes huge overhead. SGRP is relatively insensitive to increment of the number, so it performs better. Considering that satellite failures are not common, PSNRP is more robust on satellite failures. The satellite failure in this paper only means LEO satellite failure. As the MEO satellites play central roles in both protocols, no failure is tolerable in MEO layer—even one would lead to the failure of the protocol. Actually, back-up MEO satellites are often deployed on MEO layer in case of failures.

6 Conclusion

In this paper, we propose a routing scheme for predictable satellite networks. Different from conventional MLSN routing protocols like SGRP, PSNRP takes full advantage of the network predictability to reduce on-board computation; also it introduces the ground Control Centers to utilize ground-based resources. The simulation results show that PSNRP obtains shorter end-to-end delays and stronger robustness on anomalies.

The future research will focus on how to solve the problem of inconsistence between the real topology and that maintained by nodes' LSDB at the initial stage of a snapshot. Another topic is how to reduce the overhead of protocol controlling data when a large number of anomalies happen within a short time.

Acknowledgments The work is jointly supported by the National Natural Science Foundation of China (Grants No. 60973145, 61004021).

References

1. Elbert BR (2004) The satellite communication application handbook. Artech House Inc., Norwood
2. Zhou Y, Sun F, Zhang B (2006) A time-division QoS routing protocol for three-layered satellite networks. Chin J Comput 29:1813–1822
3. Chang HS, Kim BW, Lee C (1998) FSA-based link assignment and routing in low-earth orbit satellite networks. IEEE Trans Veh Technol 47:1037–1048
4. Werner M, Delucchi C, Vegel H (1997) ATM-based routing in LEO/MEO satellite networks with intersatellite links. IEEE J Sel Areas Commun 15:69–81
5. Gounder V, Prakash R, Abu-Amara H (1999) Routing in LEO-based satellite networks. In: Proceedings of IEEE emerging technologies symposium on wireless communications and systems. IEEE Press, pp 91–96
6. Hashimoto Y (1998) Design of IP-based routing in a LEO satellite network. In: Proceedings of 3rd international workshop on satellite-based information services, Dallas, pp 81–88
7. Ekici E, Akyildiz IF, Bender MD (2000) Datagram routing algorithm for LEO satellite networks. In: Proceedings of IEEE INFOCOM 2000. IEEE Press, pp 500–508
8. Zhu L, Wang R (2004) The research of satellite routing algorithm. Microcomput Dev 14:9–11
9. Reeves CR (ed) (1993) Modern heuristic techniques for combitiorial problems. Blackwell Scientific Publications, Oxford
10. Fischer D, Basin D, Engel T (2008) Topology dynamics and routing for predictable mobile networks. In: Proceedings of ICNP 2008. IEEE Communications Society, Orlando, pp 207–217
11. Ekici E, Akyildiz IF, Bender MD (2002) MLSR: a novel routing algorithm for multi-layered satellite IP networks. IEEE Trans Networking 18:411–424
12. Chen C, Ekici E, Akyildiz IF (2002) Satellite grouping and routing protocol for LEO/MEO satellite IP networks. In: Proceedings of 5th ACM international workshop on wireless mobile multimedia (WoWMoM'2002). pp 109–116
13. Long F (2010) Research on satellite network robust QoS-aware routing, PhD thesis. Tsinghua University, Beijing

14. North J (1994) The Fontana history of astronomy and cosmology. Fontana Press, London, pp 309–310
15. Long F, Xiong N, Athanasios VV, Yang LT, Sun F (2009) A sustainable heuristic QoS routing algorithm for pervasive multi-layered satellite wireless networks. Wireless Netw 14:1–17
16. OSPF protocol analysis, RFC (July 1991) Internet Engineering Task Force (IETF) Request for Comments 1245

Improved ICP Algorithm with Bounded Rotation Angle for 2D Point Set Registration

Chunjia Zhang, Shaoyi Du, Jianru Xue and Xiaolin Qi

Abstract This paper presents a more robust iterative closest point (ICP) approach for 2D point set registration. An inequality constraint of the rotation angle is introduced into the least square registration model which is solved by an extended ICP algorithm. At each iterative step of the algorithm, a closed-form solution for the rotation is obtained according to the monotonicity of the model with respect to the rotation angle. The proposed approach extends the convergence domain of the ICP algorithm, and it can be used much more widely. A series of 2D point set experiments on part B of MPEG-7 CE-shape-1 dataset prove that the proposed method is much more robust than ICP without increasing the computational complexity.

Keywords Iterative closest point · Point set registration · Rotation angle

1 Introduction

Point set registration plays an important role in computer vision, pattern recognition, and image processing. The Iterative Closest Point (ICP) algorithm [1–3] is a robust and efficient method for the registration problem, and has been applied

C. Zhang (✉) · S. Du · J. Xue · X. Qi
Institute of Artificial Intelligence and Robotics, Xi'an Jiaotong University, Xi'an, Shaanxi, China
e-mail: cjzhang.china@gmail.com

S. Du
e-mail: dushaoyi@gmail.com

J. Xue
e-mail: jrxue@gmail.com

X. Qi
e-mail: xlqi@gmail.com

F. Sun et al. (eds.), *Foundations and Practical Applications of Cognitive Systems and Information Processing*, Advances in Intelligent Systems and Computing 215,
DOI: 10.1007/978-3-642-37835-5_45,

widely. A lot of work has been done to improve the robustness. For example, Sharp et al. [4] used the Euclidean invariant features to reduce the probability of being trapped into a local minimum, and Silva et al. [5] reduced the influence of initial value and outlier arising by combining genetic algorithm with a new evaluation metric. Some other scholars devote to reducing the computational complexity, for example, Fitzgibbon [6] adopted the Levenberg–Marquardt to minimum the registration error, and Jost et al. [7] presented a coarse to fine multi-resolution approach to speed up the neighbor search. Moreover, the ICP algorithm is extended to the partial registration [8] and the non-rigid registration [9]. However, the convergence domain of these algorithms is quite narrow, and the solutions are easily being trapped into the local minimum.

To solve the aforementioned problem, a new registration model with the boundary of rotation angle is introduced, and a novel ICP algorithm with bounded rotation angle is proposed to compute the model. At each iterative step of this algorithm, the corresponding relationship between two point sets is determined first, and then a closed-form solution for the rotation angle is obtained according to the boundary of the rotation angle and the monotonicity of the model. The proposed approach is robust and fast for 2D rigid point set registration, and proved by a number of experiments based on part B of MPEG-7 CE-shape-1 dataset.

The rest of the paper is organized as follows. In Sect. 2, the least square (LS) problem for point set registration is presented and the ICP algorithm is introduced. In Sect. 3, the LS problem with bounded rotation angle and our solution for 2D point set registration are proposed. In Sect. 4, experiments based on part B of MPEG-7 CE-shape-1 are carried out to demonstrate the robustness and computational efficiency of the proposed algorithm. In Sect. 5, a conclusion is given.

2 The ICP Algorithm

2.1 Point Set Registration Problem

The general statement of the point set registration problem is presented as follows. Given two point sets in $\mathbb{R}^n$, one is a model point set $A \triangleq \{a_i\}$, $(i = 1, \cdots, N_a)$ and the other is a data point set $B \triangleq \{b_i\}$, $(i = 1, \cdots, N_b)$, the registration is to compute a transformation F which best aligns B with A, so the LS problem is presented as follows:

$$\min_{F} \sum_{i=1}^{N_b} ||F(\vec{b}_i) - \Phi\{A, F(\vec{b}_i)\}||^2 \tag{1}$$

Where $F(\vec{b}_i)$ transforms the data point set B to align with the model point set A, $\Phi\{A, F(\vec{b}_i)\}$ is a point in A which matches $F(\vec{b}_i)$ best.

In rigid registration, the transformation F in (1) is expressed as $F(\vec{b}_i) = R\vec{b}_i + \vec{t}$, where $R \in \mathbb{R}^{n\times n}$ is the rotation matrix and $\vec{t} \in \mathbb{R}^n$ is the translation vector. The point set registration is formulated in the following:

$$\begin{aligned} &\min_{R,\vec{t},c(i)\in\{1,2,\cdots,N_a\}} \sum_{i=1}^{N_b} ||(R\vec{b}_i + \vec{t}) - \vec{a}_{c(i)}||^2 \\ &s.t. \quad R^T R = I_m, \det(R) = 1 \end{aligned} \tag{2}$$

2.2 The ICP Algorithm

The ICP algorithm is efficient in dealing with the rigid registration problem (2). To achieve the point set registration, the ICP algorithm iteratively computes the optimal rotation matrix R and translation vector $\vec{t}$ by the following two steps:

Step 1: For R_k and $\vec{t}_k$, find the best corresponding point in A for each point in B:

$$c_k(i) = \arg\min_{j\in\{1,2,\cdots N_a\}} ||(R_k\vec{b}_i + \vec{t}_k) - \vec{a}_j||^2 \tag{3}$$

Step 2: Calculate the new rotation matrix R_{k+1} and translation vector $\vec{t}_{k+1}$ by the following formulation according to the corresponding relationship $\{i, c_k(i)\}$:

$$(R_{k+1}, \vec{t}_{k+1}) = \arg\min_{R_{k+1}\in\mathbb{R}^{n\times n},\vec{t}_{k+1}\in\mathbb{R}^n} \sum_{i=1}^{N_b} ||(R_{k+1}\vec{b}_i + \vec{t}_{k+1}) - \vec{a}_{c_k(i)}||^2 \tag{4}$$

3 A New ICP Algorithm

In this section, a novel model is proposed to describe the bounded rotation angle registration problem, and then a closed-form solution is presented.

3.1 The Proposed ICP Algorithm

The ICP algorithm is fast and accurate, but it is not robust enough. To improve the robustness, a new 2D point set registration model with bounded rotation angle is proposed:

$$\begin{aligned} &\min_{R,\vec{t},c(i)\in\{1,2,\cdots,N_a\}} \sum_{i=1}^{N_b} ||(R(\theta)\vec{b}_i + \vec{t}) - \vec{a}_{c(i)}||^2 \\ &s.t. \quad R(\theta)^T R(\theta) = I_m,\ \det(R(\theta)) = 1 \\ &\theta \in [\theta_b - \Delta\theta, \theta_b + \Delta\theta] \end{aligned} \tag{5}$$

where $R(\theta) = \begin{bmatrix} \cos\theta & -\sin\theta \\ \sin\theta & \cos\theta \end{bmatrix}$, θ is the rotation angle, $\theta_b - \Delta\theta$ and $\theta_b + \Delta\theta$ present the lower and upper bound, respectively. The boundary could be acquired by prior information. In general, it can be computed by principal component analysis (PCA) [1].

The LS problem with inequality constraint (5) can be solved as follows.

Step 1: For $R_k(\theta)$ and $\vec{t}_k$, find the corresponding relationship between A and B:

$$c_k(i) = \arg\min_{j\in\{1,2,\cdots N_a\}} ||(R_k(\theta)\vec{b}_i + \vec{t}_k) - \vec{a}_j||^2 \tag{6}$$

This step could be solved by k-D tree [10] or Delaunay tessellation [11].

Step 2: Compute the new rotation matrix $R_{k+1}(\theta)$ and translation vector $\vec{t}_{k+1}$ as follows:

$$\begin{aligned} (R_{k+1}(\theta), \vec{t}_{k+1}) = \quad & \arg\min \quad \sum_{i=1}^{N_b} ||(R(\theta)\vec{b}_i + \vec{t}) - \vec{a}_{c_k(i)}||^2 \\ & R(\theta)^T R(\theta) = I_m, \\ & \det(R(\theta)) = 1, \\ & \theta \in [\theta_b - \Delta\theta, \theta_b + \Delta\theta], \\ & \vec{t} \in \mathbb{R}^n \end{aligned} \tag{7}$$

This is the key step of the proposed algorithm because Eq. (7) is an inequality constraint optimization problem which is difficult to be solved. Similar to the ICP algorithm, it is easily proved that the proposed algorithm is monotonic convergence [1].

3.2 Transformation Computation

To solve the registration problem with inequality constraint (7), a Lemma is given to eliminate the translation vector $\vec{t}$:

Lemma : Given two point sets $\{\vec{m}_i\}_{i=1}^N$ and $\{\vec{n}_i\}_{i=1}^N$, the function $F(\vec{t}) = \sum_{i=1}^{N} ||(\vec{n}_i + \vec{t}) - \vec{m}_i||^2$ has minimum value when $\vec{t} = \frac{1}{N}(-\sum_{i=1}^{N} \vec{n}_i + \sum_{i=1}^{N} \vec{m}_i)$.

According to the lemma, the minimum value of $F(\theta) = \sum_{i=1}^{N_b} ||(R(\theta)\vec{b}_i + \vec{t}) - \vec{a}_{c(i)}||^2$ is obtained when $\vec{t} = \frac{1}{N_b}(-R\sum_{i=1}^{N_b}\vec{b}_i + \sum_{i=1}^{N_b}\vec{a}_{c(i)})$. Therefore,

$$F(\theta) = \sum_{i=1}^{N_b} ||R(\theta)(\vec{b}_i - \frac{1}{N_b}\sum_{i=1}^{N_b}\vec{b}_i) - (\vec{a}_{c(i)} - \frac{1}{N_b}\sum_{i=1}^{N_b}\vec{a}_{c(i)})||^2.$$

Let $\vec{p}_i = \vec{b}_i - \frac{1}{N_b}\sum_{i=1}^{N_b}\vec{b}_i$ and $\vec{m}_i = \vec{a}_{c(i)} - \frac{1}{N_b}\sum_{i=1}^{N_b}\vec{a}_{c(i)}$. Hence,

$$F(\theta) = \sum_{i=1}^{N_b} ||R(\theta)\vec{p}_i - \vec{m}_i||^2 \tag{8}$$

To find out the optimal solution of (8), partial derivative of θ is computed as follows:

$$\frac{\partial F(\theta)}{\partial(\theta)} = \sum_{i=1}^{N_b}(-\vec{m}_i^T\frac{\partial R(\theta)}{\partial(\theta)}\vec{p}_i - (\vec{m}_i^T\frac{\partial R(\theta)}{\partial(\theta)}\vec{p}_i)^T).$$
$$= 0$$

According to $\vec{m}_i^T\frac{\partial R(\theta)}{\partial(\theta)}\vec{p}_i = (\vec{m}_i^T\frac{\partial R(\theta)}{\partial(\theta)}\vec{p}_i)^T$, we have

$$\frac{\partial F(\theta)}{\partial(\theta)} = -2 \times \sum_{i=1}^{N_b}\vec{m}_i^T\frac{\partial R(\theta)}{\partial(\theta)}\vec{p}_i \tag{9}$$

Furthermore, for 2D rigid rotation matrix, we also have $\frac{\partial R(\theta)}{\partial\theta} = \begin{bmatrix} -\sin\theta & -\cos\theta \\ \cos\theta & -\sin\theta \end{bmatrix}$.

Suppose that $\vec{m}_i = (x_{m_i}, y_{m_i})^T$ and $\vec{p}_i = (x_{p_i}, y_{p_i})^T$, therefore,

$$\frac{\partial F(R(\theta))}{\partial(\theta)} = 2\sin(\theta - \psi_i).$$

where $\psi_i = \arctan\left(\frac{\sum_{i=1}^{N_b}(y_{m_i}x_{p_i} - x_{m_i}y_{p_i})}{\sum_{i=1}^{N_b}(x_{m_i}x_{p_i} + y_{m_i}y_{p_i})}\right)$.

It is obvious that ψ_i is the optimal solution for the special corresponding relationship between A and B. $F(\theta)$ is a monotonically decreasing function when $\theta \in [\psi_i - \pi, \psi_i)$, and it is a monotonically increasing function when $\theta \in (\psi_i, \psi_i + \pi]$.

According to the monotonicity of $F(\theta)$, the rotation angle θ_i is determined by judging where ψ_i belongs to:

Case 1: $\psi_i \in [\theta_b - \Delta\theta, \theta_b + \Delta\theta],\ \theta_i = \psi_i$.
Case 2: $\psi_i < \bar{\theta} - \Delta\theta,\ \theta_i = \bar{\theta} - \Delta\theta$.
Case 3: $\psi_i > \bar{\theta} + \Delta\theta,\ \theta_i = \bar{\theta} + \Delta\theta$.

In case 1, ψ_i belongs to the boundary, and it means that the transformation $F(\theta)$ is converging to the global optimal value. For both of cases 2 and 3, ψ_i does not belong to the boundary, meaning that the transformation $F(\theta)$ is not converging to the global optimal value. Hence, at each iterative step according to the monotonicity of $F(\theta)$, the proper bound is selected as the rotation angle.

Finally, the translation $\vec{t}$ is computed as follows:

$$\vec{t}_i = \frac{1}{N_b}\left(-R(\theta_i)\sum_{i=1}^{N_b}\vec{b}_i + \sum_{i=1}^{N_b}\vec{a}_{c(i)}\right).$$

4 Experiment Results

The experiments of 2D point set registration on part B of MPEG-7 CE-shape-1 dataset [12] are carried out to test the proposed algorithm. Some results are presented in this section to demonstrate the robustness and computational efficiency of the proposed algorithm.

First of all, two rigid point sets are selected randomly. One is the model point set and the other is the data point set. Then the data point set is registered to the model point set by ICP and the proposed algorithm, respectively. A comparison is done to demo the robustness of the proposed algorithm. Some results are presented in Table 1, Figs. 1 and 2.

In Table 1, it can be seen that RMS of two algorithms on Bird are similar, because the ICP algorithm has a good initial value and so it can converge to the minimum. Figure 1 shows the results of this kind of registration. However, RMS on Chicken and Deer in Table 1 show that the ICP algorithm fails without a good initial value, while our algorithm still converges to the minimum, which are illustrated in Fig. 2. Those results show that the proposed algorithm is much more robust than the ICP algorithm.

The convergence analysis of two algorithms on Bird and Chicken is presented in Fig. 3. They show that the proposed algorithm has a similar monotonic convergence and computation complexity with ICP algorithm. The reason is that both of them have a similar computation process.

Table 1 Comparison of constraint, rotation angle and RMS on Bird, Chicken and Deer

	Constraint		Rotation angle		RMS	
	Proposed	ICP	Proposed	ICP	Proposed	ICP
Bird	$\theta_b = 28.34, \Delta\theta = 20$	$\theta_{start} = 28.34$	24.409	24.409	3.186	3.202
Chicken	$\theta_b = 34.05, \Delta\theta = 20$	$\theta_{start} = 34.05$	35.04	−68.31	0.238	76.301
Deer	$\theta_b = -92.07, \Delta\theta = 20$	$\theta_{start} = -92.07$	−90.003	−164.84	0.361	4285.3

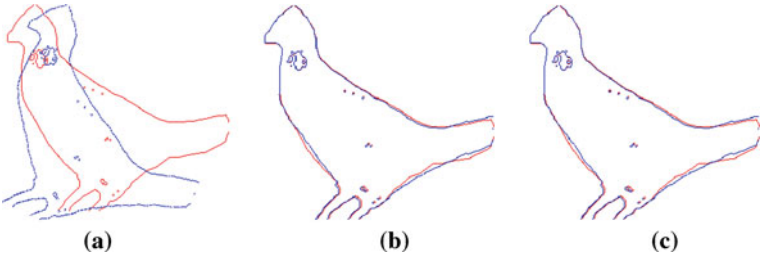

Fig. 1 Registration results of ICP and the proposed algorithm on Bird. **a** Original point set. **b** Registration result of ICP. **c** Registration result of the proposed algorithm

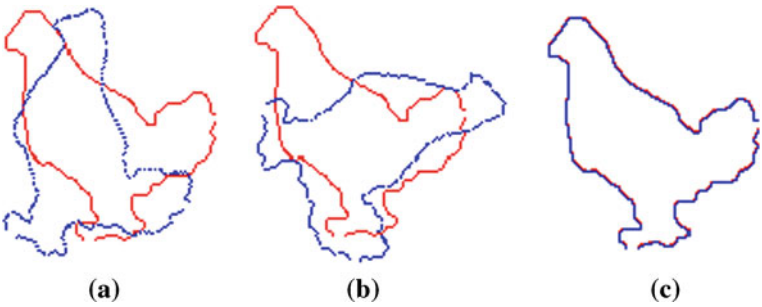

Fig. 2 Registration results of ICP and the proposed algorithm on Chicken. **a** Original point set. **b** Registration result of ICP. **c** Registration result of the proposed algorithm

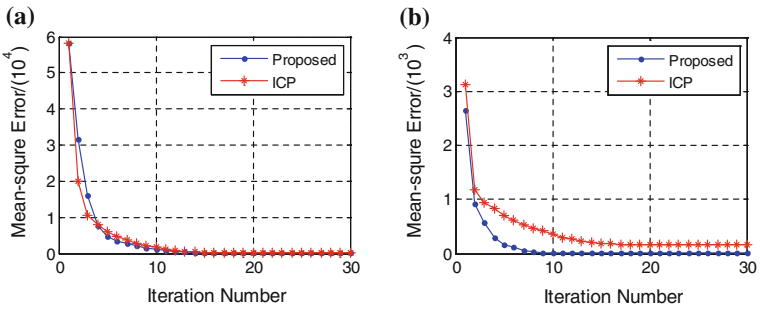

Fig. 3 Convergence results of ICP and the proposed algorithm on Bird and Chicken. **a** Convergence result on Bird. **b** Convergence result on Chicken

5 Conclusion

This paper proposes an improved ICP algorithm which is more robust for 2D point set registration without increasing the computation complexity. The proposed algorithm solves the registration problem with inequality constraint iteratively.

At each iterative step, it computes a closed-form solution for rigid transformation. The future work is to apply this novel approach to 3D point set registration.

Acknowledgments This work is supported by the National Basic Research Program of China under Grant No. 2012CB316400 and the National Natural Science Foundation of China under Grant Nos. 61005014, 90920301, and 61005002.

References

1. Besl PJ, McKay ND (1992) A method for registration of 3-D shapes. IEEE Trans Pattern Anal Mach Intell 14:239–256
2. Chen Y, Medioni G (1991) Object modeling by registration of multiple range images. Sacramento, CA, pp 2724–2729
3. Zhang Z (1994) Iterative point matching for registration of free-form curves and surfaces. Int J Comput Vision 13:119–152
4. Fitzgibbon AW (2001) Robust registration of 2D and 3D point sets. Image Vis Comput 21:1145–1153
5. Jost T, Hugli H (2003) A multi-resolution ICP with heuristic closest point search for fast and robust 3D registration of range images. In: Proceedings of 4th international conference on 3-D digital imaging and modeling. pp 427–433
6. Sharp GC, Lee SW, Wehe DK (2002) ICP registration using invariant features. IEEE Trans Pattern Anal Mach Intell 24:90–102
7. Silva L, Bellon ORP, Boyer KL (2005) Precision range image registration using a robust surface interpenetration measure and enhanced genetic algorithms. IEEE Trans Pattern Anal Mach Intell 27:762–776
8. Phillips JM, Ran L, Tomasi C (2007) Outlier robust ICP for minimizing fractional RMSD. In: Proceedings of 6th international conference on 3-D digital imaging and modeling. pp 427–434
9. Du S, Zheng N, Ying S, Liu J (2010) Affine iterative closest point algorithm for point set registration. Pattern Recogn Lett 31:791–799
10. Nuchter A, Lingemann K, Hertzberg J (2007) Cached k-d tree search for ICP algorithms. In: Proceedings of 6th international conference on 3-D digital imaging and modeling. pp 419–426
11. Barber CB, Dobkin DP, Huhdanpaa H (1996) The quickhull algorithm for convex hulls. ACM Trans Math Softw 22:469–483
12. Database of MPEG-7. http://mpeg.chiariglione.org/

Obstacle Detection for On-Road Vehicle Based on Range and Visual Information Fusion

Lipu Zhou

Abstract Obstacle detection is very important for Advanced Driving Assistance Systems (ADAS) and Unmanned Ground Vehicles (UGV) in on-road scene. The motion of vehicles is restricted by a pair of lane markings. This constraint makes obstacle detection in the on-road scene difference to the one in other robot application. Objects between lane markings are the most emergent obstacles and should be taken more attention. In this paper, we present an effective and efficient method to fuse lane marking information obtained from camera with LIDAR data to discriminate obstacles as within lane markings and outside lane markings.

Keywords Obstacle detection · UGV · ADAS · Lane detection

1 Introduction

As the increasing number of cars, traffic accidents become more frequent. Safety is the first thing concerned by car manufactures. Obstacle detection is the key component to avoid collisions in ADAS and UGVs. It is also an important element in robot field. However, in the on-road scene, behaviors of vehicles must obey traffic rules. The route of vehicles is restricted by a pair of lane markings. Objects in front of a vehicle may not be emergent obstacles, as shown in Figs. 1 and 2, thus the position and motion of an object relative to the lane is much more important than the ones relative to the vehicle. Objects outside a lane, such as trees, traffic signs, streetlights, vehicles moving parallel in a neighborhood lane, and pedestrians walking along a road may not be potential obstacles. Objects inside the same

L. Zhou (✉)
State Key Laboratory of Intelligent Technology and Systems, Tsinghua National Laboratory for Information Science and Technology, Department of Computer Science and Technology, Tsinghua University, Beijing 100084, China
e-mail: zlp09@mails.tsinghua.edu.cn

F. Sun et al. (eds.), *Foundations and Practical Applications of Cognitive Systems and Information Processing*, Advances in Intelligent Systems and Computing 215,
DOI: 10.1007/978-3-642-37835-5_46,

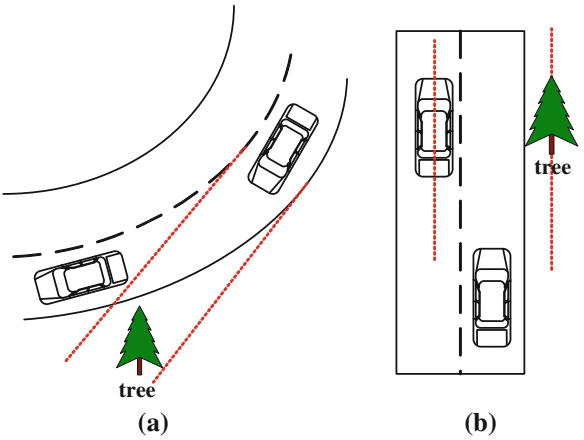

Fig. 1 **a** The real obstacle inside a lane is missed. Object, represented as a tree, in front of the vehicle is detected incorrectly as obstacle. **b** False alarm when not consider the lane information

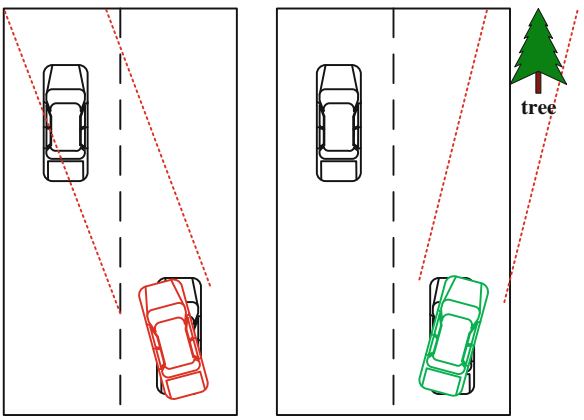

Fig. 2 When the position of a vehicle is even slightly titled, objects in front of a vehicle will be incorrectly classified as emergent obstacles if the lane information is not considered

lane with a vehicle have a higher priority and should be distinguished with the ones outside the lane.

Camera is an important device for obstacle detection and is well studied. In [1], a rear obstacles detection system using a hierarchical detecting strategy was presented. In [2], moving obstacle was detected depending on the relative motion between cameras and obstacles. In [3], "Relative In coming Angle" was introduced to detect the crossing obstacle. In [4], a real-time obstacle detection method using dense stereo vision and optical flow was proposed. However, camera cannot provide the precise location and motion of an obstacle which is important to estimate the risk of an obstacle [5].

Lidar is also used in obstacle detection application. In [5], risk of point clouds was estimated to generate the obstacle map. In [6], a self-supervised obstacle detection method using monocular vision and sparse laser data was presented. This method was used in humanoid navigation. In [7], height-length-density (HLD) was proposed for positive and negative obstacle detection. In [8], Negative Obstacle

Detector (NODR) was presented in off-road environment. These methods focused on providing potential hazard for the motion of a robot in the off-road scene. However, lane constraint should be considered in the on-road scene.

In recent years, Cameras and LIDARs have become common devices for environmental perception of various applications. They provide complementary information. LIDARs have a wide angular view and provide accurate range information. The data size is small and can be processed fast. Cameras offer color and texture of a scene. Position, orientation, and motion of an object can be easily extracted from range data. However, land markings cannot be observed from LIDARs. They can be detected by camera. Naturally, fusion of such complementary information can help intelligent vehicles to understand the scene and increases the detection rate and decreases the false alarm. Two contributions are presented in this paper. First, the homography transformation matrix between a road plane and its image is deduced. Conversion of the lane marking form the image plane to the road plane is given for different lane models. Second, an efficient and effective method is present to discriminate obstacles as within lane markings and outside lane markings.

The rest of the paper is organized as follows. In Sect. 2, basic notations and equations are presented. In Sect. 3, conversion of lane marking from image plane to road plane is introduced. Obstacle detection algorithm is presented in Sect. 4. Experimental results is given is Sect. 5. At last, we draw conclusions.

2 Basic Notation

The relative alignment between a lidar and a camera is important to convert an observed lane marking in the 2D image coordinate system to a 3D word coordinate system. We ignore the distortion factors of the lens and use the usual pinhole model to represent the camera. The relationship between a 3D lidar points $\mathbf{P}_l = [x, y, z]^T$ and the corresponding 2D pixel $\mathbf{p}_u = [u, v]^T$ can be described as:

$$\mathbf{p}_u = s\mathbf{K}(\mathbf{R}\mathbf{P}_l + \mathbf{t}), \tag{1}$$

where s is a scale factor, $\mathbf{K}$ is camera intrinsic parameters, $\mathbf{R}$ is the rotation matrix, and $\mathbf{t}$ is the translation matrix. $\mathbf{K}$ can be obtained by the camera intrinsic calibration [9], and $\mathbf{R}$ and $\mathbf{t}$ can be acquired though the extrinsic calibration between a camera and a lidar [10].

3 Conversion of Lane Markings from Image Plane to Road Plane

In this section, we detail the conversion of lane markings from image plane to road plane for different lane models. Homography matrix between the image plane and the road plane is computed. Instead of constructing bird's view road image, lanes

are directly detected in the perspective image. Then the detected lanes are converted to the road plane through the homography. This strategy can save the time used to transform perspective image into bird's eye road image and avoid the truncation or discretization error in the transformation process.

3.1 Homography Between Image Plane and Road Plane

Assume the xy plane of the lidar coordinate system is parallel or approximately parallel to the road plane. We introduce a new coordinate system referred to as road coordinate system which has the origin $[0, 0, -h]$ where h is the height of the lidar from the road plane. It has the same orientation as the lidar coordinate frame and is just a pure translation. We use $\mathbf{P}_c$, $\mathbf{P}_l$ and $\mathbf{P}_r$ to represent the coordinates of a 3D point in the coordinate frame of camera, lidar and road, respectively. The alignment of the three coordinate frames is shown in Fig. 3. The coordinate transformation between the camera and lidar coordinate frame has the form:

$$\begin{pmatrix} \mathbf{P}_c \\ 1 \end{pmatrix} = \begin{pmatrix} \mathbf{R} & \mathbf{t} \\ \mathbf{0}^T & 1 \end{pmatrix} \begin{pmatrix} \mathbf{P}_l \\ 1 \end{pmatrix}. \tag{2}$$

The relationship between the lidar and road coordinate frame can be represented as:

$$\begin{pmatrix} \mathbf{P}_l \\ 1 \end{pmatrix} = \begin{pmatrix} \mathbf{I} & \mathbf{t}_h \\ \mathbf{0}^T & 1 \end{pmatrix} \begin{pmatrix} \mathbf{P}_r \\ 1 \end{pmatrix} = \begin{pmatrix} 1 & 0 & 0 & 0 \\ 0 & 1 & 0 & 0 \\ 0 & 0 & 1 & -h \\ 0 & 0 & 0 & 1 \end{pmatrix} \begin{pmatrix} \mathbf{P}_r \\ 1 \end{pmatrix}, \tag{3}$$

where $\mathbf{t}_h = [0, 0, -h]^t$. Substituting (3) into (2), we obtain the rigid transformation from the road coordinate frame to camera coordinate frame as below:

$$\begin{pmatrix} \mathbf{P}_c \\ 1 \end{pmatrix} = \begin{pmatrix} \mathbf{R} & \mathbf{R}\mathbf{t}_h + \mathbf{t} \\ \mathbf{0}^T & 1 \end{pmatrix} \begin{pmatrix} \mathbf{P}_r \\ 1 \end{pmatrix} = \begin{pmatrix} \mathbf{R} & -h \cdot \mathbf{r}_3 + \mathbf{t} \\ \mathbf{0}^T & 1 \end{pmatrix} \begin{pmatrix} \mathbf{P}_r \\ 1 \end{pmatrix}, \tag{4}$$

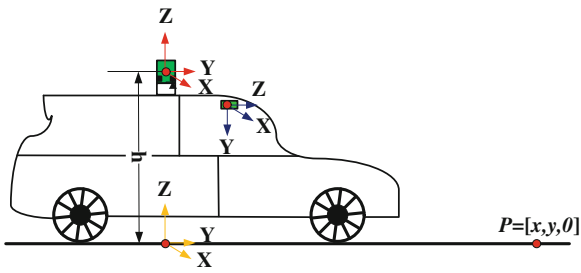

Fig. 3 The alignment of camera, lidar and road coordinate frames

where $\mathbf{r}_3$ is the third column of $\mathbf{R}$. A point on the road plane has the form $\mathbf{P}_r = [x, y, 0]^T$. Using the pinhole model (1), the relationship between a point on the road plane and the corresponding pixel can be described as:

$$\mathbf{p}_u = \begin{bmatrix} u \\ v \\ 1 \end{bmatrix} = s\mathbf{K}(\,\mathbf{r}_1 \quad \mathbf{r}_2 \quad \mathbf{r}_3 \quad \mathbf{t}_c^r\,)\begin{pmatrix} x \\ y \\ 0 \\ 1 \end{pmatrix} = s\mathbf{K}(\,\mathbf{r}_1 \quad \mathbf{r}_2 \quad \mathbf{t}_c^r\,)\begin{pmatrix} x \\ y \\ 1 \end{pmatrix}, \tag{5}$$

where $\mathbf{r}_1$, $\mathbf{r}_2$ and $\mathbf{r}_3$ are the three columns of $\mathbf{R}$ and $\mathbf{t}_c^r = -h \cdot \mathbf{r}_3 + \mathbf{t}$. So a point on the road $\mathbf{p}_c = [x, y, 1]^T$ and its image can be related by a homography matrix **H:**

$$\mathbf{p}_u = s\mathbf{H}\mathbf{p}_c, \tag{6}$$

where $\mathbf{H} = \mathbf{K}(\,\mathbf{r}_1 \quad \mathbf{r}_2 \quad \mathbf{t}_c^r\,)$.

3.2 Conversion for the Line Model of Lane Markings

Generally, except the turning, lane markings can be represented by the line model. Vehicles are constrained by a pair of lane markings. Lane markings are parallel in the road plane. However, they intersect at vanish point in the image plane because of perspective distortion. We denote the *i*th lane marking on the road plane as $\mathbf{l}_r^i$ and the corresponding line on the image plane as $\mathbf{l}_c^i$. When $\mathbf{l}_c^i$ is detected, $\mathbf{l}_c^i$ can be obtained by the result of projective geometry [11]:

$$\mathbf{l}_r^i = \mathbf{H}^T\mathbf{l}_c^i \tag{7}$$

3.3 Conversion of Conic Model of Lane Markings

At the turning, lane markings can be properly approximated by conic, such as parabola and hyperbola. The general homogenous equation of a conic can be represented as:

$$ax_1^2 + bx_1x_2 + cx_2^2 + dx_1x_3 + ex_2x_3 + fx_3^2 = 0. \tag{8}$$

The corresponding matrix form is:

$$\mathbf{x}^T\mathbf{C}\mathbf{x} = 0, \tag{9}$$

where $\mathbf{x} = [x_1, x_2, x_3]^T$ and $\mathbf{C} = \begin{bmatrix} a & b/2 & d/2 \\ b/2 & c & e/2 \\ d/2 & e/2 & f \end{bmatrix}$.

We refer to the ith conic in the road plane as $\mathbf{C}_r^i$ and its image as $\mathbf{C}_c^i$. When $\mathbf{C}_c^i$ is detected, $\mathbf{C}_r^i$ can be calculated using the result of projective geometry [11]:

$$\mathbf{C}_r^i = \mathbf{H}^T \mathbf{C}_c^i \mathbf{H} \tag{10}$$

4 Obstacle Detection

When the lane markings $\mathbf{l}_c^i$ or $\mathbf{C}_c^i$ are detected in the image plane, $\mathbf{l}_r^i$ or $\mathbf{C}_r^i$ can be calculated by Eqs. (7) or (10). Obstacles are discriminated by their positions relative to the lane. Generally, obstacles between the pair of lane markings are more important than the ones aside the lane markings. According to the positions of obstacles, the intelligent vehicle make different decisions, such as ignoring the unimportant ones, emergency stop, velocity decrease, or lane change.

A point $\mathbf{P}_l$ perceived by a laser scan is first converted to the road coordinate frame. Denote its coordinates as $\mathbf{P}_r = [x, y, z]^T$. Then this point is projected onto the road plane. Using the homogeneous representation, the projected point can be represented as $\mathbf{p}_r = [x, y, 1]^T$. To simplify notation, we use the same symbol for line model and conic model discriminative function, defined as $f_r^i(\mathbf{p}_r) = \mathbf{p}_r^T \cdot \mathbf{l}_r^i$ or $f_r^i(\mathbf{p}_r) = \mathbf{p}_r^T \mathbf{C} \mathbf{p}_r$. When $\mathbf{p}_r$ locates between a pair of lane markings, it lies at the different side of the two curves. $f_r^1(\mathbf{p}_r)$ and $f_r^2(\mathbf{p}_r)$ will have different signs, thus $f_r^1(\mathbf{p}_r) \cdot f_r^2(\mathbf{p}_r) \leq 0$. The equation occur when $\mathbf{p}_r$ is on one of the lane markings. On the other hand, when $\mathbf{p}_r$is aside the lane markings, $\mathbf{p}_r$ is at the same side of the lane marking pair, so $f_r^1(\mathbf{p}_r) \cdot f_r^2(\mathbf{p}_r) > 0$. We summarize the algorithm as follow:

(1) Convert the laser point $\mathbf{P}_l$ into the road coordinate frame and obtain $\mathbf{P}_r = [x, y, z]^T$.
(2) If the z value of $\mathbf{P}_r$ is larger than a certain threshold, project $\mathbf{P}_r$ into the road plane and get $\mathbf{p}_r$.
(3) Calculate the sign of $f_r^1(\mathbf{p}_r) \cdot f_r^2(\mathbf{p}_r)$. If $f_r^1(\mathbf{p}_r) \cdot f_r^2(\mathbf{p}_r) \leq 0$, $\mathbf{P}_l$ is inside the lane marking pair. Otherwise, it is outside the lane marking pair.

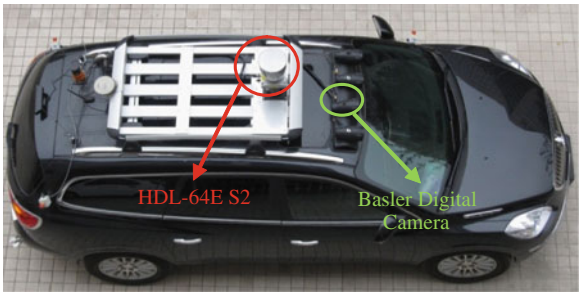

Fig. 4 Alignment of the HDL-64E S2 lidar and the Basler digital camera

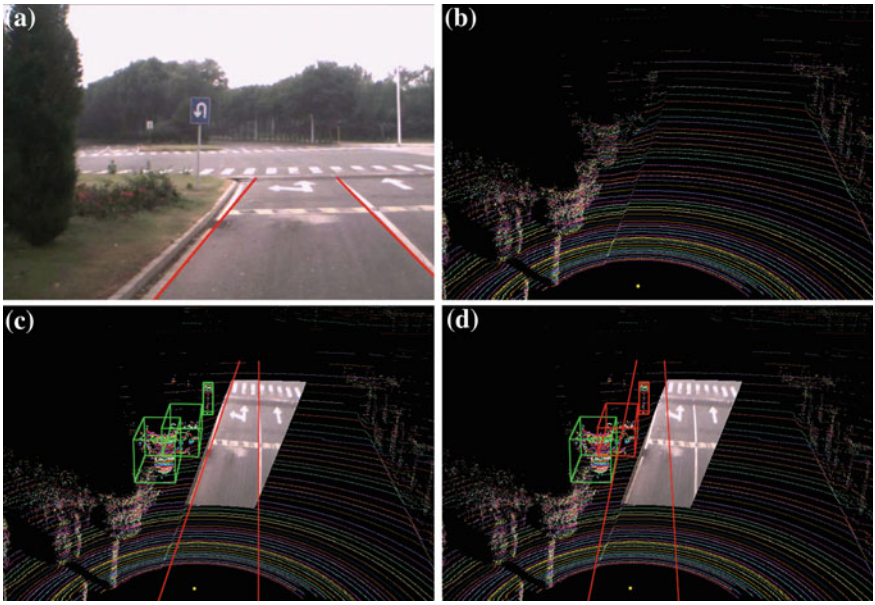

Fig. 5 Obstacle detection combining lane marking using line model. An object inside the *red lines* is represented as a *red box* and an object outside the *red lines* is represented as a *green box*. **a** The original image with the *red lines* representing lane markings. **b** The original laser point cloud. **c** Convert the lane markings into the road coordinate system. The position of road sign, trees, and bush relative to the lane are correctly classified. **d** The range in front of the vehicle is described by the *red line*. The road sign and bush was incorrectly classified as emergency obstacle, since they appear on the vehicle routine. However, they will not impact on driving

Clustering [12, 13] are used in these labeled point cloud and bounding box can be used to give a simple representation of an object.

The proposed obstacle detection method is efficient. Lane marking detection is a key component in ADAS and UGV. Thus, the lane marking information can be obtained from this module. The homography transformation matrix can be calculated after calibration. The conversion of lane markings from image plane to road plane only involves simple matrix multiplications. Assume N laser points obtained from the LIDAR. The point cloud discrimination process is $O(N)$ for scalar multiplication and addition.

5 Experimental Results

We validated our algorithm using a HDL-64E S2 lidar and a Basler digital camera with 8.5 mm lens. The HDL-64E S2 lidar provides range measurements with 0.09° angle resolution and distance precision less than 20 mm. The resolution of our camera is 750 × 480. Figure 4 shows the alignment of these two sensors. Objects

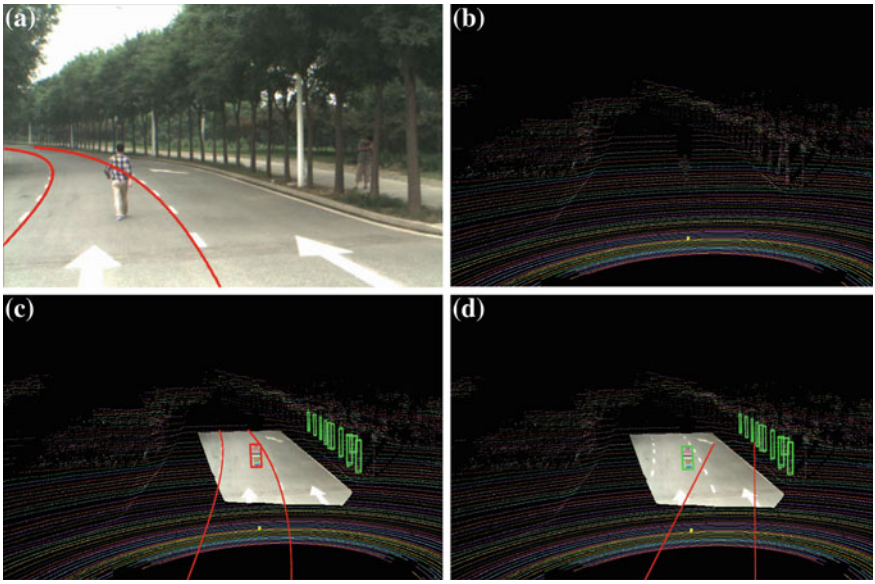

Fig. 6 Obstacle detection combining lane marking using conic model. An object inside the *red lines* is represented as a *red box* and an object outside the *red lines* is represented as a *green box*. **a** The original image with the *red lines* representing lane markings. **b** The original laser point cloud. **c** Convert lane markings into road coordinate system. The position of trees and pedestrian relative to the lane were correctly classified. **d** The range in front of the vehicle is described by a pair of *red lines*. The importance of the pedestrian was underestimated, since they appear not on the vehicle routine. The pedestrian in the lane was ignored. A terrible accident would have happened, if correct action had not been taken

observed by both sensors were processed. To validate the conversion formulas for different lane models and the obstacle detection algorithm, lane markings were manually extracted in the following experiments.

5.1 Obstacle Detection Using Lane Marking with Line Model

In the first experiment, we validated our algorithm for line model. Laser points and the corresponding images were recorded simultaneously. The vehicle was slightly tilted. Figure 5 shows the detection results. Lane markings were precisely converted into the road coordinate. Objects along the road were correctly classified when using the lane marking information, as shown in Fig. 5c. If just positions of objects with respect to the vehicle had been taken into account, the bush and traffic sign wound have been considered as emergent obstacles, as shown in Fig. 5d. However, they are just still objects outside the lane and generally have no hazard to vehicles.

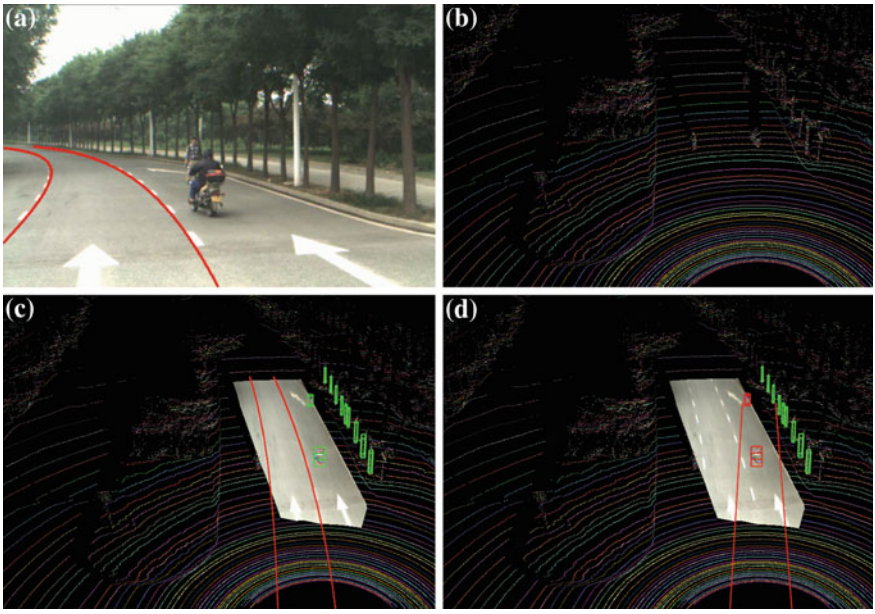

Fig. 7 Obstacle detection combining lane marking using conic model. **a** The original image with the *red lines* representing lane markings. **b** The original laser point cloud. **c** Convert lane markings into road coordinate system. The position of trees, a pedestrian and autobike outside the lane were correctly classified. The motion of the vehicle was safe, since no obstacle was between the lane markings. **d** The range in front of the vehicle is described by a pair of *red lines*. The pedestrian and autobike were incorrectly classified as emergency obstacles, since they appear on the vehicle routine. However, they will not impact on driving

5.2 Obstacle Detection Using Lane Marking with Conic Model

In Fig. 6, the conic in the image plane was accurately converted into the road plane. The pedestrian between the lane markings was correctly recognized as an emergent obstacle, as show in Fig. 6c. If we had just considered the position of an object relative to a vehicle, the importance of the man as an obstacle would have been underestimated, as shown in Fig. 6d. If the incorrect action had been taken in this situation, traffic accident would have happened.

In Fig.7, an opposite situation is illustrated. The autobike in the neighborhood lane was correctly recognized as an unimportant obstacle, as the lane marking information was taken into account, as shown in Fig. 7c. However, it would be detected as an emergent obstacle, if we had just considered its position relative to the vehicle, as shown in Fig. 7d. If an emergent stop had been taken, backing crash would have happened in this situation.

6 Conclusion

In this paper, we propose an obstacle detection strategy based on the fusion of LIDAR data and camera information for the on-road scene. According to positions of obstacles relative to the lane, they are divided into two categories, obstacles inside and obstacles outside the lane. A virtual coordinate system referred to as road coordinate system is introduced. Lane markings in the image plane are converted into this coordinate frame. The homography transformation matrix between the image plane and road plane is deduced. The analytic transformation formulas for different lane models are given. A discriminative function is presented to label laser points according to their position with respect to a lane. The experimental results validate the conversion algorithm and obstacle classification algorithm for different lane models.

Acknowledgments This work was supported in part by National Science Foundation of China (NSFC) under Grant No. 90820305 and by the National High-Tech R&D Program of China under Grant No. 2011AA041001.

References

1. Zhang YK, Hong CY, Weyrich N (2011) A single camera based rear obstacle detection system.In: IEEE Intelligent vehicles symposium, Jun 2011, pp 485–490
2. Nishigaki M, Aloimonos Y (2010) Moving obstacle detection using cameras for driver assistance system. In: IEEE Intelligent Vehicles Symposium, Jun 2010, pp 805–812
3. Sato I, Yamano C, Yanagawa H (2011) Crossing obstacle detection with a vehicle-mounted camera. In: IEEE Intelligent Vehicles Symposium, Jun 2011, pp 60–65
4. Pantilie CD, Nedevschi S (2010) Real-time obstacle detection in complex scenarios using dense stereo vision and optical flow. In: Proceedings of international IEEE conference on intelligent transportation systems, Sep 2010, pp 439–444
5. Choi J, Lee J, Kim D et al (2012) Environment-detection-and-mapping algorithm for autonomous driving in rural or off-road environment. IEEE Trans Intell Transp Syst 13(2):974–982
6. Maier D, Bennewitz M, Stachniss C (2011) Self-supervised obstacle detection for humanoid navigation using monocular vision and sparse laser data. In: Proceedings of IEEE international conference on robotics and automation, May 2011, pp 1263–1269
7. Morton RD, Olson E (2011) Positive and negative obstacle detection using the HLD classifier. In: Proceedings of the IEEE/RSJ international conference on intelligent robots and systems, Sep 2011, pp 1579–1584
8. Larson J, Trivedi M (2011) Lidar based off-road negative obstacle detection and analysis. In: Proceedings of IEEE international conference on intelligent transportation systems, Oct 2011, pp 192–197
9. Zhang ZY (2000) A flexible new technique for camera calibration. IEEE Trans Pattern Anal Mach Intell 22(11):1330–1334
10. Zhou LP, Deng ZD (2012) Extrinsic calibration of a camera and a lidar based on decoupling the rotation from the translation. In: IEEE Intelligent Vehicles Symposium, Jun 2012
11. Hartley R, Zisserman A (2003) Multiple view geometry in computer vision. CUP, Cambridge

12. Klasing K, Wollherr D, Buss M (2008) A clustering method for efficient segmentation of 3D laser data. In: Proceedings of IEEE international conference on robotics and automation, May 2008, pp 4043–4048
13. Zhu XL, Zhao HJ, Liu YM, Zhao YP, Zha HB (2010) Segmentation and classification of range image from an intelligent vehicle in urban environment. In: Proceedings of IEEE/RSJ international conference on intelligent robots and systems, Oct 2010, pp 1457–1462

Decoupled Parameter Estimation for Coherently Distributed Source

Yinghua Han, Jinkuan Wang and Qiang Zhao

Abstract A computationally efficient method for the problem of estimating the parameters—the central direction of arrival (DOA) and angular spread of coherently distributed source is presented. The proposed method is based on Schur–Hadamard product which enables the estimation of the central DOA decoupled from that of angular spread of the source. So an underlying rotational invariance structure is exploited. Then the key idea is to apply the propagator method to estimate the central DOA, which only requires linear operations. The angular spread is estimated by a proposed second-order statistics sequently, from which the closed solution of angular spread is derived. An advantage of this method over the classical subspace-based algorithm, such as ESPRIT and MUSIC for distributed source, is that it does not apply any searching. Numerical examples illustrate the performance of the method.

Keywords Distributed source · The central DOA · Angular spread · Propagator method · Second-order statistics

1 Introduction

DOA estimation algorithms have been extensively studied in the past due to their widespread applications. Among the well-known methods, DOA estimation techniques have usually been developed for far-field point sources which travel along a single path to the antenna array [1–3]. However, in applications such as wireless communications, radar and sonar, signal reflection, and scattering phenomena at the source vicinity degrade the performance of any array signal

Y. Han (✉) · J. Wang · Q. Zhao
College of Computer and Communication Engineering, Northeastern University at Qinhuangdao, Qinhuangdao, China
e-mail: yhhan723@126.com

F. Sun et al. (eds.), *Foundations and Practical Applications of Cognitive Systems and Information Processing*, Advances in Intelligent Systems and Computing 215,
DOI: 10.1007/978-3-642-37835-5_47,

processing algorithm that uses a point source model. In such complex situation, a distributed source model will be more appropriate [4–6].

In general, distribute sources have been classified into coherently and incoherently distributed source. For example, depending on the relationship between the channel coherently time and the observation period, the sources can be viewed either as coherently distributed or incoherently distributed. A source is called coherently distributed if the signal components arriving from different directions are replicas of the same signal, whereas in the incoherently distributed source case, all signals coming from different directions are assumed to be uncorrelated. Indeed, if the channel coherency time much smaller than the observation period, then the incoherently distributed model is relevant. In the opposite case, the coherency distributed model or a partially coherent model can be used.

A number of investigators have proposed distributed source modeling, and several parameter estimation techniques have been proposed in the literature [7–15]. To begin with, attempts for coherently distributed source modeling and parameter estimation have been accomplished in [9], where the central DOAs and angular spreads are estimated by algorithms based on MUSIC using a uniform linear array. However, this algorithm needs two-dimensional joint searching and assumes that the multiple sources must have identical and known angular signal intensity function. Other robust techniques using the array geometry have recently been developed. A typical example is low-complexity parameter estimation with ESPRIT technique [11], which employs eigenvalue decomposition with two uniform linear arrays. The ESPRIT algorithm is still computationally extensive and time consuming especially when the number of antenna array elements is larger than the number of incident signals. An asymptotic maximum likelihood for joint estimation of the central DOA and angular spreads of multiple distributed sources is presented in [12]. Though it has best precision, the computationally load is high.

Recently, many low-complexity methods are proposed to reduce the computational burden of estimators [13–15]. For example, the decoupled COMET-EXIP [14] uses two successive one-dimensional searches instead of a two-dimensional search for parameter estimation of a single incoherently distributed source.

The aim of this paper is to develop a computationally simple parameter estimation algorithm of coherently distributed source. First, we use the propagator method to find the estimation of the central DOA, and then second-order statistics is proposed to estimate the angular spread. Hence the method is a low-complex estimator that does not need any searching in one- or two-dimensional parameter space.

2 Problem Statement and Preliminaries

The conventional data model assumes that the signal impinging upon an array of sensors to be narrow-band and emitted from a point source in the far-field region. The complex envelope of the array output can be written as

$$\boldsymbol{X}(t) = \sum_{i=1}^{q} \boldsymbol{S}(t) + \boldsymbol{N}(t) \tag{1}$$

where $\boldsymbol{X}(t)$ is the array snapshot vector, $\boldsymbol{S}_i(t)$ is the vector that describes the contribution of the ith signal source to the array output, and $\boldsymbol{N}(t)$ is the Gaussian white noise.

In point source model, the baseband signal of the ith source is modeled as

$$\boldsymbol{S}_i(t) = s_i(t)\boldsymbol{a}(\theta_i) \tag{2}$$

where $s_i(t)$ is the complex envelope of the ith source, θ_i is its DOA, and $\boldsymbol{a}(\theta) = [1, \exp(-j2\pi(d/\lambda)\sin\theta), \cdots, \exp(-j2\pi(M-1)(d/\lambda)\sin\theta)]^{\mathrm{T}}$ is the corresponding steering vector, M is the number of sensors, d is the distance between two adjacent sensors, λ is the wavelength of the impinging signal.

However, in many environments for modern radio communications, the transmitted signal is often obstructed by buildings, vehicles, trees, etc., and/or reflected by rough surfaces. Hence, the absence of a single Line-Of-Sight (LOS) ray will violate the classical point source assumption. The receiver is likely to experience a spatially dispersed signal consisting of several arriving rays spreading around the central DOA as Fig. 1. In such cases, a distributed source model is appropriate.

In distributed source model, the source energy is considered to be spread over some angular volume. Hence, $\boldsymbol{S}_i(t)$ is written as

$$\boldsymbol{S}_i(t) = \int_{\vartheta \in \Theta} \boldsymbol{a}(\vartheta)\varsigma(\vartheta, \boldsymbol{\psi}_i, t)\mathrm{d}\vartheta \tag{3}$$

where Θ is the set of the steering vector over some parameter space of interest, $\varsigma(\vartheta, \boldsymbol{\psi}_i, t)$ is a complex random angular-temporal signal intensity which can be expressed as

$$\varsigma(\vartheta, \boldsymbol{\psi}_i, t) = s_i(t)\ell(\vartheta, \boldsymbol{\psi}_i) \tag{4}$$

under the coherently distributed source assumptions, and $\ell(\vartheta, \boldsymbol{\psi}_i)$ is the deterministic angular signal intensity, $\boldsymbol{\psi}_i$ is the location parameter vector.

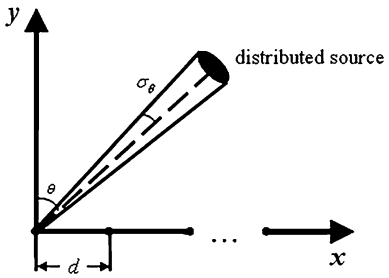

Fig. 1 A distributed source model

In terms of the steering vector, the coherently distributed source model can be expressed as

$$\boldsymbol{b}(\boldsymbol{\psi}_i) = \int_{\vartheta \in \Theta} \boldsymbol{a}(\vartheta)\ell(\vartheta, \boldsymbol{\psi}_i)\mathrm{d}\vartheta \tag{5}$$

As a common example of the coherently distributed source, assume that the deterministic angular signal intensity $\ell(\vartheta, \boldsymbol{\psi}_i)$ has the Gaussian shape

$$\ell(\vartheta, \boldsymbol{\psi}_i) = \frac{1}{\sqrt{2\pi}\sigma_{\theta_i}} \exp\left(-\frac{(\vartheta - \theta_i)^2}{2\sigma_{\theta_i}^2}\right) \tag{6}$$

Here location parameter vector $\boldsymbol{\psi}_i = (\theta_i, \sigma_{\theta_i})$, θ_i is the central DOA, and σ_{θ_i} is angular spread.

3 Decoupled Parameter Estimation for Coherently Distributed Source

In general, an optimum estimation method for point or distributed sources can provide an excellent performance at the cost of intensive computation. Since the computational complexity increases dramatically with high-dimensional parameters, we have to sometimes find suboptimum methods to reduce the computational cost, while sustaining the estimation performance within a tolerable level. It is noteworthy that a considerable simplification is possible by exploiting and utilizing the special array structure of the array geometry in the parameter estimation under distributed source model also.

In this paper, we consider an array of $2M$ sensors (M doublets) as in [11]. Assume that the two sensors in each doublet are identical and have the same gain, phase, and sensitivity pattern and are separated by a constant displacement d_1. The two induced subarrays are denoted by X and Y.

First, with the change of variables $\vartheta - \theta = \tilde{\theta}$, the closed form of the steering vector for subarray X can be written as

$$\begin{aligned}
[\boldsymbol{b}_X(\boldsymbol{\psi})]_k &\approx \exp(-j2\pi(d/\lambda)(k-1)\sin\theta) \\
&\times \int_{-\pi/2}^{\pi/2} \exp\left(-j2\pi(d/\lambda)(k-1)\tilde{\theta}\cos\theta\right) \\
&\times \frac{1}{\sqrt{2\pi}\sigma_\theta} \exp\left(-\frac{\tilde{\theta}^2}{2\sigma_{\tilde{\theta}}^2}\right)\mathrm{d}\tilde{\theta} \\
&= \exp(-j2\pi(d/\lambda)(k-1)\sin\theta) \times [\boldsymbol{h}_X]_k
\end{aligned} \tag{7}$$

and the kth element of $\boldsymbol{h}_X$is

$$[\boldsymbol{h}_X]_k = \int_{-\pi/2}^{\pi/2} \exp\left(-j2\pi(d/\lambda)(k-1)\tilde{\theta}\cos\theta\right) \times \frac{1}{\sqrt{2\pi}\sigma_\theta}\exp\left(-\frac{\tilde{\theta}^2}{2\sigma_\theta^2}\right)d\tilde{\theta} \tag{8}$$

$\boldsymbol{h}_X$is a real-valued matrix because of the symmetry assumption on angular signal intensity.

Using the integral formula [16]

$$\int_{-\infty}^{\infty} \exp\left(-f^2x^2\right)\exp[jp(x+\alpha)]\mathrm{d}x = \sqrt{\pi}\exp\left(-p^2/\left(4f^2\right)\right)\exp(jp\alpha)/f \tag{9}$$

Equation (8) can be written as

$$[\boldsymbol{h}_X]_k = \exp\left(-2\pi^2(d/\lambda)^2(k-1)^2\cos^2\theta\sigma_\theta^2\right) \tag{10}$$

So in matrix notation, the steering vector of distributed source in (7) can be written as follows,

$$\boldsymbol{b}_X(\boldsymbol{\psi}) \approx \boldsymbol{a}_X(\theta) \odot \boldsymbol{h}_X \tag{11}$$

where $\boldsymbol{a}_X(\theta)$ is the steering vector of point source, and $\odot$ is the Schur–Hadamard or element product.

Similarly, the received signal vector for subarray Y can be expressed as

$$\boldsymbol{Y}(t) = \sum_{i=1}^{q}\int_{\vartheta\in\Theta} \boldsymbol{a}(\vartheta)\ell(\vartheta,\boldsymbol{\psi}_i)\times\exp(-j2\pi(d_1/\lambda)\cos\vartheta)s_i(t)\mathrm{d}\vartheta + \boldsymbol{N}_\mathrm{Y}(\mathrm{t}) \tag{12}$$

The steering vector can be shown as

$$\begin{aligned}\boldsymbol{b}_Y(\boldsymbol{\psi}_i) &= \int_{\vartheta\in\Theta} \boldsymbol{a}_Y(\vartheta)\exp(-j2\pi(d_1/\lambda)\cos\vartheta) \times \ell_i(\vartheta;\boldsymbol{\psi}_i)\mathrm{d}\vartheta \\ &\approx \boldsymbol{b}_X(\boldsymbol{\psi}_i)\exp(-j2\pi(d_1/\lambda)\cos\theta_i)\end{aligned} \tag{13}$$

and in matrix form is

$$\boldsymbol{b}_Y = \boldsymbol{b}_X\Phi \tag{14}$$

where $\Phi = \mathrm{diag}(\exp(-j2\pi(d_1/\lambda)\cos\theta_1), \cdots \exp\left(-j2\pi(d_1/\lambda)\cos\theta_q\right))$.

The matrices Φ can be found by employing the propagator method [17] whose computational complexity is smaller than that of the subspace eigen analysis such as MUSIC and ESPRIT algorithms.

The propagator method makes a partition of the steering vector $\boldsymbol{b}_X$ and $\boldsymbol{b}_X$ as follows,

$$\begin{bmatrix} \boldsymbol{b}_X \\ \boldsymbol{b}_Y \end{bmatrix} = \begin{bmatrix} \boldsymbol{b}_{X1}^{\mathrm{T}} & \boldsymbol{b}_{X2}^{\mathrm{T}} & (\boldsymbol{b}_{Y1})^{\mathrm{T}} & (\boldsymbol{b}_{Y2})^{\mathrm{T}} \end{bmatrix}^{\mathrm{T}} \tag{15}$$

and $\boldsymbol{b}_{Y1} = \boldsymbol{b}_{X1}\Phi$, $\boldsymbol{b}_{Y2} = \boldsymbol{b}_{X2}\Phi$, where $\boldsymbol{b}_{X1}$, $\boldsymbol{b}_{X2}$, $\boldsymbol{b}_{Y1}$, $\boldsymbol{b}_{Y2}$ are submatrices of dimension $q \times q$, $(M-q) \times q$, $q \times q$, $(M-q) \times q$, respectively.

Let $\boldsymbol{Z}(t)$ denotes grouping the array output as

$$\boldsymbol{Z}(t) = \begin{bmatrix} \boldsymbol{X}(t) \\ \boldsymbol{Y}(t) \end{bmatrix} \tag{16}$$

In practical situations, the true covariance matrix of $\boldsymbol{Z}(t)$ unavailable but can be estimated. Therefore, the sample covariance matrix with N snapshots is defined as

$$\widehat{\boldsymbol{R}}_{ZZ} = \frac{1}{N}\sum_{t=1}^{N} \boldsymbol{Z}(t)\boldsymbol{Z}^{\mathrm{H}}(t) \tag{17}$$

3.1 The Central DOA Estimation

Under the hypothesis that $\boldsymbol{b}_{X1}$ is a $q \times q$ non-singular matrix, and the propagator is the unique linear operator which can be written as

$$\boldsymbol{p}^{\mathrm{H}}\boldsymbol{b}_{X1} = \begin{bmatrix} \boldsymbol{b}_{X2}^{\mathrm{T}} & (\boldsymbol{b}_{X1}\Phi)^{\mathrm{T}} & (\boldsymbol{b}_{X2}\Phi)^{\mathrm{T}} \end{bmatrix}^{\mathrm{T}} \tag{18}$$

We can partition $\boldsymbol{p}$ as follows,

$$\boldsymbol{p}^{\mathrm{H}} = \begin{bmatrix} \boldsymbol{p}_1^{\mathrm{T}} & \boldsymbol{p}_2^{\mathrm{T}} & \boldsymbol{p}_3^{\mathrm{T}} \end{bmatrix}^{\mathrm{T}} \tag{19}$$

where the dimension of $\boldsymbol{p}_1$, $\boldsymbol{p}_2$ and $\boldsymbol{p}_3$ are identical with the dimensional of $\boldsymbol{b}_{X2}$, $\boldsymbol{b}_{X1}\Phi$, $\boldsymbol{b}_{X2}\Phi$, respectively.

According to (18) and (19), we can write the following equations,

$$\boldsymbol{p}_1\boldsymbol{b}_{X1} = \boldsymbol{b}_{X2} \tag{20}$$

$$\boldsymbol{p}_2\boldsymbol{b}_{X1} = \boldsymbol{b}_{X1}\Phi \tag{21}$$

$$\boldsymbol{p}_3\boldsymbol{b}_{X1} = \boldsymbol{b}_{X2}\Phi \tag{22}$$

Using pair (20) and (22), we can find that

$$\boldsymbol{p}_1^{\dagger}\boldsymbol{p}_3\boldsymbol{b}_{X1} = \boldsymbol{b}_{X1}\Phi \tag{23}$$

where $[\cdot]^{\dagger}$denotes the pseudoinverse.

Equations (21) and (23) imply that the diagonal elements in the diagonal matrix Φ can be estimated by finding the eigenvalues of each matrix $\boldsymbol{p}_2$ and $\boldsymbol{p}_1^{\dagger}\boldsymbol{p}_3$. Using

$\boldsymbol{p}_1^{\dagger}\boldsymbol{p}_3$ will yield more accurate results than using $\boldsymbol{p}_2$, so the central DOA can be easily found as

$$\widehat{\theta}_i = \arccos(-\arg(\mu_i)/(2\pi(d_1/\lambda))) \tag{24}$$

where μ_i denotes the ith eigenvalue of $\boldsymbol{p}_1^{\dagger}\boldsymbol{p}_3$.

In addition, let $\widehat{\boldsymbol{p}}$ denotes the propagator estimate matrix based on the covariance matrix of $\widehat{\boldsymbol{R}}_{ZZ}$. The partition of $\widehat{\boldsymbol{R}}_{ZZ}$ can be written as

$$\widehat{\boldsymbol{R}}_{ZZ} = \begin{bmatrix} \widehat{\boldsymbol{G}} & \widehat{\boldsymbol{H}} \end{bmatrix} \tag{25}$$

where $\widehat{\boldsymbol{G}}$ and $\widehat{\boldsymbol{H}}$ are submatrices of dimensional $2M \times q$ and $2M \times (2M - q)$, respectively. The propagator estimate matrix $\widehat{\boldsymbol{p}}$ can be obtained by minimizing the following cost functions

$$\widehat{\boldsymbol{p}} = \|\boldsymbol{H} - \boldsymbol{G}\widehat{\boldsymbol{P}}\|^2 \tag{26}$$

So the optimum propagator estimate matrix can be found by applying the least square method on (26) as

$$\widehat{\boldsymbol{p}} = \left(\boldsymbol{G}^{\mathrm{H}}\boldsymbol{G}\right)^{-1}\boldsymbol{G}^{\mathrm{H}}\boldsymbol{H} \tag{27}$$

3.2 The Angular Spread Estimation

When we estimate the two parameters of coherently distributed source, we have to generally solve a 2D optimization problem. Furthermore, the computational complexity grows rapidly as the number of sources increases. On the other hand, if we have some preliminary information on either the central DOA or angular spread, it is anticipated that we can estimate the other one with much reduced complexity and computation.

In this paper, once the central DOA is estimated by (24), we can obtain angular spread by constructing second-order statistics for a single distributed source.

Let $r_1(k)$denotes the spatial correlation coefficient defined as

$$\begin{aligned} & r_1(k) \\ =& E\left(\boldsymbol{Z}_{k+1}(t)\boldsymbol{Z}_{k+1}^{\mathrm{H}}(t)\right) \\ =& E\left(s(t)s^*(t)\left(\exp\left(-2\pi^2(d/\lambda)^2k^2\cos^2\theta\sigma_\theta^2\right)\right)^2\right) \end{aligned} \tag{28}$$

where $k \in [1, M-1]$ and $\boldsymbol{Z}_{k+1}(t)$denotes the received data as in (16). Other correlation sequences can be used as follows,

$$\begin{aligned} & r_2(k) \\ =& E\left(\boldsymbol{Z}_{(k+M+1)}(t)\boldsymbol{Z}^{\mathrm{H}}_{(k+M+1)}(t)\right) \\ =& E\left(s(t)s^*(t)\left(\exp\left(-2\pi^2(d/\lambda)^2k^2\cos^2\theta\sigma_\theta^2\right)\right)^2\right) \end{aligned} \tag{29}$$

With the estimated central DOA $\widehat{\theta}$ in turn, we use (30) to estimate angular spread.

$$\widehat{\sigma}_\theta = \frac{1}{2(M-2)}\sum_{k=1}^{M-2}\left(\sqrt{\frac{\ln\left(\frac{r_1(k+1)}{r_1(k)}\right)}{-2\pi^2(d/\lambda)^2\cos^2\left(\widehat{\theta}\right)(2k+1)}}+\sqrt{\frac{\ln\left(\frac{r_2(k+1)}{r_2(k)}\right)}{-2\pi^2(d/\lambda)^2\cos^2\left(\widehat{\theta}\right)(2k+1)}}\right) \tag{30}$$

The proposed method based on (24) and (30) can be simplified to a fast procedure without any searching.

3.3 Computational Advantages

The primary computational advantage of the proposed algorithm is that it eliminates the search procedure in all previous methods (DSPE, ML, ESPRIT for distributed source). The proposed algorithm produces signal parameter estimates directly in terms of eigenvalues and second-order statistics. This involves computing covariance matrix, the optimum propagator estimating by least square method and eigenvalue decomposition, which need computations of the order $10Mq^2+M^2q+M^3-q^3+2q(M-1)^2$. On the other hand, ESPRIT for distributed source and the other high-resolution techniques require a search, and it is this search that is computationally expensive. For example, the ESPRIT algorithm involves computations of the order $4Mq^2+8M^3+8q^3+10q^3+(M^2+M)\times A$, A is the total steps for searching. The significant computational advantage of the proposed become even more pronounced in multidimensional parameter estimation where the computational load grows linearly with dimension in proposed algorithm, while that of ESPRIT for distributed source grows exponentially.

4 Simulation Results

In this section, we investigate the performance of the proposed algorithm through some simulation experiments. The two subarrays are uniform linear arrays, and

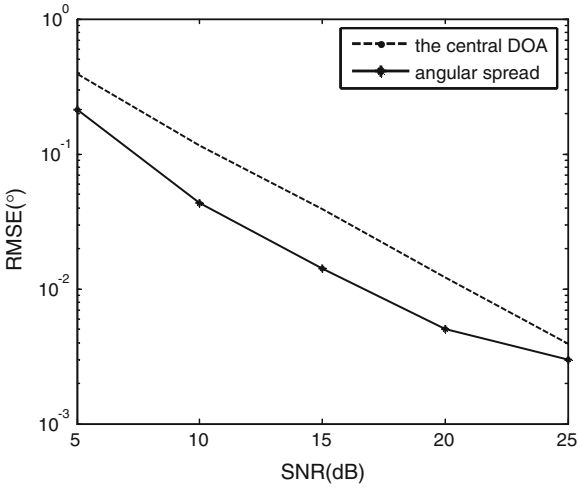

Fig. 2 RMSEs for the central DOA and angular spread estimates versus SNR

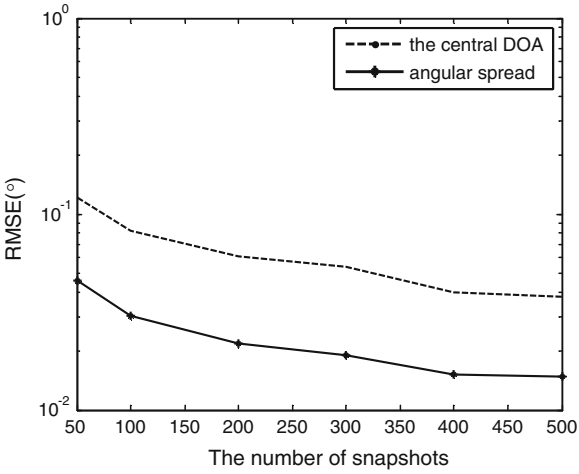

Fig. 3 RMSEs for the central DOA and angular spread estimates versus the number of snapshots

each one consists of 8 sensors. The distance between the two arrays is $0.1\,\lambda$, and the spacing between adjacent sensors in each subarray is 0.5λ.

We have considered a single narrowband coherently distributed source. The source has Gaussian shaped angular signal intensity functions with parameters $\boldsymbol{\psi} = (25^\circ, 3^\circ)$. The plots in Figs. 2, 3, and 4 show the theoretical root-mean square error (RMSE) of the central DOA and angular spread estimates.

The proposed method is a suboptimum method and is applicable when there exists a special array geometry, while classical subspace algorithms can be used with arbitrary array geometry and generally provide almost optimum performance at the expense of higher computational complexity. So there is always a tradeoff between the performance and computational complexity. The proposed

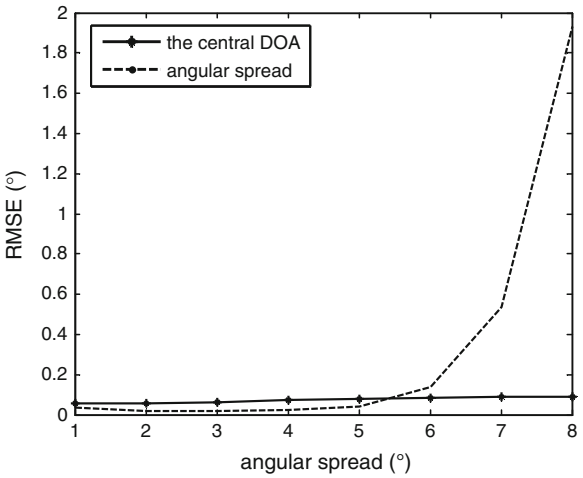

Fig. 4 RMSEs for the central DOA and angular spread estimates versus angular spread

suboptimum method has reduced computational cost while sustaining the estimation performance within a tolerable level as in Figs. 2, 3, and 4.

First, the influence of the SNR on the performance is shown in Fig. 2 when $N = 500$. As it can be seen, the proposed algorithm performs better when the SNR becomes stronger. Since the proposed second-order statistics reduces the effects of the noise, the proposed algorithm has a substantially better estimation performance.

Second, let us consider the influence of the number of snapshots on the performance in Fig. 3 assuming that SNR = 15 dB. It is observed that the RMSEs in proposed method are rather small even when the number of snapshot is not large.

Third, Fig. 4 shows the RMSEs of the central DOA and angular spread. We have assumed that the number of snapshots $N = 500$, SNR = 15 dB. As angular spread increases from 1° to 8°, the performance of the proposed method degrades. However, it is clear that when the angular spread becomes large, the proposed algorithm can still give effective estimation.

5 Conclusions

In this paper, we considered the estimation of the parameters of a spatially distributed source with a view to provide a statistically and computationally efficient algorithm. Toward this end, we have proposed a low-complexity algorithm estimating the central DOA and angular spread one by one without any peak-finding searching.

The proposed algorithm requires a preprocessing stage at which the estimates of the central DOA are obtained. In this step, we have employed the propagator which only requires linear operations. And then a second-order statistics is

proposed for estimating angular spread. The proposed method provides good estimation performance and has been shown to be useful also in situation where the ratio of array size to source number is large.

Acknowledgments This work was supported by the National Natural Science Foundation of China under Grant No. 60904035, 61004052, and 61104005, by Natural Science Foundation of Liaoning Province and Hebei Province under Grant No.20102064 and F2011501052, by The Central University Fundamental Research Foundation, under Grant. N110423004 and by Research Fund for the Doctoral Program of Higher Education of China under Grant No. 20110042120015.

References

1. Ko YH, Kim YJ, Yoo HI, Yang WY, Cho YS (2010) 2-D DOA estimation with cell searching for a mobile relay station with uniform circular array. IEEE Tran Commun 58(10):2805–2809
2. Cidronali A, Maddio S, Giorgetti G, Manes G (2010) Analysis and performance of a smart antenna for 2.45-GHz single-anchor indoor positioning. IEEE Trans Microw Theory Tech 58(1):21–31
3. Costa M, Koivunen V, Richter A (2009) Low complexity azimuth and elevation for a arbitrary array configurations. In: Proceedings of ICASSP2009, pp 2185–2188
4. Asztely D, Ottersten B (1998) The effects of local scattering on direction of arrival estimation with MUSIC and ESPRIT. In: Proceedings of ICASSP1998, pp 3333–3336
5. Xiong Y, Zhang GY, Tang B, Cheng H (2011) Blind identification and DOA estimation for array sources in presence of scattering. J Syst Eng Electron 22(3):393–397
6. Hassanien A, Shahbazpanahi S, Gershman AB (2004) A generalized Capon estimator for localization of multiple spread sources. IEEE Trans Signal Process 52(1):280–283
7. Lee J, Joung J, Kim JD (2008) A method for the direction-of-arrival estimation of incoherently distributed sources. IEEE Trans Veh Technol 57(5):2885–2893
8. Souden M, Affes S, Benesty J (2008) A two-stage approach to estimate the angles of arrival and the angular spreads of locally scatters sources. IEEE Trans Signal Process 56(5):1968–1983
9. Valaee S, Champagne B, Kabal P (1995) Parameter localization of distributed sources. IEEE Trans Signal Process 43:2144–2153
10. Raich R, Goldberg J, Messor H (2000) Bearing estimation for a distributed source: modeling, inherent accuracy limitations and algorithm. IEEE Trans Signal Process 48(2):429–441
11. Shahbazpanahi S, Valaee S, Bastani MH (2001) Distributed source localization using ESPRIT algorithm. IEEE Trans Signal Process 49(10):2169–2178
12. Sieskul BT (2010) An asymptotic maximum likelihood for joint estimation of nominal angles and angular spreads of multiple spatially distributed sources. IEEE Trans Veh Technol 59(3):1534–1538
13. Zoubir A, Wang Y, Charge P (2007) Spatially distributed sources localization with a subspace based estimator without eigendecomposition. In: Proceedings of ICASSP2007, pp 1085–1088
14. Shahbazpanahi S, Valaee S, Gershman AB (2004) A covariance fitting approach to parametric localization of multiple incoherently distributed sources. IEEE Trans Signal Process 52(3):592–600
15. Zoubir A, Wang Y (2008) Robust generalized Capon algorithm for estimating the angular parameters of multiple incoherently distributed sources. IET Signal Process 2:163–168

16. Gradshteyn IS, Ryzhik IM (1980) Table of integrals, series, and products. Academic Press, Orlando
17. Marcos S, Marsal A, Benidir M (1995) The propagator method for source bearing estimation. Signal Process 42:121–138

A Novel Blind Image Restoration Algorithm Using A SVR-Based Noise Reduction Technique

You Sheng Xia and Shi Quan Bin

Abstract In many applications, the received image is degraded by unknown blur and noise. Traditional blind image deconvolution algorithms have drawback of noise amplification. For robustness against the influence of noise, this paper proposes a novel blind image deconvolution algorithm by combining the support vector regression (SVR) approach and the total variation approach. The proposed algorithm has a lower computational complexity and a good performance in image denoising and image deblurring. Illustrative examples show that the proposed blind image deconvolution algorithm and has better performance in improvement signal-to-noise ratio than two traditional blind image restoration algorithms.

Keywords Blind image restoration · Noise reduction · Support vector regression · Total variation approach

1 Introduction

Image restoration has been an important image processing contents [1]. In many imaging applications, the received image is usually degraded by blur and noise. So, there is a need for the blur removal and noise removal techniques to improve the quality of the received image, in the field of medical imaging, astronomical speckle imaging, remote sensing, microscopy imaging, among others [2–4]. This image formation process can be modeled as follows:

$$g(x,y) = f(x,y) * h(x,y) + n(x,y), (x,y) \in \Omega \tag{1}$$

Y. S. Xia (✉) · S. Q. Bin
College of Mathematics and Computer Science, Fuzhou University, Fuzhou, China
e-mail: ysxia2001@yahoo.com

F. Sun et al. (eds.), *Foundations and Practical Applications of Cognitive Systems and Information Processing*, Advances in Intelligent Systems and Computing 215,
DOI: 10.1007/978-3-642-37835-5_48,

where (x, y) is the discrete pixel coordinate of the image frame, $f(x, y)$ is the original image, $\Omega \subset R^2$ is the support of the image, $g(x, y)$ is the degraded image, $h(x, y)$ is the point spreading function (PSF), $*$ is the discrete two-dimensional linear convolution operator, and $n(x, y)$ is additional noise. In practice, the blurred image may be corrupted by impulse noise due to bit errors in transmission, malfunctioning pixel elements in camera sensors, etc. Impulsive noise is non-Gaussian [2]. One type model is called Salt-and pepper noise model:

$$n(x,y) = \begin{cases} 0, & \text{with probability } 1-r \\ \eta_{\max}, & \text{with probability } r/2 \\ \eta_{\min}, & \text{with probability } r/2 \end{cases} \tag{2}$$

where $r \in [0, 1]$ and $[\eta_{\min}, \eta_{\max}]$ is the gray-level value range of image $f(x, y)$. Another type model is called random-valued impulse noise model:

$$n(x,y) = \begin{cases} 0, & \text{with probability } 1-r \\ \eta(x,y), & \text{with probability } r \end{cases} \tag{3}$$

where $\eta(x, y)$ is a uniformly distributed random variable in $[\eta_{\min}, \eta_{\max}]$. The blur may arise from atmospheric turbulence, relative motion between a camera and the object, or a camera out of focus [4]. The atmospheric turbulence blur is given by

$$h(i,j) = K \exp(-\frac{i^2 + j^2}{\sigma^2})$$

and the motion blur is given by

$$h(i,j) = \begin{cases} 1/L^2, & \text{if } -L/2 \le i,j \le L/2 \\ 0, & \text{Otherwise} \end{cases} \tag{4}$$

The mean filter is known to be the best one for removing Gaussian white noise from noisy images and the Kalman filter is another popular approach. But they are not appropriate for ill-conditioned problem from image restoration since the ill-conditioned nature of the problem can cause a large error on image estimate [1]. To overcome such difficulty, the traditional regularization methods have been widely developed under the assumption that the blur is known a priori. However, it is difficult to accurately measure the degradation using on-line identification techniques. This lead to the process of restoring an unknown image only using the degraded image given little or no prior knowledge about the blur, known as blind image restoration. The task for blind image restoration is to remove the effects of the blur and noise without given blur and noise information.

Blind image deconvolution study can be traced back to early image observation techniques without noise case. They estimate the blurs based on periodic zero crossings of frequency measures such as cepstrum or bispectrum [4]. Since the blind deconvolution technique was presented, various blind image restoration methods have been developed for its engineering applications. The blind image

restoration methods may be divided into three main categories: the ARMA parametric approach [5], the iterative blind deconvolution (IBD) approach [6–12], and the multichannel blind restoration approach [13]. In this paper, we focus on the single-channel IBD approaches. At present, three popular IBD methods include the nonnegative and support constraints recursive inverse filtering (NAS-RIF) approach, the double regularization (DR) approach, and the total variation (TV) approach. The NAS-RIF approach was proposed by Kunder and Hatzinakos [6]. The NAS-RIF approach can minimize convex cost function. On the other hand, it requires the image object to have a known support in a uniform background. The DR approach was presented by You and Kaveh [7] and the TV approach was developed by Chan and Wong [8, 9]. The TV approach may be viewed as a modification of the DR approach to achieve edge preservation. It was reported that three IBD approaches all have a good performance in deburing under optimal regularization parameters and without noise. But when noise exists and its level is not very low, the quality of restored images given by them is not good because of the drawback of noise amplification. For robustness against the influence of noise, this paper proposes a novel blind image deconvolution algorithm based on the support vector regression (SSVR) approach and the total variation (TV) approach. Compared with the existing blind image deconvolution using support vector regression [14], the proposed algorithm combines the total variation technique and the SSVR noise reduction technique so that it has thus a good performance in image debluring and denoising. Illustrative examples show that the proposed blind image deconvolution algorithm is efficient in producing better image estimate and has better performance in improvement signal-to-noise ratio than two traditional blind image iterative algorithm.

This paper is divided into five sections. In next Section, we describe the SVR method for noise reduction. In the third Section, we review two traditional blind image restoration approaches. In the fourth Section, we propose a novel blind image restoration approach. In five Section, two illustrative examples are discussed. Conclusions are found in six Section.

2 SVR Method for Noise Reduction

Let $z(i,j) = f(x,y) * h(x,y)$. Then the degradation image model defined in (1) may be written as the following noisy image model:

$$g(i,j) = z(i,j) + n(i,j), \tag{5}$$

where $z(i,j)$ is the blurred image without noiseness, $g(i,j)$ is a noisy image, and $n(i,j)$ is additive noise which may be Gaussian or non-Gaussian noise. Many image denoising methods were developed under a Gaussian noise assumption [15–26]. For example, the total variational method and the wavelet-based image denoising method. In recent years, support vector regression (SVR) algorithm for

image denoising has been studied because it has a better performance in function approximation [27–31]. Given training data $(\mathbf{X}_1;y_1),...,(\mathbf{X}_l;y_l)$ where $\mathbf{X}_i$ are input attribute (feature) vectors and y_i are the associated target values. A SVR is to determine the following prediction function:

$$g(\mathbf{x}) = \sum_{i=1}^{N} a_i^* K(\mathbf{x}, \mathbf{x}_i) + b, \tag{6}$$

where $K(\cdot,\cdot)$ is a Gaussian kernel function and $\{a_i^*\}$ are optimal solutions to the following quadratic optimization problem:

$$\begin{aligned} \text{Min} \quad & \frac{1}{2}\sum_{i=1}^{N}\sum_{j=1}^{N} a_i a_j K(\mathbf{x}_i, \mathbf{x}_j) - \sum_{i=1}^{N} a_i y_i + \epsilon \sum_{i=1}^{N} (a_i)^2 \\ s.t. \quad & \sum_{i=1}^{N} a_i = 0, -c \le a_i \le c (i = 1, \ldots, n) \end{aligned} \tag{7}$$

where $\epsilon > 0$ a design parameter for the tradeoff between model complexity and training error.

We thus propose using a fast SVR method for image denoising given in [31]. For each pixel of the image, we consider a neighborhood window around it. We choose the window sizes of 3×3. A two-dimensional ($2D$) gray level image can be regarded as a continuous function $y = f(\mathbf{X}) : R2 \rightarrow R1$, where the input $\mathbf{X}$ is a $2D$ vector that equals the row and column indices of a pixel, and the output y is a scalar value indicating the gray level of that pixel. We denote the row and column indices of the selected window as the input feature vector $\mathbf{X}$ of SVR, and let the target value y be the corresponding pixel value. As for the neighborhood of coordinates i, j, all the neighborhood elements are considered as the input vectors of LS-SVM. Thus we can construct the nonlinear formula between input coordinate vectors and the pixel centered at the neighborhood window. For any pixel except for those near the boundaries of the image, training the SVR model for current pixel using the training set is made from the $\mathbf{X} - y$ pairs in selected window. Therefore, the value of current pixel is estimated by the SVR model.

3 Existing Blind Image Restoration Methods for Image Deblurring

Existing traditional blind image restoration algorithms include the nonnegative and support constraints recursive inverse filtering (NAS-RIF) approach, the double regularization (DR) approach, and the total variation (TV) approach. The NAS-RIF approach minimizes convex cost function but requires the image object to have a known support in a uniform background. The DR approach minimizes the following regularization cost function:

$$J_1(\mathbf{g},\mathbf{h}) = \|\mathbf{h} * \mathbf{f} - \mathbf{g}\|_2^2 + \lambda\|Q\mathbf{f}\|_2^2 + \gamma\|P\mathbf{h}\|_2^2 \tag{8}$$

where $\| \bullet \|_2$ is the Euclidean norm (also called L_2 norm). The first term on the right-hand side of (8) is the noise error term between the observed image and the blurred image, the second term and the third term are the regularization terms for the image and the blur, respectively, Q and P in this term are called the regularization operators and are usually a highpass filter, and $\lambda > 0$ and $\gamma > 0$ are the regularization parameters that control the tradeoff between the error term and the regularization terms. To preserve edges well in the restored image, the TV approach minimizes the following TV cost function:

$$J(\mathbf{g},\mathbf{h}) = \|\mathbf{h} * \mathbf{f} - \mathbf{g}\|_2^2 + \lambda\|\mathbf{f}\|_{TV} + \gamma\|\mathbf{h}\|_{TV} \tag{9}$$

where $\| \cdot \|_2$ is L_2 norm and $\|\mathbf{f}\|_{TV}$ is the discretization of the continuous TV term of an image defined by

$$\int_{\Omega} \sqrt{f_x^2 + f_y^2}\,dxdy, \tag{10}$$

where Ω is the support of the image. The three methods have a good performance in deburing under optimal regularization parameter and noiseless conditions. In recent years some improved IBD works on the TV method for blind image restoration were developed, but they focus on algorithm implementation and TV term modification [2, 9], and thus there is a drawback of noise amplification when noise level is not very low.

4 Proposed Algorithm for Blind Image Restoration

To overcome the drawback of noise amplification, we propose a novel blind image restoration algorithm based a SVR-based noise reduction technique. Let '**g**' denotes the corrupted image. The proposed blind image restoration algorithm is described as follows:

I. Image denoising step:

(1) Select a $2D$ sliding window $\mathbf{S}$ with size $W_k \times W_k$ as the training set, where $\mathbf{X}$ is the neighborhood pixels coordinates in the selected window and y is the corresponding pixel value.
(2) Compute support vectors (SVs) $\mathbf{a}^*$ and the bias b^* by solving (7).
(3) Compute the denoised value by using the SVR function:

$$\hat{f}(\mathbf{X}) = \sum_{l=1}^{W_k}\sum_{m=1}^{W_k} a_{lm}^* K(\mathbf{X}, \mathbf{X}_{lm}) + b^*$$

II. Image deblurring step:

Let initial image $\mathbf{f}^0 := \hat{\mathbf{f}}(\mathbf{X})$ and set initial PSF: $\mathbf{h}^0$. For $k = 1, 2, 3, \ldots, L$

(1) Solve for $\mathbf{f}^{(k)}$:

$$\mathbf{f}^{(k)} = arg \min_{\mathbf{f}} \|\mathbf{h}^{(k-1)} * \mathbf{f} - \mathbf{g}\|_2^2 + \lambda \|\mathbf{f}\|_{TV} \tag{11}$$

(2) Solve for $\mathbf{h}^{(k)}$:

$$\mathbf{h}^{(k)} = arg \min_{\mathbf{h}} \|\mathbf{h} * \mathbf{f}^{(k-1)} - \mathbf{g}\|_2^2 + \gamma \|\mathbf{h}\|_{TV} \tag{12}$$

(3) If $|\mathbf{f}^{(k)} - \mathbf{f}^{(k-1)}|/|\mathbf{f}^{(k-1)}| \geq \epsilon$ and $k < L$, let k:=k+1, goto Step 1. Otherwise, output image estimate $\mathbf{f}^{(k)}$.

In image deblurring step, the gradient of the TV term is given by

$$\frac{\partial \|f\|_{TV}}{\partial f} = -\nabla \frac{\nabla f}{|\nabla f|} = -\frac{f_{xx} f_x^2 - 2 f_{xy} f_x f_y + f_{yy} f_y^2}{(f_x^2 + f_y^2 + \rho)^{3/2}}$$

and

$$\frac{\partial \|h\|_{TV}}{\partial h} = -\nabla \frac{\nabla h}{|\nabla h|} = -\frac{h_{xx} h_x^2 - 2 h_{xy} h_x h_y + h_{yy} h_y^2}{(h_x^2 + h_y^2 + \rho)^{3/2}}$$

where $\rho > 0$ is a constant to avoid the non-differentiability of the TV term at zero. The gradient of the cost function defined in (9) can be computed by

$$\begin{aligned} \frac{\partial J(f,h)}{\partial f} =& -2(g(x,y) - f(x,y) * h(x,y)) * h(-x,-y) \\ & - \nabla \frac{\nabla f(x,y)}{|\nabla f(x,y)|} \end{aligned}$$

and

$$\begin{aligned} \frac{\partial J(f,h)}{\partial h(x,y)} =& -2(g(x,y) - f(x,y) * h(x,y)) * f(-x,-y) \\ & - \nabla \frac{\nabla h(x,y)}{|\nabla h(x,y)|} \end{aligned}$$

respectively.

5 Experimental Results

In this section, we give illustrative examples to demonstrate the effectiveness of the proposed algorithm. The simulation is conducted in MATLAB.

For evaluating the performance of the proposed algorithm, the computed results are compared by visual quality subjectively and by the improvement in SNR:

$$\text{ISNR} = 10log_{10}\frac{\|\mathbf{g}-\mathbf{f}\|_2^2}{\|\mathbf{f}^*-\mathbf{f}\|_2^2},$$

where $\mathbf{f}$ represents the true image, $\mathbf{f}^*$ represents the estimated image, and $\mathbf{g}$ is the observed image.

Example 1. Consider a 256 by 256 pixels Lena image. The original image is degraded by 7×7 Gaussian blur with standard derivation $= 7$ and is added impulse noise with $\sigma^2 = 0.1$ and Gaussian noise with $\sigma^2 = 10$, respectively. Fig. 1A(a) and Fig. 1B(a) display noisy blurred images, respectively in impulse and Gaussian noise environments.

For a comparison, we perform the SVR denoising algorithm, the TV algorithm, and the proposed algorithm under same parameters: $\lambda = 0.0004$ and $\gamma = 10^8$. Figure 1 a displays restored images in the Pepper noise case, respectively by the SVR denoising algorithm, the TV algorithm, and the proposed algorithm.

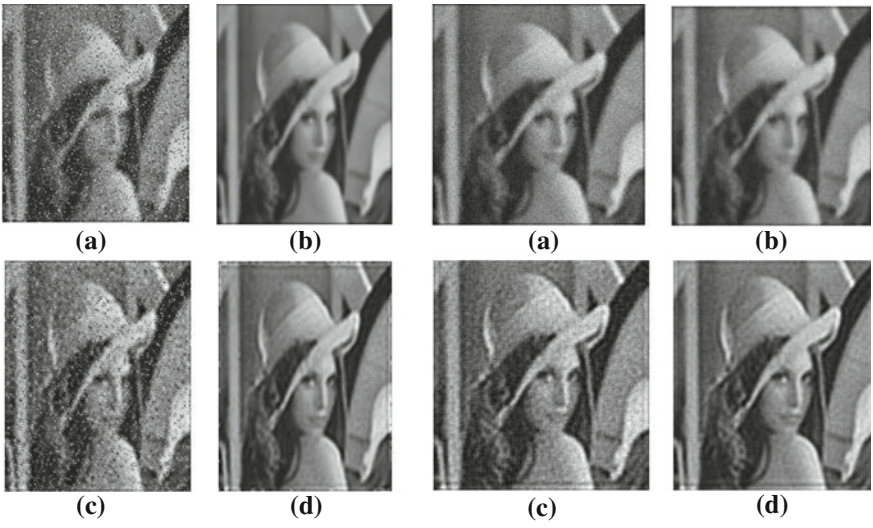

Fig. 1 Restored results under two noise environments in Example 1.: **A(a)** and **B(a)** noisy blurred images; **A(b)** and **B(b)** by the SVR denoising algorithm; **A(c)** and **B(c)** by the TV algorithm; **A(d)** and **B(d)** by the proposed algorithm

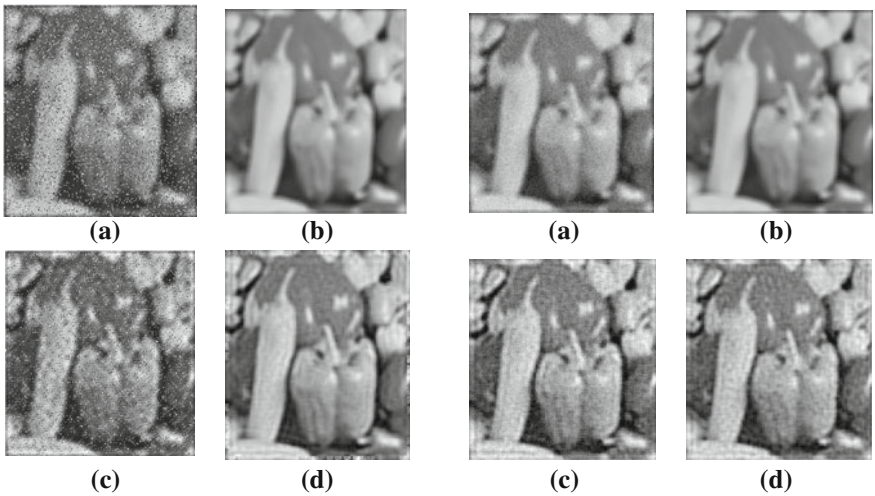

Fig. 2 Restored results under Gaussian noise environment in Example 2.: **b** by the SVR denoising algorithm; **c** by the TV algorithm; **d** by the proposed algorithm. **A** Pepper noise environment. **B** Gaussian noise environment

Table 1 Comparison of ISNR results by three algorithms

	Algorithm	Lena	Pepper
Impluse noise	TV algorithm	1.8142	2.9823
	Proposed algorithm	5.005	5.4850
Gaussian noise	TV algorithm	4.5204	4.9049
	Proposed algorithm	5.9099	6.1885

Figure 1b displays restored images in the Gaussian noise case, respectively by the SVR denoising algorithm, the proposed algorithm, and the proposed algorithm. It is seen that the proposed algorithm can give a better image estimate than the traditional TV algorithm. Furthermore, Table 1 displays ISNR results of the two algorithms. We can see that the proposed algorithm has better performance in both noise and blur removal than the TV algorithm also.

Example 2. Consider a 512 by 512 pixels Pepper image. The original image is degraded by 9×9 Gaussian blur with standard derivation$= 9$ and is added impulse noise with $\sigma^2 = 0.1$ and Gaussian noise with $\sigma^2 = 10$, respectively. Fig. 2(a):(a) and Fig. 2(b):(a) display noisy blurred images, respectively.

For a comparison, we perform the SVR denoising algorithm, the proposed TV algorithm, and the proposed algorithm under same parameters: $\lambda = 0.0004$ and $\gamma = 10^8$. Fig. 2a displays restored images in the Pepper noise case, respectively by the SVR denoising algorithm, the TV algorithm, and the proposed algorithm.

Fig.2b displays restored images in the Gaussian noise case, respectively by the SVR denoising algorithm, the proposed algorithm, and the proposed algorithm. As seen, the proposed algorithm can give a better image estimate than the traditional TV algorithm. Furthermore, Table 1 displays ISNR results of the two algorithms. We can see that the proposed algorithm has better performance in both noise and blur removal than the TV algorithm also.

6 Conclusion

In this paper, we have proposed an efficient blind image deconvolution approach to join a support vector regression noise reduction technique and a total variation technique. The proposed algorithm has a lower computational complexity and a good performance in image denoising and deblurring. Illustrative examples confirm that the proposed algorithm is efficient in producing better image estimate and has better performance in improvement signal-to-noise ratio than two traditional blind image restoration algorithms.

Acknowledgments This work is supported in part by the National Natural Science Foundation of China under Grant No. 61179037.

References

1. Andrews HC, Hunt BR (1977) Digital image restoration. Prentice-Hall, New York
2. Aujol JE, Gilboa G, Chan T, Osher S (2006) Structure,-texture image decomposition modeling, algorithms, and parameter selection. Int J Comput Vision 67:111–136
3. Kundur D, Hatzinakos D (1996) Blind image deconvolution. IEEE Signal Process Mag 13:43
4. Campisi P, Egiazarian K (2007) Blind image deconvolution: theory and applications. CRC Press, Boca Raton
5. Tekalp AM, Kaufman H, Woods JW (1986) Identification of image and blur parameters for the restoration of noncausal blurs. IEEE Trans Acoust Speech Signal Process 34:963–968
6. Kundur D, Hatzinakos D (1998) A novel blind deconvolution scheme for image restoration using recursive filtering. IEEE Trans Signal Process 46:375
7. You Y-L, Kaveh M (1996) A regularization approach to joint blur identification and image restoration. IEEE Trans Image Process 5:416
8. Chan TF, Wong C-K (1998) Total variation blind deconvolution. IEEE Trans Image Process 7:370
9. He L, Marquina A, OSher SJ (2005) Blind deconvolution using TV regularization and Bregman iteration, Int J Imaging Syst Technol 15:74–83
10. Chen L, Yap KH (2005) A soft double regularization approach to parametric blind image deconvolution. IEEE Trans Image Process 14:624–633
11. Chow TWS , Li X-D, Ng K-T (2001) Double-regularization approach for blind restoration of multichannel imagery. In: IEEE transactions. Circuits and systems I:fundantmental theory and applications 48:1075

12. Jinglian Z, Xia YS (2010) A two-dimensional algorithm for blind image restoration using a novel mixed L1 regularization approach. In: International congress on image and signal processing, Yantai, China
13. Sroubek F, Flusser J (2003) Multichannel blind iterative image restoration. IEEE Trans Image Process 12:1094–1106
14. Dalong L, Russell MM, Steven S (2005) Blind image deconvolution using support vector regression. ICASSP 2:113–116
15. Rudin LI, Osher S, Fatemi E (1992) Nonlinear total variation based noise removal algorithms. Phys D 60:259–268
16. Gilboa G, Zeevi YY, Sochen N (2003) Texture preserving variational denoising using an adaptive fidelity term. In: Proceedings of the VLSM
17. Liu J, Huan Z, Huang H, Zhang H (2009) An adaptive method for recovering image from mixed noisy data. Int J Comput Vis 85:182–191
18. Strong DM, Chan TF (1996) Spatially and scale adaptive total variation based regularization and anisotropic diffusion in image processing. UCLA CAM Report 96–46
19. Ghouti L, Bouridane A (2005) Two-step variance-adaptive image denoising. In: Proceedings of the ICIP2005
20. Hashemi M, Beheshti S (2010) Adaptive noise variance estimation in BayesShrink. IEEE signal process lett 17(1):12–15
21. Chang SG, Yu B, Vetterli M (2000) Adaptive wavelet thresholding for image denoising and compression. IEEE Trans Image Process 9(9):1532–1546
22. Chang SG, Bin Y, Vetterli M (2000) Spatially adaptive wavelet thresholding with context modeling for image denoising. IEEE Trans Image Process 9(9):1522–1531
23. Hamza A, Krim H (2001) Image denoising: A nonlinear robust statistical approach. IEEE Trans Signal Process 49(12):3045–3054
24. Hou Z, Koh TS (2004) Image denoising using robust regression. IEEE Signal Process Lett 11(2):243–246
25. Rabie T (2005) Robust estimation approach for blind denoising. IEEE Trans Image Process 14(11):1755–1765
26. Kulkarni RK, Meher S, Nair JM (2010) An algorithm for image denoising by robust estimator. Eur J Sci Res ISSN 1450–216X 39(3):372–380
27. Dalong L (2009) Support vector regression based image denoising. Image Vis Comput 27:623–627
28. Wang Y, Cheung Y, Liu H (eds) (2007) Image denoising based on wavelet support vector machine. CIS 2006, LNAI 4456, pp 963–971
29. Zeng G, Zhao R (2007) Image denoising using least squares wavelet support vector machines. Chin Opt Lett 5(11):632–635
30. Vapnik V (1995) The nature of statistical learning theory. Springer, New York
31. Wu HQ, Xia YS (2011) A simplified SVR method for blind image denoising. In: International congress on image and signal processing. Shanghai, China, pp 47–50

Effects of Music's Emotional Styles and Tempo on Driving Behavior and Eye Movement: A Driving Simulation Study

Meng Yang, Jianqiao Wang, Yuqi Xia, Fan Yang and Xuemin Zhang

Abstract This study investigated the interaction of music emotional styles and tempo in behavior and eye movement in 3D driving simulator. The main results indicated that music emotional styles affected driving behavior and eye movement in both slow tempo and fast tempo conditions, but the means of emotional styles affecting driving behavior and eye movement differed on tempo. There was significant emotional styles difference on the number of mistakes and mean fixation duration in fast tempo condition, while there was emotional styles effect on time perception and vertical spread of visual search in slow tempo condition. According to these results, we suggested that drivers should choose peaceful and cheerful music while driving.

Keywords Music emotional styles · Music tempo · Driving behavior · Eye movement

1 Introduction

Nowadays automobiles have played an important role in our daily life, which attracted psychologists to focus on the factors affecting driving. Researchers have studied three kinds of factors: (1) outside of the vehicle (road conditions, weather,

M. Yang · J. Wang · Y. Xia · X. Zhang (✉)
School of Psychology and Beijing Key Lab of Applied Experimental Psychology, Beijing Normal University, Beijing 100875, China
e-mail: xmzhang@bnu.edu.cn

X. Zhang
State Key Lab of Cognitive Neuroscience and Learning, Beijing Normal University, Beijing 100875, China

F. Yang
School of Mathematical Sciences, Beijing Normal University, Beijing 100875, China

F. Sun et al. (eds.), *Foundations and Practical Applications of Cognitive Systems and Information Processing*, Advances in Intelligent Systems and Computing 215,
DOI: 10.1007/978-3-642-37835-5_49,

etc.) [1, 2]; (2) inside of the individuals (personality, experience, age, alcohol, drugs, etc.) [3–7]; (3) Inside of the vehicle between the former two factors (mobile phone, passengers, etc.) [8, 9]. Among the factors of 'inside of the vehicle', music, because of its uniqueness, deserves more attention.

Getting into the car and turning on the video has already become a common behavior for modern drivers [10–13]. Thus, effects of background music on driving behavior have attracted the attention of psychologists. Previous studies narrowed down to music physical properties such as intension [14, 15] and tempo [16, 17]. However, some studies lead to contradictory results. As for the effects of intension on driving, for example, Spinney [18] proved that moderate-intensity music could promote driving, while Beh and Hirst [14] argued that low-intensity music could promote driving. It seems that it is impossible to reveal music effects by simply studying its physical properties. In fact, music's psychological property, namely emotional effects, also plays an important role.

Music represents and causes different emotional states. Expressing emotion is the most important characteristic of music. Compared to other stimulus, music has a lot of advantages in evoking listeners' emotion, such as high consistency among tests, high arousal, and high diversity of emotion evoked [19–21]. Zatorr and Bermudez's [22] PET study shows that music's emotional effect has neuro-physiological basis, which means music emotion effect is stable.

Driving demands high-quality attention processing [23]. In recent studies, impacts of emotion on cognition, especially on attention, have been studied by many researchers [24, 25]. These studies demonstrate that negative emotion leads to narrower span of attention, longer reaction time, and fewer risk behaviors. By contrast, positive emotion leads to wider span of attention, shorter reaction time, and more risk behaviors [26, 27]. Ellison-Potter, Bell and Deffenbacher [28] revealed that emotion and anonymity affected aggressive driving behavior significantly by using driving simulations. Besides anger, other emotions like joy and sadness also affect driving safety. Mesken [29] found that in natural conditions, joy ranked the third to affect driving behavior, following anger and anxiety. The study of depression patients found that sadness interfered in driving behavior, which resulted in longer reaction time and more accidents [30].

Music's emotional effects on driving safety have been also considered recently. Pêcher et al. [31] used joy, sadness, and neutral music excerpts to study how music emotion affected driving behavior. The results showed that the participants' driving speed was the slowest with joyful music, and the fastest with neutral music. This finding was inconsistent with the research result when music tempo was regarded as a major independent variable. As we know, music's emotional styles are associated with tempo closely: fast tempo music often expresses happy emotion, while slow tempo music often expresses sad emotion. When researchers treated tempo as an independent variable, the result was that fast tempo music increased speed and the probability of traffic accidents [16, 17]. These results may be caused by the music's dual characteristics including physical property (tempo) and psychological property (emotional styles). Tempo makes drivers speed up unconsciously by disturbing their estimation of speed and time; on the other hand,

emotional styles affect the current task by widening or narrowing the span of attention. However, few studies have investigated these two factors together, which may cause contradictions regarding music's impacts on driving.

Therefore, an experiment involving two factors should have been designed in this study. One factor is "tempo" with high tempo and low tempo as levels; the other is music's emotional styles with positive emotion and negative emotion as levels. However, we chose another way to analysis data, because tempo affects the expression of emotions, as we mentioned. Taking negative emotion for example, fast tempo normally expresses irritation or boredom, and slow tempo expresses sadness or depressiveness. This phenomenon does not meet the prerequisite for multifactor experiment design, so in this study we only investigated effects of different emotions on driving behavior under fast or slow tempo music conditions separately. Furthermore, we recorded and analyzed the eye movement's data to illustrate participants' visual attention process when they were driving. Among behavior variables, speed and number of mistakes are commonly used as two indicators, but speed has direct impacts on eye movements, so that drivers have to widen the horizontal spread of search and narrow the vertical spread of search in order to cope with the objects emerged in front of eyes when driving fast [32]. This leads to the misunderstanding about the inferences of music effect on attention span from eye movement data. To prevent this happening and control speed in different conditions, we chose roads with many turns and intersections to reduce the probability to speed up, ensuring that eye movements were caused by music rather than the road environment. According to previous studies, we have known that the reason why drivers change the speed is that music disturbs their time perception, so we chose drivers' time perception (that is, the error between actual driving time and estimated driving time) as the index predicting the driving speed. Eye movement data, such as mean fixation duration (indicating the difficulty of processing the information), saccade amplitude (indicating the span of attention), and horizontal/vertical spread of search (indicating the processing mode of road condition) were also selected as indicators to reflect drivers' visual activities.

2 Method

2.1 Participants

Eight male participants from Beijing Normal University aged between 18 and 23 years old (Mean = 21.5, SD = 1.31) participated in the experiment. All participants had a valid Chinese driving license for at least 1 year and had covered at least 5,000 km by driving. They all had normal vision or corrected normal vision. None of them major in music, or take drugs during the experiment. All participants completed a questionnaire to report basic information before the experiment.

2.2 Stimuli

Four music excerpts which were used as four experimental conditions were selected from sixteen music excerpts without lyrics in pre-test by using Self-assessment Manikin scale with 15 subjects including 7 male and 8 female. They were slow-sad, slow-joyful, fast-passionate, and fast-boring styles. Every excerpt of music was played repeatedly during the driving process. All the music experts playing orders are randomized for each participant during the simulated driving process.

To control the driving speed, we selected a "city road" which had more red lights and turns as the designate route from 3D-driving simulator which could automatically record the number of mistakes according to the real traffic rules.

2.3 Apparatus

Present experiment took place in a visualization room equipped with a Tobii 1750 eye tracker (17″ LCD Monitor, maximum resolution is 1280 × 1024, refresh rate is 50 Hz, fixations' minimum duration was set to 100 ms) and two computers (core2 CPU, 17″ LCD Monitors, resolution is 1024 × 768, refresh rate is 85 Hz). The car simulation software called "3D driving simulator" was running on the Tobii's eye tracker screen, and the hardware included steering wheel, gas pedal, and break pedal which come from Be-top Be3169, as shown in Fig. 1. The software of TET Server and Clear View of Tobii 1750 eye tracker recorded and exported the data of eye movements. 3D driving simulator counted the number of mistakes automatically, and the stopwatch was used to measure the time that participants spent to complete every lap.

Fig. 1 Screenshot of the 3D-driving simulator chose in present experiment and the car simulation with steering wheel and pedal

2.4 Procedures

There were controlled variables in this experiment; that is, participants' familiarity and preference of the music, recorded by five-point scale presented in the questionnaire before the experiment. The main experimental tasks were driving fast and safely in the provided simulation under the premise of obeying traffic rules to complete the designated route. Participants were provided with a music order after completing the questionnaire, and then they were seated in front of the simulator, adjusted posture to ensure the eye tracker could detect their eye movements. In order to familiarize themselves with the simulator, all participants drove along the route twice before the experiment. Every turn had clear direction instructions so that there was no need for participants to memorize the route. Participants' eye movements were calibrated by a 5-point calibration screen. Experiment requirements and rules were further explained to the participants to make sure that they were clear. After participants had understood the requirements and operation rules, the experiment began. Participants drove along the designated route (start/end point was clearly marked) for four times with one kind of music excerpt, played to 70 dB, and repeated until the journey was finished each time. After finishing a lap, participants were asked to complete a questionnaire to take down their familiarity and preference to the music. In fact, experimenters stressed the questionnaire was irrelevant with results in order to prevent participants from deliberating attention to music.

Microsoft excel 2003, SPSS16.0 and MatLab7.10 were used to analyze the data of collected behaviors and eye movements.

3 Results

Two independent paired sample *t* tests were conducted for slow tempo and fast tempo music. The former kind was joyful or sad, while the latter kind was irritating or boring. An alpha level of 0.05 was used for all statistical tests.

3.1 Controlled Variables

In order to examine the differences of the four music styles in terms of participants' familiarity and preference, we conducted repeated analyses of variance (ANOVA) with music styles as the within-subject factor and found no significant differences, which meant the familiarity and preference were controlled. Similarly, there were no significant emotional differences in two kinds of tempo.

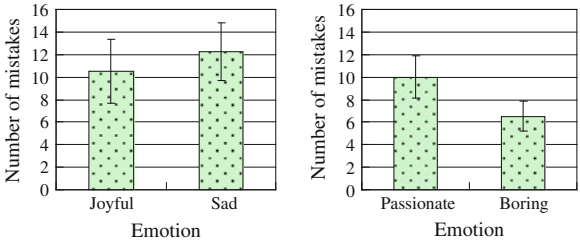

Fig. 2 Number of mistakes as a function of music emotion in different tempo conditions (*left*-slow and *right*-fast)

3.2 Number of Mistakes

Descriptive statistics of the number of mistakes were shown in Fig. 2. Paired sample t tests indicated that there was no significant emotional difference in slow tempo condition [$t(7) = 0.439$, $p > 0.05$], while there was significant emotion difference in fast tempo condition [$t(7) = 2.646$, $p < 0.05$]. Results revealed that emotion was unimportant for the number of mistakes in slow tempo condition, while it played an essential role in fast tempo condition. This inconsistency may be caused by the level of arousal: the arousal level of the slow tempo music was lower than that of the fast tempo music, so the emotional effect was no longer obvious.

3.3 Time perception

Time perception is the error between actual driving time and estimated driving time. The longer time perception is, the higher the speed is, and the more likely the driver will slow down. Descriptive statistics of time perception were shown in Fig. 3. Paired sample *t* tests indicated that there was significant emotion difference in slow tempo condition [$t(7) = 2.093$, $p < 0.05$], while there was no significant difference in fast tempo condition [$t(7) = 0.130$, $p > 0.05$]. Results above reveal that emotion was weaker than tempo when affecting the time perception. When the tempo was slow, joyful emotion shortens participants' time perception; when the tempo was fast, emotion was unimportant for time perception because tempo itself disturbs it by increasing arousal [33].

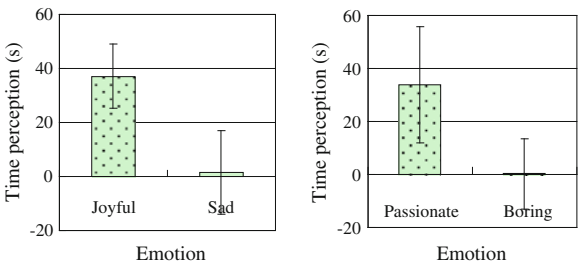

Fig. 3 Time perception as a function of music emotion in different tempo conditions (*left*-slow and *right*-fast)

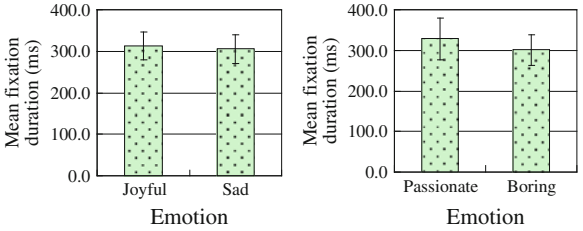

Fig. 4 Mean fixation duration as a function of music emotion in different tempo conditions (*left*-slow and *right*-fast)

3.4 Mean Fixation Duration

Mean fixation duration is the result that the sum of all valid fixations' duration divided by the number of valid fixations. It is a reflection of the difficulty of processing stimulus while driving. Descriptive statistics of mean fixation duration were shown in Fig. 4. Paired sample *t* tests indicated that there was no significant emotional difference in slow tempo condition [$t(7) = 0.501, p > 0.05$], while there was marginally significant emotion difference in fast tempo condition [$t(7) = 1.826, p = 0.056$]. Results above reveal that emotion was unimportant for difficulty of processing information in driving in slow tempo condition, while compared to boring, passionate emotion increased the difficulty of processing in fast tempo condition. This consists with the result about the number of mistakes, the reason of which may be that emotion affected the difficulty of processing and thereby affected the number of mistakes.

3.5 Saccade Amplitude

Saccade amplitude is the average of the distance between each pair of adjacent fixation points. It reflects the span of attention. Descriptive statistics of saccade amplitude were shown in Fig. 5. Paired sample *t* tests indicated that there was no significant emotion difference in slow or fast condition [$t(7) = -0.262, p > 0.05$; $t(7) = 0.223, p > 0.05$]. Results above revealed that emotion was unimportant for experienced drivers' span of attention.

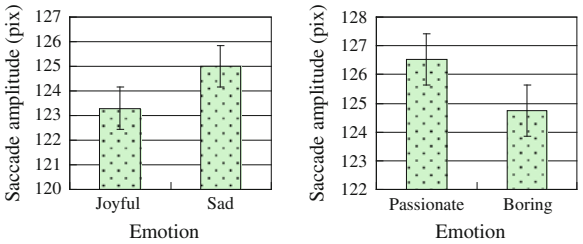

Fig. 5 Saccade amplitude as a function of music emotion in different tempo conditions (*left*-slow and *right*-fast)

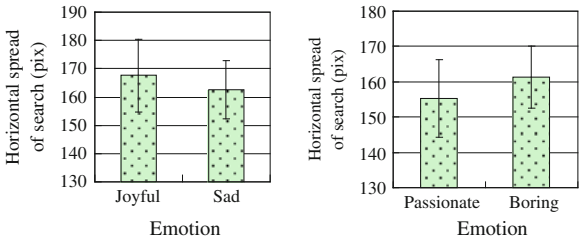

Fig. 6 Horizontal spread of search as a function of music emotion in different tempo conditions (*left*-slow and *right*-fast)

3.6 Horizontal Spread of Search

Horizontal spread of search is the standard deviation of all the valid fixations' locations in abscissa (both axes presented screen positions measure in pixels). It is a reflection of the span of attention and search mode in the horizontal direction. Descriptive statistics of horizontal spread of search were shown in Fig. 6. Paired sample *t* tests indicated that there was no significant emotion difference in slow or fast condition [$t(7) = 0.579,\ p > 0.05;\ t(7) = 1.244,\ p > 0.05$]. Results above revealed that emotion was unimportant for experienced drivers' span of attention and search mode in horizontal direction.

3.7 Vertical Spread of Search

Vertical spread of search is the standard deviation of all the valid fixations' locations in ordinate. It is a reflection of the span of attention and search mode in the vertical direction, and especially the attention distribution to faraway objects while driving. Descriptive statistics of horizontal spread of search were shown in Fig. 7. Paired sample *t* tests indicated that there was significant emotion difference in slow tempo condition [$t(7) = 2.268,\ p < 0.05$], while there was no significant emotion difference in fast tempo condition [$t(7) = 0.564, p > 0.05$]. Results above revealed that emotion was unimportant for attention distribution to faraway objects in fast tempo condition, while in slow tempo condition, compared to joyful music, sad music increased it. This finding can be explained with the results of time perception. In slow tempo condition, joyful music shortened participants' time

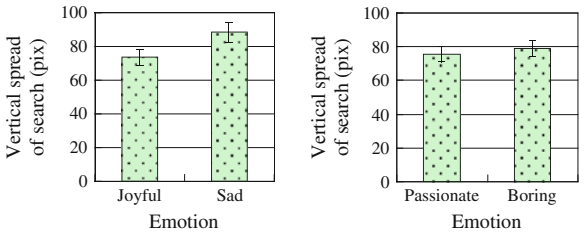

Fig. 7 Vertical spread of search as a function of music emotion in different tempo conditions (*left*-slow and *right*-fast)

perception; in other words, it made them feel the speed was faster. This anxious feeling prevented them from distributing attention to faraway objects, because they were struggling to cope with the objects emerging in the immediate. Sad music, however, made participants' time perception more objective, and brought on a wider attention. On the contrary, this phenomenon disappeared in fast tempo condition because of the tension and the great arousal caused by fast tempo.

4 Discussion

This study aimed to explore the effects of music expressing different emotions with different tempos on driving behaviors and eye movements. There were two pairs of similar patterns: the number of mistakes is consistent with the mean fixation duration, and time perception is coordinated as vertical spread of search. There was no emotion effect on horizontal spread of search or saccade amplitude.

The similar pattern between the number of mistakes and mean fixation duration was that emotional effects only occurred with fast tempo music. In other words, there was no emotion difference with slow tempo music, while there was significant emotion difference with fast tempo music, indicating that passionate music increased the number of mistakes and mean fixation duration. We think this distinction resulted from the different degree of emotion arousal. The driving behaviors in fast tempo music condition accorded with the research result conducted by Brodsky [16] and North, Hargreaves [17], who argued that positive emotion hindered driving behavior, but Vermeulen (2010) refuted the opinion, who proved that positive music could improve driving performance [27]. Contradictions above can also be explained by music arousal: when music arousal was low, positive emotion promoted driving performance; when music arousal was high, the result was opposite. We tend to drive safely in good mood; on the other hand, when we drive with eagerness, we are more likely to take risks, which will cause more mistakes. Moreover, frequent mistakes may also caused by the weak ability of cognition processing that was determined by the excitement, as indicated by the data of eye movements as well.

The similar pattern of time perception and vertical spread of search was that emotional effect only occurred in slow tempo music condition. In other words, there was no emotion difference in fast tempo music condition, while there was significant emotion differences in slow tempo music condition, indicating that joyful music decreased driving speed and attention distributed to faraway objects. We think this distinction resulted from the fact that emotion played a weaker role than tempo. In fast tempo condition, both passionate and boring music forced participants to have a sense of urgency, making time perception had nothing to do with emotion. Result of time perception in slow tempo music condition consisted with what Pêcher et al. [31] found, that is, participants drove more slowly in joyful music. However, that the attention span was narrower with joyful music than with sad music did not coordinate with Bulmash's [30] study. Contradictions above

may be due to the different modes to cope with sad emotion between depression patients and psychologically healthy people. When people felt sad, they would change perceptual and reaction mode to get them out of this negative mood [34], but depression patients selected by Bulmash did not have this ability. Sad emotion evoked insecurity to experienced drivers when they were immersed in sad music, so that they would decrease the feeling of insecurity by taking cognition strategies, which mainly consisted of widening attention, especially prospective attention to danger. In this way, there was more attention contributed to faraway objects. Combined with the result of mistake number, we can find that this prospective attention of emotion evocation did not benefit driving safety but seemed to be a waste of cognition resource.

In previous studies, we have found that dependent variables collected in studies of driving affected each other [32]. Among these dependent variables, speed is the most commonly used one and its impacts on other variables were the most powerful. In this study, we controlled the speed, aiming to explore the emotion impact only. Results showed that, when there was no speed difference, there was no attention span difference, but difference of mistakes still existed. Taking into account our previous study and discussions above, we can infer that attention span is the result of driving behavior rather than cause, which is decided by speed; the number of mistakes are determined by the processing difficulty of stimulus rather than attention span.

In summary, we have reached the following conclusions: Music's emotional styles affected driving behavior and eye movement with the same tempo; music's emotional styles affected driving behavior and eye movement in different ways with different tempos; emotion effects were significant in affecting the number of mistakes and mean fixation duration in fast tempo music condition, while emotion effects were significant in affecting time perception and vertical spread of search in slow tempo music condition. Thus, we suggest drivers to listen to peaceful and cheerful music while driving. This study still had limitations, such as the small sample which might increase the possibility of β error and simulation equipment with low external validity which could not completely simulated all driving conditions. Future studies will contribute more efforts to these aspects.

Acknowledgments The present research was supported by national project of undergraduates innovation research to Meng Yang (Supervised by Xuemin Zhang).

References

1. Konstantopoulos P, Chapman P, Crundall D (2010) Driver's visual attention as a function of driving experience and visibility. Using a driving simulator to explore drivers' eye movements in day, night and rain driving. Accid Anal Prev 42:827–832
2. Salvucc D, Liu A (2002) The time course of a lane change: driver control and eye-movement behavior. Transp Res Part F 5:123–132

3. Borowsky A, Shinar D, Oron-Gilad T (2010) Age, skill, and hazard perception in driving. Accid Anal Prev 42:1240–1249
4. Chapman PR, Underwood G (1998) Visual search of driving situations: danger and experience. Perception 27(8):951–964
5. Furr-Holden D, Voas RB, Kelley-Baker T, Miller B (2006) Drug and alcohol-impaired driving among electronic music dance event attendees. Drug Alcohol Depend 85:83–86
6. Lamers CTJ, Ramaekers JG (2001) Visual search and urban city driving under the influence of marijuana and alcohol. Hum Psychopharmacol 16:393–401
7. Nabi H, Consoli SM, Chastang J-F, Chiron M, Lafont S, Lagarde E (2005) Type A behavior pattern, risky driving behaviors, and serious road traffic accidents: a prospective study of the GAZEL cohort. Am J Epidemiol 161:864–870
8. Spence C, Read L (2003) Speech shadowing while driving: on the difficulty of splitting attention between eye and ear. Psychol Sci 14(3):251–256
9. Strayer DL, Drews FA, Johnston WA (2003) Cell phone-induced failures of visual attention during simulated driving. J Exp Psychol 9(1):23–32
10. Dibben N, Williamson VJ (2007) An exploratory survey of in-vehicle music listening. Psycholog Music 35:1–19
11. Sloboda JA (1999) Everyday uses of music listening: a preliminary study. In: Suk Won Yi (ed) Music, mind, and science. Seoul: Western Music Institute, Seoul, pp 354–369
12. Sloboda JA, O'Neill SA, Ivaldi A (2001) Functions of music in everyday life: an exploratory study using the experience sampling method. Musicae Scientiae 5:9–32
13. Sloboda JA, O'Neill SA, Ivaldi A (2000) Functions of music in everyday life: an exploratory study using the experience sampling method. In: Woods C, Luck G, Brochard R, Seddon F, Sloboda JA (eds) Proceedings of the sixth international conference on music perception and cognition. Keele University, Staffordshire, UK, CD–ROM
14. Beh HC, Hirst R (1999) Performance on driving-related tasks during music. Ergonomics 42:1087–1098
15. Stamu MJ, Brotons M (2000) The effect of music amplitude on the relaxation response. J Music Ther 37:22–39
16. Brodsky W (2002) The effects of music tempo on simulated driving performance and vehicular control. Transp Res Part F 4(4):219–241
17. North A, Hargreaves D (1999) Can music move people: the effects of musical complexity and silence on waiting time. Environ Behav 31:136–149
18. Spinney L (1997) Pump down the volume. New Sci 155:22
19. Koelsch S (2005) Investigating emotion with music: neuroscientific approaches. Ann N Y Acad Sci 1060:412–418
20. Panksepp J (1995) The emotional sources of "Chills" induced by music. Music Percept 13(2):171–207
21. Baumgartner T, Esslen M, Jäncke L (2006) From emotion perception to emotion experience: emotions evoked by pictures and classical music. Int J Psychophysiol 60(1):34–43
22. Zatorre R, Bermudez P (1999) Emotional responses to pleasant and unpleasant music correlate with activity in limbic brain regions. Nat Neurosci 2(4):382–387
23. Chilsholm SL, Caird JK, Lockhart J (2008) The effects of practice with MP3 players on driving performance. Accid Anal Prev 40:704–713
24. Griskevicius V, Shiota MN, Neufeld SL (2010) Influence of different positive emotions on persuasion processing: a functional evolutionary approach. Emotion 10(2):190–206
25. Yates A, Ashwin C, Fox E (2010) Does emotion processing require attention? The effects of fear conditioning and perceptual load. Emotion 10(6):822–830
26. Slovic P, Peters E, Finucane ML, MacGregor DG (2005) Affect, risk, and decision making. Health Psychol 24:35–40
27. Vermeulen N (2010) Current positive and negative affective states modulate attention: an attention blink study. Personality Individ Differ 49(5):542–545
28. Ellison-Potter P, Bell P, Deffenbacher JL (2001) The effects of trait driving anger, anonymity, and aggressive stimuli on aggressive driving behavior. J Appl Soc Psychol 31:431–443

29. Mesken J (2006) Determinants and consequences of drivers' emotions. SWOV-Dissertatiereeks, Leidschendam, Nederland
30. Bulmash EL, Moller HJ, Kayumov L, Shen J, Wang X, Shapiro CM (2006) Psychomotor disturbance in depression: assessment using a driving simulator paradigm. J Affect Disord 93:213–218
31. Pêcher C, Lemercier C, Cellier J-M (2009) Emotions drive attention: effects on driver's behavior. Saf Sci 47:1254–1259
32. Yang M, Wang J-Q, Xia Y-Q, Yang F, Zhang X-M (2012) Effects of music's tempo and participants' familiarity with language on driving behavior and eye-movement. Psychol Sci 34(5):1056–1061 in Chinese
33. Mella N, Conty L, Pouthas V (2011) The role of physiological arousal in time perception: Psychophysiological evidence from an emotion regulation paradigm. Brian Cogn 75(2):182–187
34. Kashdan TB, Zvolensky MJ, Mcleish AC (2008) Anxiety sensitivity and affect regulatory strategies: Individual and interactive risk factors for anxiety-related symptoms. J Anxiety Disord 22(3):429–440

An Improved HOG Based Pedestrian Detector

Chao Gao, Fengcai Qiao, Xin Zhang and Hui Wang

Abstract Despite being widely adopted and rigorously followed in many successful pedestrian detectors, the original HOG (Histogram of Oriented Gradients) descriptor are in fact NOT optimally tuned for pedestrian detection. To address this issue, we quantitatively investigate the interplay among different HOG parameters, in particular that among the cell size, aspect ratio, and detection window size, which makes it possible to jointly tune these parameters to achieve better pedestrian detection performance. In addition, we extend the training procedure of the original HOG-based detector of Dalal et al. through presenting an automatic positive sample generation algorithm, introducing LSVM (Latent SVM) to iteratively optimize the positive training samples, and adopting a hard negative mining method. To verify the effectiveness of our improved detector, we conduct extensive experiments on INRIA Person, TUD-Brussels and Caltech Pedestrians datasets. On all these datasets, our detector outperforms significantly the original HOG detector of Dalal et al.

Keywords Pedestrian detection · HOG parameter tuning · Latent SVM · Full image evaluation

1 Introduction

Persons are the most important interested objects in many image/video understanding applications, including auto navigation [1], robotics, and surveillance [2], etc. In this paper, we focus on the detection of pedestrians (i.e. persons in upright poses, as shown in Fig. 1), which is also an important area of machine vision

C. Gao (✉) · F. Qiao · X. Zhang · H. Wang
College of Information Systems and Management, National University of Defense Technology, Changsha, China
e-mail: bladegao@gmail.com

F. Sun et al. (eds.), *Foundations and Practical Applications of Cognitive Systems and Information Processing*, Advances in Intelligent Systems and Computing 215,
DOI: 10.1007/978-3-642-37835-5_50,

(a) (b) (c) (d)

Fig. 1 Example images and annotations from three pedestrian detection datasets, INRIA Person (**a**) [3], Caltech Pedestrians (**b, c**) [4] and TUD-Brussels (**d**) [5]

research. Despite impressive progress has been achieved in recent years, the keys ensuring good detection performance are still not fully revealed.

As evaluated in a recent survey on pedestrian detection [6], no single feature has been shown to outperform HOG. This is the reason for that nearly all modern detectors employ some form of gradient histograms. Moreover, the pedestrian detector [7–10] using original or variant HOG usually adopt the same parameters as Dalal in [11], in particular the cell size, aspect ratio, and detection window size. However, note that the optimal parameters of HOG are determined in [11] through evaluating the per-window (PW) performance on the INRIA Person dataset. This parameter tuning process is problematic for pedestrian detection due to (1), as argued by Dollar et al. [6], the PW evaluation metric is commonly used to compare classifiers as opposed to detectors, and the more proper metric per image (PI) for the full image detection performance evaluation is only weakly related with PW metric; and (2) the INRIA Person dataset is mainly built for *people* detection rather than *pedestrian* detection. Thus, the HOG parameters determined by Dalal et al. in [11] and widely adopted by recent pedestrian detectors may NOT suit well to pedestrian detection.

To find out the optimal parameter setting of HOG for pedestrian detection, the present paper makes two main contributions. First we quantitatively investigate the inter-play among different HOG parameters, in particular that among the cell size, aspect ratio, and detection window size, which makes it possible to jointly tune these parameters to achieve better pedestrian detection performance. We notice that some previous paper use the log-mean aspect ratios of the training dataset, e.g. 0.33 for INRIA Person [11], 0.5 for TUD-Brussels [5]. However, the log-mean aspect ratio of training dataset is not the "optimal" aspect of detection window, as demonstrated in Sect. 2.1 and verified in Sect. 4.2.

The second main contribution is to propose an algorithm to automatically collect positive examples for pedestrian detector training, which is detailed in Sect. 3.1. In evaluation, it is shown that our detector pushes down the miss rate from 46 to 41 % at 0.1 false positive per-image (fppi) on INRIA Person, using automatically collected positive examples. Furthermore, the miss rates are further pushed forward to 36 % at 0.1 fppi by using the optimally tuned parameters. Moreover, the improved detector pushes down the miss rates at 0.1 fppi by 8 % and 3 % on the two most challenging pedestrian datasets, TUD-Brussels and Caltech Pedestrians respectively.

1.1 Related Work

The HOG features [3] are widely adopted by many successful pedestrian detectors which utilize it in different forms. Wojek and Shiele [12] showed how a combination of Haar-like feature, shapelets, shape context and HOG feature outperforms any individual feature. Walk et al. [13] extended this framework by additionally combining local color self-similarity and the motion feature. Likewise, Wu and Nevatia [14] automatically combined HOG, edgelet and covariance features. Wang et al. [15] combined a texture descriptor based on local binary patterns LBP [16] with HOG. Additionally, a linear SVM classifier was modified to perform basic occlusion reasoning. In addition to HOG and LBP, Hussain et al. [17] used local ternary patterns to combine with HOG. In [18], Ott et al. added color information and implicit segmentation feature with a performance improvement over pure HOG. Felzenszwalb et al. [7, 9] proposed a discriminative trained, multi-scale and deformable part model by utilizing HOG as the descriptor of each deformable part of interested objects. As reported in those previous works, they have achieved better detection performance by combine HOG feature with other complementary cues such as motion and texture. What is more, in all the detectors mentioned above, the authors adopt the default parameter setting of HOG given by Dalal et al. in [3, 11]. The capability of the pure HOG feature for pedestrian detection is rarely further explored.

2 HOG Parameter Tuning

2.1 Aspect and Size of Detection Window

The pedestrians in real world can be captured from any viewpoints, at any distance and in any pose. Therefore, the pedestrians are with different aspects, as shown in Fig. 2. Thus, the aspect ratio and size of the detection window should be carefully chosen to achieve better detection performance.

Essentially, the HOG feature is isotropic while using square cell and block. This means that the ideal HOG feature with detection window D should capture the appearance variations of pedestrians in horizontal and vertical directions equally. Based on this assumption, we can have the following inferences.

Denote the size of the detection window D as $bb_0 = (w_0, h_0)$. Its aspect ratio is defined as $r_0 = w_0/h_0$. To roughly align different pedestrians in D, for a given one bounded by a rectangle of size $bb_i = (w_i, h_i)$, we adopt the following aspect preserving rescaling scheme:

$$\begin{aligned} bb_i^{'} &= \left(w_i^{'}, h_i^{'}\right) \\ &= (w_i f_i, h_i f_i), \end{aligned} \tag{1}$$

Fig. 2 The pedestrians with different aspects. See text for details

where $f_i = \min(w_0/w_i, h_0/h_i)$, as shown in Fig. 3. That is

- When $r_0 \geq r_i$, as shown in Fig. 3a, we have $f_i = h_0/h_i$. Consequently, we have $w_i^{'} = w_i f_i \leq w_0$ and $h_i^{'} = h_0$. The rescaled bounding box is shorter in the horizontal direction by a difference

$$\begin{aligned} \Delta w_i^{'} &= w_0 - w_i f_i = w_0 - w_i \cdot h_0/h_i \\ &= w_0 - h_0 \cdot w_i/h_i = w_0 - h_0 \cdot r_i \\ &= h_0 \cdot r_0 - h_0 \cdot r_i \\ &= h_0 \cdot (r_0 - r_i). \end{aligned} \tag{2}$$

- Similarly, as shown in Fig. 3b, when $r_0 < r_i$, we have $f_i = w_0/w_i$. The rescaled bounding box is shorter in the vertical direction by a difference

(a) **(b)**

Fig. 3 The aspect preserving rescaling scheme. See text for details. **a** $r_0 \geq r_i$. **b** $r_0 < r_i$

$$\begin{aligned}\Delta h_i^{'} &= h_0 - h_i f_i = h_0 - h_i \cdot w_0/w_i \\ &= w_0 \cdot (h_0/w_0) - w_0 \cdot (h_i/w_i) \\ &= w_0/r_0 - w_0/r_i \\ &= w_0 \cdot (1/r_0 - 1/r_i).\end{aligned} \tag{3}$$

Denote the maximum and the minimum of the aspect ratios of bounding boxes in a given training data set as $r_{\max}$ and $r_{\min}$, respectively. According to the isotropy property of the HOG feature, if constraining differences in the horizontal and vertical directions be equal, we have

$$h_0 \cdot (r_0 - r_i) = w_0 \cdot (1/r_0 - 1/r_i). \tag{4}$$

From the Eq. (4), we can easily obtain

$$r_0 = \frac{r_{\min} + 1}{r_{\max} + 1} \cdot r_{\max}. \tag{5}$$

Furthermore, if constraining the horizontal and vertical differences be equal to $2k$ times of the side length of a cell, we can have

$$\begin{aligned}h_0 &= \frac{2k}{r_0 - r_{\min}} \cdot csl, \\ w_0 &= \frac{2k}{1/r_0 - 1/r_{\max}} \cdot csl,\end{aligned} \tag{6}$$

in which k is a scalar which determines the size of the ideal detection window.

In practical, we use the discretized version of Eq. (6), which can be rewritten as

$$\begin{aligned}h_0 &= \mathbf{round}\left(\frac{2k}{r_0 - r_{\min}}\right) \cdot csl, \\ w_0 &= \mathbf{round}\left(\frac{2k}{1/r_0 - 1/r_{\max}}\right) \cdot csl,\end{aligned} \tag{7}$$

2.2 Padding as Context

In [11], it was shown to be beneficial to add some padding as context around the pedestrians. However, for large pedestrians, there is sufficient local image evidence to en-code the pedestrians. On the contrary, for small pedestrians, local image evidence may be uninformative due to motion blur, CCD noise, etc. Therefore, the scene context can be helpful to improve the detection performance.

This suggests us that context information itself should be used in a *scale-variant* manner [10].

On the other hand, the padding around the pedestrian is actually background noise. It will hurt the discriminative power of the HOG descriptor if we add too much background as padding for small pedestrians. Besides, it is inevitable to increase the length of the pedestrian descriptor by adding padding to the pedestrians, which will make the computation burden much heavier in the training and testing procedure. Therefore, we have to search for the best trade-off between the discriminative power and the computation burden experimentally.

3 Pedestrian Detector Training

Now we consider the problem of training pedestrian detector from images with bounding boxes around the pedestrians. This is the type of data available in the pedestrian detection datasets, i.e. INRIA Person [3], TUD-MotionPairs (the training set of TUD-Brussels) [5] and Caltech Pedestrians [4].

We describe a procedure for automatically collecting the training examples and learning the parameters of the pedestrian detector. Training examples are obtained from the feature pyramid for each positive training image automatically, as shown in Sect. 3.1. We adopt a latent SVM model to optimize the pedestrian detector iteratively in Sect. 3.2, using the automatically collected training examples.

3.1 Automatic Collection of Training Samples

The training examples are given by positive bounding boxes P and a set of background images N. P is a set of pairs (I, B), where I is an image and B is a bounding box for a pedestrian in I, as shown in Fig. 4. Different from [3] and [11], we collect the training examples automatically from the feature pyramid for each training image.

Given a training image I, we first construct a multi-scale image pyramid with λ layers in an octave. The image in the i-th layer is generated by rescaling I by a factor $r = 2^{-i/r}$ using bilinear interpolation. The feature pyramid is constructed by computing HOG map from each layer of the multi-scale image pyramid.

For each pair $(I, B) \in P$ in a feature pyramid, we define the filter f at location (i, j, l) as a positive sample x if the detection window D overlaps with rescaled bounding box B at least α percent. Thus, there are usually many detection windows

Fig. 4 All feasible positive training samples for a pedestrian. **a** The annotated pedestrian; **b** The feasible detection windows for the annotated pedestrian in feature pyramid. The *green rectangle* is the ground truth bounding box of the pedestrian, and the *red rectangles* are the detection windows

at different locations, including at different scales that satisfy the definition above, as shown in Fig. 4. By treating the location of the detection window as a latent variable, we can define set $Z(x)$ as all of the possible positive examples x for a pair $(I, B) \in P$.

Now consider a background image $I \in N$. Since there is no pedestrian in any location, we can define a negative sample for each location (i, j, l) in a feature pyramid. Note that there are a very large number of negative examples obtained from each background image. This is consistent with the requirement that a pedestrian detector should have a low false positive rate.

Through the procedure described above, we obtain the training samples $Z(x), y$, $y = \pm 1$. In practice, we construct the feature pyramid by setting $\lambda_p = 15$ and $\lambda_n = 15$ for the positive training images and background images respectively. The overlapping rate $\alpha = 70$.

3.2 Detector Parameter Learning

The algorithm of detector parameter learning is outlined in Algorithm 1. The training procedure is based on the latent SVM model [9]. The outermost loop implements the whole pedestrian detector training procedure. Line 3–9 implements the positive optimization step. Line 10 implements the detector initialization step. Line 11–17 implements the hard negative mining step.

Algorithm 1 *Algorithm of Detector Parameter Learning*

Input:
Positive examples $P = (Z(x_1), B_1), \ldots, (Z(x_n), B_n)$;
Negative images N
Output:
Pedestrian detector w
Initialize pedestrian detector $w = \phi$;
for opt_i:=1 to opt_max **do**
  $F_p = \phi$;
  for i:=1 to n **do**
    Add $PositiveOptimization(w, Z(x_i))$ to F_p;
  end for
  if F_p converges **then**
    break;
  end if
  w:=$TrainInitialDetector(F_p, N)$;
  for $mine\_i$:=1 to $mine\_max$ **do**
    F_n:=$HardNegativeMining(w, N)$;
    if $|F_n| < t$ **then**
      break;
    end if
    w:=$UpdateDetector(F_p, F_n)$;
  end for
end for

In function *PositiveOptimization*, we optimize the positive samples over $Z(x_i)$ by selecting the highest scoring latent value w.r.t. the trained model w. If the model w is empty, we heuristically select the positive example x_i in $Z(x_i)$ that the detection window of is best aligned with the bounding box B.

In function *TrainInitialDetector*, we train an initial pedestrian detector w with *SVMLight* [19]. The training dataset is consisted of the optimized positive examples F_p and a set of negative samples which are down sampled randomly from the feature pyramids of N.

In analogy to [9], we define hard and easy negative instances of the negative training examples from the feature pyramids of N relative to a trained detector w as follows.

$$\begin{aligned} H(w,N) &= \{x \in N | f_w(x) \leq -1\}, \\ E(w,N) &= \{x \in N | f_w(x) < -1\}, \end{aligned} \tag{8}$$

in which $f_w(x)$ is the SVM classification score of example x w.r.t. to the model w. $H(w,N)$ is the set of hard negative examples from that are incorrectly classified or inside the margin of the classifier defined by w. $E(w,N)$ is the set of negative examples from N that are correctly classified and outside the margin. In function *HardNegativeMining*, we find the negative examples in $H(w,N)$ and add them to F_n.

In function *UpdateDetector*, we update w by training a new pedestrian detector, using the optimized positive examples and the found hard negative examples in F_n. In practical, if the hard negative examples exceed memory limits, we select the hard negative examples from with lower classification score until we reach a memory limit; otherwise, we use all hard negative examples in F_n.

4 Experiments

For evaluation, we mainly focus on two dataset, TUD-Brussels dataset [5] and Caltech Pedestrians dataset [4], which are arguably the most realistic and most challenging available datasets, Caltech Pedestrians also being by far the largest. We also show results on the popular INRIA Person dataset [3].

For full image detection, we use a sliding window over multiple scales, with a step size of one cell length and a scale step of $2^{1/15}$. To detect pedestrians smaller than the detection window, we upscale the input images. We use mean shift NMS (Non-maximal suppression) [11] to suppress multiple nearby detections. We use the full image evaluation protocol provided in [6] to evaluate detection performance and compare with other detectors.

4.1 Evaluation Setup

For evaluation on TUD-Brussels and Caltech Pedestrians, we use the pedestrian detector trained on TUD-MotionPairs [5]. As for the INRIA Person database, we use the corresponding training set.

The maximum and the minimum aspects on TUD-MotionParis are 0.23 and 0.62 respectively, while the ones on INRIA Person are 0.17 and 0.77. According to Eq. (5), we can get the "optimal" aspect ratios for TUD-Motion-Pairs and INRIA Person, 0.51 and 0.47 respectively. Note that the "optimal" aspect for INRIA Person is quite different with the one that used in [11].

Similarly, we can determine the "optimal" size of the detection window according to Eq. (7). Considering that most pedestrians in Caltech Pedestrians and TUD-Brussels testing set are below 80 pixels, the detect window should not be large. On the other hand, to keep the invariance of the HOG feature, the side length of cell should not be too small. Experimentally, we set the cell side length to be 6 pixels, and the detection window of size 102×48 for training on TUD-MotionPairs.

We verify the effectiveness of HOG parameter tuning in Sect. 4.2. In addition, we found that the performance of the algorithms based pure HOG feature is not very sensitive to the change testing data size. Thus, to accelerate the verifications below, we use a down sampling rate 3 on TUD-Brussels.

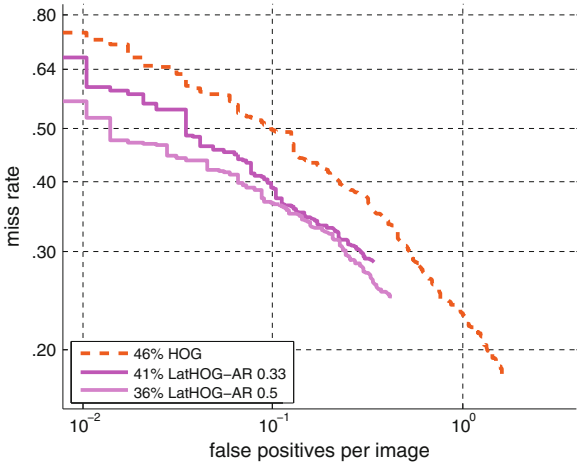

Fig. 5 INRIA Person, impact of aspect ratio. See text for details

4.2 Parameter Verification

Aspect ratio. We use INRIA Person dataset to verify the inference on "optimal" aspect ratio of the detection window in Sect. 2.1. To avoid the influence of other factor, we use the same HOG parameters except the aspect ratio. According to Eq. (5), the "optimal" aspect is 0.5 on INRIA Person dataset. In [11], Dalal et. al. use an aspect 0.33, which is the log-mean aspect ratio on INRIA Person. As shown in Fig. 5, we achieve 64 % detection rate at 0.1 fppi with aspect ratio 0.5, outperforming the one with aspect ratio 0.33 by 5 %.

Padding as context. As can be seen in Fig. 6, the padding does not always bring performance improvement. We push the miss rate from 80 to 73 % on TUD-Brussels by adding padding to the pedestrians (shown in Fig. 6a). As shown in Fig. 6b, the detector without padding outperforms the one with padding by 6 % for the big pedestrian (height over 80 pixels). However, on the contrary, the detector with padding surpasses the one without padding by 2 % for small pedestrians (height below 80 pixels), as shown in Fig. 6c.

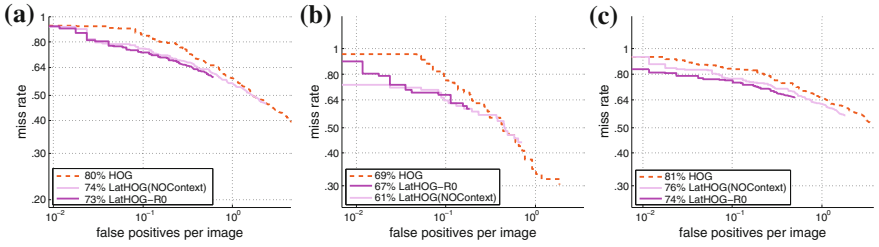

Fig. 6 TUD-Brussels, padding as context. See the text for details. **a** TUD overall. **b** TUD large. **c** TUD small

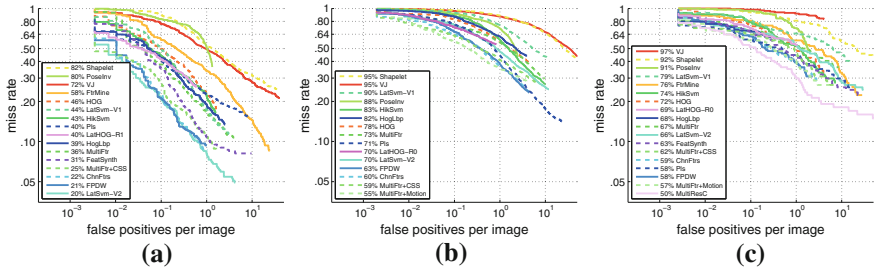

Fig. 7 Full Image Results, see text for details. **a** On INRIA Person. **b** On TUD-Brussels. **c** On Caltech Pedestrian

This phenomenon is consistent with the inferences we drew in Sect. 2.2: It can brings notable benefit for the small pedestrian detection by adding padding as contextual information. For big pedestrians, there is sufficient local image evidence to encode. Therefore, it is not necessary to add padding as context for large pedestrian detection.

4.3 Performance Evaluation

For all subsequent experiments on TUD-Brussels and Caltech Pedestrians, we use the optimally tuned HOG parameters. As for INRIA Person dataset, we remove the padding from pedestrians to maximize performance. The resulting pedestrian detector outperforms the original HOG detector notably. We refer to the resulting method as LatHOG-R0.

INRIA Person. The per-image results of our method LatHOG-R0, along with the results of the other 15 algorithms are shown in Fig. 7. LatHOG-R0 achieve about 83 % detect rate at 1 fppi, and outperforms the original HOG detector by 10 % at 0.1 fppi. Quite surprisingly, the detection performance of our proposed pedestrian detector even notably outperforms many previous works using multiple features in combination. This is due to the fact that the pedestrians in INRIA Person are most over 100 pixels in height, which make pure HOG feature encode pedestrians pretty well.

TUD-Brussels. Fig. 7 shows that performance on TUD-Brussels dataset. Using the pure HOG based pedestrian detector trained with the optimally tuned parameter, our detector LatHOG-R0 outperforms the original HOG detector by 8% at 0.1 fppi. Note that most of the pedestrians in TUD-Brussels are below 100 pixels in height, we add padding around the pedestrians. It improves the detection performance apparently, as shown in Fig. 6.

Caltech Pedestrians. Fig. 7 shows the performance on the "reasonable" subset of Caltech Pedestrians, which is the most popular portion of the data. It consists of pedestrians of over 50 pixels in height, which are fully visible or less than 35 %

Fig. 8 Sample detections on the three pedestrian datasets, see text for details. **a** INRIA Person. **b** TUD-Brussels. **c** Caltech Pedestrian

occluded. By using the pedestrian detector trained on TUD-MotionParis, our detector LatHOG-R0 outperforms the original HOG detector notably: 5 % at 0.01 fppi, 4.3 % at 0.1 fppi on the subset sampled from the Caltech Pedestrians testing data set. We notice that the training set for TUD-Brussels and Caltech Pedestrians are quite different: most of the pedestrians in TUD-MotionPairs are over 100 pixels in height, while most of the pedestrians in the training set of Caltech Pedestrians are under 80 pixels in height. Therefore, the detection performance will be further improved if we train pedestrian detector on the training dataset of Caltech Pedestrians for full image detection on Caltech Pedestrians.

Some sample detections on the three pedestrian datasets are shown in Fig. 8. The top row shows the images without any false positive or false negative. As we can see, the "good" detections are most fired for the pedestrians with fine and clear contours of head and shoulders, even for the pedestrians with apparent occlusion. The bottom row shows the images with typical false positive or false negative detections. As can be seen, the pedestrians with blur contours, dramatic appearance changes and partial occlusions are opt to be missed, which is a common drawback of the global descriptor based detector. Another interesting finding is that many false positives are occurred at the location with round or arch contours, which is quite similar to the contours of human head or shoulder.

5 Conclusion

Our paper improves the performance of pure HOG feature based pedestrian detector mainly by quantitatively investigating the interplay of the HOG parameters: cell size, aspect ratio and size of the detection window. The experiments results in Sect. 4.2 verified the inference we drew. Concerning pedestrian detector training, we describe a procedure for automatically collecting the training examples and learning the parameters of the pedestrian detector using a latent SVM model. By using the optimized HOG feature, our detector outperforms the original HOG detector on the challenging pedestrian datasets, TUD-Brussels and Caltech Pedestrians notably.

In future work, we plan to explore ways of combining the pure HOG feature with other additional features, such as the multiple types of low-level features [5, 20, 21]. On a more conceptual level, we will look into ways of handling significant partial occlusion which is a weakness of our current detector (as indeed of all global detectors we are aware of). Another important direction is to detect pedestrians over large scale range, especially the small pedestrians which are important in safely auto-navigating and many other applications.

Acknowledgments This work was supported by the National Science Foundation of China (NSFC) under grant number 60902091.

References

1. Gavrila DM, Munder S (2007) Multi-cue pedestrian detection and tracking from a moving vehicle. Int J Comput Vision 73(1):41–59
2. Enzweiler M, Eigenstetter A, Schiele B, Gavrila D (2010) Multi-cue pedestrian classification with partial occlusion handling. In: Computer vision and pattern recognition (CVPR), 2010 IEEE Conference on, June 2010, pp 990–997
3. Dalal N, Triggs B (2005) Histograms of oriented gradients for human detection. In: Computer vision and pattern recognition, 2005. CVPR 2005. IEEE computer society conference on, vol 1. June 2005, pp 886–893
4. Dollar P, Wojek C, Schiele B, Perona P (2009) Pedestrian detection: a benchmark. In: Computer vision and pattern recognition, 2009. CVPR 2009. IEEE Conference on, June 2009, pp 304–311
5. Wojek C, Walk S, Schiele B (2009) Multi-cue onboard pedestrian detection. In: Computer vision and pattern recognition, 2009. CVPR 2009. IEEE conference on, June 2009, pp 794–801
6. Dollár P, Wojek C, Schiele B, Perona P (2011) Pedestrian detection: an evaluation of the state of the art. PAMI 99(PrePrints)
7. Felzenszwalb PF, McAllester DA, Ramanan D (2008) A discriminatively trained, multiscale, deformable part model. In: 2008 IEEE computer society conference on computer vision and pattern recognition (CVPR 2008), Anchorage, Alaska, USA, IEEE Computer Society (2008), 24–26 June 2008
8. Andriluka M, Roth S, Schiele B (2009) Pictorial structures revisited: people detection and articulated pose estimation. In: (2009) IEEE computer society conference on computer vision and pattern recognition (CVPR 2009), Miami, Florida, USA, IEEE 2009, 20–25 June 2009, pp 1014–1021
9. Felzenszwalb PF, Girshick RB, McAllester DA, Ramanan D (2010) Object detection with discriminatively trained part-based models. IEEE Trans Pattern Anal Mach Intell 32(9):1627–1645
10. Park D, Ramanan D, Fowlkes C (2010) Multiresolution models for object detection. In: Proceedings of the 11th European conference on computer vision: Part IV. ECCV'10, Berlin, pp 241–254
11. Dalal N (2006) Finding people in images and videos. PhD thesis, Institut National Polytechnique de Grenoble, July 2006
12. Wojek C, Schiele B (2008) A performance evaluation of single and multi-feature people detection. In: Proceedings of the 30th DAGM symposium on pattern recognition, Berlin, pp 82–91

13. Walk S, Majer N, Schindler K, Schiele B (2010) New features and insights for pedestrian detection. In: Computer vision and pattern recognition (CVPR), 2010 IEEE conference on, June 2010, pp 1030–1037
14. Wu B, Nevatia R (2008) Optimizing discrimination-efficiency tradeoff in integrating heterogeneous local features for object detection. In: Computer vision and pattern recognition, 2008. CVPR 2008. IEEE conference on, June 2008, pp 1–8
15. Wang X, Han TX, Yan S (2009) An hog-lbp human detector with partial occlusion handling. In: ICCV (2009) pp 32–39
16. Ojala T, Pietikainen M, Maenpaa T (2002) Multiresolution gray-scale and rotation invariant texture classification with local binary patterns. IEEE Trans Pattern Anal Mach Intell 24(7):971–987
17. Hussain SU, Triggs B (September 2010) Feature sets and dimensionality reduction for visual object detection. In: Conference British Machine Vision (ed) BMVC 2010, August, 2010. BMVA Press, Aberystwyth, Royaume-Uni, pp 1–10
18. Ott P, Everingham M (2009) Implicit color segmentation features for pedestrian and object detection. In: Computer vision, 2009 IEEE 12th international conference on, 29 Sept–2 Oct 2009, pp 723–730
19. Joachims T (1999) Advances in kernel methods. MIT Press, Cambridge, MA, USA, pp 169–184
20. Dollár P, Tu Z, Perona P, Belongie S (2009) Integral channel features. In: BMVC
21. Schwartz WR, Kembhavi A, Harwood D, Davis LS (2009) Human detection using partial least squares analysis. In: Computer vision, 2009 IEEE 12th international conference on, 29 Sept–2 Oct 2009, pp 24–31

A Reconfigurable Array Synthesis Method Using the Correlation Weightings of Smooth Local Trigonometric Base

Sheng Hong, Bo Zhang and Hongqi Yang

Abstract This paper introduces a reconfigurable array synthesis method using the correlation weightings of Smooth Local Trigonometric Base (SLTB) for line antenna array and investigates its beam pattern characteristics. The beam pattern can be reconfigured by adjusting the overlapping coefficiency r of the bell-shaped function, the number K and the frequency spacing Δf of the SLTB. A fast and convenient reconfigurable array synthesis algorithm is proposed according to the evolvement rule of the beam pattern. The proposed method provides a nearly optimum first sidelobe level and gradually decaying sidelobes compared with Chebyshev weighting. Moreover, its computational complexity is $O(N \bullet K^2)$ while the one of Chebyshev is $O(N^3)$.

Keywords Smooth local trigonometric · Reconfiguration · Array synthesis · Smoothness

1 Introduction

The traditional classical array synthesis method comprises of spectral weightings, array polynomials method, pattern sampling processing, minimum beamwidth for specified sidelobe level, least squares error pattern synthesis, minimax design, null steering, adaptive beamforming, etc. [1, 2]. Spectral weightings method is a simple and effective method which uses samples of different spectral windows to assign the weightings for array elements. Many spectral window functions are used

S. Hong · H. Yang
Science & Technology Laboratory on Reliability & Environmental Engineering, School of Reliability and System Engineering, Beijing, China

B. Zhang (✉)
School of Electronics and Information Engineering, Beihang University, Beijing, China
e-mail: bozhang@buaa.edu.cn

F. Sun et al. (eds.), *Foundations and Practical Applications of Cognitive Systems and Information Processing*, Advances in Intelligent Systems and Computing 215,
DOI: 10.1007/978-3-642-37835-5_51,

frequently in the weighting, including Cosine-m window, Hann window, Hamming window, Blackman-Harris window, Chebyshev window, Kaiser window, and so on [1]. The bell-shaped window function [3, 4], is an infinitely continuous differentiable function with characteristics of smoothness and compact support merit, which is formed by a combination of smooth rising cutoff window function and uniform window function. Smooth Local Trigonometric Base (SLTB) consists of the trigonometric function multiplied by the bell-shaped window function [5]. Owing to the SLTB's spectrum convergence, it is widely used in many fields, like wavelets methods [6, 7], image processing [8], speech signal compression and processing [9–12], electromagnetic scattering modeling [3]. Qing Chang, etc. [5], use SLTB in OFDM transceiver which has a much more rapid attenuation outside the spectral bandwidth. It is known that the array's weighting and its frequency-wavenumber response are Discrete Fourier Transform (DFT) pair [1]. The result in [5] demonstrates that the spectrum convergence of the LTT-OFDM symbol using SLTB is better than the DFT-OFDM symbol with raised cosine window. It attracts the reader to explore the beam pattern using SLTB as array's weighting by transferring the frequency spectrum convergence to beam pattern convergence. However, there is no paper to adopt the SLTB weighting to form directional beam in antenna array and no data to investigate the effect of SLTB weighting.

We propose a novel array synthesis method using the correlation of SLTB as weightings and investigate the beam pattern characteristics by adjusting the overlapping coefficiency r of the bell-shaped function, the number K and the frequency spacing Δf of the SLTB. Since the bell-shaped window function has the ability to preserve the spectrum convergence [5], the radiation beam pattern using SLTB also owns good beam pattern convergence, which can be reconfigured by adjusting the parameter r, K and Δf.

This paper is organized as following sections. In Sect. 2, SLTB is introduced to demonstrate its definition, construction method, and mathematics characteristics. Then, the array synthesis method using the correlation weightings of SLTB in Sect. 3 is introduced. In Sect. 4, the reconfigurable array synthesis is quantitatively evaluated by adjusting the overlapping coefficiency r of the bell-shaped function, the number K and the frequency spacing Δf of the SLTB. And a fast and convenient reconfigurable array synthesis algorithm is proposed according to the evolvement rule of the beam pattern. Finally, the conclusion is showed in the Sect. 5.

2 The Model of the Smooth Local Trigonometric Base

Bell-shaped window function is a smooth and compactly supported window function [5]. The smoothness of the bell-shaped window improves the convergence of the Fourier coefficients in the spectral domain without creating any discontinuities at the endpoints of the sampled signal [3].

The rising smooth cutoff window function is introduced in [3] as following,

$$f_{\sin}(t) = \begin{cases} 0, & t \le -1 \\ \sin\left[\frac{\pi}{4}(1+t)\right], & -1 < t < 1 \\ 1, & t \ge 1. \end{cases} \tag{1}$$

By repeatedly replacing t with $\sin(\pi t/2)$ in (1), we can obtain arbitrary d-times continuously differentiable function. All the differentiable functions form the derivation function sets of (1). And they are expressed in (2),

$$f^{(0)}(t) = f_{\sin}(t), \;\; f^{(k+1)}(t) = f^{(k)}\left(\sin\left(\frac{\pi}{2}t\right)\right) \tag{2}$$

The smooth bell-shaped window function is defined by

$$b_j(t) = f_j\left(\frac{t-\alpha_j}{\varepsilon_j}\right) f_{j+1}\left(\frac{\alpha_{j+1}-t}{\varepsilon_{j+1}}\right) \tag{3}$$

where the bell-shaped window function is supported on interval $\left[\alpha_j - \varepsilon_j, \alpha_{j+1} + \varepsilon_{j+1}\right]$, α_j is the middle points of left-side rising smooth cutoff function in the horizontal axis, ε_j is the half interval length of left-side rising cutoff function, α_{j+1} is the middle points of right-side rising cutoff function in the horizontal axis and ε_{j+1} is the half interval length of right-side rising cutoff function.

We may also write the bell-shaped window function in another way as

$$b_j(t) = \begin{cases} f_j\left(\frac{t-\alpha_j}{\varepsilon_j}\right), & t \in \left[\alpha_j - \varepsilon_j, \alpha_j + \varepsilon_j\right) \\ 1, & t \in \left[\alpha_j + \varepsilon_j, \alpha_{j+1} - \varepsilon_{j+1}\right) \\ f_{j+1}\left(\frac{\alpha_{j+1}-t}{\varepsilon_{j+1}}\right), & t \in \left[\alpha_{j+1} - \varepsilon_{j+1}, \alpha_{j+1} + \varepsilon_{j+1}\right) \\ 0, & \text{otherwise.} \end{cases} \tag{4}$$

In this paper, for all examples we use $f_j(t) = f_{j+1}(t) = \sin[(\pi/4)(1 + \sin(\pi/2)t)] = f(t)$. Also, we adopt $\varepsilon_j = \varepsilon_{j+1} = r$, which satisfies $0 \le r \le \left(a_{j+1} - a_j\right)/2$. r is called as the overlapping coefficiency of the bell-shaped function. In Fig. 1, a bell-shaped window function is shown with $a_j = 0$, $a_{j+1} = 1$, and $r = 0.3 \in [0, 0.5]$.

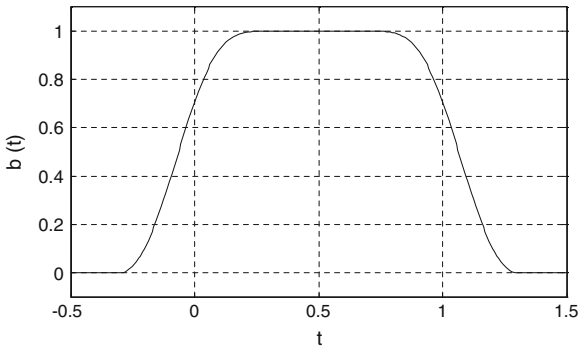

Fig. 1 A bell-shaped window function with $a_j = 0$, $a_{j+1} = 1$ and $r = 0.3$

The SLTB on the interval $I_j = [\alpha_j, \alpha_{j+1}]$ is expressed as [5, 12],

$$\Psi_{j,k}(t) = \sqrt{\frac{2}{|I_j|}} b_j(t) \times \cos\left[\frac{2\pi}{|I_j|} \times \Delta f \times \left(k + \frac{1}{2}\right)(t - \alpha_j)\right] \tag{5}$$

where $\Psi_{j,k}(t)$ is the kth basis function of the jth time interval I_j and Δf is the frequency spacing of SLTB. The sum of a set of SLTBs is

$$s(t) = \sum_{k=1}^{K} \Psi_{j,k}(t) = \sqrt{\frac{2}{|I_j|}} b_j(t) \times \sum_{k=1}^{K} \cos\left[\frac{2\pi}{|I_j|} \times \Delta f \times \left(k + \frac{1}{2}\right)(t - \alpha_j)\right] \tag{6}$$

where K is the number of SLTB in the set of SLTBs. When I_j satisfies $I_j = [0, 1]$, the auto-correlation function of $s(t)$ is expressed as

$$\begin{aligned} R(\tau) &= \int_{-\infty}^{\infty} s(t)s(t+\tau)\mathrm{d}t \\ &= 2\sum_{k1=1}^{K}\sum_{k2=1}^{K} \int_{-\infty}^{\infty} b_j(t)b_j(t+\tau) \times \cos\left[2\pi \times \Delta f \times \left(k1 + \frac{1}{2}\right)t\right] \\ &\quad \times \cos\left[2\pi \times \Delta f \times \left(k2 + \frac{1}{2}\right)(t+\tau)\right]\mathrm{d}t \end{aligned} \tag{7}$$

Furthermore, a SLTB function and a positive auto-correlation function $|R(\tau)|$ of $K = 16$ are shown respectively in Figs. 2 and 3, where the parameters are chosen as $a_j = 0$, $a_{j+1} = 1$, and $r = 0.2$.

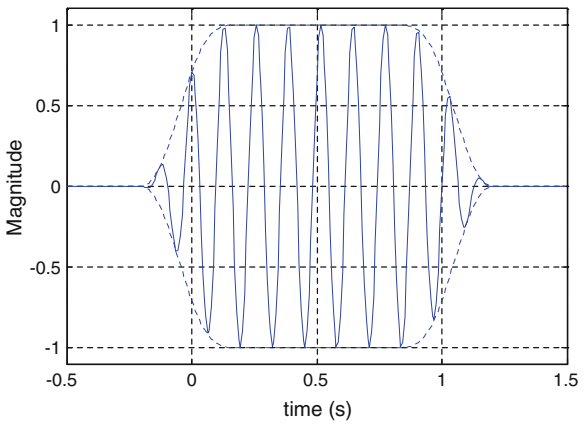

Fig. 2 A smooth local trigonometric base with $a_j = 0$, $a_{j+1} = 1$ and $r = 0.2$

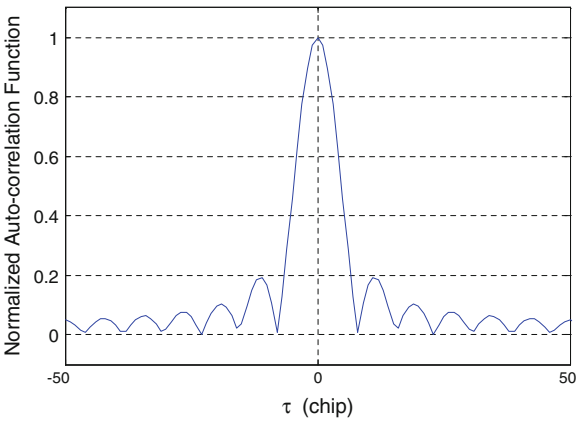

Fig. 3 Auto-correlation function $|R(\tau)|$ with $a_j = 0$, $a_{j+1} = 1$ and $r = 0.2$

3 The Array Synthesis Method Based on the Correlation Weightings of SLTB

The spectral weightings array synthesis method is that each element of the array is multiplied with a weighting to form the desirable beam pattern. Figure 4 demonstrates the spectral weighting array synthesis structure. Without special statement in the following section, the array synthesis method demonstrated in this paper applies to linear antenna array with equally half wavelength spacing. For simplicity and without loss of generality, each antenna element is supposed as an omnidirectional radiation pattern in order to show the effect of the array factor using spectral weighting.

Moreover, the beam pattern for uniform line array with equally spacing can be expressed as [1],

$$B_u(u) = \mathbf{w}^H \mathbf{v}_u(u) = e^{-j\left(\frac{N-1}{2}\right)\frac{2\pi d}{\lambda}u} \sum_{n=0}^{N-1} w^*[n] e^{jn\frac{2\pi d}{\lambda}u}, \tag{8}$$

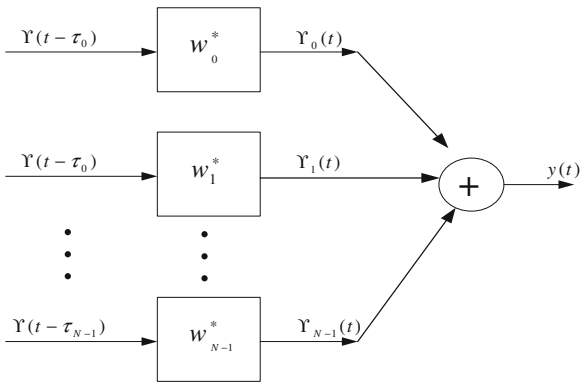

Fig. 4 The spectral weighting array synthesis structure

where $\mathbf{w}$ is the array weighting vector, $\mathbf{v}_u(u)$ is the array manifold vector and $u = \cos\theta,\ -1 \le u \le 1$.

The frequency-wavenumber response $\Upsilon(\omega, k)$ is the Fourier transform of the array weightings $w[n]$ [1]. And the array weightings $w[n]$ can be obtained by the inverse Fourier transform of the frequency-wavenumber response $\Upsilon(\omega, k)$. Hence, spectral weightings method exploits the Fourier transform relationships between the frequency-wave number response function and the weighting function. Furthermore, the beam pattern for an array is the frequency-wave response function evaluated versus the direction [1] as follows,

$$B_u(w:\theta,\phi) = \Upsilon(w,\mathbf{k})\Big|_{k=\frac{2\pi}{\lambda}\mathbf{a}(\theta,\phi)} \tag{9}$$

where $\mathbf{a}(\theta,\phi)$ is a unit vector with spherical coordinate angles θ, ϕ. Thus, there is an indirectly mapping relationship between the weighting function and the beam pattern.

Owing to SLTB's good spectrum convergence [5], it attracts us to form the beam pattern using SLTB when we need compact beam convergence. Because the negative weighting would make the beam pattern divergence, we use the mainlobe samples of SLTB's positive correlation $|R(\tau)|$ of K bases functions as weightings. Hence, the beam pattern can be expressed as

$$\begin{aligned} B_u(u) &= e^{-j\left(\frac{N-1}{2}\right)\frac{2\pi d}{\lambda}u}\sum_{n=0}^{N-1} w^*[n]e^{jn\frac{2\pi d}{\lambda}u} \\ &= e^{-j\left(\frac{N-1}{2}\right)\frac{2\pi d}{\lambda}u}\sum_{n=0}^{N-1} |R[n]|^* e^{jn\frac{2\pi d}{\lambda}u} \\ &= e^{-j\left(\frac{N-1}{2}\right)\frac{2\pi d}{\lambda}u}\sum_{n=0}^{N-1} |R[n]| e^{jn\frac{2\pi d}{\lambda}u} \end{aligned} \tag{10}$$

where $|R[n]|$ is the discrete sample with equal spacing of the mainlobe of $|R(\tau)|$ with K bases functions.

4 Computer Simulation and Analysis

4.1 The Beam Pattern with Regard to SLTBs' Parameters

Computer simulation has been carried out to analyze the array synthesis effect using the correlation weightings of SLTB with regard to parameter K, Δf and r. Without loss of generality, we show the beam pattern using different parameter K, Δf and r for a nine-element line array with equal half wavelength spacing and mainlobe maxima at $\theta = 0°$ in Fig. 5. The proposed array synthesis uses the equally sampled mainlobe values of the SLTBs' correlation function $|R(\tau)|$ as

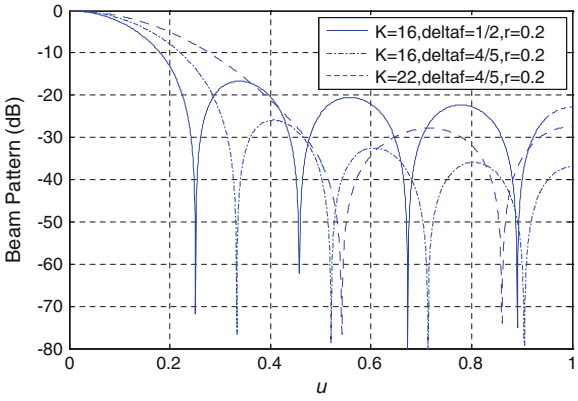

Fig. 5 The proposed beam pattern with different K, Δf and $r = 0.2$

weightings. We can see from Fig. 5 that the mainlobe beamwidth of the beam pattern increases and its sidelobe level decreases in a large range as K and Δf increases. Meantime, the corresponding spectrum bandwidth of the same set of SLTBs also increases in a large range when K and Δf increases, which demonstrates the parallelism mapping relationship between frequency spectrum and beam pattern.

Furthermore, we analyze the quantitative relationship between the shape parameter of the proposed beam pattern and the parameter K and Δf. When $K = 1$, the beamwidth between the first left-side null and the first right-side null, BWNN1, is one-to-one correspondence with Δf, which is also direct proportion to the parameter Δf. Similarly, the beamwidth increment ΔBW between BWNNK of K bases and BWNNK-1 of $K - 1$ bases, is a constant and direct proportion to the parameter Δf. Through the simulation data of BWNNK, BWNN1, and ΔBW, we easily obtain an approximate formula of BWNNK of K bases for a specific Δf with a tiny approach error ε,

$$\mathrm{BWNN}_K(\Delta f) = \mathrm{BWNN}_1(\Delta f) + (K-1) * \Delta\mathrm{BW}(\Delta f) + \varepsilon. \tag{11}$$

In Fig. 6, the mainlobe beamwidth and sidelobes' level of the proposed beam pattern changes as r changes. The mainlobe beamwidth mildly decreases when r changes in a large dynamic range from 0.03 to 0.5. Likely, the sidelobe level slightly changes in the same dynamic range of r. The narrower mainlobe beamwidth can prevent the interference signal from adjacent direction coming into the antenna array and the lower sidelobe level can prevent the strong interference signal coming into the antenna array from the direction of the sidelobe, which are always a pair of mutually exclusive parameters. The slight tradeoff between the mainlobe beamwidth and the sidelobe level can be obtained by changing r, which implies a kind of fine adjusting for beam pattern.

Moreover, we investigate the shape parameter changing tendency of the beam pattern with different r in Fig. 6. As seen from Fig. 6, BWNN_{16} decreases sharply almost 0.17 as r changes from 0.03 to 0.1 while it decreases relatively mildly as

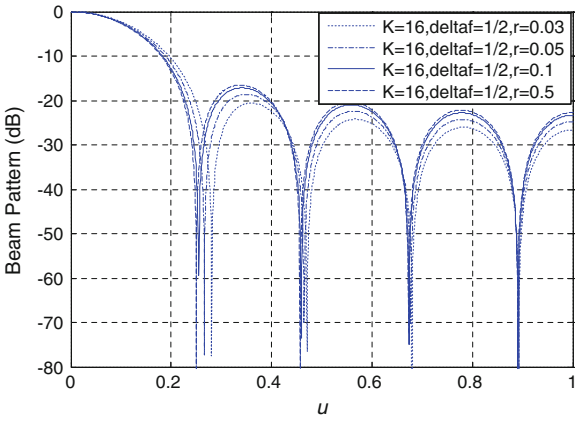

Fig. 6 The proposed beam pattern with different r and $K = 16$, $\Delta f = 0.5$

r changes from 0.1 to 0.5. By contraries, the first sidelobe level increases sharply almost 4 dB as r changes from 0.03 to 0.1 while it increases relatively mildly as $r$changes from 0.1 to 0.5. The change rule of the proposed beam pattern with regard to r provides a complementary means to reduce beamwidth error ε in (11) and approach the desired $\mathrm{BWNN_K}$ by selecting a suitable r.

4.2 The Array Synthesis Algorithm by SLTBs' Parameters

The evolvement rule in Figs. 5 and 6 reveals a kind of reconfigurable array synthesis method. The beam pattern of antenna array can be adjusted by parameter K, Δf and r. The specific reconfiguration algorithm for array synthesis includes four steps as follows,

(1) For an N-element array when N is odd, sample the right half mainlobe of $|R(\tau)|$ with equally spacing and symmetrically map them as the whole N weightings $|R[n]|$. Thus, the beam pattern is

$$B_u(u) = \sum_{n=-\frac{N-1}{2}}^{\frac{N-1}{2}} |R[n]| e^{jn\frac{2\pi d}{\lambda}u} \tag{12}$$

(2) Change K and Δf so that $|R[n]|$ changes to make the BWNN of the beam pattern largely fit the desirable one according to (11) with an approach error ε, which is a *coarse adjusting* procedure.

(3) Change r so that $|R[n]|$ changes to make the beam pattern gradually approach the desirable one to reduce the approach error ε, which is a *fine adjusting* procedure. And $|R[n]|$ is definitely confirmed with the fixed parameter K, Δf and r, according to Eqs. (1)–(7).

(4) The last step is to get the array weighting by the following way,

$$\omega[n] = |R[n]|, \quad n = -\frac{N-1}{2}, \ldots, \frac{N-1}{2}, \quad \text{where } \omega[0] = 1 \tag{13}$$

We evaluate the effect of the proposed array synthesis algorithm compared with frequently used spectral weighting. The line array beam pattern using Chebyshev weighting is showed as a reference. Chebyshev weighting is an optimum array synthesis method in the sense that (a) if the sidelobe level is specified, the beamwidth is minimized; or (b) if the first null is specified, the sidelobe level is minimized [13, 14]. We compare the beam pattern of the correlated SLTB weighting with Chebyshev weighting in Fig. 7. We can see from the figure, when BWNN of the proposed beam pattern is equal to the one using Chebyshev weighting, the first sidelobe level of the correlated SLTB is -23.33 dB with $K = 5$, $\Delta f = 2$ and $r = 0.02$, nearly approaching Chebyshev optimal first sidelobe level -25 dB. The absolute error of the first sidelobe level compared with the optimal sidelobe is about 1.67 dB, and the relative error is 6.7 %. It means the proposed correlated SLTB weighting can provide a nearly optimal sidelobe level. Meantime, the sidelobs of the proposed beam pattern gradually decay as u increases while the ones of Chebyshev weighting are with uniform height. In many applications, we would prefer that the sidelobes decay rather than remain constant. The motivation for decaying sidelobes is to reduce the effect of strong interferers that are located at angles that are significantly different from the mainlobe maxima direction. Besides, the number of operations to compute Chebyshev weighting is of $O(N^3)$ owing to N order inverse matrix [1]. However, the computational complexity of Correlated SLTB is $O(N{\cdot}K^2)$, which is less than Chebyshev weighting when $K < N$ as Δf is evaluated as a big frequency spacing. In the simulation above, the computational complexity of Correlated SLTB is $O(9{\cdot}5^2)$ while the one of Chebyshev is $O(9^3)$.

The proposed reconfiguration array synthesis algorithm fits the mainlobe beamwidth requirements first by changing K and Δf. Then it changes r to make the beam pattern gradually approach the desirable sidelobe level requirements. The reconfiguration feature of the array synthesis using the correlation weightings of SLTB provides a fast and convenient solution to fit the desirable beam pattern.

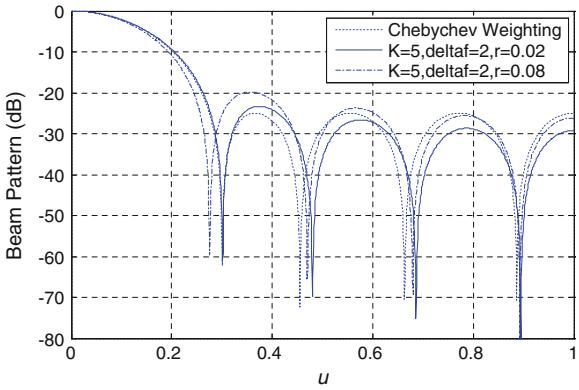

Fig. 7 The comparison between the proposed beam pattern with different r and the one with Hann weighting, $N = 9$

5 Conclusion

This paper proposes a reconfigurable array synthesis method using the correlation weightings of SLTB and investigates its beam pattern characteristics. The beam pattern can be reconfigured by adjusting the overlapping coefficiency r of the bell-shaped function, the number K, and the frequency spacing Δf of the SLTB. The reconfiguration scheme mainly includes two parts, the coarse adjusting procedure to satisfy BWNN requirement with suitable K and Δf and the fine adjusting procedure to reduce the BWNN approach error with suitable r, which forms a fast and convenient array synthesis algorithm. Besides, through the comparison of the cost and complexity of the array synthesis using the correlated SLTB weighting and the optimum Chebyshev weighting, the proposed method provides a nearly optimum beam pattern without significant loss in the first sidelobe level with the same beamwidth as Chebyshev in the beam space. The sidelobs of the proposed beam pattern gradually decay as u increases while Chebyshev has equal height sidelobes. Hence, regardless of the first sidelobe, it owns better capability to suppress interference from the direction of other sidelobes compared with Chebyshev. Moreover, the computational complexity of Correlated SLTB is less than Chebyshev weighting when $K < N$.

Acknowledgments The authors are highly thankful for the financial support of NSFC No. 61171070 and Fundamental Research Funds for the Central Universities under grant No. YWF-11-03-Q-063, China.

References

1. Van Trees H (2002) Optimum array processing. Wiley Online Library, New York, pp 90–159
2. Mudumbai R, Hespanha J, Madhow U, Barriac G (2010) Distributed transmit beamforming using feedback control. IEEE Trans Inf Theor 56:411–426
3. Pan GW, Tretiakov YV, Gilbert B (2003) Smooth local cosine based Galerkin method for scattering problems. IEEE Trans Antennas Propag 51:1177–1184
4. Wickerhauser MV (1994) Adapted wavelet analysis from theory to software. A.K.Peters, Wellesley
5. Chang Q, Yongbo T, Wei QI, Dirong C (2009) A new transceiver for OFDM systems using smooth local trigonometric transforms. IEICE Trans Commun 92:662–665
6. Coifman RR, Meyer Y (1991) "Remarques sur l'analyse de Fourier à fenêtre," Comptes rendus de l'Académie des sciences. Série 1, Mathématique 312:259–261
7. Auscher P, Weiss G, Wickerhauser MV (1991) Local sine and cosine bases of Coifman and Meyer and the construction of smooth wavelets. In: Proceedings of the 1991 in wavelets: a tutorial in theory and applications, pp 237–256
8. Aharoni G, Averbuch A, Coifman R, Israeli M (1993) Local cosine transform—a method for the reduction of the blocking effect in JPEG. J Math Imaging Vis 3:7–38
9. Lienard JS (1987) Speech analysis and reconstruction using short-time, elementary waveforms. In: Proceedings of the 1987 acoustics, speech, and signal processing, IEEE international conference on ICASSP'87, pp 948–951
10. Rodet X (1984) Time-domain formant-wave-function synthesis. Comput Music J 8:9–14

11. Malvar HS (1990) Lapped transforms for efficient transform/subband coding. IEEE Trans Acoust Speech Signal Process 38:969–978
12. Wesfreid E, Wickerhauser MV (1993) Adapted local trigonometric transforms and speech processing. IEEE Trans Signal Process 41:3596–3600
13. Dolph CL (1946) A current distribution for broadside arrays which optimizes the relationship between beam width and side-lobe level. Proc IRE 34:335–348
14. Bevelacqua PJ, Balanis CA (2007) Minimum sidelobe levels for linear arrays. IEEE Trans Antennas Propag 55:3442–3449

A Multi-channel SSVEP-Based Brain–Computer Interface Using a Canonical Correlation Analysis in the Frequency Domain

Guang Chen, Dandan Song and Lejian Liao

Abstract Brain–computer interface (BCI) is a new way for man–machine interaction with wide applications, in which steady-state visual evoked potentials (SSVEP) is a promising option. However, many characteristics of SSVEP show great user variation. So parameter optimization and channel selection for each subject were applied to improve the performance of BCI. These optimizations limit the practical applicability of the SSVEP-based BCI. The use of a canonical correlation analysis (CCA) method for multi-channel SSVEP in the time domain detection showed highly increased detection accuracy, but it is sensitive to the noise when the stimulate frequency is low. In this paper, a method of CCA in the frequency domain is presented for classifying multi-channel SSVEPs. First overlapping average is conducted on the original training signals. Then fast Fourier transform (FFT) is used to transform the signals from time domain to frequency domain to produce the reference data. Finally, according to the correlation coefficients of the new data and the references in the frequency domain, the SSVEP is classified. The experimental results show the enhanced accuracy of our method when applied to low stimulate frequencies.

Keywords BCI · SSVEP · Overlapping average · FFT · CCA in frequency domain

G. Chen · D. Song (✉) · L. Liao
Beijing Engineering Research Center of High Volume Language Information Processing and Cloud Computing Applications, Beijing Lab of Intelligent Information Technology, School of Computer Science, Beijing Institute of Technology, Beijing, China
e-mail: sdd@bit.edu.cn

G. Chen
e-mail: 20082969@smail.bit.edu.cn

L. Liao
e-mail: liaolj@bit.edu.cn

F. Sun et al. (eds.), *Foundations and Practical Applications of Cognitive Systems and Information Processing*, Advances in Intelligent Systems and Computing 215,
DOI: 10.1007/978-3-642-37835-5_52,

1 Introduction

To control an external device, brain–computer interface (BCI) is the most direct way as the communication is conducted directly from a human or animal brain. In BCI research, noninvasive scalp electroencephalogram (EEG) measurements have become a popular option because of its harmless to the users.

Steady-state visual evoked potentials (SSVEP) is one of the most commonly used signals in EEG-based BCI systems [1]. It is a periodic response to a visual stimulus modulated at a frequency higher than 6 Hz [2]. It can be recorded from the surface of the scalp and has the same fundamental frequency as the visual stimulus as well as its harmonics.

In recent years, using SSVEP in BCI systems attracts much more attentions [3–16]. The SSVEP-based BCI system has many advantages, such as a higher SNR ratio and a higher information transfer rate. These advantages of the SSVEP-based BCI make it a promising option in BCI applications.

However, many characteristics of SSVEP, such as the amplitude, distribution, and available frequency range, always have various values for different users [2]. In order to improve the performance of BCI, parameter optimization and channel selection for each subject have been widely used in previous researches [2, 6, 13]. These optimizations constraint the practical applicability of the SSVEP-based BCI.

A multi-channel SSVEP-based BCI may be able to solve this problem. Recently, many methods were proposed for SSVEP stimulus frequency identification from multi-channel EEG signals [13–15]. A particular interest is canonical correlation analysis (CCA). CCA was first applied to SSVEP by Lin et al. [8]. In their study, training data were used to optimize the CCA parameters, and it performs better than the power spectrum density analysis (PSDA) using bipolar channels. However, a time-consuming channel selection procedure was needed in the training stage, and the optimal eight channels are determined for each subject.

Another CCA-based study was carried out by Binet et al. in [13]. Therein, no training data were needed and a fixed set of nine channels over the occipital cortex were used for all subjects. But when applied to signals in which the stimulus frequency is low, it showed to be sensitive to the noise and needs to be improved. A study aimed at further improving the performance of the BCI system in [13] is introduced in [16]. The contribution of [16] is to propose an effective method for estimating the SSVEP response phase based on the apparent latency, which is the time delay due to the conduction through the visual pathway. However, it has a high requirement in the acquisition of the signals, which is not widely satisfied.

In this paper, a method of CCA in the frequency domain for classifying SSVEPs using EEG signals is presented. After overlapping average conducting on the original training signals, fast Fourier transform (FFT) is used to transform the signals from time domain to frequency domain to produce the reference data. According to the correlation coefficients of the new data and the references in the frequency domain, the SSVEP is classified.

The advantage of our method includes: (1) it does not need channel location selection and parameter optimization to extract the frequency information from multi-channel EEG signals in contrast to traditional methods; (2) it is free from the influence of low frequency noise which affects the accuracy of the method analyzed in the time domain [13]. The experimental results validate the effectiveness of our method.

2 BCI System Based on the SSVEP

2.1 The Basic Composition of the Brain–Computer Interface System

Figure 1 shows the basic structure of the BCI system. According to the function of each module, the system can be divided into four parts: Signal acquisition, Signal preprocessing, Frequency identification, and Control command generation. For the generated command, the control signal has a wide application, but is not our research focus.

2.2 Visual Stimuli

In the experiment, the screen has several (K) checkerboards shown in the Fig. 2. And the flipping frequencies of the checkerboards are $f1, f2\ldots$ and f_K ($f1 < f2 < \ldots < f_K$).

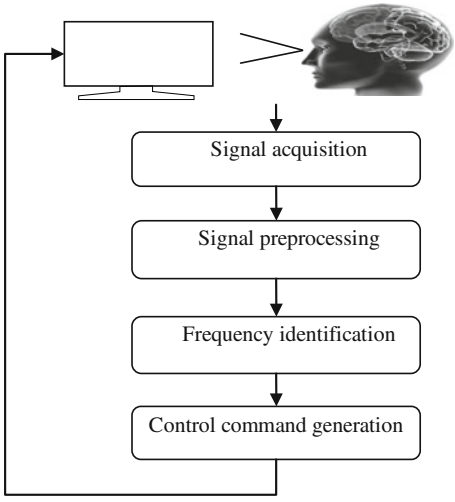

Fig. 1 Basic structure of the SSVEP-based BCI system

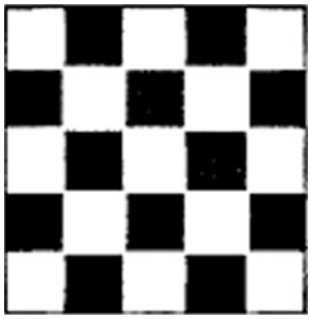

Fig. 2 The checkerboard used in the experiment

Different SSVEPs can be produced by shifting our interest or attention to one of these checkerboards.

3 Method

In our method, overlapping average is first conducted on the original training signals under each flipping frequency. Then FFT is used to transform the signals from time domain to frequency domain, and the reference data are attained. Finally, the new SSVEPs data are classified to be under the same frequency with one of the references, if they have the highest correlation coefficient in the frequency domain.

3.1 Overlapping Average

When the spectrum range of useful signal and noise does not intersect, digital filters could extract signal from noise. In controversy, we must use another way to remove the noise. In our method, overlapping average of multiple training samples is first used to suppress noise.

Figure 3 shows an example of multi-channel EEG signals under frequency of 8 Hz, which is sampled in 2 s with 256 points per second. Each signal corresponds to a channel, and there are 16 channels in the example. The x-coordinate denotes the sampling time points, and y-coordinate denotes the voltage value. It can be found that the waveforms of electrodes are very different, and have lots of spike and random component. Suppose one channel of the single record of EEG signal $s(n)$ contains useful signal and noise:

$$s(n) = s_u(n) + s_n(n), \quad n = 1, 2, \ldots, N, \tag{1}$$

where N is the number of sampling points, $s_u(n)$ is the useful signal, and $s_n(n)$ is the noise. Suppose the noise is random white noise which complies Gaussian

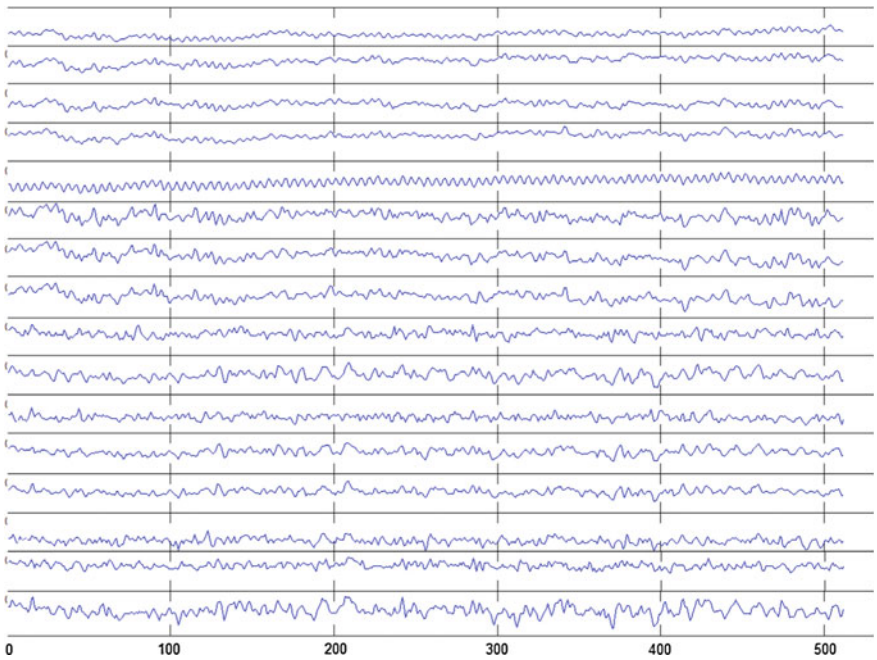

Fig. 3 An example of multi-channel EEG signals

distribution whose mean value is zero and variance is δ^2. Then the signal-to-noise (SNR) ratio of an input signal will be:

$$\mathrm{SNR}_{\mathrm{in}} = S/\delta^2, \tag{2}$$

where S is the power spectrum of the useful signal $s_u(n)$.

Then if there are M training samples $s_1(n), s_2(n), \ldots, s_M(n)$for each channel of a subject, overlapping average is conducted on these training samples:

$$x(n) = \frac{1}{M}\sum_{m=1}^{M} s_m(n), \tag{3}$$

where $x(n)$ denotes one channel of multi-channel EEG signals after M times overlapping, with $n = 1, 2,\ldots,N$.

After the overlapping average, the output will be:

$$x(n) = \overline{s_u(n)} + \frac{1}{\sqrt{M}}\overline{\overline{s_n(n)}} \quad (1 \le k \le m), \tag{4}$$

where M is the overlapping times, specifically set as the number of training samples in our method. $\overline{s_u(n)}$ is the average of useful signals, and $\overline{\overline{s_n(n)}}$ is the effective value of noise.

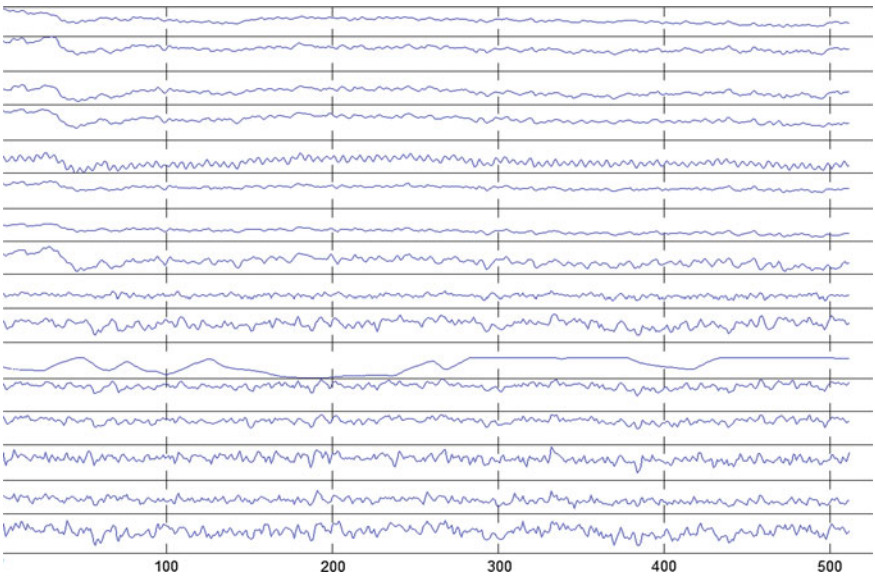

Fig. 4 Signals after M times overlapping average. The *x*-coordinate denotes the time points. The *y*-coordinate denotes the voltage value

Then the SNR ratio of the output signal will be:

$$\mathrm{SNR}_{\mathrm{out}} = \frac{S}{No} = S \Big/ \left(\frac{1}{M}\delta^2\right) = M\frac{S}{\delta^2}. \tag{5}$$

It shows that, after M times overlapping average, the SNR ratio has been improved by M times. Therefore, the SNR ratio of periodic signals or repeatable signals can be improved after several overlapping average. And the more times overlapping average executed, the higher SNR ratio is. So, we can extract extremely weak signal from strong noise with enough overlapping average times.

Taking the signals in Fig. 3 for example, the signals after overlapping average are presented in Fig. 4. Compared to Fig. 3, the waveforms are shown to be more smooth and clearer, with fewer noises. However, there is no universality of the waveforms. In order to find the frequency characteristics of the data, we then transform the signals from time domain to frequency domain.

3.2 FFT

The Discrete Fourier Transform (DFT) is one of the widely used analysis methods in design and implementation of digital signal processing systems. The DFT of a signal can be directly computed by (6) where $x(n)$ is the output signal of the

previous overlapping average step, $X(i)$ denotes the DFT output in the frequency domain, and N is the total number of sampled input points.

$$X(i) = \sum_{n=0}^{N-1} x(n) e^{-j2\pi kn/N}, \quad i = 1, 2, \ldots, N \tag{6}$$

For N points DFT, the number of plural multiplication is the square of the N. Put N point DFT into several short DFT can make the square times reduce greatly and the rotating factor has obvious periodical and symmetry. Therefore, FFT, is currently a widely used efficient way to calculate DFT of a signal, is used in our method.

Denoted $W_N^k = e^{-j\frac{2\pi}{N}k}$, and

$$\begin{aligned} x_1(r) &= x(2r), \qquad r = 0, 1, \ldots, \frac{N}{2} - 1 \\ x_2(r) &= x(2r+1), \quad r = 0, 1, \ldots, \frac{N}{2} - 1. \end{aligned} \tag{7}$$

To simplify the description, we suppose N is $N = 2^d$, where d is a natural number. Then,

$$\begin{aligned} X(k) &= \sum_{n=0,2,\ldots,N-2} x(n) W_N^{kn} + \sum_{n=1,3,\ldots,N-1} x(n) W_N^{kn} \\ &= \sum_{r=0}^{N/2-1} x(2r) W_N^{2kr} + \sum_{r=0}^{N/2-1} x(2r+1) W_N^{k(2r+1)} \\ &= \sum_{r=0}^{N/2-1} x_1(r) W_N^{2kr} + W_N^k \sum_{r=0}^{N/2-1} x_2(r) W_N^{2kr}. \end{aligned} \tag{8}$$

Additionally, because

$$W_N^{2kr} = e^{-j\frac{2\pi}{N}2kr} = e^{-j\frac{2\pi}{\frac{N}{2}}kr} = W_{N/2}^{kr} \tag{9}$$

then,

$$\begin{aligned} X(k) &= \sum_{r=0}^{N/2-1} x_1(r) W_{N/2}^{kr} + W_N^k \sum_{r=0}^{N/2-1} x_2(r) W_{N/2}^{kr} \\ &= X_1(k) + W_N^k X_2(k), \end{aligned} \tag{10}$$

where $X_1(k)$ and $X_2(k)$ are DFT of $x_1(r)$ and $x_2(r)$, respectively.

Then the execution is more efficient. And similarly, $X_1(k)$ and $X_2(k)$ could be deduced. Now the number of plural multiplication is $N \log 2\ N$. When N is very large, FFT can reduce the number of calculation greatly.

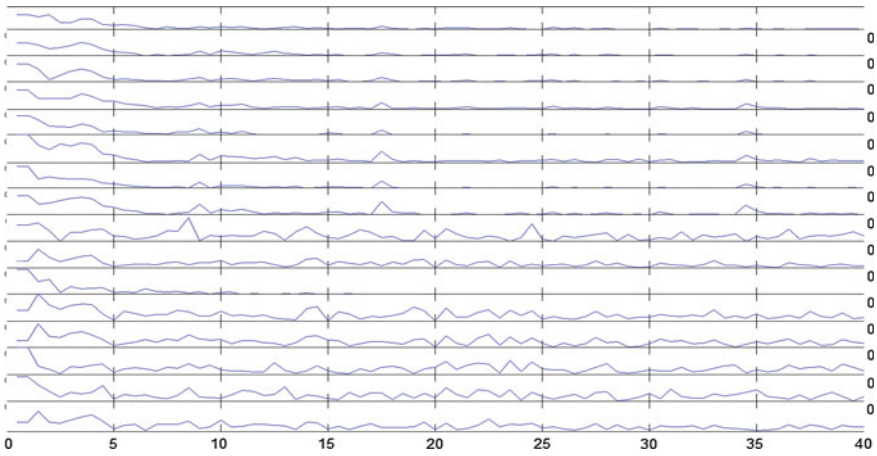

Fig. 5 The reference signals attained with the previous example of 8 Hz after FFT. The *x*-coordinate denotes the frequency, and the y-coordinate denotes the amplitude

Taking the previous signal as the example again, let input be the multichannel EEG signals after overlapping average (shown in Fig. 4), the output signals after FFT in the frequency domain are illustrated in Fig. 5.

As the SSVEP has the same fundamental frequency with the visual stimulus as well as its harmonics, there are commonly spikes of signals at these frequency coordinates.

Signals in Fig. 5 are the reference data corresponding to the previous example under stimulus frequency 8 Hz. The references corresponding to other stimulating frequencies can be obtained in the same way. As the signals of the top 8 channels are shown to be more distinctive, these channels are selected for later signal correlation analysis for all subjects and all frequencies.

3.3 CCA

CCA is a multivariable statistical method used when there are two sets of data, which may have some underlying correlation. It finds a pair of linear combinations for two sets, so that the correlation between the two canonical variables is maximized. CCA extends ordinary correlation to two sets of variables and is widely used in statistical and information mining [14, 15].

Fast Fourier Transform is also applied to transform the new test data under analysis, which is a single record of multichannel EEG signals, from time domain to frequency domain.

Then CCA is applied to calculate the correlation coefficients of test data and the training references in the frequency domain. Only 5–40 Hz of the frequency spectrogram is considered, because the frequencies of SSVEPs concentrate on 5–60 Hz.

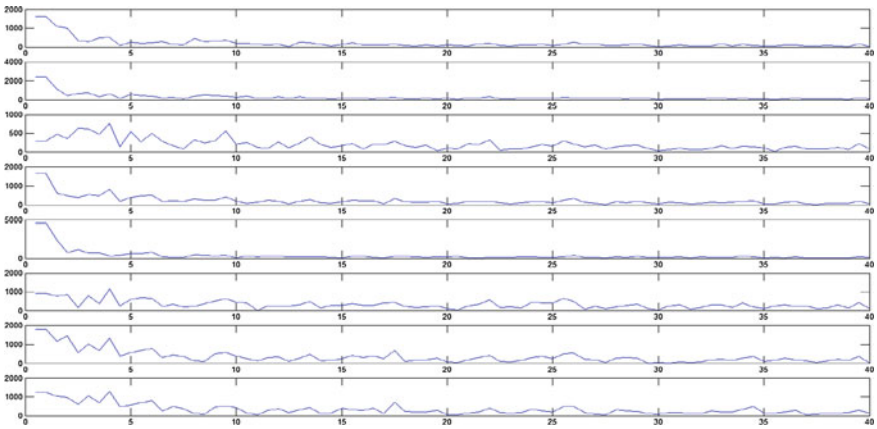

Fig. 6 An example test data transformed in frequency domain of stimulus frequency of 8 Hz

The method of calculating linear correlation coefficient can be divided into three kinds: Pearson correlation coefficient, Spearman correlation coefficient, and Kendall correlation coefficient. In our method, we use Pearson correlation coefficient to measure the related degree between test data and training references. Pearson correlation coefficient is defined as:

$$\rho_{XY} = \frac{N\sum XY - \sum X \sum Y}{\sqrt{\sum X_i^2 - \frac{\left(\sum X_i\right)^2}{N}}\sqrt{\sum Y_i^2 - \frac{\left(\sum Y_i\right)^2}{N}}}, \tag{11}$$

where X and Y are, respectively, the reference signal (shown in Fig. 5) and the test signal (shown in Fig. 6) in our method.

According to the correlation coefficients, the SSVEPs data are classified. Figure 7 shows the Pearson correlation coefficients of four test data. So the figure has four parts, each part shows the correlation coefficient of a single recording with four reference data under relevant potential stimulus frequencies. From the columnar values, it is easy to tell that the stimulate frequency of the test data is 8 Hz.

4 Experiments and Results

In this section, we describe experiments on real world data to demonstrate the effectiveness of our method. Data sets and evaluation method used in our experiments are described first. A comparative experiment is then introduced briefly. Afterward, our experimental results are presented. Finally, comparison between our method and the comparative method is provided, as well as a discussion afterward.

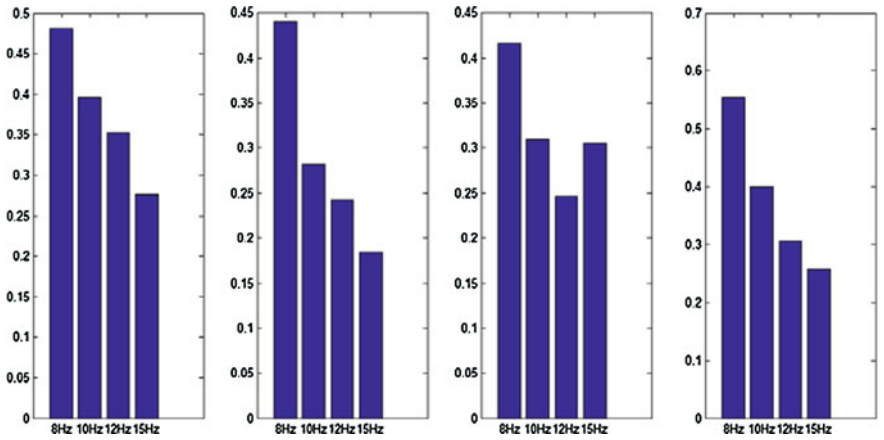

Fig. 7 The correlation coefficient of four test data and the references of four potential stimulus frequencies

4.1 Data Set

In the experiment, the screen has four checkerboards as shown in the Fig. 2. And the flipping frequencies of the checkerboards are 8, 10, 12, and 15 Hz, respectively. Four subjects shift their attentions to the four checkerboards to produce different SSVEPs. The sampling rate was 256 Hz. There is 2 s EEG data for each single record of EEG. Each subject has four training datasets and four test datasets, respectively, correspond to the four stimulus frequencies. Each dataset include several record of multichannel electroencephalography (EEG) signals under the certain stimulate frequency.

4.2 Evaluation Metric

The experimental evaluation metric is the classification accuracy r.

$$r = m_c/m * 100\ \%, \tag{12}$$

where m_c is the number of the test data identified correctly, and m is the number of EEG signal recordings included in a test dataset of the subject.

4.3 Comparative Experiment

A method of CCA in the time domain is recently presented in paper [13] for classifying SSVEPs using multichannel EEG signals. We describe this method as

Table 1 Classification accuracies of CCA in the time domain (CCA_T) in [13]

Classification accuracy	Stimulate frequency			
Subject	8 Hz (%)	10 Hz (%)	12 Hz (%)	15 Hz (%)
S1	25	94.1	97	87.5
S2	25	88.6	97	87.5
S3	10	94.1	97	91.2
S4	25	100	91.7	87.5

CCA_T in short. The method does not need any training data, just reference signals constructed on potential signals. Specifically, the reference signal Y of frequency f can be obtained by using (13).

$$Y(f) = \begin{pmatrix} \sin(2\pi \cdot f \cdot q \cdot T_s) \\ \cos(2\pi \cdot f \cdot q \cdot T_s) \\ \sin(2\pi \cdot 2f \cdot q \cdot T_s) \\ \cos(2\pi \cdot 2f \cdot q \cdot T_s) \\ \cdot \\ \cdot \\ \cdot \\ \sin(2\pi \cdot N_h f \cdot q \cdot T_s) \\ \cos(2\pi \cdot N_h f \cdot q \cdot T_s) \end{pmatrix}, \tag{13}$$

where f is the potential stimulate frequency, N and N_h denote the number of time points, and the number of harmonics being considered, where $q = [1,2,\ldots,N]$ and T_s denotes the time interval between two consecutive sampling points.

The test EEG data using in this comparative method is the same with our method, as introduced in the previous Data Set section. Then the SSVEP is classified according to the correlation coefficient of test data and the references.

By using the comparative CCA classification method in the time domain, the classification results are listed in Table 1. As it is the state-of-art SSVEP classification method, the classification accuracy of this method is relatively high for 10, 12, and 15 Hz signals. However, its classification accuracy is low when the stimulate frequency is 8 Hz. We think one possible reason for this is as the frequency of most noise is low, the noise has a deep infect in the waveforms when the stimulate frequency is low. The method in [16] is not performed because our data used in our experiment is not appropriate.

4.4 Results of our Method: CCA in the Frequency Domain

The classification accuracy of our method—CCA in the frequency domain is given in Table 2. The method is abbreviated as CCA_F for the convenience of description.

Table 2 Classification accuracies of our method—CCA in the frequency domain (CCA_F)

Classification accuracy	Stimulate frequency			
Subject	8 Hz (%)	10 Hz (%)	12 Hz (%)	15 Hz (%)
S1	87.5	88.2	50	100
S2	100	97.7	82.35	100
S3	50	64.7	50	23.5
S4	75	95.8	83.3	95.8

The classification accuracy of our method is low when the stimulate frequency is 12 Hz. There is a very large chance to misjudge 12 Hz signals to 10 Hz. The reason is that in the spectrum charts of 10 and 12 Hz, peaks of their waves are very close.

For the frequency of 15 Hz, the classification accuracy of subject *S*3 is quite low by our method. When we checked the signals, we found their spectrums have peak values in 10 and 12 Hz harmonics, which make the signals misclassified to these frequencies.

The good news is that, for the 8 Hz signals, our method performs really well, especially in contrast to the bad performance of the CCA_T method for 8 Hz signals.

4.5 Methods Comparison

The average classification accuracy for the four subjects by our method (CCA_F) and the comparative method (CCA_T) are illustrated in Fig. 8.

On the average level, as expected, our CCA_F method performs a little worse than the CCA_T method for 10, 12, and 15 Hz, especially for the 12 Hz signals. It shows the disadvantage of our method when distinguishing between close stimulus frequencies.

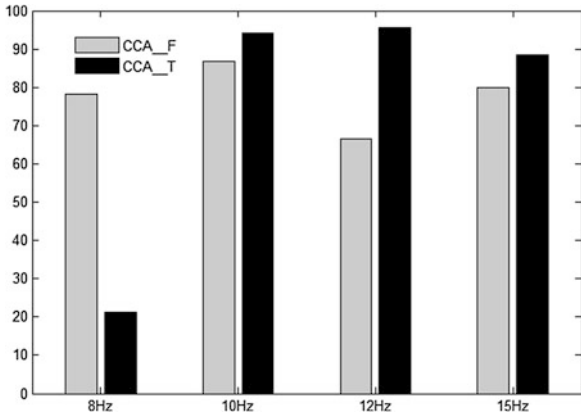

Fig. 8 The average classification accuracy results of the two methods under different stimulus frequency. *x*-coordinate denotes the stimulate frequency. *y*-coordinate denotes the classification accuracy

But our method CCA_F performs greatly better than the CCA_T method when the stimulus frequency is low. This demonstrates the effectiveness of our method distinguishing low frequency signals with similar noises.

5 Conclusion

A multi-channel SSVEP-based BCI by using a CCA in the frequency domain is designed in this paper. First overlapping average is conducted on the original training signals, and then FFT is performed to get the references. After the test data is transformed from time domain to frequency domain, it is classified according to its correlation coefficients to the references.

When applied to real data, our method performs greatly better than the comparative method when the stimulus frequency is low, which demonstrates its effectiveness of distinguishing low frequency signals with similar noises.

In our future work, we will provide a framework with the combination of our method and the comparative one, by utilizing their advantages. And experiments on more subjects will be conducted.

Acknowledgments This work was supported in part by the National Science Foundation (Grant No. 61003168), Beijing Natural Science Foundation (Grant No. 4112050), and Excellent Researcher Award Program and Basic Research Foundation of Beijing Institute of Technology.

References

1. Wolpaw JR, Birbaumer N, McFarland DJ, Pfurtscheller G, Vaughan TM (2002) Brain–computer interfaces for communication and control. Clin Neurophysiol 113:767–791
2. Wang Y, Wang R, Gao X, Gao S (2006) A practical VEP-based brain–computer interface. IEEE Trans Neural Syst Rehabil Eng 14:234–240
3. Middendorf M, McMillan G, Calhoun G, Jones K (2000) Brain–computer interfaces based on the steady-state visual-evoked response. IEEE Trans Rehabil Eng 8:211–214
4. Kelly S, Lalor E, Finucane C, McDarby G, Reilly R (2005) Visual spatial attention control in an independent brain–computer interface. IEEE Trans Biomed Eng 52:1588–1596
5. Müller-Putz G, Scherer R, Brauneis C, Pfurtscheller G (2005) Steady-state visual evoked potential (SSVEP)-based communication: impact of harmonic frequency components. Neural Eng 2:123–130
6. Cheng M, Gao X, Gao S (2005) Design and implementation of a brain–computer interface with high transfer rates. IEEE Trans Biomed Eng 49:1181–1186
7. Friman O, Volosyak I, Graser A (2007) Multiple channel detection of steady-state visual evoked potentials for brain–computer interfaces. IEEE Trans Biomed Eng 54:742–750
8. Sutter EE (1992) The brain response interface: communication through visually-induced electrical brain response. Microcomput Appl 15:31–45
9. Trejo L, Rosipal R, Matthews B (2006) Brain–computer interfaces for 1-D and 2-D cursor control: designs using volitional control of the EEG spectrum or steady-state visual evoked potentials. IEEE Trans Neural Syst Rehabil Eng 14:225–229

10. Kluge T, Hartmann M (2007) Phase coherent detection of steady-state evoked potentials: experimental results and application to brain–computer interfaces. In: Proceedings of the 3rd international IEEE EMBS neural engineering conference, pp 425–429
11. Muller-Putz GR, Pfurtscheller G (2008) Control of an electrical prosthesis with an SSVEP-based BCI. IEEE Trans Biomed Eng 55:361–364
12. Wu Z, Yao D (2008) Frequency detection with stability coefficient for steady-state visual evoked potential (SSVEP)-based BCIs. IEEE J Neural Eng 5:36–43
13. Lin Z, Zhang C, Wu W, Gao X (2008) Frequency recognition based on canonical correlation analysis for SSVEP-based BCIs. IEEE Trans Biomed Eng 53:2610–2614
14. Storch H, Zwiers F (2002) Statistical analysis in climate research. Cambridge University Press, Cambridge
15. Friman O, Cedefamn J, Lundberg P, Borga M, Knutsson H (2001) Detection of neural activity in functional MRI using canonical correlation analysis. Magn Reson Med 45:323–330
16. Pan J, Gao X, Duan F et al (2011) Enhancing the classification accuracy of steady-state visual evoked potential-based brain–computer interfaces using phase constrained canonical correlation analysis. J Neural Eng 8(3): 036–027

Acquiring Brain Signals of Imagining Humanoid Robot Walking Behavior via Cerebot

Wei Li, Yunyi Li, Genshe Chen, Qinghao Meng, Ming Zeng and Fuchun Sun

Abstract Control of humanoid robot behavior with the mind begins a new era of robotics research. One of the critical issues in this research is how to acquire the brain signals with high quality which are correlated to humanoid robot behavior. In order to improve subjects' concentration on their mental activities during tests, we develop a stimuli module in the Cerebot system, consisting of a Cerebus neural data acquisition system and a Kumotek robot with 20 degrees of freedom or a NAO robot with 25 degrees of freedom. We present the experimental procedures for acquiring brain signals of imagining humanoid robot walking behavior by using movies of robot walking or real robot walking activities. We record two groups of brain signals correlated to mental activities of six robot walking behavior. Finally, we present a demonstration of controlling the humanoid robot walking behavior using the phase coding mechanisms of the *Delta* rhythms.

Keywords Mind control · Humanoid robot · Robot walking behavior · Brainwaves · Phase coding

W. Li · Q. Meng · M. Zeng
School of Electrical Engineering and Automation, Institute of Robotics and Autonomous System (IRAS), Tianjin University, Tianjin, China

W. Li (✉)
Department of Computer and Electrical Engineering and Computer Science, California State University, Bakersfield, 9001 Stockdale Hwy, Bakersfield, CA 93311-1022, USA
e-mail: wli@cs.csubak.edu

Y. Li
Department of Psychology and Neuroscience, Duke University, 417 Chapel Drive, Durham, NC 27708-0086, USA

G. Chen
I-Fusion Technologies, Inc, Germantown, MD 20874, USA

F. Sun
State Key Laboratory of Intelligent Technology and Systems, Tsinghua University, Beijing, China

F. Sun et al. (eds.), *Foundations and Practical Applications of Cognitive Systems and Information Processing*, Advances in Intelligent Systems and Computing 215,
DOI: 10.1007/978-3-642-37835-5_53,

1 Introduction

Recently, there has been an increasing interest in controlling robots through neural signals. The works [1–3] propose and review directly employing cortical neurons to control a robotic manipulator. The research groups [4–6] report the navigation of mobile robots with thoughts, including the control of a wheelchair [7–9]. The article [10] presents an example of humanoid robot control through brain signals.

Comparing with manipulators and mobile robots, humanoid robots are more advanced as they are created to imitate some of the same physical and mental tasks that humans undergo daily [11], but control of humanoid robots is much more complex. Humanoid robots are being developed to perform some complicated tasks like personal assistance, where they should be able to assist the sick and elderly, and dirty or dangerous jobs.

In order to investigate relationships between human mental activities and humanoid robot walking behavior, we develop the Cerebot system as shown in Figs. 1 and 2, consisting of a Cerebus neural data acquisition system and a Kumotek robot with 20 degrees of freedom or a NAO robot with 25 degrees of freedom [12].

One of the critical issues in control of humanoid robot with thoughts is how to acquire the brain signals with high quality which are correlated to humanoid robot behavior. It is very important to improve subjects' concentration on mental activities during experiments. In this paper, we present procedures how to use the Cerebot to conduct experiments on acquiring brain signals correlated mental activities of six robot walking behavior. In order to improve the quality of neural signals of imaging humanoid robot walking behavior, we use movies of robot walking behavior or real robot walking activities to stimulate the subjects' attention to their mental activities.

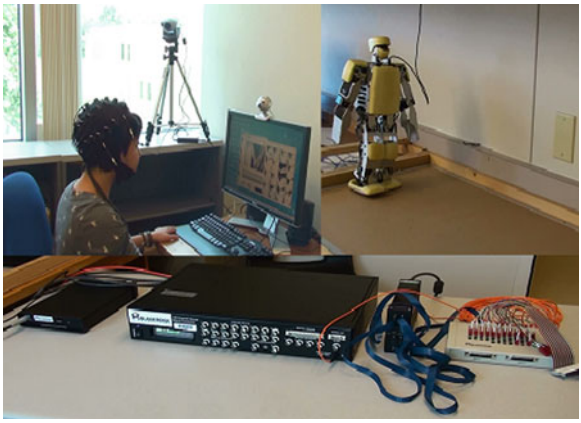

Fig. 1 Cerebot consists of a Cerebus^{TM} data acquisition system and a humanoid robot

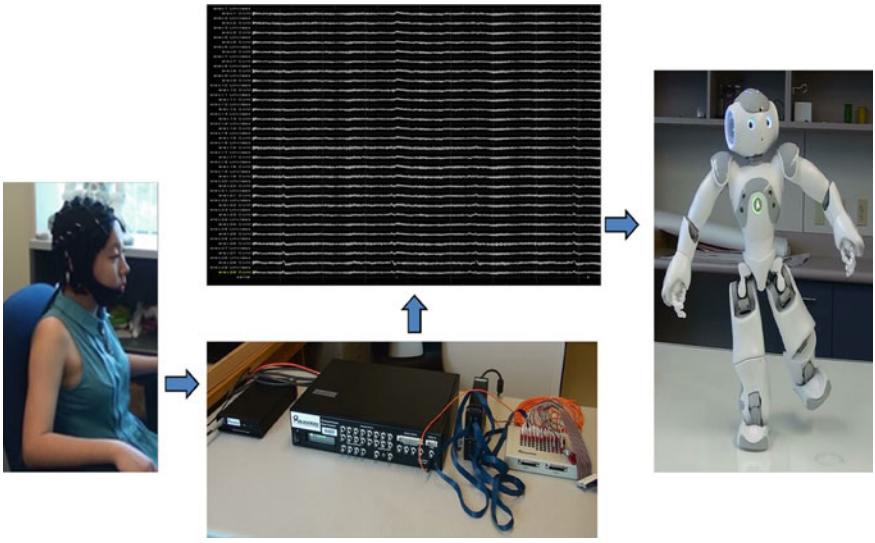

Fig. 2 NAO humanoid robot based Cerebot

2 Cerebot

The Cerebot consists of a Cerebus^{TM} Data Acquisition System with a 32 micro-electrodes cap and a humanoid robot [13]. The Cerebus^{TM}, manufactured by Blackrock Microsystem, includes an amplifier, an amplifier power supply, and neural signal processor, as shown in the bottom window of Fig. 1. This system is capable of recording from both surface and extracellular microelectrodes, and the system provides several online processing options for neural signals including noise cancellation, adjustable digital filters, simultaneous extraction of spike and field potential recordings from microelectrodes, and automatic/manual online spike classification. The Cerebus is easily scalable from 8 to 256 channels of action potentials and field potentials (with other experimental data) in real time.

The Cerebot includes a KT-X PC humanoid robot manufactured by Kumotek which has 20 degrees of freedom (DOFs), 12 DOFs located on hips, knees, and ankles, for humanoid robot walking, 6 DOFs on shoulders and arms for arms motion, and 2 DOFs for head yaw and pitch motion. The KT-X PC incorporates a 1.6 GHz Atom Z530 processor, memory expansion slots, video input for vision, speakers, a 60 MHz motor controller, three axis gyro/accelerometer chip, a 1.3 MP CMOS camera, six high-torque/titanium gear motors in the legs, and an external urethane foam casing to protect the robots internal PC and equipment from shock, as shown in the right-upper window of Fig. 1. The onboard PC computer provides a 16 GB hard disk and two USB ports, which connect a wireless adaptor and an additional flash drive. The onboard PC computer hidden in its torso allows us to run programs under Windows or Linux operating systems, to

develop programs in C++ and Python, and to control the robot motion real time or based on defined behaviors.

An alternative humanoid robot used in the Cerebot mind-controlled system is NAO H25 robot from Aldebaran Robotics [12], as shown in Fig. 2. The NAO robot is equipped standard with an embedded computer and WIFI connection. The NAO is fully autonomous and can establish a secure connection to the Internet to download and broadcast content. With 25 degrees of freedom, the NAO is capable of executing a wide range of movements, including walking, sitting, standing up, dancing, avoiding obstacles, kicking, seizing objects, etc. The NAO humanoid robot has two cameras allowing him to capture and send photos, video streams, recognize colored objects, detect and recognize faces, and communicate with the PC or the web for downloading files, behaviors, sending images in real time, etc. The NAO robot can be controlled via Choregraphe wholly designed and developed by Aldebaran Robotics. Choregraphe accepts Python language programs as well as can directly call C++ modules developed separately. In addition, the Webots™ software can also simulate the NAO robot behaviors before executing the real robot.

Both of the Cerebus™ data acquisition system and KT-X PC or NAO humanoid robots provide software development kits (SDKs) in both Matlab and C++ programming environments. Matlab suits to analyze brain signals offline and to investigate pattern features of mental activities using a variety of toolboxes. The C++ language environment is good for integrating the software NAOsim or Webots™ for simulation and to control a humanoid robot via brainwaves in real time.

3 Stimuli Module

Biological studies provide the useful research results to understand motor cortex of human brain. The foundation of robot control using brainwaves is the motor-related rhythms. Scalp-recorded electroencephalogram (EEG) signals reflect the combined synaptic and axonal activity of groups of neurons whose features can be used to control robot activities [14]. The primary motor cortex (also known as M1), a strip located on the precentral gyrus of the frontal lobe is an important brain region for the control of movement in humans. M1 maps the body topographically, meaning that the ventral end of the strip controls the mouth and face and the other end the legs and feet, with the rest of the body represented in between. The amount of representation is not proportional to the size of the body part. For example, the trunk is represented by only a small region on the primary motor cortex, because humans do not generally use the trunk for fine, precise movements or a wide range of motion. On the other hand, the fingers are greatly represented on M1, because the fingers are sensitive appendages and are used for many different movements. The primary motor cortex is thought to control both muscles and movements [15].

The nonprimary motor cortex is located just adjacent to the primary cortex and is important in the sequencing of movements. The premotor cortex (PMA) has been implicated in movements that require external cues. This region also contains

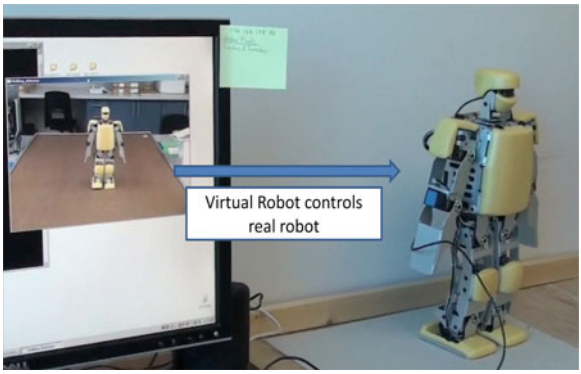

Fig. 3 Stimuli module of the Cerebot system

mirror neurons, which are activated both when one is performing a movement and when he or she is observing someone else do the same movement; in this case, the brain is utilizing visual cues [16]. In contrast, the supplementary motor area (SMA) is utilized for movements that are under internal control, such as doing some sort of action from memory [17].

For control of humanoid robot via brainwaves, our previous experiments in work [18] show that the quality of recorded data highly depends on subject concentration on mental activities. In this paper, we develop a visual stimuli module to improve the subjects' attention to their mental activities for acquiring neural signals of imaging robot walking behavior. Figure 3 shows such a program module in the Cerebot system. This module uses robot movements in video clips to control the real robot walking behavior. We record six short movie clips regarding robot walking behavior: "turn left," "shift left," "turn right," "shift right," "walking forward," and "walking backward." Our stimuli module plays the six robot walking behavior sequentially or randomly. When the humanoid robot in each movie starts a given walking behavior, the stimuli module sends out a command to the real humanoid robot to activate the same walking behavior.

The module also generates two other types of signals. The first type includes six voice messages: "Starting turn left," "Start shift left," "Starting turn right," "Starting shift right," "Starting walking forward," and "Starting walking backward." When a movie clip in the module starts playing a robot walking activity it synchronously speaks its corresponding voice message to a human subject because this voice message as an auditory stimuli signal activates the subject's mental activity on the robot walking behavior displayed on a monitor. The stimuli module also sends a digital code to the Cerebus system when the module starts the robot walking behavior. This digital code as a mark indicates which piece of brain signals are related to its corresponding imagination of robot walking behavior. These marks are very important to extract the features of mental activities. Figure 4 shows the recorded brain signals of imagining humanoid robot walking behavior as well as by the corresponding digital codes that indicate possible subject's mental activities of turn left, turn right, and walking forward.

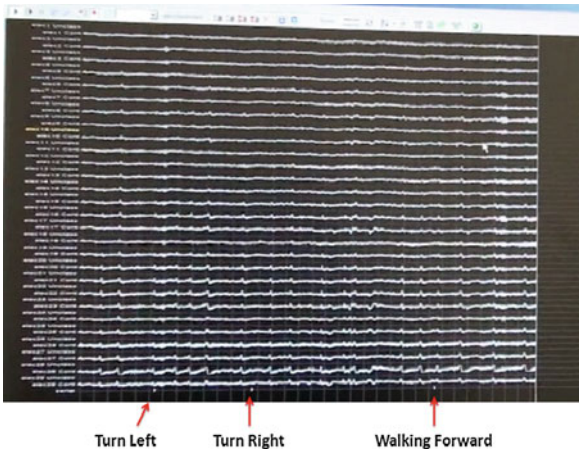

Fig. 4 Brain signal intervals of imaging humanoid walking behavior: *turn left*, *turn right*, and *walking forward* indicated by their corresponding digital codes

The stimuli module can also control the real humanoid robot walking activities to initiate human subject's imagination of robot walking behavior. In our further experiment, we will use the real robot activities to draw the human subject's attention to mental activities as the real robot walking activities may provide more effective 3D scenes for acquiring brain signals of imagining humanoid robot walking behavior.

4 Acquiring Neural Signals

In this paper, we report two groups of experiments on acquiring brain signals. For the first group, we implement three humanoid robot walking behavior to record human brain signals of imagining "turning right," "turning left," and "walking forward." A human subject starts imagining "turning right," "turning left," or "walking forward," by watching the robot walking activities in the movie clips when the stimuli module speaks their corresponding messages. During these mental activities, the subject also simultaneously moves its right hand, left hand, or both hands, which also represent the mental activities of "turning right," "turning left," and "walking forward," respectively. A CCD camera also synchronously takes these hand postures. These hand postures in the video clips can be used as additional information to determine the time intervals for mental activities of imagining "turning right," "turning left," or "walking forward," which are useful for recognizing robot walking behavior from the brainwaves (decoding brainwaves).

The recorded brainwaves addressed in the first group may include muscular signals caused by the subject's hand movements. The second group of experiments is to acquire brain signals of imagining robot walking behavior exclusive muscular signals, the human subject only imagine the robot walking behavior by watching the scenes displayed by the stimuli. The second group of experiments records the

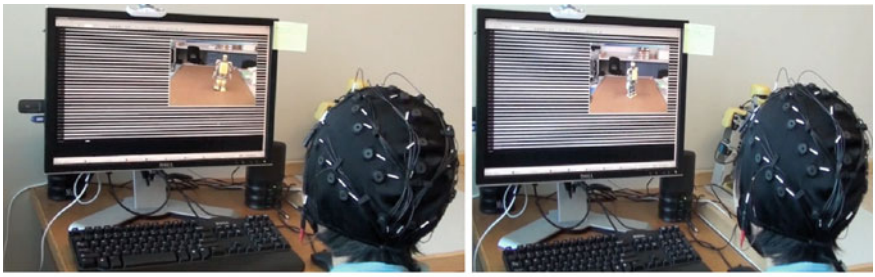

Fig. 5 Acquiring brain signals when the subject is staring at the robot walking scenes displayed by the stimuli module. **a** Imagining shift left behavior. **b** Imagining turn left behavior

brain signals of "true imagination" because the human subject does not move his hands. For the second group, we acquire the brain signals correlated to six different of humanoid robot walking behavior: "turn left," "shift left," "turn right," "shift right," and "walking forward." Figure 5 shows that acquiring brain signals when the subject is staring at the robot "turn left" and "shift left" walking activities displayed by the stimuli module.

We will use brain signals recorded in the two groups of experiments to investigate biological assumptions: "motor homunculus" and "sensory homunculus," respectively, which may be related to particular areas in the motor cortex associated with function of particular limbs and with sensory function of different limbs.

5 Processing Brain Signals

When using an EEG to acquiring brain signals, a large-scale neuronal synchronization is detectable, i.e., several tens of thousands of neurons need to fire at approximately the same time with respect to a neuronal population that has approximately the same spatial orientation. It is believed that the theory of oscillations represents one of the essential mechanisms of brain operation. These oscillations or oscillatory activity can be classified into different frequency bands and are referred to as the brain rhythms: ([0.5–3.0 Hz]—*Delta*, [4.0–7.0 Hz]—*Theta*, [8.0–12.0 Hz]—*Alpha*, [13.0–30.0 Hz]—*Beta*, [30.0–50.0 Hz]—*Gamma*. *Mu* rhythm ranges 8.0–13.0 Hz and partly overlaps with other frequencies. Some analyses have also demonstrated that the *Mu* rhythm is usually associated with 18.0–25.0 Hz in *Beta* rhythms. Because *Mu*/*Beta* rhythm changes are associated with normal motor/sensory function, they could be good signal features of controlling robot motion. *Gamma* rhythms are thought to represent binding of different populations of neurons together into a network for the purpose of carrying out a certain cognitive or motor function.

Besides the mechanisms of oscillations, synchronization, and binding, the newest insight into the brain's informational exchange and coding suggests a mechanism that could represent a general information-coding scheme and is based on the phase coding of the content in the oscillatory activity. The theory of phase coding has already been explored in working-memory processes; however, it is assumed that similar coding patterns are present during other cognitive actions too. Briefly, the idea behind the phase coding is that the phase characteristics of the synchronized oscillations in the brain that originate from two or more different brain areas could carry the information relevant to the completion of a certain task currently being performed [19] (Fig. 6).

In this paper, we use discrete wavelet transforms (DWT) to decompose the recorded brain signals into different frequency band rhythms [20]. The DWT means choosing subsets of the scales (s) and positions (p) of the function $\psi(t)$:

$$\psi_{(s,p)}(t) = s^2\psi(t)\left(2^{\frac{s}{2}}(t-p)\right) \tag{1}$$

Choosing scales and positions are based on powers of two, which are called dyadic scales and positions $\{s_j = 2^{-j};\ \ p_{j,k} = 2^{-j}k\}$, where j and k are integers). As an example, Fig. 7 shows the *Delta* and *Alpha* band rhythms of brain signals recorded from a subject.

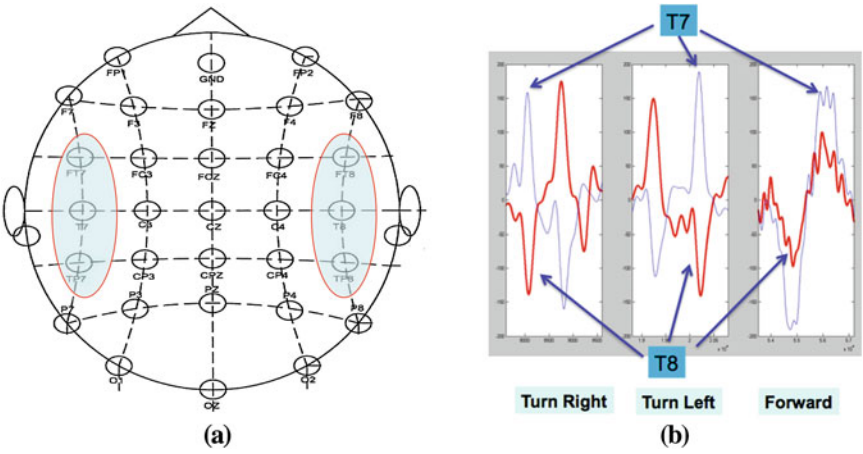

Fig. 6 **a** Electrodes located at the left brain and right brain; **b** phase relationships of the *Delta* rhythms of brainwaves correlated to mental activities

6 Control of Humanoid Robot via Phase Coding

The recent study [21] shows that the relative phase of slow ongoing rhythms at which these (temporal or population) responses occurred provided much additional and complementary information. Such nested codes combining spike-train patterns with the phase of firing were not only most informative, but also most robust to sensory noise added to the stimulus. The precise timing (phase) of slow rhythms is related to the stimulus more than the amplitude, suggesting that phase might play a more important role in sensory coding than energy.

We use the DWT algorithm to process the human subject's brainwaves from the first group to extract the *Delta* rhythms of the brainwaves recorded from electrodes located at the left brain and right brain, e.g., T7 and T8, as shown in the top two panels of Fig. 7. These brainwaves include the three mental activities: turning right, turning left, and walking forward. We further investigate their phase relationships of the *Delta* rhythms. The left brain signals in Fig. 7 present the brain mental activity when the human subject is thinking "turning right." For this pattern, the phase of brain signals at T7 is leading to the one of brain signals at T8. The middle pattern represents the brain mental activity when the human subject is thinking "turning left." For this pattern, the phase of brain signals at T8 is leading to the one of brain signals at T7. The right pattern shows the brain mental activity when the human subject was thinking "walking forward." In this case, both of the brain signals at T7 and T8 have the close phases. The mental activities can be

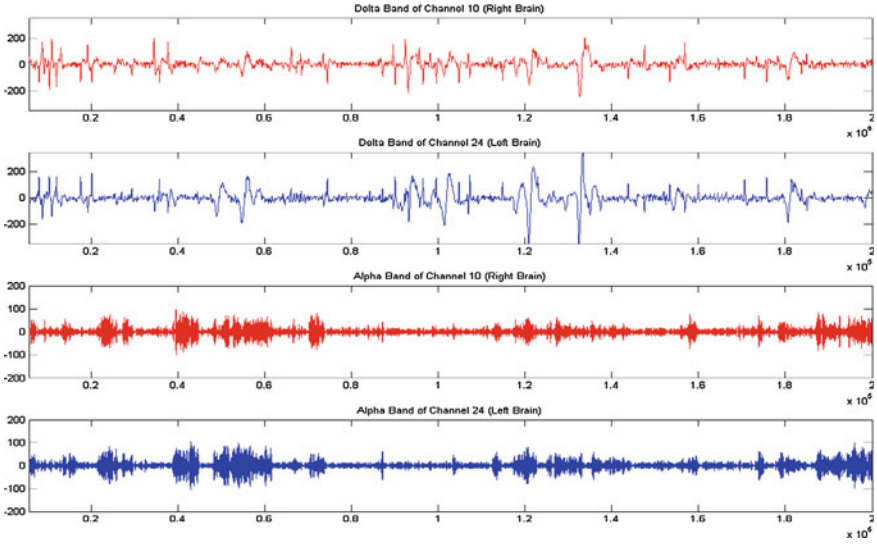

Fig. 7 *Delta* and *Alpha* band rhythms of brain signals recorded at electrodes T7 in *red* and T8 in *blue*

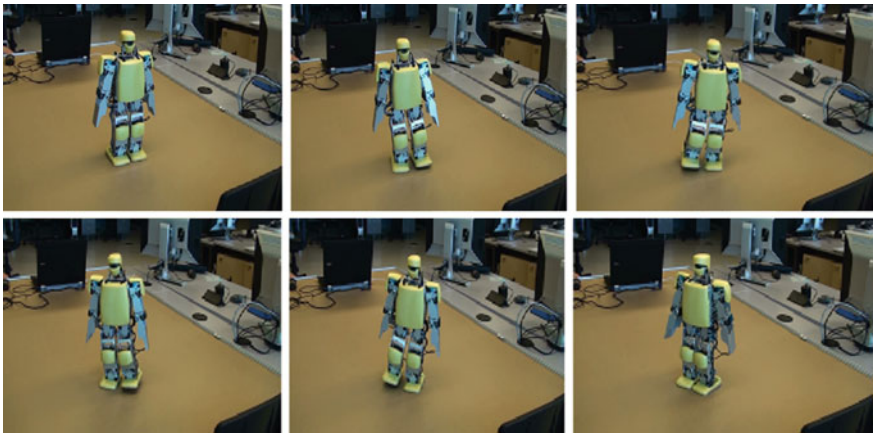

Fig. 8 Control of robot *turning left* with imagination

identified by the digital codes generated by the stimuli module and/or the video clips taken by the CCD camera during the subject mental activities. Our analyses also indicate that the brainwaves recorded at electrodes FT7, T7, and TP7 on the left half scalp (channel 25, 24, and 18) are very similar; while the brainwaves recorded at electrodes FT8, T8, and TP8 on the right half scalp (channel 17, 10, and 9) are very similar. As an example, we use these phase differences of the *Delta* rhythms between T7 and T8, FT7 and FT8, and TP7 and TP8 to control robot walking behaviors: turning right, turning left, and walking forward [13]. Figure 8 shows the turn left walking controlled by the brainwaves.

7 Conclusions

This paper presents the strategies for acquiring brain signals of imagining humanoid robot walking behavior by the embedded stimuli module in the Cerebot system. Our further work will present the detailed analysis on the experiments data and the phase coding based algorithms for control of humanoid robot activities with thoughts.

Acknowledgments We would like to thank Dr. Meifang Ma from Blackrock Microsystems for his help in conducting the experiments.

References

1. Chapin JK, Moxon KA, Markowitz RS, Nicolelis MAL (1999) Real-time control of a robot arm using simultaneously recorded neurons in the motor cortex. Nat Neurosci 2:664–670

2. Wessberg J, Stambaugh CR, Kralik JD, Beck PD, Laubach M, Chapin JK, Kim J, Biggs SJ, Srinivassan MA, Nicolelis MAL (2000) Real-time prediction of hand trajectory by ensembles of cortical neurons in primates. Nature 408:361–365
3. Lebedev MA, Nicolelis MAL (2006) Brain-machine interfaces: past present and future. Trends Neurosci 29:536–546
4. Millán JdR, Renkens F, Mouriño J, Gersterner W (2004) Noninvasive brain-actuated control of a mobile robot by human EEG. IEEE Trans Biomed Eng 51(6):1026–1033
5. Tanaka K, Matsunaga K, Hori S (2005) Electroencephalogram-based control of a mobile robot. Electr Eng Jpn 152(3):39–46
6. Barbosa AOG, Achanccaray DR, Meggiolaro MA (2010) Activation of a mobile robot through a brain computer interface. In: Proceedings of 2010 IEEE international conference on robotics and automation, pp 4815–4821
7. Rebsamen B, Burdet E, Guan C, Teo CL, Zeng Q, Laugier MAC (2007) Controlling a wheelchair using a BCI with low information transfer rate. In: Professional of IEEE 10th international conference on rehabilitation robotics, pp 1003–1008
8. Galán F, Nuttin M, Lew E, Ferrez PW, Vanacker G, Philips J, Millán JdR (2008) A brain-actuated wheelchair: asynchronous and non-invasive brain–computer interfaces for continuous control of robots. Clin Neurophysiol 119(9):2159–2169
9. Iturrate I, Antelis JM, Kubler A, Minguez J (2009) A noninvasive brain-actuated wheelchair based on a P300 neurophysiological protocol and automated navigation. IEEE Trans Rob 25(3):614–627
10. Bell CJ, Shenoy P, Chalodhorn R, Rao RPN (2008) Control of a humanoid robot by a noninvasive brain-computer interface in humans. J Neural Eng 5(2):214–220
11. Hirai K, Hirose M, Haikawa Y, Takenaka T (1998) The development of Honda humanoid robot. In: Proceedings of 1998 IEEE international conference on robotics and automation, pp 1321–1326
12. Li W, Jaramillo C, Li Y (2012) Development of mind control system for humanoid robot through a brain computer interface. In: Proceedings of second international conference on intelligent system design and engineering application, pp 679–682
13. Li W, Jaramillo C, Li Y (2011) A brain computer interface based humanoid robot control system. In: Proceedings of the IASTED international conference on robotics (Robo 2011), pp 390–396
14. Garcia GN (2004) Direct brain-computer communication through scalp recorded EEG signals. Doctor's thesis, Department of Electricity, Ecoloe Polytechnique Federale de Lausanne, Switzerland
15. Breedlove M, Rosenweig M, Watson N (2007) Biological psychology: an introduction to behavioral, cognitive, and clinical neuroscience. Sianuer Associates, Inc., Sunderland
16. Buccino G, Lui F, Canessa N, Patteri I, Lagravinese G, Benuzzi F, Porro CA, Rizzolatti G (2004) Neural circuits involved in the recognition of actions performed by nonconspecifics: an FMRI study. J Cogn Neurosc 16:114–126
17. Halsband U, Matsuzaka Y, Tanji J (1994) Neuronal activity in the primate supplementary, pre-supplementary and premotor cortex during externally and internally instructed sequential movements. Neurosci Res 20:149–155
18. Li W, Li Y, Chen G, Shen D, Blasch E, Pham K, Lynch R (2012) Acquiring neural signals for developing a perception and cognition model. In: Proceedings of SPIE (sensors and systems for space applications), Vol 8385, pp 1–8
19. Logar V, Beli A (2011) Visuo-Motor tasks in a brain-computer interface analysis. In: Fazel-Rezai R (ed) Recent advances in brain computer interface systems, InTech, New York, USA
20. Shaker MM (2005) EEG waves classifier using wavelet transform and Fourier transform. Int J Biol Life Sci 1(2):85–90
21. Kayser C, Montemurro MA, Logothetis NK, Panzeri S (2009) Spike-phase coding boosts and stabilizes information carried by spatial and temporal spike patterns. Neuron 61(4):597–608

Multimodal Mixed Conditional Random Field Model for Category-Independent Object Detection

Jian-Hua Zhang, Jian-Wei Zhang, Sheng-Yong Chen and Ying Hu

Abstract Category-independent object detection is extremely useful for many robot vision tasks. Most existing methods rank a lot of regions by measuring their object-likeness. However, to obtain a sufficient object covering rate too many regions need to be sampled. In this paper, we present a novel method that directly detects and localizes category-independent objects. We develop a novel model which is named as "mixed robust higher-order conditional random field" model which combines 2D and 3D data into a uniform framework. A set of novel features is developed based on 2D and 3D saliency and oversegments. The potentials used in this model are computed from these features. Extensive experiments are carried out on a public RGB-D dataset. By comparison with state-of-the-art ranking methods, the experimental results show the comparable performance of category-independent object detection without sampling a large number of extra regions.

Keywords Multimodality · Category-independent · Object segmentation · Conditional random fields

This work is founded by the DFG German Research Foundation (grant #1247) International Research Training Group CINACS (Cross-modal Interactions in Natural and Artificial Cognitive Systems)

J.-H. Zhang (✉) · J.-W. Zhang
Group TAMS, Department of Informatics, University of Hamburg, Hamburg, Germany
e-mail: jzhang@informatik.uni-hamburg.de

J.-W. Zhang
e-mail: zhang@informatik.uni-hamburg.de

S.-Y. Chen
College of Computer Science, Zhejiang University of Technology, Hangzhou, China
e-mail: sy@ieee.org

Y. Hu
Shenzhen Institutes of Advanced Technology, Chinese Academy of Sciences, Shenzhen, China
e-mail: ying.hu@siat.ac.cn

F. Sun et al. (eds.), *Foundations and Practical Applications of Cognitive Systems and Information Processing*, Advances in Intelligent Systems and Computing 215,
DOI: 10.1007/978-3-642-37835-5_54,

1 Introduction

To detect and localize objects without recognizing them in a scene is an important ability for humans, which raises a challenging problem: how to accurately detect category-independent objects. If this problem can be efficiently solved, many following tasks, such as object recognition (e.g. [5]), object describing (e.g. [8]), and object tracking (e.g. [2]) could be improved. Thus many researchers proposed diverse methods to detect category-independent objects, such as objectness ranking (e.g. [1, 19, 27]), structure segmentation (e.g. [6, 7]), and salient object detection (e.g. [10]). When humans localize objects in a scene, 3D information is indispensable. Most of these methods only take into account 2D images. Although two methods [6, 27] utilize 2D and 3D data, they do not take full advantage of the spatial consistency between 2D and 3D data. Furthermore, most of these methods are based on a procedure that ranks a lot of regions sampling from an image by measuring their object-likeness. They can achieve high object covering rates but the accuracy is very low, and consequently cannot be directly used for object localization.

In this paper, we focus on detecting category-independent objects and find their accurate positions based on both 2D and 3D data. As convenient devices that can obtain RGB+D (red, green, blue, + depth) data simultaneously emerge, such as Microsoft Kinect, they provide a chance for a robot vision system to efficiently integrate 3D and 2D data to improve object detection. Given an RGB+D image, a point belonging to an object in 2D space must have a corresponding point in 3D space belonging to the same object. Furthermore, in 3D space points near to the corresponding points also have high probability to belong to the same object. This means there is a spatial consistency between 2D and 3D data, which motivates a novel method that combines multimodal data in a uniform model.

We propose a novel mixed robust higher order condition random field (MRH-CRF) model that overcomes these aforementioned problems and obtains promising category-independent object detection in both 2D and 3D space. This model makes use of the 2D superpixels and 3D supervoxels as basic nodes for decreasing computational costs. The 2D saliency, superpixels and boundaries, and 3D saliency and supervoxels are computed first as category-independent object features. Then the unary, pairwise, and higher order clique potentials are generated. After infering the MRH-CRF model, the 2D and 3D labeling results are simultaneously obtained. The pixel-wise results can then be produced by combining 2D and 3D results at pixel-level. Unlike the general figure/ground segmentation methods (e.g. [3, 12, 20]), three labels, the object, the background, and the boundary, are used in the proposed method. Benefited from using three labels, the object instances can be easily distinguished from the segmenting results. We evaluate the proposed method in a public RGB+D dataset [15]. By comparison with state-of-the-art methods, our experimental results show a comparable performance for the proposed method without sampling extra regions.

1.1 Related Work

Recently, more and more approaches detecting and localizing category-independent objects have been proposed. They can be roughly divided into three groups: salient object detection based on visual saliency [10, 11], object-likeness measurement based on structure regions [3, 6, 7, 16, 22], object-likeness ranking based on sliding windows [1, 19, 27].

The salient object detection is based on the human visual attention mechanism by which humans can rapidly attend to the region with highest distinctiveness. Since visual attention theories proposed and applied in computer vision by Itti et al. [13], all subsequent methods follow one or several of the four basic principles of human visual attention summarized by Goferman et al. [11], which are local low-level considerations, global considerations, visual organization rules, and high-level factors [11]. Although visual saliency can be regarded as a good category-independent feature, it is not sufficient to use the saliency as sole feature to precisely detect all objects of interest, since salient object detection methods may fail to detect only one object in an image [11] or detect part of background as objects [10].

The second class method is first to over-segment images or 3D data (e.g. point cloud or depth map) into oversegments by some unsupervised segmentation algorithms ([9, 23]). Then the regions of the combination of adjacent oversegments are measured for containing whole objects. Unlike the salient object detection, these methods can detect more than one object regardless of their categories. However, these methods rely heavily on the results of oversegments. Thus small objects and objects with a similar color or texture to background may not be detected accurately. To improve the oversegments, they employ hierarchical segmentation [7], multi-scale segmentation [3] or utilize multimodal data [6, 22].

The objectness ranking method was first proposed by Alex et al. [1] and combines several local cues into a naive Bayesian model to sample windows in an image with high probability of containing objects by the sliding window approach. It is further improved by Rathu et al. [19] by more elaborate cues and Zhang et al. [27] by multimodal and global cues. Although output windows of objectness ranking methods can cover most objects, too many windows need to be sampled. To cover 70 % percent of objects one thousand windows with the highest objectness measurement need to be sampled as reported in [19]. Thus these objectness ranking methods cannot be directly used for category-independent object detection.

2 Formulation of the MRH-CRF Model

Given an image I and a corresponding point cloud T, we represent them by two sets of oversegments $\mathbf{S}_I = \{s_1^I, s_2^I, \ldots, s_{N_I}^I\}$ and $\mathbf{S}_T = \{s_1^T, s_2^T, \ldots, s_{N_T}^T\}$, where N_I and N_T are the number of oversegments of the image I and the point cloud T. $\mathbf{X}_I$ and $\mathbf{X}_T$

denote a discrete random field on an image I and a point cloud T, which are defined over two sets of vertices $\mathscr{V}_I = \{1, 2, \ldots, N_I\}$ and $\mathscr{V}_T = \{1, 2, \ldots, N_T\}$, respectively. Denote neighborhood systems by ε_I and ε_T where vertices $i \in \mathscr{V}_I$ and $m \in \mathscr{V}_T$ correspond to oversegments $s_i^I \in \mathbf{S}_I$ and $s_m^T \in \mathbf{S}_T$, respectively.

Random variables $X_i^I \in \mathbf{X}_I$ and $X_m^T \in \mathbf{X}_T$ associated with vertices $i \in \mathscr{V}_I$ and $m \in \mathscr{V}_T$ will take values from the label sets $\mathscr{L}_I = \{l_1, l_2, \ldots, l_k\}$ and $\mathscr{L}_T = \{l_1, l_2, \ldots, l_k\}$, respectively, were in this study $k = 3$ for three kinds of labels. The neighborhood systems ε_I and ε_T consist of variables directly connected by edges in random fields $\mathbf{X}_I$ and $\mathbf{X}_T$ respectively. A set of random variables $\mathbf{X}_{c_I}^I$ $\mathbf{X}_{c_T}^T$ which are conditionally dependent on each other forms cliques c_I and c_T in different modalities respectively. Each random variable will be assigned a label and the configurations of labels are denoted by $\mathbf{x}_I$ and $\mathbf{x}_T$ which take values from the set $\mathbf{L} = \mathscr{L}_I^N$ and $\mathbf{L} = \mathscr{L}_T^M$.

The proposed MRH-CRF model is a higher order conditional random field model, which Gibbs energy function is defined as:

$$E(\mathbf{x}_d) = \sum_{i \in \mathscr{V}_d} \psi_i^d(x_i^d) + \sum_{(i,j) \in \varepsilon_d} \psi_{ij}^d(x_i^d, x_j^d) + \sum_{c_d \in \mathscr{C}_d} \psi_{c_d}^d(\mathbf{x}_{c_d}^d) \tag{1}$$

Here $\mathscr{V}_d$ is the set of all segments and ε_d is the set of all edges connecting the segments $i, j \in \mathscr{V}_d$. A clique c_d is defined over a segment i and all adjacent segments connecting to it.

The unary potential ψ_i^d in (1) is defined as the negative log of the likelihood of a label being assigned to segment s_i^d. We employ the visual saliency as category-independent features from which the unary potential of this model is computed. The unary potential of each segment is defined as:

$$\psi_i^d(x_i^d) = -\log(p(x_i^d | F_i^{u_d})) \tag{2}$$

where the probability $p(x_i^d | F_i^{u_d})$ is computed by multi-class support vector machine [4] and $F_i^{u_d}$ is the saliency feature of the i-th segment of a 2D image or a 3D point cloud, computed as the weighted sum of saliency within this segment.

The pairwise potential $\psi_{ij}^d(x_i^d, x_j^d)$ is also computed from category-independent features. We employ object boundaries as edge features, from which the pairwise potential is defined as the Potts model:

$$\psi_{ij}^d(x_i^d, x_j^d) = \begin{cases} 0 & \text{if } x_i^d = x_j^d, \\ \theta_p^d + \theta_v^d \exp(-\theta_\beta^d ||F_{i,j}^{p^d}||^2) & \text{otherwise}, \end{cases} \tag{3}$$

where $F_{i,j}^{p^d}$ is the pairwise feature between segments i and j, which is computed from boundary features along with the edge between two segments. The model parameters θ_p^d, θ_v^d and θ_β^d are learned from training data.

In [14], Kohli et al. proved that the higher order CRF model can obtain a better performance than that of the pairwise one by adding an extra higher order

potential, and provided an efficient algorithm to solve it. In this study, we also use the robust P^n potential which is defined as:

$$\psi^d_{c_d}(x^d_{c_d}) = \begin{cases} N_i(x^d_{c_d})\frac{1}{Q}\gamma_{\max} & \text{if } N_i(x^d_{c_d}) \leq Q, \\ \gamma_{\max} & \text{otherwise}, \end{cases} \tag{4}$$

where $N_i(\mathbf{x}^d_{c_d})$ denotes the number of nodes which have different labels from the dominant label in the clique c_d, and can be calculated by $N_i(\mathbf{x}^d_{c_d}) = \min_k(|c_d| - n_k(\mathbf{x}^d_{c_d}))$. Here $|c|$ is the number of all nodes in clique c_d and $n_k(\mathbf{x}^d_{c_d})$ is the number of nodes taking label l_k. The truncation parameter denoted by Q is used to control the rigidity of this higher order potential. The γ_{max} is defined as:

$$\gamma_{max} = |c_d|^{\theta^d_\alpha}(\theta^d_{hp} + \theta^d_{hv}\exp(-\theta^d_{h\beta}||F^{h^d}_{c_d})||^2)) \tag{5}$$

where $F^{h^d}_{c_d}$ is the clique feature which is computed from object boundaries on all segments belonging to clique c_d. The parameters θ^d_α, θ^d_{hp}, θ^d_{hv}, and $\theta^d_{h\beta}$ are also learned from training data.

3 Multimodal Features

3.1 Saliency and Oversegments

Visual saliency indicates the distinctiveness of one part with respect to other parts in an image. In general, foreground objects have higher saliency while background objects get a lower one. However, 2D saliency is computed from color and brightness. Thus some objects of interest may have low saliency, while some background areas with surrounding noises may have high saliency. Therefore using both 2D and 3D saliency can detect foreground objects more robustly than using only unimodal saliency. 2D saliency is computed by the Li et al. algorithm [17]. To extend this method to deal with 3D data, we use 3D information as features. Saliency can be defined as the local contrast between a region and its surroundings. We employ two kinds of 3D information, the normal direction and depth value of each point, as features to compute 3D saliency.

All pixels in a superpixel belonging to the same object [21] is a basic assumption for many object detection methods (e.g. [1, 16]). Unfortunately, it is not always true in many cases. Using both 2D and 3D oversegments can improve the robustness of object detection. Therefore, here the algorithm in [26] is employed to compute 2D oversegments and extended to compute 3D oversegments. This algorithm treats the segmenting task as a label assigned procedure, which uses pixel values as features. The segments obtained by this algorithm have more regular size, which can align object boundaries better. To extend this algorithm to deal with 3D point clouds, we use both normal directions and depth values as features.

3.2 Unary Features

After we obtain 2D and 3D saliency and oversegments, the unary features can be computed for unary potentials in both modalities. Given a 2D segment s_i^I and 2D saliency map I_s for the image I, the 2D unary feature for this segment is defined as:

$$F_i^{u_I} = \frac{\sum_{j \in s_i^I} I_{s,j}/\sigma_j^2}{|s_i^I|} \tag{6}$$

where $|s_i^I|$ denotes the number of pixels in the segment s_i^I, $I_{s,j}$ is the saliency of the j-th pixel in s_i^I, and σ_j denotes the weight for the j-th pixel which is defined as $\sigma_j = d_j/3$ where the d_j is the Euclidean distance between pixel j and the mass of segment s_i^I. The 3D unary feature has the similar definition given a 3D segment s_m^T and 3D saliency map T_s:

$$F_m^{u_T} = \frac{\sum_{n \in s_m^T} T_{s,n}/\sigma_n^2}{|s_m^T|} \tag{7}$$

Note that in (7) σ_n is computed from the Euclidean distance between point n and the mass of segment s_m^T in 3D space.

3.3 Pairwise Features

We use object boundaries to evaluate how likely it is for two adjacent segments to take the same label. For the 2D image, the object boundaries are explicitly computed by the algorithm global probability of boundary (gpb) proposed in [18]. For the 3D point cloud data, since there is no efficient method to explicitly extract object boundaries, we implicitly take them into account when computing 3D pairwise features.

At first we explain how to formulate the 2D pairwise features. Given a gpb map B^I and two adjacent segments $\{s_i^I, s_j^I\} \in \mathbf{S}_I$, three kinds of features are computed first for each point x in the edge $E_{i,j}$ between two segments, then they are integrated into one formulation:

$$F_{i,j}^{p_I} = \frac{1}{|E_{i,j}|} \sum_{x \in E_{i,j}} (t_x \cdot (1 + \cos\theta_x)/d_x) \tag{8}$$

where d_x denotes the distance of a point x to the nearest boundary in gpb map B^I, t_x is the value of the nearest boundary in B^I, and θ_x is the radian difference between the tangent to the edge point x and the tangent to the nearest boundary, as illustrated in Fig. 1. By this equation, the closer distance, higher gpb value, and smaller radian difference result in higher values for 2D pairwise feature which means there

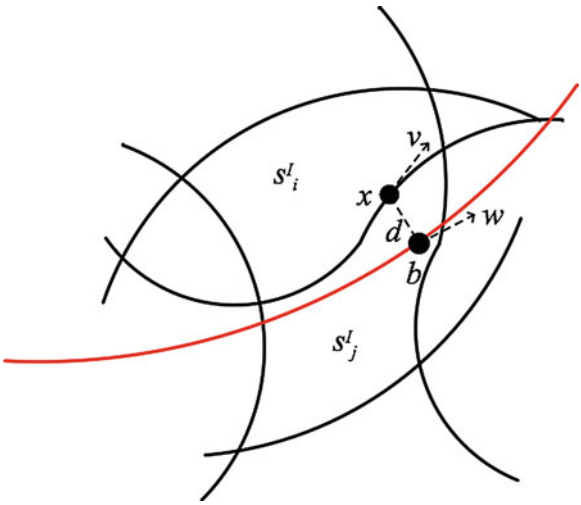

Fig. 1 2D pairwise feature. The *black curve* between two segments is the edge with one point x marked. The *red curve* is the object boundary computed by gpb. b denotes the nearest object boundary to x. d is the distance. v and w are the tangent of x and b, respectively

is a higher probability of boundary between the two segments. Note that (8) also normalizes the 2D pairwise feature to the range $[0, 1]$.

Given two adjacent 3D segments $\{s_m^T, s_n^T\} \in \mathbf{S}_T$, two kinds of features are considered. The first is the Chi-square distance of the point normal histogram between two adjacent segments. We transform a point normal from cartesian coordinates to spherical coordinates by the following equations:

$$r = \sqrt{n_x^2 + n_y^2 + n_z^2}, \varphi = \arctan n_y/n_x, \theta = \arccos n_z/r \tag{9}$$

where $\varphi \in [0, 2\pi]$ and $\theta \in [0, \pi]$. Since r is always 1 for all point normals, the histogram of normals in one segment is constructed by only φ and θ as:

$$H_m^{norm}(i) = \frac{\sum |p_j|}{|s_m^T|} \qquad (p_j \in s_m^T, \{\varphi_j, \theta_j\} \in bin(i)) \tag{10}$$

where the histogram has 72 bins by dividing φ into 12 equal portions and dividing θ into 6 equal protions. Then we have the Chi-square distance of the normal histogram of two adjacent segments which is defined as:

$$d_{m,n}^{norm} = \frac{1}{2}\sum_{i=1}^{72} \frac{(H_m^{norm}(i) - H_n^{norm}(i))^2}{H_m^{norm}(i) + H_n^{norm}(i)} \tag{11}$$

The second feature is computed from the difference in the point cloud density of two segments, which is defined as:

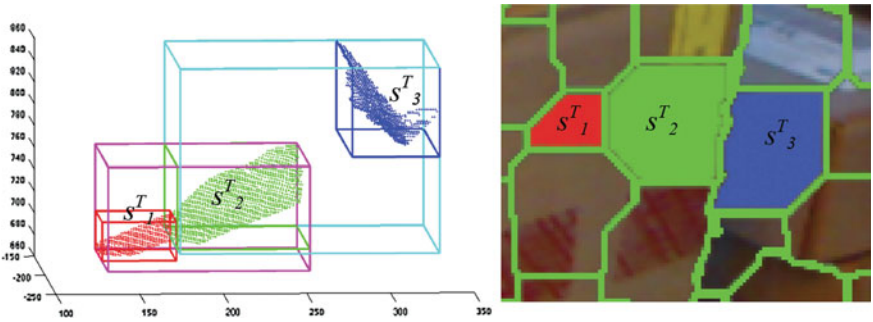

Fig. 2 Features of the difference in point density. The *right picture* shows three adjacent segments whose point clouds in 3D space are shown in the *left picture*.

$$d^{dens}_{m,n} = \exp(-\frac{D_{m,n}}{D_m + D_n})$$
$$D_{m,n} = \frac{|s^T_m|}{V_{box(s^T_m)}} \qquad D_{m,n} = \frac{|s^T_{m,n}|}{V_{box(s^T_m + s^T_n)}} \tag{12}$$

where D_m and D_n denote the point density of the segment s^T_m and s^T_n, $D_{m,n}$ denotes the joint point density of the joint segment $s^T_m + s^T_n$, and $V_{box(s^T_m)}$ is the volume of the minimal box containing all points in the segment s^T_m.

This feature is motivated by the following observation. If two adjacent segments are in the same object, their point density and their joint point density are more similar than that of two segments not in the same object. As shown in Fig. 2, we consider the three segments s^T_1, s^T_2, and s^T_3. The former two segments are in the same object and the last is in another object. It is obvious that s^T_1 and s^T_2 are closer to each other and hence the difference between $D_1 + D_2$ and $D_{1,2}$ is also smaller than that computed from s^T_2 and s^T_3 .

Finally, we normalize two features to the range [0,1] by $(d^{feat}_{m,n} - \min d^{feat})/(\max d^{feat} - \min d^{feat})$ and compute the average of three features as a 3D pairwise feature.

$$F^{p_T}_{m,n} = (\widetilde{d}^{norm}_{m,n} + \widetilde{d}^{dens}_{m,n})/2 \tag{13}$$

where $\widetilde{d}^{feat}_{m,n}$ denotes the normalized value of $d^{feat}_{m,n}$.

3.4 Higher Order Features

The higher order potential is defined on an entire clique, so the higher order feature is also computed from this clique. The higher order potential penalizes that the variables associated with segments in a clique do not have the same label.

Therefore the higher order feature will have a higher value if not all segments in a clique are in the same object, otherwise the value is lower. A natural solution of the higher order feature is to count the boundary in a clique, since the more boundaries there are, the more possible it becomes for the clique to straddle more than one objects. In this study, the 2D and 3D higher order features are defined as the mean values of all pairwise features between the segment centered at a clique and all its adjacent segments:

$$\begin{aligned} F_{c_i}^{h_I} &= \frac{1}{|c|} \sum_{j \in c_i \backslash i} F_{i,j}^{p_I} \\ F_{c_m}^{h_T} &= \frac{1}{|c|} \sum_{n \in c_m \backslash m} F_{m,n}^{p_T} \end{aligned} \tag{14}$$

where $c_i \backslash i$ means all segments but s_i^I in clique c_i.

4 Experiments

4.1 Model Inference and Parameter Learning

In this study we employ the same algorithm proposed in [14] for model inference (Readers can refer to it for details). There is a set of parameters in our MRH-CRF model that needs to be learned from training data. A simple method to set these parameters is to cross-validate every combination of all parameters; however, due to the large number of parameters there is a very high-dimensional parameter space to be exhaustively searched, which is obviously infeasible. Thus we employ a heuristic method, piecewise training [25], which has been successfully used in [14] and [24]. The particular steps of learning parameters from training data are the following. We first train the optimal parameters for each single modality separately. The pairwise potential parameters are learned by using unary and pairwise potentials. Next the parameters of higher order potentials are learned by using unary and higher order potentials. Then we train the ratio between unary, pairwise, and higher order potentials. The last step is to train the weight w_d. The final trained parameters and ratios for the RGB-D dataset are listed here: $\theta_p^I = 0.15$, $\theta_v^I = 12.0$, $\theta_\beta^I = 16.0$, $\theta_\alpha^I = 0.25$, $\theta_{hp}^I = 0.25$, $\theta_{hv}^I = 8.0$, $\theta_{h\beta}^I = 2.0$, $\theta_p^T = 0.4$, $\theta_v^T = 12.0$, $\theta_\beta^T = 7.5$, $\theta_\alpha^T = 1.0$, $\theta_{hp}^T = 0.5$, $\theta_{hv}^T = 4.0$, $\theta_{h\beta}^T = 12.0$, $w_I = 0.42$, $w_T = 0.58$.

4.2 Evaluation of the Proposed Model

We evaluate the performance of category-independent object detection for the proposed MRH-CRF model by comparison with a state-of-the-art method (i.e. [3]). All experiments are based on a public RGB+D dataset [15]. The data in the RGB+D dataset is obtained by a Kinect style 3D camera. The RGB and depth values are synchronized and alligned with 640×480 resolution. There are four classes of indoor scenes and 300 common household objects in it. Since the data is originally recorded in video sequences, we extract 200 images with significant difference in our experiments. 100 randomly selected images are used as the training set and the rest are used for testing.

We follow the criterion used in [3] to evaluate the performance at the pixel level. For the 'CPMC' method, the covering scores are computed by:

$$C(S, S'(r)) = \frac{1}{N} \sum_{R \in S} |R| \overset{\star}{\max}_{R' \in S'(r)} O(R, R') \tag{15}$$

where S and S' denote the set of ground truth segments and the set of machine segments, respectively, N denotes the total number of pixels of all annotated objects in one image, $|R|$ is the number of pixels in the ground truth segment R, and O is the overlap measure between two regions which is defined as:

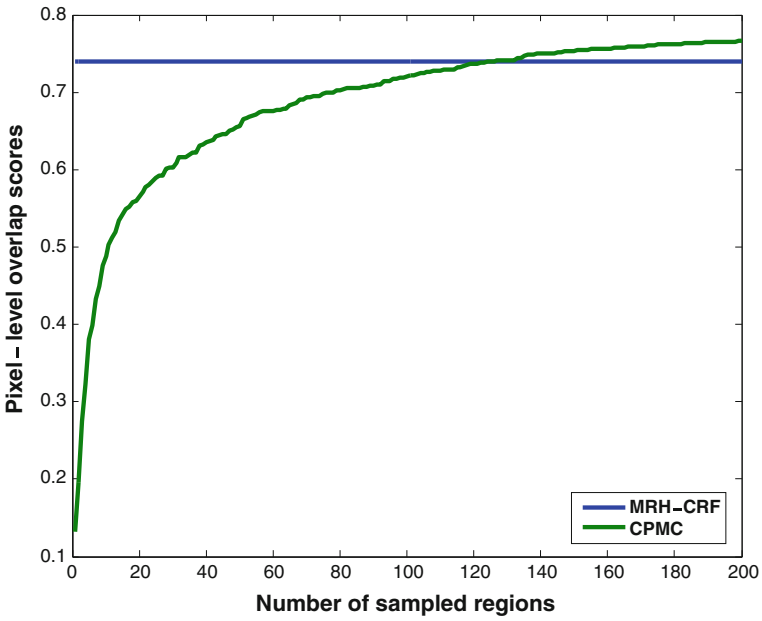

Fig. 3 Comparison of overlap scores

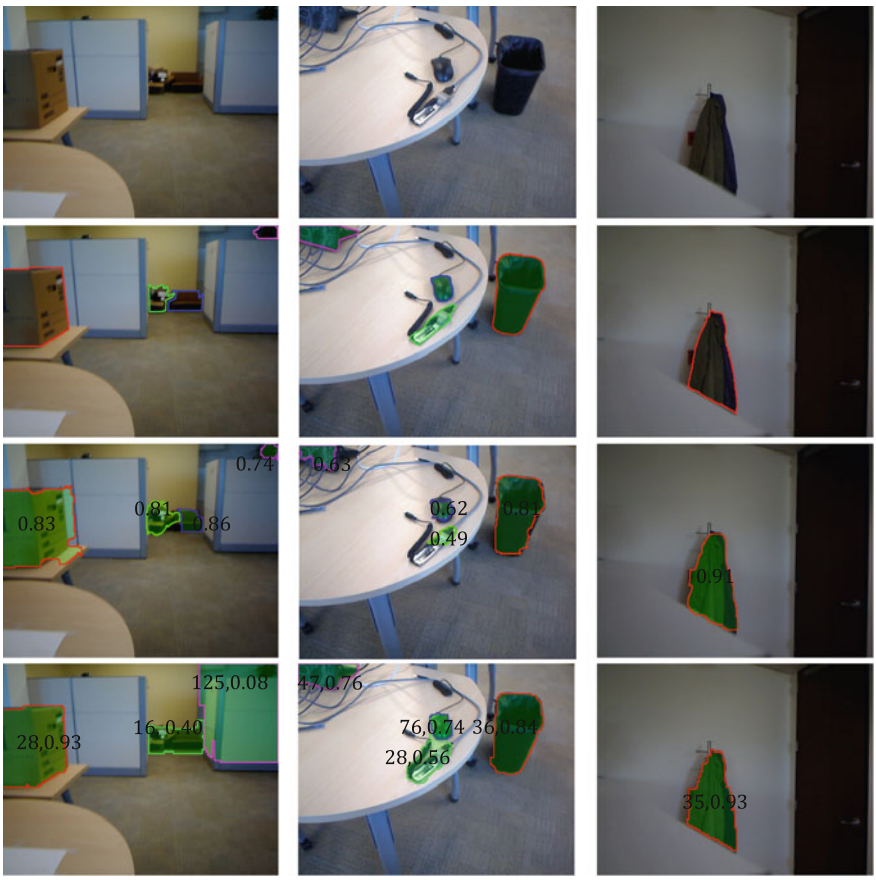

Fig. 4 Some examples of detected results. From *top to bottom*, these pictures are original images, ground truth, results of the proposed method, and results of 'CPMC'

$$O(S, G) = \frac{|S \cap G|}{|S \cup G|} \tag{16}$$

Figure 3 shows results similar to that of the object-level comparison. The 'MRH-CRF' method has comparable scores with respect to the 'CPMC' method when it samples 200 regions. The overlap score is more than 73 % which implies that the proposed method can be practically used for category-independent object detection.

Finally, some examples of detected regions by different methods are illustrated in Fig. 4. Each group of pictures, from top to bottom, consists of original images, ground truth, results of 'MRH-CRF', and results of 'CPMC'. Each detected object instance is marked by different solid curves and green transparent covers. The decimal in each object indicates the overlapping or covering score computed by

Eqs. (15) and (16). For the method 'CPMC', we sample the region from the sampled region pool with the best measuring scores and also give the ranking place by the integer number before their scores. The 'CPMC' method yields some better results than the proposed method; however, as shown in the figure, most of these best regions are located outside of the top 20 in the region pool. This implies that to get an accurate detection of objects, more inaccurate regions may be sampled first. On the other hand, the proposed method can detect and localize objects without sampling useless regions.

5 Conclusion

In this paper we developed a novel category-independent object detection method based on a set of novel category-independent features. To overcome the limitation of 2D saliency and superpixels, we extended algorithms to compute 3D saliency and oversegments. Based on 2D and 3D saliency and oversegments and boundary information, a set of novel features, including unary, pairwise, and higher order clique features are developed. Then the proposed MRH-CRF model integrates 2D and 3D data into a uniform framework and simultaneously labels them. This novel model takes into account spatial consistency in 2D and 3D space and achieves better detection results. By comparison with state-of-the-art methods, the extensive experiments show that the novel model performs better.

References

1. Alexe B, Deselaers T, Ferrari V (2010) What is an object ?. In: Proceedings of IEEE conference on computer vision and pattern recognition, pp 73–80
2. Babenko B, Yang MH, Belongie S (2011) Robust object tracking with online multiple instance learning. IEEE Trans Pattern Anal Mach Intell 33(8):1619–1632
3. Carreira J, Sminchisescu C (2010) Constrained parametric min-cuts for automatic object segmentation. IEEE Trans Pattern Anal Mach Intell Early Access. doi:10.1109/TPAMI.2011.231
4. Chang CC, Lin CJ LIBSVM : a library for support vector machines 2001. http://www.csie.ntu.edu.tw/∼cjlin/libsvm
5. Choi MJ, Torralba A, Willsky AS (Feb. 2012) A tree-based context model for object recognition. IEEE Trans Pattern Anal Mach Intell 34(2):240–252
6. Collet A, Srinivasay SS , Hebert M (2011) Structure discovery in multi-modal data: a region-based approach. In: Proceedings of IEEE international conference robotics and automation, pp 5695–5702, 2011
7. Endres I, Hoiem D (2010) Category independent object roposals. In: Proceedings of European conference on computer vision, pp 575–588, 2010
8. Farhadi A, Endres I, Hoiem D, Forsyth D (2009) Describing objects by their attributes. In: Proceedings of IEEE on conference computer vision and pattern recognition, pp 1778–1785
9. Felzenszwalb P, Huttenlocher D (Sep. 2004) Efficient graph-based image segmentation. Int J Comput Vis 59(2):167–181

10. Feng J, Wei Y, Tao L, Zhang C, Sun J (2011) Salient object detection by composition. In: Proceedings of IEEE international conference on computer vision, 2011
11. Goferman S, Zelnik-Manor L, Tal A (2010) Context-aware saliency detection. IEEE Trans Pattern Anal Mach Intell Early Access. doi:10.1109/TPAMI.2011.272
12. Ion A, Carreira J, Sminchisescu C (2011) Image segmentation by figure-ground composition into maximal cliques. In: Proceedings of IEEE international conference on computer vision, 2011
13. Itti L, Koch C, Niebur E (Nov. 1998) A model of saliency-based visual attention for rapid scene analysis. IEEE Trans Pattern Anal Mach Intell 20(11):1254–1259
14. Kohli P, Ladicky L, Torr PHS (2009) Robust higher order potentials for enforcing label consistency. Int J Comput Vis 82(3):302–324
15. Lai k, Bo L, Ren X, Fox D (2011) A large-scale hierarchical multi-view RGB-D object dataset. In: Proceedings of IEEE international conference on robotics and automation, pp 1817–1824, 2011
16. Levinshtein A, Sminchisescu C, Dickinson S (2010) Optimal contour closure by superpixel grouping. In: Proceedings of European conference computer vision, pp 480–493, 2010
17. Li Y, Yan J, Zhou Y (2009) Visual saliency based on conditional entropy. In: Proceedings of Asian conference on computer vision, 2009
18. Maire M, Arbelaez P, Fowlkes C, Malik J (2008) Using contours to detect and localize junctions in natural images. In: Proceedings of IEEE conference on computer vision and pattern recognition, 2008
19. Rahtu E, Kannala J, Blaschko M (2011) Learning a category independent object detection cascade. In: Proceedings of IEEE international conference computer vision
20. Ren X, Fowlkes C, Malik J (2006) Figure/ground assignment in natural images. In: Proceedings of European conference computer vision, 2006
21. Russell BC, Efros AA, Sivic J, Freeman WT, Zisserman A (2006) Using multiple segmentations to discover objects and their extent in image collections. In: CVPR, 2006
22. Saenko K, Karayev S, Jia Y, Shyr A, Janoch A, Long J, Fritz M, Darrell T (2011) Practical 3-D object detection using category and instance-level appearance models. In: Proceedings of IEEE international conference intelligent robots and systems, pp , 2011
23. Shi J, Malik J (Aug. 2000) Normalized cuts and image segmentation. IEEE Trans Pattern Anal Mach Intell 22(8):888–905
24. Shotton J, Winn J, Rother C, Criminisi A (2009) TextonBoost for image understanding: multi-class object recognition and segmentation by jointly modeling texture, layout, and context. Int J Comput Vis 81(1):2–23
25. Sutton C, McCallum A (2005) Piecewise training for undirected models. In: Proceedings of annual conference on uncertainty in artificial intelligence, pp 568–575, 2005
26. Veksler O, Boykov Y, Mehrani P (2010) Superpixels and supervoxels in an energy optimization framework. In: Proceedings of European conference on computer vision, pp 211–224, 2010
27. Zhang JH, Xiao J, Zhang J, Zhang H, Chen SY (2011) Integrate multi-modal cues for category-independent object detection and localization. In: Proceedigs of IEEE international conference intelligent robots and systems, pp 801–806, 2011

Research on Orbiting Information Procession of Satellites Based on Parallel Management

Yining Song and Dongdong Yan

Abstract The orbit attribution is the most important information on space object. Therefore, parallel management is channeled when complicated and systematic projects are decided and evaluated. Its method and process are applied to the study of system simulation. Traditionally, large-scale simulation and control of the system depended on single model simulation and traditional control approaches for making the target system under control at the only past time. However, the parallel management methods' application will get the system under control and be accurate for a long time in the future. The paper briefly reviews ACP theory and data-based iterative learning control, then points out the necessity and feasibility of the combination of parallel control and iterative control by putting out the structure of NN iterative learning controller. The space objects prove the methods by calculating the orbit attribute at the end of the paper. This paper focuses on parallel management principles and makes further studies of its implementation methods for trying to offer some theory achievements and practical experiences for future researches.

Keywords Parallel management · Iterative control · Learning control · Space object information processing

1 Introduction

Nowadays, both the theory and method of parallel management system have gained key breakthroughs based on parallel management theory. Meanwhile, great improvements have been obtained in practice: such as basic ideas, concepts, and operation framework of parallel system method (Feiyue Wang), which have been a

Y. Song (✉) · D. Yan
The Academy of Equipment of PLA, Beijing, China
e-mail: syn@mail.ustc.edu.cn

F. Sun et al. (eds.), *Foundations and Practical Applications of Cognitive Systems and Information Processing*, Advances in Intelligent Systems and Computing 215,
DOI: 10.1007/978-3-642-37835-5_55,

workable way to manage and control complicated systems; social computation and parallel management system which has been an important research subject in 22 strategic technology issues in the 2050 technology roadmap. Hence, researches related to such fields will still be a hot subject and attract wide attention [1, 2].

Recently, parallel management is mainly applied to simulate and control complicated systems, such as process monitoring and behavior management in engineering and construction, composition control in agriculture and manufacture industry, fire prevention and control, security control in urban rail transit, analysis and warning in social emergency system, national strategic analysis, and so on. Besides, PMS is used in these fields.

In existing parallel management studies, great achievements have been gained in system mode, analysis, and parallel execution. At the same time, it has won good theory accumulations and social benefits.

In this paper, we analyze parallel management of complicated systems, including electricity, traffic, and petrochemical industry. The result indicates that most systems continue to use standard method system, artificial system, computational experiments, parallel execution (ACP), and theory system to make studies. However, no further studies are related to decision intervention, decision feedback, system evaluation, and risk evaluation in theory method of parallel management principle. Therefore, this paper focuses on parallel management, and applies its ideas and methods to the process of management decisions and evaluations. Through comparative studies, orbit calculation methods are developed on the basis of parallel execution and former researches. Furthermore, operational problems in the practice of parallel management are solved.

2 Methodology

The study principle and methods of parallel management are put forward by the Chinese Science Academy Automatic Institute which combines artificial intelligence with control management. It is a theoretic system which establishes model according to artificial systems, stimulates with computers, and undertakes in parallel way. As a framework, parallel management is suitable for model establishment, analysis, control, and management for complicated systems. Generally, we name it as parallel management if ACP theory is applied into complicated production system.

When ACP theory is put into practice, usually, it is processed as follows:

(1) Establish a suitable model system and form artificial system's framework.
(2) Use computing simulative method and software technology to design corresponding computational way. Besides, computer experiment simulation is adopted to analyze practical system and study its disciplines.
(3) Artificial system and real system execute in a parallel way and control the practical situation.

As mentioned above, it is a must to set up a systematic work mechanism when parallel management method is applied in information processing. Besides, its work process should be structured so that parallel satellite system can be formed.

3 Parallel Execution Algorithm

3.1 Formulas

Neural network theory, as a branch of intelligent control, with its unique non-traditional expression way and inherent ability to learn caused extensive concern of the field of control, and the application fields to reach unprecedented breadth, especially in artificial intelligence, automatic control, computer science, information processing, robot, and pattern recognition of typical application.

Neural network in the role of the control study fields can be divided into:

(1) Indirect Self-tuning Control

By using the neural network computing power of the estimator of conventional controller parameters optimization solution, so as to achieve the conventional controller parameters or structure adjustment. Scheme advantage can in time obtain the satisfactory in order of magnitude real-time vector parameter, and convergence has nothing to do with the number of parameters.

(2) Feed-forward Direct Control

Using neural network modeling capability for system inverse dynamics modeling can make the entire closed-loop system input/output mapping for the identical mapping, so as to achieve the tracking control. Its advantage is to take full advantage of the modeling capabilities of neural networks. It is insufficient as the robustness is not good in the beginning.

(3) Inverse Dynamic Control

The inverse dynamic neural network model of the plant works as a controller and be put serially before the plant. The disadvantage is that the control structure requires the plant dynamic reversible, due to the inverse dynamic characteristics of the plant does not always exist; besides, reversibility study of nonlinear system is difficult.

(4) Model Reference Adaptive Control

This control structure and linear system model reference adaptive control system are all the same, only to be accused of object identification model for neural network.

(5) Feedforward-Feedback Joint Neural Network Control

It is a kind of neural network feedforward control, which makes the advance of the system initial robustness. When the system works, the neural network parameters are getting error calibration online.

(6) Predictive Neural Network Control

The neural network predictor establishes the prediction model of the nonlinear plant. Then online correction can finally forecast the output of the plant for a certain length of time in the future by the current control inputs.

Neural networks with the capability of approaching arbitrarily nonlinear mapping and learning and adapting to the dynamic characteristics of the position of uncertain systems, can learn and adapt to the dynamic characteristics of the systems with uncertain position. By applying neural network theory and using the neural network to estimate the expectations of the system control input, we can get the iterative learning control input of the system. Then by continuous improving the control input in this way, the actual output of the system only requires fewer iterations to achieve the required accuracy. The structure of the neural network iterative learning controller is shown in Fig. 1.

Neural network iterative learning controller based on the collected within the control of the former $K-2$, $K-1$, K error $e_{K-2}(t)$, $e_{K-1}(t)$, $e_K(t)$ as the input sample of neural networks, in the case of off-line network training. Three-layer neural network can be used in order to ensure the convergence of the neural network controller, the hidden layer nodes are S-shaped transfer function and output layer nodes using a linear transfer function. Neural network according to the first few cycles the error $e_{K-2}(t)$, $e_{K-1}(t)$, $e_K(t)$ to provide the nonlinear term approximation the $u_K^{ff}(\mathrm{t})$. Controller works as follows as shown in Fig. 2.

3.2 Neural Network Based on LM Algorithms

The LM algorithm is a kind of improved Gaussian-Newton method, it can make BP neural network learning number is greatly reduced and the precision and stability in also have greatly improved. The original BP algorithm gradient descent

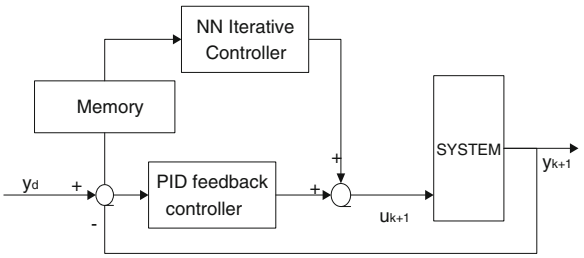

Fig. 1 Structure of the neural network iterative learning controller

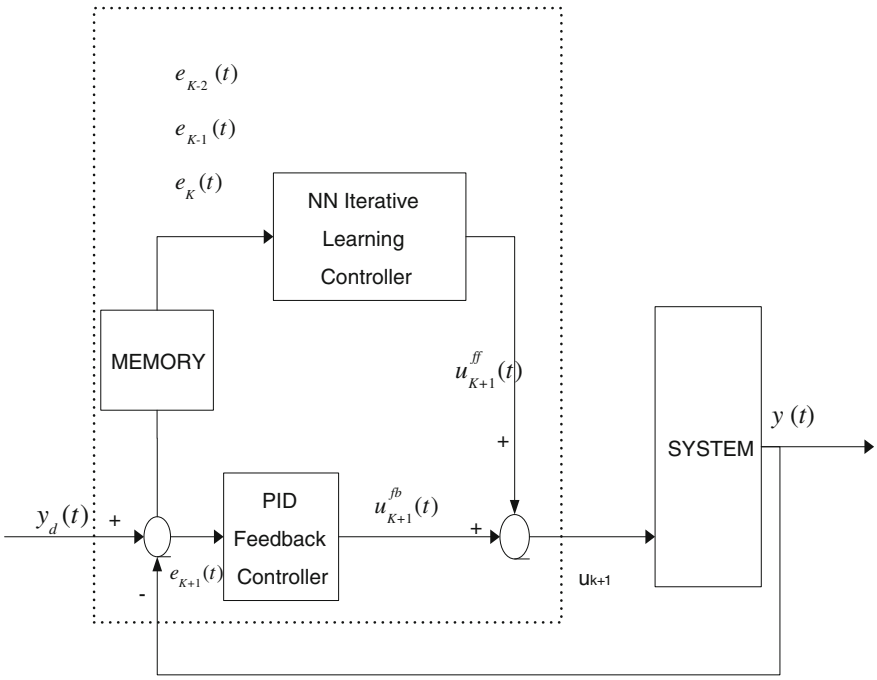

Fig. 2 Schematic diagrams of the neural network iterative learning controller

of thoughts make slow convergence speed shortcomings, the improved method is of two kinds: heuristic learning method (such as drive the amount of gradient algorithm) and more effective optimization algorithm (such as conjugate gradient and Newton method), etc. LM it is will the gradient descending method and Gaussian-Newton method, which can meet the requirements of the local convergence and meet the global properties.

3.3 The Basic Principles of LM algorithm

Make $x^{(m)}$ as the mth iterations of the weights and the threshold vector, vector $x^{(m+1)}$ as the modified new weights and thresholds.

$$x^{(m+1)} = x^{(m)} + \Delta x \tag{1}$$

$$\Delta x = -\left[J^T(x)J(x) + \mu I\right]^{-1} J(x)e(x) \tag{2}$$

$$J(x) = \begin{vmatrix} \frac{\partial e_1(x)}{\partial x_1} & \frac{\partial e_1(x)}{\partial x_2} & \cdots & \frac{\partial e_1(x)}{\partial x_n} \\ \frac{\partial e_2(x)}{\partial x_1} & \frac{\partial e_2(x)}{\partial x_2} & \cdots & \frac{\partial e_2(x)}{\partial x_n} \\ \vdots & \vdots & \ddots & \vdots \\ \frac{\partial e_N(x)}{\partial x_1} & \frac{\partial e_N(x)}{\partial x_2} & \cdots & \frac{\partial e_N(x)}{\partial x_n} \end{vmatrix} \tag{3}$$

Among them, μ is a constant, I is the unit array. And when $\mu = 0$, it comes to the Gaussian-Newton method; Due to LM algorithm using the approximate of second order derivative information, it speeds on the few even one hundred times than the gradient descending method. As to $[J^T(x)J(x) + \mu I]$ is positive, so there must be solutions of $\Delta x = -[J^T(x)J(x) + \mu I]^{-1}J(x)e(x)$. Since then, this method is better than Gaussian-Newton method which needs to test the conditions of whether the rank of $J^T(x)J(x)$ is full.

3.4 The Calculation Consumption of LM Algorithm

(a) Given the allowable value of training error, ε, β, μ_0, and the initial weights and threshold vector x^0, set $k = 0$, $\mu = \mu_0$.
(b) Calculate the network output and error index function $E(x^{(m)})$.
(c) Calculate the Jacobian matrix $J(x)$.
(d) Calculate Δx and $E(x^{(m)})$.
(e) Judge $E\left(x^{(m)}\right) < \varepsilon$, and if it is true, jump to step (g). If not, make $x^{(m+1)}$ for the value of weight and threshold to calculating error index function $E\left(x^{(m+1)}\right) = x^{(m+1)}E\left(x^{(m)}\right)$.
(f) If $E\left(x^{(m+1)}\right) < E\left(x^{(m)}\right)$, then set $m = m + 1$, $\mu = \mu/\beta$, and back to step (b), if not, set $x^{(m+1)} = x^{(m)}$, $\mu = \mu\beta$, and back to step (d).
(g) End.

4 Calculation of Orbit Information by Learning Methods

Orbit attribute is the important property of space objects. Research on this is the basis of research for space science. Therefore, take the debris and other space objects as examples for the study of space objects' orbit calculation.

4.1 The Calculation Consumption of LM Algorithm

In a right the inertial frame, according to Newton's second law, the satellite perturbation motion equation for:

$$F = m\ddot{r} = F_0 + f_g + f_m + f_s + f_d + f_v + f_t. \tag{4}$$

As:

- m is the mass property of satellite.
- F_0 is the earth gravity center.
- f_g is the earth's gravity in addition to the center of gravity.
- f_m is the moon's gravity.
- f_S is the sun's gravity.
- f_d is the atmospheric drag.
- f_v is the solar radiation pressure.
- f_t is the additional force from the earth tides.

Set the orbit elements of the satellite for σ, then the mean elements are,

$$\overline{\sigma} = \sigma - \Delta\sigma_S. \tag{5}$$

With the orbit elements as the form of $a, i, \Omega, \xi = e\cos\omega, \eta = -e\sin\omega, \lambda = M + \omega$. Then the orbit elements $\bar{\sigma}_0$ of the init time t_0 are as follows.

$$\bar{\sigma}_0 = \sigma_0 - \left[\Delta\sigma_0^{(1)}\right]_0. \tag{6}$$

And the init orbit elements $\bar{\sigma}^{(1)}$ of the mean orbit elements $\bar{\sigma}^{(2)}$ at the time t are as follows.

$$\left.\begin{aligned}
\overline{a}^{(1)} &= \overline{a_0} \\
\overline{i}^{(1)} &= \overline{i_0} \\
\overline{\Omega}^{(1)} &= \overline{\Omega_0} + \Omega_1 T \\
\overline{\xi}^{(1)} &= \overline{\xi_0}\cos(\omega_1 T) + \overline{\eta_0}\sin(\omega_1 T) \\
\overline{\eta}^{(1)} &= \overline{\eta_0}\cos(\omega_1 T) - \overline{\xi_0}\sin(\omega_1 T) \\
\overline{\lambda}^{(1)} &= \overline{\lambda_0} + (1+\lambda_1)T + \frac{1}{2}\dot{n}(t-t_0)^2 + \frac{1}{6}\ddot{n}(t-t_0)^3 + \frac{1}{24}\dddot{n}(t-t_0)^4 \\
T &= \overline{n_0}(t-t_0), \overline{n_0} = (\overline{a_0})^{-\frac{3}{2}}
\end{aligned}\right\} \tag{7}$$

the mean orbit elements $\overline{\sigma}^{(2)}$ at the time t are as follows

$$\left.\begin{aligned}
\overline{a}^{(2)} &= \overline{a}^{(1)} + (a_{22} + a_{23})(t - t_0) \\
\overline{i}^{(2)} &= \overline{i}^{(1)} + (i_{20} + i_{21} + i_{22} + i_{23} + i_{24})(t - t_0) \\
\overline{\Omega}^{(2)} &= \overline{\Omega}^{(1)} + (\Omega_{20} + \Omega_{21} + \Omega_{22} + \Omega_{23} + \Omega_{24})(t - t_0) \\
\overline{\xi}^{(2)} &= \overline{\xi}^{(1)} + (\xi_{20} + \xi_{21} + \xi_{22} + \xi_{23} + \xi_{24})(t - t_0) \\
\overline{\eta}^{(2)} &= \overline{\eta}^{(1)} + (\eta_{20} + \eta_{21} + \eta_{22} + \eta_{23} + \eta_{24})(t - t_0) \\
\overline{\lambda}^{(2)} &= \overline{\lambda}^{(1)} + (\lambda_{20} + \lambda_{21} + \lambda_{22} + \lambda_{23} + \lambda_{24})(t - t_0)
\end{aligned}\right\} \tag{8}$$

$$\sigma(t) = \overline{\sigma}^{(2)} - \Delta\sigma_S^{(1)}(t). \tag{9}$$

4.2 Orbit Data Processing

Orbit determination, the first spacecraft observations of ground stations for data processing, data processing, including removing the outliers, removes some of the patently unreasonable data (including atmospheric refraction correction and measurement of certain concept of light amended). Then do the initial orbit calculation, and second, first, as the initial value of the orbital simulation for real-time orbit to monitor the fast and accurate orbit parameters to determine the spatial objectives in the design orbit. The last are the orbit correction and orbit determination of main content. Its mission is to observe data from a series of longer time intervals and a set of time roughly track the root of the number (or coordinates, speed), making use of perturbation theory to calculate the orbital elements on time (or coordinates, speed) correction, in order to get the precise moment of the orbital elements (or coordinates, speed). Figure 3 based on the design of time domain and the simple iterative domain iteration algorithm process schematic diagram as Fig. 4 at the end of the paper.

4.3 Simulation Results

First, we list some typical space objects information to make the space information cleared to be studied [3] (Table 1).

All space objects are classified by NORAD as near-Earth (period less than 225 min) or deep-space (period greater than or equal 225 min). Depending on the period, the NORAD element sets are automatically generated with the near-Earth or deep-space model. The user can then calculate the satellite period and know which prediction model to use.

Five mathematical models for prediction of satellite position and velocity are available. The first of these, SGP, was developed by Hilton & Kuhlman (1966) and

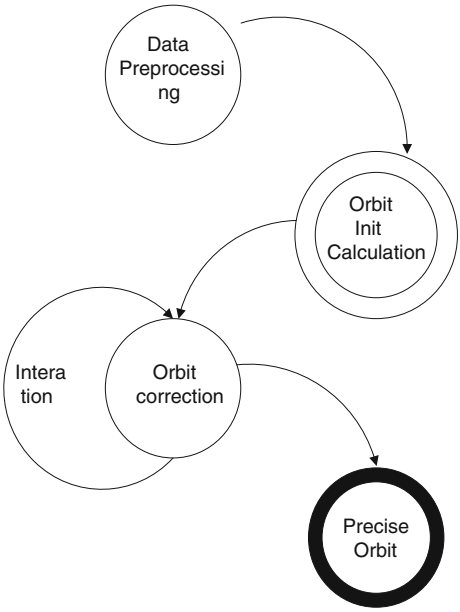

Fig. 3 Data processing

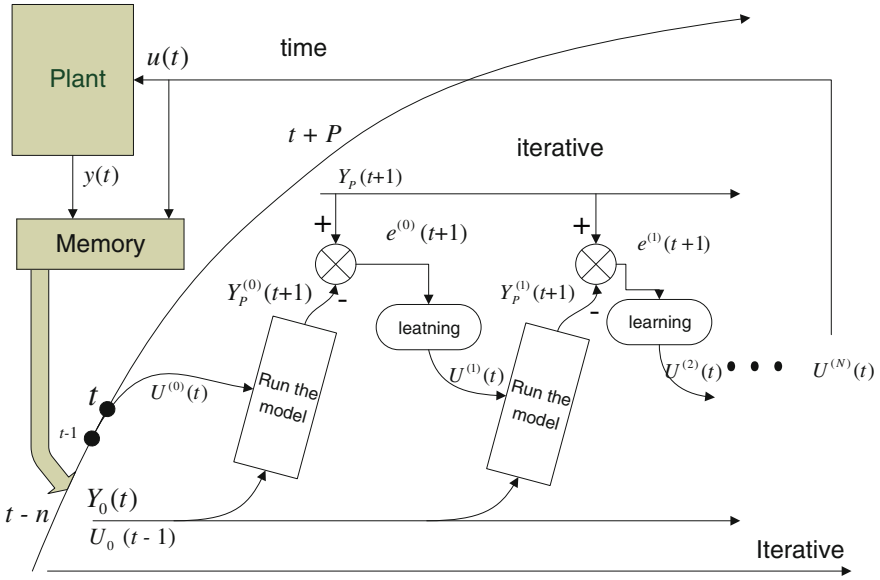

Fig. 4 Flowchart of iterative learning controller working process

Table 1 Typical space debris' informations

SSC numbers	Type	Generation times (years)	Owned country	Altitude of apogee (km)	Altitude of perigee (km)
27634	Debris	2002	CH	352	318
27784	3rd Stage	2003	USA	698	690
27479	Debris	1963	USA	1068	1058
26858	Centaur motor	2001	USA	10108	9811
27620	4th stage	2002	CIS	19109	19096
27780	4th stage	2003	CIS	35863	35776
27814	3rd stage	2003	CH	41608	217

Table 2 (ID 27634) Orbit calculation

27634	B^*	i (°)	Ω (°)	e	ω (°)	M (°)	n (revs/day)
STK (a)	16717-2	42.4362	346.8894	0035548	276.2936	153.7571	15.77934101
Single (SGP4)	50509-4	42.4343	346.8743	0033629	275.9274	154.1021	15.77943064
SGP4 (b)	17918-3	42.4362	346.8903	0035394	275.9677	154.0826	15.77934057
SGP8 (c)	18491-3	42.4363	346.8921	0043536	276.0563	154.1982	15.77837876

Table 3 (ID 27634) Orbit calculation

Days	1	2	3	4	5
B^*	17125-4	17158-4	17402-4	17631-4	17933-4
i (°)	42.4363	42.4363	42.4362	42.4362	42.4356
Ω (°)	346.8844	346.8858	346.8872	346.8909	346.8981
e	0034892	0036236	0037618	0039157	0040289
ω (°)	275.9420	275.9425	275.9480	275.9540	275.9735
M (°)	154.0848	154.0852	154.0904	154.0964	154.1159
n(revs/day)	15.77942761	15.77940589	15.77930319	15.77917511	15.778957
a (km)	6714.407229	6714.413388	6714.442523	6714.478859	6714.540858

is used for near-Earth satellites. This model uses a simplification of the work of Kozai (1959) for its gravitational model and it takes the drag effect on mean motion as linear in time. This assumption dictates a quadratic variation of mean anomaly with time. The drag effect on eccentricity is modeled in such a way that perigee height remains constant. After all, the SGP model calculates the TLE data can get us the relatively precise orbit data.

By using the methods in this paper, we take the TLE data as the init input, and then through the learning iterative controller, we finally get the results of the orbit of the space objects. The results are shown as follow forms.

5 Conclusion

Parallel management method is significant both in the theory and practice. It is formed with parallel management ideas. The application of parallel management in information processing perfects practical application results. Besides, the application of parallel management ideas has been widened greatly with parallel system of space objects.

Regarding this study, more studies and expansions are needed in the following aspects:

(1) Existing prototype of computer simulative system. How to apply project methods to parallel management decision system quickly.
(2) During the model establishment and computation for complicated systems, the complexity of information processing proposition is increasing rapidly which is difficult for computational methods and system simulative technology.
(3) Existing iteration approach of the parallel execution is prototype system and needs popularization and wide application.

As a processing method, parallel management is being popularized and applied recently, especially in society. This study involves many subjects and has a wide perspective with a higher system complexity. It is an important. It is the key way to solve social issues in large-scale companies. This system will surely promote parallel management to support the needs of management decision and evaluation application (Tables 2, 3).

References

1. Wang FY (2007) Toward a paradigm shift in social computing: the ACP approach. IEEE Intell Syst 22(5):65–67
2. Wang FY (2004) Social computing: concepts, contents, and methods. Int J Intell Control Syst 9(2):91–96
3. Klinkrad H (1997) One year of conjunction events of ERS-1 and ERS-2 with objects of the USSPACECOM catalog. In: Proceeding of the 2nd European conference on space debris

Multi-sensor Multi-Target Detection Based on Joint Probability Density

Can Xu, Zhi Li and Lei Shi

Abstract Joint probability density algorithm (JPDA) is extended to multi-sensor multi-target detection based on 'Clean' method. Key content and characteristic of JPDA in false intersection points eliminating are introduced. An iterative method for multi-sensor multi-target detection is put forward. Based on target that has been detected by peak searching, an inverse probability density function is proposed which is able to eliminate both the detected target and false intersection points. A new joint probability density matrix is constructed and all the targets can be detected through iterative process. The feasibility and validity are verified through simulation.

Keywords Multi-sensor multi-target detection · Inverse joint probability density · Clean method

1 Introduction

For multi-sensor multi-target system, targets detection is a complex problem for the incompletion of measurements from passive sensors. Many algorithms have been proposed, such as linear least squares (LLS) approach [1], traditional maximum likelihood approach (TML) [2], and other approaches based on the two approaches. These approaches have been proved to be useful in practice. However, approaches mentioned above are designed for special kinds of sensors only.

A method of localization approach based on maximum joint probability density is put forward in [3]. Joint probability density of sensors is used to solve the problem of localization. The method is applicable to passive sensors only and

C. Xu (✉) · Z. Li · L. Shi
The Academy of Equipment, Beijing, China
e-mail: dacangedangshan@yahoo.com.cn

F. Sun et al. (eds.), *Foundations and Practical Applications of Cognitive Systems and Information Processing*, Advances in Intelligent Systems and Computing 215,
DOI: 10.1007/978-3-642-37835-5_56,

many approximations are made in order to adopt LLS method. A more universal localization algorithm that suits to different kinds of sensors based on JPD is given in [4]. Although the algorithm has been verified by some simulation experiments, there are some key problems still remaining unresolved. One problem is false intersection point's elimination, as a common problem in data fusion area. Many special methods have been put forward to solve the problem such as association algorithm in [5] and cross-location algorithm in [6]. Algorithms of eliminating false intersection points based on redundant information are discoursed in [7] and reference there in. As JPDA is an algorithm based on random probability density, peak values varied according to measurement errors and this makes multi-target detection difficult.

In this paper, we put forward a resolution to make JPDA more applicable. We introduce key contents of JPDA in Sect. 2 and propose false intersection point problem in Sect. 3. An iterative algorithm is proposed based on 'Clean' idea to perform multi-sensor multi-target detection in Sect. 4.

2 Joint Probability Density Algorithm

2.1 Measurement Distribution

In order to estimate target position, three basic measurements may be obtained in local sphere coordinates (X_s, Y_s, Z_s) for a common sensor, i.e., range (R), elevation (θ), and azimuth (φ) are shown in Fig. 1 as follows. (X, Y, Z) is the global Cartesian coordinates. Point A lies in (X_s, Y_s)-plane and AT is perpendicular to (X_s, Y_s)-plane. The Cartesian coordinates we mentioned is global Cartesian coordinates, the sphere polar coordinates is local sphere coordinates of sensor without exception in this paper.

Because of effects inside and outside of the sensor system, measurement noise always exits. Gauss distribution is a common distribution used in practice and has been proved to be credible. It assumes that the measurement noise obey Gauss (normal) distribution.

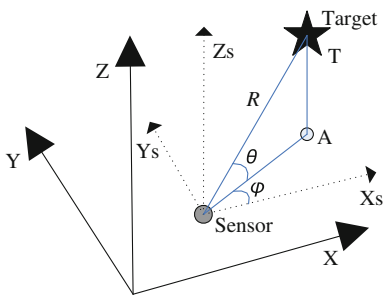

Fig. 1 Target in local sphere polar coordinates and global Cartesian coordinates

(1) Range

When range measurement r_i is obtained, the probability density function in local sphere polar coordinates is:

$$p(r|r_i) = \frac{1}{\sqrt{2\pi}\sigma_{ri}} \exp\left[-\frac{(r-r_i)^2}{2\sigma_{ri}^2}\right] \tag{1}$$

where σ_{ri} is the accuracy of range measurement, $r = f_r(\mathbf{X}, i) = \sqrt{(x - x0(i))^2 + (y - y0(i))^2 + (z - z0(i))^2}$ is the range between the ith sensor and point $\mathbf{X} = (x, y, z)^{\mathrm{T}}$ in Cartesian coordinates, ($x0(i)$, $y0(i)$ $z0(i)$) is the coordinate of the ith sensor.

(2) Elevation and azimuth

When measurements θ_i (elevation) and ϕ_i (azimuth) are obtained, PDF(s) in local sphere polar coordinates are:

$$\begin{aligned} p(\theta|\theta_i) &= \frac{1}{\sqrt{2\pi}\sigma_{\theta i}} \exp\left[-\frac{(\theta-\theta_i)^2}{2\sigma_{\theta i}^2}\right] \\ p(\varphi|\varphi_i) &= \frac{1}{\sqrt{2\pi}\sigma_{\varphi i}} \exp\left[-\frac{(\varphi-\varphi_i)^2}{2\sigma_{\varphi i}^2}\right] \end{aligned} \tag{2}$$

where $\sigma_{\theta i}$ and $\sigma_{\varphi i}$ is the accuracy of elevation and azimuth measurement, respectively, $\theta = f_\theta(\mathbf{X}, i) = \arcsin\left[(z - z0(i))/\sqrt{(x - x0(i))^2 + (y - y0(i))^2 + (z - z0(i))^2}\right]$ and $\varphi = f_\varphi(\mathbf{X}, i) = \arctan((y - y0(i))/(x - x0(i)))$ are elevation and azimuth angles of spatial point **X,** respectively.

Key note. When the directions of axis are not the same with the global Cartesian coordinates, a transformation is needed.

(3) Mapping probability density

From the relationship between (x, y, z) and (r, θ, φ), we can express the probability density in sphere polar coordinates with **X**:

$$\begin{aligned} p(r|r_i)_{r=f_r(\mathbf{X},i)} &= \frac{1}{\sqrt{2\pi}\sigma_{ri}} \exp\left[-\frac{(f_r(\mathbf{X},i)-r_i)^2}{2\sigma_{ri}^2}\right] \\ p(\theta|\theta_i)|_{\theta=f_\theta(\mathbf{X},i)} &= \frac{1}{\sqrt{2\pi}\sigma_{\theta i}} \exp\left[-\frac{f_\theta(\mathbf{X},i)-\theta_i)^2}{2\sigma_{\theta i}^2}\right] \\ p(\varphi|\varphi_i)|_{\varphi=f_\varphi(\mathbf{X},i)} &= \frac{1}{\sqrt{2\pi}\sigma_{\varphi i}} \exp\left[-\frac{(f_\varphi(\mathbf{X},i)-\varphi_i)^2}{2\sigma_{\varphi i}^2}\right] \end{aligned} \tag{3}$$

For every spatial point in Cartesian coordinates, the probability density in local sphere polar coordinates can be obtained from the expression above. The expression what we got here, although in the term of (x, y, z) in Cartesian coordinates, means probability density in local sphere polar coordinates.

It is very necessary to point out that the probability density in sphere polar coordinates draw as (3) does not means probability density in Cartesian coordinates. However, mapping the value of PDF in sphere polar coordinates into Cartesian coordinates is meaningful when we want to locate a target in Cartesian coordinates with multi-sensor. In order to make clear in concept, we call the mapping probability density function in Cartesian coordinates as "MPDF".

2.2 Joint Probability Density of Multi-sensor

According to statistical theory, if the elements are independent from each other, joint probability density function can be obtained by multiplying all the MPDFs as follows:

$$p(x, y, z|r_1, \theta_1, \varphi_1, \ldots, r_L, \theta_L, \varphi_L) = \prod_{i=1}^{L} p_i(x, y, z|r_i, \theta_i, \varphi_i) = \prod_{i=1}^{L} P_{\mathrm{i}} \tag{4}$$

where L is the number of sensors.

If a sensor cannot provide one of the measurements, the MPDF is assumed to be unit.

When the ith sensor has M measurements synchronously, in order to make all measurements protuberant in probability space, all MPDFs should be added up and the whole MPDF of the ith sensor can be expressed as:

$$P_i = \sum_{m=1}^{M} P_{im} \tag{5}$$

where P_{im} is the MPDF of the mth measurement from the ith sensor.

3 False Intersection Points Elimination

3.1 Realization of JPDA with False Intersection Points

In order to indicate the result of MPDF, take two sensors for two targets in two-dimension with configuration in Table 1 for example. The first sensor gets range measurements only and the second sensor gets azimuth measurements only.

It assumes that all sensors work independently and every sensor gets two measurements, false intersection points appear as sensors cannot provide enough

Table 1 Simulation configuration

Items	Values
Targets position	(20, 20) km; (30, 20) km
The 1st sensor: position and measure accuracy	(0, 0) km; 100 m (range only)
The 2nd sensor: position and measure accuracy	(10, 0) km; 1° (azimuth only)

information about targets. Figure 2a is the contour of two sensors' overlapping PDF and Fig. 2b is the JPDA contour. Except for two real targets, the other two false interaction points are detected too. As the information provided by two sensors is not enough, false interaction points appear.

False intersection points will explode with large number of targets in practice. Take two sensors above for example, when n targets exist, n^2 points will be detected. This makes real targets detection hard in practice. There are already several methods to eliminate false intersection points as we mentioned in Sect. 1. One powerful method is the association method when more sensors are added. But more sensors bring about high computation burden in traditional method. In order to make JPDA more practical, we will discuss performance of JPDA in false intersection points eliminating with redundant information.

3.2 False Intersection Points Elimination with JPDA

This part we will take only three azimuth sensors located at XOY plane for two independent and identical targets for example. Redundant information is generated to locate targets. The probability density of azimuth only sensor in global coordinates is a line and the line width is determined by its' accuracy. In order to illustrate clearly, a sketch map is given out in Fig. 3.

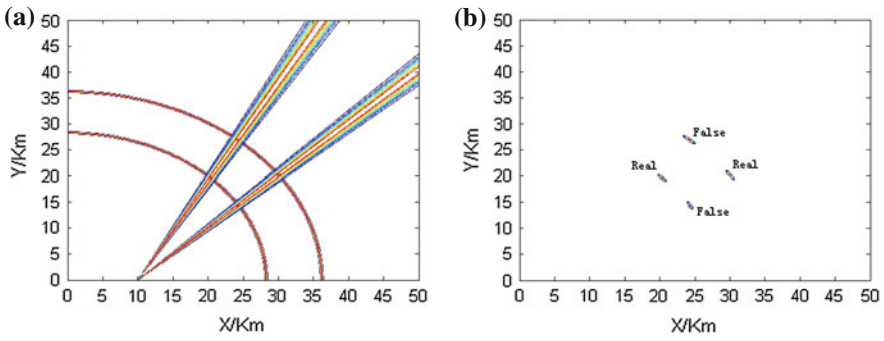

Fig. 2 Localization results with two ghost points. **a** Overlap PDF contour of two sensors. **b** JPDF contour of two sensors

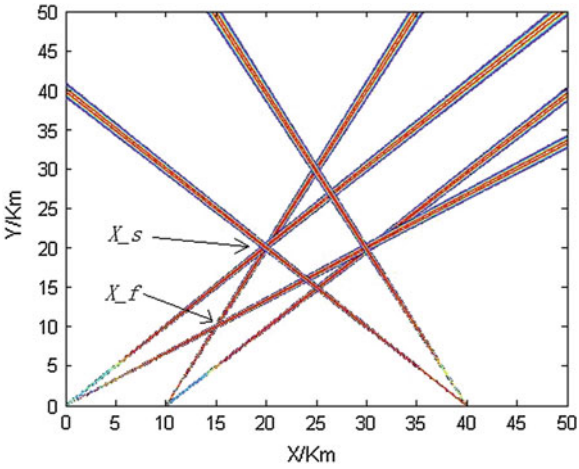

Fig. 3 Overlap probability of three sensors for two targets

It is obviously known that two unparalleled lines will intersect only once. Only the point corresponding to real target could be the intersection points of all the sensors. JMPD at $\mathbf{X}$ can be expressed as follows:

$$\mathrm{JMP}_s(\mathbf{X}) = \prod_{i=1}^{3} \mathrm{MP}_i(\mathbf{X}) \tag{6}$$

where $\mathrm{MP}_i(\mathbf{X})$ is mapping probability density of the ith sensor.

When $\mathbf{X}$ locates around real target such as $\mathbf{X}\_s$ in Fig. 3, all the mapping probability density functions in (6) has large value according to the characteristic of Gauss distribution. But when $\mathbf{X}$ locates around false intersection point such as $\mathbf{X}\_f$, the mapping probability density functions of the third sensor at (40, 0) km is very small. So the joint mapping probability density is far less than the value at $\mathbf{X}\_s$ and false intersection points are eliminated.

4 Multi-sensor Multi-target Detection Algorithm

From the expressions (1)–(3), for the situation of multi-sensor multi-target, joint probability density may vary widely as sensor measurement error is a random variable. When a sensor has large measurement error, MPD will be small. An example is given out in Fig. 4 to indicate the difference between different targets. Three peaks appeared in MPD domain, but the values vary widely. What's more, this makes the false intersection points generated by precise measurement appear as the interfering factors for other targets detection.

For multi-sensor multi-target situation, peak searching can be used to locate the target with maximum value only and the other targets are hard to detect. Based on

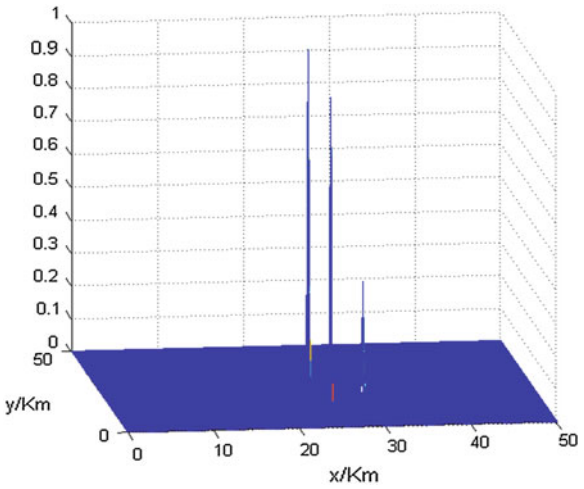

Fig. 4 Multi-sensor multi-target detection

the idea of detecting targets one by one which is also known as 'Clean' method, we proposed a new algorithm which is able to solve all the problems above.

When JMPD is obtained, the process of the algorithm can be decomposed into four steps as follows:

Step 1: Locate the first target through peak searching. As we analyzed in Sect. 3, the value of intersection points is far less than real targets. So the point corresponding to the maximum value must be a real target. We denote the point as $\mathbf{X}_1$ and the JMPD matrix as $\mathbf{P}_1$;

Step 2: For $1 < m < M$ (M is the maximum number of measurements from one of the sensors), construct *virtual measurement values* with point $\mathbf{X}_m$ and denote them as r_i, θ_i, φ_i for the ith sensor ($i = 1, 2, \ldots, L$). Constructs three functions as following:

$$
\begin{aligned}
p_{\text{inv}}(r|r_i)_{r=f_r(\mathbf{X},i)} &= \frac{1}{\sqrt{2\pi}\sigma_{ri}}\left\{1-\exp\left[-\frac{(f_r(\mathbf{X},\,i)-r_i)^2}{2\sigma_{ri}^2}\right]\right\} \\
p_{\text{inv}}(\theta|\theta_i)|_{\theta=f_\theta(\mathbf{X},i)} &= \frac{1}{\sqrt{2\pi}\sigma_{\theta i}}\left\{1-\exp\left[-\frac{f_\theta((\mathbf{X},\,i)-\theta_i)^2}{2\sigma_{\theta i}^2}\right]\right\} \\
p_{\text{inv}}(\varphi|\varphi_i)|_{\varphi=f_\varphi(\mathbf{X},i)} &= \frac{1}{\sqrt{2\pi}\sigma_{\varphi i}}\left\{1-\exp\left[-\frac{(f_\varphi(\mathbf{X},\,i)-\varphi_i)^2}{2\sigma_{\varphi i}^2}\right]\right\}
\end{aligned}
\tag{7}
$$

Here we denote the functions as *inverse probability density functions*.

Step 3: The corresponding inverse joint probability density matrix can also be formed in the same way with (4), and we denote it as $\mathbf{P}_{\text{inv}}$, the new JMPD matrix can be formed by:

Table 2 Multi-target detection parameters

Items	Values
Targets position	(25, 10) km; (30, 20) km; (25, 30) km
The 1st sensor: position and measure accuracy	(0, 0) km; 0.2°; (azimuth only sensor)
The 2nd sensor: position and measure accuracy	(0, 0) km; 100 m; (range only sensor)
The 3rd sensor: position and measure accuracy	(45, 0) km; 0.2°; (azimuth only sensor)
The 4th sensor: position and measure accuracy	(45, 0)km; 100 m; (range only sensor)

$$\mathbf{P}_i = \mathbf{P}_{i-1} \cdot \mathbf{P}_{\text{inv}} \tag{8}$$

where '·' means the matrix multiplication of elements.

Step 4: Locate the mth target by peak value searching and denote as $\mathbf{X}_i$. If $m < M$, continue to Step 2, else come to the end.

The construction of the inverse probability density function is the key process of the algorithm. From the expression of the inverse probability density, we can see that, for the point $\mathbf{X}$ in Cartesian coordinates, the value is small when $f(\mathbf{X}, i)$ appeared near the virtual measurements and the value approach to $1/\sqrt{2\pi\sigma_i^2}$ when $f(\mathbf{X}, i)$ locate far away from the virtual measurements. When inverse MPD matrix $\mathbf{P}_{\text{inv}}$ is multiplied with true JMPD matrix, the value near targets that have been detected already is eliminated. When peak searching is performed, the second real target can be detected and located soon.

We take four sensors to three targets for example to validate the algorithm. Here we assume one sensor could obtain one kind of measurement only. Parameters are given out in Table 2.

The results are shown out in Figs. 5, 6, and 7.

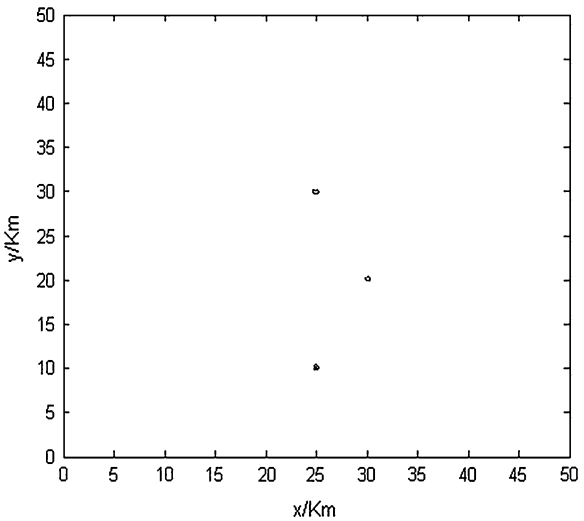

Fig. 5 Origin contour of MPD

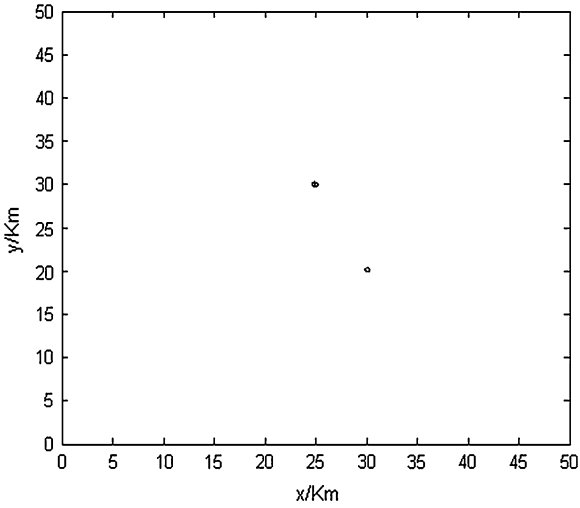

Fig. 6 Contour of MPD after the first peak searching

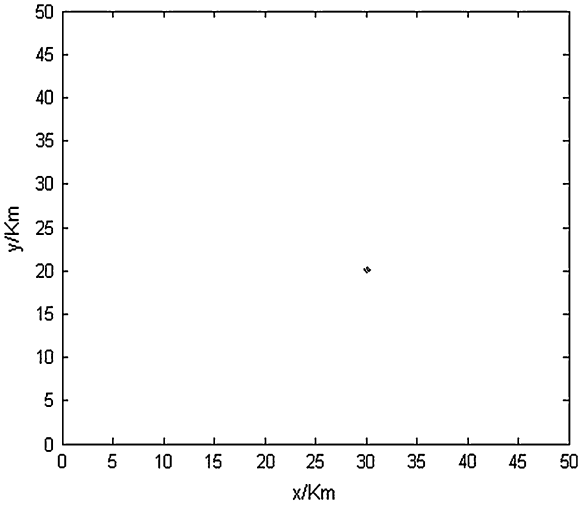

Fig. 7 Contour of MPD after the second peak searching

Figure 5 is the origin contours of MPD generated by JPDA, three targets with different value appear and the false intersection points are eliminated. Figure 6 is the result after the first peak searching and multiplied by the inverse MPD matrix. Target at (25, 10) km is detected and then is eliminated by inverse MPD matrix. Figure 7 is the result after the second iterative process. The target at (25, 30) km is detected and the last target at (30, 20) km is left.

What's more, from the conclusion we draw about false intersection point and real point, we find that the value of real target is much larger than intersection point, the detect results can be confirmed to be real targets and the method still working with false intersection points.

As there is no limitation on sensor type or number, the new method proposed here is an universal method which can be used to perform multi-sensor multi-target detection and location.

References

1. Bar-Shalom Y, Li XR (1995) Multitarget-multisensor tracking: principles and techniques. YBS Publishing, Storrs
2. Gavish M, Weiss AJ (1992) Performance analysis of bearing-only target location algorithms. IEEE Trans Aerosp Electron Syst 28(3):817–827
3. Zeng Z-Y, Chen H, Cai X (2007) New method of multi-stations positioning based on the maximum of joint probability density (in Chinese). Electron Inform Counter Technol 22(5):11–14
4. Zhao Z, Wang X (2009) A multi-sensor localization algorithm based on joint probability density (in Chinese). Chine J Sens Actuators 10(22):1146–1150
5. Li B-B, Wang ZY, Wen X (2008) Fast data association algorithm for passive sensors (in Chinese). Chin J Sens Actuators 21(7):1160–1163
6. Tan K, Chen H, Cai X-X (2009) Research into the algorithm of false points elimination in three-station cross location (in Chinese). Shipboard Electron Countermeas 32(4):80–84
7. Bishop AN, Pathirana PN (2007) Localization of emitters via the intersection of bearing lines: aghost elimination approach. IEEE Trans Veh Technol 56(5):l–5

Robot Learning of Everyday Object Manipulation Using Kinect

Nan Chen, Ying Hu, Jun Zhang and Jianwei Zhang

Abstract In this paper, we provide a solution of teaching a robot to perform tasks through human demonstration. On the one hand, we consider many everyday complex task manipulations made up of manipulation primitives, consisting of a series of sequential rotations and translations. On the other hand, we design demonstration primitives which decompose a demonstrated task. We use Kinect sensor to locate some hot points' position of a teacher's hand during demonstration, in order to gain the axes of those rotations and translations which will support the manipulation primitives that will contribute to building task descriptors. Based on this, we quote a descriptor to represent this manipulation primitive. We also teach the robot where to start and where to end once a manipulation primitive is operating via recording the special two points' coordinates in a real scene while demonstration, which could reinforce robots' learning to those effective and sequential demonstrations and shorten the learning time. One manipulation primitive corresponds with one demonstration primitive. Two kinds of primitives will be connected to the axes of trajectory. After that, we perform experiments to discuss the universality of this framework.

Keywords Robot learning · Human demonstration · Kinect

N. Chen (✉) · Y. Hu · J. Zhang
Shenzhen Institutes of Advanced Technology, Chinese Academy of Sciences, Shenzhen, China
e-mail: nan.chen@siat.ac.cn

N. Chen · Y. Hu · J. Zhang
The Chinese University of Hong Kong, Hong Kong, China

J. Zhang
TAMS, Department of Informatics, University of Hamburg, Hamburg, Germany

F. Sun et al. (eds.), *Foundations and Practical Applications of Cognitive Systems and Information Processing*, Advances in Intelligent Systems and Computing 215,
DOI: 10.1007/978-3-642-37835-5_57,

1 Introduction

Robot learning is a hot topic in the field of robotics research. So far, many researchers have invented different learning methods to improve the robots' ability of operating tasks in their special purposes.

Nowadays, the area of robotics is rapidly developing from industrial environments into indoor environments. Indoor service robots are helping humans in doing meaningful jobs, such as opening doors, opening drawers, pushing buttons, etc. With their help, people can free themselves from many daily chores and enjoy comfortable and convenient lives. Many types of service robots have been developed based on different uses. However, they require researchers who are those robotic experts to teach them skills in a professional channel, and also in a special environment. Most of the previous work usually solves that problem either at a high level [1–3] (i.e. based on completing special tasks, such as opening doors) or at a low level [4, 5] (i.e. based on special robot systems with special physical motor movement, such as humanoid robots). For common users, who do not have professional equipment and professional knowledge, a normal way for automatic robot learning to transfer human knowledge into an internal generic representation is needed.

As our robot is going to be used in indoor environments, non-expert users will have to teach them to perform everyday object-operating tasks. Considering many indoor tasks can be modeled as sequential rotations and translations with the axes of manipulation trajectories as shown in Fig. 1, hence, for those manipulation primitives, to calculate the axis and to organize them in a task chain appear significant. In order to improve robot flexibility and adaptability, we employ a new Learning from demonstration (LfD) technique. In high-level, we design demonstration primitives to abstract complex tasks. In low-level, we design manipulation primitives to extract human's motion. Also, Kinect sensor [6, 7] is used as an indoor 3D measuring device to locate the position of the user's hand.

The rest of this paper is organized as follows. In Sect. 2, some background knowledge is discussed. Section 3, proposes a design of demonstration primitives and manipulation primitives to describe the task. In Sect. 4, we provide a method

(a) **(b)** **(c)**

Fig. 1 Axis of trajectory of everyday object manipulation is annotated in the following images. **a** Drawer. **b** Switch. **c** Cupboard

to track the human hand's trajectory and obtain those primitives in one task. In Sect. 5, experiments describing how a robot learns to manipulate everyday objects are given. Conclusions and future work are discussed in Sect. 6.

2 Background and Related Work

LfD, programming by demonstration (PbD) or Learning by demonstration (LbD) is a mechanism that combines learning techniques with human–robot interaction [8]. The LfD learning problem contains two fundamental phases: gathering the examples, and deriving policies from such examples which are sequences of state-action pairs that are recorded during the teacher's demonstrated behavior.

There are many teaching methods for collecting the examples and then mapping them to the robots. Traditional methods include human tele-operation via a joystick [9] to accomplish a tele-operated task, receiving manipulation primitives by analysis of features in sensor feedback. Another approach commonly used in the field of direct teaching field is that, the robot behavior is shaped or molded by directly moving the joints of the robot to obtain the desired behavior [10]. An imitation technique in which sensors located on the executing body is also used to record the teacher execution [11, 12] by introducing different approaches in which a human wearing sensor controls a real robot arm.

A direct mapping will often not be possible, as the robot (learner) and human (teacher) will likely differ in sensing or structures. For example, the camera on the robot will neither detect state changes in the same manner as a human teacher's eyes, nor will its gripper apply force in the same manner as a human hand.

In our work, we only use a Kinect sensor [7] to track the movements of the user's hand when showing how to perform a particular task to the robot.

Kinect is an infrared structured light 3D scanner. The IR transmitter sends out infrared structured light carrying encoded information in the form of varying light patterns, a speckle pattern. Kinect uses IR light to build the same image as normal cameras but each color of the pixels identifies the distance between that part of the image and the camera, called a depth image. The information contained in the depth image is so accurate and precise that researchers like to use them to track the joints of the human skeleton. OpenNI [13, 14] is the framework which provides APIs connecting different kinds of middleware to Kinect motion tracking hardware. NITE [15] is such a good middleware which serves functions to track one person with 15 human skeleton joints in a 3D scene.

Different from the simple human movement imitation, our system could decompose complex demonstrations into discrete points in demonstration primitives, and calculate the axes of the rotations and translations producing manipulation primitives automatically.

3 Design of Primitives and Task Descriptors

A. **Demonstration Primitive**

In our study, because fast motions and complex kicks or close contact might cause the hand tracking to fail in Kinect, we change the continuous hand tracking trajectory to sequence of discrete points. Importantly, if the hand keeps static at one place while touching object during human demonstration in the real world, Kinect will record a ball of point cloud rather than only one point. Some method to process those point clouds is needed. In the follow-up experiment, Mean-Shift is chosen to get one point representing one point cloud at one demonstration state.

A task demonstration primitive D, can be defined as follows:

$$D = <p_1, p_2, p_3, \ldots, p_n>$$

where

$p_i = \left[p_{x_i}, p_{y_i}, p_{z_i}\right]$ is a point in 3D space where the moving hand is located at one demonstration state. Specially, p_1 records the hand's starting position while p_n records the position when one demonstration primitive is finished, which presents the two most important critical states during the robot learning.

B. **Manipulation Primitive**

In everyday life, operation tasks on indoor objects, such as opening doors, opening drawers, even opening door curtains, could be abstracted into translation or rotation. We call each of these translations or rotations a manipulation primitive.

Also, complex tasks, such as first opening the door, then taking the cup out, and sending to the designated place, could be artificially decomposed into series manipulation primitives during human demonstration. We define one manipulation primitive, similar to [17].

$$M = <\text{pos}, \text{dir}, m_s, m_e>$$

where

$\text{pos} = \left[p_{x_{\text{axis}}}, p_{y_{\text{axis}}}, p_{z_{\text{axis}}}\right]$ is a point in 3D space where the rotation axis is located.
$\text{dir} = \left[d_{x_{\text{axis}}}, d_{y_{\text{axis}}}, d_{z_{\text{axis}}}\right]$ is a direction for both rotation and translation axis.
$m_s = [m_{x_s}, m_{y_s}, m_{z_s}]$ is the starting point in 3D space while robot movement, corresponding p_1 in one demonstration primitive.
$m_e = [m_{x_e}, m_{y_e}, m_{z_e}]$ is the ending point in 3D space while robot movement, corresponding p_n in one demonstration primitive.

C. **Task Descriptor**

When the robot has to deal with a complex task chain, a complex manipulation trajectory descriptor T, could be defined as a set of certain P:

$$T = <M_1, M_2, M_3, \ldots, M_n>$$

where

$M_i \quad (i = 1, 2, 3, \ldots, n)$ is one demonstration primitive composing the complex manipulation trajectory T. The ending position m_e of M_i is also the starting position m_s of M_{i+1}.

4 Robot Learning to Manipulate Tasks

As shown in Fig. 2, in this section, we first collect everyday object demonstration primitives using Kinect. As the noises are disturbing, data are recorded as point clouds around the true hand's position in 3D space. Adaptive bandwidth Mean-Shift [19] is applied as a recursive clustering algorithm, using a Gaussian kernel as a gradient estimate which is proved as one form of kernel functions to assure asymptotically unbiased, consistent, and uniformly consistent estimates [20]. After door's axis and the starting (ending) position of the subtask are calculated through PCA analysis on demonstration primitives, manipulation primitives consisting of the task descriptor are concluded after a coordinate conversion between Kinect and KuKa.

A. **Human Demonstration**

Skeleton tracking is a complex task and the official documentation of NITE does not explain how it works. However, by performing experiments and analyzing the

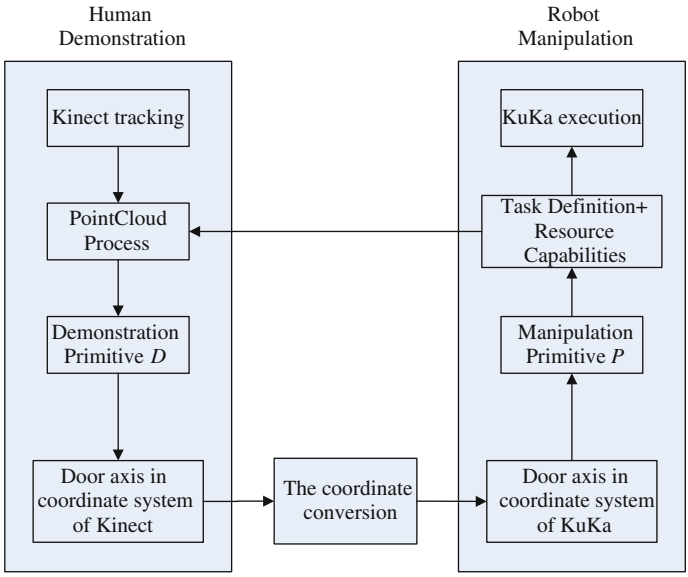

Fig. 2 Robot learning of manipulation

source code of OpenNI, I assume the processing technique might be as follows. NITE extracts the human body in a rectangular form from a precise depth map generated from Kinect sensor. Then it initially calibrates 15 joints of the human's body and the related distances between them through the human "Psi" pose. By knowing the position of each joint from the previous frame, the ranges of each joint's current position in the next frame are estimated. Finally, it extracts the skeleton joints' positions by computer vision technology (centerline extraction, image thinning might be included).

We assume what the robot sees is the motion of discrete points on the object and the human hand.

Considering that skeleton tracking through NITE has many limitations, as described in [15], we simplify our work with continuous tracking to some hot points' positioning during demonstration. Our interest is how to gain high-precision human hand coordinates in some special positions.

The human hand, which can technically be seen as a device with more than 20 DOF, forms the most effective, general purpose, interaction tool for HCI (Human Computer Interaction) [18]. As Fig. 3 shows, keeping a fixed hand gesture while manipulating objects in one demonstration primitive, we can locate the hand's position as a rigid body in our work, regardless of whether the object is articulated or not articulated. We can get human hand coordinates in a 3D scene when it is static at some hot point.

B. **Learning Demonstration Primitive**

As noises exist when extracting the hand position from depth images, such as variation in background, body parameters, infrared lighting, scene structure, and object orientation exacerbate, we generally record a ball of point cloud rather than one point.

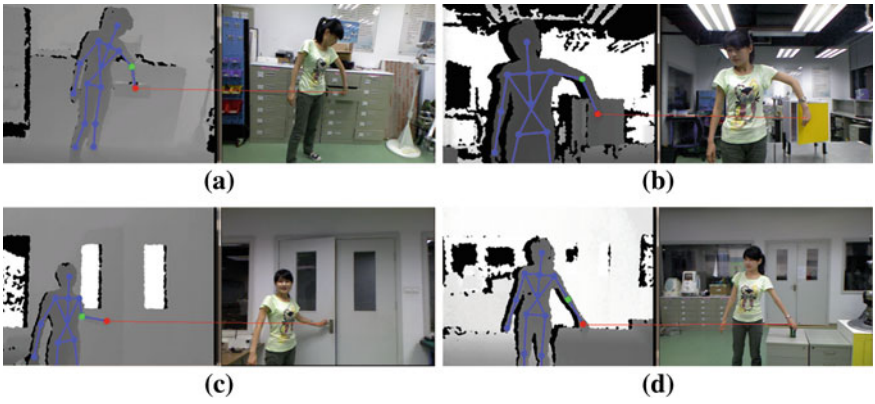

Fig. 3 The *right* columns of **a–d** display the color images from kinect; while the *left* columns of **a–d** are the corresponding depth images from Kinect, with skeleton joints positions overlaid on them. Especially, the *red* point records the position of the hand manipulating objects during demonstration, the corresponding relationship showing by the *red line*

In each cluster, we can calculate the mean value as the hand's potential coordinate, composing one point in the potential hand's trajectory. Similar to [17], we can learn the direction of manipulation primitive's axis through PCA analysis on the eigenvector of the potential hand's trajectory. Also, we can learn whether the trajectory is a translation or a rotation through PCA analysis on the eigenvalues of the potential hand's trajectory.

To gain the accurate axis's position, the cluster which represents the position of points could be projection to the plane perpendicular to the axis, as $\{x_i\}_{i=1\ldots n}$. We apply the adaptive bandwidth Mean-Shift [20], an algorithm relying on nonparametric techniques to obtain density gradient estimates, to gain the point around which the region has the maximum density, which is stored as p_i in D.

In this paper, we use the Gaussian probability density kernel function with zero mean and identity covariance matrix.

After projection, the 2D point cloud x is obtained in each cluster, to get a point p in D, the iteration algorithm is as follows:

1. h_i initialized with a fixed bandwidth h_0 and a pilot estimate $\hat{f}$.
2. Compute the intermediate variable λ.
3. For each data point x_i, compute h_i.
4. p_1 initialized with the location of interest fixed point before iteration, then compute p_j until $||p_{j+1} - p_j|| < \varepsilon$ which is viewed as convergence, stop iteration, so it is stored as a point in a demonstration primitive.

C. **Learning Manipulation Primitive**

Given the demonstration primitive, after the dir is known, we can make a circle fitting in the plane if it is a rotation which contains the points in the demonstration primitive, to get the center as pos of the human hand trajectory. As for translation, it does not need a specific point to locate the origin of the axis. Considering the distance between the human hand and the true position of handle when manipulation, we define a constant $\nabla l = [\nabla l_x, \nabla l_y, \nabla l_z]$, which is influenced by the user's grasping gesture.

So the manipulation primitive M in the coordinate system of Kinect is:

dir = the dir of demonstration axis.

pos = pos of the human hand's trajectory -∇l;

$$m_s = p_1 - \nabla l;$$

$$m_e = p_n - \nabla l;$$

If the camera lens of Kinect face against the object's surface vertically, according to the statistics analysis, generally, $\nabla l_x = 0$, $\nabla l_y = 0$, $\nabla l_z \in [5,\ 10\,\text{cm}]$.

5 Experiments and Initial Results

We have designed two experiments to discuss the universality of this framework. Our grasping platform is established with three units, which is consisted of a Kinect for Xbox 360, a KUKA robot arm with powerful 6-axis joints, and a two-finger parallel gripper. We use open source project OpenNI to capture the location of the human hand during demonstration and open source project OpenCV [21] to display the process, as in Fig. 3. Sensor Kinect [22] is chosen as the Kinect's device.

In each experiment, when the user gives a demonstration in front of Kinect, a very challenging problem is estimating the 3D position of the hand as an input device for the demonstration primitives. The estimation relies extensively on posture and viewpoint restrictions to avoid critical occlusions and needs to keep the appearance of the hand in a reasonable range. Our solution is that designing two specific gestures to grasp the object's handle, as in Fig. 4, through which only the back of the hand is visible from Kinect and the locating is stable through experiment. Also, ∇l can be measured.

Before the robot executes the task, the manipulation primitive's coordinate system is needed to translate from Kinect to KUKA through a coordinate conversion process.

A. Learning a Translation

In this experiment, either the drawer's handle or its corner can be chosen as the human hand's grasping position in the period of demonstration. While task execution, considering the normal work scope of KUKA robot arm and the two-finger parallel gripper, the drawer's handle is chosen as the robot's grasping point. Figure 5a–c shows the 3D model with the translation axis learned by our algorithm.

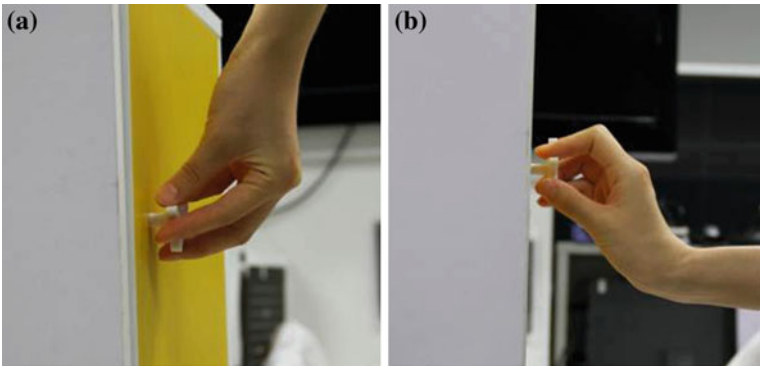

Fig. 4 **a**, **b** Show two types of hand gestures while grasping

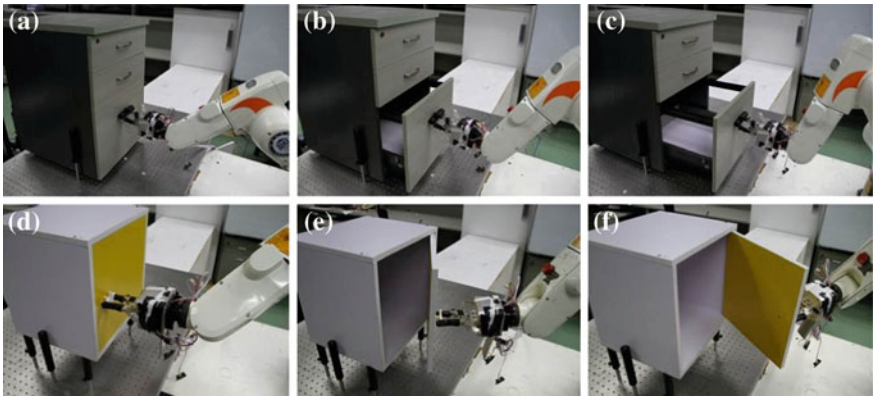

Fig. 5 Experiment. **a–c** Show the robot opening a drawer as a translation. **d–f** Show the robot opening a drawer as a rotation

B. **Learning a Rotation**

In this experiment, the door handle is chosen as the human hand grasping position in the period of demonstration and the robot's grasping position in the period of manipulation. Figure 5d–f shows the cupboard door opened by the robot after the task descriptor has been learned by our algorithm.

6 Conclusion and Future Work

In this paper, we present a framework for Robot Learning by Demonstration, to solve the problem of learning a mapping between world state and actions that lies at the heart of many robotics applications. First, the demonstration primitives are collected from user's setting examples using Kinect during human demonstration. Second, a generic task descriptor consisting manipulation primitives is deduced from demonstration primitives during robot manipulation. Finally, the robot automatically learns skills to perform the task from the task descriptor.

In the future, we will obtain intensive research combining vision and haptic technology. Especially for those handles sharing similar geometries, we can use ICP method or other shape matching techniques to make our approach more generic. This makes our framework extendable to a more general case where task descriptors are not generated based on one specific object but are capable of being applied to many other similar objects.

Acknowledgments This research is supported by National Natural Science Foundation of China (No. 61210013, 61105130), Guangdong Innovative Research Team Program (No. 201001D0104 648280). Key Fundamental Research Program of Shenzhen (No. JC201005270357A)

References

1. Klingbeil E, Saxena A, Ng AY (2008) Learning to open new doors. In: RSJ workshop on robot manipulation
2. Jain A, Kemp CC (2009) Pulling open novel doors and drawers with equilibrium point control. In: 9th IEEE-RAS international conference on Humanoid Robots, pp 498–505
3. Quigley M, Batra S, Gould S, Klingbeil E, Le Q, Wellman A, Ng AY (2009) High-accuracy 3D sensing for mobile manipulation: improving object detection and door opening. In: Proceedings of the IEEE international conference on Robotics and automation, ICRA '09, pp 2816–2822
4. Asfour T, Berns K, Dillmann R (2000) The humanoid robot armar: design and control. In: International conference on Humanoid Robot
5. Kaneko K, Kanehiro F, Kajita S, Hirukawa H, Kawasaki T, Hirata M, Akachi K, Isozumi T (2004) Humanoid robot HRP-2. In: Proceedings of the IEEE international conference on Robotics and automation, ICRA '04, vol 2, pp 1083−1090
6. Microsoft (2010) Kinect for X-BOX 360. http://www.xbox.com/en-US/kinect
7. Wikipedia. Kinect, http://en.wikipedia.org/wiki/Kinect
8. Argall B, Chernova S, Veloso M, Browning B (2009) A survey of robot learning from demonstration. Robot Auton Syst 57(5):469–483
9. Pook PK, Ballard DH (1993) Recognizing teleoperated manipulations. In: Proceedings of the IEEE international conference on Robotics and automation, vol 2, pp 578–585
10. Billard A, Calinon S, Guenter F (2006) Discriminative and adaptive imitation in uni-manual and bi-manual tasks. Robot Auton Syst 54(5):370–384
11. Aleotti J, Caselli S (2006) Robust trajectory learning and approximation for robot programming by demonstration. Robot Auton Syst 54(5):409–413
12. Calinon S, D'halluin F, Sauser EL, Caldwell DG, Billard AG (2010) Learning and Reproduction of Gestures by Imitation. Robotics Automation Magazine, IEEE 17(2):44–54
13. Openni homepage. http://www.openni.org/
14. PrimeSense (2010) OpenNI User Guide
15. PrimeSense (2010) Prime sensor NITE 1.3 algorithms notes, 1st edn
16. Sutton RS, Barto AG (1998) Reinforcement learning: an introduction. The MIT Press, Cambridge
17. Dang H, Allen PK, (2010) Robot learning of everyday object manipulations via human demonstration. In: IEEE/RSJ international conference on intelligent Robots and systems (IROS), pp 1284–1289
18. Erol A, Bebis G, Nicolescu M, Boyle RD, Twombly X (2005) A review on vision-based full DOF hand motion estimation. In: IEEE computer society conference on computer vision and pattern recognition—workshops, CVPR workshops, p 75, pp 25–25
19. Comaniciu D, Ramesh V, Meer P (2001) The variable bandwidth mean shift and data-driven scale selection. In: Proceedings of the eighth IEEE international conference on computer vision, ICCV 2001, vol 1, pp 438–445
20. Fukunaga K, Hostetler LD (1975) The estimation of the gradient of a density function, with applications in pattern recognition. IEEE Trans Inf Theory 21:32–40
21. Opencv homepage. http://opencv.willowgarage.com/wiki/
22. SensorKinect. http://github.com/avin2/SensorKinect

Research and Development of Automatic Driving System for Intelligent Vehicles

Weizhong Zhang, Tao Mei, Huawei Liang, Bichun Li, Jian Huang, Zhaosheng Xu, Yi Ding and Wei Liu

Abstract An innovative universal automatic driving system for intelligent vehicles is designed in this research. With a few mechanical modifications of four subsystems, i.e., steering system, breaking system, throttle system, and gearing system of the original manned vehicles, and the installation of an automatic control device, this system is finally established by connecting each subsystem and upper computer via CAN bus. It is proved by vehicle tests that upper computer can precisely control the underlying subsystem through automatic driving system, and this system can be used not only for vehicle bench test, but also for automatic driving of intelligent vehicles, which establishes a foundation for further researches of unmanned and intelligent control of vehicles.

Keywords Intelligent vehicle · Versatility · Automatic driving · Steering control

W. Zhang (✉) · T. Mei
Chinese Academy of Sciences, Institute of Intelligent Machines, Hefei, China
e-mail: wzzhang@iim.ac.cn

T. Mei
e-mail: tmei@iim.ac.cn

W. Zhang · T. Mei
University of Science and Technology of China, Hefei, China

T. Mei · H. Liang · B. Li · J. Huang · Z. Xu · Y. Ding · W. Liu
Chinese Academy of Science, Institute of Advanced Manufacturing Technology, Hefei, China
e-mail: hwliang@iim.ac.cn

B. Li
e-mail: bcli@iim.ac.cn

F. Sun et al. (eds.), *Foundations and Practical Applications of Cognitive Systems and Information Processing*, Advances in Intelligent Systems and Computing 215,
DOI: 10.1007/978-3-642-37835-5_58,

1 Introduction

The perception technology is important for the intelligent vehicle development, and the machine vision is the most important part of the intelligent vehicle environment perceptual system [1, 2]. Along with the development of theories and technologies of vision, artificial intelligence, and automatic control, more and more intelligent algorithms are designed which are more effective than before to improve the ability of intelligent vehicles to be intelligent controlled continuously, and the development also promotes the intelligent vehicle from remote control to semi-autonomous control and fully autonomous control [3]. In the process of the development of intelligent vehicle, the performance of underlying automatic driving system is always a key factor which will influence the vehicle's intelligent control ability. The automatic driving system can receive instructions from the upper computer, and control the vehicle's movement parameters, such as the states of steering, speed, and gearing. As the ultimate executive of all motions, the effectiveness of the automatic driving system has a direct effect on the performance of the intelligent vehicle, e.g., whether it can complete the upper computer instructions accurately and timely. The automatic driving system is therefore the foundation of the intelligent vehicle's capabilities including perception, planning, reasoning and decision-making, and so on, and is also one of the core systems of the intelligent vehicles [4, 5].

Traditional automatic driving system consists of steering system, breaking system, throttle system, and gearing system, and controls vehicles through adding a series of complex mechanical systems such as motor, gear reducer, machinery to the original manned vehicles. The automatic driving system of the ABD Company of the United Kingdom is mainly used in vehicle tests but only applies to limited vehicle types. The automatic driving system developed by the Kairos Company of the U.S. is mainly used in the modification of the intelligent vehicles, but its steering precision is not satisfactory, and transmission is not stable. The automatic driving systems developed by the Staler of German and the Horibo of Japan have the ability to control vehicles, but not in real-time, and can only be used for vehicle bench tests. The automatic driving system for "Intelligent Pioneer" developed by the Institute of Advanced Manufacturing Technology of Chinese Academy of Science is based on the mechanical structure of the original manned vehicle with extensive modifications and is prone to adversely impact the performance of the original manned vehicle. Faced with many problems that exist in the automatic driving system, this research is to explore and achieve a more rational design of an automatic driving system [6–8].

2 Overall Scheme

In order to enable the intelligent vehicle to complete a variety of independent actions in a complex environment, a layered architecture including the perception-planning layer, execution layer, and so on, is designed. The perception-planning

layer produces intelligent planning and motion instructions. The major components of the perception-planning layer include the visual perception equipment and the upper computer. Based on the expectations of motion instructions, the execution layer controls underlying actuator action. The execution layer is mainly composed of the automatic control system and its corresponding execution subsystems.

The automatic driving system requires for the perception-planning to make perception-planning decision every 100 ms time and produce a movement instruction set, which includes the expectations of steering angle, the throttle opening, the braking amount, and the gearing position. (This requires the execution layer within 100 ms should quickly and accurately perceive the perception-planning layer planning expectations.) In order to achieve this goal the original manned vehicle needs necessary mechanical modifications and automatic control devices during the process of designing the execution layer. By these modifications, the original manned vehicle is transformed into an intelligent vehicle. The intelligent vehicle can receive steering, speed, braking, and other instructions and perform the corresponding action through the automatic driving system. The design of the automatic driving system should meet the following requirements:

- Control precision and reaction time of the execution layer, provided by the perception-planning layer.
- The mechanical modifications of the original manned vehicle should be minimum.
- The performance of the original manned vehicle should not be affected.
- Maintaining high versatility, reliability, and stability.

The overall scheme of the automatic driving system is shown in Fig. 1. It can get vehicle location information and speed information through the GPS equipment, wheel speed sensors, or other sensing equipment. Through the trajectory generator it can get vehicle intended trajectory information. Trajectory generator calculates the position and velocity requirements of the preview points. The lateral controller and longitudinal controller complete the calculation of the control parameters. The direction control and speed control parameters of the vehicle will be sent to execution system by the multiplexer. In this way, automatic driving system controls the vehicle running according to a predefined trajectory. The main function of each module is as follows:

- Input modules: the connection of the GPS device, wheel speed sensors, or other sensing equipment to determine the location and other status of the vehicle.
- Control module: mainly responsible for seeking a preview point in the predefined trajectory and calculate control parameters. The calculation parameters are sent via CAN bus.
- Output modules: the connection between control and execution system, including the steering control output, braking control output, throttle control output, and gearing control output.
- Other expansion modules: a light and horn control, and ignition control by relays of the vehicle.

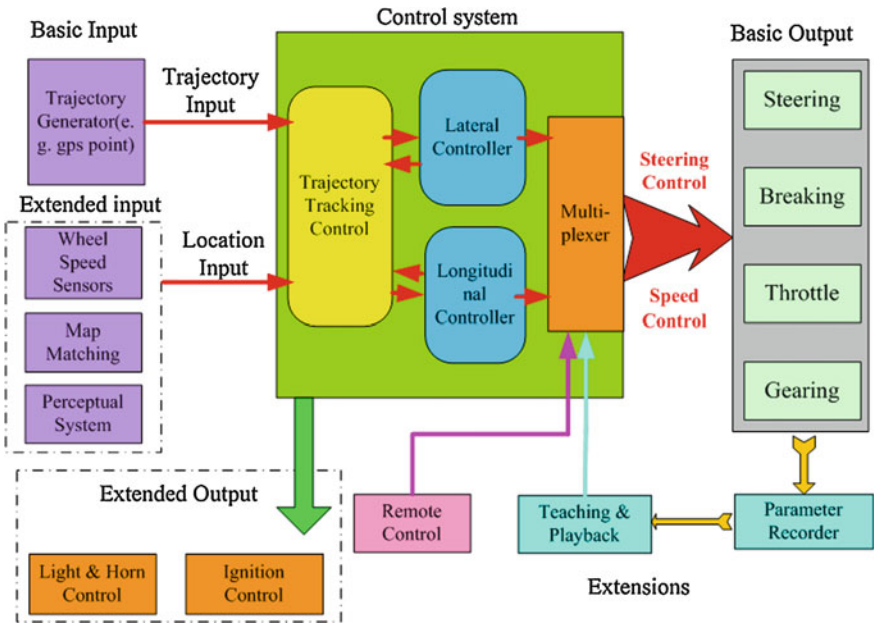

Fig. 1 The overall scheme of the automatic driving system

3 Control System

3.1 Controller Hardware

The Freescale MCS12XDP512MAL microcontroller shown in Fig. 2 is the core component of the automatic driving system, which can let external auxiliary circuits control the execution system. Finally, the automatic driving function is achieved. The entire system includes a serial communication module (SCI), a CAN bus module (MSCAN12), a timer module, an SPI bus module, a PWM module, and a co-processor module (XGATE) [9]. The main function of each module is as follows:

- The serial communication module (SCI) communicates with the onboard GPS device (CPT) to receive GPS data.
- CAN bus module (MSCAN12), divided into two CAN bus modules which are called CAN0 and CAN4. CAN0 bus module communicates with the upper track sending system, receiver trajectory path and sends the vehicle status information (GPS position, speed, and heading) to the upper computer; In addition, the upper computer can also send control mode instructions to specify the controller a machine mode (trajectory tracking mode, the path acquisition mode, the direct control mode, and the implementation of the system back to the zero mode);

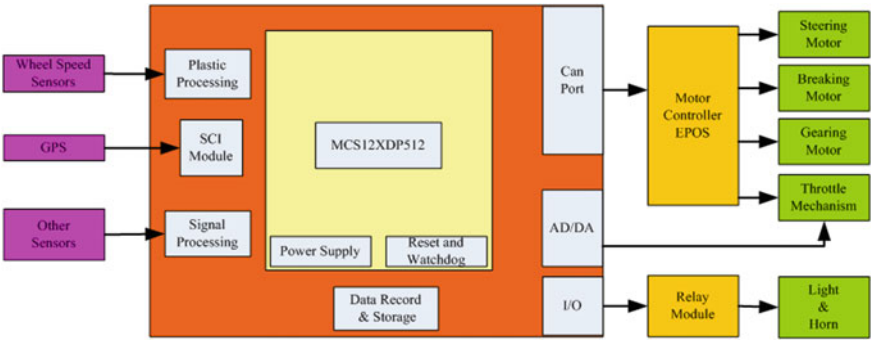

Fig. 2 Controller hardware system block diagram

CAN4 bus module communicates with motor controller, outputs the motor control parameters.

- Timer module is used for regularly scanning the keyboard operation and interrupt management of other modules.
- SPI bus module, used for the data storage device (SD card).
- PWM module, used for the buzzer and wheel speed encoder control.
- Co-processor module (XGATE) separately deal with the CAN0 interrupted trajectory path data, reducing the data processing time of the system.

3.2 Controller Software

The controller software shown in Fig. 3 is the core of the automatic driving system. The main function performed by the controller software is as follows:

- To receive GPS signal every 100 ms, parse out the vehicle's current position, velocity, and heading information.
- To receive the path trajectory points sent by the upper computer, and then parse and store the information.
- To find the preview points based on the vehicle's current position and intended track.
- To calculate the vehicle's lateral control and longitudinal control parameters based on the preview points.
- To control the execution system by calculating the lateral control and longitudinal control parameters, outputs control instructions.
- To record and store the driving status information in a real-time manner.

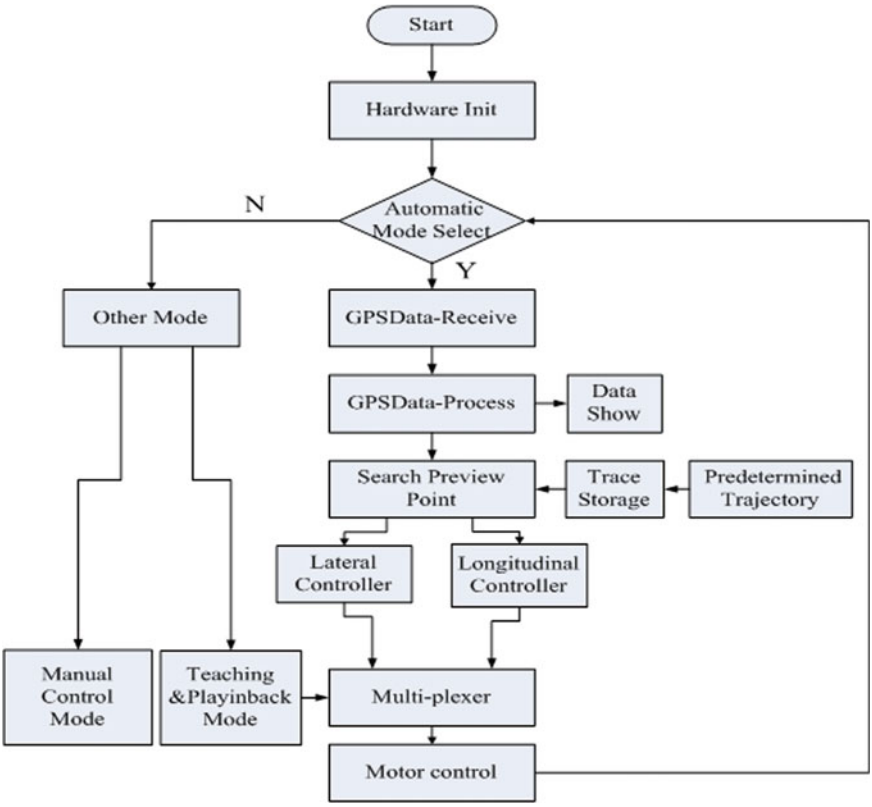

Fig. 3 Control software flowchart

4 Execution System

In order to simplify the installation process and maximize the versatility of the system, a method of modular design is adopted in the development of the execution system. The execution system shown in Fig. 4 consists of four subsystems, i.e., steering system, breaking system,throttle system, and gearing system [10].

The steering system shown in Fig. 5 with synchronous belt transmission is directly installed on the steering wheel in order to make full use of interior space and minimize the influence on the manual driving mode as much as possible owing to the automatic driving system. In this way, the steering system can be installed in many different vehicles with high steering control precision, which mainly consists of DC servo motor, gear reducer, electromagnetic clutch, synchronous belt and encoder, etc.

Sharing a similar mechanical structure, the breaking, throttle, and gearing systems shown in Fig. 5 utilize a flexible shaft with certain flexibility. The three subsystems use DC servo motors to drive ball screws and then pull the flexible

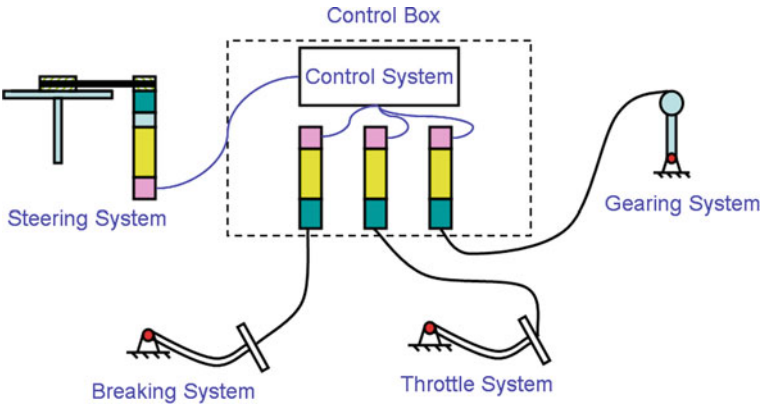

Fig. 4 Schematic diagram of the execution system

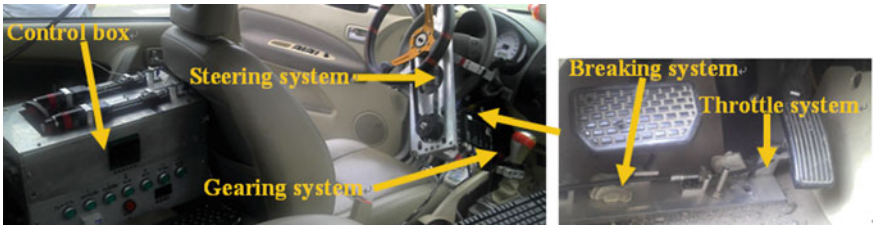

Fig. 5 The execution system

shafts. Different specifications of the flexible shafts are connected to the brake pedal, the gas pedal, and the gear knob, which are in different states by controlling of flexible shaft in different positions in order to achieve speed and gearing control of the intelligent vehicles. The three subsystems consist of DC servo motors, ball screw, flexible shafts and encoders, etc., whose main parts are integrated in the control box. In this way, not only the easiness of the installation of the three subsystems and the versatility of the system are guaranteed, but the functional independence between the manual driving and automatic driving modes is secured.

5 Vehicle Tests

In order to ensure the relative independence of the vehicle test, cameras, laser radars, and other sensing equipments are not used to generate path trajectories in real-time. Instead, the vehicle positioning device (SPAN-CPT) is used to pre-collect trajectory data set, including the track point position information and velocity information. Once track data is loaded, the upper computer sends the planned track data to the control system via CAN bus. Based on the track data and

Fig. 6 Test track of the vehicle

the position and speed information, the control system tracks the position and speed of the vehicle, provides both lateral and longitudinal control parameters, and finally completes the automatic driving of the vehicle on a predetermined path. Figure 6 depicts the test track of the vehicle and the straight path is about 300 m, the curves are about 1,200 m, and the total length is about 1,500 m.

Under the automatic driving mode, SD card records part of the vehicle track data, including latitudes, longitudes, headings, and speed information. See Table 1 for details.

Lateral control test consists of the straight line test and curve test. In the process of straight line test, the average speed is set to four kinds of circumstances, i.e., low speed (15 km/h), medium speed 1 (35 km/h), medium speed 2 (50 km/h), and high speed (80 km/h) to test the lateral control precision of vehicle in all kinds of

Table 1 Part of the data about SD card record

Latitude	Longitude	Heading (North declination)	Speed (m/s)
31.818923132	117.128479713	178.772528514	0.11895
31.818923568	117.128481080	178.794638984	0.12886
31.818896904	117.128473439	176.253454441	2.00286
31.818895079	117.128473596	176.112071448	2.05744
31.818829588	117.128480760	174.201816601	3.04548
31.818806946	117.128483148	174.863372476	3.24682
31.818173316	117.128494761	179.417047024	5.06178
31.815174147	117.128522499	178.052994253	8.04338
31.812290068	117.128520871	179.363770022	11.0041
31.813911031	117.128654341	180.463478212	14.0154

Table 2 Lateral control precision in straight lane

Average speed (km/h)	15	35	50	80
RMS of lateral control (m)	0.18	0.21	0.25	0.28

Table 3 Lateral control precision in curves

Types	Common curve (>90°)	Right-angled curve (=90°)	U-turn (<90°)
RMS of lateral control (m)	0.29	0.35	0.44

Table 4 Longitudinal control precision

Setting speed (m/s)	2.5	5.5	8	11	14	22
Real speed (minimum) (m/s)	1.84142	5.22533	7.77735	10.4112	13.2154	20.9821
Real speed (maximum) (m/s)	2.94660	5.98913	8.59982	11.1199	14.2838	22.8734
RMS of longitudinal control (m/s)	0.47823	0.45782	0.42327	0.35328	0.40319	0.49021

turning circumstances. In the process of curve test, the speed is set to idle speed (<20 km/h) to test the lateral control precision of various turning conditions.

Tables 2 and 3 show that the RMS of lateral control in straight lane is less than 0.3 m in all kinds of speeds and less than 0.5 m in curves with idle speed. The tests show that the automatic driving can meet the requirements of perception-planning layer on the lateral control precision and speed of the execution layer.

Our test of longitudinal control is implemented on a straight lane about 500 m. We obtained real speed-tracking data under the setting speed of 2.5, 5.5, 8, 11, 14, and 22 m/s in the same road type, respectively. When the vehicle travels stably, the upper computer sends the speed instructions, and then obtains the accuracy of longitudinal control by contrasting with the true vehicle speed. The RMS of longitudinal control is less than 0.5 m/s in different setting speeds, as shown in Table 4, it can meet the requirements of automatic driving.

After a series of road tests over 3,000 km within 4 months, the intelligent vehicle has proved itself as a robust platform which can travel on both structured and unstructured roads at a speed of 50 km/h. Under any circumstances, all four underlying subsystems operate flawlessly. The system perfectly meets all requirements of the underlying control system for intelligent vehicles.

6 Conclusion

An innovative universal automatic driving system for intelligent vehicle is designed in this research. The steering system with synchronous belt transmission is directly installed on the steering wheel, which uses electromagnetic clutch for two modes of switch, i.e., manual driving and automatic driving. The braking system, the throttle system, and the gear system use DC servo motors to drive ball

screws and then pull the flexible shafts to control the braking, throttle and gearing states. The automatic driving system uses CAN bus to connect all four execution systems. The design method of the automatic driving system has advantages of good versatility, without complex mechanical design, making small changes to the original manned vehicle, which obtains the effects of high control precision, short development cycle, and low cost. It is proved by vehicle tests that the intelligent vehicle equipped with this system can drive within a specified path. The research experience can also provide useful reference for other construction of similar automated driving and remote control platforms.

Acknowledgments This project is supported by National Natural Science Foundation of China (Grant No. 91120307, No. 50908222) and the control theory and method research on trajectory tracking of vehicular automatic driving system, Dean Foundation of Hefei Institutes of Physical Science, Chinese Academy of Sciences. The authors would like to acknowledge the countless other support staff members at Technical Center for Intelligent vehicle, Institute of Advanced Manufacturing Technology, CAS who contributed their expertise and skills to help make the Research and Development of Automatic Driving System for Intelligent Vehicles a successful and invaluable facility.

References

1. Lu YM, Jiangye WH, Bo Z (2001) A survey: vision based road following. J Pattern Recogn Artif Intell 14(2):186–193
2. Lixia M, Sun F, Yu S (2010) Survey on road image interpretation based on monocular vision. J Comput Appl 30(6):1552–1555
3. Wang H, Zeng L, Tian W (2004) Application of artificial intelligence in automatic drive for intelligent vehicles. Control Theory Appl 23(6):5–8
4. Ye W, Liu H, Sun F, He K (2011) Unstructured road detection using co-learning. J Image Graph 16(5):792–799
5. Wang H, Wang X, Zhang B, Sun J (1995) A method for planning the path of mobile robot moving on general terrain. J Softw 6(3):173–178
6. Villegas C, Akar M, Shorten RN (2007) A robust PI controller for emulating lateral dynamics of vehicles. In: Proceedings of the 2007 IEEE intelligent vehicles symposium, Istanbul, Turkey, pp 828–833
7. Thiel W, Grof S, Honenberg G (1998) Investigations on robot drivers for vehicle exhaust emission measurement in comparison to the driving strategies of human drivers. SAE paper, No. 982642
8. Stiller C, Färber G, Kammel S (2007) Cooperative cognitive automobiles. In: Proceedings of the IEEE intelligent vehicles symposium, IEEE Press, Istanbul, Turkey, pp 215–220
9. Zhang W, Liu J, Bian Y (2009) Study on vehicle braking plans for automatic driving. Appl Res Comput 26(11):4215–4217
10. Kou C, Chen Z, Yang M, Lei NI (2011) Design of vehicle automatic driving device based on inertial navigation system. Inf Technol 2:69–71

The Application of V Test Method in Detecting Auditory Steady-State Response

Jun Ying, Zheng Yan, Guangyu Bin and Xiaorong Gao

Abstract Auditory steady-state response (ASSR) is a kind of signal which is phase-locked to the stimulus onset. Consequently, the methods of detecting ASSR are generally based on the feature of phase-locking. In this paper, ASSR in 40 and 90 Hz were recorded from 13 subjects. The phase values were calculated while the subjects attended to the tones. And it was found that besides S7, for each frequency, the phase of ASSR were fairly constant across all 12 subjects. For examples, the phase of ASSR responding to 40 Hz was mainly distributed around 3/4pi. Based on the results, the method of *V* test was introduced in this paper. By comparing the results obtained by *V* test and Rayleigh test, we found that *V* test is a more effective method for detecting ASSR.

Keywords Auditory steady-state response · *V* test · Rayleigh test · Phase-locked

1 Introduction

The auditory steady-state response (ASSR) elicited by trains of clicks or amplitude-modulated (AM) tones, is an oscillatory brain response with a significant increase in amplitude at stimulus repetition rates [1]. Phase-lock is one of the most

J. Ying · X. Gao (✉)
Department of Biomedical Engineering, Tsinghua University, Beijing, China
e-mail: gxr-dea@tsinghua.edu.cn

Z. Yan
Institute of Information Engineering and Technology, Huaqiao University, Xiamen, China

G. Bin
School of Life Science and Bio-engineering, Beijing University of Technology, Beijing, China

J. Ying
Division of Medical Logistics, PLA General Hospital, Beijing, China

F. Sun et al. (eds.), *Foundations and Practical Applications of Cognitive Systems and Information Processing*, Advances in Intelligent Systems and Computing 215,
DOI: 10.1007/978-3-642-37835-5_59,

important features of ASSR. In general, after hearing each tone, the brain signals which are phase-locked with the stimulus could be observed [2]. In clinic, ASSR has extensive application, such as testing hearing sensitivity and as a marker of the state of consciousness during anesthesia. ASSR is of low amplitude ($\leq$1 μV) and signal-to-noise ratio (SNR). Therefore, it has become the key points to detect ASSR fast and accurately [3]. Usually, most of the detecting methods are based on the characteristic of phase-locking of ASSR.

In recent years, some reports are in line with a theory, which concluded that steady-state visual evoked potentials (SSVEPs) are not generated by amplitude modulation; instead, they are primarily due to phase alignment of the ongoing background brain signals [4]. Chuan Jia et al. indicated that under the condition of stimuli of same frequencies and phases, measured and reference phases are distributed fairly consistent across subjects; it turns out that the latency of SSVEP are similar across subjects when attending to the same visual stimulation [5]. More and more researchers have recognized that the phase information of SSVEP is helpful in understanding SSVEP mechanism and improving the target identification accuracy for SSVEP-based brain–computer interface (BCI) [6].

In fact, SSVEP is a kind of steady-state evoked potentials (SSEPs) as well as ASSR. Generally, the principle of all SSEPs is following a principle somewhat similar to SSVEPs. It has seen that the importance of phase studying in SSVEPs. However, the study of phase information was not well studied for ASSR.

In this paper, we further investigate the responding phase in ASSR. First, in order to confirm the phase consistency between different subjects, the phases were calculated from EEG data. Furthermore, *V* test was proposed to detect ASSR. *V* test is similar to the Rayleigh test which is a traditional method in ASSR detecting. The difference between *V* test and Rayleigh test is that *V* test is assumed to have a known mean direction. Due to the additional information used, the *V* test is more powerful than the Rayleigh test. Finally, a comparison was performed between *V* test and Rayleigh test. And it was found that *V* test is a more effective method for detecting ASSR.

2 Method

2.1 Subjects

Thirteen volunteers with normal hearing, nine males and four females, aged between 20 and 30 years (mean age 25, SD 3.8) participated in the experiments. All participants sat in a comfortable armchair in a shielded and quiet room.

2.2 EEG Recording

Multichannel EEG signals were recorded with a Synamps2 (NeuroScan Inc.) system. In the experiment, 64 channels were placed according to international 10–20 electrode system. The reference channel was on the nasal. The impedance was kept below 10 kΩ. Data was recorded at a sampling rate of 1000 Hz and then band passed filtered between 0.05 and 200 Hz.

2.3 Experimental Paradigm

For acquisition of better ASSR responding, instead of trains of clicks, repeated chirp were utilized in our experiment. Stimuli were delivered binaurally through the headphones at intensity of 60 dB. The sound played for a duration of 50 s and the silent inter-stimulus intervals (ISI) was 5 s. For each subject, both 40 and 90 Hz were carried out under the same conditions. The chirp signals were created based on cochlear traveling wave theory proposed by Don et al. [7]. The sounds were produced by the digital signal processor (DSP) TMS320C5515 (TI, Inc.). The sounds had been tested and found to be precise enough to allow one to control for errors within 5 μs. For headphones, the Etymotic Research ER2 insert earphones were selected because it can effectively avoid the electromagnetic interference.

2.4 Data Processing

2.4.1 SNR analysis

The data were checked prior to analysis by visual scoring. Signals contaminated by artifacts were excluded from further analysis. The ASSR topographies for the responses to the frequencies were plotted to investigate the maximal ASSR SNR distribution. We define the SNR as the ratio between the power at the signal frequency and the average power at adjacent 40 frequency bins [8].

2.4.2 Rayleigh Test

The Rayleigh test which is used for testing the significance of the mean direction in a cycle histogram is a common statistical method for detecting ASSR [9]. Let $\phi_1, \phi_2, \ldots, \phi_N$ refer to a set of samples. Hence, the test statistic R could be described in detail in the following form:

$$\mathrm{R} = \sqrt{\left(\frac{1}{N}\sum_{i=1}^{N}\cos\phi_i\right)^2 + \left(\frac{1}{N}\sum_{i=1}^{N}\sin\phi_i\right)^2} \tag{1}$$

The value of R obtained from Eq. (1) indicates the distribution of φ: (1) If φ follows circular uniform distribution, the value of R approaches 0; (2) otherwise, when ϕ has a certain direction, R tend to be 1. On the basis of that feature, R could be served as a parameter for testing if the angle variables have a significant direction. The approximate p-value is computed as:

$$P = 1 - \exp\left[\sqrt{(1 + 4N + 4(N^2 - R^2N^2))} - (1 + 2N)\right] \tag{2}$$

Here, the statistical significance level was set to 0.05. As a consequence, the samples show a remarkable direction when $P < 0.05$.

2.4.3 V test

The V test for circular uniformity is similar to the Rayleigh test with the difference that under the hypothesis is assumed to have a known mean direction [10]. It is important that the mean direction has to be known in advance. The test statistic V is computed as follows:

$$V = R\cos(\bar{\phi} - \bar{\phi}_A) \tag{3}$$

where R is calculated from Eq. (1), where $\bar{\phi}$ is mean direction of the set of samples. It is important to note that the mean indicates the mean angular direction and is obtained as follows:

$$\cos\bar{\phi} + j\sin\bar{\phi} = \frac{1}{N}\sum_{i=1}^{N}(\cos\phi_i + j\sin\phi_i) \tag{4}$$

In fact, the value of R indicates the phase clustering. And the value computed from $\cos(\bar{\phi} - \bar{\phi}_A)$ shows the difference between the mean and the expectation value. As V increases, the mean direction tends to be $\bar{\phi}_A$. The significance level could be expressed as:

$$P = 1 - \mathrm{normcdf}\left(V\sqrt{\frac{2}{N}}\right) \tag{5}$$

where, normcdf means the probability density function of standard normal distribution.

2.4.4 ASSR detecting strategy

For each subject, the datasets were extracted from corresponding trials. Finally, 50 segments of 1 s-data were obtained. The phases $\phi_1, \phi_2, \ldots, \phi_{50}$ are computed with the fast Fourier transform (FFT). The detecting scheme is as follows: (1) calculates the averaged phase distribution for each subject; (2) based on the knowledge of phase distribution obtained from step1, the V test was carried out to test the significance level $P(n)$ using the 50 1 s-segments. For the Rayleigh test, it does not need any prior knowledge. However, in order to compare the two methods, we also used the 50 1 s-segments to perform the Rayleigh test; and (3) obtain the detecting time. The process kept going until $P(n_{\text{term}}) < 0.05$ was observed for the first time. And the time c was just the detecting time of ASSR we required. In our study, both the Rayleigh and V test were realized by the CircStat toolbox which is based on Matlab environment.

3 Results

3.1 The SNR of ASSR

The ASSR SNR for the responses to specific frequency were computed and plotted. Figure 1 shows the maximal ASSR SNR mainly occurred at frontal-central and parietal-occipital regions presenting with a symmetrical distribution. Moreover, for 90 Hz, the distribution is more widely, instead of concentrating at central area. The distribution results are consistent with the findings of Herdman [11].

3.2 The Distribution of Phase

The phase distribution averaged for 13 subjects was plotted in Fig. 2.

As shown in Fig. 2, besides the black rectangle, the phase distributes rather closely, varying steadily in a certain range from 1/2 to 3/4π at 40 Hz and 7/4 to 2π at 90 Hz. And the mean directions for 40 and 90 Hz are 0.73 and 1.77π, respectively.

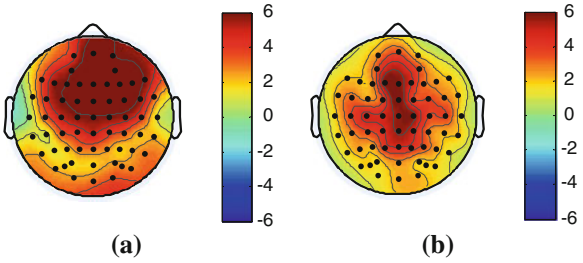

Fig. 1 Topographic plots: ASSR SNR for responses to 40 Hz (**a**) and 90 Hz (**b**)

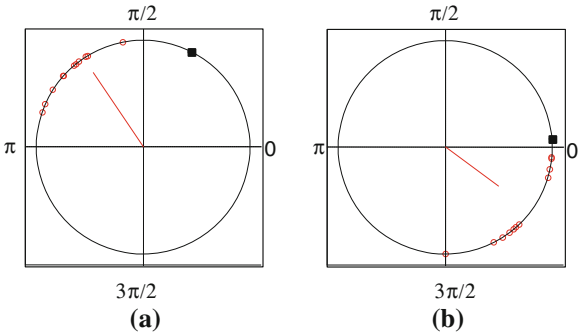

Fig. 2 The phase distribution of ASSR of 13 subjects. **a** Phase distribution of ASSR induced by 40 Hz. **b** Phase distribution of ASSR induced by 90 Hz

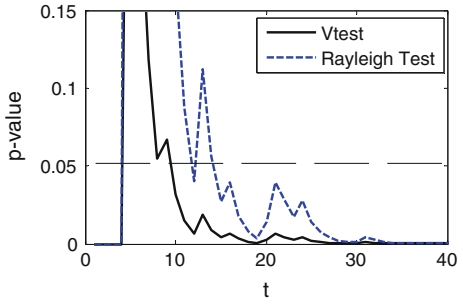

Fig. 3 Relationship between *p*-value and time obtained by *V* test and Rayleigh test

3.3 The Comparison of V *Test and Rayleigh Test*

V test was performed using the mean phase computed previously. And Rayleigh test was calculated as previously described. The relationship between *p*-value and time obtained by *V* test and Rayleigh test was plotted in Fig. 3. And the time at $P(n_{\text{term}}) < 0.05$ was shown in Table 1. As shown in Table 1, for most subjects, the average of detecting time using *V* test is smaller than using Rayleigh test, especially when the responding amplitude is lower at the situation of 90 Hz stimuli. However, for S7, the *V* test showed no advantage over the Rayleigh test. In Table 1, the mean time 1 was the results averaged across all 13 subjects. When the result of S7 is not considered, the mean time 2 obtained indicated the *V* test is superior to the Rayleigh test significantly.

3.4 Discussion and Conclusion

Similar to SSVEP, ASSR has the features of phase-locking and steady phase difference. Furthermore, the phase directions are stable between subjects. The results indicated that *V* test could detect ASSR faster and more effective. Due to the additional information used, the *V* test is more powerful than the traditional Rayleigh test method in detecting ASSR.

Table 1 Comparison of detecting time using *V* test and Rayleigh test

	V test		Rayleigh test	
Subject	40 Hz	90 Hz	40 Hz	90 Hz
S1	5	24	7	25
S2	9	9	10	10
S3	>50	11	>50	8
S4	5	16	7	45
S5	6	33	7	>50
S6	5	11	6	>50
S7	>50	24	23	24
S8	5	8	7	10
S9	42	>50	43	>50
S10	9	21	9	>50
S11	17	9	25	12
S12	5	6	7	8
S13	8	10	9	13
Mean time 1	16.6	17.8	16.1	27
Mean time 2	13.8	17.3	15.6	27.6

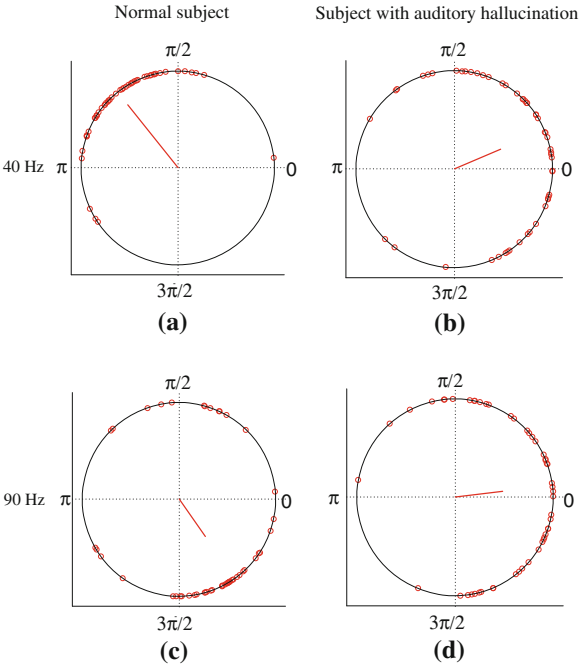

Fig. 4 The phase distribution of ASSR of normal subjects and S7 with auditory hallucination. **a** ASSR induced by 40 Hz. **b** ASSR induced by 90 Hz

However, while the phase distribution is not stable, the result obtained by the Rayleigh test is better. The reason is that there is no advance information included in the Rayleigh test. For example, the result obtained by *V* test was not good for the

subject S7 in our study. As shown in Fig. 4, for S7, compared to other subjects, the phase was widely distributed in all four quadrants showing no characteristics of stable. Therefore, the results were not good using *V* test which need reasonable advance information.

We learnt later that S7 experiences intermittent auditory hallucination. The auditory hallucination is a form of hallucination that involves perceiving sounds without auditory stimulus. A common form of auditory hallucination is hearing one or more talking voices. This may be responsible for the results of unstable distribution of phase.

Generally, the latency and auditory conduction time are basically the same. Therefore, for normal subject, the phase distributions are consistent. In our study, for 40 and 90 Hz, the phases were distributed in the fourth and second quadrants, respectively. Actually, due to the system latency, the distribution area may vary at different experiment systems.

In our study, we found that the phase distribution is stable. Based on that phenomenon, the method of *V* test could be used to detect the ASSR. Furthermore, with the advance information used, the *V* test is more powerful than Rayleigh test. However, there is one limitation about *V* test: in order to ensure correct and better result, the reasonable advance information is needed. And in the absence of prior knowledge, the Rayleigh test is superior to *V* test.

Acknowledgments This work was supported by the National Basic Research Program of China (Grant No. 2011CB933204) and National Natural Science Foundation of China (Grant No. 90820304). The authors would like to thank Xiaogang Chen for his comments and suggestions.

References

1. Picton TW (2003) Human auditory steady-state responses. Int J Audiol 42:177–219
2. Ross B, Herdman AT, Pantev C (2005) Stimulus induced desynchronization of human auditory 40 Hz steady-state responses. J Neurophysiol 94:4082–4093
3. Galambos R (1981) A 40 Hz auditory potential recorded from human scalp. Nicolet Potentials 1:12
4. Moratti S, Clementz BA, Gao Y, Ortiz T, Keil A (2007) Neural mechanisms of evoked oscillations: stability and interaction with transient events. Hum Brain Mapp 28:1318–1333
5. Jia C, Gao XR, Hong B, Gao SK (2011) Frequency and phase mixed coding in SSVEP-based brain-computer interface. Trans Biomed Eng 58:200–207
6. Kluge T, Hartmann M (2007) Phase coherent detection of steady-state evoked potentials: experimental results and application to brain-computer interfaces. In: Proceedings of the 3rd international IEEE EMBS neural engineering conference, pp 425–429
7. Don M, Kwong B, Tanaka C (2005) A diagnostic test for meniere's disease and cochlear hydrops: impaired high-pass noise masking of auditory brainstem response. Otol Neurotol 26:711–722
8. Lins OG, Picton TW, Boucher BL, Durieux-Smith A, Champagne SC, Moran LM, Perez-Abalo MC, Martin V, Savio G (1996) Frequency-specific audiometry using steady-state responses. Ear Hear 17:81–96

9. Cebulla M, Stürzebecher E, Elberling C (2006) Objective detection of auditory steady-state responses: comparison of one-sample and q-sample tests. J Am Acad Audiol 17:93–103
10. Philipp B (2009) CircStat: a MATLAB toolbox for circular statistics. J Stat Softw 31:10–19
11. Herdman AT, Lins O, Van Roon P (2002) Intracerebral sources of human auditory steady-state responses. Brain Topogr 15:69–86

Neural Network-Based Adaptive Dynamic Surface Control for Inverted Pendulum System

Enping Wei, Tieshan Li, Junfang Li, Yancai Hu and Qiang Li

Abstract In this paper, a novel neural network (NN)-based adaptive dynamic surface control (DSC) is proposed for inverted pendulum system. This scheme overcomes the problem of "explosion of complexity" which is inherent in the traditional backstepping technique. Meanwhile, the effect of input saturation constrains is considered in the control design. All the signals in the closed-loop system are proved uniformly ultimately bounded. Finally, the experimental platform simulation results are used to demonstrate the effectiveness of the proposed scheme.

Keywords Inverted pendulum system · Neural network · Dynamic surface control · Input saturation

1 Introduction

Inverted pendulum system has the characteristics of absolute instability, high-degree, multivariable, strong coupling, and nonlinearity, and it is an ideal model to test the control theory and application. The research for control techniques for inverted pendulum has important practical meaning. So, it is widely concerned by scholars and experts.

In the past several years, there were considerable literatures to study the control design of the inverted pendulum. Many control theories and methods were used for the control research for the inverted pendulum system. In [1], a supervisory hybrid/switching control strategy was applied for asymptotic stabilization of the inverted pendulum, and the controller was obtained by Jacobian linearization or exact

E. Wei (✉) · T. Li · J. Li · Y. Hu · Q. Li
Navigaion College, Dalian Maritime University, Dalian, China
e-mail: weienping@yahoo.cn

F. Sun et al. (eds.), *Foundations and Practical Applications of Cognitive Systems and Information Processing*, Advances in Intelligent Systems and Computing 215,
DOI: 10.1007/978-3-642-37835-5_60,

feedback linearization to stabilize the pendulum around its upright position. Global stabilization methods of inverted pendulum system using powerful integrator backstepping procedure (IBS) were proposed in [2, 3]. However, this technique suffers the problem of "explosion of complexity" besides putting stringent condition on certain system functions [4]. The control law obtained through a cumbersome design procedure is usually very complicated. Multiple sliding surfaces (MSS) control in [5] is similar to integrator backstepping, avoiding the phenomenon of "explosion of complexity", but it falls short of Integrator backstepping in terms of theoretical rigor. Concept of dynamic surface control (DSC), a dynamic extension to MSS, introduced by Swaroop et al. [4] resolved these issues by using low-pass filters. It addresses not only the issue of "explosion of complexity" associated with Integrator backstepping, but also solves the problem of *i*th state reference (desired) trajectory derivatives numerically. It is simple, more intuitive and applies to a more general class of systems.

Besides, in practice, actuator saturation is one of the most important nonsmooth nonlinearities which usually appears in many industry control systems. This problem is of great importance because almost all practical control systems have limitations on the amplitudes of control inputs, and such limitations can cause serious deterioration of control performances and even destroy the stability of the control systems [6]. So we cannot ignore it in the control design.

In this paper, by incorporating DSC technique into a neural network (NN)-based adaptive control design framework, a DSC NN-based adaptive controller is proposed for inverted pendulum system. Meanwhile, considering the actual condition of the implementation of the project, we will address this problem for inverted pendulum system in the presence of input saturation by taking saturation into consideration in controller design. Finally, stability analysis shows that our control law can guarantee the uniformly ultimate boundedness of the solution of the closed-loop system and make the tracking error arbitrarily small.

2 Problem Formulation

Consider the following inverted pendulum system:

$$\begin{cases} \dot{x}_1 = x_2 \\ \dot{x}_2 = x_3 - a\sin(x_1) - q\cos(x_1) + d_2(t) \\ \dot{x}_3 = -x_3 + u(v(t)) + d_3(t) \\ y = x_1 \end{cases} \tag{1}$$

where x_1, x_2 denote the angular position and rate of the Inverted pendulum, and x_3 denotes the the motor shaft angle. $u(v(\mathrm{t}))$ denotes the plant input subject to saturation type nonlinearly described by [7] which is used to represent the motor torque. a and q are the system's unknown parameters, and $d_2(t)$ and $d_3(t)$ both are the uncertain terms of the system's external disturbance, $y \in R$ is the output of this system.

The inverted pendulum plus driven motor is a simple system. This model was employed at the first time by Gutman [8] when he discussed the design of robust control of uncertain nonlinear system, but he did not take the influence of driven motor. Yang [9] also studied this system when he discussed small-gain approach to robust adaptive fuzzy control for strict-feedback nonlinear systems, but he did not consider the effect of input saturation constrains. In this paper, a novel NN-based adaptive DSC is proposed for the inverted pendulum system. Meanwhile, the effect of input saturation constrains is considered in the control design.

According to [10], the saturation is approximated by a smooth function defined as

$$g(v) = u_M \times \tanh\left(\frac{v}{u_M}\right) = u_M \frac{e^{v/u_M} - e^{-v/u_M}}{e^{v/u_M} + e^{-v/u_M}} \tag{2}$$

In order to achieve the objective of tracking, we augment the plant to consider the saturation function and transform the plant as follows

$$\begin{cases} \dot{x}_1 = x_2 \\ \dot{x}_2 = x_3 - a\sin(x_1) - q\cos(x_1) + d_2(t) \\ \dot{x}_3 = -x_3 + v(t) + \Delta u + d_3(t) \\ y = x_1 \end{cases} \tag{3}$$

where $\Delta u = g(v) - v$.

The control objective is, for a given reference input $y_r(t)$, $t \geq 0$, which is a sufficiently smooth function of t and y_r, $\dot{y}_r$, $\ddot{y}_r$ are bounded for $t \geq 0$, proposing a neural network-based adaptive control law such that the out put $y(t) = x_1$ track the reference input y_r with a prescribed small error.

3 Adaptive DSC Design

In this section, we will incorporate the DSC technique and a neural network-based adaptive control design scheme for the third-order system described by (3). The recursive design procedure contains 3 steps. From Step 1 to Step 2, virtual control α_2 and α_3 are designed at each step. Finally, an overall control law v is constructed at step 3.

Step 1: Consider the first equation in (3), i.e.,

Let

$$z_1 = x_1 - y_r \tag{4}$$

which is called the error surface with y_r as the desired trajectory. Choose virtual control α_2 as follow:

$$\alpha_2 = -c_1 z_1 + \dot{y}_r \tag{5}$$

Let α_2 pass through a first-order filter with time constant $\in_2$

$$\in_2 \dot{\phi}_2 + \phi_2 = \alpha_2 \quad \phi_2(0) = \alpha_2(0) \tag{6}$$

Step 2: Define $f_2(x_1, x_2) = -a\sin(x_1) - q\cos(x_1)$, Given a compact set $\Omega_{x2} \in R^2$, let θ_2^* and ε_2^* be such that for any $(x_1, x_2) \in \Omega_{x2}$

$$f_2(x_1, x_2) = \theta_2^{*T} \varphi_2(x_1, x_2) + \varepsilon_2^* \tag{7}$$

With $\left|\varepsilon_2^*\right| \leq \varepsilon_m$. Let

$$z_2 = x_2 - \phi_2 \tag{8}$$

which is called the second error surface. Then

$$\dot{z}_2 = x_3 + f_2(x_1, x_2) + d_2(t) - \dot{\phi}_2 \tag{9}$$

Choose a virtual control α_3 as follows:

$$\alpha_3 = -c_2 z_2 - z_1 - \hat{\theta}_2^T \varphi_2(x_1, x_2) + \dot{\phi}_2 - d_2^* \tanh\left(\frac{d_2^* z_2}{\delta}\right) \tag{10}$$

where $\hat{\theta}_2$ is the estimation of θ_2^* and is updated as follows:

$$\dot{\hat{\theta}}_2 = \Gamma_2 \varphi_2(x_1, x_2) z_2 - \sigma \Gamma_2 \hat{\theta}_2 \tag{11}$$

with any constant matrix $\Gamma_2 = \Gamma_2^T > 0$.

Introduce a new state variable ϕ_3 and let α_3 pass through a first-order filter with time constant $\in_3$ to obtain φ_3

$$\in_3 \dot{\phi}_3 + \phi_3 = \alpha_3 \quad \phi_3(0) = \alpha_3(0) \tag{12}$$

Step 3: The final control law will be derived in this step. Define $f_3(x_1, x_2, x_3) = -x_3$. Given a compact set $\Omega_{x3} \in R^3$, let θ_3^* and ε_3^* be such that for any $(x_1, x_2, x_3) \in \Omega_{x3}$

$$f_3(x_1, x_2, x_3) + \Delta u = \theta_3^{*T} \varphi_3(x_1, x_2, x_3) + \varepsilon_3^* \tag{13}$$

With $\left|\varepsilon_3^*\right| \leq \varepsilon_m$. Define the third error surface z_3 to be

$$z_3 = x_3 - \phi_3 \tag{14}$$

Then

$$\dot{z}_3 = f_3(x_1, x_2, x_3) + v(t) + \Delta u + d_3(t) - \dot{\phi}_3 \tag{15}$$

$$v = -z_2 - \hat{\theta}_3^T \varphi_3(x_1, x_2, x_3) + \dot{\phi}_3 - c_3 z_3 - d_3^* \tanh\left(\frac{d_3^* z_3}{\delta}\right) \tag{16}$$

where $\hat{\theta}_3$ is the estimation of θ_3^* and is updated as follows:

$$\dot{\hat{\theta}}_3 = \Gamma_3 \varphi_3(x_1, x_2, x_3) z_3 - \sigma \Gamma_3 \hat{\theta}_3 \tag{17}$$

4 Stability Analysis

In order to establish that the closed-loop system still retain the uniformly ultimate boundedness property, we first introduce the closed-loop system. Define the estimation error as

$$\tilde{\theta}_i = \hat{\theta}_i - \theta_i^*, \quad i = 1, \ldots, n. \tag{18}$$

Define

$$y_2 = \phi_2 - \alpha_2 = \phi_2 + c_1 z_1 - \dot{y}_r \tag{19}$$

$$y_3 = \phi_3 - \alpha_3 = \phi_3 + \hat{\theta}_2^T \varphi_2(x_1, x_2) + c_2 z_2 + \frac{y_2}{\in_2} + d_2^* \tanh\left(\frac{d_2^* z_2}{\delta}\right) \tag{20}$$

Noting that

$$\dot{\phi}_i = \frac{\alpha_i - \phi_i}{\in_i} = -\frac{y_i}{\in_i}, \quad i = 2, \ldots, n \tag{21}$$

Let

$$\dot{y}_2 = \dot{\phi}_2 - \dot{\alpha}_2 = \dot{\phi}_2 + c_1 \dot{z}_1 - \ddot{y}_r = -\frac{y_2}{\in_2} + B_2\left(z_1, y_2, \hat{\theta}_1, y_r, \dot{y}_r, \ddot{y}_r\right) \tag{22}$$

where B_2 is a continuous function as follows

$$B_2\left(z_1, y_2, \hat{\theta}_1, y_r, \dot{y}_r, \ddot{y}_r\right) = c_1 \dot{z}_1 - \ddot{y}_r \tag{23}$$

$$\dot{y}_3 = \dot{\phi}_3 - \dot{\alpha}_3 = -\frac{y_3}{\in_3} + B_3\left(z_1, z_2, y_2, \hat{\theta}_2, \hat{\theta}_3, y_r, \dot{y}_r, \ddot{y}_r\right) \tag{24}$$

where B_3 is a continuous function as follows

$$B_3\left(z_1,\, z_2,\, y_2,\, \hat{\theta}_2,\, \hat{\theta}_3,\, y_r,\, \dot{y}_r,\, \ddot{y}_r\right) = \dot{\hat{\theta}}_2^T \varphi_2(x_1,\, x_2) + \hat{\theta}_2^T \frac{\partial \varphi_2}{\partial(x_1,\, x_2)} \begin{bmatrix} \dot{x}_1 \\ \dot{x}_2 \end{bmatrix} + c_2 \dot{z}_2 + \frac{\dot{y}_2}{\in_2} + \frac{d_2^{*2}}{\delta}\left(1/\cosh^2\left(\frac{d_2^* z_2}{\delta}\right)\right)\dot{z}_2 \tag{25}$$

Given ε_m, let $\theta_i^* \in R^{N_i}$, $\quad i = 2, 3$ be in the compact set with $\Omega_{xi} \in R^i$ and $\left|\varepsilon_i^*\right| \le \varepsilon_m$. Assume there exists a known positive number such that θ_M, for all $i = 2, 3$

$$\left\|\theta_i^*\right\| \le \theta_M \tag{26}$$

Let y_r be a sufficiently smooth function of t and $y_r(t)$, $\dot{y}_r(t)$, $\ddot{y}_r(t)$ be bounded for $t \ge 0$. Consider the (22) and (24). Given any positive number p, for all initial conditions satisfying $\sum_{j=1}^{3} z_j^2 + \sum_{j=2}^{3} \tilde{\theta}_j^T \Gamma_j^{-1} \tilde{\theta}_j + \sum_{j=1}^{2} y_{j+1}^2 \le 2p$, there exist $c_i, \in_{i+1}, \Gamma_i$ and σ such that the solution of the closed-loop system is uniformly ultimately bounded, and the steady-state tracking error is smaller than a prescribed error bound.

Proof Consider the Lyapunov function candidate

$$V = \frac{1}{2}\sum_{i=1}^{3} z_i^2 + \frac{1}{2}\sum_{i=2}^{3} \tilde{\theta}_i^T \Gamma_i^{-1} \tilde{\theta}_i + \frac{1}{2}\sum_{i=1}^{2} y_{i+1}^2 \tag{27}$$

$$\begin{aligned} \dot{V} = \sum_{i=1}^{n} z_i \dot{z}_i + \sum_{i=2}^{3} \tilde{\theta}_i^T \Gamma_i^{-1} \dot{\tilde{\theta}}_i + \sum_{i=1}^{2} y_{i+1} \dot{y}_{i+1} = \sum_{i=1}^{3} -c_i z_i^2 \\ + \sum_{i=2}^{3}\left[z_i\left(\varepsilon_i^* + d_i\right) - z_i d_i^* \tanh\left(\frac{d_i^* z_i}{\delta}\right) + \left(-\tilde{\theta}_i^T \varphi_i(x_1, \ldots, x_i) z_i + \tilde{\theta}_i^T \Gamma_i^{-1} \dot{\hat{\theta}}_i\right)\right] \\ + \sum_{i=1}^{2}\left(-\frac{y_{i+1}^2}{\in_{i+1}} + \left|y_{i+1} B_{i+1}\right|\right) \end{aligned} \tag{28}$$

Substituting $\dot{\hat{\theta}}_i = \Gamma_i \varphi_i(x_1, \ldots, x_i) z_i - \sigma \Gamma_i \hat{\theta}_i \quad i = 2, 3$ then we can get

$$\begin{aligned} \dot{V} = \sum_{i=1}^{3} -c_i z_i^2 + \sum_{i=2}^{3}\left[z_i(\varepsilon_i^* + d_i) - z_i d_i^* \tanh\left(\frac{d_i^* z_i}{\delta}\right) - \left(\sigma \tilde{\theta}_i^T \hat{\theta}_i\right)\right] \\ + \sum_{i=1}^{2}\left(-\frac{y_{i+1}^2}{\in_{i+1}} + \left|y_{i+1} B_{i+1}\right|\right) \end{aligned} \tag{29}$$

Let $\left|\varepsilon_i^*\right| \le \varepsilon_{im}$, $|d_i(t)| \le d_{im}$ and $d_i^* = \varepsilon_{im} + d_{im}$, then

$$\left(\varepsilon_i^* + d_i(t)\right)z_i \le |(\varepsilon_{im} + d_{im})z_i| = \left|d_i^* z_i\right| \le 0.2785\,\delta + d_i^* z_i \tanh\left(\frac{d_i^* z_i}{\delta}\right) \tag{30}$$

$$\dot{V} \le \sum_{i=1}^{3} -c_i z_i^2 + \sum_{i=2}^{3}\left(0.2785\,\delta - \sigma\tilde{\theta}_i^T\hat{\theta}_i\right) + \sum_{i=1}^{2}\left(-\frac{y_{i+1}^2}{\in_{i+1}} + |y_{i+1}B_{i+1}|\right) \tag{31}$$

Since $|B_i|$ has a maximum M_i on $\Pi \times \Pi_i$ [7]. Using $2\tilde{\theta}_i^T\hat{\theta}_i \ge \left\|\tilde{\theta}_i\right\|^2 - \left\|\theta_i^*\right\|^2$ gives

$$\begin{aligned}\dot{V} &\le \sum_{i=1}^{3} -c_i z_i^2 + \sum_{i=2}^{3}\left[0.2785\,\delta - \frac{\sigma}{2}\left(\left\|\tilde{\theta}_i\right\|^2 - \left\|\theta_i^*\right\|^2\right)\right] + \sum_{i=1}^{2}\left(-\frac{y_{i+1}^2}{\in_{i+1}} + |y_{i+1}B_{i+1}|\right)\\ &\le \sum_{i=1}^{3} -c_i z_i^2 + \sum_{i=2}^{3}\left[-\frac{\sigma}{2\lambda_{\max}\left(\Gamma_i^{-1}\right)}\tilde{\theta}_i^T\Gamma_i^{-1}\tilde{\theta} + \frac{\sigma}{2}\left\|\theta_i^*\right\|^2 + 0.2785\,\delta\right]\\ &\quad + \sum_{i=1}^{2}\left(-\frac{y_{i+1}^2}{\in_{i+1}} + |y_{i+1}B_{i+1}|\right)\end{aligned} \tag{32}$$

Let $\frac{\sigma}{2}\left\|\theta_i^*\right\|^2 + 0.2785\,\delta = e_i$. Noting $\left\|\theta_i^*\right\| \le \theta_M$ gives

$$\mathrm{e}_i \le \frac{\sigma}{2}\theta_M^2 + 0.2785\,\delta = e_M \tag{33}$$

Let $\sigma/2\lambda_{\max}(\Gamma_i^{-1}) = c_0$. Then

$$\dot{V} \le \sum_{i=1}^{3} -c_0 z_i^2 + \sum_{i=2}^{3}\left(-c_0\tilde{\theta}_i^T\Gamma_i^{-1}\tilde{\theta} + e_M\right) + \sum_{i=1}^{2}\left(-\frac{y_{i+1}^2}{\in_{i+1}} + |y_{i+1}B_{i+1}|\right) \tag{34}$$

Let $\frac{1}{\in_{i+1}} = \frac{M_{i+1}^2}{2\eta} + c_0$. For any positive η, $\left(y_{i+1}^2 B_{i+1}^2/2\eta\right) + (\eta/2) \ge |y_{i+1}B_{i+1}|$.

$$\begin{aligned}\dot{V} &\le \sum_{i=1}^{3} -c_0 z_i^2 + \sum_{i=2}^{3}\left(-c_0\tilde{\theta}_i^T\Gamma_i^{-1}\tilde{\theta} + e_M\right)\\ &\quad + \sum_{i=1}^{2}\left[\frac{\eta}{2} - c_0 y_{i+1}^2 - \left(1 - \frac{B_{i+1}^2}{M_{i+1}^2}\right)\frac{M_{i+1}^2 y_{i+1}^2}{2\eta}\right]\end{aligned} \tag{35}$$

Define $V\left(z_1, \ldots, z_n,\ y_2, \ldots y_n,\ \tilde{\theta}_1, \ldots, \tilde{\theta}_n\right) = p, |B_{i+1}| < M_{i+1}$. We have

$$\dot{V} \le \sum_{i=1}^{3} -c_0 z_i^2 - \sum_{i=2}^{3} c_0\tilde{\theta}_i^T\Gamma_i^{-1}\tilde{\theta} + 2e_M + \eta + \sum_{i=1}^{2}\left(-c_0 y_{i+1}^2\right) = -2c_0 V + 2e_M + \eta \tag{36}$$

$$0 \le V(t) \le (2e_M + \eta)/2c_0 \tag{37}$$

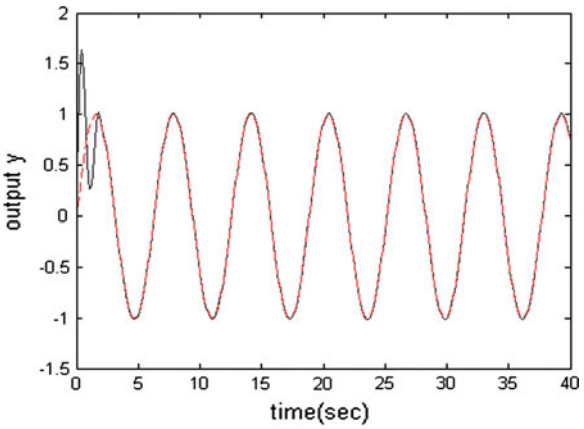

Fig. 1 Simulation results for pendulum system with motor: system output y and reference signal y_r

Actually, the Eqs. (36) and (37) means that $V(t)$ is bounded (please refer to [11] for details). Thus, all signals of the closed-loop system are proved uniformly ultimately bounded. Moreover, we can appropriately choose the design parameters c_i, Γ_i^{-1}, σ etc make the tracking error arbitrarily small. This concludes the proof simply.

5 Numerical Simulation of Inverted Pendulum

In the simulation, the initial conditions for $a = 11$, $q = 2$, $d_2(t) = \sin(t)$, $d_3 = 5\sin(t)$. The initial conditions of x_1, x_2, x_3 are 0.2, 2π, 0, respectively.

Choose the control parameters $c_1 = c_2 = c_3 = 5$, $\in_2 = \in_3 = 0.005$, $d_2^* = d_3^* = 6$, $\delta = 0.5$, $u_M = 40$.

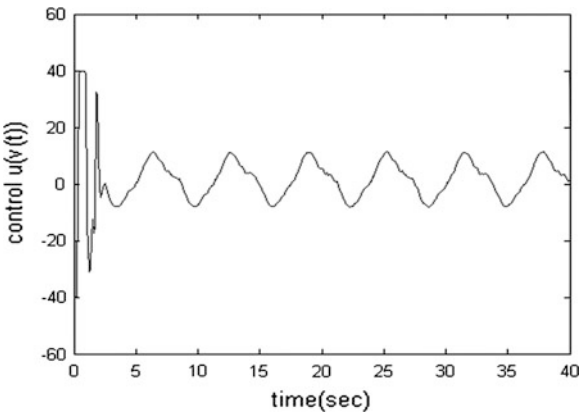

Fig. 2 Simulation results for pendulum system with driven motor: control u

From Fig. 1, we can see that after a short transit process, a good tracking and a small tracking error performance is obtained. Figure 2 is the trajectories of the control $u(v(t))$ with input saturation.

6 Conclusions

In this paper, the adaptive tracking control for the inverted pendulum has been investigated. By employing the NN approximation to address the uncertainty of the system, and DSC technique to eliminate the problem of "explosion of complexity" caused by the traditional backstepping approach, an adaptive neural tracking controller has been explored. In addition, the effect of input saturation constrains is considered in this control design. All the signals of the closed-loop system are guaranteed to be uniformly ultimately bounded. By adjusting the parameters, the tracking error may be made arbitrarily small. Simulation results for the driven inverted pendulum system are presented to demonstrate the good tracking performance of the proposed scheme.

Acknowledgments This work is supported in part by the National Natural Science Foundation of China (Grant No. 51179019, 60874056), the Natural Science Foundation of Liaoning Province (Grant No. 20102012), the Program for Liaoning Excellent Talents in University (LNET) (Grant No. LR2012016), and the Fundamental Research Funds for the Central Universities (2011QN097).

References

1. Spong MW, Corke P, Lozano R (2001) Nonlinear control of the inertia wheel pendulum. Automatica 37(11):1845–1851
2. Alberto I (1985) Nonlinear control systems, 2nd edn. Springer, Berlin
3. Sontag ED, Sussman HJ (1988) Further comments on the stability of the angular velocity of a rigid body. Syst Control Lett 12:213–217
4. Swaroop D, Gerdes JC, Yip PP, Hedrick JK (1997) Dynamic surface control of nonlinear systems. Proc Am Control Conf 5:3028–3034
5. Wonand M, Hedrick JK (1996) Multiple surface sliding control of a class of uncertain nonlinear systems. Int J Control 64(4):693–706
6. Gao WZ, Selmic RR (2006) Neural network control of a class of nonlinear systems with actuator saturation. IEEE Trans Neural Netw 17(1):147–156
7. Wang D, Huang J (2005) Neural network-based adaptive dynamic surface control for a class of uncertain nonlinear systems in strict-feedback form. IEEE Trans Neural Netw 16(1):195–202
8. Gutman S (1979) Uncertain dynamical system—A Lyapunov min max approach. IEEE Trans Automat Control AC-24:437–443
9. Yang Y, Feng G, Ren J (2004) A combined backstepping and small-gain approach to robust adaptive fuzzy control for strict-feedback nonlinear systems. IEEE Trans Syst Man Cybern 34(3):1596–1601

10. Zhou J, Er MJ, Zhou Y (2006) Adaptive neural network control of uncertain nonlinear systems in the presence of input saturation. In: Proceeding of the 9th international conference on control, automation, Robotics and vision, ICARCV '06, pp 1–5
11. Qu Z (1998) Robust control of nonlinear uncertain systems. Wiley, New York

Unmanned Aircraft Vehicle Path Planning Based on SVM Algorithm

Yanhong Chen, Wei Zu, Guoliang Fan and Hongxing Chang

Abstract This paper describes an approach of using image processing and patters classification techniques for navigating the unmanned aircraft vehicle in known irregular environment. In the case of 2D path planning, a feasible flight path connecting the start and goal point can be regarded as a separating surface that divides the space into two regions. This suggests a dual problem of first dividing the whole space into such two regions and then picking up the boundary as a path. We use support vector machine to solve this dual problem. SVM can generate a nonlinear separating surface based on the margin maximization principle. First, we generate a novel search space which contains flyable and no-fly regions from 3D surface of minimum risk and pick up key obstacle points as samples. Second, a safe and smooth path is generated through SVM. Results from simulations show that the path planner is able to plan an optimal path efficiently due to the simplicity of the search space.

Keywords Path planning · Image processing · Support vector machine · Surface of minimum risk

Y. Chen (✉) · W. Zu · G. Fan · H. Chang
Institute of Automation, Chinese Academy of Sciences, Beijing, China
e-mail: Yanhongchen100@yeah.net

W. Zu
e-mail: wei.zu@ia.ac.cn

G. Fan
e-mail: guoliang.fan@ia.ac.cn

H. Chang
e-mail: hongxing.chang@ia.ac.cn

F. Sun et al. (eds.), *Foundations and Practical Applications of Cognitive Systems and Information Processing*, Advances in Intelligent Systems and Computing 215,
DOI: 10.1007/978-3-642-37835-5_61,

1 Introduction

The path planning technology is an important branch of aerial robot research field. The so-called path planning of unmanned aircraft vehicle (UAV) is to search an optimum or approximate optimum collision-free path from start point to the destination according to certain constraints [1]. A good path planning algorithm for UAV must possess several important attributes, making its design a multi-objective optimization problem [2]. When execute low-altitude penetration mission, the path planned not only need to meet the requirements of low altitude and try to avoid the threats and obstacles, but also need to consider constraints due to the aircraft's dynamics and kinematics. Path planning has emerged as one of the most challenging problems in the development of UAV, especially in 3D environment.

A lot of research efforts have been devoted to the path planning problem over the past two decades. However, the path planning problem in three-dimensional environments can be identified into three main approaches, which are the following:

- Intelligent methods
- Geometric methods
- Potential field methods

Each method has its own advantages and disadvantages: intelligent methods do not require complex mathematical calculations, but it is slow to converge; geometric methods, such as the Voronoi graph algorithm, can find the optimal path in the initial flight paths, but it is time-consuming to expand V-diagrams in searching space; potential function method is elegant when used in an online collision scheme, but it is difficult to construct the potential function.

Most of the above-mentioned methods, generally, first construct a data structure to describe the search space, and then find the best trajectory under appropriate evaluation functions. This paper looks at path planning in a different viewpoint. Generally, the paths in horizontal and vertical plane are generated, respectively, due to the efficiency. Let us consider a collision-free path in horizontal plane as a safe corridor which divides the whole space into two regions: one on the left and the other on the right side of the path. We can view the division of the whole space as a two-class classification problem. We use support vector machine (SVM) as a classifier. SVM is a maximum margin classifier and can generate nonlinear separating surface. These properties make SVM able to produce a safe and smooth path far away from the obstacles. However, it needs pre and post-processing for applying SVM to path planning.

In this paper, we proposed a two-step method to generate path through irregular territory illustrated in Fig. 1a. First, we generate a 2D search space to represent the 3D flight environment. It can solve the challenging high-dimensional problems efficiently at the expense of completeness. A method is also introduced to pick up

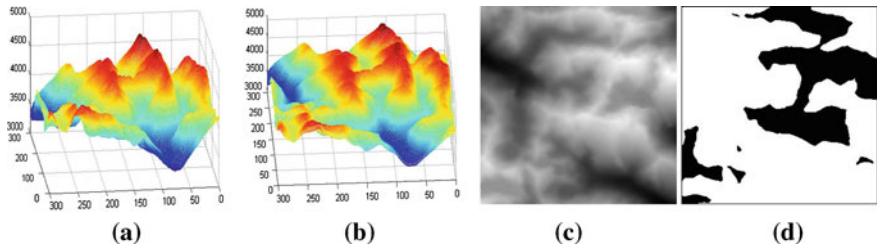

Fig. 1 **a** The original terrain surface in DEM. **b** The SOMR derived from the surface in DEM. (**c**) The *gray image* derived from the SOMR. **d** The safe-map image derived from the *gray image*

key obstacle points as samples in 2D search space. Then we take further advantage of SVM to generate a feasible path.

The remainder of this paper is organized as follow: in Sect. 2, we present a methodology for the creation of the search space and give the details of generating a smooth path by SVM. Section 3 provides the experimental results. Finally, Sect. 4 summarizes the contribution of this paper and the future work.

2 Path Planning Algorithm

The path planning approach taken in this work is carried out in two steps. A surface of minimum risk (SOMR) is constructed based on the terrain model. Any curve including the optimal path on the SOMR satisfies the dynamics of the aircraft. If we can find the horizontal projection of optimal path, then the feasible 3D flyable path can be obtained through correspondence. In the first step, we generate a safe-map which contains flyable and no-fly zones based on the SOMR, as is shown in Fig. 1d. The points on the outline of no-fly zones are treat as obstacle points. A set of samples is generated by picking up the labeled key obstacle points. In the second step, an initial path is determined from SVM through the separating surface. By fine tuning the initial path, an optimal and smooth path can be quickly generated.

2.1 Surface of Minimum Risk

The proposed path planning algorithm starts with a preprocessing step. This preprocessing step can minimize the online computation time by pregenerating a new search space that contains all the information which will be used during the path planning. It involves analyzing and representing the environment. We use Digital Elevation Models (DEM) [3] to present surrounding environments. The basic idea consists of griding the search space and assigning an altitude to each cell in the

grid. The position of grid point is given by the vector X_d^i with components x_d, y_d, H_d.

The concept of SOMR was first proposed by Menon et al. [4]. The algorithm developed in [5] takes advantage of the established technology for a safe and reliable SOMR generation. Paths on this minimum risk surface maximize the probability of survival for UAV while satisfying appropriate flight path constraints.

The SOMR is defined as a new surface on which each grid has safe distances H_{de} to the obstacles in its neighborhood, the gradient magnitude S_i and the curvature ρ_h of each grid point should also be confined in appropriate domains. The first term H_{de} ensures the aircraft not to crash into the terrain and minimizes the altitude above sea level that causes the algorithm to seek low-altitude penetration path. The second term S_i makes the path satisfy the climb and pitch angle constraints. The third term ρ_h limits the maximal vertical acceleration of the aircraft when it follows the planned path.

The position of SOMR is given by the vector X_s^i with components x_s, y_s, H_s. The value of H_s can be determined by:

$$\begin{cases} h \le H_{\text{de}} = \min\limits_{(x_i,y_i)\in R} \sqrt{(x_s - x_i)^2 + (y_s - y_i)^2 + (H_s - H_i)^2} \le H \\ s_{\min} < s_i = \dfrac{\left(H_s^i - H_s^{i-1}\right)}{l} < s_{\max} \\ \rho_{h\_\min} < \rho_h = \dfrac{\left|H_s''(x,y)\right|}{\left(1 + H_s'(x,y)\right)^{3/2}} < \rho_{h\_\max}, \text{where} \quad \rho_{h\_\max} = \dfrac{n_z - g}{V^2} \\ H_i = f(x_i, y_i), [x_i, y_i, H_i] \in X_d^i \end{cases} \tag{1}$$

Where R is the region contains the neighbors of point (x_s, y_s), H_i is the altitude of terrain in the DEM. h and H are predefined minimal−maximal safety distances. l is the horizontal distance of point (x_i, y_i) and (x_{i-1}, y_{i-1}). n_z is the maximal vertical acceleration of the aircraft, g is gravity, and V is the speed of the aircraft. The motions of UAV are limited on this new surface. The SOMR is smoother and higher than the original terrain surface, as shown in Fig. 1b.

However, the approach using SOMR to 3D planning suffers from the curse of dimensionality, making real-time implementation a challenge. Because the greater the dimension of the search space is, the more complex the path planning problem will be. We propose a novel spatial representation which can squeeze 3D surfaces into 2D map, then we simplify the 2D map to get the safe-map. It can solve the challenging high-dimensional problems efficiently without losing the main obstacles information. The safe-map is a map in planar domain for simplifying the computation. And it is used as new search space to navigate the robot among those obstacles and find an optimal path.

2.2 Safe-Map

We project the SOMR into 2D gray image, depicted in Fig. 1c. The component H_s of the vector X_s^i can be determined by x_s, y_s, then the vector X_s^i can be related to the image coordinates. We present the SOMR with an 8-bits gray image.

$$\frac{I(x_s, y_s)}{255} = \frac{H(x_s, y_s) - H_{\min}}{H_{\max} - H_{\min}} \tag{2}$$

Where $I(x_s, y_s)$ is the image intensity and indicates the altitude from the sea level at point (x_s, y_s) .

We assume that it is unnecessary to search the regions that are too high from the sea level. In order to further improve the efficiency of the path planning, we get a safe-map by narrow down the search space according to the altitude, as shown in Fig. 1d. The safe-map is represented by a binary image. This image is obtained by threshold which attempts to identify the prohibited region for aircraft. The expected altitude from ground for the flyable robot reaches maximum at the threshold value. We define white region as safe-region and black region as no-fly region. The safe-map makes sure that the path planner finds a collision-free path. The path planner searches the optimal path outside the no-fly region.

2.3 Support Vector Machine

Support vector machine is a binary classification method that finds the optimal separating hyperplane based on the principle of margin maximization [6, 7].

Suppose that we have a group of training samples: $D = \{(x_1, t_1), (x_2, t_2), \ldots, (x_n, t_n)\}$, $x_i \in R^m$, $t_i \in \{-1, 1\}$ they can be separated by a hyperplane $w^T x + b = 0$. If the training data are linearly separable, there exist parameters w and b that satisfy:

$$t_i\left(\mathrm{w^T x_i} + \mathrm{b}\right) \geq 1(\mathrm{i} = 1, 2, \ldots, \mathrm{n}) \tag{3}$$

Using such parameters, the two classes are separated by two hyperplanes H_1 : $w^T x + b = 1$ and $H_2 : w^T x + b = -1$, and no data exists between the two hyperplanes. Since the distance between the hyperplanes is $\rho = 2/\|w\|$, the optimal parameters can be determined by minimizing the objective function:

$$\begin{aligned} &\min_w L(w) = \|w\|^2 \Big/ 2, \\ &s.t.\, t_i\left(w^T x_i + b\right) \geq 1,\ i = 1, 2, \cdots, n \end{aligned} \tag{4}$$

A solution to this problem is given by solving the following dual problem:

$$\begin{aligned} &\min_{w} L_D(\alpha) = \frac{1}{2}\sum_{i,j=1}^{n} \alpha_i \alpha_j t_i t_j x_i^T x_j - \sum_{i=1}^{n} \alpha_i \\ &s.t. \sum_{i=1}^{n} \alpha_i t_i = 0, \alpha_i \geq 0, i = 1, 2, \ldots, n \end{aligned} \tag{5}$$

The training data x_i with non-zero α_i are on either one of the hyperplanes H_1 or H_2; such data are called support vectors because they are the only data that determine the parameters. From these data, a discrimination function is given by (6) in which S is the set of support vectors.

$$y = \text{sign}\left(w^T X + b\right) = \text{sign}\left(\sum_{i \in S} \alpha_i t_i x_i^T x + b\right) \tag{6}$$

If a nonlinear separating surface is to be determined, kernel tricks can be used. By using appropriate kernel functions, we can change the problem of finding a nonlinear separating surface in the original space into finding a linear separating hyperplane in the high-dimensional space, thus reducing the calculation cost and making it possible to obtain an optimal nonlinear separating surface in the original space.

Let ϕ be the mapping from the original to the high-dimensional space. Such a mapping exists for some class of kernel function K, that is:

$$K(x_1, x_2) = \phi^T(x_1)\phi(x_2) \tag{7}$$

For the discrimination in the high-dimensional space, the original objective function (5) is modified to:

$$\begin{aligned} &\min_{\alpha} L_D(\alpha) = \frac{1}{2}\sum_{i,j=1}^{n} \alpha_i \alpha_i t_i t_j \phi^T(x_i)\phi(x_j) - \sum_{i=1}^{n} \alpha_i \\ &s.t. \sum_{i=1}^{n} \alpha_i t_i = 0, \alpha_i \geq 0, i = 1, 2, \ldots, n \end{aligned} \tag{8}$$

And the discrimination function is modified as

$$y = \text{sign}\left(\sum_{i \in S} \alpha_i t_i K(x_i, x_j) + b\right) \tag{9}$$

Since all necessary calculations in the high-dimensional space are given by the calculation of the kernel function in the original space, we can determine nonlinear separating surfaces without explicitly representing the high-dimensional space.

2.4 Applying SVM to Path Planning

To use SVM in path planning problems, we should preprocess the safe-map previously obtained. Let y be the output of the following expression [this is actually the argument of the sign function in (9)] [7]:

$$y = \sum_{i \in S} \alpha_i t_i K(x_i, x_j) + b \tag{10}$$

Based on the value of y, the whole space is divided into the following three regions:

- Region of class one where $y \geq 1$.
- Region of class two where $y \leq -1$.
- Intermediate region where $-1 < y < 1$.

If we can generate these regions so that all obstacle points are in regions of class one or class two, a collision-free path can be found inside intermediate regions. For this purpose, we divide obstacle points into two classes; samples for support vector learning are generated from both the two classes. We also set virtual obstacles around the start and goal point so that they lie in intermediate regions.

In general, however, even if both a start and a goal point lie inside intermediate regions, the collision-free path generated by extracting SVM separating surface may not exactly derive from the start point and end in goal point. Such a case happens mainly because the distribution of obstacle points on both sides of the surface is not regular. To cope with this, we fine tuning the start and end part of the separating surface to get a flyable path.

Once the labeled samples are obtained, the next step is to generate an actual path. The details of path planning algorithm are as follows:

(1) Outline of the algorithm: Since we have got the binary image of safe-map that contains flyable and no-fly zones. We then obtain obstacle points from the profile of the no-fly zones. All obstacle points should be divided into two classes, labeled as class one or class two. We treat the labeled key obstacles as samples and feed them to SVM to calculate a separating surface. The procedure of the algorithm is as follows:

   (a) Pick up the key obstacle points from the profile of the no-fly zones and generate samples.
   (b) Set virtual obstacles around the start and the goal point.
   (c) Apply SVM to generate discrimination function and extract a separating surface by analyzing the learned model.
   (d) Fine tuning the separating surface then get the feasible path in 2D and 3D We will explain each step in detail.

(2) Pick up the key obstacle points and sample generation: Fig. 1d shows the binary image of safe-map, and Fig. 2a shows the closed lines of the no-fly

zone profiles. First, we divide the closed line (closed line 6 in Fig. 2a) that contains the start and goal points into two parts by the very two points as shown in Fig. 2a, one part belongs to class one and the other belongs to class two. Second, we label the line connect the start and goal points as l, to each of the rest closed lines, we calculate the number of obstacle points n_1 and n_2 on both sides of l, respectively. If $n_1 \geq n_2$, then all the obstacle points on this closed line are labeled as class one, otherwise the obstacle points are labeled as class two. After all the obstacle points are labeled through the above method, key obstacle points are picked up by corner detection. The main purposes to do this are to prohibit the aircraft from traversing the no-fly zones and cut down the number of obstacle points used as training samples. The result of two-class classification is shown in Fig. 2b.

(3) Setting virtual obstacle points around start and goal point: We set virtual obstacle points around the start and the goal point so that the separating line generated by SVM is closed to the start and goal point. More concretely, we put *N class one* (on one side) and *N class two* points (on the other side) at a certain distance from the start or goal point and in parallel to the direction of exit angle or incidence angle, as shown in Fig. 2b.

(4) Applying SVM and analyzing the learning result: We then apply SVM learning algorithm to the generated samples. By this learning, we get a set of support vectors and their weights; they constitute a discrimination function to determine to which region each point belongs. The separating surface, which is the separating line in 2D, represents candidates of collision-free paths. The separating surface is not, however, explicitly represented by the model. We therefore determine the separating line by searching for the point where value y in (10) is zero. We grid the planar search space with fixed length d_s, and calculate the value y of each grid point. Then we pick up the grid points where $y = 0$ and log the coordinate of these points. The set of these grid points make up the separating line.

(5) Fine tuning the separating line to get the feasible path: Despite we have set virtual obstacle points around the start and goal point, these two points may slightly wander away from the separating line. To cope with this, we fine tuning the start and end part of the separating line. Get the distance s between the first point of the separating line and the start point, move the first ten points

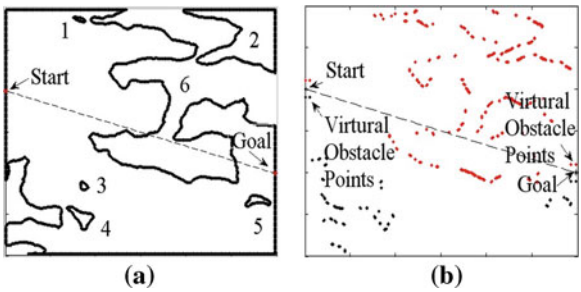

Fig. 2 **a** The outlines of no-fly regions deprived from the safe-map. **b** The result of the two-class classification and the virtual obstacle points set on both sides of start and goal point

of the line toward the start point with changeable step. The first step is s, reduce the length at every step by $0.1 \times s$, until the step turns to zero. And the same is done to the goal point. By fine tuning the separating line we get the feasible path in 2D. Since we have obtained the SOMR, the 3D flyable path on the SOMR can be found by correspondence.

3 Experimental Results

In order to demonstrate the performance of the algorithm described in the previous section, the experimental results are given. In this simulation, a map of size 27×27 km was discretized uniformly by 90 m to generate the search space. The kernel function used in SVM is a Gaussian kernel. The number N of samples for each virtual obstacle is 2.

We illustrate in Fig. 3 the results of the path planning. As we can see from the picture, the projection of the planned path in planar plane is smooth and far away

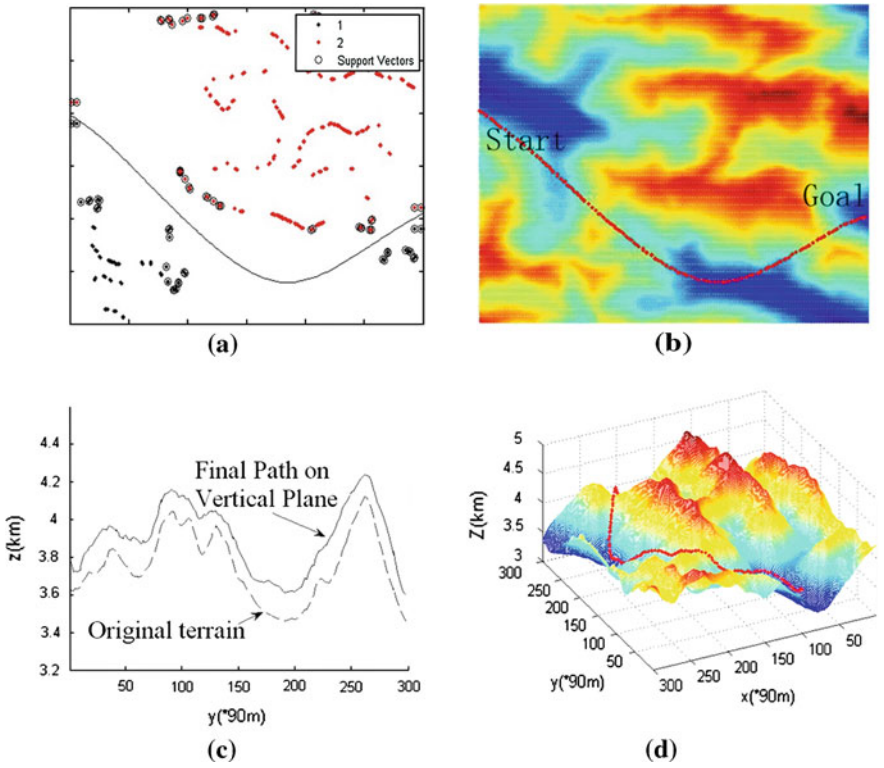

Fig. 3 **a** Path on the safe-map. **b** Path on the horizontal plane. **c** Path on the vertical plane. **d** Path in 3D

from the obstacles. The altitudes of path have been constraint on the SOMR surface. In Fig. 3c, the top line is the SOMR profile along the path in the vertical plane. It indicates the altitude of a smooth path. The bottom line is the original terrain on the vertical plane. The two lines have same shape in the horizontal plane. The path in Fig. 3d shows that the path planning approach proposed in this paper is feasible.

4 Conclusions

In this paper, we have presented a unique approach of applying SVM to the UAV path planning problem in a known environment. SVM has a nice property of generating a nonlinear separating surface based on the margin maximization principle. This property makes it suitable to generate a safe and smooth path. We have described detailed approach for using this property in robot path planning. Our method includes offline and online computation. Offline computation exploits the prior knowledge about the environment, providing surface of minimal risk for further search. Online computation exploits the 2D information provided by SOMR providing the optimal path for robot. A simulation has been provided to illustrate that the proposed approach can indeed produce an optimal path. Proper approach of extracting key obstacle points in complicated environment and reduction of planning cost are the future works.

Acknowledgments This work was supported by Knowledge innovation project of Chinese Academy of Sciences (YYYJ-1122).

References

1. Jingwen T, Meijuan G, Erhong L (2007) Dynamic collision avoidance path planning for mobile robot based on multi-sensor data fusion by support vector machine. In: IEEE international conference on mechatronics and automation, Harbin, pp 2779–2783
2. Scott A, Bortoff (2000) Path planning for UAVs. In: Proceedings of the American control conference, Chicago, pp 364–368
3. Bruno S, Mario M, Gianluca D, Jonh Koo T (2001) Vision based navigation for an unmanned aerial vehicle. In: Proceedings of the IEEE international conference on robotics and automation, Seoul, pp 1757–1765
4. Menon PKA, Kim E, Cheng VHL (1991) Optimal trajectory synthesis for terrain-following. J Guid Control Dyna 4(14):807–813
5. Zhizhong H, Kehu X, Chunlin S (2000) A smooth algorithm of digital terrain model used in low-altitude penetration. J Nanjing Univ Aeronaut Astronaut 32(5):493–498
6. Chris B (2006) Pattern recognition and machine learning. Springer, Berlin
7. Jun M (2006) Support vector path planning. In: IEEE international conference on intelligent robots and systems, Beijing, pp 2894–2899

Modeling Passenger Flow Distribution Based on Disaggregate Model for Urban Rail Transit

Da-lei Wang, En-jian Yao, Yang Yang and Yong-sheng Zhang

Abstract It is widely recognized that one of the most effective ways to solve urban traffic problems is developing public transport system, especially urban rail transit system. The estimation of passenger flow distribution, as an important part of travel demand analysis of urban rail transit, is the prerequisite of the operation organization and management of urban rail transit system, especially when a new line is put into operation. This paper proposes a new passenger flow distribution model, which is based on disaggregate model approach and conforms the aggregated historical passenger flow data to disaggregate data through representative individual method. Influencing factors including travel time, attracted traffic flow, land-use type, intensity around station, and so on are considered. Using the historical passenger flow data of urban railway system in Beijing before and after Line 4 is put into operation, the model is built and the estimation accuracy evaluated. The result shows that the disaggregate model is more accurate than the conventional aggregate single restraint gravitational model.

Keywords Urban transit system · Estimation of passenger flow distribution · Disaggregate model · Representative individual method

D. Wang (✉) · E. Yao · Y. Yang · Y. Zhang
School of Traffic and Transportation, Beijing Jiaotong University, Beijing, China
e-mail: 11120993@mail.bjtu.edu.cn

E. Yao
e-mail: enjyao@bjtu.edu.cn

Y. Yang
e-mail: 10120958@bjtu.edu.cn

Y. Zhang
e-mail: 11121028@bjtu.edu.cn

E. Yao
State Key Laboratory of Rail Traffic Control and Safety, Beijing Jiaotong University, Beijing, China

F. Sun et al. (eds.), *Foundations and Practical Applications of Cognitive Systems and Information Processing*, Advances in Intelligent Systems and Computing 215,
DOI: 10.1007/978-3-642-37835-5_62,

1 Introduction

In order to solve urban traffic problems caused by rapid growth of car ownership, more and more urban rail transit systems have been constructed in China's big cities to alleviate road traffic congestion. The estimation of travel demand, known as the most important step in feasibility analysis of urban rail transit project, can also evaluate the matching degree between the traffic demand and the new network. The estimation of passenger flow is a prerequisite of successfully opening of the new line, and also makes positive contribution to the stable operation of urban rail transit system in the future.

Compared to disaggregate model, the conventional four-step method or the modification based on it is much more widely applied in the travel demand forecast for rail transit system [1, 2]. As one step of conventional four-step method, the estimation of passenger flow distribution plays an important role. Nowadays, the gravitational model is commonly used in traffic distribution forecast. For example, Zou and Sun propose the solution approach, algorithms based on the standard single restraint gravitational model and the doubly restraint gravitational model [3]. However, the gravitational model is determined by a single factor, and the relationship between parameters is set subjectively, so the model cannot reflect the forming mechanism of passenger flow objectively. There are complex factors influencing passenger flow distribution, which brought the nonlinearity problem. Li et al. propose a forecast model based on RBF neural network, take T15 train as example, and the forecast of passenger traffic volume in seat level is taken [4]. However, the method is completely data-driven, and cannot be explained exactly.

The research of disaggregate model was first proposed in the early 1960s, McFadden from Massachusetts made great progress on the theoretical study in the 1970s, leading Manheim, Ben-Akiva, and Lerman to bring the disaggregate model into practice [5]. The disaggregate model is the product of analysis of disaggregate data, which is constructed by the original data based on the actual traffic individual, also known as discrete choice model. The foundation of the disaggregate model is the theory of consumers and financial performance [6] and the random utility theory [7]. With clear hypothesis as the foundation, choosing the factors related to the personal decision as the influencing factors, the model overcomes the disadvantage of the conventional aggregate method, becoming more and more widespread in the field of travel demand forecast. On the other hand, the disaggregate method requires sufficient precision and huge sample size. Taking a lot of time to set the independent variables and calibrate the parameters, together with the complex calculation, limiting the application of the disaggregate model, most of it is used in trip mode structure forecast [8, 9].

Almost all the disaggregate analysis are based on the data which are not aggregated or expand processed, described as disaggregate data [10]. The conventional four-step method is an aggregate approach for transportation planning analysis, and the data used in model's estimation is in aggregate form. Almost all

the transportation analyses were based on the aggregate data before the emergence of discrete choice modeling approach. When being applied, the aggregate form data cannot be used directly in the disaggregate method, it needs several methods to deal with the original aggregate data. In 2005, Yao and Takayuki proposed an integrated intercity travel demand modeling system which combines estimation across multiple data sources such as SP, RP, and aggregate data [11].

This paper develops a disaggregate model for passenger flow distribution of urban rail transit based on historical aggregated passenger flow data, which is collected by Automatic Fare Collection (AFC) system. The passenger flow distribution is described as the result of destination station choice from each departure station. When the model is established, travel time, attracted traffic flow, land-use type, intensity around station, and so on are considered. Combining with the passenger flow data of railway system in Beijing collected before and after Line 4 is put into operation, the prediction accuracy of the disaggregate model is evaluated.

2 The Passenger Flow Distribution Model

2.1 The Theory of Disaggregate Method

As the basic units in the traffic behavior determining process, travelers will choose the maximal utility scheme, and the scheme utility is determined by the scheme and travelers' characteristics. When it comes to the passenger flow distribution model, the distribution is the result of the selection of the destination; the passengers will select the most probable station as the travel destination.

In discrete choice models, the selection process is based on the random utility function, which is expressed as

$$U_{\text{in}} = V_{\text{in}} + \varepsilon_{\text{in}} \tag{1}$$

where V_{in} is the fixed utility of scheme X_{in} (which include the social and economic characteristics of the passenger and value of the scheme), and ε_{in} that obeys a certain probability distribution, is the random term. Random utility shows the sensation evaluation value in the selection process.

In the concrete form, a utility function can be determined by one or more function form expressions; considering the result analysis and parameter calibration, in this paper, linear function is chosen as a utility function expression form, which is expressed as

$$V_{\text{in}} = \sum_{k=1}^{K} \theta_k X_{k_{\text{in}}} \tag{2}$$

where $X_{k_{\text{in}}}$ is the scheme set; θ_k is the undetermined parameter. In the article, the factors affecting the passenger flow distribution forecast is the travel time between the original station and the destination, the attribute and scale of the stations, etc.

When fixed utility V_{in} and the random term is mutual independence, and V_{in} obey Gumbel distribution, it can be deduced that the probability of scheme V_{in} can be expressed as

$$P_{\text{in}} = \frac{\exp(V_{\text{in}})}{\sum_{j \in c_n} \exp(V_{\text{in}})}. \tag{3}$$

Compared with the conventional aggregate model, disaggregate method simulates the selection process of passengers; it can reflect people's choice characteristics, and thus is much more suitable for OD distribution forecast.

2.2 Representative Individual Method

The conventional four-step method is an aggregate approach for transportation planning analysis, and the data used in model's estimation are in aggregate form. Almost all the transportation analyses were based on the aggregate data before the emergence of discrete choice modeling approach. Although some problems in the aggregate data are pointed out, such as the inefficiency in the data use and the problem of ecological correlation, the advantage in controlling the total amount of travel demand and higher statistical reliability make aggregate data still play an important role in transportation studies. Moreover, most real-world decisions are based (at least in part) on the forecast of some aggregate demand (aggregate demand is the accumulation of individuals' decision) but not the prediction at individual level. Therefore, although modeling travel behavior with the disaggregate data is a key aspect of demand analysis, the advantages of aggregate data in total amount controlling and statistical reliability should also be considered in the estimation of travel demand model. In terms of data collection, compared with disaggregate data, aggregation data are more likely to acquire, thus the disaggregate model combining with aggregate data for the rail transit passenger flow distribution forecast has certain advantages.

Although the model can make significance, there is a problem that the aggregate data cannot be used for estimation directly. It needs a method to transform the aggregate data into disaggregate form. For the case when the OD volumes and operation information of each OD pair are known, based on the concept of representative individual, all the travelers with the same origin and destination choice are recognized as a group of persons with homogeneous properties, and their behaviors can be reflected by a representative individual. With this consideration, a record of aggregate data is viewed as the choice result of a representative individual and then used for disaggregate model's estimation. Obviously, a record of data actually represents a number of physical individuals' choice results, and cannot be used directly in the estimation of model as usual disaggregate data. With the framework of WESML [12], a weight factor is introduced into the likelihood function of aggregate dataset to calibrate the bias

between the sample and population data. The maximum likelihood function with weight factor is expressed as

$$L(\theta) = \sum_{n} \sum_{i} \delta_{\text{in}} w(g) \ln P(i|X_{\text{in}}, \theta) \tag{4}$$

$$w(g) = \frac{Q(g)}{H(g)} = \text{rows} \cdot \frac{\text{trip}(g)}{\text{trips}} \tag{5}$$

where

$w(g)$ is the weight for a representative individual stratum g;
$Q(g) = \text{trip}(g)/\text{trips}$ is the population proportion, $\text{trip}(g)$ is the travel volume in pair $O_{\text{m}}D_{\text{n}}$, trips is the total travel volume;
$H(g) = 1/\text{rows}$ is the sampling proportion for stratum g, and rows is the number of representative individuals.

2.3 Model Estimation

2.3.1 Utility Function

The utility function value for each OD pair will affect the passengers' choice of destination; selecting proper influencing factors and determining the utility function form is an important part of the model derivation for passengers from a constant original site; the attracted traffic flow of the destination can reflect the attraction ability, the greater the amount of the destination, the more passengers probably choose it. The selection results are as follows: more people choose to go to the station, thus the OD flow is bigger. Through the analysis of data, it can be found that the passenger flow distribution presents the "the farther the smaller" phenomenon, that is, passengers tend to choose the destination which has shorter travel time. In addition, the land-use type and intensity around the origin and destination station will also have influence on passengers' choice. When a new line is put into operation, the geographical position will cause the OD volume which across the new line and existing network is relatively smaller, so the flag variable is defined to reflect this characteristic. In detail, when origin and destination stations belong to different types of lines (i.e. existing line or new line), the value is 0; otherwise it will be 1. Therefore, the model can be applied to the passenger flow distribution forecast when a new line is added to the network. Finally, five factors including travel time, traffic attraction, the land-use type and intensity around the origin and destination station, and the flag variable are selected as the explanatory variables of utility function. As to the form of utility function, considering the result analysis and parameter calibration, linear function is chosen as a utility function expression form expressed as

Table 1 The influencing factors

Name	Travel time (h)	Traffic attraction (10,000 persons)	Land-use type	Land-use intensity	Flag variable
Symbol	T	D_j	XZ	GM	k
Parameter	β	Φ	ρ	σ	γ

$$f(C_{ij}) = \beta T/3600 + \phi D_j/10^4 + \rho XZ + \sigma GM + \gamma \times k \tag{6}$$

where $f(C_{ij})$ is the utility function; XZ is a dummy variable reflecting the land-use types around the origin and destination stations (the types of land-use are divided into three kinds: for residence, for commerce, or for residence and commerce. When the type of the origin and destination station are different or both the types are for residence and commerce, the value is 1, otherwise 0); GM is a dummy variable related to the land-use intensities around the origin and destination stations (when both the traffic attraction of the origin and destination station are greater than 30,000 persons, the value is 1, otherwise 0); β, Φ, ρ, σ, γ are undefined parameters. For other variables refer to Table 1.

2.3.2 Estimation Results

In order to reduce the particularity of the data, the paper uses the average data of a whole week from July 11 to 17, 2010. The aggregate data has be transformed into a disaggregate form, which is then used to estimate a disaggregate logit destination choice model. Moreover, there are too many destination alternatives (123 alternatives) to be dealt with in a discrete choice model. In a large choice set context, it has been proved that estimation may be conducted on a subset of alternatives without loss of parameter consistency. The destination alternative set therefore comprises the actually chosen destination and nine additional destinations randomly selected from the set of non-chosen destinations. The estimation results of the destination choice model are presented in Table 2.

The result shows that: (1) the adjusted likelihood ratios show that all models have satisfactory goodness-of-fit and (2) all parameters are statistically significant and consistent with their hypothesized effects on utility. The parameter of the traffic attraction is positive, reflects the positive correlation between OD volume and traffic attraction, when at the same conditions, the greater the traffic attraction amount, the higher the selected probability of this station. On the other hand, the

Table 2 Estimation results for destination choice

Explanatory variable	D_j	T	r	XZ	GM
Parameter	0.2365	−0.9718	−0.4436	0.2688	0.2493
t-Statistic	46.201	−23.201	−15.157	11.365	8.797

The adjusted likelihood ratios: 0.08

Table 3 The accuracy analysis of passenger flow distribution (person)

The type of error	Monday	Tuesday	Wednesday	Thursday	Friday	Saturday	Sunday	Average
From existing network to new lines	43	51	52	53	51	55	47	48
From new lines to existing network	43	53	53	54	52	56	48	49
Inter the new lines	98	123	123	123	119	124	106	115
Inter the existing network	80	126	127	128	123	130	89	113
The average error of the whole OD pairs	70	106	107	107	103	109	78	95

parameter of travel time is negative, it shows the negative correlation between OD flow and travel time. The utility function can be expressed as

$$f(C_{ij}) = -0.9718T/3600 + 0.2365D_j/10^4 + 0.2688XZ + 0.2493GM - 0.4436k. \tag{7}$$

The passenger flow distribution can be expressed as

$$q_{ij} = \frac{\exp(f(C_{ij}))}{\sum \exp(f(C_{ij}))} \times O_i \tag{8}$$

where q_{ij} is the OD flow, O_i is the traffic generation of the original station.

2.3.3 Evaluation

Based on the disaggregate model, the passenger flow distribution of Line 4 can be forecasted and compared to the real OD matrix, the accuracy is analyzed. Except the average error of the whole OD pairs, according to the type of lines the origin and destination belong to, the errors are calculated in four kinds. The average absolute error is shown in Table 3.

It can be concluded that the prediction is particularly outstanding when the OD pairs across the new lines and the existing network; the all day long prediction error can be controlled with less than 56 persons. The prediction errors for the OD pairs with origin and destination stations both in the existing network are under 130 persons. Considering that the OD flow in the existing network is larger, the relative prediction errors are under 40 %, which is within acceptable limits. For the lack of data, the errors for the OD pairs with origin and destination stations both in new line are relatively larger.

Table 4 shows the error comparison between the single restraint gravitational model and the disaggregate model. It can be obviously concluded that the disaggregate method is much more accurate, especially the forecast across the new line and the existing network.

Table 4 The error comparison (person)

The type of error	Single restraint gravitational model	Disaggregate model	The improvement of precision (%)
From existing network to new lines	65	48	26.2
From new lines to existing network	69	49	29.0
Inter new lines	205	115	44.9
Inter the existing network	139	113	18.7
The average error of the whole OD pairs	121	95	21.5

3 Conclusion

Based on the aggregate data, this paper proposes a disaggregate method which is used for rail transit passenger flow distribution forecast. With the help of representative individual method, the aggregate data is transformed into disaggregate form, a weight is added into the model. When the model is established, five influencing factors are considered, including travel time, attracted traffic flow, land-use type and intensity around station, and a flag variable. Combined with the passenger flow data of railway system in Beijing collected before and after Line 4 is put into operation, the parameters are defined. Through the accuracy analysis, the method proposed in the paper is suitable for passenger flow distribution forecast. Compared with single restraint gravitational model, the prediction accuracy is greatly improved. The errors for four types of OD pairs are all reduced and the prediction accuracy is improved by 21.5 % averagely. Especially, the prediction error reduces 90 persons for the OD pair with origin station and destination station both in the new lines.

Acknowledgments This research is supported by the State Key Laboratory of Rail Traffic Control and Safety (Contract No. RCS2011ZT012), 973 Program (No. 2012CB725403) and National Key Technology R&D Program (No. 2011BAG01B01).

References

1. Yao Z (1996) Road and traffic engineering systems analysis. China Communications Press, Beijing
2. Li Q (2011) The comparison of urban transit demand forecasting method. Technol Econ Areas Commun 1(13):54–57
3. Zou W, Sun J, Hu L (2006) The solution approach and application of gravitational model in the passenger distribution forecast. Comput Commun 2(24):47–51
4. Li X, Lv X, Liu D (2011) Forecast of railway short-term passenger row based on RBF neural network. Railway Transp Econ 6(33):86–89
5. Ben-Akiva M, Lerman S (1985) Discrete choice analysis: theory and application to travel demand. MIT Press, Cambridge, pp 100–130
6. Lancaster K (1966) A new approach to consumer theory. J Polit Econ 74(2):132–157
7. McFadden D (1974) Conditional logit analysis of qualitative choice behavior. Front Econom 1(2):105–142
8. Jia H, Gong B, Zong F (2007) Disaggregate modeling of traffic mode choice and its application. J Jilin Univ (Engineering and Technology Edition) 6(37):1288–1293
9. Ren G, Zhou Z, Zhang H (2011) Application of discrete choice model in trip mode structure forecast: a case study of Bengbu. J Southeast Univ (English Edition) 27(1):83–87
10. Guan H (2004) Disaggregate model: a tool of traffic behavior analysis, vol 10. China Communications Press, Beijing, pp 1–2
11. Yao E, Takayuki M (2005) A study of an integrated intercity travel demand model. Transp Res A 39:367–381
12. Manski C, Lerman S (1977) The estimation of choice probabilities from choice-based samples. Econometrica 45:1977–1988

Information Consensus in Distributed Systems Under Local Communication and Switching Topologies

Shijie Zhang and Yi Ning

Abstract This paper deals with the Information consensus problem in distributed systems under local communication and dynamically switching interaction topologies. We show conditions under which consensus is reached under switching directed information exchange topologies. We propose distributed model predictive control schemes that take into account constraints on the agents input and show that they guarantee consensus under mild assumptions. Simulation results show that the proposed scheme is effective under both fixed and dynamically switching interaction topologies.

Keywords Information consensus · Distributed systems · Communication · Topologies

1 Introduction

As an inherently distributed strategy for multi-vehicle coordination, consensus algorithms have been studied extensively in the context of cooperative control of multi-vehicle systems during the last few decades [1–5]. Dramatic developments in communication and computation technology relax the restrictions on information exchanges between spatially distributed agents. The possibility has been identified that simple and inexpensive systems can carry out complicated tasks through collaboration that may be too difficult for single system. Advantages

S. Zhang (✉) · Y. Ning
Research Institute of Robotics, Henan University of Technology, Zhengzhou, China
e-mail: zhangshijie@haut.edn.cn

Y. Ning
e-mail: robot@haut.edn.cn

F. Sun et al. (eds.), *Foundations and Practical Applications of Cognitive Systems and Information Processing*, Advances in Intelligent Systems and Computing 215,
DOI: 10.1007/978-3-642-37835-5_63,

include simple structure, low cost, enhanced functionality, and the flexibility in fault tolerance [6].

As an important and basic part of distributed multi-agent cooperative control, consensus has been studied extensively [7–11]. In a consensus problem, a set of dynamic agents seeks to agree upon certain quantities of interests based upon shared information. Those algorithms only require local neighbor-to-neighbor information exchange between the vehicles. Consensus problems have a history in the computer science literature and have recently found applications in cooperative control of multi-agent systems. Consensus Seeking problems in multi-agent systems are firstly studied using algebraic graph theory and matrix theory [12–14]. In [12], digraphs are employed to model information flow, and the graph topology is assumed to deterministically switch over time. It is shown that consensus is achieved if the digraph is always connected and balanced. In [13], sufficient conditions are given for consensus of the heading angles of a group of agents under undirected dynamically changing topologies. In [14], the consensus algorithms for the directed dynamically changing interaction topologies are developed in the context of linear continuous and discrete-time vehicle systems. However, most of them do not exploit optimal control ideas, do not account for input constraints,which in many cases have to be included in the problem formulation due to actuator limitations.

In this paper, We propose a distributed model predictive control schemes that take into account constraints on the agents input and show that they guarantee consensus under mild assumptions. It is shown that the agent can reach consensus under the consensus seeking algorithm we proposed if the interaction topologies of the multi-agent systems always has a spring tree.

The rest of this paper is organized as follows: In Sect. 2, the distributed consensus problem is defined. Section 3 analyze the consensus seeking algorithm based on model predictive control. Some simulation results are presented in Sect. 4 to show its performance. Finally, Sect. 5 concludes the paper.

2 Preliminary

2.1 Basic Concepts of Graph Theory

A *directed graph* $G = (V, E)$ is composed by a finite vertex set V, and an edge set $E \subseteq V^2$. Suppose there are n vertices in V, each vertex is labeled by an integer $i \in \{1, 2, \ldots, n\}$. n is the *order* of the graph. Each edge can be denoted by a pair of distinct vertices (v_i, v_j) where v_i is the *head* and v_j is the *tail*. If $(v_i, v_j) \in E \Longleftrightarrow (v_j, v_i) \in E$, the graph is called *symmetric* or *undirected*. A graph G is said to be *complete* if every possible edge exists.

For directed graph G, if edge $(v_i, v_j) \in E$, then v_j is one of the *neighbors* of v_i. The set of neighbors of v_i is denoted by $N(i) = \{v_j \in V : (v_i, v_j) \in E\}$. Directed

graphs over a vertex set can be categorized according to their connectivity properties. A *strong path* in a directed graph is a sequence of distinct vertices $[v_0, \ldots, v_r]$ where $(v_{i-1}, v_i) \in E$ for any $i \in \{1, 2, \ldots, r-1\}$. A *weak path* is also a sequence of distinct vertices $[v_0, \ldots, v_r]$ as long as either (v_{i-1}, v_i) or (v_i, v_{i-1}) belongs to E. A directed graph is *strongly connected* if any two ordered vertices can be joined by a strong path, and is *weakly connected* if any two ordered vertices in the graph can be joined by a weak path. A *rooted directed spanning tree* for directed graph G is a subgraph $G_r = (V, E_r)$ where E_r is a subset of E that connects, without any cycle, all vertices in G so that each vertex, except the root, has one and only one out-coming edge.

2.2 Preliminary Results

For sake of completeness, next we summarize some results provided in [15] that will enable us to prove consensus under the MPC schemes we proposed. Assume the individual agents share a common state space X, which is assumed to be finite dimensional Euclidean. The dynamics of the multi-agent systems including a team of N_a agents is

$$\dot{x}(t) = f(t, x(t)) \tag{1}$$

where $x(t) = [x_1(t)^T, x_2(t)^T, \ldots, x_{N_a}(t)^T]^T \in \mathbb{R}^{N_a n}$ is the states of system (1). $x_i(t) \in \mathbb{R}^n$, $\forall i = \{1, \ldots, N_a\}$. Assume that $f = [f_1^T, f_2^T, \ldots, f_{N_a}^T]^T$ is continuous.

We say that system (1) can reach consensus if $\forall i \neq j$, when $t \to \infty$, $\|x_i(t) - x_j(t)\| \to 0$.

System (1) does not capture the constraints imposed by the limited interagent communication. In order to incorporate the limited interagent communication in the model, it is common to introduce a sequence of directed graphs $G(t) = \langle V, E(t) \rangle$ with common node set $V = \{1, \ldots, N_a\}$ describe each agent. The directed graph $G(t) = \langle V, E(t) \rangle$ characterizes the communication links at time t.

The following assumption relates the sequence of communication graphs $G(t)$ with the system.

Assumption 1: Associated to each directed graph $G(t)$, and for every subsystem $i \in \{1, 2, \ldots, N_a\}$, each state $x \in X^{N_a}$, $X \in \mathbb{R}^n$, there is a compact set $e_i(G(t))(x) \subseteq X$ satisfying

(1) $x(s; x(t)) \in e_i(G(t))(x)$, $\forall x \in X^{N_a}, s \in [t, t+T]$;
(2) If $x_i = x_j$, $j \in N_G(i)$, then $e_i(G(t))(x_1, x_2, \ldots, x_{N_a}) = \{x_i\}$;
(3) If x_i and x_j, $j \in N_G(i)$ are not all equal, then $e_i(G(t))(x_1, x_2, \ldots, x_{N_a}) \in Ri\big(Co\big(\{x_i\} \cup \{x_j, j \in N_G(i)\}\big)\big)$, where $Co(A)$ and $Ri(A)$ denote the convex hull and the relative interior of the set A respectively;
(4) $e_i(G(t))(x)$ is continuous.

3 Information Consensus Under Distributed MPC

3.1 Problem Statement

In this paper we consider a team of N_a agents with uncoupled dynamics. The centralized system dynamics is

$$\dot{x}(t) = f(x(t), u(t)), \tag{2}$$

with state $x(t) \in \mathbb{R}^{nN_a}$ and control $u(t) \in \mathbb{R}^{mN_a}$. Now we decouple the centralized system into N_a subsystems as $x = (x_1, x_2, \ldots, x_{N_a})$, $u = (u_1, u_2, \ldots, u_{N_a})$, and $f = (f_1, f_2, \ldots, f_{N_a})$, with

$$\dot{x}_i(t) = f_i(x_i(t), u_i(t)), \forall i = 1, \ldots, N_a. \tag{3}$$

where each subsystem is referred as an agent, and $x_i(t) \in \mathbb{R}^n$ and $u_i(t) \in \mathbb{R}^m$ are the state and the control of agent i, respectively.

Based on the model predictive control theorem, it is easy to transform the consensus problem to an online optimization problem as follow:

Problem 1: According to system (1), $\forall i \neq j$, find a optimal control $u^*(t)$ such that:

$$J^*(x(t), u^*(t)) = \min_{u(t)} J^x(x(t), u(t)) + J^u(u(t)),$$

where

$$J^x(x(t), u(t)) = q \int_t^{t+T} \sum_{i \neq j} \left\| x_i(\tau) - x_j(\tau) \right\|^2 \mathrm{d}\tau,$$

$$J^u(u(t)) = r \int_t^{t+T} \left\| u(\tau) \right\|^2 \mathrm{d}\tau$$

and $\forall t \in [t, t+T]$, satisfying

$$\begin{aligned} \dot{x}(t) &= f(x(t), u(t)), \\ x(t) &\in X, \\ u(t) &\in U. \end{aligned}$$

where $q > 0$ and $r > 0$ are weights. X and U are the states and input constraint set respectively.

The above problem is a centralized scheme for the consensus seeking problem of multi-agent systems. Now we want to decompose the centralized problem into a distributed implementation. Note that in a distributed scheme, the optimal problem

of agent i is not only depend on $x_i(t)$, but also depend on the neighbor's states $x_j(t)$, $j \in N_G(i)$. Firstly, define the object function as:

$$J_i(x_i(t), u_i(t)) = J_i^x(x_i(t), u_i(t)) + J_i^u(u_i(t)), \tag{4}$$

where

$$J_i^x(x_i(t), u_i(t)) = q_i \int_t^{t+T} \|x_i(\tau) - z_i(\tau)\|^2 d\tau,$$

$$J_i^u(u_i(t)) = r_i \int_t^{t+T} \|u_i(\tau)\|^2 d\tau,$$

where $q_i > 0$ and $r_i > 0$ are weights. $z_i(t) = K_i(G(t))x(t)$, where $K_i(G(t))$ is the ith block matrix of $K(G) = [K_1(G(t))^T, K_2(G(t))^T, \ldots, K_{N_a}(G(t))^T]^T$. Then the distributed optimal problem is formulated as follow:

Problem 2: $\forall i \in \{1, 2, \ldots, N_a\}$, find a optimal control $u_i^*(t)$ such that:

$$J_i^*\left(x_i(t), u_i^*(t)\right) = \min_{u_i(t)} J_i(x_i(t), u_i(t)) \tag{5}$$

and $\forall t \in [t, t+T]$, satisfying

$$\begin{aligned} \dot{x}_i(t) &= f_i(x_i(t), u_i(t)), \\ x_i(t) &\in X_i, \\ u_i(t) &\in U_i, \end{aligned}$$

where X_i and U_i are the states and input constraint set respectively.

3.2 Distributed Information Consensus Algorithm

To deal with the distributed consensus problem 2, we give the following algorithm:

Algorithm 1: (Distributed Consensus Algorithm)

Step1: $\forall i \in \{1, 2, \cdots, N_a\}$, give the initial states $x_i(0)$, and the predictive horizon T, and the update period $\delta \in (0, T)$;

Step2: Solve problem 2 to compute the optimal control trajectory $u_i^*(t), t \in [0, \delta]$, and the optimal state trajectory $x_i^*(t), t \in [0, \delta]$;

Step3: Transmit the optimal state trajectory $x_i^*(t), t \in [0, \delta]$ to its neighbor, and receive the neighbor's optimal states $x_j^*(t), j \in N_G(i), t \in [0, \delta]$;

Step4: Take the current state as initial state, goto Step2, and repeat the above procedure.

3.3 Main Results

Assumption 1 plays an important role in the distributed consensus analysis. Based on Assumption 1, we have the following lemma.

Lemma 1 *Consider the directed graphs $G(t)$ assort with multi-agent system (2), and a continuous function f satisfying Assumption 1. The convex hull of the individual agents' states, denoted by $\tilde{V}(x) = Co\{x_1, x_2, \ldots, x_n\}$ is an invariant set with respect to system (2).*

Lemma 2 *Consider the closed-loop multi-agent system corresponding to (2) and the optimal control trajectory $u_i^*(t)$*

$$\dot{x}(t) = f(t, x(t)),$$

where

$$f(t, x(t)) = \begin{bmatrix} f_1(t, x(t)) \\ f_2(t, x(t)) \\ \cdots \\ f_{N_a}(t, x(t)) \end{bmatrix},$$
$$f_i(t, x(t)) = f_i(t, x_i(t), u_i^*(t)).$$

Then, $f(t, x(t))$ satisfy Assumption 1.

Proof The four condition in Assumption 1 will be verified one by one. Firstly, use the notations in Assumption 1, denote $X = \mathbb{R}^n$, $e_i(G(t))(x) = \{x_i(s, x_i(t))\}$, $\forall s \in [t, t+T]$, then the first term in Assumption 1 can be verified.

Next, if $x_i(t) = x_j(t)$, $\forall j \in N_G(i)$, it means that $z_i(t) = x_i(t)$. From(), we have $J_i(x(t), 0) = 0$, and hence the optimal inputs $u_i^*(t) = 0$, it implies that $x_i(s, x(t)) = x_i$, $\forall s \in [t, t+T]$, then the second term in Assumption 1 can be verified.

If there exists $j \in N_G(i)$ such that $x_i(t) \neq x_j(t)$, then we have $z_i(t) \neq x_i(t)$. Denote $u_i(t), t \in [t, t+T]$ is a feasible control for problem 2, then the state trajectory corresponding to the feasible control is denoted by $x_i(s; x(t)), s \in [t, t+T]$. Firstly, we show that the optimal state trajectory $x_i^*(s; x(t)), s \in [t, t+T]$ corresponding to the optimal control $u_i^*(t), t \in [t, t+T]$ is the shortest trajectory trending to $z_i(t)$. Assume by contradiction that the optimal state trajectory $x_i^*(s; x(t)), s \in [t, t+T]$ is the shortest trajectory trending to $z_i(t)$, then there exit another trajectory $\bar{x}_i(s; x(t)), s \in [t, t+T]$ such that

$$\|\bar{x}_i(t_k + \delta) - z_i(t)\| \leq \left\|x_i^*(t_k + \delta) - z_i(t)\right\|$$
$$\|\bar{x}_i(t_{k+1} + \delta) - \bar{x}_i(t_k + \delta)\| \leq \left\|x_i^*(t_{k+1} + \delta) - x_i^*(t_k + \delta)\right\|$$

where $t_{k+1} = t_k + \delta$. This means $J_i^x(\bar{x}_i(t), \bar{u}_i(t)) \le J_i^x\big(x_i^*(t), u_i^*(t)\big)$ and $J_i^u(\bar{u}_i(t)) \le J_i^u\big(u_i^*(t)\big)$, repeat the above procedure until find the optimal state trajectory $\bar{x}_i(s; x(t)) = x_i^*(s; x(t)), s \in [t, t+T]$. Next, we show that $z_i(t) \neq x_i(t)$ implies $u_i^*(s; x(t)) \neq 0, s \in [t, t+\delta)$. This will be proved by first showing that $u_i^*(t) \neq 0, t \in [t, t+T]$. This will be proved by first showing that $u_i^*(t) \neq 0, t \in [t, t+T]$. If $u_i^*(t) = 0, t \in [t, t+T]$, then

$$J_i\big(x(t), u_i^*(t)\big) = q_i \int_t^{t+T} \|x_i(\tau) - z_i(t)\|^2 d\tau.$$

Consider the input sequence

$$\bar{u}_i(t) = [\alpha(x_i(t) - z_i(t))^T, 0^T, \ldots, 0^T]^T, 0 < \alpha < 1,$$

the state trajectory corresponding to $\bar{u}_i(t)$ is denoted by $\bar{x}_i(t)$, then

$$J_i(\bar{x}_i(t), \bar{u}_i(t)) = \Big(q_i(1-\alpha)^2 + r_i\alpha^2\Big) \int_t^{t+T} \|\bar{x}_i(\tau) - z_i(\tau)\|^2 \mathrm{d}\tau,$$

if

$$\alpha < \frac{2q_i}{q_i + r_i},$$

then we have $J_i(\bar{x}_i(t), \bar{u}_i(t)) < J_i\big(x(t), u_i^*(t)\big)$, therefore, $u_i^*(t) \neq 0, t \in [t, t+T]$. Similarity, it can be shown that $u_i^*(s; x(t)) \neq 0, s \in [t, t+\delta)$.

Finally, item 4 in Assumption 1 is verified by assume that f is continuous.

Lemma 3 [12] *A directed graph $G(t) = \langle V, E(t)\rangle$ has a spanning tree if and only if for every nonempty, disjoint subsets $V_1, V_2 \subset V$ satisfy $N_G(V_1) \cup N_G(V_2) \neq \Phi$.*

Now based on the above lemma, we state the main result of the paper.

Theorem 1 *Consider the directed graphs $G(t)$ assort with the multi-agent system (2), system (2) graphscan reach consensus under the distributed consensus algorithm 1 if and only if the directed $G(t)$ has a spanning tree at any time t.*

Proof ($\Leftarrow$) Assume that at some time t_k, the directed graphs $G(t)$ assort with the multi-agent system (2) does not has a spanning tree. By Lemma 3, there exit nonempty, disjoint subsets V_1 and V_2 such that $N_G(V_1) = \Phi, N_G(V_2) = \Phi$. Let the initial time be t_k and analyze the trajectory of the subsystem in V_1 and V_2. Assume that V_1 correspond to subsystem i and V_2 correspond to subsystem j, then take two different initial states for subsystem i and j as $x_i(t_k)$ and $x_j(t_k)$ respectively. Lemma 1 implies at time $t_{k+1}, x_i(t_{k+1}) = x_i(t_k), x_j(t_{k+1}) = x_j(t_k)$, then by the arbitrary of k, system (2) can not reach consensus.

($\Rightarrow$) Assume that at any time t_k, the directed graphs $G(t)$ assort with the multi-agent system has a spanning tree. We want to show that $t \to \infty$, $\left\|x_i(t) - x_j(t)\right\| \to 0$ under the distributed consensus algorithm 1. Denote $x^*(t)$ be the optimal state trajectory of the close-loop system. Then it is equal to show that $\tilde{V}(x^*(t))$ is a singleton. By Lemma 3, we have $N_G(V_1) \cup N_G(V_2) \cup \cdots \cup N_G(V_{N_a}) = \{1, 2, \ldots, N_a\}$, then under the optimal control $u^*(t)$, $\forall i \neq j, z_i(t) \to z_j(t) \to$ constant, this implies $x^*(t) \to$ constant, then $\tilde{V}(x^*(t))$ is a singleton.

4 Simulation

To show the effectiveness and efficiency of the proposed distributed consensus algorithm, the following simulations are performed.

Consider a team of 5 subsystems with uncoupled dynamics

$$\dot{x}_i = A_i x_i + B_i u_i, i = 1, 2, \ldots, 5.$$

where x_i and u_i are the state and control input of the ith subsystem respectively, and

$$A_i = \begin{bmatrix} 0 & 1 \\ 0 & 0 \end{bmatrix}, B_i = \begin{bmatrix} 0 \\ 1 \end{bmatrix}.$$

The initial state of the five subsystems are: $x_1(0) = [-20, 30]^T x_2(0) = [-30, 25]^T x_3(0) = [40, -10]^T x_4(0) = [70, -36]^T x_5(0) = [100, -58]^T$. Assume the predictive horizon $T = 5$, and the update period $\delta = 0.1$. The information communication interaction topologies among the five subsystems is shown in Fig. 1.

Then we have

$$A(G) = \begin{bmatrix} 0 & 0 & 0 & 1 & 0 \\ 1 & 0 & 0 & 0 & 0 \\ 0 & 1 & 0 & 0 & 0 \\ 0 & 0 & 0 & 0 & 1 \\ 0 & 0 & 1 & 0 & 0 \end{bmatrix}, \tilde{K}(G) = \begin{bmatrix} \frac{1}{2} & 0 & 0 & \frac{1}{2} & 0 \\ \frac{1}{2} & \frac{1}{2} & 0 & 0 & 0 \\ 0 & \frac{1}{2} & \frac{1}{2} & 0 & 0 \\ 0 & 0 & 0 & \frac{1}{2} & \frac{1}{2} \\ 0 & 0 & \frac{1}{2} & 0 & \frac{1}{2} \end{bmatrix}.$$

In the first simulation, Let $q_i = 1$, $r_i = 1$, $\forall i = 1, 2, \ldots, 5$. The input constraint sets $U_i = \{u_i(t) || u_i(t)| < 10, i = 1, 2, \ldots, 5\}$. Under the distributed consensus algorithm 1, the trajectories of each subsystem and their neighbors are shown in Fig. 2, 3, 4, 5 and 6. The trajectories of system under the distributed consensus algorithm 1 are shown in Fig. 7. It can be seen that all the states can reach consensus under the distributed consensus algorithm.

In the second simulation, we consider the case that the interaction topologies among the five agents are dynamical changing. Assume that at the first ten

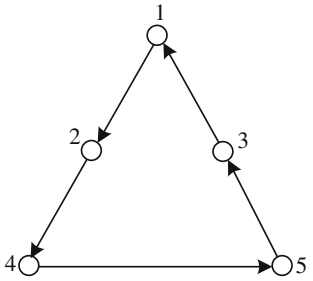

Fig. 1 Information communication graph among the five subsystems

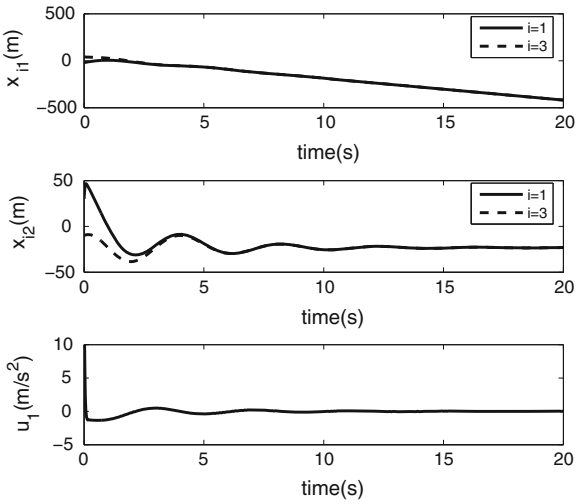

Fig. 2 The trajectories of subsystem 1 and its neighbor

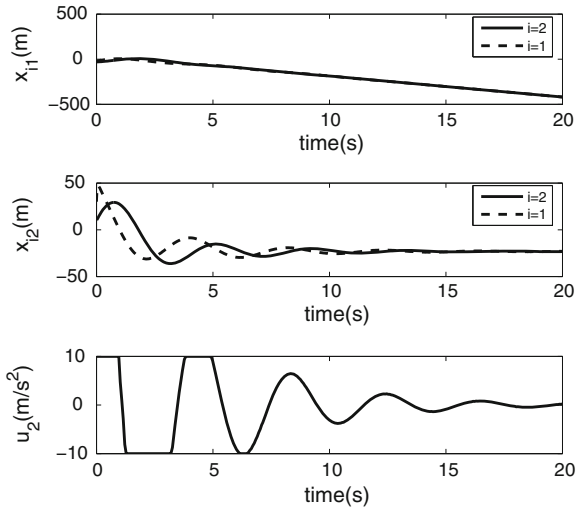

Fig. 3 The trajectories of subsystem 2 and its neighbor

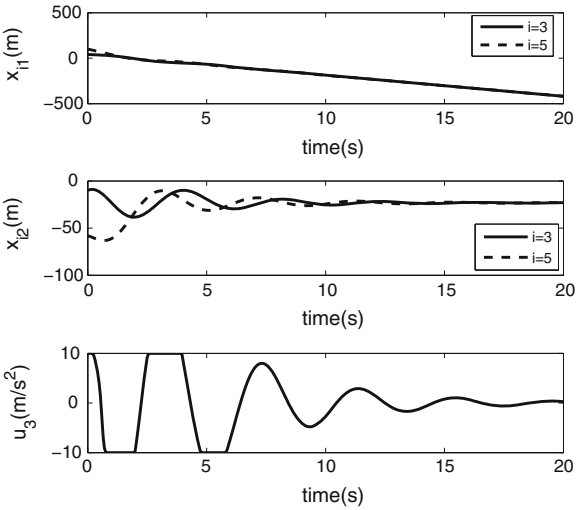

Fig. 4 The trajectories of subsystem 3 and its neighbor

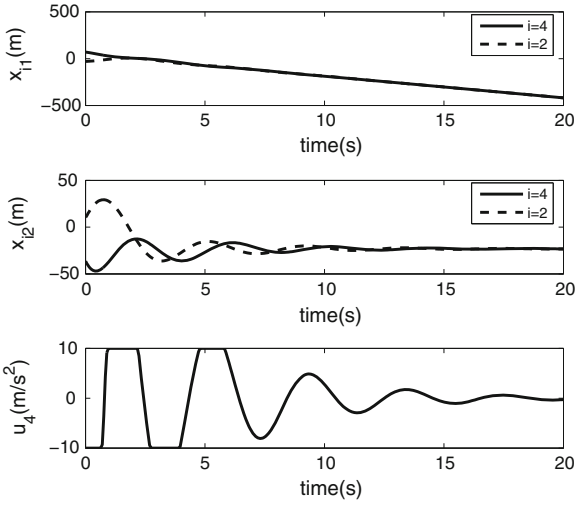

Fig. 5 The trajectories of subsystem 4 and its neighbor

seconds, the interaction topologies is shown in Fig. 1, ten seconds later, the interaction topologies is shown in Fig. 8. Using the same algorithm, The trajectories of system under the distributed consensus algorithm 1 are shown in Fig. 9. It can be seen that all the states can reach consensus even the interaction topologies are dynamical changing.

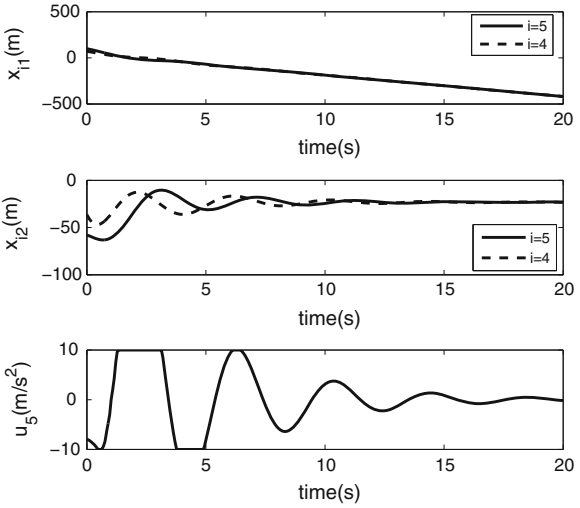

Fig. 6 The trajectories of subsystem 5 and its neighbor

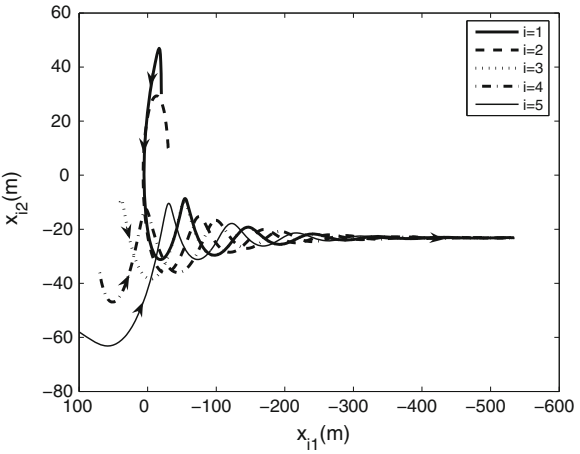

Fig. 7 The trajectories of all the subsystems under fixed interaction topologies

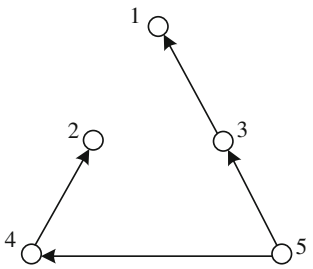

Fig. 8 Information communication graph among the five subsystems after ten second

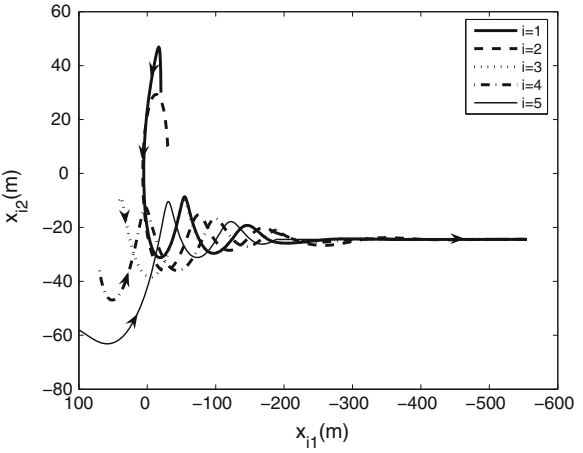

Fig. 9 The trajectories of all the subsystems under dynamical switching interaction topologies

5 Conclusions

This paper have proposed a information consensus algorithm in distributed systems. It can be shown that consensus can be achieved via distributed control using local information under fixed or dynamically switching interaction topologies. Simulation results are given in order to show the effectiveness of the proposed consensus algorithms. Future work will address the effect of time delay in those algorithms and the applications in multi-vehicle coordination problems.

Acknowledgments This work was supported by the National Natural Science Foundation of China (61075083), and Henan Province Innovation and Technology Fund for Outstanding Scholarship (0421000500), and the Key Scientific Research Projects of Henan University of technology (09XZD008), and the Science Foundation of Henan University of Technology (150166).

References

1. Tanner HG, Sandoval R (2011) Coordinated standoff tracking of moving targets: control laws and information architectures. J Guidance Control Dyn 32(4):56–69
2. Olfati-Saber R (2006) Flocking for multi-agent dynamic systems: algorithms and theory. IEEE Trans Autom Control 51:401–420
3. Redding J, Geramifard A, Undurti A (2010) An intelligent cooperative control architecture. In: Proceedings of the 2010 American control conference, pp 57–62
4. Hatta H, Uemura S, Kabayashi H (2010) Cooperative control of distribution system with customer equipments to reduce reverse power flow from distributed generation. In: IEEE PES general meeting, PES 2010, pp 2519–2535
5. Farineli A, Fujii H, Tomoyasu N, Pagello E (2010) Cooperative control through objective achievement. Robot Auton Syst 58:910–920
6. Michael N, Belta C, Kumar Z (2005) Controlling three dimensional swarms of robots. In: IEEE international conference on robotics and automation, Orlando, Florida, pp 964–969

7. Olfati-Saber R, Fax JA, Murray RM (2004) Consensus and cooperation in networked multi-agent systems. IEEE Trans Autom Control 49(9):1520–1533
8. Jadbabaie A, Lin J, Morse AS (2003) Coordination of groups of mobile autonomous agents using nearest neighbor rules. IEEE Trans Autom Control 48:988–1001
9. Ren W, Beard RW (2005) Consensus seeking in multiagent systems under dynamically changing interaction topologies. IEEE Trans Autom Control 50(5):655–661
10. Ren W (2010) Multi-vehicle consensus with a time-varying reference state. Syst Control Lett 56(7–8):474–483
11. Cameron SR, Luca F, Jonathan P (2009) Reaching consensus with imprecise probabilities over a network. In: AIAA guidance, navigation, and control conference, Chicago, Illinois, pp 1053–1075, 10–13 Aug
12. Fang L, Antsaklis PJ (2005) Information consensus of asynchronous discrete-time multi-agent systems. In: Proceedings of the American control conference, Portland, OR, June, pp 1883–1888
13. Dimarogonas D, Johanson KH (2008) Quantized agreement under time-varying communication topology. In: Proceedings of the 2008 American control conference, pp 4376–4381, 11–13
14. Blondel VD, Hendrickx JM, Olshevsky A, Tsitsiklis JN (2005) Converegence in multiagent coordination, consensus, and flocking. In: Proceedingds of the 44th IEEE conference on decision and control, Seville, Spain, 12–15 Dec 2005
15. Moreau L (2004) Stability of continuous-time distributed consensus algorithms. In: Proceedings of the 43th IEEE conference on decision and control, Atlantis, Paradise Island, Bahamas, pp 3998–4003

How Can We Find the Origin of a Path We Visually Traveled? The Effect of the Visual Environment on Path Integration

Huiting Zhang and Kan Zhang

Abstract To examine the effect of different visual information on path integration, we built four virtual environments with purecolor, texture, landmarks, and both texture and landmarks as visual cues, and used a point-to-origin task to estimate people's performance on path integration. Though constant bias existed under all visual environments, people were found to use different strategies according to different visual environments. To point back to the origin of the path, visual path integration was more likely to be achieved in the environments containing landmarks or both texture and landmarks, while in the environments with only texture or pure-colors, people turned to rely on temporal duration and the layout of the path. It was suggested that landmarks were more useful visual cues in virtual navigation.

Keywords Visual environment · Visual path integration · Point-to-origin task · Landmarks

1 Introduction

For mobile animals, navigation is a survival activity that is involved in their everyday life. When animals explore the environment, they need to keep continuously aware of the location of their home that they can return to their home after forage, and then over time they learn the layout of the surrounding environment [1].

H. Zhang (✉) · K. Zhang
Institute of Psychology, Chinese Academy of Sciences, Beijing, China
e-mail: zhanghuiting@psych.ac.cn

K. Zhang
e-mail: zhangk@psych.ac.cn

H. Zhang
Graduate University of Chinese Academy of Sciences, Beijing, China

F. Sun et al. (eds.), *Foundations and Practical Applications of Cognitive Systems and Information Processing*, Advances in Intelligent Systems and Computing 215,
DOI: 10.1007/978-3-642-37835-5_64,

Path integration is one of the important navigation strategies in which information about one's velocity or acceleration is integrated to estimate the distance traveled and angles turned from a starting point [2]. Information used in path integration process could be the internal cues such as proprioception, motor commands, or vestibular information from blind walking [3, 4], external cues such as visual information from the simulated self-motion displays [1, 5–9], or combination of all these sources.

According to Gibson's theory of ecological optics that an observer could assess the speed and direction of movement through the environment from 'optic flow', the changing pattern of coherent motion on the retina during locomotion [10]. In principle, as long as eye height remains constant, a given amount of optic flow corresponds to the distance traveled and angle turned, homing can be successfully performed by integrating the optic flow [1].

The proposal has been tested in extensive studies. For the distance traveled, results from previous studies suggest that humans can use optical information for accurate distance discrimination [11, 12], reproduction [5, 6], and estimation [8, 13]. For the turned angles, it has not yet reached a consistent conclusion on how well people estimate the turned angles with vision alone. Studies by Bakker et al. [14] examined the roles of both the body senses and visual information in reproducing turns. The most accurate rotations were produced when participants physically turned through the desired angle, regardless of whether this was coupled with visual information in a head mounted display. With vision alone, on the other hand, participants increasingly overshot the angles to be turned. However, using half-cylindrical 180° projection screen, optic flow information alone proved to be sufficient for untrained participants to perform turns with negligible systematic errors, irrespective of movement velocity [5].

More studies have focused on the combination of translation and rotation in the path integration and the role visual sense playing in it. Triangle completion is a commonly used paradigm for this combination: participants travel along two sides of a given triangle and experience the turn between these two sides, then they need to find the shortest way back to the starting position [15]. And similar tasks were also commonly used, such as triangular pointing task and point-to-origin task. People's performance on the triangle completion task was found to be more inaccurate with vision alone than with body sense, and errors were found either on the final turn of the homing path or the homing distance. Using a homing task to examine the efficiency of purely visual mechanism in a simulated three-dimension environment, the underestimation of the final turn was found to be considerably stronger under purely visual conditions when compared to results of the blind-walking studies by Loomis et al. [3, 16]. Also, when asked to turn and face to the origin after a two-segment path with a turn between segments, the simulated optic flow was found not by itself sufficient to induce spatial updating that support correct turn responses [17]. In contrast, in Riecke et al.'s study [5], path integration by optic flow was sufficient for accurately updating rotations, but homing distances were biased toward the mean response.

Comparing the studies above, one key issue that influences people's visual path integration is the field of view, and it has been addressed in previous study (see

Ref. [5] for detail). Another important element is the type of the visual stimuli. The visual environment Péruch et al. [16] used contained no textured surfaces, and hence minimal optic flow. The virtual environment used by Klatzky et al. [17] was a field of vertical posts resting on the ground plane. And the virtual environments used in Riecke et al.'s study [5] were varied from a 3D field of blobs to a natural scene of a town.

Optic flow is generated during the visual self-motion that the radial pattern of optic flow from the surrounding uniquely specifies the direction of the movement, and the rate of optic flow specifies the speed [1]. A texture ground provides the basic optic flow, while an environment with stationary and distinguishable objects contains different patterns of optic flow, such as elevation angle of the base of the objects in the field of view [1], which could also be used for moving direction and velocity judgments. One previous study addressed the question on the effect of different visual information that they varied the richness of the visual information in the virtual environment, with no texture (arena N), texture on the wall (arena W) or floor (arena F), or on both of them (arena B), and found that homing was more accurate in a richly textured environment (arena B) than it was with less visual information for translation (arena W) or rotation (arena F), or with minimal optic flow (arena N) [1]. However, in this study, different visual environments were used to test the separate effects of the rotational and translational flow and only texture or a single post (arena P, see details in Experiment 2 [1]) was used in their virtual environments.

No systematic comparison concerning the effect of different types of visual information on visual path integration has been done yet. In this paper, we are aimed at investigating the visual aspect of the path integration process, and comparing the influence of different visual information. On one hand, richer visual environment, with both texture and landmark information for example, would be more effective for people to perceive the distance and the turn path than environments with one kind or rare visual cues. On the other hand, texture environment and environment containing landmarks differ from the patterns of optic flow generated during self-movement, and landmarks offer additional information that they represent specific locations in the space, so landmarks are expected be more useful cues during visual navigation. In addition, we used curved tunnels and a point-to-origin task to test people's ability of tracking back the start from the path integration process with pure visual information in virtual reality.

2 Method

2.1 Participants

Participants in this experiment all had normal or corrected-to-normal vision. Twenty undergraduate students (10 males and 10 females) from the University of Illinois at Urbana-Champaign (UIUC) voluntarily participated in this experiment. All participants signed the consent form and compensated with course credits.

2.2 Apparatus and Virtual Environment

The experiment was performed on an ACPI x64-based PC, running a C++ program using openGL. Subjects were seated in a dimly illuminated room in front of a 17-inch display monitor rendered with 72 Hz refresh rate, a resolution of 1024 × 768 pixel, and a graphical field of view of 40° × 30°.

The virtual environment was a hallway-like tunnel, with width of 2 m and height of 3.2 m (the simulated eye height was defined as 1.6 ms[1]). Four different tunnels were built, with inner radius as 6 or 12 m in each turning direction. There were four visual environments setup by mapping with different cues on the walls. In the *Purecolor* condition, the color of the ceiling and the floor was gray, and the walls were green and blue. In the *Texture* condition, we used a black-and-white texture with random dense patterns pasted on all four walls. In the *Landmark* condition (Fig. 1), all four walls were the same solid gray color, and there were four shapes, one on each wall, in the order of a blue rectangle on the left wall (right-turned tunnel) or right wall (left-turned tunnel), a red circle on the floor, a green triangle on the right wall (right-turned tunnel) or left wall (left-turned tunnel), and a yellow star on the ceiling. The positions of the four shapes were fixed for all trials. They were set in the middle of the wall with distance of 50, 500, 950, and 1400 pixel, respectively, (about 0.625, 6.25, 11.875, and 17.5 m) from the start point. The last, the *both* condition, was the combination of the texture and the landmark condition.

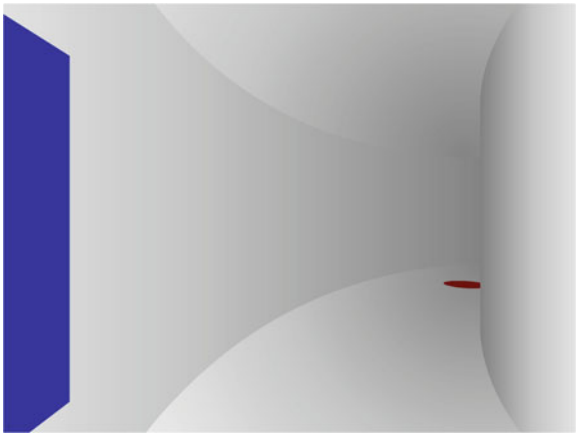

Fig. 1 Sample view of the tunnel in the landmark condition (Only half of the *blue rectangle* was shown in this image. The distance between the *blue rectangle* and the *red circle* was larger in the real experiment. We made them closer in this image only for illustration)

[1] Units were used to describe the layout of the tunnel and make comparison of different lengths of distance. To notice, the virtual scale is different from the scale in a real world. "Meter" here is an analogy for better understanding.

2.3 Task, Design, and Procedure

In every trial, participants first saw a simulated self-movement in one of the four visual environments automatically traveling for a certain amount of distance and then finished a point-to-origin task. The simulated self-motion phase was initiated by pressing the "SPACE" key on the keyboard by the participants, which was followed by a fixation screen for 500 ms before the test stimuli appeared. The movement stopped automatically. The locomotion speed was randomly chosen between 1 and 1.5 m/s for each simulated movement, and was kept constant during the trip. Then the point-to-origin task followed. A two-dimension arrow appeared on the screen pointing up (12 o'clock direction) at first. This arrow represented participants' facing direction at the end of the movement. Participants were asked to image they were at the terminal point of the path they just visually traveled and rotate the arrow with the mouse to let it point back to the origin of the path, and press "SPACE" to confirm their rotation response.

A two-factor within-subject design were used, 4 visual environments × 6 paths. With the 6-m radius tunnel, the traveled distances were 6, 12, 18, and 24 m, which corresponded to 151.35°, 122.71°, 94.06°, and 65.41° as the correct point-to-origin responses. Within the 12-m radius tunnel, the traveled distances were 12 and 24 m, and the correct response angles were 151.35° and 122.71°. The unmatched setting between the 6-m radius tunnel and the 12-m radius tunnel was due to two reasons. The increasing distance, from 6 to 12 m for example, in the 12-m radius tunnel did not change the pointing angles much enough for people to discriminate. Second, distance longer than 24 m would take a long time to perceive and the accuracy for the path integration would be affected. All 24 conditions were randomized within a session, and tested for three times. The direction of the tunnel was counterbalanced between subjects. Since the direction of tunnel was with less interest in the current study and found to have no significant effect on participants' performance, we collapsed data from these two directions for the following analysis. There were six trials of practice before the formal test session to help participants familiarize the procedure and understand the task. Participants reported no difficulty to understand and perform this task. No feedback was given about their performance or accuracy. The whole experiment lasted about 30 min.

3 Results

Data from the point-to-origin task was circular degree from 0° to 359°, with 0° referred to facing ahead and 180° as right behind (Fig. 2). In order to complete this task, people were allowed to use different strategies, to either update their reference frame or not (termed as "turner" or "non-turner", see details [18]), and their strategies were found in this previous study to be kept consistently throughout the whole experiment. In the current experiment, participants were not asked to use

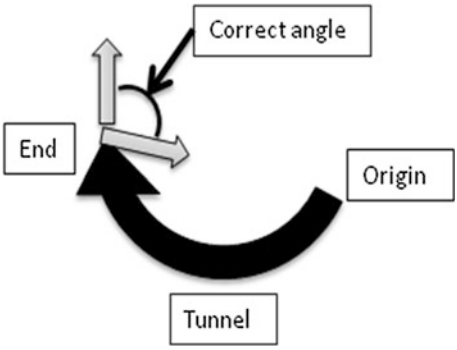

Fig. 2 Illustration of the tunnel and the point-to-origin task

one specific reference frame strategy, however, all of them were found as the same as in Gramann's study to consistently use one of the strategies to complete the task except one participant in one session, and the data from that session were eliminated (48 out of 1920 data points). There were 11 non-turners and 8 tuners. Based on their accuracy, there were no favorable strategies, and also we did not intend to discuss the issue of reference frame in this paper. We collapsed the data from these two groups in the following analysis.

In this experiment, we used four curved tunnels, with two inner-radiuses turning into two directions. Four travel distances were applied to the 6-m radius tunnels and led to the path of approximate 1/6, 1/3, 1/2, and 2/3 of the whole circle, and two travel distances for the 12-m radius tunnels that turned 1/6 and 1/3 of the circle. First, we analyzed the bias results on the signed errors, and then we conducted a regression analysis to further investigate what information people used to estimate the origin of the path in different visual environments.

3.1 Signed Errors

Signed error was calculated by minus the correct point-to-origin angle from participants' rotation angle to evaluate the bias. Positive value represented the overestimation of the correct angle and negative value meant participants underestimated the correct angle.

A repeated measures ANOVAs (4 visual cues × 6 paths; 4 angles in the 6-m radius tunnels, and 2 angles in the 12-m radius tunnels) were conducted on the signed errors (Fig. 3). There was only a significant main effect of the paths ($F_{(5,95)} = 43.942$, $p < 0.001$), that as the turning angle getting larger, participants' bias changed from overestimation to increasing underestimation. Neither the effect of the visual cue ($F_{(3,57)} = 0.190$, $p = 0.902$) nor the interaction of these two factors ($F_{(15,285)} = 1.114$, $p = 0.317$) was significant.

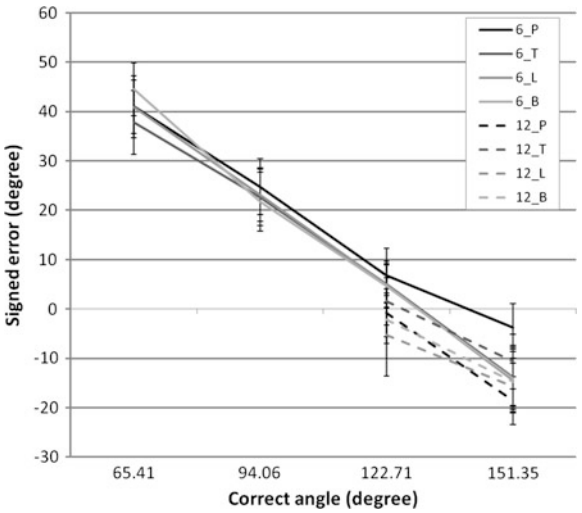

Fig. 3 The signed errors as a function of correct angle under four visual environments and two tunnel radiuses (6_p: radius = 6 m and visual environment = purecolor, etc.)

3.2 Regression

We tried to explore further what information participants used to track the origin of the path. The direct information would be derived from path integration based on optic flow resulting in the correct response of the pointing angle, and many species were found to be able to naturally and well perform the path integration process. The correct pointing angle in the current experiment was decided by the physical stimulus and experimental manipulation. Meanwhile, participants could also rely on the temporal information that longer duration of the simulated movement represented the larger turn. Furthermore, another perceivable information related to the pointing angle was the curvature of the tunnel which could be assessed during the simulated movement based on the inside view of the tunnel. All participants reported to have noticed there were different tunnels, more curved ones and less curved ones. Therefore, we ran a linear regression analysis for the participants' point-to-origin angle with correct pointing angle, traveling duration and radius as predictors for every participant in every condition. If participants were able to perform the path integration and react well by pointing back to the origin, their pointing response should be highly correlated to the correct pointing angle; if they were completely lost when there was only visual information taking them traveling and they still tried to figure out the origin of the path, their response might be correlated to the movement duration and the radius instead of the correct pointing angle. The βs of these three factors were used for the following analysis. Larger value of the β (both positive value and negative value) represents higher correlation between this factor and the response angle of the participant.

One-sample *t*-test was first carried out to test whether the beta value was significant from 0 and the results were showed in Fig. 4. In the purecolor and texture conditions, the β of the correct angle was not significant from 0, while in

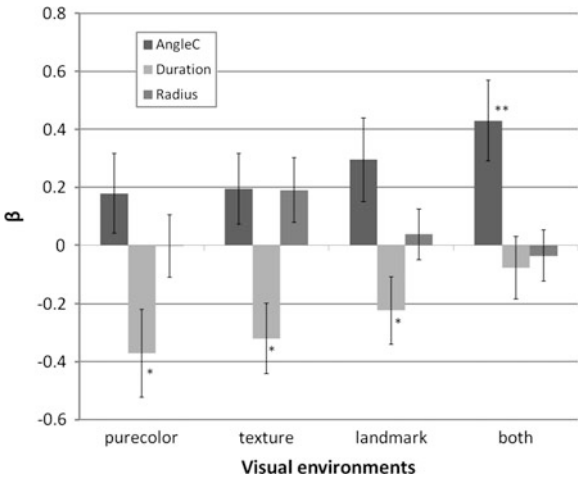

Fig. 4 The β of the correct angle, traveling duration and radius as a function of visual environment and the result of the one-sample *t*-test of β ($^{\#}\ p < 0.1$; $^{*}\ p < 0.05$; $^{**}\ p < .01$)

landmark and both conditions, the β of the correct angle was marginally significant or significant larger than 0. On the other hand, in the first three conditions, the βs of the traveling duration were significantly smaller than 0, but the β of the traveling duration in the both condition was not different from 0.

Separated repeated measures ANOVA on the factor of visual environment, were conducted on the βs of the correct angle, traveling duration, and radius, respectively (Fig. 4). No significant effect of the visual environment was found (correct angle: $F_{(3,57)} = 0.841$, $p = 0.477$; duration: $F_{(3,57)} = 1.259$, $p = 0.297$; radius: $F_{(3,57)} = 1.248$, $p = 0.301$).

4 Discussion

This experiment was aimed at investigating the effect of different visual environment on the path integration process, in specific, on the judgment of the origin of the path. Four visual environments were set up, from the simplest one with only solid colors, to the richest one with both texture and landmarks on the walls. Correct pointing angles were from 65.41° to 151.35° and there was 30 degree difference between every correct pointing angle.

From the signed error results, participants showed a constant bias on pointing back to the start position when they visually traveled along a path for a certain distance. We found only a significant effect of the turning angle on the bias, that participants overestimated the small turn and underestimated the large turn. This result was consistent with the findings of the previous studies using pointing task [19, 20] or triangular completion task [1, 5] with visual input alone. For the paths with larger turns in this experiment, the biased increased up to 40°. However, larger errors were expected according to previous research on both visual path

integration [14, 16] and path integration with body sense [3, 21]. The increasing inaccuracy was also found in previous studies with pointing task [19, 20]. Furthermore, from the bias results, people actually showed similar performance under different visual environments in all paths.

In the current study, we used different tunnels that the turning angle was determined by both the curvature of the tunnel and the distance traveled. In our previous study with the same tunnel and visual environment setting, people were proved to have accurate perception of the traveled distance in the virtual environments especially when there were landmarks or both landmark and texture presented (the paper is under review). And in the current study, participants reported to have clear sense of the two curvatures. Therefore, it might support the previous finding that vision alone was not sufficient for people to perform path integration as accurate as they did when the body sense is involved [16, 17]. However, the results that people showed difficulty in visual path integration might also be due to the specific requirement of the task that people needed to imagine their heading change changing a certain angle, and then figured out where the start was according to their imagined heading. Judgment based on imaged heading was proved to be difficult because of the conflict between the physical heading from the sense of their body and the imagined heading [17]. Several studies have demonstrated that responding in accordance with imagined heading changes was much slower and less accurate compared with physical rotation of the body [22, 23]. Further study would be needed to investigate the potential influence of the task we used.

In addition to the bias results, more interesting finding of the current study was the mediated effect of the visual environments on the strategy that participants were found to make use of different information under different visual environments. There were three major kinds of information from the simulated movement that helped to estimate the origin of the path: optic flow for path integration process, traveling duration, and radius of the tunnel. Regression was carried out to investigate which information was used by the participants under different visual environments. ANOVA failed to find any strong effect of the visual environments on the correlation of the correct point angle, duration, or radius with participants' response pointing angle. However, the one-sample *t*-test revealed a trend that when there were landmarks in the environments, people were more able to perform path integration for tracking back to origin of the path they visually traveled, while when there were only pure-colors or texture instead of landmarks, people used the traveling duration to infer the angle turned overall and the position of the origin.

As we mentioned before, similar as texture, a landmark also generates optic flow during self-motion, however, it offers more. Landmarks specify the particular positions in an environment and help people to displace themselves and plan for their next action (for example, turn left at the fountain) [24]. Therefore, landmarks could help people to be more aware of the environment as well as their own location during movement. Similar to our findings, previous study using another path integration task found that when participants were asked to make a shortcut after learning two outbound legs, they performed more accurately under the landmark condition (forest world) than under the texture condition (dessert world)

in reproducing the learned outbound legs and making the shortcut [25]. Therefore, when navigating in an environment that contains several silent landmarks, it would be easy for people to perceive the movement and the path.

One limitation in our current study was we did not consider the influence of people's strategy of the updating of the reference frame. Though it was found that whether to adapt the updated frame of reference did not make difference on people's judgment of the origin of the path [18], the updates of the reference frame might still have potential influence in our experiment. The current study was not preliminary designed for the issue, but we do believe it is a significant question for further exploration. Also, only desktop virtual reality was used in the current study, and it would be necessary to validate the findings with more immersive virtual reality technology.

Acknowledgments We would like to thank Dr. Frances Wang from University of Illinois at Urbana-Champaign for the instructions and constructive suggestions on our study. Special thanks are given to our participants for their patience and valuable time.

References

1. Kearns MJ, Warren WH, Duchon AP, Tarr MJ (2002) Path integration from optic flow and body senses in a homing task. Perception 31:349–374
2. Loomis JM, Klatzky RL, Golledge RG, Philbeck JW (1999) Human navigation by path integration. In: Golledge RG (ed) Wayfinding: cognitive mapping and spatial behavior. Johns Hopkins University Press, Baltimore, pp 125–151
3. Loomis JM, Klatzky RL, Golledge RG, Cicinelli JG, Pellegrino JW, Fry PA (1993) Nonvisual navigation by blind and sighted: assessment of path integration ability. J Exp Psychol Gen 122(1):73–91
4. Rieser JJ, Ashmead DH, Taylor CR, Youngquist GA (1990) Visual perception and the guidance of locomotion without vision to previously seen target. Perception 19:675–689
5. Riecke BE, van Veen HACH, Bülthoff HH (2002) Visual homing is possible without landmarks: a path integration study in virtual reality. Presence 11(5):443–473
6. Ellmore TM, McNaughton BL (2004) Human path integration by optic flow. Spatial Cogn 4(3):255–272
7. Frenz H, Lappe M (2005) Absolute travel distance from optic flow. Vis Res 45:1679–1692
8. Lappe M, Frenz H, Bührmann T, Kolesnik M (2005) Virtual odometry from visual flow. In: Rogowitz BE, Pappas TN, Daly SJ (eds) Human vision and electronic imaging, vol 5666. Proceedings of the SPIE/IS&T conference on human vision and electronic imaging, vol X, pp 493–502
9. Frenz H, Lappe M, Kolesnik M, Bührmann T (2007) Estimation of travel distance from visual motion in virtual environments. ACM Trans Appl Percept 4(1), Article 3
10. Gibson JJ (1950) Perception of the visual world. Houghton Mifflin, Boston
11. Bremmer F, Lappe M (1990) The use of optical velocities for distance discrimination and reproduction during visually simulated self motion. Exp Brain Res 127:33–42
12. Frenz H, Bremmer F, Lappe M (2003) Discrimination of travel distances from 'situated' optic flow. Vis Res 43:2173–2183
13. Redlick PF, Jenkin M, Harris RL (2001) Humans can use optic flow to estimate distance of travel. Vis Res 41:213–219

14. Bakker NH, Werkhoven PJ, Passenier PO (1999) The effects of proprioceptive and visual feedback on geographical orientation in virtual environments. Presence 8(1):36–53
15. Klatzky RL, Loomis JM, Golledge RG (1997) Encoding spatial representations through nonvisually guided locomotion: tests of human path integration. In: Medin D (ed) The psychology of learning and motivation. Academic Press, San Diego, pp 41–84
16. Péruch P, May M, Wartenberg F (1997) Homing in virtual environments: effects of field of view and path layout. Perception 26:301–311
17. Klatzky RL, Loomis JM, Beall AC, Chance SS, Golledge RG (1998) Spatial updating of self-position and orientation during real, imagined and virtual locomotion. Psychol Sci 9(4):293–298
18. Gramann K, Müller HJ, Eick E, Schönebeck B (2005) Evidence of separable spatial representations in a virtual navigation task. J Exp Psychol Hum Percept Perform 31(6):1199–1223
19. Wiener JM, Mallot HA (2006) Path complexity does not impair visual path integration. Spatial Cogn Comput 6(4):333–346
20. Riecke BE (2008) Consistent left-right reversals for visual path integration in virtual reality: more than a failure to update one's heading? Presence 17(2):143–175
21. Sholl MJ (1989) The relation between horizontality and rod-and-frame and vestibular navigational performance. J Exp Psychol Learn Mem Cogn 15:110–125
22. Easton RD, Sholl MJ (1995) Object-array structure, frames of reference, and retrieval of spatial knowledge. J Exp Psychol Learn Mem Cogn 21:483–500
23. Farrell MJ, Robertson IH (1998) Mental rotation and the automatic updating of body-centered spatial relationships. J Exp Psychol Learn Mem Cogn 24:227–233
24. Stankiewicz BJ, Kalia AA (2007) Acquisition of structural versus object landmark knowledge. J Exp Psychol Hum Percept Perform 33(2):378–390
25. Foo P, Warren WH, Duchon A, Tarr MJ (2005) Do humans integrate routes into a cognitive map? Map- versus landmark-based navigation of novel shortcuts. J Exp Psychol Learn Mem Cogn 31(2):195–215

Missile Turbofan Engine Fault Diagnosis Technology and Its Application

Rui Cheng and Jiayuan Dan

Abstract This paper retrospects the domestic and overseas development process of the fault diagnosis technology. Combined with today's cruise missile with turbofan engine production, testing, and use of the actual characteristics of fault diagnosis technology research and analysis in the field range of applications, the value and significance of the shells with the turbofan engine fault diagnosis technology are introduced. In addition, this paper focused on the instance of the class fault diagnosis system study. And the development trends of future missile turbofan engine fault diagnosis technologies are summarized.

Keywords Turbofan engine · Diagnostic system · Fault diagnosis approach

1 Introduction

Cruise missiles as the family's new weapon of missile weapons, in the beginning of the birth of concern, have been widely used in modern warfare, its main power plant using missile turbofan engine. With the continued progress and development of science and technology, especially the rapid advancement of computer technology and the popularity, missile turbofan engine fault diagnosis technology

R. Cheng (✉) · J. Dan
Beijing Institute of Technology School of Astronautics, Beijing 100081, People's Republic of China
e-mail: 4537768@qq.com

J. Dan
e-mail: sjy1919@bit.edu.cn

F. Sun et al. (eds.), *Foundations and Practical Applications of Cognitive Systems and Information Processing*, Advances in Intelligent Systems and Computing 215,
DOI: 10.1007/978-3-642-37835-5_65,

came into being, the detection, monitoring, and diagnostic engine working conditions to become a reality, and can be in the design, production stages to complete and accurate fault location, reduce the risk of technology applications to improve the effectiveness of equipment expenditures, in use, to ensure the safety of personnel and equipment during maintenance, to shorten equipment maintenance time and enhance the troops' ability to fight.

2 The History and Status Quo of a Fault Diagnosis Technology at Home and Abroad

2.1 Foreign Developments

Fault diagnosis technology was born in the late 1960s, the United Kingdom, from the beginning of the birth, due to its failure to identify and forecast the practicality and the resulting huge economic, military, and social benefits received widespread attention. The United States since the Apollo program in 1961, there was a series of accidents caused by equipment failure, and by the U.S. Naval Research Laboratory (ONR) in 1967 under the auspices of the NASA (NASA), established under the auspices of the American Society of Mechanical fault prevention group (MFPG), and is actively engaged in the development of technical diagnostics. The United Kingdom in the 1960s–1970s, led the British to Collacott machine health and condition monitoring Association (MHMG & CMA) first began to study the fault diagnosis technology, with a leading position in the UK in friction and wear, automotive and aircraft generator monitoring, and diagnosis. Japan's Nippon Steel developed diagnostic technology since 1971, in 1976, reached the practical Japanese diagnostic techniques leading position in the steel, chemical, and railway departments.

2.2 Domestic Developments

The start of fault diagnosis technology in China is later. The first device diagnostic technology symposium appeared in 1979, which really started from 1983 in Nanjing. Fault diagnosis technology in China after 30 years of research and development in certain diagnostic research is quite distinctive, and the formation of a number of domestic monitoring and diagnostic products, especially intelligent fault diagnosis expert system, power system, petrochemical system metallurgical systems, as well as the high-tech industry in the nuclear-powered power plants, the aviation sector and the manned space project has been widely used.

3 The Significance of the Turbofan Engine Fault Diagnosis Methods

3.1 Missile Turbofan Engine Fault Type and Diagnostic Significance

Missile turbofan engines of the type of fault is very complex, points, according to the failure mode can be roughly divided into the failure of the structure type (such as cracks, wear, corrosion, imbalance, misalignment, etc.) and parametric faults (such as stall surge resonance over-temperature, etc.). From our shells with the aviation engine failure statistics found that structured total failure is 60–70 %; the parametric faults account for about 10 % of the total failure of $\sim$20 %.

Reliable missile turbofan engine work is the basic guarantee of missile weapons to complete scheduled tasks, the damage effect, although such engine design technology and reliability of the technology is improving, but failed due to the engine causes flight and trade stories still time occur. Therefore, playing with the important significance of the turbofan engine fault diagnosis is: First, to ensure the safety of personnel and equipment; complete fault location accurately and rapidly estimate the degree of failure, reduce maintenance time, to ensure sustained combat capability of the missile; reduce technology security costs, reduced life cycle cost; accumulation of existing equipment failure characteristics and diagnostic experience, to provide design guidance on the reliability, security equipment development for the next generation, and existing equipment modification.

3.2 Mail Approaches

In accordance with the international fault diagnosis the authoritative German Frank professor's point of view, the existing shells with the aero-engine fault diagnosis method is divided into a dynamic mathematical model-based method, based on the method of signal analysis and processing and knowledge-based intelligent diagnosis method (Fig. 1) the following three types of methods in the main method to be introduced.

(1) Knowledge-based intelligent diagnosis approach

(a) Diagnosis-based expert system
The expert system in recent years is one of the most significant achievements in the field of fault diagnosis, including diagnostic knowledge expression method of diagnostic reasoning, uncertainty reasoning, and diagnosis knowledge. With the development of computer science and artificial intelligence, the expert system-based approaches for fault diagnosis method to overcome the excessive dependence of the model-based fault diagnosis model, effective method of fault detection.

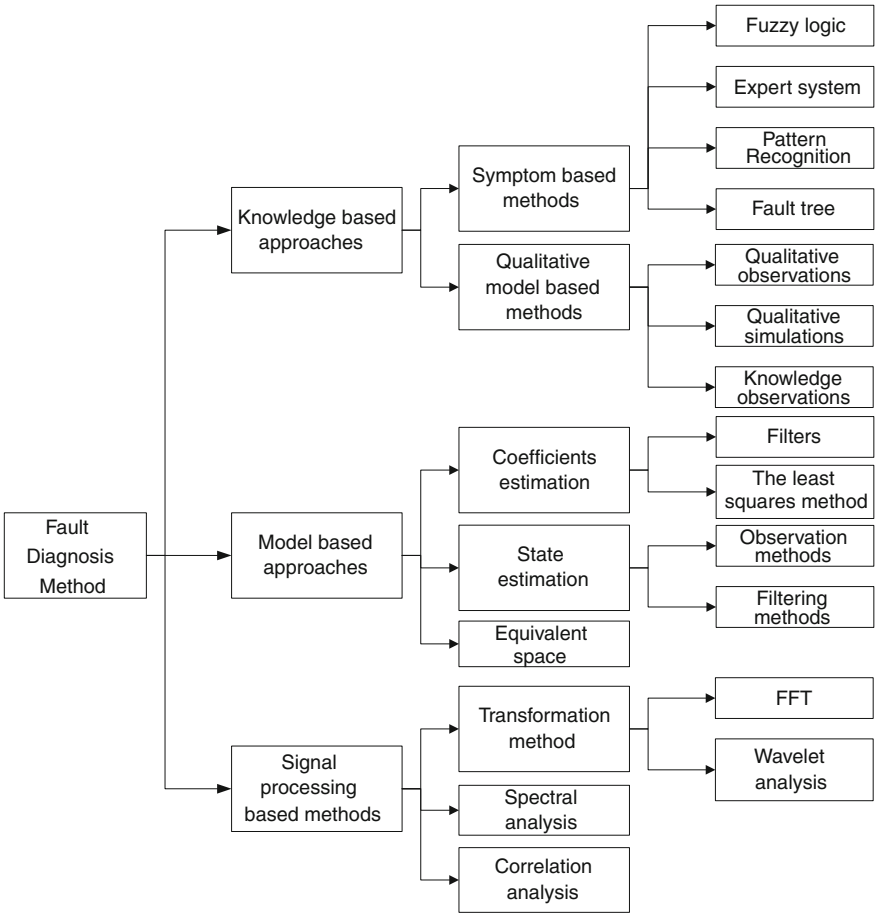

Fig. 1 Introduction of the aero-engine fault diagnosis

(b) Based on pattern recognition diagnosis
This is a static fault diagnosis method-based pattern recognition technology, its critical failure mode selection and extraction of the characteristic quantities. The method is divided into off-line analysis and on-line analysis of the two phases. Feature vector set through off-line analysis to determine the fault status of the expression system described in the failure mode, and to the feature vector set vector, thereby forming a fault set of the reference pattern, and determine the distinction identify these failure modes vector discriminant function, and then through line diagnostic real-time extraction of the feature vector of the fault by the discriminant function of the fault, separate localization.

(c) The fault tree analysis-based diagnostic method
The fault tree is a system or device-specific event that does not want the logical structure between the event and its various subsystems or component failure events, to be a part of the reasons formed through structural diagram of a system failure, the overall tree gradually detailed breakdown. This is a graphic interpretation of the method, system failure, and a variety of factors causing the failure image plotted in the fault chart to intuitively reflect the fault, components, systems, and factors, because of the relationship between the quantitative calculation fault degree of probability and reason.

(d) Diagnostic method based on fuzzy math
Some signs space of fuzzy set theory and fault state space mapping relationship by signs to diagnose the problem. The fuzzy set theory is not yet mature, usually only a rule of thumb, and a large number of test is to be determined. Further, because the system itself is uncertain and vague in information, and you want it on a sign and characteristic parameters of its upper and lower limits and appropriate membership function, application limitations. But with the perfection of the fuzzy set theory, it is believed that the method has a bright future.

(e) Artificial neural network-based diagnostic method
The late 1980s to the early 1990s witnessed the developments of real practicality of a fault diagnosis method. Because neural network has a principle, fault-tolerant the structure topology robustness, Lenovo, speculate, memory, adaptive, self-learning, parallel, and they deal with complex patterns, to the actual existence of a large number of multiple faults in engineering, multi-process, sudden failure to play a larger role in the monitoring, and diagnosis of large and complex machines and systems.

(2) Dynamic mathematical model-based methods
The method is based on the modern control theory and modern optimization methods for guidance, based on the mathematical model of the engine, the observer(s), the equivalent space equation Kalman filter parameter model estimation and recognition method produces residuals, then the residual evaluation and decision-making is based on certain criteria or threshold, the fault diagnosis.

(3) The method based on the signal analysis process
Engine I/O signal model with the source of the fault in the amplitude, phase, frequency, and correlation on a certain relationship exists some kind of signal processing method and feature extraction method for fault detection and isolation. In recent years, when a fault occurs, it can be applied here in brief based on signal processing methods.

(a) Wavelet analysis method
Wavelet analysis is a time-domain analysis methods, singularity analysis applies to non-stationary signals. Engine fault diagnosis, the commonly used detection signal such as a vibration signal and a speed fluctuation

signal wavelet transformation is performed. The removal of a singular point caused due to input change in the converted signal, the rest of the singular point is a point of failure.

(b) Kullback Information Criterion (KDI) detection failure
This criterion can measure the coefficient of variation, in the absence of unmodeled dynamic characteristics and threshold comparison, can effectively detect faults. But if there is unmodeled dynamic characteristics, KDI volatile threshold test will no longer apply.

(c) Using δ operator
Multiply orthogonal projection vector set, based on the minimum M in the the δ operator constructed Hilbert space that derived the complete trellis filter as fault detection filter, with the first element of the backward prediction error vector δ operator described as a residual, and adaptive noise canceling technology residuals as only fault sensitive.

(d) Principal component analysis method
Principal component analysis (PCA) is the core of the fault diagnosis method based on multivariate statistical process control, the basic idea is: the process of historical data using principal component analysis method to establish the main element model under normal circumstances, once the measured signal with the main Element Model conflicts, it can be judged that a fault occurs, through data analysis separable failure.

4 The Key Issues of the Turbofan Engine Fault Diagnosis Technology

Missile turbofan engine fault diagnosis technology development, has undergone the original diagnostic phase, after the diagnostic phase of analysis and estimates based on the material life, is currently in sensing, computer technology, and intelligent diagnostic phase.

Diagnosis-based sensors and computer technology began in the mid-1960s, and the more mature, the stage based on sensor technology and dynamic testing techniques, based on the basis of computer signal processing as a means, the main symptom of access to information and transform processing enabling equipment diagnosis and analysis, but its still signal detection and data processing mainly the lack of intelligence, therefore, gave birth to the development of intelligent diagnostic technology.

Intelligent diagnostic technology was born in the late twentieth century, artificial intelligence (AI) technology to support, based on expert knowledge, a knowledge processing and knowledge reasoning as the core of new diagnostic technologies. It appears not only to solve some of the problems that cannot be solved by traditional diagnostic techniques, but has also brought new vitality to the

development of the diagnostic field. It is not difficult to find that the technology started late, but there are still a lot of heavy and difficult problems to be solved.

4.1 Robust Fault Diagnosis Problem

The robustness of fault diagnosis is an important issue faced by all the fault diagnosis theory, method, and system. The concept of robust fault diagnosis (RFD) method is based on a mathematical model for the first time. Currently, it only get to use the entire mechanical system, hydraulic system, hydraulic control system based on the mathematical model of the control system, there is no practical application. RFD is an effective way to solve the practical application of the fault diagnosis, and effective way to improve the performance of fault diagnosis system that began in the early 1980s, after decades of research and development, made a lot of research, also carried out a number of applied research where some scholars have done a useful exploration in the RFD.

4.2 The Knowledge-Access Issue of Fault Diagnosis

Intelligent diagnostic technology, care only about whether there is sufficient knowledge of their match with the application of diagnostic knowledge expression, "reflects the practical application of some intelligence to simulate the kind of intelligent behavior" smart system technology The specific targeted it smart performance and intelligent separated. Will find that when the need to improve the flexibility of intelligent diagnostic system, the applicability, versatility, and robustness of the dangers of such a fragmented.

As we all know, in the field of AI, knowledge acquisition has become a "bottleneck" problem of the construction of expert systems. Automatic knowledge acquisition is the focus and difficult to implement intelligent diagnosis. Judging from the current situation, the machine learning is one of the most intelligent features and the most cutting-edge research direction that solve the heavy and difficult problem, once the diagnosis system has self-learning ability to learn new knowledge from the environmental changes, it constantly adjusted to achieve self-improvement, to improve the level of intelligence of the fault diagnosis system.

4.3 Uncertain Knowledge Processing

There is often a lot of uncertainty in the, information or random, vague or incomplete fault diagnosis process. How uncertainty knowledge expression and processing, is always diagnostic studies in the field of hot issues. Although there is

a lot of uncertainty theory a better application of the actual fault diagnosis expert system, but the problem is still not a very effective solution, effective, reasonable, and uncertain knowledge processing, there is a huge research potential.

5 Missile Turbofan Engine Fault Diagnosis Technology Applications

Turbofan engine is the main power plant of cruise missiles, which belong to the scope of aero gas turbine engines, state-of-the-art technology, complex structure, and a wide range of various failure modes exposed through the engine combustion process maintenance forces, oil leakage failure, and design professionals. Review and summary of the fault system exposed engine in the development, production, testing, use and maintenance process, the establishment of engine failure database, build a fault tree, the preparation of the fault diagnosis software, can achieve fast fault inquiries, diagnosis, location, can improve the level of troops fault disposal and maintenance support capabilities, shorten the fault repair cycle, and improve the combat effectiveness of troops to provide technical support.

5.1 Establishing the Turbofan Engine Fault Library

Delivery of maintenance and troops engine batch production engines use focused, comprehensive, and systematic collection of various failures exposed in the development, production, testing, use, and maintenance of process information, in accordance with the engine block, transmission system, power supply system, start the ignition system, the fuel control system and lubrication system 6 induction system fault information, sorting and classification. Basis GJB241-87 aviation turbojet and turbofan engines generic specification provisions, takes into account the characteristics of the actual use of the turbofan engine failure criterion requirements clear, its failure into a performance type, structure, and system failure.

Based on the data, the number of gas turbine engine performance fail is about 10–20 % of the total number. Turbofan engine performance type of failure mode: the engine cannot be completed within the given time starter; given flight conditions, and control voltage $\mu_y$value of thrust instability, changes more than the required value (instantaneous or continuous), or even turn off. Turbofan engine performance type of failure mode: fan, compressor blades crack, fracture; compressor titanium fire failure; combustion chamber formation failure; turbine blade cracks, fracture; turbine blades ablation; turbine disk crack fault; pressure turbine blades The locking piece windshield chip groove blade root and the low-pressure

turbine shroud tabs break; exceeds the required value of machine vibration and bearing failure.

(a) Lubrication system failure modes. Common failure is excessive oil consumption, seal oil, high oil temperature, fuel supply, oil pressure pulsation, oil blocked ventilation system blocking the oil pump is not normal work.
(b) Fuel control system failure modes, common faults when integrated controller control circuit failure, sensor indicates distortion, oil regulator components stuck oil pressure pulsation, the seal at the oil spill. Multiple fuel control system failure, accounting for about 50 % of the engine failure, and the cause of the malfunction is not easy to find, and the diversification of failure modes.
(c) Ignition starting system failure modes, common failure mode of the circuit is not turned on, the EED tube misfire, ignition energy is not enough.
(d) Transmission system failure modes, common failure mode is a parts failure of gears, spline gears, spline Part tooth surface and excessive wear, fatigue fracture, impact damage.
(e) Power supply system failure modes, common failure mode between the generator excitation winding and the field winding and shell, insulation between the winding and the case dropped, the generator bearing damage and short circuit, open circuit.

5.2 Shells Turbofan Engine Fault Diagnosis System Software Development

Turbofan engine fault diagnosis software system have two major forces in the testing process fault diagnosis positioning; retrieval query past failures. Turbofan engine forces the failure of the repair process characteristics, the research method of fault diagnosis system software to achieve to VB, Author ware, and Office software development platform, the development of the visual fault diagnosis system software, fault diagnosis, and queries. Take advantage of the VB6 development of a set of system software using fuzzy query technology, minimum cut set separation technology, concise method based on the probability of sequencing technology and expert system, fault retrieval functions. Author ware multimedia programming techniques, according to the fault tree model, fault diagnosis and localization of the layer-by-layer depth.

Fault diagnosis query software the VB6 software development system development, fault data access so choose the Access database program using ADO dynamic link library technology to establish a connection with the database access and query the database.

6 Missile Aero-Engine Fault Diagnosis Technology Trends

Accompanied by the development of science and technology, bomb aviation engines has become more advanced and complex, to ensure the maintenance and security requirements it is also increasing. The current development of fault diagnosis technology is mainly characterized by the following trends:

6.1 Real-Time Availability

Terms for missile aero-engine is its reliability, safety-critical, rapidly changing engine test state, therefore, the fault should be able to do real-time. Not only require on-line real-time diagnostics in real time, but to improve the diagnostic reaction speed, and improve the efficiency of diagnosis, to gain time for maintenance strategy formulation. Real-time diagnosis of a way of using the system since the detection of Technology (BIT), it can automatically detect internal failure of equipment or system, located in the diagnosis, thus greatly improving the level of real-time diagnosis.

6.2 Intelligent

Basic requirements of intelligent fault diagnosis in the absence of the circumstances of experts in the field, can be accurate, prompt, and complete diagnostic tasks independently; further requirement is a diagnostic system during operation, the semi-autonomous or fully autonomous learn new experts in the field knowledge, to achieve self-improvement, and constantly improve the accuracy of fault diagnosis.

6.3 Systematic

Fault diagnosis systematic meaning: mutual authentication due to the diversification of the fault information, the use of different diagnostic methods may also be conflicting, therefore, to be emphasized that the multiple faults signs information the systematized fusion, improve diagnostic accuracy; shells with complex equipment such as aero-engine problems are often intertwined, therefore, to emphasize multiple faults parallel diagnostic capabilities, and the ability to distinguish between partial failures and system failures in the diagnostic process.

6.4 Network

The network is an important development direction of fault diagnosis technology. Difficult fault diagnosis of speed and accuracy, and make full use of the space, network resources, necessary to the development, and application of a joint Internet-based remote diagnostic technology. Currently, the new fault diagnosis technology based on the Internet of Things in the ascendant, in the office in the near future, the engine remote maintenance, testing, and troubleshooting may become a reality.

7 Conclusions

Bomb aero engine fault diagnosis is a very practical emerging research area, although after years of painstaking research of experts in the field, both in theoretical research in the application of engineering practice made great progress. But there are still many unresolved theory and engineering applications of technical problems with the computer technology, testing technology, signal processing technology, information theory, cybernetics, reliability theory, and systems engineering to be done more in-depth research. The development of modern science and technology will greatly enrich bomb aviation as the basis of engine fault diagnosis theory and engineering technology, aviation engine diagnostic technology that makes the bombs more perfect.

References

1. Zhang F (2003) Aviation equipment failure diagnostics. National Defense Industry Press, Beijing
2. Cheng ceremony, Wei C (2003) Aviation engine condition monitoring and fault diagnosis. Air Force Engineering University Engineering Institute, Xi'an
3. Doman (1997) Analysis and testing of the flight test failure. National Defense Command Institute of Technology, Beijing
4. Kwong (1991) Modern machine fault diagnostics. Science Press, Beijing
5. Yuan MM (2006) Introduction to artificial intelligence and expert systems. Tsinghua University Press, Beijing
6. Sun C, Wang X (2007) Typical flight structural failure analysis and design improvements. Aviation Industry Press, Beijing
7. Wang P (2001) Intelligent fault diagnosis system theory and methods. Metallurgical Industry Press, Beijing
8. Yang J (2004) Equipment intelligent fault diagnosis technology. National Defense Industry Press, Beijing
9. The equipment series pipeline Committee (2008) Aero-engine. Aviation Industry Press, Beijing

A Novel Acquisition Scheme for a GPS Software Receiver Based on Two Stand-Alone One-Dimensional Search Processes

Zhiguo Liu, Dacheng Luo, Shicheng Wang, Zhanxin Cheng and Lihua Chen

Abstract To improve the capturing speed of a GPS software receiver, a novel acquisition scheme is presented. First, by compensating the frequency of the intermediate frequency signal to improve its cyclicity, the signal-to-noise ratio (SNR) of the intermediate frequency signal can be improved by using coherent average algorithm. Second, the C/A code start of every satellite is searched through the delay−multiply configuration, then the delay and accumulation unit is put forward to pretreat the multi-frequency signals. Lastly, the separation and estimation of Doppler-shift components are fulfilled by frequency domain analysis on post-treatment signals; therefore, the two-dimensional searching process in conventional acquisition scheme is transformed into two one-dimensional searching processes in the proposed acquisition scheme. In the proposed acquisition scheme, a shorted fast Fourier transform (FFT) version is adopted, which can greatly reduce the computation burden without degradation on performance. Sampled data from GPS receiver and simulated GPS signals are used for simulation experiments. Simulation results indicate that the proposed acquisition scheme is an effective one by much decreasing the acquisition time.

Keywords GPS software receiver · Signal acquisition · Two-dimensional searching · Doppler frequency

1 Introduction

The Global Positioning System (GPS) has been one of the most excellent navigation systems at present. It is widely used for its outstanding navigation performance in military and civil applications. Originally, GPS receivers consist of a

Z. Liu (✉) · D. Luo · S. Wang · Z. Cheng · L. Chen
Xi'an Research Institute of High-tech, Hongqing Town, Xi'an 710025, Shaanxi, China
e-mail: lzgc@163.com

F. Sun et al. (eds.), *Foundations and Practical Applications of Cognitive Systems and Information Processing*, Advances in Intelligent Systems and Computing 215,
DOI: 10.1007/978-3-642-37835-5_66,

Radio Frequency (RF) front-end, an Applications Specific Integrated Circuit (AISC) for signal processing, and a CPU core for higher level functions. However, design flexibility of the GPS receiver is constrained by an AISC that is hardwires with predefined acquisition and tracking channels, correlator, and control loop characteristics. So a software GPS receiver is the best solution for currently GPS receiver design.

In the design of a software GPS receiver, first operation is the signal acquisition that decides either the presence or the absence of the signal under test. Most acquisition schemes based on the principle that the local receiver replicates the GPS signal with different PRN codes and performs correlation with the incoming signal, then compares these correlation process yields various peaks with a detection threshold to test for acquisition success. These acquisition schemes also provide a rough estimation of the code delay and the Doppler frequency of the incoming signal. But the phase of the received signal relative to the available replica sequence, owing to additional modulation such as a Doppler effect and/or a receiver clock inaccuracy, can have any possible value due to uncertainties in time and position. It is also possible that the receiver may not know the exact apparent satellite frequencies or which of the possible satellites are visible in the sky.

The basic idea of signal acquisition is to search over a predicted time-frequency uncertainty zone [1]. The incoming signal and the local code are correlated for a predetermined time interval with a candidate code-phase and frequency assumptions. After the integration, a statistical test is applied to the correlation results to determine if a signal acquisition has been reached or not. If it has been, the acquisition is terminated and the receiver starts the tracking stage; if not, the search continues and moves to the next code-phase and frequency option. Therefore, those acquisition schemes are based on the two-dimensional searching process, which must do a search in several code-phase and frequency planes, one plane for each possible satellite.

In this paper, the two-dimensional searching process in conventional acquisition scheme is transformed into two one-dimensional searching processes, thus improves the capturing speed.

2 A Novel Fast Acquisition Scheme

2.1 Frequency Compensating and Coherent Average Filter

The acquisition process contains three steps: First, the improving of the signal-to-noise ratio (SNR) of the Intermediate Frequency (IF) samples by compensating its frequency. Second, the searching of the initial point of the C/A code through the utilization of delay and multiply method. Third, estimating the Doppler frequency components with the delay and accumulation unit after the removing of C/A code. Figure 1 shows the block diagram of this acquisition scheme.

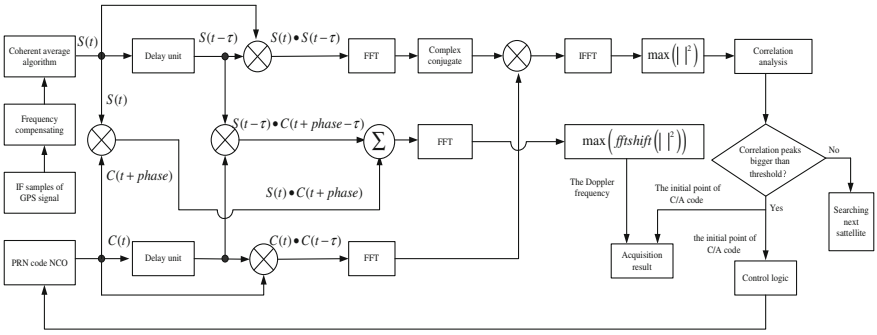

Fig. 1 Architecture of GPS fast acquisition scheme

To a satellite signal, the signals of other satellites are noises. So the received IF signal can be expressed as:

$$s_{\mathrm{IF}}(t) = \sqrt{P}C_i(t)D_i(t)\cos[2\pi(f_{\mathrm{IF}} + f_{di})t + \theta_i] + u_i(t) \tag{1}$$

where P is the total signal power, $C_i(t)$ is the normalized C/A code of satellite i, $C_i(t) \in \{-1, 1\}$, f_{IF} is the intermediate frequency of carrier, f_{di} is the carrier Doppler, and θ_i is the initial carrier phase, $u_i(t)$ represents the Gaussian white noise with the equalizing value of zero and the variance of σ_u^2. If the sampling frequency is f_s, the sample points per 1 ms signal is N, the total ms of the signal for acquisition is M, Eq. (1) can be expressed in complex representation as:

$$s_i(n) = \sqrt{P}D_i(nt_s)C_i(nt_s)\mathrm{e}^{j2\pi(f_{\mathrm{IF}}+f_{di})nt_s} + u_i(nt_s) \tag{2}$$

where $t_s = 1/f_s$ is the periodic time, $Nt_s = 1\,\mathrm{ms}$, $n \in [0, MN-1]$. The SNR of $s_i(n)$ can be expressed as:

$$\mathrm{SNR} = \frac{P}{\sigma_u^2} \tag{3}$$

Because of the navigation data bit period is 20 ms, the 180° phase changes potentially occur every 20 ms. But it occurs at most once between two continuous 10 ms signals. So the duration of coherent integration is typically limited in 10 ms signals, that is to say $M \leq 10$.

To be simple, assuming $D_i(nt_s) = 1$ in the M ms incoming signals for acquisition, multiply discrete signal $s_k(n)$ with $p_k(n)$ which is frequency compensated signal generated locally, the new signal $s_i'(n)$ can be expressed as:

$$\begin{aligned} s_i'(n) &= \sqrt{P}p_i(n)s_i(n) \\ &= C_i(nt_s)\mathrm{e}^{j2\pi(f_{\mathrm{IF}}+f_{di}+\Delta f)nt_s} + u_i(nt_s)\mathrm{e}^{j2\pi\Delta f nt_s} \end{aligned} \tag{4}$$

where $p_i(n) = e^{j2\pi\Delta f nt_s}$, $\quad n = 0, 1, \ldots, N-1$. The coherent average result in

$$\begin{aligned} Y_i(n) &= \frac{1}{M}\sqrt{P}\sum_{k=0}^{M-1} s_i'(n+kN) \\ &= \frac{1}{M}\sqrt{P}s_i'(n)\sum_{k=0}^{M-1} \mathrm{e}^{j2\pi(f_{\mathrm{IF}}+f_{di}+\Delta f)kNt_s} + \frac{1}{M}\sum_{k=0}^{M-1} u_i(nt_s)\mathrm{e}^{j2\pi\Delta f\,(n+kN)t_s} \end{aligned} \tag{5}$$

Provided the delay time Δf is chosen appropriately, the following equation is guaranteed:

$$\mathrm{e}^{j2\pi(f_{\mathrm{IF}}+f_{di}+\Delta f)Nt_s} \approx 1 \tag{6}$$

Equation (4) can be written as follows:

$$Y_i(n) = s_i'(n) + u'(n) \tag{7}$$

where $u'(n) = \frac{1}{M}\sum_{k=0}^{M-1} u_i(nt_s)\mathrm{e}^{j2\pi\Delta f\ (n+kN)t_s}$, $u'(n)$, is also the Gaussian white noise with the equalizing value of zero and the variance of σ_u^2/M. The SNR of $Y_i(n)$ can be expressed as:

$$\mathrm{SNR} = \frac{P}{\sigma_u^2/M} = M \cdot \frac{P}{\sigma_u^2} \tag{8}$$

Obviously, compared with $s_i'(n)$, $Y_i(n)$ has the same characteristics, but enlarges M times in SNR.

2.2 Estimation of the Code Delay

Ignoring the impact of noise and assuming $D_i(t) = 1$, the incoming signal contains two satellites here in [3]:

$$s(t) = \sqrt{2}C_1(t)\cos(2\pi f_1 t) + \sqrt{2}C_2(t)\cos(2\pi f_2 t) \tag{9}$$

where $f_{di} \cdot i = 1, 2$ is the Doppler shift of satellite i, $f_i = f_{\mathrm{IF}} + f_{di}$, $i = 1, 2$ is the carrier frequency with Doppler shift. The code delay and carrier phase shift are ignored in Eq. (9), the slightly shifted version of the incoming IF signal is represented as:

$$\begin{aligned} s(t-\tau) = {} & C_1(t-\tau)\cos(2\pi f_1(t-\tau)) \\ & + C_2(t-\tau)\cos(2\pi f_2(t-\tau)) \end{aligned} \tag{10}$$

where τ is the sample delay. The product of the incoming IF signal and its delayed version can be expressed in four parts:

$$s(t)s(t-\tau) = \mathrm{item1} + \mathrm{item2} + \mathrm{item3} + \mathrm{item4} \tag{11}$$

there into

$$\begin{aligned}
\text{item1} &= C_1(t)C_1(t-\tau)\{\cos(2\pi f_1\tau) - \cos[2\pi f_1(2t-\tau)]\} \\
\text{item2} &= C_2(t)C_2(t-\tau)\{\cos(2\pi f_2\tau) - \cos[2\pi f_2(2t-\tau)]\} \\
\text{item3} &= C_1(t)C_2(t-\tau)\{\cos(2\pi f_2\tau + 2\pi f_1 t - 2\pi f_2 t) - \cos[2\pi(f_1+f_2)t-\tau]\} \\
\text{item4} &= C_2(t)C_1(t-\tau)\{\cos(2\pi f_2\tau + 2\pi f_2 t - 2\pi f_1 t) - \cos[2\pi(f_1+f_2)t-\tau]\}
\end{aligned}$$

From the item1 to item4, the high-frequency terms, such as $\cos[2\pi f_1(2t-\tau)]$ in item1,$\cos[2\pi f_2(2t-\tau)]$ in item2, item3 and item4, can be easily filtered out by the pre-detection filter (accumulate and dump). So Eq. (11) can be expressed as:

$$\begin{aligned}
s(t)s(t-\tau) = {} & C_1(t)C_1(t-\tau)\cos(2\pi f_1\tau) \\
& + C_2(t)C_2(t-\tau)\cos(2\pi f_2\tau)
\end{aligned} \tag{12}$$

If the sample delay τ will be carefully chosen, $|\cos(2\pi f_i\tau)|$ $(i = 0, 1, 2)$ is close to unity. Actually, $\cos(2\pi f_i\tau)$ can be considered to be as one part of the incoming signal amplitude which is expected to be as high as possible. Since the f_{IF} is known according to the front-end frequency plan, a series of sample delay values can be found to meet this requirement. Then Eq. (12) can be rearranged as:

$$s(t)s(t-\tau) = C_1(t)C_1(t-\tau) + C_2(t)C_2(t-\tau) \tag{13}$$

where $C_i(t)C_i(t-\tau)$ $i = 1, 2$ belongs to the same family as the Gold code, and the code delay is the same as that of $C_i(t)$. Then its autocorrelation and cross-correlation can be used to find the code delay.

If the incoming signal contains more than two satellites, it will come to a similar conclusion.

2.3 Estimation of the Doppler Frequency

Proverbially speaking, acquisition process for a certain satellite i, once the code delay of C/A code is found, the Influence of $C_i(t)$ can be removed by multiplied with the $C_i'(t)$ duplicated locally which has the same stuct of $C_i(t)$, that is $C_i'(t) = C_i(t)$.

Taken the acquisition process for satellite 1 for example, by multiplied with $C_1(t)$, Eq. (9) can be expressed as:

$$\begin{aligned}
h(t) &= [C_1(t)\cos(2\pi f_1 t) + C_2(t)\cos(2\pi f_2 t) + u(t)] \times C_1(t) \\
&= \cos(2\pi f_1 t) + C_1(t)C_2(t)\cos(2\pi f_2 t) + u(t)C_1(t)
\end{aligned} \tag{14}$$

If the effect of noise is not too strong, the frequency component f_1 in Eq. (14) can be found from either FFT or DFT. This method appears excellent and attractive, but unfortunately the GPS signal consists of the superposition of all GPS

signals in view of the antenna, and is processed by parallel channels in the receiver, then the real RF signal of GPS is mixed-frequency signal which contains several satellites' frequency components with almost the same power. So the effect of frequency component f_2 cannot be ignored. So frequency domain analysis cannot distinguish f_1 from $h(t)$ in Eq. (14). Therefore, delay and accumulation unit is put forward to accomplish the frequency components separation and selectable estimation.

The output signal after pretreatment of delay and accumulation unit can be written as follows:

$$\begin{aligned} h'(t) &= h(t) + h(t-\tau) \\ &= \cos(2\pi f_1 t) + C_1(t)C_2(t)\cos(2\pi f_2 t) + \cos(2\pi f_1 t)\cos(2\pi f_1 t) \\ &\quad + \sin(2\pi f_1 t)\sin(2\pi f_1 t) + C_1(t-\tau)C_2(t-\tau)\cos(2\pi f_2 t)\cos(2\pi f_2 \tau) \\ &\quad + C_1(t-\tau)C_2(t-\tau)\sin(2\pi f_2 t)\sin(2\pi f_2 \tau) + \xi(t) \end{aligned} \tag{15}$$

In the above equation, the noise signals in $h'(t)$ is $\xi(t)$, and $\xi(t) = C_1(t)n(t) + C_1(t-\tau)n(t-\tau)$. Similar to Eq. (12), if the sample delay τ will be carefully chosen, $|\cos(2\pi f_i \tau)|$ $(i = 0, 1, 2)$ is close to unity, that is

$$|\cos(2\pi f_i \tau)| \approx 1, |\sin(2\pi f_i \tau)| \approx 0, i = 1, 2 \tag{16}$$

Inserting Eq. (16) into Eq. (15) yields

$$h(t)' = 2\cos(2\pi f_1 t) + c_1(t)c_2(t)\cos(2\pi f_2 t) + c_1(t-\tau)c_2(t-\tau)\cos(2\pi f_2 t) + \xi(t) \tag{17}$$

As dissertated before, $C_1(t)C_2(t)$ is belongs to the same family as the Gold code which is also evaluated by ± 1 compared Eq. (17) with Eq. (14), it is apparently that the frequency component f_1 is selectable enhanced and f_2 is weakened. Now the frequency component $f_1$can be easily identified through FFT analysis.

Thus, the whole fast acquisition process of mixed-frequency GPS signals is completed.

2.4 Performance Analysis

Commonly speaking, we consider calculation burden is depend on the times of FFT and IFFT. So the performance comparison of common FFT fast acquisition based on two-dimensional searching process and the presented acquisition one-dimensional searching process is mentioned in theory.

Approximately, assuming the maximum Doppler velocity result from the movement of orbit is 0.9 km/s, and the vehicle move toward the earth is about 1 km/s. Thus the maximum Doppler shift is [4].

Table 1 Contrast of two acquisition schemes

	Operation times FFT	Doppler accuracy IFFT	Doppler accuracy (Hz)
Common FFT fast acquisition	704	672	500
Proposed acquisition	38	37	<100

$$f_{d\max} = \frac{f_l \upsilon_{r\max}}{c} = \frac{1575.42\,\text{MHz} \times (1000 + 900)\,\text{m/s}}{3 \times 10^8\, m/s} \approx 10\,\text{kHz} \tag{18}$$

The Doppler frequency searching range is $f_0 \pm 10\,\text{KHz}$, the step length of searching process is selected as 500 Hz and C/A code frequency is 1.023 MHz. Taken the real GPS signal supplied by [6] which contains five satellites as acquisition source and based on these hypotheses, the calculation times when utilizing those three acquisition methods are contrastively noted in Table 1 [5].

3 Simulation and Result

Using the real Intermediate Frequency GPS signal as acquisition source, which is collected using Zarlink GP2015 RF IC and Cypress FX2 USB interface board, with the intermediate frequency of 1.405 MHz and the sampling frequency of 5.7142 MHz, the acquisition time of common FFT fast acquisition is 143.6 s and the acquisition result is suggested in Table 2, meanwhile the acquisition time of proposed acquisition scheme is 6.4 s and the acquisition result is suggested in Fig. 2.

The acquisition result of proposed acquisition scheme is suggested in Figs. 4 and 5.

Table 2 and Figs. 2, 3, 4, 5 show the similar acquisition results of common FFT fast acqusition and the proposed acquisition scheme, and indicate the validity of proposed acquisition scheme in code delay estimating process.

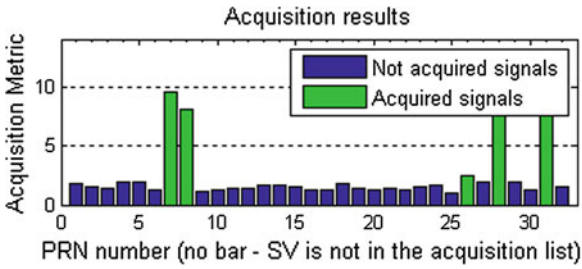

Fig. 2 Acquisition result of proposed acquisition scheme

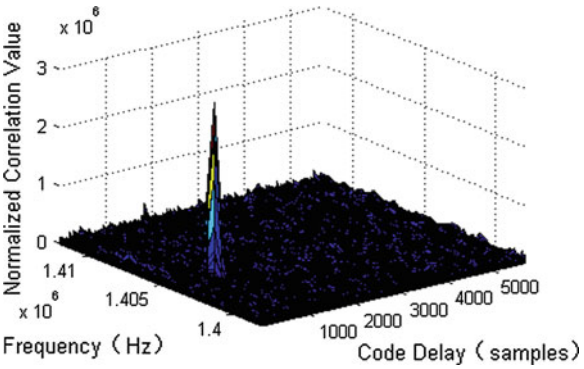

Fig. 3 Acquisition result of satellite 7, step size = 500 Hz

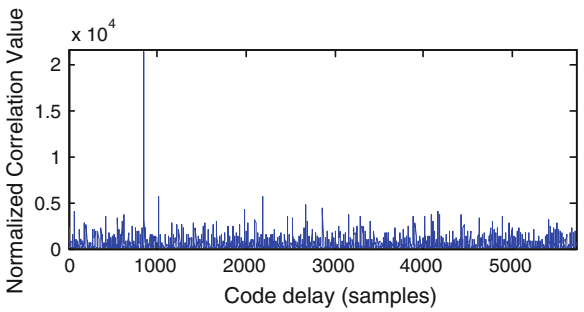

Fig. 4 Estimation the code delay of satellite 7

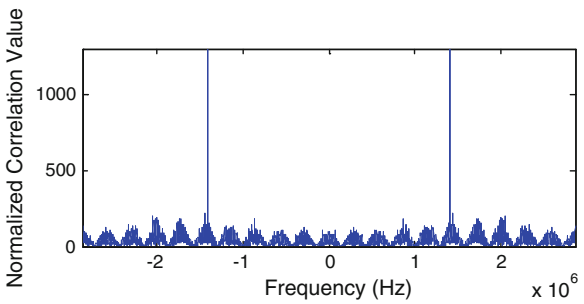

Fig. 5 Estimation the frequency of satellite 7

Table 2 Acquisition result of common FFT fast acquisition

Channel	PRN	Frequency	Doppler	Code Delay	PRN
1	31	1.40542e+006	421	484	31
2	28	1.40516e+006	160	5670	28
3	7	1.40395e+006	−1050	854	7
4	8	1.40665e+006	1653	495	8
5	26	1.40516e+006	160	1209	26

4 Conclusions

A novel acquisition scheme based on two stand-alone one-dimensional search processes for a GPS software receiver has been described. Simulation results show that the performance of proposed acquisition scheme is similar with the common FFT fast acqusition, but the acquisition speed is much faster than that of the common FFT fast acqusition.

References

1. Kaplan ED (ed) (1996) Understanding GPS: principles and applications (book style). Artech House, Boston, pp 111–124
2. Bo Z, Gerard L (2004) Acquisition schemes for a GPS L5 software receiver. In: Proceedings of ION GNSS 2004 (Session A3), Long Beach, CA, 21–24 Sept
3. Martin N, Leblond V, Guillotel G (2003) BOC (x,y) signal acquisition techniques and performances. In: Proceedings of ION GPS 2003, Portland, OR, USA Sep 2003
4. Bao J, Yen T (2000) Fundamentals of global positioning system receivers: a software approach. Wiley Interscience Publication, New York, pp 146–155
5. Gong G-H, Li S-K (2005) GPS signal C/A code phase measurement using FFT and circular convolution. J Commun 26:77–79 (in Chinese)
6. Yong Z, Lin B-J, Xu Z-H (2006) Study on simulation of signal search and acquisition in software GPS receiver. J Syst Simul 18:2647–2648 (in Chinese)
7. Tsui JBY (2000) Fundamentals of global positioning system receivers: a software approach. Wiley, New York, pp 115–120, 146–148
8. Hegarty C, Tran M, Van Dierendonck AJ (2003) Acquisition algorithms for the GPS l5 signal. In: Proceedings of ION GPS/GNSS, Sept 2003, Portland, OR, pp 165–177

In-hand Manipulation Action Gist Extraction from a Data-Glove

Gang Cheng, Norman Hendrich and Jianwei Zhang

Abstract The process of different human manipulating a specific object in hand obeys very similar operating steps. The hand movement can be modeled and generalized into action gist to guide other human or robots to execute the specific in-hand manipulation task. This paper suggests a kind of action gist similar to the way humans learn to represent the five finger hand motions in in-hand manipulation. Our method is based on Gaussian Markov Random Field that processes data-glove values to obtain the action gist. Several experiments are carried out to discuss the performance of the proposed methods.

1 Introduction

The word *gist* means the essential part of an idea or experience. Different from *hand gesture*, the *in-hand manipulation action gist* is a concept with kinetic property. It represents the key hand motions in any given manipulation task and widely adapts to different hands. The manipulation process is generalized as several compact meta motions. On the one hand, this makes it easy to remember, on the other hand it can be translated from one entity to another, just as the knowledge passing from the teacher to the student.

As we know, in the mechanism of the human hand, the motions and forces are governed by the neuromuscluar apparatus, refer to [15]. The movement of the hand is continuous, but according to human cognition, it can be classified as infinite

G. Cheng (✉) · N. Hendrich · J. Zhang
Department of Informatics, Group TAMS, University of Hamburg,
22527 Hamburg, Germany
e-mail: cheng@informatik.uni-hamburg.de

N. Hendrich
e-mail: hendrich@informatik.uni-hamburg.de

J. Zhang
e-mail: zhang@informatik.uni-hamburg.de

F. Sun et al. (eds.), *Foundations and Practical Applications of Cognitive Systems and Information Processing*, Advances in Intelligent Systems and Computing 215,
DOI: 10.1007/978-3-642-37835-5_67,

types of motions in the brain. For example, as the muscles tightening up and relaxing, or the fingers closing and opening. Then in the specific application, the possible solution sequence is recalled and executed. The object in question is touched and released by the hand components over time. When the touching motion is executed, an interacting force is generated between the object and the hand, and the neuromuscluar system keeps the hand in a proper *force applying state* that does not damage the hand itself but still holds the object firmly.

In our lab we have a five-finger air muscle hand from the Shadow Robot Company,[1] it is very similar to the human hand and better protected against damage even when overforce is applied. With a humanoid hand, a robot can implement much more human-like object manipulation than before. Because of the high degree-of-freedom, a multi-finger robot hand can perform more dexterous skills rather than grasping, holding or translating the object from one place to another. It can rotate, or shift objects and perform other advanced in-hand movements. These manipulation skills depend on the cooperation of five fingers and the palm, and in the process of in-hand manipulation, the roles are hand and object. The hand plays the role of control, and changing the object state is the aim of the manipulation. Therefore here the manipulation process is considered as a *State-Action Model* [4, 6, 8], meaning that the whole process is divided into states which are changed through actions. The action is equal to hand movement, and the state is supposed to be the criterion of how the process proceeds. Hand movement can be considered as a continuous hand joint angle variation, with countless angle combinations between each joint pair. The movement leads the manipulation process from one state to another state until the final target of the application is achieved.

The method can be applied in both human analysis and the control of robots with humanoid hands. However, it is unrealistic to map the motion exactly as from the demonstrator because of the different hand sizes. It can be imagined different-sized hands can interact with the object from different distances, obviously it can result in different gaps with a same pose. Actually in developing their hand skills, humans have the ability to learn from others and to practice by themselves. Nobody can memorize the detailed joint angles of their hands, but they can remember the key motions which are related to the moving tendency of each finger. We consider this kind of motions as in-hand manipulation action gist.

This paper proposes a cognitively feasible in-hand manipulation action gist definition for a robot with an extremely life-like humanoid hand, to enable it to learn in-hand manipulation with a small amount of key information. The action gist is expected to be universal for all in-hand movements regardless of whether it is simple (grasping) or complex (finger-gaiting). The structure of this paper is organized into several sections. After the following related work, the definition of meta motion is given, which is an element of the in-hand manipulation action gist. Then the modeling process is introduced, and experiments are carried out to discuss the performance of the algorithms. The final part is the conclusion and future work.

[1] http://www.shadowrobot.com/

2 Related Work

There are multiple ways to generate a manipulation model.

One kind of model is to plan the motion in continuous space including the position and the speed of each relative component. The major stream is the dynamic movement primitive (DMP) framework introduced by Ijspeert et al. [3] and Schaal [12], in which the movement is recorded and represented with a set of differential equations. The position and the speed is controlled in terms of the immediate position and speed feedback. Pastor et al. [9] expanded the model into a manipulation control application so that the hand can grasp and place the object in the destined area. To include obstacle avoidance in this job, an extra item is added in the system equation, which causes the form of the framework to change with the task. Different from the separate models to deal with multiple tasks, [1] applied Locally Weighted Regression to generate the movement, and the manipulating process is divided into several steps by the perceptual input. Rather than generalizing a trajectory in Cartesian or joint angle space, [2] considered the joint velocity space and enables the robot to accomplish similar tasks. As a result, this method can produce smoother trajectories than others.

The above frameworks consist of models depending on precise perception of spatial manipulator trajectories. However, for muscle control, it tracks the trajectory related to the moving tendency, not the position. Therefore, DMP does not offer any significant advantages to the target of this paper.

Another branch but a relatively older one is the generalized motor program (GMP), see [13, 14] here the overall process is guided by invariant features. Park et al. [7] extended this model with the symbolic motion structure representation (SMSR) algorithm. The body movement is tracked and segmented according to the joint angles, and then the values are used to plan a novel similar application. However, the SMSR only extracts the body motion into simple joint angle variations such as increasing, decreasing and stationary. Therefore, it would have difficulties when dealing with the multiple links cooperation application because it does not consider this kind of application so much. Different from simply defining the motion, it is possible to have a related higher semantic model. Qu and Nussbaum [10] applied Fuzzy-Logic Control to execute the motion sequence, and this idea was examined in a 2D five-segment body model by simulation. The above methods suppose that the motion sequence to an application is fixed, but actually humans can have many ways of completing a specific application. What we need are the most effective or common methods of the teacher.

Mah and Mussa-Ivaldi [5] indicated that humans learn motion by way of muscle control, not the position perception, therefore to know the posture variation (joint angle) is more important than the absolute posture. Thus the motion tendency oriented model is more feasible than DMP.

Once the model is decided on, the next problem is how to sense the movement. Many studies concentrate on sensing from the robot, for example, [1],[9] or [2]. However, for fingers, it is not convenient to directly move the robotic fingers to

find the result. Another channel is vision, the components are tracked to complete the motion behavior model. For example, Klien [11] employed color pattern on the demonstrator to track the human motion. It is promising to use vision to analyze hand motion, but the visual processing itself is a challenging topic which increases the difficulty of model generation.

A quick way to know the finger movement is using a data-glove, it can sense every finger joint relation in each data frame. Based on this kind of sensing channel, our study intends to generate an action gist model to represent human in-hand manipulation behavior.

3 Meta Motion Definition

To establish a set of hand motions which presents the hand posture transformation in in-hand manipulation, we intend to construct the model as follows.

1. It covers all possible movements of a hand
2. Each motion in the set is unambiguous from other motions
3. The motion involves the relative joint angle variation but no absolute position information.

An exception to the above is the idle pose. When the motion remains static for a while, we have to decide whether it is "move, stop and move again", or consider it as moving continuously. Our strategy is to analyze the movement without static motions first, and in the second loop to find the static section following certain rules.

Supposed that the hand has the form of five fingers and one palm, the palm stays still, then the movement is equal to the cooperation of the five fingers. The basic movement of each finger can be classified as open or close, and in terms of the moving direction at the *proximal phalange end* related to the palm, every finger has the same motion definition. Specifically, the coordinate origin of the thumb is different from the other four fingers because of its diverse position on the palm.

Shown in Fig. 1, we project the finger motion into two-dimensional space because the finger ends are fixed on the palm. In the X–Y plane, the finger direction is classified as four directions as the four quadrants in the Cartesian coordinate; plus with the open, close and the idle period, each finger has nine types of meta motions. To ensure the motion model a uniform form, the X axis and the Y axis in the moving direction related to the coordinate origin is either parallel or vertical to the palm plane.

4 Action Gist from Data-Glove

Here the action gist is defined as the key meta motions between two adjacent states. Guided by the action gist, the object is manipulated from the begin state to the end state.

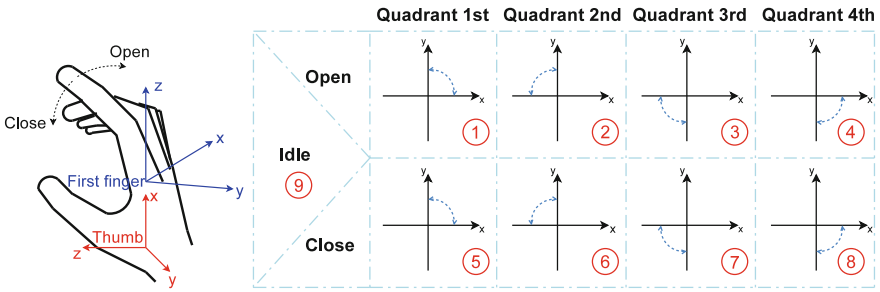

Fig. 1 Meta motion definition. Five fingers move related to the palm, so we describe their moving directions in coordinates. The thumb in the *red* coordinate is different from the other four fingers due to its special location in the hand. In each finger, two flex/ext-joints are modeled as one parameter as open or close, and the abduction angle cooperates with the metacarpal-proximal angle to form a 2D projected direction (*blue arc* indicates the directional range in the quadrant). The idle motion is specifically set apart and labeled as 9

The data-glove is a direct way to perceive the hand movement, as the data is measured by the joint angle value. Therefore, the values from the data-glove become the source for analyzing the hand movement in in-hand manipulation applications.

Corresponding to the degree of freedom, each finger has several joint values from the data-glove. However, according to the general law, the distal-intermediate and proximal-intermediate angles increase in close movement, decrease in open movement, and the varieties of metacarpal-proximal and abductional angles indicate the moving direction in the *X*–*Y* plane of the finger.

Different from the ideal environment, the acquired data-glove value can not be directly applied in the analysis. One reason for this is for the sensor noise, another one is the issue from the human operator, e.g. a hand tremor in slight operation, a short but unnecessary movement during manipulation, or at the moment the finger starts to touch the object, the value may be abnormal. Therefore a Gaussian Markov Random Field based algorithm is proposed to extract the action gist of each finger, it can effectively decrease the negative impact from the mentioned issues and provide a concise meta motion sequence. This algorithm considers each value frame from the data-glove as a node, every node can influence the other nodes on which meta motion they belong to, the nearer nodes have the stronger impacts, the criteria are based on the single meta motion similarity and the node distance, the node relationship according to the assumption is illustrated in Fig. 2.

The single meta motion similarity of each node can be presented as:

$$I_i^j = \begin{cases} \sum_{k \in \mathbf{F_g}} \left| v_i^k \right| + \varepsilon, & C_{k \in \mathbf{F_g}}^j (v_i^k) = 1 \\ 0 \qquad\qquad\quad , & \text{else} \end{cases} \tag{1}$$

Here I_i^j is the intensity of node i that is similar to meta motion j, v_i^k is the kth glove value difference (current value minus previous value) in node i. The kth value from the data-glove sensor should belong to one finger $\mathbf{F_g}$, $\varepsilon > 0$ promises the value of

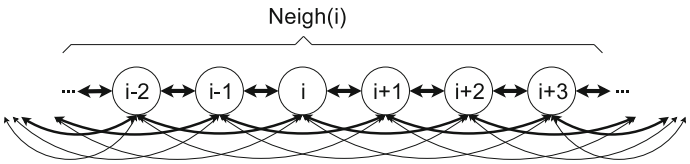

Fig. 2 Node relationship according to Gaussian MRF. Supposing each data-glove value is a node, then each node is related to other nodes in the neighboring set Neigh$(\cdot)$. With the impact factor obeying Gaussian distribution, the linewidth indicating the strength of the impact factor, we can see that the nodes sitting closer have stronger influence

intensity is always above 0. This value is not critical but should be a low value, we suggest to fix $\varepsilon = 0.05$ as experience.

Additionally, $C(\mathbf{v})$ is the conditions that the finger joint angle difference stay in the range of the corresponding meta motion j. Assuming that there are always four values $v_1, v_2, v_3, v_4 \in \mathbf{v}$ standing for the joint angle variation in five fingers, they are mapped correctly with v_i^k. Commonly, v_1 is for distal-intermediate, v_2 is for proximal-intermediate, v_3 indicates abduction and v_4 is for the metacarpal-proximal angle difference. Specifically, for the thumb values in the data-glove, in order to have a uniform expression, the rotation angle is considered as v_3. Besides, the abduction value v_4 should be adjusted as an identical increasing direction according to the meta motion definition, then the conditions $C(\mathbf{v})$ are listed in the right table of Fig. 3. v_1 has a less important effect here because when the object is manipulated, it is easy for the finger tips touching the object are easily to create a contra direction with v_2, but v_2 is related stably. Whether the finger is open or close mainly depends on the movement between the proximal and intermediate joints. In the table, "$\times$" means v_1 can be any value in this condition.

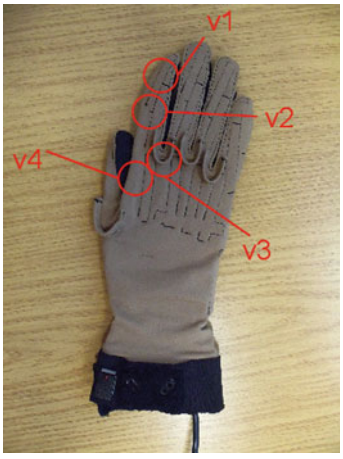

metamotion	v_1	v_2	v_3	v_4
1	$\times$	< 0 $= 0$	$\geqslant 0$	$\geqslant 0$
2	$\times$	< 0 $= 0$	$\leqslant 0$	$\geqslant 0$
3	$\times$	< 0 $= 0$	$\leqslant 0$	$\leqslant 0$
4	$\times$	< 0 $= 0$	$\geqslant 0$	$\leqslant 0$
5	$\times$	> 0 $= 0$	$\geqslant 0$	$\geqslant 0$
6	$\times$	> 0 $= 0$	$\leqslant 0$	$\geqslant 0$
7	$\times$	> 0 $= 0$	$\leqslant 0$	$\leqslant 0$
8	$\times$	> 0 $= 0$	$\geqslant 0$	$\leqslant 0$

Fig. 3 An example of the finger joint angle difference in the first finger. v_1 is for distal-intermediate, v_2 is for proximal-intermediate, v_3 indicates abduction between first finger and middle finger, v_4 is for metacarpal-proximal

For the data-glove, we have to mention that the abduction angle is not the absolute angle related to the palm. That means v_3 is not working perfectly, but in this study we do not consider it as a critical problem.

When the single similarities of all nodes are calculated, the influence from other nodes can be obtained by:

$$P_i^j = \sum_{t \in \mathbf{Neigh(i)}} I_t^j G(t, i, \sigma) \tag{2}$$

where $G(t, i, \sigma) = \frac{1}{\sigma\sqrt{2\pi}} e^{-\frac{(t-i)^2}{2\sigma^2}}$ is the typical Gaussian distribution form, $\mathbf{Neigh}(i)$ is the node set near node i (refer to Fig. 2). Because the concerned action gist locates between each adjacent state pair, it is actually set as the entire glove value sequence. Besides σ is a parameter representing the area one node can primarily impact with, it also means the shortest single motion execution time corresponding to the data-glove sensing speed. Then the likelihood of meta motion j at each node can be compared to find the best meta motion segmentation.

In addition to the action gist analysis, the idle motion is processed independently from the eight kinetic motions mentioned above. The Gaussian MRF based method can also be employed here, but according to the experimental experience, to find a frequent value as high as desired in the sliding window is a better solution. To realize this method, the first step is also to have the single similarities of each node to be similar to Eq. 1, but the intensity of meta motion 9 at node i becomes as $I_i^9 = 1$ and the condition becomes $C(\mathbf{v}) = \mathbf{1} \iff \mathbf{v} = \mathbf{0}$. Thus the idle sections can be determined by the following condition:

$$\sum_{t \in \mathbf{N}eigh(i)} I_t^9 > \text{threshold} \tag{3}$$

Thus node i stays idle when the sum of single intensities is larger than *threshold*. Here $\mathbf{N}eigh(i)$ is set to be at the range of d_{sw}, which is the size of the sliding window, then d_{sw} nodes are taken into consideration to find the idle section. In addition, all adjacent idle nodes are merged as an idle section, but if the length of idle sections is shorter than a single motion execution time σ, this section should be considered as not idle. Commonly, we find that threshold $= 0.90$ and $d_{\text{sw}} = 20$ fit most cases.

Using the proposed process, the action gist can be extracted from the raw data-glove values.

5 Experiment

Different kinds of objects are used to examine the proposed method, the hand movement involves from *clearly moving without object* to *complex finger gaiting*. The corresponding action gists are extracted from the glove values automatically, and they all agree with our expectation. In order to make a intuitive view, here we

Fig. 4 Unscrewing different-sized bottle screw caps. The thumb, first, middle and ring finger participate in this scenario. Each screw cap is rotated as around 90° anticlockwisely, and this process is defined as a trial

just take *bottle screw cap unscrewing* as an example. There are four different-sized bottle screw caps as Fig. 4, a participant rotates the caps by four fingers for many times. After several trials we list several typical results through the proposed method as in Fig. 5.

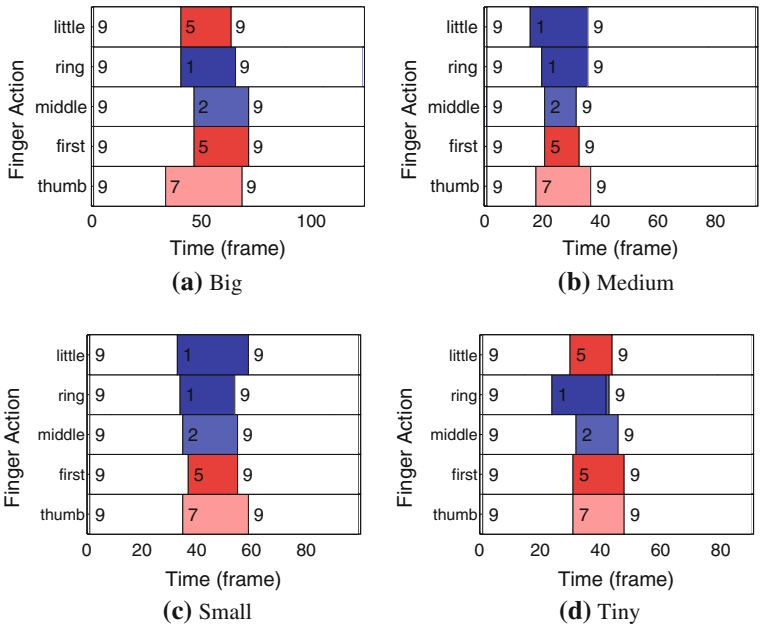

Fig. 5 Action gists of bottle screw cap unscrewing. Each action gist is composed of the meta motions of five fingers, each meta motion is represented by different color rectangles with the corresponding type number. The *x*-axis is a time axis indicating the cyber-glove frame number. Taking idle motion into consideration, we find that the action gists from four trials look similar. The common meta motions are motion *7* in the thumb, *5* in the first finger, *2* in the middle finger, and *1* in the ring finger. **a** Big, **b** medium, **c** small, **d** tiny

There are countless ways to move the fingers to reconfigure the object achieving to the goal state, but for the transfer to a robotic hand one solution is enough to guide the manipulation. Furthermore, by the result of bottle screw cap unscrewing we can see for different-sized caps unscrewing it does exist similar action gists. Therefore, we can demonstrate the scenario-specific finger-gaiting movement many times and find the popular action gist. In this case, the common one has stronger adaptability for the robotic hand, which is in different size from human hand, to complete the task.

Among the parameters in the algorithm, σ is the only one depending on the application. As we mentioned in the previous section, this parameter is relevant to movement speed and data-glove framerate. Higher σ merges more short terms, but meanwhile we risk losing critical short meta motions. On this point the value selection should be considered carefully. We enumerate all possible values and compare the extraction results for several typical applications, finally we find that the configuration of σ is not so strict. For most cases the extraction results are same, otherwise the length of meta motion changes slowly with σ variation. Thus it is not necessary to check every possible value (e.g. from 1 to 20 for 20 trials), instead, we can set $\sigma = 5$ to acquire the details, and then set $\sigma = 10$, 20 or even more to get the general context.

6 Conclusion and Future Work

This study concentrates on action gist extraction from the demonstration of in-hand manipulation. Different from the manipulator trajectory planning, this model works in a fuzzy way to guide the finger movement. It gives the manipulator a related loosely explored space to implement the task, and from the view of human in-hand manipulation, it is more similar to the mechanism of the human hand.

This action gist model is being examined by simulation and real robot tests. When the action gist is mapped back to robotic hand control, it is supposed to work as guidelines because it provides the meta motions of each finger in order. Different-sized hands apply different joint angles to execute the manipulation, but the meta motion is always correct to indicate the finger movement direction. In every trial we give the robot quantized parameters according to a fixed meta motion sequence, and through iterations the parameters are refined to ensure the correct state transition.

The model currently is built from the value of a data-glove. One disadvantage is that the human demonstrator wearing the data-glove has a different feeling and executes the movement unnaturally, and difficult manipulation applications are hardly handled. Another drawback is related to the four abduction angles in the data-glove, which are angles between two fingers, not the absolute angle related to the palm. From this point, we do not guarantee that the finger movement perception is always correct. Hence to fuse the result from other sensors, especially tactile sensing, is another direction for developing the model further.

Acknowledgments This work is partially supported by the European FP7 project HANDLE ICT-236410. Gang Cheng acknowledges financial support by Chinese Scholarship Council.

References

1. Gams A, Ude A (2009) Generalization of example movements with dynamic systems. In: IEEE-RAS international conference on humanoid robots, pp 28–33
2. Gielniak M, Liu C, Thomaz A (2010) Stylized motion generalization through adaptation of velocity profiles. In: IEEE international symposium on robots and human interactive communications, pp 304–309
3. Ijspeert AJ, Nakanishi J, Schaal S (2002) Movement imitation with nonlinear dynamical systems in humanoid robots. In: IEEE international conference on robotics and automation, pp 1398–1403
4. Kjellström H, Romero J, Kragic D (2011) Visual object-action recognition: inferring object affordances from human demonstration. Comput Vis Image Underst 115(1):81–90
5. Mah CD, Mussa-Ivaldi FA (2003) Generalization of object manipulation skills learned without limb motion. J Neurosci 23(12):4821–4825
6. Ogawara K, Takamatsu J, Kimura H, Ikeuchi K (2002) Modeling manipulation interactions by hidden markov models. In: Proceedings of IEEE/RSJ international conference on intelligent robots and systems, vol 2, pp 1096–1101
7. Park W, Chaffin DB, Martin BJ, Faraway JJ (2005) A computer algorithm for representing spatial-temporal structure of human motion and a motion generalization method. J Biomech 38(11):2321–2329
8. Pastor P, Kalakrishnan M, Chitta S, Theodorou E, Schaal S (2011) Skill learning and task outcome prediction for manipulation. In: Proceedings of IEEE international conference on robotics and automation, pp 3828–3834
9. Pastor P, Hoffmann H, Asfour T, Schaal S (2009) Learning and generalization of motor skills by learning from demonstration. In: Proceedings of IEEE international conference on robotics and automation, pp 1293–1298
10. Qu X, Nussbaum M (2009) Simulating human lifting motions using fuzzy-logic control. IEEE Trans Syst Man Cybern Part A Syst Hum 39(1):109–118
11. Riley M, Cheng G (2011) Extracting and generalizing primitive actions from sparse demonstration. In: IEEE-RAS international conference on humanoid robots, pp 630–635
12. Schaal S, Ijspeert A, Billard A (2003) Computational approaches to motor learning by imitation. Philos Trans R Soc B Biol Sci 358(1431):537–547
13. Schmidt R, Lee T (1999) Motor control and learning: a behavioral emphasis. Human Kinetics, Champaign
14. Schmidt RA (1975) A schema theory of discrete motor skill learning. Psychol Rev 82(4):225–260
15. Taylor CL, Schwarz RJ (1955) The anatomy and mechanics of the human hand. Artif limbs 2(2):22–35

Development of an Intelligent Omnivision Surveillance System

Hannes Bistry and Jianwei Zhang

Abstract This publication describes an innovative intelligent omnivision video system, that stitches the images of four cameras together, resulting in one seamless image. This way the system generates a 360° view of the scene. An additional automatically controlled pan-tilt-zoom-camera provides a high resolution view of user defined regions of interest (ROI). In addition to the fusion of multiple camera images, the system has intelligent features like object detection and region-of-interest detection. The software architecture features configurable pipelines of image processing functions. All different steps in the pipeline like decoding, feature extraction, encoding, and visualization are implemented as modules inside this pipeline. It is easily possible to rearrange the pipeline and add new functions to the overall system. The pan-tilt-zoom camera is controlled by an embedded system that has been developed for this system. GPU-accelerated processing elements allows real-time panorama stitching. We show the application of our system in the field of maritime surveillance, but the system can also be used for robots.

1 Introduction

For many applications, a wide view of the scene yields significant advantages. In the field of surveillance, wide angle and omnidirectional camera systems can provide all significant information in one video stream. Having one video stream is much easier to supervise for the staff than having multiple streams.

H. Bistry (✉) · J. Zhang
Department of Informatics, University of Hamburg, Vogt-Koelln-Strae 30,
22527 Hamburg, Germany
e-mail: bistry@informatik.uni-hamburg.de
URL: http://www.informatik.uni-hamburg.de

J. Zhang
e-mail: zhang@informatik.uni-hamburg.de

F. Sun et al. (eds.), *Foundations and Practical Applications of Cognitive Systems and Information Processing*, Advances in Intelligent Systems and Computing 215,
DOI: 10.1007/978-3-642-37835-5_68,

The challenge of the research work was to set up a surveillance system for use on a ship. The system has to be installed on a pole on board of the ship and shall provide an omnidirectional view of the scene. The image of a pan-tilt-zoom-camera shall be overlaid onto the video stream in order to display image details of a region of interest. In addition to that, intelligent feature detection algorithms will be implemented into the system.

In our previous research work we focused on intelligent cameras for robot systems [1, 2] and surveillance [3]. Due to the underlying architecture that we developed, it is easy to set up image processing systems and reuse functions that have already been implemented [4].

The remainder of this paper is organized as follows: In Sect. 2 we introduce approaches of related research projects. Section 3 gives an overview of the developed system, the hardware setup, and the software architecture. In Sect. 4 we introduce the special features of the system and show experimental results. A conclusion on the achievements and an outlook to future research is given in Sect. 5.

2 Related Research

There are different approaches of generating wide angle images using digital cameras. One possibility, that is also applied in the system described in this paper, is to use multiple cameras and to stitch the images together into a panoramic image. The FlyCam is a ring of five inexpensive colour cameras [5]. Each of the images is transformed and the tiles are combined to a panoramic image. At the borders of the image, a cross fading algorithm is applied. In this research project, the resolution of the cameras has to be reduced due to the computational load.

Another method of generating panoramic images is the use of hyperboloidal mirrors [6]. One camera is placed below the mirror. It is possible to create a seamless panoramic image by back-transformation, but the resolution is quite limited.

A surveillance system based on a fish-eye lens is described in [7]. The system features DSP-based processing and an advanced background subtraction algorithm.

Many research projects focus on adding intelligent functions to surveillance systems. In [8] a surveillance system that features real-time detection and tracking of multiple people is introduced. The authors showed their approach of classifying the activities of the people. Objects that are carried and placed by the people can also be detected. In the evaluation, the system achieved real-time performance on a regular PC. People tracking is also a well-known topic in the field of robotics [9–11].

There are also research projects on the system architecture of image processing systems. One example—not directly related to surveillance—is shown in [12]. A framework is presented where image processing tasks can be configured in a graphical editor and can be carried out on distributed systems. During runtime, the execution time of the steps is monitored, and considered in the distribution of tasks. As an application, a setup for depth reconstruction using a stereo camera system is presented.

In [13] a system is introduced, where multiple image processing tasks are carried out on the data stream from a camera (face detection, object detection, background subtraction, compression). Using classical scheduling, not all tasks can be carried out in time. The authors propose an approach, where the different tasks are classified according to the maximum acceptable latency. During test runs, the execution time is measured and the system tries to find a scheduling strategy that meets the requirement of all tasks.

3 System Setup

This chapter describes the system setup in terms of hardware and software.

3.1 Description of Hardware

The setup of the system is shown and explained in Fig. 1. The 360 ° image is captured by four IP-cameras (Sanyo HD2100P). Each of these cameras covers a $> 90°$ field of the scene.

As all cameras provide compressed video streams, there are no bandwidth issues, as the Gigabit uplink to the PC can easily handle five video streams and control data.

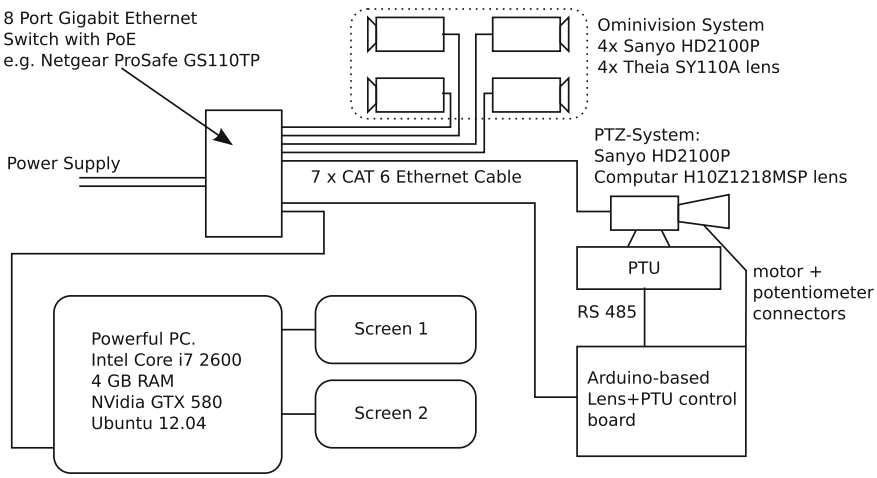

Fig. 1 Hardware setup of the intelligent omnivision system. The five cameras, the embedded system for PTZ control and the control PC are connected to a Power-Over-Ethernet-Switch. This way only (neglecting power supply) one network cable needs to be installed between the control PC and the rest of the hardware. The link between the embedded system and the pan-tilt-unit is a serial RS485 connection. The zoom-lens provides connections to the zoom/focus motors and potentiometers; these are also connected to the embedded system

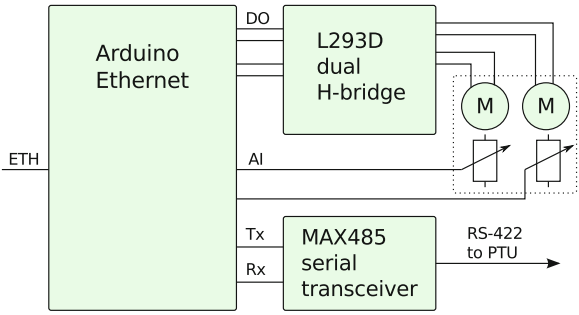

Fig. 2 The structure of the embedded system for PTZ control. In the figure the power supply of the different components is omitted for better clarity. (*ETH* ethernet, *DO* digital output, *AI* analog input, *Rx* serial receive, *Tx* serial transmit)

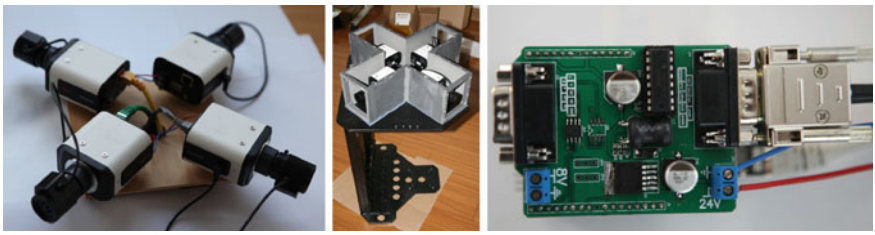

Fig. 3 A test setup of the four cameras (*left*), the housing (*middle*, designed by Kunshan Robotechn Intelligent Technology Co.), and the embedded system for PTZ control (*right*, circuit developed by Johannes Liebrecht, board layout by Kunshan Robotechn Intelligent Technology Co.)

Due to certain image quality and zoom range requirements, it was necessary to use a FullHD IP camera and a zoom lens. For this combination there is no ready-to-use solution for zoom and focus control. An embedded system has been designed to control the zoom lens as well as the movement of the pan-tilt-unit. There are few zoom lenses for the C-mount standard featuring motorized zoom and focus control. One of them is the Computar H10Z1218MSP, which features a focal range of 12–120 mm, motor-driven zoom and focus, and potentiometers to measure the current zoom and focus setting. This way it becomes possible to implement a system that approaches a desired setting automatically.

The embedded system is based on an Arduino Ethernet microcontroller, extended by custom hardware. The motors are connected using an H-bridge circuit and the potentiometers are read out using the analog input ports of the microcontroller.

One additional feature of the embedded controller is the possibility to connect a PTU via an RS485/422-based serial interface. Therefore, it is not necessary to have a direct serial connection between the control PC and the PTU. The commands can be sent via Ethernet, so the cabling effort will be reduced. In order to support the RS485/422, an additional transceiver chip is integrated into the embedded system.

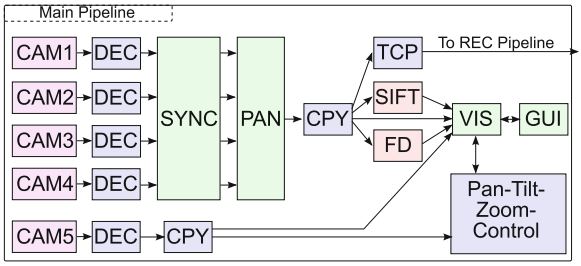

Fig. 4 Simplified pipeline setup of the intelligent surveillance system; the most important elements are shown with their connections, as shown in this figure. There are many more elements involved than those shown in this figure. As decoding is done by several elements, some elements need different colourspace and there are measures to ensure that the PTZ image is only decoded if it is activated in the GUI. Elements that are used in this setup: CAMx, access to the IP cameras; DEC, parsing of RTSP protocol, decoding of h264; SYNC, forward a group of 4 frames, drop otherwise; CPY, duplicate image to be used in multiple downstream elements; PAN, panorama generation, calculate one image from four images; TCP, send data via a TCP connection; VIS, overlay PTZ image, mark detected features; GUI, provide control widgets, control recording

On the control PC a virtual COM port is created. The PTU control software can access the PTU as if it was connected directly to the PC.

The structure of the embedded system is shown in Fig. 2. Images of the cameras, the housing, and the developed embedded system are shown in Fig. 3.

3.2 Software Setup

For the development of the intelligent omnivision camera system we are using a lot of modular processing functions developed for use in smart camera systems and service robots [4]. This is possible, since all software components are implemented as modules, that can be reused in different contexts. In the following, we describe the basics of our software system.

Our general idea is to provide module-based image processing functions that are connected to a pipeline. These pipelines can also be set up across network connections.

The software is written for Linux, but could also be transferred to other operating systems. Transfer and processing of image data will be done within the GStreamer [14] framework. This open-source multimedia framework is used by many multimedia applications under Linux. Many functions needed for this application are already implemented in GStreamer, like format conversion, image resizing, encoding, decoding, timing issues, and network data transmission. The GStreamer framework is plugin-based, so the functionality can be expanded by new elements, which can also define their own data types. There is also the possibility to set up branched pipelines where data of one image are processed by many elements in parallel.

4 Features of the System

In the following subsections we will introduce the main features of the system and their implementation.

4.1 GPU Accelerated Stitching of Panorama Image

In this processing step, the system needs to generate a panorama image from the four raw images acquired by the cameras. The information about the geometry of the camera setup and the types of lenses is included in a configuration file generated by the open source panorama stitching application Hugin.[1]

The performance of the CPU-based stitching was evaluated using the command line tool from Hugin with the defined configuration file. In the following table, the duration of the stitching procedure is shown.

System	Execution time (s)
Intel Core i5 750	0.90
Intel Xeon E31245	0.55
Intel Atom N270	11.47

With these tests it can be shown that a real-time capable solution using these algorithms is not possible. Even with more powerful CPUs it seems impossible to reach execution times in the magnitude of 0.05 s (for 20 fps). Therefore, we had to investigate an alternative solution for real-time panorama stitching. We implemented a GPU-based stitching algorithm that generates a lookup-table (LUT) at startup. The whole procedure works as follows:

- Offline Calibration (once)
  - take four Snapshots
  - manually/semi-automatically configure panorama stitching in Hugin, save configuration file
  - generate LUT with sub-pixel accuracy from configuration file using a script
- Online Initialization (once at startup)
  - allocate GPU memory (4 + 1 image buffers)
  - upload LUT

[1] Hugin—Panorama photo stitcher; hugin.sourceforge.net.

Fig. 5 This image shows the result of panorama stitching and has a resolution of 2556 × 470 pixel. The camera system is mounted on the pole of a ship. The image also shows a color correction algorithm that has not been implemented in the GPU-accelerated code yet. In some areas, the blending is not perfect. This could be improved by a better calibration of the lens distortion.

- Online Processing (each frame)
  - 4× upload YUV buffers
  - 4× colourspace conversion to RGB
  - panorama stitching, subpixel accuracy
  - download panorama

Executing all processing steps for each frame takes 7 ms on an NVidia GTX580 (11 ms on an NVidia GTS450) including upload and download. The algorithm is parallelized very efficiently, one output pixel can be computed by one of the shaders of the GPU (NVidia GTX580 has 512 shaders clocked at about 1.5 GHz). Theoretically, this GPU is capable of stitching together > 100 panoramas per second. Due to an OpenCL-based implementation, the code could also be used for devices of other vendors. A generated PTZ image is shown in Fig. 5.

4.2 Object Detection

In order to detect known objects in the image, we implemented an advanced algorithm for object detection. This can either be used to generate user notifications if a known object is detected, or to supervise whether one object of the scene has been moved. In several research projects, Scale Invariant Feature Transform (SIFT) has proven to be a powerful, but also computationally intensive algorithm [15–17]. The general idea of the SIFT algorithm is to find significant points in an image and describe them in a way so that the description is invariant to rotation, translation and scaling. Extracted features of images can be compared to features from a sample image in order to find corresponding points. If multiple corresponding points can be found, a transformation matrix can be calculated. We implemented a processing element that compares the detected features of the current image to the features of all image files in a folder. Detected objects can be displayed in the GUI.

4.3 Person Detection

Detecting persons is another important feature of an intelligent surveillance system. Unlike in the task of object detection, the targets are not known exactly, as the persons may be unknown. Therefore, a person detection element has been set up using Haar classifiers [18] that are implemented in the OpenCV framework [19]. Prior tests have shown that running the face detection algorithms with a reduced resolution is sufficient for a robust detection. This way we can save processing time and thus computing capacity for real-time critical tasks. Within this element we can load different training datasets, e.g. for faces, faces in profile view or upper bodies.

4.4 Scheduling

In order to achieve real-time stitching and display of the panoramic video, we need to take some measures in our image processing pipeline. Some algorithms like object- and face detection may not run in real-time. Thus, we have to drop frames, if processing of a previous frame is still in progress. After the processing has finished, the newest available frame will be processed. This way, it is ensured that the frame processing queue does not grow. The recording function is scheduled to allow frames queueing up to a certain point, in order to compensate for load variation of the system and to avoid frame drops.

4.5 Recording

As we are using the GStreamer-framework, it is easy to implement recording functions. Recording is implemented as a separate pipeline that runs detached from the main pipeline. This way, recording can be started and stopped independently. Several tests have been performed to find a good compromise between data rate and CPU load. It is possible to choose different codecs (e.g. h264, MJPEG, MPEG2, Theora, h263) and there is also the possibility to reduce resolution and frame rate. Trials showed that h264 yielded acceptable results with the following settings:

- recording resolution 1880 $\times$ 384
- 10 frames per second
- tuned to be less CPU-intensive
- bitrate 3000 kBit per second

Using these settings, it is possible to save one hour of video in 1.35 GByte. Considering the size of modern HDDs, this is quite moderate.

4.6 Autofocus

There are several options to control the functions of the PTZ camera. Besides the possibilities of controlling the focus with a slider in the GUI or choosing predefined values from a look-up table, an autofocus algorithm is implemented. Within this mode, the sharpness of the image is analyzed while the focus setting is changed. We take the difference between two neighboring pixels as a measurement for image sharpness. As a first step, the image is filtered with a Sobel operator and the absolute of the value will be determined. This way, points with high contrast will be detected in the image. In the next step we sum up all the pixel values of the filtered image and take the resulting integer as a measure. The higher this value, the sharper the image. During the procedure, the focus will move from the lowest setting to the highest setting. The received values are assigned to the focus settings. In the last step, the focus setting with the maximum value is chosen.

4.7 PTZ Image

One of the main features of the system is to provide close-up views of user defined regions-of-interest (ROI). These can be selected in the main software by dragging a rectangle in the main image or by double-clicking on a detected image feature. This way, the system will automatically try to calculate the setting for the PTU-unit and the zoom lens.

$$\text{pan} = \left(\frac{x_r + x_l}{2} - \frac{\text{width}}{2}\right) * \frac{\text{hfov}}{\text{width}}$$

In this equation width is the width of the panorama image, hfov is the horizontal field of view, in our case 360°, x_r and x_l are the right and left border of the ROI.

Analogous to this we can define

$$\text{tilt} = \left(\frac{y_d + y_u}{2} - \frac{\text{height}}{2}\right) * \frac{\text{hfov}}{\text{width}}$$

given that the aspect ratio of one pixel is 1 : 1, height is the height of the panorama image, x_u and y_d are the upper and lower borders of the ROI.

The desired horizontal field of view of the PTZ-camera is calculated as follows:

$$\text{PTZfov} = \begin{cases} \dfrac{x_r - x_l}{\text{width}} * \text{hfov} & \text{if } \dfrac{x_r - x_l}{y_d - y_u} \geq \dfrac{\text{PTZwidth}}{\text{PTZheight}} \\ \dfrac{y_d - y_u}{\text{height}} * \text{hfov} & \text{else} \end{cases}$$

where PTZwidth and PTZheight are width and height of the pan-tilt-zoom camera, the other variables are defined as in the prior equations. As the aspect ratio of the user-drawn rectangle will probably differ from the aspect ratio of the PTZ-camera,

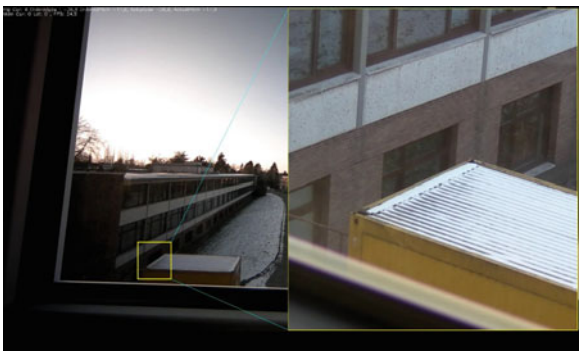

Fig. 6 The PTZ-overlay function is shown. The ROI is choosen by the user. After the PTU, zoom and focus have been adjusted, the image is overlayed

we need to distinguish between two cases. This way the desired horizontal field of view is calculated in a way that it always covers the full user-drawn rectangle.

Having the desired horizontal field of view, it is possible to calculate the corresponding focal length as follows:

$$f = \frac{d}{2.0 * \tan(\frac{\pi * \text{fov}}{360.0})}$$

where d is the horizontal width of the image sensor, and fov is the desired horizontal field of view. This value will be provided to the PTZ control routine. An image where the PTZ-camera automatically adjusted to a user-defined region is shown in Fig. 6.

5 Conclusion

In this publication we showed our research on an intelligent omnivision camera system. We showed how this system can be used in a surveillance scenario. One of the most important findings was, that there are a lot of parallels between surveillance and robotics and many implemented functions can be reused. Due to the fact that we are using the modular framework GStreamer, it was easy to access the IP cameras and it was also possible to add state-of-the-art features like h264 recording. Using an OpenCL accelerated panorama stitching algorithm and our scheduling functions, it became possible to get a real-time view of the scene, while all other detection algorithms run as fast as possible.

There are several options to enhance the system. Due to the modular pipeline setup, it is also possible to add dedicated PCs that are only used for detection of image features. This way, computationally intensive image processing functions can be executed without the risk of disturbing real-time critical tasks.

The system can also be used for different types of camera systems. They could be equipped with wide-angle lenses or spherical mirrors. In the software setup,

only the elements for generating the image need to be exchanged, the rest of the software as well as the GUI can be reused.

One possibility to have a next-generation surveillance systems would be to access even more cameras and to fuse the image of the different cameras with awareness of the three-dimensional structures in the scene.

Acknowledgments The authors would like to thank their student assistant Johannes Liebrecht for designing the PTZ control board during his thesis, Andreas Maeder for the calibration of the panorama stitching routine, Gang Cheng for contributing the PTU control code, and the Group Kunshan Robotechn Intelligent Technology Co., Ltd. for performing real-world testing in a maritime scenario.

References

1. Bistry H, Zhang J (2009) Task oriented control of smart camera systems in the context of mobile service robots. In: IEEE/RSJ international conference on intelligent robots and systems, IROS 2009, pp 3844–3849
2. Bistry H, Zhang J (2010) A cloud computing approach to complex robot vision tasks using smart camera systems. In: IEEE/RSJ international conference on intelligent robots and systems, IROS 2010, pp 3195–3200
3. Bistry H, Vietze F, Zhang J (2009) Towards intelligent high resolution surveillance cameras. In: Künzel M, Michel B (eds) Safety and security systems in Europe, number 10 in micromaterials and nanomaterials. Micro Materials at Fraunhofer IZM Berlin and Fraunhofer ENAS Chemnitz, pp 76–79
4. Maeder A, Bistry H, Zhang J (2008) Intelligent vision systems for robotic applications. Int J Inf Acquis 5(3):259–267
5. Foote J, Kimber D (2000) Flycam: practical panoramic video and automatic camera control. In: IEEE international conference on multimedia and expo, 2000. ICME 2000, vol 3. IEEE, pp 1419–1422
6. Yamazawa K, Yagi Y, Yachida M (1993) Omnidirectional imaging with hyperboloidal projection. In: Proceedings of the 1993 IEEE/RSJ international conference on intelligent robots and systems' 93, IROS'93, vol 2. IEEE, pp 1029–1034
7. Wu J, Yang K, Xiang Q, Zhang N (2009) Design of object surveillance system based on enhanced fish-eye lens. Chin Optics Lett 7(2):142–145
8. Haritaoglu I, Harwood D, Davis LS (2000) W^4: real-time surveillance of people and their activities. IEEE Trans Pattern Anal Mach Intell 22(8):809–830
9. Weser M, Westhoff D, Hüser M, Zhang J (2006) Real-time fusion of multimodal tracking data and generalization of motion patterns for trajectory prediction. In: Proceeding of the IEEE international conference on information acquisition (ICIA), Shandong, China, August 2006
10. Huang YH, Hu M, Chong HL, Jia XM, Ma JX, Liu WL (2012) A survey of robot visual tracking algorithm. Key Eng Mater 501:577–582
11. Huang J, Ponce SP, Park SI, Cao Y, Quek F (2008) GPU-accelerated computation for robust motion tracking using the CUDA framework. In: Proceedings of the IET international conference on visual information engineering
12. Torres F, Candelas F, Puente S, Jiménez L, Fernández C, Agulló R (1999) Simulation and scheduling of real-time computer vision algorithms. Computer vision systems, pp 98–114
13. Xu R, Jin J (2005) Scheduling latency insensitive computer vision tasks. Parallel and distributed processing and applications, pp 1089–1100

14. Taymans W, Baker S, Wingo A, Bultje R, Kost S (2008) Gstreamer application development manual (0.10.21.3). http://gstreamer.freedesktop.org
15. Lowe DG (1999) Object recognition from local scale-invariant features. Int Conf Comput Vis 2:1150–1157
16. Schleicher D, Bergasa LM, Barea R, Lopez E, Ocaña M, Nuevo J (2007) Real-time wide-angle stereo visual SLAM on large environments using SIFT features correction. In: Proceedings of the IEEE/RSJ international conference on international robots and system, Oct 2007, pp 3878–3883
17. Kuehnle J, Verl A, Xue Z, Ruehl S, Zoellner JM, Dillmann R, Grundmann T, Eidenberger R, Zoellner RD (2009) 6d object localization and obstacle detection for collision-free manipulation with a mobile, service robot, pp 1–6
18. Viola P, Jones M (2001) Rapid object detection using a boosted cascade of simple features. In: IEEE Computer society conference on computer vision and pattern recognition, vol 1
19. Bradski G (2000) The openCV library. Doct Dobbs J 25(11):120–126

Active Scene Analysis Based on Multi-Sensor Fusion and Mixed Reality on Mobile Systems

Denis Klimentjew, Sebastian Rockel and Jianwei Zhang

Abstract The approach presented shows possible ways of improving scene analysis to achieve more reliable and accurate object recognition in the context of mobile robotics. The centralized architecture combines different feature detectors with active modalities, such as change of perspective or influencing the scene. It opens possibilities for the use of 2D detectors and extends the results to 3D. In combination with mixed reality, it offers the possibility of evaluation of the developed system as well as increased efficiency. The architecture developed and the preliminary results are presented. The work goes a step in the direction of active intelligent perception.

Keywords Scene analysis · Object detection · Mixed reality · Active perception · Clustering and recognition · 3D modeling

1 Introduction

The detection and recognition of stationary objects is necessary in many scenarios and everyday tasks in mobile robotics. Many different algorithms and methods have been developed recently but nevertheless, no approach for stationary-object recognition meets all of the requirements of mobile robotics. Each method has its

D. Klimentjew (✉) · S. Rockel · J. Zhang
TAMS Group, University of Hamburg, Vogt-Koelln-Straße 30
22527 Hamburg, Germany
e-mail: klimentjew@informatik.uni-hamburg.de
URL: http://tams.informatik.uni-hamburg.de

S. Rockel
e-mail: rockel@informatik.uni-hamburg.de

J. Zhang
e-mail: zhang@informatik.uni-hamburg.de

F. Sun et al. (eds.), *Foundations and Practical Applications of Cognitive Systems and Information Processing*, Advances in Intelligent Systems and Computing 215,
DOI: 10.1007/978-3-642-37835-5_69,

disadvantages and depends upon boundary conditions. A perfect object recognition system must be able to accurately classify an object in its environment and to deliver the object's exact position and orientation (in relation to the main robot coordinate system).

In search of the "Holy Grail" of scene analysis and object recognition, the idea of combining the use of several algorithms and methods with the possibility of changing the view and/or actively interfering with the object in the scene is the most promising prospect. The authors do not know of any existing architecture or implemented system that has this combination of facilities. There are several approaches that combine different methods, such as the combination of volumetric models and SIFT features in RoboEarth.[1] Another example is the so-called project recognition kitchen from Willow Garage.[2] The project consists of two different pipelines of 2D and 3D data processing algorithms. Each pipeline combines different algorithms.

Many existing methods for simultaneous recognition of objects try to match features using a database [1, 2] and may also integrate stereo cameras, time of flight cameras, thermal cameras, etc. [3]. However, all of these methods have limitations; one method, for example, works only with rotationally symmetrical objects. Other algorithms cannot handle unknown objects and yet others work only with unknown objects.

The approach we present tries to extend the existing state-of-the-art and shows a possible way to improve scene analysis and to achieve more reliable and accurate object recognition. This paper presents a novel approach to increasing object recognition efficiency by simultaneously using multiple algorithms and by active interference with scene objects. The possible architecture and the first preliminary results are presented. The work goes a step in the direction of active intelligent perception.

2 Possible Approach and Architecture

While based on well-known object recognition methods, the work presented uses a new architecture to investigate optimal object recognition strategies. It includes novel approaches, such as changing the view and actively interfering with the environment.

Figure 1 presents the object recognition architecture including both new and traditional means of object detection. The upper part illustrates the perception of the complete environment and the regions of interest (ROI). The scenario is limited to an indoor scene, such as an office environment. In this case the ROIs are planar surfaces, places where interesting objects are most likely to be found. There

[1] http://www.roboearth.org/

[2] http://ecto.willowgarage.com/recognition/user.html

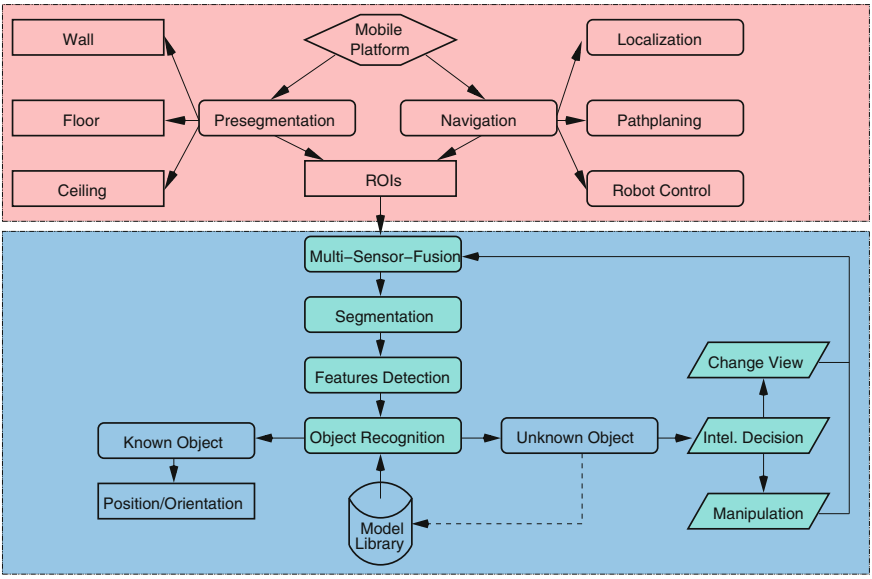

Fig. 1 Visualization of developed architecture

are many existing approaches to 3D environment mapping. We use our own approach [4] that navigates in the 2D environment and automatically creates a 3D map. The advantage of this approach is that it guarantees that all surrounding objects are mapped. On detection of the ROIs, the robot will navigate to those locations according to the assigned task. The upper part of the architecture shows the state in which the robot has been placed in front of the ROI.

The lower part of the architecture starts with "sensor fusion". The aim of gaining as much information as possible is achieved by using many different 2D and 3D feature detectors. The approach used is introduced in the Sect. 3 and combines rgb and depth information. According to future requirements, further sensors can also be adopted, for example other cameras or laser range finders. An interesting possibility is the integration of a thermal camera in order to gain another sensor modality. Thus the depths, color, and thermal information is available. The combination of depth and color information allows many more possibilities for scene analysis. After sensor fusion, planar surfaces are detected and removed as soon as the 3D data are segmented. Further processing steps (to reduce the complexity) operate only on recently detected clusters. In the next step the 2D and 3D feature detectors can be applied, singly or in combination; as single components; in combination with other methods of the same kind; and as combinations of different methods. Of course, each additional method increases the possibility of successful scene analysis. However, when no detector succeeds, the system must decide between changing the view perspective and active influence through a manipulator in order to change the spatial relationships between objects

under investigation. In either case, data acquisition, fusion, and clustering must be repeated before feature detection can be reapplied.

It is clear that the system is powerful and can deliver more usable results than state-of-the-art methods. An open question is the selection of an optimal, efficient strategy within the presented architecture. Success depends upon on many parameters, the number of which grows with the number of methods included and combined. A mathematical calculation of the best capabilities is not given; the problem is NP complete. The authors suggest that the use of physical simulation and mixed reality can help to reduce problem complexity and to find an efficient solution. More details are presented in Sect. 5.

3 Multi-sensor Fusion

Before defining the object recognition process, the necessary input has to be specified. The more information the input includes, the higher the probability of finding characteristic features in it. We concentrate on the Kinect-like sensors (see Sect. 6), combination of structured light (PrimeSense sensor), and rgb images.

The pseudo-code presented below emphasizes the multimodal fusion of both sensors. The calibration process uses a calibration body consisting of a colored planar surface and some holes with predefined alignments. The calibration body is shown in Fig. 2.

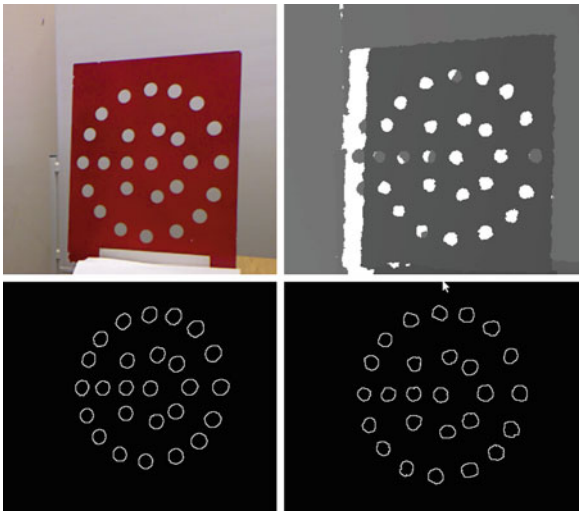

Fig. 2 Upper images show the rgb and depth image respectively. The lower images visualize the found holes in rgb and depth image

Algorithm 1 The calibration algorithm for Kinect-like sensors

procedure CALIBRATION(RGB-D)
    Synchronized data acquisition of RGB and depth information.
    RGB:
    Transform to HSV color space.
    Generate a histogram.
    Sorting to white, black, gray, and other pixels.
    Fore- / background separation.
    Reduce to ROI (calibration body in foreground).
    Finding a rgb-holes.
    Sorting a rgb-holes.
    Depth:
    Transform the distances to standard values (m)
    Generate a binary image (if depth between $0.60\,m - 1.2\,m$ then 1 else 0).
    Reduce to ROI through remove the lines (if number of 0 values $> 99\,\%$).
    Finding a depth-holes (growing).
    Sorting a depth-holes.
    Both:
    Check and remove of false-positives.
    Calculation of hole centers.
    Calculation of and finding the minimal distance between RGB- and depth hole centers.
    Generate the corresponding pairs.
    Calculation of homogeneous transformation matrices (with help of RANSAC, 7/8 point, and LMEDS algorithms).
    Return the **homogeneous transformation matrices**.
end procedure

After the detection of corresponding points (center of circles in rgb and of holes in depth images) the fundamental matrix can be calculated. The RANSAC, 7/8 Point, and LMEDS (Least Median of Squares) algorithms have been implemented and tested with the best results delivered by the RANSAC algorithm. Eventually, the user receives a colored point cloud with two each other registered depth and color information.

Evaluation of the calibration method is difficult. On the one hand, the information content of one voxel grows with distance; on the other hand, the perspective change (baseline) has negative character (parallax effect). In practical applications, the quality of the method has been verified and shows great potential. The algorithm is fast and simple to use: the user just has to place the calibration body $0.60 - 1.2\,\mathrm{m}$ in front of the sensor and start the application. Hence, calibration process is completely automated and can easily be repeated on demand. The resulting homogeneous transformation matrix is automatically updated and the platform is ready to use.

4 Approach

In the work presented, the 3D image will be seen as a one dimension expanded 2D image. Consequently, the same model is used for 3D point clouds as is used for an image. So an image I can be seen as the sum of several components:

$$F_{i,f}(\overrightarrow{x}) = \alpha \cdot BG_{i,f}(\overrightarrow{x}) + N_{i,f}(\overrightarrow{x}) + T_{i,f}(\overrightarrow{x}) \tag{1}$$

or simplified

$$F_i = T_i + BG_i + N_i \tag{2}$$

where F denotes the image, T_i the foreground region, BG_i the background, and N_i the camera noise at frame number i. The advantages of this approach are the retention of the relation between neighboring voxels and the possibility of using the know-how of 2D image processing and the many existing pertinent algorithms [5].

4.1 Preliminary Work

The calibration procedure described below delivers colored point clouds. The results can be seen in the middle image of Fig. 3. To reduce complexity and increase efficiency, planar surfaces are recognized and removed in the first step. Afterwards, cluster segmentation is applied to the remaining voxels. The methods based on calculation of Euclidean distance show good results and excellent performance. Such found clusters are used for further processing. Of course, the clusters can be under segmented and hence can contain more than one object, specifically in case of occlusion. Nevertheless, the architecture allows the use of any suitable segmentation algorithm. The authors see pre-segmentation as a precondition for applying the feature detectors, because the clusters offer an excellent basis for further processing.

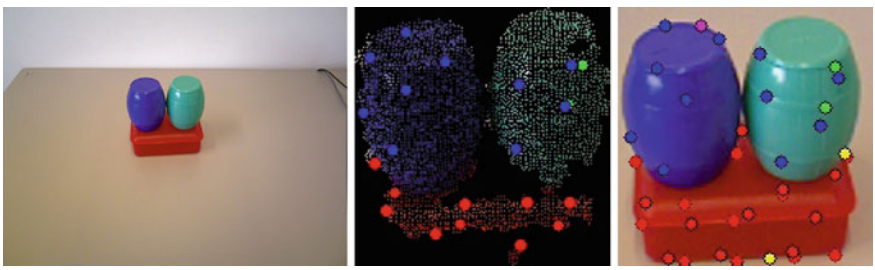

Fig. 3 Visualization of results for clustering, depth, and color segmentation. The *left* image shows the original scene. The image in the *middle* visualize the depth segmentation with the registered color information. Rights the corresponded ROI taken from the original color image

Naturally, the characteristics of the sensors in use affects the course of object recognition. In the present case, the depth resolution of the PrimeSense sensor is only $\frac{1}{4}$ of its color resolution. That is a reason for the many black pixels in the middle image of Fig. 3. This circumstance prevents the application of some image processing algorithms or can falsify their results. To compensate for this disadvantage, the method presented transfers the bounding boxes of each cluster to the color image. The results are the ROIs from the color image.

For the calculation, the homogeneous and projecting matrices are used. The procedure consists of the following steps: At first, under assumptions of ideal conditions, the so-called pinhole camera model is used. The focus lies on the projection of an object point $(x, y, z)^T$ to the position $(u, v)^T$ in the image frame. The procedure starts with the transformation of an object point $(x, y, z)^T$ in the camera frame to the point $(x', y')^T$ in the image frame with the focal length of $f = 1$. With this, $x' = \frac{x}{z}$ and $y' = \frac{y}{z}$. Thereby, the emitted brightness of the object point $(x, y, z)^T$ will be mapped to the position $(x', y')^T$.

The same layer will also be used for the calculation of lens distortion. In order to that the point at position $(x', y')^T$ is transformed into $(x'', y'')^T$.

$$x'' = x'(1 + k_1 r^2 + k_2 r^4 + k_3 r^6) + 2p_1 x' y' + p_2(r2 + 2x'^2) \tag{3}$$

$$y'' = y'(1 + k_1 r^2 + k_2 r^4 + k_3 r^6) + p_1(r^2 + 2y'^2) + 2p_2 x' y', \tag{4}$$

where $r^2 = x'^2 + y'^2$; (k_1, k_2, k_3) are the coefficients of radial and (p_1, p_2) of the tangential distortion.

Finally, the points of the distorted image are mapped, with the help of intrinsic parameters, to position $(u, v)^T$ of the 2D camera sensor.

$$u = f_x x'' + c_x \tag{5}$$

and

$$v = f_y y'' + c_y, \tag{6}$$

where (c_x, c_y) are coordinates of the principal point and (f_x, f_y) is a principal distance in pixel.

Consequently, the procedure finds the corresponding ROI inside the original color image, providing that the parameters of intrinsic calibration are correct. The work on the ROIs reduces the run time and increases the efficiency. Figure 3 visualizes the results of clustering, depth, and color segmentation. On the left side the original image is presented. The middle image shows the depth segmentation with the projected color information on it. On the right is the corresponding ROI from the original color image. With the naked eye it can be seen, that the two images contain more information than only one of them. The single colored circles visualize color information found at the corresponding positions.

The presented calculation projects a bounding box from the point clouds to a corresponding box in the image. Unfortunately, there is no possibility to reconstruct depth information from the 2D image. Nevertheless, for the use of the results from the 2D image processing algorithm this possibility is strictly needed. To provide the depth information, a structure like $[x_1, y_1, z_1, r_1, g_1, b_1, , x_n, y_n, z_n, r_n, g_n, b_n]$ is created and filled using the bounding box transformation. This allows each feature detector to switch permanently between 2D and 3D images and to achieve the best possible results. For example, the 2D edge detector is applied to the image. This kind of algorithms is robust and very fast. Nevertheless, the methods search for image brightness changes and produce a lot false positives. To improve the results, the edges detected can be evaluated with the help of depth information. In this case, the fast 2D algorithm is used as a surface based method. The 3D method can be applied only on interesting regions, thus the complexity can be reduced. Moreover, at each step of the architecture the manipulator can be included to enable dedicated manipulation inside the scene.

In almost the same manner as using 2D and 3D information, the system needs a centralized place for all object relevant information. To provide the necessary information a database is needed. This database must hold the following attributes per item: 3D mesh, images, color, and other necessary data belonging to an object. The resulting system shall have the ability not only to read the data from the database, but also to complete the data for one object or insert the new objects into the database during run time.

4.2 Single Components/Features Detectors

One of the difficulties with Euclidean distance-based methods applies when the distance between objects is below a specified threshold. An over sized threshold results in under segmentation. On the other hand, the threshold depends on the distance between sensor and object and must be not too low. One extreme example of another difficulty represents an occlusion, in this case the clustering is useless and the employment of other 2/3D feature detection algorithms is necessary. In resent years, two 2D feature detection algorithms have been widely used. The SIFT [6] and the SURF [7] algorithms are robust and fast and deliver practical results. Both feature detectors are similar to each other. The difference between them is that the SURF Detector uses a 2D Haar wavelet that makes it possible to use the integral images. Therefore, the SURF is faster compared to the SIFT detector and has constant run time.

Figure 4 visualizes object recognition with the SIFT feature detector. The methods can compensate partial occlusions under the condition that enough features are found. Three objects are recognized, the recognition of the bottle in the background fails, because the insufficient features are found. The bounding boxes are correctly transformed into the input image despite partial occlusions. Objects with complex texturing are excellently suited qualified for this kind of method.

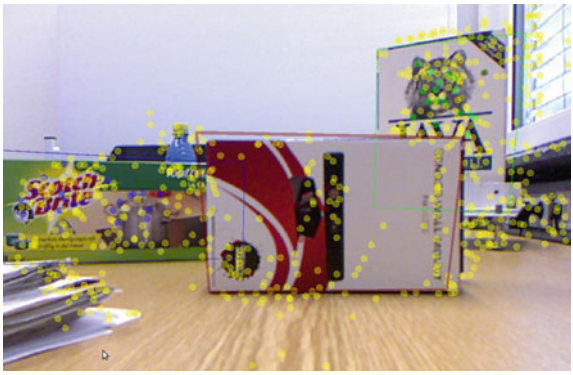

Fig. 4 Object detection with the SURF/SIFT feature detector

Fundamentally, all possible algorithms can be included and used with the developed architecture. The algorithms considered are based on edge and corner detectors, color recognition, silhouettes, principal component analysis (pca), etc. Most of these methods are well-known, efficiently implemented, and fast. Through ROS[3] as a common framework the integration of methods is simple and consistent. The big advantage lies in the possibility to use algorithms with different input information such as color, texture, size, shape, and so on. So information about different object properties can be obtained and fused. An overview of different 2D methods with significant comparison can be found in [8].

Object recognition in 3D point clouds is a relatively new research field. The input data from the pure point cloud are voxels and the neighbor relations between them. Therefore after the clustering, the size, curve, and shape information is compared. The changes between normal vectors help to determine information about curve and shape as well as possible edges and corners. There are many algorithms to compare the similarity between point clouds. The common methods are based on the so-called Iterative Closest Point (ICP). An examination of different ICP-based algorithms can be found in [9].

The more detectors that are implemented, integrated and used, the higher the probability of the successful scene analysis. Nevertheless, the developed architecture opens a possibility to go a step further through the combination of different methods. It starts with edge and corner detection in 2D and verification of the resulting hypothesis in 3D. But more complex combination are thinkable. Also the manipulator may be integrated. So the recognized object can be removed in the scene. Recursive application is promising and is under study.

The next interesting point is the handling of unknown objects. The fused sensor information and the mobile platform can be used to create the necessary information for the database. The robot can move around the table or rotate the object with the manipulator. The resulting data, such as a registered 3D model or images from different perspective, can be stored directly in the database. The absent

[3] http://www.ros.org

information, such as the category, can be applied from the user or a learning algorithm.

Anyway these possibilities are not utilized. What can be done if despite the large number of detectors and their combinations, no useful information deliver? The architecture provides two further possibilities. The first is a change of perspective, after which the scene analysis can be restarted. The second is active influence of the scene to change the correlation between objects. Re-application of the analysis algorithms is promising, too.

5 Scene Analysis and Mixed Reality

When the robot meets unknown scenes it needs a strategy for further analysis. In this work we define that a scene contains a ROI, i.e. a robot with sensors, a table, and an unknown amount of objects on it. To further specify the domain we restrict objects to be of a-priori known models in a database. Even with that knowledge, trial and error to find the best view on the scene, manipulate it or test multiple feature detectors is expensive in the real environment. Expensive here can be seen in terms of time and electricity for the robot. To reduce these 'costs' we combine in this work a simulation of the scene with the real-world environment, and thus employ a mixed reality scenario [10] where the simulation is updated by real-world sensing data and simulation results are employed in the real environment.

In this section, multiple approaches of exploiting the simulation in order to gain an efficient strategy for the scene analysis will be introduced. Finally the approach used will be introduced.

5.1 Generation/Extraction of Difficult Scenes for Evaluation

With the help of simulation trails and depending on specific criteria, 'difficult' scenes will be selected out of randomly generated situations. Only these difficult scenes will then be evaluation in the real environment with the presented system.

Difficult scenes include situations where objects occlude each other or are stacked on top of each other (Fig. 5).

5.2 Generation of a Scene Memory

With the a-priori defined objects in the database, scenes with random combinations of objects are created. Each scene is stored in a 'global memory' and this memory is then online searched for certain criteria to find appropriate scenes in the memory fitting the currently observed situation in the real environment.

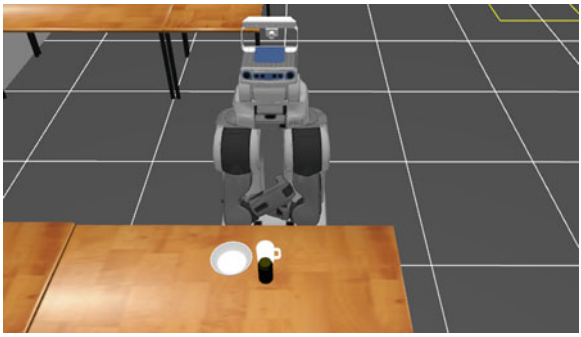

Fig. 5 Example scene in the simulation. Here a special situation is shown: Object occlusion

5.3 Finding the Next Best View

Often scenes with unknown objects on top of a table cannot sufficiently be analyzed because of the perspective, i.e., the view does not allow the scene to be completely segmented. Finding the next best view (NBV) is a problem that many scientists in the graphics and robotics community have faced. Here based on the volumetric model any approach to solve the NBV can be applied. Therefore, the 3D point cloud will be used as an input to define the volume. The next best views will then be calculated according to specific criteria. In order to validate these views each has to be tested with the robot. A view includes a goal position for the robot and a position is constrained by the robot shape and its environment, e.g., a table. Instead of giving the robot the goal position of the next best view we validate it first in the simulation. If for some reason the navigation cannot proceed to this position, e.g., because it is too close to an obstacle, it will be adapted and tested again. Eventually, a valid goal position will be found and passed to the real robot in order to find a trajectory and proceed to the NBV. The NBV problem is a local optimization problem and NP hard. It is often solved approximately by an algorithm selecting the view that maximizes a view metric [11]. Whereas in state-of-the-art NBV solutions, it is a challenge to evaluate the view metric for a large set of views, in the simulation each view can be evaluated by testing the planned view according to the feature detectors applied. The domain of possible views has to be restricted nonetheless. Defining NBV algorithms is not the focus of this work.

5.4 Finding a Strategy to Successfully Manipulate the Scene

In order to grasp an object or to move it the robot situation has to fulfill some preconditions. First, it has to be in reach of the object which is defined by the robot arms' workspace. If the object is not within reach, no manipulation can be performed. The problem can be reduced to that of finding a suitable manipulation pose. The simulation allows the testing of different robot poses and hence the choice of the optimal pose.

6 Implementation and Evaluation

The work presented benefits from the use of robot operating system (ROS) as a framework. For the evaluation, the PR2 [4] robot from Willow Garage is used. ROS provides algorithms for object detection based on the RANSAC method, for example table detection, as well as Euclidean distance using segmentation. Other advantages of using ROS are the integrated image processing library, OpenCV,[5] and the 3D processing library PCL.[6] Parts of the algorithms are used directly, while others have been adapted or integrated as part of this work like the extended ICP (ICP^2). The ROS structure allows all feature detectors and other modalities to be started in parallel, limitations arising only from the available computational capacity.

In this work, we concentrate on Kinect-like sensors (ASUS Xtion Pro Live in the case of our PR2). The advantage is the high acquisition rate of 30 fps for color and depth information simultaneously. Fusion is implemented in C/C++ for hole detection and rgb images. For the calculation of the fundamental matrix the OpenCV library is used. After calibration, the results are immediately available inside the ROS structure.

The database is realized in PostgreSQL,[7] with versions 8.4 and 9.2 integrated and tested. It is possible to connect, extend, and modify the database during run time. Inside the database, the size, color, and if available, the weight and balance information, as well as the 3D model, images taken from different perspectives and SIFT/SURF bag for each object are available attributes.

The first evaluation idea is to show that the implemented part of the architecture already goes beyond state-of-the-art methods. Therefore, three different scenarios are created to show the possibilities of the work. All of the scenarios have partial occlusion and the first segmentation delivers an under segmented cluster. In the first scenario, one of the feature detectors recognized an object as a part of the cluster. The manipulator is used to grasp the object and put it away. After re-applying the developed system, the rest of the objects can be successfully recognized. Figure 6 visualizes the individual steps of the first scenario.

The second evaluation scenario used the possibility to change the perspective. The colored point cloud after the robot has moved allows individual objects to be segmented and recognized using icp-based comparison with the database, as shown in Fig. 7.

For the third scenario, no practical information can be obtained from the feature detectors. As a last resort, the manipulator influences the scene and changes the relation between the objects. After re-applying segmentation and feature detectors the objects can be recognized. Figure 8 shows the individual steps as well as the results.

[4] http://www.willowgarage.com/pages/pr2/overview

[5] http://opencv.willowgarage.com/wiki/

[6] http://pointclouds.org/

[7] http://www.postgresql.org/

Fig. 6 The *left upper* image shows the under segmented cluster, the recognition of single objects is not possible. The SIFT/SURF detector recognized the bottle (bounding box in the *right upper* image). In the *left lower* image the manipulation with the PR2 is visualized. The robot grasps a bottle and removes it from the scene. After re-applying the segmentation and feature detection the rest of the objects can be recognized

Fig. 7 The *left* image shows the partial occluded scene. The segmentation delivers an under segmented cluster. After the perspective change the recognition can be applied successfully. The right images show the visualization of a successful recognition in the image (*top*) and the point cloud (*down*)

These experiments show clearly that the developed architecture has great potential. Of course, many detectors and/or segmentation algorithms can and must still be integrated and the system can be improved. The right hand image in Fig. 8 shows that the orientation of the left cup is inaccurate. Consequently, it is possible that the calculation of grasp can fail. Nevertheless, the system opens enormous possibilities for mobile robotics.

Fig. 8 The *left* image shows the under segmented scene, the feature detectors deliver no useful information. The recognition is not possible. The *middle* image visualizes the influence in the scene with the manipulator. After re-applying the segmentation and feature detectors the objects can be recognized

It is conceivable that with the growing number of detectors as well as segmentation the system becomes complicated. Not all components can be run in parallel, because not enough computation power can be provided. The same problem results from the possible combination and chaining of single components. From this point of view, the search for the best possible strategy for scene analysis is one of the open problems, as already described in Sect. 5. The next open questions are the evaluation and its required metrics. The authors think that the use of a physical simulation and the mixed reality approach can help an efficient solution to be found. At first the system can be evaluated with or without involving any hardware components. It can be examined with ideal sensors as well as with noisy real sensor data. Moreover, mixed reality can be seen as an omniscient concept. According to this, a meaningful scene with interesting relationships between objects can be selected. Using this, the optimal/best possible strategy can be found and verified under realistic conditions. The evaluation approach, using mixed reality, improves during run time. It can be used also to evaluate similar architectures. Moreover, the evaluation concept can be applied to compare different systems or implementation approaches.

7 Conclusion and Future Work

The paper presents a new approach to the improvement of active scene analysis and object recognition. The architecture developed allows different modalities and components to be combined in a centralized manner. Of course, one of the next steps is to produce a well-integrated system. Furthermore, the mixed reality approach can be used to evaluate the system and to make it more efficient. The final step is to create a global evaluation metric to compare this kind of system to others. The first step is now done and the authors are working hard to realize all of their proposed ambitions.

The first results show promising data and the authors hope to achieve the next step in the direction of active intelligent perception.

Acknowledgments The authors would like to thank William Morris for his structural feedback and Robert Wieczoreck for supporting the implementation of the calibration procedure. This work has been conducted as part of RACE, funded under the European Community's Seventh Framework Programme FP7-ICT-2011-7 under grant agreement n 287752 (http://www.project-race.eu/).

References

1. Rusu RB, Bradski G, Thibaux R, Hsu J (2010) Fast 3D recognition and pose using the viewpoint feature histogram. Proceedings of IROS
2. Sun M, Xu B, Bradski G, Savarese S (2010) Depth-encoded hough voting for joint object detection and shape recovery. Proceedings of ECCV
3. Rusu RB, Blodow N, Marton ZC, Beetz M (2009) Close-range scene segmentation and reconstruction of 3D point cloud maps for mobile manipulation in domestic environments. Proceedings of IROS
4. Michalicek G, Klimentjew D, Zhang J (2011) A 3D simultaneous localization and mapping exploration system. In: Proceedings of the IEEE international conference on robotics and biomimetics (IEEE-ROBIO), Phuket, Thailand, pp 1059–1065, ISBN: 978-4577-2137-3, 7-11 Dec 2011
5. Klimentjew D, Zhang J (2011) Adaptive sensor-fusion of depth and color information for cognitive robotics. In: Proceedings of the IEEE international conference on robotics and biomimetics (IEEE-ROBIO), Phuket, Thailand, pp 957–962, ISBN: 978-4577-2137-3, 7-11 Dec 2011
6. Lowe DG (2004) Distinctive image features from scale-invariant keypoints. Int J Comput Vis 60:91–110
7. Bay H, Tuytelaars T, Van Gool L (2006) Speeded up robust features, Proceedings of the 9th European conference on computer vision. Springer, New York
8. Roth PM, Winter M (2008) Survey of appearance-based methods for object recognition, Technical report ICG-TR-01/08. Graz University of Technology, Austria
9. Rusinkiewicz S, Levoy M (2001) Efficient variants of the ICP algorithm, Third international conference on 3D digital imaging and modeling (3DIM 2001). Quebec City, Canada
10. Rockel S, Klimentjew D, Zhang J (2012) A multi-robot platform for mobile robots-a novel evaluation and development approach with multi-agent technology. Proceedings of the IEEE international conference on multisensor fusion and integration for intelligent systems (MFI), University of Hamburg, Hamburg, Germany, In
11. Low K-L, Lastra A (2006) Efficient constraint evaluation algorithms for hierarchical next-best-view planning 3D data processing, visualization, and transmission, third international symposium on, vol., no., pp. 830–837, 14–16 June 2006, doi:10.1109/3DPVT.2006.52

Object Learning with Natural Language in a Distributed Intelligent System: A Case Study of Human-Robot Interaction

Stefan Heinrich, Pascal Folleher, Peer Springstübe, Erik Strahl, Johannes Twiefel, Cornelius Weber and Stefan Wermter

Abstract The development of humanoid robots for helping humans as well as for understanding the human cognitive system is of significant interest in science and technology. How to bridge the large gap between the needs of a natural human-robot interaction and the capabilities of recent humanoid platforms is an important but open question. In this paper we describe a system to teach a robot, based on a dialogue in natural language about its real environment in real time. For this, we integrate a fast object recognition method for the NAO humanoid robot and a hybrid ensemble learning mechanism. With a qualitative analysis we show the effectiveness of our system.

Keywords Ensemble learning · Human-robot interaction · Language

S. Heinrich (✉) · P. Folleher · P. Springstübe · E. Strahl · J. Twiefel · C. Weber · S. Wermter
Department of Informatics, Knowledge Technology, University of Hamburg,
Vogt-Kölln-Straße 30 D - 22527 Hamburg, Germany
e-mail: heinrich@informatik.uni-hamburg.de
URL: http://www.informatik.uni-hamburg.de/WTM/

P. Folleher
e-mail: 6follehe@informatik.uni-hamburg.de

P. Springstübe
e-mail: 3springs@informatik.uni-hamburg.de

E. Strahl
e-mail: strahl@informatik.uni-hamburg.de

J. Twiefel
e-mail: 7twiefel@informatik.uni-hamburg.de

C. Weber
e-mail: weber@informatik.uni-hamburg.de

S. Wermter
e-mail: wermter@informatik.uni-hamburg.de

F. Sun et al. (eds.), *Foundations and Practical Applications of Cognitive Systems and Information Processing*, Advances in Intelligent Systems and Computing 215,
DOI: 10.1007/978-3-642-37835-5_70,

1 Introduction

The interest in robots as assistants or companions has grown tremendously during the last years. Robots are developed to support humans in households as well as in healthcare and therapy [11]. In addition, research progresses in the direction of cognitive systems to understand cognitive functions in humans as well as to create robots that can interact with humans naturally [10].

For the development of an intelligent system that can fulfil these criteria, we have to bridge the large gap between the needs for human-robot interaction (for example based on a dialogue in natural language) and the technical capabilities of modern humanoid platforms and computing machines. The questions of how such a system can be designed and how state-of-the-art methods from machine learning and information processing can be integrated remains open [7].

To approach these questions, in this student's show case we developed a complex distributed system that is able to incorporate a humanoid robot, different standard machines and recent frameworks for various tasks. As a novel contribution we developed and included object detection and hybrid ensemble learning mechanisms that are able to operate in real time and within a real world environment. We show the effectiveness of these mechanisms in a qualitative analysis.

2 Scenario

Our research focuses on human-robot interaction in a real world scenario with real time conditions to learn about communication and grounding of language as well as about effective learned situated interaction [8]. Here a humanoid robot NAO[1] is supposed to learn cues about objects in its environment based on natural language and visual information, and to recognise and classify similar objects correctly (see Fig. 1a for an overview). The learning process is guided by a dialogue with a human teacher about some objects (compare Fig. 1b).

The teacher can inform the robot about unknown objects, and is also able to confirm the correct classification and thus the correct pointing to objects, giving the robot the opportunity to become more certain with its decisions over time:

- **Teaching Dialog:** A user can request the robot to *learn*. The robot then asks what he is supposed to learn and the user states an object category (e.g. **<This is an apple>**). The robot then asks the user to verify the linguistic expression the robot has understood for the object in the field of view. After verification (e.g. **<Right>**) by the user the robot will learn the object.

[1] The NAO is a 57 cm tall humanoid robot with, 25 *degrees of freedom* (DOF), two VGA cameras, and four microphones, developed for academic purposes—www.aldebaran-robotics.com.

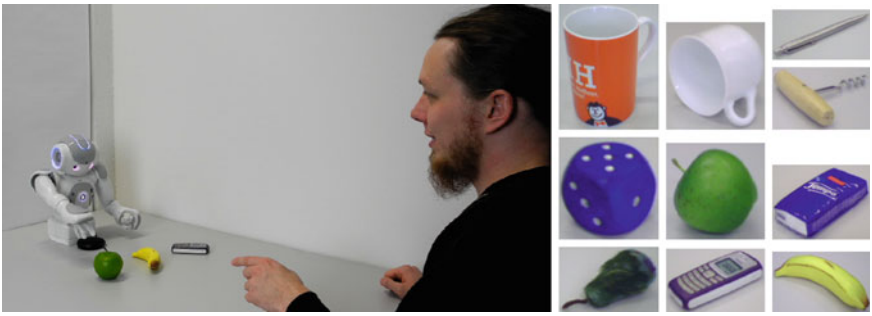

(a) (b)

Fig. 1 Scenario of learning objects by natural language in human-robot interaction. **a** Learner and teacher. **b** Objects

- **Classification Dialog:** A user can also ask the robot to *classify* an object. The robot responds by reporting a description of the object in the field of view based on recently learned experiences.
- **Find Dialog:** In addition a user can request the robot to *find* an object among a number of different objects in the field of view. If the robot recognises the described object, then it will report a relative position and point to the object. Otherwise it will express his uncertainty about the requested object.

3 Architecture of the Distributed Intelligent System

The described scenario demands a lot of capabilities of an intelligent system: First of all the robot has to observe the scene and determine objects of different levels of complexity under fairly different light conditions in real time. Secondly, the system has to provide reliable speech recognition and the ability to speak to the human in natural language. Thirdly, the system must learn objects very fast and also be scalable to a reasonable number of objects. Finally, the system has to incorporate all capabilities in a coherent interaction scheme.

To achieve the goals we set up a distributed system of up to 16 service nodes, written in ROS,[2] both on the NAO robot and some standard PCs. The system can be divided into the four modules *core*, *vision*, *motion*, and *interface* (see Fig. 2 for an overview).

- **Core:** The heart of the system is the *Controller* that implements the logic of the dialogue by means of a finite state machine, set up by SMACH.[3] A database is

[2] The *Robot Operating System* (ROS) is a middle-ware for the use with various robotic platforms; ROS supports different programming languages and multiple operating systems as well as multiple hardware elements—www.ros.org.

[3] *SMACH* is a python-based library for building hierarchical state machines—www.ros.org/wiki/smach/.

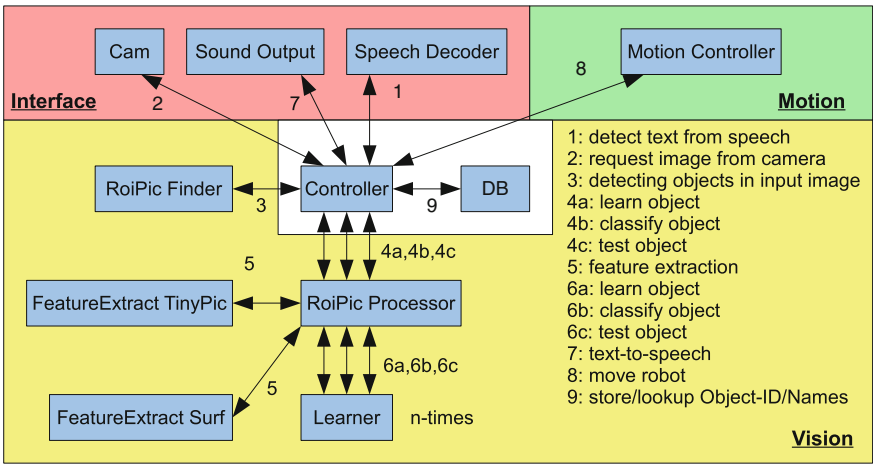

Fig. 2 An overview of the system components

used to store training data of items that a user wanted the robot to learn and to allow for a qualitative evaluation.

- **Interface:** To interact with the real world the Controller can request the camera system to get real time images from the NAO, can request to recognise speech with the employed PocketSphinx[4] with a hybrid decoder [5], and command the NAO's text-to-speech system to respond with speech.
- **Vision:** The Controller can request the vision system to determine a small extract from the image called *Region of Interest Picture* (RoiPic). For this task the *RoiPicFinder* isolates image regions by thresholding over certain ranges of hue, saturation, and value (*HSV*) for binarising in relevant parts and background, and applies the contour finder from OpenCV[5] for segmentation [9]. Note: Here, one also could use more precise but less fast methods like connected component labelling or clustering [4]. Finally, the RoiPicFinder computes the axis aligned bounding boxes, which are used to crop and return the RoiPic. Figure 3a–c visualise the processing steps. Furthermore, the vision system offers a multiple-purpose feature extracting module that can determine various features from the RoiPic to return an input for a learner in the hybrid ensemble learning system. The learning system is realised by the *RoiPicProcessor* and can combine an arbitrary number of learners based on different features.
- **Motion:** The motion controller can be requested to move the robot body in the environment, e.g. to point to an object with the arm.

[4] *PocketSphinx* is an open source *automatic speech recognition* (ASR) system, optimised for hand-held devices and robots—www.cmusphinx.sourceforge.net.

[5] The *Open Source Computer Vision* (OpenCV) library is a framework for state-of-the-art computer vision algorithms—www.opencv.willowgarage.com/wiki/.

All modules are interconnected but distributed and autonomous, allowing to extend the system, e.g. with different feature extractors or to enrich the robot's behaviour by a more capable motion, thus offering a richer interaction with the environment. However, the central idea here is to research into learning objects by natural language, thus the focus of this study is on the hybrid ensemble.

4 Hybrid Ensemble Learning

For the learning we developed a hybrid ensemble system based on a set of neural associator networks called *Learners* [3]. Each network is a three-layer MLP that takes the result of a feature extractor as input and computes the classification *confidences* for a chosen number of classes as output. The ensemble votes for the class $c \in C$ with the highest confidence $o_{\text{ensemble,c}}$, which is determined as follows:

$$o_{\text{ensemble,c}} = \frac{\max_{l \in L}\left(o_{l,c} \cdot g_l\right)}{\sum_{l \in L}\left(o_{l,c} \cdot g_l\right)} \quad , \tag{1}$$

where for every Learner $l \in L$ the output o is weighted by a chosen value g.

For the neural Learners we employed ENCOG,[6] while for the feature extractors we developed three different own types of features ourselves, as described below:

Pixel Pattern Features: The simplest features we extract from a RoiPic is the pixel pattern of the object. To determine these features for the so called *TiniPic*, we scaled the isolated image from a RoiPic to the fixed size of 16×16 pixels with RGB values. The resulting 768 data points were normalised to floating point values within $[-1, 1]$ and could be fed into a Learner. Figure 3 presents the steps to determine the scaled TinyPic.

Colour and Texture Features: For the human, eye colour and textural characteristics of an object are important [6]. Based on this bio-informed concept we developed a sophisticated extractor to determine twelve colour and texture features

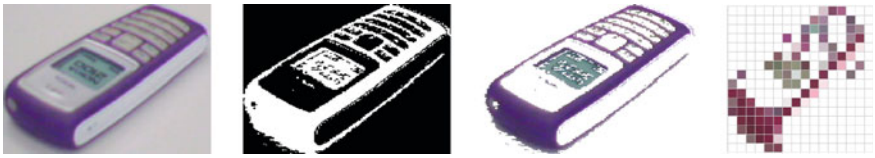

Fig. 3 Region of interest processed to determine a 16×16 pixel pattern. **a** Region of interest. **b** Threshold filter. **c** Isolated object. **d** Scaled

[6] *ENCOG* is a machine learning library focused on advanced neural networks and recent training methods—www.heatonresearch.com/encog/.

Table 1 Developed colour and texture features

Proportion of coloured pixels being of a certain colour (for six, nine, and twelve colours—each for 0° and 30°)	Proportion of pixels that have colour information (exceeding saturation and brightness threshold)
sine of average colour of coloured pixels	*cosine* of average colour of coloured pixels
Average brightness of object	Average saturation of object
Average brightness of coloured pixels	Average saturation of coloured pixels
Average grey value (average brightness of not coloured pixels)	Proportion of pixels, which are part of the object (not background)
Colour spectrum of coloured pixels	Brightness spectrum of not coloured pixels

from a RoiPic as detailed in Table 1. For all features we normalised the values to the interval $[-1, 1]$ to be able to input them to a Learner.

The "proportion of colour" features are calculated by dividing the colour space in six, nine, and twelve colours respectively. Further proportion of colour features are computed by shifting the HSV colour value by 30 before assigning it to the new colour space. The proportion of saturation and brightness is achieved by dividing their spaces in eight components. The test for matching the twelve colours is done by comparison to the HSV scale. The intervals for the colours are centred around 0° (red), 30° (orange), etc. and overlap as the intervals span $\pm 20°$ from the centre. With this method a pixel can be both e.g. red and orange, which is close to what happens in human perception.

Standardised SURF features: The conventional *SURF* [2] algorithm is able to robustly detect and recognise local features of an object in an image. However, the format of the conventional SURF features makes it impossible to combine SURF with many other learning methods, e.g. associator networks, because the dimensionality of the representation for a specific object is not known a-priori. Usually SURF results in a very large set of features for a complex object and a very small set of features for plain objects. To overcome this issue we standardised the output of the SURF extractor as follows:

We reduced the 64 double values to eight double values by summing up blocks of eight numbers and determined a seven bit number, where each bit represents a rise (bit set to 1) or a fall (bit set to 0). The remaining highest bit in the byte was determined by the Laplacian, which was calculated by the SURF extractor. The resulting kind-of "hash" (256 bits) is consistent in sparseness, leads to an unique characterisations of an object, and can be fed to a Learner.

5 Evaluation

To evaluate the system we tested its behaviour in a number of dialogues with different human teachers and observed a very natural interaction and good learning success without notable delays: The computations of the system are performed in parallel to the speech output, providing a real-time response at any time.

To offer a more comparable evaluation we also ran several experiments to quantify the object detection and object learning capabilities. For all experiments we set up the system with an ensemble consisting of five colour and texture Learners, three pixel pattern Learners, and two standardised SURF Learners. The neural networks underlying these *classifiers* have been specified with 100 hidden nodes, 21 output nodes, sigmoidal transfer functions, and randomised weights in $[-0.25, 0.25]$. They have been trained with RPROP [3] for either a maximum of 100 epochs or until a mean error of at most $\epsilon = 0.01$ was reached.

5.1 Object Detection

To evaluate the quality of our detected objects by means of the determined region of interest (dimensions and position), we developed the following metric:

$$q = \frac{A_{RF} - |A_{RF} - A_{GT}|}{A_{GT} + |A_{RF} - A_{GT}| + d_e(POS_{GT}, POS_{RF})}, \tag{2}$$

where A is the area in pixels, d_e the euclidean distance, POS the bounding box reference point, RF the results of the RoiPicFinder, and GT the ideal result.

For all ten objects we collected 20 samples covering different rotation and scaling as well as different lighting conditions in our standard lab environment (compare Fig. 1) and ran two experiments. In the first experiment we employed the near optimal grey scale value during the thresholding step, while in the second experiment we used HSV values. For five representative objects the results of the quality of the obtained regions of interest are shown in Table 2, pointing out that our developed method led to:

(a) a good object detection for most objects—except for objects with high diversity in the texture—with near optimal values (in 0.074 s), and
(b) an overall very good object detection with HSV values (in 0.71 s).

Table 2 Results for the quality q of determined regions of interest

Object class	average	min	max
Thresholding based on near optimal grey scale values			
Apple	0.886	0.552	0.989
Banana	0.111	−0.383	0.986
Dice	0.903	0.683	0.999
Mobile	0.793	0.446	0.998
Pear	0.690	0.252	0.996
Thresholding based on HSV values			
Apple	0.945	0.675	0.997
Banana	0.859	0.671	0.994
Dice	0.960	0.909	0.987
Mobile	0.949	0.844	0.996
Pear	0.959	0.824	1.000

5.2 Object Learning and Generalisation

For testing the generalisation capabilities we used the standard metrics precision $p_{\text{precision}} = tp/(tp + fp)$ and recall $p_{\text{recall}} = tp/(tp + fn)$, where we defined all correct classifications as *tp* (true positives), all classifications for an incorrect class as *fp* (false positives), and all classifications with a *confidence* $o < 0.45$ as *fn* (false negatives).

For every object we divided the set of samples into a training set with 15 samples and a test set with 5 samples and conducted two experiments. In the first one we trained and tested with all objects, while in the second we trained and tested only with the three very similar objects "Dice", "Mobile", and "Tissue". The results show that for a diverse set of objects the colour and texture classifiers achieve very good results, still performing good for similar objects. The hybrid ensemble leads to good up to very good results in all settings (see Table 3).

Table 3 Classification results on the test set for all and similar objects

Classifier	$p_{\text{precision}}$	p_{recall}
For all objects		
Pixel pattern	0.590	0.976
Color & Texture	0.984	1.000
Standardised SURF	0.391	0.895
Ensemble	0.979	0.939
For similar objects		
Pixel pattern	0.644	1.000
Color & Texture	0.893	1.000
Standardised SURF	0.621	1.000
Ensemble	1.000	1.000

6 Conclusion

In this paper we investigated the needs for human-robot interaction and developed a distributed intelligent system to enable a humanoid robot to learn about its environment by a human teacher via a dialogue. The combination of recent frameworks and a number of specially developed methods for object detection and learning led to a system working in real time and in a real environment.

For the object detection we learned that using simple well elaborated methods already can alleviate the problem of real time processing tremendously. Finding good parameters e.g. for thresholding still is an issue but can be overcome by more recent methods once they can be computed very fast [4]. The learning with hybrid ensembles works well and taught us to take very diverse classifiers into account, which are also inspired by human capabilities, e.g. the processing of texture information [6]. A very diverse or even multi-modal set of classifiers needs to be

integrated in a smart way, but this can be solved with other learning mechanisms on top, e.g. advanced self-organising networks [1].

In the future we aim to push further the natural interaction of the robot. A robot could, for instance, explore a whole room on its own and learn about objects by touching and manipulating them. This can help to understand the behaviour of young children and the need for autonomous learning systems [10].

Acknowledgments The authors would like to thank Sven Magg and Nils Meins for very inspiring as well as very helpful discussions. This work has been partially supported by the KSERA project funded by the European Commission under n° 2010-248085 and by the RobotDoC project funded by Marie Curie ITN under 235065.

References

1. Bauer J, Weber C, Wermter S (2012) A som-based model for multi-sensory integration in the superior colliculus. In: Proceedings of the 2012 international joint conference on neural networks (IJCNN), IEEE, Brisbane, Australia, June 2012, pp 1–8
2. Bay H, Tuytelaars T, Gool LV (2006) Surf: speeded up robust features. Comput Vis Image Und 110(3):404–417
3. Du KL, Swamy MNS (2006) Neural networks in a softcomputing framework. Springer, New York
4. He L, Chao Y, Suzuki K, Wu K (2009) Fast connected-component labeling. Pattern Recogn 42(9):1977–1987
5. Heinrich S, Wermter S (2011) Towards robust speech recognition for human-robot interaction. In: Proceedings of the IROS2011 workshop on cognitive neuroscience robotics (CNR), San Francisco, CA, USA, Sept 2011, pp 29–34
6. Mel BW (1997) SEEMORE: Combining color, shape and texture histogramming in a neurally-inspired approach to visual object recognition. Neural Comput 9(4):777–804
7. Pfeifer R, Bongard J, Berry D (2011) Designing intelligence: why brains aren't enough. GRIN Verlag, Munich
8. Spranger M, Loetzsch M, Steels L (2012) A perceptual system for language game experiments. In: Language grounding in robots, Springer, NY, pp 89–110
9. Suzuki S, Abe K (1985) Topological structural analysis of digitized binary images by border following. Comput Vis Graph Image Process 30(1):32–46
10. Vernon D, von Hofsten C, Fadiga L (2011) A roadmap for cognitive development in Humanoid robots. Springer, Heidelberg
11. Wada K, Shibata T (2008) Social and physiological influences of living with seal robots in an elderly care house for two months. Gerontechnology 7(2):235

Verbally Assisting Virtual-Environment Tactile Maps: A Cross-Linguistic and Cross-Cultural Study

Kris Lohmann, Junlei Yu, Matthias Kerzel, Dangxiao Wang and Christopher Habel

Abstract The Verbally Assisting Virtual-Environment Tactile Maps (VAVETaM) approach proposes to increase the effectiveness of tactile maps by realizing an intelligent multi-modal tactile map system that generates assisting utterances that generates assisting utterances acquiring survey knowledge from virtual tactile maps. Two experiments in German conducted with blindfolded sighted people and with blind and visually impaired people show that both types of participants benefit from verbal assistance. In this paper, we report an experiment testing the adaptation of the German prototype to be useable by Chinese native speakers. This study shows that the VAVETaM system can be adapted to Chinese language with comparable small effort. The Chinese participants' achievement in acquiring survey knowledge is comparable to those of the participants in the German study. This supports the view that human processing of representationally multi-modal information is comparable between different cultures and languages.

K. Lohmann (✉) · J. Yu · M. Kerzel · C. Habel
Department of Informatics, University of Hamburg, Hamburg, Germany
e-mail: lohmann@informatik.uni-hamburg.de

J. Yu
e-mail: jyu@informatik.uni-hamburg.de

M. Kerzel
e-mail: kerzel@informatik.uni-hamburg.de

C. Habel
e-mail: habel@informatik.uni-hamburg.de

D. Wang
State Key Lab of Virtual Reality Technology and Systems, Beihang University, Beijing, China
e-mail: hapticwang@buaa.edu.cn

F. Sun et al. (eds.), *Foundations and Practical Applications of Cognitive Systems and Information Processing,* Advances in Intelligent Systems and Computing 215,
DOI: 10.1007/978-3-642-37835-5_71,

Keywords Spatial knowledge acquisition · Virtual tactile map · Audio-tactile map · Multi-modal interface · Verbal assisting utterances · Virtual haptics

1 Introduction

Maps are important and highly successful means to acquire spatial knowledge about environments. Today, in the time of geographical information systems and the WWW, maps are more ubiquitous and easy to access than ever before. But, traditionally, printed maps as well as their modern counterparts, such as Google Map, are primarily designed and realized for sighted people. To provide access to adequate spatial information for blind and visually impaired people, tactile maps are used as substitutes [4]. Since reading tactile maps can be complicated and time consuming, tactile maps accessible via virtual haptic environments have been developed and verified to be usable by people with special needs [5]. Such maps can be generated on the basis of data available online [7].

To increase the effectiveness of spatial knowledge acquisition from tactile maps in virtual haptic environments, we developed the Verbally Assisting Virtual-Environment Tactile Map (VAVETaM) system, which combines spatial language and virtual variants of tactile maps [6, 9, 11]. The virtual variants of tactile maps can be perceived using the Sensable Phantom Omni haptic device (www.sensable.com). This device is placed on the desktop and allows a map user to explore three-dimensional virtual objects via force-feedback. In our case, the virtual objects are virtual variants of tactile maps generated on the basis of 3D models similar to those used in computer games and visual virtual environments. Objects on the maps are displayed as indentations and groves on a planar surface. To interact with these maps, the user holds and moves a pen-like handle attached to a small robotic arm mounted on the base of the device. The handle can be moved in all three dimensions. Sensors in the device measure the position of the handle and servomotors generate appropriate force-feedback, so that perceiving the virtual tactile map is enabled. The interaction can be pictured approximately like the exploration of a real object with a pen.

Empirical research conducted with assisting utterances in German has shown that blindfolded sighted people benefit from verbal assistance only with respect to their knowledge about landmarks (such as buildings), but not in their knowledge about tracks (such as streets) [10]. In contrast, blind and visually impaired people benefit in both types of spatial knowledge [8].

In this paper, we report on the potential for adapting the first, German-oriented, VAVETaM prototype to be useable by Chinese native speakers. Chinese instead of German assisting utterances were given and user experiments were conducted in China with Chinese native speakers. The results of the study, that has a cross-cultural and cross-linguistic perspective, have important implications. They show that the VAVETaM system for non-visual map access can be adapted to Chinese

language with comparable small effort and still be comparable efficient—besides all syntactic and semantic differences between the languages. Furthermore, they show that human processing of representationally multi-modal information (i.e., information that combines different representational systems, e.g., maps and language, see [1] for a discussion of representational modalities) is comparable between different cultures and languages.

2 Method

2.1 Participants

The data of 24 participants was evaluated (17 males, mean age: 25.4 years, SD: 2.7 years). All participants were compensated on a monetary basis. They were naïve about the purpose of the experiment. All participants gave written informed consent and reported to speak Chinese on a native-speaker level. All participants used their self-reported primary hand for the exploration of the virtual tactile map. Only one participant reported to be left-handed.

2.2 Materials and Procedure

Maps. The virtual tactile maps were explored using the Phantom haptic device. The material was similar to the experiment that was previously performed with German assistance [10], in the following referred to as the German-assistance experiment. The maps used were the same as those used in the German-assistance experiment. The maps included five tracks (track is a more general term for street-like structures) and six potential landmarks (one tree and five buildings). See Fig. 1 for a visualization of the maps used.

Assisting Utterances. The assistances were recorded before the study. They were given in Chinese, spoken by a 24-year-old male native Chinese speaker. The participants heard the utterances via headphones.

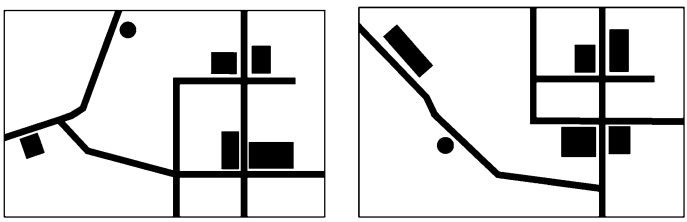

Fig. 1 Visualization of the two maps (map 1 to the *left* and map 2 to the *right*) used in the experiment

Two sets of typical Chinese names that could be used for both maps were created (the number of streets and potential landmarks is identical on both maps). The set of assisting utterances that was used is a translated version of those used in the German study. The assisting utterances are grouped by message classes. A message class is defined by the information that an utterance of a class expresses. In the context of the present paper, the identification message class is important. An utterance of the identification message class informs the user of the virtual tactile map about the identity of the map object that is explored. Usually, this is done by stating the proper name of the map object in combination with a demonstrative. If an object does not have a proper name, e.g., an intersection, it can often be identified by referring to related other objects that carry proper names. For the intersection example, these are the names of the streets that form the intersection (see example (1d) below). A detailed discussion of the other message classes is out of the scope of this paper (see [9], for a detailed discussion of message classes). In the following, the assisting utterances that were included in the two different assistance conditions are discussed.

In the *identification-assistance condition* that provided the baseline for the described study, only utterances of the identification message class were included. Example (1a) is an English counterpart[1] of an assisting utterance that was given when the map object representing the street named 'Main Street' was explored. Examples (1b) and (1c) are translations of identification messages for the frame of the map and the building called 'JFK High School'. In the present study, in addition to streets and landmarks that carry a proper name, intersections and dead ends were identified. For example, crossings were identified by utterances such as (1d) and dead ends were identified by utterance such as (1e).

(1a) This is Main Street.
(1b) This is the left map frame.
(1c) This is JFK High School.
(1d) This is the crossing Main Street Madison Avenue.
(1e) This is the dead end that forms the right end of Madison Avenue.

Additional information was given in the *extended-assistance condition*. (2a)–(2f) are examples for English counterparts of assisting utterances given in this condition when track objects were explored. (3a) and (3b) are translations of assisting utterances stated when a potential-landmark object was explored.

The extended-assistance condition included verbal information about the extend of tracks, i.e., what determines the end of a track was uttered [see example (2b)]. The set of utterances included information about the intersections a track had and spatial relations with other tracks and landmarks [see examples (2a), (2c),

[1] See the Appendix for examples of German and Chinese items used in the language specific experiments. The English counterparts in the paper are used to present the approach and the empirical studies independent from the linguistic characteristics of Chinese and German.

and (2d)]. Furthermore, for parts of tracks that were close to landmarks or between landmarks, assisting utterances were given that stated this relation [see (2f)].

For potential landmarks, the set of utterances in the extended-assistance condition included utterances that stated the relation to other map objects [see (3a)] and, if appropriate, the global location in the map [see (3b)].

(2a) Main Street is parallel to Hill Street.
(2b) Main Street ends to the left at an intersection with Church Street, and to the right in a dead end.
(2c) Below Main Street, there are JFK High School and St. Mary Church.
(2d) Main Street intersects with Madison Avenue.
(2e) This is the intersection between Main Street and Madison Avenue.
(2f) Now, you are between JFK High School and St. Mary Church.
(3a) JFK High School is located below Main Street.
(3b) St. Mary Church is located in the upper part of the map.

The experimenter started the playback of the utterances using custom-built software developed for that purpose. The experimenter saw the hand movement of the map user as a moving red dot on a visualization of the map. The experimenter started an utterance when the participant explored the corresponding map object. Color-indication was used to state which button belonged to which object on the map.

Earlier empirical studies indicated that if a map object is explored, giving information of the identification message class should precede any other information. Hence, the experimenter started an utterance of the identification class prior to any other assistance in the extended-assistance condition. The other utterances for that object were given in the order that the experimenter found most appropriate. However, we avoided unnatural repetitions of utterances. To ease this, the buttons for utterances that were started once were marked in the interface.

Sketch-Mapping Task. Following the exploration with one of the assistance conditions described, the spatial knowledge that the participants gained by the exploration of the map was tested. First, participants were asked to sketch the map they learned as precisely as possible. They were instructed to include all they remember. For a discussion of the reliability of sketch maps as testing methods for spatial knowledge see [2]. The frame defining the dimensions of the map was printed on the paper for sketching.

All 48 sketches were evaluated by two independent raters. The rating was performed in two respects: (1) to what degree does the sketch resemble the original map concerning the course of roads, their parallelism, and the junctions they have and (2) to what degree are potential landmarks represented at the correct position? The rating was performed on a 5-point Likert-type scale. A rating of 1 is associated with ‘does not reflect the original’ and 5 is associated with ‘reflects the original precisely’.

Configuration-Questions Task. After participants completed the sketch map, they were asked to answer to questions about configurations of map objects. The

full test consisted of 20 questions. Where it was possible, those questions asked for object configurations between objects that were not explicitly stated in the pre-recorded assisting utterances. The experimenter stated the questions in a predetermined individual random order. 10 questions involved spatial relations including potential landmarks and 10 were only about the configuration of and relations between tracks. The answering options were 'yes', 'do not know', and 'no'. 10 questions were answered correctly with a 'no' and 10 questions with a 'yes'. A correct 'yes' and correct 'no' were evaluated as correct answers. A wrong 'yes', a wrong 'no', and 'do not know' were evaluated as wrong answers.

In the experimental procedure, each set of names occurred with each map. Therefore, 4 sets with 20 configuration questions were developed. The questions of those sets were matched with each other. For example, question 1 always asked for the relation of two landmarks that were relatively distant to each other and was always correctly answered with 'yes' and question 17 always asked if two streets are parallel and was always correctly answered with 'no'. Two sets of questions were created for each map. This resulted from the use of two different name sets, as described above. The individual questions for each name set always asked for a spatially equivalent fact. For example, in map 1 for name set 1 question 1 was 'Is the oak tree left of JFK High School?' (English names are used for illustrative purposes). In name set 2, the map object that was the 'oak' in name set 1 was called 'beech'. The map object that was called 'JFK High School' in name set 1 was called 'St. Patrick Church'. Consequently, question 1 for the map 1 with name set 2 was: 'Is the beech tree left of St. Patrick Church?'

Procedure. The experiment was performed as a repeated-measures experiment with assistance condition as within-subject variable. This design was chosen to overcome the problem of individual differences in the ability to understand virtual tactile maps resulting from differences in spatial abilities (see [13], for a discussion of individual differences in spatial abilities).

To avoid carry-over effects, two different maps and name sets were used for the different experimental conditions. To control for order effects that bias the main research question, the experiment was fully counterbalanced concerning the order of assistance conditions, maps, and name sets. Accordingly, the second learning procedure was performed with the map, the assistance condition, and the name set that were not used in the first condition. Consequently, the extended-assistance condition occurred as often as first learning condition as the identification-assistance condition. Furthermore, map 1 and name set 1 occurred as often as map 2 and name set 2.

To ensure that the participants understood the haptic interaction with the multimodal system, they were trained in different aspects of it. To conclude the training, participants were tested for their ability to identify the shape of objects (such as a triangle and a square) and to follow a complex track structure without leaving it while receiving and following assistance given by the experimenter. The training procedure including the training test took 30–60 min.

After a short break, participants read written instructions about the time they had for exploration and the tasks they had to solve after map learning. The

information about the tasks was included to minimize order effects resulting from knowledge of the tasks from the first condition. For the same purpose, an example map similar to the ones used in the experimental conditions was printed on the instructions. Participants were instructed to read the map in a way that they would find the route from each potential landmark to each other.

Each exploration was limited to 8 min. Participants were informed when they had 2 min left. After the first exploration, first the relation-questions task was performed, then participants created the sketch map. A 10-min break was made before the participants performed the second exploration under the same time constraint as the first exploration.

3 Results

3.1 Configuration-Questions Task

Taking all questions into account, the average result showed that participants were able to answer significantly more questions correctly ($t(23) = 5.03$, $p < 0.001$) when they learned the map under the extended-assistance condition and the effect is large ($r = 0.72$) (according to [3]).

An item reliability analysis was performed to control for reliability of the scales. For reasons that are explained in the remainder of this section, questions only about tracks and questions involving potential landmarks were regarded as two subscales and the reliability analysis was performed independently for each of the subscales. Two questions were excluded from further analysis as they did not increase overall reliability of the subscales. For the following analysis of the data, we assumed that the name set and the maps do not have an effect on the items (no significant effects of the map or the name set used were found in the analysis of the remaining 18 questions).

In the German-assistance experiment, the assistance condition had a strong effect on some, but not on all of the questions. Whereas the answers to the landmark-related questions showed large differences between the conditions, the answers to the questions that only involved tracks did not. Screening the dataset of the Chinese-assistance experiment, this finding could be replicated.

For the two resulting types of knowledge, two subscales were constructed and tested for reliability by calculating Cronbach's alpha. Since the questions involving landmarks differed from those involving only tracks, these subscales are named the landmark subscale and the track subscale. The landmark subscale with the remaining nine items provides a good reliability ($\alpha = 0.848$). The track subscale with the remaining nine items provides an acceptable reliability ($\alpha = 0.704$). See [10] for an English translations of the questions (of the set presented there, question 8 was excluded in the current experiment to improve reliability). Figure 2 shows the mean number of correct answers to the configuration questions after the learning conditions and for the two subscales. The figure indicates that extended

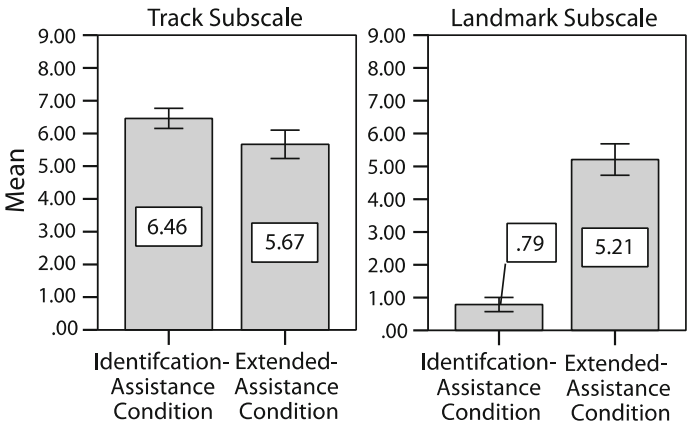

Fig. 2 Mean number of correct answers in the track subscale and in the landmark subscale of the configuration-question task. *Error bars* represent the standard error of the mean

assistance leads to a larger amount of correctly localized landmarks and the knowledge about the track structure is comparable between learning conditions.

Separate mixed-design ANOVAs were calculated for each subscale. In both subscales, there were no significant main effects of gender, order of conditions, order of the maps used, or the order of the set of names ($p > 0.05$). Therefore, these variables were stepwise excluded from the model for further analysis. Effects of handedness was not evaluated as only one left-handed person took part in the experiment.

In the track subscale, there was a non-significant trend that participants performed worse in the extended-assistance condition than in the identification-assistance condition ($F(1,23) = 3.61$, $p = 0.07$, $r = 0.37$).

In contrast, there was a highly significant and large effect of the assistance condition on the amount of correct answers in the landmark subscale ($F(1,23) = 69.10$, $p < 0.001$, $r = 0.87$). Participants were able to answer more questions correctly after having learned the map in the extended-assistance condition (Fig. 2).

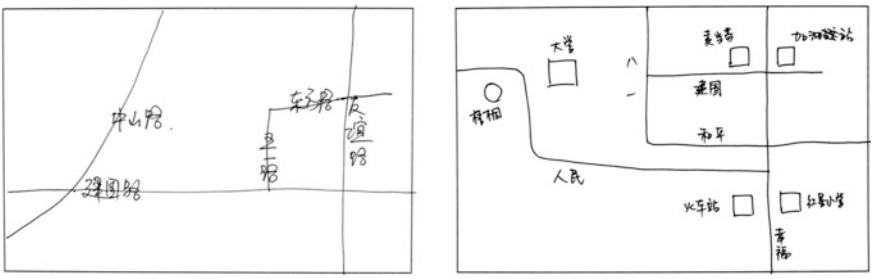

Fig. 3 Example of a participant's sketch of map 1 after learning the map in the identification-assistance condition and example of a participants sketch of map 2 after learning the map in the extended-assistance condition

3.2 Sketch-Mapping Task

Two native Chinese raters evaluated the sketches (for examples, see Fig. 3). The intraclass-correlation coefficient was calculated to test the agreement between the raters. The agreements of the track ratings ($ICC(3,1) = 0.81$) and of the potential-landmark ratings ($ICC(3,1) = 0.95$) were calculated separately [12]. Both agreements are good. The values of the raters were averaged before the analysis. Figure 4 shows the mean ratings of the sketches. The values suggest that the sketches reflected knowledge about potential landmarks better when the map was learned under the extended-assistance condition.

Separate mixed-design ANOVAs were calculated for the landmark-configuration ratings and the track-structure ratings. In both ratings, there were no significant main effects of gender, handedness, the order of the maps used, or the order of the conditions. Therefore, these variables were stepwise excluded from the model for further analysis.

Concerning how well the track structure was reflected, no significant effect of the set of names was present in the data. Therefore, this between-subjects variable was excluded from the model as well. No significant effects of assistance condition were found ($F(1,23) = 0.84$, $p > 0.05$, $r = 0.19$).

In contrast, the mean rating of how well the landmarks are represented in the sketches showed a significant main effect of the set of names used in the extended condition. Participants who performed the experiment in a setting in which name set 2 was used in the extended condition performed significantly better than participants which learned the map in the extended condition with the name set 1 ($F(1,22) = 4.82$, $p < 0.05$, $r = 0.42$). Additionally, an interaction effect of assistance condition and name set was present in the data. Again, participants who performed the experiment in a setting in which the name set 2 was used in the

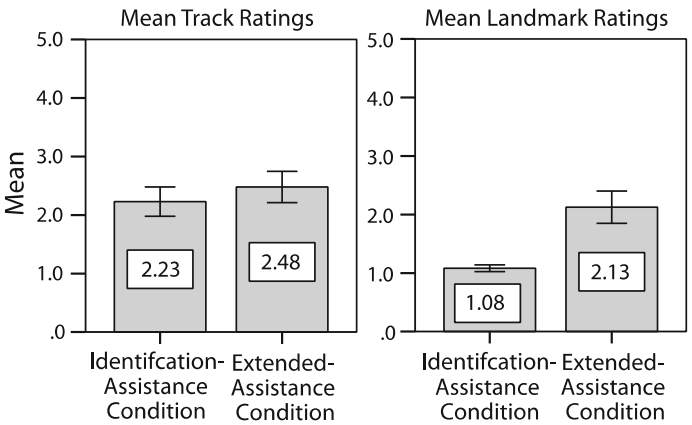

Fig. 4 Mean ratings of the track structure and the landmark configuration on the sketches. *Error bars* represent the standard error of the mean

extended condition performed significantly better than participants which learned the map in the extended condition with the first name set ($F(1,22) = 5.24$, $p < 0.05$, $r = 0.44$).

Most important for the purpose of the study, the ratings for how well potential landmarks were reflected in the sketches were significantly affected by the assistance condition ($F(1,22) = 16.71$, $p < 0.001$, $r = 0.65$).

4 Conclusion

The study reported follows a study previously conducted in the German language. Both studies were performed with blindfolded participants. The reported study conducted in the Chinese language confirmed the finding that knowledge gained using the VAVETaM system consists of two subtypes: (1) knowledge about the structure of tracks and (2) knowledge about the configuration of potential landmarks. A clear effect of extended assistance is found in this study: Participants scored higher in all tests assessing the knowledge about potential landmarks. In contrast to the clear effect in the knowledge about potential landmarks, no test showed a significant effect of assistance condition on track knowledge. Rather, there is a non-significant trend in the data of the configuration questions that participants scored lower in questions of the track subscale. However, overall, participants benefit from extended assistance.

The study reported was performed in the framework of the development of the VAVETaM system, which is intended to help blind and visually impaired people. The results indicate that the system could be adapted to the Chinese language: Generally, the results are in line with the results obtained in the experiment conducted in Germany. This also indicates that the processing of representationally multi-modal information is to some extent culture and language independent.

A.1 5 Appendix

Table A.1 Name sets used in the German-assistance experiment [10] and corresponding name sets used in the Chinese-assistance experiment

	German names and English translation		Chinese names and English translation	
Name set 1	Poststraße	Post street	人民路	Renmin road
	Humboldtstraße	Humboldt street	解放路	Jiefang road
	Eiche	Oak	梧桐树	Parasol tree
	Hauptbahnhof	Central railway station	火车站	Railway station
	Christus-Kirche	Christ church	加油站	Gas station

(continued)

Table A.1 (continued)

	German names and English translation		Chinese names and English translation	
	Berthold-Brecht-Schule	Berthold-Brecht-school	红星小学	Hongxing primary school
Name set 2	Dorfstraße	Village street	东方路	Dongfang road
	Bergstraße	Hill street	建国路	Jianguo road
	Buche	Beech	柳树	Willow
	Rathaus	Town hall	法院	Court of justice
	Gedächtnis-Kirche	Memorial church	银行	Bank
	Anne-Frank-Schule	Anne-Frank-school	科技小学	Keji primary school

References

1. Bernsen NO (1994) Foundations of multimodal representations: a taxonomy of representational modalities. Interact Comput 6(4):347–371
2. Blades M (1990) The reliability of data collected from sketch maps. J Environ Psychol 10 (4):327–339
3. Cohen J (1992) A power primer. Psychol Bull 112(1):155–159
4. Espinosa MA, Ungar S, Ochaita E, Blades M, Spencer C (1998) Comparing methods for introducing blind and visually impaired people to unfamiliar urban environments. J Environ Psychol 18:277–287
5. De Felice F, Renna F, Attolico G, Distante A (2007) A haptic/acoustic application to allow blind the access to spatial information. In: World haptics conference, pp 310–315
6. Habel C, Kerzel M, Lohmann K (2010) Verbal assistance in tactile-map explorations: a case for visual representations and reasoning. In: Proceedings of AAAI workshop on visual representations and reasoning 2010, Menlo Park, CA, USA
7. Kaklanis N, Votis K, Moschonas P, Tzovaras D (2011) HapticRiaMaps: towards interactive exploration of web world maps for the visually impaired. In: Proceedings of the international cross-disciplinary conference on web accessibility, Hyderabad, India
8. Lohmann K (2013) Verbally assisting virtual tactile maps. An interface for visually impaired people. Dissertation, Universität Hamburg
9. Lohmann K, Eschenbach C, Habel C (2011) Linking spatial haptic perception to linguistic representations: assisting utterances for tactile-map explorations. In: Egenhofer M, Giudice N, Moratz R, Worboys M (eds) Spatial information theory. Springer, Berlin, pp 328–349
10. Lohmann K, Habel C (2012) Extended verbal assistance facilitates knowledge acquisition of virtual tactile maps. In: Stachniss C, Schill K, Uttal DH (eds) Spatial cognition 2012. Springer, Berlin, pp 299–318
11. Lohmann K, Kerzel M, Habel C (2012) Verbally assisted virtual-environment tactile maps: a prototype system. In: Graf C, Giudice NA, Schmid F (eds) Proceedings of spatial knowledge acquisition with limited information displays 2012, Seeon, Germany
12. Shrout PE, Fleiss JL (1979) Intraclass correlations: uses in assessing rater reliability. Psychol Bull 86(2):420–428
13. Wen W, Ishikawa T, Sato T (2011) Working memory in spatial knowledge acquisition: differences in encoding processes and sense of direction. Appl Cogn Psychol 25:654–662

Structural Similarity-Optimal Total Variation Algorithm for Image Denoising

Yu Shao, Fuchun Sun, Hongbo Li and Ying Liu

Abstract Image denoising is a traditional problem which has been tackled using a variety of conceptual frameworks and computational tools. Total variation-based methods have proven to be efficacious toward solving image noise removal problems. Its purpose is to remove unnecessary detail and achieve optimal performance in terms of mean squared error (MSE), a metric that has been widely criticized in the literature due to its poor performance as an image visual quality assessment. In this work, we use structural similarity (SSIM) index, a more accurate perceptual image measure, by incorporating it into the total variation framework. Specifically, the proposed optimization problem solves the problem of minimizing the total gradient norm of restored image and at the same time maximizing the SSIM index value between input and reconstructed images. Furthermore, a gradient descent algorithm is developed to solve this unconstrained minimization problem and attain SSIM-optimal reconstructed images. The image denoising experiment results clearly demonstrate that the proposed SSIM-optimal total variation algorithm achieves better SSIM performance and better perceptual quality than the corresponding MSE-optimal method.

Keywords Image denoising · Total variation · Structural similarity · Gradient descent

1 Introduction

The total variation minimization model [1] is a regularization approach capable of preserving edges and removing noise in a given image. This model has proven to be successful in a wide range of applications in image processing. Mean squared

Y. Shao (✉) · F. Sun · H. Li · Y. Liu
State Key Laboratory of Intelligence Technology and Systems, Department of Computer Science and Technology, Tsinghua University, Beijing 100084, People's Republic of China
e-mail: shaoyu2011@foxmail.com

F. Sun et al. (eds.), *Foundations and Practical Applications of Cognitive Systems and Information Processing*, Advances in Intelligent Systems and Computing 215,
DOI: 10.1007/978-3-642-37835-5_72,

error (MSE) has been the most popular metric used in total variation algorithms. The methods are developed and optimized to generate the output image that has minimum MSE with respect to the target image [2–6]. However, MSE is not the best choice when it comes to image quality assessment (IQA) and signal approximation tasks since MSE optimized algorithms do not necessarily produce images with the highest visual quality [2]. Among the recent objective perceptual measures, the SSIM index [7] as a powerful perceptual distortion metric has the simplest formulation and has gained widespread popularity in a wide range of practical applications. The design of SSIM is inspired by the performance of the human visual system (HVS). Since most images are intended for viewing by the human eye, using this metric in designing image processing algorithms instinctively takes into account the properties of the HVS.

SSIM has a number of attractive mathematical properties [8], making it easier to be used in optimization tasks than other state-of-the-art perceptual IQA measures. However, much less has been done on using SSIM as an optimization criterion in the design and optimization of image processing algorithms and systems. It is natural to consider replacing the MSE with SSIM in total variation framework. In fact, owing to its analytic simplicity [9], this can be done with relative ease with the SSIM index. Rehman [10] incorporates the SSIM index into the framework of non-local means (NLM) [11] image denoising. In [12], a closed-form linear estimator was derived that maximizes a statistical version of the SSIM index, called statSSIM, as an alternative to the MSE solution. There have also been several attempts to incorporate SSIM in optimization frameworks in order to improve perceived image quality in image denoising [13, 14]. Several important mathematical properties of SSIM index have also been investigated in [15]. For example, the gradient of SSIM with respect to the image has been derived and used in iterative optimization procedures [16]. However, in general, deep analysis of the mathematical properties of SSIM is seriously lacking. In practice, SSIM is often used as a black box in optimization tasks as merely an adhesive control unit outside the main optimization module. Consequently, the potentials of SSIM-optimization have not been fully exploited, far behind its widespread usage as purely an assessment or comparison tool in other applications.

Since MSE is used as the data-fidelity term of optimization function in classical total variation, the resulting output image might not have the best perceptual quality. This motivated us to replace the role of MSE with SSIM in the total variation framework. Ideally, total variation optimizing algorithms with respect to the SSIM index should guarantee the desired level of visual quality. In this article, we provide solutions to these problems and use image denoising as a application to demonstrate the proposed framework. We compare the performance of the SSIM-optimal denoiser with the ubiquitous MSE-optimal denoiser and demonstrate the gain in visual quality offered by the proposed method.

The paper is organized as follows. The principle of total variation based image denoising is introduced in Sect. 2. Section 3 presents the proposed SSIM-optimal total variation framework. The experiments are analyzed in Sect. 4 and conclusions are drawn in Sect. 5.

2 Total Variation-Based Image Denoising

In image denoising problems, the goal is to estimate an original image $\mathbf{X}$ from an observed noisy image $\mathbf{Y}$. The noise-contaminated image is obtained using the following equation:

$$\mathbf{Y} = \mathbf{X} + \mathbf{N}, \tag{1}$$

where $\mathbf{Y}$ is the observed distorted image, $\mathbf{X}$ is the noise-free image, and $\mathbf{N}$ is additive Gaussian noise. Our goal is to remove the noise from distorted image and recover as much as possible of $\mathbf{X}$, from our knowledge of the statistics of the noise $\mathbf{N}$, and the observed image $\mathbf{Y}$. The problem of recovering $\mathbf{X}$ from $\mathbf{Y}$ is ill-posed. To make the problem mathematically sound, a cost function as the goal for minimization needs to be defined. Several methods have been proposed to solve this ill-conditioning problem and recover $\mathbf{X}$. Most of them can be classified as regularization methods. A classical regularization algorithm is the total variation proposed by Rudin-Osher-Fatemi [1] to solve the following minimization problem:

$$E_{\mathrm{TV}}(\mathbf{X}) = \int_{\Omega} |\nabla \mathbf{X}| \mathrm{d}x\mathrm{d}y + \lambda \int_{\Omega} \frac{1}{2}(\mathbf{X} - \mathbf{Y})^2 \mathrm{d}x\mathrm{d}y, \tag{2}$$

where the parameter λ is positive. We can interpret λ^{-1} as a penalization parameter which controls the trade-off between the goodness of fit of the constraint and the smoothness term given by the total variation. The first term is the regularization term which gives a prior model of the reconstructed image, and the last term is data-fidelity term which measures the dissimilarity between input and reconstructed image. This algorithm seeks an equilibrium state of an energy functional comprised of the TV norm of the image $\mathbf{X}$ and the fidelity of this image to the noisy input image $\mathbf{Y}$.

The regularization term in (2) can also be generalized by the Φ-formulation with the function. Its corresponding objective function is

$$E_{\Phi}(\mathbf{X}) = \int_{\Omega} \Phi(|\nabla \mathbf{X}|) \mathrm{d}x\mathrm{d}y + \lambda \int_{\Omega} \frac{1}{2}(\mathbf{X} - \mathbf{Y})^2 \mathrm{d}x\mathrm{d}y, \tag{3}$$

its Euler–Lagrange equation is given by

$$\mathrm{div}\left(\Phi'(\nabla \mathbf{X}) \frac{\nabla \mathbf{X}}{|\nabla \mathbf{X}|}\right) - \lambda(\mathbf{X} - \mathbf{Y}) = 0, \tag{4}$$

the actual Φ function which we employed in this paper is $\Phi(x) = x$, and $\Phi'(x) = 1$. The solution procedure uses a differential equation where parameter evolution along with the time, or equivalently, the gradient descent partial differential equation (PDE) method.

$$\frac{\partial \mathbf{X}}{\partial \mathrm{t}} = \mathrm{div}\left(\Phi'(\nabla \mathbf{X}) \frac{\nabla \mathbf{X}}{|\nabla \mathbf{X}|}\right) - \lambda(\mathbf{X} - \mathbf{Y}). \tag{5}$$

This means we can get a denoised image through iterative solution of equations given by (5).

3 The Proposed Method

In this section, we will incorporate SSIM as our quality measure to construct the data-fidelity term in total variation framework. Similar to the MSE-optimal way, we need to calculate the derivative of the data-fidelity term. First, the concept of SSIM is simply reviewed. Then, we propose the optimization problem for SSIM-optimal total variation, which is solved using a gradient descent approach.

3.1 Structural Similarity

The SSIM index is usually computed for local image patches, and these values are then combined to produce a quality measure for the whole image. For two image patches $\mathbf{x}$ and $\mathbf{y}$, the expression for SSIM index is

$$\text{SSIM}\ (\mathbf{x},\mathbf{y}) = \frac{(2\mu_x\mu_y + C_1)(2\sigma_{xy} + C_2)}{(\mu_x^2 + \mu_y^2 + C_1)(\sigma_x^2 + \sigma_y^2 + C_2)}, \tag{6}$$

where μ_x, σ_x^2, and σ_{xy} represent the sample mean of the components of $\mathbf{x}$, the sample standard variance of $\mathbf{x}$, and the sample covariance of $\mathbf{x}$ and $\mathbf{y}$, respectively. The small constants C_1 and C_2 are given by $C_1 = (K_1R)^2$ and $C_2 = (K_2R)^2$, respectively. Here, R is the dynamic range of the pixel values (e.g., $R = 255$ for 8 bits/pixel grayscale images), and $K_1 \ll 1$ and $K_2 \ll 1$ are two scalar constants ($K_1 = 0.01$ and $K_2 = 0.03$ in the current implementation of SSIM). The constants C_1 and C_2 are the saturation effect of the HVS.

In the SSIM implementation that Wang provided online, [17] where

$$\begin{aligned} &\mu_x = w * x, \mu_y = w * y, \sigma_{xy} = w * (x - \mu_x)(y - \mu_y) = w * (xy) - \mu_x\mu_y, \\ &\sigma_x^2 = w * (x - \mu_x)^2 = w * x^2 - \mu_x^2, \sigma_y^2 = w * (y - \mu_y)^2 = w * y^2 - \mu_y^2, \end{aligned} \tag{7}$$

in which w is a symmetric low-pass kernel (e.g., 11×11 normalized Gaussian kernel). '$*$' denotes convolution, σ_x^2 and μ_x are defined similarly.

For a local SSIM measure as in Eq. (6), we define

$$\begin{aligned} A_1(\mathbf{x},\mathbf{y}) &= 2\mu_x\mu_y + C_1, A_2(\mathbf{x},\mathbf{y}) = 2\sigma_{xy} + C_2, \\ B_1(\mathbf{x},\mathbf{y}) &= \mu_x^2 + \mu_y^2 + C_1, B_2(\mathbf{x},\mathbf{y}) = \sigma_x^2 + \sigma_y^2 + C_2, \\ N(\mathbf{x},\mathbf{y}) &= A_1(\mathbf{x},\mathbf{y})A_2(\mathbf{x},\mathbf{y}), D(\mathbf{x},\mathbf{y}) = B_1(\mathbf{x},\mathbf{y})B_2(\mathbf{x},\mathbf{y}). \end{aligned} \tag{8}$$

Although (6) gives the SSIM index between two windows, SSIM is a local quality measure when it is applied using a sliding window, it provides us with a quality map that reflects the variation of local quality over the whole image. It can also be considered as the formula for ($\mathrm{SSIM}_{\mathrm{map}}$), using element-wise addition and multiplication, with the parameters defined in (6). Let $\mathbf{x}$ and $\mathbf{y}$ be column vector representations of two image patches (e.g., 11×11 windows) extracted from the same spatial location from images $\mathbf{X}$ and $\mathbf{Y}$, respectively. At each point, map $\mathrm{SSIM}_{\mathrm{map}}$ is an indication of the local similarity of the input images. The global SSIM is computed by pooling (averaging) the local $\mathrm{SSIM}_{\mathrm{map}}$. The global SSIM or SSIM index for an image $\mathbf{Y}$, with respect to the reference image $\mathbf{X}$, is given by the following equation:

$$\mathrm{SSIM}(\mathbf{X}, \mathbf{Y}) = \frac{1}{M} \sum_{i,j} \mathrm{SSIM}_{\mathrm{map}}(\mathbf{X}, \mathbf{Y}; i, j), \tag{9}$$

here, M is the number of pixels in either of the input images $\mathbf{X}$ or $\mathbf{Y}$, and $\mathrm{SSIM}_{\mathrm{map}}(\mathbf{X}, \mathbf{Y}; i, j)$ is the value of SSIM index for windows centered at (i, j) from input images $\mathbf{X}$ and $\mathbf{Y}$.

The average of the SSIM values across the image gives the final quality measure. The design philosophy of the SSIM index is to admit the fact that natural images are highly structured, and that the measure of structural correlation (between the reference and the distorted image) is very crucial in deciding the overall image visual quality. Further, the SSIM index measures quality locally and is able to capture local dissimilarities better than other global image quality measures such as MSE or PSNR. Though SSIM index has a form that is more complicated than that of MSE, it still remains analytically tractable as discussed in the next section, especially when we can deduce the deviation of SSIM index. These important features make the SSIM index attractive to work with in image denoising application.

3.2 SSIM-Optimal Total Variation

The normal option for data-fidelity term is the MSE in regularization approach. To convert this to a perceptual optimization problem is straightforwardly replacing MSE with a perceptual IQA measure function. The solution of (3) demands the proximity between the noisy image $\mathbf{Y}$ and the output image $\mathbf{X}$, thus enforcing the global reconstruction constraint.

What we are concerned about here is the definition of the distance function, which should not only reflect perceptual image distortions (since in most applications, human eyes are the ultimate consumers of images), but should also possess good mathematical properties (so that finding optimal solutions is a manageable task). Note that $1–\mathrm{SSIM}(\cdot, \cdot)$ is used in [10] for image sparse

representation. This is motivated by the fact that 1–SSIM$(\cdot,\cdot)$ is a squared variance-normalized ℓ_2 distance [15].

As studied earlier, we propose a modified total variation method which incorporates SSIM into the procedure. The fact that $\mathrm{SSIM}(\mathbf{X},\mathbf{Y}) = 1$ only if $\mathbf{X} = \mathbf{Y}$ suggests that the function $1 - \mathrm{SSIM}(\mathbf{X},\mathbf{Y})$ could be considered a measure of the distance between $\mathbf{X}$ and $\mathbf{Y}$, so, we defined SSIM-optimal total variation as follows:

$$E(\mathbf{X}) = \int_{\Omega} \Phi(|\nabla \mathbf{X}|)\mathrm{d}x\mathrm{d}y + \lambda[1 - \mathrm{SSIM}(\mathbf{X},\mathbf{Y})]. \tag{10}$$

This optimization problem defined in Eq. (10) produces a good compromise between the TV norm of recovered image and correlation of obtained image in the maximal SSIM sense. We use a gradient descent approach to solve the optimization problem given by (10). If having the gradient of SSIM, the gradient descent approach is used with an iterative procedure. The update equation is given by

$$\frac{\partial \mathbf{X}}{\partial \mathrm{t}} = \mathrm{div}\left(\Phi'(\nabla \mathbf{X})\frac{\nabla \mathbf{X}}{|\nabla \mathbf{X}|}\right) - \lambda \partial_{\mathbf{X}} \mathrm{SSIM}(\mathbf{X},\mathbf{Y}). \tag{11}$$

In order to apply the constrained gradient descent algorithm, we need to calculate the gradients of the image quality models with respect to the image. Here the gradients are represented as matrix that have the same dimension as the images. Based on the formulation of SSIM index given above, taking the derivative of Eq. (9) with respect to $\mathbf{X}$, we have

$$\begin{aligned}\partial_{\mathbf{X}} \mathrm{SSIM}(\mathbf{X},\mathbf{Y}) = \frac{2}{M}\Bigg[&\left(w * \frac{A_1}{D}\right)\mathbf{Y} + \left(w * \frac{-\mathrm{SSIM}_{\mathrm{map}}}{B_2}\right)\mathbf{X} \\ &+ w * \frac{\mu_{\mathbf{X}}(A_2 - A_1) - \mu_{\mathbf{Y}}(B_2 - B_1)\mathrm{SSIM}_{\mathrm{map}}}{D}\Bigg],\end{aligned} \tag{12}$$

where A_1, A_2, B_1, B_2 and D are defined in Eq. (8), M is the number of pixels in either of the input images. This is a closed-form and computationally simple formula for SSIM gradient derived by breaking SSIM into linear terms. More details regarding the computation of SSIM gradient can be found in [16, 18].

If we choose $\Phi(x) = x$, then

$$\mathrm{div}\left(\Phi'(\nabla \mathbf{X})\frac{\nabla \mathbf{X}}{|\nabla \mathbf{X}|}\right) = \mathrm{div}\left(\frac{\nabla \mathbf{X}}{|\nabla \mathbf{X}|}\right) = \frac{\mathbf{X}_{ii}\mathbf{X}_j^2 - 2\mathbf{X}_i\mathbf{X}_j\mathbf{X}_{ij} + \mathbf{X}_{jj}\mathbf{X}_i^2}{\left(\mathbf{X}_i^2 + \mathbf{X}_j^2\right)^{3/2}}. \tag{13}$$

Since the problem is convex, the steady-state solution of the gradient descent is the minimizer of the problem. Therefore, the minimizer can be obtained numerically by evolving a finite difference approximation of this PDE. We initialize $\hat{\mathbf{X}}_0 = \mathbf{Y}$. The gradient descent is performed by iterating

$$\hat{\mathbf{X}}_{k+1} = \hat{\mathbf{X}}_k + \mathrm{d}t\mathrm{div}\left(\Phi'\left(\nabla\hat{\mathbf{X}}_k\right)\frac{\nabla\hat{\mathbf{X}}_k}{\left|\nabla\hat{\mathbf{X}}_k\right|}\right) - \mathrm{d}t\lambda\partial_{\mathbf{X}}\mathrm{SSIM}\left(\hat{\mathbf{X}}_k, \mathbf{Y}\right), \qquad (14)$$

where $\mathrm{d}t$ is a small positive timestep parameter. In our experiments, we find this gradient-based approach is well-behaved and it takes only a few iterations for $\mathbf{X}$ to converge to a stationary point.

4 Results

4.1 Experiment

The MSE and SSIM-optimal total variation algorithms are represented as MSE-optimal TV and SSIM-optimal TV, respectively. To provide visual comparisons of the denoising algorithms, the denoised results for image *Lena* are shown in Fig. 1, where the denoised images using MSE-optimal TV and proposed SSIM-optimal TV methods along with corresponding SSIM maps are presented. An original *Lena* image (a) is contaminated by noise and (b) denoised by two denoising algorithms, resulting in (d) and (f), respectively. The SSIM-based quality maps of the noisy and denoised images are shown in (c), (e), and (g), respectively, where brighter indicates better local quality (or lower distortion).

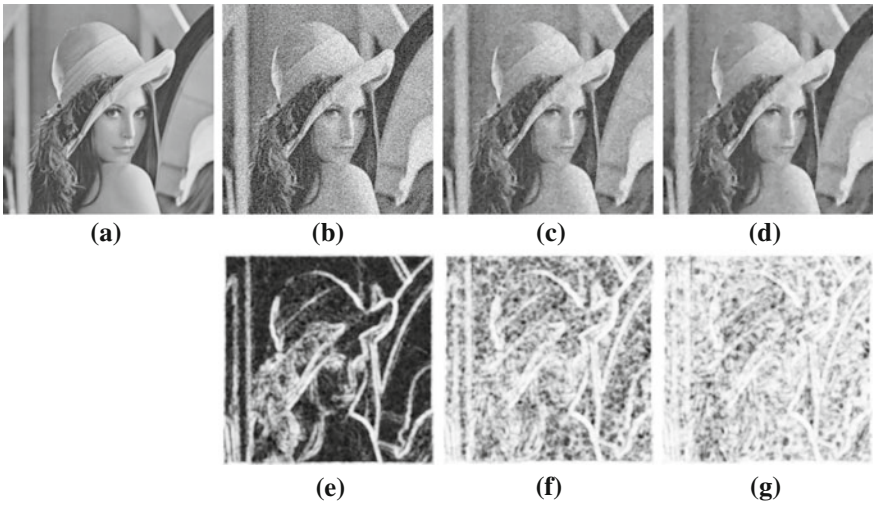

Fig. 1 Visual comparison of denoising results. **a** Original image; **b** noisy image; **c** SSIM map of noisy image; **d** MSE-optimal TV method; **e** SSIM map of MSE-optimal TV method; **f** SSIM-optimal TV; **g** SSIM map of SSIM-optimal TV method

The SSIM map help identify where in the image the denoisers yield the most improvement. The visual quality improvement is also reflected in the corresponding SSIM maps, which provide useful guidance on how local image quality is improved over space and how one denoiser outperforms the other. For instance, by comparing (e) and (g), we observe significant improvement of SSIM-optimal denoising on the smooth regions as well as the hat texture regions at the center part of the image. It can also be seen from the SSIM maps the areas which are relatively more structured and retain more details. Since they benefit more from the proposed denoising algorithm, the SSIM quality measure used as a fidelity term is better at calculating the similarity of structures compared to MSE. We test image denoising algorithms for *Lena* with additive white Gaussian noise(AWGN) standard deviation ranging from 15 to 40. The performance comparison between MSE-optimal TV and proposed SSIM-optimal TV is shown in Fig. 2. It can be observed that the proposed SSIM-optimal TV method achieves better performance than MSE-optimal TV in terms of SSIM which is expected to imply better perceptual quality of the denoised image. It is also interesting to observe RMSE improvements, though RMSE is not the optimization goal of the proposed method. The proposed image denoising scheme is tested on various images for thoroughness and fairness of our comparison study. We selected a large set of test images with size 512 $\times$ 512. Figure 3 lists eight example images in our experiments. Table 1 gives the objective quality comparison with respect to RMSE and SSIM of the two methods. From Table 1, we can clearly see that for all instances the proposed SSIM-optimal TV algorithm consistently produces better SSIM and RMSE results than MSE-optimal TV. It is worth noticing that for *Girl* and *Crowd* image, the proposed method gains 0.13 and 0.10, respectively, over the MSE-optimal method in SSIM index.

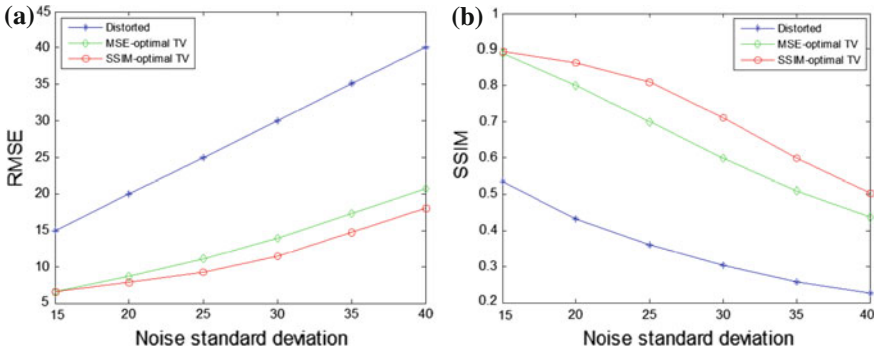

Fig. 2 For a 256 $\times$ 256 size Lena image , distorted with AWGN and restored using MSE-optimal and proposed SSIM-optimal total variation. **a** Variation of denoised images RMSE with noise standard deviation. **b** Variation of denoised images SSIM index with noise standard deviation

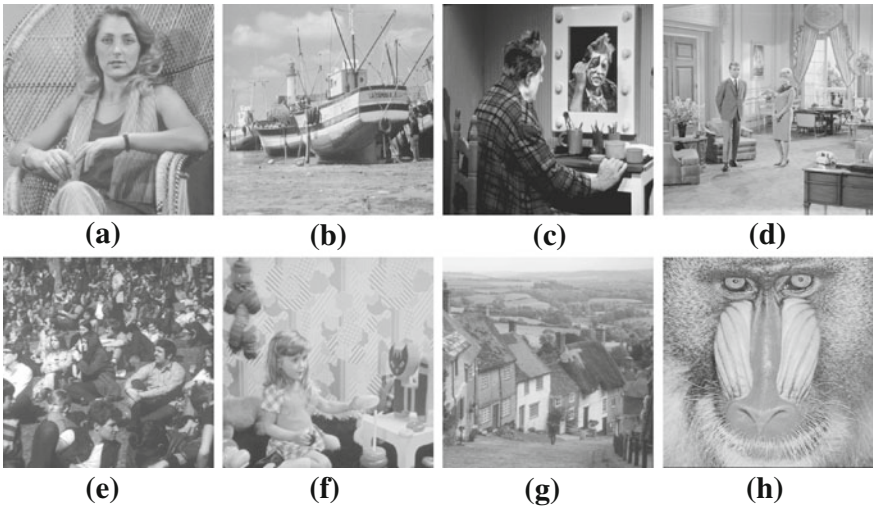

Fig. 3 Images used for our experiments. **a** Barbara2, **b** boat, **c** clown, **d** couple, **e** crowd, **f** girl, **g** goldhill, and **h** mandrill

Table 1 SSIM and RMSE comparisons of image denoising results

Image	RMSE comparison			SSIM comparison		
	Distorted	TV	Our	Distorted	TV	Our
Barbara2	30.00	15.42	13.84	0.3500	0.6109	0.6774
Boat	30.00	14.56	12.44	0.2986	0.5640	0.6455
Clown	30.00	14.08	12.14	0.2630	0.5236	0.5822
Couple	30.00	14.77	12.82	0.3191	0.5849	0.6582
Crowd	30.00	14.25	11.97	0.3050	0.5982	0.7010
Girl	30.00	13.46	10.70	0.2304	0.5409	0.6681
Goldhill	30.00	14.26	12.03	0.2728	0.5539	0.6339
Mandrill	30.00	18.38	18.01	0.4745	0.6279	0.6322

4.2 Discussion

The design of the SSIM-optimal TV was motivated by the fact that the SSIM index is a better perceptual image quality metric than the ubiquitous MSE measure. From the denoising results, it is clear that optimizing a perceptual distortion measure is more meaningful for image data. The gain in image quality can be explained as follows: the SSIM-optimal solution strives to maximize the local mean, variance, and structure in the denoised images, with respect to the reference. The local MSE-optimal solution, on the other hand, does not differentiate between the signal and the noise, thereby resulting in smoothing of important structural information while denoising and restoring images.

It must be taken into account that this is only an early attempt along a new but promising direction. The main contribution of the current work is mostly in the general framework and theoretical development. Since regular item encapsulates in itself the prior knowledge about the image to be restored, significant improvement in visual quality can be expected by improving the design and construction process of data-fidelity term based on SSIM index. A SSIM-optimal regularization term will capture structures contained in the image in a better way and the restoration task will result in sharper output image. Further improvement is also expected in the future when some of the advanced mathematical properties of SSIM and normalized metrics [19] are incorporated into the optimization framework.

5 Conclusion

In this article, We proposed a SSIM-optimal total variation method for image denoising. The key of our approach is to replace the role of MSE with SSIM as the data-fidelity term in total variation method. According to our knowledge, this is the first attempt to introduce SSIM index in the total variation optimization mechanism. We developed a gradient descent approach to obtain the optimal solution. The visual quality of our results is significantly better than MSE-optimal methods. Our experimental results demonstrate the promises of the proposed approach and also indicate the potentials of replacing the ubiquitous MSE with SSIM as the optimization criterion in image processing applications. While the SSIM-optimal framework presented here has been applied to image denoising, the solution can also be applied or extended to other important applications such as image inpainting, image deblurring, image super resolution, etc.

Acknowledgments This study was funded by National Basic Research Program of China (973 Program) under Grant 2012CB821206.

References

1. Rudin LI, Osher S, Fatemi E (1992) Nonlinear total variation based noise removal algorithms. Physica D 60(1–4):259–259
2. Wang Z, Bovik AC (2009) Mean squared error: love it or leave it? A new look at signal fidelity measures. IEEE Signal Process Mag 26(1):98–117
3. Caselles V (2006) Total variation based image denoising and restoration. In: Proceedings on the international congress of mathematicians, vol 3, pp 1453–1472.
4. Rodriguez P, Wohlberg B (2009) Efficient minimization method for a generalized total variation functional. IEEE Trans Image Process 18(2):322–332
5. Farsiu S, Robinson MD, Elad M, Milanfar P (2004) Fast and robust multiframe super resolution. IEEE Trans Image Process 13(10):1327–1344

6. Marquina A, Osher SJ (2008) Image super-resolution by TV-regularization and bregman iteration. J Sci Comput 37(3):367–382
7. Wang Z, Bovik AC, Sheikh HR, Simoncelli EP (2004) Image quality assessment: from error visibility to structural similarity. IEEE Trans Image Process 13(4):600–612
8. Wang Z, Simoncelli EP (2004) Stimulus synthesis for efficient evaluation and refinement of perceptual image quality metrics. Human vision and electronic imaging IX. Proc SPIE 5292:99–108
9. Wang Z (2011) Applications of objective image quality assessment methods. IEEE Signal Process Mag 28(6):137–142
10. Rehman A, Wang Z (2011) SSIM-based non-local means image denoising. In: 18th IEEE international conference on image processing (ICIP), pp 217–220.
11. Buades A, Coll B, More JM (2005) A non-local algorithm for image denoising. Proceedings of the IEEE computer society conference on computer vision and pattern recognition, San Diego, United states, In, pp 60–65
12. Channappayya SS, Bovik AC, Caramanis C, Heath RW (2008) Design of linear equalizers optimized for the structural similarity index. IEEE Trans Image Process 17(6):857–872
13. Channappayya SS, Bovik AC, Heath RW Jr (2006) A linear estimator optimized for the structural similarity index and its application to image denoising. In: International conference on image processing (ICIP), Atlanta, United states, pp 2637–2640
14. Rehman A, Rostami M, Wang Z, Brunet D (2012) Vrscay ER (2012) SSIM-inspired image restoration using sparse representation. EURASIP J Adv Signal Process 1:16
15. Brunet D, Vrscay ER, Wang Z (2011) A class of image metrics based on the structural similarity quality index. In: 8th international conference on image analysis and recognition, pp 100–110
16. Wang Z, Simoncelli EP (2008) Maximum differentiation (MAD) competition methodology for comparing computational models of perceptual quantities. J Vision 8(12):1–13
17. Wang Z, Bovik AC, Sheikh HR, Simoncelli EP, https://ece.uwaterloo.ca/z70wang/research/ssim/
18. Avanaki AN (2009) Exact global histogram specification optimize for structural similarity. Opt Rev 16(6):613–621
19. Brunet D, Vrscay ER, Wang Z (2012) On the mathematical properties of the structural similarity index. IEEE Trans Image Process 21(4):1488–1499

Dexterous Robotic-Hand Grasp Learning Using Piecewise Linear Dynamic Systems Model

Wei Xiao, Fuchun Sun, Huaping Liu and Chao He

Abstract Learning from sensor data plays an important role in the field of robotic research, especially in dexterous robotic hand grasping. The manuscript puts efforts on learning from tactile dynamic process during robotic hand grasping. A piecewise linear dynamic systems and a group of models are presented, under the guidance of which, proper gesture according to different types of targets could then be selected to facilitate stable and accurate grasping. This is evaluated on the experimental testbed and shows promising results.

1 Introduction

Robot research, including robotic hand and its applications, which is always in the forward position of the robot research frontier, has occupied researchers for two decades. Robotic hand can perform more accurate and sophisticated manipulation tasks under the guidance of artificial intelligence (AI). Just like humans have a good command of grasping after several attempts, with experiences accumulating, robotic hand can also exhibit "intelligence" and capabilities to a certain extent

W. Xiao (✉) · F. Sun · H. Liu · C. He
Tsinghua National Laboratory for Information Science and Technology, The State Key Laboratory of Intelligent Technology and Systems, Department of Computer Science and Technology, Tsinghua University, Beijing 100084, People's Republic of China
e-mail: 2011xiaowei@gmail.com

F. Sun
e-mail: fcsun@mail.tsinghua.edu.cn

H. Liu
e-mail: hpliu@mail.tsinghua.edu.cn

C. He
e-mail: tianhechao@sina.com

F. Sun et al. (eds.), *Foundations and Practical Applications of Cognitive Systems and Information Processing*, Advances in Intelligent Systems and Computing 215,
DOI: 10.1007/978-3-642-37835-5_73,

with the help of pattern analysis, machine learning, and other technologies within the AI domain. Grasping with dexterous robotic hand is a significant skill for robots, both in industrial and home area.

As summarized in [1], for robotic hand, identifying suitable contact locations, hand pose (both position and orientation), and force-exertion strategies are confronted with three main sets of constraints: (a) constraints due to limited capabilities of the dexterous hand, (b) constraints due to object geometry and material characteristics, and (c) constraints due to the task requirements. Analyzing, modeling, and integrating multi-sensor data can greatly alleviate all these constraints mentioned before. Many efforts have been made on how to perform accurate and stable grasping with the help of some kinds of sensors, e.g., in [2] visual sensing has been widely used, and tactile sensing is used in [3]. Our robotic hand system setup is shown in Fig. 1a, and we are trying to learn from tactile data sampled by tactile sensors (see Fig. 1b) mounted on the surface of each finger and palm of robotic hand, and accomplish target stable grasping, using our 7 DOF Schunk^{TM} manipulator and 4 DOF BarrettHand^{TM}. After several training, the most probable object type of an unknown target could be inferred with its corresponding hand pose and then BarrettHand^{TM} performs stable and accurate grasping.

In this paper, we present a learning method based on the proposed model inspired by Dynamic Bayesian Networks (DBNs) and Linear Dynamical Systems LDSs to recognize the target in order to further select a grasp gesture. It is demonstrated that the knowledge of target type can be inferred from data of tactile sensor. The state of the art and contributions of our work are discussed in Sect. 2. This is followed by a detailed presentation of the theoretical framework in Sect. 3, and we present the results of experimental evaluation and analyze the data collected from real target grasping in Sect. 4. Finally, we summarize our work and propose our future plan of work in Sect. 5. Important statements are that an earlier version of this paper was presented at the IEEE First International Conference on Cognitive Systems and Information Processing, and this revised version adds more details of how to construct a group model based on the proposed model and its applications.

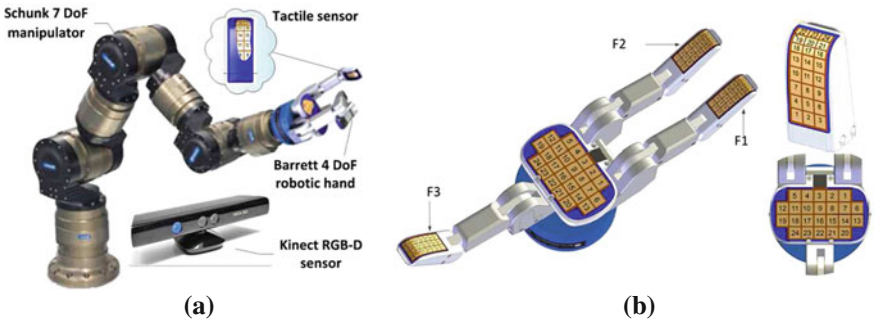

Fig. 1 Dexterous robotic hand grasp system and tactile sensor profile of BarrettHand. **a** Grasp system. **b** Robotic hand

2 Related Work

In order to establish a framework of stable grasp gesture learning, one touchy issue confronting us is how to improve our powers of perception on stable grasping and recognition of the relationship between sensor data and stable grasping gesture evaluation mechanism. The remainder of the section will introduce the prior effort on this issue together with our attempt and contribution. In the area of robotic object grasping, there has been a lot of effort during the past decades. In [4], Antonio Bicchi summarized the evolution of robotic hand grasping, with critical evaluation of what in the author's view are the leading ideas and emerging trends privileged with respect to exhaustiveness of citations. As stated in [5], most grasp planning approaches first model the target object shape with a number of primitives such as rectangle [6] or super-quadrics [7] to facilitate grasping, hand pose (both position and orientation), and force-exertion strategies are then generated based on analytical grasp quality measures, which rely heavily on accurate knowledge of the contacts between the hand and the target object in order to estimate the stability of a hand pose and corresponding magnitude of force. Distribution and magnitude of tactile data from each finger of robotic hand reflect the meticulous state of fingertips and the object, therefore, this type of sensor should receive higher priority especially in accurate and stable grasping. [5] and [8] report related researches, yet they put more emphasis on the importance of information from contact region, while ignoring the important role of visual information modeling shape of the object and helping to orchestrate manipulator approaching the target object. Moreover, in [3] and [5], a system that integrates grasp planning and online grasp stability assessment is presented.

In short, sensor data modeling and integration such as vision, tactile, and other types of sensors would be beneficial to analyzing stability and reliability of robotic grasping, for example, tactile data is always useful in reflecting meticulous state of fingertips and the object on the contact surface, while visual information often covers the shortage of tactile data when getting into the target scope before contacting.

In this paper, we model the tactile time-series during the process of grasping in order to judge the type of the target and select stable grasping gesture. The proposed so-called piecewise LDSs could better describe the distribution and magnitude of tactile data time-series and finally we evaluate the method.

3 Theoretical Framework

As mentioned above, how to model the tactile time-series data during the whole grasping process is a tough nut to crack. Here we present a comparison diagram between rigid and nonrigid target tactile time-series data starting from the moment when we operate the manipulator approaching the target until the end of the grasp,

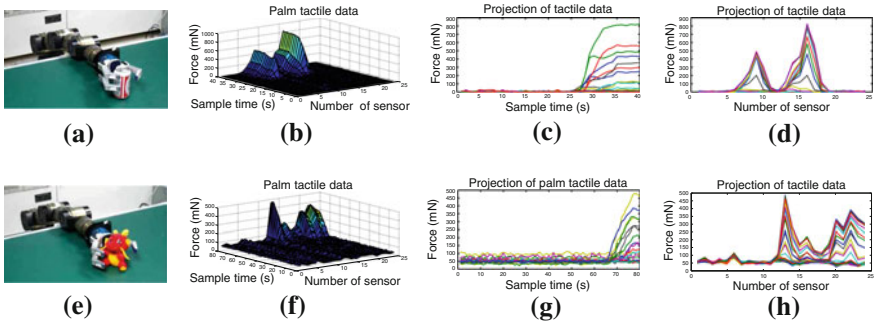

Fig. 2 Rigid and nonrigid object grasping data analysis. **a** Rigid. **b** Distribution. **c** Projection. **d** Projection. **e** Nonrigid. **f** Distribution. **g** Projection. **h** Projection

which means the fingers are closed and the joints do not move any more (see Fig. 2 for details). Figure 2b and f describes tactile data time-series of palm corresponding to rigid and nonrigid object, respectively. Figure 2c and d are projections of Fig. 2b along different axes, and the same results are Fig. 2g and h. It is observed that the distribution and magnitude of tactile-force are similar, except that the nonrigid has more peak value. This is because when the nonrigid object is wrapped by the entire hand tightly, the palm holds more contact point than it does in the situation of rigid. A distinguishing characteristic of tactile data observations (hereafter also called fingerprints) exhibits temporal correlations, modeling of which is the main challenge of dynamical systems analysis. Accurate models of these time-series fingerprints allow us to perform a variety of useful tasks, such as distribution comparison, stability recognition and prediction, gesture of the hand selection, and grasp planning. To ensure stable grasping hand pose learning and selecting, a proper model, accurately describing the changing pattern of tactile information during the whole grasping process, seems to be important. The following paragraphs put emphasis on finding this proper model.

3.1 Typical Model

One of the powerful approaches for modeling these dynamical time-series data is DBNs or LVMs assuming its observations are noisy emissions from an underlying latent variable that evolves over time and represents the state of the system [8]. Here, we briefly introduce DBNs, and how we should improve it for better analyzing the dynamical grasping process. DBNs originate from Bayesian networks (BNs). When we use BNs for analyzing the causality between random variables and time-series data, we find it is not suitable for modeling dynamic process, though causality analysis is still effective. To overcome the limitation, a modified BNs was proposed from the perspective of BNs, as a generalization of LDSs and

HMMs, namely DBNs [9]. A DBNs model could be viewed as time-series BNs model, that is to say, every time slice of DBNs is a BN, and the transition of BN between the two consecutive time t and $t + 1$ is standard first-order Markov process. For clear and simple analysis, typically, it is assumed that variables at time $t + 1$ are only related to the variables of time t. See Fig. 3.

Two useful examples of DBNs for dynamical systems are HMMs and LDSs. Different from HMMs, LDSs assume a continuous latent variable that evolves linearly with Gaussian noise, which makes LDSs adept at modeling smoothly evolving dynamical systems. Also unlike HMMs, matrix-factorization-based (e.g. singular value decomposition) approaches to learning LDSs make it easy to perform model approximation. Another distinction from HMMs is that conventional learning algorithms for the LDS do not guarantee stable parameters for modeling its dynamics [8, 10].

As an example of DBNs, LDSs could be easily depicted as follows, see Fig. 3b. The hidden state set of X and observable state set of Y are all evolving with time. Every time t, the observable Y_t is generated heavily based on state X_t, disturbed by Gaussian noise. Also, in the dynamic of hidden state set X, every time t, X_t is also generated based on X_{t-1} and disturbed by Gaussian noise. As we can see, LDSs could perfectly model the data that exhibits time correlations.

As stated above, fingerprints exhibit temporal correlations, which provide more possibilities of using the core ideas of LDSs that observations are noisy emissions from an underlying latent variable that evolves over time and represents the real state of the system. Inspired by [10], we are trying to model tactile time-series data, using so-called piecewise LDSs (switched LDSs or multi-LDSs), better "interpreting" and "understanding" data series to infer a joint stochastic model that generates it, and furthermore, find relationship between distribution of fingerprints and grasping stability.

As illustrated in Fig. 2c and g, fingerprints time-series present apparent variation regularly over time, which could be mainly divided into three phases: (1) "Inception", during which, manipulator is approaching the target object, and robotic hand does not get into its workspace, so tactile data is mainly composed of

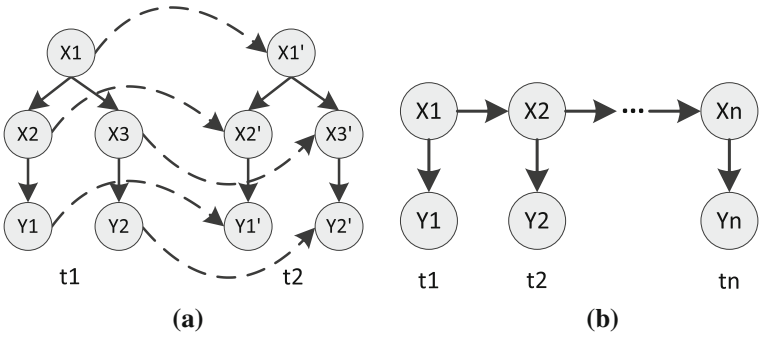

Fig. 3 Structure of DBNs (**a**) and LDSs (**b**)

zero wandering of sensors and turbulent noise; (2) "Ascent", which is a transient process where robotic hand comes into contact with the object and along with the increase in contacting area, the average value of exerting force also increases, until threshold set is reached beforehand in order to protect tactile sensor from abnormal contacting. Finally, (3) "Plateau", which is the other steady state, yet different form inception phase. In plateau phase, robotic hand has already grasped the target object, and due to the force threshold, does not exert greater force but keeps the same magnitude as the one in the ending of ascent phase.

3.2 Methodology

For convenience, we define a sole time slice at t in DBNs first, and then take the factor of time evolving into account. Let $\{\mathbf{y}(t)\}_{t=1\ldots\tau}$, $\mathbf{y}(t) \in \mathbb{R}^m$, be a time-sequence tactile τ data with additive white Gaussian observation noise, i.e., each time slice $\mathbf{y}(t)$ could be divided into two parts $\mathbf{y}(t) = \mathbf{p}(t) + \mathbf{w}(t)$: $\mathbf{p}(t) \in \mathbb{R}^m$ is pure observation; $\mathbf{w}(t) \in \mathbb{R}^m$ is white Gaussian observation noise. And $\{\mathbf{x}(t)\}_{t=1\ldots\tau}$, $\mathbf{x}(t) \in \mathbb{R}^n, (m \gg n)$, be a time-sequence underlying latent variable. We treat $\mathbf{y}(t)$ as noisy emission from $\mathbf{x}(t)$ that evolves over time and represents the real state of the system. Furthermore, it is assumed that observation function $\mathbf{C} \in \mathbb{R}^{m\times n}$: $\mathbf{p}(t) = \mathbf{C}\mathbf{x}(t)$ is linear, which means each dimension in $\mathbf{p}(t)$ is a linear combination of $\mathbf{x}(t)$. This is the so-called linear-Gaussian assumption. What about $\mathbf{x}(t)$? Yes, it is also linear-Gaussian, which means transition function $\mathbf{A} \in \mathbb{R}^{n\times n}$: $\mathbf{x}(t+1) = \mathbf{A}\mathbf{x}(t) + \mathbf{v}(t)$, $\mathbf{v}(t) \in \mathbb{R}^n$ is linear, and each dimension in $\mathbf{x}(t+1)$ is a linear combination of $\mathbf{x}(t)$ plus addictive Gaussian process noise $\mathbf{v}(t)$. This is also known as Kalman filter model or LDSs:

$$\begin{cases} \mathbf{x}(t+1) = \mathbf{A}\mathbf{x}(t) + \mathbf{v}(t) \\ \mathbf{y}(t) = \mathbf{C}\mathbf{x}(t) + \mathbf{w}(t) \end{cases} \tag{1}$$

Detailed information about LDSs can be found in [10] and [12].

Piecewise LDSs comprises a collection of subsystems described by linear dynamics, together with a switching rule that specifies the switching between the subsystems. Piecewise LDSs have the advantage to accurately cope with complex dynamic process or systems with large uncertainties, especially the process comprising different phases show obviously different characteristics. Mathematically, piecewise LDSs can be described as:

$$\begin{cases} \mathbf{x}(t+1) = \mathbf{A}_{\sigma}\mathbf{x}(t) + \mathbf{v}(t) \\ \mathbf{y}(t) = \mathbf{C}_{\sigma}\mathbf{x}(t) + \mathbf{w}(t) \end{cases} \tag{2}$$

with the switching signal:

$$\sigma(t_+) = \sigma(\mathbf{x}(t)|\mathbf{y}(t), \sigma(t_-)), \quad \forall\, t \tag{3}$$

where $\mathbf{x}(t)$, $\mathbf{v}(t)$, and $\mathbf{w}(t)$ are the same as the ones previously mentioned, while $\mathbf{A}_\sigma$ and $\mathbf{C}_\sigma$ are of a collection of $\{\mathbf{A}_i\}$ and $\{\mathbf{C}_i\}$, and system (2) can be simply denoted as $\Sigma(\mathbf{A}_i, \mathbf{C}_i)_{\mathcal{I}}$. Matrix pair $(\mathbf{A}_k, \mathbf{C}_k)$ for $k \in \mathcal{I}$ is referred to as one of the subsystems of (2). $\sigma(t_+)$ it only depends on its past value $\sigma(t_-)$, latent state $\mathbf{x}(t)$ and observation $\mathbf{y}(t)$. If $\sigma(t) = i$, we would say that the ith subsystem is *active* at time t. It is clear that at any instant, there is one (and only one) active subsystem [11].

The performance of the overall system relies on every subsystem and the switching series. Different switching signals may incur totally different system behaviors. Here we adopt time-driven switching law to model the dynamic fingerprints called piecewise LDSs with time-driven switching law. Within every time slot, our dynamic fingerprints take on different types of system characteristic respectively. As stated in typical model subsection, we have divided the time-series into three phase: (1) Inception, (2) Ascent and (3) Plateau, hence the corresponding time-driven switching law should be: $\sigma(t) = 1$, when $t \in \mathit{Inception}$; $\sigma(t) = 2$, when $t \in \mathit{Ascent}$; $\sigma(t) = 3$, when $t \in \mathit{Plateau}$.

It is observed that the model (2) captures the gist of distribution and magnitude of tactile data. To be specific, the whole process is divided into three phases, where each phase is an LDSs dynamic process. Different choice of filters ϕ can induce different types of LDSs dynamic processes. A model, whether accurate or not, depends mainly on whether it captures the significant information of a dynamic process. The rest, which is partly inspired by [10] and its successful application in dynamic texture, would be emphasized on how to deal with every phase ("Inception," "Ascent," and "Plateau") and its application in robotic hand grasping.

Taking single phase into account, say, "Plateau," is useful for application such as target selection. We adopt linear filters $\mathbf{C}$ to reconstruct observations in the preliminary study phase, see (4).

$$\mathbf{p}(t) = \sum_{i=1}^{n} \mathbf{x}_i(t)\mathbf{c}_i = \mathbf{C}\mathbf{x}(t) \tag{4}$$

where $\{\mathbf{C}\} = [c_1, \ldots, c_n] \in \mathbb{R}^{m\times n}$. Furthermore, we assume there exist symmetric positive-definite matrices $\mathbf{Q} \in \mathbb{R}^{n\times n}$ and $R \in \mathbb{R}^{m\times m}$ such that

$$\begin{cases} \mathbf{x}(t+1) = \mathbf{A}\mathbf{x}(t) + \mathbf{v}(t) \\ \mathbf{y}(t) = \mathbf{C}\mathbf{x}(t) + \mathbf{w}(t) \end{cases} \tag{5}$$

where $\mathbf{v}(t) \sim \mathcal{N}(0, \mathbf{Q})$ and $\mathbf{w}(t) \sim \mathcal{N}(0, \mathbf{R})$. Therefore, the problem of modeling the fingerprints has been transformed into parameters estimation of $\mathbf{A}$, $\mathbf{C}$, $\mathbf{Q}$, $\mathbf{R}$ from the observations $\mathbf{y}(1), \ldots, \mathbf{y}(\tau)$:

$$\begin{aligned}\hat{\mathbf{A}}, \hat{\mathbf{C}}, \hat{\mathbf{Q}}, \hat{\mathbf{R}} &= \arg \max_{\mathbf{A},\mathbf{C},Q,R} \log p(\mathbf{y}(1), \ldots, \mathbf{y}(\tau)) \\ &= \lim_{t\to\infty} \arg \min_{\mathbf{A},\mathbf{C},\mathbf{Q},\mathbf{R}} E \parallel \mathbf{y}(t+1) - \mathbf{C}\mathbf{x}(t+1|t)\|^2 \\ &\quad s.t. \quad Eq.(1)\end{aligned} \tag{6}$$

According to the matrix theory, the choice of **A**, **C**, **Q**, **R** is not unique. Using similitude transformation, we obtain a family of **A** with $\mathbf{PAP}^{-1}$, **C** with $\mathbf{CP}^{-1}$, **Q** with $\mathbf{PQP}^T$ and **R** with $\mathbf{PRP}^T$ (**P** is similitude transformation matrix). However, we could choose a so-called canonical model that represents each equivalent one. The canonical model is more convenient and efficient for analyzation, numeration, simulation, and prediction of dynamical system behavior. Detailed analytic solution can be found in the authors' publication [12].

We have hitherto modeled the tactile process of single grasping of one target using piecewise LDSs, which, in fact, establishes a mapping relation between single grasping G_j and model parameter $(\mathbf{A}^j, \mathbf{C}^j)$, where j is the jth grasping. In order to give a comprehensive tactile description of the same target, multi-direction graspings are adopted, i.e., we perform graspings from four typical directions: top, sideways, oblique upper direction, and oblique lower direction. All these j tactile time-series could then be modeled and described by a group of model parameters $\Sigma(\mathbf{A}^j, \mathbf{C}^j)$. Therefore, $\Sigma(\mathbf{A}^j, \mathbf{C}^j)$ could be viewed as a descriptor to a specific target, although it is redundant and not perfectly complete. Then we select proper model parameters from $\Sigma(\mathbf{A}^j, \mathbf{C}^j)$ in the meaning of high classification accuracy, to constitute a relative small family of models: $(\mathbf{A}^1, \cdots, \mathbf{A}^4)_k^{tactile}$ and $(\mathbf{C}^1, \cdots, \mathbf{C}^4)_k^{tactile}$ as a set of basis function to describe all the graspings performed on the target k. All these $(\mathbf{A}^1, \cdots, \mathbf{A}^4)_k^{tactile}$ and $(\mathbf{C}^1, \cdots, \mathbf{C}^4)_k^{tactile}$ belong to different targets k, where $k = 1, 2, \cdots K$, could form a compressed group of models. Let $\mathbf{A}_{tactile} = \sum_{k=1}^{K} (\mathbf{A}^1, \cdots, \mathbf{A}^4)_k^{tactile}$ and $\mathbf{C}_{tactile} = \sum_{k=1}^{K} (\mathbf{C}^1, \cdots, \mathbf{C}^4)_k^{tactile}$ be all these $(\mathbf{A}^1, \cdots, \mathbf{A}^j)_k^{tactile}$ and $(\mathbf{C}^1, \cdots, \mathbf{C}^j)_k^{tactile}$, respectively, by which any targets k could be described.

$\mathbf{A}_{tactile}$ specifies how hidden states evolve in feature space; while $\mathbf{C}_{tactile}$ builds a bridge between feature space and observation space, by which raw tactile data in observation space could be mapped into lower dimensional feature space. Although raw multi-direction grasping tactile data of a specific target are mapped as different points in feature space, which is specified by $\mathbf{C}_{tactile}$, changing rules of these points are more or less similar, which is specified by $\mathbf{A}_{tactile}$; points mapped from raw tactile data of different types of targets are of disaffinity dramatically, due to differences between targets in shape, weight, hardness, and roughness, for such is what we exploit to perform target classification.

4 Experimental Evaluation

In consideration of the high-accuracy in the 'Plateau' phase, the proposed model could be used for target classification. According to different target objects, different $\hat{\mathbf{C}}$ could be trained based on target objects. That means we could set up mapping between $\hat{\mathbf{C}}$ and target object. By discriminating among different $\hat{\mathbf{C}}$, corresponding target could then be obtained. Experimental test is detailed below, we have sampled ten different types of targets and select 'Plateau' phase for training every $\hat{\mathbf{C}}_1$–$\hat{\mathbf{C}}_{10}$, which constitutes the base of every observation data space. We can project observation data to these bases in order to discriminate different objects by calculating consistency. See Fig. 4, after projecting onto every base $\hat{\mathbf{C}}_1$–$\hat{\mathbf{C}}_{10}$, the outcome(coordinates) exhibits high consistency with $\hat{\mathbf{C}}_6$, within a narrow range of data jitter. Once the target object is identified, proper hand-pose could be selected, and take subsequent action accordingly.

To verify the classification accuracy of group models, we set up a date set with 40 different types of targets. After extracting parameter group $\mathbf{C}_{tactile}$ and $\mathbf{C}_{depth}$, we adopt leave-one-out cross validation strategy to test its accuracy. Raw depth data is sampled by Kinect™. The comparison result is shown in Fig. 5, and it is observed that tactile group models $\mathbf{C}_{tactile}$ achieve more classification accuracy

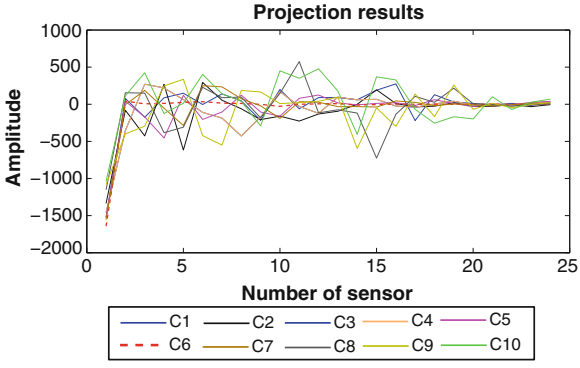

Fig. 4 Projection results to different $\hat{\mathbf{C}}$

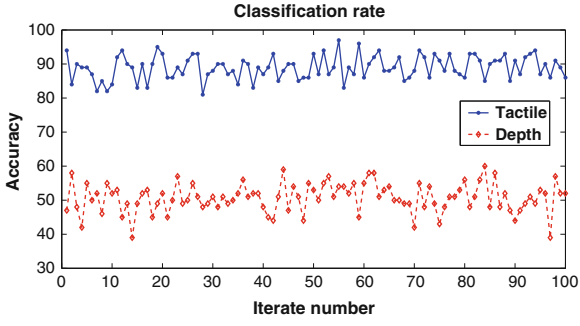

Fig. 5 Classification comparison of different modalities

Table 1 Classification statistics

	Tactile	Depth
Mean (%)	89.08	50.09
Variance (%)	1.05	1.49

than depth group models $\mathbf{C}_{depth}$, which suggests the mapping relationships $\mathbf{C}_{tactile}$ between feature space $\mathbf{X}$ and observation space $\mathbf{Y}$ has an ideal property of discrimination. Statistical comparison is shown in Table 1.

5 Conclusions and Future Work

In this paper, we propose a novel piecewise LDSs model for analyzing the tactile time-series. During different phases of dynamic process, underlying latent variable evolves along different state trajectories restrained by different system parameter matrices of $\mathbf{A}$ and $\mathbf{C}$. Therefore, we combine a piecewise LDSs and switched systems in order to better represent and "understand" the whole dynamic process of tactile time-series. Different types of experiments testify its feasibility and efficiency. While manipulator's monotonous approaching style conveys dextrous hand performing grasping in the same direction, which causes different grasping to show a similar fingerprint pattern, therefore its applications are limited. The future work will focus on these limitations and how to construct comprehensive mapping between sole target and different fingerprint patterns.

Acknowledgments This work was jointly supported by Tsinghua Self-innovation Project (Grant No. 20111081111) and the National Natural Science Foundation of China (Grants No. 61210013, 61075027).

References

1. Salimi S, Bone GM (2008) Kinematic enveloping grasp planning method for robotic dexterous hands and three-dimensional objects. Robotica 26:331–344
2. Lippiello V, Ruggiero F, Villani L (2009) Floating visual grasp of unknow objects. In: IEEE international conference on intelligent robots and systems, IEEE Press, New York, pp 1290–1295
3. Bekiroglu Y, Detry R, Kragic D (2011) Learning tactile characterizations of object- and pose-specific grasps. In: IEEE international conference on intelligent robots and systems, IEEE Press, New York, pp 1554–1560
4. Bicchi A (2000) Hands for dexterous manipulation and robust grasping: a difficult road toward simplicity. IEEE Trans Rob Autom 16:652–662
5. Bekiroglu Y, Huebner K, Kragic D (2011) Integrating grasp planning with online stability assessment using tactile sensing. In: IEEE international conference on robotics and automation, IEEE Press, New York, pp 4750–4755

6. Huebner K, Kragic D (2008) Selection of robot pre-grasp using box-based shape approximation. In: IEEE international conference on intelligent robots and systems, IEEE Press, New York, pp 1765–1770
7. Goldfeder C, Allen PK, Lackner C, Pelossof R (2007) Grasp planning via decomposition trees. In: IEEE international conference on robotics and automation, IEEE Press, New York, pp 4679–4684
8. Siddiqi SM (2009) Learning latent variable and predictive models of dynamical systems. Ph.D. dissertation, School of Computer Science Robotics Institute, Carnegie Mellon Univ., Pittsburgh, PA
9. Zhang Y, Ji Q (2006) Active and dynamic information fusion for multisensor systems with dynamic Bayesian Networks. IEEE Trans Syst Man Cybern Part B Cybern 36:467–472
10. Doretto G, Chiuso A, Wu Y, Soatto S (2003) Dynamic textures. Int J Comput Vision 51:91–109
11. Sun Z, Ge SS (2005) Analysis and synthesis of switched linear control systems. Automatica 41:181–195
12. Xiao W, Sun FC, Liu HP, Liu HY, He C (2012) Dexterous robotic hand grasp modeling using piecewise linear dynamic model. In: 2012 international conference on multisensor fusion and information integration, IEEE Press, New York, pp 52–57

Low-Rank Matrix Recovery for Traffic Sign Recognition in Image Sequences

Deli Pei, Fuchun Sun and Huaping Liu

Abstract We consider the problem of traffic sign recognition in image sequences. In many cases, image sequences of traffic signs can be collected from consecutive videos and these images have high correlation with each other. While traditional traffic sign recognition approaches focus on how to extract better features and design more powerful classifiers, most of these methods neglected this correlation. In this paper, we introduce the low-rank matrix recovery model to exploit the correlation among images with similar appearances to enhance feature representation. By recovering the underlying low-rank matrix from the original feature matrix consists of feature vectors of image sequences, we are able to attenuate the influence of corruption, such as noise and motion blur. Experiments are conducted on GTSRB dataset to evaluate our method, and noticeable performance gain is observed by using low-rank matrix recovered from original matrix. We obtain very impressive results on several super-class accuracy while get comparable performance with state-of-the-art results on global accuracy.

Keywords Computer vision · Traffic sign recognition · Low rank matrix recovery

D. Pei (✉)
Department of Computer Science and Technology, Tsinghua University, Beijing 100084, China
e-mail: newrockwolf@gmail.com

F. Sun
State Key Laboratory of Intelligent Technology and Systems, Beijing 100084, China

H. Liu
Tsinghua National Laboratory for Information Science and Technology, Beijing 100084, China

F. Sun et al. (eds.), *Foundations and Practical Applications of Cognitive Systems and Information Processing*, Advances in Intelligent Systems and Computing 215,
DOI: 10.1007/978-3-642-37835-5_74,

1 Introduction

Automatic recognition of traffic signs (TSs) belongs to one of the major objectives of driver assisting systems. Much research has been done to develop real time and accurate systems for this purpose. Traffic signs are planar rigid objects with different shapes and colors. The information provided by the road signs is encoded in their visual traits: shape, color, and pictogram. Several car manufacturers have adopted the Advanced Driver Assistance System which includes traffic sign recognition. For instance, in 2008, Mobileye partnered with Continental AG to launch three features in the BMW seven series, namely, a lane departure warning, speed limit information based on traffic sign detection, and intelligent headlight control.[1] However, traffic sign recognition in an uncontrolled environment is still an open changeling problem.

Traffic sign recognition usually starts with detection, rectification, and then finally recognition. A tracking method can also be used to speed up recognition as a smaller area of the detected object can be targeted for recognition. Since we are focusing on traffic sign recognition in this paper, no further discussion is given on detection, rectification, or tracking. Research on traffic sign recognition started in the last century. An old survey which was modified for the last time in May 1999, can be found in [1]. Since a wide variety of traffic sign recognition techniques have been proposed in the literature during the past decade, we do not try to give a comprehensive literature survey, but instead concentrate on several background works most relevant to the present research. Please refer to Refs. [2–4] and the references therein for recent advances in this area.

Although various machine learning approaches have been proposed to solve traffic sign recognition, it is very difficult to compare the actual performance of these as there is neither a standardized dataset nor a standardized procedure for evaluating performance. Very recently, the German Traffic Sign Recognition Benchmark (GTSRB), a large life-like dataset of more than 50,000 traffic sign images in 43 classes, was created [5]. This dataset, the biggest and most varied database for traffic sign recognition so far, was originally developed for a multi-category classification competition held at IJCNN 2011. The methods used by the participants who achieved the best results are briefly described and compared to human traffic sign recognition performance and baseline results in [5]. Currently, representative approaches used with the GTSRB include a committee of neural networks [6], convolution neural networks [7], K-d trees and random forests [8], intersection kernel SVM [5], sparse representation-based classification [5], and so on. The best recognition result for the final stage achieves to 99.46 % accuracy, which is even higher than human recognition performance results (98.84 %).

Another difference between GTSRB dataset and other traffic sign dataset is that these traffic sign images are collected from videos recorded while driving on different types of roads, and therefore the sequential information of these

[1] http://mobileye.com/technology/applications/traffic-sign-detection/

consecutive images are preserved. That is to say, for a particular traffic sign instance, sequential images are collected in the dataset. While current methods focus on how to extract discriminative features and design more powerful classifiers, most of the existing algorithms neglected these cues in image sequences. The methods using single frame only usually lead to inaccurate results and are sensitive to corruptions. In the dynamic environment, the temporal information can be used to dramatically improve the reliability of traffic sign localization and recognition. Reference [9] used the maximum likelihood estimation to fuse the temporal information. To simply the solution, they assumed that detection results in difference frames are independent. References [10] and [11] utilized the template matching and color distance transformation to design similar temporal fusion approaches. Reference [12] introduced the confidence value for the detection results in different frames. Reference [13] introduced a weighting strategy to fuse detection results in different frames. However, all of these approaches are heuristic and fail to exploit the intrinsic relation between frames.

Very recently, the low-rank decomposition attracts a lot of attentions from the communities of machine learning and signal processing. Based on the low-rank matrix recovery and completion, robust principle component analysis was proposed to recover the underlying low-rank structure in the data. It has been successfully used for background modeling [14, 15], salient object detection [16, 17], and image alignment [18].

In this paper, we exploit the correlation among image sequences to enhance the feature representation for traffic sign recognition. By recovering the underlying low-rank matrix from the original feature matrix consists of feature vectors of image sequences, we are able to attenuate the influence of corruption, such as noise and motion blur, and observed a obvious performance gain with simple linear classification method.

This paper is organized as follows: In this section, we introduce the traffic sign recognition task and related work. Some representative approaches in recent years are specified. In Sect. 2, we detail the low-rank matrix recovery model and how to apply it in our traffic sign recognition, optimization, and classifier used in our model is also discussed. The experimental results are given in Sect. 3, where we evaluate our approach on GTSRB dataset. In Sect. 4, conclusions are made and some future research issues are discussed.

2 Model

2.1 Low-Rank Matrix Recovery

We start by defining the notation in this model. Consider a $m \times n$ matrix $\boldsymbol{D}$ of rank r observed from the true underlying matrix $\boldsymbol{X}$, where $r < min(m, n)$. In many engineering applications, the observation procedure is often corrupted by errors or

noise, which can be described by a simplified model, $\boldsymbol{D} = \boldsymbol{X} + \boldsymbol{E}$, where $\boldsymbol{E}$ is a sparse corruption matrix. Our goal is to recover this underlying matrix $\boldsymbol{X}$ from the noisy observation with the help of low-rank property.

Ideally, we want to recovery the low-rank matrix $\boldsymbol{X}$ by optimizing the following problem:

$$\begin{array}{ll} min_{\boldsymbol{X},\boldsymbol{E}} & rank(\boldsymbol{X}) + \gamma \|\boldsymbol{E}\|_0 \\ s.t. & \boldsymbol{D} = \boldsymbol{X} + \boldsymbol{E} \end{array} \tag{1}$$

where γ is weighting parameter, the rank $rank(\boldsymbol{X}) = \#\{\sigma_i(\boldsymbol{X}) \neq 0\}$ is computed by counting all non-zero singular values and $\|\boldsymbol{E}\|_0 = \#\{\boldsymbol{E}_{i,j} \neq 0\}$ is the number of nonzero elements in matrix E.

However, this optimization problem is NP hard and therefore intractable. Fazel et al. [19] showed that, by approximating the rank by the sum of the singular values of the matrix, matrix rank minimization problem can be then reduced to an Semidefinite Program (SDP), hence efficiently solved. Candes et al. [20] further developed it and proposed Robust Principal Component Analysis (RPCA) algorithm to recover a low rank matrix from corrupted observation $\boldsymbol{D} = \boldsymbol{A} + \boldsymbol{E}$, where the corruption matrix E is unknown and the nonzeros error value can be arbitrarily large, but is assumed to be sparse. The model is described as follows:

$$\begin{array}{ll} min_{\boldsymbol{X},\boldsymbol{E}} & \|\boldsymbol{X}\|_* + \gamma \|\boldsymbol{E}\|_1 \\ s.t. & \boldsymbol{D} = \boldsymbol{X} + \boldsymbol{E} \end{array} \tag{2}$$

where the rank of matrix is replaced by the sum of singular values $\|\boldsymbol{X}\|_* = \sum_i \sigma_i(\boldsymbol{X})$ and the L0-norm of the corruption matrix $\boldsymbol{E}$ is approximated by L1-norm $\|\boldsymbol{E}\|_1 = \sum_{ij} |\boldsymbol{E}_{i,j}|$.

2.2 Image Recovery in Traffic Sign Recognition

Most of the image classification methods focus on how to extract more discriminative features and design more powerful classifiers to prompt recognition performance, these approaches treat each image separately without considering the correlations in image sequences and therefore are very sensitive to corruptions such as noise, motion blur, and occlusion. On the other hand, in many applications, images are collected consecutively from videos, such as traffic sign images from on-board cameras and handheld devices. These temporally consecutive images are highly correlated to each other because of the appearance similarity, therefore, the matrix consisted of image feature vectors are supposed to be low-rank. By exploiting the correlation, it is possible to alleviate corruption caused during observation and enhance feature representation and subsequently improve recognition performance, which is neglected by most of the existing approaches for traffic sign recognition (Fig. 1).

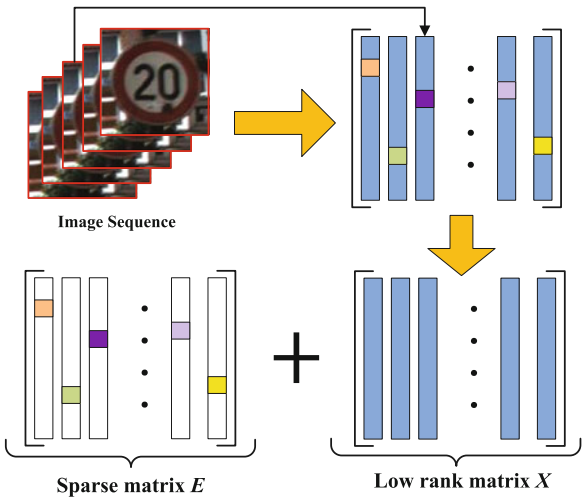

Fig. 1 The framework of our method

In our application, we are trying to utilize the sequence information with the help of low-rank matrix recovery model. Each traffic sign image is represented by vector of length k, which could be original pixel values or feature extracted from the image. We group n image vectors into a $k \times n$ matrix $\boldsymbol{D}$. We assume the underlying matrix $\boldsymbol{X}$ of the observed matrix $\boldsymbol{D}$ has much lower rank $rank(\boldsymbol{X}) << min(m, n)$ and can be recovered from the corruption with low-rank matrix recovery. The observation process is described by a simplified model $\boldsymbol{D} = \boldsymbol{X} + \boldsymbol{E}$, where $\boldsymbol{E}$ is the sparse corruption matrix and the nonzero values could be arbitrarily large. We use the model described in Eq. (2) and recover the low-rank matrix $\boldsymbol{X}$ by solving the optimization problem. Then the underlying image representation $\boldsymbol{X}$ is used to replace the original image representation in training and prediction procedure.

2.3 Optimization and Classification

There are various methods to solve the Robust PCA problem, such as Augmented Lagrange Multiplier (ALM), Accelerated Proximal Gradient (APG), Dual Method and Singular Value Thresholding (SVT) et al. A simple comparison of the speed and accuracy of different implementations can be found in [21]. In our application, we adopt the Augmented Lagrange Multiplier (ALM) method, which solved the Robust PCA problem via convex optimization that minimizes a combination of the nuclear norm and the L1-norm. For more details we refer the reader to [22].

For the multi-class classification task, we use Logistic Regression (LR) model in liblinear package [23], which is an efficient linear model for multi-class classification task. Given the feature representation of a image X_i, the probability of taking label $y \in C = \{c_1, c_2, \ldots, c_k\}$ can be computed by the following LR model:

$$P(y|\boldsymbol{x}) = \begin{cases} \frac{exp(\beta_{l0}+\beta_y^T \boldsymbol{x}_i)}{1+\sum_{t=c_1}^{c_{K-1}} exp(\beta_{t0}+\beta_t^T \boldsymbol{x}_i)}, & \text{if } y = c_1, ..., c_{k-1} \\ \frac{1}{1+\sum_{t=c_1}^{c_{K-1}} exp(\beta_{t0}+\beta_t^T \boldsymbol{x}_i)}, & \text{if } y = c_k \end{cases} \tag{3}$$

Where β is the learned parameter for the logistic regression. The label with the largest probability then is assigned to the image.

3 Experimental Results

To demonstrate the effectiveness of our method, we evaluate it on the German Sign Recognition Benchmark (GTSRB) dataset [24], which is released for the "German Traffic Sign Recognition Benchmark" competition held at IJCNN 2011 and gains increasing attention in the last 2 years. The GTSRB dataset for online competition stage contains more than 40,000 images labeled with 43 classes. Images are collected from video sequences recoded on real road driving with various illumination and distances and the temporal information is also preserved. Due to various recording distances, the size of the traffic sign images varies between 15×15 and 222×193 pixels. Following the protocol in [24], the 43-class traffic signs are further grouped into six super-classes: *Speed limits, Other prohibitions, Derestriction, Mandatory, Danger, Unique*, and accuracy of each super-class is also computed in addition to global accuracy. We use the standard split of the training/test dataset released with the dataset (Fig. 2).

We use the pre-calculated HOG feature provided along with the GTSRB dataset to represent the image, which is computed by scaling the image to a size of 40×40 pixels and converting to grayscale. A image is decomposed into 5×5 pixel cells and within each cell gradient orientation is accumulated into 8 bins. 2×2 cells are grouped together to form a block and cells are locally normalized within a block. To obtain a dense representation of the image, blocks have 50 % overlap in both X and Y axis, resulting in a 1,568 dimension feature vector.

The baseline used in our experiments is original HOG features with logistic regression classifier and no other sequence information is used. The logistic

Fig. 2 Selected presentative 43-class traffic sign images in GTSRB dataset

Table 1 Quantitative results on the GTSRB dataset

	Speed limits	Prohibitions	Derestriction	Mandatory	Danger	Unique	Global
Committee of CNNs	99.47	**99.93**	99.72	**99.89**	99.07	99.22	99.46
Human performance	98.32	99.87	98.89	100.0	99.21	**100.0**	99.22
HOG feature	99.52	98.50	99.00	95.28	99.36	99.70	95.44
LRMR	**99.70**	99.46	**100.0**	96.22	**99.68**	99.95	96.70

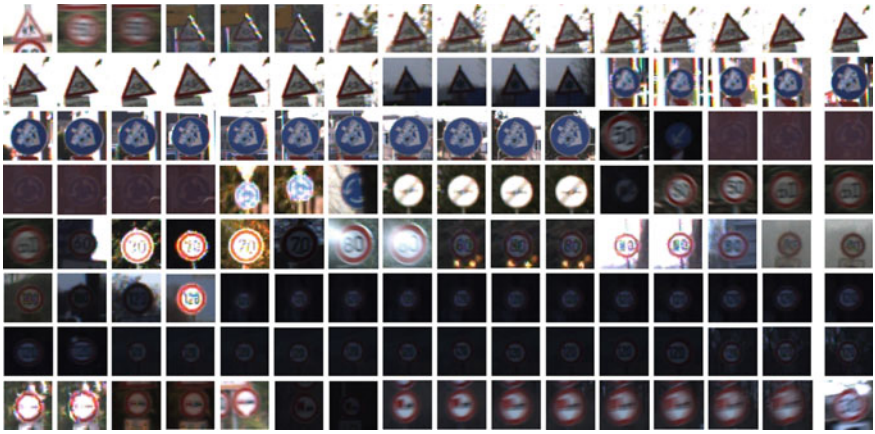

Fig. 3 Qualitative results of incorrect classified images of our method

regression is much simpler and faster than other classifiers used in state-of-the-art approaches, such as convolutional neural network (CNN) [7, 25], which is more complicated in designing multiple layers and takes longer time for training. As shown in Table 1, the global accuracy of the original HOG feature is 95.45 %, which is very close to the accuracy of LDA classifier, 95.68 %, reported in [5].

To recover the low-rank matrix from sequence images, we group feature vectors from image sequences to get the observed matrix $\boldsymbol{D}$. After low-rank matrix $\boldsymbol{X}$ is obtained by solving the optimization problem 2, the feature vector of each image in $\boldsymbol{X}$ is treated separately as new training instance. Then the logistic regression is still used to train and predict the traffic signs. By introducing low-rank matrix recovery to remove noisy and motion blur, we observe 1.3 % performance gain to 96.70 %, as shown in Table 1. Note that although our method does not outperform the state-of-the-art algorithm on global accuracy, we are able to outperform it on 3 out of 6 super-class accuracy, which achieves impressive 100 % accuracy.

A possible explanation is that by applying low-rank matrix recovery model to original image feature representation, differences of traffic signs within the same super-class are also attenuated while removing noise and other possible corruptions. Thus, instead of misclassifying to any other traffic sign classes with similar appearance, our method tends to misclassified two classes of same super-classes.

Above experiments show that with the correlation among image sequences, we can relief the effect of illuminate change, noise, and motion blur to enhance the representation of image feature, and therefore promotes the recognition performance. However, when most of images in the same video track are seriously degenerated during recording, our low-rank matrix recovery will fail to work. Figure 3 shows some traffic sign instances that our method fail to recognize correctly. As shown in the figure, some images are seriously degenerate because of low resolution, motion blur, occlusion, and low illumination et al. and cannot be recognized easily even by human eyes.

4 Conclusion

In this paper, we introduce the low-rank matrix recovery model to exploit the correlation among images with similar appearances to enhance feature representation. By recovering a low-rank matrix from the original feature matrix that consists of feature vectors of image sequences, we are able to to exploit the correlation among images with similar appearances, which is neglected by most of the existing methods, and to attenuate the influence of corruptions, such as noise and motion blur. We evaluate our methods on GTSRB dataset, and observed noticeable performance gain by using low-rank matrix recovered from original HOG feature representation. Moreover, we obtain very impressive results on several super-class accuracy while get comparable performance with state-of-the-art results of global accuracy.

Acknowledgments This work was jointly supported by the National Key Project for Basic Research of China (Grant No: 2013CB329403), the National Natural Science Foundation of China (Grants No.90820304, 61075027, 91120011), the Tsinghua Self-innovation Project (Grant No:20111081111), and the Tsinghua National Laboratory for Information Science and Technology (TNList) Cross-discipline Foundation (No. 042003023).

References

1. Paclik P (1999) Road sign recognition survey. http://euler.fd.cvut.cz/research/rs2/files/skoda-rs-survey.html
2. Kardkovacs ZT, Paroczi Z, Varga E, Siegler A, Lucz P (2011) Real-time traffic sign recognition system. In: proceedings of second international conference on cognitive infocommunications(CogInfoCom), pp 1–5
3. Maldonado-Bascon S, Lafuente-Arroyo S, Gil-Jimenez P, Gomez-Moreno H, Lopez-Ferreras F (2007) Road-sign detection and recognition based on support vector machines. IEEE Trans Intell Trans Syst 8(2):264–278
4. Ruta A, Li Y, Liu X (2010) Robust class similarity measure for traffic sign recognition. IEEE Trans Intell Trans Syst 11(4):846–855

5. Stallkamp J, Schlipsing M, Salmen J, Igel C, Man versus computer: benchmarking machine learning algorithms for traffic sign recognition. Neural Netw (in press)
6. Ciresan D, Meier U, Mascim J, Schmidhuber J (2011) A committee of neural networks for traffic sign classification. In: Proceedings of international joint conference on neural networks (IJCNN), pp 1918–1921
7. Sermanet P, LeCun Y (2011) Traffic sign recognition with multi-scale convolutional networks. In: Proceedings of the international joint conferece on neural networks (IJCNN), pp 2809–2813
8. Zaklouta F, Stanciulescu B, Hamdoun O (2011) Traffic sign classification using k-d trees and random forests. In: Proceedings of the international joint conference on neural networks (IJCNN), pp 2151–2155
9. Bahlmann C, Zhu Y, Ramesh V, Pellkofer M, Koehler T (2005) A system for traffic sign detection, tracking, and recognition using color, shape, and motion information. In: Proceedings of IEEE intelligent vehicles symposium, pp 255–260
10. Ruta A, Li Y, Liu X (2008) Detection, tracking and recognition of traffic signs from video input. In: Proceedings of international IEEE conference on intelligent transportation systems, School of Information Systems, pp 55–60
11. Ruta A, Li Y, Liu X (2010) Real-time traffic sign recognition from video by class-specific discriminative features. Pattern Recognit 43(1):416–430
12. Moutarde F, Bargeton A, Herbin A, Chanussot L (2007) Robust on-vehicle real-time visual detection of American and European speed limit signs, with a modular traffic signs recognition system. In: Proceedings of IEEE intelligent vehicles symposium, pp 1122–1126
13. Lafuente-Arroyo S, Maldonado-Bascon S, Gil-Jimenez P, Acevedo-Rodriguez J, Lopez-Sastre RJ (2007) A tracking system for automated inventory of road signs. In: Proceedings of the IEEE intelligent vehicles symposium, pp 166–171
14. Zhou X, Yang C, Yu W, Moving object detection by detecting contiguous outliers in the low-rank representation. IEEE Trans Pattern Anal Mach Intell (in press)
15. Cui X, Huang J, Zhang S, Metaxas D (2012) Background subtraction using low rank and group sparsity constraints. In: Proceedings of the European conference on computer vision (ECCV)
16. Shen X, Wu Y (2012) A unified approach to salient object detection via low rank matrix recovery. In: Proceedings of the computer vision and pattern recognition (CVPR)
17. Yan J, Zhu M, Liu H, Liu Y (2010) Visual saliency detection via sparsity pursuit. IEEE Signal Process Lett 17(8):739–742
18. Peng Y, Ganesh A, Wright J, Ma Y (2010) Robust alignment by sparse and low-rank decomposition for linearly correlated images. In: Proceedings of the computer vision and pattern recognition (CVPR)
19. Fazel M, Hindi H, Boyd SP (2001) A rank minimization heuristic with application to minimum order system approximation. In: Proceedings of the american control conference (ACC), pp 4734–4739
20. Candes E, Li X, Ma Y, Wright J (2011) Robust principal component analysis? J ACM 58:1–37
21. http://perception.csl.illinois.edu/matrix-rank/sample_code.html, 2012
22. Lin Z, Chen M, Ma Y (2009) The augmented lagrange multiplier method for exact recovery of corrupted low-rank matrices. Technical report, UIUC UILU-ENG-09-2215, arXiv:1009.5055
23. Fan RE, Chang KW, Hsieh CJ, Wang XR, Lin CJ (2008) LIBLINEAR: a library for large linear classification. J Mach Learn Res 9:1871–1874
24. Stallkamp J, Schlipsing M, Salmen J, Igel C (2011) The German traffic sign recognition benchmark: a multi-class classification competition. In: Proceedings of the international joint conference on neural networks (IJCNN), pp 1453–1460
25. Ciresan DC, Meier U, Gambardella LM, Schmidhuber J (2010) Deep, big, simple neural nets for handwritten digit recognition. Neural Comput 22:3207–3220

Locality-Constrained Linear Coding with Spatial Pyramid Matching for SAR Image Classification

Shanshan Zhang, Fuchun Sun and Huaping Liu

Abstract We propose a linear spatial pyramid matching using locality-constraint linear coding for SAR image classification based on MSTAR database. Recently, works have little consideration about targets' randomly distributed poses when applying sparse coding in coding scheme. We do the preprocessing of pose estimation to generate over-complete codebook and therefore reduce reconstruction error. SIFT descriptors extracted from images are projected into its local-coordinate system by Locality-constrained linear coding instead of sparse coding. Locality constraint ensures similar patches will share similar codes. The codes are then pooled within each sub-region partitioned according to spatial pyramid and concatenated to form the final feature vectors. We use max-pooling which is more salient and robust to local translation. With linear SVM classifier, the proposed approach achieves better performance than traditional ScSPM method.

Keywords SAR recognition · Locality-constrained linear coding · Spatial pyramid matching

1 Introduction

Synthetic Aperture Radar (SAR) systems play a significant role in many areas, especially in military defense, due to their all weather, 24 h a day, and high resolution capability. Research on automatic target recognition (ATR) using SAR sensors remains an active domain. In this paper, we propose a novel SAR ATR method based on the locality-constrained linear coding and spatial pyramid

S. Zhang (✉) · F. Sun · H. Liu
State Key Laboratory of Intelligent Technology and Systems, Department of Computer Science and Technology, Tsinghua University, Beijing, People's Republic of China
e-mail: zhangssthu@sina.com

F. Sun et al. (eds.), *Foundations and Practical Applications of Cognitive Systems and Information Processing*, Advances in Intelligent Systems and Computing 215,
DOI: 10.1007/978-3-642-37835-5_75,

matching, which yields good results on the moving and stationary target acquisition and recognition (MSTAR) standard public release database.

MSTAR standard database provides an opportunity to promote and access progress in SAR ATR development [1]. Targets in MSTAR standard database have randomly distributed poses ranging from 0° to 360°, which creates great challenge to recognition. Earlier days, one commonly used approach is the template-based method. The representative works were done by American Air Force Research Laboratory. In this approach, several templates around various angles are designed and the "best matching" class was selected after registering the given target across all stored templates. The drawback is obvious that the great amount of templates undermine computational efficiency. As classifiers prevail, researchers focus on applying popular classifiers, for example, SVM [2] and Adaboost [3], to solve SAR ATR problem. These feature-based methods outperform traditional template-based approaches and achieve robust results. It is believed that efficient features guarantee successful classification, therefore, a great amount of the literature has been devoted to investigate proper feature extraction, examples include 2-D DFT coefficients [3], PCA vectors [4], and pyramid representation [5]. There are two ways used to solve random pose problem, one is to find rotation-invariant features; the other is to preprocess images and rotate all targets to referent angle.

Enlightened by the principle of parsimony [6] and related work in face recognition [7], Thiagarajan uses sparse representation for automatic target classification in SAR images, aiming to avoid explicit pose estimation [8]. However, unlike the over complete dictionary used to represent test sample in John Wright's face recognition task, atoms in the dictionary based on MSTAR data are not sufficient due to limited amount of samples at certain range of poses. To some extent, it degrades to template-based method because only few training samples (one or two in some extreme cases) could be used to correctly represent test target.

Peter Knee applies sparse coding with spatial pyramid matching in SAR images [9]. Spatial pyramid matching, an improvement of BoF [10], locates features to specific zones to get spatial information and has made remarkable success [11]. By introducing sparse coding to replace vector quantization in coding process, Jianchao Yang proposes linear spatial pyramid matching, reducing the complexity of SVMs to O(n). Nonetheless, when the similar work is implemented on MSTAR database, the best recognition result occurs at pyramid level $= 1$ which infers that SPM has reduced to BoF. It is because the variety of poses hinders the effect of SPM. According to spatial information, targets from the same class differ in great extent due to the randomly distributed poses; therefore, there are not sufficient samples in codebook to represent the give target at certain pose. Besides, the author indicates that there is no benefit in the use of more than one sparse coefficient during encoding, which infers that, against the co-representation principle of Sc, the given target could only be represented by single basis.

In this paper, we preprocess targets to referent aspect of angle to get over complete dictionary. SIFT descriptors are extracted to represent SAR images. Noticing that locality is of equal importance as sparsity [12], We apply Locality-constrained Linear Coding (LLC) to address locality constraint in coding scheme.

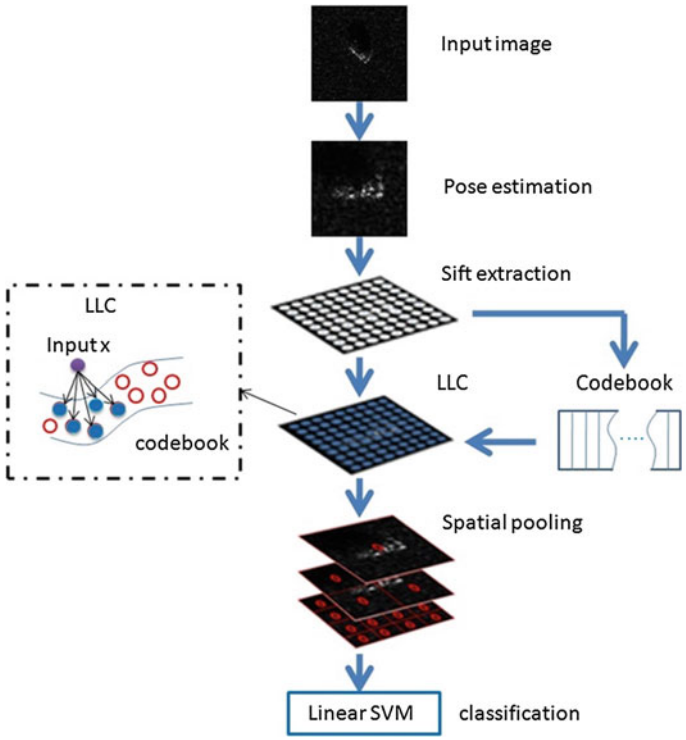

Fig. 1 *Left* a model of LLC coding scheme which selects basis similar to input descriptor. *Right* flowchart of locality-constrained linear coding with spatial pyramid matching

The codes are then processed by spatial pyramid matching with max-pooling. The final feature vectors are the concatenation of vectors from each spatial layer and feed to a linear SVM classifier. The flowchart is illustrated in Fig. 1.

The remainder of the paper is organized as follows: Sect. 2 depicts the preprocessing of MSTAR data; Sect. 3 introduces LLC algorithm and its usage in SAR image classification; Sect. 4 presents the construct of features vector by spatial pyramid matching and max-pooling. In Sect. 5, we will validate our approach by experiment on MSTAR data. Conclusion and further discussion will be presented in Sect. 6.

2 Data Preprocessing

We extract SIFT descriptors to represent SAR image. Although SIFT features are invariant to scale, orientation and affine distortion, they are located to particular sub-region in spatial pyramid matching algorithm. It loses the rotate-invariance. Therefore, the pose estimation is crucial. We first estimate targets' angle and rotate them to referent aspect angle.

2.1 Pose Estimation

We assume target's contour to be rectangle and thus its angle is determined by the longest edge. It is hard to detect edges in SAR image, different from optical image which have clear edge information, hence a series of preprocessing is necessary. We first segment targets from noisy background and then detect longest edge to receive its angle. Specific steps are shown in Fig. 2.

Step 1: Intensity equalization

Because SAR images differ from chip to chip, we equalize the intensity to 0–1 by standard histogram equalization method. By employing a monotonic, nonlinear mapping, this method modifies the dynamic range and contrast of an image and therefore uniform outputs images' distribution of intensities.

Step 2: Smoothing

We apply a mean filter to intensity equalized images to reduce noises.

Step 3: Rough segmentation

Segment the targets by a predefined threshold and thus get images containing pixels larger than threshold only.

Step 4: Fine segmentation

To enhance the segmentation precision, we apply fine segmentation to the targets from roughly partition. Here, two types of approach could be applied. (a) morphology method: it is an effective way to explore targets contour information. Noises in background could be eliminated by opening and closing operation, while targets inner parts could be connected to guarantee the integration. (b) threshold segmentation: calculate the median pixel in targets after Step 3 as the fine segmentation threshold. The median is more appropriate to be the threshold than the mean because the latter one could easily be affected by some extremely high pixels which in many cases are noises.

Step 5: Edge detection and longest edge extraction

Detect edge by Prewitt edge operator. Next, extract target edges by Hough transform method, find the longest edge and compute its relative angle to X-axis which denotes the target pose.

An example of intermediate results shows in Fig. 3. The second line depicts the results of applying morphological operation as fine segmentation, while the third line shows the results of applying threshold segmentation in fine segmentation step. The latter one gives more accurate results, hence, this method was chosen as fine segmentation. We compare the pose estimation with manually estimation

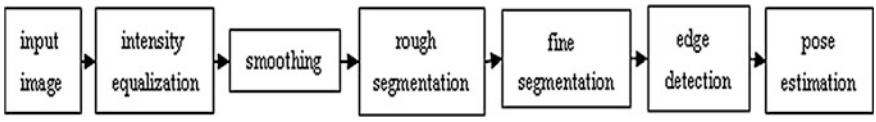

Fig. 2 Flowchart of edge detection

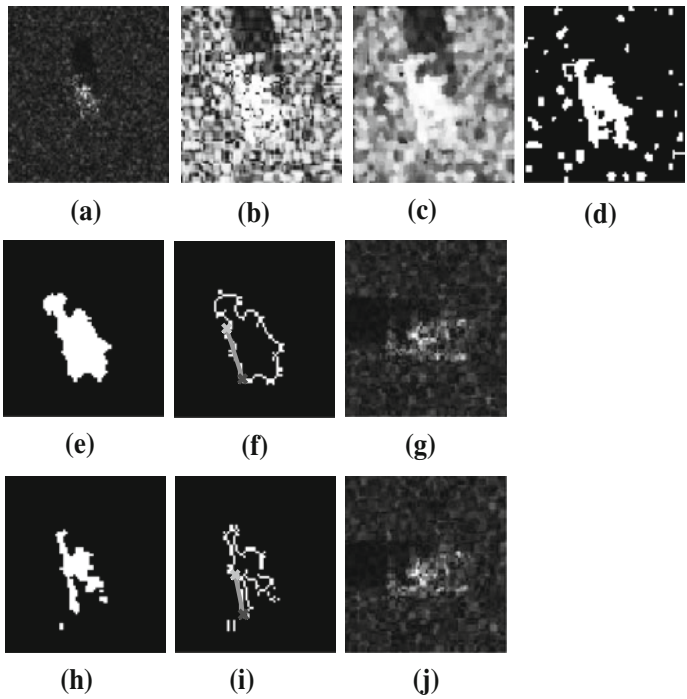

Fig. 3 An example of intermediate results. **a** Original image. **b** Histogram equalization. **c** Mean filter. **d** Roughly segmented. **e** Morphological operation. **f** Edge detection. **g** Rotated result. **h** Fine segment. **i** Edge detection2. **j** Rotated result2

result. The mean of the error is 2.38° with the standard deviation of 7.06°. Finally, all targets are rotated to referent pose of 180°. Because no information about target head is provided, therefore, there is 180° uncertainty remained in our estimation procedure. That is to say, we cannot distinguish heading north with heading west.

2.2 Local Image Features

Unlike traditional scale-invariant feature transform, we do not detect interest points, instead, we place a dense regular grid on images to compute inside SIFT descriptors. Specifically, 16×16 pixel patches computed over a grid with spacing of six pixels are extracted and account for one SIFT descriptor. K-means clustering are performed to form codebook from a random subset of patches in training set. Typical codebook sizes for our experiments are $M = 100$, $M = 200$, $M = 400$.

3 Code Generation by Locality-Constrained Linear Coding

The aim of code generation is finding a proper way to represent the extracted features, in this paper, SIFT descriptors. Let $X = [x_1, x_2, \ldots, x_N] \in R^{D\times N}$ be a set of D-dimensional SIFT descriptors, $B = [b_1, b_2, \ldots, b_M] \in R^{D\times M}$ be a M-entry codebook generated from K-means clustering algorithm. Different image representation could be generated by different coding schemes. Specifically, vector quantization (VQ) method was prevalent before the development of sparse coding, and recently locality principle attracts more attention which brings LLC algorithm into hotspot. We introduce briefly in this section about these three kinds of coding scheme and explain the reason to choose LLC in our approach.

3.1 Coding Descriptors in VQ

In VQ, each descriptor is exclusively assigned to one prototype generated by K-means clustering from training data. In another words, it solves the following constrained least square fitting problem:

$$\arg\min_{C} \sum_{i=1}^{N} ||x_i - Bc_i||^2 \tag{1}$$

$$s.t.\ ||c_i||_{l_0} = 1, ||c_i||_{l_1} = 1,\ c_i \geq 0, \forall i$$

where $C = [c_1, c_2, \ldots, c_M] \in R^{M\times N}$ is the codes for X. $||c_i||_{l_0} = 1$ means there could be only one non-zero element in each code c_i and x_i could be represented exclusively by this prototype. One common implementation is to find the nearest neighbor.

However, it will bring a great amount of quantization errors which hinder the accurate classification. Besides, computational complexity is increased because non-linear kernel projection is required in classification step.

3.2 Coding Descriptors in SC

In order to conquer the problem of quantization loss of VQ, sparse representation theory, aiming to approximate a target using a linear combination of elements from a sufficient large collection, is applied in coding scheme.

$$\arg\min_{C} \sum_{i=1}^{N} ||x_i - Bc_i||^2 + \lambda||c_i||_{l_1} \tag{2}$$

The restriction of $||c_i||_{l_0} = 1$ in (1) is relaxed by using a sparsity regularization term. The problem transforms to find the best co-representation of given target through minimizing the l_1 norm of C. Thus, the test sample could be more accurate represented because the relationships between different bases are considered. Accordingly, linear SVM classifier suffices the requirement.

Nevertheless, the drawback of Sc is obvious that the regulation term of l_1 norm is not smooth. In another word, this sparsity-prior method may select quite different bases for similar patches.

3.3 Coding Descriptors in LLC

Locality should be taken greater attention than sparsity when considering the representation of given targets [13]. LLC implement such principle by adding a locality constraint to criteria (2):

$$\begin{aligned} &\arg\min_{C} \sum_{i=1}^{N} ||x_i - Bc_i||^2 + \lambda ||d_i \odot c_i||^2 \\ &s.t. 1^T c_i = 1, \forall i \end{aligned} \tag{3}$$

$$d_i = \exp\left(\frac{\text{dist}(x_i, B)}{\sigma}\right)$$

where $\odot$ denotes the element multiplication, $d_i \in R^M$ is the locality adaptor which assess the similarity distance between base elements and input descriptor. $\text{dist}(x_i, B)$ is the Euclidean distance between x_i and b_j. $\text{dist}(x_i,\ B) = [\text{dist}(x_i,\ b_1),\ \ldots,\ \text{dist}(x_i,\ b_M)]^T$. Parameter σ adjusts weight decay speed. Small coefficients below the threshold are forced to be zero in real practice.

Similar to Sc, LLC has better reconstruction ability than VQ by selecting multi-elements in dictionary. The introducing of locality adaptor guarantees the elements captured are nearest and most similar to the given target, thus ensure the accurate representation. As proved in [12], LLC algorithm is very fast.

4 Spatial Pooling

As each descriptor is represented by a M-dimensional vectors, the next step is aggregating them together to form the final feature vector. We use special pyramid scheme and max-pooling to concatenate all the descriptors.

4.1 Spatial Pyramid Matching

In the original BoF method, the final feature vectors of images are orderless collection of local features. However, each descriptor contains significant spatial information, its coordinates in the respective image, which is discarded. It is believed that the full use of such information could enhance classification result. The SPM method partitions an image into several segments in different scales. $2^l \times 2^l$ grids are placed over images (l denotes the pyramid level). It is obvious that features extracted from finer level provide more precise spatial information. Hence, the weight associated to level l is set to be $\frac{1}{2^{L-l}}$, inversely proportional to cell width at that level to encourage features found at smaller cells. Let $z_l \in R^M$ depicts the vector of level l after pooled by certain algorithm, in this paper which refer to max-pooling. The final representation V of given image is a long vector formed by concatenating of weighted z_l from all levels, $V = \left[\frac{1}{2^L} z_0, \ldots, z_L\right] \in R^M \sum_{l=0}^{L} 4^l$.

4.2 Max-Pooling

Let $C \in R^{N \times M}$ be the representation of descriptors in a set X after LLC, where N denotes the number of SIFT descriptors in one grid of level l. Different pooling functions $z = F(C)$ yield different image statistics. We choose max-pooling function.

$z_j = \max\{|c_{1j}|, |c_{2j}|, \ldots, |c_{Nj}|\}$ where z_j is the jth element of z, c_{ij} is the element at ith row and jth column in C. It is proved that max-pooling method could form more salient and robust statistics.

5 Experimental Results

In this section, we report results based on MSTAR standard SAR image database including three types of vehicles, namely, BMP2, BTR70, and T72. We choose the same training data and testing data as those used in [9], illustrated specifically in Table 1. Training data is formed by the collection of single variant of each target type at 17° depression angle while testing data by all variants for each target type at 15° depression angle. In preprocessing step, all targets are rotated automatically to the referent angle of 180°. Then, 128-dimensional SIFT descriptors are extracted from 16 × 16 patches and encoded by LLC processing, the number of neighbors is set to 5. In the SPM step, the codes of each sub-region are pooled together to form features for corresponding layer and concatenated to get final image representation. Max-pooling function is used. Spatial pyramid is set to

Table 1 Training and testing data

Training			Testing		
BMP2 (SN_9653)	BTR70	T72 (SN_132)	BMP2	BTR70	T72
233	233	232	587	196	582

3-level. The dictionary used in code generation is formed by k-means clustering. A linear SVM is used to get SVM classifier.

To validate the effect of pose estimation preprocessing, we do experiment with two methods:

1. ScSPM: the original SPM with sparse coding, the same as the work proposed in [9];
2. ScSPM2: add the preprocessing of pose estimation to ScSPM.

We set the entry of codebook to be $M = 200$. The recognition rate of ScSPM2 is 82.10 %, which remarkably outperforms the result of ScSPM (67.84 %).

Due to the different setting of specific parameters, we do not achieve the result proposed in [9]. However, we could compare our method to ScSPM based on results in [9]. The entries of codebook are set to $M = 100$, $M = 200$, and $M = 400$. Classification results are showed in Table 2. We create a 3-level pyramid with grids of 1×1, 2×2, 4×4 at each layer, while [9] do experiment on 1-level, 5-level, and 10-level, the best results of ScSPM are selected with its pyramid level denoted in the parenthesis.

The proposed method performs better than ScSPM approach. The pose estimation preprocessing enhances the representation ability in coding step. As mentioned before, earlier work of ScSPM does not take the pose variation into consideration which leads to great reconstruction error because samples at certain scope are not sufficient to reconstruct the given target with given pose. Our approach ameliorates the problem by rotating all images automatically to referent angle. Though the accuracy is not 100 %, it fulfills the task to provide abundant samples to represent given target. Besides, we highlight the locality in coding scheme by introducing locality constraint in LLC method. The locality adaptor guarantees that similar patches will have similar codes and enhances classification accuracy.

Table 2 Classification results

	M = 100	M = 200	M = 400
ScSPM	78.32 %(L = 5)	80.29 %(L = 1)	81.54 %(L = 1)
LLC (%)	86.00	87.70	88.66

6 Conclusion

In this paper, we propose a LLC-SPM approach with pose preprocessing for SAR image classification. All targets are rotated to referent angle to provide adequate samples in codebook and therefore the reconstruction errors are reduced in coding layer. We improve the traditional sparse coding step by applying locality-constraint linear coding which adds locality constraint to select similar bases in codebook. Experiment results based on MSTAR database outperform the result of ScSPM.

The future work includes the following issue: first, better code generation algorithms remain to be investigated; second, other pyramid partition method could be attempted, such as circle instead of grid considering target rotation of SAR images.

References

1. Ross T, Worrell S, Velten V, Mossing J, Bryant M (1998) Standard SAR ATR evaluation experiments using the MSTAR public release data set. In: Proceedings of SPIE, algorithms for synthetic aperture radar imagery V, vol 3370. Orlando, FL, pp 566–573
2. Bryant M, Garber F (1999) SVM classifier applied to the MSTAR public data set. In: Proceedings of SPIE, algorithms for synthetic aperture radar imagery VI, vol 3721. Orlando, FL, pp 355–360
3. Sun Y, Liu Z, Todorovic S, Li J (2007) Adaptive boosting for SAR automatic target recognition. IEEE Trans Aerosp Electron Syst 43:1
4. Wei G, Qi Q, Jiang L, Zhang P (2008) A new method of SAR image target recognition based on adaboost algorithm. In: Geoscience and remote sensing symposium
5. Yin H, Cao Y, Sun H (2011) Combining pyramid representation and AdaBoost for urban scene classification using high-resolution synthetic aperture radar images. IET Radar Sonar Navig 5(1):58–64
6. Cande‘s E (2006) Compressive sampling. In: Proceedings of the international congress of mathematicians, Madrid, Spain, pp 1433–1452
7. Wright J, Yang AY, Ganesh A, Sastry SS, Ma Y (2009) Robust face recognition via sparse representation. IEEE Trans Pattern Anal Mach Intell 31(2):210–227
8. Thiagarajan JJ, Ramamurthy KN, Knee P, Spanias A, Berisha V (2010) Sparse representations for automatic target classification in SAR images. In: Proceedings of IEEE 4th international symposium on communications, control and signal processing (ISCCSP), pp 1–4
9. Knee P, Thiagarajan JJ, Ramamurthy KN, Spanias A (2011) SAR target classification using sparse representations and spatial pyramids. In: Radar conference (RADAR), pp 294–298
10. Lazebnik S, Schmid C, Ponce J (2006) Beyond bags of features: spatial pyramid matching for recognizing natural scene categories. In: Proceedings of CVPR’06, vol 2, New York, pp 2169–21785
11. Yang J, Yu K, Gong Y, Huang T (2009) Linear spatial pyramid matching using sparse coding for image classification. In: Proceedings of IEEE conference on computer vision and pattern recognition, CVPR, pp 1794–1801
12. Wang J, Yang J, Yu K, Lv F, Huang T, Gong Y (2010) Locality-constrained linear coding for image classification. 2010 IEEE conference on computer vision and pattern recognition
13. Yu K, Zhang T, Gong Y. (2009) Nonlinear learning using local coordinate coding. In: Advances in neural information processing systems, vol 22, pp 2223–2231

Quantitative Evaluation of Interictal High Frequency Oscillations in Scalp EEGs for Epileptogenic Region Localization

Yaozhang Pan, Cuntai Guan, How-Lung Eng, Shuzhi Sam Ge, Yen Ling Ng and Derrick Wei Shih Chan

Abstract Electroencephalography is a commonly used tool for presurgical evaluation of epilepsy patients. In this paper, we present a quantitative evaluation of interictal high frequency oscillations (HFOs) in scalp Electroencephalographies (EEGs) for epileptogenic region localization. We process multichannel EEGs using time–frequency spectral analysis in order to detect HFOs in each EEG channel. Comparison between the results of time–frequency analysis and visual assessment is performed to verify the reliability of time–frequency analysis. Later, *t*-test and Pearson correlation analysis are performed to analyze the relationships between ictal HFOs and interictal HFOs. The high correlations between interictal and ictal HFOs imply that interictal HFOs, like ictal HFOs, are valuable in

Y. Pan (✉) · C. Guan · H.-L. Eng
Institute for Infocomm Research, Agency for Science, Technology and Research (ASTAR), 1 Fusionopolis Way, #21-01 Connexis, Singapore 138632, Singapore
e-mail: yzpan@i2r.a-star.edu.sg

C. Guan
e-mail: ctguan@i2r.a-star.edu.sg

H.-L. Eng
e-mail: hleng@i2r.a-star.edu.sg

S. S. Ge
Department of Electrical and Computer Engineering, National University of Singapore, Singapore 117576, Singapore
e-mail: samge@nus.edu.sg

S. S. Ge
The Robotics Institute and School of Computer Science and Engineering, University of Electronic Science and Technology of China, Chengdu 11813, China

Y. L. Ng · D. W. S. Chan
KK Women's and Children's Hospital, 100 Bukit Timah Road, Singapore 229899, Singapore
e-mail: Derrick.Chan.WS@kkh.com.sg

D. W. S. Chan
e-mail: Ng.Yen.Ling@kkh.com.sg

F. Sun et al. (eds.), *Foundations and Practical Applications of Cognitive Systems and Information Processing*, Advances in Intelligent Systems and Computing 215,
DOI: 10.1007/978-3-642-37835-5_76,

localizing the epileptogenic region. As a result, scalp interictal HFOs are valuable in epileptogenic region localization for presurgical evaluation of epilepsy patients. It holds great potential for reducing the long delay before patients can be referred for surgery.

Keywords High frequency oscillations · Scalp EEGs · Epileptogenic region localization

1 Introduction

Epilepsy is a common neurologic disorder affecting more than 1 % of the world population. Although antiepileptic drug (AED) is the most popular treatment of epilepsy, 40 % of epilepsy patients are pharmacoresistant. For these patients with pharmacoresistant seizures, surgery is a highly effective treatment instead of AED. However, a successful epilepsy surgery necessitates the accurate delineation of the epileptogenic region. Reliable biomarkers are needed to identify potential surgical candidates and localize the epileptogenic regions as early as possible after AED fails. A commonly used biomarker is the interictal EEG spike, which however is not reliable for localizing the extent of an epileptogenic region because it is difficult to differentiate two types of interictal epileptic discharges: those originating from the ictal onset zone; and those propagated from other regions or irritative regions [5, 10].

High frequency oscillations (HFOs) are oscillatory activities on EEG above 25 Hz. HFOs can be subgrouped into gamma waves, ripples and fast ripples, etc. A gamma wave is a pattern of neural oscillation in humans with a frequency range between 25 and 100 Hz, though 40 Hz is prototypical. Ripple is HFO in the 80–200 Hz range, reflecting inhibitory field potentials, which synchronize neuronal activity [3]. HFOs of 250–600 Hz, which are referred to as fast ripples (FRs), are pathologic signals reflecting summated action potentials of spontaneously bursting neurons [3].

Clinical studies using direct brain recordings during presurgical evaluation have found ripples and FRs to be valuable in identifying the epileptogenic region [2, 3]. It has also been shown in [5, 10] that HFOs, with or without interictal spikes, are more reliable in identifying epileptogenic region than interictal spikes alone and even more reliable than ictal onset in determining the extent of brain tissue that must be resected.

HFOs in patients with focal epilepsies have been reported with ECoG recordings [9, 10]. In [6], HFOs' changes have been extracted based on a simple statistics of time–frequency representation. In [8], a reviewer-dependent approach for detection of HFOs has been proposed. In [4], HFOs have been detected using swarmed neural-network features.

Till recently, HFOs analysis has been confined to ECoG, which has limited its utility as a biomarker. Analysis of scalp EEG has demonstrated possibility to detect HFOs from scalp EEGs [1, 7]. In [1], Andrade-Valenca et al. have studied scalp EEGs recordings of 15 patients with focal epilepsy, and analyzed the rates of gamma waves (40–80 Hz) and ripples ($> 80\,Hz$) by visually rating the number of spikes, gamma waves, and ripples per minute for each channel of scalp EEGs. However, inspecting the bulky multichannel EEG data visually is very tedious and time-consuming. In another work [7], HFOs in scalp EEGs recorded during slow-wave sleep (CSWS) have been investigated through visual analysis as well as time–frequency spectral analysis. However, the reliability of using the scalp EEG to identify the epileptogenic region is still an open question.

In this paper, we present a quantitative evaluation of HFOs in scalp EEGs in localizing epileptogenic region. Following [7], the quantitative analysis is based on a time–frequency spectral analysis of scalp EEGs recorded from 6 epilepsy patients. Comparison between the results of time–frequency analysis and visual assessment is performed to verify the reliability of time–frequency analysis. Furthermore, we use paired t-test and Pearson correlation analysis to look for relationships between the frequency-power characteristics of ictal and interictal HFOs. The results of t-test demonstrate significant differences between ictal and interictal HFOs in both values of peak frequency and corresponding power. This fact implies that the HFOs can be valuable for differentiating the ictal and interictal states. The Pearson correlation analysis shows high correlations between ictal and interictal HFOs. The high correlations imply that interictal HFOs, similar to ictal HFOs, hold potential in localizing the epileptogenic region.

Our results demonstrate the potential of using interictal HFOs of scalp EEGs as a biomarker of noninvasive localization of the epileptogenic region. The HFOs in interictal EEG are quite promising for detecting the epileptogenic region once it is proved to be reliable. The interictal EEGs have many advantages in localizing the epileptogenic region compare to ictal EEGs. They have less muscle artifacts. Moreover, they make it possible to diagnose epilepsy without waiting subsequent seizures and long-term presurgical evaluation. Thus, the findings in this paper would help to justify earlier surgical treatment and thereby reduce the long delay before patients are referred for surgery [2].

2 Methods

2.1 EEGs Recording

The EEGs recording was conducted at the KK Women's and Children's Hospital (KKH), Singapore. We recruited those pediatric epileptic patients with informed consent obtained from their guardians. The patients were subject to the standard video-EEG monitoring in the epilepsy monitoring unit (EMU) of KKH. Long-term

Table 1 Selected patients and patient characteristics

Patient no.	Age^a	N_s^b	Diagnosis
P003	12	3	Lennox Gastaut syndrome
P004	9	13	Right temporal lobe focal
P006	9	10	Right frontal lobe focal
P023	8	2	Left fronto-central focal
P025	5	10	Right fronto-central-vertex focal
P027	11	6	Left frontal lobe focal

[a] *The* age here is refer to age of screening
[b] N_s is total number of seizures of one patient

EEGs were recorded by 32 electrodes placed on scalp according to the international 10–20 system. All data were stored on a hard disk with 256 or 512 sampling rate.

The subjects recruited so far are 27 patients with diagnosis of different types of seizures. We focus only on focal seizure in this study. After careful assessment by the EEG technologist, six epileptic patients aged between 5 and 12 years (three male, three female) are selected for this analytic work with 44 seizure events and frequently occurred HFOs in both ictal and interictal states. The related information of the patients are listed in Table 1.

2.2 Visual Assessment of EEGs

Each patient's EEGs are assessed visually. Seizure events are identified from the standard video-EEG system by a EEG technologist. EEGs are marked as ictal or interictal periods. In addition, some of the visible HFOs are also marked. The conventional EEG traces (10 s per page) are initially reviewed to identify the ictal events, as shown in Figs. 1a and 2a. Then, the traces are temporally expanded to 2 s per page in order to study the details of activity faster than 25 Hz (see Figs. 1b and 2b).

In interictal period, the HFOs are relatively clear, as shown in Fig. 2. But due to the large amount of artifacts during ictal state, the HFOs cannot be found easily by visual checking as in Fig. 1. We need to extract HFOs from EEG back ground noises in order to further study HFOs in epileptic EEGs.

2.3 Time–Frequency Analysis

We investigate the time evolution of the high-frequency power spectrum of the ictal and interictal activity by applying the Gabor transform, which is the Fourier transform with a sliding Gaussian window. For EEGs with 256 Hz sampling rate,

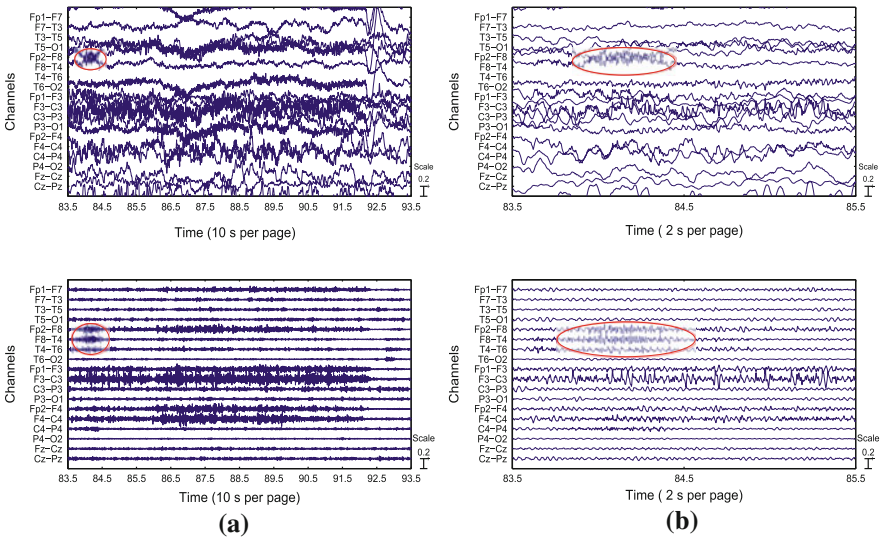

Fig. 1 Ictal EEGs of P025 (sampling rate 512 Hz): the *above row* is after 0.5–198 Hz bandpass filtering, the *below row* is after 20–198 Hz bandpass filtering **a** P025 ictal EEGs with 10 s window. **b** P025 ictal EEGs with 2 s window

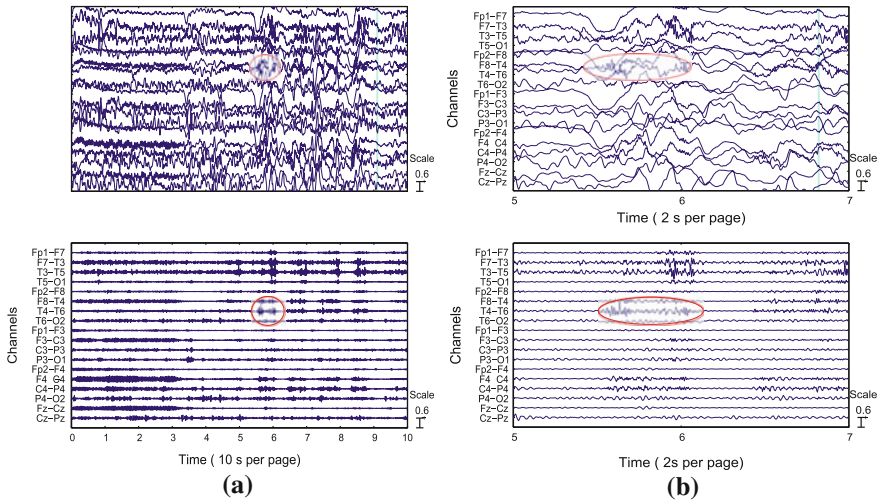

Fig. 2 Interictal EEGs of P006 (sampling rate 256 Hz): the *above row* is after 0.5–98 Hz bandpass filtering, the *below row* is after 20–98 Hz bandpass filtering **a** P006 interictal EEGs with 10 s window. **b** P006 interictal EEGs with 2 s window

we apply Fourier transform with a 500 ms wide Gaussian window (contains 128 data points, the frequency resolution is 2 Hz) and 10–100 Hz frequency range to the raw EEG data. For EEGs with 512 Hz sampling rate, we apply Fourier

transform with a 250 ms wide Gaussian window (contains 128 data points, the frequency resolution is 4 Hz) and 10–200 Hz frequency range. All computations are performed using a program written in-house for MATLAB 2010a (MathWorks Inc., Natick, MA).

3 Results

3.1 Comparison of Time–Frequency Analysis and Visual Assessment

A typical example of ictal EEGs which contains HFOs is shown in Fig. 1, and a typical example of interictal EEGs containing HFOs is shown in Fig. 2. We show the signal with both 10 and 2 s window respectively. Red circles in the figures are used to mark out the visually inspected HFOs.

For the HFOs marked in Fig. 1, we plot the spectrograms of the corresponding channels: Fp2-F8, F8-T4, T4-T6, as shown in Fig. 3.

For the HFOs marked in Fig. 2, we plot the spectrograms of the corresponding channels: Fp2-F8, F8-T4, T4-T6, as shown in Fig. 4.

HFOs are identified as clearly visible red spectral spots with frequencies faster than 20 Hz that are surrounded by an area of low power. From Figs. 3 and 4, we can find the clear red spots at the same time points of visually marked red circles in Figs. 1 and 2. This indicates that time–frequency analysis obtains reliable results as visual assessment.

3.2 Relationship of Ictal HFOs and Interictal HFOs

We compare the frequencies and power values of the HFO peaks in the spectrograms of interictal period with those of ictal period. For each event (a period of ictal HFOs or interictal HFOs, according to one spectrogram), we pick the point

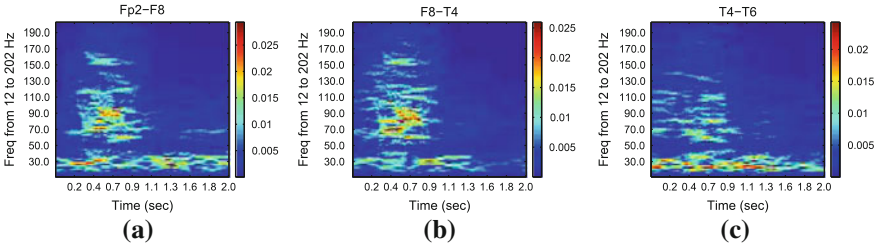

Fig. 3 Time–frequency spectrograms of EEGs in ictal state of P025, with sampling rate of 512 Hz and bandpass filtering of 20–198 Hz **a** Fp2-F8, **b** F8-T4, and **c** T4-T6

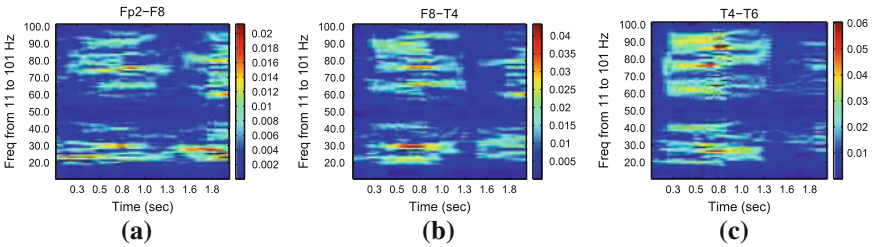

Fig. 4 Time–frequency spectrograms of EEGs in interictal state of P006, with sampling rate of 256 Hz and bandpass filtering of 20–98 Hz **a** Fp2-F8, **b** F8-T4, and **c** T4-T6

Table 2 EEG observations and their associated HFOs: ictal and interictal

Patient id	N_i	N_{in}	Ictal channels involved	Interictal channels involved	Ictal (frequency (Hz)/power)	Interictal (frequency (Hz)/power)
P003	3	3	F3-C3, F4-C4	F3-C3, F4-C4	103.81/2.92 e-2	85.14/1.78 e-2
P004	5	3	T4-T6	T4-T6	55.95/2.15 e-2	43.35/1.42 e-2
P006	12	3	T4-T6, F8-T6	Fp2-F8, F8-T4	79.60/3.12 e-2	65.88/2.06 e-2
P023	2	3	Fp1-F7, Fp1-F3	F7-T3, F3-C3	76.86/2.14 e-2	47.91/1.70 e-2
P025	2	4	Fp2-F8, F8-T4	F4-C4, Fz-Cz	74.28/1.77 e-2	33.27/1.16 e-2
P027	4	9	Fp1-F3	Fp1-F7, Fp1-F3	92.47/2.78 e-2	58.08/2.59 e-2

N_i is total number of ictal periods with HFOs analyzed for one patient
N_{in} is total number of interictal periods with HFOs analyzed for one patient
Paired t-test between highest frequencies during ictal and interictal periods obtains p-*value* $= 0.0328$, and that for corresponding power values is p-*value* $= 0.0423$
Pearson correlation coefficient for frequencies between ictal and interictal periods is $\gamma = 0.7808$ and that for power values is $\gamma = 0.7550$

with highest value in the spectrogram, and record the corresponding value (power) and frequency of that point. Then, for each patient with several events, we compute the average value of all events' power and frequency.

The average peak frequency and corresponding power value of ictal HFOs and interictal HFOs of each patient are shown in the sixth and seventh column of Table 2. The frequencies and powers of the total six patient are then analyzed using a paired t-test and Pearson correlation analysis between ictal HFOs and interictal HFOs.

For paired t-test, relationships are considered statistically significant if $p < 0.05$. From the result of Table 2, HFOs detected during ictal period have significantly higher frequencies ($p = 0.0328$) and more power ($p = 0.0423$) than those detected during interictal period. This provides us evidence that HFOs can be used to differentiate interictal and ictal state for seizure detection.

For Pearson correlation analysis, larger Pearson correlation coefficient (range between [0, 1]) implies higher correlation between two data sets. From the result of

Table 2, the Pearson correlation coefficients are computed. Results $\gamma = 0.7808$ for frequency and $\gamma = 0.7550$ for power are obtained, which indicates that the frequencies and powers in interictal HFOs and ictal HFOs are highly correlated.

We also demonstrate in Table 2 that the channels involved in ictal HFOs (column four) and interictal HFOs (column five) are similar, which indicates that HFOs largely remain in the same region during interictal and ictal periods.

4 Conclusion

In this paper, we presented a quantitative evaluation of interictal scalp EEG for Epileptogenic Region Localization. The analysis was based on time–frequency spectral analysis of scalp EEG recorded from six epilepsy patients. The results of time–frequency analysis and visual assessment were compared to verify reliability of the time–frequency analysis. A paired *t*-test of peak frequencies and powers between ictal HFOs and interictal HFOs demonstrated that ictal HFOs had significantly higher frequencies ($p = 0.0328$) and more power ($p = 0.0423$) than interictal HFOs. Pearson correlation analysis demonstrated high correlations ($\gamma = 0.7808$ for frequency and $\gamma = 0.7550$ for power) between ictal and interictal HFOs. In conclusion, scalp interictal HFOs could be considered as an effective biomarker in epileptogenic region localization. In further study, investigations based on larger dataset using more advanced methods are worth performing.

References

1. Andrade-Valenca LP, Dubeau F, Mari F, Zelmann R, Gotman J (2011) Interictal scalp fast oscillations as a marker of the seizure onset zone. Neurology 77:524–531
2. Cendes F, Engel J (2011) Extending applications for high-frequency oscillations. Neurology 77:518–519
3. Engel JJ, Bragin A, Staba R, Mody I (2009) High-frequency oscillations: what is normal and what is not? Epilepsia 50:598–604
4. Firpi H, Smart O, Worreli G, Marsh E, Dlugos D, Litt B (2007) High-frequency oscillations detected in epileptic networks using swarmed neural-network features. Ann Biomed Eng 35(9):1573–1584
5. Jacobs J, LeVan P, Chander R, Hall J, Dubeau F, Gotman J (2008) Interictal high-frequency oscillations (80–500 Hz) are an indicator of seizure onset areas independent of spikes in the human epileptic brain. Epilepsia 49:1893–1907
6. Kobayashi K, Jacobs J, Gotman J (2009) Detection of changes of high-frequency activity by statistical time–frequency analysis in epileptic spikes. Clin Neurophysiol 120:1070–1077
7. Kobayashi K, Watanabe Y, Inoue T, Oka M, Yoshinaga H, Ohtsuka Y (2010) Scalp-recorded high-frequency oscillations in childhood sleep-induced electrical status epilepticus. Epilepsia 51:2190–2194
8. Le Van Quyen M, Bragin A (2007) Analysis of dynamic brain oscillations: methodological advances. Trends Neurosci 30:365–373

9. Valderrama M, Quyen MV (2011) High-frequency oscillations and interictal spikes in partial epilepsy: joining the benefits. Clin Neurophysiol 122(1):3–4
10. Zijlmans M, Jacobs J, Kahn YU, Zelmann R, Dubeau F, Gotman J (2011) Ictal and interictal high frequency oscillations in patients with focal epilepsy. Clin Neurophysiol 122:664–671

Erratum to: A Cognitive-Heuristic Framework for Optimization of Spaceplane-System Configurations

Ali Sarosh, Yun-Feng Dong and Shi-Ming Chen

Erratum to:
Chapter 'A Cognitive-Heuristic Framework for Optimization of Spaceplane-System Configurations' in: F. Sun et al. (eds.), *Foundations and Practical Applications of Cognitive Systems and Information Processing*, DOI 10.1007/978-3-642-37835-5_42

In the original version, country name in the affiliation of the first author "Dr. Ali Sarosh" is unfortunately wrong. It should read as "Pakistan" instead of "China".

The online version of the original chapter can be found under DOI 10.1007/978-3-642-37835-5_42

A. Sarosh (✉)
Department of Aerospace Engineering, College of Aeronautical Engineering, National University of Sciences and Technology (NUST), PAF Academy Risalpur, 24080 KPK, Pakistan
e-mail: alisarosh@sa.buaa.edu.cn

Y.-F. Dong · S.-M. Chen
Department of Flight Vehicle Design, School of Astronautics, Beihang University (BUAA), 37 Xueyuan Road, Beijing 100191, China
e-mail: sinosat@buaa.edu.cn

S.-M. Chen
e-mail: csm7531@sa.buaa.edu.cn

F. Sun et al. (eds.), *Foundations and Practical Applications of Cognitive Systems and Information Processing*, Advances in Intelligent Systems and Computing 215,
DOI: 10.1007/978-3-642-37835-5_77,